Water Science and Technology Library

Vijay P. Singh
Shalini Yadav
Ram Narayan Yadava *Editors*

Hydrologic Modeling

Select Proceedings of ICWEES-2016

Springer

Water Science and Technology Library

Volume 81

The aim of the Water Science and Technology Library is to provide a forum for dissemination of the state-of-the-art of topics of current interest in the area of water science and technology. This is accomplished through publication of reference books and monographs, authored or edited. Occasionally also proceedings volumes are accepted for publication in the series.

Water Science and Technology Library encompasses a wide range of topics dealing with science as well as socio-economic aspects of water, environment, and ecology. Both the water quantity and quality issues are relevant and are embraced by Water Science and Technology Library. The emphasis may be on either the scientific content, or techniques of solution, or both. There is increasing emphasis these days on processes and Water Science and Technology Library is committed to promoting this emphasis by publishing books emphasizing scientific discussions of physical, chemical, and/or biological aspects of water resources. Likewise, current or emerging solution techniques receive high priority. Interdisciplinary coverage is encouraged. Case studies contributing to our knowledge of water science and technology are also embraced by the series. Innovative ideas and novel techniques are of particular interest.

Comments or suggestions for future volumes are welcomed.

Vijay P. Singh, Department of Biological and Agricultural Engineering & Zachry Department of Civil Engineering, Texas A&M University, USA
Email: vsingh@tamu.edu

More information about this series at http://www.springer.com/series/6689

Vijay P. Singh · Shalini Yadav
Ram Narayan Yadava
Editors

Hydrologic Modeling

Select Proceedings of ICWEES-2016

Springer

Editors
Vijay P. Singh
Department of Biological and Agricultural Engineering, and Zachry Department of Civil Engineering
Texas A&M University
College Station, TX
USA

Ram Narayan Yadava
AISECT University
Hazaribagh, Jharkhand
India

Shalini Yadav
Department of Civil Engineering
AISECT University
Bhopal, Madhya Pradesh
India

ISSN 0921-092X ISSN 1872-4663 (electronic)
Water Science and Technology Library
ISBN 978-981-10-5800-4 ISBN 978-981-10-5801-1 (eBook)
https://doi.org/10.1007/978-981-10-5801-1

Library of Congress Control Number: 2017947024

Printed on acid-free paper

This Springer imprint is published by Springer Nature
The registered company is Springer Nature Singapore Pte Ltd.
The registered company address is: 152 Beach Road, #21-01/04 Gateway East, Singapore 189721, Singapore

Preface

Fundamental to sustainable economic development, functioning of healthy ecosystems, reliable agricultural productivity, dependable power generation, maintenance of desirable environmental quality, continuing industrial growth, enjoyment of quality lifestyle, and renewal of land and air resources is water. With growing population, demands for water for agriculture and industry are skyrocketing. On the other hand, freshwater resources per capita are decreasing. There is therefore a need for effective water resources management strategies. These strategies must also consider the nexus between water, energy, environment, food, and society. With these considerations in mind, the International Conference on Water, Environment, Energy and Society (WEES-2016) was organized at AISECT University, Bhopal, Madhya Pradesh, India, from March 15 to 18, 2016. The conference was fifth in the series and had several objectives.

The first objective was to provide a forum to not only engineers, scientists, and researchers, but also practitioners, planners, managers, administrators, and policy makers from around the world for discussion of problems pertaining to water, environment, and energy that are vital for the sustenance and development of society.

Second, the Government of India has embarked upon two large projects one on cleaning of River Ganga and the other on cleaning River Yamuna. Further, it is allocating large funds for irrigation projects with the aim to bring sufficient good quality water to all farmers. These are huge ambitious projects and require consideration of all aspects of water, environment, and energy as well as society, including economics, culture, religion, politics, administration, law.

Third, when water resources projects are developed, it is important to ensure that these projects achieve their intended objectives without causing deleterious environmental consequences, such as waterlogging, salinization, loss of wetlands, sedimentation of reservoirs, loss of biodiversity.

Fourth, the combination of rising demand for water and increasing concern for environmental quality compels that water resources projects are planned, designed, executed, and managed, keeping changing conditions in mind, especially climate change and social and economic changes.

Fifth, water resources projects are investment-intensive, and it is therefore important to take a stock of how the built projects have fared and the lessons that can be learnt so that future projects are even better. This requires an open and frank discussion among all sectors and stakeholders.

Sixth, we wanted to reinforce that water, environment, energy, and society constitute a continuum and water is central to this continuum. Water resources projects are therefore inherently interdisciplinary and must be so dealt with.

Seventh, a conference like this offers an opportunity to renew old friendships and make new ones, exchange ideas and experiences, develop collaborations, and enrich ourselves both socially and intellectually. We have much to learn from each other.

Now the question may be: Why India and why Bhopal? India has had a long tradition of excellence spanning several millennia in the construction of water resources projects. Because of her vast size, high climatic variability encompassing six seasons, extreme landscape variability from flat plains to the highest mountains in the world, and large river systems, India offers a rich natural laboratory for water resources investigations.

India is a vast country, full of contrasts. She is diverse yet harmonious, mysterious yet charming, old yet beautiful, ancient yet modern. Nowhere can we find as high mountains as snowcapped Himalayas in the north, the confluence of three seas and large temples in the south, long and fine sand beaches in the east as well as architectural gems in the west. The entire country is dotted with unsurpassable monuments, temples, mosques, palaces, and forts and fortresses that offer a glimpse of India's past and present.

Bhopal is located in almost the center of India and is situated between Narmada River and Betwa River. It is a capital of Madhya Pradesh and has a rich, several century-long history. It is a fascinating amalgam of scenic beauty, old historic city, and modern urban planning. All things considered, the venue of the conference could not have been better.

We received an overwhelming response to our call for papers. The number of abstracts received exceeded 450. Each abstract was reviewed, and about two-thirds of them, deemed appropriate to the theme of the conference, were selected. This led to the submission of about 300 full-length papers. The subject matter of the papers was divided into more than 40 topics, encompassing virtually all major aspects of water and environment as well energy. Each topic comprised a number of contributed papers and in some cases state-of-the-art papers. These papers provided a natural blend to reflect a coherent body of knowledge on that topic.

The papers contained in this volume, "Hydrologic Modelling," represent one part of the conference proceedings. The other parts are embodied in six companion volumes entitled, "Energy and Environment," "Groundwater," "Environmental Pollution," "Water Quality Management," "Climate Change Impacts," and "Water Resources Management." Arrangement of contributions in these seven books was a natural consequence of the diversity of papers presented at the conference and the topics covered. These books can be treated almost independently, although significant interconnectedness exists among them.

This volume contains seven parts. The first part deals with some aspects of rainfall analysis, including rainfall probability distribution, local rainfall interception, and analysis for reservoir release. Part 2 is on evapotranspiration and discusses development of neural network models, errors, and sensitivity. Part 3 focuses on various aspects of urban runoff, including hydrologic impacts, storm water management, and drainage systems. Part 4 deals with soil erosion and sediment, covering mineralogical composition, geostatistical analysis, land use impacts, and land use mapping. Part 5 treats remote sensing and GIS applications to different hydrologic problems. Watershed runoff and floods are discussed in Part 6, encompassing hydraulic, experimental, and theoretical aspects. Water modeling constitutes the concluding Part 7. SWAT, Xinanjiang, and SCS-CN models are discussed.

The book will be of interest to researchers and practitioners in the field of water resources, hydrology, environmental resources, agricultural engineering, watershed management, earth sciences, as well as those engaged in natural resources planning and management. Graduate students and those wishing to conduct further research in water and environment and their development and management may find the book to be of value.

WEES-16 attracted a large number of nationally and internationally well-known people who have long been at the forefront of environmental and water resources education, research, teaching, planning, development, management, and practice. It is hoped that long and productive personal associations and friendships will be developed as a result of this conference.

College Station, USA — Vijay P. Singh, Conference Chair

Bhopal, India — Shalini Yadav, Conference Organizing Secretary

Hazaribagh, India — Ram Narayan Yadava, Conference Co-Chair

Sponsors and Co-Sponsors

The International Conference on Water, Environment, Energy and Society was jointly organized by the AISECT University, Bhopal (M.P.), India, and Texas A&M University, Texas, USA, in association with ICE WaRM, Adelaide, Australia. It was partially supported by the International Atomic Energy Agency (IAEA), Vienna, Austria; AISECT University, Bhopal; M.P. Council of Science and Technology (MPCOST); Environmental Planning and Coordination Organization (EPCO), Government of Madhya Pradesh; National Bank for Agriculture and Rural Development (NABARD), Mumbai; Maulana Azad National Institute of Technology (MANIT), Bhopal; and National Thermal Power Corporation (NTPC), Noida, India. We are grateful to all these sponsors for their cooperation and providing partial financial support that led to the grand success to the ICWEES-2016.

Acknowledgements

We express our sincere gratitude to Shri Santosh Choubey, Chancellor, and Dr. V. K. Verma, Vice Chancellor, Board of Governing Body, and Board of Management of the AISECT University, Bhopal, India, for providing their continuous guidance and full organizational support in successfully organizing this International Conference on Water, Environment, Energy and Society on the AISECT University campus in Bhopal, India.

We are also grateful to the Department of Biological and Agricultural Engineering and Zachry Department of Civil Engineering, Texas A&M University, College Station, Texas, USA, and International Centre of Excellence in Water Management (ICE WaRM), Australia, for their institutional cooperation and support in organizing the ICWEES-2016.

We wish to take this opportunity to express our sincere appreciation to all the members of the Local Organization Committee for helping with transportation, lodging, food, and a whole host of other logistics. We must express our appreciation to the Members of Advisory Committee, Members of the National and International Technical Committees for sharing their pearls of wisdom with us during the course of the conference.

Numerous other people contributed to the conference in one way or another, and lack of space does not allow us to list all of them here. We are also immensely grateful to all the invited keynote speakers and directors/heads of institutions for supporting and permitting research scholars, scientists and faculty members from their organizations for delivering keynote lectures and participating in the conference, submitting and presenting technical papers. The success of the conference is the direct result of their collective efforts. The session chairmen and co-chairmen administered the sessions in a positive, constructive, and professional manner. We owe our deep gratitude to all of these individuals and their organizations.

We are thankful to Shri Amitabh Saxena, Pro-Vice Chancellor, Dr. Vijay Singh, Registrar, and Dr. Basant Singh, School of Engineering and Technology, AISECT University, who provided expertise that greatly helped with the conference organization. We are also thankful to all the heads of other schools, faculty member and

staff of the AISECT University for the highly appreciable assistance in different organizing committees of the conference. We also express our sincere thanks to all the reviewers at national and international levels who reviewed and moderated the papers submitted to the conference. Their constructive evaluation and suggestions improved the manuscripts significantly.

Contents

Part I Rainfall Analysis

Rainfall Probability Distribution Analysis in Selected Lateral Command Area of Upper Krishna Project (Karnataka), India 3
N. K. Rajeshkumar, P. Balakrishnan, G. V. Srinivas Reddy, B. S. Polise Gowdar and U. Satishkumar

Analyzing Rainfall and Reservoir Release Pattern for Ajwa Reservoir: A Case Study 13
Pushkar Sharma and Sanskriti Mujumdar

Preliminary Investigations on Localized Rainfall Interception Losses Under Real Field Observations 21
M. L. Gaur and Saket Kumar

Probabilistic Estimation of Design Daily Runoff from Bamhani Watershed, India 37
Sarita Gajbhiye Meshram and Vijay P. Singh

Part II Evapotranspiration

Development of Generalized Higher-Order Neural Network-Based Models for Estimating Pan Evaporation 55
Sirisha Adamala, N. S. Raghuwanshi and Ashok Mishra

Sensitivity Analysis of FAO-56 Penman–Monteith Reference Evapotranspiration Estimates Using Monte Carlo Simulations 73
Gicy M. Kovoor and Lakshman Nandagiri

Quantification of Error in Estimation of Reference Crop Evapotranspiration by Class A Pan Evaporimeter and Its Correction 85
S. Praharaj, P. K. Mohanty and B. C. Sahoo

Part III Urban Runoff

Spatial and Temporal Analyses of Impervious Surface Area on Hydrological Regime of Urban Watersheds 99
Tauseef A. Ansari and Y. B. Katpatal

An Assessment of Hydrological Impacts Due to Changes in the Urban Sprawl in Bhopal City and its Peripheral Urban-Rural Fringe 111
L. Patel, S. Goyal and T. Thomas

Simulation of Urban Drainage System Using Disaggregated Rainfall Data 123
Vinay Ashok Rangari, K. Veerendra Gopi, N. V. Umamahesh and Ajey Kumar Patel

Investigation of Drainage for Structures, Lithology and Priority (Flood and Landslide) Assessment Using Geospatial Technology, J&K, NW Himalaya 135
Umair Ali and Syed Ahmad Ali

Hydrologic Design Parameters Database for Water Harvesting Structures in Madhya Pradesh 161
Ramadhar Singh, Karan Singh and D. M. Bhandarkar

Application of Storm Water Management Model to an Urban Catchment 175
V. Swathi, K. Srinivasa Raju and Ajit Pratap Singh

Part IV Soil Erosion and Sediment

A Study of Erosional Depositional Activity and Land Use Mapping of Majuli River Island Using Landsat Data 187
Dipsikha Devi, Nilutpal Phukan and Bibhash Sarma

Study of Soil Erosion and Deposition Around an Island in a Natural Stream 201
Snigdhadip Ghosh, Saptarshi Das and Vijay Kumar Dwivedi

Impact Assessment of Alternate Land Cover and Management Practices on Soil Erosion: A Case Study 211
T. R. Nayak, R. K. Jaiswal, R. V. Galkate and T. Thomas

Geostatistical Analysis of River Sedimentation Behavior in Kerala State 225
Mathew K. Jose, T. Chandramohan, B. K. Purandara and B. Venkatesh

Study of Mineralogical Composition of Sediment in Brahmaputra River in Urban Stretch of Guwahati City, Assam, India 243
Mamata Das and Triptimoni Borah

Part V Remote Sensing and GIS Applications

Hypsometric Analysis for Assessing Erosion Status of Watershed Using Geographical Information System 263
S. K. Sharma, S. Gajbhiye, S. Tignath and R. J. Patil

Assessment of Different Bathymetry Statistical Models Using Landsat-8 Multispectral Images 277
Omar Makboul, Abdelazim Negm, Saleh Mesbah and Mohamed Mohasseb

Estimation of Minimum and Maximum Air Temperature Using MODIS Remote Sensing Imagery and Geographical Information System (GIS) 291
P. Sardhara Bharatkumar, P. Dholariya Jay, M. K. Tiwari and M. L. Gaur

A RS and GIS Approaches for the Estimation of Runoff and Soil Erosion in SA-13 Watershed 307
H. N. Bhange and V. V. Deshmukh

Rainwater Harvesting Structure Site Suitability Using Remote Sensing and GIS 331
B. K. Gavit, R. C. Purohit, P. K. Singh, Mahesh Kothari and H. K. Jain

Land Surface Temperature Estimation Using Remote Sensing Data 343
Vijay Solanky, Sangeeta Singh and S. K. Katiyar

Watershed Prioritization of Wardha River Basin, Maharashtra, India Using Morphometric Parameters: A Remote Sensing and GIS-Based Approach 353
B. S. Manjare, S. Khan, S. A. Jawadand and M. A. Padhye

Flood Assessment of Lolab Valley from Watershed Characterization Using Remote Sensing and GIS Techniques 367
Mannan Bashir Wani, Syed Ahmad Ali and Umair Ali

Delineation of Paleochannels in Periyar River Basin of Kerala Using Remote Sensing and Electrical Resistivity Methods 391
C. P. Priju, Jiby Francis, P. R. Arun and N. B. Narasimha Prasad

Application of EO-1 Hyperion Data for Mapping and Discrimination of Agricultural Crops 401
H. Ramesh and P. P. Soorya

Geomatica-Based Approach for Automatic Extraction of Lineaments from ASTER-GDEM Data, in Part of Al-Rawdah, Shabwah, Southeast Yemen 423
Mohammed Sultan Alshayef and Akram Javed

Part VI Watershed Runoff and Floods

Morpho-Mathematical Analysis of Bharar River Basin District Chhatarpur-Central India 437
Pradeep Kumar Jain

Application of Principal Component Analysis for Grouping of Morphometric Parameters and Prioritization of Watershed 447
Sarita Gajbhiye Meshram and S. K. Sharma

Velocity Distribution in Vortex Chamber at High Water Abstraction Ratio 459
Mohammad Athar and Shivani Srotriya

Performance Appraisal of Friction Factor Estimators 475
Abhishek Mishra, Aditya Deshpande and Bimlesh Kumar

Experimental Investigations of Wave Height Attenuation by Submerged Artificial Vegetation 499
Beena Mary John, I. Mohit Babu, Kiran G. Shirlal and Subba Rao

Developing Rating Curves for Nubia Lake, Sudan, Using RS/GIS 511
Mohamed Elsahabi, Abdelazim Negm and Kamal Ali

A Spreadsheet Approach for Prediction of Rating Curve Parameters 525
Mohammad Muzzammil, Javed Alam and Mohammad Zakwan

Experimental Study on Role of Emergent Artificial Coastal Vegetation in Controlling Wave Run Up 535
Beena Mary John, R. T. Arun Vignesh, Kiran G. Shirlal and Subba Rao

Development of Regional Soil Water Retention (SWR) Characteristics 543
R. K. Jaiswal, T. Thomas, R. V. Galkate, S. Singh and J. V. Tyagi

Revision of Empirical Coefficients of Commonly Used Flood Formulae Using Flow Data from Karnataka Rivers 555
T. Chandramohan, Mathew K. Jose, B. K. Purandara and B. Venkatesh

Reservoir Inflow Forecasting Using Extreme Learning Machines 565
Mukesh Kumar Tiwari and Sanjeet Kumar

Quantifying Discontinuity, Connectivity, Variability, and Hierarchy in Overland Flow Generation: Comparison of Different Modeling Methods 587
Xuefeng Chu

Nondimensional UH-Based Smoothing of *S*-Curve-Derived UH Oscillations 605
P. R. Patil, S. K. Mishra, Nayan Sharma and Vijay P. Singh

Fuzzy-Based Comprehensive Evaluation of Environmental Flow Alteration 621
Kairong Lin, Fan Zhang, Qiang Zhang, Xinjun Tu and Yang Hu

Part VII Watershed Modeling

Spatial Characters of a Tropical River Basin, South-West Coast of India 641
Girish Gopinath, N. Ramisha, Ajith G. Nair and N. P. Jesiya

Streamflow Estimation Using SWAT Model Over Seonath River Basin, Chhattisgarh, India 659
Sabyasachi Swain, Mani Kant Verma and M. K. Verma

Revisiting the Soil Conservation Service Curve Number Method 667
S. K. Mishra, Vijay P. Singh and P. K. Singh

Hydrological Impacts of Rejuvenating Degraded Hilly Watershed in Shivalik Region 695
A. K. Tiwari and V. K. Bhatt

Modeling of a River Basin Using SWAT Model 707
B. Venkatesh, T. Chandramohan, B. K. Purandara, Mathew K. Jose and P. C. Nayak

Performance of the Xinanjiang Model 715
A. Ahirwar, M. K. Jain and M. Perumal

About the Editors

Prof. Vijay P. Singh is a Distinguished Professor, Regents Professor, Caroline and William N. Lehrer Distinguished Chair in Water Engineering, Department of Biological and Agricultural Engineering & Zachry Department of Civil Engineering, Texas A&M University, USA. He received his B.S., M.S., Ph.D., and D.Sc. degrees in engineering. He is a registered professional engineer, a registered professional hydrologist, and an Honorary Diplomate of American Academy of Water Resources Engineers.

Professor Singh has extensively published the results of an extraordinary range of his scientific pursuits. He has published more than 900 journal articles; 25 textbooks; 60 edited reference books, including the massive Encyclopedia of Snow, Ice and Glaciers and Handbook of Applied Hydrology; 104 book chapters; 314 conference papers; and 72 technical reports in the areas of hydrology, ground water, hydraulics, irrigation engineering, environmental engineering, and water resources.

For his scientific contributions to the development and management of water resources and promoting the cause of their conservation and sustainable use, he has received more than 90 national and international awards and numerous honors, including the Arid Lands Hydraulic Engineering Award, Ven Te Chow Award, Richard R. Torrens Award, Norman Medal, and EWRI Lifetime Achievement Award, all given by American Society of Civil Engineers; Ray K. Linsley Award and Founder's Award, given by American Institute of Hydrology; Crystal Drop Award, given by International Water Resources Association; and Outstanding Distinguished Scientist Award, given by Sigma Xi, among others. He has received three honorary doctorates. He is a Distinguished Member of ASCE and a fellow of EWRI, AWRA, IWRS, ISAE, IASWC, and IE and holds membership in 16 additional professional associations. He is a fellow/member of 10 international science/engineering academies. He has served as President and Senior Vice President of the American Institute of Hydrology (AIH). Currently, he is editor-in-chief of two book series and three journals and serves on editorial boards of 20 other journals.

Professor Singh has visited and delivered invited lectures in almost all parts of the world but just a sample: Switzerland, the Czech Republic, Hungary, Austria, India, Italy, France, England, China, Singapore, Brazil, and Australia.

Prof. Shalini Yadav is a Professor and Head of the Department of Civil Engineering, AISECT University, Bhopal, India. Her research interests include solid and hazardous waste management, construction management, environmental quality, and water resources. She has executed a variety of research projects/consultancy in environmental and water science and technology and has got rich experience in planning, formulating, organizing, executing, and management of R&D programs, seminars, and conferences at national and international levels. She has got to her credit guiding an appreciable number of M.Tech. and Ph.D. students. She has published more than 10 journal articles and 30 technical reports. Dr. Shalini has also visited and delivered invited lectures at different institutes/universities in India and abroad, such as Australia, South Korea, and Kenya.

Professor Shalini Yadav graduated with a B.Sc. in Science from the Bhopal University. She earned her M.Sc. in Applied Chemistry with specialization in Environmental Science from Bhopal University, and M.Tech. in Civil Engineering with specialization in Environmental Engineering from Malaviya National Institute of Technology, Jaipur, India, in 2000. Then she pursued the degree of Ph.D. in Civil Engineering from Rajiv Gandhi Technical University, Bhopal, India, in 2011. Also, she is a recipient of national fellowships and awards. She is a reviewer for many international journals. She has been recognized for one and half decades of leadership in research, teaching, and service to the Environmental Engineering Profession.

Dr. Ram Narayan Yadava holds position of Vice Chancellor of the AISECT University, Hazaribagh, Jharkhand. His research interests include solid mechanics, environmental quality and water resources, hydrologic modelling, environmental sciences, and R&D planning and management. Yadava has executed a variety of research/consultancy projects in the area of water resources planning and management, environment, remote sensing, mathematical modelling, technology forecasting, etc.

He has got adequate experience in establishing institutes/organizations, planning, formulating, organizing, executing, and management of R&D programs, seminars, symposia, conferences at national and international levels. He has got to his credit guiding a number of M.Tech. and Ph.D. students in the area of Mathematical Sciences and Earth Sciences. Dr. Yadava has visited and delivered invited lectures at different institutes/universities in India and abroad, such as USA, Canada, United Kingdom, Thailand, Germany, South Korea, Malaysia, Singapore, South Africa, Costa Rica, and Australia.

He earned an M.Sc. in Mathematics with specialization in Special Functions and Relativity from Banaras Hindu University, India, in 1970 and a Ph.D. in Mathematics with specialization in Fracture Mechanics from Indian Institute of Technology, Bombay, India, in 1975. Also, he is the recipient of Raman Research Fellowship and other awards. Dr. Yadava has been recognized for three and half

decades of leadership in research and service to the hydrologic and water resources profession. Dr. Yadava's contribution to the state of the art has been significant in many different specialty areas, including water resources management, environmental sciences, irrigation science, soil and water conservation engineering, and mathematical modelling. He has published more than 90 journal articles; 4 textbooks; and 7 edited reference books.

Part I
Rainfall Analysis

Rainfall Probability Distribution Analysis in Selected Lateral Command Area of Upper Krishna Project (Karnataka), India

N. K. Rajeshkumar, P. Balakrishnan, G. V. Srinivas Reddy, B. S. Polise Gowdar and U. Satishkumar

Abstract In India, occurrence and distribution of rainfall is erratic, seasonally variable, and temporal in nature, which is one of the most important natural input resources for agricultural production. To study the behavior of rainfall variability, the rainfall data of 37 years (1978–2014) were analyzed for Gabbur, Raichur (Karnataka), India. Hence, frequency analysis was carried out for best-fit distribution through software for probability density functions viz Weibull, lognormal, Gamma, log-Pearson type III, Gumbel, and Weibull 3 parameter (3P) distributions. The expected values were compared with the observed values, and goodness of fit was determined by chi-square test. The results showed that the log-Pearson type III distribution was the best-fit probability distribution to forecast annual weekly rainfall for different return periods. Based on the best-fit probability distribution, the minimum rainfall of 141.3 mm in a year can be expected to occur with 99% probability at one-year return period. The maximum of 515-mm rainfall can be received with 50% probability for every 2-year return period, and 1160.1-mm rainfall can be received by 0.5% probability at every 200-year return period. The results of this study would be useful for agricultural scientists, decision makers, policy planners, and researchers in agricultural crop planning, canal constructions, and operation management for irrigation and drainage systems in the semiarid plain region of the Karnataka.

Keywords Rainfall · Return period · Frequency · Probability distribution

N. K. Rajeshkumar (✉) · P. Balakrishnan · G. V. Srinivas Reddy · B. S. Polise Gowdar
U. Satishkumar
Department of Soil and Water Engineering, College of Agricultural Engineering,
University of Agricultural Sciences, Raichur 584102, Karnataka, India
e-mail: rajeshmtechster@gmail.com

V. P. Singh et al. (eds.), *Hydrologic Modeling*, Water Science
and Technology Library 81, https://doi.org/10.1007/978-981-10-5801-1_1

Introduction

Rainfall is one of the major precipitation forms of hydrological events occurring as stochastic natural phenomena occurring in India. Unequal rainfall variation throughout the year is one of the important problems in hydrology which deals with the interpreting past records of hydrological events in terms of future probabilities of occurrence through time series and probability models. Analysis of rainfall and determination of variation in annual, seasonal, monthly, and weekly rainfall of a region and time is well known, and this inter-annual variability of monsoonal rainfall has considerable impact on agricultural production, water management, and energy generation, estimating design command area and cropping pattern. Similarly, the weekly rainfall analysis gives more useful information in crop planning.

Though the rainfall is erratic and varies with time and space, it is very much essential to predict return periods using various probability distributions (Upadhaya and Singh 1998). Probability and frequency analysis of rainfall data enables us to determine the expected rainfall at various chances (Bhakar et al. 2008). Such information can also be used to prevent floods and droughts and applied to crop planning and designing of water resources related to hydrological engineering such as reservoir capacity and canal carrying capacity design, flood control work, and soil and water conservation planning (Agarwal et al. 1988; Dabral et al. 2009). Therefore, probability analysis of rainfall is necessary for solving various water management problems and to access the crop failure due to the deficit or excess rainfall. Scientific prediction of rain and crop planning done analytically may prove a significant tool in the hands of farmers for better economic returns (Bhakar et al. 2008). Frequency analysis of rainfall data has been attempted for different return periods (Nemichandrappa et al. 2010; Vivekananda 2012). Probability and frequency analysis of rainfall data enables us to determine the expected rainfall at various chances. The probability distribution functions most commonly used to estimate the rainfall frequency are Weibull, normal, lognormal, log-Pearson type III, and Gumbel distributions (Bhim et al. 2012; Mahdavi et al. 2010; Subudhi et al. 2012; Mandal et al. 2013; Mishra et al. 2013).

Earlier workers work out the weekly rainfall probabilities for different agroclimatic regions (Ray et al. 1980; Kar et al. 2014). Gupta et al. (1975) suggested that the rainfall at 80% probability can safely be taken as assured rainfall, while that of 50% probability is the medium limit for taking dry risk. According to Von Braun (1991) recommended that a 10% decrease in monsoonal rainfall for a long period there is 4.4 % decrease in the national food production. Therefore, an attempt has been made for probability analysis of long-term rainfall data of Gabbur station for decision support system risk proof technologies for irrigated agriculture of Upper Krishna Project (UKP) of Raichur district.

Materials and Methods

The study area is the command area of the branch distributary 5 of the tail-end distributary 18, starting at chainage of 23.33 km in the UKP Narayanapur Right Bank Canal (NRBC) starting at the right flank of Narayanapur dam. The study area is located in Gabbur village at an altitude of 389 m from mean sea level, Devadurga taluk, Raichur district between 16° 16′52.280″ to 16° 17′50.895″N latitudes and 77° 09′20.312″ to 77° 30′50″E longitudes (Fig. 1). The soils of the study area are sandy soils in the head region and black soils in the tail region (clay content 46–55%). The climate is semiarid tropical with an average rainfall of 534.3 mm. The monthly evaporation varies from 141 to 273 mm and is maximum during April–May. The area receives 86% of annual rainfall during southwest monsoon (*kharif*), i.e., from June to October, 6% during *rabi,* and 8% during summer. The annual mean maximum and minimum monthly relative humidity of the region are 73.7% (Sept) and 39.6% (April), respectively. The annual mean maximum and minimum monthly mean daily temperatures in the study area are 39.7 °C (May) and 15.5 °C (Dec), respectively.

The region as a whole lies in a low rainfall area, and the annual average rainfall was 534.3 mm. Time series rainfall records for the period of 1978–2015 (37 years) was analyzed to study the behavior daily rainfall data from Gabbur rain gauge station. Hence, frequency analysis was carried out for best-fit distribution through VT-fit software. The probability analysis can be used for predicting the occurrence of rainfall events of the available data with the help of statistical analysis. Several distributions have been suggested for hydrological analysis. Based on the theoretical probability distributions, it could be possible to predict the rainfall of different magnitudes and return periods. The most suitable distribution to represent the observed data may depend on rainfall pattern of the place.

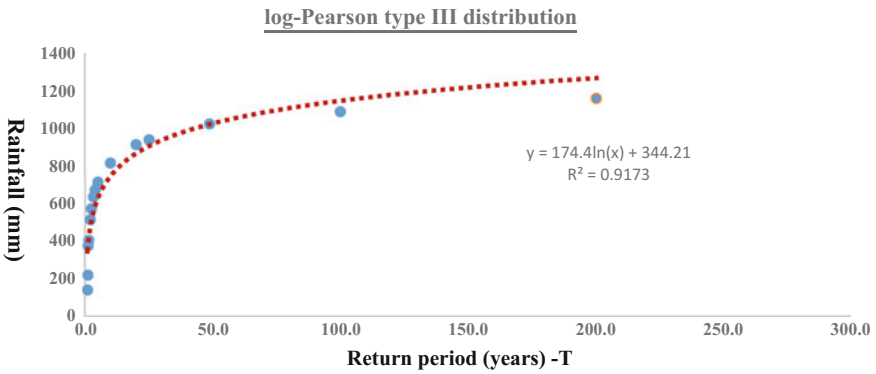

Fig. 1 Annual rainfall analysis for Gabbur by log-Pearson type III distribution

Test for Goodness of Fit for Probability Distributions

Out of the selected four probability distribution methods, the best-fitting probability density function was selected based on goodness-of-fit test procedure. A number of statistical tests are available for testing the best-fit distribution. In this study, chi-square test was selected among the most commonly useful procedures for testing goodness-of-fit test. The test statistic (χ^2) has been estimated from the expression:

$$\chi^2 = \sum_{h=1}^{k} \frac{(O_h - E_h)^2}{E_h} \tag{3.2}$$

where

k number of years,
O_h observed values in hth year,
E_h expected value in hth year.

The data were analyzed by computer-based VT-fit software used for fitting probability distribution functions that also provide goodness-of-fit tests. The probability density functions viz Weibull, Gamma, Gumbel, lognormal, 3-parameter Weibull, log-Pearson type III distributions which were used for analysis and compared with the Weibull (observed one) for deciding the best-fit distribution are shown below.

Distribution	Probability density function
Weibull distribution	$P = \left(\frac{m}{N+1}\right)$
Gamma distribution	$P(X) = \left(\frac{X^a e^{\frac{-x}{b}}}{b^{a+1}\Gamma(a+1)}\right)$
Gumbel distribution	$f(X) = \frac{e^{-\frac{(X-\gamma)}{\beta}} - e^{-\frac{(-X-\gamma)}{\beta}}}{\beta}$
Lognormal distribution	$P(X) = \frac{1}{\sigma_y e^y \sqrt{2\pi}} e - \left(\frac{y}{\mu y}\right)^2 / 2\sigma_y^2$
Log-Pearson type III distribution	$f(X) = \frac{e^{\frac{\gamma}{\beta}} X^{\beta-1}}{\beta\Gamma(\alpha)} \left(\frac{\ln X-\gamma}{\beta}\right)^{\alpha-1}$
Three-parameter Weibull distribution	$f(x) = \frac{\beta}{\eta}\left(\frac{X-\gamma}{\eta}\right)^{\beta-1} e^{-\left(\frac{X-\gamma}{\eta}\right)\beta}$

Using the best-fit distribution identified for rainfall, the lowest chi-square value distribution was considered to be the best-fit distribution, and the rainfall magnitudes at different probabilities were computed.

Confidence Limits

Since the value of the variate for a given return period, 'x_t' determined by the above-said probability best-fit distribution values can have errors due to the limited sample data used as an estimate of the confidence limits of the desirable. The confidence interval indicates the limits about the calculated value between which the true value can be said to lie with a specific probability. Based on sampling errors for confidence probability 'c', the confidence interval of the variate x_t is bounded by values x_1 and x_2 given by the following equation.

$$x_{1/2} = x_T \pm f(c)S_e$$

where

$f(c)$ = function of the confidence probability 'c' determined by using the table of normal variates.

$$\text{Se} = \text{probable error} = b\left(\sigma\frac{n-1}{\sqrt{N}}\right)$$

$$b = \sqrt{1 + 1.3K + 1.1K^2}$$

$$K = \text{frequency factor given by } K = \frac{y_T - y_n}{S_n}$$

σ_{n-1} Standard deviation of the sample,
N Sample size.

Rainfall at various probability levels (25, 50, 75, and 90) based on the above methodology rainfall at various probability levels (50, 60, 70, 75, 90, and 99%) for annual basis has been worked out and are presented in Table 1. The rainfall at 70% probability was generally used for agricultural planning, and hence, the same is considered in the present investigation to suggest crop planning.

Results and Discussions

Rainfall Analysis

The analysis of annual rainfall data of the 37-year period for the study area Gabbur revealed that the log-Pearson type III distribution was the best-fit distribution with minimum chi-square value (23.7). This function was useful for studying the rainfall pattern among the various probability distribution functions considered viz log-normal, log-Pearson type III, Gamma, Gumbel, and Weibull 3 parameter (3P) distributions in comparison with the Weibull distribution as observed one. The best-fit distributions followed by log-Pearson type III distribution were Gumbel,

Table 1 Computation of annual rainfall in the study area at different probabilities for finding best-fit distribution

Return period	Probability	Rainfall (mm)						Chi-square value $(O - E)^2/E$				
		Log normal	Gamma	Log-Pearson type III	Gumbel	Weibull	Weibull three parameter	Log normal	Gamma	Log-Pearson type III	Gumbel	Weibull three parameter
1	99	180.8	150.9	141.3	198.7	122.1	188.3	19.1	5.5	2.6	29.5	23.3
1	95	242.3	211.9	219.7	267.2	214.6	231.0	3.2	0.0	0.1	10.4	1.2
1	75	367.6	341.5	376.1	390.0	389.7	355.4	1.3	6.8	0.5	0.0	3.3
1	70	392.1	370.2	405.0	412.4	419.8	382.1	1.9	6.6	0.5	0.1	3.7
2	50	491.2	449.8	515.0	500.4	528.2	489.9	2.8	13.7	0.3	1.5	3.0
3	40	547.7	502.9	572.7	549.0	581.8	549.8	2.1	12.4	0.1	2.0	1.9
3	30	615.4	560.1	636.0	606.3	639.4	619.0	0.9	11.2	0.0	1.8	0.7
4	25	656.4	625.8	673.0	640.5	671.4	659.4	0.3	3.3	0.0	1.5	0.2
5	20	705.2	664.3	715.0	681.0	707.0	706.1	0.0	2.7	0.1	1.0	0.0
10	10	852.0	709.0	816.0	800.5	800.2	836.9	3.1	11.7	0.3	0.0	1.6
20	5	995.9	835.7	914.0	915.2	876.5	952.6	14.3	2.0	1.5	1.6	6.1
25	4	1042.2	986.0	940.0	951.6	898.5	987.5	19.8	7.8	1.8	3.0	8.0
50	2	1187.2	1091.6	1020.2	1063.7	961.2	1090.3	43.0	15.6	3.4	9.9	15.3
100	1	1334.7	1192.4	1090.0	1174.9	1017.1	1186.1	75.6	25.8	4.9	21.2	24.1
200	1	1485.7	1289.5	1160.1	1285.7	1067.6	1276.2	117.7	38.2	7.4	37.0	34.1
								305	163.3	23.7	120.5	126.4

O observed, *E* expected total

Weibull 3 parameters (3P), and Gamma distributions with the chi-square values of 120.5, 126.4, 163.3, and 305.2 as shown in Table 1.

The best-fit regression analysis equation for the study area was developed using the log-Pearson type III distribution which is given by the formula.

$$y = 174.4 \ln(x) + 344.21$$

where

y Rainfall mm
x Return period.

The equation was used to estimate rainfall at different probabilities in the study area, and then the same was shown in Fig. 2. As the value of the regression coefficient is $R^2 = 0.9173$ in log-Pearson type III distribution-based on regression models, which can be used to predict probable rainfall for different return periods. The log-Pearson type III distribution estimated the probable annual rainfall magnitudes of 1160.1, 1090.0, 1020.2, 940.0, 914.0, 816.0, 715.0, 673.6, 636.9, 572.6, 515.0, 405.0, 376.1, 219.7, and 141.3 mm for the return periods 200, 100, 50, 25, 20, 10, 5, 4, 3.3, 2.5, 1.4, 1.3. 1.05 and 1.01 years respectively.

Further, using the log-Pearson type III distribution, the magnitudes of weekly rainfall at different probability levels were worked out. The mean annual rainfall of 534.3 mm was found to occur at the probability of 42.4%. Generally, the rainfall at 70% probability is considered for agricultural planning. The estimated weekly rainfall values at this probability ranged from 0 to 25.1 mm. The mean standard weekly rainfall and the estimates of standard weekly rainfall over a year at different probability levels were calculated. The analysis revealed that the mean maximum weekly rainfall values at 50, 70, 75, 90, 95, 99% probability levels were 28.6, 25.1, 23.6, 14.7, 10.9, 8.9, 2.8, and 1.4 mm during the 38th week, respectively (Fig. 2).

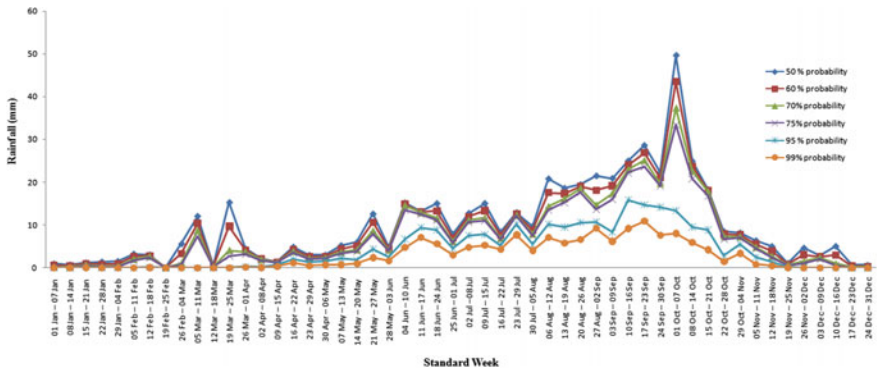

Fig. 2 Mean standard weekly rainfall over a year at different probability levels

During the period between 23rd and 42nd weeks except 26, 29, and 31st weeks, 17 weeks in a year the rainfall equal to or more than 10 mm could be received. As expected, these periods coincided with the southwest monsoon season. The monsoon in this part of the region starts from June first/second week, which was clearly revealed from the rainfall analysis that the 23rd week (04–10 June) coincided with that period with a mean rainfall of 16.3 mm and at an acceptable 70% probability, the rainfall of 14.6 mm could be expected during that week.

The mean weekly rainfall was >10 mm during the period from 23rd week to 42nd week (15–21 Oct). Further, it was noticed that even >15 mm could be anticipated during the same period, except during 26th (25–01 Jul), 29th (16–22 Jul), and 31st weeks (30 Jul–05 Aug), which coincided with *kharif* season. On an average, maximum peak weekly rainfall of 41.3 mm could be expected during the 38th week (17–23 Sep). At 70% probability, >15 mm rainfall could be expected during the period from 33rd (13–19 Aug) to 42nd week (15–21 Oct) except 35th week (27 Aug–02 Sep).

During the years wherein average weekly rainfall is >15–30 mm, *kharif* crops could be expected to be sown during the beginning of the month of June (23rd week) onwards. Later, during the month of October till the third week, i.e., 42nd week, the southwest monsoon promises wet spells (35.4–18.2 mm), around that time the sowing of *rabi* crops could be expected to be taken up. The recession of southwest monsoon would start during week (22–28 Oct) and continue. Later on even during northeast monsoon, no significant rains useful for crop growth would be expected. This trend was found to continue till the summer by the end of May month. The analysis also gave information on probable rainfall excesses help in the canal water operation for saving water in the canal command area, harvested in farm ponds and utilized during lean periods. Based on this, the effective rainfall could be estimated and appropriate cropping pattern for upper, middle, and tail reaches arrived at with consideration of the canal water availability and irrigation requirement to be met out from the canal flow in the study area.

The confidence limit analysis regarding rainfall pattern following the log-Pearson type III distribution indicated that as the confidence probability increased, the confidence interval also increased and an increase in return period caused the confidence band to spread on either side of the value as shown in Table 2 which is helpful for finding out errors in the probability distribution.

The rainfall analysis would be useful in finding out the best-fit distribution representing the rainfall pattern, which in turn would be helpful in arriving at the magnitudes of weekly rainfall at different probabilities. For agricultural planning, the rainfall at 70% probability with a 30% risk could be taken up for evolving appropriate cropping pattern for upper, middle, and tail reaches by considering both the availability of canal water supplies and effective rainfall. This information is helpful for judging the suitable time of sowing of crops, intercultural operation planning and harvesting of crops at suitable time during kharif and rabi seasons. The irrigation water requirements to be met out from canal water supplies could be estimated accordingly.

Table 2 Confidence limits for annual rainfall at different probability levels using log-Pearson type III distribution

Parameter confidence limits	Different probability levels (%)								
	Mean	50	70	75	95	99	99.5	99.8	99.9
XT, mm	534.3	515.9	405.6	376.0	219.6	141.7	101.6	22.7	1.4
T, Yr	2.25	2.00	1.43	1.33	1.05	1.01	1.01	1.00	1.00
Y_T	0.53	0.37	−0.19	−0.33	−1.10	−1.53	−1.67	−1.83	−1.93
K	−0.02	−0.16	−0.63	−0.75	−1.41	−1.78	−1.90	−2.04	−2.13
B	0.99	0.91	0.79	0.80	1.17	1.48	1.59	1.71	1.80
Se	73.35	64.90	44.21	41.87	35.54	29.0	22.3	5.38	0.36
X_1 mm, 80%	628.3	599.1	462.3	429.7	265.1	178.9	130.2	29.6	1.9
X_2 mm, 80%	440.2	432.7	348.9	322.4	174.0	104.5	72.9	15.8	1.0
X_1 mm, 95%	678.0	643.1	492.3	458.1	289.2	198.6	145.3	33.2	2.1
X_2 mm, 95%	390.5	388.7	319.0	294.0	149.9	84.8	57.8	12.1	0.7

Conclusion

By considering best-fit probability distribution, the weekly rainfall observation, the effective rainfall and net irrigation requirement were estimated by after meeting all the losses required for meeting the irrigation requirements could be supplied from the canal water. This would not only minimize the deep percolation losses in the upper and middle reaches thereby would facilitate declining of the water table to solve drainage problems, but also would enhance the canal water supplies to the lower reaches to reduce the tail-end problems and also help in developing cropping planning decisions and estimating the design flow rate for maximizing crop production.

Acknowledgements The authors are grateful to the Science and Engineering Research Board, Department of Science and Technology, Government of India, for providing financial assistance in Young Scientist Scheme.

References

Agarwal MC, Katiyar VS, Rambabu (1988) Probability analysis of annual maximum daily rainfall of U.P., Himalaya. Indian J Soil Conserv 16(1):35–42

Bhakar SR, Iqbal M, Mukesh D, Bansal AK (2008) Probability analysis of rainfall at Kota. Indian J Agric Res 42:201–206

Bhim S, Deepak R, Amol V (2012) Probability analysis for estimation of annual one day maximum rainfall of Jhalarapatan area of Rajasthan, India. Plant Arch 12(2):1093–1100

Dabral PP, Mautushi P, Singh RP (2009) Probability analysis for one day to seven consecutive day's annual maximum rainfall for Doimukh (Itanagar), Arunachal Pradesh. J Indian Water Resour 2:9–15

Gupta RK, Rambabu, Tejwani KG (1975) Weekly rainfall of India for crop planning programme. Soil Conserv Digest 3:31–39

Kar SK, Sahoo DP, Subudhi CR (2014) Weekly analysis for crop planning using markovs chain model for Kandhamal district of Orissa, India. Int J Eng Res Appl 9(4):139–145

Mahdavi M, Khaled O, Sadeghi SAN, Bakhtiar K (2010) Determining suitable probability distribution models for annual precipitation data (a case study of Mazandaran and Golestan Provinces). J Sustain Develop 3(1):157–168

Mandal KG, Padhi J, Kumar A, Sahoo DK (2013) Analysing rainfall events and soil characteristics for water resources management in a canal irrigated area. J Water Res Ocean Sci 2(1):1–8

Mishra PK, Khare D, Kandu S, Shukla R (2013) Statistical and probability analysis of rainfall for planning in a canal command area. Agric Sustain Develop 1(2):45–52

Nemichandrappa M, Ballakrishnan P, Senthilvel S (2010) Probability and confidence limit analysis of rainfall in Raichur region, Karnataka. J Agric Sci 23(5):737–741

Ray CR, Senapati PC, Lal R (1980) Rainfall analysis for crop planning, Gopalpur (Orissa). J Agric Eng 17:1–8

Subudhi CR, Sahoo M, Senapati SC (2012) Rainfall probability analysis for crop planning in Kandhamal district of Orissa, India. Indian J Soil Cons 40(3):247–251

Upadhaya A, Singh SR (1998) Estimation of consecutive day maximum rainfall by various methods and their comparison. Indian J Soil Conserv 26:193–201

Vivekananda N (2012) Intercomparison of extreme value distributions for estimation of ADMR. Int J Appl Eng Technol 2(1):30–37

Von Braun J (1991) A policy agenda for famine prevention in Africa. Food Policy Statement No.13, IFPRI, Washington DC

Analyzing Rainfall and Reservoir Release Pattern for Ajwa Reservoir: A Case Study

Pushkar Sharma and Sanskriti Mujumdar

Abstract The rainfall pattern of a catchment is the governing parameter for the quantity of water stored or released from any reservoir. However, along with the rainfall of the current year, the rainfall of the previous year also plays a vital role in deciding the releases. The Ajwa Reservoir is one of the main sources of water supply for the city of Vadodara—the cultural capital of Gujarat aspiring to become a smart city soon. The reservoir accounts for nearly 40% of the water supply to the city. The city of Vadodara is growing at a very fast pace, and the water supply will play an important role in its growth. With an average annual rainfall of 950 mm, it usually faces shortage of water in peak summers which is the case of most of the cities in the country. The study attempts to analyze the rainfall pattern as well as the pattern of releases from the Ajwa Reservoir together. A data of 24 years has been used for this purpose. The conclusions can be useful for devising a long-term strategy for the reservoir operation policy of the Ajwa Dam.

Introduction

Vadodara is the third largest city in the state of Gujarat, with an area of 149 km^2 (vmc.gov.in) and a population of 17 lakh (vmc.gov.in), located between Ahmedabad and Surat. Post-independence, the city has experienced rapid population growth and significant metamorphoses. Though the existence of Vadodara can be traced back to the second century BC, its existence as a city dates back to 1816 when it came under British Rule. The modernization of the city began in 1882 with His Highness Late Shrimant Maharaja Sayajirao Gaekwad—III ascending the throne of the Baroda State.

P. Sharma · S. Mujumdar (✉)
Civil Engineering Department, Faculty of Technology and Engineering,
Maharaja Sayajirao University of Baroda, Vadodara 390001, Gujarat, India
e-mail: sanskritimujumdar@yahoo.co.in

P. Sharma
e-mail: pushkarsharma2014@gmail.com

V. P. Singh et al. (eds.), *Hydrologic Modeling*, Water Science
and Technology Library 81, https://doi.org/10.1007/978-981-10-5801-1_2

Ajwa (Sayaji) Sarovar

Ajwa Sarovar is an earthen dam built by His Highness Late Shrimant Maharaja Sayajirao Gaekwad—III. A survey of this project was undertaken by Mr. Sadashivaji in 1883. The scheme was sanctioned on November 26, 1884, and the work was commenced in January 1885 and completed in months of March 1892 (Vadodara Mahanagar Seva Sadan). The reservoir is located 20 km northeast of Vadodara with waste weir and outlet works. The works were designed to afford a daily supply of 13.63 million liters (3 million gallons) to 120,000 consumers (Vadodara Mahanagar Seva Sadan).

Impounding Reservoir

The catchment area of Shri Sayaji Sarovar is 95 km^2 (36.67 sq. miles). The loss of water by evaporation assumed to be 1.82 m (72 inches) annually, and the earthen embankment is 4389 m (14,400 ft.) in length and 17.06 m (56 ft.) maximum height. The capacity of reservoir up to R.L. 63.40 m (208.00 ft.) is 1287 Mcft and that at R.L. 64.31 m (211.00 ft.) is 1717 Mcft. The top width is 4.87 m (16 ft.). The top of the embankment is at R.L. 67.81 m (222.50 ft.). The sill of the outlet valve is at R.L. 55.78 m (183.00 ft.). The inner slope is 3:1 and 2:1 on the outer side. The inner toe is pitched with 0.23 m (9 inch) bricks up to the R.L. 65.83 m (216 ft.). The water spread at R.L. 64.31 m (211.00 ft.) is 5.40 sq. miles. The water in the lake has risen to R.L. 65.83 m (216.00 ft.) in the year 1927 owing to heavy rains. The land between the dam and contour R.L. 65.83 m (216.00 ft.) belongs to Municipality (Vadodara Mahanagar Seva Sadan).

Waste Weir

The waste weir is 244 m (800 ft.) length and 30.50 m (100 ft.) in width. There are 62 shutter, each 3.05 m (10 ft.) and 0.91 m (3 ft.) in height. The shutters are fixed with chains at two points. The chains are carried over pulleys and tied to the floats. The floats are circular each 0.91 m (3 ft.) in dia and 1.82 m (6 ft.) in height. All of them are filled with sand, gravel. The quantity of sand for each float is manipulated according to the requirements. The width of the paving is 28.65 m (94 ft.) which is made of concrete. The waste weir is automatically operated, and the overflow level is 64.31 m (211 ft.) (Vadodara Mahanagar Seva Sadan).

Literature Review

Bharali (2015) has estimated the reservoir storage capacity for the Dibang Multipurpose Dam site in the Dibang River Basin, Arunachal Pradesh. The inflow mass curve is plotted, and the slope line is converted on horizontal axis to make residual mass curve. Also, the calculations by sequent peak algorithm method are done to obtain the reservoir capacity. The reservoir storage capacity is calculated for monthly variation flow for different years, and graph is plotted to calculate the maximum storage capacity. Mehta et al. (2014) have used HEC-RAS to evaluate the flood conveyance performance of Tapi river for lower reach of approximately 6 km length within Surat city from weir cum causeway to Sardar Bridge with the past flood data of Tapi River. Vogel et al. (1999) all have used the annual and monthly flow records to obtain storage-yield curves and compared it with standardized net inflow and coefficient of variation of net inflow C_v to characterize the refill properties of storage reservoirs in USA. Coefficient of variation of net inflow C_v of a river can be used to calculate the design capacity of the reservoir with the help of annual fluctuations in stream flow alone regardless of stream size.

Suleiman and Ifabiyi (2015) have obtained the spatiotemporal trends of Shiroro Dam with the hydro-meteorological data available. Statistical analysis of rainfall, inflow, reservoir storage, and turbine release are done, and the correlation regression analysis is used to develop models for the variables. Pancholi et al. (2015) all have calculated the minimum and maximum runoffs for the Vishwamitri River watershed for the period of 1990–2013. Minimum and maximum values of yearly computed average rainfall, land use/land cover, and hydrological soil maps layers are used in GIS environment to estimate CN. Universal Soil Loss Equation is used to calculate the soil loss from the watershed per hectare per year and the regions with severe soil erosion is also obtained.

Data Collection

The daily rainfall data of the monsoon period for the four raingauge stations located in the catchment of Ajwa Reservoir is collected for the period of 1991–2014. Figure 1 shows the location of the rain gauges in the catchment. Table 1 shows the details of the four rainguage stations. The hourly level of dam for the monsoon period is collected for the period of 1991–2014. The weir-discharge table and the specifications of Sayaji Sarovar are collected.

Analysis

Subramanya (2015), 'Engineering Hydrology' book is used for all types of calculation of formulas. The average depth of rainfall for the catchment was calculated by arithmetic mean method. Table 2 shows the average depth of rainfall for the catchment for the study period of 24 years.

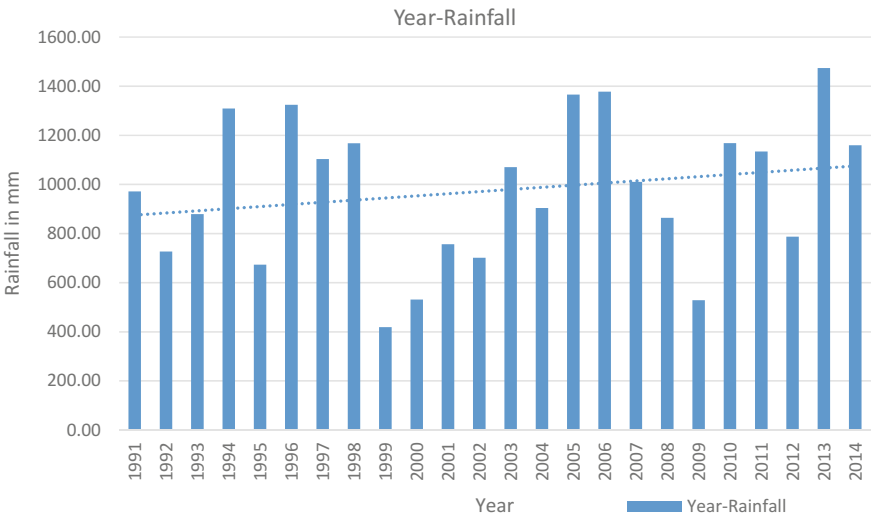

Fig. 1 Average rainfall versus year

Table 1 Location of raingauges in catchment of Ajwa Reservoir

Position No.	Place	Latitude	Longitude	Elevation in m
1	Ajwa	22° 24′ 45″	73° 23′ 12″	64
2	Pratappura	22° 29′ 51″	73° 23′ 21″	74
3	Halol	22° 30′ 42″	73° 27′ 51″	90
4	Ghansarvaav	22° 26′ 25″	73° 29′ 1″	110

Table 2 Average rainfall of raingauge stations

Position No. in Fig. 1.	Place	Avg. rainfall from 1991 to 2014 (mm)
1	Ajwa	1010
2	Pratappura	938
3	Halol	1059
4	Ghansarvaav	894.25

Here in Table 2, average rainfall for individual rain gauge station is calculated as shown below for Ajwa station:

$$\text{Average rainf all for rain gauge station at Ajwa (mm)} = \frac{y_1 + y_2 + \cdots + y_n}{n}$$

where

y yearly rain fall in mm
n no. of years

The average rainfall in Fig. 1 is calculated by arithmetic mean method for all the stations for each year from 1991 to 2014.

$$\text{Average rainf all for catchment of Ajwa reservoir (mm)} = \frac{y_1 + y_2 + y_3 + y_4}{4}$$

where

y_1 yearly rainfall for Ajwa station in mm
y_2 yearly rainfall for Pratapura station
y_3 yearly rainfall for Halol station
y_4 yearly rainfall for Gansarvaav station.

In this manner, average rainfall for each year is calculated and plotted and average for 24 years is obtained as 975 mm.

From graph shown in Fig. 2a, we can get the maximum level obtained by reservoir in each year, and from this level we can get the maximum discharge from waste weir for that particular level of Ajwa Reservoir in graph of Fig. 2b. During high flows, water flowing in the reservoir exceeds its overflow level of 64.31 m and release from waste weir starts as water keeps accumulating from catchment. Due to heavy releases from waste weir, the river Vishwamitri gets flooded. The river flows through the Vadodara city meeting the Arabian Sea at Pingalwada. In this paper, we have calculated the yearly release through dam for a period of 1991–2014 by interpolating the level of the dam in elevation-discharge curve in Fig. 2b. Hourly level of dam is obtained from Municipality Authority (Vadodara Mahanagar Seva Sadan) for each year, and with this level, hourly discharge is calculated and total discharge is obtained for the whole year by summing hourly discharge.

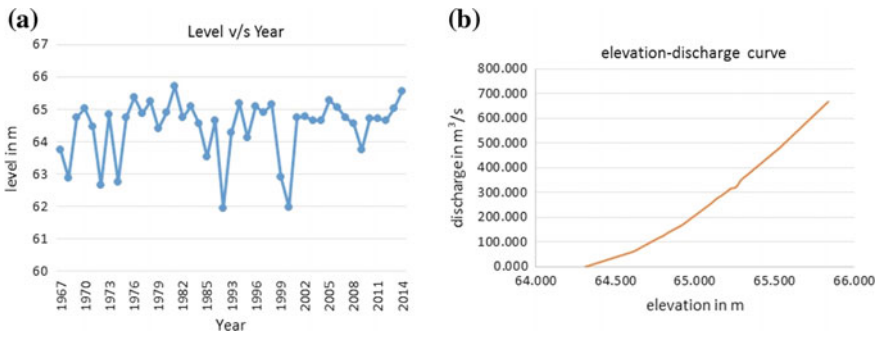

Fig. 2 **a** Yearly maximum level of Ajwa Reservoir and **b** elevation-discharge curve for waste weir of Ajwa Reservoir

Results and Conclusion

From Fig. 1, it can be seen that average rainfall for Ajwa catchment area is 975 mm (1991–2014) and the rainfall varies from 419 to 1474 mm. The trendline shows that the rainfall has increased from 850 to 1050 mm in a span of 24 years and there is a steady rise. From Fig. 2a, b, the maximum discharge which the downstream river can face in near future can be used for modification in river cross section so as to increase its capacity and protect the downstream region from flooding. From Fig. 3, it can be seen that 1992 and 1993 are drought year and thus storage in the reservoir was very less. Therefore, although year 1994 has rainfall above average annual rainfall of 975 mm (1991–2014), there is no overflow from the dam due to the previous year deficit. Thus, in year 1994, overflow has not occurred as compared to other years. Results are unusual for 1996, 1997, and 1998, which give an indication that either there may be some errors in discharge data for these years or water may have been released for special purpose. Thus, because of this error, the trendline in Fig. 4 has correlation coefficient of 0.48, which is very less. Further from year 1999, the rainfall and discharge follow a pattern shown by trendline in Fig. 5 which has correlation coefficient of 0.7 which is fairly good enough. With this equation, future discharge for a given rainfall can be predicted and data can be used for planning of release from the dam.

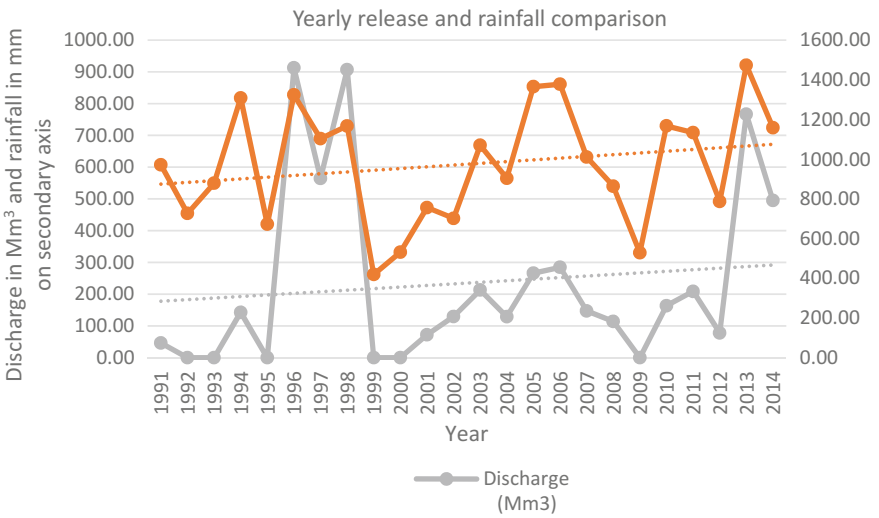

Fig. 3 Release versus year and discharge versus year

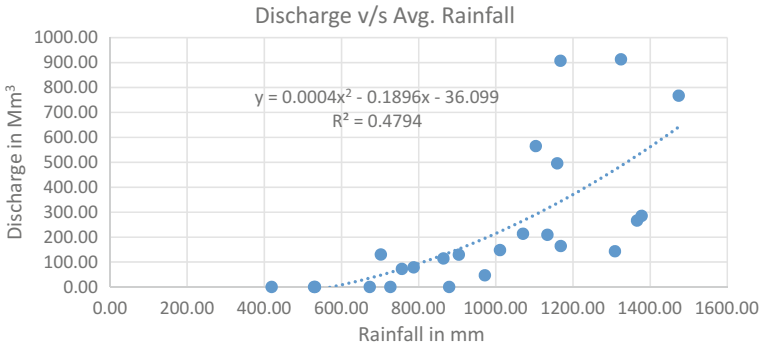

Fig. 4 Discharge versus rainfall for 1991–2014

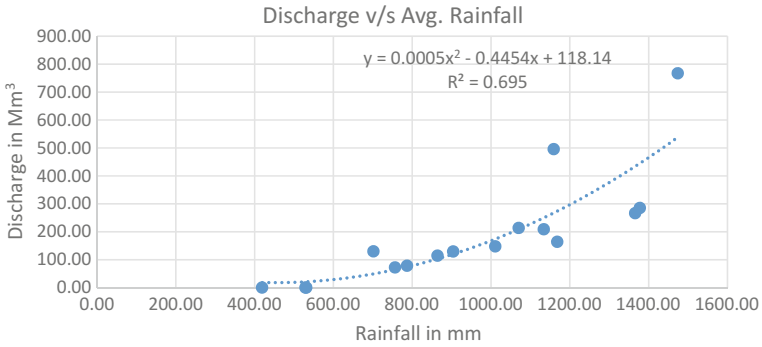

Fig. 5 Discharge versus rainfall for 1999–2014

References

Bharali B (2015) Estimation of reservoir storage capacity by using residual mass curve. J Civil Eng Environ Technol 2(10):15–18

Mehta DJ, Ramani M, Joshi M (2014) Application of 1-D Hec-Ras model in design of Channels. Int J Innov Res Adv Eng 1(7):103–107

Pancholi VH, Lodha PP, Prakash I (2015) Estimation of runoff and soil erosion for Vishwamitri river watershed, Western India using RS and GIS. Am J Water Sci Eng 1(2):7–14

Subramanya K (2015) Engineering hydrology (Fourth edition). McGraw Hill Education (India) Private Limited, New Delhi, pp 40, 41, 197–206

Suleiman YM, Ifabiyi IP (2015) The role of rainfall variability in reservoir storage management at Shiroro Hydropower Dam, Nigeria. Momona Ethiopian J Scie 7(1):55–63

Vogel RM, Lane M, Ravindiran RS, Kirshen P (1999) Storage reservoir behavior in the United States. J Water Resour Plan Manage 125(5):245–254

Preliminary Investigations on Localized Rainfall Interception Losses Under Real Field Observations

M. L. Gaur and Saket Kumar

Abstract Even under prevailing advanced science era, hydrological loss functions remain the weakest link and thus governs the ultimate success of any rainfall-runoff modeling on natural catchments. Among various such loss functions, interception happens to be the first and foremost element, on which research efforts are almost negligible, being truer for India and particularly middle Gujarat region. Present study is a preliminary effort, where field-based experimentations were conceived and conducted during rainy season of 2014, by adopting natural trees of different varieties and equipping them with certain low-cost alternative simple gauging setups to record daily magnitudes of stemflows, throughfalls and rainfalls. Two diverse sites were earmarked at newly developed College of Agricultural Engineering and Technology (CAET) Godhra in Gujarat, encompassing about 40 trees of 13 different types/varieties at 2 different sites. Simplified standard protocols and methodological steps were adhered, for measuring the stemflows, throughfalls, and actual rainfalls during active monsoon. Canopy interception (daily) was determined along with stemflow, by equipping the tree barks with reused half-cut tires and flexible plastic pipes and containers beneath it. Appropriately measured tree canopy area and rainfall were utilized in computations. Preliminary results as obtained and communicated herein are indeed an effort to visualize and attempt gap filling for this mistreated hydrological component. The observed range of average values of stemflows and throughfalls was found extremely heterogeneous depending upon rainstorms as well as physiological attributes of trees (8–20 and 5–35%, respectively). Though the individual observed values of intercepted rains remained small, but their cumulative magnitudes had visible hydrological impacts (soil moisture patterns, infiltration patter, overland flows, and re-distribution of raindrops) on land surface located beneath the tree canopy. Results revealed significant influences of vegetative physiognomies on several such impacts from intercepted rainfall, owing to heterogeneous trees and their physiological architecture (canopy area, tree height, types and shape of leaves, bark/branches).

M. L. Gaur (✉) · S. Kumar
Department of Soil & Water Engineering, College of Agricultural Engineering and Technology, Anand Agricultural University, Godhra 389001, Gujarat, India
e-mail: mlgaur@yahoo.com

V. P. Singh et al. (eds.), *Hydrologic Modeling*, Water Science and Technology Library 81, https://doi.org/10.1007/978-981-10-5801-1_3

The qualitative analysis of intercepted rainwater was also performed and reported herein. Larger trees such as *azadirachta indica* (neem), *mangifera indica* (mango), tamarind (emlee), *Saraca asoca* (ashoka) showed higher interception magnitudes, even for identical rains, showing influence of their high aerodynamic roughness. The observed magnitudes and patterns of rainfall interception from this study are expected to be of vital utilities for futuristic hydrological modeling efforts in study region.

Introduction

In the field of hydrology, interception by trees/plants is deliberated essentially in view of two aspects; (1) as component of catchment water balance and (2) as element of water flow in the atmosphere-tree stand-soil system. In dynamic hydrology, the concept of interception embraces the processes ongoing within whole catchment area and includes long-term periods of precipitation as well as of water evaporation from plant surfaces, even during the periods in between rainstorms (Okonski 2007). Interception topic has been widely contemplated in textbooks (Crockford and Richardson 2000), where it is well recognized that in any natural catchment, it remains very difficult to get evaluate it. It happens because of the reason that it requires ground-observed data, which often remained a neglected area, presuming magnitude of interception as almost negligible. Under prevailing climatic change situations, such assumption could never be a wise/correct postulation, as it all together imposes high degrees of uncertainties/imbalances in hydrological processes/constituents. Hence, the rainfall interception is believed to play an important role in the water balance of catchments and plant ecosystems as whole. It is often defined as the rainwater that is retained on vegetation canopies and lost to atmosphere as water vapor (Rao 1987). Caldier (1979) and Gash et al. (1980) reported that owing to higher interception losses, there could be a reduction in water yield even up to almost a zero level after forestation. On the other hand, for Indian conditions, Rao (1987) has reported that a similar reverse impact could occur due to conversion of forest into agricultural lands. If we traverse the previous research reviews, it is evident that there exist very vague/uncertain estimates of interception losses, which remain confined and applicable to local situations only, without any potential for its wider extrapolations. Reporting all such estimates here is considered out of scope; moreover, for Indian conditions, such observations are hardly available.

Asdak (2010) reported that rainfall interception loss in the tropical rain forests remains about 11% of total rainfall and solely depended upon kind of plant. The highest levels of rainfall interception (@ 30% of total rains) are reported for natural forests, which ultimately gets re-evaporated back into the atmosphere. Variability in respect of stemflows and throughfalls was too found extremely uncertain and poorly gauged; the throughfall percentage also increases significantly with decreasing tree height in tropical forest (Horton 1938). There can be enormous reasons with which

the quantum and rates of intercepted water vary. Researchers have well demonstrated that it varies not only with forest type, but also with geographical location. But still, it remained an important factor of hydrological cycle, and majority of hydrological models demand its proper parameterization (Wang et al. 2007), which indeed remains a big challenge for hydrologists. If we visualize the physics of interception, it is quite evident that when rain falls on forest canopies, a proportion reaches the forest floor as throughfall (TF) and stemflow (SF), and the remainder is retained on canopy and subsequently evaporated. TF being part of gross rainfall (GR) drips from foliage or branches of canopy or reaches the forest floor by passing directly through tree canopies (Ahmadi et al. 2009; Rao 1987). SF too remains yet another important constituent of GR, whose volumetric magnitudes, under a tree/vegetation are greatly influenced by specific physiological attributes of trees/vegetation, namely species, crown size, leaf shape and its orientation, branch angle, and also the bark roughness (Levia and Frost 2010). Rao et al. (2012) reported certain important findings on rain interception over bamboo plants in the location nearer to present study.

There exists a plethora of review out of which only few bits are being portrayed here. Fathizadeh et al. (2013) studied hydrological balance of forest ecosystems on seasonal variability of rainfall interception and canopy storage capacity by individual trees, where interception was accounted for 84.9 mm (20%) of GR that significantly differed between the leaf (47.4 mm or 30% of GR) versus leafless (37.7 mm or 14% of GR) periods. Panwar et al. (2012) attempted a study on partitioning of rainfall and runoff measurement in *Terminalia chebula* (8 × 8 m) and *Emblica officinalis* (6 × 6 m) plantations with additional measurements on TF, SF, and canopy interception. TF was measured by placing collectors beneath tree canopy, and SF was collected by diverting water flowing through stem to a collector. Ramser's samplers were established to collect runoff water and compare runoff among 2 plantations, where it was reported that SF varied from 0.5 to 3.7% in *T. chebula* and 0.3 to 3.2% of GR in *E. officinalis*-based system. TF was reported slightly higher in *E. officinalis* (90–97.5%) as compared to *T. chebula* (86.64–97.8%). Wani and Manhas (2012) revealed some results on observations of rainfall interception in relation to the tree architecture and other features for *Pinus wallichiana* stand in Dal Lake catchment in Kashmir Himalayas, where SF (mm) was significantly influenced by tree diameter at breast height (DBH, cm), tree height (m), nature of bark, and attachment angles of lateral branches in tree height. Smooth-barked trees gave about 5% more of SF than rough-barked ones. TF was found negatively correlated with downward branching pattern. Of the total average rainfall of 66.5 mm during the course of study, TF, SF, and interception for whole tree stand were reported as 26.7, 36.3, and 36.9%, respectively. Interception percentage decreased significantly with increase in rainfall. Gurav et al. (2012) studied the partitioning of GR into TF and canopy interception loss in 2 different shade levels of Indian coffee agroforests. TF ranged from 84 to 91%, and interception loss ranged from 8.9 to 15.7% of GR in the high and low shade levels of coffee agroforestry systems. TF was reported significantly higher, and interception loss was significantly lower in high-shade-level system compared to low-shade-level

system. Alfiansyah et al. (2012) studied pattern of rainfall interception on plants/trees in a coffee plantation in Indonesia adopting 15-year-old plants of 1.5 m height 4.56-m^2 canopy area. Rainfall interception loss was determined based on water balance approach of daily rainfall, TF and SF data, followed by empirical regression equation between rainfall interception loss and rainfall to arrive a model to estimate rainfall interception loss. It was reported that coffee plants can intercept even 76% of annual rainfall. Global estimates were presented giving an interesting finding that the interception loss is responsible for evaporation of about 13% of total incoming rainfall over broadleaf evergreen forests, 19% in broadleaf deciduous forests, and 22% in needle leaf forests. Zhang et al. (2009) performed the similar studies in China, on rainfall interception loss by shrubs, and found that TF passes through crowns, adopting 73 rain events and giving canopy water storage capacities in the ranges of 0.52–0.68 mm, and free TF coefficient in between 0.47 and 0.62 for prevailing vegetation. Friesen et al. (2008) revealed canopy interception as 60% of annual rainfall.

Vegetation in tropical regions often represents a type of ecosystem that has a large influence on hydrological processes (Jetten 1996), which mostly remains a physical process, but sometimes chemical too. The trees intercept a large part of the rainfall, whose internal circulation involves the transfer of nutrients from the vegetation to the soil through the process of canopy leaching, defined as rainfall on the canopy that passes through it and reaches the soil surface by directly falling or through stemflow (Parker 1983). In these steps of internal circulation, process remains continuous and most likely involves the recycling of nutrients over rainy periods. As described by Casartelli et al. (2008), the chemistry of precipitation is a concern in developing countries, because it is an efficient mechanism of removing pollutants from the air. The majority of studies published in western parts of globe are giving importance to chemistry of precipitation looking at solute contribution to the biogeochemistry cycle in order to explain nutrient input to ecosystem. Dry and wet deposition of water on leaves can be an important nutrient source for plants and soils.

Measuring and Modeling Interception

To model the interception, three kinds of models are explained by the researchers. First the conceptual Rutter model and its revised sparse canopy version; second, the often used analytical, i.e., Gash model (original and revised sparse canopy version); finally the third one under the categories of stochastically based models. Today, interception is one of the most underestimated processes in rainfall-runoff analysis. It has often been disregarded in hydrological models because it is difficult to measure. Models that consider interceptions take it as a minor flux and either combine it with evaporation and transpiration or take it as a fixed percentage of rainfall. It is commonly accepted that interception volume is directly related to the size of the surface of the aboveground plant part. In earlier studies, there were

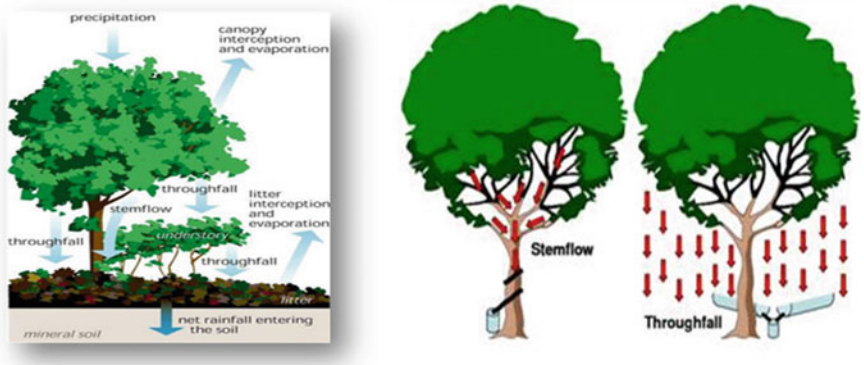

Fig. 1 Conceptual process framework of interception losses

efforts undertaken to describe tree surface area based on its similarity to other tree or stand biometric features. Telkehaimanot et al. (1991) had assumed a linear relationship between interception and number of trees per hectare. At the present time, in the majority of the studies on interception, the crown area is determined with the use of leaf area index, and it is later regressed/correlated with interception magnitudes. There have been certain base models too that amply describe the interception volume. Same could be generally divided into two main groups: (1) based on physical features of the process of water interception by tree canopy (Rutter et al. 1971; Gash 1979; Gash et al. 1980) and further modified and (2) regression equations of purely academic character or further founded on natural determinants (Horton 1938; Calder 1986). The Sacramento model, for instance, combines interception with the upper soil's tension water volume. Disregarding or lumping up interception with other processes introduces errors in hydrological modeling. Researchers have many a time revealed that evaporation of intercepted precipitation merely replaced transpiration, and that interception does not need to be considered as an additional 'loss' separate from transpiration (Gaurav et al. 2012; Gash et al. 1995; Hormann et al. 1996 and Yoshida et al. 1996) . A broad simplistic conceptual process framework of interception losses is depicted in Fig. 1, which is kept in focus taking timescale of interception as short, ending within hours after rainfall. A study carried out by Owens et al. (2005) revealed that 35% of the bulk rainfall falling on Juniper trees can be intercepted by tree canopy.

Material and Method

Description of Study Area

The study was performed in CAET campus Godhra (latitude 22.50N; longitude 73.40E; MSL 121 m) and its experimental research farm Kakanpur (latitude 22.50;

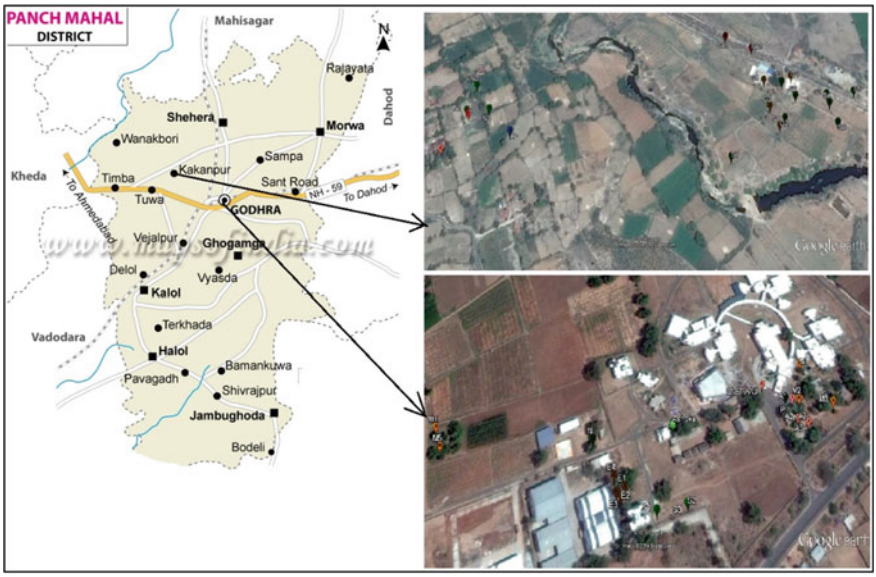

Fig. 2 Geographical and location details of study area as well as identified trees there in

longitude 73.30E; MSL 70 m). The representative geographical details of study sites are illustrated in Fig. 2, where the spatial distribution of identified trees as adopted in the study is reflected. The detailed information of location of trees was earmarked with GPS to depict about 40 natural trees as adopted in this study.

Measuring Physiological Attributes of Trees Under Study

A large number of natural trees (7 nos at CAET, Godhra, and 8 nos at Instruction Farm CAET, Kakanpur) were identified and adopted in this study, which were having tremendous variations in their physiological attributes. A condensed pictorial scenario of these trees is illustrated in Fig. 3, incorporating their spatial configurations and standard botanical nomenclature as well. Height measurement of trees under study at two specific sites was performed by using tangent clinometers, levels, and levelling staff/measuring taps. Canopy area of the trees was determined by number of canopy diameter measurements using measure tap and vertical ranging rods simultaneously. Crown projection area (CPA) was estimated for individual trees which were later utilized for calculation of the SF equivalent depth. The standard method of measuring the CPA is to surface (Delphis and Levia 2004). The corresponding SF depth of each selected tree was measured by dividing the collected SF volume by the CPA. Finally, the SF depths of the 9 selected trees were averaged to determine the mean SF depth for each event.

Fig. 3 Physiological look of representative trees as adopted for observing rainfall interception at two different sites. (*words in parenthesis are botanical name*) (location of trees 1–7 @ CAET Godhra Campus; 8–15 @ Kakanpur Farm of CAET)

Measuring Interception Components

Measuring the interception components like SF and TF needed a thorough effort to adjudge the best suitable simpler means where some of the innovative options were evolved, and accordingly, measuring systems were fabricated and installed on pre-identified trees at two specific study sites. Low-cost-used materials like worn-out tubes/tires and used containers/plastic canes and tubes were procured and suitably utilized in the study, after their need-based fabrication/assemble for the intended purpose. The structural configurations of these setups were made extremely simple (Fig. 3), where the magnitudes of rainfall, stemflows, and throughfalls were computed by having a regular observation on important rainy days at fixed point of time (8–8.30 am). The stemflows stored inside the plastic canes were suitably measured in its volumetric units and later converted to depths by using the measured dimensions of projected tree canopy areas of individual trees. Similarly, the measurements for throughfalls were conducted by placing the tin containers in different quadrants beneath the trees and measuring TF volumes periodically. The materials utilized for fabrication of interception measuring complements included plastic sheets, trays, tubes, cans, nonrecording rain gauges, and other sampling means. The observations from standard recording type rain gauge as well as automatic weather station (installed at CAET Godhra and Kakanpur farm) were too utilized for the purpose.

To analyze the qualitative attributes of intercepted rainwater in contrast to nonintercepted water, standard methods were adopted while collecting and conducting analysis of the water samples. Digital oven dryer, digital weighing balance, measuring cylinders, glass beaker/stick bold marker, digital PH conductivity, temperature meter, and other facilities in water quality laboratory were suitably used to obtain certain basic attributes. Parameters like pH and total solids for intercepted and nonintercepted rainwater were worked out utilizing pH meter and water sample oven drying/weighing, respectively. Similarly, dissolved oxygen too was evaluated for above-cited two groups of sampled rainwater.

The gross precipitation was measured in the open field, away from canopy influences. SF was measured by an open flap of tire wrapped around the trunk of tree, and nails are placed outside of wrapped flap of tire with the help of hammer and to control leakage water by M-seal and pipe placed into gallon. During rainfall, the SF was stored into wrapped flap and delivered water into gallon through pipe, which could be later measured volumetrically. Measuring TF was a bit difficult because the canopy of various trees was not homogeneous, but it was attempted by placing number of containers (fixed cross-sectional area) under canopies.

Result and Discussion

Rainfall

Though there observed a plethora of rainfall records at both the study sites, the number of rainy events during the year of study were remained extremely limited. Out of those, only 10 storms with maximum possible common dates were identified with sizeable observed rainfall at both the study sites, and looking into accomplishment of feasible observations in regard to stemflows, throughfalls, and other sampling on said dates. The observed 24-h precipitation on these dates for both the study sites is illustrated in Table 1. Results show that range of observed rainfall depths across 18 different storms was varying in the range of 2.8–37.0 mm with sizeable differences at 2 study sites even on similar dates. Owing to various field limitations/constraints, the storm size and data ranges remain a bit small, but generated and used in best possible manner.

Quantitative Variations in Interception Components

The quantitative variations in net interception values were highly heterogamous and did not have any set trends. The values were influenced by many parameters including tree physiology as well as the prevailing storm characteristics. These values were arrived after measuring the components like throughfalls and the stemflows on various trees as adopted in this study. In all about 40 trees were identified out of which observations could be feasible on 38, across August and September months of 2014 active monsoon period. The in-depth description in regard to observed values and their trends is summarized in below given paragraphs:

Throughfall Values: The preliminary analysis of observed records revealed that the throughfall values were changing a lot depending upon the integrated effects of plant physiological parameters as well as input rainwater values. In general, the values of throughfall were ranging from two in all sets of conditions at Godhra campus. The stemflow in mango trees was significant and was in the range of 0.15–3.75%, which could be having further scope of refinement. The similar values of stemflows in almond trees were in the range of 0.05–0.78% of rain. The values in regard to eucalyptus were in the range of 1.57–13.76%, which is of special significance to depict the role of tree architecture. The values of stemflows in sahjan tree were in between 0.41 and 2.51 and in neem trees 0.03 and 0.33% which is of very interesting to reflect partitioning factors of rains, may be specific density pattern of leaves and branches. In Peepal trees, it was 0.32–2.12%, while in ashoka trees it was 0.21–2.4%. The date-wise as well as tree-wise variability of TF for CAET, Godhra, as well as Kakanpur site is illustrated in Fig. 4, which is self-speaking in its contents.

Table 1 Observed values of daily rainfall at two study sites

Storm dates/study sites	Observed values of 24-h rainfall in mm on different dates at 2 sites									
	18.08.2014	24.08.2014	26.08.2014	27.08.2014	30.08.2014	31.08.2014	1.09.2014	2.09.2014	5.09.2014	8.09.2014
CAET Godhra (18 trees)	–	11.4	26.0	6.2	29.4	23.2	10.4	12.0	16.2	–
Kakanpur farm (20 trees)	4.4	10.4	2.8	28.0	29.4	23.2	12.0	4.0	28.0	37.0

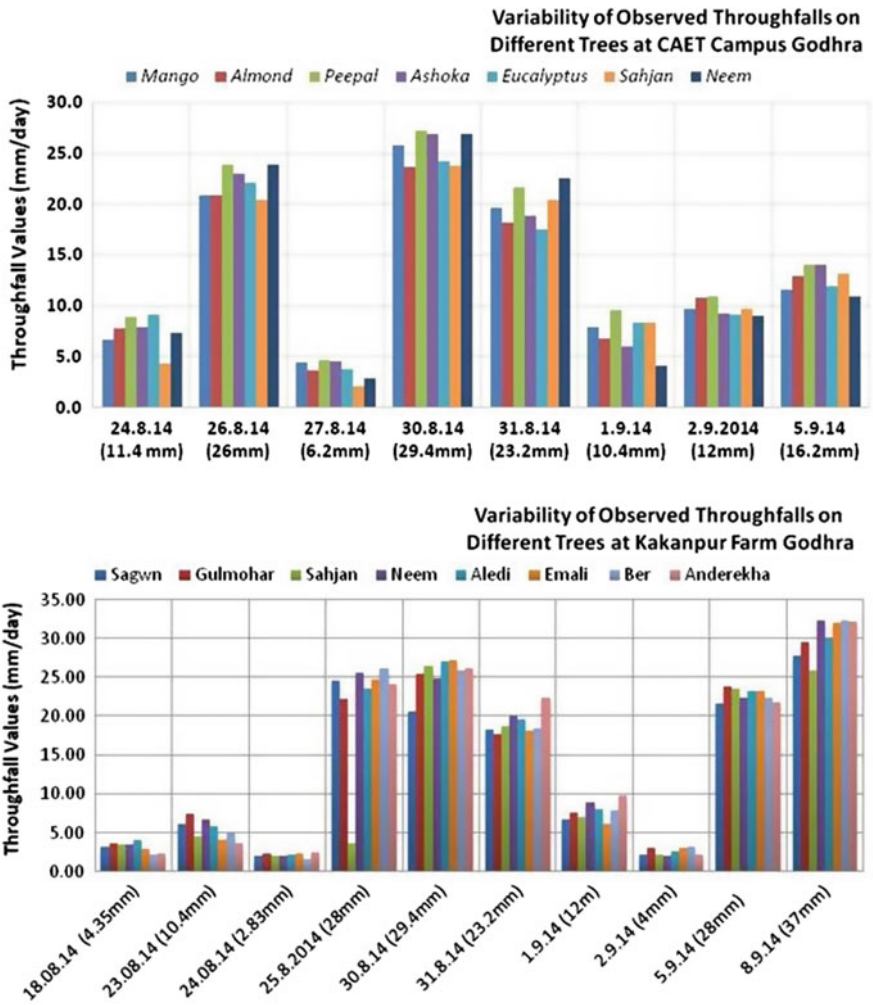

Fig. 4 Variability of observed throughfalls on different trees at two study sites

Stemflow Values: For CAET, Godhra site, the composite range of SF magnitudes across various trees as well as period of observation was found to vary between 0.5 and 7% depending upon the prevailing combinations of settings. Eucalyptus, Ashoka, and Mango trees gave higher magnitudes of stemflows in comparison to other trees. It indirectly reflected reduced interception losses on these trees when compare to other trees under study area. For Kakanpur site, the composite range of SF magnitudes across various trees as well as period of observation was found to vary between 0.1 and 8.5% depending upon the prevailing combinations of settings. sagwan, sahjan, and neem trees gave higher magnitudes of throughfalls in comparison to other trees. It was due to the higher density of leaves with closed

overlapping to offer larger surface catchments for catching raindrops. It indirectly reflected reduced interception losses on these trees when compare to other trees under study area. The date-wise as well as tree-wise variability of SF at both the study sites is illustrated in Fig. 5, which is self-speaking in its contents.

Net Interception Values: At Godhra site, the interception components were observed on 18 trees (Mango-5, Almond-3, Peepal-1, Ashoka-1, Eucalyptus-4, sahjan-3, and Neem-1). Results revealed that magnitudes of daily interception

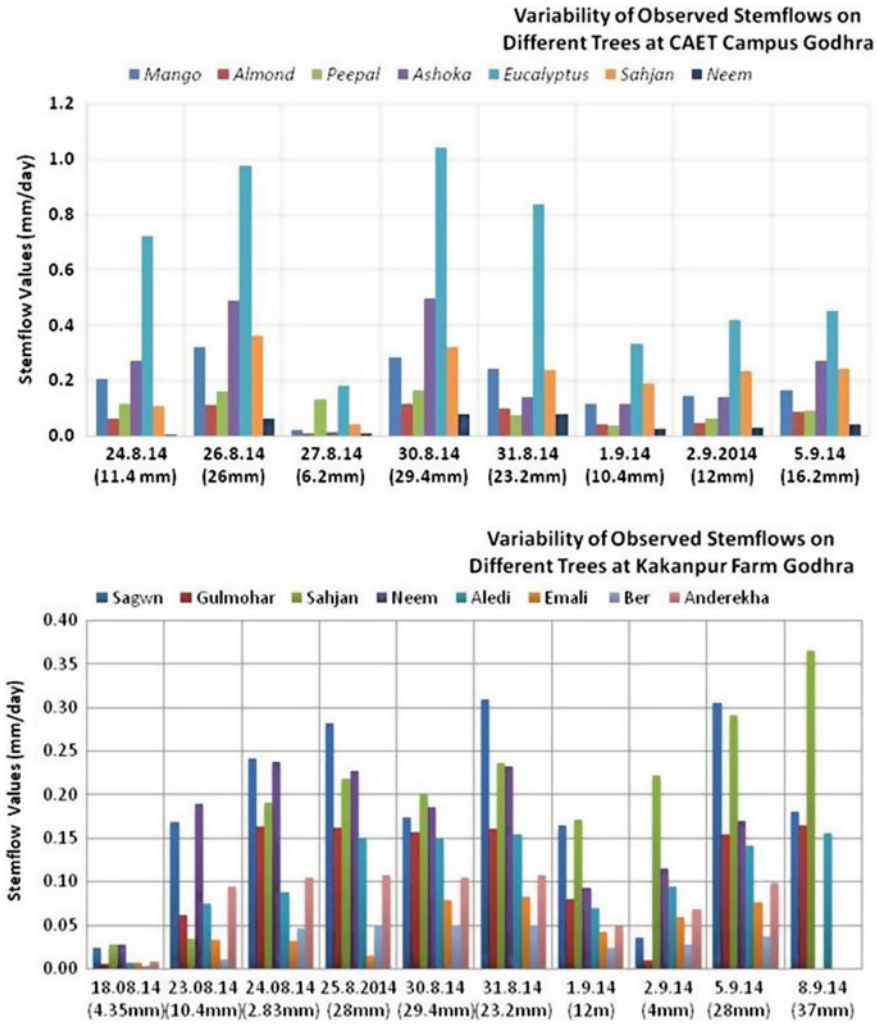

Fig. 5 Variability of observed stemflows on different trees at two study sites

values varied widely across the types of trees with significant influences of input rainfall. On mango trees, it varied in the range of 1.1–6.8 mm per day while facing storms in the ranges/magnitudes. Similar ranges of values for Almond, Peepal, Ashoka, Eucalyptus, sahjan, and Neem were found as 0.4–7.1, 0.8–2.3, 1.6–4.3, 0.6–8.6, 1.0–9.6 mm, respectively. The net magnitudes of so arrived interception values were having multiple influences from tree physiological constituents as well as storm characteristics. The variations in regard to total interception values worked out for various trees at Godhra campus were found in the range of 3.36 to as high as 60% of input rainfall values. It was highly depended upon the magnitude of rainfall and its temporal spread in particular the earlier day rains and later on the basis of plant physiological architecture at specific location under study. Similarly for Kakanpur experimental farm location, the interception components were observed on 20 trees (sagwan-7, Gulmohar-4, sahjan-2, Neem-3, aledi-1, emali-1, ber-1, anderekha-1). Results revealed that magnitudes of daily interception values varied widely across the types of trees with significant influences of input rainfall. On mango trees, it varied in the range of 1.1–6.8 mm per day while facing storms in the ranges/magnitudes. Similar ranges of value for sagwan, Gulmohar, sahjan, Neem, aledi, emali, ber, and anderekha were found as 0.2–8.9, 02–6.9, 0.2–7.7, 0.1–6.9, 0.3–6.9, 0.8–6.5, and 0.7–7.7 mm, respectively. The net magnitudes of so arrived interception values were having multiple influences from tree physiological constituents and storm characteristics.

Qualitative Variations in Intercepted Water

Some of the important quality parameters/indicators of intercepted rainfall were judged to reveal variations in pH, appearance, dissolved oxygen, and total solids. An interesting fact was observed while evaluating the pH values of samples of direct rainfall, and the intercepted and throughfall part of rainwater. By coming in contact with stems, barks, and leaves, the pH of water was significantly altered and increased even up to 25–30% of normal values as in original rainwater. These variations were found to get significantly influenced by types and varieties of trees whose external and internal physiological architectures were different as depicted in various pictorial illustrations (Fig. 6). Intercepted rainwater continuously travelled over or along leaves and tree bark till it reaches either to ground or back to atmosphere. Chemistry of intercepted precipitation used to be an efficient mechanism of removing pollutants from the air and its transportation toward soil surface or soil columns too.

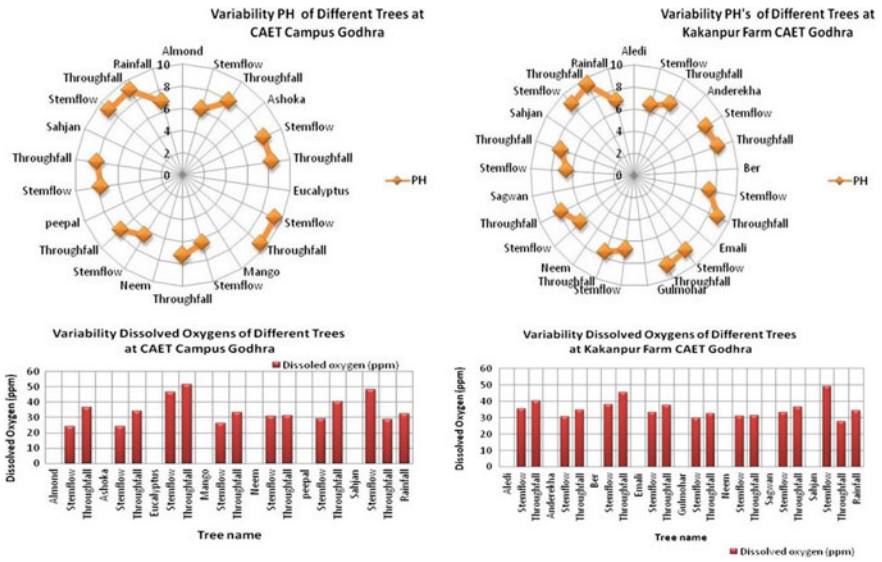

Fig. 6 Variability of pH and dissolved oxygen in intercepted rainwater for different trees

Conclusions

The process of interception by vegetation is an important factor in hydrological models, but very fewer efforts are made for its reliable quantitative estimations. Hydrological models could provide more accurate results if this important gap of hydrological observation is fulfilled by putting realistic data for the region under study. The present study was a preliminary effort and performed at two locations in middle Gujarat region of western India by encompassing about 38 natural trees and observing rainfall and its interception components using 10 natural storms as observed during active monsoon in 2014. Types and species of trees were identified and earmarked for observing the magnitudes of stemflows, throughfalls, and at last the interception values on daily basis for 10 daily events. The trees at Godhra campus were Mango, Almond, sahjan, Neem, Ashoka, Peepal, and Eucalyptus, while at Kakanpur these were aledi, anderekha, sagwan, ber, emali, Neem, Gulmohar, and sahjan. Magnitudes of daily interception values varied widely across the types of trees with significant influences of input rainfall. On mango trees, it varied in the range of 1.1–6.8 mm per day, while for sagwan, gulmohar, sahjan, neem, aledi, emali, ber, and anderekha trees, these were found as 0.2–8.9, 02–6.9, 0.2–7.7, 0.1–6.9, 0.3–6.9, 0.8–6.5, and 0.7–7.7 mm, respectively. Although the collected data and its results are only from one short season with thin records, still these preliminary findings provided certain logical ranges of values to unfold this undiscovered part of hydrological cycle in the region. Futuristic studies will supplement these observations and could yield better local estimates for improving

modeling framework on rainfall-runoff studies, provoking researchers to lay line of sight toward this important hydrological parameter. Results from this preliminary study, visualized 'Leaf Area' as one of the most dominating variable to influence magnitude & intensities of rainfall interceptions. Present benchmark information was generated during active monsoon period, and it might be further researched & refined for its futuristic extension in similar neighbourhood.

References

Ahmadi MT, Attarod, P, Marvi-Mohadjer MR, Rahmani R, Fathi J (2009) Partitioning rainfall into throughfall, stemflow and interception loss in an oriental beech (fagus orientalis lipsky) forest during the growing season. Turk J Agric 33:557–568

Alfiansyah Y, Rizalihadi MBC, Benara R (2012) Preliminary study on rainfall interception loss and water yield analysis on Arabica coffee plants in central Aceh regency, Indonesia. Aceh Int J Sci and Technol 1(3):94–97. ISSN:2088-9860

Asdak C (2010) Hydrology and watershed management. Gadjah Mada University Press, Yogyakarta (The fifth print (revision)

Calder IR (1986) A stochastic model of rainfall interception. J Hydrol 89:65–71

Caldier IR (1979) Do trees use more water than grass? Water Serv 83:11–14

Casartelli MR, Mirlean N, Peralba MC Barrionuevo S, Gomezrey MX, Madeira M (2008) An assessment of the chemical composition of precipitation and throughfall in rural-industrial gradient in wet subtropics (southern Brazil). Environ Monit Assess 144:105–116. http://dx.doi.org/10.1007/s10661-007-9949-y

Crockford RH, Richardson DP (2000) Partitioning of rainfall into throughfall, stemflow and interception: effect of forest type, ground cover and climate. Hydrol Process 14:2903–2920

Edwards KA, Classen GA, Schroten EHJ (1983) The water resource in tropical Africa and its exploitation. ILCA research report No. 6. International Livestock Centre for Africa

Fathizadeh1 O, Attarod P, Pypker TG, Darvishsefat1 AA, Zahedi Amiri G (2013) Seasonal variability of rainfall interception and canopy storage capacity measured under individual oak (quercus brantii) trees in Western Iran. J Agri Sci Tech 15:175–188

Friesen J, van Beek C, Selker J, Savenije HHG, van de Giesen N (2008) Tree rainfall interception measured by stem compression. Water Resour 44:W00D15. doi:10.1029/2008WR007074

Gash JHC (1979) An analytical model of rainfall interception by forests. Quarter J R Meteorol Soc 105:43–55

Gash JHC, Wright IR, Llyod CR (1980) Comparative estimates of interception loss from three coniferous forests in Great Britain. J Hydrol 48:89–105

Gash JHC, Lloyd CR, Lauchaud G (1995) Estimation sparse forest rainfall interception with an analytical model. J Hydrol 170:79–86

Gaurav M, Sachin Kumar MD, Kushalappa CG, Vaast P (2012) Throughfall and interception loss in relation to different canopy levels of coffee agroforestry systems. Int J Environ Sci 1(3):145–149

Hormann G, Branding A, Clemen T, Herbst M, Hinrichs A, Thamm F (1996) Calculation and simulation of wind controlled canopy interception loss of a beech forest in Northern Germany. Agric Forest Meteorol 79:131–148

Horton RI (1938) Interpretation and application of runoff plot experiments with reference to soil erosion problems. J Soil Sci Soc Am Proc 3:340–349

Jetten VG (1996) Interception of tropical rain forest performance of a canopy water balance model. Hydrol Process 10:671–685. http://dx.doi.org/10.1002/(SICI)1099-1085(199605)10:5

Levia DF, Frost EE (2010) A review and evaluation of stemflow literature in the hydrologic and biogeochemical cycles of forested and agricultural ecosystems. J Hydrol 274:1–29

Okonski B (2007) Hydrological response to land use changes in central European lowland forest catchments. J Environ Eng Landscape Manag 15(1):3–13

Owens MK, Lyons RK, Alejandro CL (2005) Rainfall partitioning within semiarid Juniper communities: effects of event size and canopy cover. Wiley, New York

Panwar P, Bhatt VK, Pal S, Prasad R (2012) Rainfall interception and runoff in *Terminalia, Chebula* and *Embilica Officinalis* based system in sandy-loam soils of lower Himalayas. Central Soil and Water Conservation Research and Training Institute Research Center, Chandigarh-160019, India

Parker GG (1983) Throughfall and stemflow in forest nutrient cycle. Adv Ecol Res 13:55–133. http://dx.doi.org/10.1016/S0065-2504(08)60108-7

Rao AS (1987) Interception losses of rainfall from cashew trees. J Hydrol 90:293–301

Rao BK, Kurothe RS, Pande VC, Kumar G (2012) Throughfall and stemflow measurement in bamboo (*Dendrocalmus strictus*) plantation Indian. J Soil Conserv 40(1):60–64

Rutter AJ, Kershaw KA, Robins PC, Morton AJ (1971) A predictive model of rainfall interception in forests. I. Derivation of the model and comparison with observations in a plantation of Corsican pine. Agric Meteorol 9:367–384

Telkehaimanot Z, Jarvis PG, Ledger DC (1991) Rainfall interception and boundary layer conductance in relation to tree spacing. J Hydrol 123:261–278

Wang A, Diao Y, Pei T, Jin C, Zhu J (2007) A semi-theoretical model of canopy rainfall interception for a broad-leaved tree. Hydrol Process 21(18):2458–2463

Wani MA, Manhas RK (2012) Rainfall interception in relation to the tree architecture of *Pinus wallichiana*. Curr Sci 103(7):821–827

Yoshida H, Hashino, M, Kajita H (1996) A simple method for estimating rainfall interception loss by linear regression model. Ann Proc J Jpn Soc Hydrol Water Resour, 112–113

Zhang Z, Li XR, Dong XJ, Jia XH, He MZ, Tan, HJ (2009) Rainfall interception by sand-stabilizing shrubs related to crown structure. Sci Cold Arid Reg 1(2):0107–0119

Probabilistic Estimation of Design Daily Runoff from Bamhani Watershed, India

Sarita Gajbhiye Meshram and Vijay P. Singh

Abstract Exact estimation of runoff is very important task in physiographic unit and watershed management (Gajbhiye et al. Int J u- e-Serv Sci Technol 7(6):47–60 2014; Gajbhiye. Int J u- e-Serv Sci Technol 8(2):11–24 2015a, Int J u- e-Serv Sci Technol 8(4):118–122 b). For the design of surface runoff storage system, probabilistic estimation of 1-day maximum runoff is essential for safe and cost effective planning. In this study, 1-day and consecutive 2 and 3 day maximum runoff from Bamhani Watershed, Madhya Pradesh (India) were computed. Daily runoff was estimated using SCS-CN model for a 200 year return period. Moreover, 1, 2, and 3-day maximum runoff was fitted with 3 probability distributions (i.e. log normal, log Pearson type III and Gumbel). The goodness of fit test (chi square) revealed that the log-Pearson type III distribution is the best fit distribution for the 1, 2 and 3 day maximum runoff from Bamhani watershed.

Keywords Daily rainfall · Runoff · Probabilistic estimation · SCS-CN model Watershed

Introduction

Soil erosion can be control by the management techniques of the watershed management planning in the catchment area (Gajbhiye et al. 2015; Sharma et al. 2014). Sediment and runoff are the two important hydrologic responses from the rainfall events occurring in the watershed (Gajbhiye et al. 2014). Rainfall generated runoff

S. G. Meshram (✉)
Department of Water Resources Development and Management,
Indian Institute of Technology Roorkee, Roorkee 247667, Uttarakhand, India
e-mail: gajbhiyesarita@gmail.com

V. P. Singh
Department of Biological and Agricultural Engineering and Zachry Department
of Civil Engineering, Texas A&M University, College Station, TX 77843-2117, USA
e-mail: vsingh@tamu.edu

V. P. Singh et al. (eds.), *Hydrologic Modeling*, Water Science
and Technology Library 81, https://doi.org/10.1007/978-981-10-5801-1_4

from a watershed is an important input for design of hydraulic structures and erosion control measures. The need for accurate information on watershed runoff have grown rapidly during the past decades because of the acceleration of watershed management programs for conservation, development, and beneficial use of all natural resources, including soil and water (Gajbhiye and Mishra 2012; Mishra et al. 2013; Gajbhiye et al. 2014a, b). On a long term basis, the change in runoff volume and its time distribution indicates dynamic changes occurring in a watershed (Deshmukh et al. 2013). The SCS-CN method computes the surface runoff volume for a given rainfall event from small agricultural, forest, and urban watersheds (SCS 1956, 1985). Rainfall is a stochastic variable and a large amount of annual rainfall data is needed for its depth duration frequency analysis. Higher the rainfall less often it occurs. Higher the recurrence interval, higher the design rainfall implying more costly project with less risk of failure. One day maximum rainfall values are of great importance for design of hydraulic structure. In the present study probability analysis of one to three consecutive days' maximum annual rainfall for different return periods is attempted to select the best probability distribution for design of hydraulic structures for the watershed.

Probability analysis is the most reliable method to predict the occurrence of future rainfall events based on the past behavior of rainfall. Analysis of one day rainfall has been carried out for different place by many researchers (Dhar and Kulkarni 1973; Ferdows et al. 2005; Patle 2008; Yadav and Saxena 2014; Sharma and Singh 2010; Nemichandrapp et al. 2010; Mayooran and Laheetharan 2014; Manikandan et al. 2015; Vivekanandan 2015; Bora and Choudhry 2015; Krishnamurthy et al. 2015) by using different probability distribution viz, Gumbel, Log normal and Log Pearson type-III.

The Soil Conservation Service (SCS) curve number (CN) method has gained general acceptance in engineering practice due to its simplicity in estimating storm water runoff depth from rainfall depth and it is supported by the United States Department of Agriculture (USDA). Originally developed from daily rainfall data from small agricultural watersheds in the Midwestern United States (Mockus 1949; Rallison 1980), this method was first introduced in 1954 (NRCS 2001). The CN method continues to be updated and amended with increasing data and research (Mishra and Singh 1999a, b; Jain et al. 2006; Gajbhiye et al. 2013), as well as innovative applications such as water quality modelling (Mishra and Singh 2003) and continuous simulations (Williams and LaSeur 1976; Hawkins 1973, 1978; Arnold et al. 1990; Mishra and Singh 2004; and others).

Biswas and Khambete (1989) computed the lowest amount of rainfall for different probability levels by fitting the gamma probability distribution to week by week total rainfall of 82 stations in a dry farming tract of Maharashtra. Lin et al. (1993) stated that in accordance with the probability distribution all stations in the same area can be classified indifferent clusters and special characteristic among clusters can have spatial relationship to a certain extent in that cluster. Chapman (1994) evaluated five daily rainfall generating models with several methods and analyzed that Srikanthan-McMahon model performed well when calibrated with long rainfall records. Duan et al. (1995) suggested that for modeling daily rainfall

amounts, the Weibull and to a lesser extent the exponential distribution were suitable. Upadhaya and Singh (1998) stated that it is possible to predict rain fall fairly accurate using various probability distributions for certain returns periods although rainfall varies with space and time and have erratic nature. Sen and Eljadid (1999) reported that for monthly rainfall in arid regions the gamma probability distribution is best fit. Ogunlela (2001) evaluated that the log-pearson type III distribution best describes the stochastic characteristics of peak daily rainfall. Tao et al. (2002) recommended the generalized extreme value model as the most suitable distribution after a systematic assessment procedure for representing extreme-values and its relatively simple method of parameter estimation. Topaloglu (2002) reported that the Gumbel probability model estimated by the method of moments and evaluated by chi-square tests was found to be the best model in the Seyhan River basin. Salami (2004) analyzed meteorological data for Texas and found that the Gumbel distribution fitted adequately both evaporation and temperature data, while for precipitation data log-Pearson type III distribution was more accurate. Lee (2005) indicated that log-Pearson type III distribution fitted 50% of the stations for the rainfall distribution characteristics of Chia-Nan plain area.

Bhakar et al. (2006) analyzed frequencies of peak rainfall of consecutive days at Banswara, Rajasthan, India, and found the gamma distribution as the best fit amongst all the distributions tested by the Chi-square value. Deidda and Puliga (2006) found for left-censored records of Sardinia that some weaknesses were evident for the generalized Pareto distribution. Kwaku et al. (2007) observed that the log-normal distribution was the best fitted probability distribution for one to five consecutive day maximum rainfall for Accra, Ghana. Hanson et al. (2008) indicated that the Pearson type III distribution fitted the full record of daily precipitation data and the Kappa distribution best described the observed distribution of wet-day daily rainfall. Olofintoye et al. (2009) found that 50% of the stations in Nigeria followed the log-Pearson type III distribution for peak daily rainfall, while 40 and 10% of the stations followed the Pearson type III and log-Gumbel distributions respectively. From the above discussion, it can be concluded that generally the Log-Pearson/Pearson type III distribution fits the data tested by Chi-square test.

Study Area

River Banjar is a tributary of River Narmada and its catchment is geographically located in Mandla district between 21°65′55″N and 22°29′00″N Latitudes and 80°22′00″E and 81°00′00″E longitudes. The watershed covers 2542 km^2 area. It is situated in the eastern part of Madhya Pradesh. The climate of Mandla district is characterized by a hot summer and general dryness except during the south-west monsoon season. Climate can be classified as sub-tropical sub-humid with an average annual rainfall of 1178 mm. About 90% of the annual rainfall is received during the monsoon season (June–October). The estimates of evapotranspiration vary from 4 mm/day in winter to 10 mm/day in summer. The area contains of both

flat and undulating lands covered with grasses, wood and cultivated land. Soils vary from black to mixed red soils. Nearly 58% of the catchment area is covered with forest. Agricultural crops are grown in 19% area, and the remaining area comes under degraded lands and water bodies (Mishra et al. 2008).

Materials and Methods

The daily runoff data of the Bamhani watershed for the period of 10 years (2001–2010) were collected from the Central Water Commission (CWC), Bhopal, India. Daily rainfall data of Bamhani watershed for the same period (2001–2010) was collected from the Meteorological Observatory of College of Agricultural Engineering, JNKVV, Jabalpur, M.P.

Estimation of Daily Design Runoff

The estimated daily runoff from the watershed under study was used to determine one-day maximum and consecutive 2 and 3-day maximum runoff. The daily runoff data were added for consecutive two and three days and thus the maximum values of 2 and 3-day runoff for each year were computed. Data of 1-day and consecutive 2 and 3-day maximum runoff were fitted to the log normal; log pearson type III and Gumbel distributions, which are widely used for maximum runoff frequency analysis (Haan 1977). The probabilities of exceedance were calculated by the Weibull method (Chow 1964):

$$p = \frac{m}{n+1} \tag{1}$$

where, p = the probability of exceedance of maximum runoff (%), m = the number of years during the period of runoff record in which the maximum runoff equaled or exceeded, and n = total number of years of runoff record.

Computation of Runoff Curve Number

First, we arrange the P-Q series in descending order of P-magnitude and compute CN (or S) for all P-Q values (exhibiting runoff factor C (= Q/P) < 1) using the SCS-CN method and assign the cumulative probability of exceedance to each value using Weibull's plotting position. We derive the CN-values corresponding to 90, 50, and 10% probabilities of exceedance of rainfall as those for wet (ARC-I), normal (ARC-II), and dry (ARC-III) conditions, respectively. Since these values are

derived from daily P-Q data, the derived CN-values correspond to 1-d rain duration. Similarly, from the daily P-Q data, two-day and three-day P-Q data series for each year were prepared by summing the rainfall and the corresponding runoff values for respective durations. For a given wetness condition and duration, we fit a suitable frequency distribution in the annual CN-series and derive the CN-values corresponding to different return periods.

Validation of Design CN Estimates

Validation of design curve number is required so that these curve numbers can be applied for the design of hydraulic structures and erosion control measures. For a given duration, we develop an annual maximum rainfall (P)-series to determine the P-values corresponding to different return periods using the above-said frequency distribution. We compute runoff (Q) from P that corresponds to the same duration and return period and CN that corresponds to the same duration, wetness condition, and return period. It is assumed that these are computed Q-values. Similarlywe develop a Q-series for a given duration to estimate the Q-values for the above-said return periods. These values may be taken as observed for comparing with computed Q value.

The best fit probability distribution was evaluated by using the following steps.

Step I: Fitting the Probability Distribution

The probability distributions viz. log-normal, log Pearson Type III and Gumbel generalized extreme value were used to determine the best fit probability distribution for rainfall.

Frequency Factors

Frequency or probability distribution helps relate the magnitude of extreme hydrological events such as floods, droughts and heavy storms along with their number of occurrence such that their chances of occurrence with time can be predicted (Singh et al. 2012). The Chow (1951) general frequency formula was used in this study to get the observed rainfall statistically. The formula used for the evaluation of expected values or frequency of occurrence of rainfall was expressed in terms of frequency factor.

If, $X\tau$ = the expected value of event or rainfall corresponding to return period (T), then

$$X_\tau = \overline{\overline{X}} + K_\tau \sigma \tag{2}$$

where, $K\tau$ = the Frequency factor, $\overline{\overline{X}}$ = the arithmetic mean of all the rainfall values in the annual series, σ = the standard deviations, T = the return period. Equation (2) is the frequency factor equation for calculating the expected value of rainfall corresponding to return period, T.

The Frequency factor, $K\tau$ depends on the return period, T and the assumed frequency distribution and $K\tau$ can be calculated by the log normal distribution, log Pearson type-III and Gumbel distributions.

Log-Normal Distribution

For the log normal distribution, the normal values were transformed into logarithmic form that is Y = ln X, where Y is normally distributed [the value of variate X was replaced by its natural logarithm]. Here Y was the magnitude of rainfalls and X was the time in months or years.

$$X_T = X_{\text{av}} + k\sigma \tag{3}$$

where X_{av} is the mean value, and k is the frequency factor and

$$\sigma = \left[\frac{\sum (X_i - X_{\text{avg}})^2}{N-1}\right]^{1/2} \tag{4}$$

in which σ is the standard deviation and N is the sample size.

The value of k is determined considering the coefficient of skewness as zero.

Log Pearson Type III Distribution

Here, the values of variate X_T for different return periods was computed by using the following relationship:

$$\log X = \log X_{\text{avg}} + k\sigma_{\log x} \tag{5}$$

Hence,

$$X_T = \text{Antilog}\, X \tag{6}$$

where, $\log X_{\text{avg}}$ = the mean of logarithmic values of observed rainfall and $\sigma_{\log X}$ = the standard deviation of these observed rainfall values and k is the frequency factor

$$k = \frac{2}{C_s}\left[\left\{\left(Z - \frac{C_s}{6}\right)\frac{C_s}{6} + 1\right\}^3 - 1\right] \tag{7}$$

Gumbel Distribution

In the Gumbel distribution, the expected rainfall is computed by the following formula

$$X_T = X_{\text{avg}}(1 + C_v K_T) \tag{8}$$

where, X_{avg} is the mean of the observed rainfall, C_V is the coefficient of variation, and K_T is frequency factor which is calculated by the formula given by Gumbel (1958) as:

$$K_T = -\frac{\sqrt{6}}{\pi}\left\{0.5772 + \ln\left[\ln\left(\frac{T}{T-1}\right)\right]\right\} \tag{9}$$

Step II: Testing the Goodness of Fit

The goodness of fit test measures the compatibility of random sample with the theoretical probability distribution. The chi-square test was used for the selection of the best fit probability distribution. The Chi-Squared statistics is defined as

$$\chi^2 = \sum_{i=1}^{k} \frac{(O_i - E_i)^2}{E_i} \tag{10}$$

where,

O_i = observed frequency

E_i = expected frequency
'i' = number of observation (1, 2, 3,…k)

Step III: Identification of Best Fit Probability Distribution

The three goodness of fit test mentioned above were used for different datasets of the maximum rainfall. The statistic of each test was computed and tested at ($\alpha = 0.01$) level of significance. Accordingly the ranking of different probability distributions was marked from 1 to 16 based on the minimum test statistic value. The distribution holding the first rank was selected for all the three tests independently. The assessments of all the probability distribution were made on the basis of total test score obtained by combining the entire three tests. The maximum score 16 was awarded to rank first probability distribution and further less scores were awarded to the distributions having ranks more than 1, that is 2–15. Thus the total scores of the entire three tests were summarized to identify the best fit distribution on the basis of the highest score obtained.

Results and Discussions

Determination of Design Curve Numbers Using Conventional Approach

To enhance the field utility of the CN-methodology, the CN values for the three wetness conditions were derived for three durations, viz., 1, 2, and 3 days, for each year and for all the four catchments separately. For a given duration and wetness condition, the annual CN-series were derived for each catchment. Then, Log-Normal (LN), Gumbel (G), and Log-Pearson type III (LPIII) frequency distributions were employed for the derivation of design CN-values corresponding to different return periods. The results are shown in Tables 1 and 2, for example, for dry condition. Based on the minimum standard error (Table 2) of rainfall and runoff and CN < 100 (Table 1) criterion, the results of Log Pearson type III distribution were adopted. It is seen from Table 1 that, for a given return period, as duration increases, the quantum CN-value decreases, and vice versa. Alternatively for a given duration, the reverse trend is apparent with the return period. Similarly, for a given return period and duration, as wetness progresses from dry to wet, the design CN-values also increase. The last inference is consistent with the general notion that CN in the existing methodology increases as the Antecedent Runoff Condition (ARC) level changes from ARC I (dry) to ARC III (wet).

Table 1 Estimation of design 1, 2, 3-day rainfall (mm), CN, and runoff values for dry condition

Return period (year)	Rainfall (LP-III)	Curve number (CN)			Qo (LP III)	Qc (LP III)
		LP-III	G	LN		
1-Day						
2	77.20	76.34	74.79	75.39	34.62	26.94
5	120.56	81.00	82.17	80.94	62.46	70.17
10	155.83	83.03	87.06	84.00	89.76	107.20
25	208.71	84.89	93.24	87.39	138.01	162.82
50	254.71	85.93	97.83	89.65	186.83	210.81
100	306.86	86.76	102.38	91.74	249.67	264.79
200	366.11	87.43	106.91	93.69	330.42	325.67
2-Day						
2	109.05	72.85	70.9	71.56	57.15	43.95
5	139.07	78.9	80.35	78.83	84.75	81.42
10	157.69	81.54	86.61	82.92	103.58	104.92
25	180.1	82.94	94.52	87.51	127.76	129.71
50	196.12	84.27	100.38	90.61	145.97	148.83
100	211.65	85.33	106.2	93.49	164.31	166.98
200	226.85	86.18	112	96.21	182.87	184.37
3-Day						
2	115.53	68.23	65.71	66.33	63.48	40.16
5	160.23	77.14	79.16	77.04	96	79.98
10	183.98	81.11	88.06	83.31	111.9	113.65
25	208.44	84.76	99.31	90.55	126.52	144.07
50	223.38	86.8	107.66	95.56	134.33	164.45
100	236.03	88.41	115.94	100.29	140.17	182.56
200	246.85	89.72	124.2	104.84	144.52	197.95

Notation: *LP-II* Log Pearson type III, *G* Gumble, *LN* Log normal distribution, *Qo* Observed runoff, *Qc* Computed runoff

Validation of Design Curve Numbers

For validation, the above design CN-values for all three wetness conditions were used in the SCS-CN equation for the determination of design runoff from the rainfall of the same return period and duration. This design runoff termed as computed design runoff (Q-computed) was compared with the conventionally derived design runoff (termed as observed runoff, Q-observed), for the same return period, from the observed annual maximum runoff series employing the same the LP-III distribution. The computed runoff values for different return periods, durations, and wetness conditions (Table 1) are plotted against the corresponding observed design runoff in Fig. 1a–c for Bamhani watershed. Both Q-observed and Q-computed (for different wetness conditions) runoff values for different durations

Table 2 Standard error for 1,2,3-day rainfall and runoff

Return period (year)	Rainfall (mm)			Run off (mm)		
	LP-III	G	LN	LP-III	G	LN
1-Day						
2	15.23	14.26	13.81	8.70	10.98	9.87
5	18.58	24.00	17.50	11.76	18.49	13.32
10	20.72	32.42	20.54	14.25	24.97	15.78
25	23.33	43.71	23.66	17.95	33.66	19.21
50	25.21	52.3	26.16	21.14	40.28	21.46
100	27.05	60.92	28.15	24.75	46.92	24.63
200	28.87	69.58	30.20	28.82	53.59	27.57
2-Day						
2	15.07	9.38	15.05	11.05	8.21	10.99
5	17.07	15.80	17.06	13.53	13.83	13.51
10	18.24	21.34	18.26	15.04	18.67	15.10
25	19.59	28.77	19.65	16.83	25.18	17.02
50	20.51	34.43	20.60	18.08	30.12	18.39
100	21.37	40.10	21.51	19.27	35.09	19.73
200	22.19	45.80	22.37	20.42	40.08	21.05
3-Day						
2	15.69	13.38	15.19	11.79	9.29	11.03
5	18.57	22.53	18.53	14.60	15.64	14.63
10	19.98	30.42	20.62	15.83	21.13	17.04
25	21.35	41.02	23.15	16.89	28.49	20.09
50	22.16	49.08	24.96	17.44	34.09	22.36
100	22.83	57.17	26.71	17.84	39.71	24.62
200	23.38	65.30	28.43	18.14	45.35	26.90

and return periods are compared through a line of perfect fit in Fig. 2a–c for the watershed. It is seen that for a given duration, the Q-computed is generally quite close to the Q-observed for all return periods for the watershed. These design CN values can be useful in field for estimation of design flood using the unit hydrograph approach for the basins requiring storm duration of the order of 1, 2, and/or 3 days.

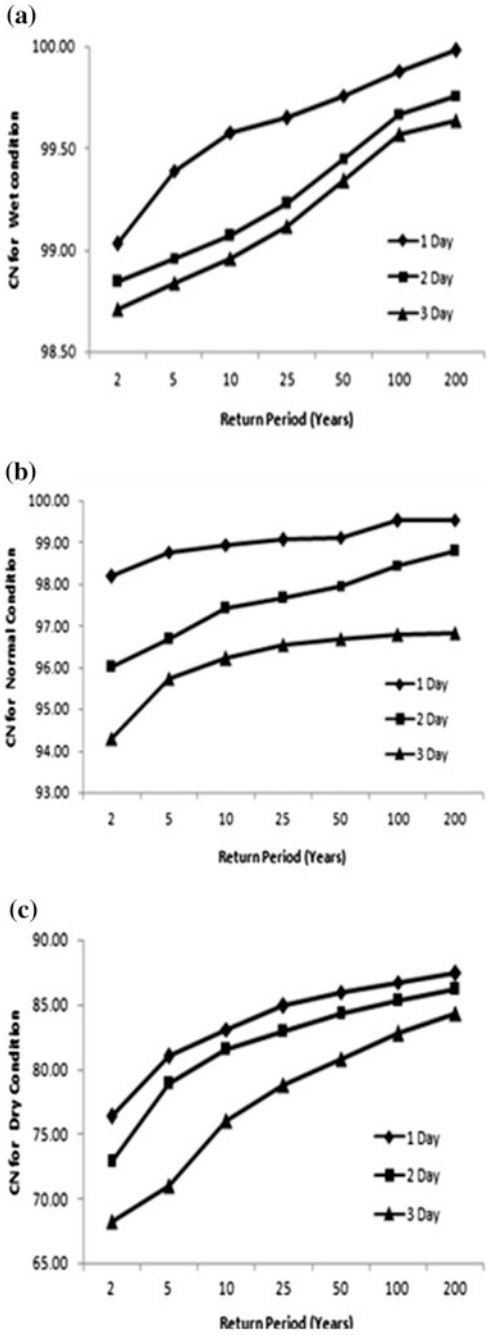

Fig. 1 Design curve number for **a** wet, **b** normal, and **c** dry condition and different return periods for Bamhani watershed

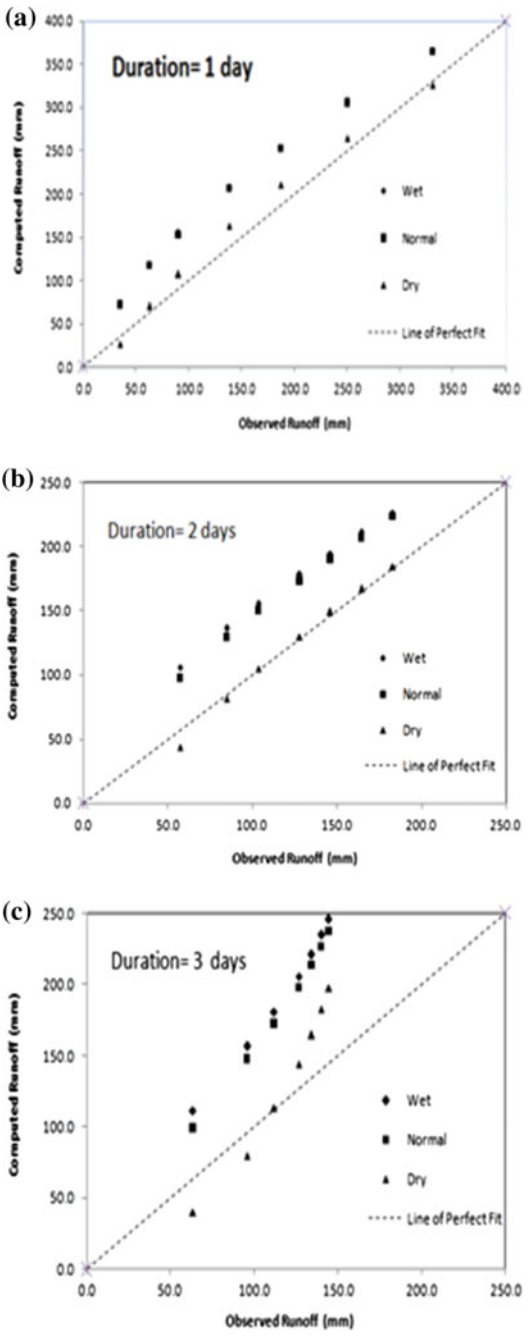

Fig. 2 Computed and observed runoff for different wetness conditions and return periods (Bamhani watershed)

Conclusion

On comparing observed and estimated runoff obtained by the SCS-CN model for Bamhani watershed, it is found that computed runoff is quite close to the observed runoff. The best fit criterion for probability distribution shows that the log Pearson type III distribution is the best fit for the estimation of one, two, and three day maximum runoff of Bamhani watershed. Finally estimates of one day and consecutive 2 and 3 day maximum runoff for the watershed are made for selected return periods. These estimates are useful for planning and designing of soil and water conservation structure in the study area.

References

Arnold JG, Williams JR, Nicks AD, Sammons NB (1990) SWRRB: a basin scale simulation model for soil and water resources management, Appendix 10. Texas A&M University Press, College Station, p 142

Bhakar SR, Bansal AK, Chhajed N, Purohit RC (2006) Frequency analysis of consecutive days maximum rainfall at Banswara, Rajasthan, India. ARPN J Eng Appl Sci 1(3):64–67

Biswas BC, Khambeta NK (1989) Distribution of short period rainfall over dry farming tract of Maharashtra. J Mah Agric Uni 12:157–168

Bora K, Choudhury P (2015) Estimation of annual maximum daily rainfall of Silchar, Assam. In: International conference on engineering trends and science and humanities (ICETSH-2015), pp 12–16

Chapman T (1994) Stochastic models for daily rainfall. National Conference Publication/The Institution of Engineers, Australia 94(15):7–12

Chow VT (1951) A generalized formula for hydrologic frequency analysis. Trans Am Geophys Union 32(2):231–237

Chow VT (1964) Handbook of applied hydrology. McGraw-Hill, New York

Deshmukh DS, Chaube UC, Hailu AE, Gudeta DA, Kassa MT (2013) Estimation and comparision of curve numbers based on dynamic land use land cover change, observed rainfall-runoff data and land slope. J Hydrol 492(7):89–101

Deidda R, Puliga M (2006) Sensitivity of goodness-of-fit statistics to rainfall data rounding off. Phys Chem Earth 31:1240–1251

Dhar ON, Kulkarni AK (1973) Monthly probabilities of intense one-day rainfall over north India. Irrig Power 30:153–156

Duan J, Sikka AK, Grant GE (1995) A comparison of stochastic models for generating daily precipitation at the H. J. Andrews experimental forest. Northwest Sci 69(4):318–329

Ferdows M, Masahiro OTA, Jahan R, Bhuiyan MNA, Hossain M (2005) Determination of probability distribution for data on rainfall and flood levels in Bangladesh. J Inst Eng Malays 66(1):61–72

Gajbhiye S, Mishra SK (2012) Application of NRSC-SCS curve number model in runoff estimation using RS and GIS. In: IEEE—international conference on advances in engineering science and management (ICAESM-2012) Nagapattinam, Tamil Nadu, March 30–31, pp 346–352

Gajbhiye S, Mishra SK, Pandey A (2013) Effect of seasonal/monthly variation on runoff Curve Number for selected watersheds of Narmada Basin. Int J Env Sci 3(6):2019–2030

Gajbhiye S, Mishra SK, Pandey A (2014a) Relationship between SCS-CN and sediment yield. Appl Water Sci 4(4):363–370

Gajbhiye S, Mishra SK, Pandey A (2014b) Hypsometric analysis of Shakkar River catchment through geographical information system. J Geol Soc India 84(2):192–196
Gajbhiye S, Sharma SK, Meshram C (2014) Prioritization of watershed through sediment yield index using RS and GIS approach. Int J u- e-Serv Sci Technol 7(6):47–60. ISSN:2005-4246
Gajbhiye S (2015a) Morphometric analysis of a Shakkar River catchment using RS and GIS. Int J u- e-Serv Sci Technol 8(2):11–24
Gajbhiye S (2015b) Estimation of surface runoff using remote sensing and geographical information system. Int J u- e-Serv Sci Technol 8(4):118–122
Gajbhiye S, Mishra SK, Pandey A (2015) Simplified sediment yield index model incorporating parameter CN. Arab J Geosci 8(4):1993–2004
Gumbel EJ (1958) Statistics of extremes. Columbia University Press, pp 375
Haan CT (1977) Statistical methods in hydrology. Affiliated East-West Press Pvt. Ltd., New Delhi
Hanson LS, Vogel R (2008) The probability distribution of daily rainfall in the United States. In: Proceedings of the world environment and water resources congress conference 2008
Hawkins RH (1973) Improved prediction of storm runoff from mountain watersheds. J Irrig Drain Div, ASCE 99(4):519–523
Hawkins RH (1978) Runoff curve numbers with varying site moisture. J Irrig Drain Div 104(4): 389–398
Jain MK, Mishra SK, Babu PS, Venugopal K, Singh VP (2006) Enhanced runoff curve number model incorporating storm duration and a nonlinear Ia-S relation. J Hydrol Eng 11(6):631–635
Krishnamurthy KN, Bhoomika RR, Gowda DM, and RajeGowda MB (2015) Fitting statistical distributions for maximum daily rainfall at GKVK station. Int J Pure Appl Res Eng Technol 3 (12):64–74
Kwaku XS, Duke O (2007) Characterization and frequency analysis of one day annual maximum and two to five consecutive days maximum rainfall of Accra, Ghana, ARPN J Eng Appl Sci 2(5):27–31
Lee C (2005) Application of rainfall frequency analysis on studying rainfall distribution characteristics of Chia-Non plain area in Southern Taiwan. J crop Environ Bioinform (2):31–38, 189 Chung Cheng Rd, Wefeng.
Lin DY, Wei LJ, Ying Z (1993) Checking the Cox model with cumulative sums of martingale-based residuals. Biometrika 80:557–572
Manikandan M, Navaneetha PV, Vinoth Kumar R (2015) Frequency analysis for assessing one day and two to seven consecutive days maximum rainfall at Coimbatore, Tamil Nadu. Life Sci Leaflets 66:34–41
Mayooran T, Laheetharan A (2014) The statistical distribution of annual maximum rainfall in Colombo district. Sri Lankan J Appl Stat 15–2:107–130
Mishra SK, Singh VP (1999a) Another look at SCS-CN method. J Hydrol Eng, ASCE 4(3): 257–264
Mishra SK, Singh VP (1999b) Behaviour of SCS-CN method in C-Ia-λ spectrum. In: International Conference Water, Environment, Ecology, Socio-economics, and Health Engineering, Korea, 18–21 October
Mishra SK, Singh VP (2003) Derivation of SCS-CN parameter S from linear Fokker Planck equation. Acta Geophysica Polonica 51(2):180–202
Mishra SK, Singh VP (2004) Long-term hydrologic simulation based on the Soil Conservation Service curve number. Hydrol Processes 18(7):1291–1313
Mishra SK, Pandey RP, Jain MK, Singh VP (2008) A rain duration and modified AMC-dependent SCS-CN procedure for long rainfall-runoff events. Water Resour Manage 22(7):861–876
Mishra SK, Gajbhiye S, Pandey A (2013) Estimation of design runoff curve numbers for Narmada watersheds (India). J Appl Water Eng Res 1(1):69–79
Mockus V (1949) Estimation of total (peak rates of) surface runoff for individual storms, Exhibit A of Appendix B, Interim Survey Report, Grand (Neosho) River Watershed, USDA, Washington, D.C.
Nemichandrapp M, Balakrishnan AP, Senthilvel S (2010) Probability and confidence limit analysis of rainfall in Raichur region, Karnataka. J Agric Sci 23(5):737–741

NRCS (2001) Engineering field handbook. National engineering handbook, Part 650, Chapter 14, Water management (Drainage)

Ogunlela AO (2001) Storchastic analysis of rainfall events in Ilorin, Nigeria. J Agric Res Dev 1(2): 39–50

Olofintoye OO, Sule BF, Salami AW (2009) Best-fit Probability distribution model for peak daily rainfall of selected cities in Nigeria. N.Y Sci J 2(3):1–12

Patle GT (2008) Probability analysis of consecutive days annual maximum rainfall for the design of surface drains in semi-arid Maharastra. Indian J Soil Conserv 36(3):144–147

Rallison RE (1980) Origin and evolution of the SCS runoff equation, Proceedings of ASCE Irrigation and Drainage Division. Paper presented at the Symposium on Watershed Management, ASCE, New York, 2:912–924

Salami AW (2004) Prediction of the annual flow regime along Asa River using probability distribution models. AMSE Periodical, Lyon, France. Modelling C- 2004, 65(2):41–56

SCS (1956, 1985) Hydrology. National engineering handbook, Supplement A, Section 4, Chapter 10. Soil Conservation Service, USDA, Washington, D.C.

Sen Z, Eljadid AG (1999) Rainfall distribution function for Libya and rainfall prediction. Hydrol Sci J 44(5):665–680

Sharma MA, Singh JB (2010) Use of Probability Distribution in Rainfall Analysis. NY Sci J 3(9): 40–49

Sharma SK, Gajbhiye S, Nema RK, Tignath S (2014) Assessing vulnerability to soil erosion of a watershed of tons river basin in Madhya Pradesh using remote sensing and GIS. Int J Environ Res Develop 4(2):153–164

Singh B, Rajpurohit D, Vasishth A, Singh A (2012) Probability analysis for estimation of annual one day maximum rainfall of Jhalarapatan area of Rajasthan, India. Plant Arch 12(2): 1093–1100

Tao DQ, Nguyen VT, Bourque A (2002) On selection of probability distributions for representing extreme precipitations in Southern Quebec. In: Annual conference of the Canadian society for civil engineering. 5–8 June 2002, pp 1–8

Topaloglu F (2002) Determining suitable Probability Distribution models for flow and precipitation Series of the Seyhan River Basin. Turk J Agric 23:189–194

Upadhaya A, Singh SR (1998) Estimation of consecutive day's maximum rainfall by various methods and their comparison. Indian J Soil Conserv 26:193–201

Vivekanandan N (2015) Frequency analysis of annual maximum flood discharge using method of moments and maximum likelihood method of gamma and extreme value family of probability distributions. Int J Math Comput Sci 1(3):141–146

Williams JD, LaSeur WV (1976) Water yield model using SCS curve numbers. J Hydraul Div 102(9): 1241–1253

Yadav RC, Saxena SC (2014) Partial duration trend analysis for yearly rainfall and its sequential distribution: a conceptual model. Open Hydrol J 8:1–7

Part II
Evapotranspiration

Development of Generalized Higher-Order Neural Network-Based Models for Estimating Pan Evaporation

Sirisha Adamala, N. S. Raghuwanshi and Ashok Mishra

Abstract It is common practice to develop artificial neural network models using location-based single dataset for both the training and testing. Based on this procedure, the developed models may perform poorly outside the training location. Therefore, this study aims at developing generalized higher-order neural network (GHNN) models for estimating pan evaporation (E_p) using pooled climate data of different locations under four agro-ecological regions in India. The inputs for the development of GHNN models include different combinations of daily climate data such as air temperature, relative humidity, wind speed, and solar radiation. Comparisons of developed GHNNs were made with the generalized first-order neural network (GFNN) and generalized multi-linear regression (GMLR) models. It is concluded that the GHNNs along with GFNNs performed better than the GMLR models. Further, GHNNs were applied to model development and model testing locations to test the generalizing capability. The testing results suggest that the GHNN models have a good generalizing capability.

Keywords Pan evaporation · Higher-order · Generalization
Agro-ecological regions

S. Adamala
Applied Engineering Department, Vignan's Foundation for Science, Technology and Research University, Vadlamudi 522213, India
e-mail: sirisha@agfe.iitkgp.ernet.in

N. S. Raghuwanshi (✉) · A. Mishra
Agricultural and Food Engineering Department, Indian Institute of Technology (IIT), Kharagpur 721302, West Bengal, India
e-mail: nsr@agfe.iitkgp.ernet.in

A. Mishra
e-mail: amishra@agfe.iitkgp.ernet.in

V. P. Singh et al. (eds.), *Hydrologic Modeling*, Water Science and Technology Library 81, https://doi.org/10.1007/978-981-10-5801-1_5

Introduction

Accurate estimation of pan evaporation (E_p) is needed to solve various hydrological and water resources related problems. The influence of several meteorological parameters [air temperature (T_{avg}), wind speed (W_s), relative humidity (RH_{avg}), and solar radiation (S_{ra})] on E_p makes the modeling of evaporation more complex due on the nonlinear nature. To deal with the complexity and nonlinearity, the artificial neural networks (ANNs) are used in E_p modeling. Depending upon the order of synaptic operation in a hidden neuron, the ANNs are classified as either first order or higher order (second or third or *N*th) (Gupta et al. 2003). The 'first-order neural networks' or 'linear neural network (LNN)' models are synonymous to feed-forward neural network (FNN).

Han and Felker (1997) demonstrated application of ANN in estimation of E_p. The authors implemented a radial basis function (RBF) neural network to model daily soil water evaporation using RH_{avg}, T_{avg}, W_s, and soil water content data as input. Bruton et al. (2000) developed FNNs to estimate daily E_p with different combinations of rainfall, T_{avg}, RH_{avg}, S_{ra}, and W_s as input. Sudheer et al. (2002) proposed ANN models with back propagation (BP) training algorithm for the prediction of Class A pan evaporation with different combinations of climate data as input. Keskin and Terzi (2006) evaluated the potential of ANNs to estimate daily E_p from measured meteorological data viz. water temperature (T_w), T_{avg}, sunshine hours (n), S_{ra}, air pressure (P_a), RH_{avg}, and W_s. Kisi (2009) investigated the abilities of multi-layer perceptron (MLP), RBF, and generalized regression neural networks (GRNN) models to estimate daily E_p using climatic variables (T_{avg}, S_{ra}, W_s, RH_{avg}, and P_a). Moghaddamnia et al. (2009) explored the ANN and adaptive neuro-fuzzy inference system (ANFIS)-based E_p estimation methods with an aid of the Gamma test. Rahimikhoob (2009) considered the MLP models for estimating the daily E_p by using maximum and minimum air temperatures (T_{max} and T_{min}) and the extraterrestrial radiation (R_a) as input. Shirsath and Singh (2010) presented the application of ANN and multi-linear regression (MLR) models comprising of various combinations of T_{max}, T_{min}, n, W_s, maximum and minimum relative humidity (RH_{max} and RH_{min}) to estimate daily E_p.

Tabari et al. (2010) aimed to estimate daily E_p using ANN and multivariate nonlinear regression methods with varying input (T_{avg}, precipitation, S_{ra}, W_s, and RH_{avg}) combinations and various training algorithms. Shirgure and Rajput (2011) reviewed thoroughly the studies on the E_p modeling using ANNs. Shiri and Kisi (2011) illustrated the abilities of ANN, genetic programming, and ANFIS models to improve the accuracy of daily E_p estimation by using various climatic variables (T_{avg}, n, S_{ra}, W_s, and RH_{avg}). Kalifa et al. (2012) developed ANN-based models to predict the E_p from various combinations of T_w, T_{avg}, W_s, RH_{avg}, and S_{ra} as input. Kim et al. (2012) demonstrated the accuracy of two types of ANNs, i.e., MLP and co-active neuro-fuzzy inference system model for estimating the daily E_p. Kumar et al. (2012) developed ANN and ANFIS models to forecast monthly potential E_p based on four explanatory climatic factors (RH_{avg}, S_{ra}, T_{avg}, and W_s) with different

combinations. Nourani and Fard (2012) examined the potential of MLP, RBF, and Elman Network for estimating daily E_p using measured climatic (RH_{avg}, S_{ra}, T_{avg}, P_a, and W_s) data. Arunkumar and Jothiprakash (2013) developed ANN, model tree, and genetic programming-based models with varying input data (reservoir evaporation values with different lags) to predict the reservoir evaporation. Chang et al. (2013) proposed a hybrid model to estimate E_p. The hybrid model combined the BP ANNs and dynamic factor analysis. Kim et al. (2013) developed MLP, GRNN, and ANFIS-based ANNs for estimating daily E_p using T_{avg}, S_{ra}, n, and merged input combinations under lag-time patterns. Kim et al. (2014) developed soft computing models, namely MLP, self-organizing map ANN model, and gene expression programming to predict daily E_p.

All of the above-cited studies used the FNN or LNN to model E_p. These neural networks are able to extract the first-order or linear correlations that exist between inputs and the synaptic weight vectors. However, the climatic variables associated with E_p exhibit high nonlinearity during modeling and these LNN models fail to extract the complete nonlinearity that is present in the data because of the linear synaptic operation. The limitations with the existing conventional E_p methods encourage the researchers to develop higher-order neural network (HNN) network models. The HNN network is a polynomial model in which the weighted sum of the products of its input vector is passed to a computational neuron instead of just a weighted sum of its input vector, as in case of conventional ANNs. This property makes the superior performance of HNNs over other conventional ANNs. The HNNs have been widely used in various fields such as pattern recognition, financial time series forecasting. Further, the HNN models have been successfully applied in hydrology to a limited extent, e.g., characterizing soil moisture dynamics (Elshorbagy and Parasuraman 2008), forecasting river discharge (Tiwari et al. 2012), reference crop evapotranspiration estimation (Adamala et al. 2014a, b, 2015a). However, the HNNs application in E_p estimation is not yet reported.

One limitation associated with the FNN and HNN models is their lack of generalizing capability because they are applicable to data from the locations which are used in training or model development (these locations are indicated as 'model development locations'). When new location data, i.e., data from locations that were not used during the model development (these locations are represented as 'model test locations') are introduced to the developed network, the network fails to provide good performance, indicating poor generalizing capacity. This limitation can be overcome by developing generalized FNN (GFNN) and generalized (GHNN) models which perform well not only for model development locations but also for model test locations. This can be achieved by considering pooled climatic data of various locations which have properties of both spatial and altitudinal variations during model development. Therefore, this study aims to develop GHNN and GFNN models for the estimation of E_p for different agro-ecological regions (AERs) of India and to test their generalizing capabilities for both the model development and testing locations.

Materials and Methods

Study Area and Climate Data

The climatic data for this study were collected from All India Coordinated Research Project on Agro-meteorology (AICRPAM), Central Research Institute for Dryland Agriculture (CRIDA), Hyderabad, Telangana, India. Data (T_{max}, T_{min}, S_{ra}, RH_{max}, RH_{min}, W_s, and E_p) for 25 climatic stations distributed over the following four AERs: semi-arid, arid, sub-humid, and humid (Fig. 1) were collected.

Table 1 presents information related to altitude, observation periods, and statistical summary of the climate data and measured E_p for the chosen locations. The altitude of selected stations varies from 10 m above msl at Mohanpur to 1600 m

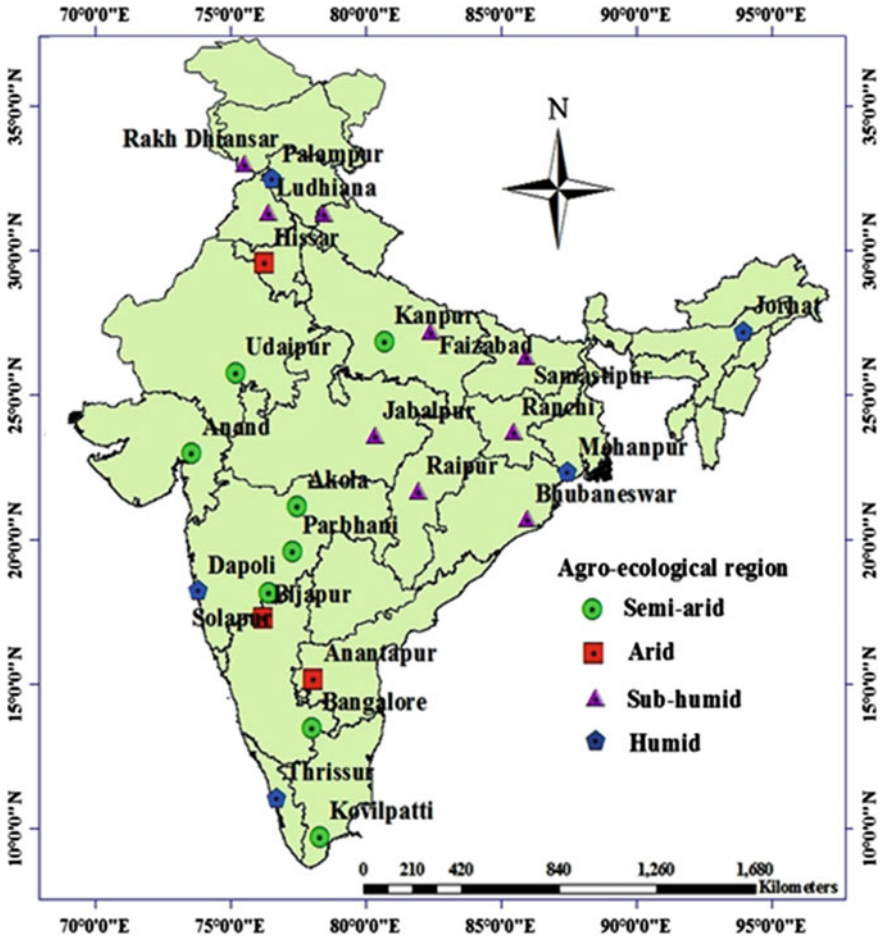

Fig. 1 Geographical locations of study sites in India

Table 1 Characteristics of daily climate data and E_p for the study locations

AER	Location	Alt. (m)	Role[a]	Period	T_{max} (°C)	T_{min} (°C)	T_{avg} (°C)	RH_{max} (%)	RH_{min} (%)	RH_{avg} (%)	W_s (km h^{-1})	S_{ra} (MJ m^{-2} day^{-1})	E_p (mm)
Semi-arid	Parbhani	423	Tr, V, Ts	2001–05	33.75	18.32	26.035	71.13	41.02	56.075	5.04	20.87	6.28
	Solapur	25	Tr, V, Ts	2001–05	34.15	20.14	27.145	73.28	45.09	59.185	6.15	18.96	7.39
	Bangalore	930	Tr, V, Ts	2001–05	28.9	17.7	23.3	89.15	47.3	68.225	8.68	18.95	5.26
	Kovilpatti	90	Tr, V, Ts	2001–05	**35.11**	23.37	29.24	80.36	48.52	64.44	6.6	19.3	6.99
	Udaipur	433	Tr, V, Ts	2001–05	31.81	16.33	24.07	72.36	36.44	54.4	3.74	19.45	5.56
	Kanpur	126	Ts	2004–05	31.5	19.04	25.27	79.59	54.08	66.835	5.6	16.95	4.78
	Anand	45	Ts	2002–05	33.66	19.73	26.695	79.74	42.23	60.985	3.62	19.86	5.73
	Akola	482	Ts	2001–03	33.93	19.88	26.905	**64.27**	37.15	50.71	8.01	**23.3**	7.14
Arid	Anantapur	350	Tr, V, Ts	2001–05	34.43	21.78	28.105	73.32	**33.91**	53.615	**9.64**	20.27	**8.38**
	Hissar	215	Tr, V, Ts	2001–05	31.17	16.23	23.7	81	44.27	62.635	5.2	17.26	5.11
	Bijapur	594	Ts	2001–04	32.32	18.98	25.65	77.91	43.73	60.82	4.26	18.97	6.96
Sub-humid	Raipur	298	Tr, V, Ts	2001–05	32.6	19.91	26.255	80.62	44.08	62.35	5.33	17.8	5.61
	Faizabad	133	Tr, V, Ts	2001–05	31.56	18.18	24.87	87.02	52.11	69.565	3.51	17.88	3.8
	Ludhiana	247	Tr, V, Ts	2001–05	30.06	17.42	23.74	83.97	49.14	66.555	4.26	18.1	4.53
	Ranichauri	**1600**	Tr, V, Ts	2001–05	**20.08**	**9.66**	14.87	81.15	61.55	71.35	4.99	16.23	2.52
	Jabalpur	393	Ts	2002–05	31.45	18.57	25.01	77.71	42.77	60.24	3.78	17.65	4.26
	Samastipur	52	Ts	2004–05	30.53	19.99	25.26	84.67	56.12	70.395	4.66	17.59	3.31
	Bhubaneshwar	25	Ts	2002–05	32.83	22.23	27.53	91.41	58.39	74.9	6.53	18.26	4.96
	Ranchi	625	Ts	2005	29.73	17.08	23.405	88.09	53.92	71.005	1.86	**3.46**	4.42
	Rakh Dhiansar	332	Ts	2005	29.1	15.4	22.25	83.46	50.02	66.74	1.76	15.68	3.58

(continued)

Table 1 (continued)

AER	Location	Alt. (m)	Role[a]	Period	T_{max} (°C)	T_{min} (°C)	T_{avg} (°C)	RH_{max} (%)	RH_{min} (%)	RH_{avg} (%)	W_s (km h^{-1})	S_{ra} (MJ m^{-2} day^{-1})	E_p (mm)
Humid	Palampur	1291	Tr, V, Ts	2001–05	24.41	13.24	18.825	69.7	57.88	63.79	5.56	16.35	3.75
	Jorhat	86	Tr, V, Ts	2001–05	27.97	19.23	23.6	92.7	**75.27**	83.985	3	14.68	**2.3**
	Mohanpur	**10**	Tr, V, Ts	2001–05	32.2	21.04	26.62	**96.18**	61.48	78.83	**1.27**	18.06	2.66
	Dapoli	250	Tr, V, Ts	2001–05	31.13	18.87	25	93.77	69.22	81.495	4.92	18.02	4.37
	Thrissur	26	Ts	2001–04	31.92	**23.38**	27.65	84.34	59.36	71.85	4.72	18	4.52

[a]*Tr* Train; *V* validation; *Ts* test

Table 2 Correlation coefficients of climate variables with E_p

AER	T_{avg}	RH_{avg}	W_s	S_{ra}
Semi-arid	0.7	−0.6	0.4	0.6
Arid	0.7	−0.6	0.4	0.5
Sub-humid	0.8	−0.7	0.4	0.7
Humid	0.3	−0.4	0.4	0.5

above msl at Ranichauri. The mean T_{min} and T_{max} range from 9.66 °C at Ranichauri to 23.38 °C at Thrissur and 20.08 °C at Ranichauri to 35.11 °C at Kovilpatti, respectively. The mean RH_{min} and RH_{max} range from 33.91% at Anantapur to 75.27% at Jorhat and 64.27% at Akola to 96.18% at Mohanpur, respectively. The mean W_s and S_{ra} range from 1.27 km h^{-1} at Mohanpur to 9.64 km h^{-1} at Anantapur and 3.46 MJ m^{-2} day^{-1} at Ranchi to 23.30 MJ m^{-2} day^{-1} at Akola, respectively. The mean E_p ranges from 2.30 mm day^{-1} at Jorhat in a humid region to 8.38 mm day^{-1} at Anantapur in an arid region.

Daily climate data (T_{avg}, RH_{avg}, W_s, and S_{ra}) of 15 locations were used to develop GHNN-based E_p models, whereas remaining 10 locations were used to test the developed models. The correlation coefficients of climatic variables with the E_p for four AERs are shown in Table 2. Among the four climatic variables, the three variables (T_{avg}, W_s, and S_{ra}) show a positive correlation and the remaining one variable (RH_{avg}) shows a negative correlation with the E_p. The degree of correlation of these climatic variables with the E_p indicates their sensitivity in estimating E_p.

Artificial Neural Network (ANN) Models

ANNs are represented as parallel distributed units with a crucial ability of learning and adaptation. The processing of information in any biological or artificial neural models involves two distinct operations: (a) synaptic operation and (b) somatic operation. In synaptic operation, different weights are assigned to each input matrix based on past experience or knowledge with an addition of bias or threshold (Fig. 2). In somatic operation, the synaptic output is applied to a nonlinear activation function (ϕ) (Tiwari et al. 2012). Mathematical representation of synaptic and somatic operations in a neural network is shown in Eqs. (1) and (2), respectively.

$$y = \sum_{i=0}^{n} w_i x_i = w_0 x_0 + w_1 x_1 + \cdots + w_n x_n \tag{1}$$

$$z = \phi[y] \tag{2}$$

where y = neural synaptic output; z = neural somatic output; w_0 = threshold weight; x_0 = constant bias (=1); x_i = neural inputs at the ith step; w_i = synaptic weights at the ith step; and ϕ = activation function (sigmoid); n = number of elements in the input vector.

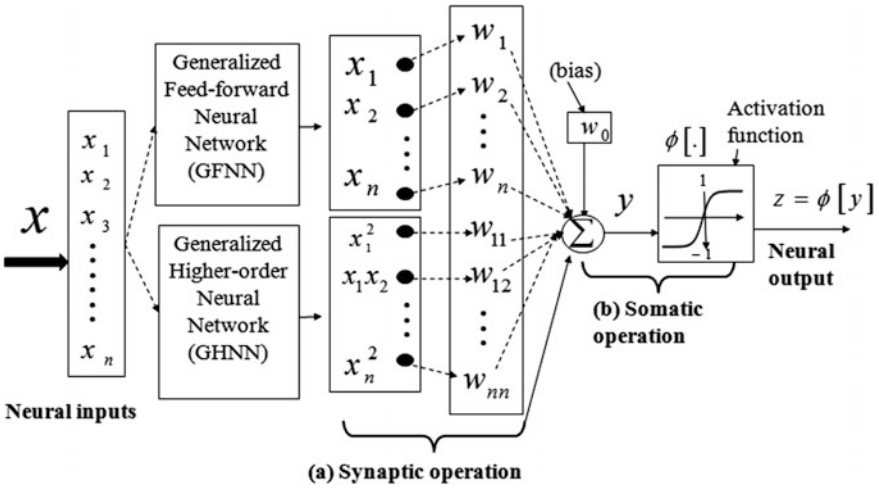

Fig. 2 Architecture of generalized synaptic neural network models (Tiwari et al. 2012)

Generalized Feed-Forward Neural Network (GFNN) Model

The GFNN model provides the neural output as a nonlinear function of the weighted linear combination of the neural inputs. In GFNN model, the synaptic operation is of the first order which means that only first-order correlations exist between the inputs and the synaptic weights of the model. Let N and n be the order and the number of inputs to the neuron, respectively. For $N = 1$, according to Redlapalli (2004) the mathematical expression of GFNN model is given as:

$$(z)_{N=1} = \phi\left(\sum_{i_1=0}^{n} w_{i_1} x_{i_1}\right) \tag{3}$$

where x_{i_1} = neural inputs at the i_1^{th} step; w_{i_1} = synaptic weights at the i_1^{th} step.

Generalized Higher-Order Neural Network (GHNN) Model

The architecture of the GHNN model is accomplished by capturing the higher-order association as well as the linear association between the elements of the input patterns. The higher-order weighted combination of the inputs will yield higher neural performance as they require fewer training passes and a smaller training set to achieve the generalization over the input domain. The synaptic operation of the GHNN embraces both the first- and second-order neural input combinations with the synaptic weights. In GHNN model, the synaptic operation in a neural unit or a

node is of the second order which means that there exists not only first order but also higher-order correlations with second-order terms between inputs and synaptic weights. For $N = 2$, the mathematical model of GHNN is represented as:

$$(z)_{N=2} = \phi\left(\sum_{i_1=0}^{n}\sum_{i_2=i_1}^{n} w_{i_1 i_2} x_{i_1} x_{i_2}\right) \tag{4}$$

where x_{i_2} = neural inputs at the i_2^{th} step; $w_{i_1 i_2}$ = synaptic weights at the $i_1 i_2^{\text{th}}$ step (Redlapalli 2004).

Data Preparation

For the development of GFNN and GHNN models for different AERs, locations having daily data for the period of 2001–2005 were chosen. The data were divided into training sets (denoted as Tr and used to adjust the weights and biases during learning), validation sets (denoted as V and used to avoid overfitting), and testing sets (denoted as Ts and used to predict with new data). The locations with 'Tr, V, Ts' role (Table 1) were used to develop GFNN and GHNN models (model development locations). These locations for the model development were selected because of the availability of a larger set of data during the study period as compared to other locations. In this study, the habitual practice of using a standard hold out strategy for dividing the data was followed as it is a very common practice in hydrological modeling (Adamala et al. 2015b). For these locations, 70 and 30% of data for the period 2001–2004 were used for training and validation, respectively. It would be more complicated to use different year of dataset for different locations. Therefore, the same 2005 year data was used for testing the performance of developed models. However, the data for the same testing (2005) year is different for the locations considering the different agro-climatic zones.

To develop GFNN and GHNN models for semi-arid, arid, sub-humid, and humid regions, respectively, the data in Table 1 were pooled as follows: (i) Parbhani, Solapur, Bangalore, Kovilpatti, and Udaipur; (ii) Anantapur and Hissar; (iii) Raipur, Faizabad, Ludhiana, and Ranichauri; and (iv) Palampur, Jorhat, Mohanpur, and Dapoli. To test the generalizing capability of the developed models (either for practical application or ….), these models were applied to data from the locations that were not used during model development. The locations with only 'Ts' role (Table 1) were used to test the generalizing capability of the developed models (model testing locations). As an example, for the locations that lie in semi-arid regions (Parbhani, Solapur, Bangalore, Kovilpatti, and Udaipur), the pooled data of 2001–2004 were used to train (including validation) the GFNN and GHNN models, while the data of 2005 were used to test these models. The generalizing capability of GFNN and GHNN models was tested using data from Kanpur, Anantapur, and Akola that were not included during development in

semi-arid region. In a similar way, different GFNN and GHNN models were developed and tested for their generalization capabilities in arid, sub-humid, and humid regions.

Criteria for Preprocessing and Estimation of Parameters

As a first step in developing GFNN and GHNN models, normalization before presenting data as input to network and denormalization after developing optimum network were performed using a Matlab built-in function called 'mapstd' which rescales data so that their mean and standard deviation become equal to 0 and 1, respectively. The inputs for developing GFNN and GHNN models were T_{avg}, RH_{avg}, S_{ra}, and W_s. This study examined eight combinations of these inputs to both models. Thus, the sensitivity of E_p on each of these variables was evaluated. The target consists of the daily values of measured E_p. Only one hidden layer was used in both the GFNN and GHNN models, as it is enough for the representation of the nonlinear relationship between climate variables and E_p. The important parameters for network training are the learning rate, which tends toward a fast, steepest-descent convergence, and the momentum, a long-range function preventing the solution from being trapped into local minima. The other parameters are activation function, error function, learning rule, and the initial weight distribution (i.e., initialization of weights). A variation in GHNN parameters had a negligible effect on the performance of these models for estimating E_p (Adamala et al. 2014b). Therefore, results concerning the model's parameters are not discussed. Sigmoidal activation function was employed in the output layer neurons. For developing GHNN-based daily E_p models, the code was written using Matlab 7.0 programming language.

Performance Evaluation

The performance evaluation of all the developed models was carried out for both the training, validation, and testing periods in order to examine their effectiveness in simulating E_p. The performance indices used for evaluating the models were: the root mean squared error (RMSE, mm day^{-1}), ratio of average output to average target E_p values (R_{ratio}), and coefficient of determination (R^2, dimensionless). A description of the aforementioned indices is provided below.

$$\text{RMSE} = \sqrt{\frac{1}{n}\sum_{i=1}^{n}(T_i - O_i)^2} \tag{8}$$

$$R^2 = \frac{\left[\sum_{i=1}^{n}\left(O_i - \overline{O}\right)\left(T_i - \overline{T}\right)\right]^2}{\sum_{i=1}^{n}\left(O_i - \overline{O}\right)^2 \sum_{i=1}^{n}\left(T_i - \overline{T}\right)^2} \tag{9}$$

$$R_{\text{ratio}} = \frac{\overline{O}}{\overline{T}} \tag{10}$$

where T_i and O_i = target (E_p) and output (E_p predictions of the GFNN and GHNN models) values at the ith step, respectively; n = number of data points; $\overline{T}$ and $\overline{O}$ = average of target and output values, respectively.

Results and Discussion

Evaporation estimation requires nonlinear mapping of different climate variables. The main advantages of using GHNN models are their flexibility and their ability to model nonlinear relationships. An important aspect of this study is to develop models for prediction of E_p using available weather data. Sudheer et al. (2002) concluded that using daily mean values of temperature and relative humidity instead of minimum and maximum values of both the parameters would not significantly reduce the performance. This observation may help to reduce drastically the data requirement for estimating the evaporation from climatic variables.

Performance of E_p Based GHNN Models

Keeping the findings of Sudheer et al. (2002) in view, in the present study the GHNN models were developed with the various combinations of T_{avg}, RH_{avg}, W_s, and S_{ra} instead of T_{max}, T_{min}, RH_{max}, RH_{min}, W_s, and S_{ra} as inputs to evaluate the effect of each of these variables on estimated E_p. A total of eight different input combinations were tried in this study. These included (i) T_{avg}, RH_{avg}, W_s, and S_{ra}; (ii) T_{avg}, RH_{avg}, and W_s; (iii) T_{avg}, RH_{avg}, and S_{ra}; (iv) T_{avg} and RH_{avg}; (v) T_{avg}; (vi) RH_{avg}; (vii) W_s; and (viii) S_{ra}. Due to poor performance of the GHNN models developed with a single input variable (input combinations v–viii), the performance results pertaining to these are not presented here. The GHNN models were compared with the GFNN models to test the relative performance of higher-order over linear (first-order) neural models. Further, the developed GHNN models were compared with the generalized multiple linear regression models (GMLR) models to evaluate the accuracy of the former models.

The optimum GHNN, GFNN, and GMLR structures were determined for each input combination and their performance statistics during testing is presented in Table 3. The comparative results of GHNN models with the GFNN models confirm the superiority of GHNN models in terms of the various performance criteria (RMSE, R^2, and R_{ratio}) for all the four input combinations under four AERs (Table 3). The reason for this is probably the capability GHNN models to capture nonlinearity, as these models use nonlinear approximation functions with the second-order polynomials (Eq. 4). The GMLR models with various input combinations showed the poorest performance with highest RMSE and lowest R^2 values for different AERs except for the arid region.

Among the all combinations, the GHNN(i) model whose inputs are the T_{avg}, RH_{avg}, W_s, and S_{ra} (input combination i) gave the highest accuracy with the smallest RMSE (mm day^{-1}) values (1.389 for semi-arid, 1.079 for sub-humid, 0.99 for humid) for all AERs except for arid region where GMLR (i) resulted in minimum RMSE of 1.429 mm day^{-1}. This shows the strong correlation of T_{avg}, RH_{avg}, W_s, and S_{ra} variables with the measured E_p values. The reason for this superior performance might be due to the inclusion of all climatic data as inputs which may have great influence on generalized models as these were developed using data from different locations.

Removing S_{ra} (input combination ii) as an input variable increased the RMSE (mm day^{-1}) to 1.451, 1.117, and 1.035 for semi-arid, sub-humid, and humid regions, respectively. Further, decreasing the number of input variables in the GHNN model continued to decrease its accuracy. Removing the climate variable W_s (input combination iii) as an input variable increased the RMSE (mm day^{-1}) to 1.510, 1.167, and 1.224 for semi-arid, sub-humid, and humid regions, respectively, and decreased the RMSE (mm day^{-1}) to 1.625 for arid region. The GHNN (iv) model which considers only two inputs furthermore increased the RMSE (mm day^{-1}) to 1.559, 1.632, 1.198, and 1.281 for semi-arid, arid, sub-humid, and humid regions, respectively. Similar performance of GHNN models was also observed with R^2 (high) statistical index. These results suggest that the performance of the developed E_p models decreased with the decrease in the input variables.

Due to the superior performance of GHNN models over the GMLR and GFNN models, the scatter plots pertaining to the GHNN models with all input combinations (i.e., i to iv) are only shown in Fig. 3, which confirms the statistics given in Table 3. The results in Fig. 3 illustrate that the agreement between the E_p predictions of the GHNN models and the measured E_p predictions was better for all regions. Although the GHNN (i) to (iv) models resulted in acceptable R^2 values for all regions except for humid region, their estimates are far from the exact 1:1 fit line. This can be clearly observed from the coefficients of their fitted equations ($y = a_0x + a_1$) where the values of a_0 and a_1 coefficients are far away from one and zero, respectively.

Table 3 Performance of GMLR-, GFNN-, and GHNN-based E_p models with different input combinations

AER	Semi-arid			Arid			Sub-humid			Humid		
Model	GMLR	GFNN	GHNN	GMLR	GFNN	GHNN	GMLR	GFNN	GHNN	GMLR	GFNN	GHNN
(i) T_{avg}, RH_{avg}, W_s, and S_{ra}												
RMSE	1.563	1.456	1.389	1.429	1.803	1.637	1.355	1.295	1.079	1.110	1.014	0.990
R^2	0.724	0.762	0.782	0.807	0.702	0.792	0.819	0.846	0.887	0.597	0.667	0.672
R_{ratio}	1.001	0.986	0.999	0.992	0.997	1.001	0.987	0.970	0.984	1.001	1.015	0.990
(ii) T_{avg}, RH_{avg}, and W_s												
RMSE	1.685	1.516	1.451	1.546	1.905	1.634	1.474	1.350	1.117	1.178	1.162	1.035
R^2	0.682	0.743	0.762	0.759	0.638	0.805	0.788	0.835	0.881	0.547	0.558	0.651
R_{ratio}	0.987	0.987	0.997	0.987	0.993	0.999	0.977	0.961	0.988	0.991	0.997	1.009
(iii) T_{avg}, RH_{avg}, and S_{ra}												
RMSE	1.710	1.569	1.510	1.467	1.847	1.625	1.459	1.385	1.167	1.385	1.359	1.224
R^2	0.669	0.723	0.743	0.781	0.664	0.804	0.790	0.822	0.866	0.377	0.405	0.517
R_{ratio}	0.999	0.983	0.988	0.992	0.997	1.001	0.986	0.954	1.009	0.984	0.991	1.029
(iv) T_{avg} and RH_{avg}												
RMSE	1.807	1.598	1.559	1.559	1.748	1.632	1.533	1.340	1.198	1.610	1.413	1.281
R^2	0.634	0.713	0.726	0.755	0.727	0.805	0.770	0.832	0.858	0.191	0.361	0.474
R_{ratio}	0.987	0.988	0.991	0.988	1.002	1.004	0.978	0.967	1.011	0.954	0.990	1.028

Note RMSE mm day^{-1}; R^2 and R_{ratio} dimensionless

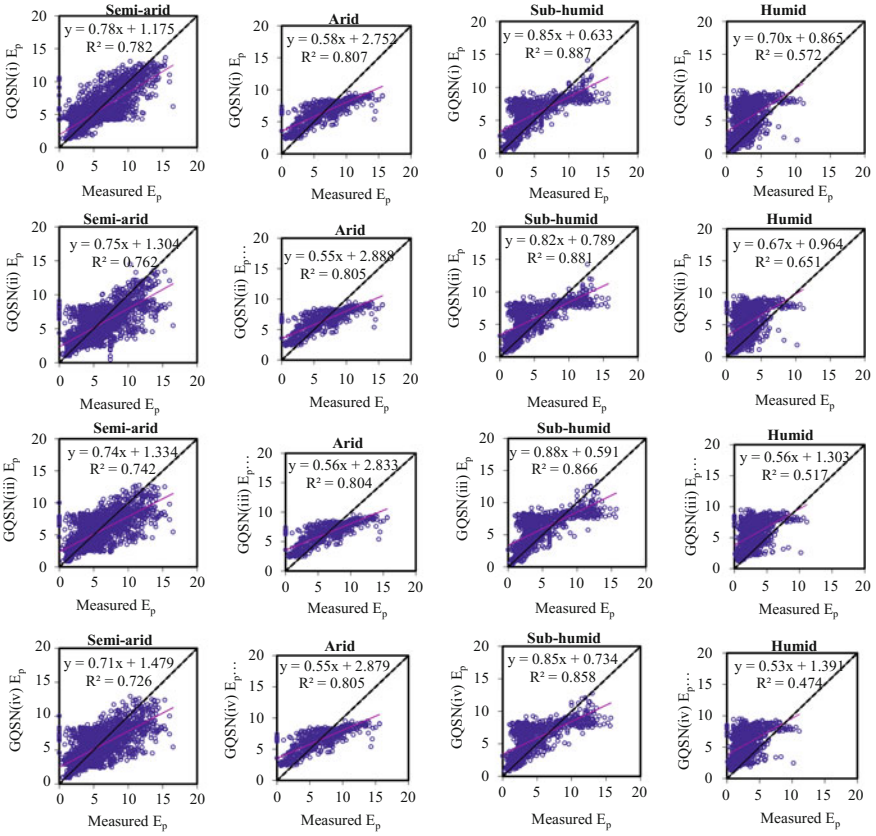

Fig. 3 Scatter plots of GHNN(i), GHNN(ii), GHNN(iii), and GHNN(iv) models estimated E_p (mm day^{-1}) with respect to measured E_p (mm day^{-1}) for four AERs

Application of GHNN Models for E_p Estimation

The best performed GHNN(i) models were applied to 15 model development and 10 model testing locations for four AERs to test their generalizing capability. The performance indices of GHNN(i) models for the model development locations are shown in Table 4. The R_{ratio} values (Table 4) suggest that the GHNN(i) model overestimated E_p values for semi-arid and humid regions and underestimated for arid and sub-humid regions. The RMSE (mm day^{-1}) values for this model ranged from 0.673 (at Ranichauri) to 3.227 (at Hissar). The performance indices of GHNN (i) models for the model testing locations are shown in Table 5. The RMSE (mm day^{-1}) values for this model ranged from 1.098 (at Samastipur) to 1.830 (at Bijapur). This indicates that the GHNN models have better generalization capability for the estimation of E_p for locations that were not used in the model development.

Table 4 Performance of GHNN(i)-based E_p model for model development locations

AER	Location	GHNN(i)		
		RMSE	R^2	R_{ratio}
Semi-arid	Parbhani	1.174	0.862	1.030
	Solapur	1.576	0.728	1.016
	Bangalore	0.973	0.625	1.016
	Kovilpatti	1.941	0.678	1.048
	Udaipur	1.180	0.885	1.022
Arid	Anantapur	1.658	0.566	0.976
	Hissar	3.227	0.217	0.918
Sub-humid	Raipur	1.008	0.929	0.998
	Faizabad	1.417	0.640	0.989
	Ludhiana	1.049	0.890	0.998
	Ranichauri	0.673	0.603	0.980
Humid	Palampur	1.098	0.706	1.092
	Jorhat	0.907	0.357	1.042
	Mohanpur	1.197	0.515	1.079
	Dapoli	1.599	0.361	1.028

Note RMSE mm day^{-1}; R^2 and R_{ratio} dimensionless

Table 5 Performance of GHNN(i)-based E_p model for model testing locations

AER	Location	GHNN(i)		
		RMSE	R^2	R_{ratio}
Semi-arid	Kanpur	1.633	0.727	1.026
	Anand	1.108	0.808	0.998
	Akola	1.662	0.861	1.022
Arid	Bijapur	1.830	0.457	0.916
Sub-humid	Jabalpur	1.413	0.791	1.019
	Samastipur	1.098	0.711	0.983
	Bhubaneswar	1.302	0.747	0.985
	Ranchi	1.290	0.808	0.983
	Rakh Dhiansar	1.103	0.740	1.003
Humid	Thrissur	1.283	0.625	1.095

Note RMSE mm day^{-1}; R^2 and R_{ratio} dimensionless

Conclusions

The ability of GHNN models corresponding to different locations in four AERs in India to estimate E_p was studied in this paper. The results illustrated that GHNN and GFNN models performed much better than the GMLR models and GHNN and GFNN models with the input combination (i), which include all variables as input performed better as compared to other combinations (ii, iii, and iv, respectively) for

all AERs. During testing of the generalizing capability of GHNN models for the model development and testing locations, the GHNN models performed better than the GFNN models for all cases. The performance of the generalized models increases with the increase of number of input variables during E_p modeling. Overall, better performance of GHNN models in comparison to GFNN and GMLR models in different AERs in India showed that these models not only have better potential but also have good generalizing capability. It may be noted that the main focus of this study was to evaluate the generalizing capability of higher-order neural networks in E_p modeling. This study does not intend to replace the well established models. Further, more studies are required to test the generalizing capability of GHNN models with limited climate data for different climatic regions of other countries.

Acknowledgements The authors wish to thank All India Coordinated Research Project on Agro-meteorology (AICRPAM), Central Research Institute for Dryland Agriculture (CRIDA), Hyderabad, Telangana, India for providing the requisite climate data to carry out this study. Also, the authors express their gratitude to the reviewers for useful comments and suggestions.

References

Adamala S, Raghuwanshi NS, Mishra A, Tiwari MK (2014a) Evapotranspiration modeling using second-order neural networks. J Hydrol Eng 19(6):1131–1140

Adamala S, Raghuwanshi NS, Mishra A, Tiwari MK (2014b) Development of generalized higher-order synaptic neural based ET_o models for different agroecological regions in India. J Irrig Drain Eng. doi:10.1061/(ASCE)IR.1943-4774.0000784

Adamala S, Raghuwanshi NS, Mishra A (2015a) Generalized quadratic synaptic neural networks for ET_o modeling. Environ Proces 2(2):309–329

Adamala S, Raghuwanshi NS, Mishra A, Tiwari MK (2015b) Closure to evapotranspiration modeling using second-order neural networks. J Hydrol Eng 20(9):07015015

Arunkumar R, Jothiprakash V (2013) Reservoir evaporation prediction using data-driven techniques. J Hydrol Eng 18:40–49

Bruton JM, McClendon RW, Hoogenboom G (2000) Estimating daily pan evaporation with artificial neural networks. Trans ASAE 43(2):491–496

Chang FJ, Sun W, Chung CH (2013) Dynamic factor analysis and artificial neural network for estimating panevaporation at multiple stations in northern Taiwan. Hydrol Sci J 58(4):1–13

Elshorbagy A, Parasuraman K (2008) On the relevance of using artificial neural networks for estimating soil moisture content. J Hydrol 362:1–18

Gupta MM, Jin L, Homma N (2003) Static and dynamic neural networks: from fundamentals to advanced theory. Wiley/IEEE Press, NY

Han H, Felker P (1997) Estimation of daily soil water evaporation using an artificial neural network. J Arid Environ 37:251–260

Kalifa EA, Abd El-Hady Rady RM, Alhayawei SA (2012) Estimation of evaporation losses from Lake Nasser: Neural network based modeling versus multivariate linear regression. J Appl Sci Res 8(5):2785–2799

Keskin ME, Terzi O (2006) Artificial neural networks models of daily pan evaporation. J Hydrol Eng 11(1):65–70

Kim S, Park K-B, Seo Y-M (2012) Estimation of pan evaporation using neural networks and climate-based models. Disaster Adv 5(3):34–43

Kim S, Shiri J, Kisi O, Singh VP (2013) Estimating daily pan evaporation using different data-driven methods and lag-time patterns. Water Resour Manage 27:2267–2286

Kim S, Shiri J, Singh VP, Kisi O, Landeras G (2014) Predicting daily pan evaporation by soft computing models with limited climatic data. Sci J, Hydrol. doi:10.1080/02626667.2014.945937

Kisi O (2009) Daily pan evaporation modelling using multi-layer perceptrons and radial basis neural networks. Hydrol Process 23:213–223

Kumar P, Kumar D, Jaipaul, Tiwari AK (2012) Evaporation estimation using artificial neural networks and adaptive neuro-fuzzy inference system techniques. Pakistan J Meteorol 8(16): 81–88

Moghaddamnia A, Gousheh MG, Piri J, Amin S, Han D (2009) Evaporation estimation using artificial neural networks and adaptive neuro-fuzzy inference system techniques. Adv Water Resour 32:88–97

Nourani V, Fard MS (2012) Sensitivity analysis of the artificial neural network outputs in simulation of the evaporation process at different climatologic regimes. Adv Eng Softw 47:127–146

Rahimikhoob A (2009) Estimating daily pan evaporation using artificial neural network in a semi-arid environment. Theor Appl Climatol 98:101–105

Redlapalli SK (2004) Development of neural units with higher-order synaptic operations and their applications to logic circuits and control problems. M.S. thesis, Department of Mechanical Engineering, University of Saskatchewan, Saskatoon, Canada

Shirgure PS, Rajput GS (2011) Evaporation modeling with neural networks—a research review. Int J Res Rev Soft Intell Comput 1(2):37–47

Shiri J, Kisi O (2011) Application of artificial intelligence to estimate daily pan evaporation using available and estimated climatic data in the Khozestan Province (South Western Iran). J Irrig Drain Eng 137(7):412–425

Shirsath PB, Singh AK (2010) A comparative study of daily pan evaporation estimation using ANN, regression and climate based models. Water Resour Manage 24:1571–1581

Sudheer KP, Gosain AK, Rangan DM, Saheb SM (2002) Modeling evaporation using an artificial neural network algorithm. Hydrol Process 16:3189–3202

Tabari H, Marofi S, Sabziparvar AA (2010) Estimation of daily pan evaporation using artificial neural network and multivariate non-linear regression. Irrig Sci 28:399–406

Tiwari MK, Song KY, Chatterjee C, Gupta MM (2012) River flow forecasting using higher-order neural networks. J Hydrol Eng 17:655–666

Sensitivity Analysis of FAO-56 Penman–Monteith Reference Evapotranspiration Estimates Using Monte Carlo Simulations

Gicy M. Kovoor and Lakshman Nandagiri

Abstract The present study used Monte Carlo (MC) simulations to characterize the sensitivity of the FAO-56 Penman–Monteith reference evapotranspiration (ET_0) model to the climate variables used in its application. The analysis was performed separately for four climate stations representing different climate regimes of India. Sensitivity indices (defined by the partial rank correlation coefficient) representing the sensitivity of ET_0 values to the various input variables were obtained as output from the analysis. Wind speed was found to be the dominant input variable at all stations except the humid one where net radiation (R_n) appeared to be crucial. The results of this study while emphasizing the need for accurate measurement of these variables for reliable estimates of ET_0 to be obtained, also provide information for evaluating the impacts of future climate changes.

Introduction

The United Nations (UN) Food and Agricultural Organization (FAO) recommends the sole use of the Penman–Monteith (PM) method for the estimation of reference crop evapotranspiration (ET_0) from ground-based climatological measurements in its paper popularly known as FAO-56 (Allen et al. 1998). The document also describes the various climate variables that are needed for the computation of ET_0 and the recommended equations for the conversion of these variables into parameters that are used in this equation. Nandagiri and Kovoor (2005) demonstrated how errors are likely to creep into ET_0 estimates if non-recommended equations are used for computing the parameters of FAO-56 PM equation. Even with such precise

G. M. Kovoor · L. Nandagiri
Department of Civil Engineering, Manipal Institute of Technology, Manipal 576104, India
e-mail: gicy.kovoor@manipal.edu

G. M. Kovoor · L. Nandagiri (✉)
Department of Applied Mechanics and Hydraulics, National Institute of Technology Karnataka, Surathkal, Mangalore 575025, India
e-mail: Lnand@rocketmail.com

V. P. Singh et al. (eds.), *Hydrologic Modeling*, Water Science and Technology Library 81, https://doi.org/10.1007/978-981-10-5801-1_6

calculations, erroneous ET_0 values can be still be obtained due to errors in input climatic data (e.g., Llasat and Synder 1998) and sampling frequency (Hupet and Vanclooster 2001). As Droogers and Allen (2002) point out, the number of climate stations in developing countries where reliable data exist for application of FAO-56 PM equation is extremely small. Therefore, understanding the effect of accuracy of the observed climatological variables on ET_0 estimates is a matter of great importance in the planning and design of irrigation schemes. However, due to nonlinearity of the PM equation and multi-collinearity effects, ET_0 estimates may exhibit different levels of sensitivity to changes/errors in different input climatic variables.

Several earlier investigators have carried out sensitivity analysis of various forms of the Penman combination equation including the FAO-56 PM equation, for estimating evaporation from open water surfaces or potential evapotranspiration or actual evapotranspiration (e.g., McCuen 1974; Saxton 1975; Coleman and DeCoursey 1976; Beven 1979; Piper 1989; Singh and Xu 1997; Goyal 2004; Irmak et al. 2006; Kwon and Choi 2011; Debnath et al. 2015). Most of these studies have implemented simple perturbation or Taylor series techniques to perform sensitivity analysis and sought to understand the relative importance of the radiation and the aerodynamic terms of the Penman combination equation. Gong et al. (2006) used a non-dimensional relative sensitivity coefficient approach to predict responses of Penman–Monteith ET_0 estimates to perturbations of four climatic variables in the Changjiang (Yangtze River) basin, China.

However, the possible existence of significant correlations between the input variables (multi-collinearity) involved in a Penman-type equation may give rise to problems in the routine application of such simple sensitivity techniques. To overcome this problem, Ahn (1996) developed a novel Taylor series-based method for sensitivity analysis for correlated input variables and used it to characterize the sensitivity of the Penman–Brutsaert evapotranspiration model using meteorological data collected from the humid South Florida region of USA. However, application of Taylor series expansion techniques of sensitivity assessment may still pose problems due to failure in the presence of nonlinearity in the relationship, difficulty in evaluating derivatives, and inaccuracies arising out of non-normal distributions of variables.

Monte Carlo (MC) simulation methods circumvent most of these problems and provide a complete statistical description of changes in the response variable due to uncertainties in the predictor variables. The advantages offered by the MC method over other sensitivity analysis techniques include the following: the ability to handle complex and nonlinear models, mechanism to incorporate correlation effects, providing an insight into model behavior, and allowing varied distributions to be specified for the input variables. Montaldo et al. (2003) used MC simulation to understand the effect of background hydrometeorological conditions on the sensitivity of evapotranspiration to model parameters. However, few studies seem to have used the MC method for the sensitivity/uncertainty analysis of FAO-56 PM ET_0 estimates.

Therefore, the present study was taken up with the intention of assessing the sensitivity of the FAO-56 PM ET_0 estimates to the uncertainties associated with the input climate variables using MC simulations. Also, in an effort to explore differences in sensitivity on account of prevailing climatic conditions, four stations each representing the dominant climate types in India—arid, semiarid, sub-humid, and humid—were selected for the analysis.

Methodology

Sensitivity Analysis

In its simplest sense, sensitivity analysis (SA) involves quantification of the change in model output corresponding to a change in one or more of the model inputs. It is the study of how the variation in the output of a model can be apportioned, qualitatively or quantitatively to different sources of variation, and of how the model depends upon the information fed into it. In other words, it tries to explain how the output varies when perturbations are introduced into the inputs. SA is carried out where it is generally very useful to know which variables mostly contribute to output variability.

Monte Carlo Analysis

Monte Carlo methods are stochastic techniques which mean that they are based on the use of random numbers and probability statistics to investigate problems. Thus, Monte Carlo analysis is based on performing multiple model evaluations with probabilistically selected model inputs and then using the results of these evaluations to quantify both the uncertainty in model predictions and also to identify the input variables that give rise to this uncertainty.

Typically, application of the Monte Carlo simulation approach involves four steps as explained below:

1. A range and distribution are selected for each input variable. These selections will be used in the next step in the generation of a sample from the input variables. If the analysis is primarily of an exploratory nature, then rather crude (e.g., uniform, normal, log-normal, triangular) distribution assumptions may be adequate.
2. A sample is generated from the ranges and distribution is specified in the first step. The result of this step is a sequence of sample elements.
3. The model is evaluated for each sample element. In essence, these model evaluations create a mapping from the analysis inputs to the analysis results that can be studied in subsequent uncertainty and sensitivity analysis.

4. The final step is sensitivity analysis that is based on an exploration of the mapping from analysis input to analysis results.

In the present study, the probability distribution functions of each of the input climatic variables were determined using the BESTFIT® software program. Jankauskas and McLafferty (1996) give a detailed description of the methods/algorithms implemented in the software. A 30-day/100 runs trial version of the software was downloaded (http://www.palisade.com/trials.asp) and used to characterize the probability distributions of all the climate variables for the four stations.

MC simulations as per the steps described above were implemented using the SimLab V2.2® software program. SimLab (Simulation Environment for Sensitivity and Uncertainty Analysis) is a free software package designed for Monte Carlo analysis. The model along with reference manual is available for download at https://ec.europa.eu/jrc/en/samo/simlab. SimLab V2.2 used in this study consists of three modules: the statistical preprocessor module, the model specification and execution module and the statistical post-processor module. These modules cover all the steps in a Monte Carlo analysis as described below:

1. The statistical preprocessor module allows the user to define the list of factors that represent the input of the model. These selections are used in the generation of a sample from the input variables.
2. The model specification module helps the user to link SimLab to an external model or define a model within the SimLab using a simple equation editor. During model execution, the software runs the model for each sample element.
3. The statistical post-processor aids in performing uncertainty analysis. One way to characterize the uncertainty is with a mean value and a variance. This processor also performs sensitivity analysis based on an exploration of the mapping from inputs to results of the analysis.

Sampling of Input Variables

This is the first step in the Monte Carlo analysis which was done with the help of SimLab V2.2. For this, the distribution describing each climate variable is entered as input into SimLab. Since the climatic variables are mutually correlated, multi-collinearity effect was also taken into account when defining the factors. SimLab has provision for expressing the correlation in three different ways: (1) the Iman-Conover method, (2) the Stein method and (3) the correlation tree method. The Iman-Conover method is considered to be the best method for generating correlated random numbers as this has been identified as the simplest and most satisfactory one in view of its efficiency and overall performance (Wu and Tsang 2004). This is used to induce a desired rank correlation between pairs of sampled

input variables using information on the correlation coefficients as determined from the observed data set.

The next step is to generate the sample set. For this again, various methods of sampling are available in SimLab. In this work, the Latin hypercube sampling for sampling correlated variables is used.

Latin hypercube sampling may be considered as a particular case of stratified sampling. The purpose of stratified sampling is to achieve a better coverage of the sample space of the input variables. The method has the advantage of ensuring that input variable has all portions of its distributions represented by input values. Latin hypercube sampling performs better than random sampling when the output is dominated by a few components of the input variables. This method ensures that each of these components is represented in a fully stratified manner, no matter which components might turn out to be important.

In this method, the range of probable values for each uncertain input parameter is divided into ordered segments of equal probability. Thus, the whole parameter space, consisting of all the uncertain parameters, is partitioned into cells having equal probability and they are sampled in an efficient manner such that each variable is sampled once from each of its possible segments, i.e., the range of each input variable x_j, $j = 1, 2, 3, \ldots, k$ is divided into N' intervals of equal marginal probability, $1/N'$, and one observation of each input variable is made in each interval using random sampling within that interval. Thus, there are N' non-overlapping realizations for each of the k input variables. One of the realizations on x_1 is randomly selected (each observation is equally likely to be selected), matched with a randomly selected realization of x_2 and so on till x_k. These collectively constitute a first sample S_1. One of the remaining realizations on x_1 is then matched at random with one of the remaining observations on x_2 and so on to get S_2. A similar procedure is followed for $S_3,\ldots, S_m$ which results in a Latin hypercube sample set. The advantage of this approach is that the random samples are generated from all the ranges of possible values, thus giving insight into the extremes of the probability distributions of the outputs.

Sensitivity Analysis

When a Monte Carlo study is being performed, propagation of the sample through the model creates a mapping from analysis inputs to analysis results. Once this mapping is generated and stored, it can be explored to determine the sensitivity of model predictions to individual input variables. More quantitative measures of sensitivity are based on regression analysis. A multivariate sample of the inputs (x) is generated by the sampling strategy (dimension $m \times k$), and the corresponding sequence of "m" output values is computed using the model under analysis. The coefficients of the regression model computed can be used to indicate the importance of individual input variables with respect to the output. These coefficients called the Standard Regression Coefficients (SRC) can be used for sensitivity

analysis when the input variables x_js are independent. But when the variables are correlated, the measure of variable importance is given by Partial Correlation Coefficients (PCC). These coefficients are based on the concepts of correlation and partial correlation, i.e., the PCC measures the correlation between the output and the selected input variable after the linear influence of other variables has been eliminated. But here again, the regression analysis often performs poorly when the relationships between the input variables are nonlinear. In this case, the value of the coefficient computed on the raw values may be low. The problem associated with poor linear fits to nonlinear data can often be avoided with the use of the rank transformations.

The rank transform is a simple procedure which involves replacing the data with their corresponding ranks, i.e., assign rank 1 to the smallest observation and continue to rank N^* for the largest observation. The usual least squares regression analysis is then performed entirely on these ranks $R(x)$. The final regression equation expresses $R(y_i)$ in terms of $R(x_k)$. Thus, the partial rank correlation coefficient (PRCC) which is the sensitivity index used in the present study is the corresponding measure of PCC when input–output relationships are built using the ranks of the variables to linearize the relation. In order to determine the PRCC between the output variable y and the pth input variable x_p, a linear regression model between y and all other inputs is first built (Eq. 1)

$$\widehat{c} = b_0 + \sum_{j \neq p} b_j x_j \tag{1}$$

where b denotes a regression coefficient and the "hat" signifies a regression-fitted variable. Next, a linear regression model is built between x_p and all other inputs (Eq. 2).

$$\widehat{c}_p = c_0 + \sum_{j \neq p} c_j x_j \tag{2}$$

where c denotes a regression coefficient. The RCC between the residuals arising out of Eqs. (1) and (2) is now free from the input–input correlations and is defined as the PRCC. Thus,

$$\text{PRCC}\left[y, x_p\right] = \text{RCC}\left[y - \widehat{y}, x - \widehat{x}_p\right] \tag{3}$$

PRCC varies over the range from −1 to +1. Values close to these limits indicate a strong influence of the input variable over the output variable. Usually, PRCC values >+0.5 or <−0.5 are considered significant. Positive or negative values are indicative of the nature of relationship (direct or inverse) between the input variable and the output variable.

Climate Data

Table 1 lists details of the climate stations considered in the analysis. These stations are drawn from a network of over 550 surface observatories operated and maintained by the India Meteorological Department (IMD), Government of India. The stations were selected to represent the major climate types prevalent in India (Subrahmanyam 1983): arid (Jodhpur), semiarid (Hyderabad), sub-humid (Bangalore), and humid (Pattambi).

All stations are equipped with standard ground-based instruments: Class A pan evaporimeter, alcohol and wet-bulb thermometers, sunshine recorder, cup anemometer, and mercury thermometers. Readings are taken twice a day at 08.30 h and 17.30 h IST. Records are transmitted from the stations to the IMD Data Centre at Pune, where data archives are maintained. Data are scrutinized and subjected to quality checks prior to supply to users.

Historical data were procured from IMD for the periods shown against each station in Table 1. Unfortunately, good quality data were unavailable for a common period for all the stations. For each station, the data set used in this study comprised daily values of maximum air temperature (T_{max}), minimum air temperature (T_{min}), maximum relative humidity (RH_{max}), minimum relative humidity (RH_{min}), actual hours of sunshine (n), and 24-h wind speed (u_2) at 2 m height. Individual data records were subjected to further screening, and integrity checks were performed on the climatic variables as per procedures described in FAO-56 (results not presented here for brevity). After discarding obvious outliers and accounting for missing records, the number of days (N_d) for which complete records were available for each station is as follows: Jodhpur—1453, Hyderabad—1044, Bangalore—1368, and Pattambi—1275. From the historical data set of the measurements, the daily averages of all the variables for the four stations were obtained from which the distribution functions of the variables T_{max} (°C), T_{min} (°C), RH_{max} (%), RH_{min} (%), and u_2 (m/s) were determined. Actual hours of sunshine (n) which is another input variable had to be handled indirectly. This variable is required in the computation of the radiation components. Since day number (J) has to be a continuous variable from 1 to 365, R_n (MJ/m^2/d) for the entire data set is calculated with measured values of n and the respective day numbers. Net radiation (R_n) computed in this manner was then treated as an input variable in the application of the MC method. The distributions of the various climate variables viz. T_{max}, T_{min}, RH_{max}, RH_{min}, u_2,

Table 1 Details of climate stations

Station	State	Latitude (N)	Longitude (E)	Altitude (m)	Climate	Data period
Jodhpur	Rajasthan	26° 18′	73° 01′	224	Arid	1984–1987
Hyderabad	Telangana	17° 32′	78° 16′	545	Semiarid	1988–1990
Bangalore	Karnataka	13° 00′	77° 37′	899	Sub-humid	1982–1985
Pattambi	Kerala	10° 48′	76° 12′	254	Humid	1985–1988

and R_n for each of the four lysimeter stations considered in this research (Jodhpur, Hyderabad, Bangalore, and Pattambi) were first determined with the help of BESTFIT® software. The software program provided a list of possible probability distribution functions (PDFs) that best fit the sample data in descending order of goodness of fit. In all cases, the PDF which was listed first was used in this study.

Other than the probability distribution functions of the input variables, inter-variable correlation coefficients that are also necessary in applying the MC method were determined from the historical observations for each climate variable. With the help of this information, sample data sets were generated using the Latin hypercube sampling method to provide input for Monte Carlo analysis. The FAO-56 PM model was then created within SimLab and executed. For each climate site, the model was executed 300 times and output was obtained in the statistical post-processor module.

Results and Discussion

Distribution Fitting and Generation of Sample Data Sets

Table 2 lists the distributions of the different climate variables for the four stations as obtained from BESTFIT®. As mentioned earlier, the distributions for each variable shown in Table 2 are the ones ranked highest by BESTFIT® in terms of goodness of fit of the PDF to observations. Parameters of the PDFs were also extracted (not shown here for brevity). These distributions were later entered into SimLab for the generation of samples by the Latin hypercube sampling technique.

The distributions were entered in terms of the type and the parameters which describe the distribution. For example, T_{max} for Jodhpur is found to have a triangular distribution. This was entered in terms of the minimum and maximum values and the mode of the distribution. Along with defining the distribution of the various factors, their correlation coefficients were also defined so that samples could be generated taking into effect the correlation as well. Correlation coefficients between the different variables both for the original data set and also for the sample data set

Table 2 Identified probability distributions for climate variables at the selected stations

Variable	Probability distribution type			
	Jodhpur	Hyderabad	Bangalore	Pattambi
T_{max}	Triangular	Triangular	Triangular	Beta general
T_{min}	Beta general	Triangular	Triangular	Weibull
RH_{max}	Triangular	Beta general	Normal	Triangular
RH_{min}	Beta general	Triangular	Beta general	Beta general
u_2	Weibull	Triangular	Weibull	Normal
R_n	Beta general	Beta general	Beta general	Beta general

Table 3 Mean and variance of variables for observed and sampled data sets for Jodhpur

Variable	Observed data set		Sampled data set	
	Mean	Variance	Mean	Variance
T_{max} (°C)	34.24	25.32	34.13	25.22
T_{min} (°C)	20.25	35.77	20.19	35.65
RH_{max} (%)	51.92	236.30	51.74	235.48
RH_{min} (%)	25.38	166.75	25.30	166.19
u_2 (m/s)	191.45	5692.19	190.81	5672.80
R_n (MJ/m^2/d)	9.65	11.42	9.62	11.38

Table 4 Statistical parameters of simulated ET_0 estimates

Station	Mean (mm/d)	Variance (mm/d)^2
Jodhpur	5.94	3.80
Hyderabad	5.44	2.73
Bangalore	4.81	1.08
Pattambi	4.34	0.54

generated by SimLab were compared (not shown here for brevity). Results indicated only minor differences in the values of the correlation coefficients indicating that the sample data sets generated are very good representations of the original data set. Similarly, observed values of mean and variance for the input variables closely match equivalent statistics for the generated samples. As an example, this comparison for Jodhpur station is shown in Table 3.

Sensitivity Analysis

The statistical parameters for the output variable (ET_0) calculated from the 300 generated values at each site are given in Table 4. It is seen that mean ET_0 increases from the humid Pattambi site to the arid Jodhpur site and the variance also exhibits an increasing trend from the humid to the arid climate with a minimum variance of 0.54 for Pattambi to a maximum of 3.80 at Jodhpur. Generated ET_0 values were processed in BESTFIT software, and the underlying PDF was identified for each site. From these results, it was found that at Pattambi and Bangalore—the humid and sub-humid locations—ET_0 values follow a normal distribution. At the semiarid Hyderabad site, ET_0 exhibits a log-normal distribution, and at the arid Jodhpur site, it follows a Weibull distribution.

Sensitivity indices (defined by the partial rank correlation coefficient) representing the sensitivity of ET_0 values to the various input variables are shown in Fig. 1. It can be noticed that the sensitivity index is positive for T_{max}, u_2, and R_n at all stations indicating that an increase in these variables leads to an increase in ET_0. On the other hand, the sensitivity index is negative at all stations for RH_{max}, RH_{min}, and T_{min} (except for Pattambi) representing an inverse relationship between them

and the output variable. For all stations except Pattambi, wind speed (u_2) appears to be the most sensitive input variable with indices significantly larger than +0.5 and reaching the highest value of +0.90 at the sub-humid Bangalore station. At the arid and semiarid locations, the sensitivity indices for wind speed are comparable: +0.84 for the arid location (Jodhpur) and +0.82 for the semiarid location (Hyderabad). At the humid location (Pattambi), net radiation (R_n) appears to be the most critical variable with a sensitivity index of 0.94 followed by wind speed with an index of 0.58. Maximum temperature (T_{max}) exhibits almost same sensitivity index at all the stations: 0.45 at Jodhpur, 0.53 at Hyderabad, 0.5 at Bangalore, and 0.51 at Pattambi. This is indicative of the fact that T_{max} is equally significant in all climates and hence is a very important variable in the determination of ET_0. The results of factor analysis presented by Nandagiri and Kovoor (2006) have also shown that temperature-related variables are the most crucial in the determination of ET_0. With regard to input variables possessing an inverse relationship with ET_0, Fig. (1)

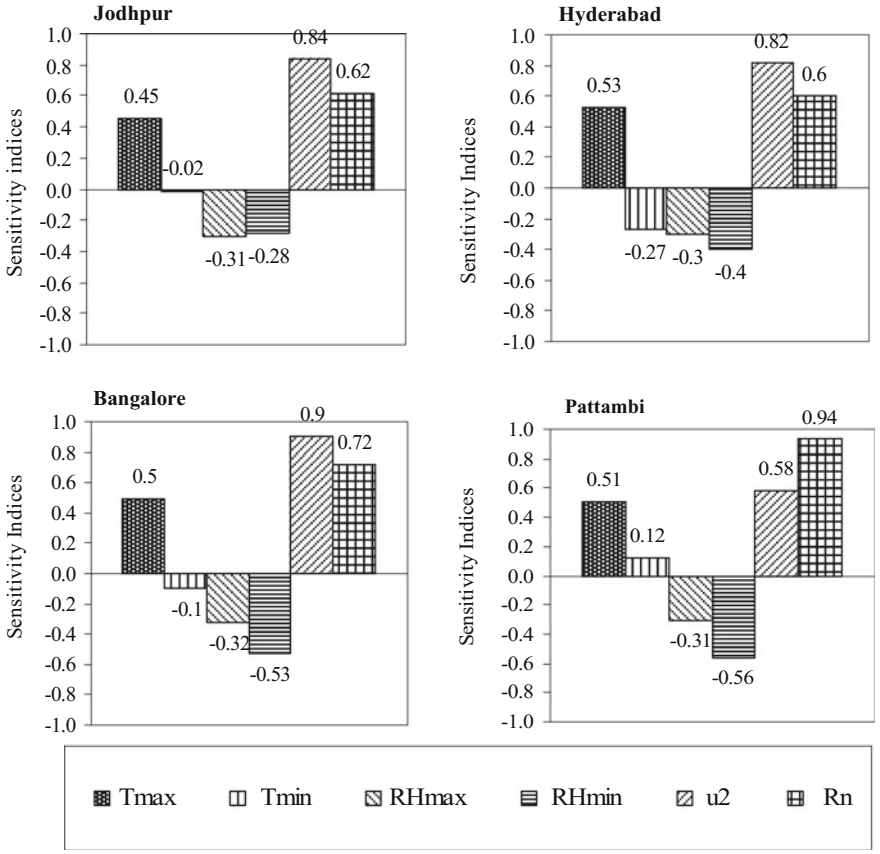

Fig. 1 Sensitivity indices for climate variables at the four stations

shows that minimum relative humidity (RH_{min}) appears to be sensitive especially at the sub-humid (Bangalore) and humid (Pattambi) locations. Minimum temperature (T_{min}) and maximum relative humidity (RH_{max}) appear to be relatively less sensitive variables at all the locations.

Undoubtedly, accuracy of all input variables is important in estimation of ET_0, but the results of the MC sensitivity analysis reveal that accuracy of measurements particularly with reference to maximum air temperature (T_{max}), wind speed (u_2), and net radiation (R_n) (or actual hours of sunshine) is critical. Also, future climate changes that bring about modifications in these climate variables may have important ramifications on crop and irrigation water requirements.

Conclusions

The present study used the Monte Carlo (MC) method to evaluate the sensitivity of FAO-56 Penman–Monteith ET_0 estimates to uncertainties in the climatic variables used as input. The analysis was carried out for four climate stations located in different climate regimes of India. Overall results clearly depict the major role played by the temperature variable in estimating reference evapotranspiration. From the viewpoint of deriving the most accurate estimates of ET_0, this study also identifies net radiation as being most critical in a humid location, whereas wind speed appears to be more important in arid, semiarid, and sub-humid climates. This study therefore emphasizes the need for accurate measurement of these variables for accurate determination of ET_0. Results of sensitivity analysis also provide crucial information on critical climate variables that need to be considered in evaluating the impact of future climate changes on irrigation water requirements of agricultural crops.

References

Ahn H (1996) Sensitivity of correlated input variables and propagated errors in evapotranspiration estimates from a humid region. Water Resour Res 32(8):2507–2516

Allen RG, Pereira LS, Raes D, Smith M (1998) Crop evapotranspiration—guidelines for computing crop water requirements. In: Food and agricultural organization of the United Nations (FAO) irrigation and drain. Paper No. 56, Rome, Italy

Beven K (1979) A sensitivity analysis of the Penman-Monteith actual evapotranspiration estimates. J Hydrol 44:169–190

Coleman G, DeCoursey DG (1976) Sensitivity and model variance analysis applied to some evaporation and evapotranspiration models. Water Resour Res 12(5):873–879

Debnath S, Adamala S, Raghuwanshi NS (2015) Sensitivity analysis of FAO-56 Penman-Monteith method for different agro-ecological regions of India. Environ Process 2(4):689–704

Droogers P, Allen RG (2002) Estimating reference evapotranspiration under inaccurate data conditions. Irrig Drain Syst 16:33–45

Gong L, Xu C, Chen D, Halldin S, Chen YD (2006) Sensitivity of the Penman-Monteith reference evapotranspiration to key climatic variables in the Changjiang (Yangtze River) basin. J Hydrol 329(3–4):620–629

Goyal RK (2004) Sensitivity of evapotranspiration to global warming: A case study of arid zone of Rajasthan (India). Agr Water Manage 69:1–11

Hupet F, Vanclooster M (2001) Effect of the sampling frequency of meteorological variables on the estimation of the reference evapotranspiration. J Hydrol 243:192–204

Irmak S, Payero JO, Martin DL, Irmak A, Howell TA (2006) Sensitivity analysis and sensitivity coefficients of standardized daily ASCE Penman-Monteith equation. J Irrig Drain Eng 132 (6):564–578

Jankauskas L, McLafferty S (1996) BESTFIT, distribution fitting software by Palisade Corporation. In: Charnes JM, Morrice DJ, Brunner DT, Swain JJ (eds) Proceedings of the 1996 Winter simulation conference, pp 551–555

Kwon H, Choi M (2011) Error assessment of climate variables for FAO 56 reference evapotranspiration. Meteorol Atmos Phys 112:81–90

Llasat MC, Synder RL (1998) Data error effects on net radiation and evapotranspiration estimation. Agr Forest Meteorol 91:209–221

McCuen RH (1974) A sensitivity and error analysis of procedures used for estimating evaporation. Water Res Bull 10(3):486–497

Montaldo N, Toninelli V, Albertson JD, Mancini M, Troch PA (2003) The effect of background hydrometeorological conditions on the sensitivity of evapotranspiration to model parameters: analysis with measurements from an Italian alpine catchment. Hydrol Earth Syst Sci 7(6): 848–861

Nandagiri L, Kovoor GM (2005) Sensitivity of Food and Agriculture Organization Penman-Monteith evapotranspiration estimates to alternative procedures for estimation of parameters. J Irrig Drain Eng 131(3):238–248

Nandagiri L, Kovoor GM (2006) Performance evaluation of reference evapotranspiration equations across a range of Indian climates. J Irrig Drain Eng 132(3):238–249

Piper BS (1989) Sensitivity of Penman estimates of evaporation to errors in input data. Agr Water Manage 15:279–300

Saxton KE (1975) Sensitivity analysis of the combination evapotranspiration equation. Agr Meteorol 15:343–353

Singh VP, Xu CY (1997) Sensitivity of mass transfer-based evaporation equations to errors in daily and monthly input data. Hydrol Process 11(11):1465–1473

Subrahmanyam VP (1983) Some aspects of water balance in the tropical monsoon climates of India. In: Proceedings of hamburg symposium, I. A. H. S. Publication No. 140, pp 325–331

Wu F-C, Tsang Y-P (2004) Second-order Monte Carlo uncertainty/variability analysis using correlated model parameters: application to salmonid embryo survival risk assessment. Ecol Model 177 (3–4):393–414

Quantification of Error in Estimation of Reference Crop Evapotranspiration by Class A Pan Evaporimeter and Its Correction

S. Praharaj, P. K. Mohanty and B. C. Sahoo

Abstract Today Penman–Monteith equation is assumed to be the most appropriate model for estimation of reference crop evapotranspiration (ET_0) across the globe. However, as the model requires many weather parameters, so it has not been percolated down to the stakeholder's level. Instead pan evaporimeter is being widely used in many parts of the world for estimating approximate ET_0 without considering the degree of error involved in this method. So an attempt has been made in the present study to quantify the percentage of error the stakeholders allowing in estimation of ET_0 as well as crop water requirement. Weekly weather data were collected for 14 years from 2001 to 14 from the crop weather observatory of Orissa University of Agriculture and Technology and put into Penman–Monteith equation for estimation of actual ET_0. Further, the weekly ET_0 values recorded at the observatory from the depletion of water level in Class A pan evaporimeter for the corresponding period were compared with the actual ET_0. It was found that the pan evaporimeter is underestimating the parameter to the tune of 50% of the actual ET_0. A regression analysis between pan ET_0 and Penman–Monteith ET_0 carried out for a period of 12 years form 2001 to 12 discloses linear relationship based on highest R^2 value (0.81) among all the relation functions. Furthermore, the regression model was validated using pan ET_0 data from the observatory for two years (2013–14) with the help of RMSE, percent deviation and Scatter plot. An average RMSE of 0.545 mm/week and percent deviation of −5.53 and 0.82% in 2013 and 2014, respectively, along with the depiction of Scatter plots in both the years depict close agreement of the model prediction with the actual ET_0 values. It is recommended to use the developed model for estimation of actual ET_0 instead of error-infested pan ET_0 for estimation of crop water requirement and scheduling irrigation in regions having similar agro-climatic conditions.

Keywords Reference crop evapotranspiration · Class A pan evaporimeter Penman–Monteith equation

S. Praharaj (✉) · P. K. Mohanty · B. C. Sahoo
College of Agricultural Engineering and Technology, Orissa University of Agriculture Engineering and Technology, Bhubaneswar, Orissa, India
e-mail: salini.praharaj3@gmail.com

V. P. Singh et al. (eds.), *Hydrologic Modeling*, Water Science and Technology Library 81, https://doi.org/10.1007/978-981-10-5801-1_7

Introduction

Agriculture accounts for more than 70% of global freshwater withdrawal (FAO 2011; Salazar et al. 2012), out of which 60% is wasted due to leaky irrigation systems and inappropriate application methods that leads to poor irrigation efficiency, decreased crop production and as a whole misuse of the scare resource. United Nations Department of Economic and Social Affairs (UNDESA) in its international decade for action 'Water for life' 2005–2015 reveals that around 700 million people in 43 countries across the globe suffer from water scarcity today.

In agriculture sector, scheduling of irrigation is considered to be the best management option for improving the present scenario of water use. Calculation of crop water requirement is not an easy task at farmer's level. As a result of an Expert Consultation held in May 1990, the FAO Penman–Monteith method is now recommended as the sole standard method for the definition and computation of the reference evapotranspiration (ET_0). The FAO Penman–Monteith method requires large number of climatic variables for calculating ET_0. But, basically, pan evaporation is widely used in agricultural meteorology due to simplicity, low cost, ease of application for irrigation scheduling. However, the density of these stations is not adequate as per recommendation even in developed countries. Complex methods of determination of appropriate timing and depth of irrigation are beyond the capacity of the farmers. The simplest method widely used across the world for estimating reference crop evaporation is pan evaporation method. But the output of the method involves an error of 15% as a whole as compared to Penman–Monteith equation (FAO 24). It may lead to magnification of error while determining the crop evapotranspiration (ETc) of the crop.

Thus, there is a need to develop a user-friendly model for the farmers describing the relationship between the evaporation rate of the pan evaporimeter in the meteorology station and the complex Penman–Monteith as it closely approximates grass ET_0 at the location evaluated, is physically based, and explicitly incorporates both physiological and aerodynamic parameters. This would help to simulate the evapotranspiration rate of the crops grown in his farm and use of the same to assess the soil moisture balance in the crop root zone on daily basis. Thus, the expected outcome would be derivation of a correct irrigation scheduling and calculation of appropriate depth of irrigation by the farmer prior to any irrigation event.

Materials and Methods

The materials used and methods adopted during the investigation are presented in this section.

Experimental Site

The experiment was conducted at the Central Research Station, Department of Agronomy, Orissa University of Agriculture and Technology, Bhubaneswar, Odisha, during the year 2013–14. The experimental site is located at 20° 15′N latitude and 82° 52′E longitude at an elevation of 25.9 m above mean sea level.

Weather Condition

Odisha is characterised by warm and moist climate with hot and humid summer and mild winter. The mean annual rainfall is about 1451 mm out of which 80% downpours during four monsoon months (June–September). The mean maximum temperature during the hottest month of May and June varies from 38 to 40 °C, and the mean minimum temperature during the colder months of December and January varies from 11 to 14 °C. The atmosphere remains quite humid throughout the year with an average relative humidity of 84%. The average wind speed above 2 m from ground level is observed to be 6.5 m s^{-1}. Occurrence of one or two cyclonic storms in each year during monsoon season is the natural climatic phenomenon, and it is mostly due to formation of low pressure at some point in the Bay of Bengal.

Theoretical Consideration

FAO Penman–Monteith equation is expressed as:

$$\mathrm{ET}_0 = \frac{0.408\Delta(R_n - G) + \gamma \frac{900}{T+273} u_2 (e_s - e_a)}{\Delta + \gamma(1 + 0.34u_2)} \quad (1)$$

where ET_0 = reference evapotranspiration [mm day^{-1}], R_n = net radiation at the crop surface [MJ m^{-2} day^{-1}], G = soil heat flux density [MJ m^{-2} day^{-1}], T = mean daily air temperature at 2 m height [°C], u_2 = wind speed at 2 m height [m s^{-1}], e_s = saturation vapour pressure [kPa], e_a = actual vapour pressure [kPa], $(e_s - e_a)$ = saturation vapour pressure deficit [kPa], Δ = slope of vapour pressure curve [kPa $°C^{-1}$], γ = psychrometric constant (kPa $°C^{-1}$).

All these data were collected for a period of 15 years (2001–2014) from the meteorological observatory in the central station of OUAT, Bhubaneswar. Apart from these data, the net radiation at the crop surface, soil heat flux, saturation and actual vapour pressure, psychrometric constant etc., were estimated based on the geographical location of the experimental site and referring some standard table values.

$$R_n = R_{ns} - R_{nl} \tag{2}$$

$$R_{ns} = 0.77Rs = 0.77(0.25 - 0.5S)R_a \tag{3}$$

$S = n/N$

$$R_{nl} = \sigma\left[\frac{T_{\max K^4} + T_{\min K^4}}{2}\right](0.34 - 0.14\sqrt{e_a})\left(1.35\frac{R_s}{R_{so}} - 0.35\right) \tag{4}$$

where R_{ns} = short-wave radiation [MJ m^{-2} day^{-1}], R_{nl} = net outgoing long-wave radiation [MJ m^{-2} day^{-1}], σ = Stefan–Boltzmann constant [4.903 $\times$ 10^{-9} MJ K^{-4} m^{-2} day^{-1}], $T_{\max}$ K = maximum absolute temperature during the 24-h period [K = °C + 273.16], $T_{\min,}$ K = minimum absolute temperature during the 24-h period [K = °C + 273.16],e_a actual vapour pressure [kPa], R_s/R_{so} relative short-wave radiation (limited to ≤ 1.0), R_s measured or calculated solar radiation [MJ m^{-2} day^{-1}], R_{so} calculated clear-sky radiation [MJ m^{-2} day^{-1}].

$$P = 101.3\left(\frac{293 - 0.0065z}{293}\right)^{526} \tag{5}$$

where P = atmospheric pressure [kPa]; z = elevation above sea level [m].

$$\gamma = \frac{c_p P}{\varepsilon\lambda} = 0.665 \times 10^{-3} P \tag{6}$$

where γ = psychrometric constant [kPa °C^{-1}], P = atmospheric pressure [kPa], λ = latent heat of vaporisation, 2.45 [MJ kg^{-1}], C_p = specific heat at constant pressure, 1.013 $\times$ 10^{-3} [MJ kg^{-1} °C^{-1}], ε = ratio molecular weight of water vapour/dry air = 0.622.

$$\text{RH} = 100\frac{e_a}{e^o(T)} \tag{7}$$

The saturation vapour pressure is related to air temperature, and the following equation has been used to determine it.

$$e^o(T) = 0.6108\exp\left[\frac{17.27T}{T + 237.3}\right] \tag{8}$$

where $e°(T)$ = saturation vapour pressure at the air temperature T [kPa]; T = air temperature [°C].

$$\Delta = \frac{4098\left[0.6108\exp\left(\frac{17.27T}{T + 237.3}\right)\right]}{(T + 237.3)^2} \tag{9}$$

where Δ = slope of saturation vapour pressure curve at air temperature T [kPa °C^{-1}]; T = air temperature [°C]; exp[..] 2.7183 (base of natural logarithm) raised to the power [..].

$$e_a = \frac{e^{o}(T_{\min})\frac{RH_{max}}{100}e^{o}(T_{\max})\frac{RH_{min}}{100}}{2} \tag{10}$$

where e_a = actual vapour pressure [kPa]; $e°$ (T_{min}) = saturation vapour pressure at daily minimum temperature [kPa]; e° (T_{max}) = saturation vapour pressure at daily maximum temperature [kPa]; RH_{max} = maximum relative humidity [%]; RH_{min} = minimum relative humidity [%].

R_a and N are functions of latitude, date and time of day. Monthly values of R_a and N throughout the year for different latitudes are taken from the standard table (Kumar and Singh 2005).

$$\text{Equivalent evaporation}\left[\text{mm day}^{-1}\right] = 0.408 \times \text{Radiation}\left[\text{MJ m}^{-2}\text{ day}^{-1}\right] \tag{11}$$

$$G = c_s\frac{T_i - T_{i-1}}{\Delta t}\Delta z \tag{12}$$

where G = soil heat flux [MJ m^{-2} day^{-1}], c_s soil heat capacity [MJ m^{-3} °C^{-1}], T_i = air temperature at time i [°C], T_{i-1} = air temperature at time $i - 1$ [°C], Δt = length of time interval [day], Δz = effective soil depth [m].

Determination of ET_0 Using US Class A Pan Evaporimeter

Daily reference crop evapotranspiration was calculated from the US Class A pan evaporimeter installed in the crop weather observatory of the central farm.

The pan evaporation is expressed as:

$$ET_0 = K_p \times E_{pan} \tag{13}$$

where K_p = pan coefficient and its value is assumed to be 0.7; E_{pan} = pan evaporation rate, mm/day.

Development of Model

Calculation of the ET_0 by both FAO Penman–Monteith equation and the US Class A pan evaporimeter was made on weekly basis for 12 years from 2001 to 2012. Using these two sets of data, the relationship between the ET_0 by Penman–Monteith

method and reference crop evapotranspiration estimated by pan evaporimeter was developed through putting the data to various relation functions such as linear, exponential, power, polynomial (2nd degree), and logarithmic inbuilt into the Microsoft Excel software. Thus, the ET_0 models were developed.

Validation of Model

This model was used to predict ET_0 using pan evaporimeter data for two years, namely 2013 and 2014. Based on a comparison study between these predicted values of ET_0 and the actual ET_0 values estimated by Penman–Monteith equation, the model validation process was carried out. Statistical methods such as root-mean-squared error (RMSE), percent deviation, Scatter plots and Nash–Sutcliffe model accuracy test were used to verify the prediction ability of the model developed.

Root-Mean-Square Deviation or Error

$$\text{RMSD} = \sqrt{\frac{\sum_{t=1}^{n} (x_{1,t} - x_{2,t})^2}{n}}. \tag{14}$$

Percent Deviation

$$\% \text{ deviation} = [(\text{Actual value} - \text{Expected value}) * 100]/\text{Expected value} \tag{15}$$

Scatter Plot

A graph of plotted points shows the relationship between two sets of data. Scatter plots are important in statistics because they can show the extent of prediction efficiency of the model through eye observation only.

Nash–Sutcliffe Model Accuracy Test

Nash–Sutcliffe model efficiency coefficient is used to assess the predictive power of hydrological models. It is defined as:

$$E = 1 - \left(\sum_{t=1}^{T} \left(Q_o^t - Q_m^t \right)^2 \div \sum_{t=1}^{T} \left(Q_o^t - Q_o^- \right)^2 \right) \quad (16)$$

where Q_o is the mean of observed discharges and Q_m is modelled discharge. Q_o^t is observed discharge at time t. Nash–Sutcliffe coefficient is an indicator of the model's ability to predict about the 1:1 line between observed and simulated data. With Nash–Sutcliffe measure, an r-square coefficient is calculated. Coefficient values equal to 1 indicate a perfect fit between observed and predicted data, and values less than or equal to 0 indicate that the model is predicting no better than using the average of the observed data.

Results and Discussion

Comparison of ET_0 Values Estimated by Penman–Monteith and Pan Evaporimeter

Weekly ET_0 values are estimated by FAO Penman–Monteith equation and pan evaporimeter for 14 years from 2001 to 2014. The average ET_0 values for each week are presented in Table 1. It is observed that in almost all the weeks, the actual ET_0 value estimated by FAO Penman–Monteith equation remains higher than the corresponding ET_0 values measured by pan evaporimeter. The fact has been illustrated through Fig. 1. It may be seen that the ET_0 values in both the methods are remaining highest during 17th week to 24th week of the year and this period coincides with the peak summer in the region. Similarly, the ET_0 values estimated by both the methods are found lying low during initial and end weeks of the year and this period coincides with peak winter in the region.

The point of concern is that the ET_0 values obtained from the pan evaporimeter throughout the year are lying considerably low as compared to the actual ET_0 estimated by FAO Penman–Monteith equation. The difference is observed to vary from 3 to 6.2 cm per week. The percent of error in estimation of ET_0 by pan evaporimeter is sometimes more than 50% in the study region. Thus, keeping the high level of error involved in estimation of ET_0 by pan evaporimeter, it is not at all recommended to use pan evaporation data as such for deciding the irrigation scheduling as well as computing the crop water requirement.

As the ET_0 values are under-predicted in all the weeks by pan evaporimeter method, so the crop water requirement estimated would be very low in comparison with the actual. The irrigation amount applied based on this value would again be inadequate as compared to the actual water requirement of the crop. Thus, the yield of crop is bound to remain below the normal yield of the crop. On the other hand, the irrigation frequency will be quicker leading to application of more water to the crop. Thus, a relationship needs to be developed between the ET_0 values observed

Table 3.1 Average weekly ET_0 values estimated by FAO Penman–Monteith and pan evaporimeter

Week no.	ET_0 pan	ET_0 P–M	Week no.	ET_0 pan	ET_0 P–M
1	2.71	3.45	27	2.79	3.32
2	2.70	3.36	28	5.25	3.74
3	2.92	3.59	29	2.62	3.66
4	2.87	3.40	30	2.87	3.62
5	2.77	3.71	31	2.85	3.56
6	2.98	4.03	32	2.85	3.51
7	3.31	4.09	33	2.86	3.53
8	3.58	4.19	34	3.19	3.80
9	3.73	4.86	35	2.79	3.67
10	3.98	4.66	36	3.27	3.55
11	4.20	4.56	37	2.76	3.64
12	4.76	4.80	38	2.68	3.57
13	4.86	4.88	39	3.05	4.34
14	5.17	5.07	40	2.87	3.62
15	5.71	5.17	41	3.08	4.12
16	5.93	5.39	42	3.10	4.26
17	6.17	5.43	43	3.02	4.16
18	6.43	5.77	44	2.81	3.69
19	6.72	5.61	45	2.80	3.51
20	6.54	5.54	46	2.87	3.67
21	6.37	5.49	47	2.87	3.84
22	6.89	5.57	48	2.85	3.55
23	6.28	4.99	49	2.82	3.37
24	5.57	4.18	50	2.75	3.29
25	4.80	4.25	51	2.82	3.26
26	3.43	3.55	52	2.88	3.36

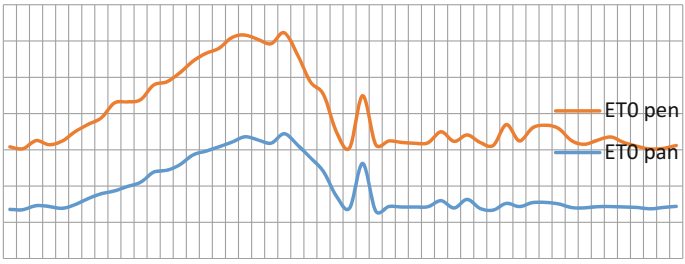

Fig. 3.1 Comparison between ET_0 measured by pan evaporimeter and estimated by FAO Penman–Monteith method

by pan evaporimeter and those of the FAO Penman–Monteith which would enable the stakeholders to compute the crop water requirement accurately and develop a correct approach for deciding irrigation scheduling for the crops grown in the zone.

Relationship Between ET_0 Calculated by Pan Evaporimeter and Penman–Monteith Methods

Average values of ET_0 estimated on weekly basis by FAO Penman–Monteith and pan evaporimeter methods were put into regression analysis, and the relationship between them is shown through Fig. 2a–e. Relationship between ET_0 measured

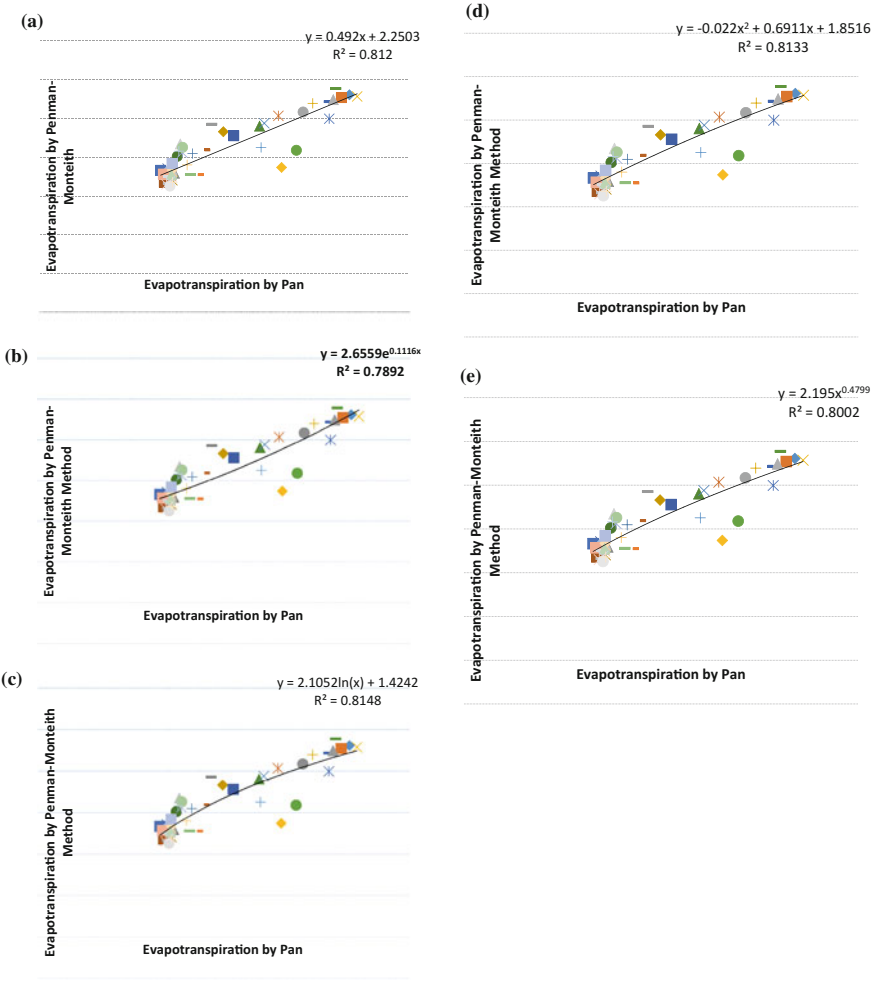

Fig. 3.2 Relationship between ET_0 estimated by FAO P–M method and pan evaporation method

by pan evaporimeter and that estimated by Penman–Monteith method had been described through various relation functions such as linear, exponential, power, polynomial (2nd degree), and logarithmic. Among the relation functions, the data set are showing a perfect matching trend under linear function based on highest value of coefficient of determination (R^2) i.e. 0.8148. In rest of the functions, though the data sets are matching, the R^2 values are found to be smaller than the former. Hence, the relation function between ET_0 estimated by FAO Penman–Monteith and pan evaporimeter is found to be linear as shown in Fig. 2a. The corresponding equation that describes the relation between the Penman–Monteith and pan evaporimeter is expressed as:

$$Y = 0.492(X) + 2.2503 \tag{17}$$

where Y = predicted ET_0 and X = ET_0 measured by pan evaporimeter.

The model developed for converting pan ET_0 to the actual ET_0 (FAO Penman–Monteith ET_0) has been validated using the pan evaporation data for two years, namely 2013 and 2014.

Validation of the Model

The developed ET_0 model was used to convert the ET_0 values obtained from the pan evaporimeter during the year 2013–2014. The predicted values thus obtained were compared with the ET_0 values estimated by FAO Penman–Monteith equation in the respective years. The estimated and predicted ET_0 values for both the years are presented in Appendix A. Statistical tools like RMSE, percent deviation, Scatter plots and Nash–Sutcliffe model accuracy test have been used in the process of validation of the model.

The values of RMSE between the predicted and actual ET_0 were found to be very less in both the years. While in case of the year 2013, the error came around 0.622 mm/week and it was 0.468 mm/week in the year 2014. It indicates that there is marginal error in using the model for prediction of the ET_0 values. In addition to it, the prediction efficiency of the model was again established by the minimal per cent deviation of −5.53% in 2013 and 0.82% in the year 2014. In the first year of simulation, the model is observed to under-predict the ET_0 values by 5.53% only, and in the year 2014, the same has been over-predicted by an amount of only 0.82%. In both the years, the deviation of the predicted ET_0 values is very less and so, it may be taken for granted that the developed model is capable of converting the pan evaporimeter ET_0 values to the actual ET_0 values as estimated by FAO Penman–Monteith equation.

Also, the strong prediction efficiency of the developed model in converting pan ET_0 to Penman–Monteith ET_0 has been established through the use of Scatter plots as shown in Figs. 3 and 4 for the year 2013 and 2014, respectively. It is depicted from Fig. 3 that the predicted values of ET_0 are both over-and

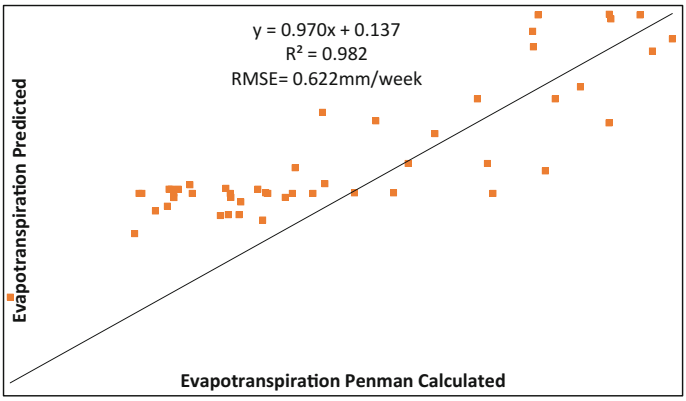

Fig. 3.3 Scatter plot of P–M ET_0 versus pan ET_0 during 2013

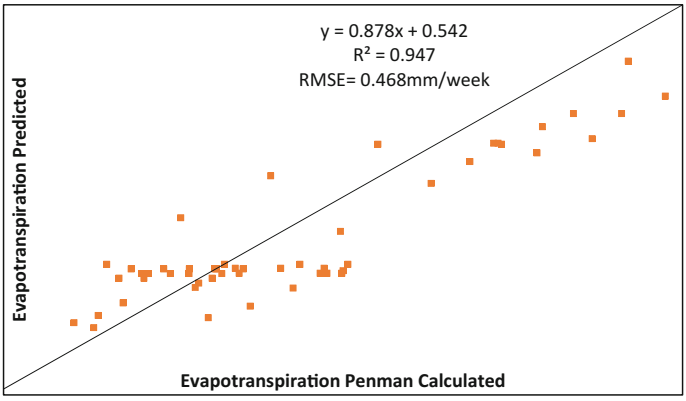

Fig. 3.4 Scatter plot of P–M ET_0 versus pan ET_0 during 2014

under-predicted but the predicted values lie close to the 1:1 line. The percent deviation is within 10%, and thus it establishes the fact that the prediction efficiency of the model is very high. Similarly, in the year 2014, the Scatter plot of ET_0 by pan evaporimeter and Penman–Monteith as illustrated in Fig. 4 indicates the minimal gap between the predicted and the actual values of ET_0. The percent deviation of only 0.82% emphatically pronounces the high-degree predictability of the model. In this case, the RMSE is still lower than the previous year. The distribution of predicted points very close to and at both sides of 1:1 line implies a high degree of prediction efficiency of the model.

Finally, the Nash–Sutcliffe model accuracy tests give r^2 value of 0.94 in the model validation process. This value is very close to unity which clearly shows accuracy of the model. From the discussion made above, it may be concluded at this point that using pan evaporimeter data for estimation of crop water requirement as

well as taking decision on irrigation scheduling should not be recommended for the study area. Whenever there is no access to Penman–Monteith ET_0 values, the developed model should be used to convert the pan ET_0 values to the actual ET_0 values correctly.

Conclusions

The following conclusions may be drawn at the end of the present study. These are:

- Measurement of ET_0 by pan evaporimeter is an erroneous approach as a high degree of difference is observed between the pan ET_0 and FAO Penman–Monteith ET_0 values throughout the year. The difference is observed to be more than 50% in almost all the weeks of the year. Hence, use of pan data for computation of crop water requirement and taking decision on irrigation scheduling involves considerable error.
- Pan ET_0 values should be put to the model developed in the present study to convert the erroneous pan ET_0 values to actual FAO Penman–Monteith ET_0 values. It is so because the model predicts the ET_0 values accurately close to the actual with minimal percent deviation (<10%) and less RMSE (<0.65 mm/week).
- The model developed in the present study may be reliably used for converting the pan ET_0 values to the actual FAO Penman–Monteith ET_0 values in the regions having similar agro-climatic conditions.

References

Allen RG, Pereira LS, Raes D, Smith M (1998) Crop evapotranspiration: guidelines for computing crop requirements. FAO irrigation and drainage paper no. 56. Food and Agriculture Organization of the United Nations, Rome, Italy

Doorenbos J, Pruitt W (1977) Crop water requirements. FAO irrigation and drainage paper no. 24. Food and Agriculture Organization of the United Nations, Rome, Italy

FAO (2011) Crop water requirement paper. Food and Agriculture Organization of the United Nations, Rome, Italy

Kumar R, Singh J (2005) Textbook of drainage Engineering. ICAR, New Delhi, pp 135–149

Mendonca JC, Esteves BS, Sousa EF (2004) Evapotranspiration (ET_0) in North Fluminense, Rio de Janerio, Brazil: a review of methodologies of the calibration for different periods of analysis. Environmental Hydrology, Lewis Publishers, USA, p 465

Smith M, Allen R, Monteith JL, Pereira LA, Perrier A, Segeren (1991) A report on the expert consultation for the revision of FAO methodologies for crop water requirements, FAO/AGL, Rome

Salazara MR, Hook JE, Garcia A, Paza JO, Chavesa B, Hoogenboom GA (2012) Estimating irrigation water use for maize in the South eastern USA: a modelling Approach. Agric Water Manag 107:11–104

Part III
Urban Runoff

Spatial and Temporal Analyses of Impervious Surface Area on Hydrological Regime of Urban Watersheds

Tauseef A. Ansari and Y. B. Katpatal

Abstract The industrialisation and urbanisation have significant impacts on hydrological regimes within the watersheds. The spatial analysis in urban watersheds is prerequisite for management of surface and subsurface water regimes. The objective of the study is to analyse the impacts of increase in impervious surface area (ISA) in urban watersheds of the Nagpur city. High-resolution satellite images were used of year 2000 and 2012. Significant increase in ISA was observed in the watersheds between 2000 and 2012 having impacts on vegetation index, runoff, CN and flash floods. Statistical analyses were used to establish the relationship between runoff, impervious surface areas, vegetation index, slope and runoff coefficient.

Keywords Runoff · SCS-CN · Potential maximum retention
Slope-based curve number

Introduction

Urbanisation in the country has rapidly increased; as a result, most of the cities have expanded in the past few years. Currently, about 3.3 billion humans reside in cities, and this figure is expected to rise to 5.0 billion by 2030 (United Nations 2008). The number of Indian mega cities will increase from the current three (Mumbai, Delhi and Kolkata) to six by the year 2021 (including Bangalore, Chennai and Hyderabad), when India will have the largest concentration of mega cities in the world (Chakrabati 2001). Expansion of the impervious surface area in the city has started to impact the surface and subsurface hydrological units in the area. In recent years, impervious surface has emerged not only as an indicator of the degree of

T. A. Ansari (✉) · Y. B. Katpatal
Department of Civil Engineering, Visvesvaraya National Institute of Technology, Nagpur 440010, India
e-mail: sirftauseef@gmail.com

Y. B. Katpatal
e-mail: ybkatpatal@rediffmail.com

V. P. Singh et al. (eds.), *Hydrologic Modeling*, Water Science and Technology Library 81, https://doi.org/10.1007/978-981-10-5801-1_8

urbanisation, but also a major indicator of environmental quality (Arnold and Gibbons 1996). Increased population is undoubtedly a source of consumption and waste generation in the city. Taubenbock et al. (2009) conducted the spatiotemporal analysis to detect the changes and similarities and dissimilarities in the urban characteristics of 12 largest cities in India through remote sensing and geographic information system (GIS). Gupta et al. (2012) assessed the greenness in urban areas using remote sensing and GIS. Ma and Xu (2010) analysed orientation and rate of variation of urban expansion of Guangzhou City for the period of 23 years. The increase of impervious surface area would lead to the increase in the volume, duration and intensity of urban runoff (Weng 2001).

Rainfall is the important source of water resources, but huge amount gets converted into runoff due to change in the land use/land cover (LU/LC). The changes in storm runoff, resulting from the LU/LC change with the development of urban areas, have also been estimated (Rongrong and Guishan 2007; Suiji et al. 2012; Yan et al. 2013; Miller et al. 2014). Soil Conservation Service curve number (SCS-CN) method is the widely used due to its low data requirement. Curve number (CN) values for runoff have been obtained experimentally using measured rainfall-runoff data over the wide range of geographic, soil and land use conditions. However, the watershed slope adjustment has not been taken into account (Huang et al. 2006). The watershed slope is an important factor determining water movement within a landscape (Huang et al. 2006). Many researchers have analysed the effect of slope under natural or artificial conditions for the same type of LU/LC. In Pakistan, Shafiq and Ahmad (2001) used three slopes (1, 5 and 10%) in silt loam soil under medium rainfall intensities and found that the runoff increases with slope. Deshmukh et al. (2013) found significant results in the runoff estimation values made by using the slope adjusted CN, as proposed by Sharpley and Williams in 1990. Mishra et al. (2014) experimentally analysed the effect of slope and LU/LC on the SCS-CN. The study area consists of ungauged watersheds; hence, it is difficult to observe the actual runoff in the watersheds. LU/LC has been changed drastically during year 2000 and 2012 due to which significant change in the impervious surface area (ISA) estimated. In this study, change in the weighted CN, slope-based CN, relationship between runoff, impervious areas, vegetation index, slope and runoff coefficient have been established using Spearman's and Pearson's statistical methods in addition to assuming the initial abstraction ratio as 0.05.

Study Area

Nagpur city in the central India is growing rapidly in "radial pattern" with open spaces covered with vegetation (Katpatal et al. 2008). There are subwatersheds of WGKN-1, WGKN-4, WGKN-5, in the study area with the total area of 290.80 km^2 considered for the present study. Nagpur has tropical wet and dry climate. Average

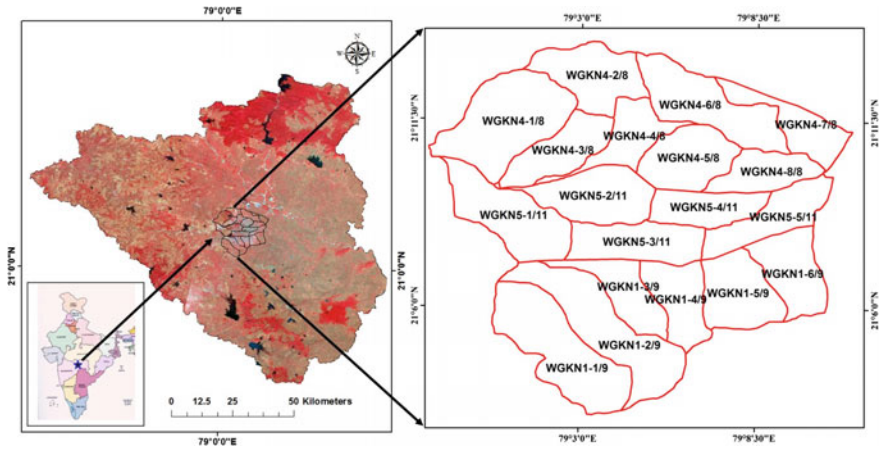

Fig. 1 Location map of the nineteen watersheds in the Nagpur urban area

annual rainfall of the Nagpur is almost 1000 mm, the maximum temperature recorded in the month of May as 47 °C. The topographic elevation of the area ranges between 335 and 210 m (Fig. 1) (Varade et al. 2013).

Soil of the Study Area

The study area has two types of soil, clayey and clay loam. Based on the moderate and moderate-to-low infiltration characteristics and more runoff potential, the soil is categorised in the *C* and *D* hydrological soil group (HSG) in the area (Fig. 2).

Methodology

The present study utilises geoinformatics technology, where high spatial resolution satellite images (Google Earth) of year 2000 and 2012 and geographic information system (GIS) have been used. SCS-CN method is used to determine the weighted CN and when slope of the watershed is considered for the year 2000 and 2012. However, CN in normal condition is compared with slope-based CN. The effect of slope and LU/LC on CN is compared for year 2000 and 2012. Runoff in normal and slope-based conditions is compared for July 2000 and July 2012 (Fig. 3).

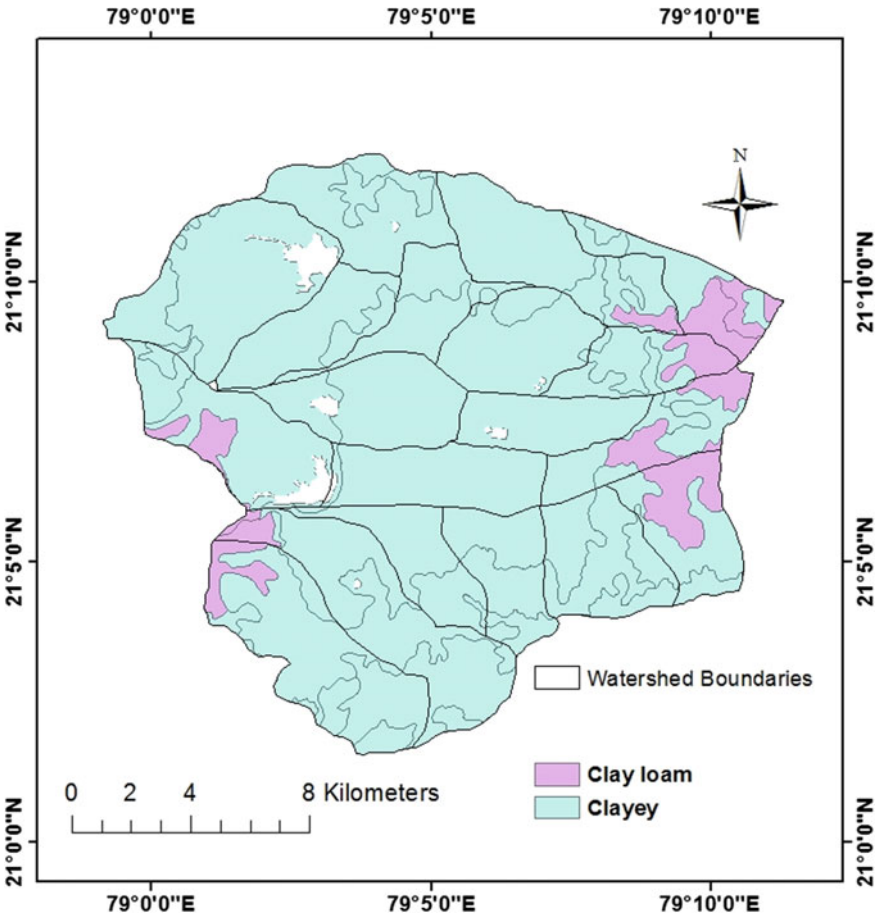

Fig. 2 Hydrologic soil group (HSG) map of the study area

Results

Following are the basic equations of SCS-CN method (Mishra et al. 2014):

$$P = I_a + F + Q, \tag{1}$$

$$\frac{Q}{(P - I_a)} = \frac{F}{S}, \tag{2}$$

$$I_a = \lambda S, \tag{3}$$

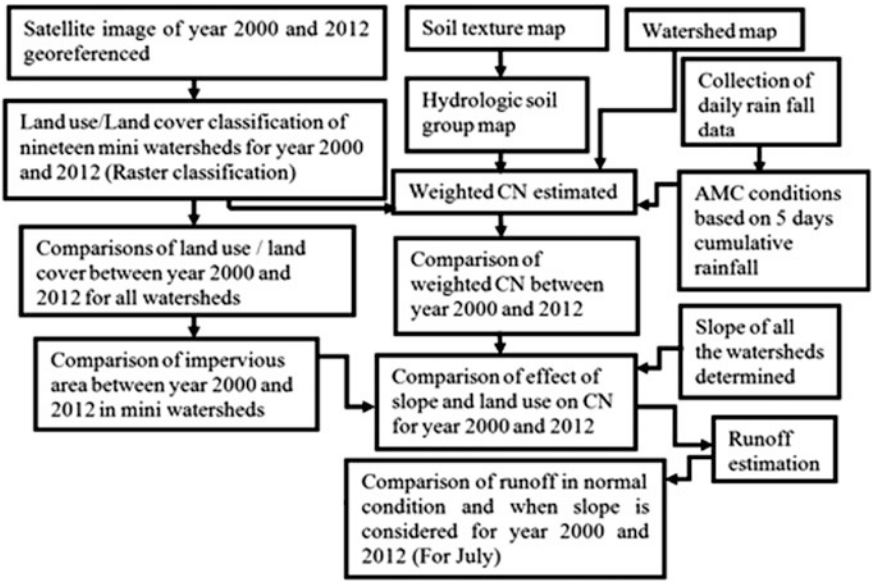

Fig. 3 Flow diagram of the complete methodology

$$Q = \frac{(P - I_a)^2}{(P - I_a + S)}, \tag{4}$$

where P = total rainfall; I_a = initial abstraction; F = cumulative infiltration excluding I_a, Q = direct runoff; and S = potential maximum retention or infiltration. Equation (4) is the general form of SCS-CN method, and it is valid when $P \geq I_a$; $Q = 0$ otherwise.

Here, the initial abstraction is taken as the 5% ($I_a = \Lambda s$ where $\lambda = 0.05$). In 1990, Sharpley and William considered slope for adjusting the CN

$$\mathrm{CN2}\alpha = \frac{1}{3}(\mathrm{CN3} - \mathrm{CN2})\left(1 - 2e^{-13.86\alpha}\right) + \mathrm{CN}, \tag{5}$$

where CN2α is the curve number when average slope is considered, CN2 and CN3 are CNs for soil moisture condition II (average) and III (wet), respectively; and $\alpha(\mathrm{mm}^{-1})$ is the average slope of watersheds. Equation (5) was used to estimate the CN2α values for all watersheds. CN3 is estimated using Eq. (6):

$$\mathrm{CN3} = \left(\mathrm{CN2}\, e^{0.00673(100-\mathrm{CN2})}\right) + \mathrm{CN2}. \tag{6}$$

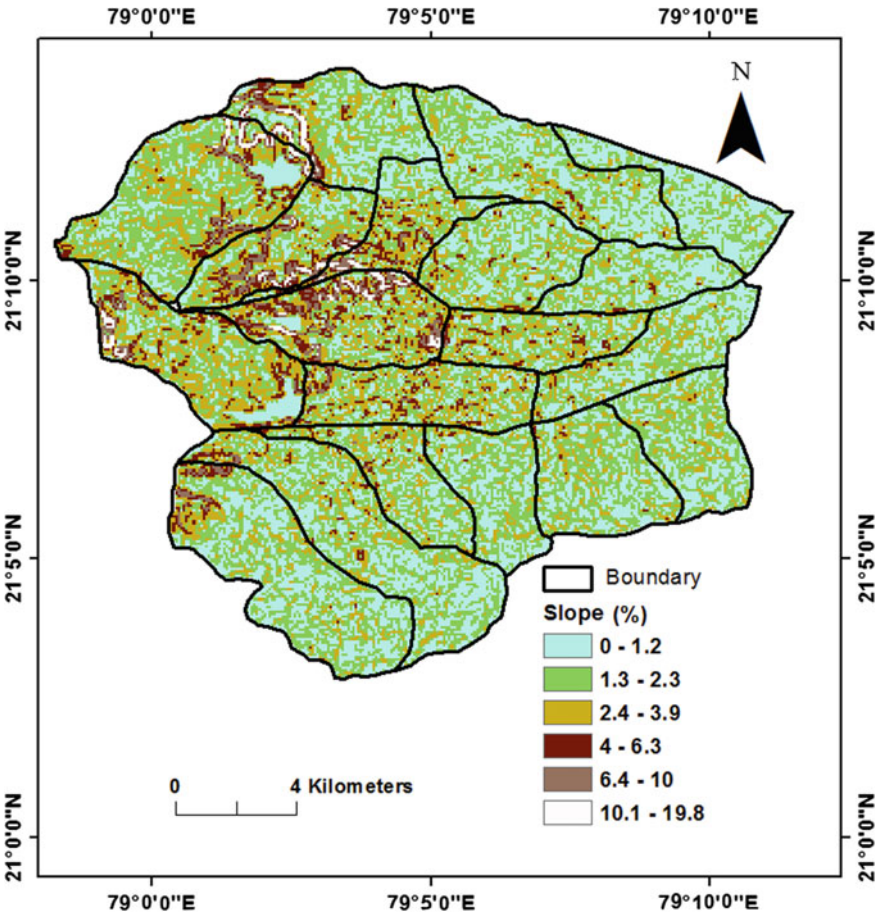

Fig. 4 Slope map of the all watersheds comes under Nagpur urban area

The slope classes in the study area have been extracted from the DEM generated from Shuttle Radar Topography Mission (SRTM) data. The slope in the area approximately varies from 0.1 to 19.8% which is classified into six classes (Figs. 4).

Comparison of Weighted CN (in Normal Condition) and CN2α (Slope-Based CN) for Year 2000 and 2012

The increase in the weighted CN values in watersheds shows changes due to change in the LU/LC during year 2000 and 2012 (Table 1). The watersheds WGKN 1-4/9, WGKN 1-5/9, WGKN 1-6/9, WGKN 4-2/8 and WGKN 4-6/8 show the change in

Table 1 Changes estimated in the weighted CN, slope-based curve number and percentage change for the weighted CN and slope-based CN (ΔCN)

Watershed codes	Weighted CN in year 2000	Weighted CN in year 2012	Percentage change in the weighted curve number (ΔCN) during 2000 and 2012	CN when slope is considered for year 2000 (CN2α)	CN when slope is considered for year 2012 (CN2α)	Percentage change in the slope-based CN during 2000 and 2012 (ΔCN)
WGKN 1-1/9	87	88	1.14	90	91	1.10
WGKN 1-2/9	89	89	0.00	91	91	0.00
WGKN 1-3/9	90	91	1.10	92	93	1.08
WGKN 1-4/9	81	**93**	**12.90**	85	94	**9.57**
WGKN 1-5/9	87	**92**	**5.43**	89	93	**4.30**
WGKN 1-6/9	85	**89**	**4.49**	87	91	**4.40**
WGKN 4-1/8	78	79	1.27	82	83	1.20
WGKN 4-2/8	76	**88**	**13.64**	79	90	**12.22**
WGKN 4-3/8	88	89	1.12	**90**	**91**	1.10
WGKN 4-4/8	89	90	1.11	**91**	**92**	1.09
WGKN 4-5/8	**93**	**93**	0.00	**94**	**94**	0.00
WGKN 4-6/8	86	**88**	2.27	89	90	1.11
WGKN 4-7/8	**90**	**91**	1.10	92	93	1.08
WGKN 4-8/8	89	90	1.11	91	92	1.09
WGKN 5-1/11	79	80	1.25	82	83	1.20
WGKN 5-2/11	85	86	1.16	88	89	1.12
WGKN 5-3/11	**91**	**92**	1.09	**92**	**93**	1.08
WGKN 5-4/11	**92**	**92**	0.00	**93**	**94**	1.06
WGKN 5-5/11	89	91	2.20	**91**	**93**	2.15

the weighted CN while WGKN 1-2/9, WGKN 4-5/8 and WGKN 5-4/11 show no change condition due to low development in the area.

Percentage Change in Weighted Curve Number (ΔCN) and Change in the CN for All Watersheds

The percentage change in the curve number between the years reflects degree in which LU/LC has changed. Suribabu and Bhaskar (2015) evaluated the percentage change in the CN for the long duration. The percentage change is calculated from Eq. (7). The watersheds WGKN 1-4/9, WGKN 1-5/9 and WGKN 1-6/9 show the maximum percentage change during year 2000 and 2012. The watersheds showing significant change values are made bold in the respective (Table 1).

$$CNi = (CNt_2 - CNt_1)/CNt_2 \times 100, \quad (7)$$

where CNt_2 and CNt_1 are the CN in the year 2012 and 2000.

Comparison of Potential Maximum Retention (S) and Runoff Depth (Q) for Year 2000 and 2012

Potential maximum retention (s) and runoff depth (Q) are calculated to analyse the differences occurred in the two different conditions (Table 2). The 5% initial abstraction assumption reflects the more potential maximum retention; then, the 20% initial abstraction and runoff of 5% initial abstraction condition show the low

Table 2 Potential maximum retention and runoff when initial abstraction is assumed 20, 5% and when slope is considered for 5% initial abstraction for July 2000

Watershed codes	Potential maximum retention (S) (when initial abstraction assumed 20%) m	Potential maximum retention (S) (when initial abstraction assumed 5%) m	Potential maximum retention (S) (initial abstraction assumed 5%, when slope considered) mm	Runoff depth (Q) for 20% initial abstraction (mm)	Runoff depth (Q) for 5% initial abstraction (mm)	Runoff depth (Q) when slope is considered for 5% initial abstraction (mm)
WGKN 1-1/9	35.17	79.79	27.14	143.86	107.59	170.89
WGKN 1-2/9	28.67	63.09	22.91	165.18	136.88	188.37
WGKN 1-3/9	25.35	54.75	19.59	177.98	140.03	204.11
WGKN 1-4/9	56.45	137.50	44.01	96.70	66.70	120.85
WGKN 1-5/9	37.09	84.82	28.62	138.34	102.59	165.38
WGKN 1-6/9	44.69	105.10	34.68	119.31	85.80	145.32
WGKN 4-1/8	69.17	173.67	53.52	78.67	53.95	101.70
WGKN 4-2/8	77.59	198.20	66.33	68.75	44.79	82.39
WGKN 4-3/8	33.29	74.91	25.69	149.58	112.85	176.57
WGKN 4-4/8	30.70	68.25	23.70	158.04	120.76	184.89
WGKN 4-5/8	18.63	38.43	14.40	**209.02**	171.89	**233.33**
WGKN 4-6/8	39.15	90.26	30.20	132.76	97.59	159.76
WGKN 4-7/8	26.41	57.39	20.40	173.74	135.85	200.07
WGKN 4-8/8	29.23	64.50	22.57	163.17	125.62	189.88
WGKN 5-1/11	67.42	168.64	52.25	81.01	53.85	103.99
WGKN 5-2/11	42.49	99.16	32.76	124.41	90.23	151.25
WGKN 5-3/11	25.11	54.17	19.40	**178.94**	140.98	**205.07**
WGKN 5-4/11	21.18	44.53	16.37	**196.32**	158.57	**221.50**
WGKN 5-5/11	29.92	66.24	23.10	160.75	123.32	187.53

Table 3 Potential maximum retention and runoff when initial abstraction is assumed 20, 5% and when slope is considered for 5% initial abstraction for July 2012

Watershed codes	Potential maximum retention (S) (when initial abstraction assumed 20%) mm	Potential maximum retention (S) (when initial abstraction assumed 5%) mm	Potential maximum retention (S) (initial abstraction assumed 5%, when slope considered) mm	Runoff depth (Q) for 20% initial abstraction (mm)	Runoff depth (Q) for 5% initial abstraction (mm)	Runoff depth when (Q) slope is considered for 5% initial abstraction (mm)
WGKN 1-1/9	32.02	71.63	24.75	98.22	78.46	117.73
WGKN 1-2/9	28.75	63.28	22.99	106.12	85.62	123.03
WGKN 1-3/9	22.28	47.21	17.25	125.43	103.48	145.23
WGKN 1-4/9	18.18	37.35	14.24	141.19	118.58	159.92
WGKN 1-5/9	21.43	45.13	16.58	128.46	106.33	148.28
WGKN 1-6/9	30.36	67.37	23.62	102.10	78.76	120.96
WGKN 4-1/8	66.09	164.81	51.22	54.46	38.84	67.70
WGKN 4-2/8	31.80	71.07	27.32	95.11	78.91	109.93
WGKN 4-3/8	30.70	68.25	23.73	101.28	81.22	120.60
WGKN 4-4/8	27.99	61.37	21.64	108.10	87.42	127.69
WGKN 4-5/8	17.91	36.71	13.86	**142.33**	119.82	**161.96**
WGKN 4-6/8	33.41	75.21	25.82	95.20	75.73	114.18
WGKN 4-7/8	23.07	49.13	17.85	123.93	101.03	142.58
WGKN 4-8/8	25.39	54.84	19.63	115.47	94.19	135.26
WGKN 5-1/11	62.73	155.22	48.69	57.39	40.57	70.59
WGKN 5-2/11	40.19	93.03	31.04	82.52	64.27	100.48
WGKN 5-3/11	21.37	45.00	16.54	128.65	106.52	148.44
WGKN 5-4/11	20.07	41.87	15.53	**133.50**	111.25	**154.14**
WGKN 5-5/11	23.88	51.11	18.47	120.14	98.52	140.66

runoff depth compared to 20% condition. However, runoff is significantly increased when slope of the watersheds is considered even at 5% initial abstraction condition for year July 2000 and 2012 (Tables 2 and 3).

Conclusions and Discussions

The study demonstrates the use of SCS-CN method and other parameters in monitoring the surface hydrological regime in urban watersheds. In Nagpur city, huge urbanisation was observed in few watersheds between years 2000 and 2012.

The following significant conclusions may be drawn based on the present study.

(1) The significant changes occurred in the impervious surfaces area (ISA) and due to the increase in ISA, CN and also runoff within the watersheds WGKN 1-4/9, WGKN 1-5/9, WGKN 1-6/9, WGKN 4-2/8, WGKN 4-5/8, WGKN 4-7/8, WGKN 5-3/11 and WGKN 5-4/11 has increased.
(2) Proper initial abstraction (5%) assumption gives the almost accurate runoff quantity.
(3) Urbanisation has adversely impacted the hydrological parameters and changing LU/LC has a profound impact on the CN and runoff.
(4) A significant increase in weighted CN and runoff depth has been observed in the watersheds due to urbanisation during 2000 and 2012.
(5) There is a marginal increase in CN values and runoff when slope is considered in SCS-CN method.

Since the development in the urban watersheds is obvious so there should be the strict guidelines for sustainable of urban area development.

References

Arnold CL Jr, Gibbons CJ (1996) Impervious surface coverage: the emergence of a key environmental indicator. J Am Plan Assoc 62:243–258

Chakrabati PGD (2001) Urban crisis in India: new initiatives for sustainable cities. Dev Pract 11(2–3):260–272

Deshmukh DS, Chaube UC, Hailu AE, Gudeta DA, Kassa MT (2013) Estimation and comparison of curve numbers based on dynamic land use land cover change, observed rainfall-runoff data and land slope. J Hydrol 492:89–101

Gupta K, Kumar P, Pathan SK, Sharma KP (2012) Urban neighborhood green index—a measure of green spaces in urban areas. Landsc Urban Plan 105:325–335

Huang M, Gallichand J, Wang Z, Goulet M (2006) A modification to the soil conservation service curve number method for steep slopes in the loess plateau of China. J Hydrol Process 20(3):579–589

Katpatal YB, Kute A, Satapathy DR (2008) Surface- and air-temperature studies in relation to land use/land cover of Nagpur urban area using landsat 5 TM data. J Urban Plan Dev 134(3): 110–118

Ma Y, Xu R (2010) Remote sensing monitoring and driving force analysis of urban expansion in Guangzhou city, China. Habitat Int 34:228–235

Miller JD, Kim H, Kjeldsen TR, Packman J, Grebby S, Dearden R (2014) Assessing the impact of urbanization on storm runoff in a peri-urban catchment using historical change in impervious cover. J Hydrol 515:59–70

Mishra SK, Chaudhary A, Shrestha RK, Pandey A, Lal M (2014) Experimental verification of the effect of slope and land use on SCS runoff curve number. Water Resour Manag 28:3407–3416

Rongrong W, Guishan Y (2007) Influence of land use/cover change on storm runoff a case study of Xitiaoxi river basin in upstream of Taihu lake watershed. J Chin Geogr Sci 17(4):349–356

Shafiq M, Ahmad B (2001) Surface runoff as affected by surface gradient and grass cover. J Eng Appl Sci 20(1):88–92

Sharpley AN, Williams JR (1990) EPIC-erosion/productivity impact calculator: 1. Model determination. US Department of Agriculture. Tech. Bull., No. 1768

Suiji W, Yunxia Y, Ming Y, Xiaokun Z (2012) Quantitative estimation of the impact of precipitation and human activities on runoff change of the Huangfuchuan river basin. J Geog Sci 22(5):906–918

Suribabu CR, Bhaskar J (2015) Evaluation of urban growth effects on surface runoff using SCS-CN method and Green-Ampt infiltration model. J Earth Sci Inf 8:609–626

Taubenbock H, Wegmann M, Roth A, Mehl H, Dech S (2009) Urbanization in India-Spatiotemporal analysis using remote sensing data. Comput Environ Urban Syst 33:179–188

United Nations (2008) World urbanization prospects: the 2007 revision. Highlights. New York: Population Division, Department of Economic and Social Affairs, United Nations. http://www.un.org/esa/population/publications/wup2007/2007WUP_Highlights_web.pdf

Varade AM, Khare YD, Mondal NC, Sarang M, Pawan W, Priti R (2013) Identification of water conservation sites in a watershed (WRJ-2) of Nagpur district, Maharashtra using geographical information system (GIS) technique. J Indian Soc Remote Sens 41(3):619–630. doi:10.1007/s12524-012-0232-5

Weng Q (2001) Modeling urban growth effect on surface runoff with the integration of remote sensing and GIS. Environ Manag 28:737–748

Yan H, Edwards FG (2013) Effects of land use change on hydrologic response at a watershed scale, Arkansas. J Hydrol Eng 18:1779–1785

An Assessment of Hydrological Impacts Due to Changes in the Urban Sprawl in Bhopal City and its Peripheral Urban-Rural Fringe

L. Patel, S. Goyal and T. Thomas

Abstract Bhopal district has been developing at a very fast pace with most of the developmental activities being concentrated in the Bhopal city and along its periphery mostly comprising of the urban-rural fringe areas. This has resulted in considerable changes in the land use in the city and its fringes, with substantial areas being converted to semi-pervious and impervious zones owing to the fast pace of urbanization. These drastic changes in the land use pattern have to a large extent changed the hydrology and drainage aspects of the city. Owing to the changes in the land use and pressures of increasing population, the runoff and drainage aspects have also been altered to some extent. Nowadays, it is very common to find large stretches of roads being submerged during small rainfall events, thereby causing hardships to the local population. An effort has therefore been made to identify the land use changes in the city and its surroundings and its possible impacts on the hydrology of the study area. The land use classification has been carried out for 1992, 2000, and 2014 using LANDSAT data with a resolution of 30 m. The changes in the land use/land cover categories were derived for three different time periods by spatial intersection of land use maps pertaining to 1992 and 2000, 2000 and 2014, and 1992 and 2014 using ERDAS Imagine 2011 and ArcInfo/ArcMap 10 software. The area under settlements has increased by 10.66% during the period between 1992 and 2014, whereas the area under wastelands decreased by 18.29% during the same period. However, the forested area initially decreased from

L. Patel (✉) · T. Thomas
Ganga Plains South Regional Centre, National Institute of Hydrology, Bhopal 462041, Madhya Pradesh, India
e-mail: lokesh.patel90@gmail.com

T. Thomas
e-mail: thomas_nih@yahoo.com

S. Goyal
Madhya Pradesh Resource Atlas Division, Madhya Pradesh Council of Science and Technology, Bhopal 462003, Madhya Pradesh, India
e-mail: sgoyalbsg@gmail.com

V. P. Singh et al. (eds.), *Hydrologic Modeling*, Water Science and Technology Library 81, https://doi.org/10.1007/978-981-10-5801-1_9

45.64 km^2 (1992) to 40.24 km^2 (2000) but subsequently increased to 48.62 km^2 in 2014. The soil conservation service-curve number (SCS-CN) method has been used to compute the surface runoff. The change in the runoff pattern has not been substantial in commensuration to these changes in the land use pattern as the runoff generation mechanism is also dominantly dependent on the rainfall pattern and its distribution and the antecedent moisture condition apart from the curve number.

Keywords Land use · Change detection · SCS-CN · LANDSAT · GIS

Introduction

Land use/land cover (LULC) changes have direct impacts on the hydrological cycle and stream water quality, and furthermore, there are also indirect impacts on climate and the related impacts of the altered climate on the hydrology of an area (Weng 2001). Therefore, LULC changes have been treated as one of the most crucial and sensitive factors for global environmental change. Urbanization is the major force that is driving LULC changes. Although urbanization due to urban sprawl provides social and economic benefits to the community, the detrimental consequences of the urbanization to the urban environment are widespread, especially in most emerging countries. Increased impervious surface in the urbanized areas can reduce the time to peak and increase the peak discharges, resulting in large and more frequent incidents of flooding (Weng 2001; Li and Wang 2009). In addition, because of the pollutants in runoff and sediments, the increase in impervious surfaces also degrades stream quality (Li and Wang 2009). Therefore, urbanized areas would become more susceptible to flood hazard under conditions of high precipitation intensity (Shi et al. 2007).

In recent decades, with a constantly accelerating increase in urban population, urbanization has become a significant urban environmental and ecological concern, especially in most developing countries. Therefore, it is of great significance to accurately map LULC changes in urbanized areas and to evaluate its impacts on surface runoff and stream quality for urban planning policy makers and water/land resource management. Due to their relatively low cost and suitability for large area mapping, satellite remote sensing (RS) images have been widely applied for detecting urban growth and accurately and timely mapping LULC changes over a long period (Yang et al. 2003). Furthermore, RS-based LULC changes mapping and also allows for a rapid assessment of its impacts on surface runoff and water quality (Li and Wang 2009).

In India, rapid urban sprawl has had a profound influence on runoff and results in larger and more frequent incidents of flooding in many urban areas. Over the past three decades, Bhopal, the capital of Madhya Pradesh, India, is one of the fastest

growing urban areas in Madhya Pradesh, and has undergone intense urbanization which has impacted the urban surface runoff. The objective of this paper is to derive LULC classification maps and further quantitatively assess the effects of LULC change on surface runoff in Bhopal city and along its periphery comprising of the urban-rural fringe areas. The LULC maps are derived from LANDSAT TM/ETM + imagery (1992, 2000 and 2014) using unsupervised classification method. To estimate the effects of LULC change on runoff, the SCS-CN approach is used in this research.

Study Area

The study area is a part of Bhopal district of Madhya Pradesh, India, and covers an area of 874.51 km^2. Bhopal city nestles in a hilly terrain, which slopes toward north and southeast. Hillocks of different altitudes are situated along the southwest and northwest portions of the city, and these hillocks form a continuous belt from Singarcholi up to Vindhyachal range. The height of Singarcholi near Lalghati is 625 M above MSL which is maximum in this area. The general ground level is, however, nearly 460 M above MSL along the southeastern and northeastern portions of the city. The remarkable topography of the city provides enchanting and panoramic views of the city and of natural scenic beauty. There are immense possibilities for landscaping and waterfront development for recreation along with beautiful hills and large number of lakes spread all over the city. Owing to this, Bhopal is also called "The City of Lakes" and the Upper Bhopal Lake is one of the biggest lakes in the country.

Large-scale developmental activities are taking place in and around Bhopal. The city is getting a modern look owing to the large number of infrastructure projects, and it has off-late turned out to be the educational hub in Central India. However, this had led to changes in the land use with agricultural land being converted into housing colonies and recreational parks and malls. The map showing the location of the study area is given in Fig. 1.

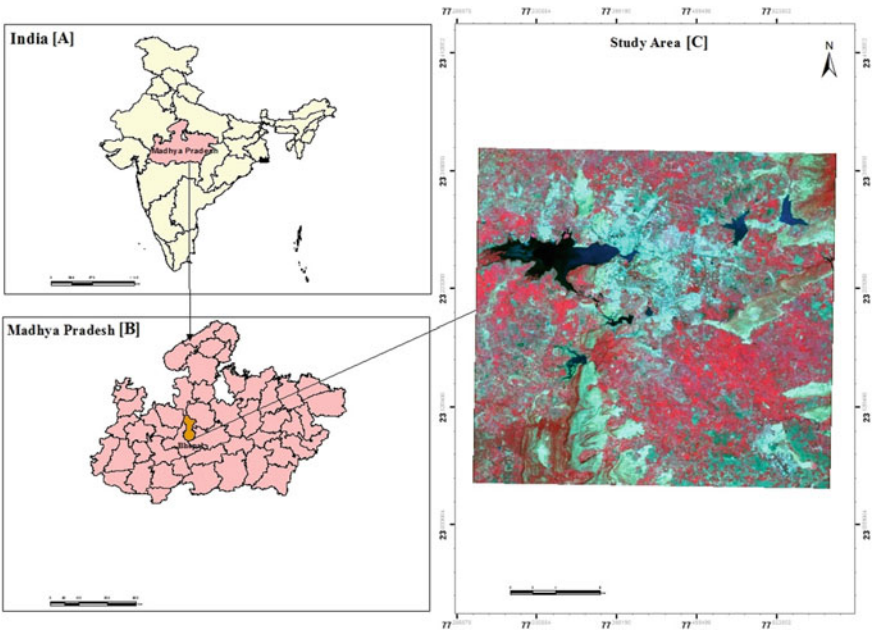

Fig. 1 Location map of the study area

Methodology

The LULC classification maps were derived from LANDSAT TM/ETM + imagery. The SCS-CN approach was used to assess the impacts of LULC changes on surface runoff due to urbanization. Figure 2 shows the data-processing framework of research on hydrological response to LULC changes. The left side of Fig. 2 depicts the data processing for LULC classification and change detection while the right side shows the flowchart of SCS-CN approach. In this paper, unsupervised classification was used to prepare LULC maps and spatial intersection (overlay analysis) was used to evaluate the temporal change of LULC in study area.

Unsupervised Classification

Visual interpretation technique was used for the mapping of land use/land cover. Prior to interpretation of multi-date satellite data, a reconnaissance survey of the study area was done to develop a classification scheme based on local knowledge and ancillary information. An interpretation key was also developed based on

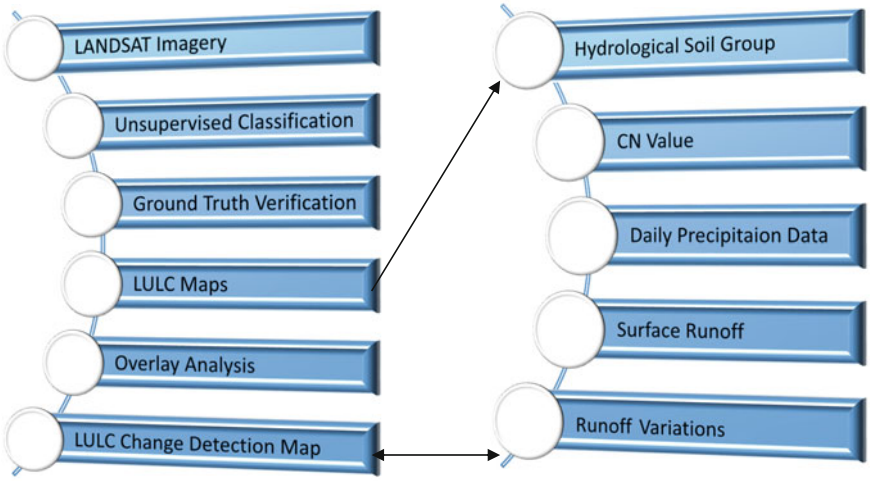

Fig. 2 Framework of research on hydrological response to LULC changes

standard photo-elements like tone, texture, size, shape, association, pattern, location to identify and map different classes. With the help of interpretation key, onscreen preliminary interpretation of satellite data was done using ERDAS IMAGINE 2011 software.

Ground Truth Verification

Entire study area was visited to get an acquaintance of different ground features and cover type with respect to satellite data. The doubtful area on preliminary interpreted maps from satellite data was carefully verified in the field. After verification, these areas were reconciled on the maps and corrections were made to obtain final maps.

Analysis, Final Map Preparation, and Area Statistics Generation

The spatial intersection method has been used for performing the overlay analysis using ArcInfo software. The final maps were prepared after reconciliation of doubtful areas observed in preliminary maps. The final maps were prepared/composed, and area statistics were generated using ArcMap 10.0 software.

SCS-CN Approach Description

The SCS-CN model was used to estimate direct runoff from daily rainfall after deriving the curve number (CN) from LULC, and hydrologic soil group data and thereafter deriving the appropriate CN for the average, wet or dry condition based on the antecedent rainfall condition. For runoff calculation, SCS-CN uses the curve number (CN) method of the US Department of Agriculture (USDA) Soil Conservation Service (SCS, now Natural Resources Conservation Service), which is a core component of many traditional hydrology models (Wang et al. 2005). The runoff equation is

$$Q = \frac{(P - I_a)^2}{(P - I_a) + S} \tag{1}$$

where Q is the runoff (mm), P is the rainfall (mm), S is the potential maximum retention (mm), and I_a is the initial abstraction (mm) and can be approximately estimated by

$$I_a = 0.2\,S \tag{2}$$

S, in mm, is related to the soil and LULC conditions and can be described by CN through:

$$S = \frac{25,400}{\mathrm{CN}} - 254 \tag{3}$$

where CN is determined by the combination of LULC and soil (hydrological soil group) information for each cell. Theoretically, CN values are between 0 and 100. However, practically, CN values range between 30 and 100. Then, SCS-CN approach uses daily rainfall and the CN to calculate the surface runoff (mm).

Results and Analysis

LULC Change

In the present study, land use/land cover of Bhopal and its peripheral area was mapped for the years 1992, 2000, and 2014. In order to monitor the changes in land use/land cover, proper care was taken in the selection of cloud-free temporal data. It was not possible to obtain the ground truth pertaining to older datasets i.e., LANDSAT 1992, therefore a novice approach to overcome the same was followed by mapping for 2000 and using it as template for the analyses of 1992 datasets.

The major land use/land cover categories identified in the study area are built-up, agriculture, forest, scrub, wasteland and water bodies and their areal extent. The

details of the various land use classes and the observed changes are presented in Table 1 and Fig. 3. In general, major area was occupied by agriculture followed by wasteland, scrub, forest, built-up land, and water bodies in the year 1992. In the years 2000 and 2014, built-up land has increased. The built-up area identified in the study area was mainly large city settlements. The total built-up area of 37.51 km^2 in 1992 increased to 130.73 km^2 in 2014. This accounted 4.29 and 14.95% of the total geographical area during 1992 and 2014, respectively. The overall increase was 10.66% of total geographical area with annual increment of 4.24 km^2/year.

Agriculture was observed mainly on plain lands and uplands and accounted 403.53 and 435.83 km^2 during 1992 and 2014, respectively, and the rate of increase in the agriculture area was 1.47 km^2/year. Wasteland is located on the uplands. The total wasteland which was 295.3 km^2 in 1992 reduced to 135.36 km^2 in 2014 and registered a decrease of −7.27 km^2/year. However, the decrease of −18.29% was noticed in wastelands during the period between 1992 and 2014. Forests are mainly located on hilly and upland areas. The total area during 1992 was 45.64 km^2 which decreased to 40.24 km^2 in 2000 which again increased in 2014 to 48.62 km^2. The scrub which was 58.77 km^2 in 1992 increased to 116.04 km^2 in 2000 and thereafter decreased to 79.40 km^2 in 2014. The area covered by water bodies was almost same during all the years, while area of reservoirs increased by 1.24% during 1992–2014.

The wasteland was observed to be 295.30 km^2 in 1992 which was reduced to 89.15 km^2 in 2000. The reason behind this transformation is because of increase in agricultural activities at those places. However, the wasteland further increased to 135.36 km^2 in 2014 because of lesser utilization of land in agricultural activities.

The transformation of a particular land use/land cover category into different categories was derived by spatial intersection of 1992–2000, 2000–2014, and 1992–2014. The built-up area increased from 37.51 km^2 in 1992 to 77.20 km^2 in 2000 which further increased to 130.73 km^2 in 2014 as a result of conversion of croplands and wasteland existing around settlements. One may expect such change in the study area on account of increase in population over a period of almost two decades.

Table 1 Area statistics of land use/land cover distribution in Bhopal during 1992, 2000, and 2014

S. No.	Land use/land cover categories	1992 area (in km^2)	2000 area (in km^2)	2014 area (in km^2)	Change 1992–2000 (%)	Change 2000–2014 (%)	Change 1992–2014 (%)
1	Agriculture	403.53	514.78	435.83	12.72	−9.03	3.69
2	Built-up	37.51	77.20	130.73	4.54	6.12	10.66
3	Forest	45.64	40.24	48.62	−0.62	0.96	0.34
4	Scrub	58.77	116.04	79.40	6.55	−4.19	2.36
5	Wasteland	295.30	89.15	135.36	−23.57	5.28	−18.29
6	Water body	33.76	37.09	44.57	0.38	0.86	1.24

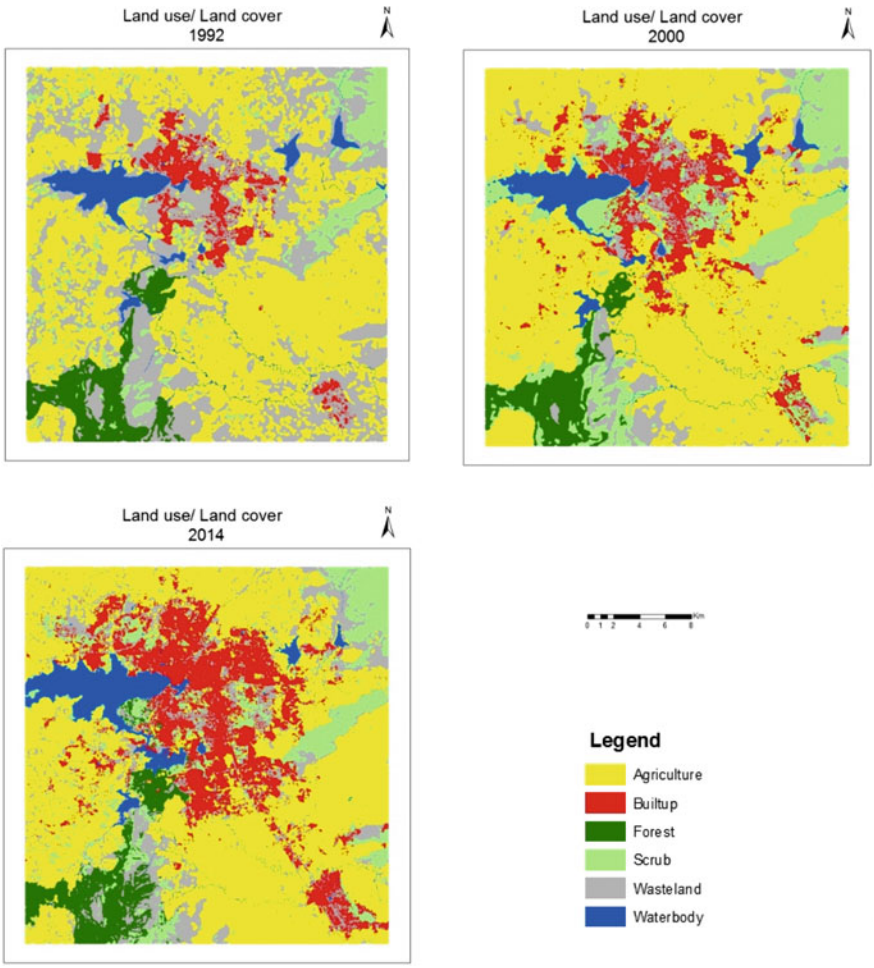

Fig. 3 LULC maps of study area in 1922, 2000, and 2014

The aerial extent of agriculture registered an increase of 12.72% of total geographical area from 1992 to 2000 and further decreased −9.03% during 2000–2014. The overall increase was 3.69% of total geographical area during 1992–2014. During these periods, major area under wasteland and small area under reservoir was transformed into cropland. However, conversion of wasteland into cropland was more during 1992–2000 than the year 2000–2014. In case of forest, the land transformation in dense, open, and scrub was observed for the period 1992–2000 and 2000–2014. During this period, dense forest converted into scrub forest and at a few places the scrub lands got converted into forest.

Estimation of SCS-CN

The direct surface water runoff has been estimated by the soil conservation service-curve number (SCS-CN) method at the outlet of the watershed. The SCS-CN method is based on the single parameter curve number (CN), which depends on the land use, land cover, soil type, and the antecedent moisture conditions prevailing in the watershed. The LULC types were derived from LANDSAT TM/ETM + imagery as described earlier. According to soil classification categories, the study area comes in very low infiltration category which is categorized by type "D" in hydrological soil group (HSG) classification. Based on this hydrological soil group and LULC, the CNs have been determined for the various combinations of land use and soil type combinations. The composite curve number (CCN) for the watershed is estimated as 78 using hydrologic soil group and land use for the AMC-II condition (average). The AMC changes to dry or wet conditions depending on the five-day antecedent rainfall.

Estimation of Direct Surface Runoff by SCS-CN

The simulated annual surface runoff of the study area estimated by SCS-CN method is 252.8 mm for the year 1992, 298.39 mm for the year 2000, and 245.24 mm for the year 2014. The ratio of annual surface runoff to that of annual rainfall calculated is 31.71, 33.98, and 27.75% for the years 1992, 2000, and 2014, respectively.

Although the change in urban area from 1992 to 2014 is very vast, which is 10.66% of the total area, the computed surface runoff has not increased in a similar proportion. The main reason of this exception is the rainfall pattern and its distribution. As the SCS-CN runoff estimation depends on the previous 5 days AMC (Antecedent Moisture Condition), and as distribution of rainfall in 2014 had been quite different from that during 2000 and 1992, the computed surface runoff during 2014 is lesser than that during 2000 and 1992. The comparison of the daily rainfall and daily computed runoff for 1992, 2000, and 2014 is given in Figs. 4, 5, and 6, respectively. From these figures, it is clear that the rainfall events in the year 2014 are in scattered manner (non-continuous) and hence the direct surface runoff peak values are smaller as compared to that during the years 1992 and 2000. Therefore, the simulated annual surface runoff had decreased even though there is a drastic increase in urban area.

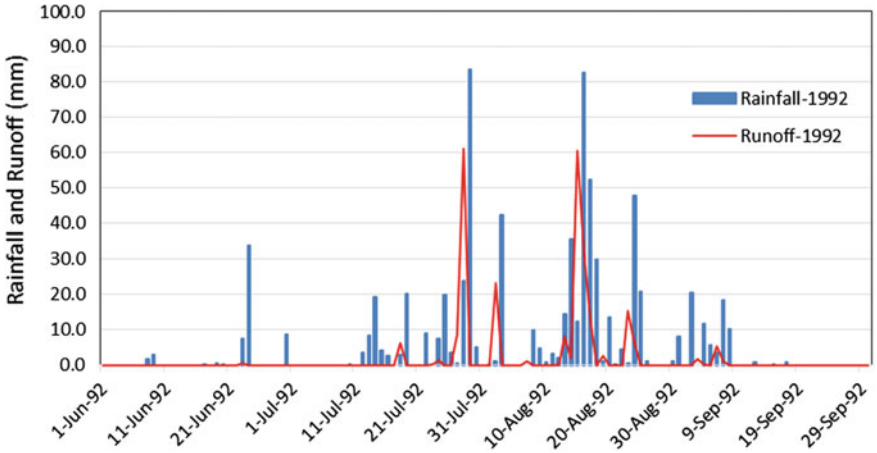

Fig. 4 Comparison of rainfall and runoff during 1992

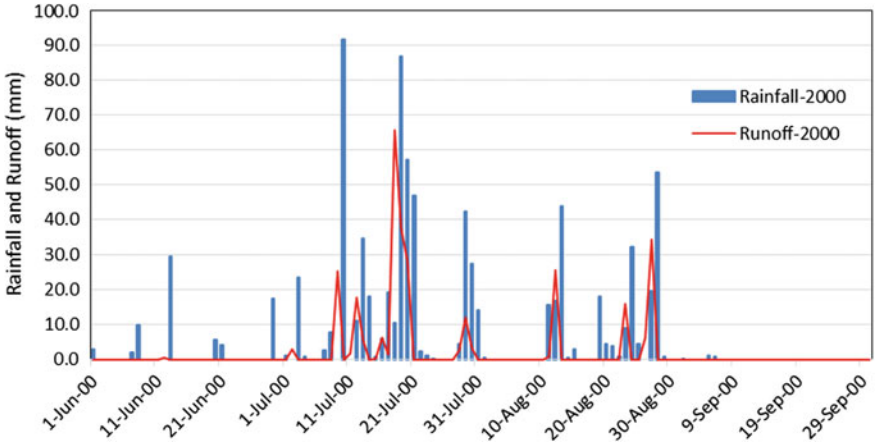

Fig. 5 Comparison of rainfall and runoff during 2000

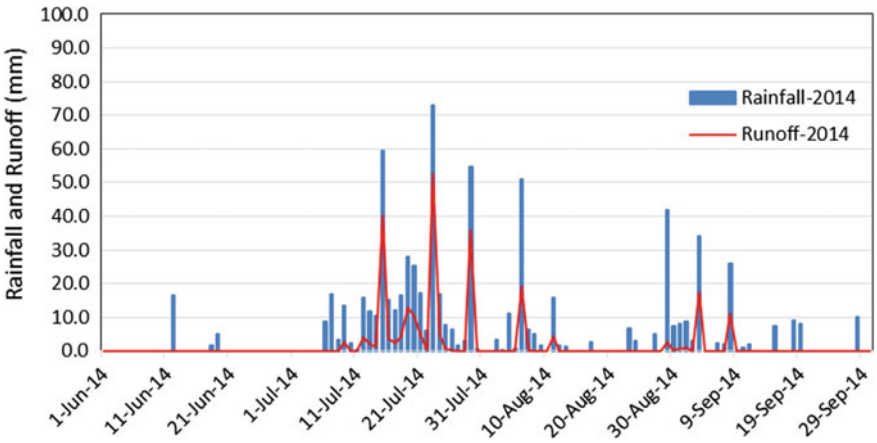

Fig. 6 Comparison of rainfall and runoff during 2014

Conclusions

This paper presents a case study to investigate the impact of LULC change on surface runoff in the fast urbanizing Bhopal city, the capital of Madhya Pradesh. The LULC maps were derived from LANDSAT TM/ETM + imagery (acquired in 1992, 2000, and 2014, respectively) using support unsupervised classification. Results indicated that the selected study area experienced rapid urbanization from 1992 to 2014. The overall increase in built-up area was 10.66% during 1992–2014. The increase was more during 2000–2014 (6.12%) than 1992–2000 (4.54%). The increase in built-up area was due to transformation of agriculture and wasteland. The SCS-CN approach was applied to simulate surface runoff variations in the study area during 1992, 2000, and 2014. As a direct result of the urbanization from 1992 to 2014, the surface runoff increased for the whole area. However, due to scattered rainfall pattern in the year 2014, changes in the runoff do not seem to be significant. This research provides a simple method for policy makers to assess potential hydrological impact of development activities for future planning of the city.

References

Li Y, Wang C (2009) Impacts of urbanization on surface runoff of the Dardenne Creek watershed, St. Charles County, Missouri. Phys Geogr 30(6):556–573

Shi P, Yuan Y, Zheng J, Wang J, Ge Y, Qiu G (2007) The effect of land use/cover change on surface runoff in Shenzhen region, China. Catena 69:31–35

Wang Y, Woonsup C, Brian MD (2005) Long-term impacts of land-use change on non-point source pollutant loads for the St. Louis metropolitan area, USA. Environ Manag 35(2):194–205

Weng Q (2001) Modeling urban growth effects on surface runoff with the integration of remote sensing and GIS. Environ Manag 28(6):737–748
Yang L, Xian G, Klaver JM, Deal B (2003) Urban land-cover change detection through sub-pixel imperviousness mapping using remotely sensed data. Photogramm Eng Remote Sens 69 (9):1003–1010

Other Studies

Dabbs DL, Gentle GC (1974) Landscape classification and plan succession Trends in Peace Athabasca Delta Can. Wildlife Service Rep. SER, pp 32–34
Gautam NC, Narayan LRA (1983) Landsat MSS data for land use/land cover inventory
Harbor JM, Grove M, Bhaduri B, Minner M (1998) Long-term hydrologic impact assessment (L-THIA) GIS. Public Works 129:52–54
Karwariya S, Goyal S (2011) Land use and land cover mapping using digital classification technique in Tikamgarh district, Madhya Pradesh, India using Remote Sensing
Sun Z (2011) Effect of LULC change on surface runoff in urbanization area. In: ASPRS 2011 annual conference Milwaukee, Wisconsin, 1–5 May 2011

Simulation of Urban Drainage System Using Disaggregated Rainfall Data

Vinay Ashok Rangari, K. Veerendra Gopi, N. V. Umamahesh and Ajey Kumar Patel

Abstract Urban flooding is one of the major challenges that India is facing every year to which a solid solution is not yet available. Rapid-growing urban areas are responsible for the ground sealing which affects the natural drainage system. As a result, all the rainwater is going to flow through drainage system. Most of the drainage network in the country is old and deteriorated that needs immediate attention. Proper design and maintenance of drainage system can solve the problem to a maximum extent. But one of the difficulties encountered in design of drainage network of urban area is unavailability of peak runoff data for shorter time intervals at most of the locations. In this study, the preliminary assessment of drainage discharge for Zone V area of Hyderabad City is carried out. Hourly precipitation data is disaggregated using artificial neural networks (ANN) in order to obtain sub-hourly data. Intensity duration frequency (IDF) curves are constructed using the disaggregated sub-hourly data. The existing drainage network is simulated in Storm Water Management Model (SWMM) to check its hydraulic performance. The simulations carried out using design hydrographs constructed from IDF curves. Results indicate that existing drainage network is inadequate at certain locations.

Keywords Urban flood · Storm water · Watershed · IDF curve · ANN

V. A. Rangari (✉) · K. Veerendra Gopi · N. V. Umamahesh · A. K. Patel
National Institute of Technology Warangal, Warangal 506004, India
e-mail: vinayrangari@gmail.com

A. K. Patel
Water & Environment Division, National Institute of Technology Warangal, Warangal 506004, India

V. P. Singh et al. (eds.), *Hydrologic Modeling*, Water Science and Technology Library 81, https://doi.org/10.1007/978-981-10-5801-1_10

Introduction

Urban flooding is a serious and growing development challenge around the globe. Flooding in urban areas can be caused by flash floods, or coastal floods, or river floods. But there is also a specific flood type that is called urban flooding. It is specific in the fact that the cause is a lack of drainage in an urban area. Rapid-growing urban areas are responsible for the ground sealing which affects the natural drainage system (Ahmed et al. 2013). As a result, all the rainwater is going to flow through drainage system. If the city sewage system and draining canals do not have the sufficient capacity to drain away the amounts of rain that are falling, it will result in spreading water in surrounding area and thus flooding. Water may even enter the sewage system in one place and then get deposited somewhere else in the city on the streets. It happens frequently and is a great disturbance to daily life in the city. Thus, it is essential to dispose of the excess water economically and efficiently in the quickest possible time. One of the ways to reduce its intensity is proper designing and maintenance of drainage system. In recent years, simple and effective modern modeling techniques have also brought great attention to the prediction of runoff with rainfall input (Wang and Altunkaynak 2012; Sun et al. 2012).

Most of the drainage network in the country is old and deteriorated that needs immediate attention. Proper design and maintenance of drainage system can solve the problem to a maximum extent. The existing stormwater network as well as in design practices must be revised considering potential shifts in extreme rainfall at the local levels (Kuo et al. 2012; Olsson et al. 2012; Peck et al. 2012). Short duration rainfall data are needed for modelling urban systems (Lall and Sharma 1996; Cowpertwait 2002). But one of the difficulties encountered in design of drainage network of urban area is unavailability of peak runoff data for shorter time intervals at most of the locations. However, hourly rainfall data is available with numerous government and private agencies which can be used to calculate design peak discharge. Thus, there is need to develop a methodology to disaggregate available rainfall data into shorter time intervals that can be used effectively for the design of drainage network in urban environment (Liew et al. 2014).

Bennis and Crobeddu (2007) presented a new runoff simulation approach based on the improvement of the rational hydrograph method. Quader and Guo (2006) used probabilistic approach for estimation of peak discharge rates in a practical design. Rumelhart et al. (1986) developed the back-propagation ANN model for disaggregation of rainfall data. Burian et al. (2001) implemented a model in ANN for the disaggregation of hourly precipitation to sub-hourly (15 min), and the model performance found good in obtaining the maximum depth and time of 15 min precipitation, when compared with two empirical precipitation disaggregation models developed by Ormsbee (1989). Later a new approach using an artificial neural network technique to improve rainfall forecast performance is presented by Hung et al. (2008). Armesh and Negaresh (2013) simulated the maximum daily rainfall in Saravan using artificial neural network (ANN) using back propagation and radial basis with Levenberg-Marquardt training algorithm. Golbahar et al. (2013) downscaled 3-h

precipitation data simulated by five combinations of global and regional climate models using artificial neural networks (ANNs) for evaluating potential changes in IDF curves for Alabama under projected future climate scenarios. Lamia and Farawn (2013) converted maximum rainfall values of each year into shorter duration (1, 2, 3, 6, and 12 h) using the reduction formula suggested by the Indian Meteorological Department (Venkata Rathnam 2000). The objective of this study is to assess the adequacy of the existing drainage system in Zone V of Hyderabad City.

Study Area and Data Used

Area chosen for the present study is a part of Hyderabad Metropolitan City known as Zone V (Fig. 1) covering the localities of Malakpet, Chanchalguda, Falaknuma, Durganagar, and a few other colonies in the southern part of the Musi River. The total area taken for study extends to 21.92 km^2. The study area is situated at latitude of 17° 20′ 42″ North, longitude of 78° 28′ 18.9″ East and at an average altitude of 468.2 m above mean sea level. The city has slope from south to east with level varying from +510.0 to 407.0 m and generally slopes towards Musi River and terrain are hilly. The drainage system in the city comprises of hierarchy of natural and man-made drains and water bodies that ultimately discharge into River Musi and Hussain Sagar Lake. Nalas are major carrier of storm water drainage system of the city.

Data of the study area is collected from different agencies. Most of the data regarding digital elevation model (DEM) map, land use-land cover map were extracted from Cartosat 30 m DEM obtained from Bhuvan. Hourly rainfall data for 43 years (1970–2013) is procured from Indian Metrological Department (IMD), while 15-min interval rainfall data for the period 1978–2007 (30 years) is obtained from GHMC. Evaporation data is obtained from Indian Metrological Department (Fig. 1).

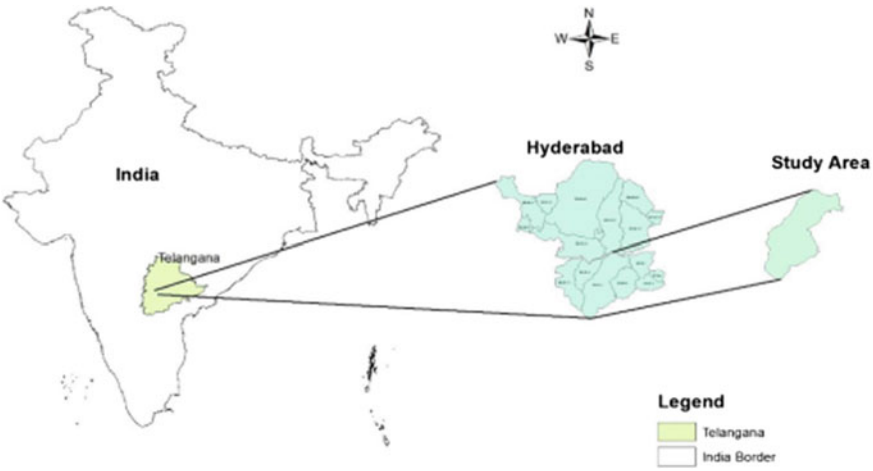

Fig. 1 Boundary map of study area

The Problem Statement

Hyderabad City is a fast-growing city and developed metropolitan city. In rainy season, drains in the city are flowing under full flow conditions and in many places due to insufficient capacities of drains; rainwater is overflowing from drains on to the roads. The main reason for flooding on roads is summarised as improper inlet arrangements, insufficient drain sections, and lack of proper storm water planning. Rainfall data for short duration is necessary for the design of drainage systems in urban environment. Sub-hourly records of rainfall data are not available for all the regions but daily or monthly rainfall data for many regions are available. In order to predict sub-hourly rainfall data, various disaggregation models are being developed by various authors. For the present study, artificial neural network (ANN) is used for development of a disaggregation model. Intensity duration frequency (IDF) curves are developed for disaggregated rainfall data to estimate the design storm. SWMM model has run for the developed IDF curves, and flooding junctions are identified.

Methodology

The methodology consists of three parts: (1) development of a disaggregation model using artificial neural network; (2) generation of intensity duration frequency (IDF) curves from the disaggregated rainfall values; and (3) carrying out capacity analysis of existing drainage system for design storm intensity considered from IDF curves.

Development of a Disaggregation Model Using Artificial Neural Network

The ANN disaggregation model developed for this study is a feed-forward back-propagation model. The model includes the three layers, namely input layer, hidden layer, and output layer. The model has the capability to learn the mapping function between a set of input-output patterns. Feed-forward neural networks (FNNs) and their associated supervised learning rules are the most widely used in pattern mapping (Rumelhart 1986; Sivakumar et al. 2001). In supervised learning, errors generated from training are used for adjustment network weights, so that actual output matches the target output. Typical view of feed-forward neural Network is shown in Fig. 2.

The hyperbolic tangent sigmoid transfer function is used to determine the behaviour between the input layer and output layer in this study which is given by Eq. 1. The Levenberg-Marquardt back-propagation training algorithm is used for

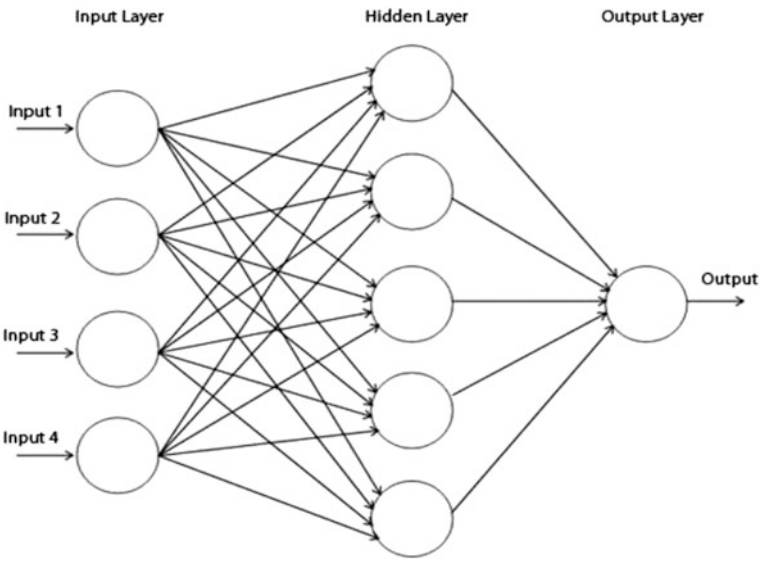

Fig. 2 Typical view of feed-forward neural network

updating weights and bias values. Finally, gradient descent with momentum weights/bias learning function is used to develop the ANN model.

$$f(x) = \tan \mathrm{sig}(x) = \frac{2}{1 + \mathrm{e}^{-2ax}} - 1 \tag{1}$$

where 'a' is the slope parameter of sigmoid function.

As input data, 1-h annual maximum rainfall for past 30 years from IMD is used as target data. As target data, 15-, 30-, 45-, and 60-min annual maximum rainfall from GHMC is taken.

Generation of Intensity Duration Frequency (IDF) Curves

The rainfall Intensity Duration Frequency (IDF) relationship is one of the most commonly used tools for the design of hydraulic and water resources engineering control structures (Bara et al. 2009; Antigha and Ogarekpe 2013; Hassanzadeh et al. 2014). Disaggregated rainfall data of 15, 30, 45, and 60 min duration for past 30 years is taken for development of IDF curves. Frequency analysis was performed for annual maximum series of rainfall data sets of different durations using best fitted distribution. IDF curves are developed for three return periods of 2, 3, and 5 years (Fig. 3).

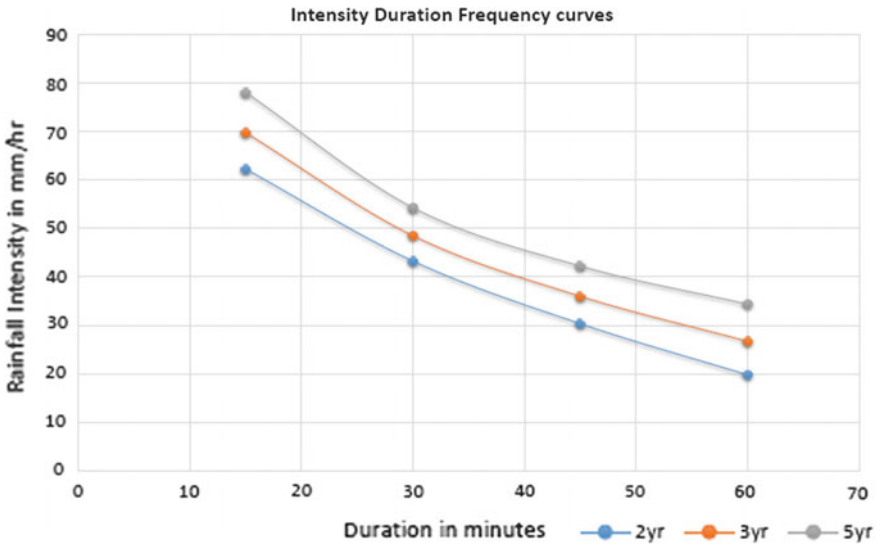

Fig. 3 IDF curves for disaggregated rainfall data

Capacity Analysis of Existing Drainage System

The total study area is divided into 47 sub-basins by considering the drainage line. Area of each sub-basin is calculated and provided as input in storm water management model (SWMM) (Rossman 2010; EPA 2013) to define the runoff from each sub-catchment (sub-basins are considered as sub-catchments in SWMM). Overland flow from each sub-catchment is calculated using rational formula, and SWMM model (Fig. 4) is simulated for the calculated flow values, and flooding junctions are identified.

Results and Discussions

ANN Model Validation

The ANN model was trained with input and target data sets using the training function given by Eq. 1. Model accuracy usually increases with an increase in training, but there is a point at which more training doesn't improve model performance, and sometimes even gets worse. Identifying this point can be done with trial and error. For the ANN model evaluated in this study, 70% of observed data was used for training, 15% for validation, and last 15% for testing. The training data set was used to adjust the weights on the network, whereas the validation data set

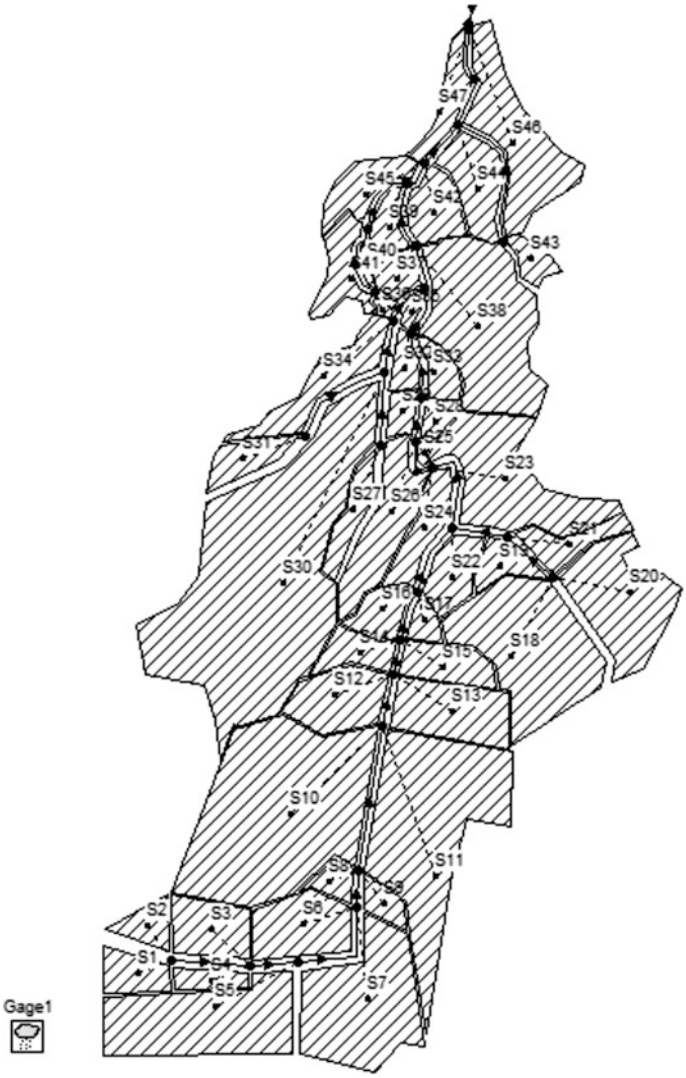

Fig. 4 SWMM model for study area

was used to minimise overfitting. The validation data set was used to verify if an increase in prediction accuracy for a data set (validation data set) that the ANN had not processed previously. If an increase in prediction accuracy using the training data set does not result in an increase in accuracy in the validation data set, the network is considered overfitted and training should be stopped. The performance

measures for evaluation of the ANN model were the Nash-Sutcliffe efficiency coefficient (NSE) and the correlation coefficient (R). The NSE and R can be calculated using the following equations:

$$\mathrm{NSE} = 1 - \frac{\left[\sum_{i=1}^{N}\left(y_{\mathrm{sim},i} - y_{\mathrm{obs},i}\right)^2\right]}{\left[\sum_{i=1}^{N}\left(y_{\mathrm{obs},i} - y_{m\mathrm{obs}}\right)^2\right]} \tag{2}$$

$$R = \frac{\left[\sum_{i=1}^{N}\left(y_{\mathrm{obs},i} - y_{m\mathrm{obs}}\right)\left(y_{\mathrm{sim},i} - y_{m\mathrm{sim}}\right)\right]}{\left[\sqrt{\sum_{i=1}^{N}\left(y_{\mathrm{obs},i} - y_{m\mathrm{obs}}\right)^2}\sqrt{\sum_{i=1}^{N}\left(y_{\mathrm{obs},i} - y_{m\mathrm{sim}}\right)^2}\right]} \tag{3}$$

where, i = number of observations; y_{obs} = observed data; y_{sim} = output of the ANN model; $\hat{y}$ = average of observed and output data.

The NSE can range from $-\infty$ to 1. An efficiency of 1 is a perfect model, whereas an efficiency of zero indicates that the model simulation is as good as the mean of observed data. If the NSE is less than zero, it means that the observed mean is a better predictor than the model. The correlation coefficient (R) ranges between +1 and −1. The statistical measures used in the error quantification are presented in Table 1. Regression plots for training, testing, and validation for different durations are shown in Fig. 5.

SWMM Simulation Results

SWMM model is simulated for design storm of 2-year return period. At each node/junction, runoff from individual sub-catchments is given as input values. Peak runoff for every sub-catchment is calculated using rational formulae for particular time of concentration for each sub-catchment, and flooding junctions are identified. Nodes flooding at particular junctions are represented in Table 2. Conduits C9, C12, C13, C14, C21, C22, and C23 have attained maximum/full depth. Simulation

Table 1 Performance criteria of ANN model for training, testing, and validation

Duration (min)	All		Training		Validation and testing		R^2
	NSE	R	NSE	R	NSE	R	
15	0.39	0.72	0.39	0.69	0.39	0.81	0.51
30	0.65	0.81	0.66	0.82	0.62	0.87	0.65
45	0.28	0.69	0.52	0.80	−0.54	0.31	0.47
60	0.40	0.71	0.37	0.69	0.52	0.80	0.50

NSE Nash-Sutcliffe model efficiency coefficient, R correlation coefficient and R^2 coefficient of determination

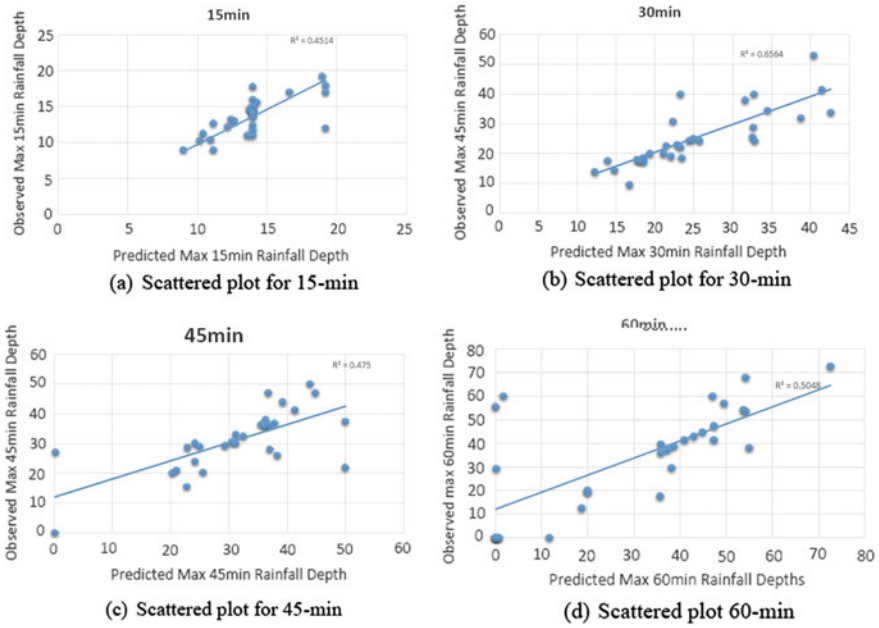

Fig. 5 Scatter plots for observed and predicted maximum rainfall depths (mm) using artificial neural network model

Table 2 Summary of flooding at junctions for 2 year design storm intensity

Node	Hours flooded	Maximum rate CMS	Hours of maximum flooding	Total flood volume 10^6 l	Hours submerged
J9	0.07	1.254	0.020139	0.157	0.07
J12	0.85	25.395	0.020139	33.512	0.85
J13	0.94	9.047	0.035417	19.756	0.94
J14	1.27	11.056	0.019444	40.146	1.27
J16	0.61	0.249	0.045833	0.373	0.62
J21	0.62	5.748	0.036111	6.452	0.62
J22	0.19	1.259	0.03125	0.486	0.19
J25	0.75	9.11	0.036806	19.274	0.75
J26	2.1	23.662	0.022917	102.566	2.10

results of 2-year return period design storm shows that maximum flooding occurring at junction 29(J29) is 309.477 l. J29 is very near to Musi River (outlet junction). Channel overflow occurred at conduit C22 with a velocity of 7.96 m/s. Peak runoff is observed at sub-catchments S10 and S38 with a rate of 2.5 and 1.96 m^3/s, and volume of runoff is 28.96 and 23.51 l.

Summary and Conclusion

Urban drainage systems have been attracting attention in both industrialised and developing countries. For designing drainage network for urban scenarios, rainfall data for shorter time interval must be considered which is unavailable for most of regions. ANN can found a useful tool in disaggregating available rainfall data into sub-hourly data. In the present study, a storm water drainage network for a part of Hyderabad City has been analysed using the well-known storm water management model. Existing drainage network for study area is taken from the GHMC. Presented results show that the drainage network of selected study area is inadequate to carry the extreme storm runoff during precipitation events. Thus, there is need of reconstructing the drainage network to carry the excess of flows. Sub-hourly rainfall data is disaggregated from one-hour rainfall data using artificial neural network model. Intensity duration frequency curves are developed using best fitted distribution (Gumbel's) for 15-, 30-, 45-, and 60-min disaggregated rainfall data. Design storm intensities are taken from IDF curves for the analysis of drainage network.

Acknowledgements This work is undertaken as a part of ITRA-Water, Media Lab Asia project entitled 'Integrated Urban Flood Management in India: Technology Driven Solution'. We also thank GHMC for sharing technical data.

References

Ahmed Z, Rao DRM, Reddy KRM, Raj YE (2013) Urban flooding—case study of Hyderabad. Glob J Eng Design Technol 2(4):63–66

Antigha RE, Ogarekpe NM (2013) Development of intensity duration frequency curves for calabar metropolis, South-South, Nigeria. Int J Eng Sci 2(3):39–42

Armesh M, Negaresh H (2013) Maximum daily rainfall simulation by using artificial neural network (case study: Saravan-Iran). Res J Environ Earth Sci 5(11):651–659

Bara M, Kohnova S, Gaal L, Szolgay J, Hlavcova K (2009) Estimation of IDF curves of extreme rainfall by simple scaling in Slovakia. Contrib Geophys Geod 39(3):187–206

Bennis S, Crobeddu E (2007) New runoff simulation model for small urban catchments. J Hydrol Eng 12(5):540–544. doi:10.1061/(ASCE)1084-0699(2007)12:5(540)

Burian BSJ, Durrans SR, Nix SJ, Pitt RE (2001) Training of artificial neural networks to perform precipitation disaggregation. J Hydrol Eng 6:43–51

Cowpertwait PSP (2002) Stochastic generation of point rainfall data at sub-daily timescales: a comparison of DRIP and NSRP, vol 63, pp 1813–1819

EPA (2013) Storm water management model (SWMM). Retrieved 1 22, 2014 from United States Environmental Protection Agency: http://www.epa.gov/nrmrl/wswrd/wq/models/swmm/

Golbahar M, Srivastava P, Fang X (2013) Developing rainfall intensity-duration-frequency (IDF) curves for Alabama under future climate scenarios using artificial neural network (ANN). J Hydrol Eng 131219231550002. doi:10.1061/(ASCE)HE.1943-5584.0000962

Hassanzadeh E, Nazemi A, Elshorbagy A (2014) Quantile-based downscaling of precipitation using genetic programming: application to IDF curves in the city of Saskatoon. J Hydrol Eng 943–955. doi:10.1061/(ASCE)HE.1943-5584.0000854

Hung NQ, Babel MS, Weesakul S, Tripathi NK (2008) An artificial neural network model for rainfall forecasting in Bangkok, Thailand. Hydrol Earth Syst Sci 13(8):1413–1425. doi:10.5194/hess-13-1413-2009

Kuo C, Gan TY, Chan S (2012) Regional intensity-duration-frequency curves derived from ensemble empirical mode decomposition and scaling property. J Hydrol Eng 415. doi:10.1061/(ASCE)HE.1943-5584.0000612

Lall U, Sharma A (1996) A nearest neighbour bootstrap for resampling hydrologic time series. Water Resour Res 32(3):679–693

Lamia AJ, Farawn MT (2013) Developing rainfall intensity-duration-frequency relationship for Basrah city, Kufa. J Eng 5(1):105–111. ISSN 2207-5528

Liew S, Raghavan SV, Liong SY (2014) Development of intensity-duration-frequency curves at ungauged sites: risk management under changing climate. Geosci Lett 1(1):8. doi:10.1186/2196-4092-1-8

Olsson J, Willen U, Kawamura A (2012) Downscaling extreme short-term regional climate model precipitation for urban hydrological applications. Hydrol Res 43(4):341–351. doi:10.2166/nh.2012.135

Ormsbee LE (1989) Rainfall disaggregation model for continuous hydrologic modeling. J Hydraul Eng 115(4):507–525

Peck A, Prodanovic P, Simonovic SP (2012) Rainfall intensity duration frequency curves under climate change: city of London, Ontario, Canada. Can Water Resour J 37(3):177–189. doi:10.4296/cwrj2011-93565

Quader A, Guo Y (2006) Peak discharge estimation using analytical probabilistic and design storm approaches. J Hydrol Eng 11(1):46–54

Rumelhart D, Hinton G, Williams R (1986) Learning representation by back propagating errors. Nature 323:533–536

Rossman L (2010) Storm water management model user's manual version 5.0. U.S. Environmental Protection Agency, Cincinnati

Sivakumar B, Sorooshian S, Gupta HV, Gao X (2001) A chaotic approach to rainfall disaggregation. Water Resour Res 37(1):61–72

Sun N, Hall M, Hong B, Zhang L (2012) Impact of SWMM catchment discretization: a case study in syracuse, NY. J Hydrol Eng (January), 121225202154001. doi:10.1061/(ASCE)HE.1943-5584.0000777

Venkata Rathnam (2000) Urban runoff simulation and sptimisation of stormwater detention ponds storage-releases. Ph.D. Thesis, NIT Warangal

Wang KH, Altunkaynak A (2012) Comparative case study of rainfall-runoff modeling between SWMM and fuzzy logic approach. J Hydrol Eng 17(2):283–291. doi:10.1061/(ASCE)HE.1943-5584.0000419

Investigation of Drainage for Structures, Lithology and Priority (Flood and Landslide) Assessment Using Geospatial Technology, J&K, NW Himalaya

Umair Ali and Syed Ahmad Ali

Abstract In the present study, drainage analysis with application in lithological and structural study using remote sensing and GIS technique has been carried out in left bank catchment (Sukhnag-Ferozpur) of River Jhelum, Kashmir Basin. The remote sensing and GIS with the aid of satellite data are emerging as the most effective and time-saving technique for drainage analysis. This technique is found applicable for the extraction of drainage basin and its drainage networks from ASTER (DEM) with the support of satellite data (IRS LISS III 2005 and Survey of Indian toposheets). Drainage analysis is found of immense utility in the examination of lithology and structures. The mean bifurcation ratio fluctuation indicates structural control in drainage development in south-west side. Low drainage density is observed in low relief and highly permeable material in north-east and high drainage density in regions having impermeable sub-surface and mountainous relief in south-west side. Lithological and lineament analysis is performed using satellite data which gave ample support to the spatial variability of lithology and the presence of structures illustrated out by drainage parameters. Moreover, mountain fronts (mainly active fronts), stream profiles (showing anomalous nature at lineament crossing) and drainage basin asymmetry (left tilt) also supported to the presence of possible structures. The dominant trend of the lineaments was observed NW–SE which concords with the trend shown by major structures traversing in and around the area. The sub-watersheds in the Sukhnag catchment (left side of River Jhelum) has been divided into three zones: high-altitude zone of rugged topography and steep slopes with hard rocks like Panjal Volcanic, Dogra slates, and limestone; middle altitude zone of Karewas; and low-altitude flood plain zone of alluvium. The chances of landsliding in the high-altitude zone are more because of high-structural, steep-slope and deep-valley topography enhanced by cutting slopes, deforestation, making road and buildings. Futher, the high-altitude basins contribute more water to plainer area and to the main river (Jhelum River) causing floods in

U. Ali (✉) · S. A. Ali
Department of Geology, Aligarh Muslim University, Aligarh 202002, India
e-mail: umairgeo121@gmail.com

V. P. Singh et al. (eds.), *Hydrologic Modeling*, Water Science and Technology Library 81, https://doi.org/10.1007/978-981-10-5801-1_11

low-lying areas, which becomes most disastrous during heavy rainfall conditions. The low-lying plainer area were found more prone to floods as observed in recent flooding (Sep 2014) in the Kashmir Valley.

Keywords Drainage network · Structures · Lithology · Flood · Landslides

Introduction

Drainage analysis provides quantitative description of the basin geometry to understand initial slope or inequalities in the rock hardness, structural controls, recent diastrophism, geological and geomorphic history of drainage basin (Strahler 1964). The morphometric study involves the evaluation of stream parameters through the measurements of various stream properties (Kumar et al. 2000; Ali et al. 2003; Ali and Pirasteh 2005; Pirasteh et al. 2007). Drainage analysis generally provides clues to structural features and lithology (Howard 1967). The underlying concept is that rivers necessarily flow from high to low elevations parallel to the maximum regional slope (regional topographic gradient). Several basic drainage patterns have been defined: dendritic, parallel, trellis, rectangular, radial/centrifugal, annular and contorted (Deffontaines and Chorowicz 1991; Howard 1967). All deviations from a dendritic pattern or flow direction oblique to the regional topographic gradient ('misfit drainage', Deffontaines et al. 1992) are considered as drainage anomalies related either to structural or to lithological discontinuities (Deffontaines et al. 1997; Pubellier et al. 1994).

Streams are highly sensitive to any change, tectonic and climatic conditions of an area, and as such they are the most powerful indicators of these activities. In any terrain, stream processes or network are controlled not only by the climatic conditions, but also the lithology and geologic structures have great control as they influence the nature of flow, erosion and sediment transportation. The permeability, the structural characteristics, and the degree of jointing/fractures also affect the extent to which the materials can be detached by fluvial processes (Derbyshire et al. 1981). Thus, the role of rock types and geologic structure in the development of stream networks can be better understood by studying the nature and type of drainage pattern and by the quantitative drainage parameters. Moreover, the drainage features mostly stream capture and beheaded streams are investigated for the identification of active fault traces (Schumm 1977; Bloom 1979).

The quantitative analysis of channel networks and drainage basins are developed from qualitative and deductive studies subsequent to the valuable contributions of (Horton 1945; Strahler 1952, 1957; Morisawa 1959; Melton 1957; Leopold and Miller 1956). The analysis of basins, as either single units or groups of basins which (taken together) comprise a distinct morphologic region, has particular relevance to geomorphology (Doornkamp and Cuchlaine 1971). Thus, the drainage networks and landform development depend on the bedrock lithology and associated varied geologic structures. Moreover, the sub-watersheds can be categorised into different

priority zones taking the various drainge parameters, lithology and structure into consideration for assesment of landslide and flood behaviour.

Landslides are one of the most significant natural damaging disasters in hilly environments (Ayala et al. 2006). In landslide hazard assessment, the main aspect is to analyse combination of factors that contribute to landslide occurrences. Geology, slope, soil cover, elevation, drainage pattern and vegetation cover are factors which may contribute alot in assessment of landslide vulnerability. Heavy rainfall and earthquakes may become variables that tend to trigger landslides quickly where other given contributing factors like steep slopes, structures and loose upper soil cover already exist. The utility of lineament mapping is one way of incorporating structural information into the landslide hazard assessment (Anbalagan and Singh 1996; Atkinson and Massari 1998; Nagarajan et al. 2000; Temesgen et al. 2001; Saha et al. 2002; Lin and Tung 2003; and others). Lineament is an extended mappable linear or curvilinear feature of a surface whose parts align in straight or nearly straight relationships that may be the expression of folds, fractures or faults in the sub-surface (Sabins 2000). Hobbs (1904) originally proposed the term lineament for significant lines of landscape caused by joints and faults, revealing the architecture of the rock basement. The most widely used definition is by O'Leary et al. (1976) who described a lineament as a mappable, linear feature of a surface whose parts are aligned in a rectilinear or slightly curvilinear relationship and which differ from the pattern of adjacent features and presumably reflect some sub-surface phenomenon. However, taking landslides as a major concern, lineaments (faults and fractures) are more important because they act as weak lines or zones and increase the chances of landslide in that particular area.

Not only the landslide assessment but the areas more prone to flood hazard can also be assessed by the application of drainage morphometry (Patel et al. 2012; Angillieri 2008; Roughani et al. 2007; Chopra et al. 2005; Alexander 1972) in association with other factors like flood plain encroachment, river bed level, upstream tributaries and deforestation. The tributaries of the river basin contribute more water in the main river causing floods in low-lying areas, with each sub-catchment having its own distinct influence on the main river due to varying drainage morphometrics (Ozdemir and Bird 2009). Since the time immemorial, floods are one of the most recurring and frequent natural calamities faced by mankind. Occurrence of flooding in any area causes serious vulnerability to economy, population and environment. In Kashmir Basin, the intense rainfall in September 2014 and March 2015 with the support of water-logging problems and low water transport capacity of river channels caused flooding in low-lying areas. The unforgotten flood in September 2014 caused massive damages to the life and property, particularly in low-lying plains. In the plainer areas, other causative factors which contribute a lot in bringing floods are land-use pattern in which uncontrolled construction along river banks and flood plains is the serious issue.

In the present study, attempts have been made to understand and evaluate the influence of bedrock lithology and geologic structures in the development of drainage networks by investigating drainage characteristics. Thus, in this study drainage analysis of the catchment is performed to decipher the relation between drainage, lithology and geologic structures with their special relation to natural disasters like landslides and floods.

Study Area

The catchment investigated in this study falls mainly in Budgam and little bit in Baramulla district, drains an area of about 1008 Km^2 and is situated between 33° 54′ to 34° 15′N and 74° 15′ 30″ to 74° 48′E coordinates (Fig. 1). The head streams of Sukhnag drain the Pir-Panjal range between the Nurpur Gali (4086 m) and the Chinamarg peak (4386 m) and also take care of the drainage of Tosha maidan. After crossing the 2200 m contour, Sukhnag Nala gets divided into a large number of streams. In the lower reaches, these branches reunite to form a few major streams. One of such stream is formed at Shulipur and is called Karshan Nadi. It is finally lost into the Hokar Sar. The parent stream of Sukhnag Nala flows in a north–north-east direction. At Path Magam, it receives a sizable tributary and then takes a

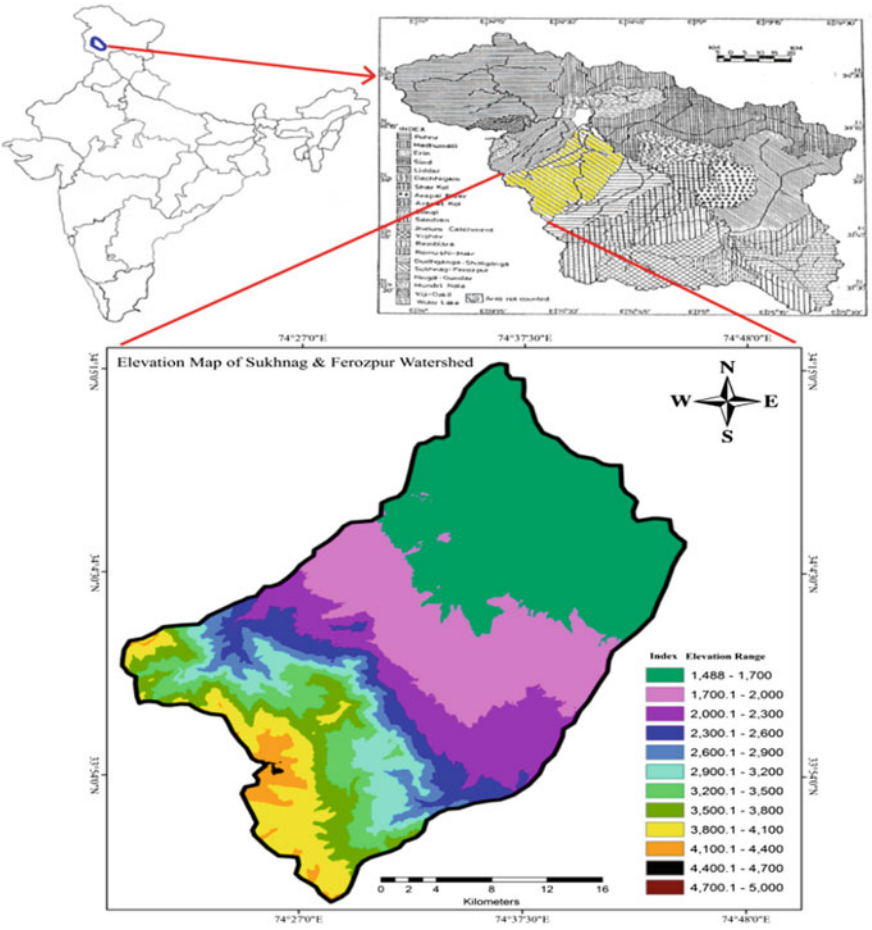

Fig. 1 Location map of study area in the Kashmir Basin, J&K

meandering course and enters the Rakh Arat and then the spill channel which takes it to Wular Lake. The Sukhnag Nala has a length of about 54 km. The Ferozpur Nala rises in the slopes of the Pir-Panjal between the Jamianwali Gali (4084 m) and Apharwat (4143 m). On entering the relatively plain area, the Ferozpur Nala gets divided into two branches which individually enter the spill channel and the marshy land.

Geological Set-up of the Area

The Kashmir Basin is diverse in lithology with the Salkhala series of Precambrian and Dogra slates of lower Cambrian age forming its basement (Wadia 1975; Krishnan 1982). These basement rocks are overlain by a more or less full sequence of rocks such as Panjal Volcanic series (Panjal trap and Agglomeratic slate), Gneissose granite, Gondwana shale, Fenestella shale, Syringothyris limestone, Permo–Triassic rocks, conglomerate beds and varved clays in various parts of Kashmir (Krishnan 1982; Lydekker 1883; Middlemiss 1910; Wadia 1975). However, most of the areas in Kashmir Basin is filled by fluvio-glacial sediments, which have been assigned group status are known as Karewas (Plio–Pleistocene) (Farooqi and Desai 1974; Bhatt 1989). These Karewas (or wuder in local dialect) lies unconformably on the older rocks and are made up of ∼1300-m-thick sequence of unconsolidated clays, sands and conglomerates with lignite beds and are covered by recent alluvium (Wadia 1975; Bhatt 1975, 1976; Singh 1982; Burbank and Johnson 1982).

For the concerned study area, the lithological map was collected from various sources and then the necessary modifications were incorporated after thorough field investigations. Geologically, the study area is quite diverse in rock types ranging from Precambrian to Recent. The commonest of the rocks present in the area are Salkhala Slates/Dogra Slates, Panjal traps, Limestone, Karewas and Alluvium. Salkhala Slates/Dogra Slates, Limestone and Panjal traps (Fig. 2) are lying in the extreme west, Karewas covers most of the area in middle and the recent alluvium has covered low-lying areas near the Jhelum River. The different structural elements like folds, faults and joints present in the area with varied orientations point towards multiphase deformation.

Data Source and Methodology

In the present study, base map showing drainage basin details (Fig. 3) has been prepared using satellite imagery (LISS III, 2005, 23.5 m), ASTER DEM 30 m resolution and SOI topographic maps (1:50,000) and field data. Softwares like ERDAS Imagine 9.3, Arc GIS 10.2 and Global mapper were used in georegistration of toposheets as well as for georectification, image processing, digitization, digital

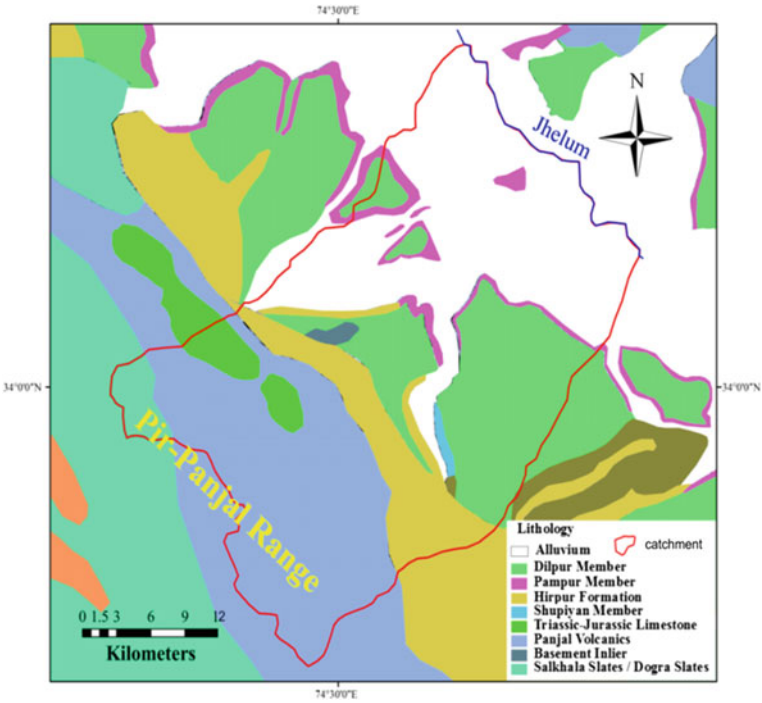

Fig. 2 Lithological set-up of the study area

image classification and composition of FCC images from satellite data. The methodology used consists of the following steps.

(a) Visual interpretation of the satellite imagery, DEM and SOI toposheets to delineate and update drainage network and to calculate morphometric and morphotectonic parameters; (b) lineament analysis from both satellite data and DEM-derived products; and (c) the assessment of co-relation between all the aspects like drainage, lithology and structures and in turn their relation with regional tectonics, landslide and flood behavior in the area.

Extraction of Watershed

The Sukhnag-Ferozpur catchment is extracted from the ASTER digital elevation model (DEM) data in Arc GIS 10.2. Various geoprocessing techniques were applied to extract the watershed area. The stepwise geoprocessing techniques essential for the extraction of the watershed are shown in Fig. 3 like fill basin, flow direction, flow accumulation, basin raster and basin raster to feature. The outcome of geoprocessing in Arc GIS 10.2 will create a polygon which is separated from other polygons by clipping technique.

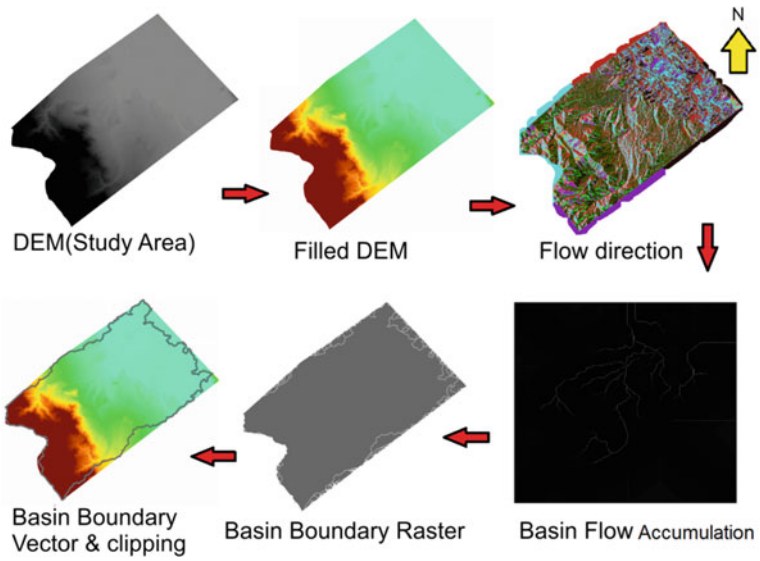

Fig. 3 Stepwise automatic extraction of catchment boundary in Arc GIS environment

Extraction of Drainage Network

The drainage network and/stream order can also be extracted automatically by a number of steps in Arc GIS 10.2 by geoprocessing tools. The result of geoprocessing technique will create a drainage network based on (Strahler 1964) stream classification. In Strahler's system of classification, a first-order stream is a stream with no tributaries, two first-order streams give birth to second-order stream, two second-order streams form third order, and so on. In the study area, the highest order stream is of sixth order (Fig. 4).

Result and Discussion

Morphometric analysis has long been believed to be important indices of surface processes. Since 1950, morphometry has been a significant instrument of structural geomorphology (Strahler 1952). It is the measurement and mathematical evaluation of the configuration of the earth's surface and of the shape and dimensions of its landforms. Robert E. Horton was the first to establish a quantitative method for analysing drainage networks. Morphometric parameter calculation and their analysis for a catchment is considered to be the most appropriate method that makes possible to understand the relationship among different aspects of the drainage pattern of the basin and to create a relative assessment of different drainage basins

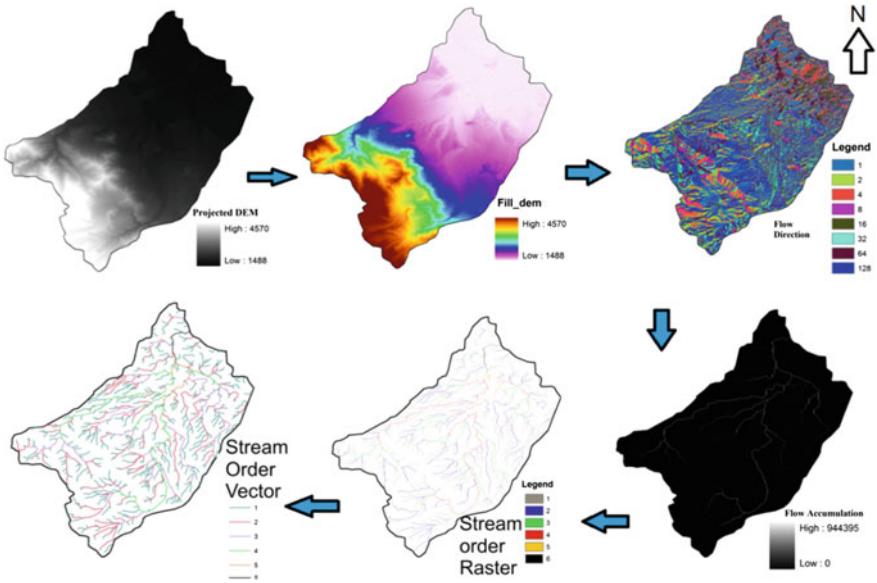

Fig. 4 Stepwise automatic stream order extraction in Arc GIS environment

developed in a variety of geological areas. Morphometry has also made it possible to define certain useful variables of drainage basins in numerical terms. The morphometric analysis of a watershed and its stream channel system can be better accomplished through the measurement of linear, areal and relief aspects of the drainage basins and contributing ground slopes.

The morphometric parameters computed include stream order (u), stream length (L_u), bifurcation ratio (R_b), circulatory ratio (R_e), stream frequency (F_s), drainage density (D_d), elongation ratio (R_e), form factor (R_f) and length of overland flow (L_o) (Table 1). Additionally, the slope and aspect map was prepared from the DEM using the aspect and slope tool in Arc GIS 10.2 spatial analyst module. Simultaneously, some of the geomorphic indices like mountain-front sinuosity index, drainage basin asymmetry, river profiles and lineament analysis are considered useful indicators of relative tectonic activity, lithology and the consequent landscape evolution of the drainage basins.

Slope Analysis

Analysis of slope is an essential parameter in morphometric studies. The slope of any landscape refers to the amount of inclination of physical feature, topographic landform to the horizontal surface. The climato-morphologinic processes in areas having lithology of varying resistance are controlling the slope element of the area;

Table 1 Drainage parameters of the catchment

Sub-watershed	D_d	R_b					Mean bifurcation ratio	F_S	R_e	Cc	Lo	Rn
		1/2	2/3	3/4	4/5	5/6						
SF1	3.46	5.97	4.83	6	0	0	3.6	4.97	0.78	1.33	0.14	4.086
SF2	2.56	4.62	5	3.5	2	0	3.02	3.27	0.99	1.16	0.19	4.303
SF3	2.32	4.80	4.42	2.33	3	0	2.91	2.73	0.73	1.32	0.22	2.691
SF4	2.37	5.00	5.00	7.00	1	0	3.6	2.72	0.72	1.39	0.21	3.618
SF5	3.04	3.61	4.43	7	1	0	3.20	2.62	0.83	1.29	0.16	3.033
SF6	3.44	4.81	3.2	2.5	2	0	2.50	3.67	0.74	1.25	0.15	6.615
SF7	2.87	4.65	4	5	1	0	2.93	3.45	0.53	1.54	0.17	5.725
SF8	3.18	3.74	2.71	3.5	1	2	2.59	3.35	0.62	1.44	0.16	5.355
SF9	2.39	4.76	2.83	2	3	0	2.52	1.74	0.47	1.63	0.21	2.024
SF10	1.14	3.43	2.8	5	1	0	2.45	0.64	0.65	1.24	0.44	0.354
SF11	2.66	5.83	2.88	4	2	0	2.94	2.15	0.58	1.40	0.19	5.152
SF12	1.74	3.46	6.5	2	1	0	2.59	0.71	0.39	1.79	0.29	1.110
SF13	0.84	3.43	3.5	2	0.5	2	2.28	0.36	0.53	1.53	0.54	0.252
SF14	0.79	3.57	3.5	2	1	1	2.21	0.28	0.52	1.56	0.63	0.353

however, tectonic processes also control the slope development. The slope map for the study area was prepared based on the DEM data that were converted into slope and aspect grids. According to Burrough (1986), slope grid is identified as the maximum rate of change in value from each cell to its neighbours. The slope counted in degree varies from 0 to 68.73 for the catchment (Fig. 5). The higher slope gradient is contributed by the hilly terrain and resistant rocks in south-west of the study area. Consecutively, the higher slope gradient areas if highly structured, during heavy rainfall, will give birth to rapid runoff and hazardous landslides.

Aspect Analysis

The aspect of a terrain is the direction to which it faces. Aspect grid is recognized as 'the downslope direction of the maximum rate of change in value from each to its neighbours' (Gorokhovich and Voustianiouk 2006). The output raster data value was used to derive the compass direction of the aspect. The value of 0° aspect is to true north, a 90° aspect is to the east, 270° are to the west and so forth. The aspect map generated in Arc GIS 10.2 for the watershed is shown in Fig. 6. The north-east- and east-facing slopes mainly occur in the study area.

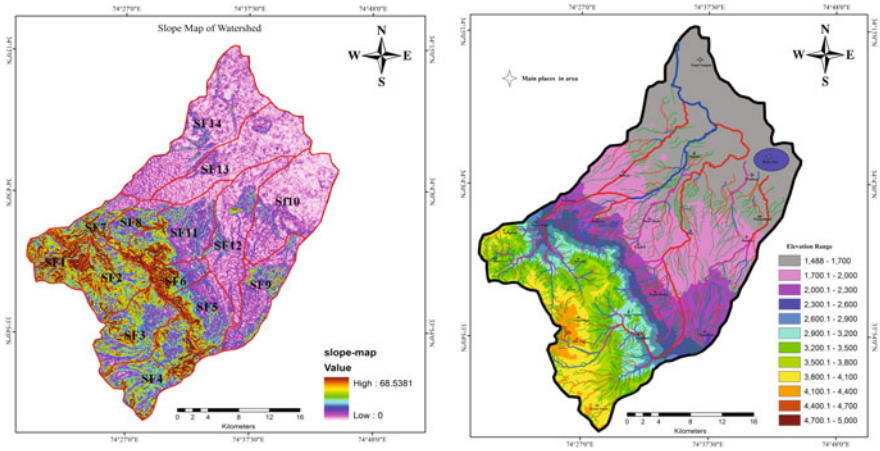

Fig. 5 Slope map showing high slope in south-west and low slope in north-east of the area

Stream Order and Number

The morphometric analysis of a watershed begins with delineation of stream orders which is based on a hierarchic ranking of streams. For stream ordering, Horton's Law in which Strahler (1952) had made some modifications was followed by designating an un-branched stream such as first-order stream, two first-order streams join to form second order, two second-order streams join together to form third order and so on. In the present study, the Strahler system of stream ranking is used for the basins. It is also noted that first-order streams are highest in number in all sub-watersheds while highest order has the lowest number. Based on the Strahler (1964) system of stream ordering, the watershed is designated as sixth order (Fig. 4) covering an area about 1000 km^2. In the hilly terrain, first-order streams are more in number, which indicates compact nature of the bedrock lithology and terrain complexity. The variation in order and size of the sub-watersheds is largely due to physiographic and structural conditions of the region.

Stream Length

The stream length was computed on the basis of the law proposed by (Horton 1945), for all the 14 sub-watersheds given in Table 2. It can be noted from the table that in each sub-watershed stream length decreases as the stream order increases (Horton 1945) except SF 1, 4, 5, 7, 8, 10, 11, 12, 13 and 14. This variation observed indicates that the flow of streams is from high altitude with lithological variations and moderately steep slopes (Singh and Singh 1997). Lineament map prepared for

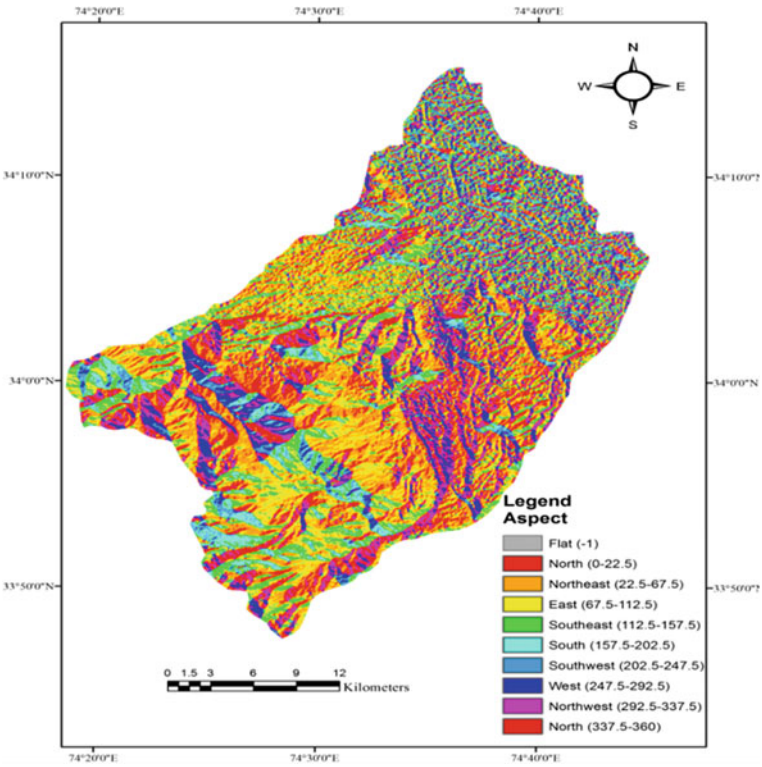

Fig. 6 Aspect map highlights dominance of north-east- and east-facing slopes in the area

the area shows that a lot of lineaments pass through the area (Fig. 11). Superimposition of the lineament map of the area over the drainage map showed that the drainage lines form straight lines at various places. A close relation was observed when lineament and drainage map was superimposed by observing that streams follow the path of lineaments at many places (Fig. 8). This deviation from the normal shape of the stream in a terrain may result in a nonlinear length-order relationship.

Bifurcation Ratio (R_b)

The term 'bifurcation ratio (R_b)' was introduced by Horton in 1932 (Horton 1932). Bifurcation ratio is related to the branching pattern of a drainage network and is defined as the ratio between the total numbers of stream segments of one order to that of the next higher order in a drainage basin (Schumn 1956). Strahler (1957) demonstrated that bifurcation ratio shows only a small variation in different regions

with different environments except where powerful geological control dominates. Lower bifurcation ratio values are the characteristics of structurally less disturbed watersheds without any distortion in drainage pattern (Nag 1998). The values of mean bifurcation ratio fluctuate from 2.21 to 3.20 suggest high degree of dissection and structural control in drainage development in uplands in south-west sub-watersheds. According to Zuchiewicz (1989), high values of bifurcation ratio can be in the territory with the presence of young tectonic movements. Thus, values of R_b indicate that the area towards SW side (Pir-Panjal) has suffered more structural disturbances. Consequently, the difference in bifurcation ratio reflects the lithological and structural variations in the watershed (Rawat et al. 2011).

The presence of structures in lithology (also covered by upper loose soil layer) brings the area in the category prone to landslides. The analysis of mean bifurcation ratio reveals the presence of high flow energy result of which does not offer ample time for infiltration, leads flood hazard during heavy rainfall. Moreover, the continuous and intense rainfall loosens the upper surface and enhances seepage of water through these structures which act as lubricant and in turn cause landsliding as observed in devastating flood (Sep 2014 and March 2015) in Jammu and Kashmir after decades of years.

Stream Frequency (F_s)

The F_s is defined as the total number of streams per unit area (Horton 1945). The direct relationship of drainage density and stream frequency with runoff processes was analysed (Melton 1958). The occurrence of stream segments depends on the nature and structure of rocks, vegetation cover, nature and amount of rainfall and soil permeability. Generally, high stream frequency is related to impermeable sub-surface material, sparse vegetation, high relief and low infiltration capacity of the region. The study revealed that the SF1, 2, 6, 7 and 8 watersheds have high stream frequency because of the fact that it falls in the zone of fluvial channels and the presence of ridges on both sides of the valley while as watershed SF10, 12, 13 and 14 has low stream frequency because of low relief. The highest value of stream frequency sub-watersheds produces faster runoff, and resultant faster runoff makes the downstream sub-watersheds more susceptible to floods.

Length of Overland Flow (L_o)

It is one the most important independent variables affecting hydrological and physiographical development of a drainage basin. It is the length of water over the ground before it gets concentrated into definite stream channels and is equal to half of drainage density (Horton 1945). The length of overland flow relates inversely to the average channel slope, and results show conformity with the same. The shorter

length of overland flow (0.14) for SF1 points out the quicker runoff process, and higher length of overland flow (0.63) for SF14 point out slower runoff process.

The sub-watersheds having lower 'L_o' and quicker runoff brings water quickly from upstream into SF10, 13 and 14 having higher 'L_o', makes them more susceptible to floods during intense rainfall. The higher 'L_o' and slower runoff gives more time for settling of mud coming with flood water as seen in recent flooding (September 2014). Thus, siltation is another serious environmental problem other than direct damage caused by flood water to everything coming in its way.

Drainage Density (D_d)

One of the essential indicators of the landform element is drainage density (D_d) which gives a numerical measurement of landscape dissection and runoff potential (Chorley 1969). This is defined as the total stream length in a given basin to the total area of the basin (Strahler 1964). It has been observed that low drainage density is associated with regions having highly permeable sub-surface material under dense vegetative cover and low relief while as high values of D_d are noted for the regions of impermeable sub-surface materials, sparse vegetation and mountainous relief (Nag 1998).

In the area, high drainage density was found in SF1, 2, 5, 6, 7, 8 and 11 because of impermeable (Hard rock's) sub-surface material (Panjal traps, limestones, slates, etc.) and mountainous relief. Drainage density map (Fig. 7) of catchment clearly indicates presence of high slope, and impermeable rock types in these sub-watersheds. Low D_d for sub-watershed SF10, 12, 13 and 14 indicates that it has highly permeable sub-surface material (Alluvium) and low relief, as observed from the lithological map (Fig. 2).

The low drainage density of sub-watershed SF13, 14, 10 and 12 may be because of indiscriminate anthropogenic influence on the land-use pattern as observed in the area. The high drainage density sub-watersheds provoke a quick flood response which results in higher runoff in downstream in these low-density areas with resultant flood vulnerability (Fig. 6) during intense rainfall (Fig. 15a).

Compactness Coefficient (C_c)

It was calculated as the basin perimeter divided by the circumference of a circle to the same area of the basin (Horton 1945). Compactness constant developed the relationship between actual hydrological basins to the exact circular basin having the same area as that of hydrological basin. The value of compactness coefficient for the sub-watersheds ranges between 1.16 and 1.79. The high values of compactness are particularly observed in the less resistant rock areas while low values are found

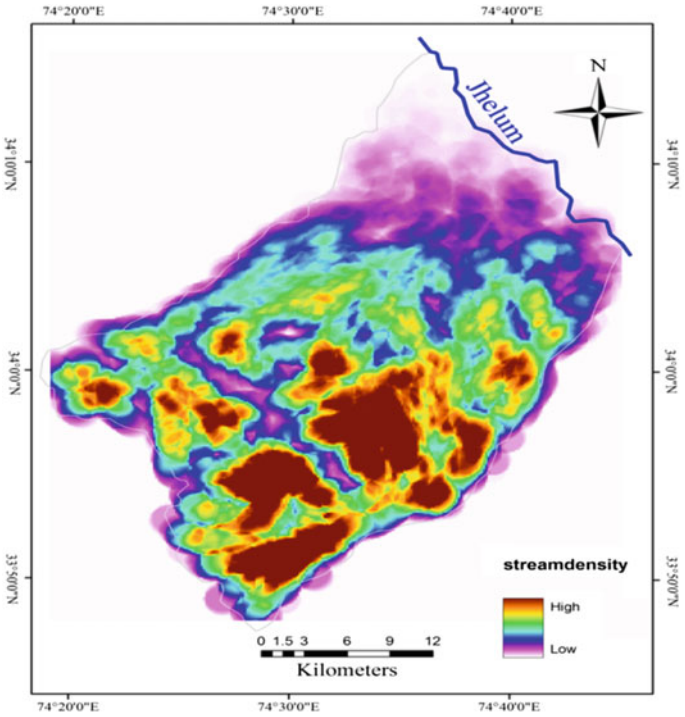

Fig. 7 Drainage density map shows high density in south-west and very low in north-east of the area

in hard rock areas. The compactness constant is higher in SF7, 9, 12, 13 and 14, suggesting their elongated nature and has enough time for discharge of water.

Elongation Ratio (R_e)

Schumn (1956) defined it as the ratio between the diameter of the circle of the same area as the drainage basin (A) and the maximum length (L) of the basin. Analysis of elongation ratio indicates that the areas with higher elongation ratio have high infiltration capacity and low runoff. A circular basin is more efficient in the discharge of runoff than an elongated basin (Singh and Singh 1997). The values of elongation ratio generally vary from 0.6 to 1.0 over a wide variety of climatic and geological conditions. Values close to 1.0 are typical of regions of very low relief, whereas values in the range 0.6–0.8 are usually associated with high-relief and steep ground slope (Strahler 1964). The value of the elongation ratio in the study area is found in the range of 0.39 to 0.99 indicating high-relief and steep ground

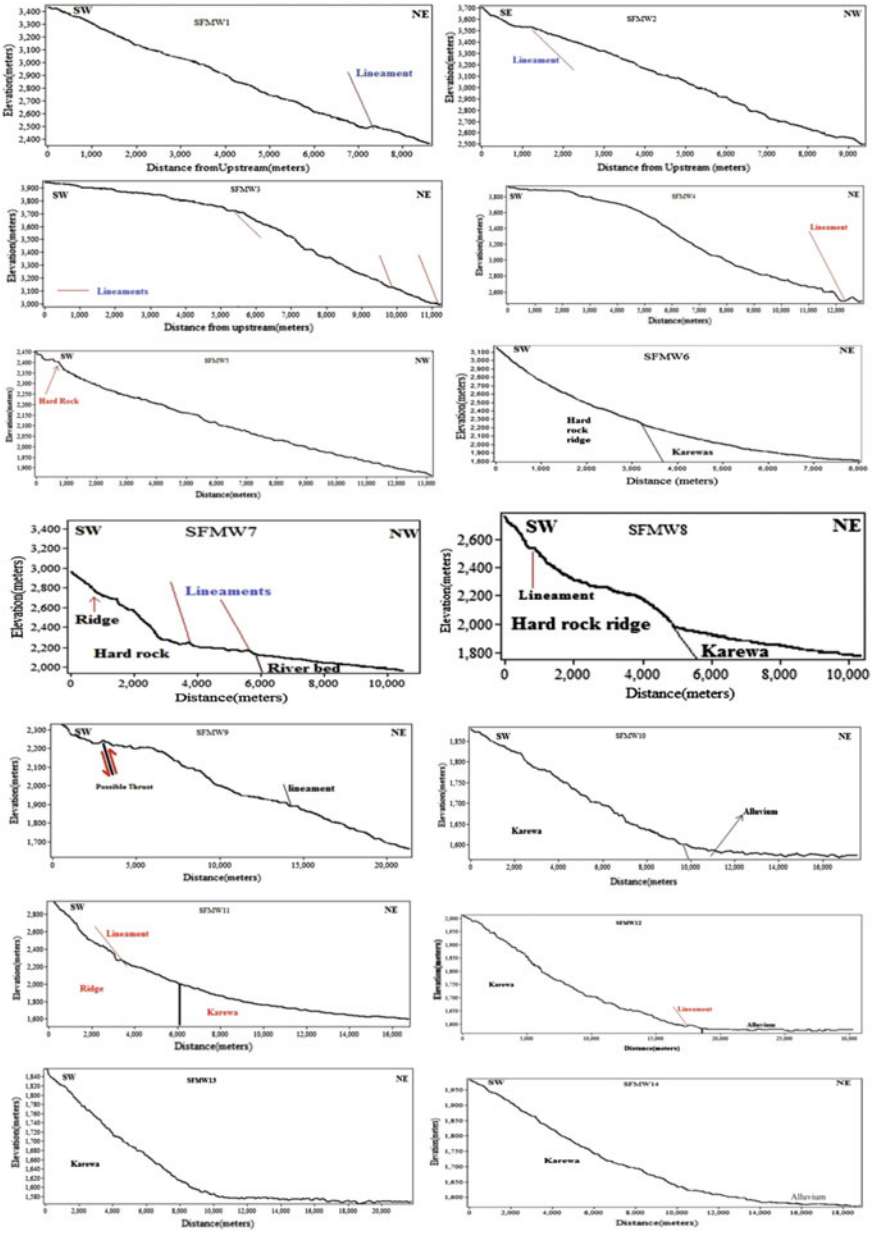

Fig. 8 Stream profiles of highest order streams of each sub-basin showing possible effect of sub-surface structure or lithological transition

slope (Fig. 5). In the present study, these values are less than 0.99; hence, all the sub-watersheds are more or less elongated in shape.

Circulatory Ratio (R_c)

Circularity ratio is defined as the ratio of the area of the basin (A) to the area of a circle (A_c) having the same circumference as the perimeter of the basin (Miller 1953). As basin shape approaches to a circle, the circulatory ratio approaches to unity (Miller 1953). Circulatory ratio (Table 2) is found in the range of 0.31–0.74 which is less than unity and indicates that the sub-watersheds are almost elongated. The high value of circulatory ratio of SF2 (0.74) can be due to delay in topographic development or maturity stages and assortment of various geological conditions. The circulatory ratio is found very much applicable parameter in the assessment of flood vulnerability of area. If circulatory ratio is higher, higher will be flood risk at a peak time at the outlet point. The outlet point of higher circulatory ratio sub-watershed becomes one of the inlet points for lower circulatory ratio sub-watershed on downstream side. This analysis reveals that the extreme downstream sub-watersheds (i.e. SF9, 12, 13 and 14) having low circulatory ratio are more prone to floods.

Longitudinal River Profiles

The longitudinal profiles (Fig. 8) of rivers have been determined using a specific tool of Arc GIS. The extraction of tectonic information is the principle goal to construct longitudinal profiles of main channels and also to interpret the lithological influence. According to (Rhea 1993; Sinha 2001), the longitudinal profile analysis, which is a graphical representation/relation of river elevation and river length, is the most commonly used technique to identify river response to tectonics. In many longitudinal river profiles, convex-up nature can be linked with the sub-surface structures and uplift (Fig. 9) and consequently effects the lithological distribution in the area. The transition of different rock types can be investigated by strictly analysing stream profiles as observed presently.

The longitudinal profiles of some main streams at some portions are highly concave upwards suggesting the tectonically active nature of the area. The longitudinal profile when showing any anomalous behaviour may be attributed either to the presence of structural element or to the lithological transition. It is also observed that some profiles show smooth stream profiles which can be attributed to either to same lithology or minute lithology change in terms of hardness. However, some river profiles also show abrupt change at the junction of steep slope (Pir-Panjal

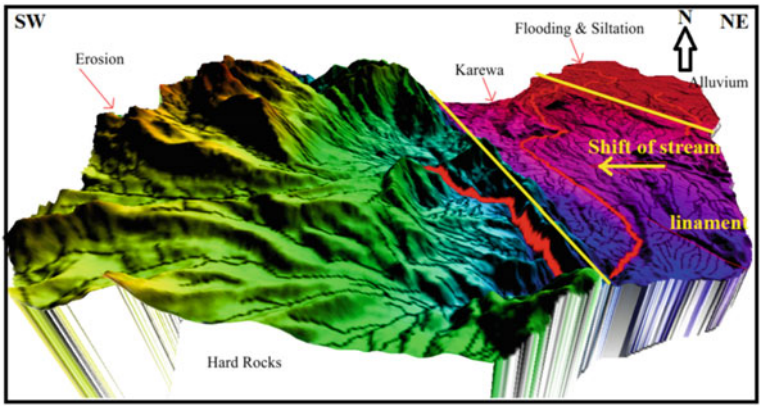

Fig. 9 3D view showing shift of drainage and highlighting three divisions to categorize the area

range side) and the Karewas plateau, that is, longitudinal profiles can also be used to show the major slope changes along its course. According to Reyaz et al. (2013), geologic structures such as lithologic boundaries and lineaments/faults also affect both the local shape of longitudinal profiles and the SL index. Therefore, deviations found in longitudinal river profile may be either related to the activity of tectonic lineaments or lithological transition.

Asymmetry Factor (A_F)

The asymmetry factor was developed to detect tectonic tilting at the scale of a drainage basin (Hare and Gardner 1985; Keller and Pinter 2002) and is defined as

$$A_F = 100(A_r/A_t),$$

where 'A_r' is the area of the basin to the right of the trunk stream that is facing downstream and 'A_t' is the total area of the drainage basin. For a stream network that formed and continues to flow in a stable setting, A_F should equal about 50, while values of A_F greater or less than 50 may suggest tilt. The A_F (65.53) reveals that tectonic activity has caused a left dipping of the drainage basin. Consequently, tributaries to the right of the main stream (Fig. 9) are longer compared to the ones to the left side of the stream with an asymmetry factor less than 50 (Keller and Pinter 2002).

Lineaments and Their Importance

Lineaments are an extended mapable linear or curvilinear feature of a surface whose parts align in straight or nearly straight relationships that may be the expression of folds, fractures or faults in the sub-surface (Sabins 2000). Geomorphologically, lineaments are defined as mappable simple or composite linear features whose parts are aligned in a rectilinear or slightly curvilinear and linear surface features such as valleys, ridges and boundaries of elevated areas, coastlines, boundaries of formation, fractures, faults and joints (Lillesand and Kiefer 1987; Peterson 1980). The lineament analysis carried out by using satellite data and DEM offers important information on sub-surface fractures that may control the movement and storage of surface and sub-surface water.

Lineaments may be continuous or discontinuous and, under certain circumstances, may be regarded as the surface manifestation of fault and fracture zones (Pal et al. 2006). In the areas having hard rock terrain, the occurrence and movement of water depend mainly on the secondary porosity and permeability resulting from folding, faulting, fracturing, etc. Thus, lineaments are the most evident structural features that are significant for movement of water (surface as well as sub-surface water). The remote sensing data have the application of offering synoptic view of large area assist in understanding and mapping the lineaments for the area. The lineaments identified (Fig. 10) from the satellite data are surface manifestation of some structural features developed in the bedrock due to tectonic stress and strain.

In the study area, the lineaments recognized are controlling the streams at many places towards Pir-Panjal side (hilly terrain) but in low-lying alluvial side where depositional processes obliterate/vanish the surface expression of these structures. The lake of expression of lineaments in any area does not mean that the area is structure less. The analysis of rose diagram (Fig. 11a, b) shows that the maximum number of lineaments on the south-western side (Pir-Panjal Range side) is having NW–SE direction. The tectonic map of the region was analysed, and it was found that Muree thrust (MBT), Panjal thrust (MCT) (Fig. 12) and many others passing in the neighbourhood of the study area show same direction on the rose diagram. By the overlay analysis, it was found that most of the lineaments are parallel to these tectonic lineaments.

The analysis of stream network illustrates that the sub-watersheds display dendritic to sub-dendritic and parallel to sub-parallel drainage pattern in different parts of the area. This variation in drainage pattern can be attributed to the presence of different rock types such as Panjal Volcanic, Slates, Limestone, Karewas and recent alluvium in the area (Fig. 13).

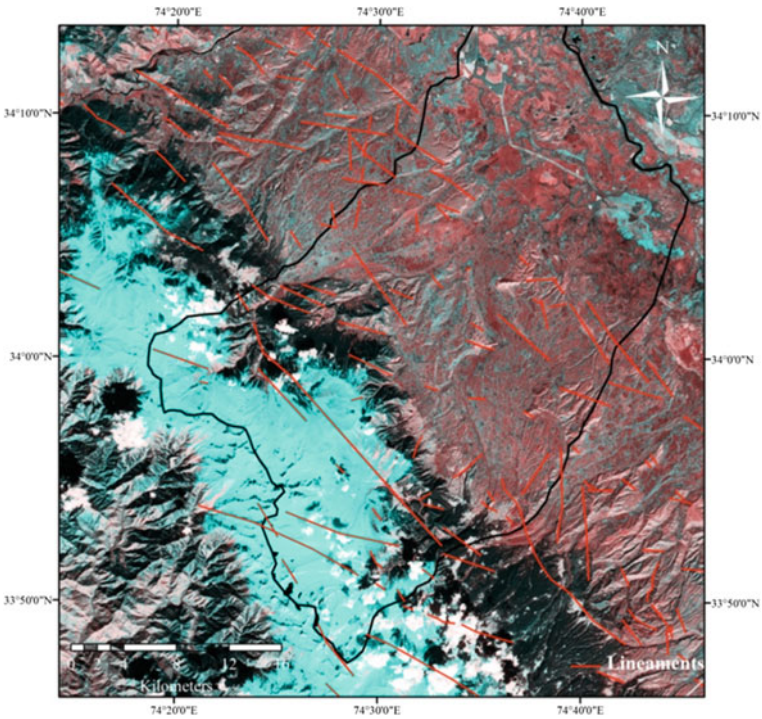

Fig. 10 Map showing the lineaments manually drawn from Sobel and Laplacian edge-enhanced images

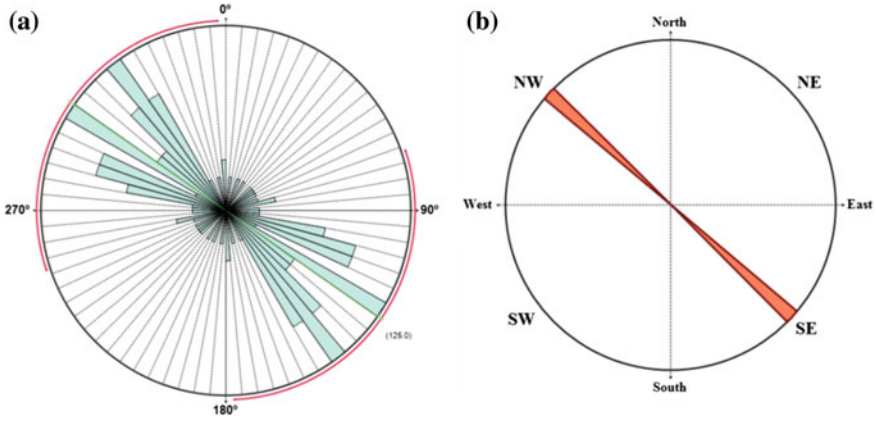

Fig. 11 **a** Rose diagram of new lineaments, **b** rose diagram of structures present in the surrounding area

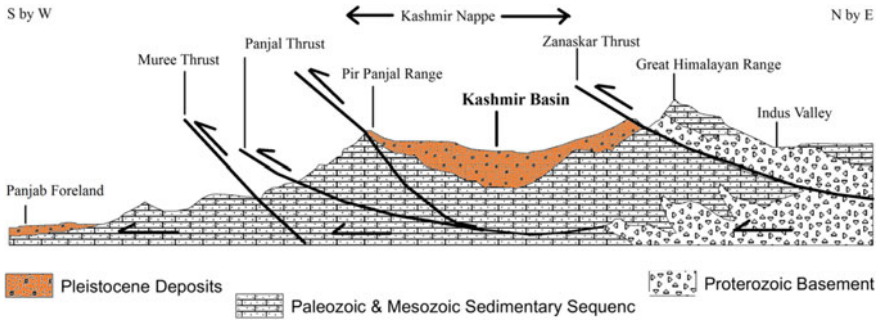

Fig. 12 Schematic section of Kashmir Valley, after Wadia 1976

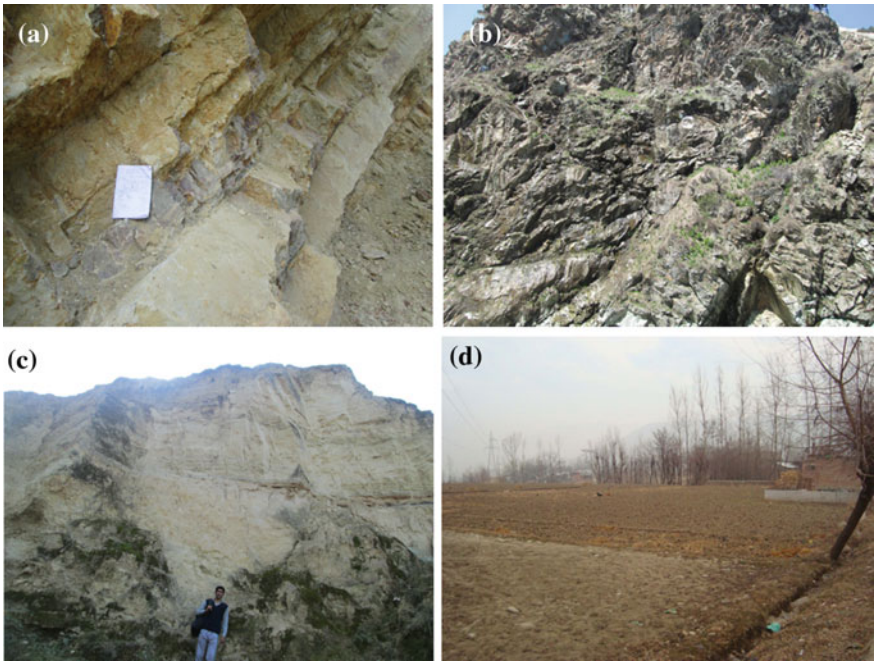

Fig. 13 Different rock types. **a** Limestone. **b** Panjal Volcanic. **c** Karewas. **d** Alluvium

Interpretations

The detailed analysis of stream pattern and the assessment of morphometry for sub-watersheds falling in different geologic terrains have clearly shown that the drainage features and its behaviour change with different lithology. The lineaments having structural advantage of being sub-surface structures such as folds, fractures and faults and geomorphological advantage of being linear ridges, linear valleys,

streams, etc., have been delineated using the remote sensing techniques like edge enhancement (Sobel and Laplacian), FCC and DEM-derived products (aspect, shaded relief map, etc.). Therefore, the advantage of drainage network with the support of satellite data allows the evaluation of geological structures and interpretation of lithology. The drainage pattern and texture can be easily identified from the terrain analysis based on satellite information. The drainage density map and lineament map reflect that the south-west side has a high drainage and lineament density, which reveals high dissection. Consequently, from the analysis of longitudinal river profiles and drainage basin asymmetry and other parameters, it can be summarized that the area has undergone high tectonic deformation (Fig. 8).

Additionally, morphometric parameters, i.e. drainage density, stream frequency, mean bifurcation ratio, drainage texture, length of overland flow, form factor, circularity ratio, elongation ratio, basin shape and compactness coefficient, are also termed as erosion risk assessment parameters used for priority zoning of sub-watersheds (Biswas et al. 1999). Additionally, the hills have steep slopes that are vulnerable to landslides (Khan et al. 2012). The cross profiles generated across the valleys present in the hilly area are mostly found to be V-shaped and U-shaped (Fig. 14). The structures associated with these valleys may also increase the landslide susceptibility in the area. The high number of lineaments (expression of weak zone) has close relation with permeability of water and increases the probability of landslides occurrence. Other important causative factors of producing landslides in hilly regions are the intensity and duration of rainfall which is the most common factor in Kashmir Basin. Taking all these parameters into consideration, the areas (sub-watersheds) more prone to landslides are coming towards the mountainous region where the geological structures are more and upper soil cover is weak.

However, when we consider the flooding as factor which is more dangerous and devastating than other natural hazards in the plainer sub-watersheds, we have to

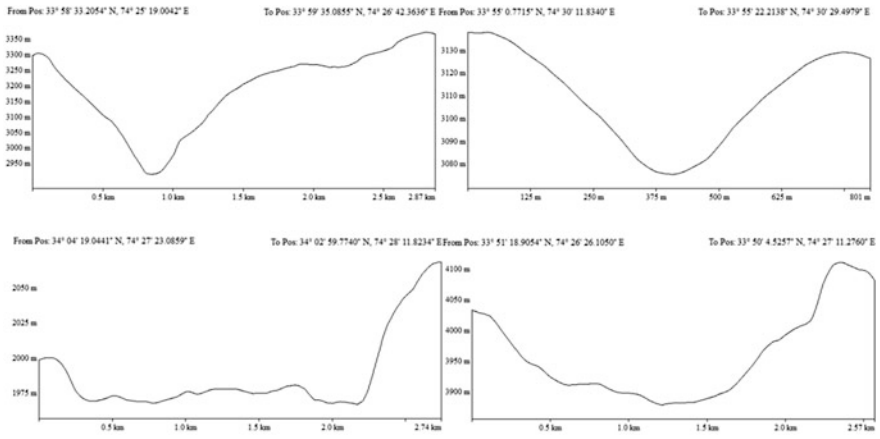

Fig. 14 V-shaped and U-shaped valleys present in the hilly areas

take the low-lying watersheds into consideration having more chances of flooding. All the water which comes from higher reaches has to drain through low-lying sub-watershed as an overbank flow because of low drainage density and ultimately reaches River Jhelum (only outlet for Kashmir Basin). At the time of heavy rain fall, River Jhelum is not able to concentrate all the flood water and in turn results overbank flow and river bank failure which causes damage to life and property. Thus, in low-lying plainer areas of the study area as well as Kashmir Basin, low stream frequency, low drainage density, slower runoff and higher overland flow are the main factors in bringing such devastating floods. At last but not the least, the settlements on river banks and flood plains and their consequence in causing floods in any area cannot be neglected (Fig. 15). The whole catchment has been categorized into three zones; south-western zone having high elevation, high slope, hard rocks and high drainage density (more chances of landsliding), medium zone and north-eastern zone having plainer topography with low drainage density (more chances of flooding).

Nevertheless, the study has also assisted in interpreting the impact of the recent tectonic activity in the catchment present in earthquake prone zone. The lineament analysis suggests that the drainage is controlled by sub-surface structures at many places. The river profiles of the highest order stream of many sub-watersheds can be

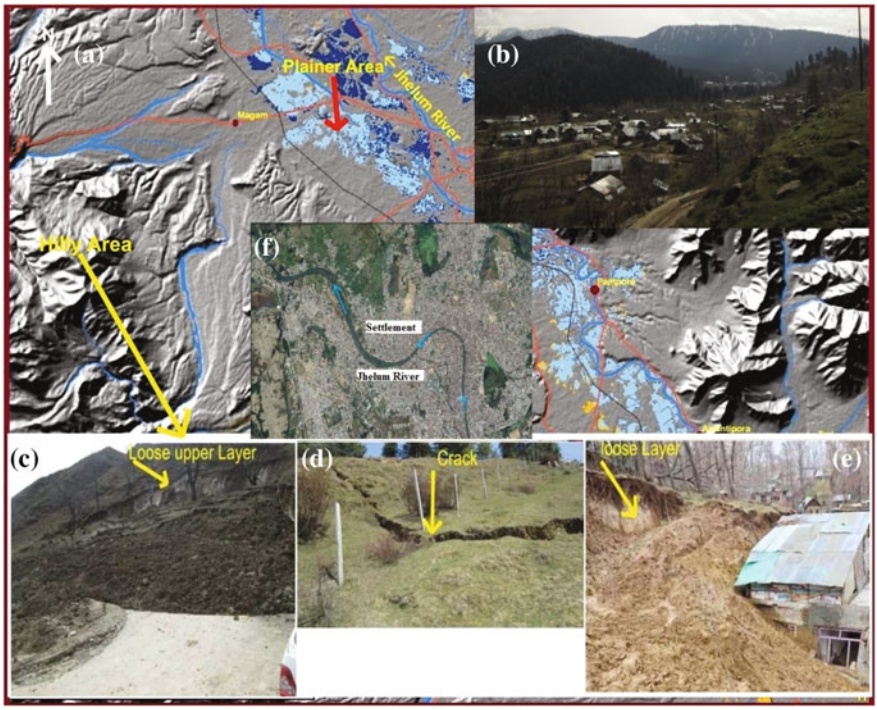

Fig. 15 Highlights 2014 and 2015 landslide and flooding. **a** Flooding in plainer area. **b**, **f** Settlement on flood plain and river banks. **c**, **d** and **e** Landslides in hilly areas

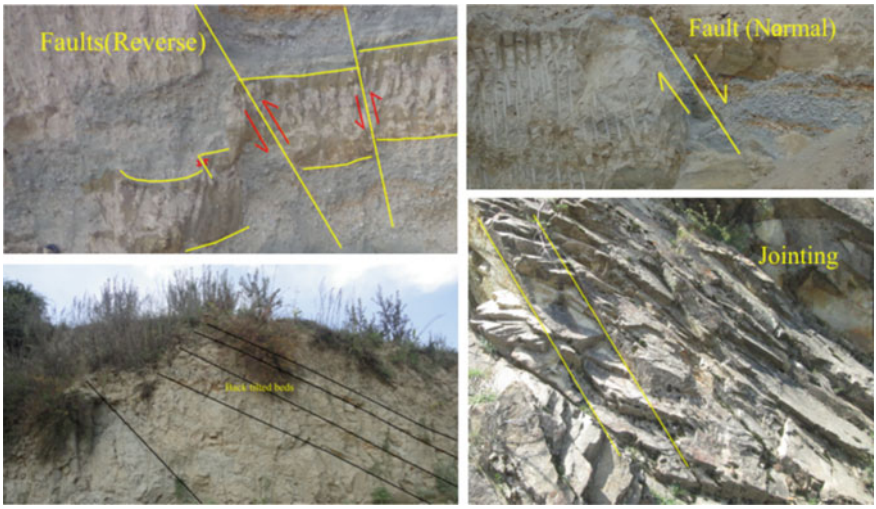

Fig. 16 Various kinds of structural features developed in response to tectonic deformation in the area

correlated with a high degree of tectonic activity. Thus, abrupt change in slope breaks in the longitudinal river profiles indicates either lithological transition and/or existence of structures with tectonic significance. The presence of active fronts and basin tilting also suggest the existence of possible structures and their effects on the topography of the catchment. Based on the field investigation, various types of structures were found in all types of rocks (Fig. 16) as an expression of neotectonism suggesting the tectonically active nature of the area. Last of all, landslide and flood vulnerability being the concern in the present study, the collective role of drainage analysis, structures and lithology has helped to read the area which may help the local inhabitants, engineers and urban planners to minimize loss of life, property and nature in the area.

Conclusion

Drainage characteristics offer basics to recognize variation in rock resistance, structural control and priority assessment (in terms landslides and floods) in any drainage basin. The thorough investigation of the drainage pattern and the evaluation of linear and areal aspects have clearly revealed that the drainage characteristics are noticeably different for each lithology type. The unusual appearance of drainage network at many places has given hint to the presence of sub-surface structures supported by geomorphic indices like river longitudinal profiles and drainage asymmetry factor. Additionally, lineament analysis performed has clearly shown that streams at many places follow the path of lineaments. It can be

concluded that at many places streams are structurally controlled and others are carving out their own path. Consequently, the assessment of rose diagram of lineaments has shown NW–SE trend which resembles to trend of major geological structures present in the region. It confirms that these lineaments and abrupt deflection in drainage courses in the area are strongly controlled by the regional tectonics of the area. Lastly, the study demonstrates the usefulness of drainage behaviour for categorizing the catchment in terms of landslide and flood struck areas. Landslides in the hilly area having high-slope, structural weak planes and loose upper soil cover (driving rapid physical erosion) result from heavy rainfall. The low drainage density, low frequency, slower runoff, higher overland flow and more human intervention like the settlements on river banks and flood plains and death of drainage channels make low-lying areas prone to floods (J&K flood 2014) during intense rainfall conditions.

References

Alexander GN (1972) Effect of catchment area on flood magnitude. J Hydrol 16:225–240

Ali SA, Pirasteh S (2005) Evaluation of ground water potential zones in parts of Pabdeh anticline, Zagros fold belt, SW Iran. Water Ethiop J Water Sci Technol 9(1):92–97

Ali SA, Rangzen K, Pirasteh S (2003) Use of digital elevation model for study of drainage morphometry and identification of stability and saturation zones in relations to landslide assessments in parts of Shahbazan Area, Zagros Belt, SW Iran. Cartograph 32(2):162–169

Anbalagan R, Singh B (1996) Landslide hazard and risk assessment mapping of mountainous terrains. A case study from Kumaun Himalaya, India. Eng Geol 43:237–246

Angillieri MYE (2008) Morphometric analysis of Colangüil river basin and flash flood hazard, San Juan, Argentina. Environ Geol 55:107–111

Atkinson PM, Massari R (1998) Generalised linear modelling of susceptibility to landsliding in the Central Apennines, Italy. Comput Geosci 24(4):373–385

Ayala IA, Chavez OE, Parrot JF (2006) Landsliding related to land-cover change: a diachronic analysis of hillslope instability distribution in the Sierra Norte, Puebla, Mexico. Catena 65:152–165

Bhatt DK (1975) On the quaternary geology of the Kashmir valley with special reference to stratigraphy and sedimentation. Geol Surv India, Misc Pub 24(1):188–203

Bhatt DK (1976) Stratigraphical status of Karewa group of Kashmir, India. Himal Geol 6:197–208

Bhatt DK (1989) Lithostratigr of the Karewa group, Kashmir valley, India and a critical review of its fossil record. Geol Surv India Mem 122:1–85

Biswas S, Sudhakar S, Desai VR (1999) Prioritization of subwatersheds based on morphometric analysis of drainage basin: a remote sensing and GIS approach. J Indian Soc Remote Sens 27 (3):155–166

Bloom AL (1979) Geomorphology. Prentice-Hall Private Ltd., India, New Delhi

Burbank DW, Johnson GD (1982) Intermontane-basin development in the past 4 Myr in the north-west Himalaya. Nature 298:432–436

Burrough PA (1986) Principles of geographical information systems for land resources assessment. Oxford University Press, New York, p 50

Chopra R, Dhiman RD, Sharma PK (2005) Morphometric analysis of sub-watersheds in Gurdaspur district, Punjab using remote sensing and GIS techniques. J Indian Soc Remote Sens 33:531–539

Chorley RJ (1969) Introduction to fluvial processes. Methuen and Co., Limited, London, p 588

Deffontaines B, Chorowich J (1991) Principles of drainage basin analysis from multisource data: application to the structural analysis of the Zaire Basin. Tectonophysics 194:237–263
Deffontaines B, Chotin P, Brahim LA, Rozanov M (1992) Investigation of active faults in Morocco using morphometric methods and drainage pattern analysis. Geol Rundsch 81 (1):199–210
Deffontaines B, Lacombe O, Angelier J, Chu HT, Mouthereau F, Lee CT, Deramond J, Lee JF, Yu MS, Liew PM (1997) Quaternary transfer faulting in the Taiwan foothills: evidence from a multisource approach. Tectonophysics 274(1):61–82
Derbyshire E, Gregory KJ, Hails JR (1981) Studies in physical geography, geomorphological processes. Butterworths, London, p 101
Doornkamp JC, Cuchlaine AMK (1971) Numerical analysis in geomorphology—an introduction. Edward Arnold, London, pp 3–20
Farooqi IA, Desai RN (1974) Stratigraphy of Karewas, India. J Geol Surv India 15(3):299–305
Gorokhovich Y, Voustianiouk A (2006) Accuracy assessment of the processed SRTM-based elevation data by CGIAR using field data from USA and Thailand and its relation to the terrain characteristics. Remote Sens Environ 104:409–415
Hare PW, Gardner TW (1985) Geomorphic indicators of vertical neotectonism along converging plate margins, Nicoya Peninsula, Costa Rica, In: Morisawa M, Hack, JT (eds) Tectonic geomorphology. Proceedings of the 15th annual binghamton geomorphology symposium. Allen and Unwin, Boston, pp 123–134
Hobbs WH (1904) Lineaments of the Atlantic border region. Geol Soc Am Bull 15:483–506
Horton RE (1932) Drainage basin characteristics. Trans Am Geophys Union 13:350–361
Horton RE (1945) Erosional development of streams and their drainage basins: hydrophysical approach to quantitative morphology. Bull Geol Soc Amer 56:275–370
Howard AD (1967) Drainage analysis in geological interpretation: a summation. Am Asso Petrol Geol Bull 51(11):2246–2259
Keller EA, Pinter N (2002) Active tectonics: earthquakes, uplift, and landscape. 2nd edition. New Jersey Prentice Hall, pp 1–362
Khan YA, Lateh H, Baten MA, Kamil AA (2012) Critical antecedent rainfall conditions for shallow landslides in Chittagong city of Bangladesh. Environ Earth Sci 67(1):97–106
Krishnan MS (1982) Geology of India and Burma. Madras, Higginbotham, p 536
Kumar R, Kumar S, Lohni AK, Neema RK, Singh AD (2000) Evaluation of geomorphological characteristics of a catchment using GIS. GIS India 9(3):13–17
Leopold LB, and Miller JP (1956) Ephimeral streams: hydraulic factors and their relation to the drainage net. US Geol Surv prof 282-A
Lillesand TM, Kiefer RW (1987) Remote sensing and image interpretation. Wiley, New York
Lin ML, Tung CC (2003) GIS-based potential analysis of the landslides induced by the Chi-Chi earthquake. Eng Geol 71:63–77
Lydekker R (1883) The geology of Kashmir and Chamba territories and the British district of Khagan. Geol Surv India Mem 22:344
Melton MA (1957) An analysis of the relations among elements of climate, surface properties and geomorphology. Proj. NR 389-042, Tech. Rep 11, Columbia University, Department of Geology, ONR, New York
Melton MA (1958) Correlation structure of morphometric properties of drainage systems and their controlling agents. J Geol 66(4):442–460
Middlemiss CS (1910) A revise of the Silurian-Trias sequence in Kashmir. Geol Surv India Rec 40:206–260
Miller V C (1953) A quantitative geomorphic study of drainage basin characteristics on the clinch mountain area, Virgina and Tennessee. Project, Tech Rep 3, Columbia University, Department of Geology, ONR, New York, NR, pp 389–402
Morisawa ME (1959) Relation on morphometric properties to runoff in the Little Mill Creek. Ohio, drainage basin. Tech. Rep. 17, Columbia University, Department of Geology, ONR, New York
Nag SK (1998) Morphometric analysis using remote sensing techniques in the Chaka sub-basin, Purulia district, West Bengal. J Indian Soc Remote Sens 1:69–76

Nagarajan R, Roy A, Kumar RV, Mukherjee A, Khire MV (2000) Landslide hazard susceptibility mapping based on terrain and climatic factors for tropical monsoon regions. Bull Eng Geol Environ 58:275–287

O'Leary DW, Friedman JD, Pohn HA (1976) Lineament, linear, lineation: some proposed new standards for old terms. Bull Geol Soc Am 87:1463–1469

Ozdemir H, Bird D (2009) Evaluation of morphometric parameters of drainage networks derived from topographic maps and DEM in point of floods. Environ Geol 56:1405–1415

Patel D, Gajjar C, Srivastava P (2012) Prioritization of malesari mini-watersheds through morphometric analysis: a remote sensing and gis perspective. Environ Earth Sci 69:2643–2656

Peterson R (1980) Lineament analysis for oil and gas exploration and production in thematic mapper images, northern territory, Australia. Photogram Eng Remote Sens 61:761–773

Pirasteh S, Ali SA, Hussaini HS (2007) Morphmetric and structural analysis in Zagros Mountains, Southwest Iran—an application of geo-information technology. J Geomat 1(2):39–44

Pubellier M, Deffontaines B, Quebral R, Rangin C (1994) Drainage network analysis and tectonics of Mindanao, southern Philippines. Geomorphology 9(4):325–342

Rawat PK, Tiwari PC, Pant CC (2011) Morphometric analysis of third order river basins using high resolution satellite imagery and gis technology: special reference to natural hazard vulnerability assessment. E-Int Sci Res J 3:(2)

Reyaz et al (2013) Morphotectonic and lithostratigraphic analysis of intermontane Karewa Basin of Kashmir Himalayas. India J Mt Sci 10(1):1–15

Rhea S (1993) Geomorphic observation of river in the Oregon coast range from a regional reconnaissance prespective. Geomorphology 27:135–150

Roughani M, Ghafouri M, Tabatabaei M (2007) An innovative methodology for the prioritization of sub-catchments for flood control. Int J Appl Earth Obs Geoinf 9:79–87

Sabins FF (2000) Remote sensing: principles and interpretation. Freeman and Company, W.H., p 494

Saha AK, Gupta RP, Arora MK (2002) GIS-based landslide hazard zonation in the Bhagirathi (Canga) Valley, Himalayas. Int J Remote Sens 23(2):357–369

Schumm SA (1956) Evolution of drainage systems and slopes in bad lands at perth Amboy. New Jersey. Bull Geol Soc Am 67:597–646

Schumm SA (1977) The fluvial system. Wiley, New York, p 338

Singh IB (1982) Sedimentation pattern in the Karewa basin, Kashmir valley, India and its geological significance. J Palaeonto Soc India 27:71–110

Singh S, Singh MC (1997) Morphometric analysis of Kanhar River basin. National Geogr J India 1:31–43

Sinha SR (2001) Neotectonic significance of longitudinal river profiles: an example from the Banas drainage basin, Rajasthan. J Geol Soci India 58:143–156

Strahler AN (1952) Dynamic basis of geomorphology. Bull Geol Soc Amer 63:923–938

Strahler AN (1957) Quantitative analysis of watershed geomorphology. Trans Amer Geophys Union 38:913–920

Strahler AN (1964) Quantitative geomorphology of drainage basin and channel networks. In: Chow VT (ed) Handbook of applied hydrology. McGraw Hill, New York, Sect. 4–11

Temesgen B, Mohammed MU, Korme T (2001) Natural hazard assessment using GIS and remote sensing methods, with particular reference to the landslides in the Wondogenet area, Ethiopia. Phys Chem Earth Part C 26:665–675

Wadia DN (1975) Geology of India, 4th edn. Tata McGraw-Hill, New Delhi (Tenth reprint)

Zuchiewicz W (1989) Morphotectonic phenomena in the polish flysch Carpathians: a case study of the Eastern Beskid Niski Mountains. Quest Geogr Spec Issue 2:155–167

Hydrologic Design Parameters Database for Water Harvesting Structures in Madhya Pradesh

Ramadhar Singh, Karan Singh and D. M. Bhandarkar

Abstract The databases of hydrologic design parameters need to be developed for proper design of water harvesting structures. Daily rainfall data for 20 years period (1991–2010) of ten identified districts of Madhya Pradesh (MP), State of India, were used for estimation of design rainfall and runoff values of various durations and different return periods. Rainfall data adequacy and randomness tests indicated that data are of adequate period and random in nature. Rainfall frequency analysis was carried out using nine probability density functions (pdfs). The best fitted pdf describing data set and giving minimum value of Chi-Square test parameter was identified for estimating the design rainfall values of different durations and frequencies (return periods). Design runoff values were estimated using NRCS-Curve Number method and design rainfall values. Peak flow rate database for 25 years return period was developed for varying catchment area (1–100 ha). The magnitudes of 1-day-maximum, 2-day-maximum and annual rainfall were estimated. The 1-day-maximum rainfall values for 25 year return period were estimated to be 257.0, 227.5, 254.5, 307.4, 255.0, 255.1, 292.5, 227.6, 346.4 and 173.0 mm for Bhopal, Indore, Raisen, Hoshangabad, Khandwa, Jabalpur, Datia, Dhar, Guna and Chhindwara districts, respectively. The annual runoff values for Bhopal, Indore and Jabalpur districts were estimated to be 322.7, 290.5 and 471.0 mm, respectively. The developed database may be used for design of water harvesting structures in Vertisols of Madhya Pradesh.

R. Singh (✉) · K. Singh · D. M. Bhandarkar
Irrigation and Drainage Engineering Division, ICAR-Central Institute of Agricultural Engineering (CIAE), Nabi Bagh, Berasia Road, Bhopal 462038, India
e-mail: rsingh067bpl@gmail.com

K. Singh
e-mail: singhkaran@yahoo.com

V. P. Singh et al. (eds.), *Hydrologic Modeling*, Water Science and Technology Library 81, https://doi.org/10.1007/978-981-10-5801-1_12

Introduction

Rainfall is a continuous random variable and is stochastic in nature. This necessitates the use of long-term rainfall data for works related to design of water harvesting structures. For best results, the length of record should be greater than the design life of the structure (Serrano 1997). Rainfall generated runoff is very important in various activities of water resources development and watershed management (Mishra et al. 2013). Rainfall intensity-duration-frequency (IDF) relationship is the most important parameter for design of various hydrologic and water harvesting structures. The typical estimation procedure for IDF curves consists of three steps as presented by Chow et al. (1988) and Singh (1992). Many researchers have developed various formulae for design rainfall/storm estimation based on the construction of IDF curve (Rakhecha and Clark 1999; Durbude 2008). Standard probability distributions commonly used for design rainfall/flood estimation are Normal, log-Normal (LN), Pearson, log-Pearson type-III (LP-III) and Extreme value type-1 (Wilson 1990; Haktan 1992; Al-Hassoun and Saleh 2011).

The soil conservation service curve number (SCS-CN) method (SCS 1956) converts rainfall to surface runoff (or rainfall-excess) using a CN derived from watershed characteristics and 5-days antecedent rainfall. This method is based on recharge capacity of a watershed. This method is selected for predicting runoff as: (i) it is a familiar procedure that has been used for many years around the world; (ii) it is computationally efficient; (iii) the required inputs are generally available and (iv) it relates runoff to soil type, land use and management practices. To derive CN values for an ungauged watershed, SCS (1956) provided tables based on the soil type, land cover and practice, hydrologic condition and antecedent moisture condition (AMC). Fairly accurate mathematical expressions (Ponce and Hawkins 1996) are also available for CN conversion from AMC-I (dry) to AMC-III (wet) or AMC-II (normal) levels. Rational method is used world wide for estimation of peak flow rate with reasonable accuracy for the watersheds having drainage area less than 1000 ha.

Rainwater harvesting technology is highly location-specific and practices evolved in a given region have a limited applicability in other regions. General guidelines are inadequate for the design and adoption of water harvesting structures in different regions of the country (Sharma et al. 2002). Water harvesting and recycling studies carried out at CIAE, Bhopal revealed that water harvesting pond of 3 m minimum depth can be constructed in 10–12% of watershed area. The minimum runoff received is about 300 mm (3000 m^3/ha) to fill up the pond every year. About 60–70% of stored water can be utilized for irrigating crop. Entire *kharif* and 50% of *rabi* crop can be irrigated twice with twofold increase in yield (Bhandarkar et al. 2005). The proper planning, design and execution of site-specific rainwater harvesting structures in country's on-going watershed development and management programmes at large scale got utmost importance. Therefore, there is a

need to develop databases of design parameters (i.e. design rainfall, runoff and peak flow rate for different durations and frequencies) considering local conditions, which will arrive at proper designs of water harvesting structures.

Materials and Methods

Study Area and Data Sources

The study area covers ten identified districts (Bhopal, Indore, Raisen, Hoshangabad, Khandwa, Jabalpur, Datia, Dhar, Guna and Chhindwara) of MP State of India. Daily rainfall data for 20 years period (1991–2010) of 10 identified districts were obtained from India Meteorological Department (IMD), Pune, India. The soil series, data on soil properties and land use and cropping patterns of the selected districts were obtained from Technical Bulletin NBSS Publication 78 of National Bureau of Soil Survey and Land Use Planning (NBSS & LUP), Nagpur and Department of Agriculture, Government of Madhya Pradesh, Bhopal.

Development of Software for Design of Water Harvesting Pond and Structures

The software for design of harvesting pond and associated structures was developed using Microsoft Visual Basic 6.0 Enterprise Edition with Service Pack 6, for 32-bit Windows operating system and Microsoft Access 2000 as back-end. Splash and main screens of the developed software are shown in Fig. 1. The software has four basic modules—hydrologic design, hydraulic design, structural design and estimation of materials and costs of water harvesting structures. Hydrologic design module consists of three sub-modules of rainfall frequency analysis for design rainfall, design runoff volume and design peak flow estimation. Hydraulic design module consists of five sub-modules for determination of storage capacity of pond, storage structure dimensions, spillway dimensions and design of earthen embankment including seepage analysis. The structural design module includes two sub-modules of structures subjected to water pressure and earth pressures for checking the stability of water harvesting structures. The materials and costs estimation module consists of four sub-modules related to different components. The software is armed with database addition and editing facility. The software uses inbuilt database for different variables of formulae/equations used in runoff and peak flow estimation for identified districts of MP, India.

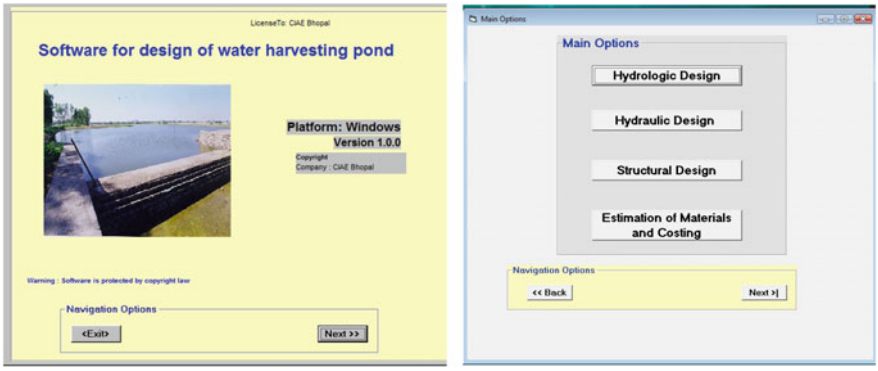

Fig. 1 Splash and main screens of the developed software

Creation of Design Rainfall Database

The daily rainfall data of identified districts were analysed. Test of adequacy and test of persistence were carried out for available data to check whether the data is of sufficient period and is of random in nature. When variable data of given period is of random in nature, then frequency analysis was carried out using probability density functions (pdfs) for estimating the design values of variables. Rainfall frequency analysis was carried out using rainfall frequency analysis module of the developed software for design of water harvesting ponds and associated structure. The following nine probability density functions (pdfs) were used for rainfall probability analysis.

- Normal (N) and Log-Normal (LN) distribution
- Extreme values type (EVT)-I and Log-extreme values type (LEVT-I) distribution.
- Exponential (EXP) and Log exponential (LEXP) distribution.
- Pearson type-III (PT-III) and Log-Pearson type-III (LPT-III) distribution.
- Weibull distribution.

Chi-square goodness-of-fit test is applied to judge the fitting of a particular probability distribution.

$$\chi^2 = \sum_{i=1}^{k} (O_i - E_i)^2 / E_i. \tag{1}$$

where

k Number of class intervals,
O_i Observed values and
E_i Expected number of observations in the ith class.

Degree of freedom (DF) = $k - p - 1$, where, p = No. of parameters of distribution.

The hypothesis that the data from the expected distribution is rejected if $\chi_c^2 > \chi_{1-\alpha,k-p-1}^2$ for α level of significance. The pdf is considered to be fitted well (accepted) if the calculated Chi-square value is less than the table value of Chi-square for DF = 2 at 95% confidence level (=5.99).

The best fitted pdf describing data set and giving minimum value of Chi-Square test parameter was identified for estimating the design values of the variable with different probability levels (return periods). Design rainfall values were estimated using following relationship:

$$X_T = X_{\text{mean}}(1 + C_{\text{v}} K_T) \tag{2}$$

where

X_T Magnitude of the variable (rainfall) having a return period T,
C_{v} Coefficient of variation and
K_T Frequency factor for a particular type of distribution function (Haan et al. 1994).

The magnitudes of 1-day-max, 2-day-max and annual rainfall at various return periods of 1, 2, 5, 10, 20 and 25 years were estimated using best fitted pdfs.

Database Creation for Design Runoff Volume and Peak Flow Rate

Design runoff values at different frequencies for various rainfall durations of identified districts of MP were estimated using design rainfall values for different durations and frequencies and Natural Resource Conservation Service Curve Number (NRCS-CN) method (earlier known as SCS-CN method) for the identified districts. For estimation of design runoff, curve numbers from recommended curve number table suggested by Ministry of Agriculture, Hydrology Division, Govt. of India (1972) were obtained for the wet soil condition, i.e. antecedent soil moisture condition (AMC-III) and good hydrologic condition and straight row crop cultivation practice (Table 1). In black soils region for estimation of design average annual runoff $I_a = 0.1S$ and for all other regions $I_a = 0.3S$ were considered.

For watersheds up to 1000 ha area, the most commonly used relation is Rational formula to estimate the peak flow rate and is given as

$$Q_{\text{p}} = \frac{\text{CIA}}{360} \tag{3}$$

Table 1 Soil and land use conditions considered in design runoff estimation

District	Soil type	Hydrologic condition	HSG	CN		LULC
				AMC-II	AMC-III	
Bhopal	Sandy clay loam	Good	C	85	94	Cultivated straight row
Indore	Clay	Good	D	89	96	Cultivated straight row
Raisen	Sand clay loam	Good	C	85	94	Cultivated straight row
Hoshangabad	Sand clay loam	Good	C	85	94	Cultivated straight row
Khandwa	Clay	Good	D	89	96	Cultivated straight row
Jabalpur	Clay	Good	D	89	96	Cultivated straight row
Datia	Sandy clay loam	Good	C	85	94	Cultivated straight row
Dhar	Sand clay loam	Good	C	85	94	Cultivated straight row
Guna	Sand clay loam	Good	C	85	94	Cultivated straight row
Chhindwara	Clay	Good	D	89	96	Cultivated straight row

where

Q_p The peak discharge in m^3/s,
I Rainfall intensity of a desired recurrence interval (return period) and for the duration of time of concentration (T_c) of the watershed in mm/h,
A Watershed area in ha,
C Coefficient varying between 0 and 1 (for agricultural cultivated land having land slope 0–5%, the C varies from 0.5 to 0.6).

The time of concentration, which is needed for selecting an appropriate value of I in the Rational formula, can be calculated by either of the following:

$$T_c = 0.0195L^{0.779}S^{-0.385} \tag{4}$$

where

T_c Time of concentration in hours,
L Maximum length of flow in m and
S The average slope of the watershed in fraction.

The rainfall intensity value as input to Rational method for a given storm duration equal to time of concentration (t_c) and return period (T-years) was estimated using following relationship:

Table 2 Intensity—duration-return period relationships, India

Zone	Station	K	a	b	N
Central zone	Bagra-Tawa	8.5704	0.2214	1.25	0.9931
	Bhopal	6.9296	0.1892	0.50	0.8767
	Indore	6.9280	0.1394	0.50	1.0651
	Jabalpur	11.379	0.1746	1.25	1.1206
	Jagdalpur	4.7065	0.1084	0.25	0.9902
	Nagpur	11.45	0.1560	1.25	1.0324
	Punasa	4.7011	0.2608	0.50	0.8653
	Raipur	4.683	0.1389	0.15	0.9284
	Thikri	6.088	0.1747	1.00	0.8587
	Central zone	7.4645	0.1712	0.75	0.9599

Source Singh et al. (1994)

$$I = \frac{KT^a}{(t_c + b)^n} \tag{5}$$

where

I Rainfall Intensity (cm/h),
T Return period (years),
t_c Storm duration equal to time of concentration (h).

The values for K, a, b and n for particular places in Central Zone were taken from Table 2.

The design peak flow database for the identified districts was created considering 25 year return period/life of water harvesting structures and catchment area up to 100 ha.

Results and Discussion

Rainfalls of Various Durations

The rainfall data of different durations for identified districts of MP are given in Table 3. During 20 years period, highest rainfall of various durations, i.e. 1-day maximum (380.0 mm), 2-day maximum (470.0 mm), monthly maximum (1031.0 mm) and average annual (1293.6 mm) were observed to be for Hoshangabad, Datia, Bhopal and Hoshangabad districts, respectively. In identified districts, Chhindwara district received lowest rainfall of 1-day maximum (200.0 mm), 2-day maximum (240.8 mm) and monthly maximum (572.8 mm), while Khandwa district received lowest average annual rainfall (827.0 mm).

Table 3 Rainfall values (mm) of different durations (based on 20 year data)

Station	1–day max	2-days max	Monthly max	Average annual rainfall
Bhopal	320.0 (Aug)	349.2 (Aug)	1031.4 (Jul)	1114.6
Indore	276.0 (Sep)	462.0 (Sep)	642.2 (Jul)	971.2
Raisen	295.2 (Jul)	415.3 (Jul)	921.0 (Jul)	1246.2
Hoshangabad	380.0 (Aug)	405.0 (Aug)	897.6 (Aug)	1293.6
Khandwa	278.0 (Sep)	338.4 (Aug)	639.0 (Sep)	827.0
Jabalpur	222.6 (Aug)	340.2 (Jul)	1022.4 (Jul)	1346.3
Datia	330.0 (Sep)	470.0 (Sep)	639.6 (Sep)	881.3
Dhar	287.2 (Jul)	349.4 (Jul)	641.1 (Jul)	847.0
Guna	317.7 (Sep)	333.7 (Sep)	610.9 (Aug)	949.2
Chhindwara	200.0 (Jul)	240.8 (Jul)	572.8 (Jul)	939.9

Table 4 Identified best fitted probability density functions (pdfs) for design rainfall estimation

S. No.	District	Rainfall duration		
		1-day-max	2-day-max	Annual
1	Bhopal	Log-EVT-I	Log-Normal	Log-EVT-I
2	Indore	Log-Normal	EVT-I	Log-Normal
3	Raisen	Log-Normal	Log-Normal	EVT-I
4	Hoshangabad	Log-Normal	Log-Normal	PT-III
5	Khandwa	PT-III	Log-Normal	Log-Normal
6	Jabalpur	Log-Normal	PT-III	Log-Normal
7	Datia	EVT-I	Log-Normal	EVT-I
8	Dhar	Log-Normal	EVT-I	Log-Normal
9	Guna	Log-Normal	PT-III	PT-III
10	Chhindwara	Log-EVT-I	Log-Normal	Normal

EVT-I Extreme value type-I distribution; *PT*-III Pearson type-III distribution

Estimation of Design Rainfall Values

Best Fitted Pdfs

The frequency analysis of rainfalls of different durations for identified 10 districts of MP was carried out using nine probability density functions (pdfs). The best fitted pdfs describing data sets of rainfall of various durations were identified based on minimum value of Chi-Square test parameter (Table 4). The data sets of rainfall of various durations were well described by Log-Normal distribution, followed by extreme value type-I (EVT-I: Gumble distribution) and Pearson type-III distribution. The design rainfall magnitudes of 1-day-maximum, 2-day-maximum and average annual rainfall for different return periods of 1, 2, 5, 10, 20 and 25 years

Table 5 Rainfall magnitudes of different duration for various return periods

District	Rainfall (mm)	Return period (year)				
		1	5	10	20	25
Bhopal	1-day-max	85.9	160.3	202.4	239.0	257.0
	2-day-max	130.8	217.4	266.6	315.5	331.4
	Annual	1010.2	1331.7	1484.5	1623.9	1666.9
Indore	1-day-max	104.5	159.8	189.6	218.3	227.5
	2-day-max	119.3	268.4	338.7	378.3	427.5
	Annual	886.7	1163.2	1297.5	1419.8	1457.7
Raisen	1-day-max	124.9	184.3	215.4	245.1	254.5
	2-day-max	167.6	256.6	304.5	350.8	365.5
	Annual	824.8	1528.8	1640.5	1704.8	1736.8
Hoshangabad	1-day-max	106.9	190.3	240.0	290.7	307.4
	2-day-max	146.0	244.0	299.9	350.7	373.8
	Annual	1071.3	1552.5	1723.3	1855.7	1921.0
Khandwa	1-day-max	80.2	161.4	202.7	237.7	255.0
	2-day-max	122.4	211.3	263.1	315.3	332.4
	Annual	741.9	1009.1	1141.9	1264.6	1302.8
Jabalpur	1-day-max	107.5	172.4	208.4	243.7	255.1
	2-day-max	121.3	229.7	271.6	304.7	321.1
	Annual	1230.0	1610.3	1794.3	1962.0	2013.9
Datia	1-day-max	78.9	182.2	230.9	258.4	292.5
	2-day-max	120.9	200.6	245.8	290.7	305.3
	Annual	737.5	1115.9	1294.4	1394.8	1519.7
Dhar	1-day-max	100.4	157.0	187.9	218.0	227.6
	2-day-max	120.8	223.6	270.1	299.3	333.3
	Annual	764.5	1026.2	1155.1	1273.6	1310.4
Guna	1-day-max	97.9	195.2	257.7	324.0	346.4
	2-day-max	182.2	312.0	387.3	463.0	487.8
	Annual	729.3	1195.7	1335.5	1438.2	1489.0
Chhindwara	1-day-max	90.8	129.1	148.8	167.2	173.0
	2-day-max	104.2	185.3	223.3	244.8	271.5
	Annual	809.8	1169.4	1313.9	1433.2	1468.0

were estimated and are given in Table 5. The graphical representation of design rainfall values of 1-day-maximum and average annual rainfall for different return periods are shown in Figs. 2 and 3, respectively.

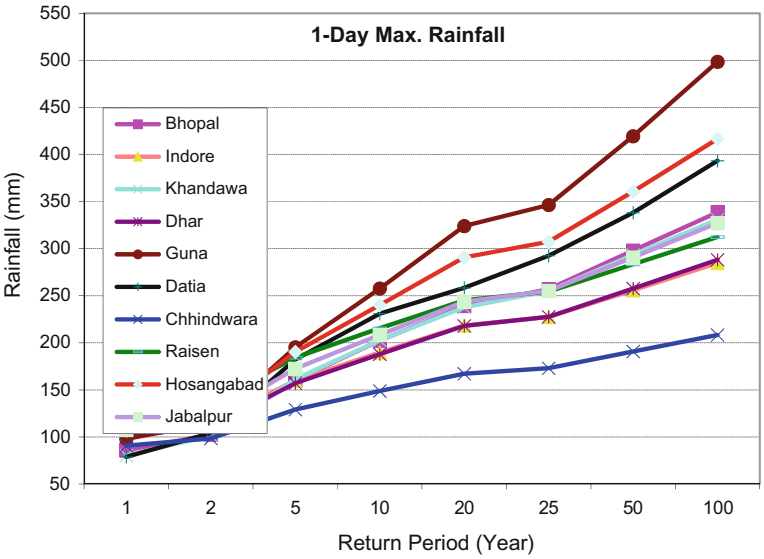

Fig. 2 1-day-maximum rainfall for different return periods

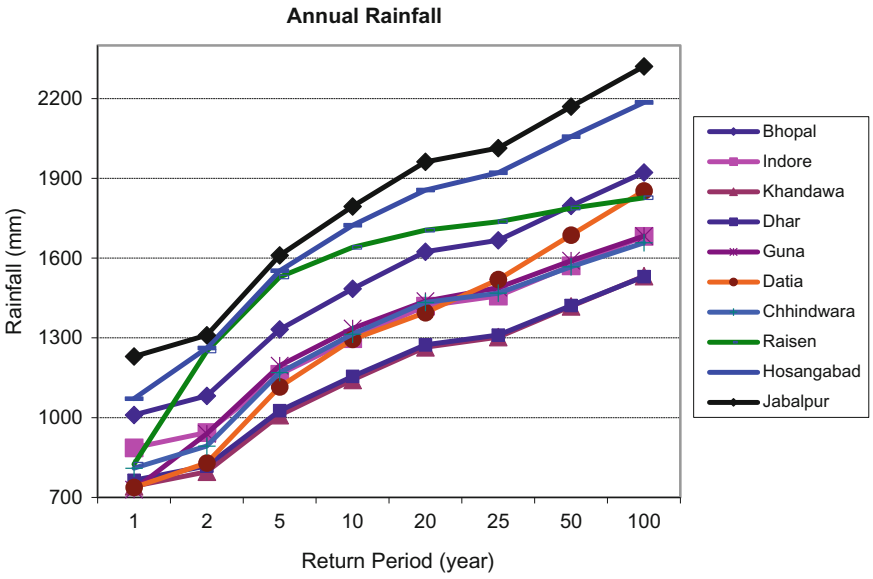

Fig. 3 Annual rainfall for different return periods

Estimation of Design Runoff Values

The design runoff values for 1-day-maximum rainfall for different return periods are given in Table 6. The annual runoff values for different return periods are given in Table 7. Using designed annual runoff volume values relationships between annual runoff and return periods have been developed for the identified area and are given in Table 8. The developed annual runoff curves for Bhopal and Chhindwara districts are shown in Fig. 4.

Estimation of Design Peak Flow Rates

Design peak flow rates for different catchments areas varying from 1 to 100 ha for 25 years return period of identified districts of MP were estimated using Rationale formula and are given Table 9. Design peak flow rate values for 25 year return period and 20 ha catchment area for Bhopal, Indore, Raisen, Hoshangabad, Khandwa, Jabalpur, Datia, Dhar, Guna and Chhindwara districts were estimated to be 3.70, 3.29, 3.09, 3.09, 3.71, 3.92, 3.09, 3.09, 3.09 and 3.71 m^3/s, respectively.

Table 6 Daily maximum runoff (mm) values for different periods

District	1	5	10	20	25
Bhopal	70.7	143.9	185.8	222.2	240.1
Indore	93.8	148.8	178.5	207.1	216.3
Raisen	108.9	167.7	198.7	228.1	237.6
Hoshangabad	91.2	173.7	223.1	273.7	290.3
Khandwa	69.8	150.4	191.5	226.5	243.7
Jabalpur	96.8	161.4	197.3	232.5	243.8
Datia	63.9	165.7	214.1	241.5	275.5
Dhar	84.9	140.7	171.4	201.3	210.9
Guna	82.4	178.6	240.8	306.9	329.3
Chhindwara	80.3	118.3	137.9	156.2	161.9

Table 7 Annual runoff values (mm) for different return periods

District	Return periods (year)				
	1	5	10	20	25
Bhopal	322.7	577.2	740.5	858.8	946.6
Indore	290.5	493.0	629.6	743.8	800.5
Raisen	395.4	718.7	896.1	1040.4	1111.1
Hoshangabad	458.0	703.9	855.1	975.1	1034.1
Khandwa	232.4	393.7	498.3	586.7	623.3
Jabalpur	470.1	756.0	932.4	1052.7	1147.3
Datia	260.0	434.5	569.2	710.0	767.4
Dhar	243.9	427.7	540.2	624.8	673.2
Guna	288.9	490.7	616.3	716.1	765.5
Chhindwara	231.8	441.8	565.6	646.1	712.0

Table 8 Relationship between annual runoff (Q in mm) and return period (T in years) for identified districts of MP

S. No.	District	Runoff–frequency relationship	Coefficient of determination (R^2)
1	Bhopal	$Q = 208.09 * \text{Log}_e(T) + 266.19$	0.991
2	Indore	$Q = 173.14 * \text{Log}_e(T) + 237.11$	0.990
3	Raisen	$Q = 232.76 * \text{Log}_e(T) + 349.86$	0.994
4	Hoshangabad	$Q = 189.35 * \text{Log}_e(T) + 411.91$	0.992
5	Khandwa	$Q = 130.46 * \text{Log}_e(T) + 198.87$	0.992
6	Jabalpur	$Q = 223.86 * \text{Log}_e(T) + 412.48$	0.991
7	Datia	$Q = 192.11 * \text{Log}_e(T) + 174.47$	0.969
8	Dhar	$Q = 140.56 * \text{Log}_e(T) + 209.96$	0.991
9	Guna	$Q = 157.31 * \text{Log}_e(T) + 248.62$	0.991
10	Chhindwara	$Q = 155.52 * \text{Log}_e(T) + 198.33$	0.992

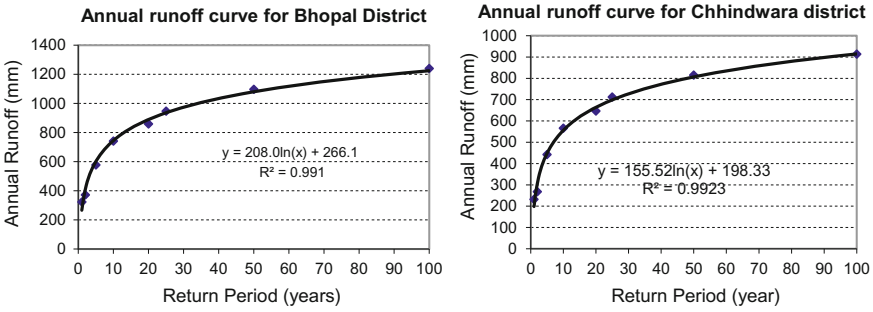

Fig. 4 Annual runoff curves for Bhopal and Chhindwara districts

Table 9 Peak flow rate (m^3/s) for 25 years return period

District/catchment area (ha)	Peak flow rate (m^3/s)							
	1	5	10	20	25	50	75	100
Bhopal	0.23	0.83	2.00	3.70	4.42	8.01	11.83	15.42
Indore	0.21	1.02	1.84	3.29	3.77	6.94	10.90	14.21
Raisen	0.18	0.90	1.67	3.09	3.63	6.84	9.97	12.94
Hoshangabad	0.18	0.90	1.67	3.09	3.63	6.84	9.97	12.94
Khandwa	0.22	1.08	2.01	3.71	4.36	8.21	11.97	15.52
Jabalpur	0.22	1.10	2.08	3.92	4.67	8.91	13.08	17.06
Datia	0.18	0.90	1.67	3.09	3.63	6.84	9.97	12.94
Dhar	0.18	0.90	1.67	3.09	3.63	6.84	9.97	12.94
Guna	0.18	0.90	1.67	3.09	3.63	6.84	9.97	12.94
Chhindwara	0.22	1.08	2.01	3.71	4.36	8.21	11.97	15.52

Summary and Conclusions

Software for the design of water harvesting pond and associated structures have been developed using Visual Basic as front-end and Microsoft Access as back-end. The software has three basic modules—hydrologic design, hydraulic design and structural design. Hydrologic design module consists of three sub-modules of rainfall frequency analysis for estimation of the design rainfall, designed runoff volume and design peak flow estimation. Daily rainfall data for 20 years period (1991–2010) of ten identified districts of Madhya Pradesh, i.e. Bhopal, Chhindwara, Datia, Dhar, Guna, Hoshangabad, Indore, Jabalpur, Khandwa and Raisen, were obtained from IMD Pune. The soil data related to soil types and their properties were obtained from NBSS & LUP Nagpur and Govt. of MP. These data were used for estimation of design rainfall, runoff volume and peak flow values of various durations and different frequencies (return periods) of 1, 2, 5, 10, 20 and 25 years using a developed software. The rainfall frequency analysis was carried out using nine probability density functions (pdfs). Natural Resource Conservation Service Curve Number (NRCS-CN) method and Rational formula were used for creating database of design runoff and peak flow rate values. Following databases for the identified districts of MP were developed.

- Design rainfalls of different durations (1-day-maximum, 2-day-maximum, monthly and annual rainfall) and frequencies (1, 2, 5, 10, 20 and 25 years).
- Design runoff volumes and peak flow rates of different durations (surface drainage coefficient, 1-day-maximum runoff and annual runoff) at different frequencies.

Acknowledgements The authors are grateful to Director, India Meteorological Department (IMD), Pune (Maharashtra), for providing daily rainfall data. The authors are also thankful to the Director, ICAR-Central Institute of Agricultural Engineering, Bhopal, for providing facilities and moral support for research work.

References

AlHassoun Saleh A (2011) Developing an Empirical Formulae to Estimate Rainfall Intensity in Riyadh Region. J King Saud Univ Eng Sci 23:81–88

Bhandarkar DM, Singh Ramadhar Reddy KS, Reddy Rao KVR (2005) Water harvesting and recycling technologies for black soils with high rainfall. In: Proceedings of the national seminar on existing water resources and technologies for enhancing agricultural production in North Central India, 2–3 April 2005, Indian Institute of Soil Science, Bhopal, pp 78–87

Chow VT, Maidment DR, Mays LW (1988) Applied hydrology. McGraw-Hill Book Company, Singapore

Durbude DG (2008) Estimation of probable maximum precipitation for planning of soil and water conservation structures. Indian J Soil Water Conserv 7(3):31–35

Haan CT, Barfield BJ, Hayes JC (1994) Design hydrology and sedimentology for small catchments. Academic Press, San Diego

Haktan YT (1992) Comparison of various flood frequency distributions using annual flood peaks data of rivers in Anatolia. J Hydrol 136:1–31

Mishra SK, Gajbhiye S, Pandey A (2013) Estimations of design runoff curve numbers for Narmada watershed (India). J Appl Water Eng Res 1(1):67–79

Ponce VM, Hawkins RH (1996) Runoff curve number: has it reached maturity? J Hydrol Eng 1 (1):11–19

Rakhecha PR, Clark C (1999) Revised estimates of one-day probable maximum precipitation (PMP) for India. Meteorol Appl 6:343–350

Serrano SE (1997) Hydrology for engineers: geologists and environmental professionals. KY: HydroScience, Lexington

SCS (1956) National engineering handbook, supplement A, (Section 4, Chapter 10), Soil Conservation Service, Washington, DC, USDA

Singh G, Venkatraman C, Sastri G, Joshi BP (1994) Manual of soil & water conservation practices. Oxford & IBH Publishing Co. Pvt. Ltd., New Delhi

Singh VP (1992) Elementary hydrology. Prentice-Hall, New Jersey

Sharma JS, Sharda VN, Sikka AK (2002) Water harvesting and recycling: Indian experiences. Published by the Director, CSWCRTI, Dehradun, (UttraKhand)

Wilson EM (1990) Engineering hydrology, 4th edn. ELBS Publishers, London

Application of Storm Water Management Model to an Urban Catchment

V. Swathi, K. Srinivasa Raju and Ajit Pratap Singh

Abstract In the present study, Storm Water Management Model (SWMM) has been explored for the catchment of BITS Pilani-Hyderabad campus, India. The catchment has been divided into various sub-catchments and are modeled for 2006 rainfall event. The study deals with a flexible set of hydraulic modeling capabilities. In particular it is used to assess infiltration using Horton method and flow routing analysis using Dynamic wave method. The storm water network with system of pipes, channels, storage works, and diversion structures were also considered. Efforts are made to identify the critical locations of overflow. The results show that there are no nodes flooded and no overflow sections in the entire catchment. It is concluded that campus storm network system has been well planned and has sufficient carrying capacity to cater the simulated rainfall event.

Introduction

Urban flooding is one of the disasters effecting mankind especially in urban areas. Metropolitan cities like Mumbai, Hyderabad, Chennai, and Kolkata in India are frequently witnessing urban floods. This may occur due to various reasons such as insufficient carrying capacity of storm drains, blockage of storm drains due to solid waste, improper planning of storm network, and changes in rainfall pattern. Thus, it

V. Swathi (✉) · K. Srinivasa Raju
Department of Civil Engineering, BITS Pilani-Hyderabad Campus,
Hyderabad 500078, India
e-mail: p201244029@hyderabad.bits-pilani.ac.in

K. Srinivasa Raju
e-mail: ksraju@hyderabad.bits-pilani.ac.in

A. P. Singh
Department of Civil Engineering, BITS Pilani-Pilani Campus, Pilani, India
e-mail: aps@pilani.bits-pilani.ac.in

V. P. Singh et al. (eds.), *Hydrologic Modeling*, Water Science
and Technology Library 81, https://doi.org/10.1007/978-981-10-5801-1_13

is very much necessary to perform the capacity analysis of the existing storm network to identify the locations of overflow so as to come up with preventory and mitigation measures. Keeping the necessity to model urban floods, several modeling softwares are developed (Borah 2011), namely, Storm Water Management Model (SWMM) (Liong et al. 1991), Hydrologic Engineering Centers-Hydrologic Modeling System (HEC-HMS) (Knebl et al. 2005), Hydrologic Engineering Centers-River Analysis System (HEC-RAS) (Tate and David 1999). The present study explored the applicability of SWMM to a case study of Birla Institute of Technology and Science (BITS), Pilani-Hyderabad Campus, India. The terrain of the campus consists of small hillocks and urban forests of Shamirpet which spreads about 200 acres of land (Swathi 2014). This paper covers literature review, description of SWMM, results followed by conclusions and acknowledgments.

Literature Review

This section deals with a brief discussion of SWMM along with review of literature. Rossman and Supply (2006) compared dynamic flow routing in both SWMM 5 and SWMM 4 for 20 sewer patterns. They found SWMM 5 produced stable results for a larger time steps than SWMM 4. Peterson and Wicks (2006) explored SWMM to a catchment in Missouri, USA. They performed various simulations with increase in dimension of conduits. Increase in dimension of conduits by 10% effected fluid flow responses. Bedient et al. (2007) modeled urban flood using two softwares HEC-HMS and SWMM. They created hydrographs in HEC-HMS which were treated as input to nodes for storm drain network in SWMM. The results obtained from study have clearly demonstrated usefulness and understanding of the storm network.

Barco et al. (2008) coupled Geographic Information System (GIS), SWMM, and optimization procedures to model a catchment in California. The time required for data management and calibration was drastically reduced. Aad et al. (2009) modeled two Best Management Practices (BMPs) rain garden and rain barrel within the sub-catchments. They simulated a rainfall event to assess the reduction in peak runoff. Rain garden was comparatively effective in reducing peak runoff and volume. Freni et al. (2010) used SWMM to simulate pressurization effect caused due to reduction in discharge at downstream. The results were compared with an experimental surge measured in a laboratory pipe. SWMM was able to model with reasonable accuracy. Gambi et al. (2011) modeled BMPs such as retention basin, green roof, and infiltration tanks in catchment of Italy to reduce peak runoff. The simulation was performed using 15 years rainfall data. Green roof was

comparatively more effective in reducing peak runoff. Ouyang et al. (2012) modeled rainfall-runoff and pollutant discharge from catchment of Beijing. The results show that impervious area is linearly proportional to runoff coefficient.

Gulbaz and Kazezyilmaz-Alhan (2013) calibrated SWMM model for Sazlidere Watershed. Calibration was done using extreme rainfall event to find sensitive parameters of SWMM. They inferred that Manning's roughness and infiltration parameters were sensitive parameters. Weilin et al. (2014) modeled storm water network of Dongguan city, China, using SWMM. They modeled for 1 and 2-year rainfall return periods. They also modeled for all critical locations of node overflow. Results show that increase in conduit diameter could cater for excess runoff. Scieranka (2013) performed hydraulic modeling of car park drainage in SWMM 5. They used dynamic wave routing approach. They concluded that introducing sewer retention could be an effective method to reduce runoff. Walsh et al. (2014) proposed SWMM modeling for rainfall-runoff simulation of rain water harvesting (RWH) for a catchment in California, USA. RWH could significantly reduce runoff, and it is inferred that runoff reductions and drain capacity are directly related to each other. Mikovitsa et al. (2014) used GIS custom tool box with SWMM to simulate city growth patterns. They analyzed differences in runoff pattern for both simulated and existing catchment of Innsbruck, Austria. Increase in impervious area resulted in twice increase in runoff volume.

Zhang and Guo (2015) used SWMM for Low Impact Development (LID). They modeled permeable pavement system for catchment of Atlanta. They concluded that SWMM needs to further improve its LID module to take into account, effect of storage capacity of under drains on infiltration. Park et al. (2015) applied SWMM and linear programming to model rainwater detention system for a rainfall of 30 years frequency. Cost-related objectives of the detention system were analyzed using linear programming. The modeling results show significant reduction in flood damage. Pathak and Chaudhari (2015) have applied SWMM to model rain garden as BMP for Mithi River sub-catchment, Mumbai, India. They calibrated and validated the model for 2009 rainfall event. Introducing rain garden resulted in significant reduction in peak runoff.

Some of the observations emanated from the literature are discussed below:

- Most of the above studies dealt with modeling BMPs and LIDs than performing the adequacy analysis of the existing system.
- Limited studies are reported for identifying critical location of overflows in the storm network and analyzing the same.
- The response of a single catchment to various rainfall events has not been discussed.

In the following section, SWMM has been described along with its modules.

Description of SWMM

SWMM is an open source model by United States Environmental Protection Agency (US-EPA). It is a dynamic rainfall-runoff model used to model hydraulic and hydrological components of a catchment. It models and simulates both single and continuous rainfall events. It is also used to model various BMPs and LIDs in the catchment. It analyzes the catchment response for various scenarios of rainfall events. The model also allows snowmelt calculations and hydraulic modeling.

There are four blocks in SWMM namely, runoff block, transport block, extran block, and storage treatment block. Runoff block deals with the evaluation of both surface and sub-surface runoff for a given rainfall event, whereas transport block incorporates effects of inflow hydrograph in a drainage system through kinematic routing. Extran is the extended transport block which performs dynamic routing. Storage/treatment block accounts for various storage, treatment functions, and pollutant loadings defined by the user (SWMM Reference Manual 2014). Thus, SWMM not only contributes in routing of flow quantities but also in functions such as routing of quality parameters, estimating dry-weather flow, estimating infiltration, assessing storage, treatment functions, and pollutant loadings.

In the present study, an application of SWMM has been explored by identifying critical locations across BITS. The methodology adopted and results obtained from the study have been discussed in the following section.

Methodology and Results

The watershed of BITS has been considered in this study. The entire watershed is divided into sub-catchments, and the storm network has been represented by conduits, junctions, and outfall. The rainfall-runoff block of SWMM has been applied to model on the basis of rainfall event for 2006. Infiltration and flow routing of the watershed have been evaluated using Horton method and Dynamic wave method, respectively. The map of the campus was obtained from the Google Earth as shown in Fig. 1. The maps are geo-referenced in Arc-GIS Version 9.1 to perform complete analysis.

Using the load image option, the back drop image of storm network is loaded. The complete storm network is drawn as line diagram in SWMM. All the data pertaining to conduits and junctions are treated as input variables. The input parameters for junction are invert elevation and maximum depth. The data required for conduits are shape, dimension, maximum depth, length, roughness, inlet offset,

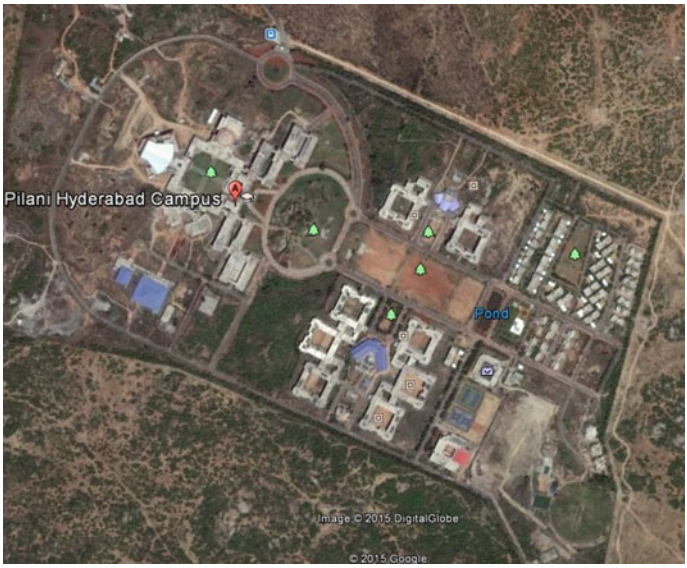

Fig. 1 BITS Google Earth image (*Source* https://earth.google.com/). Accessed on 3.5.2014

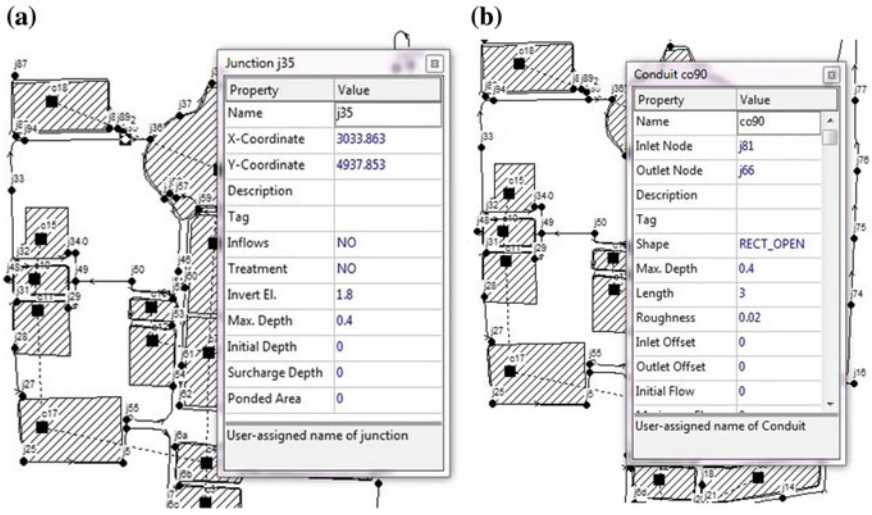

Fig. 2 **a**, **b** Data entry option in SWMM at various junctions and conduits

outlet offset, and maximum flow as shown in Fig. 2a, b. The required data are obtained from the storm network plan of the campus. The catchment is divided into 18 sub-catchments based on their discharge point, storm network, and drainage pattern as shown in Fig. 3. The model is run successfully after all the inputs are given.

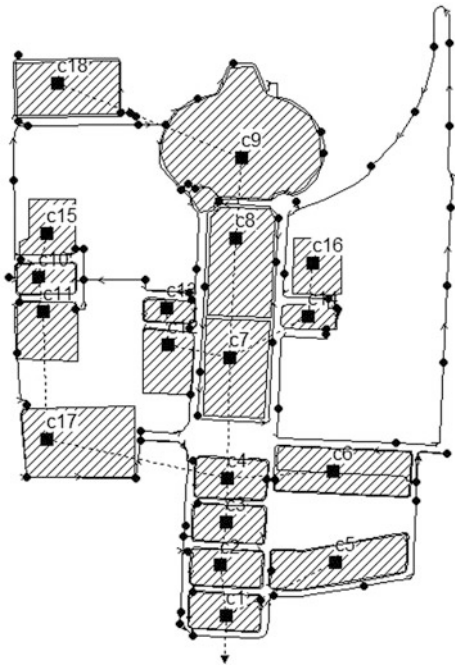

Fig. 3 Catchments visualization in SWMM (*C* denotes catchment)

The maximum peak runoff from sub-catchments 1–18 are 32.40, 33.42, 33.42, 33.42, 33.45, 33.45, 33.48, 1.47, 32.72, 32.13, 33.37, 33.00, 29.86, 29.36, 3.45, 29.86, 3.45 and 33.43 m^3/s respectively as shown in Fig. 4a, b. The highest peak runoff is obtained from sub-catchment 7 with 33.48 m^3/s and least peak runoff was obtained from sub-catchment 8 with 1.47 m^3/s. The peak runoff obtained and respective peak time for all catchments are summarized in Fig. 5a, b. For the rainfall events simulated, node floodings were nil in the obtained model results for the rainfall event simulated. This implies no flooding scenario.

Figure 5a shows the peak runoff from all the catchments. It can be inferred that catchment 7 has highest peak runoff of 33.48 m^3/s, and catchment 8 has a least runoff of 1.47 m^3/s.

Figure 5b shows the time taken by catchments to obtain peak runoff, and it is inferred that all the catchments have attained peak runoff at 2.5 h.

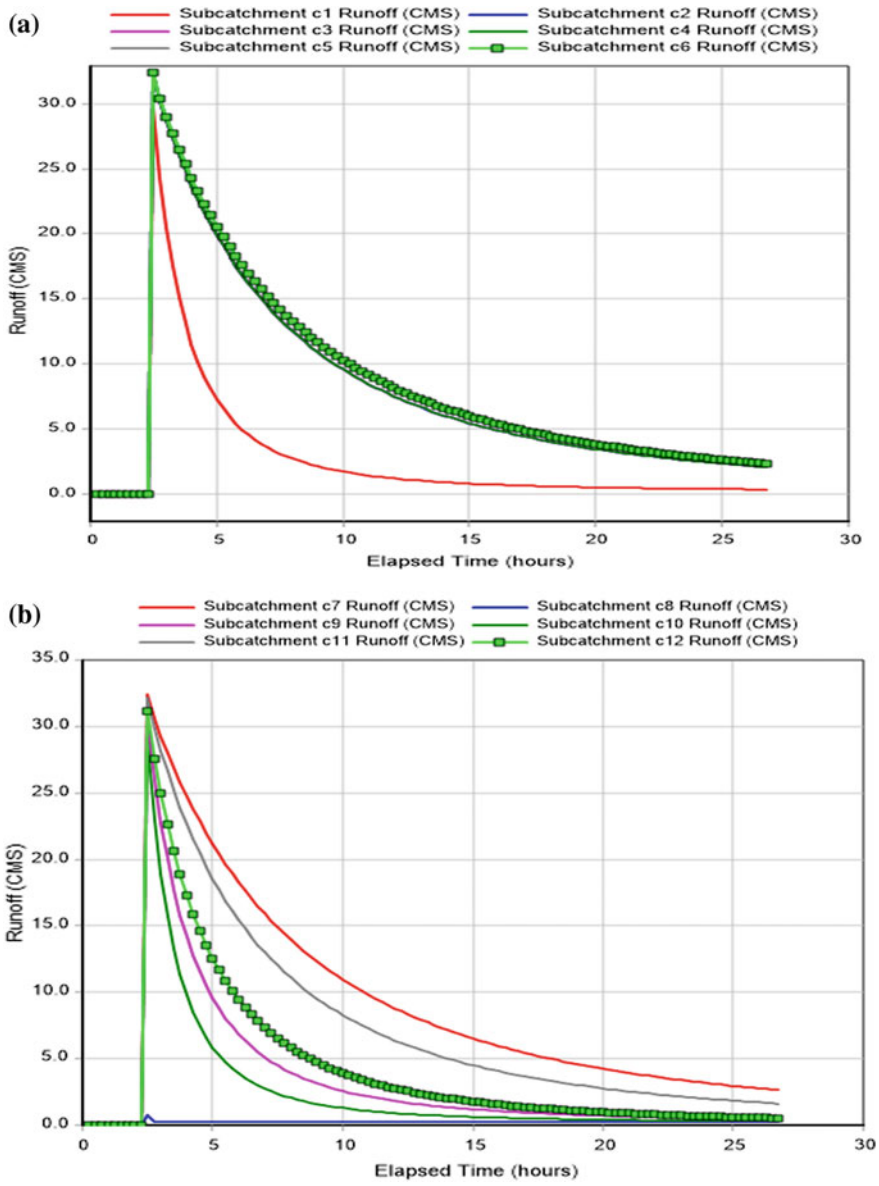

Fig. 4 **a** Runoff pattern from sub-catchment 1 to sub-catchment. **b** Runoff pattern from sub-catchment 7 to sub-catchment 12. **c** Runoff pattern from sub-catchment 13 to sub-catchment 18

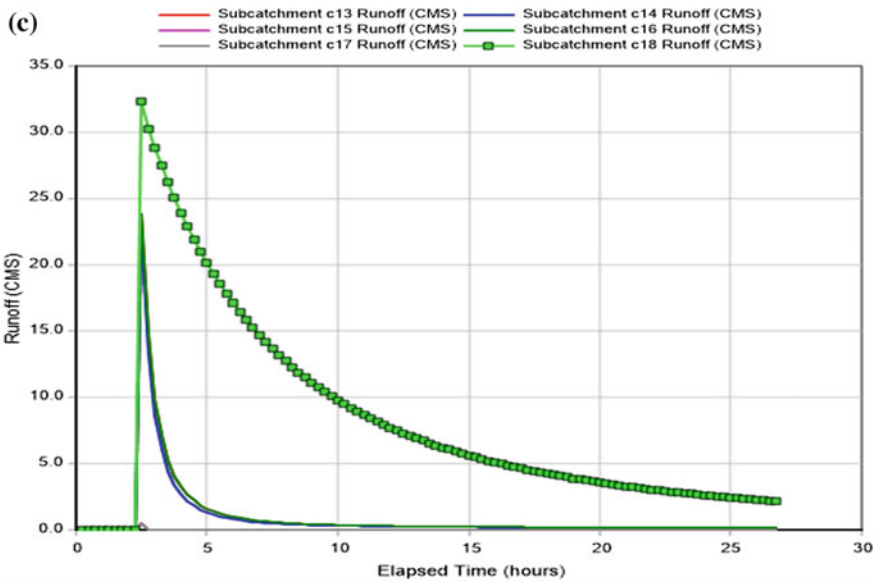

Fig. 4 (continued)

Conclusions

The SWMM model is applied for the catchment of BITS. Dynamic wave routing and Horton approaches were applied to analyze flow routing and infiltration processes. The case study of BITS presented showed that SWMM is well suited for urban catchments especially when it is modeled as a single watershed even under uncalibrated condition. The results show that there are no nodes flooded in the entire catchment and there are no overflow sections. Thus, the campus storm network system has been well planned and has sufficient carrying capacity to cater the simulated rainfall event.

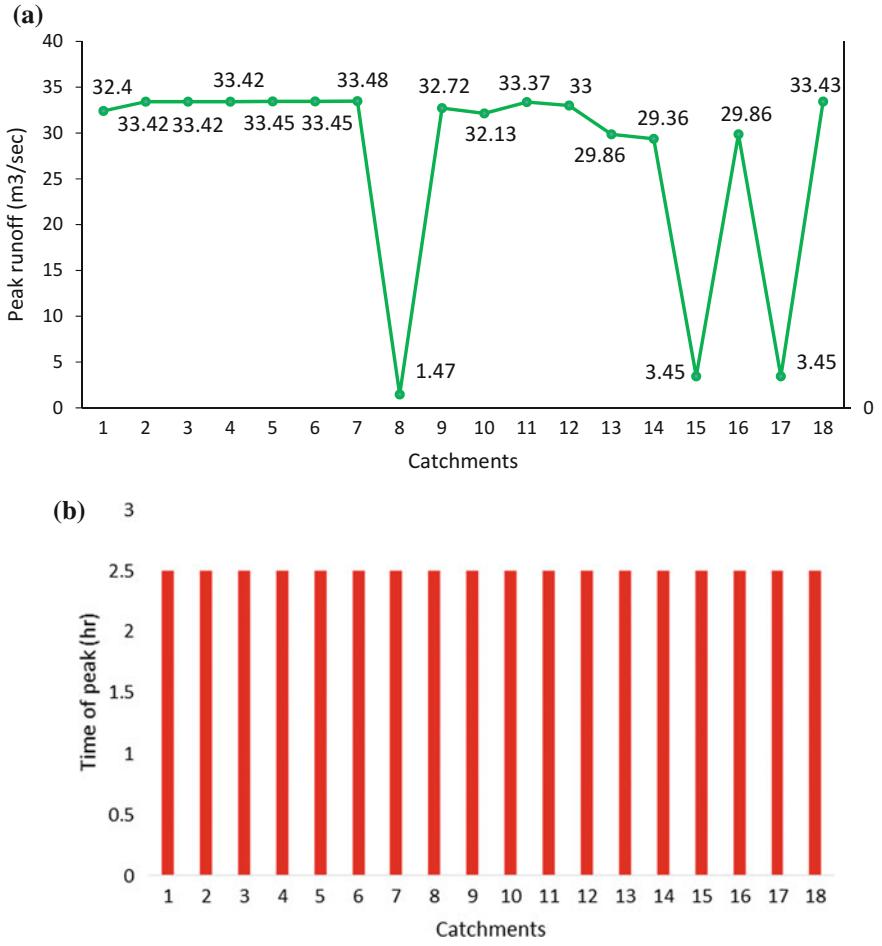

Fig. 5 **a** Graph showing peak runoff from catchments. **b** Graph showing time taken to attain peak runoff from catchments

Acknowledgements This work is supported by Information Technology Research Academy (ITRA), Government of India under, ITRA-Water grant ITRA/15(68)/Water/IUFM/01 dated Sep 20, 2013, Integrated Urban Flood Management in India: Technology Driven Solutions. Special acknowledgements to Sri K.V. Rao, Facilities Manager BITS, for providing the necessary data in the form of drainage plan of the campus. First author thanks Google Earth for enabling to download Google images. The authors thank EPA for providing SWMM as open source software and also India Meteorological Department for providing rainfall data.

References

Aad MPA, Suidan MT, Shuster WD (2009) Modeling techniques of best management practices: rain barrels and rain gardens using EPA SWMM-5. J Hydrol Eng 15(6):434–443

Barco J, Wong KM, Stenstrom MK (2008) Automatic calibration of the US EPA SWMM model for a large urban catchment. J Hydrol Eng 134(4):466–474

Bedient PB, Holder AW, Thompson JF, Fang Z (2007) Modeling of storm-water response under large tail water conditions: case study for the texas medical center. J Hydrol Eng 12(3): 256–266

Borah DK (2011) Hydrologic procedures of storm event watershed models: a comprehensive review and comparison. Hyd Pros 25(22):3472–3489

Freni G, Ferreri GB, Tomaselli P (2010) Ability of software SWMM to simulate transient sewer smooth pressurization. Novatech, France

Gambi G, Maglionico M, Tondelli S (2011) Water management in local development plans: the case of the old fruit and vegetable market in Bologna. Pro Engg 21:1110–1117

Gulbaz S, Kazezyilmaz-Alhan CM (2013) Calibrated hydrodynamic model for sazlidere watershed in Istanbul and investigation of urbanization effects. J Hydrol Eng 18(1):75–84

Google Earth. https://earth.google.com/. Accessed on 3.5.2014

Knebl MR, Yang ZL, Hutchison K, Maidment DR (2005) Regional scale flood modeling using NEXRAD rainfall, GIS, and HEC-HMS/RAS: a case study for the San Antonio River Basin Summer 2002 storm event. J Env Mang 75(4):325–336

Liong SY, Chan WT, Lum LH (1991) Knowledge-based system for SWMM runoff component calibration. J Water Resour Plann Manage 117(5):507–524

Mikovitsa C, Raucha W, Kleidorfer M (2014) Dynamics in urban development, population growth and their influences on urban water infrastructure. Pro Eng 70:1147–1156

Ouyang W, Guo B, Hao F, Huang H, Li J, Gong Y (2012) Modeling urban storm rainfall runoff from diverse underlying surfaces and application for control design in Beijing. J Water Resour Plann Manage 113:467–473

Park SH, Lee HD, Kim MC, Park SH, Koo J (2015) A study on optimal design methodology of multi-objective rainwater detention system using SWMM and linear programming. Adv Sci Technol Lett 99:101–104

Pathak H, Chaudhari P (2015) Simulation of best management practices using SWMM. Int Res J Eng Technol 2(1), 129–132

Peterson EW, Wicks CM (2006) Assessing the importance of conduit geometry and physical parameters in karst systems using the storm water management model (SWMM). J Hydrol 329 (1):294–305

Rossman LA, Supply W (2006) Storm water management model, quality assurance report: dynamic wave flow routing. US Environmental Protection Agency, Office of Research and Development, National Research Management Research Laboratory

Scieranka G (2013) Modeling storage channel using SWMM 5. Archit Civ Eng Environ 6(1):87–94

Swathi V (2014) Application of SWMM in urban flood management. M.E thesis, BITS Pilani Hyderabad Campus, Hyderabad, India

SWMM Reference Manual. http://www.epa.gov/water-research/storm-water-management-model-swmm. Accessed on 2.4.2014

Tate EC, David RM(1999) Floodplain mapping using HEC-RAS and ArcView GIS. Master's thesis, University of Texas at Austin

Walsh T, Pomeroy AC, Burian S (2014) Hydrologic modeling analysis of a passive, residential rainwater harvesting program in an urbanized, semi-arid watershed. J Hydrol 508:240–253

Weilin L, Xiaowen Z, Changhong W, Zhaoli W (2014) Simulation and application on storm flood in Dongguan city based on SWMM. In: International Conference on Mechatronics, Electronic, Industrial and Control Engineering. Atlantis Press

Zhang S, Guo Y (2015) SWMM simulation of the storm water volume control performance of permeable pavement systems. J Hydrol Eng 20(8):06014010

Part IV
Soil Erosion and Sediment

A Study of Erosional Depositional Activity and Land Use Mapping of Majuli River Island Using Landsat Data

Dipsikha Devi, Nilutpal Phukan and Bibhash Sarma

Abstract Majuli is the largest inhabited river island in India. It is surrounded by Subansiri on the north, Brahmaputra on the south and a spill channel called Kherkatia Xuti on north east. Majuli has been declared as the 35th district of Assam in May 2017. In other words Majuli is the first river island district in India. Since, time immemorial erosion is a continuous process. Majuli has been facing immense threat due to environmental and social consequences of bank line migration. Erosion have been shrinking its landmass significantly. Along with erosion, other problems that Majuli is facing are flood, breaching of embankments, sand casting, etc. Satellite data are considered as major inputs to this study. This paper enunciates the changes in land area in different years using remote sensing and GIS technology. This has revealed the dramatic change in reduction of land area. The land use land cover area is also shown.

Keywords Majuli · Subansiri · Erosion · Flood · Remote sensing
GIS technology

Introduction

Majuli is the largest inhabited river island in India surrounded by Subansiri on the north, Brahmaputra on the south and a spill channel called Kherkatia Xuti on north east. The island is about 200 km east of state's largest city, Guwahati. Majuli has

D. Devi (✉) · N. Phukan
Department of Civil Engineering, Assam Engineering College,
Guwahati 781013, Assam, India
e-mail: devidipsikha@yahoo.in

N. Phukan
e-mail: neilphukan@gmail.com

B. Sarma
Department of Civil Engineering, Assam Engineering College, Guwahati, India
e-mail: bsghy@yahoo.co.in

V. P. Singh et al. (eds.), *Hydrologic Modeling*, Water Science
and Technology Library 81, https://doi.org/10.1007/978-981-10-5801-1_14

been the cultural capital of Assamese civilization since sixteenth century. Sankardeva, a pioneer of medieval age Neo-Vaishnavite Movement preached a monotheist form of Hinduism called Vaishnavism and established monasteries and hermitages known as Satras.

River migration is an acute problem in Assam. The fluvial system of alluvial plains of Assam tends to dissipate large amount of energy and as a result of this the rivers frequently found to be shifting their banklines, thereby causing erosion. Erosion is a serious threat for existence of Majuli. Many structural measures are undertaken by Brahmaputra Board and Water Resource Department of Assam to reduce the erosional activity at Majuli. Spurs are used to deflect the flow away from the island. These spurs require regular maintenance due to very high hydrodynamic forces of river. Embankment is used as a flood mitigation measure. The siltation measures in the form of R.C.C. porcupines have shown mixed results. Erosion in this region was not much before 1950 earthquake in Assam but became active thereafter. Intense braiding characteristic of Brahmaputra coupled with silt and sand strata of banks is the main cause of erosion. The composition and characteristic of bed materials and presence of vegetative cover determine the erosion rate.

Origin

Majuli was a part of large area at the beginning of the seventh century. It was a long piece of land called Majuli (land between two parallel rivers). Sarma and Phukan (2004) gave a comprehensive account on the origin and geomorphological changes including erosion and deposition in Majuli Island. The island was formed due to continuous deposition of sands and changing course of rivers, namely Brahmaputra to the north and one of the tributaries Dihang flowing south of Majuli. There was a catastrophic flood in 1750 that continued for 15 days, mentioned in the historical texts. As a result of this severe flood, the Brahmaputra splits into two anabranches —one flowing through the original channel and other flowing through Dihang channel resulting in formation of the island. The northern channel which was previously the Brahmaputra became Luit Xuti. In course of time it became to be known as Kherkatia Xuti and Dihang expanded to become Brahmaputra River.

Problem

The problems of flood in the island can be summarized as below:

1. Inundation of large areas due to spilling of banks of the Brahmaputra and simultaneously overflowing of the banks of its tributaries.
2. Drainage congestion at the outfall of the tributaries during high stages of the River Brahmaputra causing flooding of low lying areas.

3. Excessive silt load in the river due to soil erosion and large scale landslides in the upper catchment areas resulting in instability of the river and erosion of its banks.
4. Due to high fluctuations of discharge and silt load coupled with braiding nature of the river, the sandbars are changing their locations frequently, making the island vulnerable to soil erosion.

Various south bank villages of Majuli Island like Tekeliphuta, Salmora, Bessamora, Burhakalita are under serious threat. Bank erosion is also caused by River Subansiri to its north. Subansiri also carries enormous silts in flood seasons, and thereby has lost her stability in plains. The north bank villages are under serious threat. It is expected that, after the commissioning of Subansiri hydropower project, the release from the reservoir would be regulated and it would contain less silt. So, the problem due to River Subansiri would be less.

Study Area

The geographical extent of study area is 26° 45′N–27° 12′N latitude and 93° 39′E–94° 35′E longitude. Majuli is bounded by Subansiri on the northwest, the Kherkatia Xuti in the northeast and the main Brahmaputra River on the south (Fig. 1).

A wetland, Majuli is a hotspot for flora and fauna, harboring many rare and endangered avifauna species including migratory birds that arrive in the winter season. The island is almost pollution free owing to lack of polluting industries and factories and also chronic rainfall. The island is under serious threat due to extensive soil erosion on its banks.

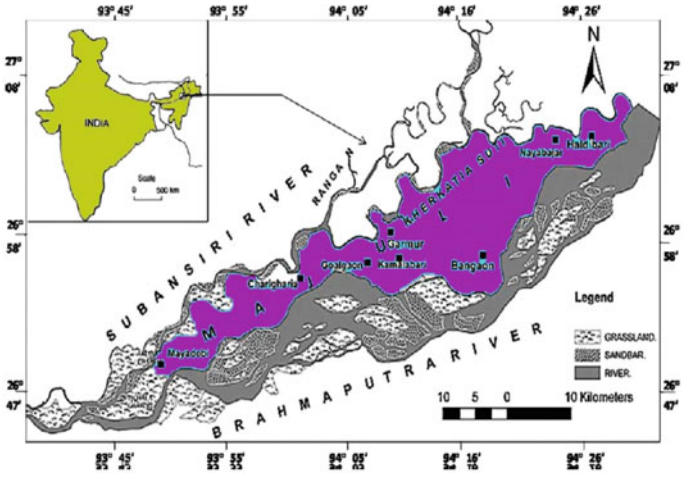

Fig. 1 Study area of Majuli. *Source* Dutta et al. (2010)

Data Used

For the study purpose, satellite imageries Landsat MSS/TM/ETM$^+$ are taken for different years.

Sattelite/sensor	Path/row	Acquisition	Spatial resolution (m)	Courtesy
Landsat MSS	135/041	07/11/1976	30	USGS
Landsat TM	135/041	31/10/1990	30	USGS
Landsat TM	135/041	02/11/2005	30	USGS
Landsat ETM$^+$	135/041	26/12/2010	30	USGS
Landsat ETM$^+$	135/041	07/11/2015	30	USGS

Methodology

Rivers are both agents and products of erosion and deposition adjusting their channel dimensions to accommodate the sediment load demand from bed banks and upland erosion (Martin 2005). Continual adjustments are made in an attempt to develop a stable dimension which the stream neither aggrades nor degrades (Rosgen 1996). Much time and effort has been devoted by many hydrologists to understand the geomorphology and the fluvial system (Wolman and Miller 1960; Leopold et al 1964; Rosgen 1996). With the advancement and upgradation in science and technology, the researches on fluvial system has been able to generate more accurate and precise results. The sciences of remote sensing, and geographic information system (GIS) have made it possible to study the remote areas and generate more accurate results. This technology has increased availability of data sources like aerial photogrammetry, satellite imageries, etc. Many researchers in recent years have used RS and GIS techniques for studying channel changes of different rivers (Goswami and Gogoi 2013).

For the study, the GIS softwares namely QGIS, ArcGIS, ErDas are used for image processing and analysis. The Landsat images are first georeferenced using WGS84 46 N datum, and polygon shape files are prepared using GIS software QGIS. The south bank of Majuli Island is divided into 33 divisions. The south bank is digitized, and the distances are measured in ArcGIS software. Erosion and deposition are then evaluated. Supervised land use classification is done in ErDas software. The south bank of Majuli is digitized. The length from each bank is measured for two years and the same is deducted to get the resultant erosion and deposition which depict the erosion and deposition. The erosion–deposition processes are analyzed in GIS softwares. Erosion is taken as positive and deposition is taken as negative.

Result and Discussions

The banklines of Majuli River Island from the year 1976 till 2015 are shown in figures above. From figures, it is cleared that a drastic change in the area of Majuli has been noticed in the years mentioned. The south bank and north bank of Majuli Island have been eroded by the combined action of mighty River Brahmaputra and River Subansiri shown in Figs. 2, 3, 4, 5 and 6.

Erosion–Deposition of Different Years

Figure 7 shows the bankline migration of Majuli Island from 1976 to 2015. The south bank of the island is vulnerable to River Brahmaputra. To know the amount of shifting of Majuli, the south bank of the Majuli is divided into 33 sections. The erosion and deposition for each section are evaluated. A quantitative comparitive analysis is carried on for two years for the evaluation of erosion and deposition process shown in Figs. 8, 9, 10, 11 and 12. From the analysis of data, it is found that a maximum erosion of 1.3 km occurred at Burha Kalita at section point 13 and an erosion of 1.3 km occurred at Katani Gaon Na Satra at section point 14 in between years 2010 and 2015. For the temporal datasets of 2005–2010, at section point 23 a maximum erosion of 1.39 km occurred near Mudoi Tanti which is a south bank area. Again an erosion of 2.19 km is found to be occurring near Mudoi Tanti at section point 23 in between time interval 2005 and 2000. In between 1990 and 2000,

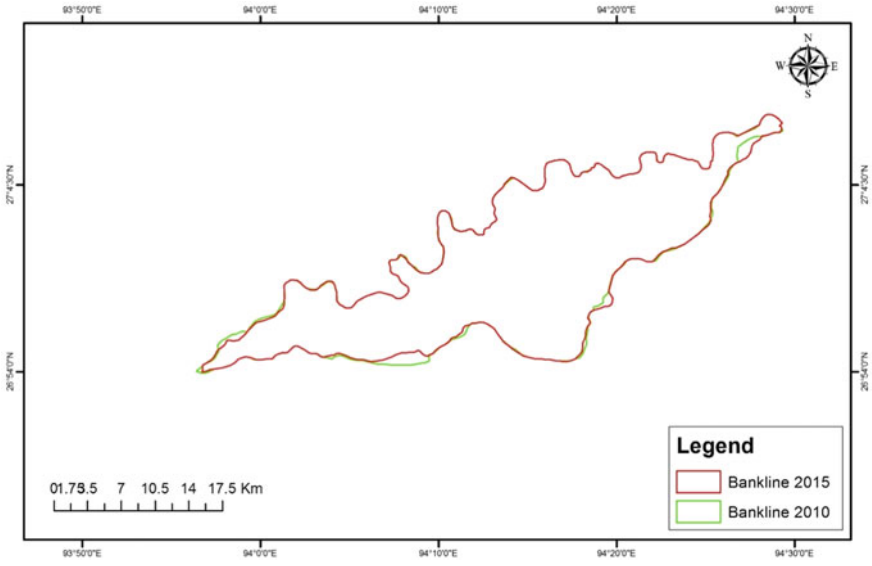

Fig. 2 Bankline of year 2015 and 2010

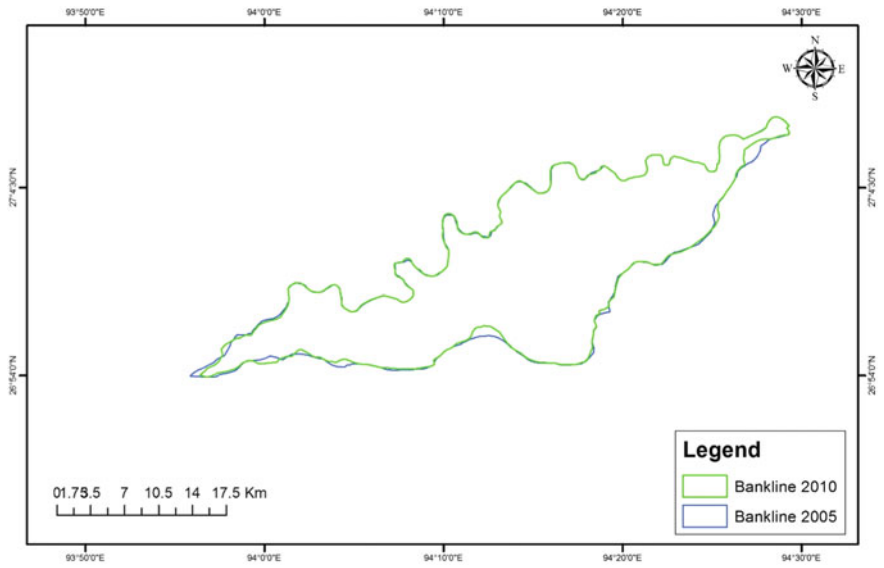

Fig. 3 Bankline of years 2010 and 2005

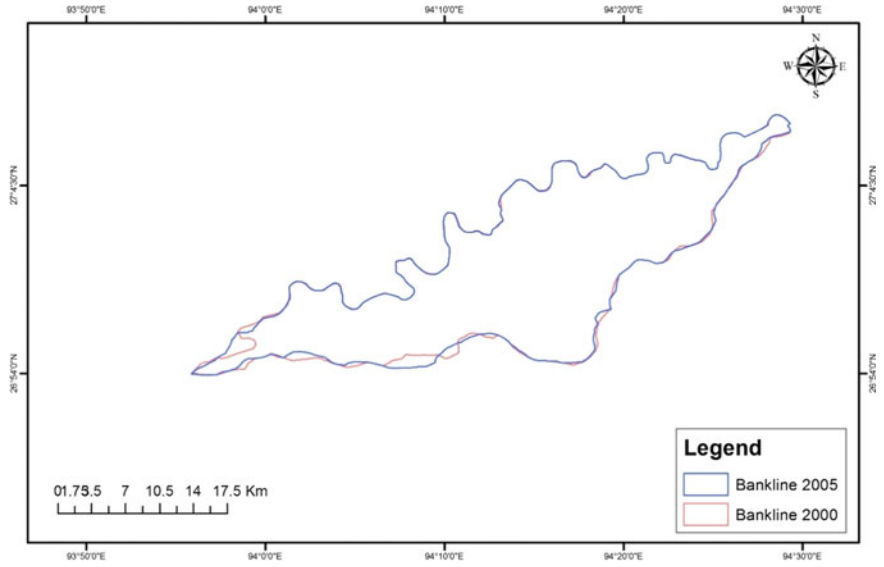

Fig. 4 Banklines of the years 2005 and 2000

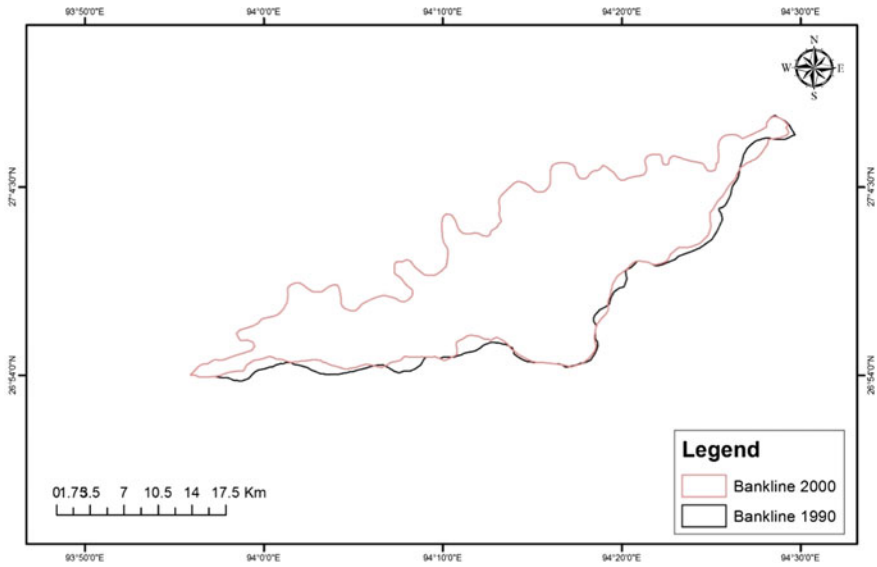

Fig. 5 Banklines of the years 2000 and 1990

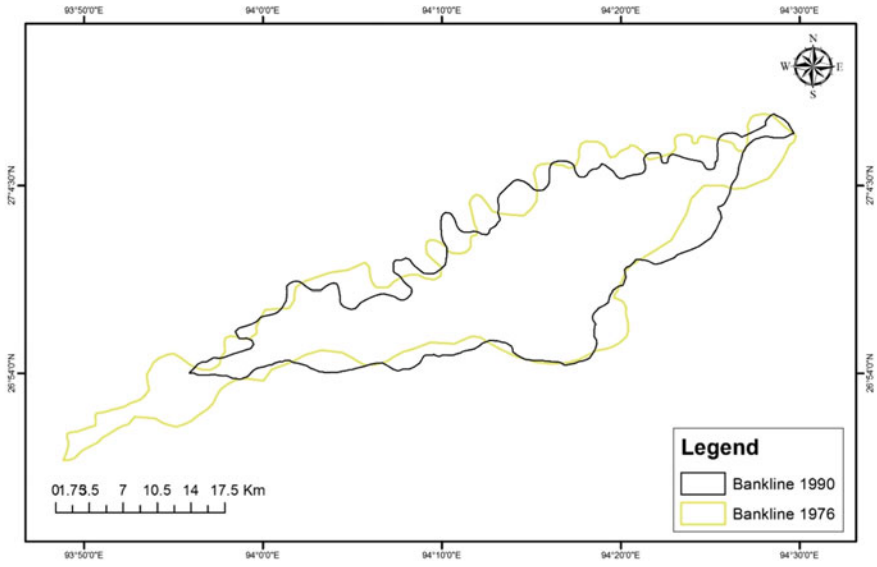

Fig. 6 Banklines of the year 1990 and 1976

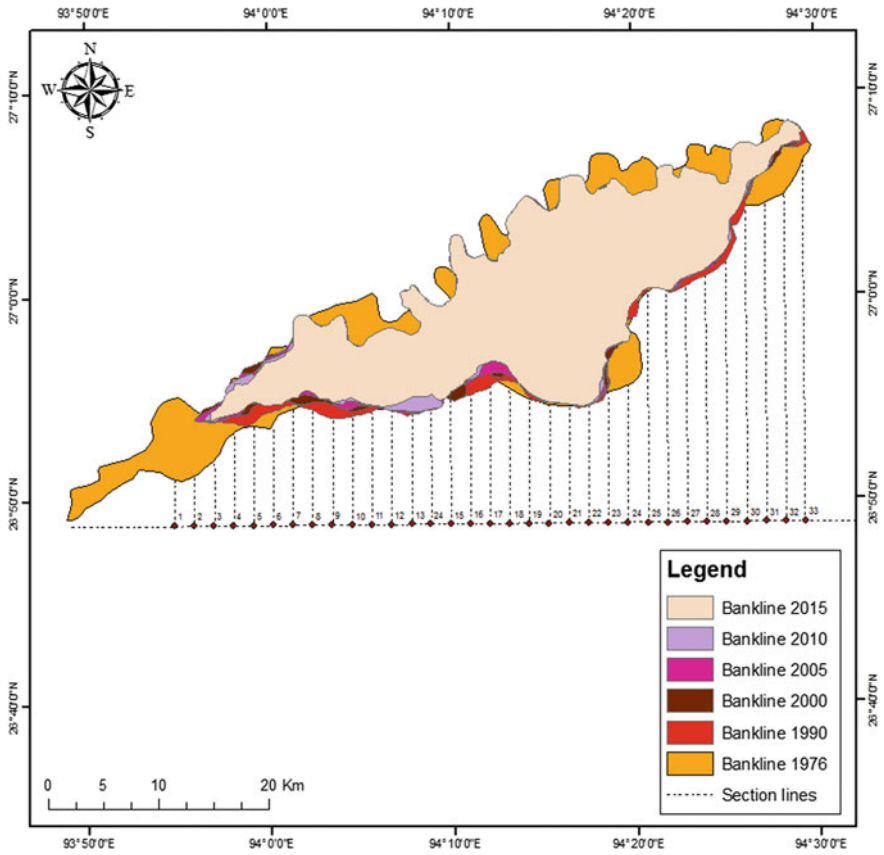

Fig. 7 Bankline shifting of Majuli Island

an erosion of 1.54 km is found to be occurred at Alimur Patir at section point 33. A maximum erosion occurred at Keturi Beel at section point 24. Maximum deposition is found to be occurred at Keturi Beel at section point 24 from 2005 to 2015. In between the years 1990 and 2000, maximum deposition is noticed at Kachari Gaon at section point 33. From 1976 to 1990, maximum deposition is found to be occurred at Mowamaria Chapori at section point 29. From Fig. 13, it is seen that 1976–2015, a maximum erosion of 61.64 km occurred and a deposition of 37.406 km occurred.

Land Use Classification

The land is used for numerous purposes like cultivation, livestock production, housing, industrial, roads, water harvesting, etc. The land use affects rates of runoff, infiltration, and types of quality of vegetation. Suitable land uses minimize the soil

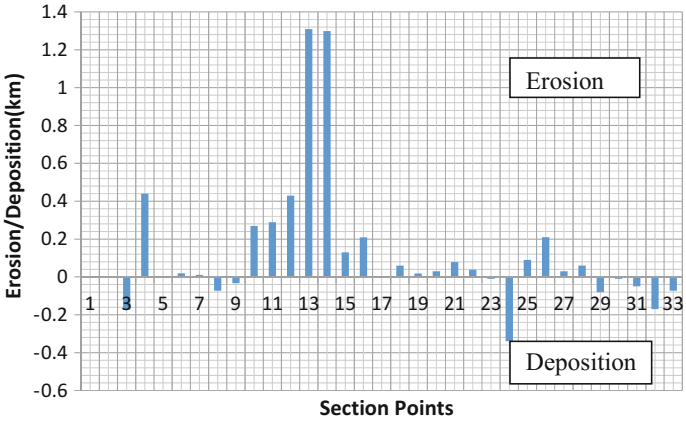

Fig. 8 Bankline shift from 2015 to 2010

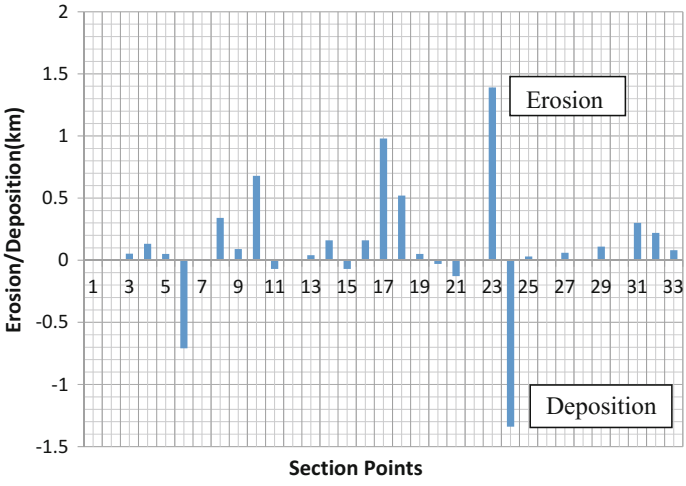

Fig. 9 Bankline shift from 2005 to 2010

erosion and reduce the runoff. Therefore, land use determination is of utmost importance (Fig. 14).

The land use map of Majuli Island is prepared with the software ErDas. For this, supervised land classification is done. A total of eight land covers have been identified in the island. From Fig. 15, it can be concluded that maximum land cover is of agricultural area which constitutes 49% of the total area, i.e., nearly half of the

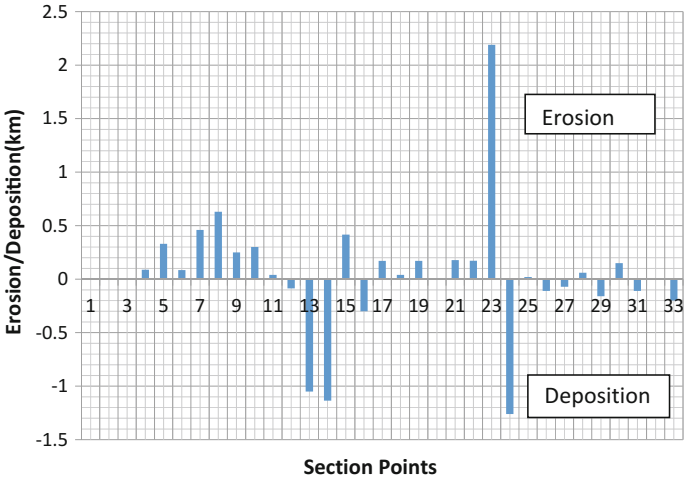

Fig. 10 Bankline shift from 2000 to 2005

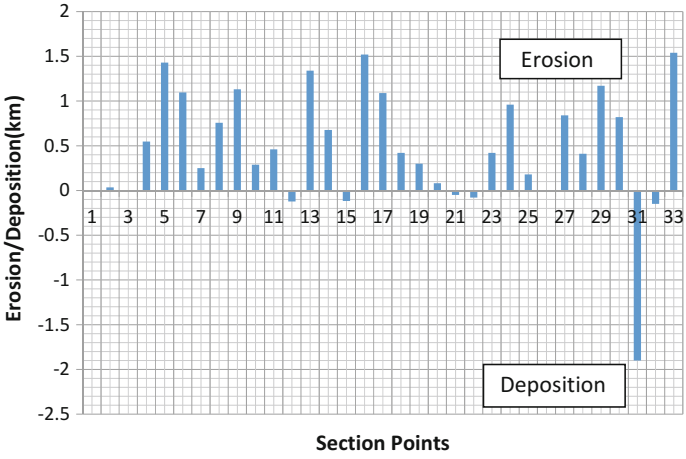

Fig. 11 Bankline shift from 1990 to 2000

total land cover which is followed by rural settlement which is 23% of the total area. The next level of land cover is swampy/marshy areas which contribute 10% of total area. Dense forest and waterbodies cover an area of about 8% of total area. River and sandbar cover around 3% of areas each.

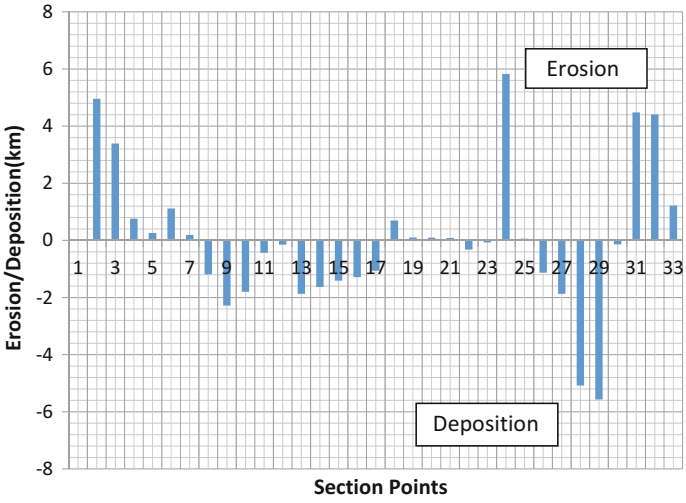

Fig. 12 Bankline shift from 1976 to 1990

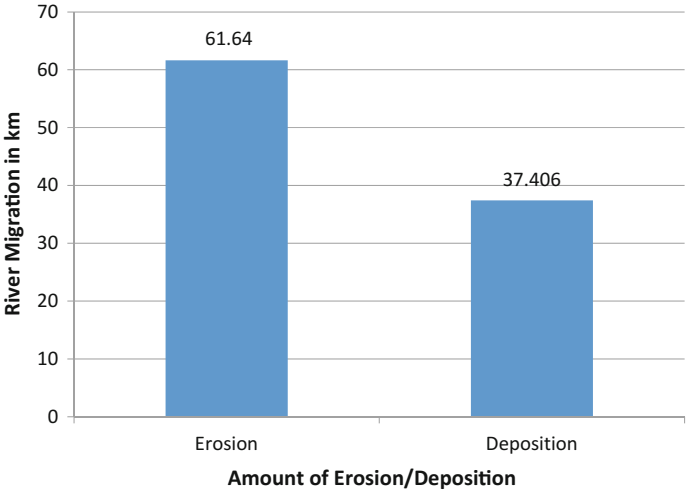

Fig. 13 Total erosion/deposition along the south bank of the Majuli River Island from 1976 to 2015

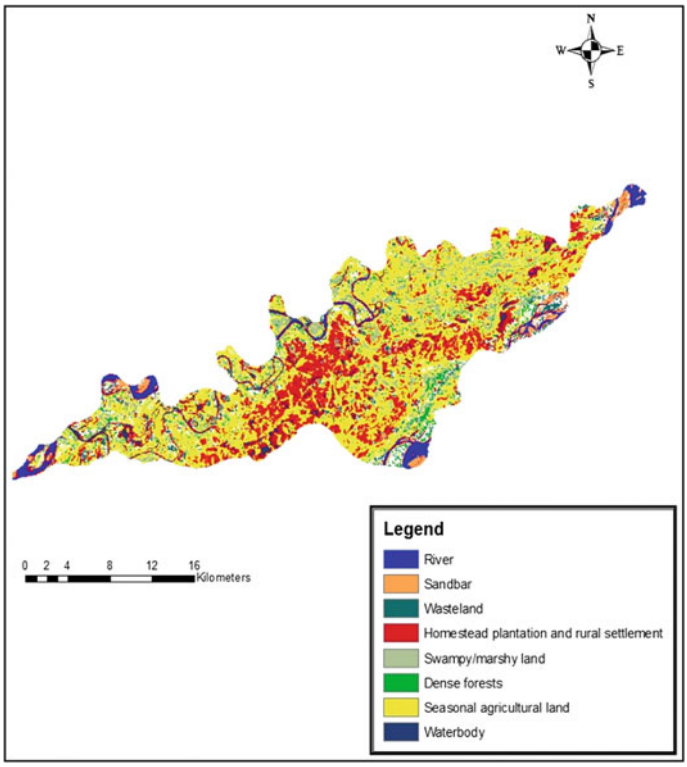

Fig. 14 Land use land cover on 31st November 2015

Area Chart

The changes in area from 1976 to 2015 have been shown in Fig. 16. In 1976, the total area of the Majuli Island has been found as 590.9 km^2, whereas in the year 2015, it has been found as 474.209 km^2. This dramatic change in the areas during these years is due to erosion. From the area chart, the average rate of erosion per year has been found to be 2.74 km/year.

Conclusion

The dwellers of Majuli Island have no fear psychosis for flood, rather they welcome flood. Flood is responsible for engenderment of loamy soil which in turn helps in fructification of the soil by a plant locally known as *Jaubon*. The specialty of this plant is that it arrests the silt particles and allows the loam to pass along with flood

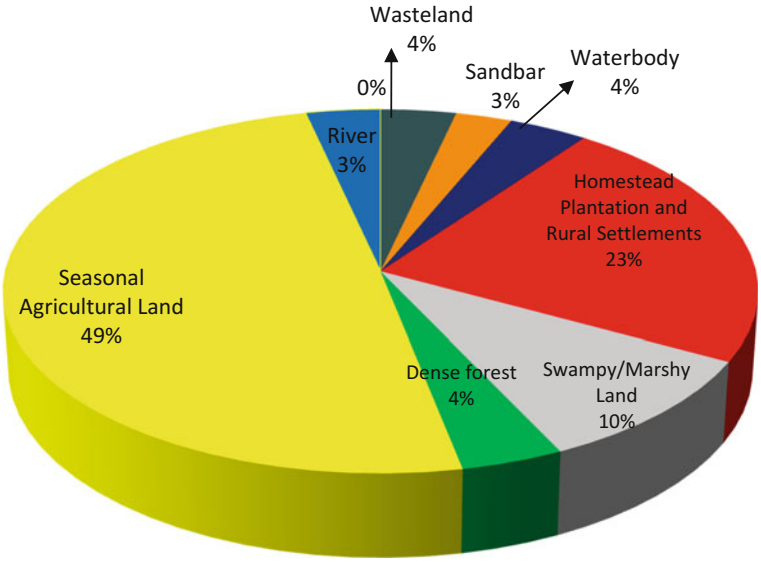

Fig. 15 Pie diagram of land use classification

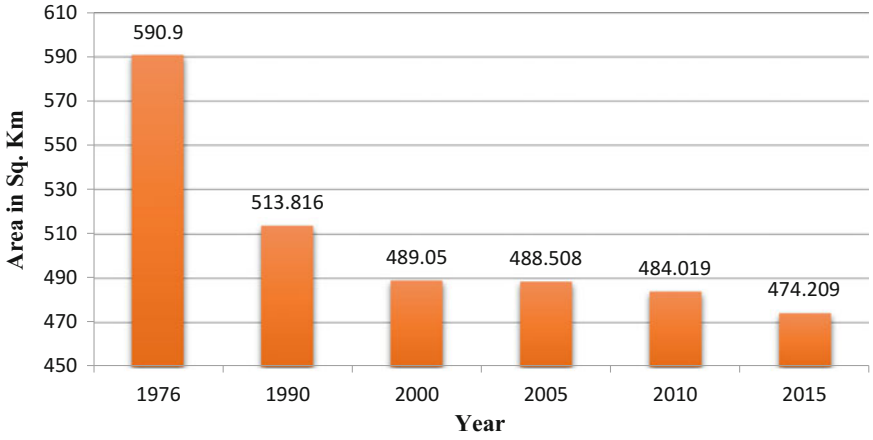

Fig. 16 Changes in area from 1975 to 2015

water which later increases the fertility of soil. Majuli is known for its agriculture. A total number of 4–5 types of crops are grown annually. Apart from agronomy, Majuli is also famous for poultry and livestock farming. Various types of tribes and communities are local inhabitants of Majuli Island and they are very much adaptive to live with flood. The Mishing communities of Majuli live in a special type of houses locally known as *Chang* ghar (stilt house). Chang ghar is houses on raised

platform above HFL made of bamboo and wood. Flood is not the prime problem in Majuli. The problem of concern is erosion.

There are various structural measures undertaken by Brahmaputra Board and Water Resource Department of Assam. Spurs are used to deflect the flow away from the island. Embankment is used as a flood mitigation measure. The siltation measures in the form of R.C.C. porcupines have been found to be effective in some areas. Majuli is a hub of culture and historical importance and also a biodiversity hotspot. Protection of this colossal river island from river erosion is of utmost importance.

References

Dutta M, Barman S, Aggarwal S (2010) A study of erosion-deposition processes around Majuli. Open Access e-J Earth Sci India 3(IV):206–216 http://www.earthscienceindia.info/; eISSN: 0974-8350

Goswami DC, Gogoi C (2013) A study on bank erosion and bank line migration pattern of the Subansiri River in Assam using remote sensing and GIS technology. Int J Eng Sci (IJES), ISSN (e): 2319-1813, ISSN(p): 2319-1805

Leopold LB, Wolman MG, Miller JP (1964) Fluvial processes in geomorphology. Dover Publications Inc., Mineola, N.Y

Martin (2005) Geospatial analysis of gravel bar deposition and channel migration within Ozark National Scenic Riverways. Master of Science, Geospatial Science submitted to Southwest Missouri State University

Rosgen D (1996) Applied river morphology. Wildland Hydrology, Pagosa Springs

Sarma A (2014) Landscape degradation of river Island Majuli, Assam (India) due to flood and erosion by river Brahmaputra and its restoration. J Med Bioeng 3(4)

Sarma JN, Phukan M (2004) Origin and some geomorphological changes of Majuli Island of the Brahmaputra river in Assam, India. Geomorphology 60:1–19

Wolman MG, Miller JP (1960) Magnitude and frequency of forces in geomorphic processes. J Geol 68:54–74

Study of Soil Erosion and Deposition Around an Island in a Natural Stream

Snigdhadip Ghosh, Saptarshi Das and Vijay Kumar Dwivedi

Abstract The main objective of this project is to study of plan form development and soil erosion and deposition around an island by conducting experiments in a mobile riverbed setup. Field measurements of velocity and turbulence vectors have carried out in this setup at NIT Durgapur. Directional current measurement (DCM) instrument and acoustic Doppler velocity (ADV) meters were used for the field measurements of velocity and turbulence particularly in the interface region between main channel and floodplain. The values of local shear velocity and roughness length for the reach under study were calculated using measured velocity data.

Keywords Soil erosion · Acoustic Doppler velocity · Shear velocity

Introduction

There are many approaches to improve ecological environment by creating diversity of river configuration in straightened rivers. As measures to create flow diversity, riverside embayment and groynes were often constructed. In order to predict changes of riverbed form and flow structures, numerical simulations became a powerful tool. For accurate application of the numerical methods, it is necessary

S. Ghosh (✉) · V. K. Dwivedi
Department of Civil Engineering, National Institute of Technology Durgapur, Durgapur 713209, West Bengal, India
e-mail: snigdhadipsuri@gmail.com

V. K. Dwivedi
e-mail: vkdwivedi10725@yahoo.co.in

S. Das
Department of Civil Engineering, Central University of Jharkhand, Brambe, Ranchi 835205, Jharkhand, India
e-mail: saptarshidas.3645@gmail.com

V. P. Singh et al. (eds.), *Hydrologic Modeling*, Water Science and Technology Library 81, https://doi.org/10.1007/978-981-10-5801-1_15

to understand resistance characteristics in actual rivers. Here we used acoustic Doppler velocimeter to measure the erosion and sedimentation characteristics of soil in mobile riverbed.

Objectives

Main objectives of this project were:

- Characterization of plan form development during stages of river flow.
- Erosion characteristics of soil around an island in a natural stream.

Literature Review

Patel and Ranga Raju (1999) carried out extensive experiments on initiation of motion and bed load transport of different fractions of sediment mixtures. They checked the accuracy of different models viz. Egiazaroff (1965), Ashida and Michiue (1972), Parker et al. (1982), Wiberg and Smith (1987), Bridge and Bennett (1992). Since the available methods did not produce satisfactory results, Patel and Ranga Raju (1999) proposed a new relationship for critical shear stress of different fractions in a mixture as

$$\frac{\tau_{*ci}}{\tau_{*c\sigma}} = \left(\frac{d_i}{d_\sigma}\right)^{-0.96}. \tag{1}$$

Here, $d_\sigma = \sigma_g d_g$ is geometric mean size of the mixture, σ_g is its geometric standard deviation, τ_{ci} is the dimensionless critical shear stress for size d_i, $\tau_{*c\sigma}$ is the dimensionless critical shear stress for size d_σ. They also proposed a graphical relationship between $\tau_{*c\sigma}$ and σ_g.

The transport of uniform sediments in suspension in open channel had been studied extensively in last four decades and is fairly well understood at present. Garde and Ranga Raju (1977) were observed the characteristics of settling perticles in laboratory flumes and natural streams that the concentration of suspended load in vertical decreased with increase in distance from the bed. The concentration of suspended sediment can be expressed in various ways as described below:

1. Absolute volume of solids per unit volume of water–sediment mixture. In this method, the dry weight of sediment in a unit volume of mixture is first determined. This can also be expressed as percentage by volume.
2. Dry weight of solids per unit volume of mixture. It is usually expressed as gm per liter, lb per cubic foot or kN per cubic meter.

3. Dry weight of solids per unit weight of mixture. This is customarily expressed in parts per million (ppm). One percent equals 10,000 ppm.
4. Dry weight of solids per unit weight of pure water equal in volume to that of sample.

Among these methods, the first and the third are commonly used for indicating the suspended sediment concentration. The concept of critical friction velocity or critical bed shear stress has long occupied a central position in sediment transport theory. Several investigations related to critical shear stress of uniform and nonuniform sediments in the absence of cohesion are available. An extensive review of different approaches for the computation of critical shear stress has been done by Garde and Ranga Raju (1977). Misri et al. (1984) have proposed a conceptual model for the effect of a particular size of sediment on the transport rates of other sizes of sediment. They analyzed the experimental data for assessing the accuracy of existing methods of computation of bed load transport. They also proposed a new method of computation. Samaga et al. (1986) measured the suspended load transport rates of individual fractions and compared with both Einstein's and Holtroff's methods. They found these methods were unsatisfactory in the present range of sediment parameters. They found a relationship existing between the dimensionless shear stress and the suspended transport rate for uniform sediment. To make this relation applicable to nonuniform sediments, a corrective multiplying factor for shear stress is introduced. The dimensionless parameters which govern this correction factor are identified, and a relation for the same is obtained. This relation can be applied to a sediment mixture of individual size portions.

Details of Experimental Setup and Materials

Flume

The experiments were conducted in the experimental setup created at National Institute of Technology, Durgapur. The setup consists of a flume 20 m long, 4 m wide, and 10 m deep. The flume has a cemented bottom and glass wall on both sides with a grid of 5 × 5 cm up to a height of 50 cm from the bottom of the flume to measure the bed profile. Experiments were done at several slopes of bed in the flume. The discharge in the flume was provided by an upstream reservoir fed by two 10″ mild steel pipes. There are two pumps of 7.5 HP each to supply water to the MS pipe from the underground reservoir. The water supply into flume was regulated with the help of a valve provided in the inlet pipe coming from reservoir. The water from the flume was drained to the reservoir through an escape channel, 41.2 m long, 1 m wide, and 0.6 m deep. Its discharge to the channel was volumetrically measured with the help of another tank provided at the downstream end of the channel. The water level and discharge through the flume were controlled by

a motor-operated sluice gate at the tailed end of the flume. Experimental soil is collected locally and analyzed. The sludge velocity instrument is Sontek acoustic Doppler velocimeter. Acoustic Doppler velocimeter (ADV) can measure three dimensional point velocities and turbulence parameters in shallow and deep water system in nearly any location in the water column and close to boundaries as long as air entertainment is minimal.

Measurements

Discharge Measurement Using V-Notch

Two 90º V-notch have been installed in the escape channel to measure discharge in the flume. The installed V-notch has been calibrated with the help of electronic flow meter.

Measurement for the Velocity Distribution

The velocity profile along the centerlines of the flume width in the approach flow was measured with the help of acoustic Doppler velocity (ADV) meter. Acoustic Doppler velocity meter is a versatile, high-precision instrument used to measure water velocity in a wide range of environments including laboratories, rivers, estuaries, and the ocean. The instrument consists of three basic elements: the probe, the signal conditioning module, and the processor. The probe is attached to the conditioning module, which contains low noise receiver enclosed in a submersible housing. The ADV conditioning module and probe are connected to the processing module using a custom shielded cable up to 10-m long. The ADV uses acoustic Doppler technology to measure flow in a small sampling volume located 5 cm from the probe. The velocity range is programmable from ± 3 to ± 250 cm/s; data can be acquired at sampling rates up to 50 Hz with no zero offset.

Measurements of Dry Density

The values of dry density were computed by using the observed value of bulk density and antecedent moisture content. The void ratio was derived from the computed value of dry density of the sediments.

Sediment Load Measurements

The sediment transported as bed load was collected in a trap placed at the downstream end of the flume just before the tail gate location. The samples of water–sediment mixture were collected in containers by traversing the depth integrating sampler over the entire width of flow. The containers were weighed to determine the weight of water–sediment mixture in them. The water was removed next from these containers after allowing the fine sediment to settle completely, which requires 24 h time. Next, the sediments were removed from these containers using filters into smaller size pans and these pans were kept in an electric oven for drying. After drying the samples, the weight of suspended sediments was measured by using an electronic balance having a least count of 0.01 g. The concentration of suspended sediment sampled in each container was determined by dividing the weight of sediment contained by the given volume/weight of water.

ADV Components, Terminology and Sampling

Sontek acoustic Doppler velocimeter (ADV) systems are of two types: field systems and lab systems. ADV field systems can be of three types: splash-proof, underwater, and autonomous (hydra) systems. The hardware for these systems is composed of two main components: signal processing hardware and probe hardware. The signal processing hardware can be contained in a splash-proof housing or an underwater canister. The probe hardware can be of three basic types: a 16-MHz micro-ADV probe, a 10-MHz ADV probe, and a 5-MHz ADV ocean probe. The signal processing hardware performs the signal generation and processing required for the Acoustic Doppler velocimeter (ADV) to make velocity measurements. This includes generating the electrical signals that are converted to acoustic energy at the transducers, digitizing the return signal, performing Doppler processing to calculate velocity, and averaging samples together before data output. The applicability of turbulence measurements by using ADV in actual rivers and laboratory flumes was verified by many researchers (e.g., Rennie et al. 2002; Kostaschuk et al. 2005; Biron et al. 1998; Goring and Nikora 2002; Song and Chiew 2001; Papanicolaou et al. 2007). It was also proved in the study that the velocity measurements using acoustic Doppler velocimeter (ADV) are reasonably accurate, and the turbulence structures have consistency even in these nonuniform flow fields.

Data Collection and Comparison

See Image 1.

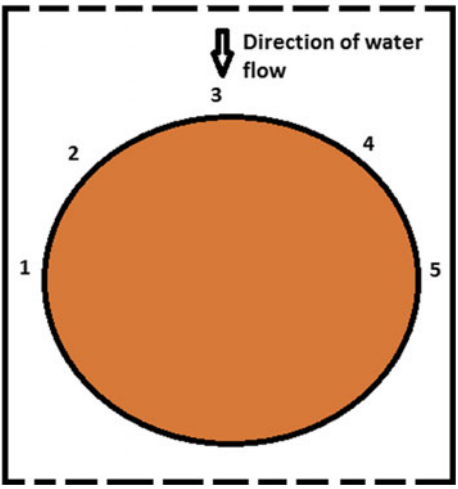

Image 1 Orientation of stations

Reading I

Mode of ADV: discharge mode.
Discharge rate: 0.118 m^3/s.
Date of test: January 1, 2016.

Where SNR is signal-to-noise ratio and spike is the sharp increment in the magnitude or concentration of Doppler in the corresponding stations around the island (Figs. 1 and 2; Table 1).

Reading II

Mode of ADV: discharge mode.
Discharge rate: 0.118 m^3/s.
Date of test: January 2, 2016 (Figs. 3 and 4; Table 2).

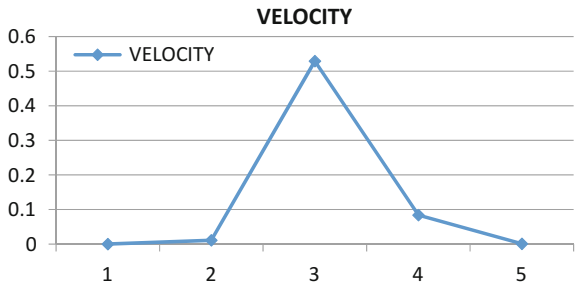

Fig. 1 Variation of velocity depending on reading I

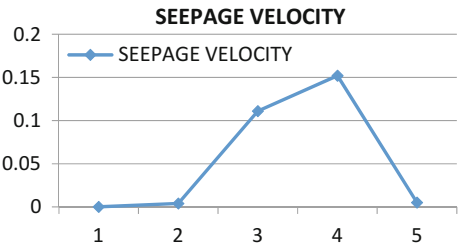

Fig. 2 Variation of seepage velocity depending on reading I

Table 1 Data recorded on January 1, 2016

Station	Velocity	Seepage velocity	Angle	SNR	Spike	Band
1	0	0	−76	30.9	0	Good
2	0.011	0.004	−13	33.7	2	Best
3	0.529	0.111	15	4.5	0	Best
4	0.084	0.152	120	0.4	0	Best
5	0.001	0.005	133	27.5	1	Best

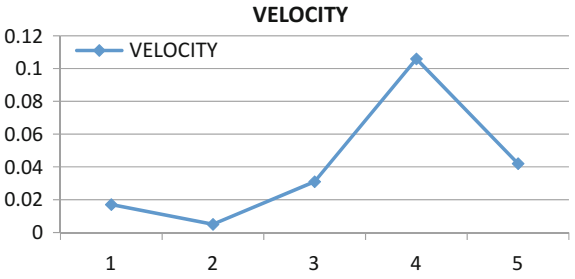

Fig. 3 Variation of velocity depending on reading II

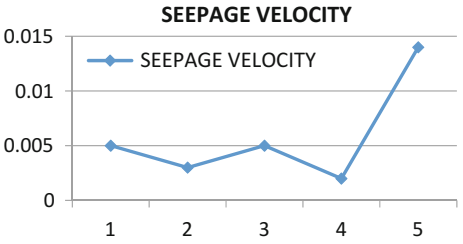

Fig. 4 Variation of velocity depending on reading II

Table 2 Data recorded on January 2, 2016

Station	Velocity	Seepage velocity	SNR	Angle	Spike	Band
1	0.017	0.005	24.5	−84	0	Good
2	0.005	0.003	16.7	5	2	Good
3	0.031	0.005	20.8	16	2	Best
4	0.106	0.002	28.8	7	0	Best
5	0.042	0.014	32.5	82	0	Best

Image 2 Before erosion and after erosion

Conclusion

The pattern of sediment velocity observed in two consecutive experiment data with the help of micro acoustic Doppler velocimeter was that the velocity of sediment particles increased at station 3 and 4 as the direction of current was directly toward the stations, whereas there were angular velocities in station 1 and 5. SNR values were inversely proportional to the velocity of settling particles. The difference between day 1 experiment data and day 2 experiment data was mainly because of the consolidation and degree of saturation of island, though the pattern of erosion and deposition were almost same (Image 2).

References

Ashida K, Michiue M (1972) Study on hydraulic resistance and bed-load transport rate in alluvial streams. Proc Japan Soc Civil Eng 1972(206):59–69

Biron PM, Lane SN, Roy AG, Bradbrook KF, Richards KS (1998) Sensitivity of bed shear stress estimated from the vertical velocity profiles: the problem of sampling resolution. Earth Surf Process Land 23:133–139

Bridge JS, Bennett SJ (1992) A model for the entrainment and transport of sediment grains of mixed sizes, shapes, and densities. Water Resour Res 28(2):337–363
Egiazaroff IV (1965) Calculation of nonuniform sediment concentrations, J Hydraul Eng 91 (4):225–247
Garde RJ, Ranga Raju KG (1977) Halsted Press, New York (Wiley Eastern Limited, New Delhi). Price: Â£1.25. No. of pages: 483. Earth Surf Proc 4(3):304–305
Goring DG, Nikora VI (2002) Despiking acoustic doppler velocimeter data. J Hydraul Eng 128 (1):117–126
Kostaschuk R, Best J, Villard P, Peakall J, Franklin M (2005) Measuring flow velocity and sediment transport with an acoustic doppler current profiler. Geomorphology 68:25–37
Misri RL, Ranga Raju KG, Garde RJ (1984) Bed load transport of coarse nonuniform sediments. J Hydraul Eng 1103:312–328
Papanicolaou AN, Elhakeem M, Hilldale R (2007) Secondary current effects on cohesive river bank erosion. Water Resour Res 43(12)
Parker G, Klingeman PC, McLean DG (1982) Bedload and size distribution in paved gravel-bed streams, J Hydraul Div Am Soc Civ Eng 108:544–571
Patel PL, Ranga Raju KG (1999) Critical tractive stress of nonuniform sediments. J Hydraul Res 37(1):39–58
Samaga BR, Ranga Raju KG, Garde RJ (1986) Suspended load transport of sediment mixtures. J Hydraul Eng 112(11):1019–1034
Song T, Chiew YM (2001) Turbulence measurement in nonuniform open-channel flow using acoustic doppler velocimeter (ADV). J Eng Mech 127(3):219–232
Rennie CD, Millar RG, Church MA (2002) Measurement of bed load velocity using an acoustic doppler current profiler. J Hydraul Eng 128:473–483
Wiberg PL, Smith JD (1987) Calculations of the critical shear stress for motion of uniform and heterogeneous sediments. Water Resour Res 23(8):1471–1480

Impact Assessment of Alternate Land Cover and Management Practices on Soil Erosion: A Case Study

T. R. Nayak, R. K. Jaiswal, R. V. Galkate and T. Thomas

Abstract Climate, soil, vegetation, topography, and man are the factors that affect soil erosion, and out of these vegetation and soil to some extent are the only factors which man can control. Fertile soil by carrying erosion fills dam reservoir and reduces dam's economical life, hence economy of country get debilitated big amount. To specify hazard and damage of soil erosion is very important for this reason. Among many environmental hazards, checking land degradation is of utmost importance as it has direct bearing on decline in productivity on arable and non-arable lands. To prevent the erosion and rapid siltation, management of water, soil cover, and vegetation resources on watershed is must. In the present study, expected soil loss from Bina river watershed of Betwa river basin has been estimated using USLE model in GIS platform. The total soil about 4% of the total geographical area of the Bina watershed was found under very severe erosion category having erosion rate more than 120 t/ha/year, whereas the average soil erosion for the Bina basin was found to be 8.7 t/ha/year. Impact of alternate land cover management practices have been analyzed by hypothetically assigning the alternate land use practices and changing the values of controlling factors of USLE model accordingly. The best management practices which increase the food production and also control the soil erosion have been suggested.

Introduction

The soil has been defined by the International Soil Science Society as: The soil is a limited and irreplaceable resource, and the growing degradation and loss of soil mean that the expanding population in many parts of the world is pressing this

T. R. Nayak (✉)
National Institute of Hydrology, Regional Centre, WALMI Campus,
Bhopal 462016, MP, India
e-mail: tejramn@yahoo.com; trnnca@gmail.com

R. K. Jaiswal · R. V. Galkate · T. Thomas
Department of Applied Mechanics and Hydraulics, National Institute of Technology
Karnataka, Surathkal, Mangaluru, India

V. P. Singh et al. (eds.), *Hydrologic Modeling*, Water Science
and Technology Library 81, https://doi.org/10.1007/978-981-10-5801-1_16

resource to its limits. In its absence in the biospheric environments, man will collapse with devastating results for humanity. Fertile soil by carrying erosion fills dam reservoir and reduces dams economical life, hence economy of country get debilitated big amount. To specify hazard and damage of soil erosion is very important for this reason (Choudhary and Nayak 2003). Among many environmental hazards, checking land degradation is of utmost importance as it has direct bearing on decline in productivity on arable and non-arable lands. It is estimated that about 80% of current degradation on agricultural land in the world is caused by soil erosion due to water (Angima et al. 2003). It is estimated that India suffers an annual loss of 13.4 million tones in the production of major cereal, oilseed, and pulses crops due to water erosion equivalent to about 2.6 billion dollars (Sharda et al. 2010).

Reservoir sedimentation, resulting from degradation of the watersheds in India, is on multiple rises as compared to the rate that was assumed at the time the projects were designed hence the catchment is deteriorated and thus the operational life of reservoir is diminished. Climate, soil, vegetation, topography, and man are the factors that affect soil erosion, and out of these vegetation and soil to some extent are the only factors which man can control. To prevent the erosion and rapid siltation, management of water, soil cover, and vegetation resources on watershed is must. USLE model and ILWIS GIS have been used for determining the quantity of soil erosion. Wang et al. (2006) used the Agricultural Policy–Environmental eXtender (APEX) model developed in the USA to investigate soil erosion effects associated with alternative land uses at the ZFG (Zi-Fang-Gully) watershed in northwestern China. The results indicated that the APEX model could be calibrated reasonably well (615% errors) to fit those areas with 50% slope within the watershed. Wijitkosum (2012) studied the impacts of land use changes on soil erosion in Pa Deng sub-district, adjacent area of Kaeng Krachan National Park, Thailand, were investigated by applying remote sensing technique, geographical information system (GIS), and the Universal Soil Loss Equation (USLE). The study results revealed that land use changes in terms of area size and pattern influenced the soil erosion risk in Pa Deng in the 1990–2010 period. The area with smaller land cover obviously showed the high risk of soil erosion than the larger land cover did.

Bina River, a major tributary of River Betwa in Bundelkhand region of Madhya Pradesh has been selected for the study. In this paper, the application of USLE model and GIS has been attempted for determining the quantity of soil erosion in present physical condition of the watershed. Subsequently, alternate land use and management practices have been applied in the vulnerable areas to control the soil erosion and impact of different land cover and management practices have been analyzed. The alternate land use management plans for soil conservation measures have been suggested for the Bina river watershed.

Study Area

Bina River is a major tributary of River Betwa in Bundelkhand region of Madhya Pradesh, which originates from Begumganj block of Raisen district and enters Sagar district at Rahatgarh block and traverses through Khurai and Bina Tehsil before confluence with River Betwa near Basoda town in Vidisha district. Presently, domestic water supply to the Rahatgarh town, Khurai town and Bina town, and industrial supply to Bina Railway Junction and Oil Refinery at Bina are met from the Bina river. Also, the irrigation demand is partially met by direct pumping of the river water. 'Bina Complex-Irrigation and Multipurpose Project' has been proposed. Under this project, four dams are proposed, the Madia dam and Chakarpur dam-cum-pickup weir on Bina River and one each on Dehra and Dhasan rivers, which are the tributaries of River Betwa. The Index map showing the Bina river watershed up to the confluence with Betwa River is shown in Fig. 1. The watershed under consideration falls between 23° 18′ to 24° 15′N latitudes and

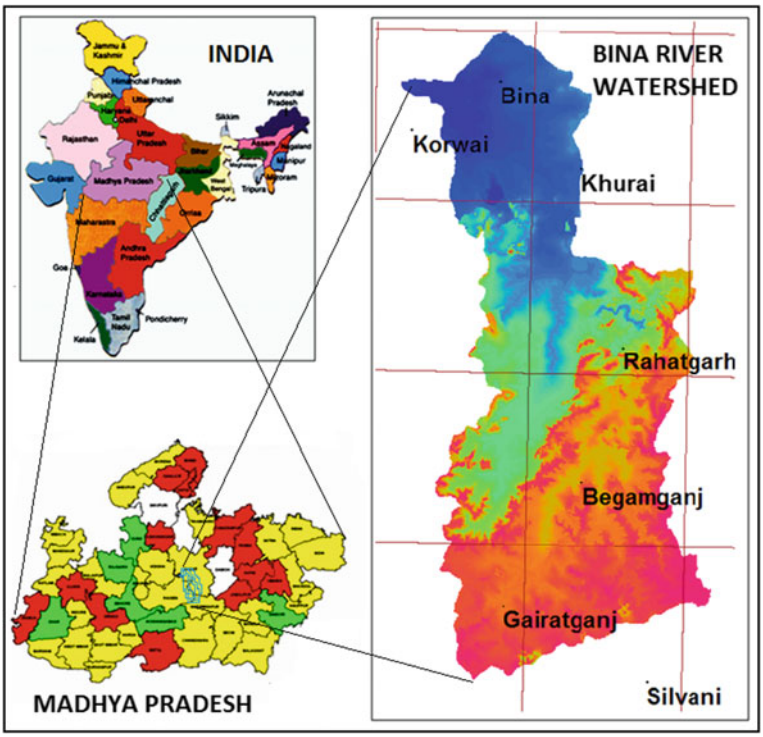

Fig. 1 Index map showing Bina river watershed

78º 03′ to 78º 32′E longitudes having total geographical area of 2817 km^2. The southern part of the watershed is dominated with hills and undulating topography with forest cover, whereas the northern part of the watershed has gentle slopping and plains with fertile agricultural lands.

The average normal annual rainfall of the area is 1329.56 mm and average 28 rainy days in a year. About 90% of the annual rainfall takes place during the monsoon period, only 5.5% of annual rainfall takes place during winter, and about 4.5% of rainfall occurs during the summer season. During winter season, the January is the coldest month with the average minimum temperature of 11.5 °C, whereas the hottest month is May with average maximum temperature up to 40.9 °C. The topography of the area is rolling to undulating. The land slope is characterized by flat topped hillocks. This topography is a result of the variation in hardness of different types of water flows. The valley land is moderately to poorly drain.

Methodology

In the present study, the well-known model for soil erosion estimation from a watershed, the Universal Soil Loss Equation (USLE) has been used. The thematic maps were prepared using remote sensing imageries, and data storage and analysis were done using ILWIS geographic information system (GIS).

The Universal Soil Loss Equation Model

In 1958, Wischmeier, a statistician with the Soil Conservation Service, was put in charge of analyzing and collating over 10,000 annual records of erosion on plots and small catchments at 46 stations on the Great Plains. The model with the greatest acceptance and use is the Universal Soil Loss Equation (USLE), developed by Agriculture Research Services (ARS) scientists Wischmeier and Smith (1978) to estimate soil erosion from fields. Mathematically, the equation is denoted as:

$$A = R * K * L * S * C * P \tag{1}$$

A Annual soil loss (tons/ha/year)
K Soil erodibility factor
S Degree of slope factor
P Conservation practice factor
R Rainfall and runoff erosivity index
L Length of slope factor
C Cropping management factor

Rainfall Erosivity Index (*R*)

R, the rainfall erosivity index, is equal to product of *E*, the kinetic energy of rainfall, and I_{30} (maximum rainfall intensity in 30 min expressed in cm per hour). This index corresponds to the potential erosion threat in a given region where sheet erosion appears on a bare plot with a 9% slope. In India, simple relationship between erosivity index (*R*) and annual or seasonal rainfall (*X*) has been developed by Singh et al. (1981) after analyzing the data collected from 45 stations distributed in different rainfall zones throughout the country (Choudhary and Nayak 2003).

$$R_a = 79 + 363.079 * X_a \tag{2}$$

$$R_s = 50 + 389.050 * X_s \tag{3}$$

For this study, seasonal rainfall index, i.e., R_s is used for *R* value.

Soil Erodibility Factor (*K*)

The *K* factor represents both susceptibility of soil to erode by an amount and rate of runoff. *K* depends on the texture and organic matter content of the soil, its permeability, and profile structure. It varies from 0.7 for the most fragile soil to 0.01 for the most firm soil. It is measured on bare reference plots 22.2 m long on 9% slopes, tilled in the direction of the slope and having received no organic matter for three years (http://www.grr.ulaval.ca). It quantifies the cohesive character of a soil type and its resistance to dislodging and transport (particle size and density dependent) due to raindrop impact and overland flow shear forces. *K* is a function of complex interaction of a substantial number of its physical and chemical properties. A simpler method to forecast *K* was presented by Wischmeier et al. (1971) which includes the particle size of the soil, organic matter content, soil structure, and profile permeability (Wischmeier et al. 1971).

The Topographic Factor (*L* and *S*)

SL, the topographical factor, depends on both the length and gradient of the slope. Value varies from 0.1 to 5 in the regular farming lands and may reach up to 20 in hilly areas. The slope length and slope steepness can be used in a single index, which expresses the ratio of soil loss as defined by (Wischmeier and Smith 1978).

$$LS = (\lambda/22.1)^{0.5} * (0.065 + 0.045G + 0.0065G^2) \quad (4)$$

where λ = slope length (m) and G = percentage slope gradient. Slope percentage layer was derived from digital elevation model (DEM) of the study area, and slope length was assumed to be fixed for each pixel (100 m). The values of G and λ will be derived from DEM.

Cropping Management Factor (*C*)

The plant cover factor, *C*, is a simple relation between erosion on bare soil and erosion observed under a cropping system. It is the ratio of soil loss from land cropped under specified conditions to corresponding loss under tilled, continuous fallow conditions. It measures the combined effect of vegetation cover and management variables. It varies from 1 on bare soil to 0.001 under forest, 0.02 under grasslands and cover plants, and 1–0.9 under root and tuber crops.

Conservation Practice Factor (*P*)

The conservation practice factor, *P*, is the ratio of soil support practice to the corresponding loss with up and down slope culture. Practices induced in this term are contouring, terracing (alternate crops on a given slope established on the contour), strip cropping. *P* is a factor that takes account of specific erosion control practices such as contour tilling or contour ridging or mounding. Value varies from 1 on bare soil with no erosion control to about 0.25 with tied ridging on a gentle slope.

Application of ILWIS GIS Tool

The integrated land and water information system (ILWIS) has the capability of analyzing the remote sensing (RS) data as well as geographic information system (GIS). ILWIS multiplies the map by overlaying these maps one over another. Hence, it becomes very essential for all maps to be rasterized with same pixel size. All the factors required for soil erosion estimation as given in Eq. 1 were calculated using ILWIS GIS software and stored as thematic maps in raster format. These maps were then multiplied together to generate the soil erosion map using Map Calculation operation. The approach is made to observe how severe the specific area is by generating a classified map of various erosion class such as 0–10, 10–20, 10–20, 20–40, 40–80, 80–120, >120. The sensitivity analysis will also be done by assigning the barren land as forest cover, agricultural land with good management

practices, etc., to see the changes in the quantity of soil erosion from the catchment area. The analysis is helpful for planning the watershed management practices, such as afforestation, contour bunding, gully plugging. Histogram of erosion map can be used in calculating the total soil erosion of the catchment. The histogram provides total number of pixels falling in each erosion intensity, the number of pixels can be multiplied with the corresponding mid value of erosion intensity to get the total soil loss.

Data Processing and Parameter Estimation

Rainfall Erosivity Factor

Total seven rain gauge stations, namely Bina, Kurwai, Khurai, Rahatgarh, Begumganj, Gairatganj, and Silvani falls in and around Bina river basin. The annual rainfall observed at these stations available for last fifteen years were collected. The seven rain gauge stations were marked on the basin map and stored as point map. The Interpolation operation on the point map was carried out by choosing the Criging interpolation method to get the distributed rainfall map in raster format. Further, using the MapCalc operation in GIS, the rainfall map was converted into the '*R*' factor map by applying Eq. 2, and the output map was named as '*R*-factor.' The average annual rainfall observed at seven rain gauge stations and corresponding *R*-factor values are given in Table 1.

Soil Erodibility Factor

The organic matter (OM) contents in these soils are reported about 2%. *K* values were determined based on locally measured soil properties and using soil erodibility factor monograph for great soil groups in India. These values were annual averaged corresponding to homogeneous different soil groups as shown in Fig. 2. *K* values for study area are shown in Table 2.

Table 1 Rainfall distribution in Bina river basin

S. No.	Rain gauge station	Average annual rainfall (mm)	*R*-factor
1	Bina	1064.1	465.3
2	Korwai	1002.5	442.9
3	Khurai	1193.3	512.2
4	Rahatgarh	1166.9	502.6
5	Begamganj	1209.2	517.9
6	Gairatganj	1183.8	508.7
7	Silvani	1067.3	466.4

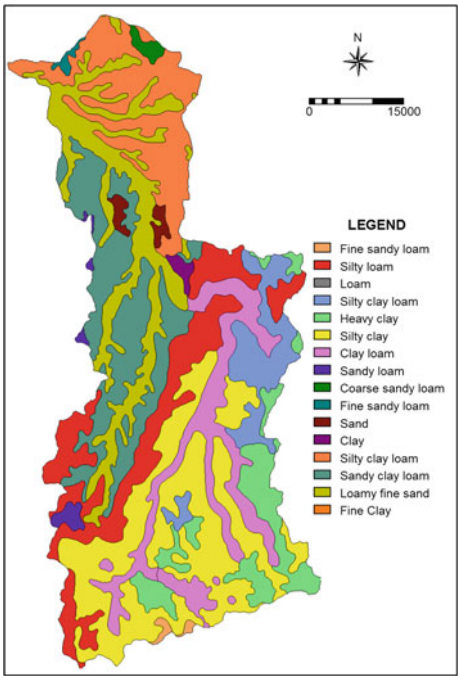

Fig. 2 Soil map of Bina river basin

Table 2 Distribution of soil class and '*K*' value

Code	soil class	Area	*K*-factor
203	Fine sandy loam	9.36	0.35
305	Silty loam	366.02	0.38
311	Silty clay loam	162.82	0.32
314	Heavy clay	203.82	0.17
315	Silty clay	580.64	0.26
317	Clay loam	291.89	0.30
325	Sandy loam	21.85	0.13
342	Coarse sandy loam	14.49	0.07
352	Fine sandy loam	7.68	0.18
355	Sand	24.02	0.02
362	Clay	12.45	0.22
376	Silty clay loam	328.18	0.32
377	Sandy clay loam	395.43	0.20
398	Loamy fine sand	389.43	0.11

Topography Factor (S, L)

Contour lines given in the Survey of India topographic maps were digitized, and the corresponding heights above mean sea level (Contour values) were assigned to each

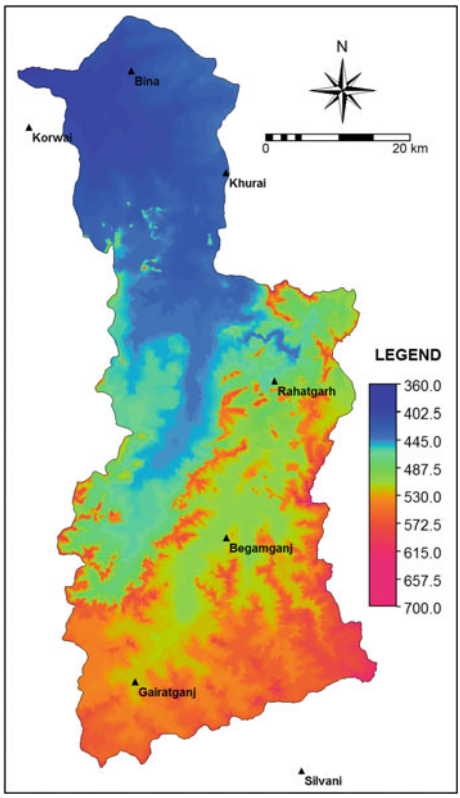

Fig. 3 Digital elevation model (DEM)

line. The contour lines at 10 m intervals and the spot heights available at some places have also been digitized and stored in vector format as segment/point maps 'isoline.' To create a digital elevation model (DEM) map, interpolation of the segment map 'isoline' was done via the operation Interpol Seg in ILWIS GIS. The DEM map thus generated is a raster map showing the elevation or height above mean sea level at each pixels in the study area as given in Fig. 3. Slope length factor map was generated by using Eq. 4.

Crop Management (Land Use) Factor

The ILWIS GIS software has the capability of digital image processing (DIP) capabilities also. The land use map was prepared by applying maximum likelihood classifier (MLC) digital classification of multi-date LISS-IV Satellite data acquired from the National Remote Sensing Centre (NRSC), Hyderabad. The land use map of Bina river watershed is given in Fig. 4, and spatial distribution of all the five land use classes is given in Table 3.

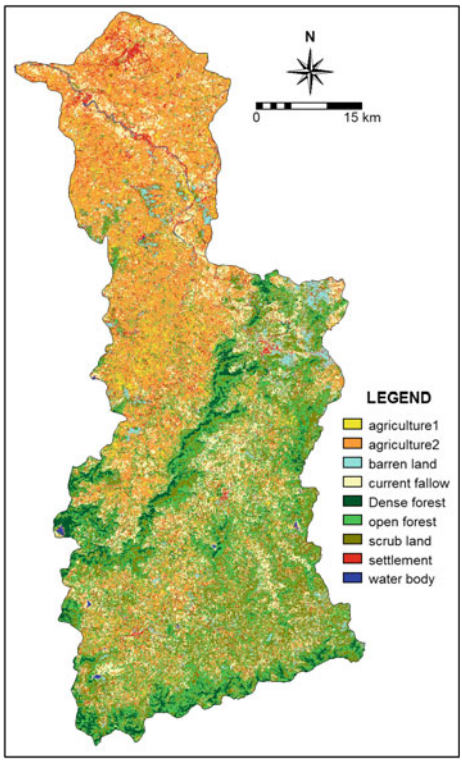

Fig. 4 Land use map of Bina river basin

Table 3 Land use map and '*C*' factor for Bina river basin

S. No.	Landuse class	Area in (km^2)	% of basin area	'*C*' factor
1	Agriculture-1	121.32	4.3	0.25
2	Agriculture-2	786.70	28.0	0.28
3	Current fallow	450.15	16.0	0.30
4	Dense forest	140.61	5.0	0.02
5	Open forest	543.76	19.4	0.05
6	Scrub land	490.28	17.5	0.15
7	Barren land	116.23	4.1	0.45
8	Settlement/rock outcrop	151.90	5.4	0.20
9	Water body	7.13	0.3	0.001

Conservation Practice Factor (P)

The classified slope map slope class was attributed to *P* factor values to create a raster map of conservation practices factor. The non-agricultural lands (forest, shrubs/bushes, and barren/grazing land) were assigned value 1.0 for *P* factor.

Results and Discussion

Estimation of Expected Soil Erosion

The various maps having the values of factors responsible for soil erosion, i.e., *R*, *K*, *LS*, *C,* and *P* were brought in the form of raster maps as affirmed previously to obtain the soil loss. Multiplying the *R*, *K,* and *LS* maps gave the potential soil erosion of the catchment. The expected soil loss map 'USLE' was obtained by multiplying all the six factor maps. The USLE map was again classified into distinct group of erosion intensities to create the classified expected soil loss, and the result has been presented in Table 4. By this assessment, it can be clearly observed that almost 4% of the catchment is prone to very severe erosion condition and 2.3% is under severe erosion situation.

The quantity of actual soil erosion calculated by USLE model comes out to be 8.72 Million tones/year. This value can be converted in terms of volume by dividing the same with the specific gravity of the sediment load, i.e., 1.1 tones/m^3. Thus, the soil erosion from the Ravishankar catchment will be 7.9 mm^3/year.

Alternative Strategies to Reduce Soil Erosion

The impact of land use/land cover changes in the watershed area can be well analyzed in GIS. However, the temporal changes cannot directly be modeled in the GIS, but the changes in values of different parameters due to change in land use/land cover can be redefined in the GIS. Expected soil loss in a watershed may be estimated by assigning the new values for cropping management practices assuming the alternate land cover. The primary purpose for conducting raster-based USLE model simulations is to assist local policymakers to change the land use within the Bina river watershed. One of the major challenges is to identify strategies

Table 4 Potential/expected soil loss of Bina river basin

S. No.	Erosion class	Erosion value (t/ha/year)	Potential soil loss		Expected soil loss	
			Area (km^2)	Percent to total area	Area (km^2)	Percent to total area
1	Very low	0–05	286.50	10.20	1959.90	69.80
2	Low	05–10	477.55	17.01	410.16	14.61
3	Moderate	10–20	1005.50	35.81	213.55	7.61
4	High	20–40	519.53	18.50	94.49	3.36
5	Very high	40–80	200.98	7.16	69.43	2.47
6	Severe	80–140	88.18	3.14	30.12	1.07
7	Very severe	>140	229.85	8.18	30.43	1.08
	Total		2808.08	100.00	2808.08	100.00

Table 5 Expected soil loss in different scenarios assumed for Bina watershed

Scenario	Assumptions on land use changes	Soil loss (t/year)	% change from base
S-I	The base	24.416	Base
S-II	All forest planting in open forest and scrubland	22.137	−9.33
S-III	Open forest in 50% scrubland and 50% barren land	23.289	−4.62
S-IV	All grain production in barren land up to 5% slope	26.444	8.31
S-V	All grass growth in barren land	25.148	3.00
S-VI	Scenario-IV with forest plantations in barren land with more than 5% slope and in scrub land	21.712	−11.07

that reconcile the inherent conflict between food production and soil protection in the area. The proposed alternatives reflect alternative land use practices. Obviously, USLE modeling cannot answer all policy questions, but it may assist with defining: (i) the environmental effects of alternative land uses and (ii) the watershed management practices.

The six land use scenarios simulated include:

- the base,
- all forest planting in open forest and scrubland,
- open forest in 50% scrubland and 50% barren land,
- all grain production in barren land up to 5% slope,
- all grass growth in barren land,
- all grain production in barren land up to 5% slope, and forest plantations in >5% slope, and in scrub land.

The USLE model has been run for all the six scenarios, and gross annual soil loss in the Bina watershed has been computed for different scenarios. The quantity of annual total soil loss in case of different scenarios has been worked out as shown in Table 5.

Discussion of Results

It is seen from the results that the forest plantations in half of the scrub land and barren land is found to be very effective measure for controlling soil erosion. The total expected soil erosion reduced by plantation (S-II) from the present value of 24.416–22.137 t/year, i.e., by 9.33%. Whereas, the grain production in barren land up to 5% (S-IV) increases the total expected soil erosion by 8.31%. But, the crop land is necessary to produce food grains for the livelihood of the local population, which increases the soil erosion. In order to keep the total soil loss at minimum, the

increase in soil loss due to increase in cropland by converting (barren land into arable land must be counter balance by planting in the high slope barren land (with >5% slope) and scrub land in the Bina watershed (S-VI), in this scenario, the total soil erosion would be reduced by 11.1%.

Acknowledgements The authors owe their gratefulness to the Director, National Institute of Hydrology, Roorkee and the Coordinator, NIH Regional Centre, Bhopal for providing institutional facilities to complete this work.

References

Angima SD, Stott DE, O'Neill MK, Ong CK, Weesies GA (2003) Soil erosion prediction using RUSLE for central Kenya highland conditions. Agric Ecosys Environ 97:295–308

Choudhary MK, Nayak TR (2003) Estimation of soil erosion in Sagar lake catchment of central india, watershed hydrology. In: proceedings of the international conference on water and environment, pp. 387–392. Bhopal, India, 15–18 Dec. http://www.grr.ulaval.ca/gae_3005/Documents/References/RUSLE/ah703_ch3.pdf

Singh G, Babu R, Chandra S (1981) Soil loss research prediction in India. Central Soil and Water Conservation Research and Training Institute, Dehradun, Bull. No. T-12/D-9

Sharda VN, Dogra P, Prakash C (2010) Assessment of production losses due to water erosion in rainfed areas of India. J Soil Water Conserv 65:79–91

Wang ED, Cheng X, Williams JR, Cheng X (2006) Predicting soil erosion for alternative land uses. J Environ Qual 35:459–467

Wijitkosum S (2012) Impacts of land use changes on soil erosion in Pa Deng sub-district, adjacent area of Kaeng Krachan national park, Thailand. Soil Water Res 7(1):10–17

Wischmeier WH, Johnson CB, Cross BV (1971) A soil erodibility nomograph for farmland and construction sites. J Soil Water Conserv 26:189–193

Wischmeier WH, Smith DD (1978) Predicting rainfall erosion losses—A guide to conservation planning. In: Agriculture handbook. No. 537, U.S. Deptartment of Agriculture, Washington D.C

Geostatistical Analysis of River Sedimentation Behavior in Kerala State

Mathew K. Jose, T. Chandramohan, B. K. Purandara and B. Venkatesh

Abstract Sediment transport is an important aspect of all fluvial systems like river flows. Sediment transportation depends on the flow conditions, ratio of densities of sediment and fluid, and the size of the particle. Analysis of sediment yield data is helpful in understanding the distributional characteristics of sedimentation in river basins. Evolving a sediment distribution relationship over the region, consisting of different catchments, may facilitate in estimating sedimentation rates at non-sampling locations. Such estimates based on geostatistical analyses would be better estimates of mass fluxes compared to those obtained through conventional methods. As processes like river sedimentation, with time-space variation, may be considered as regionalized variables, geostatistical techniques can be effectively utilized in analyzing such variables to bring out their spatial structure. In the present study, geostatistical analysis of sediment yield data from sixteen river basins of the State of Kerala has been undertaken with a view to reveal the spatial and temporal distribution pattern of sedimentation in the region. The mean annual rainfall in the region is above 3000 mm, and it varies from west to east as well as from south to north. Therefore, the sedimentation behavior also is expected to vary. Geostatistical analysis has been carried out for distinct cases based on regional and seasonal variations. Northern and southern regions were treated separately. Also, seasonal variations with regard to SW and NE monsoons were also considered. The geostatistical analyses revealed that the sedimentation characteristics in Kerala river catchments tend to increase from north to south during NE monsoon. However, during SW monsoon, northern region yielded more sediment. The quantitative increment in sediment yield toward the southern parts of the state may be attributed to the rainfall characteristics.

M. K. Jose (✉) · T. Chandramohan · B. K. Purandara · B. Venkatesh
National Institute of Hydrology, Regional Centre, Belgaum 590019, Karnataka, India
e-mail: mathewkjose@gmail.com

V. P. Singh et al. (eds.), *Hydrologic Modeling*, Water Science and Technology Library 81, https://doi.org/10.1007/978-981-10-5801-1_17

Introduction

Sediment is natural material disintegrated by weathering and erosion. It is transported by action of wind, water, or by the force of gravity acting on the particles. Sizes of sediment particles vary from pebbles and gravel to silt and clay. Sediment transport is an inseparable part of fluvial systems like river flows. Transportation of sediment starts when the shear stress acting on the bed exceeds the critical shear stress of the bed material. The sediment moves in the direction of flow from high region to low region. The modes of transport can be classified into different categories like *Contact load* (sediment particles that roll or slide along the bed for some time, then come to rest and again start rolling or sliding), *Saltation load* (sediment particles hopping or bouncing along the bed thereby losing contact with the bed for sometime), *Bed load* (sediment moved on or near the bed), *Suspended load* (sediment moving in suspension in the fluid).

Sediment transport is a variable because as it is constantly subject to changes. Sediment transport can be altered by other external factors. Sediment load varies due to geological and geomorphological characteristics. The alteration to sediment transport can come from changes in water flow, water level, weather events, and human influence. The rainfall/precipitation characteristics, flow conditions in the river, ratio of densities of sediment and fluid, size distribution of sediment particles, etc., affect the sediment transportation process in river systems.

The observation and measurement of sediment yield from various rivers are being carried out in the country by various State agencies as well as Central agencies like Central Water Commission. The methods and equipment used for sampling suspended sediment are different from those used for deposited sediments due to different discharges. Discharge measurement is generally carried out by current meters; also sampling methods and measurements of the quantity of sediment in transport are different. The reason for these differences reflects the fact that sediment sampling methods depend on the particle distributed in depth which is carried out by integrated samplers, instantaneous grab samplers, pump samplers, and sedimentation traps, whereas sediment quantity focuses on the sediment particle fraction by sieve analysis which is not depth-dependent.

Analysis of sediment yield data facilitates to understand the distributional characteristics of sedimentation in river basins. Evolving a sediment distribution relationship over the region, consisting of different catchments, may be helpful in estimating sedimentation rates at non-sampling locations. Such estimates are being carried out using different statistical techniques. However, geostatistical analyses (Cressie 1991; Jose 1993; French 1995; Goovaerts 1997) would be better estimates of mass fluxes compared to those obtained through conventional methods. This kind of analysis is possible, as processes like river sedimentation with time-space variation may be considered as regionalized variables (Deutsch and Journel 1998) and estimation of two dimensional semivariograms allows the spatial scale of variability to be incorporated into interpolated sedimentation surfaces (French et al 1995). This enables more accurate estimation of mass fluxes compared to such estimations using

conventional methods. Therefore, geostatistical techniques can be effectively utilized in analyzing such variables to bring out their spatial structure.

Objective

The analysis of sediment yield data of long periods over a large area is helpful in investigating and understanding the distributional characteristics and behavioral pattern of sedimentation in river basins in a region. In the presented study, geostatistical analysis of sediment yield data from sixteen river basins of the State of Kerala has been undertaken with a view to reveal the spatial and temporal distribution pattern of sedimentation in the region.

Study Area

The study area consists of various river basins of Kerala state situated in the humid tropics and bound by 8° 18′N & 12° 48′N and 74° 52′ & 77° 22′E. In the study area, there are 41 rivers flowing westward and three rivers flowing eastward originating in the Western Ghats. The study area under consideration has highly undulating features with altitudes varying from sea level to thousands of meters. Based on topography, the area may be categorized into low land area, mid land area and high ranges. Since the region is characterized by steep slopes consisting of mountains and valleys, generation and transport of sediment is an integral aspect of river flows. The state is characterized by distinct rainfall patterns consisting of SW monsoon during June to September (denoted as Season-1) and NE monsoon during October to December (denoted as Season-2). The nature of rainfall, their intensities, and spatial distribution vary between these two seasons.

The mean annual rainfall in the study area is more than 3000 mm. The rainfall varies from about 900 mm in the southern parts to 3500 mm in the northern parts of the State. Further, there is spatial variation in the rainfall from coastal area to the high ranges due to orographic influences. The rainfall varies between 1400 and 6000 mm in the west to east direction. The overall rainfall contribution during SW monsoon is about 70% and NE monsoon is 25%. The contribution of NE monsoon in the southern parts of the state is much higher than that of north Kerala. Therefore, the sedimentation behavior also is expected to vary in time and space.

Geological formations in the study area are crystalline rocks, sedimentary rocks, and laterite. In the low lying areas and river valleys, recent and sub-recent sediment formations also exist. The land use patterns observed in the state can be classified into arable land, forest land, agricultural plantation, grassland, and waste land.

The present study utilizes sediment and flow data of 16 rivers from the state. The data was recorded over a period during 1989–2007 by the Central Water Commission (CWC). The sediment data had been obtained using sampling method

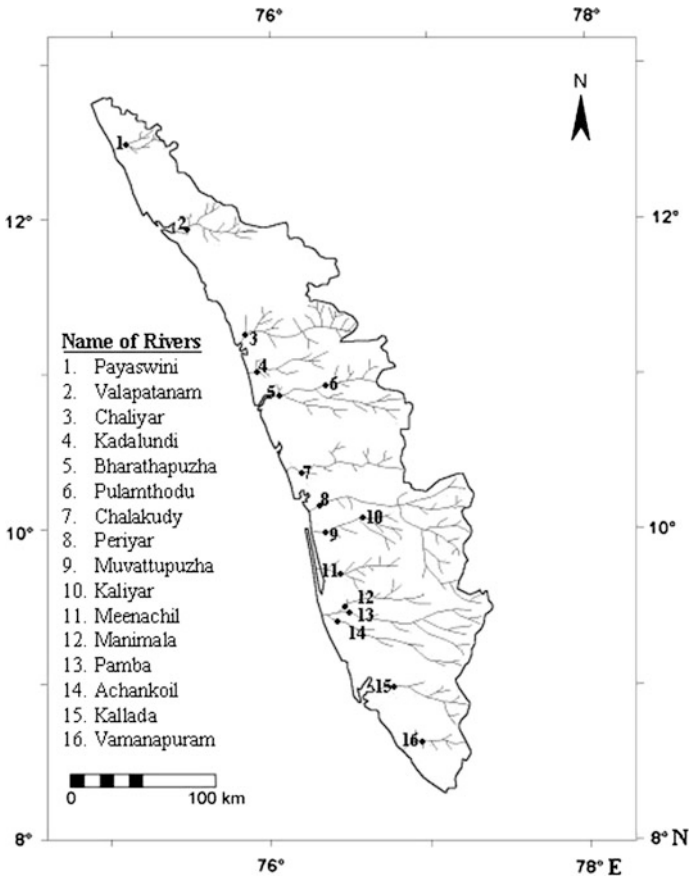

Fig. 1 Study area indicating sediment data sampling locations (Ref: C & SRO, CWC)

at the discharge measurement locations. The daily samples collected were subjected to laboratory analysis and the concentration levels for fine, medium, and coarse particles for the suspended load (Fig. 1).

Methodology

Geostatistics is the application of probabilistic methods to regionalized variables (Matheron 1963). Regionalized variables are variables that have an attribute value and a location in a two- or three-dimensional space. Geostatistics is also described sometimes as a set of techniques/tools used to analyze and predict values of a variable distributed in space or in time. With geostatistics, we can explore our sample data by constructing variogram models and producing interpolated surfaces.

Variogram

The variogram (or semivariogram) (Cressie 1991) is a function that describes spatial autocorrelation of a regional (geo referenced) variable. Autocorrelation is the correlation between elements of a series and others from the same series separated from them by a given interval. Variogram contains the property of *intrinsic stationarity* which indicates the natural increase in variance between observations of a regional variable as distance increases from each observation.

Construction of variogram includes two stages such as calculating empirical variogram and model fitting (Gringarten and Deutsch 2001; Isaaks and Srivastava 1992; Oliver and Webster 1986). The empirical variogram provides a description of how the data is related (correlated) with distance. The semivariogram function, $\gamma(h)$, was originally defined by Matheron (1963) as half the average squared difference between points separated by a distance h. The semivariogram is calculated as:

$$\gamma(h) = \frac{1}{2|N(h)|}\sum_{N(h)}\left(z_i - z_j\right)^2$$

where $N(h)$ is the set of all pair-wise Euclidean distance $i - j = h$, $|N(h)|$ is the number of distinct pairs in $N(h)$, and z_i and z_j are data values at spatial locations i and j, respectively. In this formulation, h represents a distance at spatial locations i and j, respectively. In this formulation, h represents a distance measure with magnitude only. Sometimes, it might be desirable to consider direction on in addition to distance. In such cases, h will be represented as the vector h, having both magnitude and direction.

Most variograms are defined through several parameters (Fig. 2); namely, the nugget effect (signifying the measurement error), the sill (representing the variance of the random field), and the range (distance at which data are no longer autocorrelated) (Fig. 3).

The methodology adopted for the present investigation is based on the geostatistical approach by considering the sediment yield from different rivers and different locations as regionalized variables (Deutsch 1998). The method of variogram analysis employed in the geostatistical techniques has been used for sediment yield data for distinct zones as well as different seasons.

Time series arise as recordings of processes which vary over time. A recording can either be a continuous trace or a set of discrete observations. We will concentrate on the case where observations are made at discrete equally spaced times. All the analyses have been carried out using SGeMS, the Stanford Geostatistical Modeling Software (Remy et al. 2008; Bohling 2007).

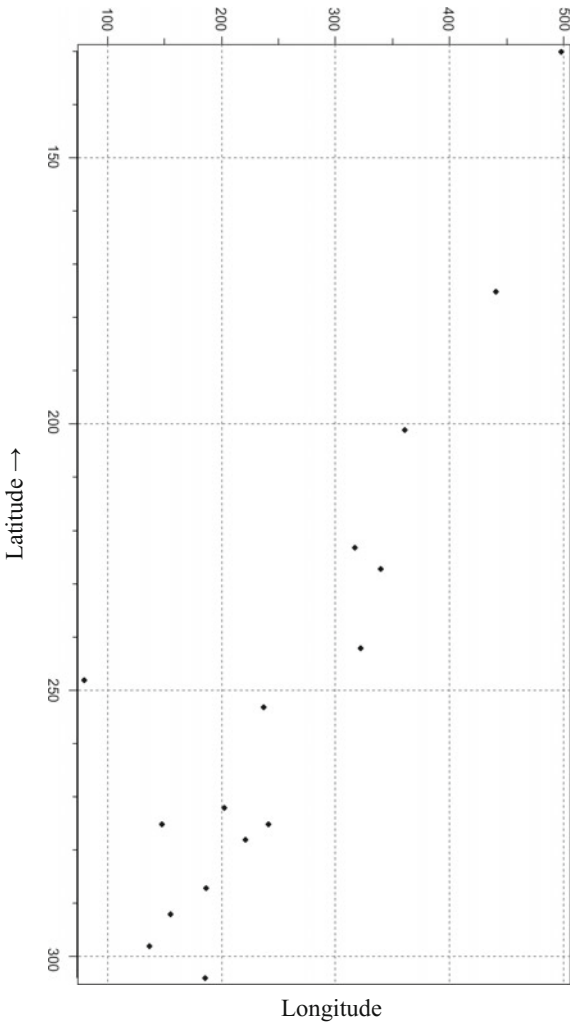

Fig. 2 Cartesian representation of location of sediment sampling points in the study area

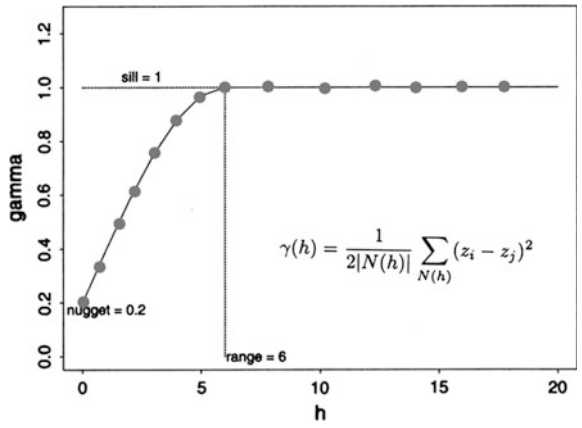

Fig. 3 Structure of a typical variogram (Ref: Bohling 2007)

The Stanford Geostatistical Modeling Software (SGeMS)

The Stanford Geostatistical Modeling Software (SGeMS) is an open-source computer package for solving problems involving spatially related variables. It provides geostatistical practitioners with a user-friendly interface, an interactive 3D visualization, and a wide selection of algorithms. SGeMS provides algorithms for multiple-point statistics. SGeMS software consists of tools like QQ plot, PP plot, scatter plot, variogram modeling, simulation techniques, Simple Kriging, Ordinary Kriging, Kriging with Trend, and Simple Kriging with Locally Varying Mean (Remy et al. 2008; Bohling 2007).

The QQ Plot

This is a graphical procedure that plots the observed values on the *X*-axis and the expected values (assuming a normal distribution) on the *Y*-axis. Note that if the sample distribution is distributed exactly like a normal distribution, the points should fall on a straight line.

The PP Plot

These are similar to QQ plots, but instead of plotting observed values, these plot cumulative probabilities (values range from 0 to 1), with observed probabilities (cumulative proportion of cases) on the *X*-axis and expected probabilities given the normal curve on the *Y*-axis. Again, if the sample were exactly normally distributed, the points would lie on a straight line.

The Scatter Plot

Scatter plots are similar to line graphs in that they use horizontal and vertical axes to plot data points. Scatter plots show how much one variable is affected by another. The relationship between two variables is called their correlation. The closer the data points come when plotted to making a straight line, the higher the correlation between the two variables, or the stronger the relationship. If the data points make a straight line going from the origin out to high *x*-and *y*-values, then the variables are said to have a positive correlation. If the line goes from a high-value on the *y*-axis down to a high-value on the *x*-axis, the variables have a negative correlation.

Computing the Empirical Variogram

The variogram for a 3D model is commonly expected to include as a minimum, three directions: (i) a vertical directional component to account for variability with respect to vertical axis; (ii) an omnidirectional component to account for global variability throughout the field, and (iii) at least one horizontal directional component covering the major directions in the field.

In order to compute the empirical variogram in the SGeMS software, it is required to provide: the number of lags, the lag separation distance, and the lag tolerance (tolerance around the lag separation). Components in the SGeMS software define the directionality of the empirical variogram: (i) azimuth: the direction on a planar surface measured between 0° and 360°, (ii) dip: the angle of descent relative to the azimuth measured between 0° and 90°, (iii) tolerance: the angle of tolerance of the directional variogram measured between 0° and 90°, and (iv) the bandwidth: the maximum width of the area resulting from the directional variogram.

Fitting the Variogram Model

The following parameters estimated from the empirical variogram model are to be provided to SGeMS software to fit the variogram model.

Nugget Effect

Initial abrupt jump to the first value at the beginning of the entire variogram model. Non-continuity only at the origin is due to either measurement error or variation at a scale smaller than the sampling distance.

Number of Structures

A variogram model may be composed using a number of (nested) variogram structures. An accurate fit to a variogram model may be best constructed using a combination of multiple model functions, especially to model variability at different scales.

Sill Contribution

Effect of the sill is the maximum variance of the variogram. Sill is the limit, represented graphically as where the function flattens out, of the variogram model after a specific distance called the range.

Type of Variogram

There are different types of variogram models. SGeMS includes models for variograms that have a sill function associated with either spherical, exponential, or Gaussian. The model type depends on the function that is used to approximate the variogram.

Ranges

Ranges along each of the three directions of the anisotropy ellipsoid in the variogram structure (maximum, medium and minimum) are used to approximate the model. Depending on the direction(s) specified these ranges help refine the shape/extent of the function.

Angles

The three angles (directions) of the 3D anisotropy ellipsoid in the variogram structure, measured in degrees, are: azimuth, dip and rake. Rotation of the angles along the orthogonal planes of a Cartesian coordinate system positions the 3D ellipsoid in space.

Kriging

Kriging is an alternative to many other point interpolation techniques. Unlike straightforward deterministic methods, such as Nearest Point, Trend Surface, Moving Average, or Moving Surface, it is a statistical method based on the theory of regionalized variables. From empirical variogram model, the interpolation function is determined. One may apply simple Kriging, conditional Kriging or any other variation depending up on the application.

Results and Analysis

The rainfall in the region varies spatially from west to east as well as from south to north and also varies temporally season-wise. Therefore, geostatistical analysis of the sediment yield data has been carried out for distinct cases based on regional and seasonal variations. Northern and southern regions were treated separately. Also,

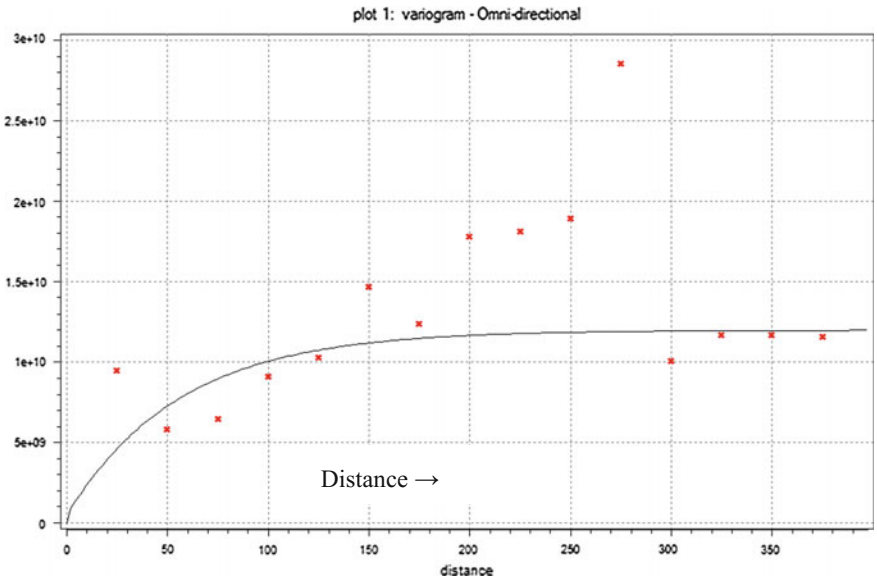

Fig. 4 Variogram model for the study area

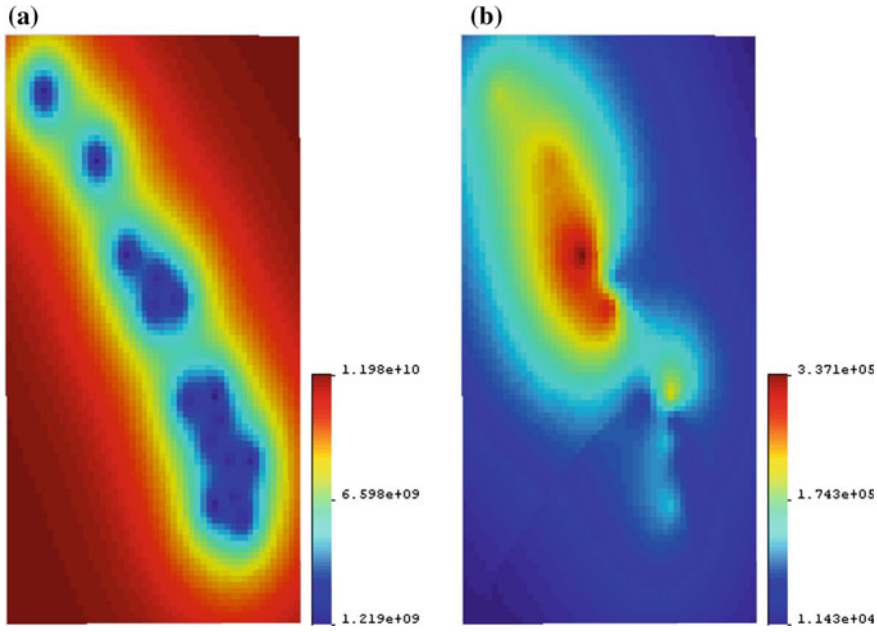

Fig. 5 **a** Kriged sediment values for the study area based on the variogram, **b** variance of the Kriged field in **a**

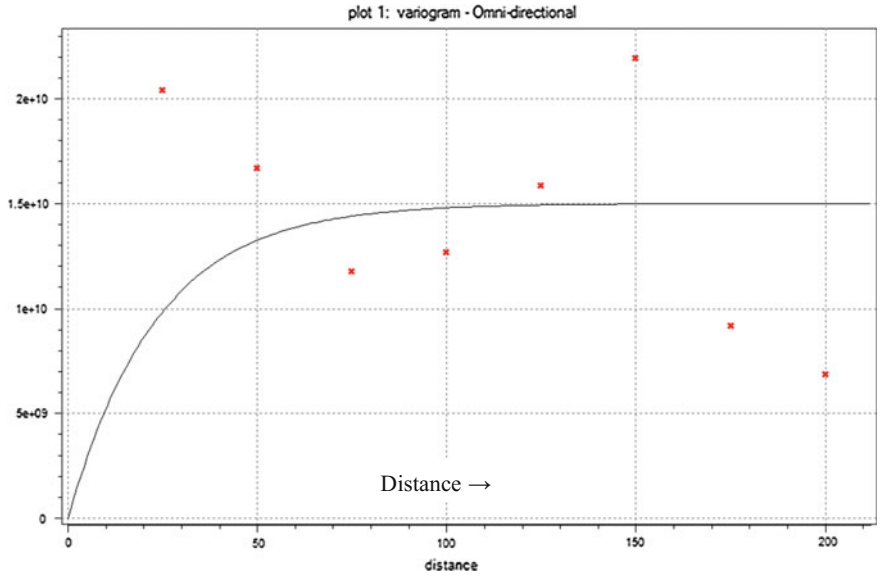

Fig. 6 Variogram model for sediment data of north region of the study area

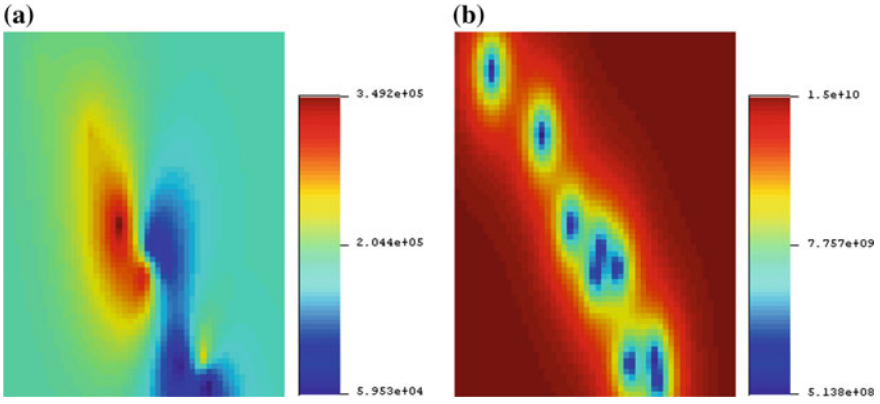

Fig. 7 **a** Kriged sediment values for the north region of the study area, **b** variance of Kriged field in **a**

seasonal variations with regard to southwest monsoon and northeast monsoon were also considered. The long-term averages of the data were computed for various locations and used for the analysis. The region was portioned into the north zone and the south zone. Also, the two monsoon seasons namely, SW monsoon and NE monsoon, were also considered separately (Figs. 4, 5, 6, 7, 8, 9, 10, 11, 12 and 13).

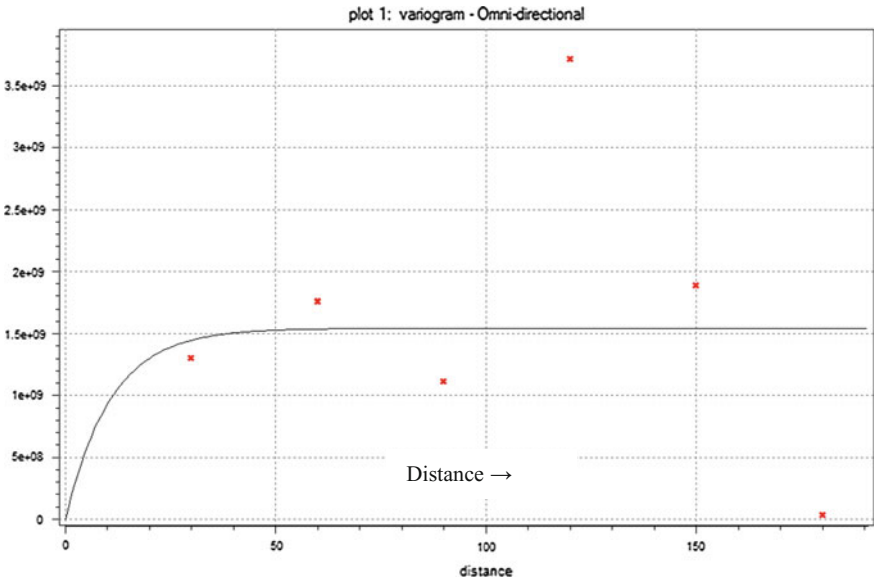

Fig. 8 Variogram model for sediment data of South region of the study area

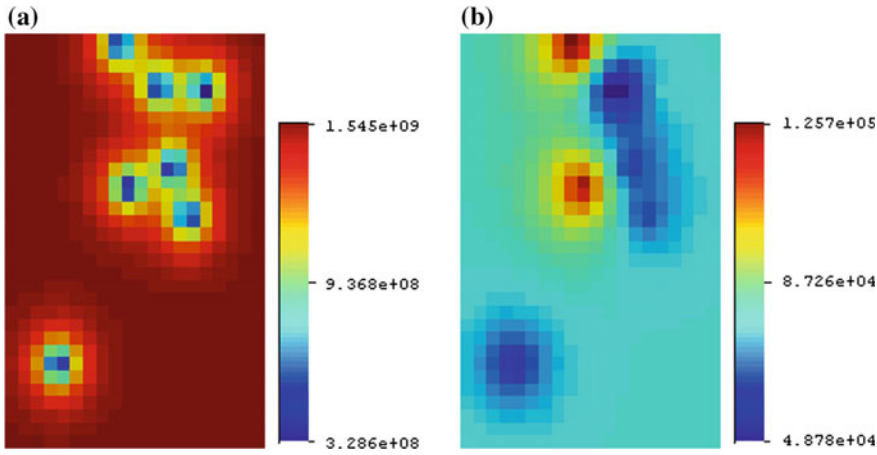

Fig. 9 **a** Kriged sediment values for south region of the study area, **b** variance of Kriged field in **a**

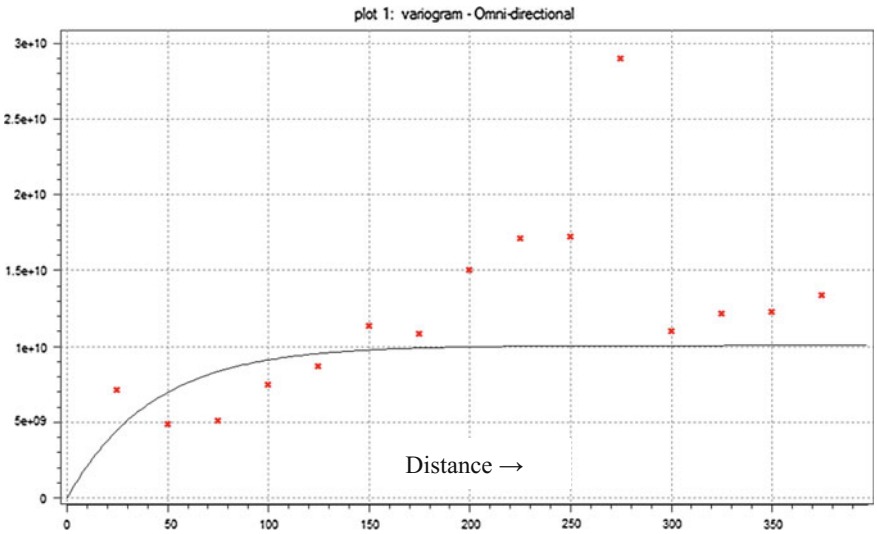

Fig. 10 Variogram model for sediment data of the study area for southwest monsoon

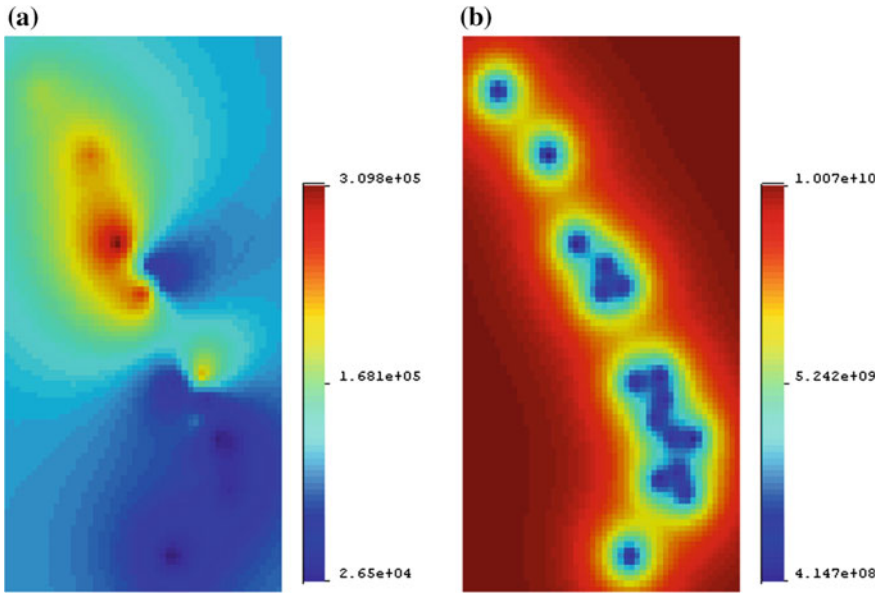

Fig. 11 **a** Kriged sediment values for the study area for southwest monsoon, **b** distribution of variance of Kriged field in **a**

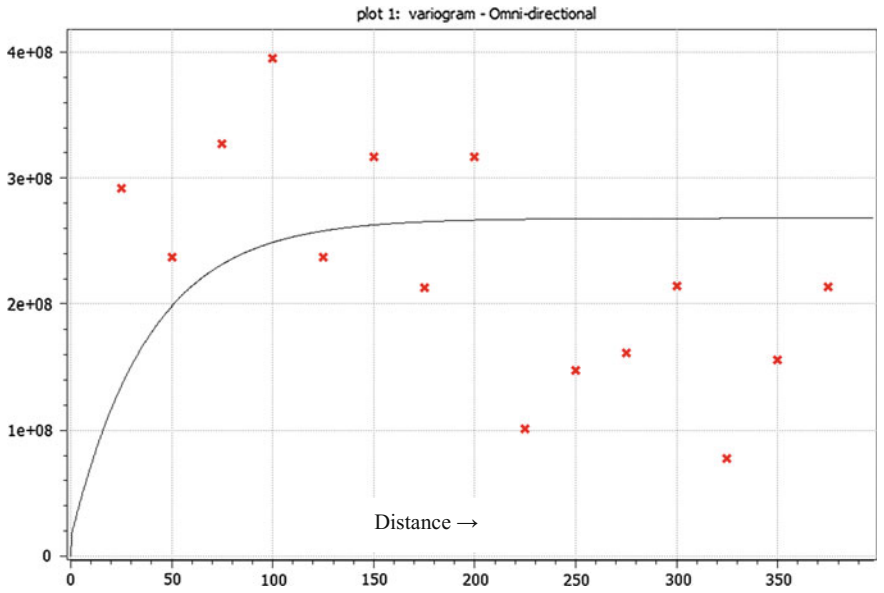

Fig. 12 Variogram model for sediment data of the study area for northeast

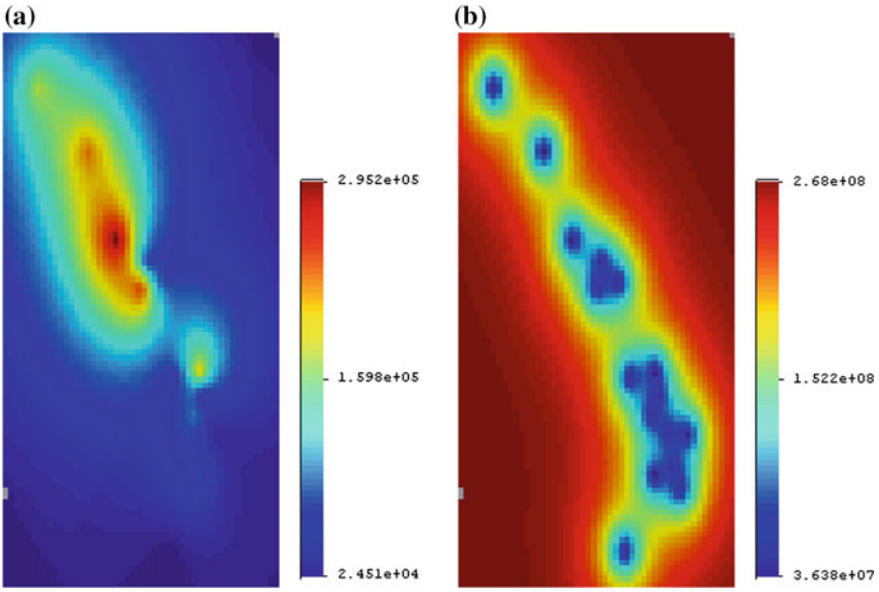

Fig. 13 **a** Kriged sediment values for the study area for NE monsoon, **b** variance of Kriged field in **a**

Discussion

Spatial analysis of sediment yield data of the study area has been carried out using geostatistical tools. The software SGeMS (Remy et al. 2008; Zhang 2011) has been utilized for the purpose. Various cases have been considered for the analysis giving due consideration to the regional variations, seasonal variations as well as monsoonal behavior in the northern and southern parts of the study area. The long-term average of the sediment data has been computed using long records of sediment data, and the long-term mean value of each data sampling location has been used for the spatial analyses. For preprocessing the data, various graphical techniques like scatter plots, QQ plots, and PP plots have been employed.

In the first case, data of the whole region is taken together and did the analysis. In the second and third cases, the study is divided into two zones of north and south regions separately to investigate any regional disparity. In the other cases, seasonal variations of the monsoonal rainfall characterized by the southwest and northeast monsoon have been analyzed separately for the whole area as well as for the designated zones also.

Using the corresponding data, empirical variograms were calculated with appropriate parameters. Using the calculated parameters, variogram models were fitted. In general, variogram models of the exponential type were found to be fitting for the various cases. The evolved variogram models were used to simulate the spatial sediment distribution using simple Kriging method. The mean and variance values for different cases are given in Table 1.

It may be seen that the mean value of north region is higher than that of the south region. Analysis of seasonal variation due to SW monsoon and NE monsoon (post monsoon) showed differences in sedimentation pattern during the two rainy seasons and also regional disparities existed. The correlation structure of the whole area revealed that the sedimentation pattern is much more consistent in the northern parts of the study area compared to the south region. North region has about 70%, south region has 45%, and whole region has 37% of spatial correlation. However, during NE monsoon, north region indicated less spatial correlation while southern region showed higher spatial correlation.

Table 1 Mean and variance values of sediment distribution for various cases

Region	Mean		Variance	
	SW monsoon	NE monsoon	SW monsoon	NE monsoon
Whole study area	112178	26309.4	1.01e10	2.5e8
North region	160998	23537.8	1.21e10	2.83e8
South region	49408.4	29873.5	9.03e8	2.28e8

Conclusion

Analysis of sediment distribution pattern of west-flowing rivers of Kerala has been carried out by giving due consideration to regional as well as seasonal aspects. The sediment data has been partitioned into regional zones as well as seasonal (SW and NE monsoonal) basis to investigate variability. North region has yielded comparatively good spatial correlation structure in both the monsoon seasons. During NE monsoon, southern region yielded more sediment compared to northern region, possibly due to intense rainfall in the south during NE monsoon. However, sediment contribution from the northern region during SW monsoon is much higher compared to the southern region. This may be attributed to the heavy orographic rainfall spells in the Western Ghats of the northern region during SW monsoon. For the south region, sediment values have a variance of about 41% during SW monsoon, while it is more than 85% during NE monsoon. Therefore, the sediment yield in the southern parts is highly variant during the NE monsoon period.

The geostatistical analyses revealed that the sedimentation characteristics in Kerala river catchments tend to increase from north to south during NE monsoon. During SW monsoon season, northern region is yielding more sediment compared to southern region. The quantitative increment in sediment yield toward the southern parts of the state during NE monsoon may be due to the high intensity of the storms during that period. The study revealed that maximum spatial correlation in north region compared to south region. Also, seasonal variation is observed between SW monsoon and post monsoon periods.

Geostatistics is a powerful tool to help us characterize spatial variability. The study demonstrates the usefulness of spatial analysis of sediment yield data over long periods in investigating and understanding the distributional characteristics and pattern of sedimentation in river basins.

References

Bohling G (2007) S-GeMS Tutorial Notes presented in Hydro-geophysics: theory, methods, and modeling, Boise State University, Kansas Geological Survey; http://people.ku.edu/~gbohling/BoiseGeostat

Cressie NAC (1991) Statistics for spatial data. Wiley, New York, pp 920

Deutsch CV, Journel AG (1998) GSLIB: geostatistical software library and users's guide. Oxford University Press, New York

French JR, Spencer T, Murray AL, Arnold NS (1995) Geostatistical analysis of sediment deposition in two small tidal wetlands, Norfolk, U.K, J Coast Res 11(2):308–321

Goovaerts P (1997) Geostatistics for natural resources evaluation. Oxford University Press, New York, p 512

Gringarten, E, Deutsch CV (2001) Variogram analysis and interpretation. Math Geol 33(4)

Isaaks EH, Srivastava RM (1992) An introduction to applied geostatistics. Oxford University Press, New York, p 561

Jose MK (1993) Random simulation of spatial rainfall, Masters' Thesis. International Institute for Infrastructural, Hydraulic and Environmental Engineering (IHE). Delft, The Netherlands, pp 99
Matheron G (1963) Principles of geostatistics. Econ Geol 58:1246–1266
Oliver MA, Webster, R (1986) Semi variograms for modeling the spatial pattern of landform and soil properties. Earth Surf Process Land 11(5):491–504
Remy N, Boucher A, Wu J (2008) Applied geostatistics with SGeMS: a user's guide. Cambridge University Press, UK
Zhang Y (2011) Introduction to Geostatistics—Course Notes

Study of Mineralogical Composition of Sediment in Brahmaputra River in Urban Stretch of Guwahati City, Assam, India

Mamata Das and Triptimoni Borah

Abstract High sediment load is an integral component of the Brahmaputra River System. Due to its sheer amount and the complex behavior of the sediment transport, its control has remained a challenge. In this study, an attempt has been made to study the mineralogical composition of suspended sediment in unban stretch of River Brahmaputra. In order to understand the properties of the sediment, Scanning electron microscope, X-ray diffractometer, Atomic Absorption Spectrometer, and Particle size distribution analysis are carried out. In the meanwhile, the composition of suspended sediment is also evaluated so as to know about the present scenario of the river system that can be used for water supply in Guwahati city. Artificial neural network (ANN) and nonlinear regression (using dataFit software) were developed, to predict both sediment concentration and concentration of chemical parameters of sediment. The nonlinear nature of suspended sediment load time series necessitates the utilization of nonlinear methods for simulating the suspended sediment load. Si, Al, Fe, Mg, Ca, Na, and K were analyzed in AAS for determining chemical composition of the sediments. Here, ANNs model is developed using the toolbox of the MATLAB software and also compared with results of dataFit software models.

Keywords Brahmaputra river · Sediment · Particle size · Mineralogy
Suspended sediment load · ANN · dataFit

M. Das (✉) · T. Borah
Department of Civil Engineering, Assam Engineering College,
Guwahati 781013, Assam, India
e-mail: mamtadas4@gmail.com

T. Borah
e-mail: btriptimoni@gmail.com

V. P. Singh et al. (eds.), *Hydrologic Modeling*, Water Science
and Technology Library 81, https://doi.org/10.1007/978-981-10-5801-1_18

Introduction

Solid particles which move or might have moved by flow channels are mainly defined as sediments (IS:4890-1968). Due to the action of water, wind, ice, and human activities like cultivation, clods and aggregates of soil of the catchment area are broken down into small particles, are thrown into suspension, and are carried away as sediment. The total amount of eroded material which travels from a source to the downstream measuring point is termed as 'sediment yield.' These sediment yields depend on significant physical features such as size, slope of the catchment's area, land use, erodibility of the soil and significant hydrologic parameters such as rainfall, runoff, peak values of runoff. However, different engineers and agriculturist face numerous problems along the channel as the sediments raise the stream bed and as a result high flood and inundation occurs. It silts up irrigation and navigation channels making them less efficient (WAPCOS 1993). Apart from this, high sediment deposit causes some tributaries to change their courses which may cause extensive hazard to the nearby areas.

The Brahmaputra is a high sediment-carrying river (Fig. 1). The average annual sediment load of Brahmaputra at Pandu, Assam, is more than 402 million tones/year (Goswami 1985). In the year 1950, the earthquake occurred in Assam (scale 8.7 richter) had drastically affected the gradient of this river, stopping the flow temporarily and bringing about high flooding and accumulation of high volume of sediments. The Brahmaputra is a typical braided river with a wide bed in which the river channels meander, the bed being 15–19 km in reaches with constructed locations where the river is confined to less than 3 km (WAPCOS 1993). The sediment load in this river system is believed to have increased due to excessive deforestation that has taken place in the upper catchments of both northern and southern tributaries (Master Plan of Brahmaputra Basin, Part I, Main stream 1986). The quantity of suspended sediment transport in the Brahmaputra is more variable than the quantity of water discharged, as revealed by the coefficient of variation, which is 0.15 for mean annual flow and 0.85 for sediment discharge for the period 1971–79 (Sarma 2005).

Over the last fifty years, extensive research has been carried out to predict bed load, suspended load, and total load. Though different sediment transport models were developed to predict the accuracy but the results obtain doesnot provide much improvement. Stummeyer et al. (2001) studied the composition of suspended matter from Ganges-Brahmaputra sediment dispersal system during low sediment transport season. They observed that chemical and mineralogical analyses of the suspended matter show changes in its composition with distance from the source. Therefore, it is essential to know the chemical parameters of the suspended load. This study mainly concerned to study the mineralogical composition of suspended sediment of River Brahmaputra in urban stretch of Guwahati city using SEM, XRD, EDX, and AAS, to analyze the particle size distribution and to estimate the sediment load using artificial neural network (ANN).

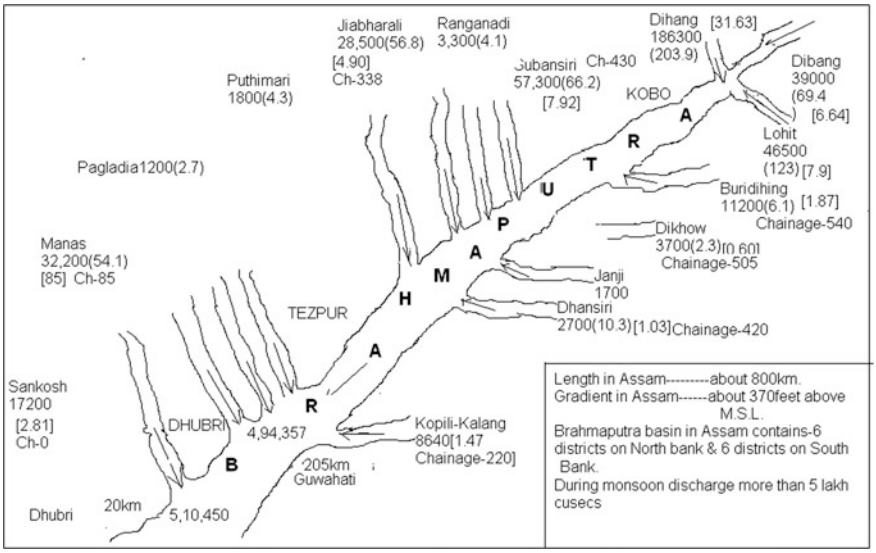

Fig. 1 Average annual water discharge (in million cubic meters), of Brahmaputra in Assam [Sediment load data, whenever available, given in *brackets*, figures in *sq. brackets* indicate percentage contribution, and figures in *parenthesis* indicate sediment load (in million tones)]

Composition of Principal Minerals in Sediments

The mineral particles in rivers are an assemblage of particles of different types, which reflects the rock types and weathering condition source areas. Mineral particles found in suspended matter and sediments are those that are resistant to weathering. Following is a list of major minerals generally present in sediments:

Quartz	SiO_2
Feldspar	$(K, Na, Ca)(Al, Si)_4O_8$
Muscovite	$KAl_2AlSi_3O_{10}(OH)_2$
Biotite	$K(Mg, Fe)_3AlSi_3O_{10}(OH)$
Orthoclase	$KAlSiO_8$
Albite	$NaAlSi_3O_8$
Anorthite	$CaAl_2Si_2O_8$
Clay minerals	
Kaolinite	$Al_4(OH)_8[Si_4O_{10}]$
Chlorite	$(Al, Mg, Fe)_3(OH)_2[(Al, Si)_4O_{10}]Mg_3(OH)$

(continued)

(continued)

Illite	$(K, H_2O)Al_2(H_2O, OH)_2[AlSi_3O_{10}]$
Montmorillonite	$(Al_{2-X}Mg_X)(OH)_2[Si_3O_{10}]$
Calcite/aragonite	$CaCO_3$
Opal	SiO_2 (amorphous)
Limonite	FeO·OH

Artificial Neural Network

Artificial neural networks are important alternatives to the traditional methods of data analysis and modeling. In this study, feed-forward back propagation (FFBP) and radial basis function (RBF) were written in MATLAB for ANN simulations.

The feed-forward back propagation has one-way connections from input to output layers. Back propagation refers to the propagation of error back through the network from output layer through hidden layers toward input layer. Back propagation needs feed-forward neural network, where in interlayer connections feed the neuron's output into the neurons in the next forward layer.

The general mathematical forms of the output units in FFBP network are as follows:

$$\text{net}_{pj}^{h} = \sum_{i=1}^{N} w_{ji}^{h} x_{pi} + \theta_j^h \tag{1}$$

where input vector, $x_p = (x_{p1}, x_{p2}, \ldots x_{pN})^t$, is applied to the input layer of the network. The input unit distributes the value to the hidden, w_{ji}^h is the weight on the connection from the ith input unit, and θ_j^h is the bias term (this term is a weight on a connection that has its input value always equal to 1).

Assume that the activation of this node is equal to the net input; then, the output of this node is

$$i_{pj} = \int_{j}^{h} \left(net_{pj}^{h} \right) \tag{2}$$

The equations for the output nodes are

$$\text{net}_{pk}^{o} = \sum_{j=1}^{L} w_{kj}^{o} i_{pj} + \theta_k^o \tag{3}$$

$$o_{pk} = \int_{k}^{o} \left(\text{net}_{pk}^{o} \right) \tag{4}$$

where the 'o' superscript refers to the quantities on the output layer.

Radial Basis Function

Radial basis function networks are alternative universal approximations widely used for function approximation. A RBF network consists of three layers, namely the input layer, a single hidden layer of nonlinear processing neurons, and the output layer. Any function can be approximated with the help of radial basis network as shown in Fig. 2. The general mathematical forms of the output units in RBF network are as follows.

Any function 'ϕ' can be approximated using RBF networks as follows

$$\phi = \sum_{k=1}^{m} w_k g_k(\|\boldsymbol{x} - \boldsymbol{x_k}\|, c_k) \tag{5}$$

where $\boldsymbol{x} = (x, y)^{\mathrm{T}}$, $\boldsymbol{x_k} = (x_k, y_k)^{\mathrm{T}}$ is a two-dimensional vector called center, $\|\boldsymbol{x} - \boldsymbol{x_k}\|$ is the Euclidian norm, $\boldsymbol{c_k}$ is called spread parameter, w_k are weights, $g_k(\|\boldsymbol{x} - \boldsymbol{x_k}\|, c_k)$ is the radial basis function (RBF), and m is the number of neurons. For each neuron in the hidden layer, Euclidean distance between the associated centers and input to the network is computed. The output of the network is computed as a weighted sum of hidden layer outputs.

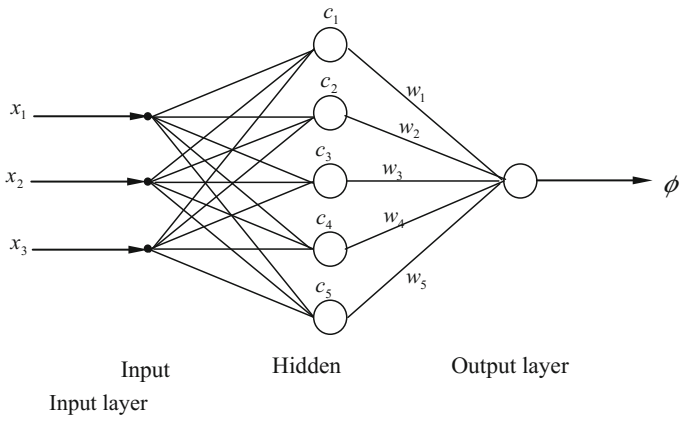

Fig. 2 Architecture of a radial basis function neural network

$$\text{Multiquadrics: } g_k(x) = \left(\|\boldsymbol{x} - \boldsymbol{x_k}\|^2 + c_k^2\right)^{1/2} \tag{6}$$

$$\text{Inverse Multiquadrics: } g_k(x) = \left(\|\boldsymbol{x} - \boldsymbol{x_k}\|^2 + c_k^2\right)^{1/2} \tag{7}$$

$$\text{Gaussians: } g_k(\boldsymbol{x}) = \mathrm{e}^{-c_k^2\|\boldsymbol{x}-\boldsymbol{x_k}\|^2} \tag{8}$$

$$\text{Thin Plate Splines: } g_k(x) = \|\boldsymbol{x} - \boldsymbol{x_k}\|^2 \log\|\boldsymbol{x} - \boldsymbol{x_k}\| \tag{9}$$

Figure 2 shows the variation of the different radial basis functions for the case with only one center (neuron) at (0.5, 0.5). Due to the RBFs spherical symmetry about the centers, they are called radial as shown in Fig. 2.

DataFit Software

dataFit is a science and engineering tool that simplifies the tasks of data plotting, regression analysis (curve fitting), and statistical analysis. Here, dataFit apart from similar curve fitting and regression programs is its ease of use. With the combination of the intuitive interface, online help, and wide range of features, it is a tool that is used effectively by both beginners and experts.

Study Area

This study is carried out in a particular location of Guwahati city that is the Pandu location. The city extends latitudinally from 26° 5′N to 26° 12′N and longitudinally from 91° 24′E to 91° 51′E. The average annual temperature is 24.2 °C with extremes ranging from 40.6 °C recorded on April 24, 2014, to 3.0 °C recorded in January, 1964. Guwahati is one of the fastest growing cities in India. The city's population grew from just 200,000 in 1971 to more than 500,000 in 1991. In the 2001 census, the city's population was 808,021. By 2012, the population of the rapidly growing metropolitan area had risen to 1.5 million. Pandu, located on the banks of the River Brahmaputra at the western part of the city, is an ancient urban area that acted as the chief military base for the Ahoms against external invasions. Due to extensive fortification ('Gorh') surrounding Pandu, it acts as a natural river harbor and is formally called Gar-Pandu. Pandu port falls under Dhubri-Sadiya National Waterway-2 and is an important terminal cum transit point for goods and cargo as well as passenger and tourist vessels. Construction of both low-level and high-level jetty of fixed terminal, capable of handling container vessels, has been completed and has further enhanced revenue generation for the city.

Collection of Sample

The samples of suspended sediment were collected accordingly for pre-monsoon and post-monsoon. Samples were collected in both cross section and longitudinal section. The concentration of suspended load not only changes from point to point in a cross section but also fluctuates from moment to moment at a fixed point (IS:4890). So while collecting the samples, utmost efforts were made to maintain the actual location at each time by using GPS (global positioning system). The samples were collected at a month interval.

The sampling points were along longitudinal section and cross section of the river. Figure 3 shows the lateral position of the sampling, and Fig. 4 shows the vertical profile of the sampling station at different points at Pandu location. In this study, feed-forward back propagation (FFBP) and radial basis function (RBF) were written in MATLAB for ANNs simulations. This includes daily discharge, top width, and velocity data describing the input and sediment load data describing the output. These models were prepared using the 10 years of CWC dataset.

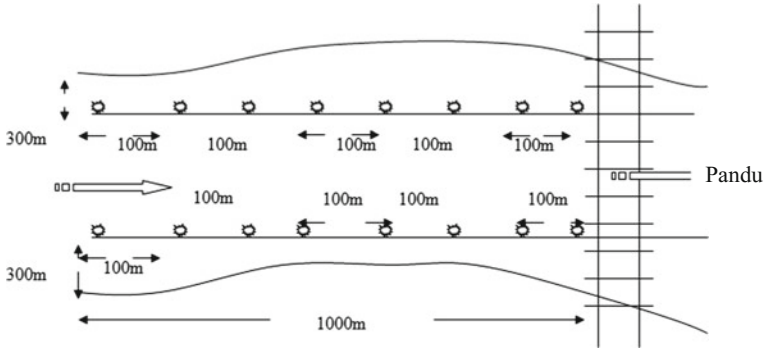

Fig. 3 Plan view of the study area with sampling location (not in scale)

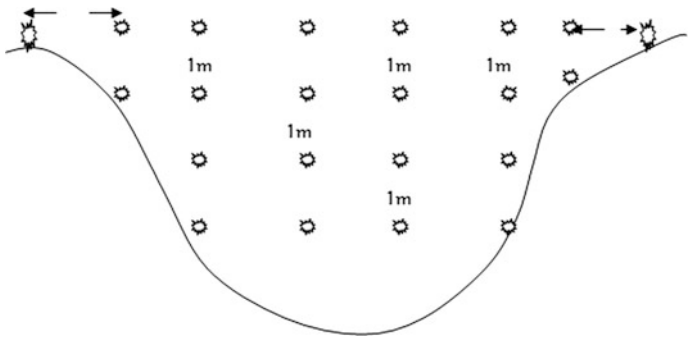

Fig. 4 Cross-sectional view of the study area with sampling location (not in scale)

Another trial is made by using the dataFit software for nonlinear interpretation. dataFit is a science and engineering tool that simplifies the tasks of data plotting, regression analysis (curve fitting), and statistical analysis.

Results and Discussion

Samples of suspended sediment and of sediment deposited on the river bank were analyzed in the laboratory to determine the grain size distribution and their mineralogical and chemical composition. The major sediment constituents were studied using scanning electron microscope (SEM), atomic absorption spectrometer (AAS), and X-ray diffractometer (XRD). These field data were eventually used for attempting predictive models. Two methods, artificial neural network (ANN) and nonlinear regression (using dataFit software), were developed, to predict both sediment concentration and concentration of chemical parameters of sediment. The neural network was trained using discharge and suspended sediment load data collected for Brahmaputra River at the downstream location, Pandu.

Mineralogy

X-ray Diffractometer (XRD) Analysis

X-ray diffraction analyses of the samples collected from the Pandu sites of River Brahmaputra in both pre-monsoon and post-monsoon period are carried out and observed that quartz represents more than 30% of all the sediments. From the observation, it is observed that quartz and clay to be the dominant minerals with lesser amount of feldspar and dolomite (Table 1). K-feldspar and plagioclase were also present. In few samples, dolomite and pyrite were present but in small amounts. Though there is likelihood of other minerals like carbonates also being present, but these were not within detectable limit in the present study. Figure 5 shows the 2θ value for the Pandu sample. The relative mineralogical composition of the sediment sample is shown in Table 1. From Table 1, it is clear that the percentage of quartz was lesser than clay percentage in Pandu.

Table 1 Relative mineralogical composition of the bulk sediment at Pandu

Bulk composition	wt%
Quartz	33.90
Feldspar	25.37
Calcite	1.02
Dolomite	Not detected
Siderite	0.6
Pyrite	1.45
Total clay	37.66

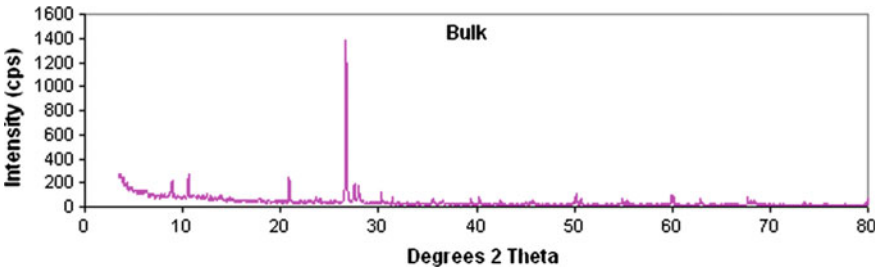

Fig. 5 Results after bulk analysis at Pandu

Fig. 6 Concentration of different elements at Pandu station by SEM

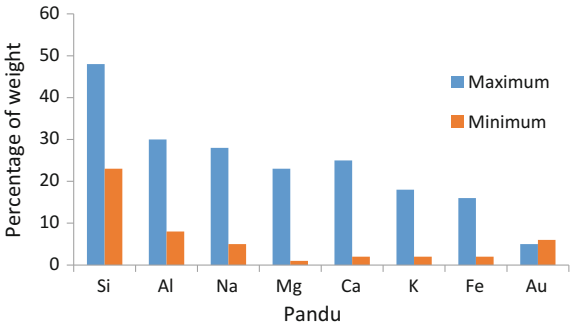

Element Analysis by SEM/EDX

Samples from Pandu site were selected for elemental analysis. Figure 6 gives the concentration of different elements in the sediment samples collected during monsoon period. From Fig. 6, it is observed that the concentration of Si is more in both pre-monsoon and post-monsoon period than the other elements Al, Na, Mg, Ca, K, Fe, and Au. The general decrease in the heavy metal concentration in the coarser fraction was likely due to increase in population of the detrital minerals, mostly quartz and feldspar derived from rock weathering (Vaithiyanathan et al. 1992).

Metal Distribution in the Sediment by Atomic Absorption Spectrophotometer (AAS) Analysis

Since EDX analysis is not fully representative of a whole location, so the analysis of concentration of metals in suspended sediment was carried out in atomic absorption spectrophotometer (AAS). The metal concentration (μg/g) of Fe, Cu, Pb, Zn, Cr, Mn, Mg, Na, K, Ca, Al, and Si of suspended sediment in Pandu location is

Table 2 Heavy metal distribution of suspended sediment in Pandu location (μg/g)

Average value	Fe	Cu	Pb	Zn	Cr	Mn	Mg	Na	K	Ca	Al	Si
Pre-monsoon	23,900	19	15	60.4	123	1352	1220	525	4563	8343	25,150	21,7750
	32,370	18.2	18.5	44.5	130	2487	1745	693	4002	9623	16,550	34,2500
	25,240	11.5	11.2	59	187	1874	1200	412	4980	8123	34,600	21,5500
	33,200	15.6	15.5	45	193	1352	1546	617	3925	8645	13,600	29,4000
	15,154	16.5	12.6	60	156	2854	1325	753	4120	8125	21,550	23,4780
Post-monsoon	44,850	18	17.2	46.2	215	2880	1540	411	4498	9123	20,500	16,2500
	35,150	17.5	19.98	84.1	222	3775	1771	450	4390	9350	34,700	29,5054
	24,750	17.9	11.7	65.8	120	3620	766	680	4010	8574	49,560	21,5600
	36,300	12.8	18.29	44	156	1845	935	475	4568	8215	22,750	21,5670
	25,350	16.55	12.95	49.75	128	2590	2918	530	4800	7893	16,050	24,6080
	23,650	18.8	16.2	52.65	254	2940	1874	440	4864	9526	57,700	29,4050
	20,550	19.35	14.8	58.2	244	1365	1231	578	4710	8935	21,700	21,5430

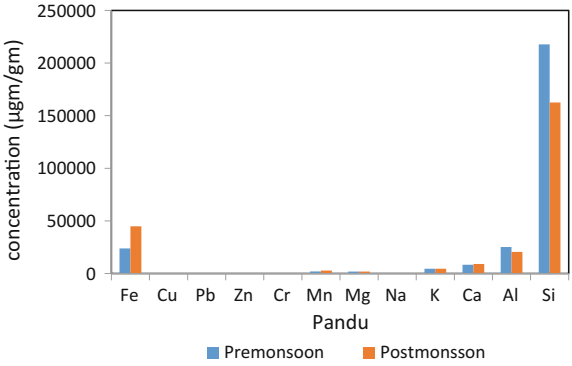

Fig. 7 Concentration of different elements at Pandu location for pre-monsoon and post-monsoon by AAS

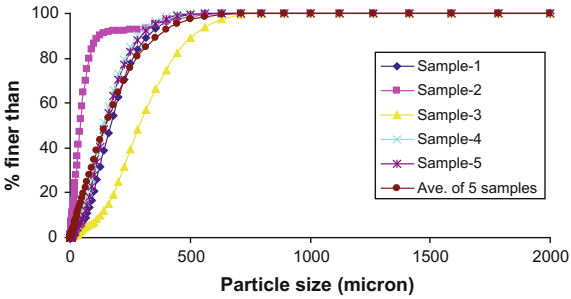

Fig. 8 Change of grain size distribution curve (five samples) at Pandu

tabulated in Table 2. The concentration of different elements at Pandu location of pre-monsoon and post-monsoon by AAS is given by Fig. 7. From Fig. 7, it was observed that Si, Al, and Fe percentage are high as compared to other metal.

Particle Size Parameters of Suspended Sediment

In the pre-monsoon and post-monsoon season, the d_{50} and d_{85} value in Pandu site varies from 5 to 10 µm and 15 to 20 µm. For all the sample, the cumulative curves stared from zero, indicating the smallest particle size of the sediment is less than 1 µm as shown in Fig. 8.

Application of ANNs to the Data

In this study, feed-forward back propagation and radial basis functions (RBF) were written in MATLAB for ANN simulations. The ANNs network structure consisted of three layers, i.e., input layer, single hidden layer, and output layer. The input layer was prepared using different hydro-metrological data. The application of the

ANNs to time series data consisted of two steps. The first step was the training of the neural networks. This includes daily discharge, top width, and velocity data describing the input and sediment load data describing the output to the network so as to obtain the interconnection weights. Once the training stage was completed, the ANNs were applied to the testing data.

Suspended Sediment Load Simulation Using Feed-Forward Back Propagation with Discharge, Top Width, and Velocity Data

Here, the suspended sediment load simulation study was carried out considering discharge, top width, and flow data. The discharge data series employed in this study are daily discharge which are collected from the CWC Dept. The training and testing periods for ANN application are from 1993–97 to 1997–98, respectively, which is given in Table 3 for model 1. To develop model 2, same code was used but with different dataset as given in Table 4. The plots obtained for testing periods FFBP with different dataset are presented in Figs. 9 and 10.

For RBF, several iteration numbers changing from 5 to 100 were tested. The iteration number equals to 80 provided best performance criteria. Various spread values between 0 and 1 were considered for RBF simulations. The spread providing best performance criteria for each RBF configuration is given in Table 5. The input and output data were scaled between −1 and +1 to overcome problems associated with upper-limit and lower-limit saturation. The performance evaluation measures were the root-mean-square error (RMSE) and the coefficient of determination (R^2) between simulated and observed sediment load.

Table 3 Training and testing for ANN application

	Training				Total	Testing		Total
Study period	93–94	94–95	95–96	96–97	500	96–97	97–98	100
No. of data	137	146	125	92		34	66	

Table 4 Training and testing for ANN application

	Training				Total	Testing
Study period	98	99	00	01	462	02
No. of data	108	121	98	135		109

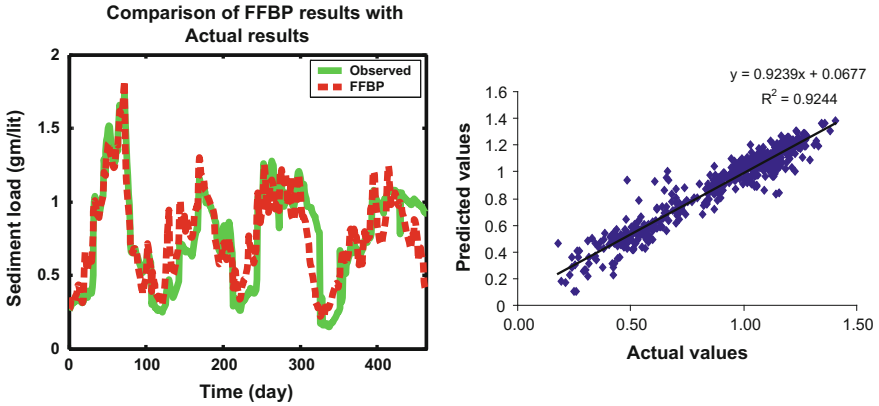

Fig. 9 Comparison of observed and FFBP predicted sediment concentration model 1

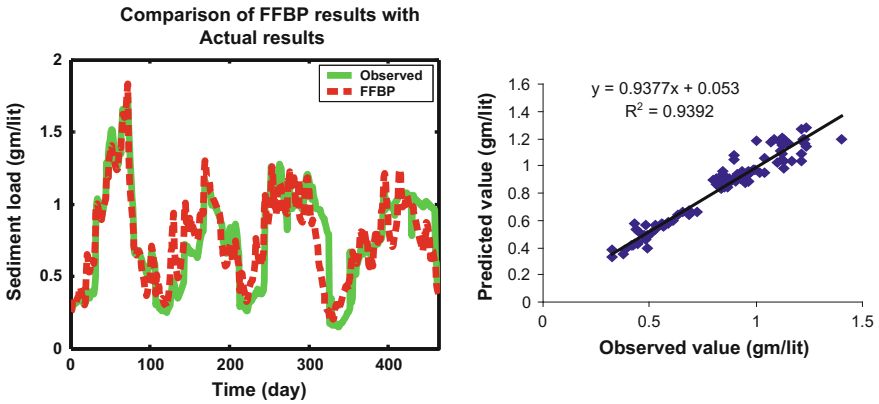

Fig. 10 Comparison of observed and FFBP predicted sediment concentration model 2

Table 5 Performance criteria (MSE and coefficient of determination) values for ANNs obtained for training and testing periods model 3

RBF						
Training				Testing		
Spread parameter	MSE	R^2	No. of neurons	Spread parameter	MSE	R^2
0.1	8.7123	0.8006	50	0.1	7.2401	0.3129
0.2	6.8466	0.8434	60	0.2	7.133	0.4563
0.3	5.4814	0.874	70	0.3	6.1257	0.6329
0.4	4.185	0.9244	80	0.4	4.135	0.8261
0.5	3.3012	0.9271	90	0.5	5.355	0.7953
0.6	2.9754	0.9319	100	0.6	6.2545	0.6563

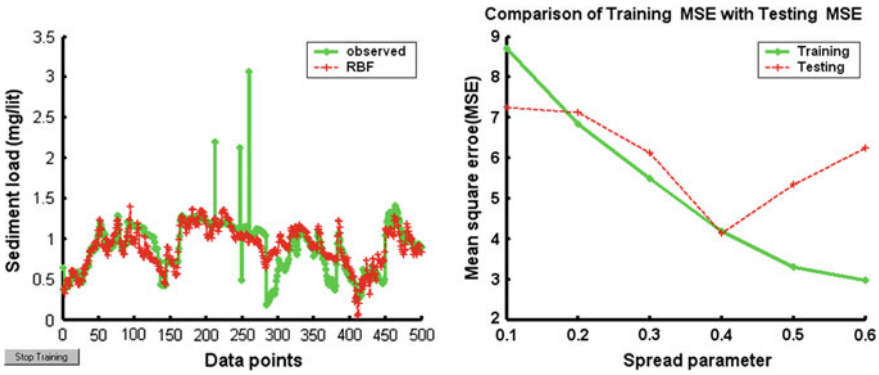

Fig. 11 Comparison of observed and RBF predicted sediment concentration at Pandu station

Suspended Sediment Load Simulation Using Radial Basis Function with Discharge, Top Width, and Velocity Data

In this part also, suspended sediment load simulation study was carried out considering discharge, top width, and velocity. The discharge data series employed in this study are daily discharged which are collected from the CWC Dept. The training and testing period are presented in Table 4.

A network structure with 0.4 spread parameter and having 80 neurons in the input layer provided the best performance criteria, i.e., lowest MSE and highest R^2 value for both training and testing. The input layer consisted of three dataset covering a time period of four years. It is observed that error percentage is gradually decreasing for training with the increase in spread parameter but in case of testing due to variation of spread parameter and neuron, first it is gradually decreasing and then it starts increasing, and this is shown in Fig. 11. The R^2 value between observed and predicted was 0.9244.

Model Using Data Fit Software

Suspended Sediment Load Evaluation Model by Using CWC Data

The first attempt was made by considering the discharge, top width, and velocity as independent variable and sediment load was considered as dependent variable.

From Figs. 12 and 13, it is clear that the input data are in excellent agreement with the obtained by the regression using dataFit software for both the model 1 and model 2.

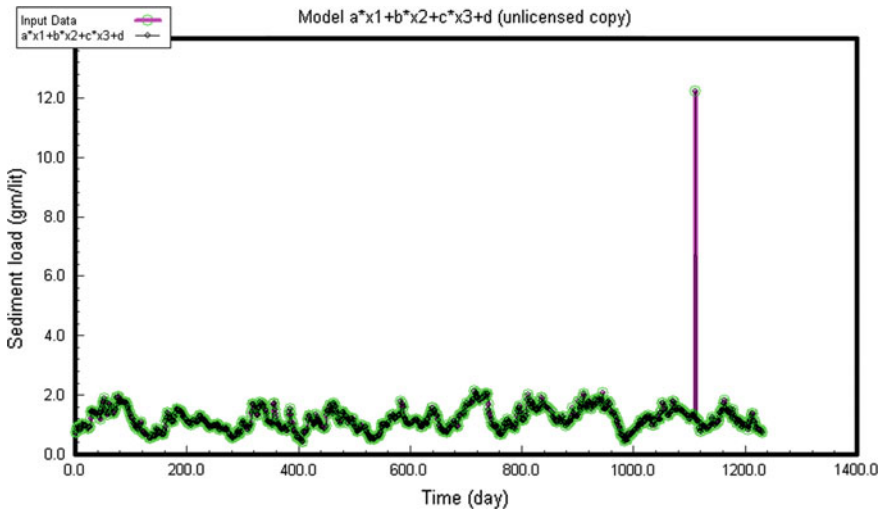

Fig. 12 Suspended sediment estimation by dataFit software for nonlinear regression for model 1

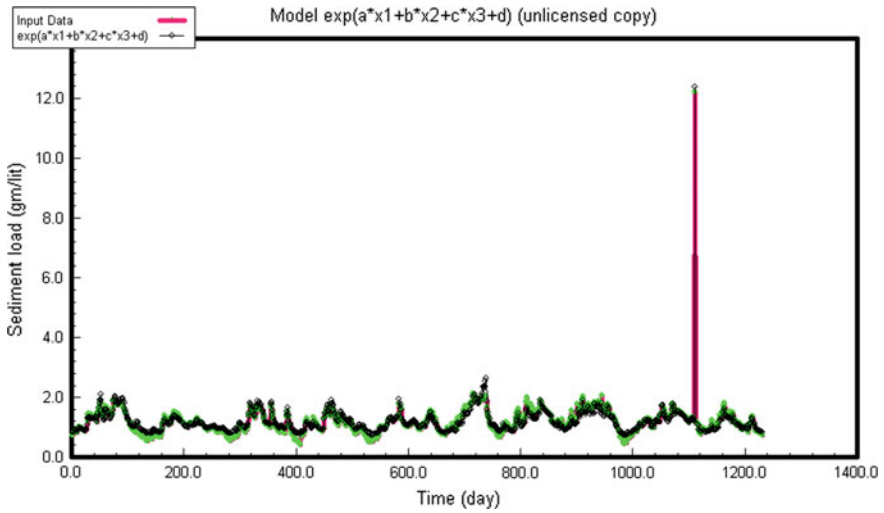

Fig. 13 Suspended sediment estimation by dataFit software for nonlinear regression for model 2

Chemical Characteristics Evaluation by Using Experimental Data

Si Model: In this model, independent variable is d_{50}, percentage of clay, and sediment concentration and dependent variable is Si percentage (%) in sediment.

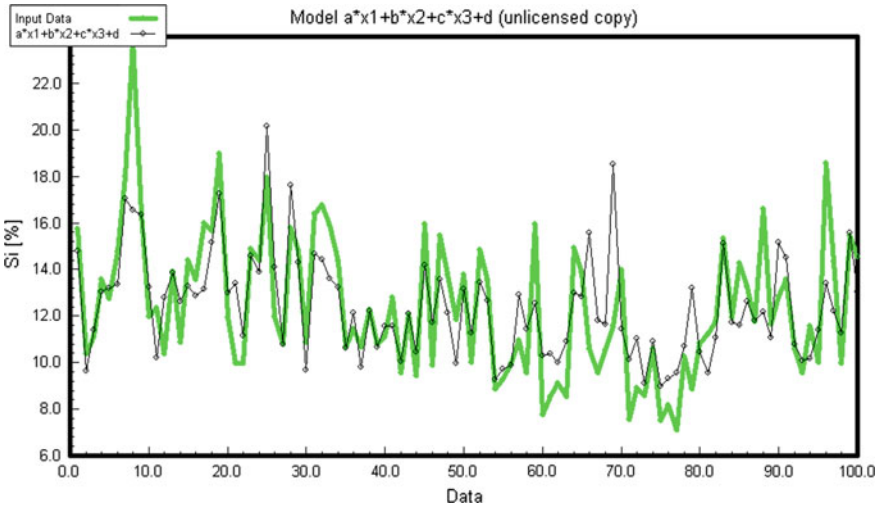

Fig. 14 Model evaluation for percentage of Si in sediment form dataFit

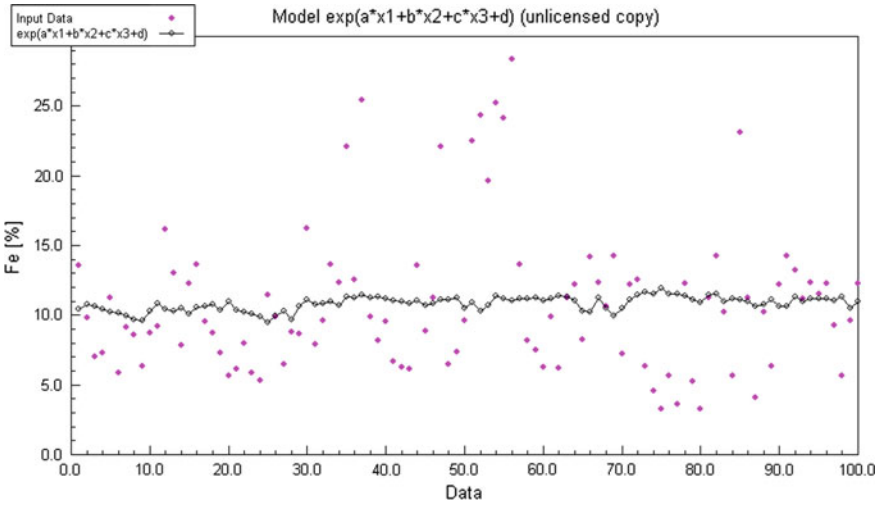

Fig. 15 Model evaluation for percentage of Fe in sediment form dataFit

Fe Model: In this model, independent variable is d_{50}, percentage of clay, and sediment concentration and dependent variable is Fe percentage (%) in sediment.

Chemical characteristics were evaluated by using the experimental data as the input data. The percentage of Si is shown in Fig. 14 from dataFit software, and Fig. 15 shows the percentage of Fe evaluated using dataFit.

Summary

From this study, it is observed that quartz and clay to be the dominant minerals with lesser amount of feldspar and dolomite, and from the particle size analysis it has been observed that in the pre-monsoon and post-monsoon season, the d_{50} and d_{85} value in Pandu site varies from 5 to 10 μm and 15 to 20 μm. The suspended sediment load simulation study was carried out considering discharge, top width, and flow data by using ANN methods (FFBP and RBF) and observed that the predicted sediment concentration values of FFBP model match with the observed values. This work provides a framework to understand the correlation of physical and chemical characteristics as well as their trend with respect to time. A more intensified sampling program using GIS tools can give clear understanding for developing their correlation.

References

Goswami DC (1985) Brahmaputra River, Assam, India: physiography, basin denundation and channel aggradation. Water Resour Res 21:959–978

Indian Standard (IS:4890-1968) Methods for measurements of suspended sediment in open channels

Kile DE, Eberl DD (2000) Quantitative mineralogy and particle-size distribution of bed sediments in the Boulder Creek Watershed, Chapter 7. Mineralogy and particle size of bed sediments. p 173–184

Master Plan of Brahmaputra Basin, Part I, Main Stream (1986)

Sarma JN (2005) Fluvial process and morphology of the Brahmaputra River in Assam, India. J Geomorphol (accepted 14 Feb 2005)

Stummeyer J, Marching V, Knabe W (2001) The composition of suspended matter from Ganges-Brahmaputra sediment dispersal system during low sediment transport season. J Chem Geol (received 2 oct 2000; accepted 9 oct 2001)

Vaithiyanathan P, Ramanathan A, Subramanian V (1992) Sediment transport in the Cauvery River basin: sediment characteristics and controlling factors (received 26 Jan 1992; accepted 25 Feb 1992)

WAPCOS (1993) Ecological and environmental studies for integrated development of Indira Gandhi Project Stage-II. Water and Power Consultancy Services (India) Limited, New Delhi

Part V
Remote Sensing and GIS Applications

Hypsometric Analysis for Assessing Erosion Status of Watershed Using Geographical Information System

S. K. Sharma, S. Gajbhiye, S. Tignath and R. J. Patil

Abstract Assessment of erosion status of the watershed is an essential prerequisite of an integrated watershed management programme. It helps in selecting suitable conservation measures to check erosion and conserve water as well as in devising best management practices in the watersheds. The geological stages of development and erosion proneness of the watersheds can be quantified by hypsometric integral. Hypsometric integral is estimated by graphical plot of the measured contour elevation and encompassed area using empirical formulae. In present study, Gusuru River watershed falling in Tons River basin located in Panna and Satna districts of Madhya Pradesh, India, was selected. The watershed was delineated into fourteen sub-watersheds and hypsometric analysis was carried out for all the sub-watersheds using digital contour maps generated in Arc/Info GIS. The hypsometric integral values of all the sub-watersheds of Gusuru River watershed range between 0.20 and 0.71. In the study area, all the three stages of erosion cycle development namely monadnock, equilibrium and youthful stages are identified.

Keywords GIS · Hypsometric analysis · Watershed · Geological stages Soil conservation

S. K. Sharma (✉)
Department of Soil and Water Engineering, College of Agricultural Engineering, J.N.K.V.V., Jabalpur, MP, India
e-mail: sharmashailesh501@gmail.com

S. Gajbhiye
Department of Water Resources Development & Management, IIT Roorkee, Roorkee, India

S. Tignath
Department of Geology, Government Science College, Jabalpur, MP, India

R. J. Patil
Department of Engineering, The University of Cambridge, Cambridge, UK

V. P. Singh et al. (eds.), *Hydrologic Modeling*, Water Science and Technology Library 81, https://doi.org/10.1007/978-981-10-5801-1_19

Introduction

Hypsometry involves measurement and analysis of the relationship between altitude and basin area in order to understand the degree of dissection and stage of the landform evolution. It helps to assess the influence of geologic and tectonic factors. Hypsometric analysis aims at developing the relationship between horizontal cross-sectional area of the watershed and its elevation in a dimensionless form permitting comparison of watersheds irrespective of scale issues (Dowling et al. 1998). Historically, hypsometry has been used as an indicator of the geomorphic form of the catchments and landforms. It is strongly dependent on the channel network and catchment geometry. Computationally, it refers to find out distribution of the elevation as a function of area occupied by each contour interval within a terrain unit. The idea of hypsometry was introduced by Langebein and Basil in the year 1947. Strahler (1952) extended it by including the percentage hypsometric curve (area-altitude curve) and the hypsometric integral.

Using dimensionless parameters, hypsometric curves can be described and compared irrespective of the true scale. Hypsometric curves are non-dimensional measures of proportion of the catchment area above a given elevation (Strahler 1952). According to Schumm (1956), Strahler (1964) and Hurtrez et al. (1999a), geomorphic and tectonic development of drainage basins in case of their forms and processes are related to hypsometric curves. Hypsometric curves have also been used to decipher age of landforms (Schumm 1956; Strahler 1952, 1964). Hypsometric curves and hypsometric integral are important indicators of watershed conditions (Ritter et al. 2002). Extent of disequilibria in the balance of erosive and tectonic forces is related to differences in the shape of hypsometric curve and integral values (Weissel et al. 1994). Comparison of the shape of hypsometric curve for different drainage basins under similar hydrologic situations gives a relative insight of the soil movement in the past of the basins (Singh and Sarangi 2008). Thus, shape of the hypsometric curve explains temporal changes in the slope of the original basin. Following analysis of shapes of hypsometric curves of numerous drainage basins, Strahler (1952) classified the basins as young (very energetic), mature (less energetic) and peneplain or distorted or old one. These shapes of hypsometric curves describe the stages of landscape evolution, which also provide an indication of erosion status of the watershed (Singh and Sarangi 2008). There is frequent variation in the shapes of hypsometric curves during early geomorphic stages of the growth, followed by minimum change, after the watershed has reached to mature stage. Convex-shaped hypsometric curves show that the watershed is reached to stabilized condition and the concave hypsometric curves point out to more proneness of watershed to the erosion processes (Hurtrez et al. 1999b).

The hypsometric integral is a geomorphological parameter classified under the geologic stages of watershed development. It is important for estimation of erosion status of watershed, and it consequently helps in prioritization of watersheds for proposing soil and water conservation activities. In addition, hypsometric integral is an indication of the ‘cycle of erosion’ (Strahler 1952; Garg 1983). The ‘cycle of

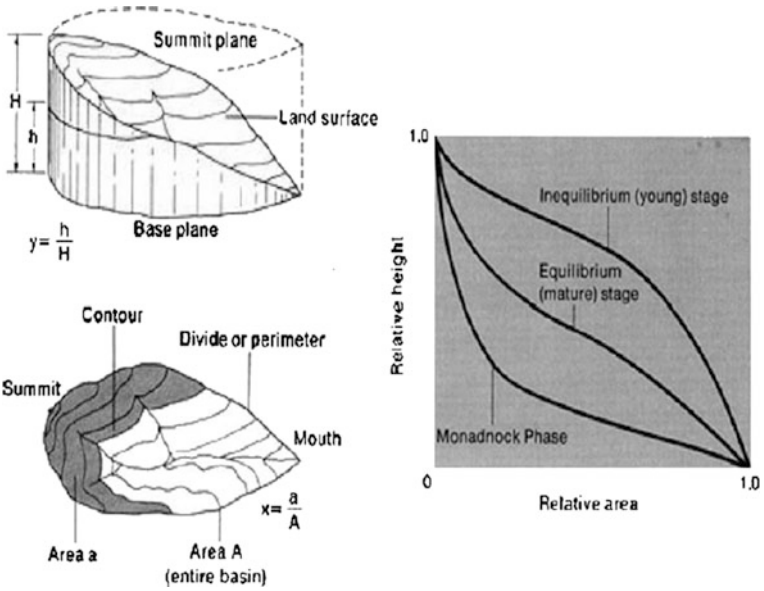

Fig. 1 Concept of hypsometric analysis and the model hypsometric curves (Ritter et al. 2002)

erosion' is the total time required for reduction of a land area to the base level, the lowest level to which streams could reduce a region if all factors remain constant except time (Fig. 1). This entire period of 'cycle of erosion' can be divided into three stages (i) fully stabilized watershed geologically called monadnock (old) ($H_{si} < 0.3$) (ii) equilibrium or mature stage (H_{si} 0.3 $\leq$ $H_{si} < 0.6$ (iii) inequilibrium or young stage ($H_{si} \geq 0.6$) in which watershed is highly susceptible to erosion (Strahler 1952). The dimensionless hypsometric integral is related to the landmass volume remaining for the whole basin (Bishop et al. 2002). Tectonic forces move rock above mean sea level, but erosion tends to move it back towards the ocean basins so a hypsometric curve is really a representation of competition between uplift and erosion. The value of hypsometric integral (the area beneath the hypsometric curve, whose value varies from 0 to 1) is an indicator of which side is dominating the competition. When the value of hypsometric integral is high, tectonic processes are dominant; when it is low, erosion processes are dominant, and when the value is intermediate (near $\sim$0.5), uplift and erosion are approximately in balance (Davis 1899). In addition, it provides a simple morphological index with respect to relative height of elevation distribution within the area that can be used in surface runoff and sediment yield prediction from watersheds (Sarangi and Bhattacharaya 2000). Hurtrez et al. (1999b) in Siwalik Hills of Central Nepal, investigated the sensitivity of hypsometry to DEMs of different resolutions and afterwards determined the control of varying drainage area on hypsometry. To explain, the watershed conditions of two watersheds in Nepal have been studied by Awasthi et al. (2002) on hypsometric curves and integrals and revealed that in the

past watershed had undergone severe erosion and are prone to soil erosion and its degradation.

While dealing with erosional topography, the hypsometric technique has been used by several researchers in India (Singh 2007; Singh et al. 2008; Sharma et al. 2010, 2011, 2013; Sarkar and Patel 2011). It can be proclaimed from these research findings that the hypsometric integral was estimated from the hypsometric curves generated using the standard graph-based area estimation procedures. However, they have not discussed effect of the hypsometric integrals on erosion status of watersheds.

Above reviews reveal that the hypsometric curve and hypsometric integral are important watershed health indicators and need to be estimated for Tons River catchments. The watersheds of Tons River catchment are vulnerable to erosion looking to its undulating topography. Further, it was also observed that there is lack of hypsometric analysis-based studies to assess the watershed health in this basin. This may be attributed to the tedious nature of data acquisition and analysis involved in estimation of hypsometric integral. However, due to advances in GIS and remote sensing image interpretation techniques, the estimation process has become easy and more accurate. Different hypsometric methods in use find their utility and superiority over one another depending upon number of factors. The region such as one selected here represents horizontal disposition of sedimentary rock piles comprising sandstone–shale–limestone with flat-topped plateau. It is specific to proterozoic belts of undisturbed rocks of the world. There is a gradual development of slope segments with a scarp segment from the top to further convex–concave association downward showing parallel regression in general.

This kind of landscape is widely distributed around the world. It is advantageous to use hypsometric analysis to assess the stage of geomorphological cycle of the overall study area on sub-units basis. It is widely known that stage of the geomorphic cycle not only changes in time, but also in space. Therefore, the assessment is scale dependant and when the study is conducted at smaller level, precision and selection of methods find special importance. With this realistic background, efforts were made in this study to compare different hypsometric integral estimation techniques and to study their effects on erosion status and geological stages of development for the Gusuru River watershed.

Materials and Methods

Description of the Study Area

Gusuru River watershed is located in parts of Panna and Satna districts of Madhya Pradesh, India, and covers an area of 155 km^2 which is bounded between 80° 32′ 50.23″E to 80° 37′ 31.14″E longitudes and 24° 6′ 32.75″N and 24° 16′ 24.07″N latitudes (Fig. 2). Maximum and minimum elevation encountered

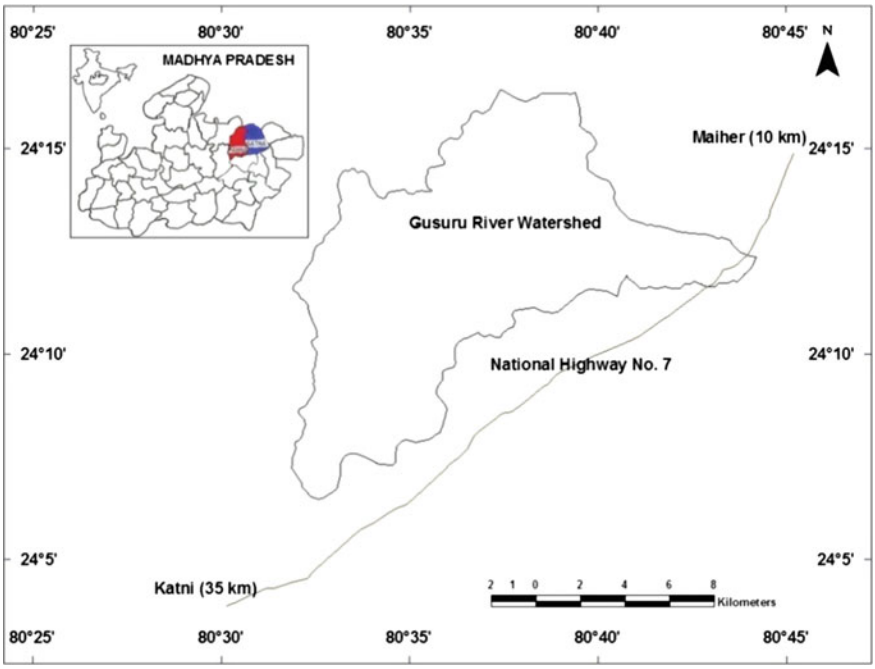

Fig. 2 Location map of study area

in the watershed is between 628 and 339 m above mean sea level. The Gusuru River stream flows from westward to eastward and joins Tons river at Sagwania village of Maihar Developmental Block. The area is represented by sandy loam soils. Geologically, the area is represented by rocks of Vindhayan super group with sandstone, shale and limestone as being the dominant litho units. The Vindhayan super group forms the northern boundary of the central Indian tectonic zone of Satpura mobile belt. In relation to Indogangetic plains, it rises to form Rewa plateau that further rises to form Bhander plateau comprising Bhander groups of rocks. In relation to Son valley in the south, it rises up as Kaimore highlands. The present study area comes down from the Bhander plateau and runs over the tract between Bhander escarpment and Kaimore highlands. Climate of the watershed is typically subtropical with hot dry summer and cool dry winter. Temperature of the area ranges between 4 °C (during December and January) and 45 °C (during May and June). Average annual precipitation of study area is 1100 mm.

Generation of DEM from the Topological Data and Watershed Delineation

Survey of India (SOI) toposheets numbered 63D/11, 63D/12 and 63D/16 were georeferenced and digitized, using capabilities of ArcInfo and ArcGIS tools to generate the topological information of the study area. Using ArcGIS, contours were digitized to have the line feature class, which was further processed using the spatial analyst toolbox to generate the digital elevation model (DEM) representing the watershed terrain (Fig. 3). Further, the developed DEM was processed to delineate the watershed and sub-watersheds using hydrology extension of spatial analyst toolbox. The digitized contour map and drainage map of the study area are shown in Figs. 4 and 5, respectively. The delineated sub-watersheds of the Gusuru river watershed marked from 1 to 14 are also shown in Fig. 5. The drainage network ordering was adopted from the Strahler's stream ordering scheme (Strahler 1964). Attribute tables of the georeferenced feature classes representing contours and their enclosed area with the sub-watersheds boundaries contained elevation and length of contours and their respective area and perimeter values. The attribute feature classes containing these values were used to plot the hypsometric curve of the sub-watersheds from which the hypsometric integrals were estimated (Fig. 6).

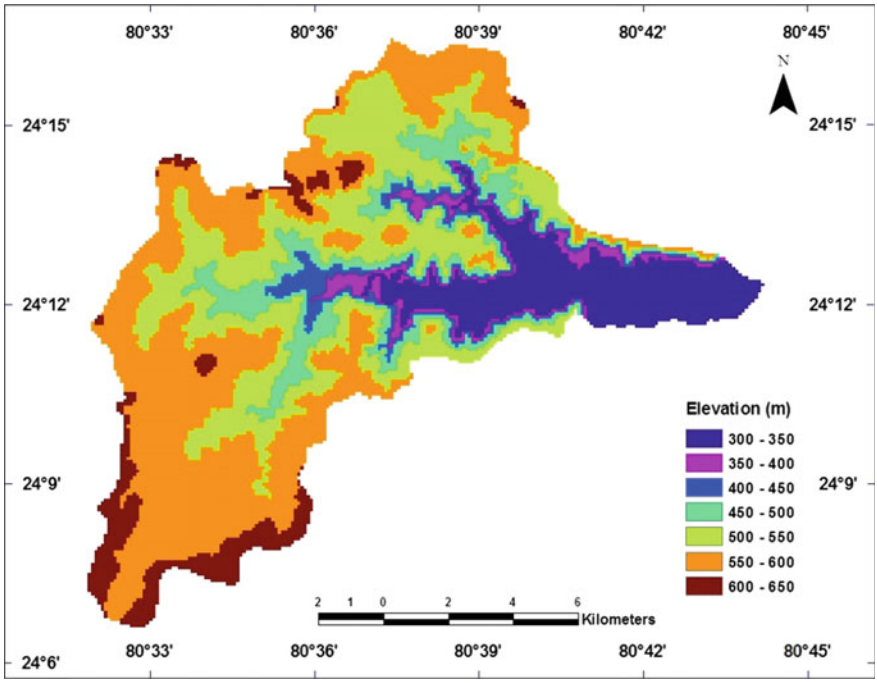

Fig. 3 Digital elevation model of study area

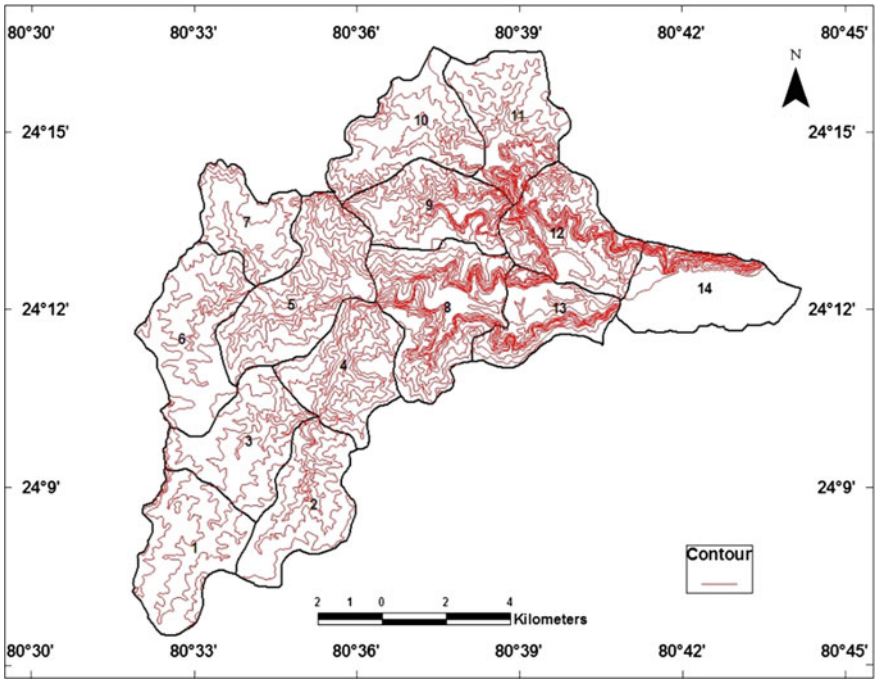

Fig. 4 Contour map of study area

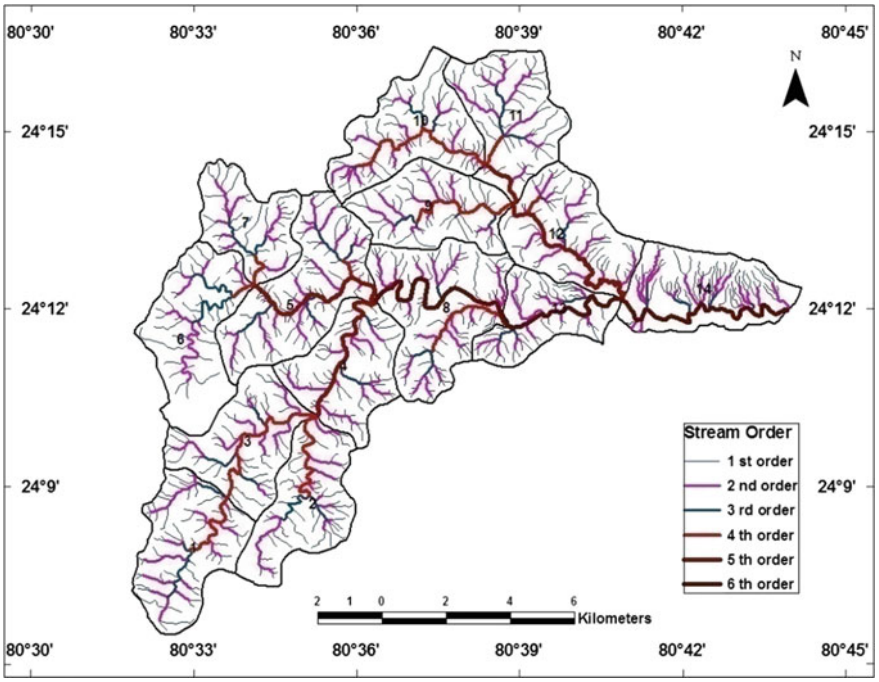

Fig. 5 Drainage network of study area

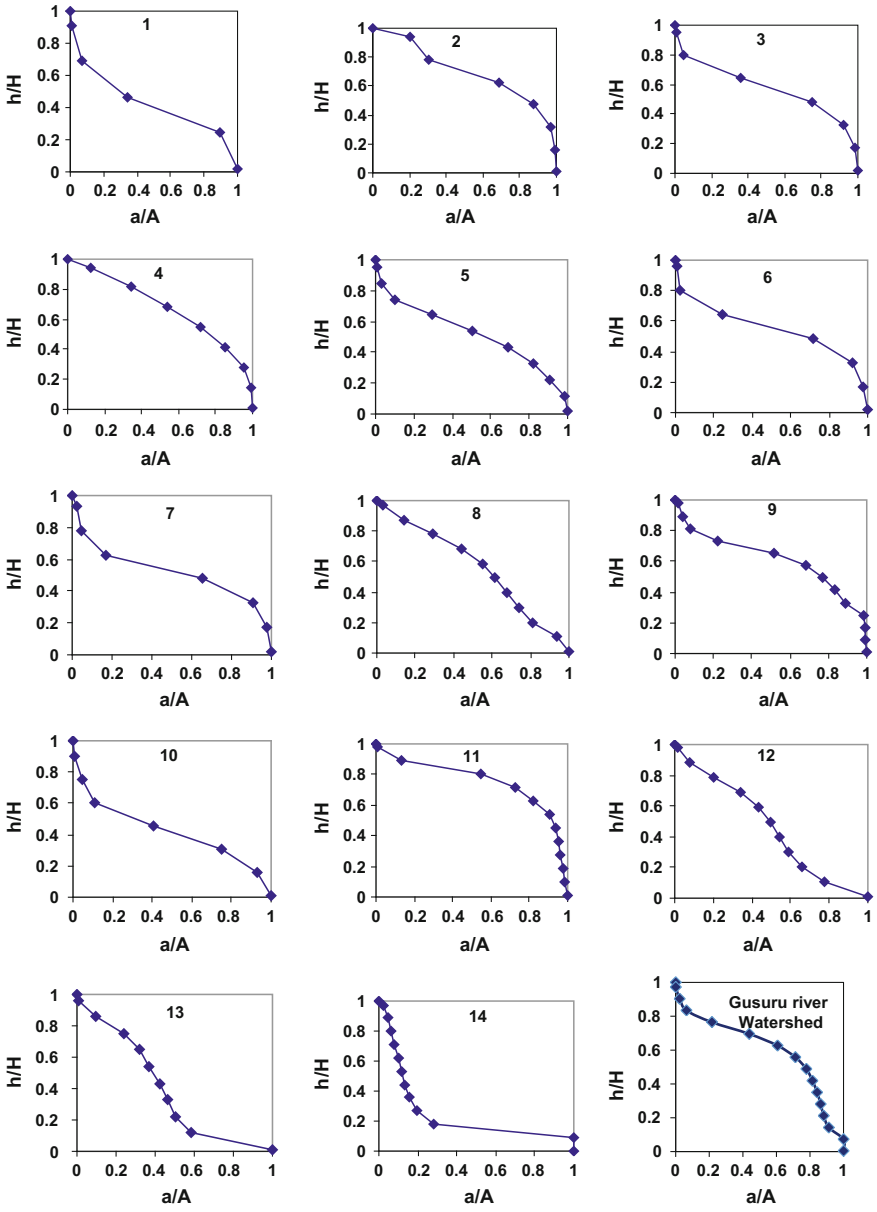

Fig. 6 Hypsometric curves of sub-watersheds and Gusuru river watershed

Plotting of Hypsometric Curves (HC) and Estimation of Hypsometric Integrals (H_{si})

Hypsometric analysis deals with the relationship between horizontal cross-sectional area of the watershed and its elevation in the dimensionless form. To create the data required for relative area and elevation analysis, digital contour maps were used. The hypsometric curve was generated by plotting the relative elevation (h/H) along the ordinate against the relative area (a/A) along the abscissa. The relative area is calculated as a ratio of the area above a particular contour (a) to the total area of the sub-watershed above outlet (A). Similarly, referring to Fig. 1, considering the watershed area to be enclosed by vertical sides and a horizontal base plane passing through the outlet, the relative elevation is obtained as the ratio of the height of a given contour (h) from the base plane to the maximum basin elevation (H), (up to the remote point of the micro-watershed from the outlet) (Ritter et al. 2002). The hypsometric integral is generated from the hypsometric curve and is proportional to the ratio of the area under the curve to the area of the entire square formed by covering it. Its unit is percentage and is obtained from the percentage hypsometric curve by measuring the area under the curve. This provided a measure of the distribution of landmass volume remaining beneath or above a basal reference plane. Hypsometric integral or the area under the curve was estimated using three methods and comparative evaluation was attempted in the present study. The methods adopted to calculate area under the curves are as follows:

Integration of Hypsometric Curve The plotted hypsometric curves were fitted with a trend line to represent an equation of the curve, and the best fitting equation was obtained for highest coefficient of determination (R^2) value. The equation was further integrated within the limits 0–1 (due to non-dimensional nature of the graph) for estimating the area under the curve. Thus, estimated area gives the hypsometric integral value of the hypsometric curve. Developed polynomial equation by fitting the hypsometric curve of the sub-watershed 1 and 2 as a sample set is shown in Fig. 7. The fitted equation was integrated within the desired limits to estimate the area under the HC. Similar procedure was adopted for other remaining 12 sub-watersheds of Gusuru River watershed. However, this method was time consuming and necessitated mathematical integration procedures and subsequent calculation within the desired limits of HC.

Use of Planimeter Equipment Planimeters are widely used by the engineers to estimate the area. In this study, digital planimeter was used. Initially, the pointer of the planimeter was rotated on the entire graph area, and readings were recorded. Further, the planimeter was rotated on the curved area beneath the hypsometric curve, and the readings were noted. Finally, the entire graph area readings were divided by the area readings below the hypsometric curve to estimate the hypsometric integral. This method was also cumbersome and time consuming in which the estimation error was also due to precision and accuracy of the equipment besides the human error.

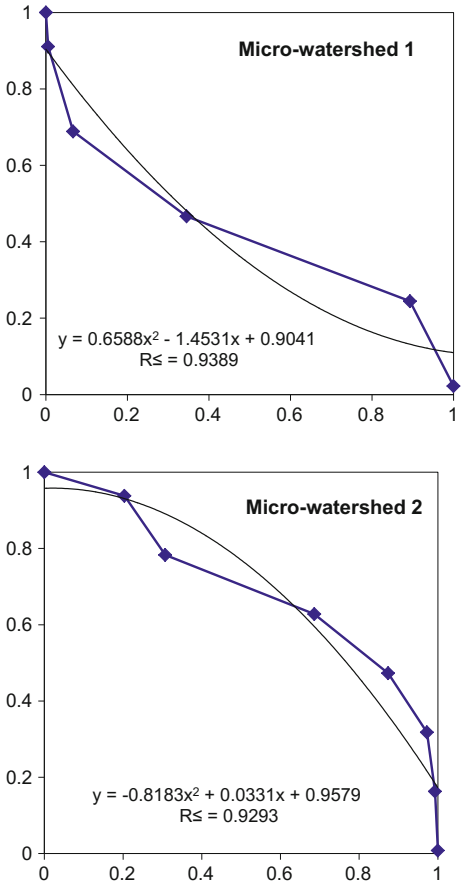

Fig. 7 Fitted equation of hypsometric curves as sample set of sub-watershed 1 and 2

Use of Elevation-Relief Ratio (E) Relationship The elevation-relief ratio method proposed by Pike and Wilson (1971) was used. The relationship is expressed as

$$E \approx H_{si} = \frac{\text{Elev}_{\text{mean}} - \text{Elev}_{\text{min}}}{\text{Elev}_{\text{max}} - \text{Elev}_{\text{min}}} \quad (1)$$

where E is the elevation-relief ratio which is equivalent to hypsometric integral H_{si}; $\text{Elev}_{\text{mean}}$ is the weighted mean elevation of the watershed calculated from the identifiable contours of the delineated sub-watersheds; Elev_{min} and Elev_{max} are the minimum and maximum elevations within the sub-watersheds.

Results and Discussion

The coordinates of hypsometric curves of the Gusuru River watershed and its fourteen sub-watersheds are plotted and presented in Fig. 6. Drainage system is approaching to the monadnock stage from the youth stage, which is evident from the hypsometric curves of these sub-watersheds and Gusuru River watershed, and it is true for most of the Tons watershed (Gusuru river is sub-watershed of Tons river). The comparison between these curves as shown in Fig. 6 indicated a marginal difference in mass removal from the sub-watersheds of the study area. It was also observed that there was a combination of convex-concavo and S-shape of the hypsometric curves for the sub-watersheds and the watershed under study.

Estimation of Hypsometric Integral (H_{si}) Values

The hypsometric integral values obtained using the three methods for the fourteen sub-watersheds of the study area are presented in Table 1. Referring to Table 1, it can be seen that there was not much difference in the estimated values of the

Table 1 Estimated hypsometric integral values of Gusuru river watershed and its sub-watersheds using three different methods

Sub-watershed No.	Area (km^2)	Elevation-relief ratio method	Integration method	Planimeter method	Geologic stages
1	11.81	0.31	0.30	0.31	Late mature or near monadnock
2	10.70	0.63	0.61	0.63	Young
3	11.13	0.49	0.49	0.49	Mature
4	10.50	0.61	0.61	0.62	Young
5	14.47	0.46	0.44	0.46	Mature
6	12.57	0.47	0.47	0.47	Mature
7	7.89	0.44	0.44	0.44	Mature
8	14.72	0.51	0.50	0.51	Mature
9	10.18	0.57	0.58	0.57	Late youthful
10	11.58	0.34	0.34	0.35	Late mature or near monadnock
11	11.07	0.71	0.71	0.72	Young
12	11.48	0.40	0.41	0.40	Mature
13	7.78	0.32	0.33	0.32	Late mature or near monadnock
14	9.24	0.20	0.20	0.20	Monadnock
Entire Gusuru river watershed	155	0.58	0.56	0.56	Late youthful

hypsometric integral for all the methods except for minor differences of 0.02 in some cases. However, the elevation-relief ratio method was observed to be less cumbersome and faster than the other two methods. Moreover, the comparison of the estimated H_{si} values from the elevation-relief ratio method and the rest two hypsometric curve-based methods revealed that there is no significant difference between the estimated hypsometric integral values. It indicated that the estimation of hypsometric integral from hypsometric curve using the ratio of areas is not always a better estimator of hypsometric integral. Therefore, the elevation-relief method could be most efficient for estimation of hypsometric integral.

Relevance of Hypsometric Integral (H_{si}) on Watershed Hydrological Responses

Surface runoff and sediment losses are two major dynamic hydrological events that are occurring in the watershed system due to erosive forces such as rainfall. The hypsometric integral value can be an indirect estimator of the erosion from the watershed systems (Singh et al. 2008). Hypsometric integral value of catchment is inversely proportional to the intensity of denudation acting on the slopes and testifies for plano-altimetric configurations of the drainage basins to be strongly dependent on the effectiveness of denudation processes (Strahler 1952; Ciccacci et al. 1988; Ohmeri 1993; D'Alessandro et al. 1988). It is observed from the H_{si} values (Table 1) that the watershed and its sub-watersheds are in the mature stage and verging upon the peneplanation or the deteriorating stage. This revealed the information that the soil erosion from the watershed and its sub-watersheds are derived primarily from the cutting of channel beds, down slope transportation of top soil and bed rock material, detachment of soil mass and incision of stream banks. Such landforms are also presents in the different sub-watersheds of the study area. Topographic evidence represents the land concavity of the study region due to river incision. The H_{si} value of the watershed indicates that 58% original rock masses still exist in the watershed. Hypsometric integral values of fourteen sub-watersheds of the study area range between 0.20 and 0.71. While comparing the standard H_{si} values of different stages the sub-watersheds 11, 2 and 4 were observed to be in youthful stage and are still in geological development. The hypsometric integral value of sub-watershed 11 is 0.71, which indicates the severity of erosion in the sub-watershed. High value of hypsometric integrals were observed in catchments, where linear incision of streams is dominant, while lowest values are typically concentrated where clay covers lead to widespread denudation on slopes (Della Seta et al. 2007). Further, sub-watersheds 11, 2 and 4 with very high value of H_{si} indicate that they are very susceptible to erosion. However, sub-watershed 9 is high-slope terrain with higher value of hypsometric integral explains its late youthful stage. Moreover, the sub-watershed 14 has reached to monadnock stage. This sub-watershed is near to the outlet of the watershed and now has a flat topography looks devastated, and in some areas, agricultural activities are going on.

The sub-watersheds 1, 10 and 13 are very near to monadnock stage as their H_{si} values are 0.31, 0.34 and 0.32, respectively. Further, sub-watersheds 3, 5, 6, 7 and 8 are in mature stage (less susceptible) and mainly attributed to human interventions in the form of construction of roads, intensive agricultural practices and deforestation activities. The hydrologic response of the sub-watersheds attaining mature stage will have slow rate of erosion unless there is very high intense storms leading to high runoff peaks (Ritter et al. 2002).

Moreover, the information of erosion status based on hypsometric integral values as discussed above can be used for watershed prioritization. Results of this study revealed that sub-watersheds 11, 2 and 4 are more prone to erosion in comparison with other sub-watersheds under study that necessitates construction of soil and water conservation structures at appropriate locations in the sub-watersheds to arrest the sediment outflows and conserve water. Sub-watersheds having hypsometric integral values more than 0.5 (i.e. approaching youthful stage) need construction of both vegetative and mechanical conservation structures to arrest sediment and to conserve water for integrated watershed management. However, the hypsometric integral values less than 0.5 (i.e. approaching monadnock stage) needs minimum mechanical and vegetative measures to arrest sediment, but may require more water harvesting structures to preserve the water at appropriate locations in the watershed for conjunctive use.

Summary and Conclusion

Hypsometric analysis of watershed expresses complexity of the denudational processes and rate of the morphological changes. Therefore, it is quite beneficial to apprehend the erosion status of watersheds and prioritize them for adopting soil and water conservation measures. But, the exercise of interpreting and comparing hypsometric curves needs special cautions due to its complex nature of computation. Out of the three methods used to compute the hypsometric integrals, the elevation-relief ratio method is most convenient because of its easiest estimation procedure in minimal time without any equipment. The estimated integral values have strong relevance on watershed erosion status leading to watershed prioritization and subsequent decisions for undertaking soil and water conservation measures, which are the prerequisites of integrated watershed management.

References

Awasthi KD, Sitaula BK, Singh BR, Bajacharaya RM (2002) Land use changes in two Nepalese watersheds: GIS and geomorphometric analysis. Land Degrd Dev 13:495–513

Bishop MP, Shroder JF, Bonk R, Olsenholler J (2002) Geomorphic change in high mountains: a western Himalayan perspective. Glob Planet Change 32:311–329

Ciccacci S, D'Alessandro L, Fredi P, Lupia Pallmaieri E (1988) Contributo dell'analisi geomorfica quantitative allo studio dei processi didenudazione nel bacino idrografico del Torrente paglia (Toscana meridonale-Lazio settentrionale). Geografica Fisica e Dinamica Quaternaria Suppl I:171–188

D'Alessassandro L, Del Monte M, Fredi P, Lupia Pallmaieri E, Peppoloni S (1988) Hypsometric analysis in the study of Italian drainage basin morphoevolution. Trans Japan Geomorphol Union 19(5):5–18

Davis WM (1899) The geographical cycle. Geogr J 14:481–504

Della Seta M, Del Monte M, Fredi P, Lupia Palmieri E (2007) Direct and indirect evaluation of denudation rates in Central Italy. CATENA 71:21–30

Dowling TI, Richardson DP, O'Sullivan A, Summerell GK, Walker J (1998) Application of the hypsometric integral and other terrain based metrices as indicators of the catchment of health: a preliminary analysis Technical report 20/98. CSIRO Land and Water Canberra

Garg SK (1983) Geology—the science of the earth. Khanna Publishers, New Delhi

Hurtrez JE, Sol C, Lucazean F (1999a) Effect of drainage area on hypsometry from an analysis of small scale drainage basins in the Siwalik hills (Central Nepal). Earth Surf Processes Landf 24:799–808

Hurtrez JE, Lucazean F, Lava J, Avouac JP (1999b) Investigation of the relationship between basin morphology, tectonic uplift and denudation from the study of an active fold belt in Siwalik hills (Central Nepal). J Geophys Res 104:799–796

Langebein WB, Basil W (1947) Topographic characteristics of drainage basins. USGS Water Supply Paper 947–C

Ohmori H (1993) Changes in the hypsometric curve through mountain building resulting from concurrent tectonics and denudation. Geomorphology 8:263–277

Pike RJ, Wilson SE (1971) Elevation—relief ratio hypsometric integral and geomorphic area-altitude analysis. Geol Soc Am Bull 82:1079–1084

Ritter DF, Kochel RC, Miller JR (2002) Process geomorphology. McGraw Hill, Boston

Sarangi A, Bhattacharaya AK (2000) Use of geomorphological parameters for sediment yield prediction from watersheds. J Soil Water Conserv 44:99–106

Sarkar A, Patel PP (2011) Topographic analysis of the Dulung river basin, vol II, no 1, 2–1 to 2–17. Traverse Geographical Institute

Schumm SA (1956) The evolution of drainage systems and slopes in badlands at Perth Amboy, New Jersey. Geol Soc Amer Bull 67:597–646

Sharma SK, Tignath S, Chaube UC (2010) Hypsometric analysis of Kanhiya Nala watershed using Geographical Information System. JNKVV Res J 44(1):97–100

Sharma SK, Seth NK, Tignath S, Pandey RP (2011) Use of geographical information system in hypsometric analysis of watershed. J Ind Wat Res Soc 31(3–4):28–32

Sharma SK, Tignath S, Gajbhiye S, Patil RJ (2013) Use of geographical information system in hypsometric analysis of Kanhiya Nala watershed. Int J Remote Sens Geosci 2(3):30–35

Singh O (2007) Geomorphological evaluation, soil erosion assessment and management in Himalayan watersheds, Himachal Pradesh. Ph.D. thesis, Jawaharlal Nehru University, New Delhi, India

Singh O, Sarangi A (2008) Hypsometric analysis of the lesser Himalayan watersheds using geographical information system. Ind J Soil Cons 36(3):148–154

Singh O, Sarangi A, Sharma MC (2008) Hypsometric integral estimation methods and its relevance on erosion status of north western Lesser Himalayan watershed. Water Res Manag 22:1545–1560

Strahler AN (1952) Hypsometric (area-altitude) analysis of erosional topography. Geologic Soc Am Bull 63:1117–1141

Strahler AN (1964) Quantitative geomorphology of drainage basins and channel networks (Editor, Chow VT) 63:1117–1141

Weissel JK, Pratson LF, Malinverno A (1994) The length scaling properties of topography. J Geophys Res 99:13997–14012

Assessment of Different Bathymetry Statistical Models Using Landsat-8 Multispectral Images

Omar Makboul, Abdelazim Negm, Saleh Mesbah and Mohamed Mohasseb

Abstract Remote sensing has many applications including bathymetry mapping in shallow water areas from multispectral images. It is considered a useful reconnaissance tool to save time and cost to be used in the preliminary survey. This paper aims at assessing the performance of three techniques used for bathymetry modeling to obtain water depth. In this research, three models are applied to obtain water depth using optical bands of Landsat-8 multispectral images. The selected algorithms (models) are principle component analysis (PCA), ratio model (RM), and 3rd polynomial model. The images are first corrected for the effects caused by atmospheric conditions and sun specular. The bands are then calibrated using ground truth measurements obtained using GPS and single-beam echo sounder in the area of the eastern harbor of Alexandria, Egypt. The study area represents a low turbid, mud bottom, and shallow water area. The three algorithms are implemented, and the results are compared with echo sounder data. The root mean square error (RMSE) is computed for the three techniques for different spectral bands combinations. RM resulted in RMSE 1.04 m using the coastal and green bands. The RMSE of PCA was 1.02 m resulted from the blue and green bands.

O. Makboul (✉) · S. Mesbah · M. Mohasseb
Arab Academy for Science, Technology and Maritime Transport,
Alexandria 21913, Egypt
e-mail: Omarm526@gmail.com

S. Mesbah
e-mail: saleh.mesbah@gmail.com

M. Mohasseb
e-mail: mohamedmohasseb@live.com

A. Negm
Water and Water Structures Engineering Department, Faculty of Engineering,
Zagazig University, Zagazig 44519, Egypt
e-mail: amnegm@zu.edu.eg; amnegm85@yahoo.com

V. P. Singh et al. (eds.), *Hydrologic Modeling*, Water Science
and Technology Library 81, https://doi.org/10.1007/978-981-10-5801-1_20

The 3rd polynomial yielded 0.91 m using from the green band. The capability of using Landsat-8 images in bathymetry was approved. In addition, the outperformance of green band usage in bathymetry was also argued.

Keywords Bathymetry · Shallow water · Harbor · Satellite images
Remote sensing and GIS

Introduction

Bathymetry data are important in many applications such as costal, marine planning and management, and nautical navigation (Green et al. 1996). Production of bathymetric maps in order to be used for navigation purposes requires accurate water depth. The conventional methods of measuring the water depths using ship-borne surveys with single- or multi-beam echo sounders can measure water depth up to 500 m (Su et al. 2008) with full bottom coverage and depth accuracy with about 1 cm. However, there are some obstacles when surveying in shallow water as the shallowness of water and bottom type as rocks and coral reefs. Moreover, ship-borne surveys are time consuming and relatively expensive (Mohamed et al. 2015).

Since 1970s, satellite remote sensing technology has been used for clear water bathymetry mapping providing an easy access and cost-effective way to bathymetry mapping especially for the fast-changing coastal environment studies (Ehses and Rooney 2015). The theory behind all bathymetric mapping using optical remote sensing is that different wavelengths of light will penetrate water with varying degrees. When the light passes through water it becomes attenuated by interaction with water column according to Beers law. Therefore, the light is reflected from the seabed in shallow water appears bright as a less amount of light has been absorbed. Conversely, deep areas appear darker (Sánchez-Carnero et al. 2014). The techniques which applied to obtain water depths are optical modeling through establishing a statistical relationship between image pixel values and ground truth measurements data. The most popular approach was proposed by Lyzenga (1978, 1981, 1985) which assumed that light attenuation is an exponential function of depth and the water quality has no variance within the image area. So, a linear relationship can be derived from the Lambert-Beer law after correcting the specular affects using near-infrared band (NIR) and removal of water column affect for single and pair wavelength bands. Stumpf et al. (2003) proposed a ratio algorithm method which uses two or more bands to determine the depth of water based on the difference in attenuation properties between bands (Vanderstraete et al. 2002) which use Jupp assumption that proposed an algorithm to determine the depth of penetration zones (DOPZ) than calibrating actual depth within (DOP) zones (Mumby 2000). However, the accuracy of the estimated water depths is limited by the

attenuation and reflectance characteristics (Philpot 1989). Attenuation coefficient is used to determine the light loss due to absorption by dissolved and particulate matter as well as scattering in pure water by particulates (Camacho 2006). The aim of this paper is to assess different models using free Landsat-8 satellite imagery to estimate shallow water depths up to 10 m. These models are PCA, RM (which were proposed by Stumpf et al. (2003)), and the 3rd order polynomial model. The three algorithms are calibrated using field data after the removal of sun glint from imagery data and atmospheric correction over sea surface area.

Materials and Methods

The Study Area

The study area is the eastern harbor located in northwest of Alexandria as shown in Fig. 1. It is a portion of the commercial port of Alexandria. The harbor is formed by two converging breakwaters. The East harbor is characterized by its shallow depth and is not navigable by the large-decked ships. It is used for fishing boats, yachts, and others. The study area is 1 km by 1 km and is located in between the coordinates (31° 12.6′N, 29° 52.9′E), (31° 12.0′N, 29° 53.4′E), (31° 12.4′N, 29° 45.3′E), (31° 12.8′N, 29° 53.9′E), UTM zones 35.

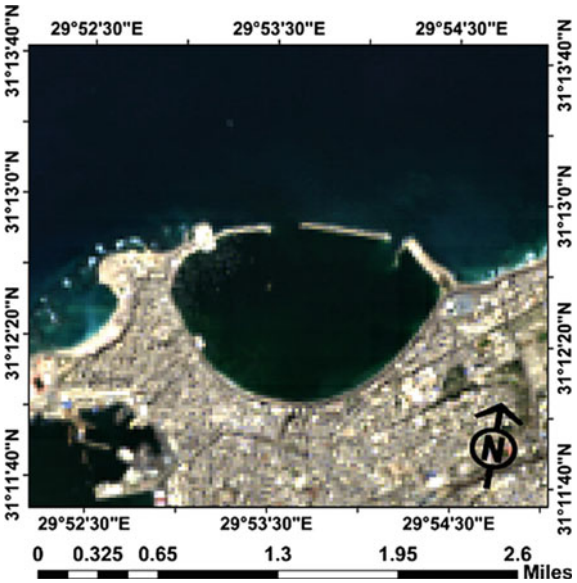

Fig. 1 Land-site 8 imagery of the study area: eastern harbor of Alexandria

Data Collection

The ground truth measurements acquisition systems consisted of laptop computers running (Hypack 2012) hydrographic survey software. Devices used in this operation are single-beam echo sounders (NAVI SOUND 210), Trimble 2000 GPS, and side scan sonar (Starfish SSS). The weather condition was clear in the morning, then partly cloudy and windy. Temperature ranged from 30 to 31 °C Breezy. Winds direction was NNE, and wind speed was 15–30 km/h. The depth average is 4.1 m, and sea bottom nature is mud. The echo sounders and DGPS were interfaced to the survey computers via RS-232 serial. The echo sounder transducers were mounted to the rails of the survey vessels amidships, and the GPS antenna was mounted directly over the transducer. The region of survey is divided into line with a total of 20 planed lines and two cross check lines according to IHO standard order (1a) as shown in Table 1. Since the density of ground truth data was about 2500 measurements of depth. The water depths below 10 m represent 97% of the total area. The depth soundings were corrected to chart datum (CD) by subtracting the local tidal height as predicted by Total Tide Software Computer Program.

The parameters "*a*" and "*b*" for each order, as given in Table 1, together with the depth "*d*" have to be introduced into the formula (1) in order to calculate the maximum allowable TVU for a specific depth

$$\mathbf{TVU} = \pm\sqrt{a^2 + (b * d)^2}, \tag{1}$$

where

- a represents portion of the uncertainty that does not vary with depth.
- b is a coefficient which represents that portion of the uncertainty that varies with depth.
- d is depth of water.
- $b \times d$ represents portion of the uncertainty that varies with depth.

Table 1 Summary of minimum standards for hydrographic surveys order (1) (International Hydrographic Bureau 2008)

Examples of typical areas	Harbors, Harbor approach channels, recommended tracks, and some coastal areas with depths up to 100 m
Horizontal accuracy (95% confidence level)	5 m + 5% of depth
Depth accuracy for reduced depths (95% confidence level)	a = 0.5 m b = 0.013
100% bottom search	Required in selected areas
System detection capability	Cubic features >2 m in depths up to 40 m; 10% of depth beyond 40 m
Maximum line spacing	3 × average depth or 25 m, whichever is greater

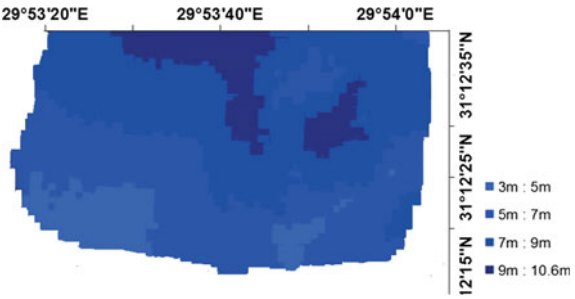

Fig. 2 Ground truth data from echo sounder

Bathymetric Data Processing

Bathymetric data as shown in Fig. 2 are processed using the (Hypack 2012) single-beam processor module. The processing steps are as follows

- Adding the raw data files to the Hypack software.
- Adding the tide measurement from the total tide software to the Hypack.
- Removing the spikes from all the survey lines.
- Filling area of survey.
- Drawing contour lines.
- Plotting the area of survey for the final graphics chart.

Sensor Data

Landsat-8 collects image data for 11 spectral bands with a 30 m spatial resolution. The bands used for detecting bathymetry in this study are coastal/aerosol (0.435–0.451 μm), blue (0.452–0.512 μm), green (0.533–0.590 μm), red (0.636–0.673 μm), and near-infrared (NIR) (0.851–0.879 μm) as shown in Fig. 1.

Methods

Imagery Data Preprocessing

Remote sensing image is affected by a variety of environmental factors such as atmosphere, sea water, and sun specular. Correction of RS images is essential to improve the precision of water depth.

Converting to Radiance

Converting the DN to the spectral radiance at the aperture (L_λ) is measured in (watts/meter squared * ster * μm) using Eq. (2):

$$L_\lambda = \mathrm{ML} * \mathrm{Qcal} + \mathrm{AL}, \tag{2}$$

where

ML Band-specific multiplicative rescaling factor from Landsat metadata files.
AL Band-specific additive rescaling factor from Landsat metadata files.
Qcal Calibrated standard product pixel values (DN).

Applying Atmospheric Correction

The solar radiation passes through the atmosphere before collected by the sensor. Wherefore images affected by several factors such as water vapor, distribution of aerosols, and visibility (Song et al. 2001). In this paper, the FLASSH model in ENVI software is used to correct the atmospheric effect that applied to the solar wavelength according to Eq. (3):

$$L = \left(\frac{A\rho}{1 - \rho_{e^S}}\right) + \left(\frac{B\rho_e}{1 - \rho_{e^S}}\right) + L_a, \tag{3}$$

where

ρ the pixel surface reflectance.
ρ_e an average surface reflectance for the pixel and a surrounding region.
S is the spherical albedo of the atmosphere.
L_a radiance back scattered by the atmosphere.

A and B are coefficients that depend on atmospheric and geometric conditions but not on the surface. A, B, S, and L_a are depending on water vapor amount. This is used in MODTRAN model using calculations that use the viewing and solar angle and the mean surface elevation measurement. The input image for FLAASH module in ENVI software must be a radiometrically calibrated radiance image and data must be in floating-point format (ENVI 2009).

Applying Sun Glint Correction

Specular reflection of solar radiation known as sun glint must be removed for accurate benthic habitat classification. Hochberg et al. (2003) provided a method to remove sun glint by using the brightness of near-infrared NIR band. Hedley et al. (2005) proposed revised method depending on Hochberg assumption that is based

on the linear relationship between NIR and visible bands using linear regression. By using linear regression, the NIR brightness (x-axis) against the visible band brightness (y-axis), are compared. The relationship would be homogeneous, otherwise, a presence of sun glint (deep water) is indicated. The slope of the regression is then used to predict the brightness in the visible band by using Eq. (4). This method is not necessary to mask out land or cloud pixels. The minimum sample size required is two pixels

$$R_i' = R_i - b_i(R_{\mathrm{NIR}} - \mathrm{MIN}_{\mathrm{NIR}}), \tag{4}$$

where

R_i' the sun glint corrected pixel brightness in b and i.
b_i the product of regression slope.
R_{NIR} corresponding pixel value in NIR band.
$\mathrm{MIN}_{\mathrm{NIR}}$ min NIR value existing in the sample.

Statistical Models

Derivation of the depth from spectral image using regressing reflectance values were checked against ground truth measurement data. In this case, three statistical models RM, PCA, and 3rd order polynomial were used to find the relation between corrected bands and ground truth data.

Ratio Model

The RM is based on the difference in absorption rates between bands. As depth increases, the band with a higher absorption rate will decrease proportionally faster than the band with a lower absorption rate. Therefore, the ratio between two bands will increase as depth increases. This method was proposed by Stumpf et al. (2003) as shown in Eq. (5)

$$Z = m1\frac{\ln(nR(\lambda 1))}{\ln(nR(\lambda 2))} - m, \tag{5}$$

where

$m1$ and m are tunable constants to scale the ratio depth.
n is a constant to assure that the logarithm is positive under any condition.

Principal Components Analysis (PCA)

Principal components analysis (PCA) is a methodology whereby the main linear factor underlying the movement of a given multi-variety data series are extracted as distinct vectors. It is used to assess data quality and discover relationship between data. PCA method assumes that change in depth explains the most variance and other factors, such as a changing bottom type, water turbidity will be secondary sources of variation (Gholamalifard et al. 2013). The PCA approach seeks the best combination of highly correlated bands (and their logarithms) in order to build a variable that captures most of variability in the area (Sánchez-Carnero et al. 2014). The values of first component are used to adjust linear expression with ground truth data.

3rd Order Polynomial

The nonlinear 3rd order polynomial has the form.

$$z = ax^3 + bx^2 + cx + d, \tag{6}$$

where $a \neq 0$ as the equation must have the term in x^3 or it would not be cubic while all of b, c, and d can be zero. The aim of using 3rd order polynomial is to increase possibilities of accuracy of depth. This method was used by Sánchez-Carnero et al. (2014) and Mohamed et al. (2015).

Results and Discussion

The Landsat-8 is prepared for water depth estimation after atmospheric correction and sun glint removal were applied. The atmospheric correction was performed in ENVI software, and the sun glint correction was performed in ARCGIS.

Ratio Method

Results of the ratio method are shown in Figs. 3 and 4 and Eq. (7). Results show good correlation between the ratios of coastal to green and ground truth measurement since the correlation coefficient $R = 0.74$. The root mean square error RMSE is 0.78 m. Furthermore, the index of determination $R^2 = 0.55$ which represents 55% of variability in the known depth can be explained by the transformed bands.

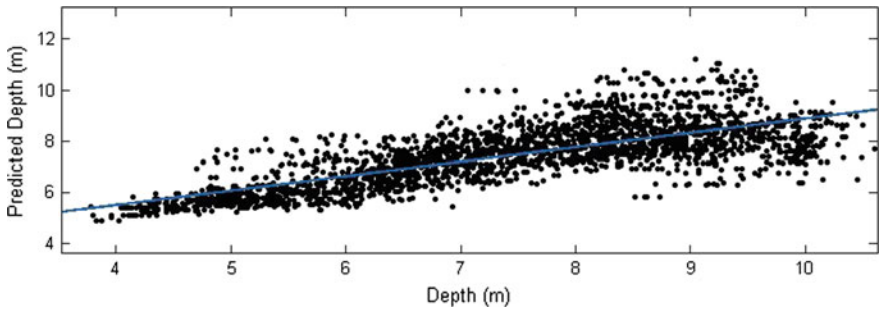

Fig. 3 Regression for coastal/green bands against predicted depth

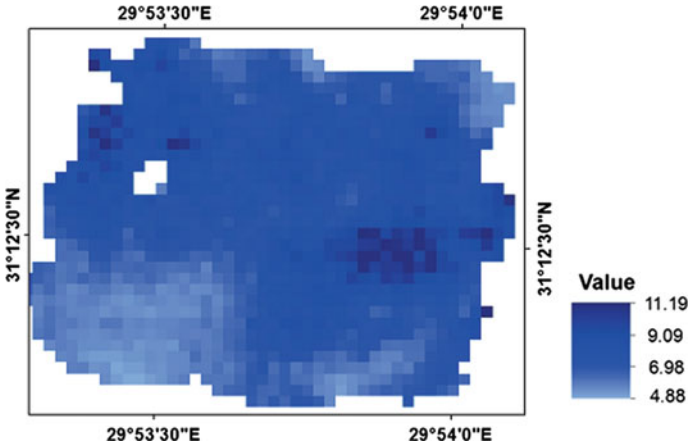

Fig. 4 The map of water depths (m) produced by RM

$$z = 2.691 * \frac{\ln(R_c)}{\ln(R_g)} + 2.985. \tag{7}$$

Principal Components Analysis

The PCA is calculated using the logarithm transform of the blue and green bands (2 and 3). As shown in Figs. 5 and 6, the resulting first component p_1 (concentrating 71% of the variance) with loadings of 0.814 for two bands is used to adjust a linear expression of the depth z in the form as shown in Eq. (8)

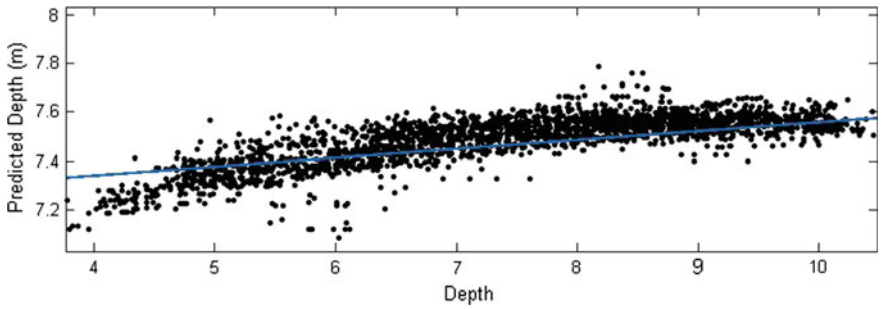

Fig. 5 Regression of first component of PCA against predicted depth

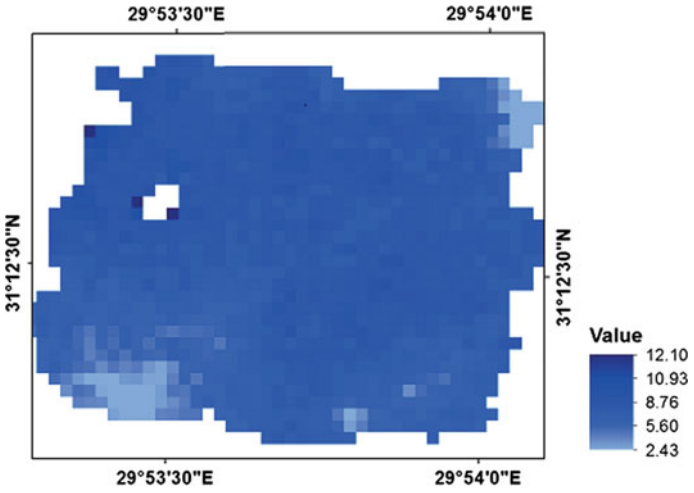

Fig. 6 The map of water depth (m) produced by PCA

$$Z = -6.861 * p1 + 20.47. \tag{8}$$

The correlation coefficient $R = -0.75$. Only 57.6% in the known depth is explained by the first component of PCA because $R^2 = 0.57$. The RMES of Eq. (8) is 1.026 m.

3rd Order Polynomial

The nonlinear 3rd order polynomial correlation between the green band logarithm (R_g) and ground truth data as shown in Figs. 6 and 7 and its form is given by Eq. (9)

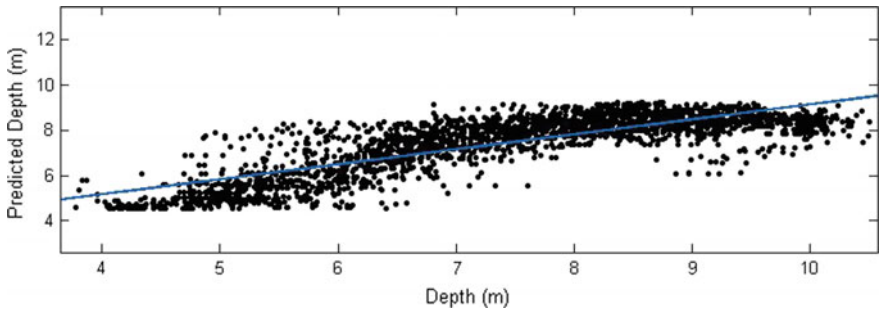

Fig. 7 Regression of green band logarithms against predicted depth

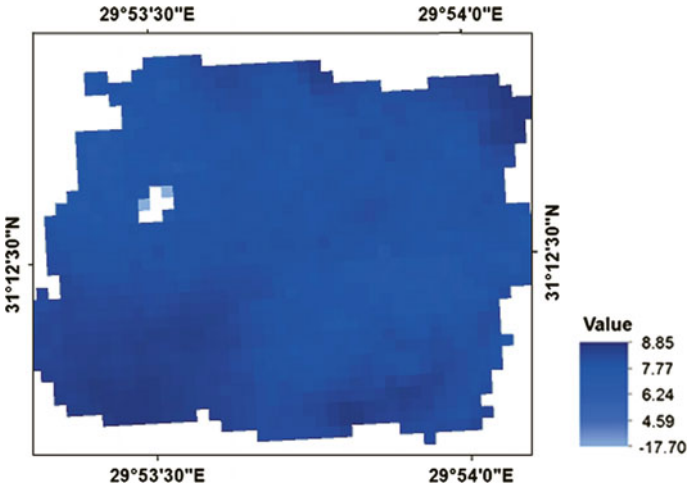

Fig. 8 The map of water depth (m) produced by 3rd order polynomial

$$z = 27.8 * R_g^3 - 43.92 * R_g^2 + 12.9 * R_g + 8.25. \quad (9)$$

Results show strong correlation between the green band and known depths with $R = 0.81$ and 66.4% in the known depth is explained by the green band logarithms as R^2 equals 0.664 and the RMSE equals 0.7419 m (Fig. 8).

The root mean square error (RMSE) values of the three methods are presented in Table 2.

Selections of bands in this study are based on absorption and scattering characteristics. For the ratio method, ratio between the coastal and green bands (R_C/R_g) is used because the coastal band has lower absorption ratio, besides it is useful for imaging shallow water (USGS 2015). The contribution of the blue band in these two areas is significant but less than the contribution of the green. The coastal band

Table 2 RMSE of the three Eqs. (7), (8), and (9)

The 3rd order polynomial method	PCA method	RM method	Method
0.741 m	1.02 m	0.787 m	RMSE

is satisfied only in the ratio method and their contribution is consistent with (Doxani et al. 2012). The red bands had no contribution as a result of high absorption and scattering ratio.

Comparison of results with the previous studies (Lyzenga et al. 2006) achieved an aggregate RMSE error of 2.3 m from a set of IKONOS images over a variety of conditions. A bathymetric map derived from WORLDVIEW-2 over depth of 14 m has RMSE of 0.33 m (Doxani et al. 2012). The bathymetric information derived from SPOT-5 has RMSE of 1.87 m over depth from 0.2 to 21.5 m (Liu et al. 2010). A bathymetric map derived from SPOT-4 images has RMSE of 0.17 m over depth from 0.4 to 2 m (Mohamed et al. 2015). The estimated bathymetry errors in these works are very variable between 0.17 and 2 m. The accurate depth was derived from highly resolution multispectral image such as WORLDVIEW-2 (having a spatial resolution 0.5 m) and SPOT-4 (having a spatial resolution 10 m). Gao (2009) proposed that the depth accuracy depends on spatial resolution and water turbidity. In this case, estimation error appears to increase with water depth with the estimates being accurate for water depth up to 7.5 m.

It is worth to compare the results with International Hydrographic Organization Standard. The maximum allowable total vertical uncertainty (TVU) for reduced depths specifies the uncertainty to be achieved to meet each order of survey. Uncertainty related to the 95% confidence level refers to the estimation of error from the combined contribution of random error and residuals from the correction of systematic error. In minimum standards for Hydrographic Surveys order 2 (for areas generally deeper than 100 m), we find that TVU for depth 10 m = 1.03 m according to Eq. (1) where a = 1 m and b = 0.023.

Conclusion

This paper assessed the performance of three modeling algorithms used for bathymetry estimation to obtain water depths. Bathymetric information retrieval from optical satellite multispectral imagery has many advantages as large surface coverage, high spatial resolution, and low cost. Three statistical models were developed to obtain water depth using optical bands of Landsat-8 multispectral images. Through the use of images available for free Landsat-8, depth estimates were derived from multispectral images with vertical accuracy of RMSE about 1.0 m. These obtained levels of vertical accuracy meet International Hydrographic Office (IHO) standards for safe navigation order 2. Bathymetric information derived from Landsat-8 imagery produced fairly accurate results. The green band out of the

tested bands proved to be the most effective for bathymetry detection of shallow depth harbors.

References

Camacho M (2006) Depth analysis of midway atoll using quick bird multi-spectral imaging over variable substrates. Available at: http://bio.research.ucsc.edu/people/potts/midway/documents/Camacho2006-Thesis.pdf

Doxani G, Papadopoulou M, Lafazani P, Pikridas C, Tsakiri-Strati M (2012) Shallow-water bathymetry over variable bottom types using multispectral worldview-2 image. In: ISPRS—international archives of the photogrammetry, remote sensing and spatial information sciences, pp 159–164. Available at: http://www.Int-Arch-Photogramm-Remote-Sens-Spatial-Inf-Sci.Net/XXXIX-B8/159/2012/

Ehses JS, Rooney JJ (2015) Depth derivation using multispectral worldview-2 satellite imagery. Civil and Environmental Engineering (June), pp 24–46

ENVI (2009) ENVI atmospheric correction module: QUAC and FLAASH user's guide. Available at: http://scholar.google.com/scholar?hl=en&btnG=Search&q=intitle:ENVI+Atmospheric+Correction+Module:+QUAC+and+FLAASH+user's+guide#0

Gao J (2009) Bathymetric mapping by means of remote sensing: methods, accuracy and limitations. Prog Phys Geogr 33(1):103–116

Gholamalifard M, Kutser T, Esmaili-Sari A, Abkar A, Naimi B (2013) Remotely sensed empirical modeling of bathymetry in the Southeastern Caspian Sea. Remote Sens 5(6):2746–2762. Available at: http://www.mdpi.com/2072-4292/5/6/2746/

Green EP et al (1996) A review of remote sensing for the assessment and management of tropical coastal resources. Coast Manag 24(1):1–40

Hedley JD, Harborne AR, Mumby PJ (2005) Technical note: simple and robust removal of sun glint for mapping shallow-water benthos. Int J Remote Sens 26(10):2107–2112

Hochberg EJ, Andréfouët S, Tyler MR (2003) Sea surface correction of high spatial resolution Ikonos images to improve bottom mapping in near-shore environments. IEEE Trans Geosci Remote Sens 41:1724–1729

Hypack Inc (2012) HYPACK hydrographic survey software user manual. Hypack Inc

International Hydeographic Bureau (2008) IHO standards for hydrographic surveys. Available at: http://arxiv.org/abs/1011.1669

Liu S, Zhang J, Ma Y (2010) Bathymetric ability of SPOT-5 multi-spectral image in shallow coastal water. In: 2010 18th international conference on geoinformatics. IEEE, pp 1–5. Available at: http://ieeexplore.ieee.org/lpdocs/epic03/wrapper.htm?arnumber=5567951

Lyzenga DR (1978) passive remote sensing techniques for mapping water depth and bottom features. Appl Opt 17:379–383

Lyzenga DR (1981) Remote sensing of bottom reflectance and water attenuation parameters in shallow water using aircraft and Landsat data. Int J Remote Sens 2(1):71–82. Available at: http://www.tandfonline.com/doi/abs/10.1080/01431168108948342

Lyzenga DR (1985) Shallow-water bathymetry using combined lidar and passive multispectral scanner data. Int J Remote Sens 6(1):115–125

Lyzenga DR, Malinas NP, Tanis FJ (2006) Multispectral bathymetry using a simple physically based algorithm. IEEE Trans Geosci Remote Sens 44(8):2251–2259

Mohamed H, Negm A, Zahran M, Saavedra Oliver C (2015) Assessment of artificial neural network for bathymetry estimation using high resolution satellite imagery in shallow lakes: case study El Burullus Lake. In: International water technology conference, pp 12–14

Mumby P, Green EP, Edwards AJ, Clark CD (2000) Remote sensing handbook for tropical coastal management (Editor, Edwards AJ). Coastal Management Sourcebooks 3, UNESCO, Paris

Philpot WD (1989) Bathymetric mapping with passive multispectral imagery. Appl Opt 28 (8):1569–1578

Sánchez-Carnero N, Ojeda-Zujar J, Rodríguez-Pérez D, Marquez-Perez J (2014) Assessment of different models for bathymetry calculation using SPOT multispectral images in a high-turbidity area: the mouth of the Guadiana Estuary. Int J Remote Sens 35(2):493–514. Available at: http://www.tandfonline.com/doi/abs/10.1080/01431161.2013.871402

Song C, Woodcock CE, Seto KC, Macomber S (2001) Classification and change detection using Landsat TM data: when and how to correct atmospheric effects? Remote Sens Environ 75 (2):230–244

Stumpf RP, Holderied K, Sinclair M (2003) Determination of water depth with high-resolution satellite imagery over variable bottom types. Limonol Oceanogr 48(1_part_2):547–556. Available at: http://www.aslo.org/lo/toc/vol_48/issue_1_part_2/0547.html

Su H, Liu H, Heyman WD (2008) Automated derivation of bathymetric information from multi-spectral satellite imagery using a non-linear inversion model. Mar Geodesy 31 (May):281–298

USGS (2015) Landsat 8 (L8) data users handbook. Available at: http://landsat.usgs.gov/documents/Landsat8DataUsersHandbook.pdf

Vanderstraete T, Goossens R, Ghabour TK (2002) Remote sensing as a tool for bathymetric mapping of coral reefs in the Red Sea (Hurghada—Egypt). In: International conference on remote sensing for marine and costal environments, pp 257–268. Available at: http://www.scopus.com/inward/record.url?eid=2-s2.0-2642550678&partnerID=tZOtx3y1

Estimation of Minimum and Maximum Air Temperature Using MODIS Remote Sensing Imagery and Geographical Information System (GIS)

P. Sardhara Bharatkumar, P. Dholariya Jay, M. K. Tiwari and M. L. Gaur

Abstract Air temperature is a useful environmental variable in a wide range of applications in areas of ecology, hydrology and atmospheric sciences. Estimating air temperature (T_a) is very important in monitoring the environment, estimating precipitation, climatic prediction, determining evapotranspiration, predicting crop yield and climatic changes, etc. Furthermore, it is the most important meteorological and climatological variable, along with radiation, in plant development, determining its spatial distribution, and conditioning agricultural soil suitability. In agro-meteorological, hydrological, hydro-meteorological studies, one of the main issues is the lack of representative temperature data. Density of the meteorological stations network is generally sparse, and installation and running cost of additional meteorological stations are very high. As a result, obtaining high spatial resolution maximum temperature (T_{max}) and minimum temperature (T_{min}) map from meteorological stations data is not possible. Remote sensing data provides synoptic spatial coverage compared to discrete spatial distribution of meteorological stations, thus encouraging researchers to make use of satellite data to fill in the gaps inherent in meteorological station data. Satellite remote sensing image is fundamentally designed to offer spatially distributed information over earth observation. Therefore, this study is carried out with the objectives to select appropriate MODIS data for simulation of temperature and with application of selected imaginary to simulate temperature in the Limkheda watershed located in the semi-arid middle region of Gujarat. Temperature data during the month of October 2010, at two sites of the Limkheda watershed are applied to explore the capabilities of MODIS satellite imagery to simulate the minimum and maximum temperature in the Limkheda watershed. It is found in this study that bands namely Day_view_angle and Emis_32 of MODIS imagery simulate minimum and maximum temperature

P. Sardhara Bharatkumar · P. Dholariya Jay · M. K. Tiwari · M. L. Gaur (✉)
Department of Soil and Water Engineering, College of Agricultural Engineering and Technology, Anand Agricultural University, Godhra 389001, Gujarat, India
e-mail: dr.mlgaur@gmail.com

V. P. Singh et al. (eds.), *Hydrologic Modeling*, Water Science and Technology Library 81, https://doi.org/10.1007/978-981-10-5801-1_21

satisfactorily. It is found in this study that Day_view_angle simulate minimum temperature very well, whereas Emis_32 band simulate both the maximum and minimum temperature very well. From this study, it is recommended that Emis_32 band would be a suitable choice to calculate temperature.

Introduction

Remote sensing of the atmosphere is nowadays carried out by means of very sophisticated sensors, using both new and broader wavelength regions, and measuring with better frequency resolution and lower noise. As a consequence, larger amounts of data have to be efficiently processed in order to optimize the retrieval performance (Del Fratea et al. 2005). A remote measurement of the atmosphere from space with high spectral resolution can give a large amount of information about the atmosphere (Gribanov and Zakharov 2004; Bastiaanssen et al. 1998).

Air temperature is a useful environmental variable in a wide range of applications in areas of ecology, hydrology and atmospheric sciences. Estimating air temperature (T_a) is very important in monitoring the environment, estimating precipitation, climatic prognoses, determining evapotranspiration, predicting crop yield (Rugege 2002), and climatic changes (Aikawa et al. 2008; Adamowski et al. 2012; Tiwari and Adamowski 2013) among others. Furthermore, it is the most important meteorological and climatological element, along with radiation, in plant development, determining its spatial distribution, and conditioning agricultural soil suitability (Lozada and Sentelhes 2008). According to Lozada and Sentelhes (2008), one of the main problems in conducting agro-meteorological studies is the lack of temperature data. These authors consider that the low density of the meteorological stations in some study areas, addition to flaws in the meteorological data series and/or short historical data series, is compromising the quality of estimation of T_a spatially distributed. Most methods to determine T_a spatial variation often use spatial interpolation and extrapolation of data from the nearest meteorological stations. The problem with T_a interpolation and extrapolation is that they depend on many local parameters that can influence its estimation spatially distributed (e.g. altitude, sun exposure, terrain concavity, and distance from the coast among others) (Marquínez et al. 2003; Del Fratea et al. 2005; Deo and Şahin 2015). Usually crop growth modelling requires spatially weather variables for whole study area, while the available weather information offers represented observe values of limited area near by meteorological station. In most case, a spatial interpolation of observed air temperature at single or multiple meteorological stations is carried out to estimate whole over area of interest. Due to the limited density of meteorological station or rarely design to cover the range of climate variability with in region, thus uncertainly spatial information available of air temperature is often present. Consequently, the output of uncertainly estimate for weather variables over study area can cause an inaccurate results when applying crop growth models over regional area.

Meteorological stations measure air temperature at two metre height above ground. However, density of the meteorological stations network is generally sparse, and installation and running cost of additional meteorological stations are very high. As a result, obtaining high spatial resolution T_{min} and T_{max} map from meteorological stations data is not possible. Satellite provides synoptic spatial coverage compared to discrete spatial distribution of meteorological stations, thus attracting researchers to make use of satellite data to fill in the gaps inherent in meteorological station data.

Satellite remote sensing image is fundamentally designed to offer spatially distributed information over earth observation. Nevertheless near surface air temperature is scarcely obtained from direct satellite observation which mainly targets to the earth surface observation. While modern remote sensing platform like Moderate-Resolution Imaging Spectroradiometer (MODIS) can estimate land surface temperature (LST) using a generalized split-window technique of thermal infra-red (TIR) channels (Wan and Dozier 1996). Many scientists have studied and reported a strong correlation between LST and near surface air temperature. Mostovoy et al. (2006) and Vancutsem et al. (2010) demonstrate the derivation of near surface air temperature from LST observed by satellite remote sensing through various regression and statistical analysis. In this study, capabilities of MODIS satellite imagery are explored to simulate the temperature in the Limkheda watershed, located in semi-arid middle region of Gujarat.

Methodology

Description of Study Area

An agricultural Limkheda watershed located in the semi-arid middle region of Gujarat, India, (Fig. 1) is selected in this study. The total area of the Limkheda watershed is 220.86 km^2. The outlet of the study area is located at latitude 22° 49′ 55″ and longitude 73° 59′ 15″ at an elevation of 207 m falling in Survey of India (SOI) toposheets No. F43I1, F43I2, F43H13 on 1:50,000 scale. Limkheda is the heart of Dahod district; it is situated on the river bank of Hadaf that is passing between Limkheda and Palli. Limkheda is 25 km west of Dahod district. Limkheda Taluka is bounded by Devgad Bariya Taluka towards south, Dhanpur Taluka towards south and Dahod Taluka towards east. Limkheda consists of 245 villages and 87 panchayats. The study area attains maximum elevation of 490 m and a minimum of 196 m above mean sea level.

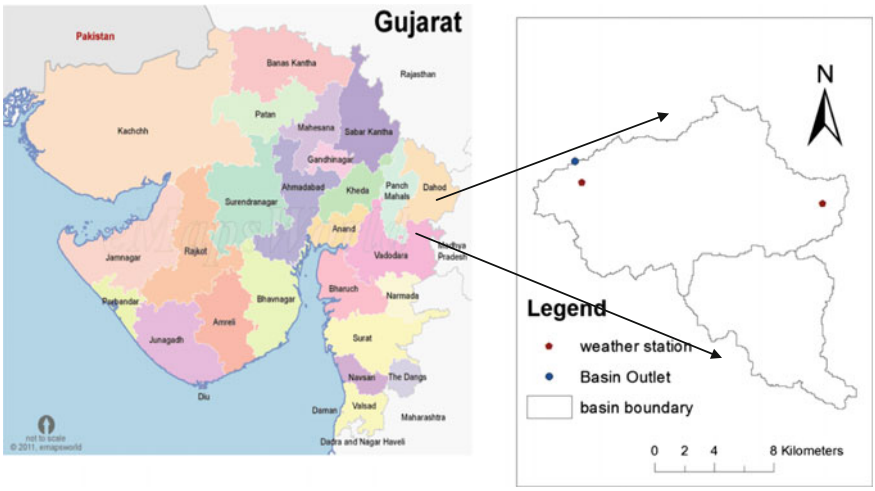

Fig. 1 Location map of the study area

Software Used

ERDAS Imagine: The Earth Resources Data Analysis System (ERDAS) imagine, an image processing software, has been extensively used for importing and exporting of different remote sensing images from one format to another, rectification of imageries, subsetting of images, and classification of images and preparation of thematic maps.

ArcMap: In the present study, ArcMap software developed by Environmental Systems Research Institute (ESRI) has been used extensively for arranging all the thematic layers in proper sequence and to perform different operations such as overlaying, intersection.

Pre-processing of Satellite Data

1. **Import of HDF format image**: The original MODIS data are provided in the Hierarchical Data Format (HDF-EOS). HDF is a multi-object file format for sharing scientific data in multi-platform distributed environments. It is import in Arcgis.
2. **Reprojection**: MODIS Land surface temperature and surface reflectance image are in sinusoidal projection and WGS84 datum. This sinusoidal projection is reprojected to Albers conical equal area and WGS84 datum.
3. **Subset**: Using AOI layer of Limkheda watershed boundary, subset area corresponding to Gujarat state has been done for all the images.

Scientific Data Sets (SDS)

The SDSs in the MYD11A1 product include LST_Day_1 km, QC_Day, Day_view_time, Day_view_angle, LST_Night_1 km, QC_Night, Night_view_time, Night_view_angle, Emis_31, Emis_32, Clear_day_cov, Clear_night_cov. Note that the scale factor and offset for Day_view_angle and Night_view_angle in V5 Level-3 MODIS LST products have been changed so that a negative sign of the viewing angle means MODIS viewing the grid from east. The view zenith angle itself is always a positive number, the zenith angle from nadir. The information of MODIS viewing the grid from east or west may be important in understanding the view angle effect in the temporal variations in LSTs, especially in rugged regions.

MODIS Description

MODIS Data: As a part of the NASA EOS project, two MODIS instruments were placed on the Terra and Aqua satellite platforms to provide information for global studies of atmosphere, land and ocean processes. Aqua passes overhead at approximately 1:30 p.m. (ascending mode) and 1:30 a.m. (descending mode) local time, whereas Terra passes at 10:30 a.m. (descending mode) and 10:30 p.m. (ascending mode) local time. The MODIS instruments have distinct advantages in terms of their global coverage, high radiometric resolution and dynamic ranges, and accurate calibration in the thermal infrared (TIR) bands. MODIS land surface temperature products provide global temperatures and emissivities with daily or quasi-daily temporal resolutions and either a 1-km spatial resolution, retrieved using the generalized split-window algorithm, or a 5-km spatial resolution, retrieved using the MODIS day/night LST algorithm. In this study, MODIS Collection-5 LSTs at a 1-km spatial resolution (MOD/MYD11A1) were evaluated, while the synchronous Collection-5 LSTs at a 5-km spatial resolution (MOD/MYD11B1) were downloaded to calculate the land surface broadband emissivity of each station based on Equation. The MOD/MYD11A1 product pixels were determined based on the location of the validation stations. Then, the validated pixels were further selected through the LST product quality control field (QC = 0) and the sensor view zenith angle field (SVZ < 40°). To calculate the broadband emissivities of the stations, emissivity data in band 29, band 31 and band 32 were selected from the MOD/MYD11B1 corresponding to the MOD/MYD11A1 pixels that had been previously selected.

MODIS Sensor

Orbit : 705 km
10.30 a.m. descending node (Terra)
01.30 p.m. ascending node (Aqua)
Sun-synchronous, near polar, circular
Scan rate : 20.3 rpm, cross track
Scan angle : +/- 55 degrees
Swath width : 2330 km (cross track) by
10 km (along track at nadir)
Size : 1.0 x 1.6 x 1.0 m
Weight : 228.7 kg
Power : 162.5 W (single orbit average)
Data rate :10.6 Mbps (peak daytime)
6.1 Mbps (orbital average)
Orbit period : 99 minutes
Quantization: 12 bits
Spatial Resolution :250 m (band 1-2) ; 500 m (band 3-7) ; 1000 m (band 8-36)

Results and Discussion

Date-Wise Pre-processing of Modis Remote Sensing Imagery to Extract Pixel Values

All the MODIS imagery obtained during the month of October are pre-processed to extract all the pixel values from two gauge stations over Limkheda watershed. Later on pixel values of two gauges are applied to simulate the temperature in these gauges. Subdatabase-10 clear day cov. (16-bit unsigned integer) on 09 October 2010, is shown in Fig. 2.

Subdatabase-10 clear day cov. (16-bit unsigned integer) for 10 and 11 October 2010, are shown in Figs. 3 and 4, respectively.

Subdatabase-10 clear day cov. (16-bit unsigned integer) for 14 and 15 October 2010, is shown in Figs. 5 and 6, respectively.

Subdatabase-10 clear day cov. (16-bit unsigned integer) for 17 and 22 October 2010, are shown in Figs. 7 and 8, respectively.

Subdatabase-10 clear day cov. (16-bit unsigned integer) for 24 and 26 October 2010, are shown in Figs. 9 and 10, respectively.

Subdatabase-10 clear day cov. (16-bit unsigned integer) for 28 and 29 October 2010, are shown in Figs. 11 and 12, respectively.

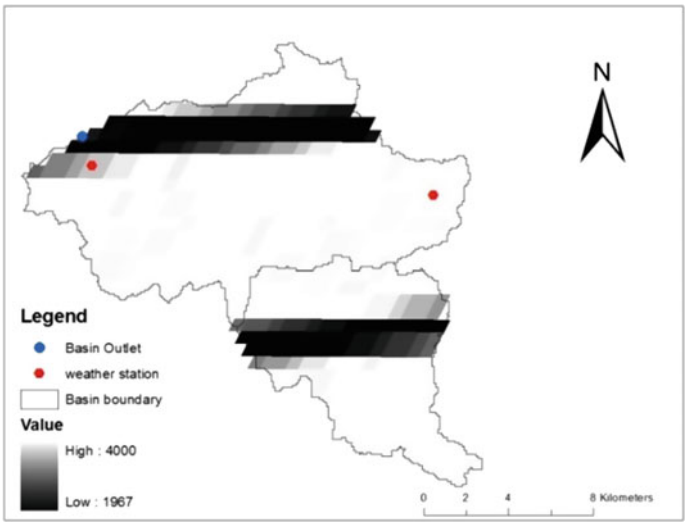

Fig. 2 Subdatabase-10 clear day cov. (16-bit unsigned integer) on 09 Oct 2010

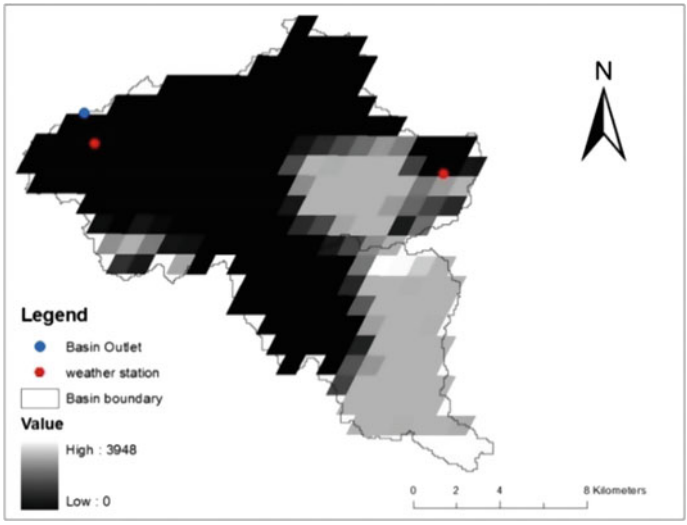

Fig. 3 Subdatabase-10 clear day cov. (16-bit unsigned integer) on 10 Oct 2010

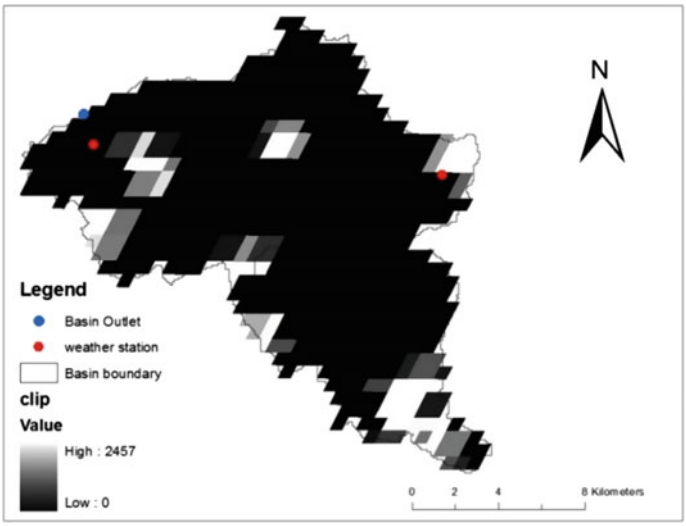

Fig. 4 Subdatabase-10 clear day cov. (16-bit unsigned integer) on 13 Oct 2010

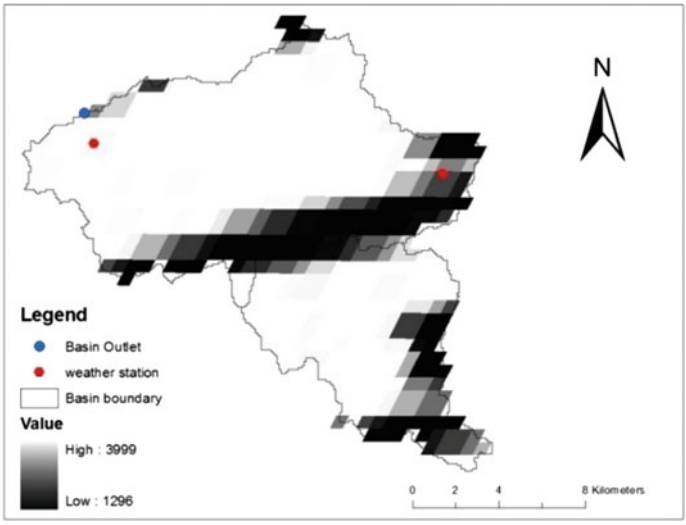

Fig. 5 Subdatabase-10 clear day cov. (16-bit unsigned integer) on 14 Oct 2010

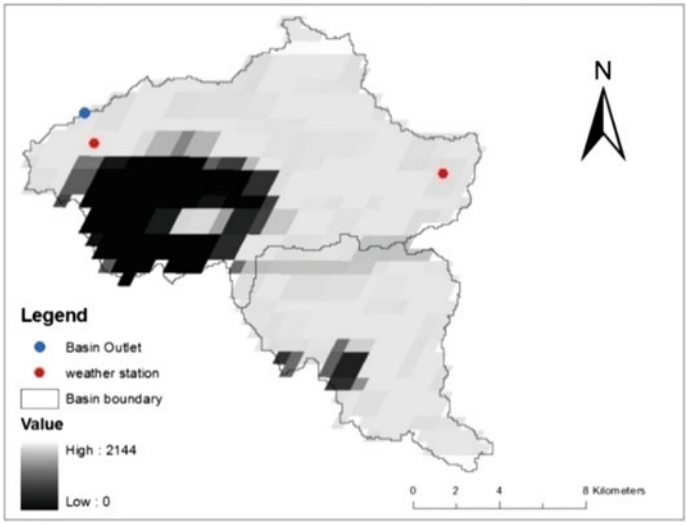

Fig. 6 Subdatabase-10 clear day cov. (16-bit unsigned integer) on 15 Oct 2010

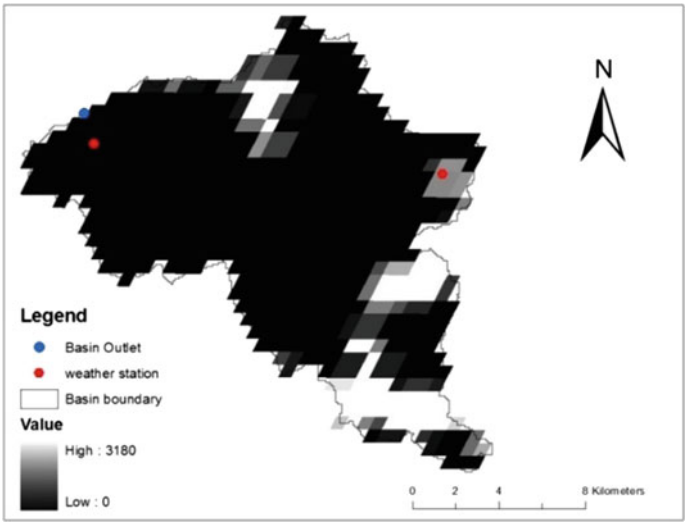

Fig. 7 Subdatabase-10 clear day cov. (16-bit unsigned integer) on 17 Oct 2010

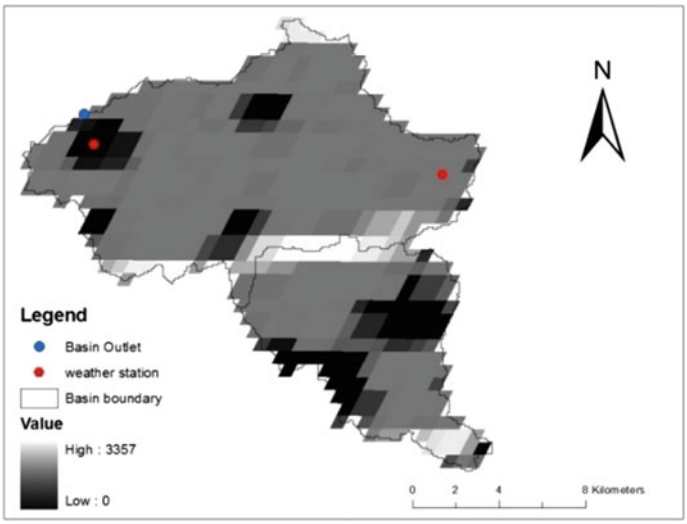

Fig. 8 Subdatabase-10 clear day cov. (16-bit unsigned integer) on 22 Oct 2010

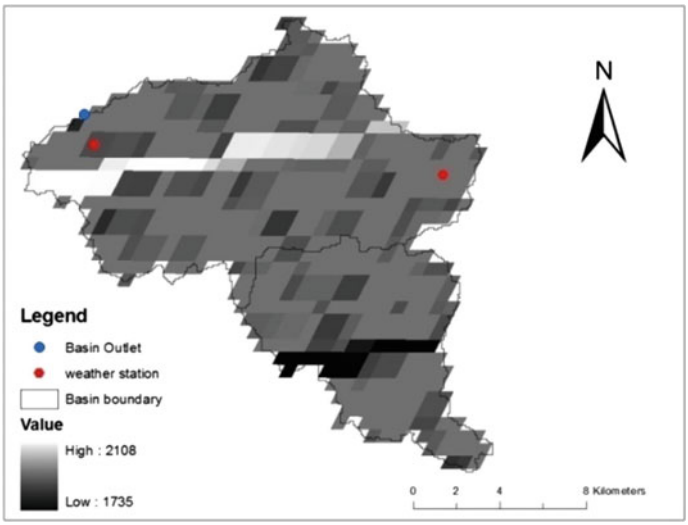

Fig. 9 Subdatabase-10 clear day cov. (16-bit unsigned integer) on 24 Oct 2010

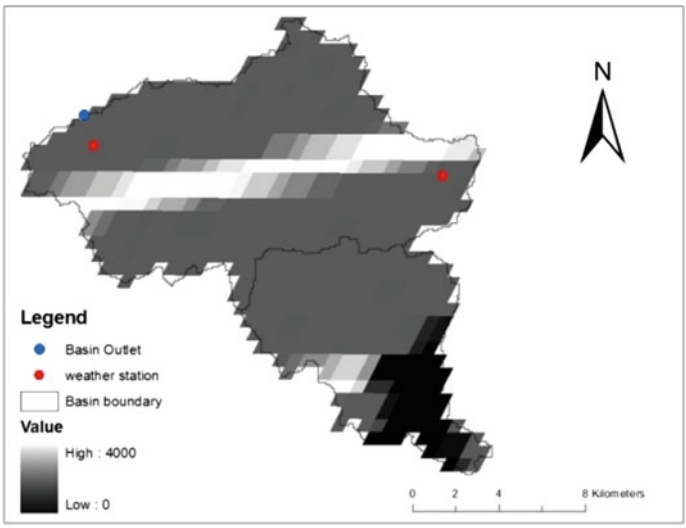

Fig. 10 Subdatabase-10 clear day cov. (16-bit unsigned integer) on 26 Oct 2010

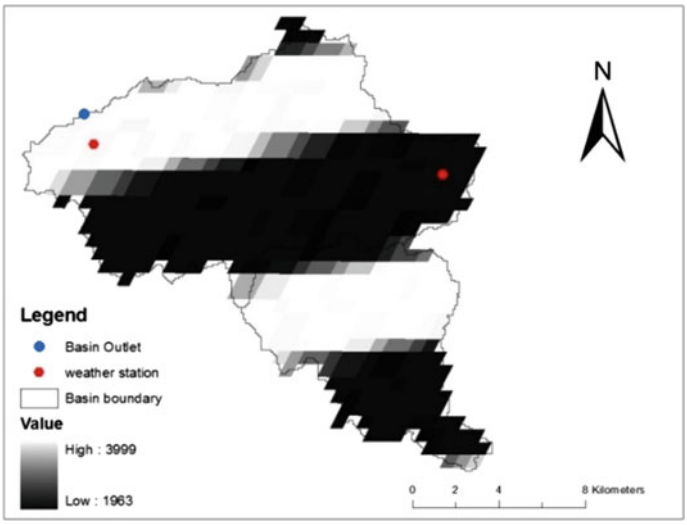

Fig. 11 Subdatabase-10 clear day cov. (16-bit unsigned integer) on 28 Oct 2010

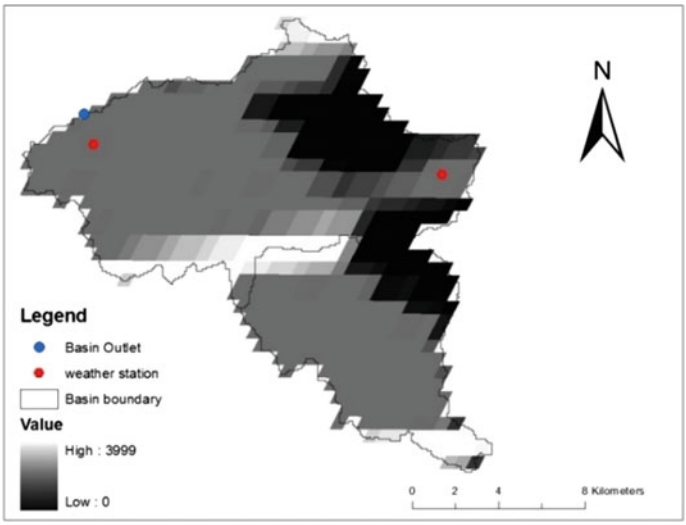

Fig. 12 Subdatabase-10 clear day cov. (16-bit unsigned integer) on 29 Oct 2010

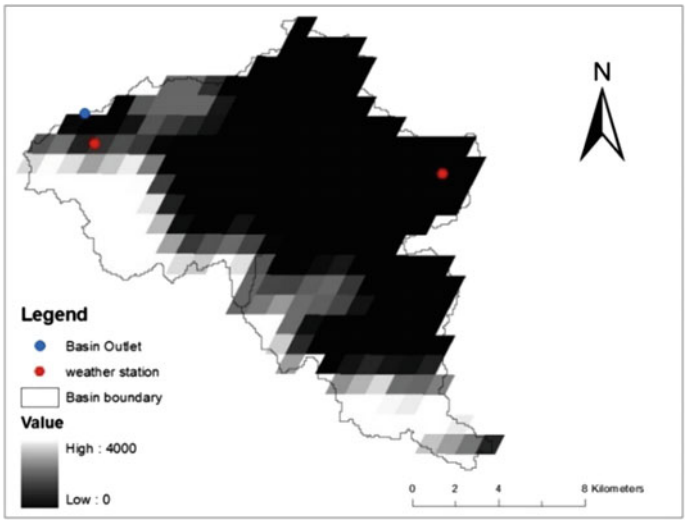

Fig. 13 Subdatabase-10 clear day cov. (16-bit unsigned integer) on 30 Oct 2010

Subdatabase-10 clear day cov. (16-bit unsigned integer) for 30 and 31 October 2010, are shown in Figs. 13 and 14, respectively.

A relationship between pixel values of all the MYD11A1 product including LST_Day_1 km, QC_Day, Day_view_time, Day_view_angle, LST_Night_1 km, QC_Night, Night_view_time, Night_view_angle, Emis_31, Emis_32, Clear_day_cov,

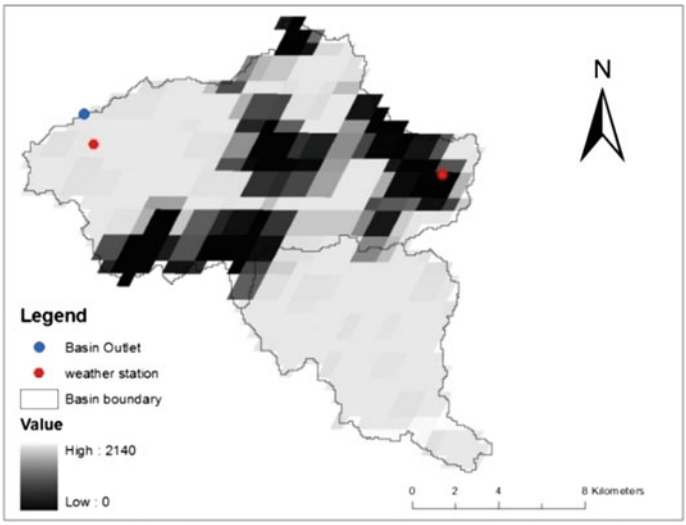

Fig. 14 Subdatabase-10 clear day cov. (16-bit unsigned integer) on 31 Oct 2010

Table 1 Date-wise maximum temperature, minimum temperature and pixel value for Dahod Subdatabase-9, EMIS_32 (8-bit unsigned integer)

Date	Location: Dahod		
	Pixel value	Max	Min
10/9/2010	136	32.0	24.0
10/10/2010	136	33.0	23.0
10/13/2010	139	34.0	25.0
10/14/2010	141	35.2	25.0
10/15/2010	142	35.6	26.0
10/17/2010	139	35.4	20.6
10/22/2010	136	34.6	19.8
10/24/2010	132	33.0	19.0
10/26/2010	134	34.8	21.0
10/28/2010	134	34.2	21.0
10/29/2010	133	34.2	20.0
10/30/2010	130	34.2	17.0
10/31/2010	128	33.4	17.0

Clear_night_cov is established and the results for Emis_32, MODIS imagery for which results were found better are shown below. Date-wise maximum temperature, minimum temperature and pixel value obtained for Dahod gauge station using Subdatabase-9, EMIS_32 (8-bit unsigned integer) are shown in Table 1.

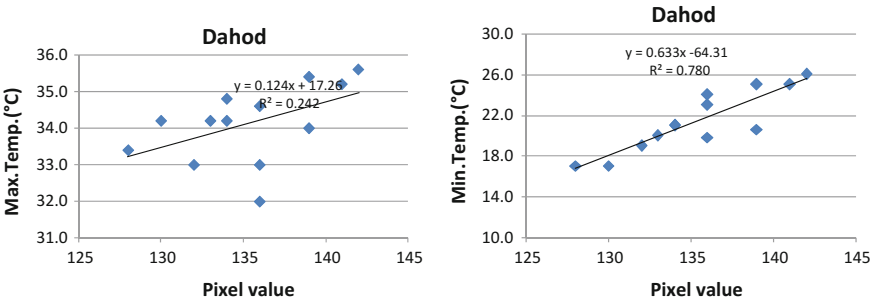

(a) MaximumTemperature Dahod (b) Minimum Temperature Dahod

Fig. 15 Relationship between pixel values and minimum and maximum temperature in Dahod gauge station using Subdatabase-9 Emis-32 (8-bit unsigned integer) MODIS imagery

Table 2 Date-wise maximum temperature, minimum temperature and pixel value for Limkheda Subdatabase-9, EMIS_32 (8-bit unsigned integer)

Date	Location: Limkheda		
	Pixel value	Max	Min
10/9/2010	143	37.00	20.50
10/10/2010	139	35.00	21.00
10/13/2010	135	33.00	20.00
10/14/2010	138	35.00	21.00
10/15/2010	140	35.00	20.50
10/17/2010	137	35.00	21.00
10/22/2010	136	35.00	20.00
10/24/2010	133	34.00	20.00
10/26/2010	138	35.00	20.00
10/28/2010	131	34.00	19.00
10/29/2010	131	34.00	18.00
10/30/2010	132	34.00	19.00
10/31/2010	133	34.00	19.50

Pixel values extracted for the Dahod gauge station are modelled to simulate maximum and minimum temperature by using regression equation. A regression model is fitted between pixel values and minimum and maximum temperature in Dahod gauge station using Subdatabase-9 Emis-32 (8-bit unsigned integer), and the results are shown in Fig. 15.

Date-wise maximum temperature, minimum temperature and pixel value obtained for Limkheda gauge station using Subdatabase-3 Day_view_angle (8-bit unsigned integer) are shown in Table 2. Similarly pixel values extracted for the

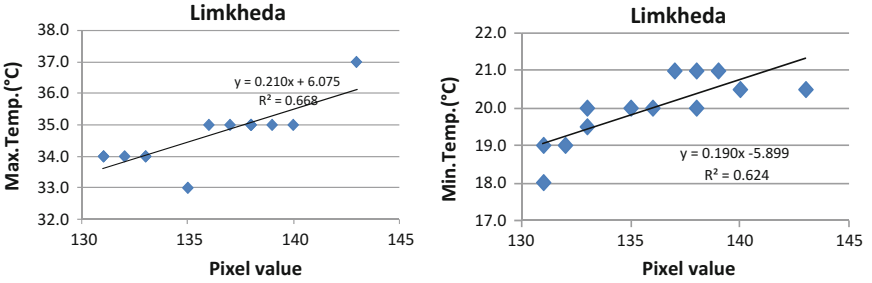

(a) Maximum Temperature Limkheda (b) Minimum Temperature Limkheda

Fig. 16 Relationship between pixel value and minimum and maximum temperature in Dahod and Limkheda gauge station using Subdatabase-9 Emis-32 (8-bit unsigned integer) MODIS imagery

Limkheda gauge station are modelled to simulate maximum and minimum temperature by using regression equation. A regression model is fitted between pixel values and minimum and maximum temperature in Limkheda gauge station using Subdatabase-9, EMIS_32 (8-bit unsigned integer) MODIS imagery, and the results are shown in Fig. 16.

Based on the scatter plot for each site in figures, the validation results derived from the temperature from the ground-measured station data in good agreement with the pixel values are derived using the MODIS imagery. In general, the regression equation is able to model the maximum and minimum temperature in both the sites, namely Dahod and Limkheda using Day_view_angle and Emis_32 MODIS remote sensing imagery. A promising agreement between the MODIS 1-km land surface temperature products (MOD/MYD11A1) and the ground-measured temperatures for the Limkheda and Dahod stations indicates the applicability of selected MODIS imagery for temperature simulation in the whole Limkheda watershed and adjoining area.

Conclusions

Capability of MODIS satellite imagery is explored to simulate the temperature in the Limkheda watershed. A relationship between pixel values of the entire MYD11A1 product including LST_Day_1 km, QC_Day, Day_view_time, Day_view_angle, LST_Night_1 km, QC_Night, Night_view_time, Night_view_angle, Emis_31, Emis_32, Clear_day_cov, Clear_night_cov is established. It is found in this study that bands, namely Day_view_angle and Emis_32, MODIS imagery are found better to simulate minimum and maximum temperature. It is found in this study that Day_view_angle simulate minimum temperature very well, whereas Emis_32 band simulate both the maximum and minimum temperature very well. From this study, it can be recommended that Emis_32 band can be used to calculate temperature

throughout the Limkheda watershed and nearby area. Estimation of distributed minimum and maximum temperature can be applied in several distributed hydrological, hydro-meteorological, crop growth modelling.

References

Adamowski J, Fung Chan H, Prasher SO, Ozga-Zielinski B, Sliusarieva A (2012) Comparison of multiple linear and nonlinear regression, autoregressive integrated moving average, artificial neural network, and wavelet artificial neural network methods for urban water demand forecasting in Montreal, Canada. Water Resour Res 48

Aikawa M, Hiraki Eiho T J, Miyazaki H (2008) Air temperature variation with time and thermally evaluated atmospheric conditions correlated with land use change in urban areas of Japan. Int J Climatol 28:789–795

Bastiaanssen WGM, Pelgrum H, Wang J, Ma Y, Moreno JF, Roerink GJ, van der Wal T (1998) A remote sensing surface energy balance algorithm for land (SEBAL). J Hydrol 212–213: 213–229

Del Fratea F, Iapaoloa M, Casadiob S, Godin-Beekmannc S, Petitdidier M (2005) Neural networks for the dimensionality reduction of GOME measurement vector in the estimation of ozone profiles. J Quant Spectrosc Radiat Transf 92:275–291

Deo RC, Şahin M (2015) Application of the artificial neural network model for prediction of monthly standardized precipitation and evapotranspiration index using hydrometeorological parameters and climate indices in eastern Australia. Atmos Res 161–162:65–81

Gribanov KG, Zakharov VI (2004) Neural network solution for temperature profile retrieval from infrared spectra with high spectral resolution. Atmos Sci Lett 5:1–11

Lozada B, Sentelhes YP (2008) Modelos de estimación de las temperaturas promedios de la mínima, maxima y media diaria para la Región andina de Venezuela. Agronomía Trop 58(2):141–153

Marquínez J, Lastra J, García P (2003) Estimation models for precipitation in mountainous regions: the use of GIS and multivariate analysis. J Hydrol 270:1–11

Mostovoy GV, King RL, Reddy KR, Kakani VG, Filippova MG (2006) Statistical estimation of daily maximum and minimum air temperatures from MODIS surface temperature data. Remote Sens Environ 114(2):449–465

Rugege D (2002) Regional analysis of maize-based land use systems for early warning applications. 118 p. Ph.D. International Institute for Geo-Information Science and Earth Observation (ITC), Wageningen University, Enschede, The Netherlands

Tiwari MK, Adamowski J (2013) Urban water demand forecasting and uncertainty assessment using ensemble wavelet-bootstrap-neural network models. Water Resour Res 49:6486–6507

Vancutsem C, Ceccato P, Dinku T, Connor SJ (2010) Evaluation of MODIS land to estimate air temperature in different ecosystems over Africa. Remote Sens Environ 114(2):449–465

Wan Z, Dozier J (1996) A generalized split-window algorithm for retrieving land surface temperature from space. IEEE Trans Geosci Remote Sens 34:892–905

A RS and GIS Approaches for the Estimation of Runoff and Soil Erosion in SA-13 Watershed

H. N. Bhange and V. V. Deshmukh

Abstract The research work was conducted for the estimation of runoff and soil loss from SA-13 watershed. SA-13 watershed has area of 213 km^2 in Ashti tahsil, Beed. The SCS curve number method and Revised USLE using RS and GIS techniques were used to find out runoff volume and soil erosion. The results show that the average rainfall for the year 2005 in the SA-13 watershed was 406.50 mm and average annual runoff was 93.52 mm, amounting 23.01% of the total rainfall received. The average annual soil loss of the SA-13 watershed is 8.2 tons/ha/year. Soil erosion is in moderate erosion risk class. The results obtained using remote sensing techniques can help decision makers to prepare resource map accurately in less time and cost.

Introduction

A watershed is a natural ecological unit composed of interrelated parts and contributes runoff water to a single point. Rainstorms generate runoff, and its occurrence and quantity are dependent on the intensity, duration, and distribution of the rainfall event. There are a number of catchment-specific factors, which have a direct effect on the occurrence and volume of runoff which includes soil type, vegetation cover, slope, and catchment's type. Runoff is one of the most important hydrologic variables used in most of the resource applications. Reliable prediction of quantity and rate of runoff from land surface into stream and river is difficult and time-consuming to obtain for ungauged watershed. However, this information is

H. N. Bhange (✉)
Department of Soil and Water Conservation Engineering, CAET, DBSKKV, Dapoli, District Ratanagiri 415712, MS, India
e-mail: harshalbhange@gmail.com

V. V. Deshmukh
Department of Soil and Water Conservation Engineering, Pad. Dr. D.Y. Patil CAET, Talsande, Kolhapur, MS, India
e-mail: vidya1723@gmail.com

V. P. Singh et al. (eds.), *Hydrologic Modeling*, Water Science and Technology Library 81, https://doi.org/10.1007/978-981-10-5801-1_22

needed in dealing with many watershed development and management problems. Conventional methods for prediction of river discharge require considerable hydrological and meteorological data. Collection of these data is expensive, time-consuming, and a difficult process.

In India, the availability of accurate information on runoff is scarcely available and that too in a few selected sites where recording and automatic hydrologic gauging stations are installed. Thus, there is an urgent need to generate information on basin runoff and silt yield for the acceleration of the watershed development and management programs (Zade et al. 2005). Most of the agricultural watersheds in India are ungauged, having no past record whatsoever of rainfall–runoff processes (Sarangi et al. 2005a, b). Non-availability of continuous rainfall and runoff records in majority of Indian watersheds has led to the development of techniques for the estimation of surface runoff from ungauged basins (Chattopadhyay and Choudhury 2006).

However, speeding up of the watershed management program for conservation and development of natural resource management has necessitated the runoff information. Remote Sensing data was provided a quick result for decision-makers before any quantification of Runoff. These tools provide significant reduction in the cost and time over the conventional methods with reliability and accuracy. So the RS and GIS techniques provide valuable modern tools in evaluation, management, and system performance of the water resources (Ingle et al. 2008). Advances in computational power and the growing availability of spatial data have made it possible to accurately predict the runoff. The possibility of rapidly combining data of different types in a geographic information system (GIS) has led to significant increase in its use in hydrological applications. The runoff depth computed for ungauged watershed using SCS-CN method in the GIS environment is used for management and conservation purposes (Ebrahimian et al. 2009). Out of several methods for runoff estimation from ungauged watershed, the curve number (CN) is an index developed by the Natural Resource Conservation Service (NRCS), to represent the potential for storm water runoff within a drainage area. The curve number method, also known as the hydrologic soil cover complex method, is a versatile and widely used procedure for runoff estimation. The CN for a drainage basin is estimated using a combination of land use, soil's permeability, and antecedent soil moisture condition (AMC).

Soil erosion is one of the most critical environmental hazards of modern times. Assessing the severity of soil erosion is difficult due to the fact that land often erodes at an imperceptible rate. In addition, some areas may be more susceptible to soil erosion than others and the rate of erosion is not the same everywhere. Vast areas of land now being cultivated may be rendered economically unproductive if the erosion of soil continues unabated.

Soil erosion is a complex phenomenon as it is governed by various natural processes, and it, in turn, results in decrease of soil fertility and reduction of crop yields. Globally, 1964.4 M ha of land is affected by human-induced degradation (UNEP 1997). Of this, 1,903 M ha is subject to soil erosion by water and

548.3 M ha by wind erosion. Each year, 75 billion tons of soil is removed due to erosion largely from agricultural land. The process of soil erosion involves detachment, transport, and subsequent deposition (Meyer and Wischmeier 1969). The consequence of soil erosion occurs both on-site and off-site (Morgan 1986). On-site effects are particularly, where the redistribution of soil within a field, the loss of soil from a field, the breakdown of soil structure, and the decline in organic matter and nutrient result in a reduction of cultivable soil depth and decline in soil fertility. Erosion also reduces available soil moisture, resulting in more drought-prone conditions. The net effect is a loss of productivity which, at first, restricts what can be grown and results in increased expenditure on fertilizers to maintain yields but later, ultimately leads to land abandonment. Off-site problems result from sedimentation downstream, which reduces the capacity of the rivers, enhances the risk of flooding, blocks irrigation canals, and reduces the design life of reservoirs.

The prevention of soil erosion, which means reducing the rate of soil loss to approximately that which would occur under natural conditions, relies on selecting appropriate strategies for soil conservation, and this, in turn, requires a thorough understanding of the processes of erosion. The factors, which influence the rate of soil erosion, are rainfall, runoff, soil, slope, plant cover, and the presence or absence of conservation measures (Morgan 1986).

Several parametric models have been developed by various scientists to predict soil erosion from drainage basins, hillslopes, and field levels. With a few exceptions, these models are based on soil type, land use, climatic and topographic information. Remote sensing technique makes it possible to measure hydrologic parameters on spatial scales. Scientific management of soil, water, and vegetation resources on watershed basis is very important to arrest erosion and rapid siltation in rivers, lakes, and estuaries.

It is, however, realized that due to financial and organizational constraints, it is not feasible to treat the entire watershed within a short time. Prioritization of watersheds on the basis of those sub-watersheds within a watershed which contribute maximum sediment yield obviously should determine our priority to evolve appropriate conservation management strategy so that maximum benefit can be derived out of any such money-time-effort making scheme. Within any particular area, there will be a considerable variation in erosion rates, but if the rates are grouped into those related to natural vegetation, cultivated land, and bare soil, each group follows a broadly similar pattern of similar variation.

Erosion is not only a function of climate alone but also depends on the frequency at which potentially erosive events coincide with ground conditions that accelerate the erosion. The most vulnerable time for erosion is the early part of the wet season when the rainfall is high, but the vegetation has not grown sufficiently to protect the soil. Generally, the period between plowing and the growth of the crop beyond the seedling stage contains an erosion risk if it coincides with heavy rainfall (Morgan 1986).

Erosion and land use change are very closely related. Rates of soil loss accelerate quickly unacceptably high levels whenever land is misused. Erosion is a natural

process but that its rate and spatial and temporal distribution depends on the interaction of physical and human circumstances.

Simple methods such as the Universal Soil Loss Equation (USLE) (Musgrave 1947), the Modified Universal Soil Loss Equation (MUSLE) (Williams 1975), or the Revised Universal Soil Loss Equation (RUSLE) (Renard et al. 1991) are frequently used for the estimation of surface erosion from catchment areas (Ferro and Minacapilli 1995; Ferro 1997; Kothyari and Jain 1997; Ferro et al. 1998). Both of these quantities are found to have large variability due to the spatial variation of rainfall and catchment heterogeneity. The use of geographical information system (GIS) methodology is well suited for the quantification of heterogeneity in the topographic and drainage features of a catchment (Shamsi 1996; Rodda et al. 1999). With this view in mind, the study was carried out with the objectives, estimation of runoff using SCS-CN and estimation of soil erosion using RUSLE, by RS and GIS from watershed. SA-13 watershed is located in Ashti tahsil, district Beed of Maharashtra. Area represents typical semiarid region of Maharashtra state and associated agroecological setup.

Watershed SA-13 lies between longitude 75° 04′ 55″ to 75° 16′ 25″E and latitude 18° 40′ 11″ to 18° 56′ 20″N. SA-13 occupies an area of about 21,300 ha (Fig. 1). The elevation of the watershed ranges from 730 m above mean sea level at northeast border and gradually decreases down to 575 m at the confluence of Sina and Talwar rivers

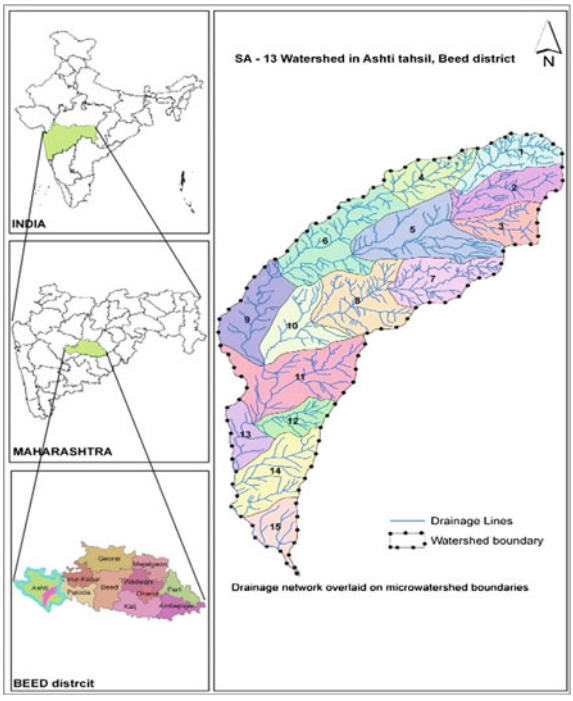

Fig. 1 Location map of study area

Materials and Methods

Watershed Delineation

Survey of India toposheets 47°N/1, 47°N/2, and 47°N/5 (1:50,000 scale) in combination with satellite image was used for watershed delineation. Contours, spot heights, and elevation along with drainage pattern exhibited on the toposheets were the guiding features for micro-watershed delineation. 15 micro-watersheds were delineated for the project area.

Land Use/Land Cover

Land use/land cover was one of the most important thematic inputs in any study as it provides the present status of land utilization and its pattern. The change in the land use/land cover is very dynamic that is why satellite remote sensing is widely used for its mapping. The multiseasonal satellite data are used to know the status of different crops in different seasons. Classification system suggested by NRSA (1989) was adopted. The preprocessing techniques need to be employed on the satellite data before it can be used for actual interpretation. Geometric correction of satellite images and enhancement used as a preprocessing step is required for further processing. ERDAS Imagine 9.1 image processing software is used for preprocessing of satellite data (ERDAS Imagine Field Guide 1998), whereas Arc GIS 9.2 suite was used for performing integration of various thematic layers which includes spatial and non-spatial analysis (ESRI User Manual 1994).

In this study, hybrid classification approach (supervised, unsupervised, and NDVI threshold) was adopted to classify the area into different land use classes. The soil map of the study area has been prepared by MRSAC under the project IMSD (Integrated Mission for Sustainable Development) as per the guidelines of NBSS and LUP (1995), AIS and LUS, and Ministry of Agriculture was used for this purpose.

Slope Extraction from SRTM DEM

The NASA Shuttle Radar Topographic Mission (SRTM) has provided digital elevation model (DEMs) for over 80% of the globe. These data are currently distributed free of charge by USGS and are available for download from the National Map Seamless Data Distribution System, or the USGS ftp site. The SRTM data are available as 3-arc second (approx. 90-m resolution) DEMs. A 1-arc second data product was also produced, but is not available for all countries. The vertical error of the DEMs is reported to be less than 16 m. The data come in two formats:

arc-formatted ASCII and GeoTIFF. (http://glcf.umiacs.umd.edu/index.shtml) SRTM DEM is used to understand the drainage networks, elevation, and generation of the slope.

Runoff Estimation by SCS Curve Number Method

The requirements for the soil conservation service (SCS) curve number (CN) method are rainfall amount and curve number. The curve number is based on the hydrologic soil group, land use treatment, and hydrologic condition. As defined by SCS soil scientists, soil was classified into four hydrologic groups (A, B, C, and D) (USDA 1985), depending on infiltration and soil classification. Land use and treatment classes were used in the preparation of hydrologic soil cover complex method.

Antecedent soil moisture condition (AMC) is an indicator of watershed wetness and availability of soil moisture storage prior to a storm and has a significant effect on runoff volume. Recognizing its significance, SCS developed a guide for adjusting CN according to AMC based on the total rainfall in the 5-day period preceding a storm. Three levels of AMC are used in the CN method: AMC-I for dry, AMC-II for normal, and AMC-III for wet conditions. Table 1 gives seasonal rainfall limits for these three antecedent soil moisture conditions.

The CN method is based on the recharge capacity of the watershed. The recharge capacity is determined by antecedent soil moisture conditions and physical characteristics of the watershed. The storage capacity (S) can be obtained from CN by using the following relationship

$$S = \frac{24,500}{\mathrm{CN}} - 245 \tag{1}$$

where

S Maximum recharge capacity of watershed after 5-day rainfall antecedent, mm
CN Curve number.

In the past 30 years, the SCS method has been used by a few researchers because it gives consistently usable results (Rao et al. 1996; Sharma et al. 2001;

Table 1 Classification of antecedent soil moisture condition

AMC	5-days Antecedent rainfall (mm)	
	Active growing season	Dormant season
I	Dry (<35)	Dry (<12.5)
II	Medium (35–52.5)	Medium (12.5–27.5)
III	Wet (>52.5)	Wet (>27.5)

Chandramohan and Durbude 2001; Sharma and Kumar 2002) for runoff estimation. Putting the value of curve number in above, the recharge capacity '*S*' was calculated. The direct runoff of the watershed was calculated using following equation.

$$\begin{aligned} Q &= 0, && \text{If } P \leq 0.2S \\ Q &= \left(\frac{P-0.2S)^2}{P+0.8S}\right) && \text{If } P \geq 0.2S \end{aligned} \tag{2}$$

where

Q Runoff depth (mm)
P Rainfall (mm)
S Maximum recharge capacity of watershed after 5-day rainfall antecedent (mm).

Generating CN Map

To generate the CN map, the hydrologic soil group and land use maps were integrated into GIS environment. An integrated, hydrologic soil cover complex method map with new polygons representing the merged soil hydrologic group and land use was generated. Weighted CN map was generated using following equation:

$$\text{CN} = \frac{\sum \text{CN}_i \times A_i}{A} \tag{3}$$

where

CN weighted curve number.
CN_i curve number from 1, 2, 3, … *i*.
A_i area with curve number CN_i
A total area of the watershed.

Antecedent Soil Moisture Condition (AMC)

The CN values for each polygon were calculated for average conditions (i.e., antecedent soil moisture condition Class II). To determine which AMC class was the most appropriately related to study area, the use of rainfall data is necessary. The CN values are documented for the case of AMC-II (USDA 1985). To calculate CN values for AMC-I and AMC-III conditions, the following equations are used (Chow et al. 2002):

$$\text{CN for AMC-I,} \quad \text{CN}_{(\text{I})} = \frac{4.2 * \text{CN}_{(\text{II})}}{10 - \left(0.058 * \text{CN}_{(\text{II})}\right)} \tag{4}$$

$$\text{CN for AMC-III,} \quad \text{CN}_{(\text{III})} = \frac{23 * \text{CN}_{(\text{II})}}{10 + \left(0.13 + \text{CN}_{(\text{II})}\right)} \tag{5}$$

where

$\text{CN}_{(\text{II})}$ curve number for normal condition,
$\text{CN}_{(\text{I})}$ curve number for dry condition, and
$\text{CN}_{(\text{III})}$ curve number for wet condition.

Slope-Adjusted CN

Slope has profound impact on the determination of CN values; therefore, incorporating slope values in CN and adjusting CN values accordingly are essential from hydrology study point of view. To achieve this, slope and CN maps were intersected to get slopes of each polygon. Since each polygon has different slopes, calculating weighted slope is needed for each polygon. Weighted slope of a polygon was computed using formula (6).

$$\text{Weighted slope} = \frac{\sum_{i=1}^{n} a_i \times s_i}{A} \tag{6}$$

where

a_i area of slope (ha)
s_i slope in percent
A polygon area (ha)

Weighted slope of polygon was applied in Eq. (8) to compute slope-adjusted CN values. Huang et al.'s (2006) approach was used to make the improvement and incorporate the slope factor into the analysis. The CN values for AMC-II condition are calculated by formula (8) considering the slope correction, and then, $\text{CN}_{(\text{II})}$ modified is converted into CN values for AMC-I and AMC-III condition by using following Eqs. (7) and (9)

$$\text{CN}_{(\text{I})} = \text{CN}_{(\text{II})} - \left(\frac{20\left(100 - \text{CN}_{(\text{II})}\right)}{\left(100 - \text{CN}_{(\text{II})} + \exp\left[2.533 - 0.0636\left(100 - \text{CN}_{(\text{II})}\right)\right]\right)} \right) \tag{7}$$

$$\text{CN}_{(\text{II})}\text{Mod-II} = \text{CN}_{(\text{II})} \left(\frac{322.79 + 15.63\alpha}{\alpha + 323.52} \right) \tag{8}$$

$$\mathrm{CN}_{(\mathrm{III})} = \mathrm{CN}_{(\mathrm{II})} \times \exp\left[0.00673\left(100 - \mathrm{CN}_{(\mathrm{II})}\right)\right] \quad (9)$$

The daily rainfall data for the year 2005 for the study area and the values of maximum potential retention, *S,* obtained from the CN for the watershed area were used for the estimation of runoff from SCS (model).

Soil Erosion by Revised Universal Soil Loss Equation (RUSLE)

In this study, RUSLE an empirical equation is a used and estimated annual soil loss in croplands (tons/ha/year) resulting from sheet and rill erosion. The RUSLE is based on the series of factors, each quantifying one or more processes and their interactions, are combined to estimate overall soil loss. The overall schemas of estimating annual soil loss using remote sensing and GIS techniques are given in Fig. 2. Annual soil loss potential from different categories of land uses has been calculated using RUSLE equation, as under:

$$A = R * K * L * S * C * P \quad (10)$$

where

A Gross amount of soil erosion (t/ha/year);
R Rainfall erosivity factor (MJ mm ha^{-1} h^{-1});

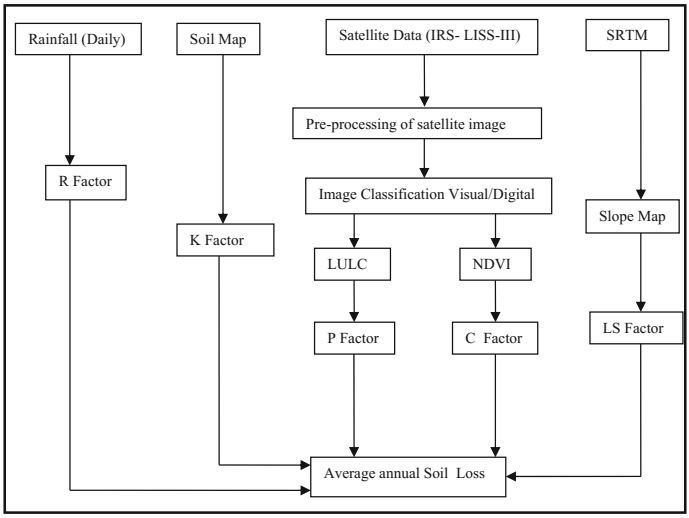

Fig. 2 Flowchart for the estimation of annual soil loss

K Soil erodibility factor (t ha h ha^{-1} MJ^{-1} mm^{-1});
L Slope length factor (dimensionless);
S Slope steepness/gradient factor
C Cover management factor (dimensionless) and
P Support practice factor (dimensionless)

R-Factor (Rainfall Erosivity Factor)

Rainfall data from nine rainfall stations surrounding the SA-13 watershed were used to calculate rainfall erosivity factor (R-value). Monthly precipitation for these stations was collected for the year 2005. The monthly precipitation surface was interpolated to determine the value of each cell. Inverse distance weighted (IDW) technique was adopted to generate interpolated rain image (rain.img) to find the R-factor.

$$\text{R-Factor} = 81.5 + [0.380^{*}(\text{rain.img})] \tag{11}$$

K-Factor (Soil Erodibilty Factor)

K values had been estimated for all the vertical layers of the soil series by using the analytical relationship for the nomograph by Atawoo and Heerasing (1997) given as below

$$100K = \left(2.1 \times 10^{4} \times (2 - \text{OM}) \times m^{1.14} + 3.25 \times (\text{St} - 2) + 2.5 \times (\text{Pt} - 3)\right) \tag{12}$$

where

K Soil erodibility (tons-year/MJ-mm),
OM % Organic matter,
Pt Permeability code,
St Soil structure code,
M A function of the primary particle size function given by
M (% silt + % sand content)

LS-Factor (Slope Length and Steepness Factor)

Slope gradient (S) and slope length (L) were determined and combined to form a single factor known as the topographic factor LS. The accuracy of estimation depends on the resolution of DEM. The LS-factor in the present study was therefore computed by using the equation stated by Moore and Wilson (1992):

$$\mathrm{LS} = (A_S/22.13)^n \times (\sin\beta/0.0896)^m \tag{13}$$

where

A_s the specific area (=Alb), defined as the upslope contributing area for an overland cell (A) per unit width normal to the flow direction (b);
β the slope gradient in degrees;
n 0.4; for 3–4% slope
m 1.3

The slope steepness factor S is evaluated by the relationship developed by McCool et al. (1987)

$$S = 10.8\sin\theta + 0.03 \quad S < 9\% \quad (\text{i.e. } \tan\theta \leq 0.09) \tag{14a}$$

$$S = (\sin\theta/\sin 5.143)^{0.6} \quad S \leq 9\% \quad (\text{i.e. } \tan\theta \geq 0.09) \tag{14b}$$

β is calculated as

$$\beta = (\sin\theta/0.0896)/\left[3.0(\sin\theta)^{0.8} + 0.56\right] \tag{15}$$

where

θ slope angle.

The combined topographic (LS) factor was computed rather than the individual slope length and slope angle factors. The inputs for the computation include the slope in percent and the slope length as a flow length.

C-Factor (Cover Management Factor)

The Normalized Difference Vegetation Index (NDVI), an indicator of the vegetation vigor and health, is used along with the following formula to generate the C-factor image for the study area (Zhou et al. 2008; Kouli et al. 2009).

$$\text{NDVI} = \frac{\text{NIR} - R}{\text{NIR} + R} \tag{16}$$

where

NDVI Normalized Difference Vegetation Index (ratio varying from −1 to +1).
NIR Near-infrared band.
R Red band

The NDVI map was generated for the watershed to formulate the linear equation between NDVI and *C*-factor. The NDVI values less than zero indicate water and other non-vegetated features, so the negative values are not considered in preparing the *C*-factor equation. With these boundary conditions, the regression equation for *C*-factor was developed.

$$C = 0 \quad \text{NDVI} \leq 0 \tag{17a}$$

$$C = -0.50\ \text{NDVI} + 1 \quad 0 < \text{NDVI} \leq 0.68 \tag{17b}$$

$$C = 0 \quad \text{NDVI} \geq 0.68. \tag{18c}$$

P-Factor (Support Practice Factor)

In this study, the watershed was broadly divided into three zones by considering the present land use/land cover practices and support factors (rabi season image reflects the management practices undertaken in the watershed in terms of soil moisture and vegetation cover). The values of conservation practice factor for different management practices were adopted for the SA-13 watershed as suggested by Haan et al. (1994). The *P*-factor was assumed by using the conservation practice of the study area, and the value of *P*-factor for strip cropping was taken as 0.37 (Stone and Hilborn 2000).

Result

Runoff Estimation

In this study, modified soil conservation system (SCS) CN model was used for rainfall–runoff estimation that considers parameter such as soil type, vegetation cover, slope, and watershed characteristics. SCS-CN provides an empirical relationship for estimating initial abstraction and runoff as a function of soil type and land use. Rainfall runoff relationship can be visualized by the factors such as initial abstraction, runoff, and actual retention. The curve number (CN) is an index

developed by the Natural Resource Conservation Service (NRCS), to represent the potential for storm water runoff within a drainage area. The CN for a drainage basin was estimated using a combination of land use, soil, and antecedent soil moisture condition (AMC).

Land Use/Land Cover

There were eight land use/land cover categories, viz. kharif, rabi, seasonal fallow, double crop, forest, wasteland, water bodies, and settlement in the study area. Watershed was dominantly agrarian in nature with other categories such as forest, wasteland, settlement, and water bodies. Agriculture categories observed in the watershed were kharif season crops, rabi season crops, seasonal fallows, and area cropped twice in a year called as double crop area. In total, 17,847.56 ha of area was demarcated as agriculture land which was 83.79% of the total area of the watershed. Seasonal cropping such as kharif, rabi, and fallows occupies about 13.04, 8.63, and 41.20%, respectively. Watershed was dominated by dry deciduous type of forest, occupying the undulating areas and hills in northern part. Based on the canopy coverage, the forest area was categorized as dense, open, and degraded forest (reported as total forest area). The total area under forest was 1127.10 ha, which was 5.29% of the total watershed area.

Wastelands were mainly the non-arable areas occupying undulating landforms and the hillslopes. The total 2039.26 has area under this category, which was 9.57% of the total watershed area. Other classes, such as settlement and water bodies, occupy about 29.60 and 256.47 ha, respectively.

Hydrologic Soil Groups

Soils of the watershed were classified into hydrologic soil groups B, C, and D based on infiltration and runoff generating potentials. Hydrologic group A was absent in the study area. Hydrologic soil groups occurring in the area are depicted in Fig. 3. HSG-C occupies highest aerial extent of about 14,820.99 ha which was 69.58% of the total geographical area of the watershed. Dominance of HSG-C indicates that the soils in the watershed have moderately fine-to-fine structure with slow rate of water transmission and with slow rate of infiltration when thoroughly wetted. HSG-C soils are spread all over the watershed in interdrainage areas where ridge line exist with moderate elevation. These areas are conspicuously cultivated for rainfed crops.

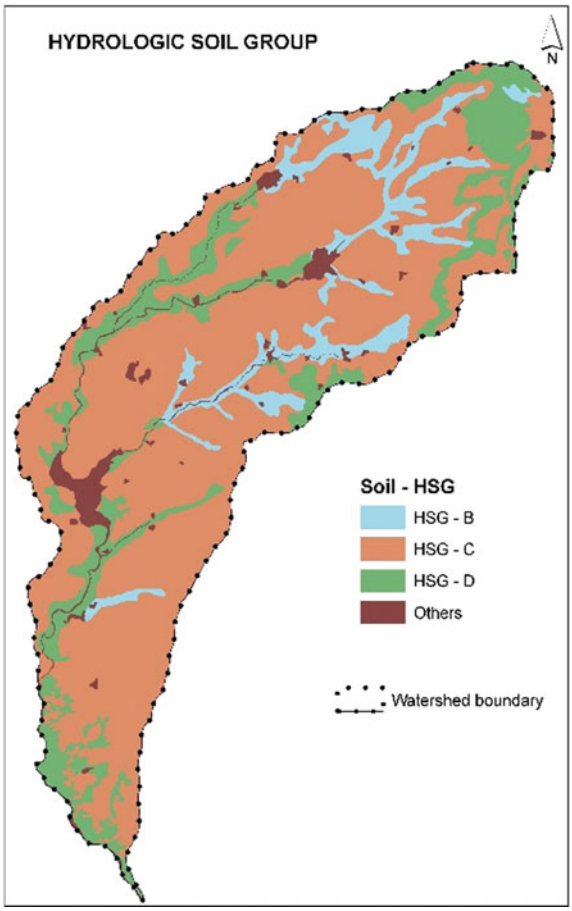

Fig. 3 Hydrological soil grouping (HSG) map of SA-13 watershed

HSG-D covers 17.65% area of watershed. Area occupied by HSG-B was very less, i.e., 1885.50 ha which was mere 8.85% of watershed. They were forming catchment zones for smaller water bodies located in the watershed.

CN Values

Composite curve number for each micro-watershed was calculated by multiplying weights according to the area occupied by each land use class and the corresponding curve numbers. The weighted CN values were further corrected using slope in m/m (initially estimated in degrees and then converted to radians). Mean slope of each micro-watershed was multiplied with weighted CN to derive

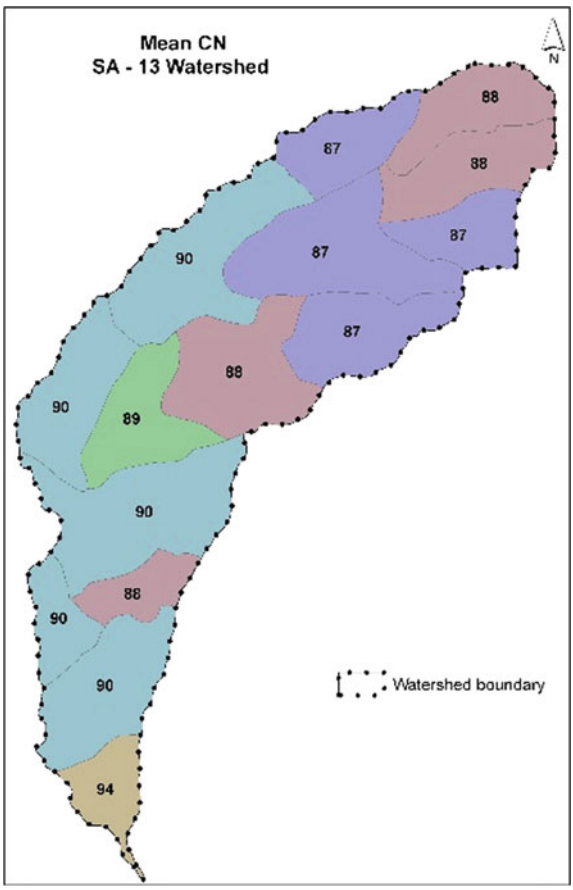

Fig. 4 Mean CN map of SA-13 watershed

slope-corrected or slope-adjusted CN values for each micro-watershed. Final CN values in each micro-watershed for AMC-II are estimated and depicted in Fig. 4.

Hydrological soil groups C and D lead to higher CN values, whereas hydrologic soil group B leads to relatively low CN values. The lowest CN was found 88, whereas highest CN was 94. This indicates that SA-13 watershed generates higher runoff for these considerable high CN values, as CN values increasing runoff would also increase. Any change in land use can alter CN values of the watershed, and accordingly, the runoff response is also favorable to generate more runoff volume. (Mellesse and Shih 2002).

Runoff Depth

The rainfall data of SA-13 watershed were obtained for the year 2005, and runoff estimation based on SCS-CN method had been carried out for 15 micro-watershed areas. Daily estimations of runoff were aggregated on monthly basis, and further cumulative scenario on rainfall, runoff, and percent runoff depth is given in Table 2.

It was observed from Table 2 that average annual rainfall in the watershed for the year 2005 was 406.50 mm, whereas average annual runoff depth was 93.52 mm for the year 2005, amounting 23.01% of the total rainfall. Micro-watershed No. 3 generates minimum runoff (i.e., 19.59%) as against micro-watershed No. 15, which has generated maximum runoff of 33.11%. Micro-watershed numbering 3, 5, 4, 2, 1, and 8 generates lower values of runoff, whereas micro-watershed, viz 15, 9, 6, 14, and 11, generated higher values of runoff.

Soil Loss Estimation

Soil loss is defined as the amount of soil lost in a specified time period over an area of land. It is expressed in units of mass per unit area (t/ha/year). This study uses the RUSLE (Revised Universal Soil Loss Equation) to estimate annual soil loss from agricultural watershed. Soil loss values estimated using RUSLE are dependent upon six major parameters, i.e. *R*-factor (rainfall and runoff), *K*-factor (soil erodibility), *L*-factor (slope length factor), *S*-factor (slope steepness), *C*-factor (cover and

Table 2 Rainfall and runoff depth for the year 2005

Micro-watershed	Rainfall (mm)	Runoff (mm)	% Runoff
1	406.5	84.19	20.71
2	406.5	85.70	21.08
3	406.5	79.63	19.59
4	406.5	80.06	19.69
5	406.5	79.99	19.68
6	406.5	102.71	25.27
7	406.5	81.36	20.01
8	406.5	87.96	21.64
9	406.5	102.84	25.30
10	406.5	96.46	23.73
11	406.5	98.97	24.35
12	406.5	89.93	22.12
13	406.5	97.16	23.90
14	406.5	101.27	24.91
15	406.5	134.58	33.11
Average	406.5	93.52	23.01

management), and *P*-factor (support practice factors). The result of individual RUSLE parameters and average annual soil loss estimated is as follows.

R-Factor (Rainfall Erosivity Factor)

The rainfall distribution was not homogeneous all over the study area; for this reason, an interpolation of annual precipitation data was applied (using IDW interpolation technique) to have a more representative rainfall distribution. The rainfall data from 9 surrounding meteorological stations were used for estimating the average annual precipitation.

R-factor map of the SA-13 watershed is depicted in Fig. 5. *R*-factor values for SA-13 watershed vary from 287 to 329, tending higher values at the northeast

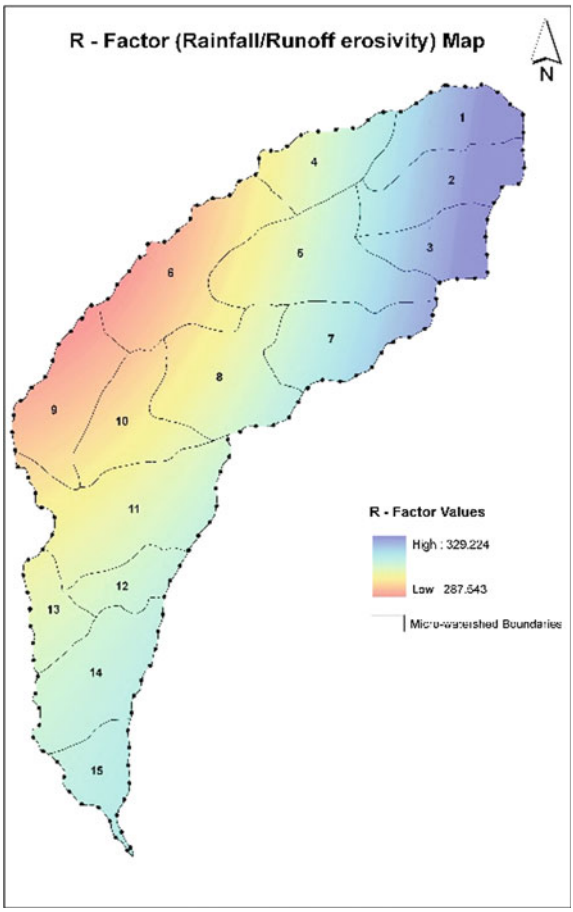

Fig. 5 *R*-factor map of SA-13 watershed

corner and gradually decreasing down to central-west part of the study area. This shows that the value of *R*-factor varies according to rainfall distribution.

K-Factor (Soil Erodability Factor)

The *K*-factor reflects the fact that different soils erode at different rates when the other factors affecting erosion remain the same. Soil texture was the principal cause affecting the *K*-factor along with soil structure, organic matter content, and permeability. A map for the *K*-factor was generated based on above soil parameters and presented in Fig. 6.

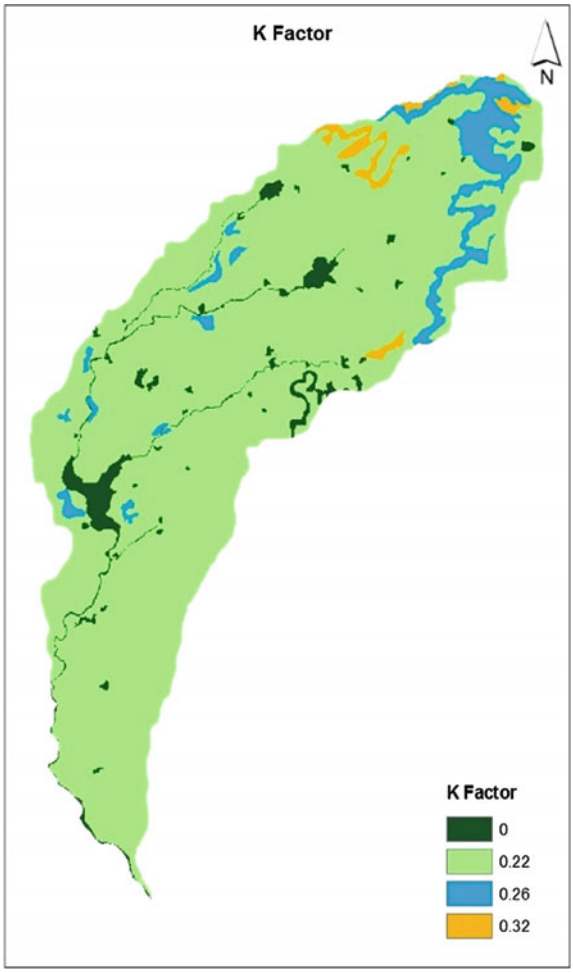

Fig. 6 *K*-factor map of SA-13 watershed

Table 3 Area statistics of *K*-factor in SA-13 watershed

S. No.	*K*-factor	Area (ha)	% Total geographical area
1	0.00	936.88	4.40
2	0.22	18707.12	87.83
3	0.26	1288.92	6.05
4	0.32	367.10	1.72
Total		21,300	100

For SA-13 watershed, *K*-factors were varying between 0.00 and 0.32, which depict soil susceptibility to erosion, the sediment transportability, and runoff rate. One assumption was made that only the topsoil layer is the most susceptible to erosion. Therefore, only the *K*-factor values for the top portion of each soil type were used. Area occupied by *K*-factors in SA-13 watershed is given in Table 3.

L-Factor (Slope Length) and S-Factor (Slope Gradient/Steepness)

L- and *S*-factors in combination are called as topographic factor, both of which are determined using DEM. Slope is varying from 0° to 79.45°. Higher slopes are concentrated on northeastern part of the watershed, whereas it is gradually decreasing toward south. The *L*- and *S*-factors in RUSLE reflect the topography of watershed. The *LS*-factor in the present study was computed for overland cells by using the equation stated by Moore and Wilson (1992). The value of *LS*-factor varies from 0 to 10. The *LS*-factor map of SA-13 watershed is depicted in Fig. 7.

C-Factor (Cover Management Factor)

The *C*-factor is the cover management factor. The cover management factor is the ratio of soil loss from an area with specified cover and management to that of an area in tilled continuous fallow. The values of *C* depend on vegetation type, stage of growth, and cover percentage and vary between 0 and 1 (Gitas et al. 2009). The value of *C*-factor varies from 0.44 to 1 depending on the NDVI.

In this study, the cover management factor *C* reflects the effect of cropping and management practices on the soil erosion rate. *C*-factor map of the watershed is presented in Fig. 8.

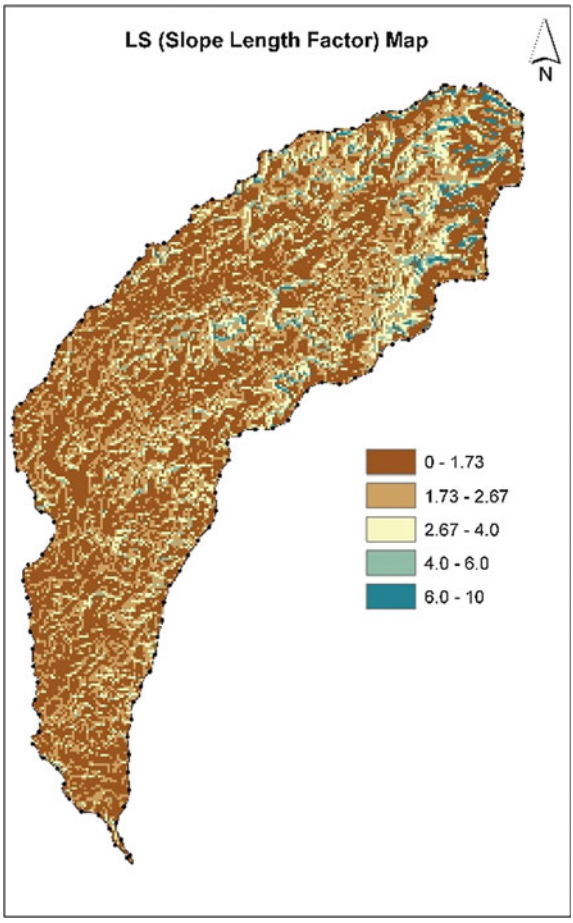

Fig. 7 Slope length factor map of SA-13 watershed

P-Factor (Support Practice Factor)

Supporting practices typically affect erosion by redirecting runoff around the slope so that it has less erosivity or by slowing down the runoff to cause deposition. The lower the *P*-factor value, the more effective the conservation practice was deemed to be at reducing soil erosion. If there are no support practices, the *P*-factor is 1.0. In this study area, most of the agricultural area was occupied by rainfed crops such as jowar, soybean, wheat, and gram fields on strip farming method. In forest areas, the *P* value 1 was assigned because there was no support practice. The *P*-factor for strip cropping of the study area was taken 0.37 (Stone and Hilborn 2000).

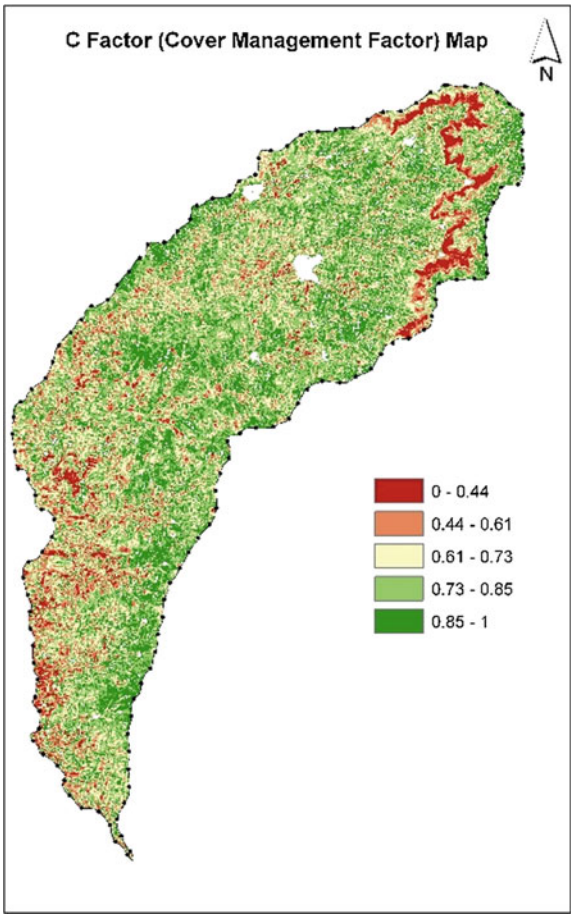

Fig. 8 *C*-factor map of SA-13 watershed

Estimation of Soil Loss

The composite term RKLSCP represents the soil erosion potential of different grid cells in the unit t/ha/year. The GIS database generated for the estimation of soil erosion such as *R*-factor, *LS*–factor, *C*-factor, and *P*-factor has been multiplied using 'Raster Calculator' in spatial analyst of ArcGIS. The final soil loss map of the watershed is given in Fig. 9. The average soil loss of the entire watershed was 8.2 t/ha/year, highest soil erosion potential of 9.97 t/ha/year was observed in micro-watershed number 4, whereas lowest potential of 5.59 t/ha/year was observed in micro-watershed number 13. Generally, the highest erosion was in areas of bare soils with upland topography where slope exceeds approximately 30°.

Soil erosion is a natural process, and the goal of any mitigation action should be for reducing erosion rates down to reasonable limits. Generally, watershed areas

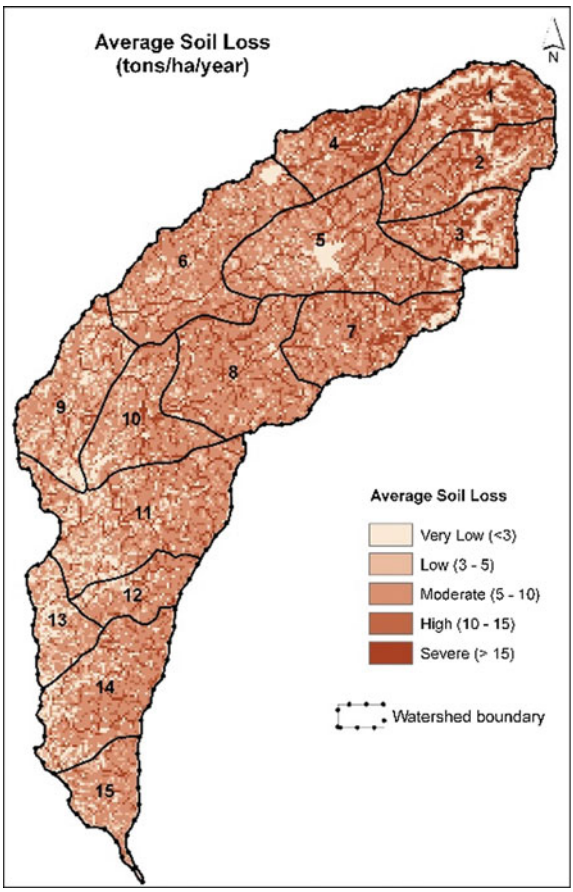

Fig. 9 Average soil loss in SA-13 watershed

which have a soil erosion potential under 3 t/ha/year are within the expected tolerable soil loss level and should be excluded from any mitigation actions. Soil erosion in present study is in moderate erosion risk class.

Conclusions

The conclusions that may be drawn are as follows:

1. Geographical information system arises as an efficient tool for the preparation of most of the input data required by the SCS curve number model;
2. The runoff estimated using SCS curve number model is comparable with the runoff measured by the conventional method for the SA-13 watershed.

3. Generally, the highest estimates of soil erosion are in areas of bare soils with upland topography where slope exceeds approximately 30°.
4. Generally, watershed areas which have soil erosion potential of less than 3 tons/ha/year are within the expected tolerable soil loss level and should be excluded from any mitigation actions.
5. Soil erosion for SA-13 watershed is in moderate erosion risk class.
6. This approach could be applied in other ungauged Indian watersheds for planning of various conservation measures.
7. This methodology can be applied to small basins. The application of remote sensing images and GIS tools is useful to approximate the land cover and potential soil erosion of the basin.

References

Atawoo MA, Heerasing JM (1997) Estimation of soil erodibility and erosivity of rainfall patterns in Mauritius. Food and Agricultural Research Council, Reduit, Mauritius

Chandramohan T, Durbude DG (2001) Estimation of runoff using small watershed models. Hydrol J 24(2):45–53

Chattopadhyay GS, Choudhury S (2006) Application of GIS and remote sensing for watershed development project—a case study. Map India 2006. http://www.gisdevelopment.net

Chow VT, Maidment DK, Mays LW (2002) Applied hydrology. McGraw- Hill Book Company, New York, USA

Ebrahimian M, See LF, Ismail MH, Malek IA (2009) Application of natural resources conservation service-curve number method for runoff estimation with GIS in the Kardeh Watershed, Iran. Eur J Sci Res 34(4):575–590

ERDAS Imagine Field Guide (1998) Przewodnik geoinformatyczny, Geosystems Polska, Warszawa

ESRI (1994) Cell based modelling with GRID. Environmental Systems Research Institute Inc., Redlands, California, USA

Ferro V (1997) Futher remarks on a distributed approach to sediment delivery. Hydrol Sci J 42(5): 633–647

Ferro V, Minacapilli M (1995) Sediment delivery processes at basin scale. Hydrol Sci J 40(6): 703–717

Ferro V, Porto P, Tusa G (1998) Testing a distributed approach for modelling sediment delivery. Hydrol Sci J 43(3):425–442

Gitas IZ, Douros K, Minakoul C, Silleos GN (2009) Multi-temporal soil erosion risk assessment In: Chalkidiki N (ed) Using a modified USLE raster model. Earsel Eproceeding, vol 81, pp 40–52

Haan CT, Barfield BJ, Hayes JC (1994) Design hydrology and sedimentology for small catchments. Academic Press, New York

Huang M, Jacgues G, Wang Z, Monique G (2006) A modification to the soil conservation service curve number method for steep slopes in the Loess Plateau of China. Hydrol Process 20(3): 579–589

Ingle PM, Chowdhary VM, Mahale DM, Thokal RT (2008) Potential of remote sensing (rs) and geographical information system (gis) techniques in command area management—a review. IE (I) J-AG 89:3–8. ISSN 0257-3431

Kothyari UC, Jain SK (1997) Sediment yield estimation using GIS. Hydrol Sci J 42(6):833–843

Kouli M, Sopios P, Vallianatos F (2009) Soil erosion prediction using the revised universal soil loss equation (RUSLE) in a geographic information system. Framework, Chania, Northwestern Crete, Greece. Environ Geol 57:483–497

McCool DK, Foster GR, Mutchle CK, Meyer LD (1987) Revised slope steepness factor for the universal soil loss equation. Trans Am Soc Agric Eng 30(5):1387–1396

Mellesse AM, Shih SF (2002) Spatially distributed storm runoff depth estimation using landsat images and GIS. Comput Electron Agric 37:173–183

Meyer LD, Wischmeier WH (1969) Mathematical simulation of the processes of soil erosion by water. Trans Am Soc Agric Eng 12(6):754–758

Moore ID, Wilson JP (1992) Length slope factor for the revised universal soil loss equation: simplified method of solution. J Soil Water Conserv 47(5):423–428

Morgan RPC (1986) Soil erosion and conservation. Longman Group Limited, pp 63–74

Musgrave G (1947) The quantitative evaluation of factors in water erosion, a first approximation. J Soil Water Conserv 2(3):133–138

NBSS and LUP (1995) Soils of Maharashtra for optimising land use. National Bureau Soil Survey Publication 54, Soils of India Series 5

NRSA (1989) Manual of Nationwide land use mapping using satellite imagery, Part I, National remote sensing agency, Hyderabad

Rao KV, Bhattacharya AK, Mishra K (1996) Runoff estimation by curve number method-case studies. J Soil Water Conserv 40:1–7

Renard KG, Foster GR, Weesies GA, Porter JP (1991) RUSLE, revised universal soil loss equation. J Soil Water Conserv 46(1):30–33

Rodda HJE, Demuth S, Shankar U (1999) The application of a GIS based decision support to predict nitrate leaching to ground water in south Germany. Hydrol Sci J 44(2):221–236

Sarangi A, Madramootoo CA, Enright P, Prasher SO, Patel RM (2005a) Performance evaluation of ANN and geomorphology-based models for runoff and sediment yield prediction for a Canadian watershed. Curr Sci 89(12):2022–2033

Sarangi A, Bhattacharya AK, Singh AK, Sambaiha A (2005b) Performance of geomorphologic instantaneous unit hydrograph (GIUH) model for estimation of surface runoff. In: International conference on recent advances in water resources development and management, pp 569–581. IIT, Roorkee, Uttaranchal, India, 23–25 Nov 2005

Shamsi UM (1996) Storm-water management implementation through modeling and GIS. J Water Résour Plann Manage ASCE 122(2):114–127

Sharma D, Kumar V (2002) Application of SCS model with GIS data base for estimation of runoff in an arid watershed. J Soil Water Conserv 30(2):141–145

Sharma T, Satya Kiran PV, Singh TP, Trivedi AV, Navalgund RR (2001) Hydrologic response of a watershed to landuse changes: a remote sensing and GIS approach. Int J Remote Sens 22(11):2095–2108

Stone RP, Hilborn D (2000) Universal soil loss equation (USLE). Ontario Ministry of Agricultural and Food original factsheet

UNEP (1997) World atlas of desertification, 2nd edn. Arnold London

USDA (1985) National engineering handbook. Soil Conservation Service, USA

Williams JR (1975) Sediment routing for agricultural watersheds. Water Resour Bull 11:965–974

Zade MR, Ray SS, Dutta S, Panigrahy S (2005) Analysis of runoff pattern for all major basins of India derived using remote sensing data. Curr Sci 88(8):1301–1305

Zhou P, Luukkanen O, Tokola T, Nieminen J (2008) Effect of vegetation cover on soil erosion in a mountainous watershed. CATENA 75(3):319–325

Rainwater Harvesting Structure Site Suitability Using Remote Sensing and GIS

B. K. Gavit, R. C. Purohit, P. K. Singh, Mahesh Kothari and H. K. Jain

Abstract Water is an important natural resource for the survival of all living beings. Watershed is the hydrogeological entity bounded by ridge line having single outlet. Digital elevation model (DEM) is defined as any digital representation of continuous variation of relief over a space. DEM is available from several sources and different spatial resolution. The ASTER DEM is one of the freely available DEM. Rainwater harvesting is important to avoid the scarcity of water. The appropriate choice of water harvesting technique depends on rainfall and its distribution, topography, land use land cover (LULC), and soil. The water harvesting conditions include the practices, viz. bunding, pitting, rainwater harvesting, water harvesting, floodwater and groundwater recharging. The paper illustrates the efficacy of remote sensing and GIS technology for suitability of rainwater harvesting structures. The study is conducted in Punad watershed, Nashik district (India). The data used are ASTER DEM, LISS-III image and SOI toposheet, soil and rainfall, etc. The study area is about 290 km^2. The watershed area falls in 46 H/14 and 46 L/2 toposheet. Average annual rainfall of the Kalwan tahsil is 780 mm. The drainage network and slope maps were derived using ASTER DEM, whereas other thematic maps LULC, road and settlements were derived using toposheet. Slope is categorized as high, medium, and low slope. All these maps were integrated in GIS environment to locate the potential suitable sites for rainwater harvesting. Adopting the IMSD guidelines, the suitable sites for percolation tank and check dam were identified in the study area.

B. K. Gavit (✉) · R. C. Purohit · P. K. Singh · M. Kothari
Department of SWE, CTAE, MPUAT, Udaipur 313001, Rajasthan, India
e-mail: bhaugavit@gmail.com

H. K. Jain
Department of Agriculture Statistics & Computer Applications, RCA, MPUAT, Udaipur 313001, Rajasthan, India

V. P. Singh et al. (eds.), *Hydrologic Modeling*, Water Science and Technology Library 81, https://doi.org/10.1007/978-981-10-5801-1_23

Introduction

Water is most noteworthy natural resources which support both human needs and economic development (Sinha et al. 2015). Hence, it should be used precisely for tomorrow's use. The natural resources like land and water are planned and managed on the basis watershed. Watershed is considered as an ideal unit for land and water resources planning and management purposes (Sharma et al. 2015). Watershed is a hydrological entity bounded by ridge line having single outlet. India is very divergent country in its physio-topographical nature and in terms of availability of natural resources. Central Water Commission divided India into 20 river basins comprising of 12 major river basins and 8 composite basins using Survey of India (SOI) toposheets and contour maps. Thereafter in 1990, AISLUS gave hydrological unit classification and came up with 35 basins. Central Water Commission (CWC), Ministry of Water Resources, GOI, and Indian Space Research Organisation (ISRO) have jointly developed Web-enabled Water Resources Information System of India (India-WRIS). India is divided into 25 basins and 101 subbasins under India-WRIS project based on digital elevation model (DEM) (Anonymous 2012). The size of watershed varies from few ha to some square kilometer. According to the catchment area, the classification of watershed is given in Table 1.

Water harvesting is nothing but the collection of surface runoff mainly for agricultural and domestic purposes. Water harvesting structures are extremely important to conserve precious natural resources like soil and water; these are depleting day by day at faster rate (Bamne et al. 2014). The water harvesting is mostly done for control of the runoff, to maintain groundwater level, to increase the vegetation, to minimize the sedimentation in the reservoirs or to store at the time of excess, and to reuse whenever required. In the case of designing and locating, the water harvesting site is very important. The identification of potential sites for water harvesting is an important step in efficient utilization and maximizing of water availability as well as land productivity in that area. The traditional fragmented approach of identification of potential sites for water harvesting is no longer viable and a more holistic approach to water management.

Table 1 System of classification of watershed in India

Category	Number	Size ranges ('000 ha)
Regions	6	25,000–1,00,000
Basin	35	3000–25,000
Catchments	112	1000–3000
Sub-catchments	500	200–1000
Watersheds	3237	50–200
Sub-watersheds	12,000	10–50
Milli-watershed	72,000	1–10
Micro-watershed	4,00,000	0.5–1

Foundation for Ecology. *Source* Book of Soil and Water Conservation 2008

The surveying of the watershed for locating the rainwater harvesting structure needs field work and as well as it takes more time. The preparation of the watershed action plan from the survey sheets is old practice. Recent technological advances have brought remote sensing and geographic information system (GIS) techniques to the forefront as tools for recommending these conservation measures (Biswas et al. 2002). Remote sensing is nothing but acquiring/gathering information about an object without in physical contact of that object. Remote sensing imagery has many applications in mapping Land Use Land Cover (LULC), agriculture, soil mapping, forestry, city planning, archeological investigations, military observation, geomorphological surveying, land cover changes, deforestation, vegetation dynamics, water quality dynamics, urban growth, etc., (Agarwal 2003). Burrough (1986) defines GIS as 'a set of tools for collecting, storing retrieving at will, transforming and displaying spatial data from the real world for a particular set of purposes.' GIS is a powerful set of tools for collecting, storing, retrieving, transforming, and displaying spatial data from the real world. The GIS data model allows the geographic features in real-world locations to be digitally represented and stored in a database so that they can be abstractly presented in map (analog) form and can also be worked with and manipulated to address some problem. Combined use of remote sensing and GIS results best solution for the complex problem.

A digital elevation model (DEM) provides digital representation of portions of earth's terrain over two-dimensional surfaces. DEM is normally generated by regular array of elevation values derived from topographic maps, aerial photographs. The DEM can be used for the extraction of the different topographic parameters such as slope, aspect, perspective three-dimensional view, hill shading, curvature, flow direction, flow accumulation, catchment area, drainage network, etc. Nowadays DEM is available freely on the Internet for whole globe in varied spatial resolution. The advanced spaceborne thermal emission reflection radiometer (ASTER) global digital elevation model (GDEM) is one of the freely available DEM on the Web portal for the whole globe. The present study was undertaken to use remote sensing and GIS technique for locating the potential sites for rainwater harvesting structure. Pandit et al. (1999) carried out a case study of Nasik Taluka, Maharashtra, using RS and GIS-based integrated watershed development. The approach aims generation of specific action plans for the development using remote sensing satellite data in connection with other conventional socioeconomic data to meet the demands of present local populations as well as to achieve the sustainable development. The scope of study is to assess natural resources potential and their spatial variation in respect to soil, water resources, LULC in slected area using IRS LISS-II data.

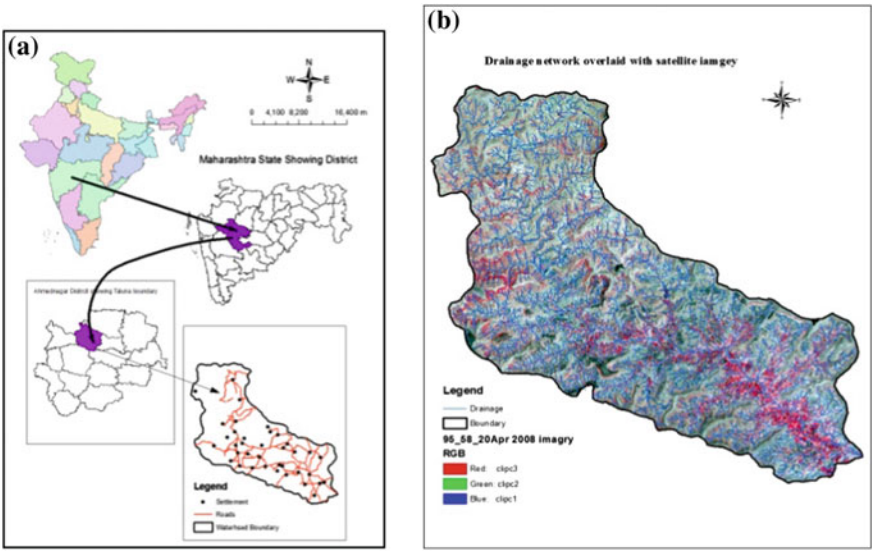

Fig. 1 **a** Location map of the study area **b** satellite imagery of study area

Study Area

The study is conducted in Punad watershed of Girna catchment in Nashik district, Maharashtra (India). The present study area is located in Nashik which is the part Kalwan block as part of Girna sub basin. The watershed falls in Survey of India toposheet No. 46 H/14 and 46 L/2 (1:50,000 scale) which is located in Kalwan tahsil. The approximate area of the watershed is 290 km^2 covering 37 villages of Kalwan tahsil. The soil in this area is mostly black soil. The area shows a wide variation in physiographical topography. Average annual rainfall of the Kalwan tahsil is 780 mm. Most of the area is under the agriculture cultivation. The major crops of the area are bajra, maize, sugarcane, onion, wheat and some seasonal vegetables, and horticultural crops. Figure 1 shows the location map of the study area.

Methodology

The present study is taken to use the efficacy of the remote sensing and GIS technique for locating the site suitability of the water harvesting structures. Rainfall in selected area is abundant but due to hilly topography its not managed properly; hence considering need this rainwater harvesting study was undertken in this study. The reduction of surface runoff can be achieved by constructing suitable structures

in the area, which automatically helps to manage the other natural resources like soil and vegetation as the watershed condition affects these resources. For the efficient management, one has to take suitable unit of management. Here, by taking watershed as a unit, the water, soil, and vegetation's can be managed efficiently, collectively, and simultaneously. The present study was planned in such a way to utilize the freely available satellite data. The ASTER DEM is used for extracting the drainage network as well to delineate the watershed, whereas settlement and road network are digitized from the Survey of India toposheet.

The LISS-III data are also taken from the Bhuvan Web portal of ISRO which gives the data in free domain. The geo-referencing and rectification of the satellite imagery as well toposheets were carried out using the image processing ERDAS Imagine 8.7 software. The roads, railway, and settlements are digitized using the toposheet in the ArcGIS 9.3 software. The drainage network, slope, and contour were derived using the ASTER DEM. The land use land cover (LULC) map is prepared using the satellite imagery. The soil data is taken from National Bureau Survey Land Use Planning, Nagpur. All those thematic layers were integrated in the GIS environment. The integrated mission for sustainable development (IMSD) technical guidelines for site selection of water conservation structure given by National Remote Sensing Agency (NRSA) (currently NRSC), India (NRSC 1995) was followed for selection of the suitable site of the water harvesting structure. On the basis of these guidelines, the following factors were selected as requirements for suitable site. The methodology adopted in this study for finding the suitable site of the structure is given in Fig. 2.

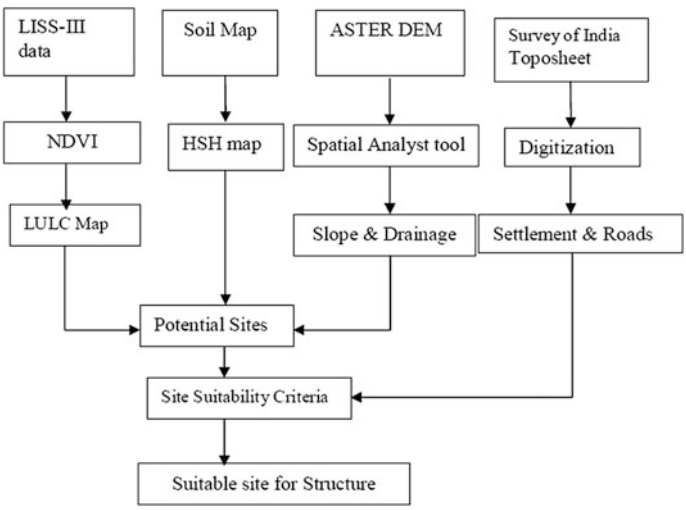

Fig. 2 Methodology flow chart

Drainage Network

The drainage network of the watershed gives the idea about the topography of that area, and it plays very important role in locating the proper site of the watershed. Hence, the drainage network is derived from the ASTER DEM (30 m) data as free. ASTER DEM of the study area is shown in Fig. 3. For the digital extraction of the drainage network, the ArcGIS 10.2 software is used. Using the ArcGIS hydrology tool, the drainage is extracted. The filling and sinking of DEM were performed prior to vectorization of the stream. After the vectorization of the drainage network, the stream ordering is done using the GIS environment. The drainage network map of the study area is shown in Fig. 4.

Soil Map

The soil map of any watershed is very important which is very helpful to get the idea about the land use as well as land of that area. The study areas soil map is collected from National Bureau of Soil Survey and Land Use Planning, (NBSS and

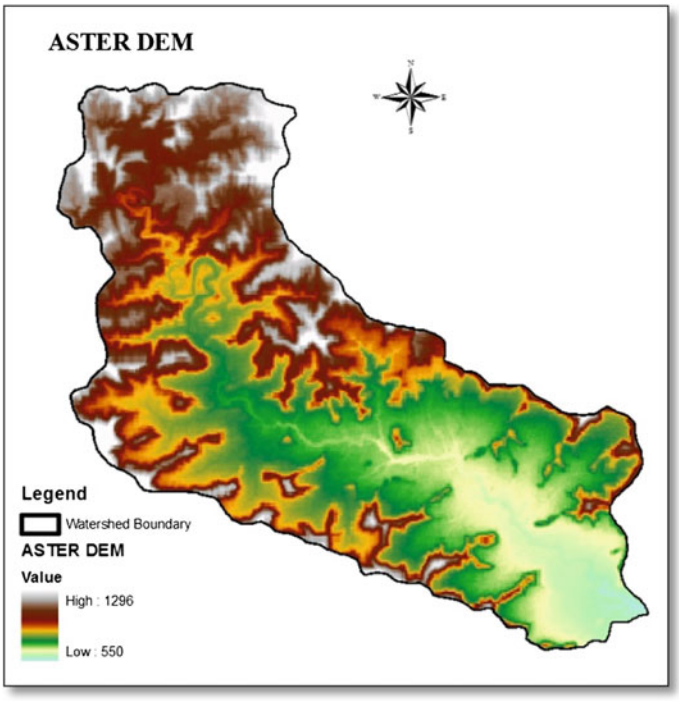

Fig. 3 ASTER DEM of the study area

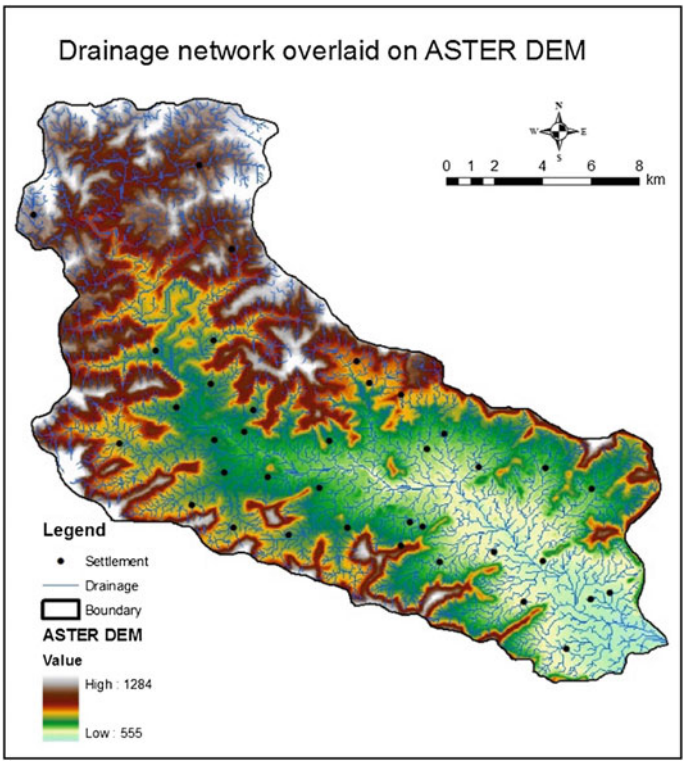

Fig. 4 Drainage map of the study area with settlements

LUP) Nagpur. The soil of the study area is mostly fertile and most land is under cultivation.

Land Use Land Cover

Land use land cover is the key component for controlling runoff and evapotranspiration from that area. The LULC tells to interpreter about the watersheds healthiness in terms of soil and natural resources. The LULC maps of that area are prepared using the LISS-III (23.5 m) satellite imagery. For preparation of the LULC map, supervised as well as unsupervised techniques of the image processing are used. Major land use land cover categories are agriculture, forest, wasteland, river, and built-up area. The LULC map of the study area is depicted in Fig. 5.

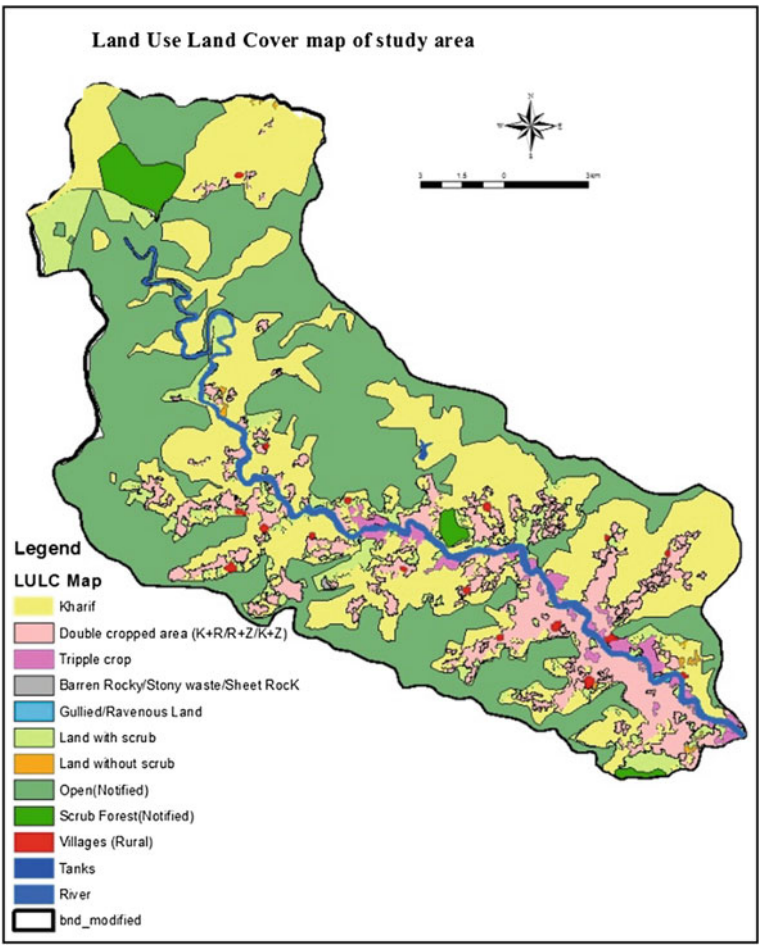

Fig. 5 Land use land cover map of the study area

Results and Discussion

All thematic layers were integrated in GIs environment using Arc GIS software as per methodology Flow chart. To adopt the suitable site selection criteria, integrated mission for sustainable development (IMSD) technical guidelines given by National Remote Sensing Agency (NRSA) (currently NRSC), India, were taken. It was found that watershed was suitable for constructing check dams. With the help of IMSD guidelines, suitable sites for check dam were identified for irrigation or drinking water purposes. The buffer of 500 m is extracted for the settlement and proposed suitable area for water harvesting structures. The buffer area is marked for settlement in order to avoid the structures location in residential area.

By extraction of buffer zones, it is possible to find out the area of interest around the entity or set of entities. Figure 6 shows the buffer areas around the settlement and agricultural land use, which show that this area should be excluded for locating water harvesting structures.

The runoff potential map was generated by integrating information on rainfall, LULC, soil groups, settlement, drainage network, and other ancillary data. The potential sites were integrated in the GIS environment. The buffer of 500 m was marked from the settlement for finding the suitable sites. As expected, barren/rocky areas with soil group class D amount to maximum runoff potentiality. The combination of open forest with soil group class C contributes the least runoff potential. In the case of current fallow and irrigated land use classes, the runoff varies depending upon the soil type and rooting depth of the plants.

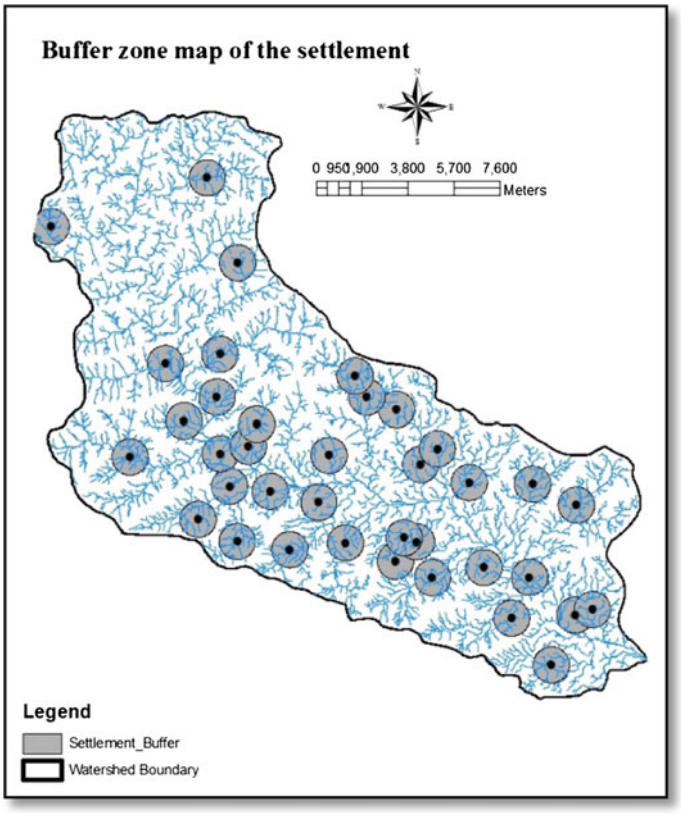

Fig. 6 Buffer map of the study area

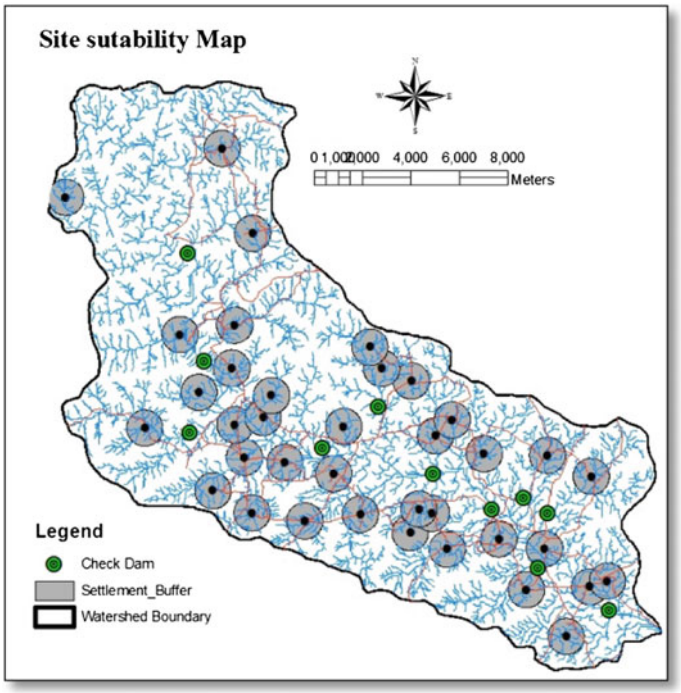

Fig. 7 Site suitability map for check dam

Site Identification

The thematic layers were assigned the weights in order to integrate it. After giving the weights, all those layers were integrated to derive the composite maps in GIS environment. Generally, water conservation structures are preferred along the streams. Location of the water conservation structure should be such that, it should get enough quantity of water and should be neither very near nor too far from settlement and agriculture area. On this map, site suitability analysis for check dam was carried out by running queries using the decision tree concept. The resultant map is shown in Fig. 7. In the field, suitable sites for these structures were identified following the IMSD guidelines.

Conclusion

The remote sensing and GIS are the advanced and recent technologies,which coupled together yields better solution for complex problems for watershed planning as well resources management. The present study shows the utility of freely

available ASTER DEM is very good source for delineation of the watershed. After adopting the integrated mission for sustainable development (IMSD) guidelines in watershed, the suitable sites for constructing the check dam for drinking, irrigation, and for drinking purposes are found. Such harvested water may be used in many watershed activities. The integrated results of the decision criteria show that suitable sites of the check dams are more or less nearer or on the drainage line. The remote sensing technique proved to be effective for generating various thematic layers relevant to sites suitability.

References

Agarwal S (2003) Satellite remote sensing and GIS application in agricultural meteorology. In: Proceedings of the training workshop, 7–11 July, Dehra Dun, India, pp 23–28

Anonymous (2012) River basin atlas of India-WRIS, RRSC-West, NRSC, ISRO, Jodhpur, India

Bamne Y, Patil KA, Vikhe SD (2014) Selection of appropriate sites for structures of water harvesting in a watershed using remote sensing and geographical information system. Int J Emerg Technol Adv Eng 4(11):270–275

Biswas S, Sudhakar S, Desai VR (2002) Remote sensing and geographic information system based approach for watershed conservation. J Surveying Eng 128:108–124

Burrough PA (1986) Principles of geographical information systems for land resources assessments. Clarendon Press, Oxford

National Remote Sensing Agency (NRSA) (1995) IMSD technical guidelines, Dept of Space, Govt of India, Balanagar, Hyderabad

Pandit DS, Jeyram A, Sinha AK, Murthy YVNK (1999) Remote sensing GIS base integrated watershed development. A case study of Nasik Taluka, Dist, Nasik of Maharashtra. In: Souvenir of state level seminar on watershed development and management past, present and future, Ahmed Nagar

Sharma SK, Gajbhiye S, Tignath S (2015) Application of principal component analysis in grouping geomorphic parameters of a watershed for hydrological modeling. Appl Water Sci 5:89–96

Sinha DD, Mohpatra SN, Pani P (2015) Site selection for suitable water harvesting structure using remote sensing and GIS. Trans Inst Indian Gographer 37(2):223–233

Land Surface Temperature Estimation Using Remote Sensing Data

Vijay Solanky, Sangeeta Singh and S. K. Katiyar

Abstract India is facing crucial problem as the other world, by the impact of Global warming which is resulting from climate change. Global warming is an increase in Earth's average surface temperature, land surface temperature (LST) plays a critical role in Global climate change and is used in a range of hydrological, meteorological, and climatological applications. As needed for most modelling and climate analysis applications. Remote sensing (RS) and geographic information system (GIS) have found wide application areas in climate change analyses also this can be used for LST calculation. There are various sensor whose data is useful in generating LST such as: advanced very high resolution radiometer (AVHRR), moderate resolution imaging spectroradiometer (MODIS), Landsat-8, and many more. LST can be estimated by using many algorithms i.e. split-window (SW), dual-angle (DA), single-channel (SC). In this paper we have used SW algorithm to estimate LST for Bhopal region using LANDSAT-8 Thermal Infrared bands. SW algorithm uses spectral radiance and emissivity of TIR bands as input for deriving LST. The spectral radiance was estimated using TIR bands and emissivity was calculated using NDVI threshold technique. Finally Land surface temperature for Bhopal region have been estimated and statistics are presented.

Keywords Remote sensing (RS) · Land surface temperature (LST)
Split window algorithm · NDVI threshold · Climate change

V. Solanky (✉) · S. Singh · S. K. Katiyar
Centre for Remote Sensing, GIS & GPS, Department of Civil Engineering,
M.A.N.I.T., Bhopal 462003, MP, India
e-mail: makusolanky@gmail.com

S. Singh
e-mail: sangeeta211.aec.it@gmail.com

S. K. Katiyar
e-mail: sunil64k@gmail.com

V. P. Singh et al. (eds.), *Hydrologic Modeling*, Water Science
and Technology Library 81, https://doi.org/10.1007/978-981-10-5801-1_24

Introduction

Over the past several decades in Remote Sensing community, land surface temperature (LST) is found to be one of the most important parameters in the physical processes of surface energy and water balance at local through global scales (Anderson et al. 2008; Brunsell and Gillies 2003; Karnieli et al. 2010; Kustas and Anderson 2009; Zhang et al. 2008). In more general terms LST can be defined as hotness of surface of earth, from RS satellite's perspective, the surface is whatever it sees when it looks through the atmosphere to the ground. LST estimation provides information about temporal and spatial variations of the surface equilibrium state and is of fundamental importance in many applications.

LST is being used in a variety of areas such as evapotranspiration, climate change, hydrological cycle, vegetation monitoring, urban climate and environmental studies, among others (Arnfield 2003; Bastiaanssen et al. 1998; Hansen et al. 2010; Kalma et al. 2008; Kogan 2001; Su 2002; Voogt and Oke 2003; Weng 2009; Weng et al. 2004). Since the launch of the Landsat-8 satellite (also known as Landsat Data Continuity Mission, LDCM) in February 2013 continuity of remote sensing data at high spatial resolution acquired by instruments on board previous Landsat satellites such as the multispectral scanner system (MSS), the thematic mapper (TM), and the enhanced thematic mapper plus (ETM+).

Landsat-8 carries two sensors, i.e., the operational land imager (OLI) and the thermal infrared sensor (TIRS). OLI collects data at a 30 m spatial resolution with eight bands located in the visible and near-infrared and in the shortwave infrared regions of the electromagnetic spectrum, plus an additional panchromatic band at 15 m spatial resolution. TIRS sensor measures the TIR radiance at 100 m spatial resolution using two bands located in the atmospheric window between 10 and 12 μm (Irons et al. 2012). Since Satellite-based thermal infrared (TIR) data is directly linked to the LST through the radiative transfer equation.

The retrieval of the LST from remotely sensed TIR data has attracted much attention, specially from Landsat-8 TIR bands. Direct estimation of LST from the radiation emitted in the TIR spectral region is difficult to perform with that accuracy, because radiances measured by the radiometers onboard satellites depend not only on surface parameters (temperature and emissivity) but also on atmospheric effects. Therefore, besides radiometric calibration and cloud screening, the determination of LSTs from space-based TIR measurements requires atmospheric corrections (Vidal 1991). In past many studies have been carried out to estimate LST from satellite derived TIR data, by using different approaches and methods (Jiménez-Muñoz and Sobrino 2003).

Before the invention of earth observation satellites (EOS), it was hard to estimate the LST of an area. Generally, it was calculated for a particular set of sample points and interpolated into isotherms to generalize the point data into area data. But now a day's remotely sensed data is being used for LST estimation by using thermal data. LST greatly affected by the increasing green house gases in the atmosphere. As it rises, it melts the glaciers and ices sheets in the polar region, it also increases flood

and sea level, Increase in LST also affects the climatic condition of the monsoon countries leading to unpredictable rainfall hence vegetation in the entire Earth surface will be affected by this (Rajeshwari and Mani 2014).

Land use/Land cover (LU/LC) of an area can be used for estimating the amount of LST. The natural and anthropogenic activities change the LU/LC of an area. It also influences LST of that area. As its value changes the local climate of the area also changes, this draws attention of many researchers to calculate the amount of LST for any particular region. In literature it has been found that many methods of LST estimation are developed and adopted some of the most widely used methods are as follow: split-window (SW), SC algorithm, Dual-Angle, Sobrino, Mao, and Submao. Most of the studies were done for urban areas and arid and semi-arid regions and in many of the studies, single thermal band was used. LST products are routinely generated from moderate-resolution satellite data (e.g., moderate resolution imaging spectroradiometer (MODIS) on the National Aeronautics and Space Administration's (NASA) Terra and Aqua platforms, Advanced Along-Track Scanning Radiometer on the European Space Agency's Environmental Satellite) because they indicate the surface energy that is available at the land–atmosphere interface (Norman and Becker 1995).

In this paper, investigations have been carried out for LST estimation using Landsat-8 TIR bands, and SW algorithm which uses NDVI Threshold technique. The rest of paper is structured as follow:

Section 2 describes LST retrieval algorithms which also covers theoretical aspects of these algorithm, details of study area, data resources and satellite data used in this study are given in Sects. 3 and 4 addresses methodology adopted for carrying out this study, Results are discussed in Sect. 5. In Section 6 concluding remarks are presented which is followed by some future recommendations.

LST Retrieval Algorithms

Previous Landsat series has single thermal band in the atmospheric window between 10 and 12 μm for TM/ETM+sensors. Landsat-8 TIRS has some advancement over previous sensors and split single thermal band into two TIR bands. Previous LST algorithms use singe channel (SC) algorithm for the retrieval of surface temperature, which is fully based on single thermal band. But in TIRS sensor SC algorithm may cause some problem because the bandwidths of TIRS bands are narrower than the previous TM/ETM+TIR band. To overcome this problem a new mathematical structure of split-window (SW) algorithm was proposed, in which two TIR bands were used instead of single TIR band. In this paper a SW algorithm has been used for LST (Land surface temperature) estimation.

Single-Channel Algorithm

The SC algorithm developed by Jiménez-Muñoz et al. (2014) for the estimation of LST. The mathematical structure of SC algorithm is:

$$T_s = \gamma[1/\varepsilon(\psi_1 L_{sen} + \psi_2) + \psi_3] + \delta \quad (1)$$

where ε is the surface emissivity and (γ, δ) are two parameters given as:

$$\gamma \approx T_{sen}^2/_{b_\gamma} L_{sen}; \quad \delta \approx T_{sen} - T_{sen}^2/b_\gamma \quad (2)$$

where T_{sen} is the at-sensor brightness temperature and ψ_1, ψ_2, and ψ_3 are atmospheric functions, given as:

$$\psi_1 = 1/\tau; \quad \psi_2 = -L_d - L_u/\tau; \quad \psi_3 = L_d \quad (3)$$

Split-Window Algorithm

The split-window algorithm proposed by based on two TIR bands typically located in the atmospheric window between 10 and 12 μm. The mathematical structure of SW algorithm is given as:

$$T_s = T_i + c_1(T_i - T_j) + c_2(T_i - T_j)^2 + c_0 + (c_3 + c_4 w)(1 - \varepsilon) + (c_5 + c_6 w)\Delta\varepsilon \quad (4)$$

where T_i and T_j are the at-sensor brightness temperatures of bands i and j, ε is the mean emissivity, and given by $\varepsilon = 0.5(\varepsilon_i + \varepsilon_j)$, $\Delta\varepsilon$ is the emissivity difference, $\Delta\varepsilon = (\varepsilon_i - \varepsilon_j)$, w is the total atmospheric water vapour content (in g cm^{-2}), and c_0–c_6 are the SW coefficients. The basic inputs to SW algorithm are brightness temperature and Land Surface Emissivity LSE.

Study Area and Data Resources

Study area selected for this study is the capital city of Indian state of Madhya Pradesh (MP) having area central point coordinates 23° 55′N Latitude and 76° 57′E Longitude. Investigations for this study have been carried out for the LANDSAT-8 satellite images and details of each test image is presented in Table 1. Study area is shown in Fig. 1 and LST retrieval algorithm is implemented in ArcGIS 10.3 software environment and ERDAS imagine version 2011 software has been used for other image analysis task.

Table 1 Details of data resources

S. No.	Sensor	Satellite	Area	Date of acquisition
1	OLI	LANDSAT-8	BHOPAL (INDIA)	23-04-2014
2	TIRS	LANDSAT-8	BHOPAL (INDIA)	23-04-2014
3	OLI	LANDSAT-8	BHOPAL (INDIA)	26-04-2015
4	TIRS	LANDSAT-8	BHOPAL (INDIA)	26-04-2015

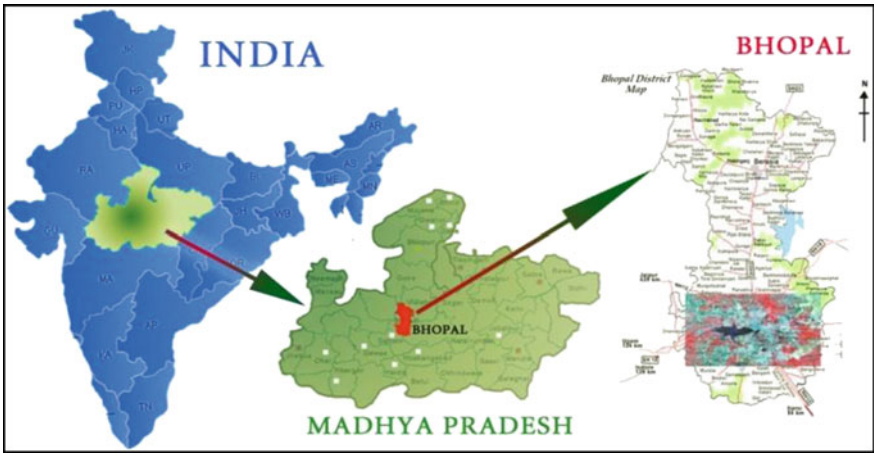

Fig. 1 Study area (Bhopal District) on map

Detailed description of satellite data used in this paper is formulated in tabular form and is shown in Table 1.

Methodology Adopted

To carry out this research work, we have used split-window (SW) algorithm for LST retrieval, procedure for each and every step involved in this process is shown in Fig. 1. LANDSAT-8 satellite images are freely available for research purpose, and can be easily downloaded by accessing the USGS (United States geological survey) website. USSG offers these images in a bundled form which have 12 different band images. For this study we have only used 4 MS (Multi-spectral) bands i.e. red, green, blue and near-infrared and 2 and TIR bands out of 12 bands. Initially OLI images are pre-processed to generate a stacked image and then a false colour composite (FCC) image is generated to clearly distinguish between different land cover features. After that sub-setting is applied to extract admin boundaries of

Bhopal district by using the generated FCC image. Then pre-processing steps are applied on TIRS bands.

After pre-processing of both data sets, NDVI map is generated using 2, 3, 4, 5 bands of LANDSAT-8 i.e. 4 MS bands by using Eq. 1. and this NDVI map is reclassified to calculate the LSE. Brightness temperature is calculated using thermal band i.e. 10 and 11, images which aids in the process of LST retrieval (Fig. 2).

NDVI (Normalized difference vegetation index) threshold technique is used to obtain land surface emissivity (LSE), from reclassified NDVI map and fractional vegetation cover (FVC) given in Eq. 6.

$$\mathrm{NDVI} = \frac{\mathrm{NDVI} - \mathrm{Red}}{\mathrm{NDVI} + \mathrm{Red}} \tag{5}$$

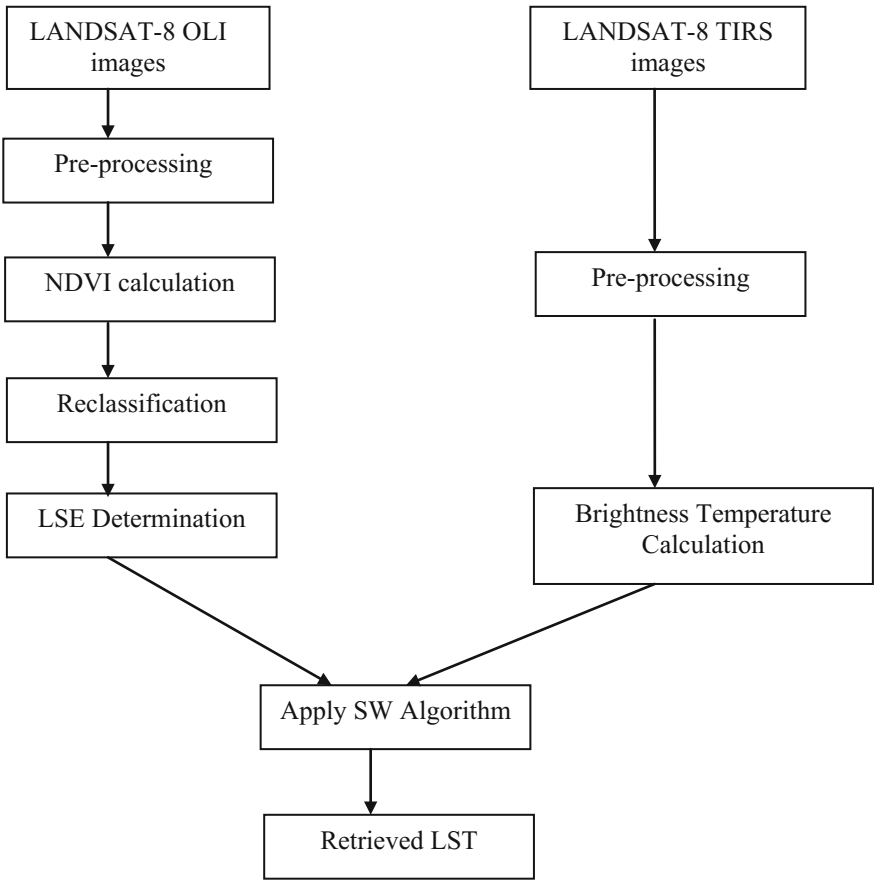

Fig. 2 Flowchart for LST retrieval using LANDSAT-8

$$FVC = \left(\frac{NDVI - NDVI_{min}}{NDVI_{max} - NDVI_{min}} \right)^2 \quad (6)$$

where

NDVI	NDVI value
$NDVI_{min}$	minimum value of NDVI
$NDVI_{max}$	maximum value of NDVI

To calculate the LST, we have given the two inputs to SW algorithm i.e. LSE and brightness surface as described in Eq. 5. And all other parameters used n formula are determined in previous steps, which have led to determination of LST for Bhopal district.

Results and Discussion

LST retrieval process is completed using SW algorithm, which is best suited algorithm for LANDSAT-8 TIR bands as found in literature. LST maps are generated for Bhopal district as shown in Fig. 3a, b, for the months April 2014 and 2015 respectively. Degree Celsius (°C) is considered as basic unit for temperature for all the analysis, since original LST calculated was in Kelvin hence a Kelvin to °C conversation is applied and results are presented in °C.

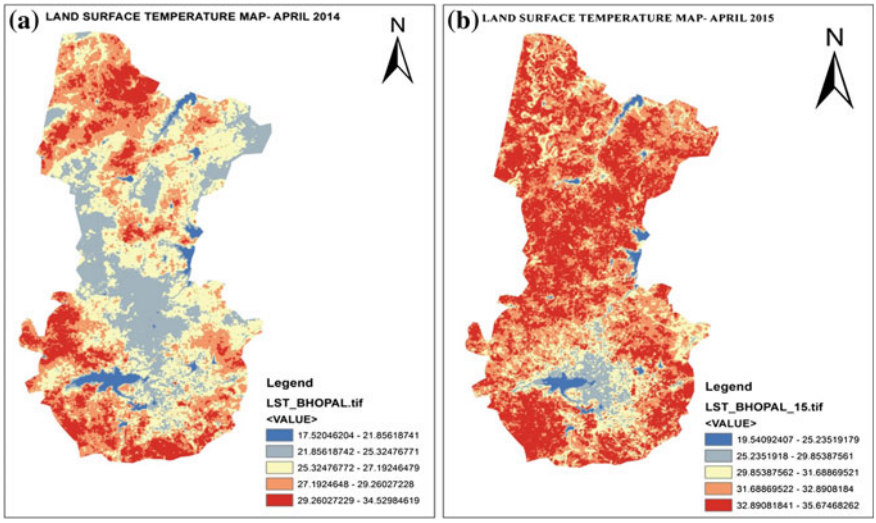

Fig. 3 **a** LST map of Bhopal district for April 2014 **b** LST map of Bhopal district for April 2015

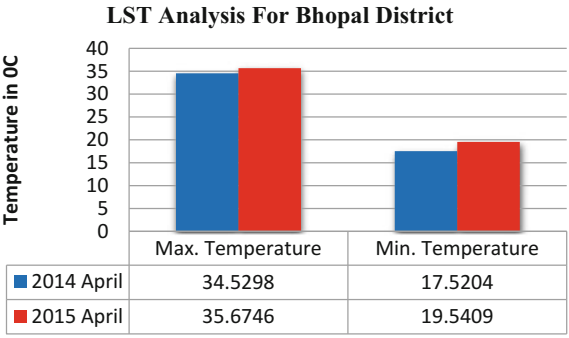

Fig. 4 Maximum and minimum temperature for Bhopal district

As per the results obtained in this paper it has been found that Land surface temperature is significantly increased within one year, i.e. for April 2014 maximum temperature was found 34.52 °C and it was found 35.67 °C that of April 2015, which shows an increase in value by 1.15 °C and shown in Fig. 4.

As shown in Fig. 4, there is a rise in maximum and minimum land surface temperature of 1.15, 2.02 °C which is not desirable. and clearly indicates that region is affecting from environmental changes.

Conclusions

LST retrieval using Split window algorithm has been investigated in this research paper and conclusions are summarised as follows:

I. Since the availability of thermal bands (TIR) of LANDSAT-8, many algorithms have been adopted for LST estimation and it has been found that Split window outperform others.
II. Estimated LST for two consecutive years i.e. 2014 and 2015 shows a significant rise in minimum and maximum temperature from which this can be inferred that region of study area i.e. Bhopal (India) is affecting from global environmental changes and need to be taken care of.
III. LST was found high in barren regions and low in agricultural, vegetated areas, also lowest value was found in water bodies, North, south region of district is having high LST as compare to east and west and central region of district is having moderate temperature values.
IV. A hybrid approach based upon SC and SW algorithms can be adopted in order to refine the results for LST retrieval.

References

Anderson MC et al (2008) A thermal-based remote sensing technique for routine mapping of land-surface carbon, water and energy fluxes from field to regional scales. Remote Sens Environ 112:4227–4241

Arnfield AJ (2003) Two decades of urban climate research: a review of turbulence, exchanges of energy and water, and the urban heat island. Int J Climatol 23:1–26

Bastiaanssen WGM et al (1998) A remote sensing surface energy balance algorithm for land (SEBAL) 1. Formulation J Hydrol 212:198–212

Brunsell NA, Gillies RR (2003) Length scale analysis of surface energy fluxes derived from remote sensing. J Hydrometeorol 4:1212–1219

Hansen J et al (2010) Global surface temperature change. Rev Geophys 48:RG4004

Irons JR et al (2012) The next landsat satellite: the landsat data continuity mission. Remote Sens Environ 122:11–21, doi:10.1016/j.rse.2011.08.026

Jiménez-Muñoz JC, Sobrino JA (2003) Split-window coefficients for land surface temperature retrieval from low-resolution thermal infrared sensors. IEEE Geo sci Remote Sens Lett 5 (4):806–809

Jiménez-Muñoz JC et al (2014) Land surface temperature retrieval methods from landsat-8 thermal infrared sensor data. IEEE Geosc Remote Sens Lett 11(10):1840–1843

Kalma JD et al (2008) Estimating land surface evaporation: a review of methods using remotely sensed surface temperature data. Surv Geophys 29:421–469

Karnieli A et al (2010) Use of NDVI and land surface temperature for drought assessment: merits and limitations. J Clim 23:618–633

Kogan FN (2001) Operational space technology for global vegetation assessment. Bull Am Meteor Soc 82:1949–1964

Kustas W, Anderson M (2009) Advances in thermal infrared remote sensing for land surface modeling. Agric For Meteorol 149:2071–2081

Norman JM, Becker F (1995) Terminology in thermal infrared remote sensing of natural surfaces. Agric For Meteorol 77(3):153–166

Rajeshwari A, Mani ND (2014) Estimation of land surface temperature of Dindigul district using Landsat 8 data. Int J Res Eng Technol 03(05). (eISSN: 2319-1163, pISSN: 2321-7308)

Su Z (2002) The surface energy balance system (SEBS) for estimation of turbulent heat fluxes. Hydrol Earth Syst Sci 6:85–100

Vidal A (1991) Atmospheric and emissivity correction of land surface temperature measured from satellite using ground measurements or satellite data. Int J Remote Sens 12:2449–2460

Voogt JA, Oke TR (2003) Thermal remote sensing of urban climates. Remote Sens Environ 86:370–384

Weng Q et al (2004) Estimation of land surface temperature–Vegetation abundance relationship for urban heat island studies. Remote Sens Environ 89:467–483

Weng Q (2009) Thermal infrared remote sensing for urban climate and environmental studies: methods, applications, and trends. ISPRS J Photogram Remote Sens 64:335–344

Zhang R et al (2008) Two improvements of an operational two-layer model for terrestrial surface heat flux retrieval. Sensors 8:6165–6187

Watershed Prioritization of Wardha River Basin, Maharashtra, India Using Morphometric Parameters: A Remote Sensing and GIS-Based Approach

B. S. Manjare, S. Khan, S. A. Jawadand and M. A. Padhye

Abstract The present investigation is an effort to prioritize the sub-watersheds of the Wardha River basin using morphometric parameters to identify water conservation measures. Delineation of potential zones for implementation of conservation measures above the entire watershed at similar occurrence is inaccessible as well as uneconomical; consequently, it is a prerequisite to apply viable technique for prioritization of sub-watersheds. In that view, the present research attempted to study various morphological characteristics and to implement geographical information system (GIS) to prioritize sub-watersheds. The Wardha River basin was delineated into 10 sub-watersheds, and morphometric parameters were derived independently for each of the sub-watersheds. For the study stream network along with their order was extracted in geospatial environment. The morphometric characterization was obtained through the measurement of distinct linear and areal aspects over the ten sub-watersheds. It showed imperative role in distinguishing the topographical and hydrological behaviour of the watershed. Based on morphometric analysis, the watershed has been classified into three categories as high, medium and low in terms of priority for conservation and management of natural resources. The result of prioritization analysis revealed that the sub-watersheds, such as SW1, SW4, SW5 and SW7, are the zones having lowest composite score and were considered under high priority which clearly indicates that it is subjected to maximum soil erosion, and hence, these may be taken for conservation measures by planners and decision makers for local-specific planning and development. Low-prioritized zone is represented by SW10, and sub-watersheds SW2, SW3, SW6, SW8 and SW9 are categorized under medium-priority zone.

Keywords Morphometric parameters · Prioritization · GIS · Remote sensing

B. S. Manjare (✉) · S. Khan · S. A. Jawadand · M. A. Padhye
Department of Geology, RTM Nagpur University, Nagpur, Maharashtra, India
e-mail: yogesh_manjare1@rediffmail.com

V. P. Singh et al. (eds.), *Hydrologic Modeling*, Water Science and Technology Library 81, https://doi.org/10.1007/978-981-10-5801-1_25

Introduction

Management of watershed encompasses various activities from watershed delineation to monitoring. Morphometric studies involve evaluation of streams through the measurements of various stream properties. Analysis of various drainage parameters, namely ordering streams and perimeter of basin, length of drainage channels, drainage density (Dd), drainage frequency, bifurcation ratio (Rb), texture ratio (*T*) and circulatory ratio (Rc) (Kumar 1999). Drainage characteristic of many river basins and sub-basins in different parts of the globe has been studied using conventional methods (Horton 1945; Strahler 1957, 1964; Krishnamurthy et al. 1996). Various scholars carried out morphometric analysis of river basins by using remote sensing and geographical information system (GIS). The large variety of factors that can affect the behaviour of a watershed falls into two categories, first the permanent characteristics of the drainage basin, such as, its size or drainage density, i.e., drainage morphometry and second, transient or variable characteristics, such as the amount of precipitation, type of land use.

Watershed prioritization and generation of water resource development plan were envisaged by integrating satellite based land use/cover, and soil information with morphological parameters of the watershed to identify suitable sites for soil and water conservation measures on a holistic approach. Prioritization is the ranking of different critical sub-watersheds according to the order in which they have to be taken up for the treatment by soil and water conservation measures.

Remote sensing and geographical information system (GIS) techniques are being effectively used in recent times in determining quantitative description of the basin geometry (Biswas et al. 1999; Obi Reddy et al. 2002; Vijith and Satheesh 2006). The high-resolution remotely sensed data coupled with topographical data analysis procedures have made satellite data-based morphometric analysis a highly effective tool to understand and manage natural resources.

The generated geo-coded resources database at watershed level in geomorphic information system (GIS) provides an excellent means of storing, retrieving and analysing spatial information. Nowadays, integration remote sensing and GIS are helpful in planning and managing land and water resources for adaptation of location specific technology. Furthermore, geographical information system (GIS) has been widely used in several geomorphologic and morphometric flood management and environment applications.

Study Area

The study area lies in the survey of India toposheet no 55 L/1, L/5, L/2, L/6, L/11 bounded by latitude 20° 20′ 0″N and 21° 0′ 0″N and longitude 78° 10′ 0″E and 78° 40′ 0″E covers an area of 950.396 km^2. The area falls in Wardha district and

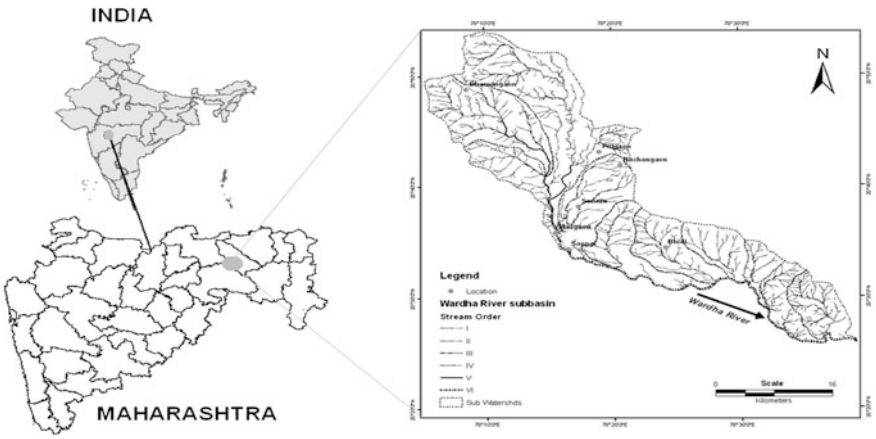

Fig. 1 Location and accessibility map of the study area

some parts of Amravati district, Maharashtra. The sub-basin mainly comprises of Deccan trap alluvium, chikli and karanja formations. These formations of Sahyadri group are highly weathered and fractured. The Wardha River forms the boundary between Amravati and Nagpur districts (Fig. 1). The basin area has been subdivided into one to ten sub-watersheds, and the morphometric parameter values are calculated and prioritized.

Morphometric Analysis

Morphometric analysis refers as the quantitative evaluation of form characteristics of the earth surface and any landform unit. This is the most common technique in basin analysis, as morphometry forms an ideal areal unit for interpretation and analysis of fluvially originated landforms where they exhibit and example of open systems of operation. The composition of the stream system of a drainage basin in expressed quantitatively with stream order, drainage density, bifurcation ration and stream length ratio (Horton 1945). For detail morphometric analysis of the drainage within Wardha River basin, sub-watersheds are delineated from the available toposheet after assigning 'stream order' to all the segments following Horton's (1945) method modified by Strahler's (1952).

Stream Order (U)

There are four different system of ordering streams that are available Gravelius (1914), Horton (1945), Strahler (1952) and Schideggar (1965). Strahler's system, which is a slightly modified of Horton system, has been followed because of its simplicity, where the smallest, unbranched fingertip streams are designated as 1st order; the confluence of two 1st order channels gives a channel segments of 2nd order; two 2nd order streams join to form a segment of 3rd order and so on. When two channels of different orders join, then the higher order is maintained. The trunk stream is the stream segment of highest order. The total Wardha drainage basin boundary and major river system are delineated from the satellite imagery and SRTM. It is found that Wardha River is 6th-order stream. The analyses of morphometric parameters are carried out for the entire 10 sub-watersheds.

Mean Stream Length (Lu)

Mean stream length of a stream channel segment of order 'u' is a dimensional property revealing the characteristic size of components of a drainage network and its contributing basin surface (Strahler 1964). The lengths of stream segments of up to 6th order are measured, and the total length as well as mean stream length (Lu) of each order is computed (Table 1). The mean stream lengths of stream increase with the increase of the order. But in some sub-watersheds showing opposite relation, higher order stream has a small mean length. These basins show variable lithology with asymmetry in nature, and these basins are found along the major structural lineament.

Bifurcation Ratio (Rb)

The bifurcation ratio is the ratio between the number of streams in one order and in the next. It is calculated by dividing the number of streams in the lower by the number in the higher of the two orders; the bifurcation ration of large basins is generally the average of the bifurcation rations of the stream orders within it. In the study area, the higher values of Rb indicate a strong structural control in the drainage development, whereas the lower values indicate that some of the area in the basin is less affected by structural disturbances (Strahler 1964; Nag 1998).

Table 1 Calculation of morphometric parameters of 10 sub-watersheds of Wardha River basin

Sub-watersheds	Bifurcation ratio (Rb)					Mean bifurcation ratio (Rbm)	Area (km^2)	Perimeter (km)	Basin length (km)	Drainage density (Dd)	Stream frequency (Fs)	Drainage texture (T)	Form factor (Rf)	Circulatory ratio (Rc)	Elongation ratio (Re)	Shape factor (Bs)	Compactness coefficient (Cc)	Length of overland flow (Lg)
	I/II	II/III	III/IV	IV/V	V/VI													
SW-1	5	2.75	4	–	–	3.92	63.217	37.79	13.04	1.04	1.14	1.91	0.38	0.55	0.69	2.69	1.36	1.93
SW-2	4.5	5	–	–	–	4.75	49.172	40.42	14.57	1.03	1.18	1.44	0.24	0.37	0.55	4.32	1.64	1.95
SW-3	5.67	3	–	–	–	4.34	28.55	29.52	11.8	0.82	0.78	0.75	0.21	0.4	0.52	4.88	1.57	2.44
SW-4	3.17	3	2	–	–	2.73	54.82	31.77	13.12	0.71	0.53	0.92	0.32	0.67	0.64	3.14	1.22	2.82
SW-5	3.42	4	3	–	–	3.48	77.53	42.14	16.19	0.68	0.75	1.38	0.3	0.54	0.62	3.39	1.36	2.95
SW-6	5.88	4	–	–	–	4.94	81.33	57.59	17.98	0.89	0.72	1.01	0.26	0.31	0.57	3.98	1.82	2.25
SW-7	5.19	2.75	–	–	–	3.97	106.87	55.27	16.93	0.76	0.69	1.33	0.38	0.44	0.69	2.69	1.52	2.64
SW-8	4.19	4.13	4	1	2	3.07	280.36	120.77	39.49	0.62	0.66	1.53	0.18	0.24	0.48	5.57	2.05	3.23
SW-9	3.89	3.86	3.5	2	–	3.32	142.74	57.61	22.94	0.79	1	2.47	0.28	0.54	0.59	3.69	1.37	2.54
SW-10	4.91	11	–	–	1	5.64	65.77	55.2	22.88	0.97	1.04	1.24	0.13	0.27	0.41	7.96	1.94	2.07

Mean Bifurcation Ratio (Rbm)

Mean bifurcation ratio (Rbm) is calculated as the arithmetic mean bifurcation ratio, and the result is tabulated corresponding to sub-order basins as shown in Table 1. Using Strahler's (1957) method, taking into consideration of actual number of streams that are involved in the ratio, mean bifurcation ratio of different sub-watersheds was calculated. The mean bifurcation ratio is in between 2.73 and 5.64. The SW4 has the lower bifurcation ratio of 2.73, and SW10 has the higher bifurcation ratio of 5.64.

Drainage Density (Dd)

Drainage density has long been recognized as topographical characteristic of fundamental significance. Dd is a measure of the texture of the network and indicates the balance between the erosive power of overland flow and the resistance of surface soils and rocks. The factors affecting drainage density include geology and density of vegetation. The vegetation density influenced drainage density by binding the surface layer and slows down the rate of overland flow, and stores some of the water for short periods of time. The effect of lithology on drainage density is marked. Permeable rocks with a high infiltration rate reduce overland flow, and consequently, drainage density is low. In sub-watersheds of Wardha River basin, SW1 is having highest drainage density, i.e., 1.04, and SW8 has lowest, i.e., 0.62. This low drainage density suggested highly permeable subsoil and coarse drainage texture. The drainage density is also governed by the factors like rock type, run-off intensity, soil type, infiltration capacity and percentage of rocky area.

Stream Frequency (Fs)

Stream frequency may be directly related to the lithological characteristics. The number of stream segments per unit area is termed stream frequency or channel frequency or drainage frequency (Fs) Horton (1945). The stream frequency (Fs) value of the sub-watersheds ranges from 0.53 (SW4) to 1.18 (SW2) (Table 1) suggests sub-watersheds having lower Fs values represent low relief and permeable sub-surface material, whereas sub-watersheds with higher Fs values show resistant/low conducting sub-surface material, sparse vegetation and high relief. The value of stream frequency (Fs) of the basin exhibits positive correlation with drainage density of the area. This indicates that with increase in stream numbers, there is an increase in drainage density.

Drainage Texture (Rt)

Horton (1945) defined drainage texture is the total number of stream segments of all order in a basin per perimeter of the basin. It is important to geomorphology which means that the relative spacing of drainage lines. Drainage texture is on the underlying lithology, infiltration capacity and relief aspect of the terrain. Smith (1950) has classified drainage texture into 5 different textures, i.e., very coarse (<2), coarse (2–4), moderate (4–6), fine (6–8) and very fine (>8). The drainage texture of entire 10 sub-watersheds is coarse to very coarse. The study area has dendritic to sub-dendritic drainage type pattern. It is characterized by a tree-like branching system in which tributaries join the gently curving mainstream at acute angles. The occurrence of this drainage system indicates homogeneous, uniform soil and rock material.

Form Factor (Rf)

Form factor is the numerical index (Horton 1932) commonly used to represent different basin shapes. The value of form factor is in between 0.13 and 0.38. Smaller the value of form factor, more elongated will be the basin. In the study area, Rf values have been found varying from 0.13 (SW10) to 0.38 (SW1, SW7), suggesting that 10 sub-watersheds represent elongated shape with lower peak flows for longer duration.

Circularity Ratio (Rc)

The circularity ratio is a similar measure as elongation ratio, originally defined by Miller (1953), as the ratio of the area of the basin to the area of the circle having same circumference as the basin perimeter. The value of circularity ratio varies from 0 (in line) to 1 (in a circle). The Rc values in sub-watershed ranges from 0.24 (SW8) to 0.67 (SW4) (Table 1). Higher the value represents more circularity in the shape of the basin and vice versa. Low, medium and high values of Rc indicate the young, mature and old stages of the life cycle of the tributary watershed.

Elongation Ratio (Re)

Schumm's (1956) used an elongation ratio (Re) defined as the ratio of diameter of a circle of the same area as the basin to the maximum basin length. The value of Re varies from 0 (in highly elongated shape) to unity, i.e., 1.0 (in the circular shape).

Thus, higher the value of elongation ratio more circular shape of the basin and vice versa. Values close to 1.0 are typical of regions of very low relief, whereas that of 0.6–0.8 are usually associated with high relief and steep ground slope (Strahler 1964). These values can be grouped into three class namely circular (>0.9), oval (0.9–0.8) and less elongated (<0.7). In the sub-watersheds of Wardha River basin, SW1 have highest value, i.e., 0.69, and SW10 lowest, i.e., 041 (Table 1). Values close to 1.0 are typical of region of very low relief, whereas values in the range 0.6–0.8 are usually associated with high relief and steep ground slope.

Basin Shape (Bs)

Basin shape is the ratio of the square of basin length (Lb) to the area of basin (A). Shape factor is greater than 1 for basins which are elongated along some characteristic length of the basin and less than 1 for basins which are perpendicular to this characteristic length. The calculated basin length in the given study area ranges from 3.69 to 7.96.

Constant of Channel Maintenance (Cc)

Schumn (1956) has used the inverse of the drainage density having the dimension of length as a property termed constant of channel maintenance. The drainage basins having higher values of this parameter, and there will be lower value of drainage density. All the values are computed and shown in Table 1. Higher value of constant channel maintenance reveals strong control of lithology with a surface of high permeability.

Length of Overland Flow (Lg)

The term length of overland is used to describe the length of flow of water over the ground before it becomes concentrated in definite stream channels. Horton (1945) expressed it as equal to half of the reciprocal of drainage density (Dd). It is an important independent variable which greatly affects the quantity of water required to exceed a certain threshold of erosion. This factor relates inversely to the average slope of the channel and is quite synonymous with the length of sheet flow to a large degree. The length of overland flow bears an effective relationship with the drainage density and constant channel maintenance. Length of overland flow in Wardha River sub-basin is 2.68, and in sub-watersheds, SW8 is having highest value, i.e., 3.23 and SW1 lowest, i.e., 1.93 (Table 1).

Watershed Prioritization

Watershed prioritization is the ranking of different sub-watersheds of a watershed according to the order in which they have to be taken up for treatment and conservation measures. Remote sensing image is geometrically rectified with respect to Survey of India (SOI) topographical map on 1:50,000 scale. The drainage pattern was initially derived from SOI toposheet and later updated using linearly stretched False Color Composite (FCC) IRS-P6 LISS IV satellite data. The drainage pattern delineated for watershed was exported to ARC GIS 10 software for morphometric analysis. For better accuracy of the thematic map, ground truth check is done for verification, and necessary modifications are made in thematic maps during post interpretation.

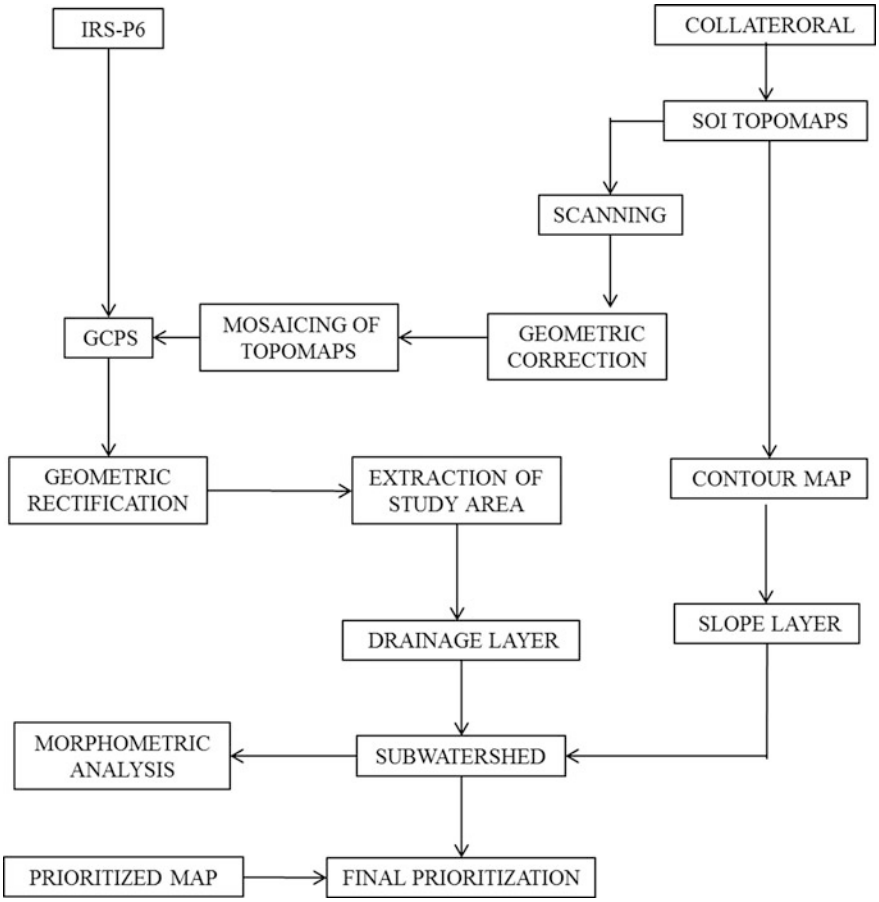

The linear parameters such as drainage density, stream frequency, bifurcation ratio, drainage texture, length of overland flow have a direct relationship with erodibility, higher the value, more is the erodibility. Shape parameters such as elongation ratio, compactness coefficient, circularity ratio, basin shape and form factor have an inverse relationship with erodibility lower the value, more is the erodibility. Compound value (Cp) has been calculated by adding the values of linear and shape parameters of each watershed. Based on average value of these parameters, sub-watersheds having the least rating value were assigned highest priority; next value was assigned second priority and so on. Prioritization rating of all the ten sub-watersheds of Wardha River basin was carried out by calculating the compound parameter values (Fig. 2).

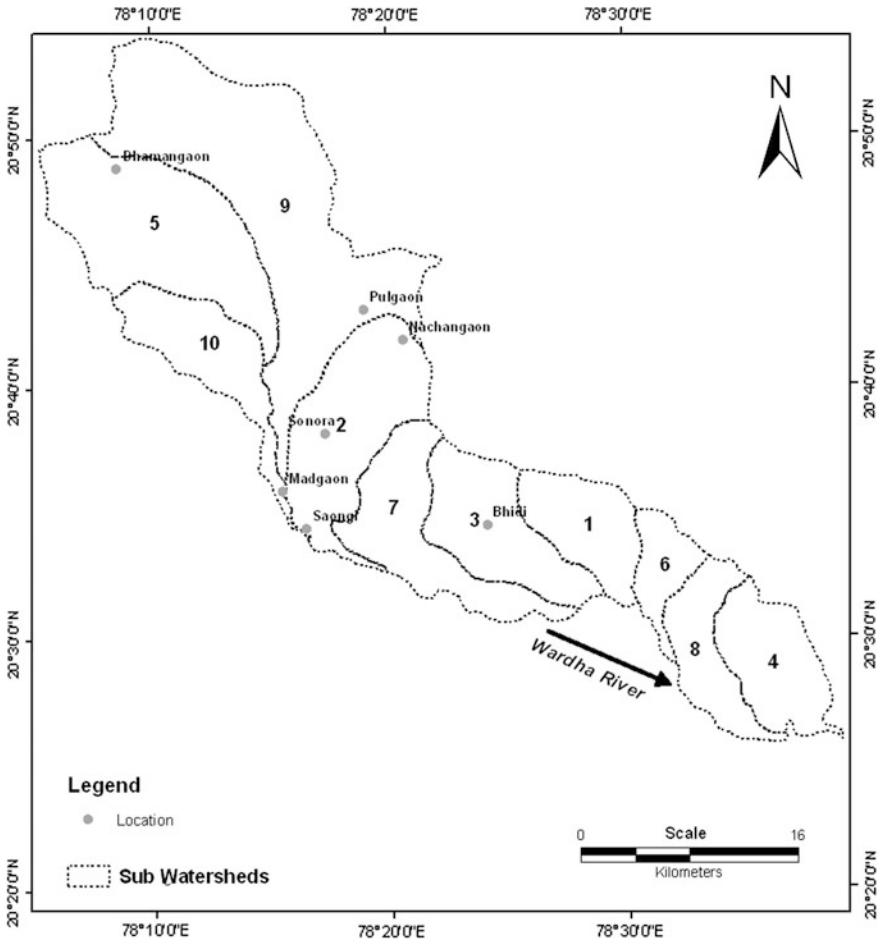

Fig. 2 Prioritized sub-watersheds of Wardha River basin

Table 2 Compound value of morphometric parameters

Sub-watersheds	Rbm	Dd	Fs	T	Rf	Rc	Re	Cc	Bs	Lg	Compound value (Cp)	Rank
SW-1	3.92	1.04	1.14	1.91	0.38	0.55	0.69	1.36	2.69	1.93	1.561	4
SW-2	4.75	1.03	1.18	1.44	0.24	0.37	0.55	1.64	4.32	1.95	1.747	8
SW-3	4.34	0.82	0.78	0.75	0.21	0.4	0.52	1.57	4.88	2.44	1.671	6
SW-4	2.73	0.71	0.53	0.92	0.32	0.67	0.64	1.22	3.14	2.82	1.37	1
SW-5	3.48	0.68	0.75	1.38	0.3	0.54	0.62	1.36	3.39	2.95	1.545	3
SW-6	4.94	0.89	0.72	1.01	0.26	0.31	0.57	1.82	3.98	2.25	1.675	7
SW-7	3.97	0.76	0.69	1.33	0.38	0.44	0.69	1.52	2.69	2.64	1.511	2
SW-8	3.07	0.62	0.66	1.53	0.18	0.24	0.48	2.05	5.57	3.23	1.763	9
SW-9	3.32	0.79	1	2.47	0.28	0.54	0.59	1.37	3.69	2.54	1.659	5
SW-10	5.64	0.97	1.04	1.24	0.13	0.27	0.41	1.94	7.96	2.07	2.167	10

All the ten sub-watersheds in the study area have been prioritized by considering the results of various morphometric parameters. The prioritization results for all ten sub-watersheds of the study area have been categorized on the basis of compound value, and the respective results of various parameters against each sub-watershed are given in Table 2 and spatial distribution of prioritization is given in Fig. 3. On the basis of priority and rank assigned to each sub-watershed, these are grouped into three categories: high, medium and low priorities. The prioritization analysis results reveal that SW1, SW4, SW5 and SW7 are the zones having lowest composite score and were considered under high priority (Table 3). They can be taken up for development and management plans on sustainable basis with immediate effect. Out of the remaining six sub-watersheds, SW2, SW3, SW6, SW8 and SW9 are

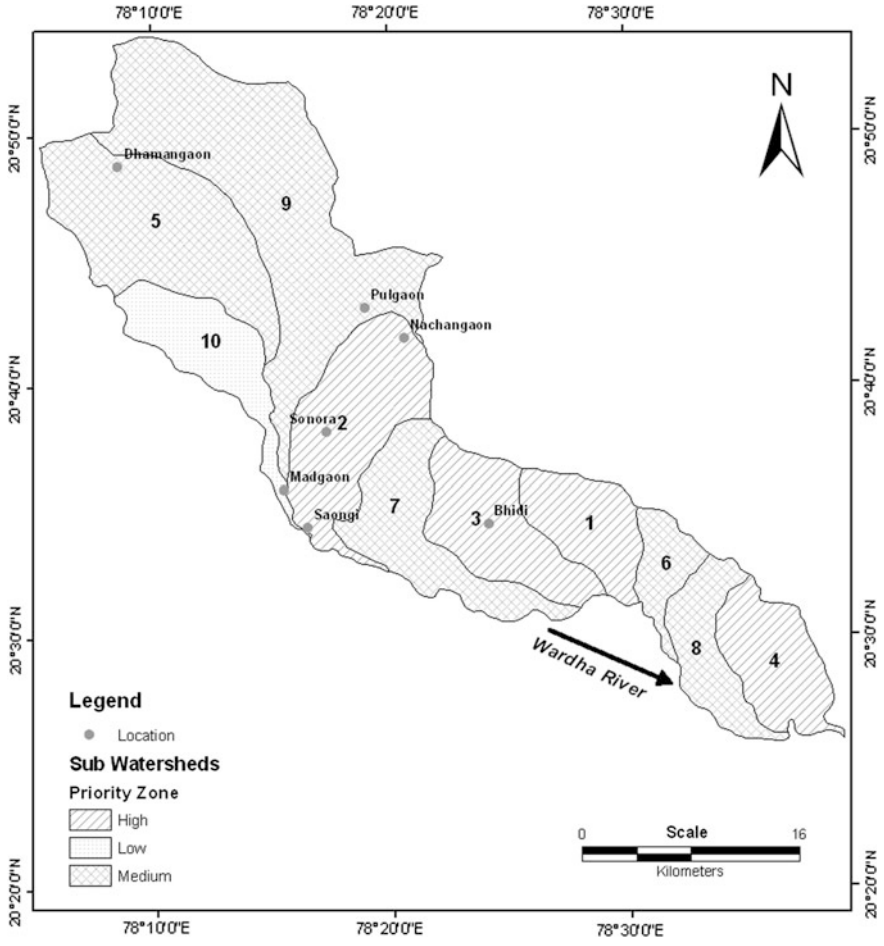

Fig. 3 Final-prioritized sub-watersheds of Wardha River basin

Table 3 Final priority of sub-watersheds

Sub-watersheds	Compound value (Cp)	Rank	Final priority
SW-1	1.561	4	High
SW-2	1.747	8	Medium
SW-3	1.671	6	Medium
SW-4	1.37	1	High
SW-5	1.545	3	High
SW-6	1.675	7	Medium
SW-7	1.511	2	High
SW-8	1.763	9	Medium
SW-9	1.659	5	Medium
SW-10	2.167	10	Low

categorized under medium priority, while low-prioritized zone is represented by SW10 (Table 3). These prioritized sub-watersheds may be taken up for development and management plans in a phased manner.

Conclusion

Satellite remote sensing has an ability of obtaining the synoptic view of a large area at one time, which is very useful in analysing the drainage morphometry. This study depicts the utility of remote sensing and GIS technique in prioritizing watershed based on morphometric analysis which could be valuable for watershed management practices. GIS has proved to be an efficient tool in drainage delineation, and this drainage has been used in the present study. Variation in the values of Rb among the sub-watersheds is ascribed to the difference in topography and geometric development. Based on the morphometric parameters, watershed prioritization was carried out. Using the composite score of these parameters, the sub-watershed having the leastrating value was assigned the highest priority number of 1; the next highest value was assigned a priority number 2 and so on. The sub-watersheds were classified into the three zones of priority, namely high, medium and low. The sub-watersheds which are falling under very high priority may be taken up for implementation of soil and water conservation measures.

References

Biswas S, Sudhakar S, Desai VR (1999) Prioritization of subwatersheds based on morphometric analysis of drainage basin—a remote sensing and GIS approach. J Indian Soc. Remote Sens 27:155–156

Gravelius H (1914) Grundrifi der gesamten Gewcisserkunde. Band I: Flufikunde (Compedium of Hydrology, vol. I. Rivers, in German). Goschen, Berlin, Germany, p 179

Horton RE (1932) Drainage basin characteristics. Trans Amer Geophys Union 13:350–361
Horton RE (1945) Erosional development of streams and their drainage basins: hydrophysical approach to quantitative morphology. Bull Geol Soc Amer 5:275–370
Kumar A (1999) Sustainable utilization of water resources in watershed perspective—a case study in Alaunja watershed, Hazaribagh. Bihar J Indian Soc Remote Sens 27(1):13–22
Krishnamurthy J, Srinivas G, Jayaram V, Chandrasekhar MG (1996) Influence of rock type and structure in the development of drainage networks in typical hard rock terrain. ITC J 3(4): 252–259
Miller VC (1953) A quantitative geomorphic study of drainage basin characteristics in the Clinch Mountain area, Varginia and Tennessee, Project NR 389042, Tech. Rept. University, Dept. of Geol., ONR, Geography Branch, New York
Nag SK (1998) Morphometric analysis using remote sensing techniques in the Chaka sub-basin purulia district, West Bengal. J Indian Soc Rem Sens 26:69–76
Obi Reddy GE, Maji AK, Gajbhiye KS (2002) GIS for morphometric analysis of rainage basins. GIS India 11(4):9–14
Scheidegger AE (1965) The algebra of stream-order numbers, Geol. Survey Research, U.S. Geol. Survey Prof. Paper 525-B, pp. B187–B189
Schumm SA (1956) Evaluation of drainage systems and slopes in bad lands at Perth Amboy, New Jersey. Bull Geol Soc Am 67:597–646
Smith KG (1950) Standards for grading texture of erosional topography. Am J Sci 248:655–668
Strahler AN (1952) Dynamic basis of geomorphology. Bull Geol Soc Am 63:923–938
Strahler AN (1957) Quantitative analysis of watershed geomorphology. Trans Amer Geophys Union 38:913–920
Strahler AN (1964) Quantitative geomorphology of drainage basins and channel networks, In: Chow VT (ed), Handbook of applied hydrology. McGraw Hill, New York, Sec 4–11, pp. 439
Vijith H, Satheesh R (2006) GIS based morphometric analysis of two major upland subwatersheds of Meena chil river in Kerala. J Indian Soc. Remote Sens 34(2):181–185

Flood Assessment of Lolab Valley from Watershed Characterization Using Remote Sensing and GIS Techniques

Mannan Bashir Wani, Syed Ahmad Ali and Umair Ali

Abstract The estimation of basin characteristics from the morphometric parameters assists in understanding the physical behavior of the watershed with respect to flooding. The remote sensing and geographical information system (GIS) are used for extraction of drainage boundary and order using ASTER digital elevation model (DEM), to evaluate the drainage characteristics. Additionally, sub-watershed-wise drainage parameters were analyzed to delineate the major influencing catchments with respect to flooding. The morphometric analysis for all the twelve sub-watersheds of the Lolab basin reveals that the sub-watersheds LSB 2, 4, 5, 10, 11 and LSB 12 are having the greater tendency to peak discharge in a short period of time because of high relief ratio (Rh), high ruggedness number, and less time of concentration (Tc). The sub-watersheds LSB1 and LSB11 having the highest drainage density (Dd), stream frequency (Fs), mean bifurcation ratio (Rbm), and infiltration number (If) cause greater runoff influence on the mainstream in the catchment. The LSB 3, 6 and LSB 7 sub-watersheds having higher form factor (Ff), medium drainage density (Dd), texture ratio (*T*), relief ratio (Rh), and time of concentration (Tc) cause moderate runoff influence toward mainstream. The study points out that DEM used in GIS environment for systematic analysis of drainage parameters offers valuable information about Lolab Basin with regard to flood assessment. This work will help in mitigating the hazard caused by flooding with respect to nature and human society. Thus, drainage characterization using remote sensing and GIS has made substantial contribution in flood monitoring and damage assessment.

Keywords Floods · Watershed · Morphometric analysis · Prioritization Remote sensing and GIS

M. B. Wani (✉) · S. A. Ali · U. Ali
Department of Geology, Aligarh Muslim University, Aligarh 202002, Uttar Pradesh, India
e-mail: mannanwani14@yahoo.in

V. P. Singh et al. (eds.), *Hydrologic Modeling*, Water Science and Technology Library 81, https://doi.org/10.1007/978-981-10-5801-1_26

Introduction

India is the worst flood-affected country in the world after Bangladesh and accounts for one-fifth of the global death count due to floods (Agarwal and Narayan 1991). Around 40 million hectares of land in the country is affected by floods; according to the National Commission on Floods (1980), an average of 18.6 million hectares of land is affected annually. The annual average cropped area affected is approximately 3.7 million hectares (Roy et al. 2008). The floods in India are caused mainly by the gambling of monsoon. Nearly, 75% of the entire Indian rainfall is concentrated over a short monsoon period of four months (June–September).

Jammu and Kashmir experienced one of the worst floods in the past 60 years, during first week of September 2014, due to unprecedented and intense rains. The Jhelum River and its tributaries were in spate and caused extensive flooding in the region. The heavy rainfall along with huge discharge of water from the several reservoirs in the Lolab Basin caused inundation and extensive damages on the agricultural lands along the river plains. Further, the tributaries of the river basin contribute more water in the main river causing floods in low lying areas, with each sub-catchment has its own distinct influence on the main river due to varying drainage morphometrics (Ozdemir and Bird 2009).

Quantitative morphometric analysis of watershed can provide information about the hydrological nature of the rocks exposed within the watershed. A drainage map of basin provides a reliable index of permeability of rocks and their relationship between rock type, structures, and their hydrological status. Watershed characterization and management requires detailed information for topography, drainage network, water divide, channel length, geomorphologic and geological setup of the area for proper watershed management and implementation plan for water conservation measures (Sreedevi et al. 2013). It is well established that the influence of drainage morphometry is very significant in understanding the landform processes, soil physical properties, and erosional characteristics. Besides, the quantitative analysis of drainage system is an important aspect of characteristic of watershed (Strahler 1964). It is important in any hydrological investigation such as assessment of groundwater potential, groundwater management, basin management, and environmental assessment.

The study of the physical behavior of the catchment helps in understanding the hydrological and geomorphic problems such as flooding, erosion, and mass movement (Eze and Efiong 2010). The morphometric analysis also supports in better understanding of hydrological characteristics of the basin (Nag and Chakraborty 2003; Sreedevi et al. 2009). Morphometric analysis is carried out through the measurement of linear, aerial, and relief aspects of the basin as done by Ali and Ali (2014); Bhatt and Ahmed (2014). Many pioneers (Horton 1945; Smith 1950; Miller 1953; Schumm 1956; Strahler 1957; Verstappen 1983; Kumar et al. 2000) have studied and developed various morphometric parameters such as stream order, basin area and perimeter, stream length, basin length, drainage density (Dd), stream frequency (Fs), bifurcation ratio (Rb), texture ratio (*T*), relief ratio (Rh),

ruggedness number (Rn), time of concentration (Tc), and infiltration number (If) to analyze the behavior of surface drainage networks and characteristic of the basin. These parameters have been utilized to prioritize the watersheds to study the flood characteristics (Alexander 1972; Chopra et al. 2005; Roughani et al. 2007; Angillieri 2008; Patel et al. 2012; Ali and Ali 2014). By prioritization of watersheds, one can conclude which watershed can lead higher amount of discharge due to an excessive amount of rainfall (Patel et al. 2012).

Surface hydrological indications are one of the promising scientific tools for assessment and management of water resources. Drainage morphometric analyses are a prerequisite for selection of water recharge site, watershed modeling, runoff modeling, watershed delineation, and groundwater prospect mapping and geotechnical investigation (Magesh et al. 2011; Thomas et al. 2012). The drainage network analysis is generally performed to understand the prevailing geological variation, topographic information, and structural set of a basin and their interrelationship. Remote sensing and GIS-based drainage basin evaluation have been carried out by number of researchers for different terrains, and it is proved to be a very scientific tool for generation of precise and updated information for characterization of drainage basin parameters (Ali et al. 2016; Grohmann 2004; Korkalainen et al. 2007; Hlaing et al. 2008; Pankaj and Kumar 2009).

The delineation of the catchment boundary and extraction of the drainage networks and catchment morphometric characteristics of the basins have been studied by using the conventional method (Horton 1945; Smith 1950; Strahler 1952; Nag 1998; Vittala et al. 2004; Amee and Dhiman 2007; Magesh et al. 2011). In recent years, the use of geographic information system (GIS) technology facilitated much to the work of hydrologists in the scientific study and management of water resources. Remote sensing and GIS are effective tools in the extraction of spatial information, especially for the delineation of catchment boundaries and extraction of drainage networks (Ahmed et al. 2010; Bertolo 2000). The use of digital elevation model (DEM) in particular has made watershed delineation a relatively smooth procedure. The representation of the terrain in an elevation format from the DEM provides excellent input for the delineation of the catchment boundary and extraction of drainage networks through the automated procedure in GIS technology. The techniques for automated extraction of drainage networks and delineation of catchment boundaries are developed since mid-eighties and have been implemented in various GIS systems and custom applications (Garbrecht and Martz 1999). In the present study, an attempt is made to delineate the catchment boundary and extraction of drainage networks from SRTM DEM for the basin using remote sensing and GIS techniques. Evaluation of morphometric parameters with respect to floods derived from the DEM is used to understand the hydrological behavior of the each sub-watershed in the Lolab Basin which influences floods in the Lahwal (Lalkul) River.

Study Area

The Lolab Valley (Figs. 1 and 2), hilly and mountainous in the north, west, and east regions is a Himalayan sub-valley and forms the northwestern corner of the Kashmir Valley, drained by the Lahwal River (locally known as Lalkul River) in the state of Jammu and Kashmir of India. It is bordered by the Kashmir Valley to the south and the Neelum Valley to the north and is separated by Nagmarg Meadows from Bandipora to the east. The Lolab Basin, formed by the flow of Lahwal (Lalkul) River, which flows from east to west, lies between 34° 43′30″ to 34° 24′0″ North latitudes and 74° 15′0″ to 74° 39′0″ East longitudes. The Lahwal (Lalkul) River has its source in the Nandmarg, the Kimsar, and the Bagalsar heights, north of the Walur. The study area has a total drainage area of 447 km^2. The mainstream of the Lolab has a length of about 30 km and flows in a westerly direction. One of its lateral tributaries is the Kalaroos Nala which originates below the peak of Nalgat (3645 m) and joins the Lolab below Khumriyal. A little before its junction with the Kahmil, which draw their waters from a series of ridges between the Shamshbari in the west and the Nowan Gali (3908 m) in the north, the Lahwal River receives the HaihomKol which flows from the north. Finally, Lahwal River in conjunction with Kahmil River near Mughalpora forms the Pohru River, which ultimately drains into the River Jhelum. Morphologically, Lolab Valley has flat to mildly undulating topography with its elevation about 1600 m a.m.s.l. The master slope in the area is toward southeast. The Lolab Basin can be divided into three major distinct physiographic units, i.e., high plateau lands, sharp ridges of hard rock, and intervening valleys and river terraces. The main ridges of the mountain ranges run in a northwest to southeast direction. The ridges are conical in shape with steep to very steep slopes in all directions. The geology of the study area is characterized by Quaternary alluvium, Karewa formations, Panjal traps, Dogra slates, and Zewan beds/Gondwana formations ranging in age from recent to Cambro-Silurian, respectively. In general, the study area experiences temperate-cum-mediterranean climate with the higher reach remaining cold throughout the year. Average minimum and maximum temperature varies from −5 to 32 °C. The winter season starts from the middle of the November, and severe winter conditions continue till the middle of February/March. The study area receives an average annual precipitation of about 700 mm in the form of rain and snow for about 60 days (Fig. 1).

Materials and Methods

The present work is basically based on morphometric analysis to evaluate the different morphometric parameters in order to assess the flood risk in Lolab Valley. For evaluation of these morphometric parameters, i.e., extraction of river basin/watershed boundary and extraction of drainage/stream network from the

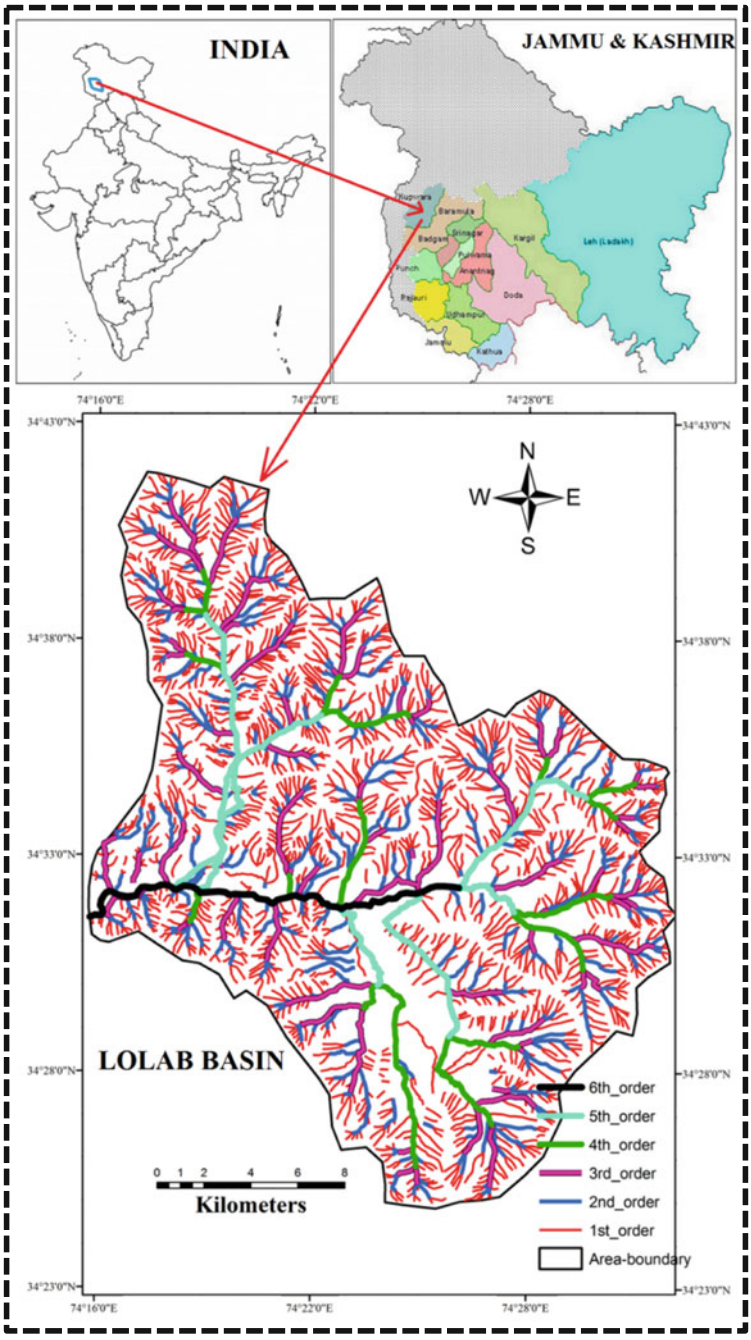

Fig. 1 Study area with river network

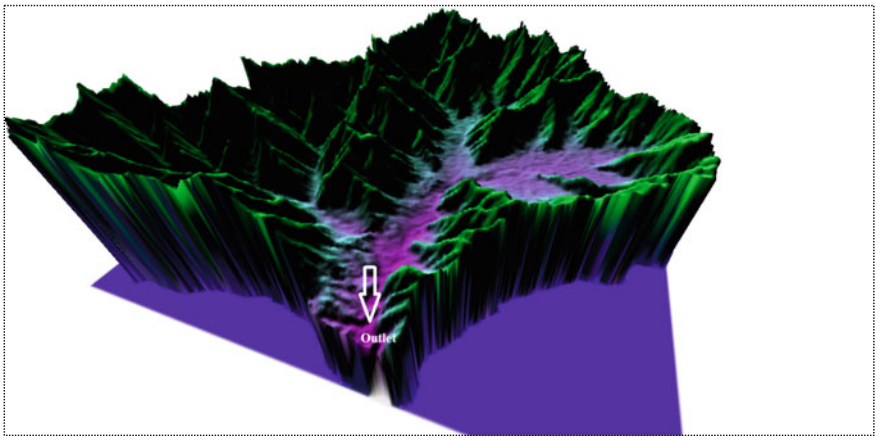

Fig. 2 Profile view of the study area showing stream concentration with main outlet

Lahwal (Lalkul) river basin using ASTER DEM data (30 m resolution) and SOI topographical maps (1:50,000), automatic extraction techniques (Maidment 2002; Ozdemir and Bird 2009; Ahmed et al. 2010) have been used. At first, Lolab watershed was delineated with the help of ARC GIS 9.3 software. Inlet and outlet are defined to demarcate Lolab Valley watershed. The DEM and the pour point are the two input parameters required for the extraction purpose. A pour point is a user-supplied point to the cells of highest flow accumulation. The pour point of the basin is shown in Fig. 3. The systematic geo-processing techniques required for the extraction of the basin are shown in Fig. 4. The result of this technique will create a polygon from the contributing area above a set of cells in a flow direction raster. Flow direction was calculated for each pixel using the filled DEM, i.e., the direction water will flow out of the pixel to one of the eight surrounding pixels (Fairfiled and Leymarie 1991). Flow direction cell contains the numerical value from 1 to 128 in an eight different directions. The output grid will have a cell value at the center cell, depending on the direction of flow (Fig. 4). The next step in hydrological modeling, i.e., flow accumulation, is used to generate a drainage network totally based on the direction of flow of each cell. The drainage network was extracted by considering the pixels greater than a threshold of 100 (Mark 1983). Further, watersheds can be delineated by giving an outlet or pour point where water flows out from a watershed and this is the lower most point in watershed. The Lolab watershed consists of twelve major sub-basins, named accordingly LSB1–LSB12 (Fig. 7, Table 1). All the twelve basins were delineated similarly as the method explained, and the morphometric analysis for each basin was carried out independently to estimate the influence of the water flow to the main river which causes floods in the lower part of the Lolab Basin.

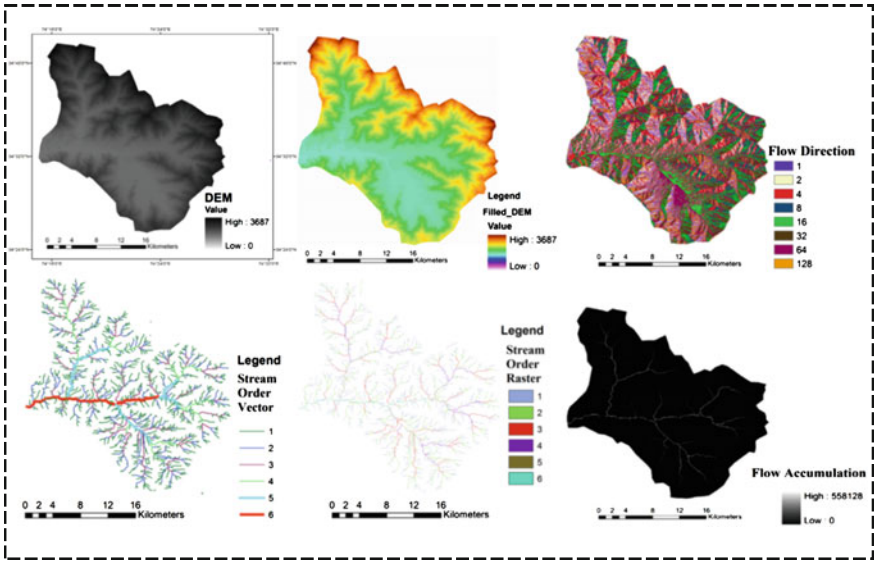

Fig. 3 Extraction of drainage networks from SRTM DEM

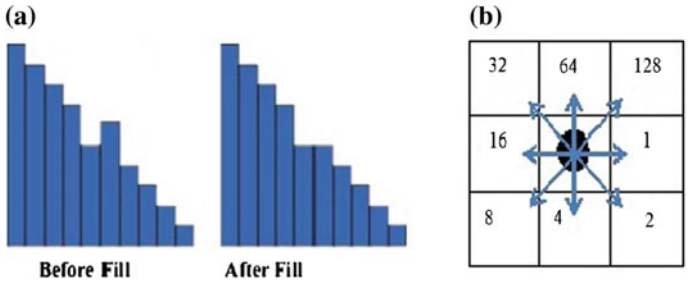

Fig. 4 Cross section of an image showing fills (**a**); flow direction in 8 directions (**b**)

Results and Discussion

The basic parameters such as stream number, stream length, catchment area, catchment perimeter, basin length, and minimum and maximum elevation of the catchment were derived from DEM and are presented in Tables 1, 2, and 3. Tables 4 and 5 are the results of the derived parameters that are achieved through the measurement of linear, aerial, and relief aspects of catchment using mathematical equations (Table 6) to analyze flood behavior in the area. Drainage pattern in Lolab Basin is characterized by irregular branching of streams in many directions with an angle less than 90º.

Table 1 Basic parameters

Sub-watershed	Basin area (km^2)	Basin perimeter (km)	Relative perimeter (Pr) = A/P	Basin length (km)	Max. elevation (m)	Min. elevation (m)
LSB1	68.81	35.51	1.93	13.73	3400	1900
LSB2	47.24	32.24	1.46	9.12	3400	1900
LSB3	57.41	36.20	1.58	9.75	3200	1700
LSB4	33.29	25.24	1.31	7.65	3200	1700
LSB5	16.76	18.39	0.91	5.23	2900	1700
LSB6	40.90	26.47	1.54	8.27	2500	1700
LSB7	15.88	17.21	0.92	7.18	2400	1700
LSB8	23.73	23.64	1.00	9.09	2400	1700
LSB9	35.75	31.21	1.14	10.27	2400	1700
LSB10	45.28	30.56	1.48	9.96	3700	1800
LSB11	28.13	27.15	1.03	4.93	2700	1600
LSB12	33.75	29.02	1.1	7.24	2700	1600
Total	446.99	332.88				

Table 2 Stream order and stream number

Watershed No.	Name of the sub-watershed	Stream order	Stream number						
			I	II	III	IV	V	VI	Total
1	LSB1	V	289	55	11	3	1	–	359
2	LSB2	V	159	34	7	3	1	–	204
3	LSB3	V	183	38	10	2	1	–	234
4	LSB4	IV	83	21	6	1	–	–	111
5	LSB5	IV	65	13	3	1	–	–	82
6	LSB6	V	120	26	8	2	1	–	157
7	LSB7	III	49	6	1	–	–	–	56
8	LSB8	IV	59	12	3	1	–	–	75
9	LSB9	V	85	19	3	1	1	–	109
10	LSB10	V	173	43	9	2	1	–	228
11	LSB11	IV	144	28	5	1	–	–	178
12	LSB12	V	101	24	5	0	2	–	132

Stream Order (U)

The Lolab Basin formed by the Lahwal (Lalkul) River is a 6th order stream covering an area of 447 km^2. The sub-watersheds LSB1, LSB2, LSB3, LSB6, LSB9, LSB10, LSB12 are having V order streams, whereas the sub-watersheds LSB4, LSB5, LSB8, LSB11 are having IV order streams and LSB7 is having III order streams (Table 2). The variation in order and size (Table 1) of the sub-watersheds is largely due to physiographic and structural conditions of the region.

Table 3 Stream length of different sub-watersheds of Lolab Basin

Watershed No.	Name of the sub-watershed	Stream length (km)						Mean stream length (Lum) = Lu/Nu
		I	II	III	IV	V	Total	
1	LSB1	187.81	38.29	23.05	4.72	7.81	261.69	0.72
2	LSB2	114.43	23.14	9.65	4.99	8.25	160.48	0.78
3	LSB3	124.09	28.50	16.64	8.79	3.25	181.29	0.77
4	LSB4	66.22	17.66	10.24	4.83	–	98.96	0.891
5	LSB5	42.85	9.15	6.08	0.89	–	58.99	0.71
6	LSB6	81.36	22.29	12.73	8.44	1.28	126.23	0.80
7	LSB7	32.86	6.02	2.33	–	–	41.22	0.73
8	LSB8	38.31	7.64	2.33	7.72	–	56.02	0.74
9	LSB9	49.64	19.08	11.01	2.79	4.60	87.13	0.79
10	LSB10	111.88	24.09	12.14	6.06	4.60	158.79	0.69
11	LSB11	72.15	19.37	8.44	1.50	–	101.47	0.57
12	LSB12	55.90	20.35	10.68	0	12.68	99.63	0.75

Table 4 Bifurcation ratios

Name of the sub-watershed	I/II	II/III	III/IV	IV/V	V/VI	Mean bifurcation ratio (Rbm) = Nu/Nu + 1
LSB1	5.25	5	3.66	3	–	4.23
LSB2	4.67	4.85	2.33	3	–	3.71
LSB3	4.81	3.8	5	2	–	3.90
LSB4	3.95	3.5	6	–	–	4.48
LSB5	5	4.33	3			4.11
LSB6	4.61	3.25	4	2		3.46
LSB7	8.16	6				7.08
LSB8	4.91	4	3			3.97
LSB9	4.47	6.33	3	1		3.70
LSB10	4.02	4.77	4.5	2		3.82
LSB11	5.14	5.6	5			5.37
LSB12	4.02	4.8	0	0		2.25

Stream length (**Lu**): The stream length was computed on the basis of the law proposed by (Horton 1945), for all the 12 sub-watersheds. As a rule, the total length of stream segments decrease as the stream order increases. In all the 12 sub-watersheds, the stream length follows Horton's law (Table 3). The highest Lu is observed in the sub-watershed LSB1 and the lowest in LSB8 (Table 3).

Stream frequency (**Fs**): Stream frequency (Fs) is an interlinking factor in predicting peak flood discharge (Patton and Baker 1976; Eze and Efiong 2010). Generally, high Fs is related to impermeable subsurface material, sparse vegetation, high relief conditions, and low infiltration capacity (Reddy et al. 2004;

Table 5 (a, b) Derived morphometric parameters

(a)

Name of the sub-watershed	Length of overland flow (Lo)	Circularity ratio (Re)	Rho coefficient (ρ)	Basin relief (H)	Drainage intensity (Di)	Drainage texture	Compactness constant (Cc)	Shape Factor (Bs)	Relief ratio (Rh)
LSB1	0.52	0.68	0.15	1.5	1.37	19.83	0.07	2.74	0.10
LSB2	0.58	0.57	0.18	1.5	1.27	14.66	0.09	1.76	0.16
LSB3	0.63	0.55	0.10	1.5	1.29	12.86	0.08	1.65	0.15
LSB4	0.67	0.65	0.09	1.5	1.12	9.91	0.10	1.76	0.19
LSB5	0.56	0.62	0.08	1.2	1.38	17.20	0.15	1.63	0.22
LSB6	0.64	0.73	0.12	0.8	1.24	11.84	0.091	1.67	0.09
LSB7	0.77	0.67	0.04	0.7	1.35	9.14	0.15	3.25	0.09
LSB8	0.84	0.53	0.31	0.7	1.33	7.45	0.14	3.48	0.07
LSB9	0.82	0.46	0.19	0.7	1.25	7.42	0.12	2.95	0.06
LSB10	0.57	0.60	0.12	1.9	1.43	17.65	0.09	2.19	0.19
LSB11	0.55	0.48	0.05	1.1	1.75	22.82	0.13	0.86	0.22
LSB12	0.67	0.50	0.13	1.1	1.32	11.54	0.12	1.55	0.15

(b)

Name of the sub-watershed	Drainage density (Dd)	Stream frequency (Fs)	Elongation ratio (Re)	Form factor (Ff)	Ruggedness number (Rn)	Time of concentrations (Tc)	Texture ratio (Dt)	Infiltration number (If)
LSB1	3.80	5.21	0.68	0.36	2.05	120.98	10.10	19.83
LSB2	3.39	4.31	0.85	0.56	1.90	75.54	6.32	14.66
LSB3	3.15	4.07	0.87	0.60	1.93	81.64	6.46	12.86
LSB4	2.97	3.33	0.85	0.56	1.68	61.76	4.39	9.91
LSB5	3.51	4.89	0.88	0.61	1.66	43.43	4.45	17.20

(continued)

Table 5 (continued)

(b)

Name of the sub-watershed	Drainage density (Dd)	Stream frequency (Fs)	Elongation ratio (Re)	Form factor (Ff)	Ruggedness number (Rn)	Time of concentrations (Tc)	Texture ratio (Dt)	Infiltration number (If)
LSB6	3.08	3.83	0.87	0.59	0.99	86.06	5.92	11.84
LSB7	2.59	3.52	0.62	0.30	0.95	77.01	3.25	9.14
LSB8	2.35	3.15	0.60	0.28	0.93	100.92	3.17	7.45
LSB9	2.43	3.04	0.65	0.33	0.87	116.18	3.49	7.42
LSB10	3.50	5.03	0.76	0.45	2.72	76.33	7.46	17.651
LSB11	3.60	6.32	1.21	1.15	1.93	42.03	6.55	22.82
LSB12	2.95	3.91	0.90	0.64	1.45	65.327	4.54	11.54

Table 6 Morphometric parameters and their mathematical expressions

S. No.	Morphometric parameters	Formula	Reference
1	Stream order	Nu	Strahler (1964)
2	Stream length	Lu	Horton (1945)
3	Bifurcation ratio (Rb)	Rb = Nu/Nu + 1	Horton (1932)
4	Stream frequency (FS)	Fs = Nu/A	Horton (1945)
5	Drainage density (Dd)	Dd = Lu/A	Horton (1945)
6	Texture ratio (*T*)	*T* = Nu/P	Smith (1950)
7	Form factor (Ff)	Ff = A/Lb2	Horton (1945)
8	Infiltration number (If)	If = Fs × Dd	Faniran (1968)
9	Relief ratio (Rh)	Rh = H/L	Schumm (1963)
10	Ruggedness number (Rn)	Rn = Bh × Dd	Schumm (1956)
11	Elongation ratio (Re)	Re = 2/Lb *$(A/Pi)^{0.5}$	Schumn (1956)
12	Circularity ratio (Rc)	Rc = 4 * Pi * A/P^2	Miller (1953)
13	Compactness coefficient (Cc)	Cc = 0.2821P/A0.5	Horton (1945)
14	Length of overland flow (Lo)	Lo = 1/Dd*2	Horton (1945)
15	Shape factor (Bs)	Bs = Lb^2/A	Horton (1945)
16	Time of concentrations (Tc)	Tc = $6.95(L^{1.15}/Bh^{0.385})$	Verstappen (1983)

Shaban et al. 2005). In Lolab Basin, the Fs values for twelve sub-watersheds vary from 3.04 to 6.32 per km^2 (Table 5). The LSB11 has the highest Fs value followed by LSB1, LSB10, LSB5, LSB2, LSB3, respectively, all having Fs > 4. A higher Fs reflects greater surface runoff and a steeper ground surface. The sub-watersheds, i.e., LSB1, LSB5, LSB2, LSB3, are having high Fs, showing that these sub-watersheds cause more water flow during the period of high intensity rainfall. This is due to their high relief with the presence of flattopped hillocks on both sides which cause more discharge of water in less amount of time. The sub-watersheds LSB4, LSB6, LSB 7, LSB8, LSB9, LSB11, and LSb12 have low Fs because of low relief and presence of more agricultural fields which causes less water flow during the period of rainfall. Finally, the results of Fs show that early peak discharges from the LSB1, LSB10, LSB5, LSB2, LSB3 catchments to the main Lahwal (Lalkul) River cause floods in the riverbanks. The remaining catchments of the Lolab Basin take a longer period to contribute peak discharge to the River because of low water flow.

Drainage density (**Dd**): The drainage density (Dd) is an important indicator of the linear scale of landform elements in a stream-eroded topography (Horton 1945). It is an essential element of drainage morphometry to study the landscape dissection, runoff potential, infiltration capacity of the land, climatic condition, and vegetation cover of the basin. The Dd indicates the closeness of spacing of channels, thus determines the time of travel by water (Horton 1932). The Dd indirectly reflects the structural framework of the underlying rocks of the watershed and is a significant factor in controlling over the landscape runoff, and its influences on the flood peak discharges (Yildiz 2004; Pallardet al. 2009). Strahler (1964) is of the opinion that a low Dd is favored in regions of highly resistant or highly permeable strata under dense vegetation and low relief, while a high Dd is supported in regions of weak or impermeable rocks under sparse vegetation and mountainous relief. In the Lolab Basin, the Dd values range from 2.35 to 3.8 km/km^2 (Fig. 5, Table 5).

The highest Dd values are present in the sub-watersheds of LSB1, followed, respectively, by LSB11, LSB10, LSB2, LSB3, and LSB6, because of the high mountainous relief and impermeable subsurface material, and their catchments will contribute more runoff in a short period of time and attain floods in the lower part of the basin. The LSB5, LSB7, LSB8, and LSB9 sub-watersheds have the lowest Dd value because of low relief and accordingly influence low runoff during the flood period. The LSB4 and LSB12 sub-watersheds having medium Dd values thus contribute an average discharge of water during flood period.

Drainage texture (**T**): The drainage texture (*T*) is a measure of closeness of the channel spacing, depending on climate, rainfall, vegetation, soil and rock type, infiltration rate, relief, and stage of development (Smith 1950). Soft or weak rocks unprotected by vegetation characterize a fine drainage texture, while massive and resistive rocks represent a coarse drainage texture (Sreedevi et al. 2009). Sparse vegetation, with an arid climate, causes a finer drainage texture than that developed on similar rocks in a humid climate. According to Dornkamp and King (1971), the *T* of the rocks depends upon the type of vegetation and the climate. On the other hand, the *T* is a product of Dd and F. Smith (1950) classifies *T* as coarse (<4 per km), intermediate (4–10 per km), fine (10–15 per km), and ultrafine (>15 per km).

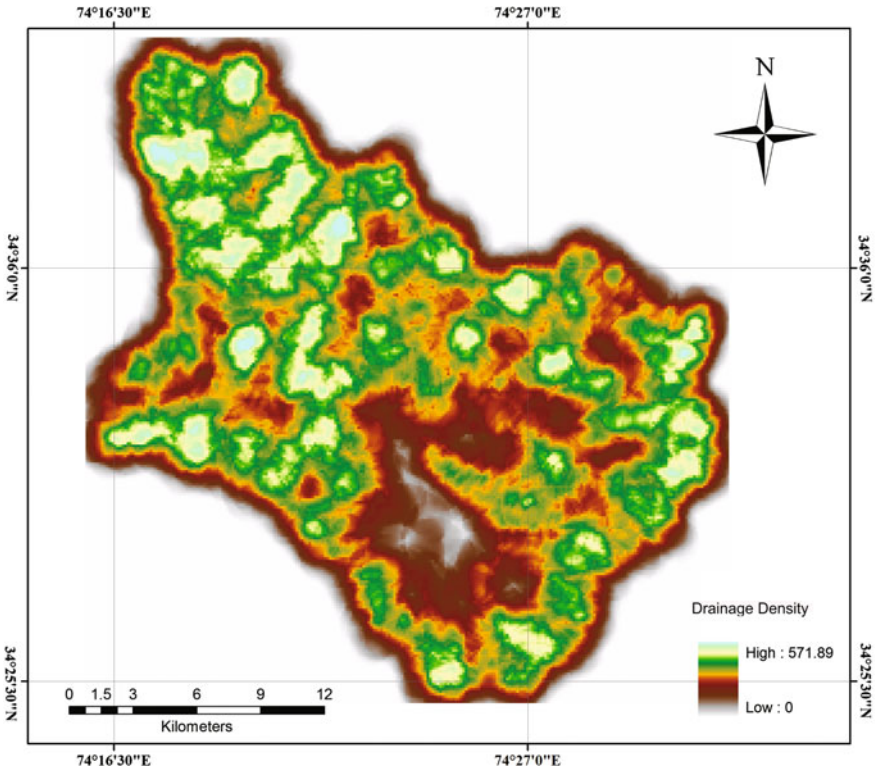

Fig. 5 Drainage density map of Lolab Basin

In the study area, the drainage texture varies from 7.42 to 22.82, indicating intermediate to ultrafine texture. (Table 5).

Bifurcation ratio (**Rb**): It is a dimensionless property and shows the degree of integration prevailing between streams of various orders in a drainage basin. Horton (1945) considered bifurcation ratio as an index of reliefs and dissections. Strahler (1964) has stated that where the Rb is between 3 and 5, geological structures do not seem to exercise a dominant control over the drainage pattern of the watershed. Rb of greater than 5 indicates structurally controlled development of a drainage network (Strahler 1957). In case of floods, the Rb plays an important role in control over the peakedness of the runoff hydrograph (Chorley 1969; Jain and Sinha 2003). The Rb of 2 is obtained for flat terrain and 3–4 for mountainous or highly dissected terrain (Horton 1945). The variation seen in Rb values (Table 4) clearly reflects the differences in the stage of geomorphic development and topographic variations (Lattif and Sherief 2012). In addition to this, the variation in Rb values within the basin is directly dependent upon the geological and the lithological development of the area (Strahler 1964).

The mean Rbm values vary from 4.6 to 7.08, indicating structural control in some of the sub-watersheds of the Valley. The higher values of Rbs (Table 4), in turn, are an indication of mature topography with a higher degree of drainage integration which attains peak discharge during the period of floods (Eze and Efiong 2010).

Length of overland flow (**Lo**): The surface water has to flow as a sheet to a certain distance before it reaches to a well-defined stream channel. This distance of travel is termed as 'length of overland flow.' If the formations are permeable and the slope is gentle, the volume of water reaching the channel will be less. Thus, the higher value of overland flow indicates poor permeability of formations. It is taken as half the reciprocal of the drainage density (Horton 1945). Length of overland flow relates inversely to the average channel slope; thus, it is one of the most important independent variables affecting hydrological and physiographical development of a drainage basin. The length of overland flow for twelve sub-watersheds ranges from 0.52 for LSB1 to 0.84 for LSB8 (Table 5). The shorter length of overland flow for LSB1 points out the quicker runoff process, and larger length of overland flow for LSB8 points out slower runoff process.

Form factor (**Ff**): Form factor (Ff) predicts the flow intensity of a basin with defined area and represents the shapes and outlines of a basin (Horton 1945; Gregory and Walling 1973). Thus, it has a direct relation with the peak discharge of the basin. For perfectly circular basin, the value of Ff would always be greater than 0.78 and the basin will be more elongated if the value turns to be smaller. The values of form factor vary from 0.28 for LSB8 to 1.15 for LSB11 (Table 7). The values of Ff for all the sub-watersheds except LSB11 are less than 0.78 depicting the sub-watersheds are elongated in shape. These elongated sub-watersheds with lower values of form factor indicate that the basin will have a flatter peak flow for longer duration. Flood flows of such elongated basins are easier to manage than those of the circular basins. The low Ff value of the sub-watersheds, viz LSB8, LSB7, LSB9, and LSB1, reveals that these watersheds have less side flow for shorter duration and high main flow for longer duration and vice versa (Reddy et al. 2004).

Elongation ratio (**Re**): It is a measure of the shape of the river basin, and it depends on the climatic and geologic types. A circular basin is more efficient in runoff discharge than an elongated basin (Singh and Singh 1997). The variations in the elongated shapes of the sub-basins within the watershed are caused by the effects of structural disturbances (Sreedevi et al. 2005). The ratio generally ranges from 0.6 to 1.0. The basins with the values of 0.6 to 0.8 are generally associated with strong relief and steep ground slopes, whereas the values in the range of 0.8 to 1.0 are typical of regions with low relief (Strahler 1964). These basins are efficient in the discharge of runoff than the elongated basin because concentration time is less in circular basins. Higher values of elongation ratio show high infiltration capacity and low runoff, whereas lower Re values are characterized by high susceptibility to erosion and sediment load (Reddy et al. 2004).

The elongation ratio (Re) values range from 0.60 for LSB8 to 1.21 for LSB11 (Table 7). The sub-watersheds LSB2, LSB3, LSB4, LSB5, LSb6, and LSb12 have

Table 7 Classification of sub-watersheds into different catagories

Priority	High	High	Medium	Medium	High	Medium	Low	Low	Low	High	High	Low
Priority Rank	10	8	7	6	9	5	4	2	1	9	11	3
Compound factor	8	6.75	6.5	6.41	7.75	5.58	5	3.08	2.5	7.75	8.08	4.5
Elongation ratio (Re)	4	6	7	6	8	7	2	1	3	5	10	9
Circulatory ratio (Rc)	11	6	5	9	8	12	10	4	1	7	2	3
Shape factor (Fs)	8	6	4	6	3	5	10	11	9	7	1	2
Time of concentration(Tc)	1	8	5	10	11	4	6	3	2	7	12	9
Infiltration number (If)	11	8	7	4	9	6	3	2	1	10	12	5
Relief ratio (Rr)	4	6	5	7	8	3	3	2	1	7	8	5
Ruggedness no. (Rn)	10	8	9	7	6	4	3	2	1	11	9	5
Mean bifurcation ratio(Rbm)	9	4	6	10	8	2	12	7	3	5	11	1
Texture ratio (T)	12	8	9	4	5	7	2	1	3	11	10	6
Form factor (Ff)	4	6	8	6	9	7	2	1	3	5	11	10
Stream frequency (Fs)	10	7	6	3	8	4	4	2	1	9	11	5
Drainage density (Dd)	12	8	7	5	10	6	3	1	2	9	11	4
Sub-watersheds	LSB1	LSB2	LSB3	LSB4	LSB5	LSB6	LSB7	LSB8	LSB9	LSB10	LSB11	LSB12

values ranging between 0.8 and 1, thus showing low relief which results in lower runoff, while the sub-watersheds LSB1, LSb7, LSb8, LSB9, and LSB10 show the values ranging between 0.6 and 0.8, thus showing high relief and steep ground slopes.

Circulatory ratio (**Rc**): The circulatory ratio (Rc) is a quantitative expression of the shape of basin which is expressed as the ratio of basin area to the area of circle, having the same perimeter as the basin. If the value of Rc is exactly 1.0, the basin is set to be a perfectly circular shape. The shape of a drainage basin mainly governs the rate at which water is supplied to the mainstream as it flows along its course from the source to the mouth. Long and narrow basins with a high bifurcation ratio are expected to have low discharges over a long time, whereas round basins with a low bifurcation ratio would be expected to have sharp peak flood discharge. The circularity ratio ranges from 0.46 for LSB9 to 0.73 for LSB6 (Table 5), which shows that the sub-watersheds are mainly elongated in shape. High value of circulatory ratio indicates the mature stages of topography. Rc is influenced by the length and frequency of streams, geological structures, land use/land cover, climate, relief, and slope of the basin. The sub-watersheds LSB2, LSB3, LSB8, LSB9, LSB10, LSB11, and LSB12 having values less than 0.60 are strongly elongated in shape resulting in low discharge of runoff.

Shape Factor: The shape factor is defined as the ratio between the squares of basin length to the basin area. The shape parameters can be used to quantify the degree of similarity of drainage basin shapes. A square-shaped drainage basin would have a shape factor (Sf) = 1, whereas the long narrow drainage basin would have a shape factor (Sf) > 1. The basin shape may influence the hydrographic shape especially for small basins. For example, if a basin is long and narrow, then it will take a longer time for water to travel from basin extremities to the outlet, and the resulting runoff hydrograph will be flatter. Runoff hydrograph is expected to be sharper with a greater peak and shorter duration for a more compact basin. A compact basin is more likely to be covered by the area of maximum rainfall intensity of local streams. The shape factor for the sub-watersheds ranges from 0.86 for LSB11 to 3.48 for LSB8 (Table 5). All the sub-watersheds except LSB11 have Sf values greater than one, which indicates that the sub-watersheds are elongated and the runoff hydrograph is expected to be flatter in this area.

Relief ratio (**Rh**): The Rh is a measure of overall steepness of the catchment. It is a good indicator of the intensity of water flows from a catchment slope. The high Rh implies on shorter lag time and attains higher peak discharge and flow velocities. With increasing relief, steeper hillslopes, and higher stream gradients, Tc of runoff decreases, thereby increasing flood peaks (Patton 1988). In the sub-watersheds of Lolab Basin, the Rh varies from 0.6 for LSB9 to 0.22 for LSB5 and LSB11 (Table 5). In general, the 'relief ratio' is the controlling factor for surface runoff. The higher the relief ratio, the higher is the surface runoff. The LSB 2, LSB 4, LSB 5, LSB 10, LSB11, and LSB 12 sub-watersheds having high Rhs indicate that the terrain contains steep slopes (Fig. 6) and the sub-watersheds with highest Rhs have a higher peak flows with greater velocities (Altin and Altin 2011). These subwatersheds contribute more water in a short period of time and cause

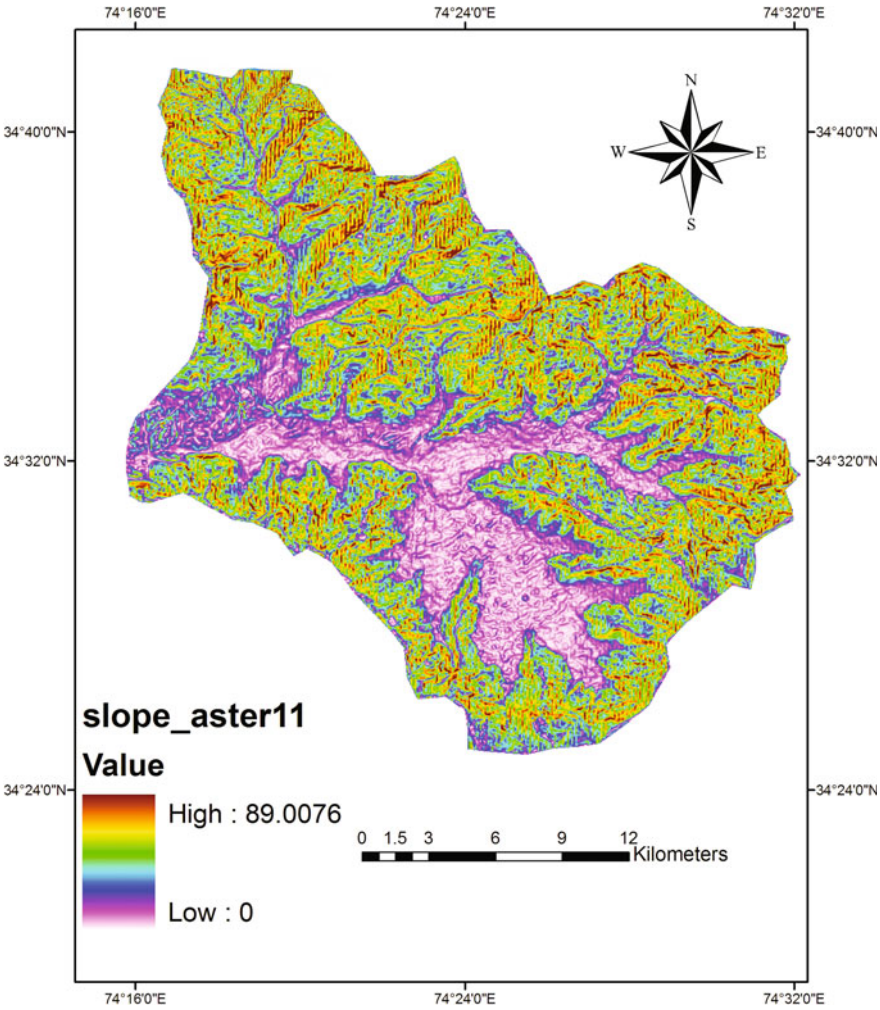

Fig. 6 Slope map of an area

floods in the lower region of the basin. The LSB3, LSB6, and LSb7 sub-watersheds have the moderate Rhs and have moderate influence on flooding. LSB8 and LSB9 sub-watersheds have low Rhs, indicating a nearly flat terrain with longer basin length, and their influence on flood is very less.

Ruggedness number (**Rn**): Rn indicates the structural complexity of the terrain in association with relief and Dd. Patton and Baker (1976) recognized that basins with high Rns with fine drainage texture might be expected to have high flood potential. In the Lolab Basin, LSB1, LSB2, LSB3, LSB10, and LSB11 have highest Rn because of the high relief and fine drainage texture and therefore possibilities of high surface flow (Table 5). The LSB4, LSB5, and LSB12 having the moderate Rn indicate that partially, the flat top surfaces or ridges (Fig. 7) and valley topography

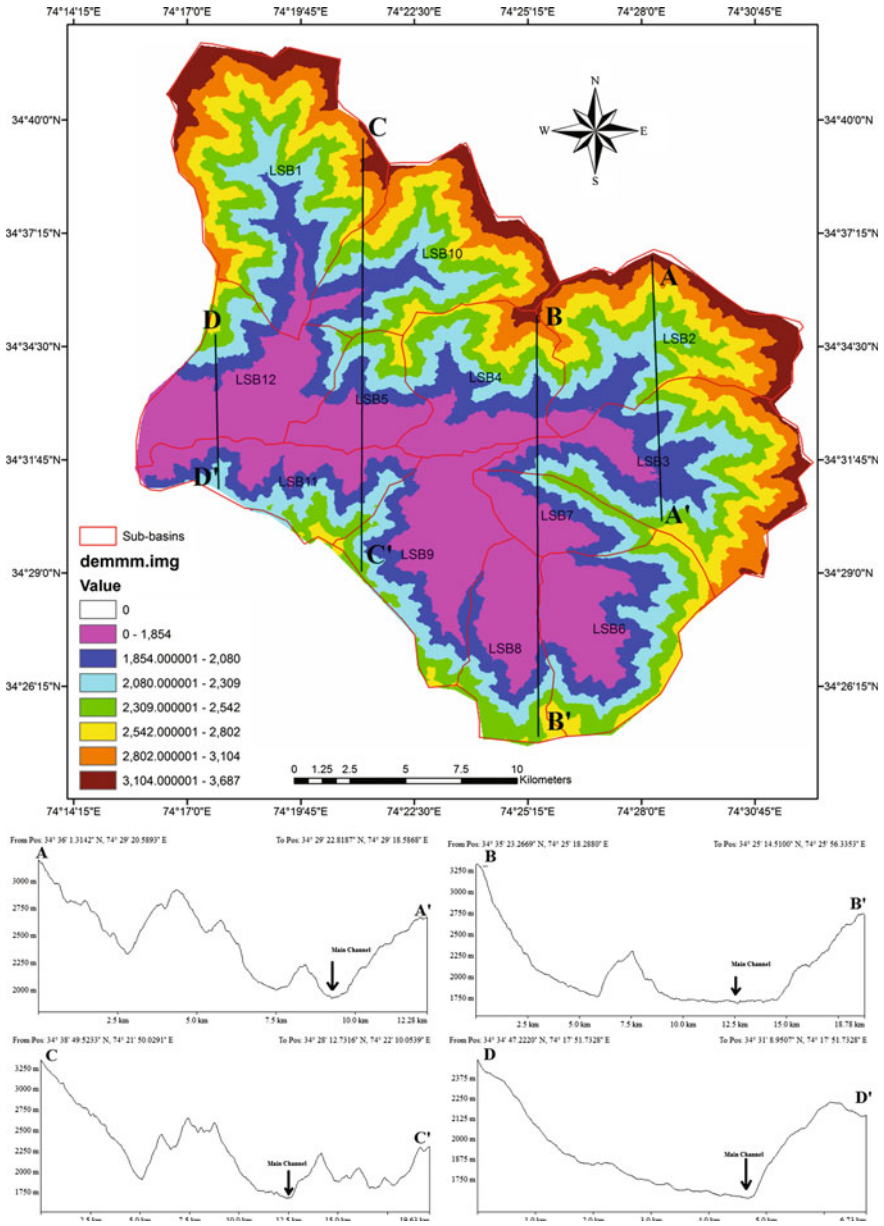

Fig. 7 Elevation map with associated graphs along lines AA', BB', CC', and DD' from source to outlet highlighting the relief aspect of Lolab Basin respectively

and moderately high degree of dissection and medium runoff are expected in these sub-watersheds, whereas LSB6, LSB7, LSB8, and LSB9 sub-watersheds have the lower Rn, indicating a lesser degree of terrain complexity causing less water flow.

Infiltration number (**If**): The product of Dd and Fs is defined as the If of a watershed and gives an idea about the infiltration characteristics of the basin. It is inversely proportional to the infiltration capacity of the basin (Romshoo et al. 2012). The higher the If, the lower will be the infiltration and the higher the runoff. In Lolab Basin, LSB1, LSB5, LSB10, and LSB 11 having the higher values for If (Table 5) indicate their low infiltration capacity which ultimately results more water flow in shorter durations during the period of intense rainfall.

Time of concentration (**Tc**): The time taken by runoff water to travel from the source of watershed to its outlet is known as the 'time of concentration.' The highest Tc value represents the greatest length of time for water to travel from the most distant point of the catchment to its outlet (Ozdemir and Bird 2009). In the Lolab Basin, lowest Tc values are observed in the sub-watersheds LSB5 and LSB11 (Table 5), showing that these catchments attain peak flows in short duration of time. The LSB1, LSB8, and LSB9 sub-watersheds having the highest Tc values signify the longer duration of flow discharges.

Compound factor and weightage: Lastly, to assess the flood influencing characteristics in each sub-watershed, morphometric parameters are taken into consideration. The parameters such as Rbm, Dd, Fs, *T*, Ff, Rn, If, and Rh have a direct relationship with flood runoff; i.e., the higher the value, the greater the runoff. Therefore, the highest value of the parameter was assigned as weightage 12, second highest value was assigned as weightage 11, and so on, and the least value was assigned as weightage 1 (Table 7). The parameter, Tc, has an inverse relationship with runoff; i.e., the lower the value, the greater the runoff. Thus, the lowest value of Tc was assigned as weightage 12, next lower value was assigned as weightage 11, and so on, and the highest value was assigned as weightage 1 (Table 7). Compound factor is calculated by summing the weightages of all parameters and then dividing the number of parameters. Basin with highest compound factor is of high priority while that with lowest compound factor is of low priority.

Thus, among the twelve sub-watersheds LSB1, LSB2, LSB 5, LSB 10 and LSB11 shows the greatest influence on the Lolab Basin during the rainy season because of high runoff parameters such as high Rh, high Rn and less Tc. The LSB11 having the highest form factor, high Rh, and less Tc causes high runoff. The LSB 3, LSB4, LSB 6, and LSB12 sub-watersheds contribute medium runoff and have medium influence toward flooding because of moderate Rh, moderate values of *T*, Rn, Tc, and moderate to high Dd, If, and mean Rb. The LSB 7, LSB 8, and LSB 9 have less influence in their runoff to the main basin because of lower values of Rh, Dd, Rn, and If. The results were mapped in GIS environment and are shown in Fig. 8 (Table 7).

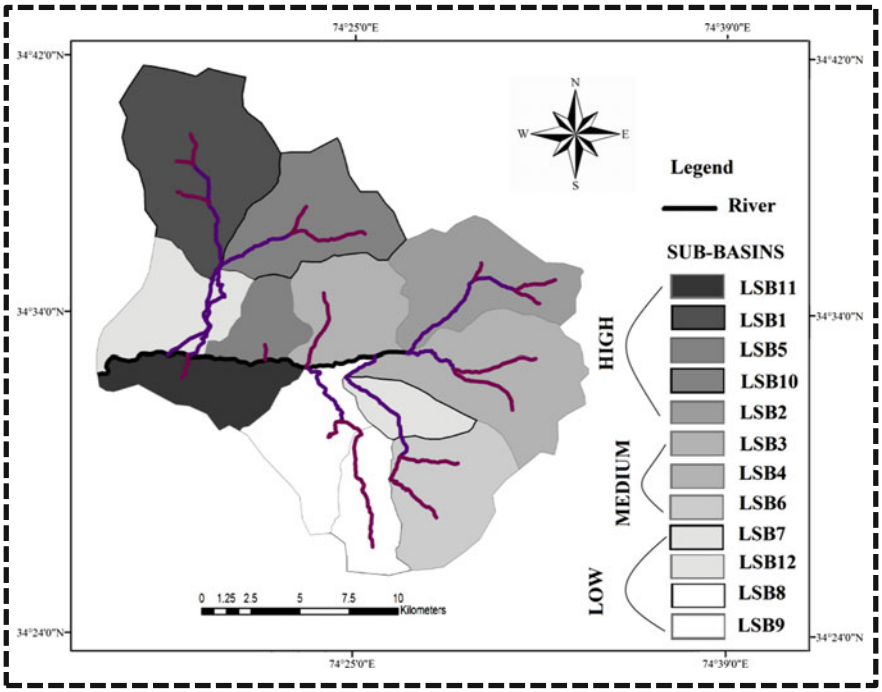

Fig. 8 Final map of higher-to-lower order of sub-watersheds which influence floods in the main Lahwal River of the Lolab Valley

Conclusion

The flood behavior analysis carried out for the Lolab watershed confirms that the watershed is having high relief and more or less elongated in shape. Drainage network of the basin exhibits as mainly dendritic type and helps to understand various terrain characteristics such as bedrock nature, infiltration capacity, runoff. Lower drainage density and stream frequency indicate high permeability rate of the different geological subsurface formations. The study of the drainage characteristics with respect to floods using the advanced techniques of GIS reveals the best method for extraction of drainage network and derivation of morphometric parameters from ASTER DEM and reduces the effort of digitization. Watershed analysis using GIS, remote sensing data, and digital elevation model (DEM) are efficient tools for understanding of any terrain parameter such as nature of bedrock, infiltration capacity, surface runoff, which helps in better understanding the status of landforms and their originating processes, drainage management, and assessment of flood hazard, planning, and management.

The present study demonstrates the usefulness of remote sensing and GIS for morphometric analysis and prioritization of the sub-watersheds of Lolab Basin in

Kashmir Valley. The morphometric characteristics of different sub-watersheds reveal their relative characteristics with respect to hydrological response of the Lolab Basin. These morphometric parameters derived from the ASTER DEM help in understanding the hydrological behavior of a Lahwal (Lalkul) River catchment which influences the floods in the Lolab Basin. The result points out that during the rainy season, there is a possibility of greater runoff in the sub-watersheds LSB1, LSB2, LSB4, LSB5, LSB10, LSB11, and LSB12, which causes floods in the lower part of the basin. Hence, to prevent floods in the flood plain in downstream to protect agricultural crops and settlements, mitigation measures should be taken in the upper streams such as early flood warning system and adaptation of advanced flood forecasting techniques for the Lolab Basin.

References

Agarwal A, Narayan S (1991) State of India's environment: floods. New Delhi: Center for Science and Environment

Ahmed SA, Chandrashekarappa KN, Raj SK, Nischitha V, Kavitha G (2010) Evaluation of morphometric parameters derived from ASTER and SRTM DEM—a study on Bandihole sub-watershed basin in Karnataka. J Indian Soc Remote Sens 38:227–238

Alexander GN (1972) Effect of catchment area on flood magnitude. J Hydrol 16:225–240

Ali SA, Alhamed M, Ali U (2016) Morphometric analysis of Abdan Basin, Almahfid basement rock, Yemen: using remote sensing and GIS. Int J Adv Remote Sens GIS 5(3):1605–1617

Ali U, Ali SA (2014) Analysis of drainage morphometry and watershed prioritization of Romushi—Sasar catchment, Kashmir Valley, India using remote sensing and GIS technology. I Jour Adv Res 2(12):5–23

Altin TB, Altin BN (2011) Drainage morphometry and its influence on landforms in volcanic terrain, Central Anatolia, Turkey. Procedia Soc Behav Sci 19:732–740

Amee KT, Dhiman SD (2007) Morphometric analysis and prioritization of mini watersheds in Mohr watershed, Gujarat using remote sensing and GIS techniques. J Indian Soc Remote Sens 35:313–321

Angillieri MYE (2008) Morphometric analysis of Colangüil river basin and flash flood hazard, San Juan, Argentina. Environ Geol 55:107–111

Bertolo F (2000) Catchment delineation and characterisation, catchment characterisation and modelling Euro landscape project. Ispra: Space Application Institute, Joint Research Center

Bhatt S, Ahmed SA (2014) Morphometric analysis to determine floods in the upper Krishna basin using Cartosat DEM. Geocarto Int 29(8):878–894

Chopra R, Dhiman RD, Sharma PK (2005) Morphometric analysis of sub-watersheds in Gurdaspur district, Punjab using remote sensing and GIS techniques. J Indian Soc Remote Sens 33:531–539

Chorley RJ (1969) Introduction tofluvial processes. Methuen and Co., Limited, London, p 588

Dornkamp JC, King CAM (1971) Numerical analyses in geomorphology: an introduction. New York: St Martins, p 372

Eze BE, Efiong J (2010) Morphometric parameters of the Calabar River basin: implication forhydrologic processes. J Geogr Geol 2:18–26

Fairfiled J, Leymarie P (1991) Drainage network from grid digital elevation models. Water Resour Res 30:1681–1692

Faniran A (1968) The index of drainage intensity–a provisional new drainage factor. Aust J Sci 31:328–330

Garbrecht J, Martz LW (1999) Digital elevation model issues in water resources modeling. Proceedings of the 19th Esri Users Conference; San Diego (CA)
Gregory KJ, Walling DE (1973) Drainage form and process: a geomorphological approach. New York (NY): Wiley, p 456
Grohmann CH (2004) Morphometric analysis in geographic information systems: applications of free software GRASS and R. Comput & Geosci 30(9–10):1055–1067
Hlaing TK, Haruyama S, Aye MM (2008) Using GIS-based distributed soil loss modeling and morphometric analysis to prioritize watershed for soil conservation in Bago river basin of lower Myanmar Front. Earth Sci China 2:465–478
Horton RE (1932) Drainage basin characteristics. Trans Am Geophys Union 13:350–361
Horton RE (1945) Erosional development of streams and their drainage basins: hydro physical approach to quantitative morphology. Bull GeolSoc Am 56:276–370
Jain V, Sinha R (2003) Evaluation of geomorphic control on flood hazard through geomorphic instantaneous unit hydrograph. Curr Sci 85:1596–1600
Korkalainen THJ, Lauren AM, Kokkonen TS (2007) A GIS based analysis of catchment properties within a drumlin field. Boreal Environ Res 12:489–500
Kumar R, Kumar S, Lohani AK, Nema RK, Singh RD (2000) Evaluation of geomorphological characteristics of a catchment using GIS. GIS India 9:13–17
Lattif AA, Sherief Y (2012) Morphometric analysis andflash floods of WadiSudr and WadiWardan, Gulf of Suez, Egypt: using digital elevation model. Arab J Geosci 5:181–195
Magesh NS, Chandrasekar N, Soundranayagam JP (2011) Morphometric evaluation of Papanasam and Manimuthar watersheds, parts of Western Ghats, Tirunelveli district, Tamil Nadu, India: a GIS approach. J Indian Soc Remote Sens 64:373–381
Maidment DR (2002) Arc Hydro: GIS for water resources. Redlands (CA): ESRI Press
Mark DM (1983) Relations between field-surveyed channel networks and map-based geomorphometric measures, Inez, Kentucky. Ann Assoc Am Geogr 73:358–372
Miller VC (1953) A quantitative geomorphic study of drainage basin characteristics in the Clinch Mountain area. Virginia and Tennessee, Proj. NR 389-402, Technical report 3, Columbia University, Department of Geology, ONR, New York (NY)
Nag SK (1998) Morphometric analysis using remote sensing techniques in the Chaka sub-basin, Purulia district, West Bengal. J Indian Soc Remote Sens 26:69–76
Nag SK, Chakraborty S (2003) Influence of rock types and structures in the development of drainage network in hard rock area. J Indian Soc Remote Sens 31:25–35
Ozdemir H, Bird D (2009) Evaluation of morphometric parameters of drainage networks derived from topographic maps and DEM in point of floods. Environ Geol 56:1405–1415
Pallard B, Castellarin A, Montanar A (2009) A look at the links between drainage density and flood statistics. Hydrol Earth Syst Sci 13:1019–1029
Pankaj A, Kumar P (2009) GIS based morphometric analysis of five major sub-watershed of Song River, Dehradun district, Uttarakhand with special reference to landslide incidences. J Indian Soc Remote Sens 37:157–166
Patel DP, Dholakia MB, Naresh N, Srivastava PK (2012) Water harvesting structure positioning by using geo-visualization concept and prioritization of mini-watersheds through morphometric analysis in the lower Tapi basin. J Indian Soc Remote Sens 40:299–312
Patton PC, Baker VR (1976) Morphometry andfloods in small drainage basins subject to diverse hydrogeomorphic controls. Water Resour Res 12:941–952
Patton PC (1988) Drainage basin morphometry andfloods. In: Baker VR, Kochel RC, Patton PC (eds) Flood geomorphology. Wiley, New York, pp 51–65
Reddy GPO, Maji AK, Gajbhiye KS (2004) Drainage morphometry and its influence on landform characteristics in a basaltic terrain, Central India—a remote sensing and GIS approach. Int J Appl Earth Obs Geoinf 6:1–16
Romshoo SA, Bhat SA, Rashid I (2012) Geoinformatics for assessing the morphometric controlon hydrological response at watershed scale in the Upper Indus basin. J Earth Syst Sci 121: 659–686

Roughani M, Ghafouri M, Tabatabaei M (2007) An innovative methodology for the prioritization of sub-catchments for flood control. Int J Appl Earth Obs Geoinf 9:79–87

Roy PS, Bhanumurthy V, Murthy CS, Kiran Chand T (2008) Space for disaster management: lessons and perspectives. J South Asia Disaster Stud 1:157–177

Schumm SA (1956) Evolution of drainage systems and slopes in badlands at Perth Amboy, New Jersey. Geol Soc Am Bull 67:597–646

Schumm SA (1963) Sinuosity of Alluvial Rivers on the Great Plains. Geol Soc Am Bull 74 (9):1089

Shaban A, Khawlie MM, Abdallah C, Awad M (2005) Hydrological and watershed characteristics of the El-Kabir River, North Lebanon. Lakes and Reservoirs: Res Manage 10(2):93–101

Singh S, Singh MC (1997) Morphometric analysis of Kanhar river basin. Nat Geogr J India 43 (1):31–43

Smith KG (1950) Standards for grading texture of erosional topography. Am J Sci 248:655–668

Sreedevi PD, Owais S, Khan HH, Ahmed S (2009) Morphometric analysis of a watershed of south India using SRTM data and GIS. J GeolSoc India 73:543–552

Sreedevi PD, Sreekanth PD, Khan HH, Ahmed S (2013) Drainage morphometry and its influence on hydrology in an semi arid region: using SRTM data and GIS. Environ Earth Sci 70(2): 839–848

Sreedevi PD, Subrahmanyam K, Ahmed S (2005) Integrated approach for delineating potential zones to explore for groundwater in the Pageru River basin, Cuddapah District, Andhra Pradesh, India. Hydrogeol J 13(3):534–543

Strahler AN (1952) Hypsometric (area-altitude) analysis of erosional topography. Geol Soc Am Bull 63: 1117–1141

Strahler AN (1957) Quantitative analysis of watershed geomorphology. Trans Am Geophys Union 38:913

Strahler AN (1964) Quantitative geomorphology of drainage basins and channel networks. In: Chow VT (ed) Handbook of applied hydrology. McGraw Hill, New York, pp 4–76

Thomas J, Joseph S, Thrivikramji K, Abe G, Kannan N (2012) Morphometrical analysis of two tropical mountain river basins of contrasting environmental settings, the southern Western Ghats India. Environ Earth Sci 66(8):2353–2366

Verstappen HTH (1983) Applied geomorphology-geomorphological surveys for environmental development. New York (NY): Elsevier, pp 57–83

Vittala SS, Govindaiah S, Gowda HH (2004) Morphometric analysis of sub-watersheds in the Pavagada area of Tumkur district, South India using remote sensing and GIS techniques. J Indian Soc Remote Sens 32:351–362

Yildiz O (2004) An investigation of the effect of drainage density on hydrologic response. Turk J Eng Environ Sci 28:85–94

Delineation of Paleochannels in Periyar River Basin of Kerala Using Remote Sensing and Electrical Resistivity Methods

C. P. Priju, Jiby Francis, P. R. Arun and N. B. Narasimha Prasad

Abstract In the present study, the paleo-river channels in the midland and coastal plain region of the Periyar and Chalakudy river basins, central Kerala, west coast of India were delineated applying remote sensing techniques and electrical resistivity methods. The river basin areas are flanked by Western Ghats in the eastern side and Lakshadweep Sea in the western side. Geologically, the area is overlain by charnockites and biotite gneiss in the midland and foothill region and fluvial and paleo-beach deposits in the western parts adjoining the sea. Laterite deposits are seen at several locations in the midland region of the basin. The main course of the river cuts across all the lithological units; the northern branch directly joins with sea and southern branch cut across older alluvial plain and reaches the Vembanad backwater system. Geomorphological mapping of the study area using IRS P6 LISS III data revealed the presence of two sets of paleochannels in the northern side of current channel of the river. The migratory trace of the river is indicated in the satellite images by the presence of meandering scars, crescent-shaped oxbow lakes in the older floodplain areas. Distinct vegetation alignment along the paleochannels is noted indicated by abrupt changes in tone and texture. Vertical electrical sounding (VES) survey was carried out at eight locations along the paleochannels demarcated. Good resistivity contrast obtained in five locations between the first and second layers. Apparent resistivity values obtained for the first layer (ρ_1) varied from 22 to 422 Ωm with thickness ~1–2 m and the second layer (ρ_2) varied from 5 to 80 Ωm with thickness ~2–7 m.

Keywords Paleochannels · Remote sensing · Vertical electrical sounding Periyar River basin · Kerala · India

C. P. Priju (✉) · J. Francis · P. R. Arun · N. B. Narasimha Prasad
Groundwater Division, Centre for Water Resources Development and Management, Kunnamangalam, Kozhikode 673571, India
e-mail: cppriju@gmail.com

V. P. Singh et al. (eds.), *Hydrologic Modeling*, Water Science and Technology Library 81, https://doi.org/10.1007/978-981-10-5801-1_27

Introduction

Paleochannels are remnant of inactive river or stream channels that have been either filled or buried by younger sediment. The sediments that the ancient channel is either cut into or buried by can be unconsolidated, semi-consolidated, consolidated or lithified materials. Paleochannels can be most easily identified as broad erosional channels into a basement which underlies a system of depositional sequences which may contain several episodes of deposition and represent meandering peneplain streams (Twidale 2004). The subsurface groundwater flow along these channels can be mapped applying geophysical and isotope techniques (Gautam 1994; IAHS 1995; Katz et al. 1998; Owen and Dahlin 2010; Rathore et al. 2010; Samadder et al. 2011). The major rivers of the world viz. Nile, Amazon, Yangtze (Chang Jiang), Mississippi and the South Asian rivers Indus, Ganga, Brahmaputra, Godavari, Krishna, Narmada, etc., have found to be shifted their course during historic and geological periods (Radhakrishna and Merh 1999).

The major objectives of the present study are to delineate paleochannels in the midland and coastal plain areas in the Periyar and Chalakudi river basins. The study also aims to understand the subsurface lithology of paleochannel formations. The study area is within the midland and coastal plain region of Periyar and Chalakudy river basins (Fig. 1). Periyar is the longest river in Kerala with 244 km in length,

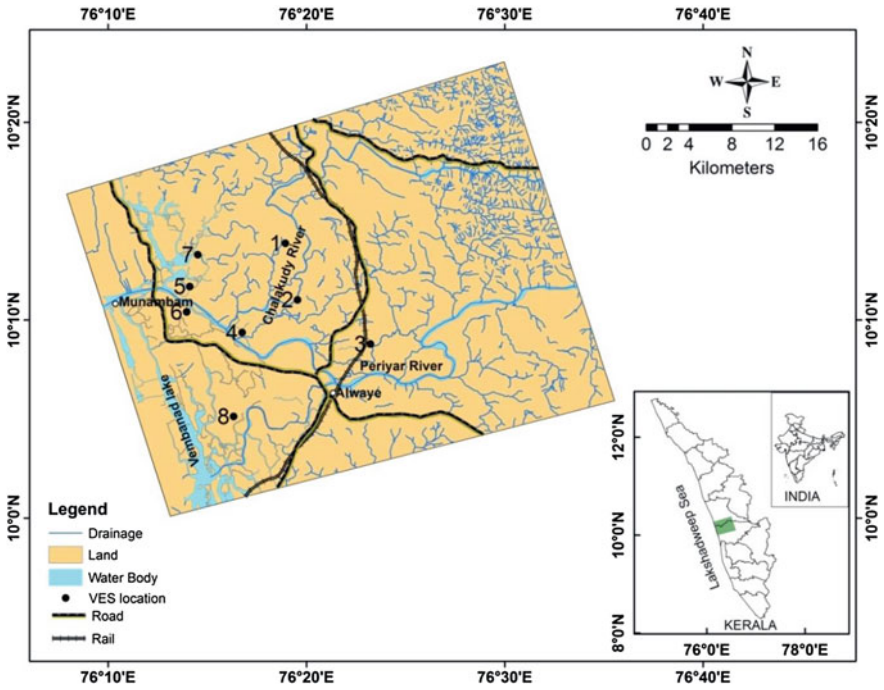

Fig. 1 Study area map showing drainage and VES locations

drains an area of 5,398 km^2. Chalakudi River has a length of 130 km, originates in the Anamalai hills of Western Ghats and it joins with Periyar River in the coastal plain region. The total drainage area of Chalakudy River is 1,704 km^2, of which 1,404 km^2 lies in Kerala and the rest in Tamil Nadu (Chattopadhyay et al. 2005). Based on the physiographic and slope maps of Kerala (*cf.* Resource Atlas of Kerala 1984), the study area can be divided into three near-parallel and north–south trending tracts, viz. the highland (>75.0 amsl), the midland (7.5 m–75.0 amsl) and the lowland (<7.5 m amsl).

Geologically, the highland area is typically underlain by crystalline rocks of Precambrian age, whereas the coastal land and parts of lower-midland in the Periyar river basin are covered by sedimentary deposits of Tertiary age. Hence, in spite of the fact that paleochannels are considered as a single geomorphological identity, the paleochannels are located with different geological conditions. The area is mainly covered with charnockites and banded biotite gneiss in the eastern part and paleo-beach deposits, tidal, fluvial and beach deposits in the western part adjoining the sea. Several dolerite intrusions are also observed in the highland/foothill areas (Figs. 2 and 3).

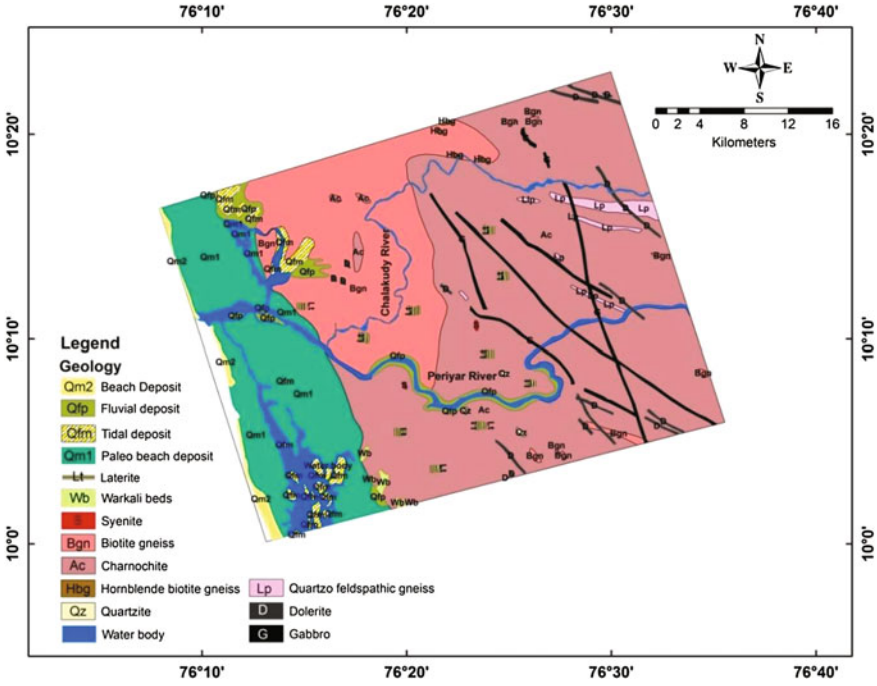

Fig. 2 Geology map of the study area

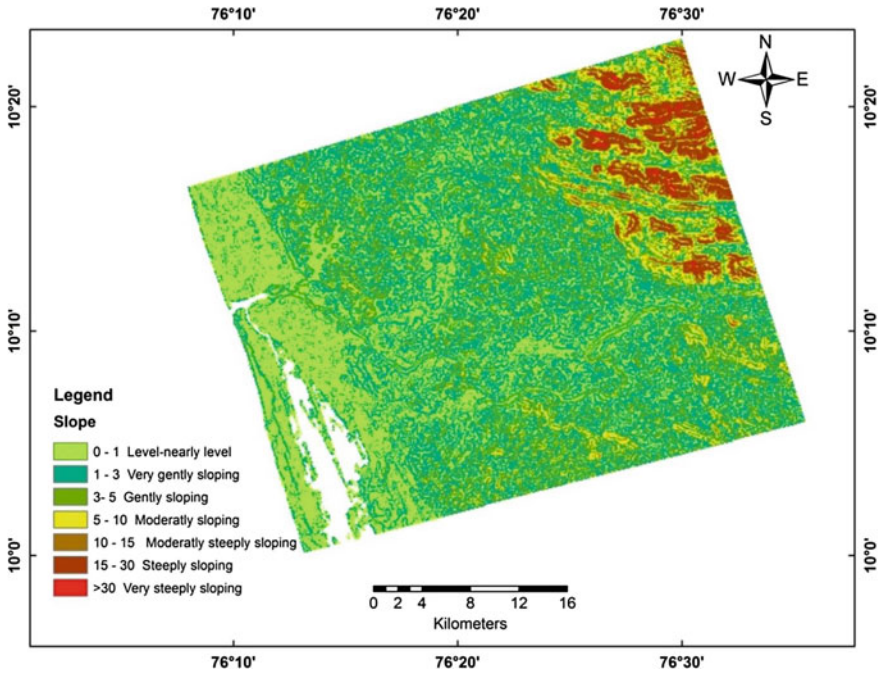

Fig. 3 Slope map of the study area

The midland and coastal plain region of Periyar and adjoining Chalakudy River basins of Central Kerala have extensive delta plains and paleo-drainages (Narayana et al. 2001; Narayana and Priju 2006; Santhosh et al. 2012; Padmalal et al. 2014). The study by Narayana et al. (2001) applying satellite remote sensing techniques revealed the presence of paleo-deltas and historical channels in the mouth of Periyar river. They have also identified shifted course of Periyar river mouth and paleo-shorelines in the region. Narayana and Priju (2006) have studied the land-forms and shoreline changes of central Kerala coast. Their study identified major changes in the river course pattern from the presence of paleo-drainage features along Periyar and adjoining Chalakudy River. Valdiya and Narayana (2007) attributed neotectonic activity for recent river course changes in central Kerala. Santhosh et al. (2012) have studied the brick and tile clay mining from the paddy lands of central Kerala especially along the paleo-river courses of Periyar and Chalakudy River.

Methodology

Geomorphological mapping of the study area was carried out using digital satellite data (IRS P6 LISS III, bands 1, 2, 3 and 4, February 2005) in combination with field information (lithology of well sections) applying image processing techniques. Level III geomorphological map of the area was prepared using Survey of India Toposheets (1:50K scale) and IRS imageries following guidelines given in NRSC Manual (2010). The remote sensing data from infrared and thermal sensors (Landsat ETM+) are also used for delineation of paleochannels. Image analysis techniques are employed to derive information on various morphological features and structural pattern in the area (SAC 1991). Field checks were carried out to verify the ground truth on information derived from remote sensing techniques. Vertical electrical sounding (VES) surveys (Schlumberger configuration) were carried out at eight locations along the paleochannels identified using Terrameter (SAS 300 C). The apparent resistivity and $AB/2$ values were plotted on double-log sheet. The layered resistivity model generated in IPI2Win software (Moscow State University) was used to interpret different resistivity layers. The apparent resistivity (ρ), thickness (h) and depth to layer interface (d) were obtained from the model. The layered resistivity model was employed to prepare subsurface resistivity sections in the paleochannel areas.

Results and Discussion

Geomorphology

Various landform units were delineated from the satellite images of the study area. In the Level I classification, the major geomorphologic units identified are plateau (36%), coastal plain (24%), pediplain (18%), piedmont zone (11%), water body (5%), denudational structural hill (4%), residual hill (1%), denudational hill (1%), rock exposure (1%), floodplain (1%), marshy area (1%), etc. In the Level III classification, landforms are further categorized into dissected lower plateau (lateritic), valley fill, piedmont zone, denudational and structural hills and residual hills in the midland region. In the coastal plain region, the landforms are further classified (Level III) into coastal alluvium, mudflats and backwaters (Fig. 4).

In the present study, the satellite images (IRS P6 LISS III and Landsat ETM+) revealed the presence of two sets of paleochannels in the northern side of current channels of Periyar and Chalakudy Rivers indicating southward migration of the river channel. The migratory trace of the river is indicated in the satellite images by

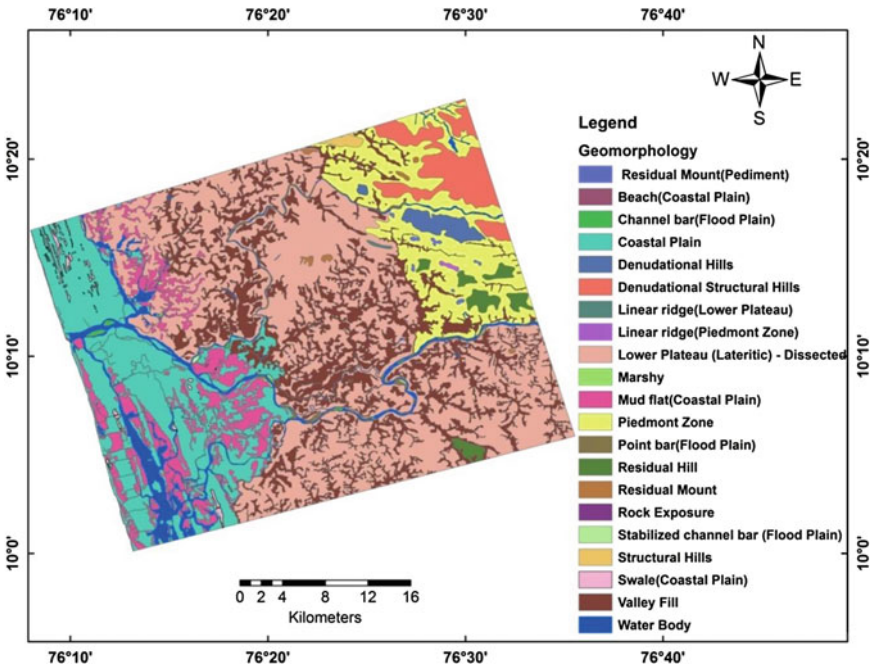

Fig. 4 Geomorphological map (level III) of the area showing various landform units

the presence of meandering scars, crescent-shaped oxbow lakes in the older floodplain areas. Distinct vegetation alignment along the paleochannels is noted indicated by abrupt changes in tone and texture (Fig. 5).

Geophysical Investigation

Semi-quantitative interpretation of the VES data concludes that majority of sounding curves are *H*-type (VES-1, VES-2, VES-3 and VES-4) indicating the presence of low resistivity sand/clay layer. The sounding curve is *Q*-type at one location (VES-6) indicating brackish nature towards depth (Fig. 6). The layered resistivity parameters (ρ, h and d values) interpreted for various resistivity layers (1, 2, 3, etc.) are shown in Table 1. Apparent resistivity values obtained for the first layer (ρ_1) varied from 22 to 422 Ωm with thickness ~1–2 m and the second layer (ρ_2) varied from 5 to 80 Ωm with thickness ~2–7 m (Table 1).

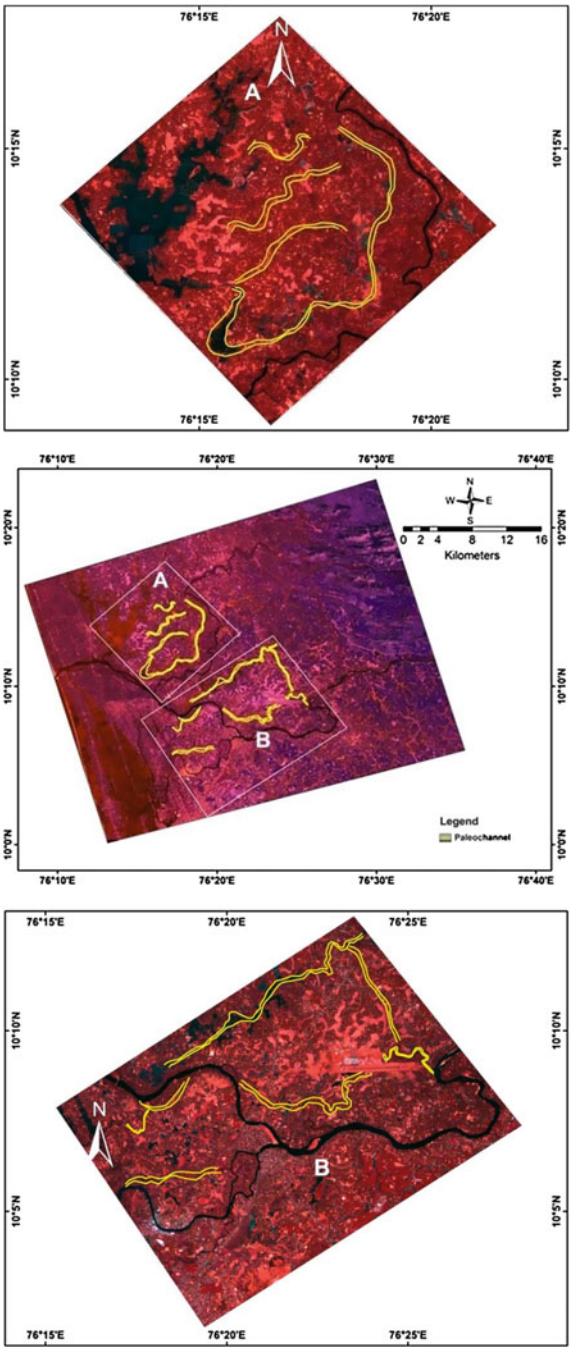

Fig. 5 Study area showing paleochannels of Chalakudy (**a**) and Periyar (**b**) river basin

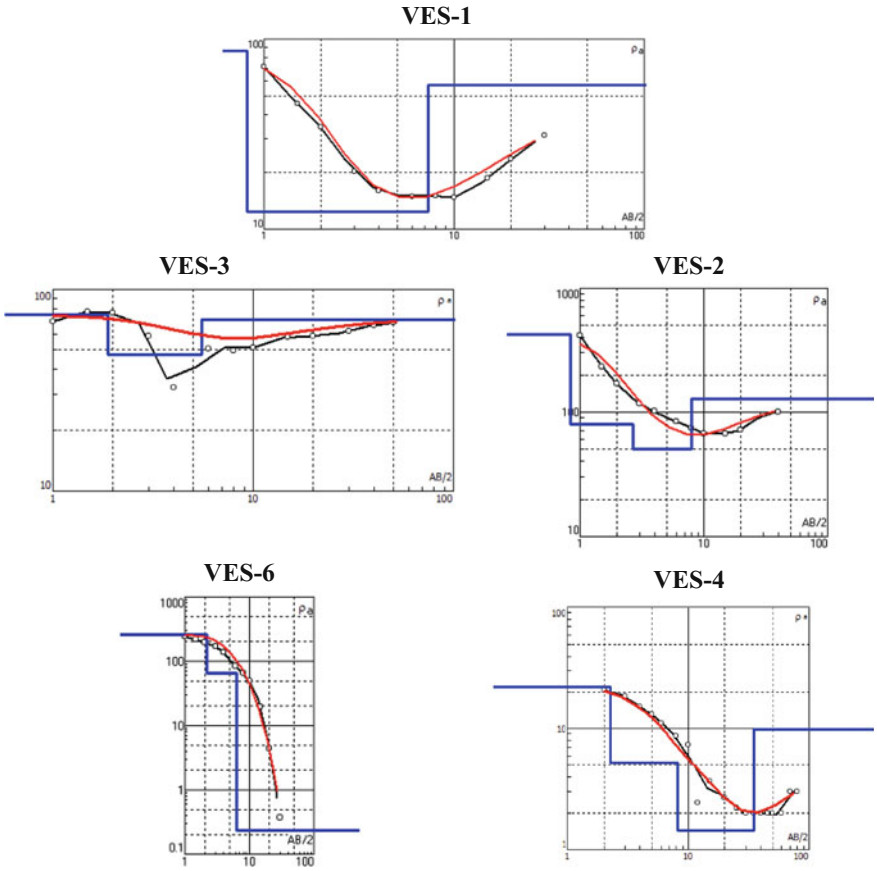

Fig. 6 VES curves and interpreted layered resistivity model

Table 1 Layered resistivity parameters (ρ, h) interpreted from VES curves

S. No.	VES no.	No. of layers	Apparent resistivity ρ (Ωm)			Thickness h (m)		
			ρ_1	ρ_2	ρ_3	h_1	h_2	h_3
1	VES-1	3	86.8	12.4	57	0.816	6.49	–
2	VES-2	4	422	79.7	50.1	0.844	1.84	5.29
3	VES-3	3	74.5	47.2	70.8	1.88	3.68	–
4	VES-4	4	22.1	5.23	1.43	2.25	5.98	26.6
5	VES-6	3	261	64.9	0.236	2.21	4.13	–

Summary and Conclusion

The study concludes the presence of two sets of paleochannels in the northern side of current channels of the Periyar and Chalakudy River. The migratory trace of the river is indicated in the satellite images by the presence of meandering scars, crescent-shaped oxbow lakes in the older floodplain areas. Vertical electrical sounding (VES) survey indicates good resistivity contrast in five locations between the layers 1 and 2. Semi-quantitative interpretation of the VES data concludes that majority of sounding curves are *H*-type (VES-1, 2, 3 and 4) indicating the presence of low resistivity second layer (sand/clay). The thickness of the first layer varied from $\sim$1 to 2 m and the second layer varied from $\sim$2 to 7 m.

Acknowledgements Authors thank Executive Director, Centre for Water Resources Development and Management (CWRDM) for the permission and extending support for publishing this work. Authors also thank Department of Science and Technology (DST), New Delhi, for research funding (Project No.SB/S4/ES-674/2013).

References

Anon (1984) Resource Atlas of Kerala. Centre for Earth Science Studies Publ., Trivandrum, India, Plates 58, 39 p

Chattopadhyay S, Rani LA, Sangeetha PV (2005) Water quality variations as linked to landuse pattern: a case study in Chalakudy River basin, Kerala. Curr Sci 89(12):2163–2169

Gautam AM (1994) Palaeochannels of Ken River as potential groundwater reservoirs and geomorphic evolution of adjoining area, Banda and Hamirpur Districts, U.P. Indian Miner 48 (3):181–184

IAHS (1995) Application of tracers in arid zone hydrology In: Adar EM, Leibundgut C (eds) IAHS Publication No. 232, Internatioal association of hydrological science, 78 p

Katz BG, Catches JS, Bullen TD, Michel RL (1998) Changes in the isotopic and chemical composition of ground water resulting from a recharge pulse from a sinking stream. J Hydrol 211:178–207

Narayana AC, Priju CP (2006) Landforms and shoreline changes inferred from satellite images along the central Kerala coast. J Geol Soc India 68:35–49

Narayana AC, Priju CP, Chakrabarti A (2001) Identification of a Palaeodelta near the mouth of Periyar river in Central Kerala. J Geol Soc India 57:545–547

NRSC (2010) Manual for national geomorphological and lineament mapping on 1:50,000 scale. National Remote Sensing Centre, Hyderabad, 120 p

Owen R, Dahlin T (2010) Inherited drainage paleo channels and preferential groundwater flow. Hydrogeol J 18(4):893–903

Padmalal D, Kumaran KPN, Limaye RB, Baburaj B, Vishnumohan S, Maya K (2014) Effect of holocene climate and sea level changes on landform evolution and human habitation: Central Kerala, India. Quat Int 325:162–178

Radhakrishna BP, Merh SS (eds) (1999) Vedic Sarasvati: evolutionary history of a lost river of northwestern India. Geol Soc India (Memoir 42), Bangalore

Rathore VS, Nathawat MS, Champatiray PK (2010) Palaeochannel detection and aquifer performance assessment in Mendha River catchment, Western India. J Hydrol 395:216–225

SAC (1991). Manual for mapping of coastal wetlands/land forms and shore line changes using satellite data, Ahmedabad, 63 p

Samadder RK, Kumar S, Gupta RP (2011) Paleochannels and their potential for artificial groundwater recharge in the western Ganga plains. J Hydrol 400(1–2):154–164

Santhosh V, Padmalal D, Baijulal B, Maya K (2012) Brick and tile clay mining from the paddy lands of Central Kerala (southwest coast of India) and emerging environmental issues. Environ Earth Sci. doi:10.1007/S/2665-012-1896-4

Twidale CR (2004) River patterns and their meaning. Earth-Sci Rev 67(3–4):159–218

Valdiya KS, Narayana AC (2007) River response to neotectonic activity: example from Kerala, India. J Geol Soc India 70(3):427–443

Application of EO-1 Hyperion Data for Mapping and Discrimination of Agricultural Crops

H. Ramesh and P. P. Soorya

Abstract Remote sensing offers an efficient and reliable means of collecting the information required for mapping, assessing and monitoring of agricultural crop conditions and production. Recent advances in remote sensing technology have led to the development of hyperspectral remote sensing imaging devices which can obtain high-resolution radiance data. This study evaluates the potential of the hyperspectral data in discrimination and mapping of agricultural crops using EO-1 Hyperion hyperspectral image over the Thalasseri Taluk, Kerala, India. Five agricultural crops such as arecanut, banana, cashew, coconut and rubber were considered for the study. The EO-1 was pre-processed using minimum noise fraction (MNF) transform to reduce the atmospheric effects on the imagery. Support vector machine classification and minimum distance classification were applied in order to perform image data classification based on different crops. The optimum wavelengths suitable for crop discrimination were derived by analysing the spectral reflectance curve as well as by using the techniques such as stepwise discriminant analysis and partial least square regression (PLSR). This study establishes that the Hyperion bands 53, 56, 62, 74, 79 and 84 are suitable for crop-type discrimination. The support vector machine classification is suitable for mapping the crops from Hyperion imagery with a higher accuracy of about 80% and above.

Keywords Hyperspectral imaging · Crop-type discrimination
Optimum wavelength · MNF transformation · SVM classification

Introduction

Identifying, mapping and monitoring of crops are important for a number of reasons. Many national and multinational agricultural organizations, insurance organizations, NGOs and regional agricultural boards have been developing crop

H. Ramesh (✉) · P. P. Soorya
Department of Applied Mechanics and Hydraulics, National Institute of Technology Karnataka, Surathkal, Mangalore 575025, India
e-mail: ramesh.hgowda@gmail.com

V. P. Singh et al. (eds.), *Hydrologic Modeling*, Water Science and Technology Library 81, https://doi.org/10.1007/978-981-10-5801-1_28

inventory maps to assess the yield and the damage. It serves the purpose of estimating yield prediction, collecting crop production statistics, simplifying crop rotation information, soil productivity mapping, identifying the factors influencing crop stress, assessment of crop damage due to storms and drought and monitoring farming activity (Barbosa et al. 1996; Enkhzaya et al. 2013). Key activities in crop monitoring include identifying and classifying the crop types and demarcating their areal extent. Traditional methods of obtaining this information in most of the countries are census and ground surveying. These methods are highly tedious, time consuming and more often subjective. In order to standardize measurements, remote sensing can provide synoptic and temporal data collection and information extraction schemes. It provides information on a regular, synoptic, temporal and in a more objective manner. The spectral reflection of a crop field will vary with respect to changes in the growth, type and crop health, and thus, it can be measured and monitored by remote sensing sensors at regular time interval.

The use of remote sensing imagery for mapping, assessing and monitoring of agricultural crop conditions and production has been steadily increasing in recent years (Van Niel and McVicar 2004). The recent advances in remote sensing field is the development of hyperspectral imaging system which provides a high-resolution satellite image with large number of bands (Datt et al. 2003). Hyperspectral remote sensing, like other spectral imaging, collects and processes information from across the electromagnetic spectrum. The Hyperspectral remote sensing images acquire simultaneously hundreds of very narrow, contiguous spectral bands throughout the visible, near-infrared (NIR), mid-infrared (MIR) and thermal infrared portions of the electromagnetic spectrum.

The Hyperion sensor on Earth Observing 1 (EO-1) satellite of the NASA's New Millennium Programme is the first hyperspectral instrument in space that covers the visible, near-infrared (NIR) and shortwave infrared (SWIR) bands between 400 and 2500 nm. The Earth Observing 1 (EO-1) satellite has three imaging sensors: the multispectral Advanced Land Imager (ALI), the hyperspectral Hyperion sensor, and the Atmospheric Corrector. The Hyperion sensor images a 7.5 km by 100 km surface area (Datt et al. 2003).

The geologists have started using the concept of hyperspectral remote sensing widely for mapping the minerals in mid-1980s to the present years. Also at that time, airborne hyperspectral data were used in vegetation studies, such as crop classification under different stress conditions (Mader et al. 2006), weeds detection, crop residues mapping and crop disease detection (Apan et al. 2004). However, the high cost and the limited coverage of airborne sensors constituting restrictive factors for their use in wider scale studies. Previous studies have indicated that forest species were classified with greater accuracy by the use of Hyperion images than multispectral data (Bing and Gong, 2007). The aim of the study is to investigate the potential of Hyperion data in discriminating and mapping agricultural crops. The specific objectives are: (i) to map the main agricultural crops appearing in the study area with Hyperion imagery, (ii) to compare various classification methods for hyperspectral image and (iii) to select optimum wavebands suitable for crop-type discrimination.

Study Area Description, Data and Tools

Study Area

The study area shown in Fig. 1 consists of a part of Thalasseri Taluk of Kannur District of Kerala State, India. It is located at latitude of 12° 1′ 23.98″N and longitude of 75°35′ 7.36″E. The entire study area covers an area of 139.547 km^2. The elevation of the study area ranges from 65 to 145 m above the mean sea level. The region is an Agro-climatic region according to planning commission of government of Kerala. The main crops growing in the area are coconut, cashew, arecanut, banana and plantation crops like rubber. The present study concentrates on the crops arecanut, banana, cashew, coconut and rubber.

Data Used

Hyperion Data: Hyperion data was downloaded from earth explorer website of USGS (http://earthexplorer.usgs.gov) over the study area. The EO-1 Hyperion hyperspectral image acquired on 21st March 2013 was collected. The image consists of 242 spectral bands, of which only 198 bands are calibrated (Ungar et al. 2003; Hina and Tiwari 2013) and the bands which are not calibrated are set to zero.

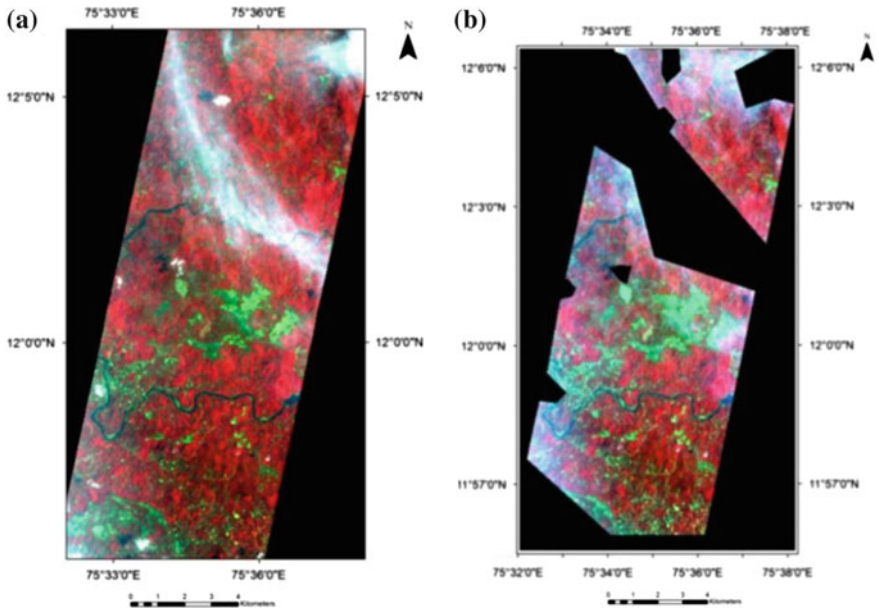

Fig. 1 Study area with Hyperion image (**a**) and after removing the clouds (**b**)

Field Data: Field visit was made to the study area on 2 March 2014. The sites in which arecanut, coconut, cashew, rubber and banana plantain are growing were recorded with GPS. The details about the field were collected from the respective farmers regarding the crop age, type of crop, disease, etc. Using the lat-long information of all the points and the corresponding area of the fields, shape files are created using ArcGIS software.

Software Used

ENVI 4.7: the Environment for Visualizing Images (ENVI) is a revolutionary image-processing system. It is suitable for the visualization, analysis and presentation of all types of digital imagery (ENVI 2004). ENVI Classic's complete image-processing package includes advanced, yet easy-to-use, spectral tools, geometric correction, terrain analysis, radar analysis, raster and vector GIS capabilities, extensive support for images from a wide variety of sources and much more. ENVI 4.7 was used to process EO-1 hyperspectral image in the present study.

ArcGIS 10: ArcGIS developed by Environmental science research institute (ERSI), USA, provides the set of comprehensive spatial analysis tools and a platform for viewing and disseminating results (ESRI 2012). ArcGIS software was used to create shape files and geo-referencing the hyperspectral image.

MATLAB 2008: MATLAB® (2012) is a high-level language and interactive environment for numerical computation, visualization and programming. Using MATLAB, helps analyse data, develop algorithms, and create models and applications (MATLAB® 2012). MATLAB is used to perform partial least square regression to determine the optimum bands for crop discrimination in the present study.

SPSS statistics 17: SPSS statistics is a software package used for statistical analysis. The software name stands for Statistical Package for the Social Sciences (SPSS 2006). The software system is developed based on the idea of using statistics to turn raw data into information that is essential for decision making. The stepwise discriminant analysis was done using SPSS software in the present study to obtain the optimal bands for crop discrimination.

Methodology

Hyperspectral sensors provide many advantages over the multispectral sensors. However, these hyperspectral sensors have their disadvantages including an increase in the number of bands (data) to be processed, relatively poor signal-to-noise ratios and an increased susceptibility to the effects of unwanted atmospheric interferences if such effects are not corrected for. As a result, the image-processing techniques for hyperspectral imagery differ somewhat from the

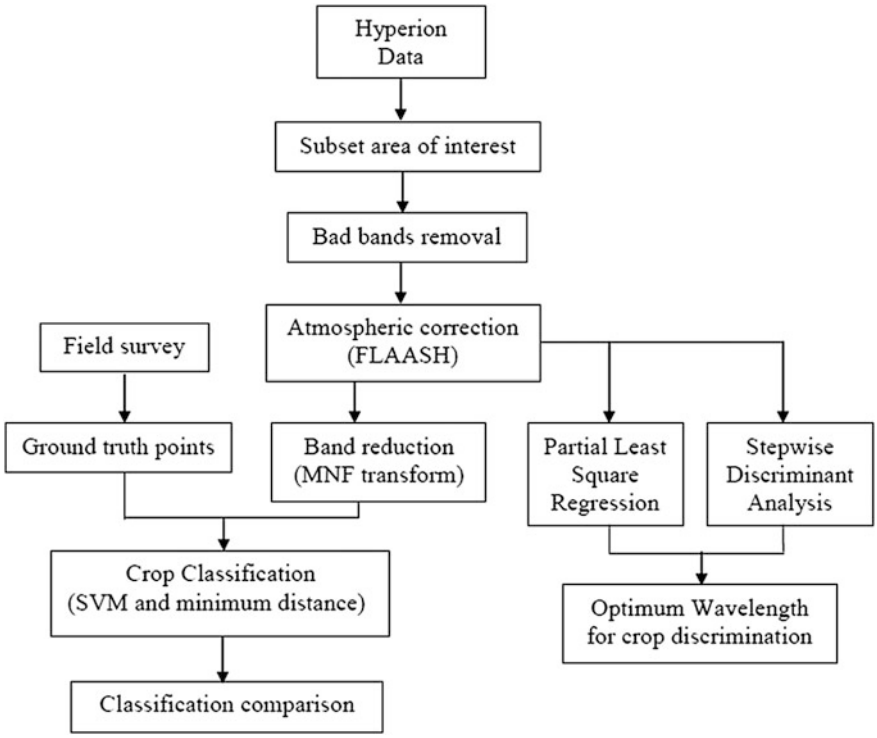

Fig. 2 Flow chart showing the methodology

image-processing techniques for multispectral imagery (Bing and Gong, 2007). Hyperspectral image analysis requires more attention to issues of atmospheric correction and relies more heavily on physical and biophysical models (Glenn et al. 2005). The overall methodology (Fig. 2) used for this study is described in this section.

Pre-processing of Hyperion Imagery

The Hyperion EO-1 data was pre-processed to correct for sensor artefacts, atmospheric and geometric effects. This was achieved through (i) Converting Hyperion level 1G/1T HDR data to ENVI format (ii) subsetting the area of interest (iii) Bad bands removal (iv) Atmospheric correction and (v) minimum noise fraction transform.

(i) **Converting Hyperion Level 1G/1T HDR data to ENVI format**

The imagery was received as a full long scene (185-km × 7.7-km strip) and at level 1 (L1GST) processing in GeoTIFF format, written as band-interleaved-by-line (BIL) files stored in 16-bit signed integer radiance values. The L1G product is radiometrically corrected, geometrically resampled and registered to a geographic map projection with elevation correction applied. The Level 1G/1T GeoTIFF Hyperion imagery was converted into ENVI format files using the Hyperion_tools. sav toolkit. The ENVI format files contain wavelength, full width half maximum and bad band information.

(ii) **Subsetting the area of interest**

Subsetting the image is the process of extracting the area of interest from the image file and removing the unnecessary part for better and fast processing. The subset data via region of interest (ROIs) tool is used to subset the data into the study area.

(iii) **Bad bands removal**

The Hyperion data consists of 242 bands, of which 155 are non-zero bands. This is due to the heavy water absorption in the VNIR and SWIR region and the spectral overlap between the two spectrometers set in the VNIR and SWIR region. Before applying the atmospheric correction model FLAASH, each band in the Hyperion data has examined by opening in the viewer window of ENVI software and have to find out the good bands and removing the bad bands.

(iv) **Atmospheric correction**

Properties such as amount of water vapour, distribution of aerosols and scene visibility must be known to compensate for atmospheric effects. Direct measurements of these atmospheric properties are rarely available; hence, there are techniques that infer them from their imprint on hyperspectral radiance data. Removal of these properties is necessary to produce an estimate of the true surface reflectance. Such atmospheric corrections are mostly applied on a pixel-by-pixel basis because each pixel in a hyperspectral image contains an independent measurement of atmospheric water vapour absorption bands. Thus, atmospheric correction is essential to convert radiance into reflectance (Agarwal and Sarup, 2011). Reflectance is the ratio of the amount of light leaving an object to the amount of light incident on the object.

There are many algorithms for atmospheric correction. The atmospheric correction algorithm was carefully implemented to model the atmospheric condition that existed during the scene acquisition. Major scene-based algorithms are IAR and ELM, and the latest is QUAC. MODTRAN is a very popular and effective atmospheric transmission model for correcting multispectral and hyperspectral data. MODTRAN-based FLAASH algorithm available in ENVI® software is very effective for Hyperion data atmospheric correction (Agarwal and Sarup, 2011). Among all atmospheric correction models, FLAASH has an upper hand and gives better comparison results, but it requires full knowledge of the area, time of flight,

sensor elevation, etc. FLAASH (fast line of sight atmospheric analysis of spectral hypercubes) is a radiative transfer model for atmospheric calibration and is the first atmospheric correction tool that corrects wavelengths in the visible through near-infrared and shortwave infrared regions, up to 3 μm (Kawishwar 2007). Unlike many other atmospheric correction programmes that interpolate radiation transfer properties from a pre-calculated database of modelling results, FLAASH incorporates the MODTRAN4 radiation transfer code (Lee et al. 1990). FLAASH supports many hyperspectral sensors such as HyMAP, AVIRIS, HYDICE, HYPERION, Probe-1, CASI and AISA along with multispectral sensors such as ASTER, IRS, Landsat, RapidEye and SPOT.

(v) **Minimum Noise Fraction Transform**

Minimum noise fraction (MNF) transforms are used to determine the inherent dimensionality of image data, to segregate noise in the data and to reduce the computational requirements for subsequent processing (Powers and Elizabeth, 2006). The MNF transform has two cascaded principal components transformations (Lee et al. 1990). The first step results in transformed data in which the noise has unit variance and no band-to-band correlations. The second step is a standard principal components transformation of the noise-whitened data. The data space can be divided into two parts: one part associated with large eigenvalues and coherent eigen images, and a complementary part with near-unity eigenvalues and noise-dominated images. By using only the coherent portions, the noise is separated from the data, thus improving spectral processing results. After performing MNF transformation, we will get an eigenvalue plot. The importance of plot is that bands with large eigenvalue (>1) contain data and bands with eigenvalue near 1 contain noise.

Image Classification

The classification procedures are applied for an image to automatically categorize all pixels in an image into different classes (Goodenough et al. 2003). Normally, multispectral and hyperspectral data are used to perform the classification, and, indeed, the spectral pattern present within the data for each pixel is used as the numerical basis for categorization (Griffin et al. 2005; Govender et al. 2008). This study used two types of supervised classification techniques, namely minimum distance classification and support vector machine (SVM) classification. The Hyperion imagery was classified using the above-stated two classifiers to map the main crops (arecanut, banana, cashew, coconut and rubber) present in the study area. Then, these two classification methods were compared by calculating the accuracy of classification.

(i) **Minimum Distance Classification**

The minimum distance classification is a supervised classification technique. The mean vectors of each reference class are used, and euclidean distance is calculated from each unknown pixel to the mean vector for each class (Li et al. 2014a, b). All pixels are classified to the nearest class unless a standard deviation or distance threshold is not specified. If standard deviation or distance threshold is specified, then the pixels which do not meet this criterion are classified into unclassified group.

(ii) **Support Vector Machine Classification**

Support vector machine (SVM) can be used to perform supervised classification on images to identify the class associated with each pixel. The complete mathematical formulation of SVM classifier is provided by (Burges 1998; Vapnick 1998; Huang et al. 2002). SVM is a classification system derived from statistical learning theory (Huang et al. 2002; Oommen et al. 2008). The basic approach in SVM is to identify a hyperplane that produces optimal separation between two classes (Yu et al. 2012). Usually in SVM, the hyperplane is developed using a subset of data called training data set, and the generalizing ability of the developed hyperplane is validated using an independent subset called testing data set. To classify a data of N dimensions, a $(N - 1)$ dimensional plane is developed in support vector classification (Mercier and Lennon, 2003). There are different algorithms for classification. These include linear classifier and nonlinear classifiers (Mercier and Lennon 2003; Oommen et al. 2008). Linear classifiers are used when the data is linearly separated. If the data are highly complex and cannot be separated linearly, nonlinear classifiers are used. The nonlinear classifiers include classification using polynomial kernels, redial basis function kernels and sigmoid kernels.

Accuracy Assessment

Usually, the accuracy of classification is found out by generating an error matrix. An error matrix is the one which compares pixels in a classified map with the information in the reference data supplied. The error matrix gives the overall accuracy, producer's accuracy, user's accuracy and Kappa coefficient (Lelong and Patrick 1998; Guo et al. 2006).

Spectral Reflectance Curve Generation

The spectral reflectance (ρ_λ) characteristics of earth surface features is quantified by measuring the part of incident energy that is reflected (Guo et al. 2006) from the

earth surface features obtained as a graph with wavelength. It is mathematically defined as:

$$\rho_\lambda = \frac{\lambda_r}{\lambda_i} \times 100 \quad (1)$$

where is ρ_λ expressed as a percentage, λ_i is the energy wavelength incident upon the object and λ_r is the energy wavelength reflected from the object.

The spectral reflectance curve provides behaviours of the spectral characteristics of an object and influence strongly on the choice of wavelength regions in which remote sensing data are acquired for a particular application (Lillesand et al. 2012). In this study, spectral reflectance curves are generated from the Hyperion image for crops arecanut, banana, cashew, coconut and rubber.

Optimum Wavelength Determination

The hyperspectral data provides reflectance in large number of bands. Therefore, it is essential to select the most optimum bands for crop discrimination (Mundt and Glenn 2007; Nellis et al. 2009). There are several data mining methods for reducing the large data volume. These methods include (1) feature selection (e.g., principal component analysis and derivative analysis); (2) partial least squares; (3) stepwise linear regressions; and (4) hyperspectral vegetation indices. These data mining method will result in (a) reduction in data dimensionality, (b) reduction in redundancy and (c) extraction of unique information. Partial least square regression and stepwise discriminant analysis were used to identify optimum wavelength in this study.

Partial Least Square Regression (PLSR)

Partial least square regression is a recent technique that combines and generates features from principal component analysis and multiple regressions. It predicts a set of dependent variables from a set of independent variables or predictors (Li et al. 2014a, b). The PLSR method was used in this study for finding the optimum bands for crop discrimination from the reflectance values of different crops. Therefore, PLS decomposes X into orthogonal scores T and loadings P and regresses Y not on X itself but on the scores T. PLSR was done using MATLAB software. The inputs were given and ran the code. The percent variance field was obtained which gives the number of PLS components. The number of components corresponding to 90% variance is used for regression analysis. The X loadings values generated will give the optimum wavelengths for crop discrimination.

Stepwise Discriminant Analysis

The multivariate analysis of variance (MANOVA) is performing to determine whether multiple levels of independent variables on their own or in combination with one another have an effect on the dependent variables. MANOVA requires that the dependent variables meet parametric requirements (Vapnick 1998; Ouardighi El et al. 2007). The most appropriate wavelength is found by carrying out the discriminant analysis to discriminate between the different level of infestation using the multivariate seperability measures such as Wilk's lambda, canonical correlation and the Pillai's trace. Wilk's lambda gives the variance of dependent variable that is not explained by the discriminant function. Wilk's lambda is between 0 and 1. Smaller value of Wilk's lambda gives greater seperability. So for the perfect separation of crops, we need a smaller value of Wilk's lambda statistic. Pillai's trace is the sum of the variance which can be explained by the calculation of discriminant variables. It calculates the amount of variance in the dependent variable which is accounted for the greatest separation of the independent variables (Powers and Elizabeth, 2006). Canonical correlation coefficient measures the strength of the overall relationship between two linear composites (canonical variates), one variate for the independent variables and one for the dependent variables. The stepwise discriminant analysis was done using SPSS software in the present study. The inputs used were the index for crop types and their spectral reflectance values.

Results and Discussion

Bad Bands Removal

The Hyperion data consists of 242 bands out of which 155 are non-zero bands. The bands those set to zero, bands in the overlap between the two spectrometers set in the VNIR and SWIR region and bands affected by atmospheric water vapour and heavy noise comprise the excluded bands. These nonzero bands are chosen for further processing and analysis.

Zeroed bands: 1–7 (355.5889–416.6401 nm), 58–78 (935.5810–922.5410 nm), 225–242 (2405.5996–2577.0747 nm).

Strong water absorption bands: 120–132 (1346.2506–1467.3330 nm), 165–182 (1800.2863–1971.7607 nm), 221–224 (2365.2051–2395.5007 nm).

So the resulted **good bands** are 8–57 (426.8158–925.4054 nm), 79 (932.6393 nm), 83–119 (972.9934–1336.1514 nm), 133–164 (1477.4318–1790.1870 nm), 183–184 (1981.8593–1991.9581 nm), 188–220 (2032.3525–2355.2065 nm).

Atmospheric Correction

FLAASH algorithm was used for the atmospheric correction. The nonzero bands are given as the input for FLAASH. The FLAASH atmospheric correction model input parameters include scene centre location, sensor type, sensor altitude, ground elevation, pixel size, flight date, flight time, atmospheric model, aerosol model, tile size used for tile processing, etc. After the FLAASH application, compare the reflectance spectrum obtained from the image before atmospheric correction (Fig. 3a) and image after atmospheric correction (Fig. 3b).

The spectrum from image after atmospheric correction shows more resemblance with the normal reflectance spectrum of vegetation. The peaks in the curve are due to higher reflectance and troughs are due to the absorption of the sunlight.

Minimum Noise Fraction (MNF) Transform

The MNF transform was applied for the FLAASH output file for reducing the data dimensionality for further processing. MNF transform was applied separately for VNIR region and SWIR region. Figure 4 shows MNF images for VNIR bands. MNF images for SWIR bands are shown in Fig. 5. Resulted 13 eigen images for VNIR and 8 eigen images for SWIR, after examination of eigenvalue plots as well as visual inspection of eigen images, were selected for further analysis. The 13 eigen images from VNIR and 8 eigen images from SWIR were stacked into a single file for applying classification techniques.

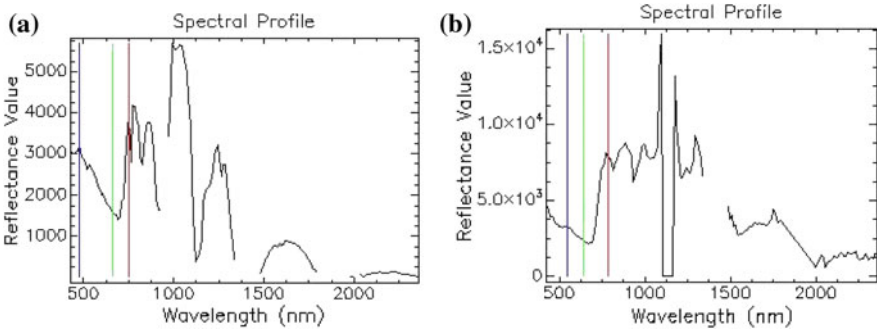

Fig. 3 Reflectance spectrum before (**a**) and after atmospheric correction (**b**)

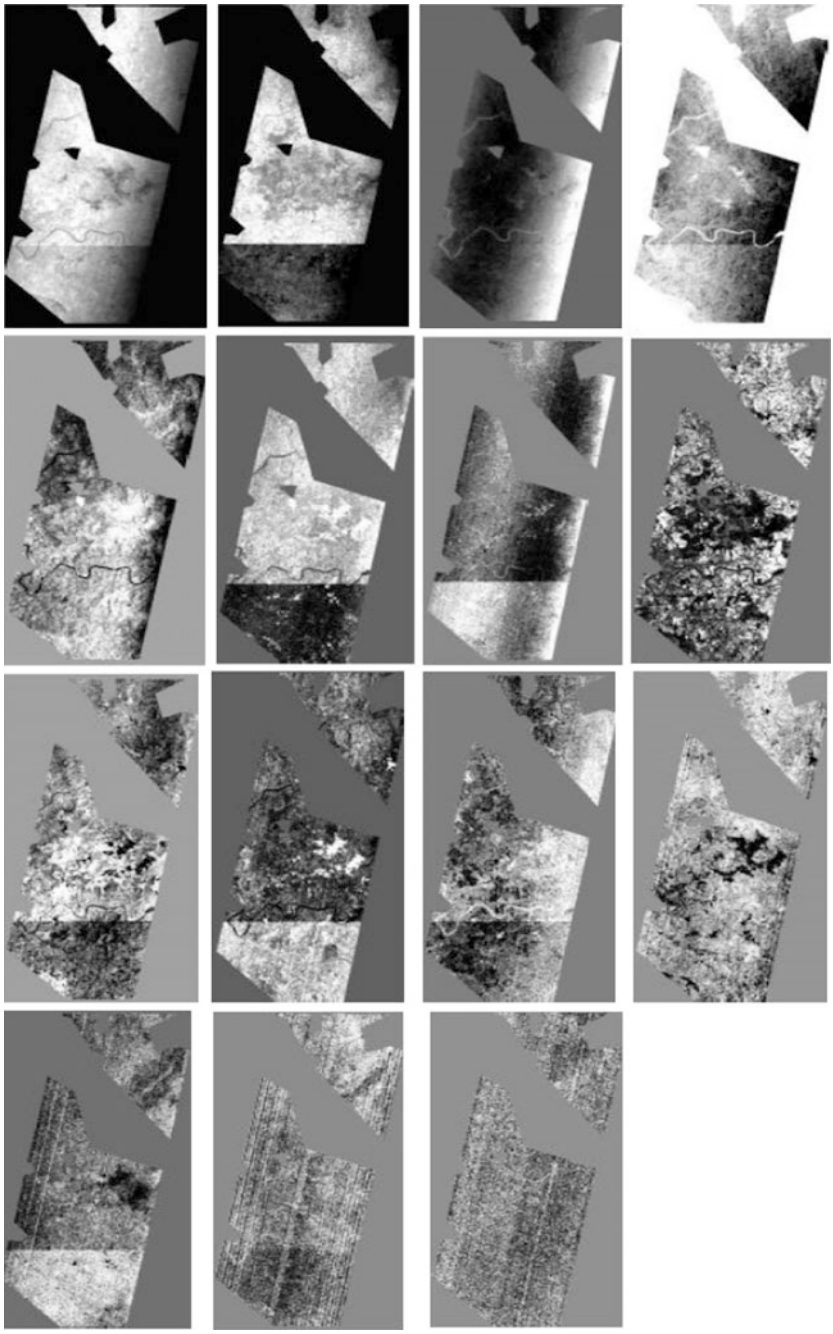

Fig. 4 MNF images for VNIR bands 1–15 (*left* to *right*)

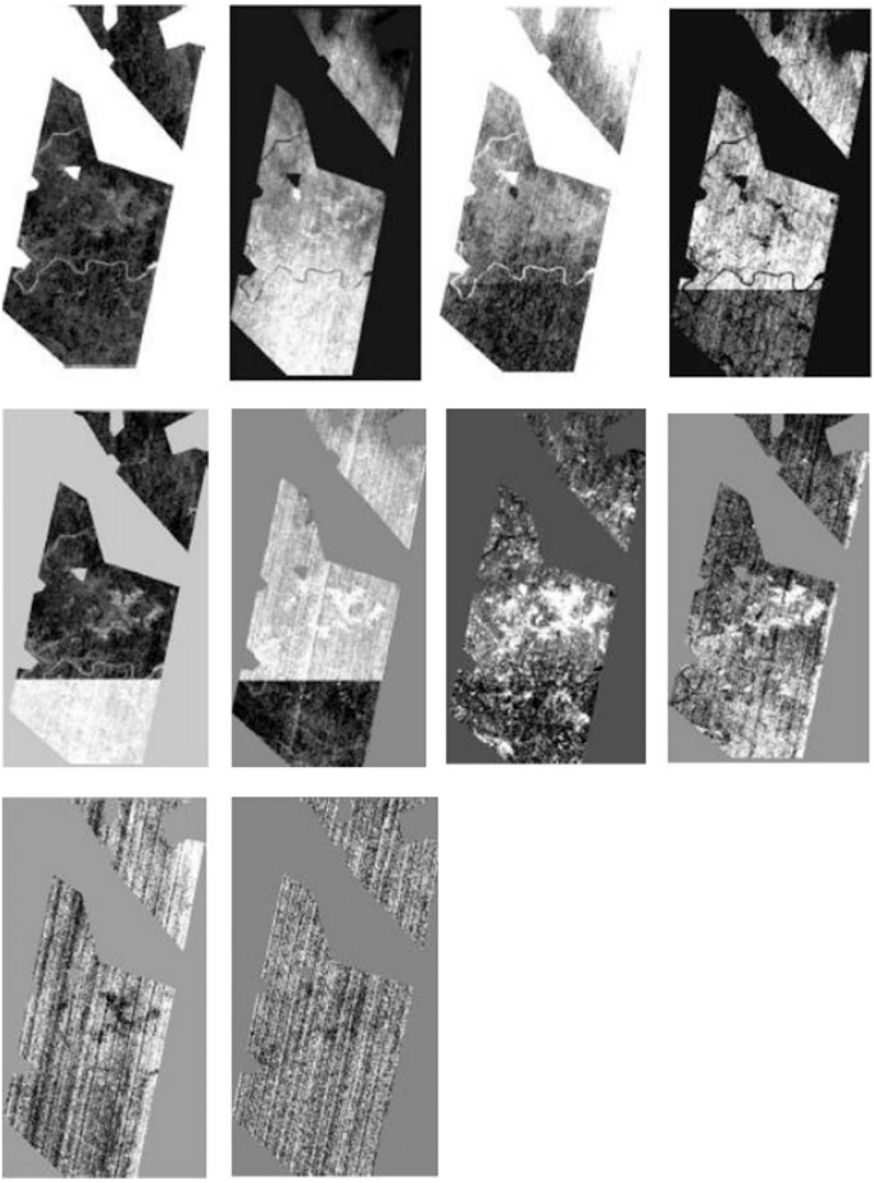

Fig. 5 MNF images for SWIR bands 1–10 (*left* to *right*)

Image Classification

The supervised classification methods such as minimum distance classification and support vector machine classification were used for the classification of the Hyperion image (Harsanyi and Chein, 1994) to obtain the crop classes (Petropoulos et al. 2012; Sankaran et al. 2010; Sankar et al. 2011). The classification techniques were applied separately for 13 eigen images consisting of 13 VNIR bands and 21 eigen images consisting 13 VNIR bands and 9 SWIR bands. The classification accuracy was also computed for each classification.

The SVM classification was performed on the Hyperion imagery to classify the different agricultural crops. Figure 6a, b shows the classified images using 13 MNF eigen images and 21 eigen images, respectively. Table 1 summarizes the accuracy assessment. The error matrix of classification using 13 MNF eigen images shows that the overall accuracy for this classification is 80.95% and Kappa coefficient is 0.75. The classification using 21 MNF eigen images gives an accuracy of 85.71% and a Kappa coefficient of 0.812. Therefore, it is concluded that the classification using 13 VNIR bands and 9 SWIR bands gives higher accuracy compared to classification using 13 VNIR bands only.

The minimum distance classification was performed on the Hyperion imagery, and the classification images are shown in Fig. 7a, b. Table 2 shows the summery accuracy assessment. The classification performed using 13 VNIR bands gave an

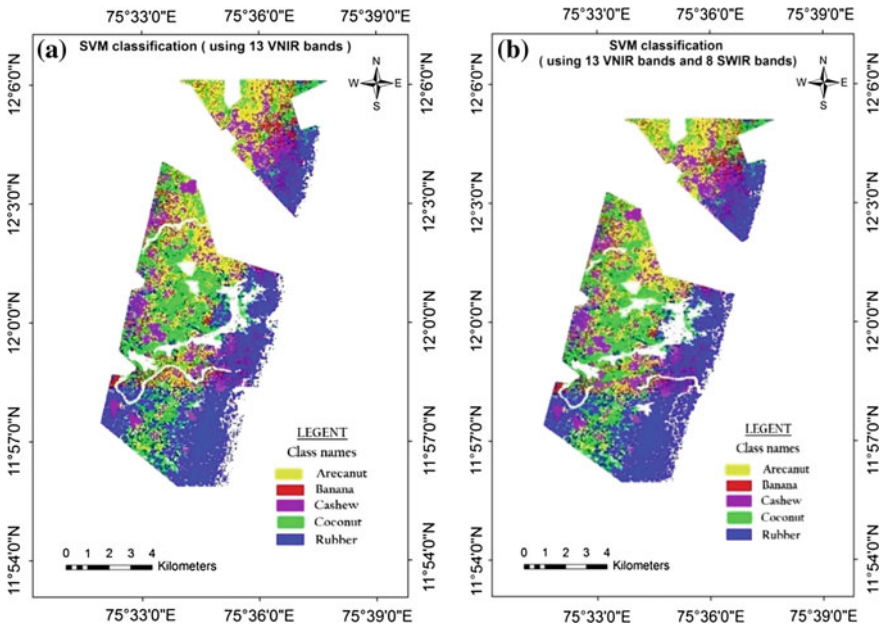

Fig. 6 SVM classified image

Table 1 Results from the accuracy assessment of support vector machine classification

Class	Using 13 MNF eigen images (13 VNIR bands)		Using 21 MNF eigen images (13 VNIR bands and 9 SWIR bands)	
	Producer's accuracy (%)	User's accuracy (%)	Producer's accuracy (%)	User's accuracy (%)
Arecanut	50	33.33	50	100
Banana	50	66.67	50	100
Cashew	66.67	100	100	75
Coconut	100	85.71	100	75
Rubber	100	100	100	100
Overall accuracy (%)	80.95		85.71	
Kappa coefficient	0.75		0.812	

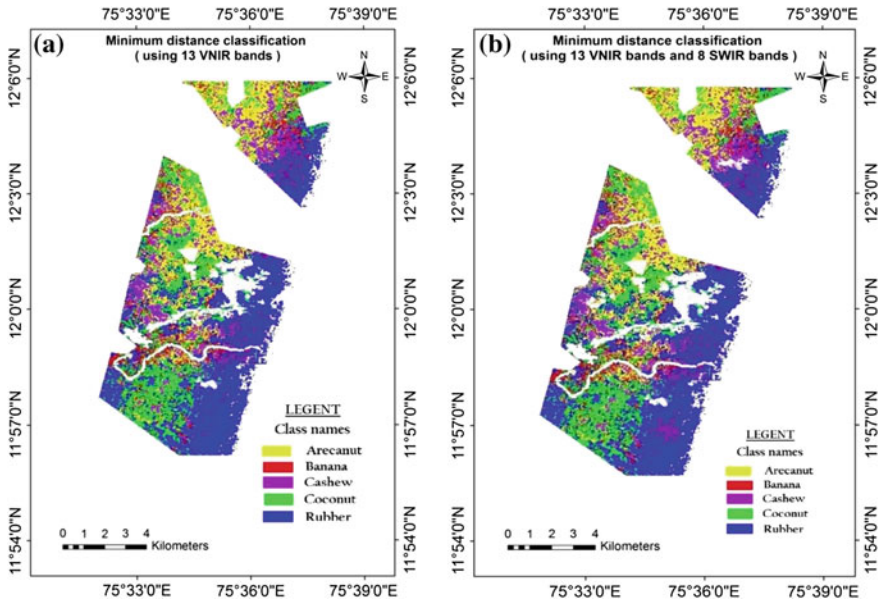

Fig. 7 Minimum distance classified image

accuracy of 73.33% with a Kappa coefficient of 0.45. The overall accuracy increased to 75.61% when classification was performed using 13 VNIR bands and 9 SWIR bands. In this classification, the Kappa coefficient obtained was 0.68. In minimum distance classification, it is concluded that the classification using 13 VNIR bands and 9 SWIR bands gives higher accuracy compared to classification using 13 VNIR bands.

The overall results showed that the SVM classifier gives better accuracy compared to minimum distance classifier, and the comparison of the Hyperion classified

Table 2 Results from the accuracy assessment of minimum distance classification

Class	Using 13 MNF eigen images (13 VNIR bands)		Using 21 MNF eigen images (13 VNIR bands and 8 SWIR bands)	
	Producer's accuracy (%)	User's accuracy (%)	Producer's accuracy (%)	User's accuracy (%)
Arecanut	58	46	100	100
Banana	100	50	33.33	50
Cashew	100	33.33	77.78	87.5
Coconut	48	43	90	52.94
Rubber	81.82	90	100	91.67
Overall accuracy (%)	73.33		75.61	
Kappa coefficient	0.45		0.68	

images which were derived from 13 MNF eigen images and 21 MNF eigen images, respectively, showed that the overall accuracy in the 21 MNF case was slightly higher.

Spectral Reflectance Curve

The vector files (or shape files) were created using the lat-long values obtained during the field visit for each crop, and it was overlaid on the Hyperion image. From each vector files corresponding to each crop, spectral reflectance curve was developed (Thenkabeil et al. 2005). The spectral reflectance curve for different crops obtained from the image is shown in Fig. 8, and also, the spectral reflectance curve developed for different ages of rubber is shown in Fig. 9. From the spectral curves of different crops (Fig. 8), it was observed that crops can be easily discriminated in the region 730–1050 nm. The rubber crop showed maximum separation from other crops at wavelength 884 nm which corresponds to Hyperion band 53. And also banana and arecanut showed almost similar spectrum. They can be distinguished at wavelength 972 nm which corresponds to Hyperion band 62. Coconut and cashew were also showed almost similar spectrum, but they can be distinguished at 915 nm which corresponds to Hyperion band 56.

An attempt has been made to develop the spectral reflectance curves for different age of rubber. The spectral reflectance curve was developed for 2 years old rubber, 3 years old rubber and 9 years old rubber (Fig. 9). From the spectra, it was observed that as the age increases reflectance increases. The curve shows distinct characteristics at 864 nm (corresponding to band 51). Hence, this may be the portion where rubber crops can be discriminated based on age.

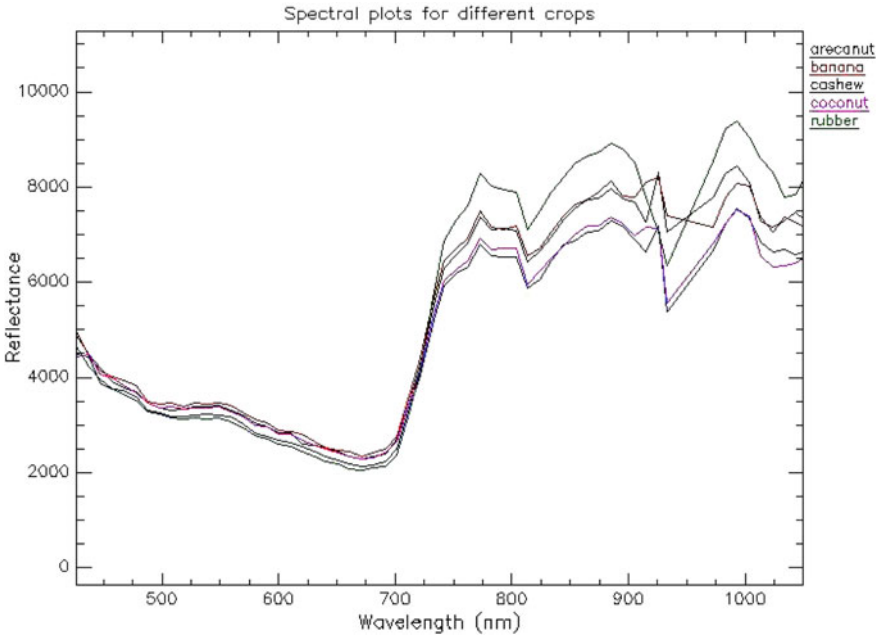

Fig. 8 Spectral curves for different crops

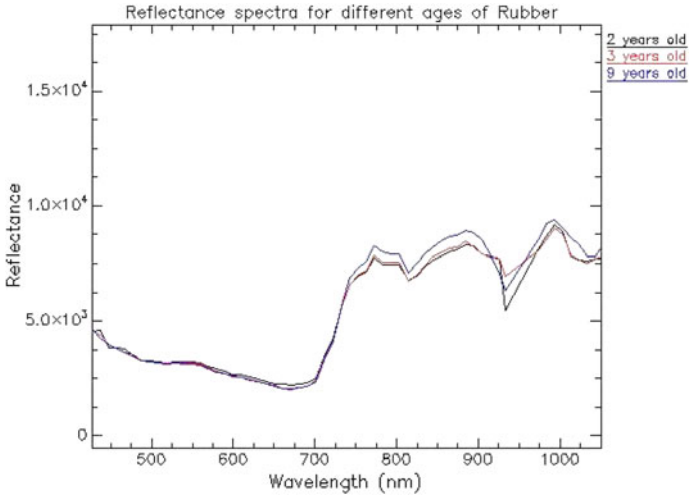

Fig. 9 Spectral curves for different ages of rubber

Optimum Wavelength Determination

To determine optimum wavelength (Thenkabeil et al. 2013) suitable for crop-type discrimination, two methods were used: partial least square regression and stepwise discriminant analysis.

(i) **Partial Least Square Regression**

Partial least square regression was done using MATLAB software to find the optimum wavelength bands for discriminating the agricultural crops. Five crops such as arecanut, banana, cashew, coconut and rubber and the corresponding reflectance spectra were the inputs for the method. The MATLAB code was developed and run for the PLSR. Two PLS components were obtained and correspondingly two optimum wavelengths were determined. The optimum wavelengths were 932 and 983 nm, and they correspond to band 79 and band 84 of Hyperion data.

(ii) **Stepwise Discriminant Analysis**

The stepwise discriminant analysis for finding the optimum wavelength bands for agricultural crop discrimination was performed using the SPSS software using different crop types and their corresponding spectral reflectance values as the inputs. The analysis was performed with the syntax developed. After running, the syntax results were generated with the values of multivariability seperability parameters. The wavelength variables were altered and again syntax was run. This process was repeated for several trials until the optimum wavelengths with maximum correlation coefficient and minimum Wilk's lambda obtained. After the inclusion of four bands, the Wilk's lambda and canonical correlations were saturated. This showed that no further inclusion of bands would increase the discrimination. The four wavelengths obtained for crop discrimination in this method are 882, 915, 932 and 983 nm.

Conclusion

The usage of remote sensing imagery for mapping, assessing and monitoring of agricultural crop conditions and production is steadily increasing in recent years. One of the recent advances in remote sensing field is the development of hyperspectral imaging system which provides high-resolution satellite imagery. This study made an attempt to evaluate the potential of hyperspectral imagery in mapping and discriminating agricultural crops. The main conclusions drawn from the study are given below.

The analysis of hyperspectral data is complex because it needs a pre-processing stage. The classification techniques such as support vector machine classification and minimum distance classification were compared on the Hyperion imagery, and

the result showed that SVM gives better results compared to minimum distance classification which infers different crops can be mapped using SVM classifier with higher accuracy. Also, results conclude that inclusion of the Hyperion SWIR bands increases the mapping or classifying accuracy.

By analysing spectral reflectance curve of different crops, it has been clearly found that rubber can be discriminated from other crops using Hyperion band 53 (wavelength 884 nm). Band 62 (wavelength 972 nm) is useful for distinguishing banana and arecanut crops. Coconut and cashew show almost similar spectrum, and they can be distinguished using band 56 (wavelength 915 nm). The results of partial least square regression and stepwise regression analysis showed that the Hyperion bands 79 (wavelength 932 nm), 84 (wavelength 983 nm), 74 (wavelength 882 nm), 56 (wavelength 915 nm) are suitable for discrimination of different crops. Overall, this study proves that high-resolution Hyperion data can be used for mapping and discrimination of agricultural crops with higher accuracies.

References

Agarwal G, Sarup J (2011) Comparison of QUAC and FLAASH atmospheric correction modules on EO-1 Hyperion data of Sanchi. Int J Adv Eng Sci Technol 4:178–186

Apan A, Held A, Markley J (2004) Detecting sugarcane "orange rust" disease using EO-1 Hyperion hyperspectral imagery. Int J Remote Sens 25(2):489–492

Barbosa PM, Casterad MA, Herrero J (1996) Performance of several Landsat 5 Thematic Mapper (TM) image classification methods for crop extent estimates in an irrigation district. Int J Remote Sens 17:3665–3674

Bing X, Gong P (2007) Land-use/land-cover classification with multispectral and hyperspectral EO-1 data. Photogram Eng Remote Sens 73(8):955–965

Burges CJ (1998) A tutorial on support vector machines for pattern recognition. In: Fayyad U (edn) Data mining and knowledge discovery. Kluwer Academic, pp 1–43

Datt B, McVicar TR, Van Niel TG, Jupp DLB, Pearlman JS (2003) Pre-processing EO-1 Hyperion hyperspectral data to support the application of agricultural indices. IEEE Trans Geosci Remote Sens 41:1246–1259

Enkhzaya T, Oyunbileg T, Tateishi R (2013) Characterization of phonological features for cropland area in Mangolia using MODIS NDVI data. In: Proceedings of the 6th international workshop on remote sensing and environmental innovations in Mongolia, June 2013, pp 18–23

ENVI User's Guide (2004) ENVI version 4.1, Sept 2004 edn

ESRI (2012) ArcGIS user manual. ESRI Inc., USA

Getting Started with MATLAB Version 7.14 (2012) The math works, Inc., Natick, MA, USA

Glenn NF, Jacob TM, Keith TW, Timothy SP (2005) Hyper spectral data processing for repeat detection of small infestations of leafy spurge. Remote Sens Environ 95:399–412

Goodenough D, Dyk A, Niemann KO, Pearlman JS (2003) Processing Hyperion and ALI for forest classification. IEEE Trans Geosci Remote Sens 41(6):1321–1331

Govender M, Chetty K, Naiken V, Bulcock H (2008) A comparison of satellite hyperspectral and multispectral remote sensing imagery for improved classification and mapping of vegetation. Water SA 34(3):147–154

Griffin MK, Burke HHK, Orloff SM, Upham CA (2005) Examples of EO-1 Hyperion data analysis. Lincoln Lab J 15

Guo B, Gunn SR, Damper RI, Nelson JDB (2006) Band selection for hyperspectral image classification using mutual information. IEEE Geosci Remote Sens Lett 3(4):522–526

Harsanyi JC and Chein CI (1994) Hyperspectral image classification and dimensionality reduction: an orthogonal subspace projection approach. IEEE Trans Geosci Remote Sens 32(4):779–785

Hina P, Tiwari PS (2013) High-resolution and hyperspectral data fusion for classification. In: Miao Q (edn) New advances in image fusion. ISBN 978–953-51-1206-8. InTech. doi:10.5772/56944

Huang C, Davis LS, Townshend JRG (2002) An assessment of support vector machines for land cover classification. Int J Remote Sens 23(4):725–749

Kawishwar P (2007) Atmospheric correction models for retrievals of calibrated spectral profiles from hyperion EO-1 data. MS thesis, ITC, The Netherlands and IIRS, Dehradun, India

Lee JB, Woodyatt AS, Berman M (1990) Enhancement of high spectral resolution remote sensing data by a noise-adjusted principal components transform. IEEE Trans Geosci Remote Sens 28:295–304

Lelong C, Patrick C (1998) Hyperspectral imaging and stress mapping in agriculture: a case study on wheat in Beauce (France). Remote Sens Environ 66:179–191

Li W, Prasad S, Tramel EW, Fowler EJ, Du Q (2014) Decision fusion for hyperspectral image classification based on minimum-distance classifiers in the wavelet domain. In: IEEE chain summit & international conference on signal and information processing, pp 162–165

Li X, Zhang Y, Bao Y, Luo J, Jin X, Xu X, Song X, Yang G (2014) Exploring the best hyperspectral features for LAI estimation using partial least squares regression. Remote Sens 6:6221–6241

Lillesand TM, Kiefer RW, Chipman JW (2012) Remote sensing and image interpretation, 6th edn. Wiley-India Publishing

Mader S, Vohland M, Jarmer T, Casper M (2006) Crop classification with hyperspectral data of the hymap sensor using different feature extraction techniques. In: Proceedings of the 2nd workshop of the EARSeL SIG on land use and land cover, Sept 2006, pp 96–101

Mercier G, Lennon M (2003) Support vector machines for hyperspectral image classification with spectral-based kernels. In: Proceedings of IEEE international symposium on geoscience and remote sensing, vol 1, pp 288–290

Mundt JT, Glenn NF (2007) Discrimination of hoary cress and determination of its detection limits via hyperspectral image processing and accuracy assessment techniques. Remote Sens Environ 98(2):398–411

Nellis MD, Price KP, Rundquis D (2009) Remote sensing of crop land agriculture. The SAGE handbook of remote sensing. SAGE Publications, Thousand Oaks, pp 801–828

Oommen T, Misra D, Navin KC, Prakash A, Sahoo B, Bandopadhyay S (2008) An objective analysis of support vector machine based classification for remote sensing. Math Geosci 40:409–424

Ouardighi ElA, Akadi ElA, Aboutajdine D (2007) Feature selection on supervised classification using Wilk's lambda statistic. In: 3rd international symposium on computational intelligence and intelligent informatics—ISCIII, pp 51–55

Powers JJ, Elizabeth KS (2006) Stepwise discriminant analysis of gas chromatographic data as an aid in classifying the flavor quality of foods. J Food Sci 33(2):207–213

Petropoulos GP, Arvanitis K, Sigrimis N (2012) Hyperion hyperspectral imagery analysis combined with machine learning classifiers for land use/cover mapping. J Expert Syst Appl 39:3800–3809

Ray SS, Jain N, Arora RK, Chavan S, Panigrahy S (2011) Utility of hyperspectral data for potato late blight disease detection. J Indian Soc Remote Sens 39(2):61

Sankaran S, Mishra A, Ehsani R, Davis C (2010) A review of advanced techniques for detecting plant diseases. Comput Electron Agric 72:1–13

SPSS-statistical package for social sciences software, SPSS Inc., USA, 2006

Thenkabeil PS, Eiden A, Christopher L (2005) Hyperion, IKONOS, ALI, and ETM + sensors in the study of African rainforests. Int J Remote Sens 90:489–498

Thenkabeil PS, Mariotto I, Gumma Murali Krishna, Middleton EM, Landis DR, Huemmrich (2013) Selection of Hyperspectral narrowbands and composition of two band vegetation indices for biophysical characterization and discrimination of crop types using field reflectance and Hyperion/EO-1 data. IEEE J Sel Top Appl Earth Obs Remote Sens 6(2):1–13

Ungar SG, Pearlman JS, Mendenhall JA, Reuter D (2003) Overview of the earth observing one (EO-1) mission. IEEE Trans Geosci Remote Sens 41:1149–1159

Van Niel GT, McVicar TR (2004) Determining temporal windows for crop discrimination with remote sensing: a case study in south-eastern Australia. Comput Electron Agric 45:91–108

Vapnick VN (1998) Statistical learning theory. Wiley, New York

Yu L, Porwal A, Holden EJ, Dentith MC (2012) Towards automatic lithological classification from remote sensing data using support vector machines. Comput Geosci 45:229–239

Geomatica-Based Approach for Automatic Extraction of Lineaments from ASTER-GDEM Data, in Part of Al-Rawdah, Shabwah, Southeast Yemen

Mohammed Sultan Alshayef and Akram Javed

Abstract Lineaments are considered one of the most important topographic features used in exploring resources such as minerals, groundwater, oil, and gas; besides, they are indicators of structural and tectonic basin. Geomatica- and GIS-based techniques have been used for extracting lineaments in part of Al-Rawdah, Shabwah, southeast Yemen. High-resolution 30-m ASTER GDEM shaded images with different sun angles are used in delineating lineaments in different distinct relief and topography. Various softwares are as follows: Arc GIS has been used for extracting various hill-shaded image and Geomatica (2013) has been used to enhance hill-shaded image and to extract lineaments using various default parameters, whereas RockWork14 has been used to indicate trend of the lineaments. Moreover, Arc GIS 10.2.2 has used for overlying, mapping, visualizing, and calculating different parameters. Eight hill-shaded images have been extracted with different sun angles. Shaded images of sun angles 0°, 45°, 90°, 135° were combined as one image for better enhancements. The next four shaded images, i.e., hill-shaded images of sun angles 180°, 225°, 270°, and 315°, were combined as one hill-shaded image. The two hill-shaded images combined were used for automatic extraction of lineaments and give N-NE and S-SE and N-NW and S-SE directions, respectively; however, they vary in their density. In addition, fault map identified NW-SE direction and was compared with last two combined hill-shaded images; when superimposed with them, it indicates that most of the lineaments are perpendicular to fault line and some match with it properly where the majority of the lineaments occur along hard rocks. The final superimposed image of all lineaments map has been classified into three types of lineaments: micro-, minor, and medium which have total number of 1040, 324 and 8 respectively with the length of 1368, 1050, and 157.5 km, respectively. Rose diagram indicated that the dominant trend of lineaments is NW-SE. The present study demonstrates the utilization of software for automated extraction of lineaments and their relationship with major structural features.

M. S. Alshayef (✉) · A. Javed
Department of Geology, AMU, Aligarh 202002, UP, India
e-mail: alshayef2014@gmail.com

V. P. Singh et al. (eds.), *Hydrologic Modeling*, Water Science and Technology Library 81, https://doi.org/10.1007/978-981-10-5801-1_29

Keywords Geomatica and GIS · Lineaments · ASTER GDEM
Shaded images · Geological fault map

Introduction

Lineaments are simply linear or curvilinear edges that may be related to geological structure (fault, joint, and line weakness), geomorphological features (cliffs, terraces, and linear valleys), tonal contrast (vegetation, soil moisture, and rock composition), human activity and/or constructions (road, tracks, buildings, mining, etc.). A digital elevation model (DEM) is a representation of the topography surface sampled in a regular grid (Zelazny 2011). Topographic attributes can be extracted from digital elevation data by applying special computer algorithms which include slope, aspect, and shaded relief algorithms (Abdulla et al. 2010). Shaded relief logarithm is a method for representing topography and becomes most widely used for lineaments extraction. The Geomatics technology comprising of remote sensing and GIS has enormous virtues and avenues in mapping and modeling the earth surface and subsurface geological process/system (Kumanan et al. 2011). The most important factor for using Geomatica is the ability to extract lineaments from raster images automatically with the spatial line option. The main advantages of lineaments extracted from satellite images are: It has the ability to extract lineaments which are not recognized by the human eyes and the processing operation is performed in a short time (Sarp 2005). In this study, the aim was to map automatic extraction of lineaments and compare it with reference to geological fault map. The presence of lineaments is considered as an important factor in oil and gas exploration, groundwater, mineral targeting and mapping seismically active areas etc.

Study Area

The study area is situated in Shabowah Province, southeastern central part of Yemen (Fig. 1) with zone 38 UTM projection, and extends from 14° 36′ to 14° 67′ N latitudes and 47° 03′ to 47° 419′E longitudes in 38 UTM grid zone covering an area of about 1492 km^2. The maximum and minimum elevations encountered in the basin are 1743 and 594 m above main sea level (MSL), respectively. The area is mainly drained by joining the main channel, river (Amqeen), and their tributaries, which flow from NW to SE directions defining the general slope of the basin. The drainage pattern is dendritic to sub-dendritic with moderate-to-high drainage texture. The general land use of the study area is agriculture; besides, some natural vegetation cover is also present in some parts of the basin.

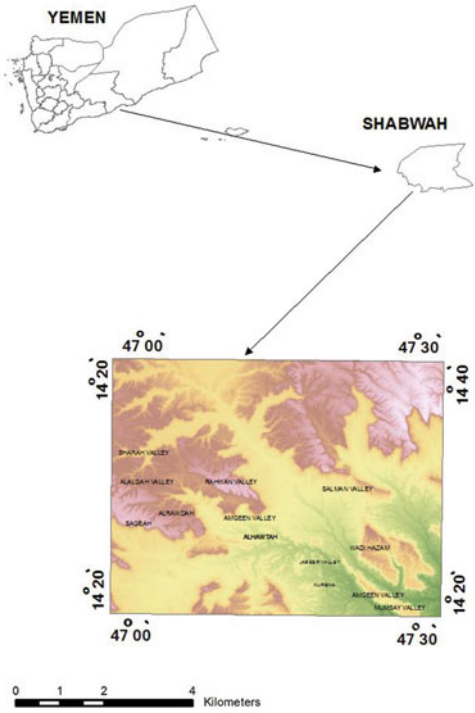

Fig. 1 Location map of the study area

Materials and Methodology

Toposheet map no. D-38-59, 1978 of survey of Yemen (SOY) on 1:100,000 scale has been used to verify the man-made linear features and for the preparation of base map. Geological map no. D-38-59, 1978 of survey of Yemen (SOY) on 1:100,000 scale has been used to digitize faults and geological units. Advanced spaceborne thermal emission and reflection radiometer (ASTER) of 30 * 30 m resolution data was downloaded from the Web site (http://www.ASTERGDEM/Data/Obtaining.html) and was subsequently used for the preparation of digital elevation model and getting hill-shaded images. Eight shaded images were extracted from DEM with varying sun angles; i.e., the first shaded image had sun angle 0° and others had 45°, 90°, 135°, 180°, 225°, 270°, and 315°, respectively. The first four shaded images, i.e., shaded images of sun angles 0°, 45°, 90°, 135°, were combined as one shaded image for more enhancement by using Arc GIS 10.2.2 and combined last four shaded images, i.e., shaded images of sun angles 180°, 225°, 270°, 315°, as one hill-shaded image. The two hill-shaded combined images have been used for automatic extraction of lineaments by using a special tool in Geomatica (2013) to extract linear features and record it as polylines in a vector segment. Various extracted lineaments have been plotted in Rockwork15 as a rose diagram to show the trend/orientation of the lineaments.

Result and Discussion

Geological Setting

The geological setup of the area comprises rocks ranging from Mesozoic to recent. The lithological unit present in the study area is river alluvium of Quaternary age which shows bright greyish color with fine-to-medium texture, curvilinear, and elongated pattern. Shale of Jiza formation OF early Eocene (Hadramut group) age represented by greenish-yellowish papery shales, with a thickness 133 m. Jawl limestone of early Eocene (Um er Radhuma formation) is represented by well-bedded limestone of thickness from 4 to 6 m. Umm er Rdumah limestone occurs in Paleocene (Hadramut group) with 220 m thickness and white and gray color. Tawilah sandstone belongs to in Cretaceous period and known as Cretaceous (Tawilah group) sandstone series with a thickness of 200 m. It shows white-yellowish and brown sandstone. Tawilah sandstone occurs over a high plateau (Beydon et al. 1998). In the study area, lineaments are concentrated in the plateau, hills, and linear ridges which represent hard rocks such as limestone, shale, and sandstone. Figure 2 shows the geological map of the study area.

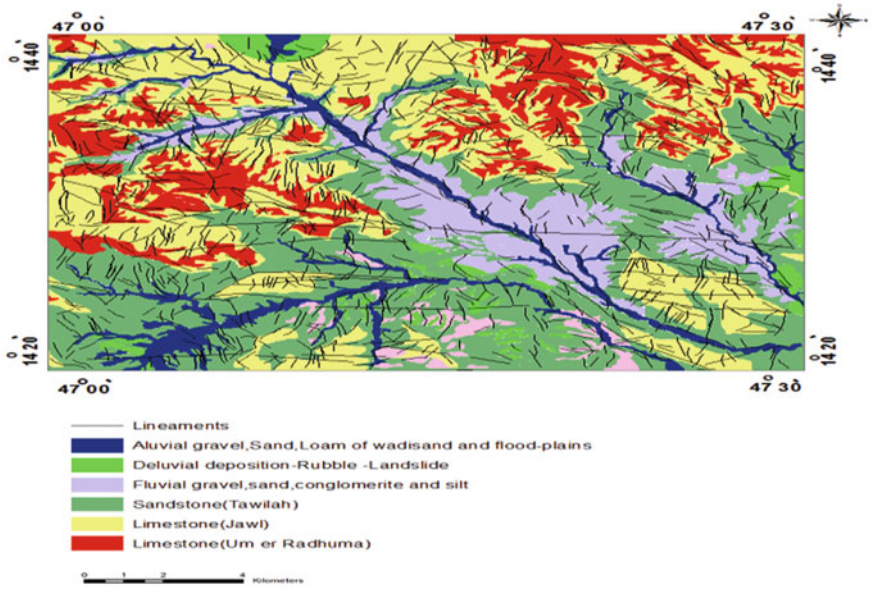

Fig. 2 Geological map of the study area (Derived from SOY geological map D 38-59)

Automatic Lineaments Extraction

Lineaments were extracted automatically using the module line of Geomatica from various sun angle shaded images which were combined together and record the output as polyline with vector segment (Fig. 3). The lineaments extraction algorithms of PCI Geomatica software consist of edge detection, thresholding, and

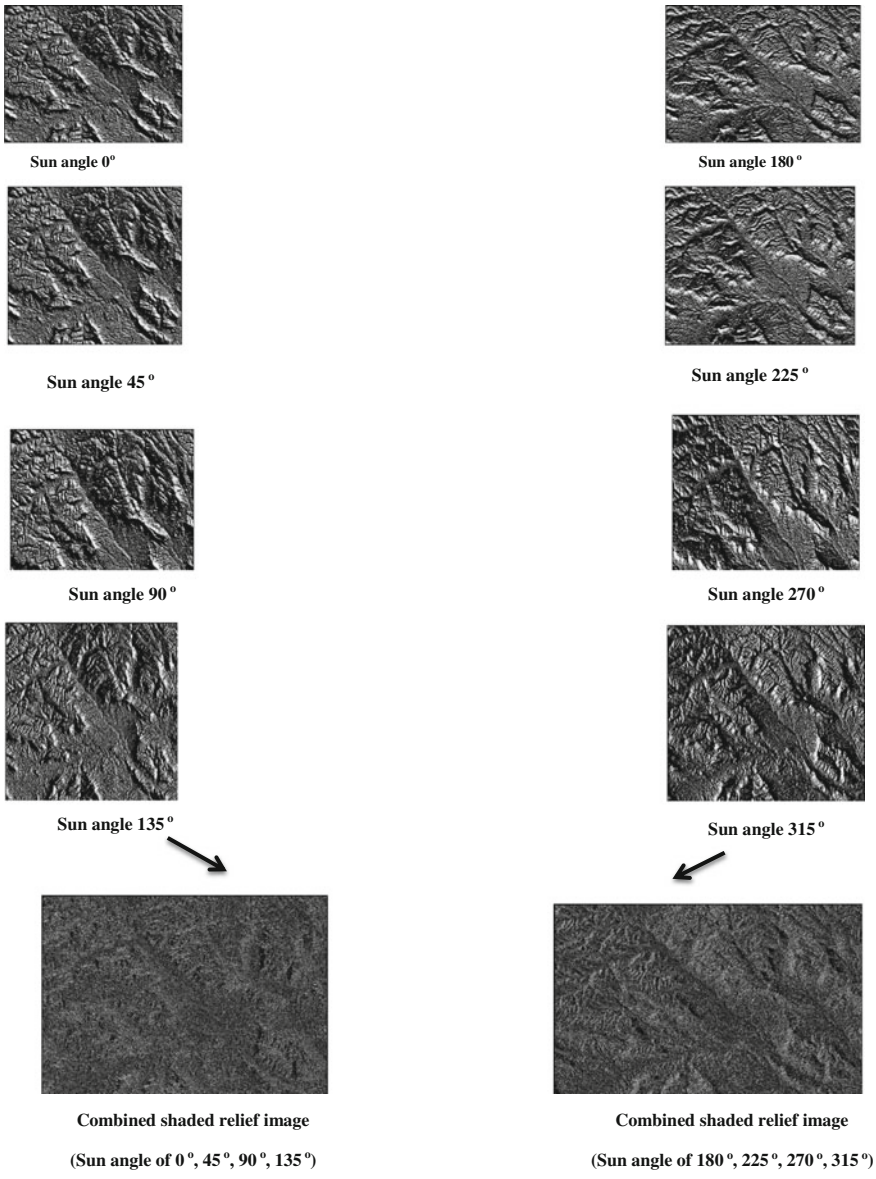

Fig. 3 DEM showing different sun angle shaded images

Table 1 Parameters of automatic extraction process

Name	Description	Values
RADI	Filter radius (pixels)	10
GTHR	Edge gradient threshold	50
LTHR	Curve length threshold (pixels)	30
FTHR	Line-fitting error threshold	3
ATHR	Angular difference threshold (degree)	30
DTHR	Linking distance threshold (pixels)	10

curve extraction steps (PCI Geomatica 2013). These steps were executed over two combined hill-shaded images under six default parameters control the automatic extraction lineaments process as shown in Table 1 applied for multi-directional sun angle hill-shaded images for more enhancement.

Lineaments Analysis

Lineaments analysis from ASTERGDEM has been done for the study area with reference to geological fault map which has variations in trend, frequency, and length. Rose diagram with statistical analysis was applied to interpret structural lineaments (Table 2). The first combined lineament image of multi-directional sun angle hill-shaded images 0°, 45°, 90°, and 135° consists of 557 lineaments with a total length of 1281.2 km, which predominately represents the N-NE and S-SE directions (Fig. 4), whereas the combined lineament image of multi-directional sun angle hill-shaded images 180°, 225°, 270°, 315° contained 768 lineaments with the length of 2386 km which represents N-NE and S-SW directions (Fig. 5). However,

Table 2 Characteristics of the automatic lineaments maps and fault map

Lineaments map	Minimum (km)	Maximum (km)	Mean	Numbers of the lineaments	Total lineaments length (km)	Orientation
Combine lineaments image of multi-directional Sun angle (0°, 45°, 90°, 135°)	0.9	3	1.3	557	1281.2	N-NE and S-SE
Combine lineaments image of multi-directional Sun angle (180°, 225°, 270°, 315°)	0.8	5.16	1.5	768	2386	N-NE and S-SW
Geological fault	0.26	32.8	3.7	150	1108	NW-SE
Total	1.96	40.96	6.5	1475	4775.2	

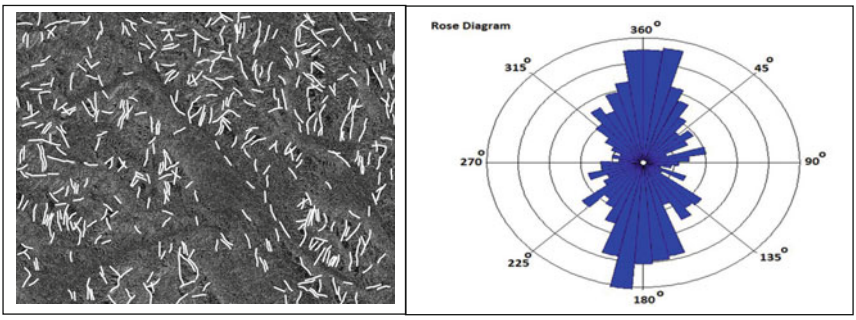

Fig. 4 Automatic lineaments of the first combined image with orientation

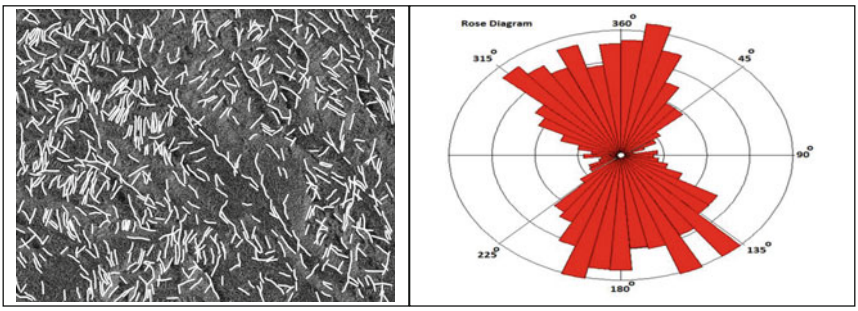

Fig. 5 Automatic lineaments of the second combined image with orientation direction

the geological fault map which has 150 lineaments with a total length of 1108 km represents NW-SE direction (Fig. 6). Overall, lineaments have been superimposed with each other which indicated that most of the lineaments are perpendicular to fault line and do not match with it properly as shown in Fig. 8. In addition, it contains 1475 lineaments with total lineaments length 4775.2 km which represent NW-SE orientation (Fig. 9). The frequency distribution is shown in Figs. 7 and 9, respectively (Table 3).

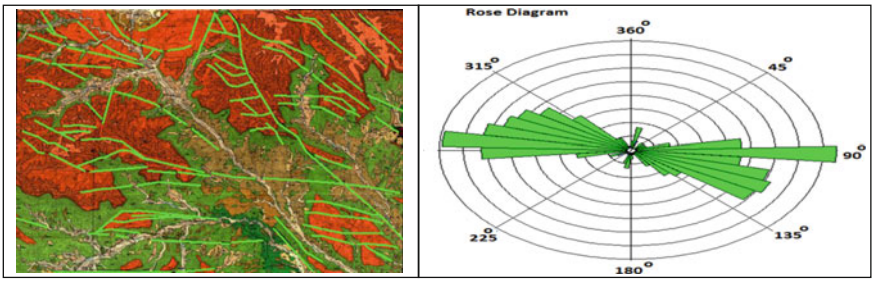

Fig. 6 Nonautomatic (digitize) geological fault map of the study area with orientation

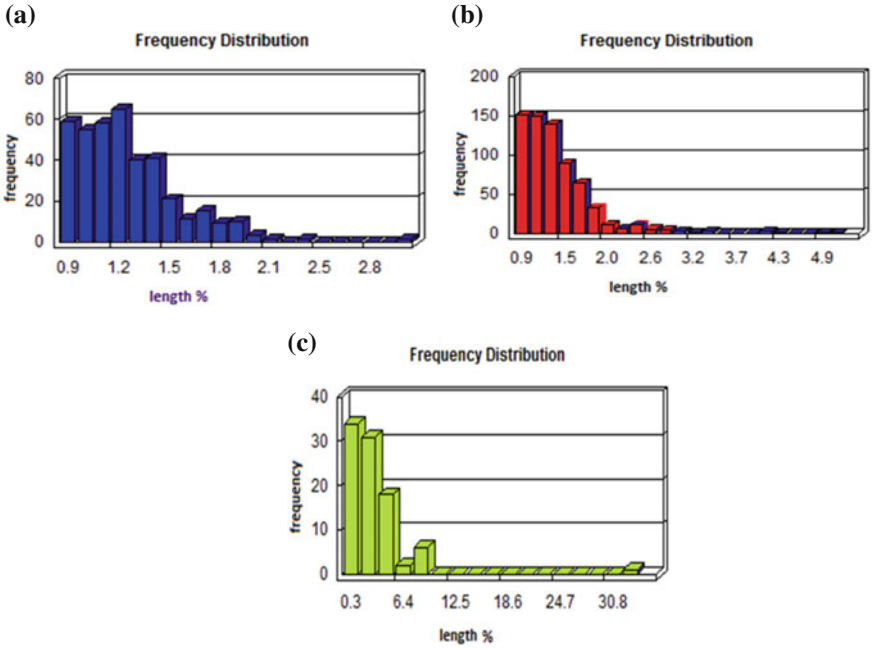

Fig. 7 Frequency distribution of lineaments of **a** the first combined image, **b** the second combined image, **c** geological fault map

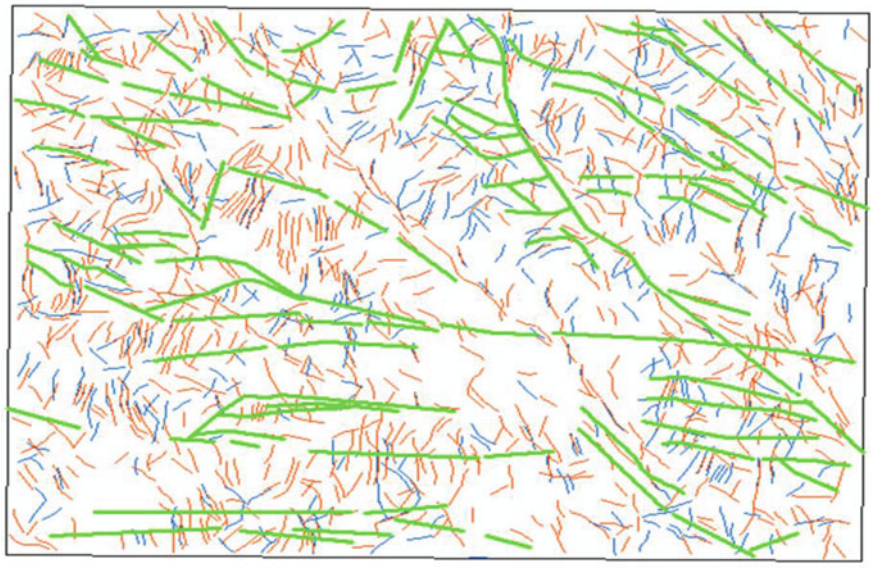

Fig. 8 Superimposed automatic extraction with geological fault map

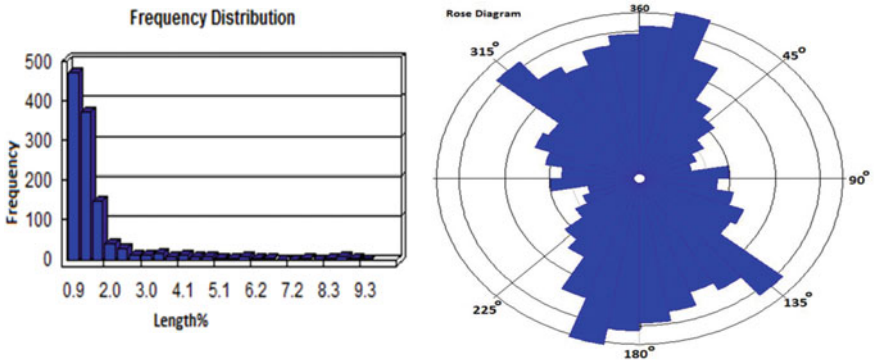

Fig. 9 Frequency distribution with rose diagram of superimposed automatic extraction with geological fault map

Table 3 Characteristics of the superimposed automatic lineaments maps and fault map

Lineaments map	Minimum (km)	Maximum (km)	Mean	Numbers of the lineaments	Total lineaments length (km)	Orientation/ trend
All lineaments maps	0.90	9.4	1.65	1475	4775	NW-SE

Lineaments Density

The lineaments density map is another method to analyze and extract lineaments (Hashim 2013). The purpose of the lineaments density analysis is to calculate the frequency of the lineaments per unit area. This is also known as lineaments frequency (Greenbaum 1985), which produces a map showing concentrations of the lineaments over an area. The lineaments density is created by spatial analyst tool in ArcGIS10.2.2 program by counting lines digitally per unit (number/km^2) area, then plotted in the respective grid centers, and contoured using the same tool. The density map of the first combined image has 215.5 which is more concentrated in NW with SE and SW, whereas the second combined image has highest lineaments density 333 concentrated in NW and SE of the study area (Fig. 10). Geological fault map shows 192.9 density which is concentrated in NW and SE.

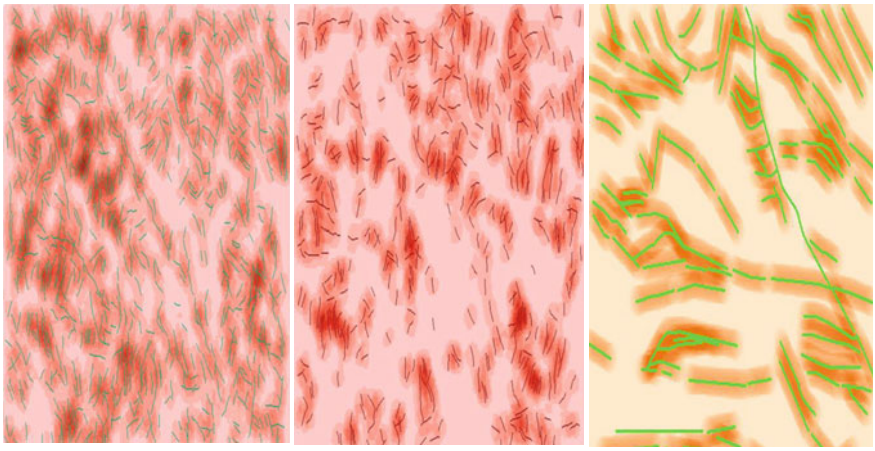

Fig. 10 Line density for lineaments extracted from ASTER GDEM and geological fault map

Lineaments Classification

The final superimposed lineament map contains of 1475 lineament with different length. These lineaments can be classified based on their length as (i) micro: <2 km, (ii) minor: 2–10 km, (iii) medium: 10–100 km, (iv) major: 100–500 km, and (v) mega: >500 km (Manjare 2013). In the present study, lineaments are classified into three classes: micro-, minor, and medium lineaments (Table 4). Moreover, classification of lineaments, rose diagram, and frequency distribution of the classified lineaments are shown in Figs. 11 and 12, respectively.

Table 4 Classification of lineaments in the study area

S. No.	Lineaments class	Numbers	%	Length (km)
1	Micro lineaments	1040	76.2	1368
2	Minor lineaments	324	23.3	1050
3	Medium lineaments	8	0.5	157.2
4	Major lineaments	–	–	–
5	Mega lineaments	–	–	–
Total		1372	100%	2575.2

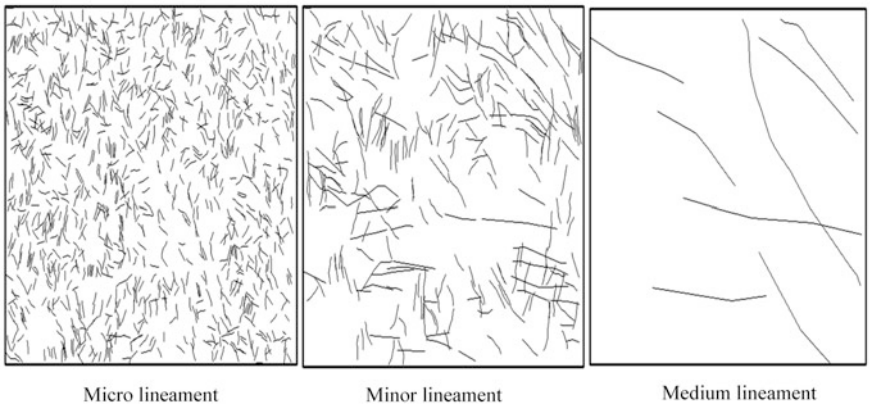

Fig. 11 Classification of lineaments in the study area

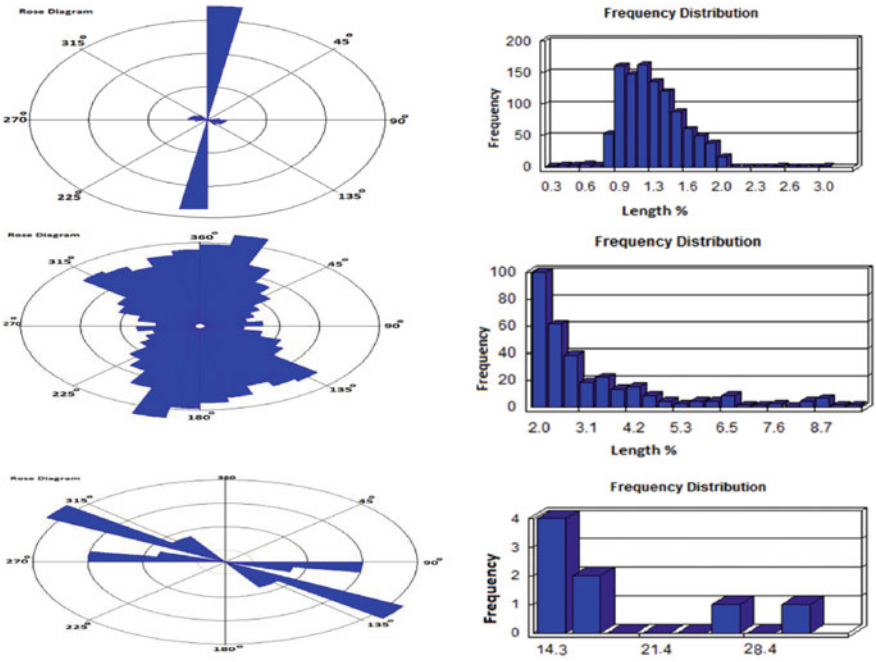

Fig. 12 Rose diagram with frequency distribution of micro, minor and medium lineaments

Conclusion

ASTER GDEM image has given evidence to lineaments identification and mapping. Numerous lineaments have been extracted and classified into micro-, minor/short, and medium lineaments where the majority of study area contains minor/short lineaments along with faults. Various parameters applied successfully to enhance and extract lineaments. Lineaments assessed by three geospatial analyses, i.e., length, density, and orientation. The study shows the utility of the ASTER GDEM and Geomatica in automatic extraction of lineaments and classifies them into various classes based on their lengths.

Acknowledgements Authors would like to thank the chairman, D/O Geology, AMU, Aligarh, for extending necessary facilities. Thanks are also due to (http://www.ASTERGDEM/Data/Obtaining.html) for ASTER data and survey of Yemen for providing toposheets.

References

Abdulla A, Akhir JM, Abdullah I (2010) Automatic mapping of lineaments using shaded relief images derived from digital elevation model (DEMs) in the Maran-Sungi Lembing area, Malaysia. EJGE 15:948–957

ASTER GEODEM website. (http://www.ASTERGDEM/Data/Obtaining.html)

Beydon ZR, As-Saruri MAL, El-Nakhal H, Al-Ganad IN, Baraba RS, Nani ASO, Al-Aawah MH (1998) International lexicon of stratigraphy-geological of Yemen. IUGS 3(34):48–229

Greenbaum D (1985) Review of remote sensing applications to groundwater exploration in basement and regolith. Br Geol Surv Rep OD 85/8, 36 pp

Hashim M, Ahmad S, Johari MAM, Pour AB (2013) Automatic lineament extraction in heavily vegetated region using landsat enhanced thematic mapper (ETM+) imagery. Adv Space Res 51:874–890

Kumanan CJ, Saravanavel J, Palanivell K (2011) Virtues of 3D GIS in mapping earth surface & subsurface geological system/process. In: 12th Esri India user conference, Richmond Hill, Canada. Relief shading website (www.reliefshading.com)

Manjare BS (2013) Mapping of lineaments in some part of Betul District, Madhya Pradesh and Amravati District of Maharashtra, Central India using remote sensing and GIS techniques. Int J Adv Remote Sens GIS 2(1):333–340

PCI Geomatica (2013) PCI Geomatica user's guide version 2013

Sarp G (2005) Lineament analysis from satellite images, north-west of Ankara. M.Sc. theses, Middle East Technological University, p 2

Zelazny EM (2011) Lineament mapping using remote sensing techniques and structural geology for CO_2 sequestration site characterization in Central New York State. M.Sc. thesis, University of New York, pp 29

Part VI
Watershed Runoff and Floods

Morpho-Mathematical Analysis of Bharar River Basin District Chhatarpur-Central India

Pradeep Kumar Jain

Abstract The area of present study is situated at and around Nowgaon town of Chhatarpur district, Madhya Pradesh. It falls on the Survey of India Toposheet No. 54 O/8 and 54 O/12. The Bharar river basin selected for investigation is bounded by longitudes 79° 20′ 15″ to 79° 33′ 30″E and latitudes 25° 01′ 30″ to 25° 07′ 00″N. The morpho-mathematical analysis of Bharar river basin has been described in linear and areal aspects. The entire drainage network is spread over granitic rocks. The data obtained from morpho-mathematical analysis satisfy Horton's laws of drainage composition. The shape parameters indicate that the basin is elongated.

Keywords Morpho-mathematical analysis · Bharar · Chhatarpur

Introduction

The area of investigation is situated in Chhatarpur district of central India lying between longitudes 79° 20′ 15″ to 79° 33′ 30″E and latitudes 25° 01′ 30″ to 25° 07′ 00″N (Fig. 1). It falls on the Survey of India Toposheet No. 54 O/8 and 54 O/12. The total area is about 135 km^2. The Bharar river basin is covered mainly by Archeans, namely Bundelkhand granites/granitoid rocks. These granites are intruded by various quartz reefs and dolerite dykes. The general trend of these intrusions is NNE–SSW and NE–SW. Morpho-mathematical analysis has been carried out to understand the geometry of the drainage basin, drainage network and texture, etc. Similar studies have been carried out by Jain (1999) for upper Urmil river basin and Singhari river basin.

P. K. Jain (✉)
Department of Geology, Govt. Maharaja Autonomous College Chhatarpur (M.P.), Chhatarpur 471001, India
e-mail: drpradeepgeol@gmail.com

V. P. Singh et al. (eds.), *Hydrologic Modeling*, Water Science and Technology Library 81, https://doi.org/10.1007/978-981-10-5801-1_30

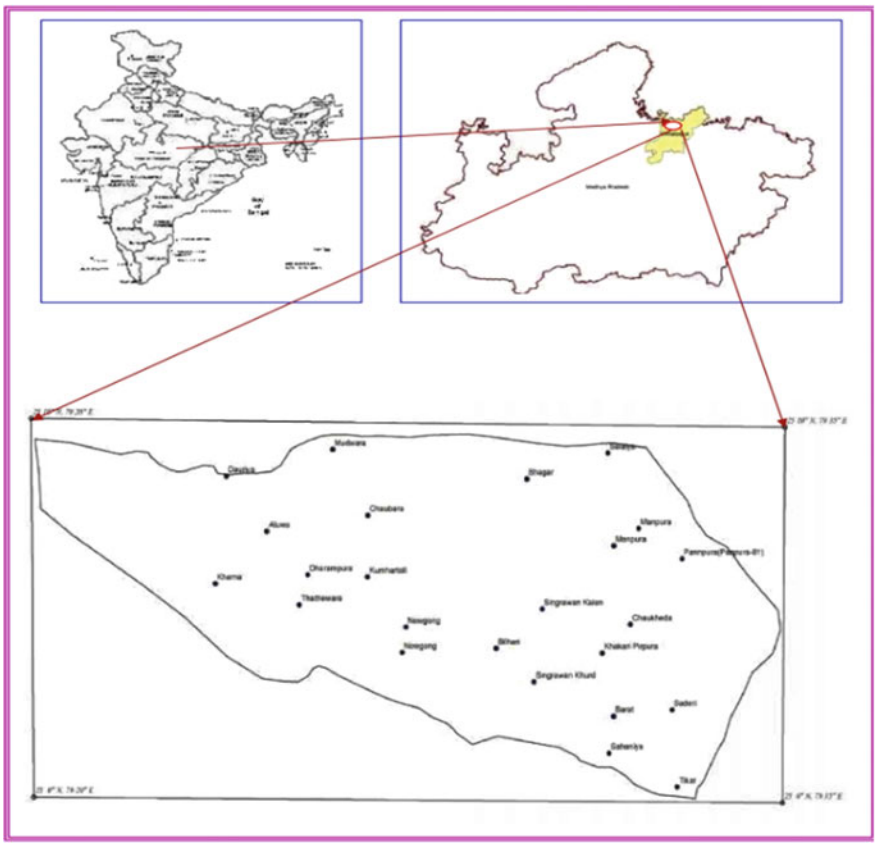

Fig. 1 Location map of Bharar river basin

Materials and Methods

The morpho-mathematical analysis of Bharar river basin has been carried out on the Survey of India Topographical map No. 54 O/8 and 54 O/12 on the scale of 2 cm to a km (1:50000). The perimeter of the Bharar river basin has been demarcated on the topographic maps. Author has followed Strahler (1957) for the present analysis. The length of stream has been measured using rotameter, and the area of Bharar drainage basin has been measured using planimeter. All the morpho-mathematical parameters have been computed using standard equations described by various workers given in Table 3.

Results and Discussion: Morpho-mathematical parameters of the Bharar river basin are as under

(A) Linear Properties

Stream Order

A stream order map is prepared following Strahler's (1957) scheme and shown in Fig. 2. It shows that the Bharar is a fourth-order stream.

Stream Number (Nu)

In accordance with Horton's (1945) law, the number of stream of each order has been counted and it is found that there is a progressive decrease in number of streams as the numerical value of stream order increases in each sub-basin (Table 1). Graphical representation of these data on semi-logarithmic paper does not yield perfect straight lines (Fig. 3). This departure suggests the presence of some sort of complexity in the resistance of the rocks of the study area.

Stream Length (*L*)

The length of various stream segments has been measured order-wise, and the total length as well as the mean length of each order has been computed. The total

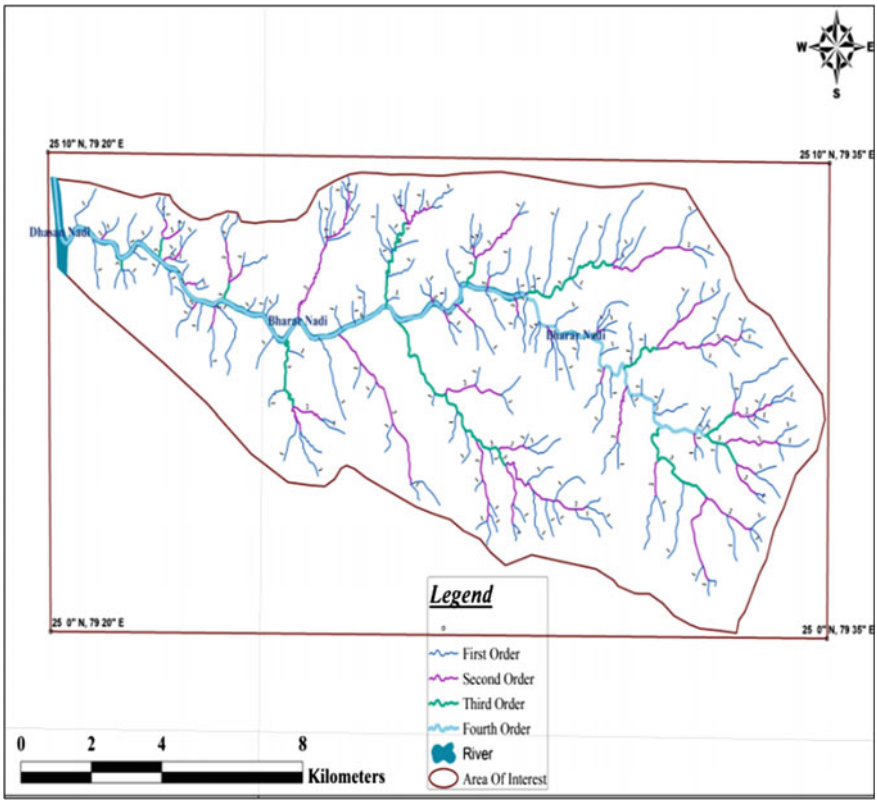

Fig. 2 Drainage map of Bharar river basin

Table 1 Linear properties of Bharar river basin

Sub-basin	Stream order (U)	No. of stream (NU)	Bifurcation ratio (R_b)	Average (R_b)	Total length of stream in km (LU)	Mean length of stream in km	Length ratio
Bharar	I	207			21.74	0.10	
	II	46	4.50	7.25	22.42	0.48	0.20
	III	14	3.28		22.01	1.57	0.30
	IV	1	14.00		2.52	2.52	0.62

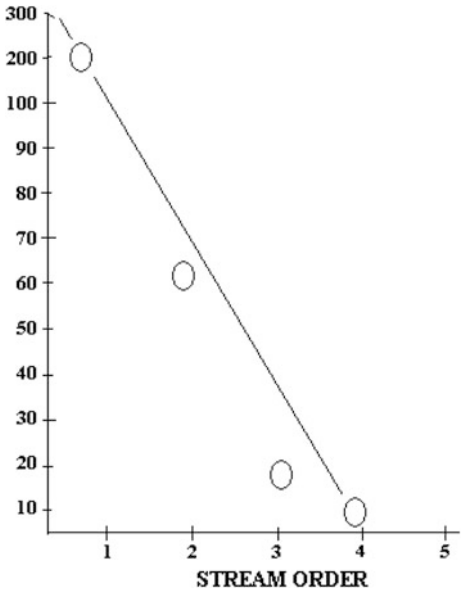

Fig. 3 Semi-log plot of stream order versus stream no.

length, mean length and length ratio are given in Table 1. Logarithmic plots of the stream length against stream order are made as suggested by Strahler (1956) and shown in Fig. 4. These plots confirm Horton's second law of stream length. The departure from perfect straight line indicates that there is a slight complexity in relief of the study area.

Length Ratio

It has been calculated for each pair of order and is given in Table 1. It has been expressed using equations described by Horton (1945) and Strahler (1952).

Bifurcation Ratio

The bifurcation ratio is given in Table 1. Table 1 reveals that bifurcation ratio ranges between 4.5 and 14 which indicates slight modification in geological structure of the study area.

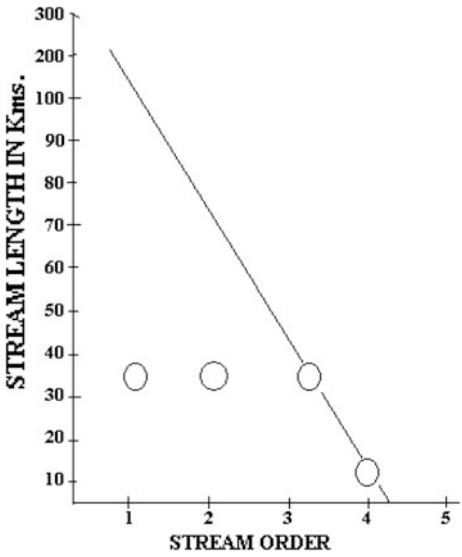

Fig. 4 Semi-log plot of stream order versus stream length

(B) Areal Properties

Mean Basin Area

The area of the drainage basin has been measured by planimeter, and it is given in Table 2. Schum (1956) established relation between the total drainage basin area and the total stream length which are supported by the contributing areas.

Basin Length (*L*)

The basin length measured by Schumm (1956) method for Bharar basin is given in Table 2.

Basin Perimeter (*P*)

The basin perimeter (*P*) has been measured for Bharar basin, and it is given in Table 2.

Basin Shape

Shape of drainage basin is largely influenced by rock types and prevalent processes. Basin shape gives an idea about potential efficiency of the drainage network. The shape of Bharar basin has been determined using the following ratios:

(1) Form Factor (FF)

The form factor has been determined as suggested by Strahler (1957), and it is given in Table 2. The value 0.58 is obtained as form factor for Bharar basin, which reveals the fact that average width of the respective sub-basin is about 58 of the respective basin length.

Table 2 Areal properties of Bharar river basin

(A)							
Sub-basin	Basin area in km^2	Basin length in km	Basin width in km	Perimeter in km	Form factor (FF)	Circularity ratio (R_c)	Elongation ratio (R_e)
Bharar	135	17.5	7.71	44.5	0.58	0.89	0.83
(B)							
Sub-basin	Lemniscate (K)	Drainage density (D_d)	Stream frequency (F)	Drainage intensity (D_I)	Constant of channel maintenance	Length of over land flow in km (L_g)	
Bharar	0.68	1.3	1.98	1.6	0.76	0.36	

(2) **Basin Circularity Ratio (R_c)**

This ratio has been obtained using the Miller (1953) equation, and it is given in Table 2. Basin circulatory ratio is 0.89 which indicates low value of circularity.

(3) **Basin Elongation Ratio (R_e)**

The elongation ratio (R_e) has been computed following Schumm (1956). The basin elongation ratio is given in Table 2. The value of elongation ratio reveals that the basin under study represent an area of low relief.

(4) **Lamniscate (K)**

The lamniscate (K) has been calculated as suggested by Chorley (1957) and mentioned in Table 2. Value of lamniscate (K) reveals that the basin is nearly rectangular in shape. On the basis of above shape parameters, it is concluded that the basin can be classified as an elongated basin.

Drainage Nature

This can be expressed as drainage density (D_d), stream frequency (F) and drainage intensity (D_i) (Carlston 1963; Greygory and Walling 1968).

(A) **Drainage Density (D_d)**

The Bharar basin has drainage density of 1.30 km. The drainage texture has been determined, and it is found that Bharar basin has very coarse texture as described by Smith (1950).

(B) **Stream Frequency (F)**

Stream frequency is 1.98 stream/km^2, which indicates low relief and rugged topography in the study area.

(C) **Drainage Intensity (D_i)**

Drainage intensity (D_i) has been calculated as described by Faniran (1968). It is 1.60.

(D) **Constant of Channel Maintenance**

It is just reciprocal of drainage density. It expresses the relationship between the drainage development and the character of the basin in so far as it retards the development of stream. It is given in Table 2.

Length of Overland Flow (L_g): The length of overland flow (L_g) has been calculated. It is 0.36 km (Table 3).

Table 3 Showing important equations used in morpho-mathematical analysis

No.	Parameter	Symbol	Equation	Whereas
1	Bifurcation ratio	R_b	$R_b = N_\mu/N_{\mu+1}$	N_μ = No. of stream segments of a given order, $N_{\mu+1}$ = No. of stream of the next higher order
2	Form factor	FF	$F_f = A/L^2$	A = Basin area, L^2 = square of the basin length (L)
3	Basin circularity	R_c	$R_c = 4\pi A/P^2$	A = Basin area, P^2 = square of the area of the circle with the same perimeter (P)
4	Basin elongation	R_e	$R_e = 2(A/\pi)^{1/2}$	A = Basin area, L = basin length
5	Lamniscate	K	$K = (K^2 - 1)^{1/2}/K$ where $K = \pi L^2/A$	A = Basin area, L = basin length
6	Drainage density	D_d	$D_d = \varepsilon L$ (km/km^2)/A	L = Total length of stream, A = area of the basin
7	Drainage intensity	D_i	$D_i = F/D_d$	F = Stream frequency, D_d = drainage density

Conclusion

On the basis of morpho-mathematical analysis, it is concluded that Bharar river basin is elongated in shape and it is a fourth-order stream. Drainage density and stream frequency indicate coarse texture, low relief and rugged topography in the study area. The result of morpho-mathematical analysis is useful in water shed management and helpful in suggesting the artificial recharge structures in the study area.

Acknowledgements The author is thankful to the reviewer for their valuable suggestions. The author also thankful to University Grant Commission (U.G.C.) Central Regional Office, Bhopal, for financial assistance as Minor Research Project vide their sanction letter No. F-MS-3/104023/XII/14-15/CRO, Bhopal. Dated 20.02.2015.

References

Carlston CW (1963) Drainage density and stream flow. US Geol Surv Prof Paper 422-c:8

Chorley RJ (1957) Illustrating the laws of morphometry. Geol Magaz 94:14–150

Faniran A (1968) The index of drainage intensity a provisional new drainage factor. Aust J Sci 31:328–330

Greygory KJ, Walling DE (1968) The variation of drainage density with in a catchment. Inst Assoc Sci Hydrol Bull 13:61–68

Horton RE (1945) Erosional development of stream and their drainage basin: hydrophysical approach to quantitative morphology. Bull Geol Soc Am 56:275–370

Jain PK (1999) Morpho-mathematical analysis of upper Urmil river basin district chhatarpur-central India. Madhya Bharti J Phys Nat Sci 43:31–40 [Dr. H.S. Gour V.V. Sagar (M.P.)]
Miller VG (1953) A quantitative geomorphic study of drainage basin characteristic of mountain area. Technical Report No. 3, Columbia University
Schumm SA (1956) A evolution of drainage system and slope and bed land, New Jersey. Bull Geol Soc Am 67:597–646
Smith KG (1950) Standards for grading texture of erosional topography. Am J Sci 248:655–668
Strahler AN (1952) Hypsometric area attitude analysis of erosional topography. Bull Geol Soc Am 63:1142–1167
Strahler AN (1956) Quantitative slop analysis. Bull Geol Soc Am 67:571–596
Strahler AN (1957) Quantitative analysis of watershed geomorphology. Trans Am Geophys Union 38:193

Application of Principal Component Analysis for Grouping of Morphometric Parameters and Prioritization of Watershed

Sarita Gajbhiye Meshram and S. K. Sharma

Abstract Remote sensing (RS) and geographic information systems (GIS) techniques have become very important these days as they aid planners and decision makers to make effective and correct decisions and designs. Principal component analysis (PCA) involves a mathematical procedure that transforms a number of (possibly) correlated variables into a (smaller) number of uncorrelated variables. It reduces the dimensionality of the data set and identifies a new meaningful underlying variable (Gajbhiye and Sharma 2015a, b; Gajbhiye 2014; Gajbhiye 2015a, b). Morphometric analysis and prioritization of the sub-watersheds of Mohgaon River Catchment, Mandla district in Madhya Pradesh State, India, are carried out using RS and GIS techniques using satellite imageries and topographic maps. In this study, we apply PCA technique for redundancy of morphometric parameters and find the more effective parameters for prioritization of the watershed. The PCA produced more effective parameter form factor (R_f), drainage texture (T) and length of overland flow (L_o). Finally, the results of PCA reflect a good look on the prioritization of watershed.

Keywords Morphometric analysis · PCA · Watershed

Introduction

The watershed management planning highlights the management techniques to control erosion in the catchment/watershed area. Lifespan of a reservoir in case of a seasonal storage dams is greatly reduced due to soil erosion in the catchment area (Gajbhiye et al. 2014a, b, c). A watershed is a physically complex system. It

S. G. Meshram (✉)
K. Banerjee Centre of Atmospheric & Ocean Studies, IIDS, Nehru Science Centre, University of Allahabad, Allahabad 211002, Uttar Pradesh, India
e-mail: gajbhiyesarita@gmail.com

S. K. Sharma
Department of Soil and Water Engineering, J.N.K.V.V., Jabalpur, MP, India

V. P. Singh et al. (eds.), *Hydrologic Modeling*, Water Science and Technology Library 81, https://doi.org/10.1007/978-981-10-5801-1_31

consists of a number of Unit Source Areas (having approximately uniform properties), and Partial and Variable Source Areas each exhibiting a different response. The juxtaposition of different source areas of contrasting topography, rock types, and land use and soil characteristics results in areal variations in watershed processes and response. Every hydrologic design is therefore different because the physical properties often vary with site.

Soil erosion is one of the most serious environmental problems in the world today, as it threatens agricultural and natural environment (Tombul 2010). It is very distressing that at a time when agricultural efforts are focused on increasing food production, soil degradation is increasing worldwide. The problem is providing in most of the world's major agricultural regions, and the problem is growing incessantly as more marginal land is brought into cultivation and, in turn, production.

A geomorphological parameter directly or indirectly reflects almost the entire watershed-based causative factor affecting run-off and sediment loss. Geomorphological analysis provides quantitative description of the basin geometry to understand initial slope or inequalities in the rock hardness, structural controls, recent diastrophism, geological and geomorphic history of drainage basin (Strahler 1964; Pandey et al. 2011). In the absence of huge hydrological data, geomorphological parameters of watershed may be helpful in characterizing a watershed as geomorphological and climatic characteristics of a basin govern the hydrological response to a considerable extent.

Micro-watersheds can be ranked based on values of different geomorphological parameters. The highest value of F_s, L_o, D_d, T, R_r, R_h, S_a, and R_N was given a rating of 1, the next highest value was given a rating of 2 and so on as these geomorphological parameters generally show positive correlation with soil erosion. The lowest value was rated last in the series of numbers. For R_f, R_e, C_c and R_c, the watershed with their least value was given a rating of 1, next higher value was given a rating 2 and so on as these parameters show negative correlation with soil erosion (Biswas et al. 2002; Nookaratnam et al. 2005; Thakker and Dhiman 2007). Prioritization and morphometric analysis using remote sensing and GIS techniques have been attempted by number of researchers (Nautiyal 1994; Srivastava and Mitra 1995; Srivastava 1997; Nag 1998; Agarwal 1998; Biswas et al. 1999; Sreedevi et al. 2001, 2005; Gajbhiye and Mishra 2012; Gajbhiye et al. 2013a, b, c; Sharma et al. 2013a, b; Sharma et al. 2014a, b; Gajbhiye et al. 2015a, b, c), and all have concluded that remote sensing and GIS are powerful tools for studying basin morphometric and continuous monitoring.

Study Area

River Narmada is one of the major rivers with 41 tributaries flowing through central parts of India. It rises from Amarkantak plateau of Maikala range in Shahdol district in Madhya Pradesh at an elevation of about 1,059 m above mean sea level. The river

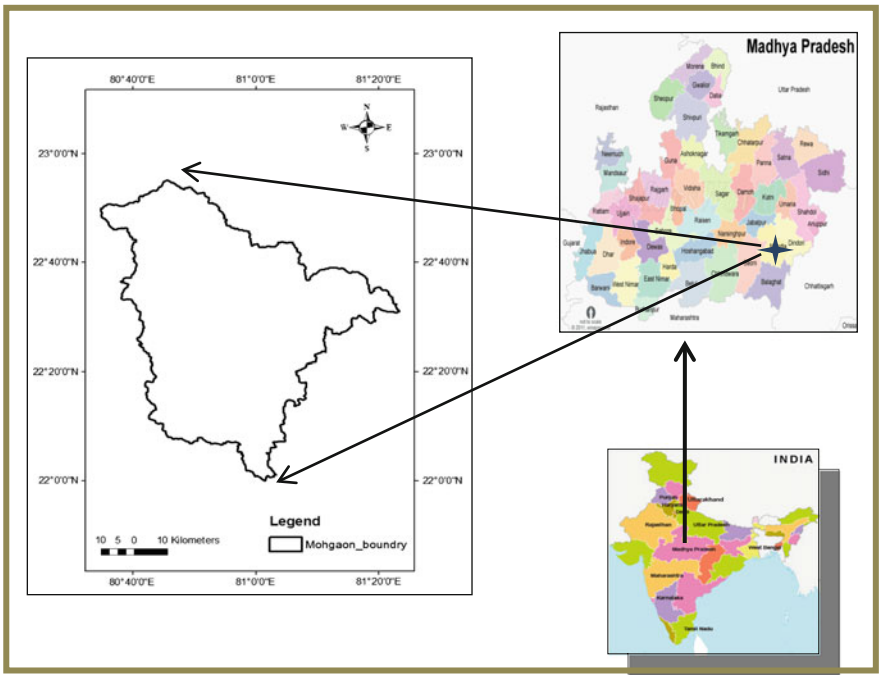

Fig. 1 Index map of the study area

travels a distance of 1,312 km before it joins to Gulf of Cambay in the Arabian Sea near Bharuch in Gujarat. The Burhner River rises in the Maikala range, south-east of Gwara village in the Mandla district of Madhya Pradesh at an elevation of about 900 m at north latitude 22° 32′ and east longitude 81° 22′. It flows in westerly direction for a total length of 177 km to join the Narmada near Manot. Its catchment area up to Mohgaon is about 3978 km^2 (Fig. 1). The elevation at Mohgaon gauging site drops to 509 m. Climate of the basin can be classified as sub-tropical and sub-humid with average annual rainfall of 1,547 mm. The evapotranspiration varies from 4 mm day in winter to 10 mm/day in summer. The catchment area comprises both flat and undulating lands covered with forest and cultivated lands. Soils are mainly red and yellow silty loam and silty clay loam. Forest and agricultural lands share nearly 58 and 42% of the catchment area, respectively.

Materials and Method

The map layers of drainage pattern along with stream order, watershed and sub-watershed boundaries and contours in the study area have been prepared in GIS environment using Arc GIS 9.3 software. The digital elevation model is obtained by

linear interpolation of contour layer which is digitized from the Survey of India topo sheets (scale 1:50,000). Various linear measurements such as area, perimeter, watershed length, drainage length and total relief (H) are calculated from the attributes table of map layers such as boundary layer, drainage layer, and digital elevation layer. With the help of these linear measurements, formula-based morphological parameters are computed for watersheds and sub-watersheds of the study area.

Principal Component Analysis: The geomorphic parameters are usually many times correlated. The correlation indicates that some of the information contained in one variable is also contained in some of the other remaining variables. The method of component analysis involves the rotation of coordinate axes to a new frame of reference in the total variable space—an orthogonal or uncorrelated transformation where each of the n original variables is describable in terms of the n new principal components. An important feature of the new components is that they account, in turn, for a maximum amount of variance of the variables. Principal component analysis is applied for all geomorphic parameters to calculate the correlation matrix and also to derive principal components. The first factor loading matrix and rotated factor loading matrix are used in this analysis.

Software Used: Arc view 3.1 power GIS software was used for creating, managing and generating different layer and maps. The Microsoft Excel was used for mathematical calculation (Gajbhiye and Mishra 2012).

Result and Discussions

Morphometric Analysis

Geomorphological parameters of sub-watersheds of Mohgaon watershed are presented in Table 1. It is evident from Table 1 that sub-watershed 1 is covering smallest (51.27 km^2) and MG 5 largest areas (631.75 km^2) among fifteen sub-watersheds of Mohgaon watershed.

The shape of the watershed governs the stream discharge and its flow hydrograph. Shape parameters considered in geomorphological analysis are form factor, elongation ratio and circulatory ratio (Table 1). The form factor, elongation ratio and circularity ratio of sub-watersheds of Mohgaon watershed show that all the sub-watersheds are more or less elongated in shape. Compactness of any watershed is expressed by compactness ratio. In Mohgaon watershed, it varies from 0.009 (MG 14) to 0.035 (MG 10).

Langbein (1947) recognized D_d as the significance factor determining the time travel by water within the basin and in case of sub-watersheds of Mohgaon watershed it varies between 2.418 km/km^2 (MG 1) and 3.357 km/km^2 (MG 8). The sub-watershed with high value of D_d indicates a well-developed network, which is conducive for quick disposal of run-off resulting in intense floods and also

Table 1 Geomorphological parameters of sub-watersheds of Mohgaon watershed

Sub-water shed	R_h	R_r	R_N	R_b	D_d	F_s	R_c	R_f	R_e	T	L_o	C_c	S_a	HI
MG 1	0.037	0.009	0.961	3.339	2.418	6.277	0.551	0.7	0.944	9.382	0.207	0.032	9.523	0.393
MG 2	0.016	0.004	1.298	5.019	3.091	7.854	0.435	0.584	0.863	28.542	0.162	0.008	13.253	0.413
MG 3	0.024	0.006	0.924	4.147	2.888	7.692	0.379	0.569	0.852	13.195	0.173	0.022	12.108	0.393
MG 4	0.023	0.005	1.014	3.869	3.17	8.058	0.483	0.702	0.946	18.324	0.158	0.016	9.797	0.5
MG 5	0.01	0.002	1.044	5.558	2.269	7.892	0.219	0.31	0.628	26.127	0.22	0.006	10.532	0.42
MG 6	0.011	0.003	1.107	4.234	2.914	7.835	0.362	0.332	0.65	27.554	0.172	0.007	11.843	0.5
MG 7	0.014	0.003	1.109	4.407	3.082	7.388	0.227	0.287	0.605	13.776	0.162	0.015	10.033	0.5
MG 8	0.01	0.002	1.276	3.951	3.357	8.016	0.268	0.376	0.692	26.151	0.149	0.007	7.558	0.557
MG 9	0.016	0.005	1.028	3.907	2.942	7.671	0.476	0.348	0.665	18.205	0.17	0.015	9.132	0.551
MG 10	0.034	0.008	0.909	3.306	3.247	7.623	0.484	0.72	0.958	10.376	0.154	0.035	6.461	0.561
MG 11	0.016	0.002	1.117	4.14	3.102	7.758	0.16	0.658	0.916	15.943	0.161	0.011	9.101	0.5
MG 12	0.015	0.005	0.849	3.759	3.144	7.637	0.462	0.356	0.674	15.095	0.159	0.019	9.586	0.375
MG 13	0.013	0.003	0.875	4.375	2.918	7.929	0.299	0.47	0.773	18.82	0.171	0.012	4.303	0.5
MG 14	0.012	0.003	0.98	4.624	3.266	8.053	0.353	0.563	0.847	24.382	0.153	0.009	9.002	0.443
MG 15	0.008	0.002	0.936	4.904	3.119	7.633	0.227	0.25	0.564	18.687	0.16	0.01	10.1	0.443

characterized by a region of weak subsurface materials, high relief and sparse vegetation (Gajbhiye et al. 2013b). In general, drainage density of the sub-watersheds suggests that sub-watershed 1 more impermeable material then the sub-watershed 8. Texture ratio (T) of sub-watersheds of Mohgaon watershed varies from 9.382 (MG 1) to 27.554 (MG 6). The values of R_h in the sub-watersheds varies from 0.008 (MG 15) to 0.037 (MG 1). Relative relief (R_r) varies from 0.002 (MG 15) to 0.009 (MG 1). Ruggedness number (R_N) expresses the roughness of sub-watersheds. In this case, R_N varies from 0.849 (MG 12) to 1.298 (MG 2). Therefore, MG 2 is more rough then the other fourteen sub-watersheds of Mohgaon watershed. Average slope of the sub-watersheds of Mohgaon watershed ranges between 4.303% (MG 13) and 13.253% (MG 2).

Intercorrelation among the Geomorphic Parameters

For obtaining the inter co-relationship among the geomorphic parameters, a correlation matrix is obtained using SPSS 14.0 Software. The correlation matrix of the fourteen geomorphic parameters of Mohgaon watershed (Table 2) reveals that strong correlations (correlation coefficient more than 0.9) exist between relief ratio (R_h) and relative relief (R_r); between R_h and C_c, S_a; between R_b and T; between D_d and L_o, C_c; between R_f and R_e. Also, good correlations (correlation coefficient more than 0.75) exist between R_h and R_f; between R_r and D_d; between D_d and R_r, F_s. Some more moderately correlated parameters (correlation coefficient more than 0.6) are R_h with R_e, T; R_r with R_N, S_a; R_N with R_c; R_b with C_c, S_a; F_s with C_c, R_c, R_e; R_c with C_c. It is very difficult at this stage to group the parameters into components and attach physical significance. Hence, in the next step, the principal component analysis has been applied to the correlation matrix.

Principal Component Analysis

The principle component analysis method was used to obtain the first factor loading matrix, and thereafter, the rotated loading matrix using orthogonal transformation. The results are shown in the following sections.

First Factor Loading Matrix

From the correlation matrix of 14 geomorphic parameters, the first unrotated factor loading matrix is obtained. It can be seen from Table 3 that the first three components whose Eigen values are greater than one, together accounting for about 92.22% of the total variance. It can be observed from Table 4a that the first

Table 2 Intercorrelation among the geomorphic parameters

	Rh	Rr	RN	Rb	Dd	Fs	Rc	Rf	Re	T	Lo	Cc	Sa	HI
Rh	1.000	0.92	−0.312	0.13	−0.188	−0.41	−0.02	0.766	0.749	−0.714	0.185	0.926	0.946	0.05
Rr	0.92	1.00	0.60	0.15	−0.80	−0.51	−0.08	−0.51	−0.50	0.17	0.83	−0.48	0.62	−0.02
RN	−0.312	0.60	1.000	0.74	0.165	−0.52	−0.61	−0.084	−0.075	0.615	−0.136	−0.528	−0.442	0.13
Rb	0.13	0.15	0.74	1.00	−0.35	−0.18	−0.33	−0.33	−0.33	0.90	0.29	−0.66	0.62	−0.04
Dd	−0.188	−0.80	0.165	−0.35	1.000	0.84	0.52	0.080	0.086	0.062	−0.994	−0.096	−0.259	−0.48
Fs	−0.41	−0.51	−0.52	−0.18	0.84	1.00	0.60	0.72	0.67	−0.28	−0.85	0.70	−0.22	−0.69
Rc	−0.02	−0.08	−0.61	−0.33	0.52	0.60	1.00	0.69	0.71	−0.31	−0.48	0.63	−0.49	−0.62
Rf	0.766	−0.51	−0.084	−0.33	0.080	0.72	0.69	1.000	0.998	−0.373	−0.072	0.559	0.549	−0.36
Re	0.749	−0.50	−0.075	−0.32	0.086	0.67	0.71	0.998	1.000	−0.349	−0.079	0.539	0.528	−0.30
T	−0.714	0.16	0.615	0.90	0.062	−0.27	−0.30	−0.373	−0.349	1.000	−0.033	−0.860	−0.823	0.10
Lo	0.185	0.83	−0.136	0.28	−0.994	−0.84	−0.48	−0.072	−0.079	−0.033	1.000	0.088	0.248	0.46
Cc	0.926	−0.45	−0.528	−0.65	−0.096	0.69	0.62	0.559	0.539	−0.860	0.088	1.000	0.966	−0.54
Sa	0.946	0.62	−0.442	0.61	−0.259	−0.22	−0.48	0.549	0.528	−0.823	0.248	0.966	1.000	−0.05
HI	0.04	−0.01	0.13	−0.03	−0.48	−0.68	−0.61	−0.36	−0.30	0.10	0.46	−0.54	−0.05	1.00

Table 3 Extraction of the component

Component	Initial eigenvalues			Extraction sums of squared loadings			Rotation sums of squared loadings		
	Total	% of variance	Cumulative (%)	Total	% of variance	Cumulative (%)	Total	% of variance	Cumulative (%)
1	4.817	53.522	53.522	4.817	53.522	53.522	3.129	34.767	34.767
2	2.139	23.771	77.293	2.139	23.771	77.293	3.094	34.374	69.141
3	1.344	14.935	92.229	1.344	14.935	92.229	2.078	23.088	92.229
4	0.521	5.790	98.019						
5	0.154	1.706	99.725						
6	0.014	0.161	99.885						
7	0.006	0.067	99.952						
8	0.004	0.040	99.992						
9	0.001	0.008	100.000						
10	00	00	100.000						
11	00	00	100.000						
12	00	00	100.000						
13	00	00	100.000						
14	00	00	100.000						

Table 4 (a) First factor loading matrix; (b) rotated factor loading matrix

(a)			
Component matrix[a]			
	Component		
	1	2	3
R_h	0.97	0.027	0.149
R_r	0.703	0.156	0.676
R_N	−0.498	0.257	0.621
R_b	0.557	0.584	−0.507
D_d	−0.184	0.931	−0.303
F_s	−0.782	0.505	−0.068
R_c	−0.669	0.366	0.461
R_f	0.745	0.403	0.48
R_e	0.727	0.412	0.492
T	−0.824	0.041	0.453
L_o	0.174	−0.924	0.334
C_c	0.95	−0.002	−0.217
S_a	0.948	−0.136	−0.09
HI	0.422	−0.721	−0.214
(b)			
Rotated component matrix[b]			
	Component		
	1	2	3
R_h	0.776	0.576	0.172
R_r	−0.132	0.57	0.127
R_N	0.132	−0.824	−0.068
R_b	−0.069	0.012	0.451
D_d	0.028	−0.087	−0.992
F_s	0.336	−0.412	−0.046
R_c	0.016	0.053	−0.355
R_f	**0.962**	0.124	−0.077
R_e	0.961	0.102	−0.083
T	−0.278	**−0.899**	0.018
L_o	−0.014	0.058	**0.996**
C_c	0.526	0.819	0.055
S_a	0.553	0.754	0.226
HI	−0.308	−0.057	−0.143

[a]First factor loading matrix
[b]Rotated factor loading matrix

component is strongly correlated (more than 0.90) with R_h, C_c and S_a and correlated satisfactorily (more than 0.75) with F_s and T, and moderately (loading more than 0.60) with R_c, R_f and R_e. It is observed that (Table 4a) some parameters are highly correlated with some components, some moderately, and some parameters do not

correlate with any component. Thus, at this stage, it is difficult to identify a physically significant component. It is necessary to rotate the first factor loading matrix to get better correlation.

Rotation of First Factor Loading Matrix

The rotated factor loading matrix is obtained by post-multiplying the transformation matrix with the selected component of first factor loading matrix. It can be observed from Table 4b that the first component is strongly correlated with R_f, second component is strongly correlated with T, and third component is strongly correlated with L_o.

Conclusion

Geomorphological parameters reveal average hydrological and geological conditions at watershed scale of the study area. For planning, development and management of watersheds for their sustainable and judicious use, planning is carried out at sub-watershed level. Mohgoan watershed was divided into a number of sub-watersheds for better understanding of hydrological behaviour and influence of geological setting on the drainage evolution pattern.

Among the geomorphological parameters, shape parameters indicate that Mohgaon less elongated shape. In general, shape of the basin affects the stream flow hydrographs and peak flows. Elongated shape suggests lower peak flows of longer duration, whereas circular shape indicates the basin will have high peak flows of shorter duration. Drainage parameters show that the geomorphic control is more than the structural control on drainage network. Slope parameters indicate that Mohgaon has more sloping topography. The PCA produced more effective parameter form factor (R_f), drainage texture (T) and length of overland flow (L_o). Finally, the results of PCA reflect a good look on the prioritization of watershed.

References

Agarwal CS (1998) Study of drainage pattern through Aerial data in Naugarh area of Varanasi District, U.P. J Indian Soc Rem Sens 26(4):168–175

Biswas S, Sudhakar S, Desai VR (1999) Prioritisation of sub watersheds based on morphometric analysis of drainage basin-aremote sensing and GIS approach. J Indian Soc Remote Sens 27:155–166

Biswas S, Sudhakar S, Desai VR (2002) Remote sensing and geographic information system based approach for watershed conservation. J Surv Eng 128(3):108–124

Gajbhiye S (2014) Estimation of Rainfall generated runoff using RS and GIS. LAMBERT Academic Publishing, Germany. ISBN 978-3-659-61084-4

Gajbhiye S (2015a) Estimation of surface runoff using remote sensing and geographical information system. Int J U-and E-Serv Sci Technol 8(4):118–122. ISSN: 2005-4246

Gajbhiye S (2015b) Morphometric analysis of a Shakkar River catchment using RS and GIS. Int J U-and E-Serv Sci Technol 8(2):11–24. ISSN: 2005-4246

Gajbhiye S, Mishra SK (2012) Application of NRSC-SCS curve number model in runoff estimation using RS & GIS. IEEE conference, Nagapattinam, Tamil Nadu, March 30–31. pp 346–352 ISBN: 978-81-909042-2-3

Gajbhiye S, Mishra SK, Pandey A (2013a) A procedure for determination of design runoff curve number for Bamhani Watershed. IEEE Conference, Bombay, 1(9):23–25

Gajbhiye S, Mishra SK, Pandey A (2013b) Prioritization of Shakkar River catchment through morphometric analysis using remote sensing and GIS techniques. IEEE Conference, Kanyakumari, 4(2):129–142

Gajbhiye S, Mishra SK, Pandey A (2013c) Effect of seasonal/monthly variation on runoff curve number for selected watersheds of Narmada Basin. Int J Environ Sci 3(6):2019–2030

Gajbhiye S, Sharma SK (2015a) Prioritization of watershed through morphometric parameters: a PCA based approach. Appl Water Sci 1–15. doi:10.1007/s13201-015-0332-9

Gajbhiye S, Sharma SK (2015b) Applicability of remote sensing and GIS approach for prioritization of watershed through sediment yield index. Int J Sci Innovative Eng Technol (1). ISBN: 978-81-904760-6-5

Gajbhiye S, Sharma SK, Meshram C (2014a) Prioritization of Watershed through sediment yield index using RS and GIS approach. Int J u-and e-Serv Sci Technol 7(6):47–60. ISSN: 2005-4246

Gajbhiye S, Mishra SK, Pandey P (2014b) Hypsometric analysis of Shakkar River catchment through geographical information system. J Geol Soc India (SCI-IF 0.596) 84(2):192–196. ISSN: 0974-6889

Gajbhiye S, Mishra SK, Pandey P (2014c) Prioritizing erosion-prone area through morphometric analysis: an RS and GIS perspective. Appl Water Sci 4(1):51–61. ISSN: 2190-5495

Gajbhiye S, Sharma SK, Tignath S (2015a) Application of remote sensing and geographical information system for generation of runoff curve number. Appl Water Sci 1–7. doi:10.1007/s13201-015-0350-7

Gajbhiye S, Sharma SK, Awasthi MK (2015b) Application of principal components analysis for interpretation and grouping of water quality parameters. Int J Hybrid Inf Technol 8(4):89–96. ISSN: 1738-9968

Gajbhiye S, Sharma SK, Tignath S, Mishra SK (2015c) Development of a geomorphological erosion index for Shakkar Watershed. Geol Soc India 86(3):361–370 (SCI-IF 0.596) ISSN: 0016-7622

Langbein WB (1947) Topographic characteristics of drainage basins.US Geol. Survey Water Supply Pap 986(C):157–159

Nag SK (1998) Morphometric analysis using remote sensing techniques in the Chaka sub-basin Purulia district, West Bengal. J Indian Soc Remot Sens 26:69–76

Nautiyal MD (1994) Morphometric analysis of a drainage basin using arial photographs: a case study of Khairkuli basin District Deharadun. J Indian Soc Remote Sens 22(4):251–262

Nookaratnam K, Srivastava YK, Venkateswa Rao V, Amminedu E, Murthy KSR (2005) Check dam positioning by prioritization of micro watersheds using SYI model and morphometric analysis: remote sensing and GIS perspective. J Indian Soc Remote Sens 33(1):25–28

Pandey A, Chowdhary VM, Mal BC, Dabral PP (2011) Remote sensing and GIS for identification of suitable sites for soil and water conservation structures. Land Degrad Dev 22(3):359–372

Sharma SK, Tignath S, Gajbhiye S, Patil R (2013a) Use of geographical information system in hypsometric analysis of Kanhiya Nala Watershed. Int J Remote Sens Geosci (IJRSG) 2(3):30–35. ISSN: 2319-3484

Sharma SK, Gajbhiye S, Tignath S (2013b) Application of principal component analysis in grouping geomorphic parameters of Uttela Watershed for hydrological modelling. Int J Remote Sens Geosci (IJRSG) 2(6):63–70. ISSN: 2319-3484

Sharma SK, Yadav A, Gajbhiye S (2014a) Remote sensing and GIS approach for prioritization of watershed. LAMBERT Academic Publishing, Germany, ISBN 978-3-659-53529-1

Sharma SK, Gajbhiye S, Tignath S (2014b) Application of principal component analysis in grouping geomorphic parameters of a watershed for hydrological modelling. Appl Water Sci 5 (1):89–96. ISSN: 2190-5495

Srivastava VK, Mitra D (1995) Study of drainage pattern of ranigang coalfield (Burdwan District) as observed on Landsat-TM/IRS LISS-III imagery. J Indian Soc Rem Sens 23(4):225–235

Sreedevi PD, Srinivasulu S, Keshva RK (2001) Hydro geomorphological and groundwater prospects of the Pageru River basin by using remote sensing data. Environ Geol 40(8): 1088–1094

Sreedevi PD, Subrahmanyam K, Shakeel A (2005) The significance of morphometric analysis for obtaining groundwater potential zones in a structurally controlled terrain. Environ Geol 47 (3):412–420

Srivastava VK (1997) Study of drainage pattern of Jharia Coalfield (Bihar), India, through remote sensing technology. J Indian Soc Rem Sens 25(1):41–46

Strahler AN (1964) Quantitative geomorphology of drainage basins and channel networks. Section 4–II. In: Chow VT (ed) Handbook of applied hydrology. McGraw-Hill, pp 4–39

Thakker AK, Dhiman SD (2007) Morphometric analysis and prioritization of mini-watersheds in Mohr watershed, Gujrat using remote sensing and GIS techniques. J Indian Soc Rem Sen 35 (4):313–321

Tombul M (2010) Prediction of erosion and sedimentation by runoff in kurukavak creek basin by the WEPP model. In: Integrated water resources management Karlsruhe 2010. International conference, 24–25 November 2010; Conference proceedings. KIT Scientific Publishing, p 315

Velocity Distribution in Vortex Chamber at High Water Abstraction Ratio

Mohammad Athar and Shivani Srotriya

Abstract Present paper deals with the results of the experimental investigation regarding the velocity distribution inside the vortex chamber-type sediment extractor at high water abstraction ratio. Data are collected in the laboratory on a vortex chamber. A programmable electromagnetic shunt (P.E.M.S.) flow meter is used to measure the velocity components along tangential and radial directions at well-defined nodal points inside the chamber. Graphs for tangential and radial velocity distributions are plotted at various depths along radius of the chamber for highest water abstraction ratio (17%). It is found that velocity distribution throughout the chamber is not uniform due to unsymmetrical positions of inlet, outlet channels, and under flow outlet. In some part of the chamber, it follows the law of Rankine vortex-type velocity distribution.

Keywords Velocity distribution · Vortex chamber · Rankine vortex
Water abstraction ratio · Tangential and radial velocities

Symbols

R_T	Radius of the vortex chamber
r	Radial spacing
r/R_T	Dimensionless radial spacing
Q_i	Discharge in the inlet channel
Q_u	Discharge in the overflow outlet
Q_u/Q_i	Discharge ratio or water abstraction ratio
z	Vertical spacing
z/Rt	Depth ratio
V_i	Velocity at the inlet of the vortex chamber

M. Athar (✉) · S. Srotriya
Department of Civil Engineering, A.M.U. Aligarh, Aligarh, India
e-mail: matharalam58@gmail.com

V. P. Singh et al. (eds.), *Hydrologic Modeling*, Water Science and Technology Library 81, https://doi.org/10.1007/978-981-10-5801-1_32

v_r Radial velocity component
vt Tangential velocity component
θ Angular spacing in degrees

Introduction

A vortex chamber is a fluidic device, which makes use of the vortices of the flow in a chamber or a basin for separation of sediment particles from the flow. A higher velocity flow is introduced tangentially into a cylindrical chamber/basin having an orifice/outlet at the center of its bottom. This gives rise to combined vortex conditions (Rankine vortex) with forced vortex near the orifice at the center and free vortex in the outer region toward the periphery. Sediment particles being heavier than water are forced toward the periphery of the chamber due to centrifugal force imparted by vortex flow to them. The secondary flow resulting due to combined vortex causes the fluid layers near the chamber periphery to move toward the outlet orifice at the center along the chamber bottom, as a result the sediment particles from the chamber periphery move with the flow along a helicoidal path toward the orifice, thereby obtaining a settling length which is longer than basin dimensions. Thus, relative higher inflow velocities can be allowed into the chamber. The sediment reaching the center of the chamber can be flushed out through the orifice continuously. Relatively, sediment-free water is allowed to leave the chamber through an outlet channel/pipe taking off from the chamber at a location of relatively higher elevation.

It was found by Athar et al. (2001) and also many other investigators (2, 3, 4, and 5) that sediment removal efficiency of a vortex chamber is increasing with increase of water abstraction ratio from 5 to 13%, but with further increase in water abstraction ratio there is no considerable increase in the efficiency. The main reason was that at very high ratio air core at the center of the orifice out let is formed which prevented the entry of the sediment into the underflow outlet channel.

Brief Review

The flow mechanism in a vortex chamber sediment extractor is similar to the Rankine vortex in which a forced vortex core is surrounded by an irrotational or free vortex zone (Julien 1985a, b). Several investigators for investigating the flow structure and similarity in vortex chambers have conducted experimental studies. Notable amongst these includes those by Anwar (1965), Cecen (1977), Daggett (1974), Julien (1985a, b), Odgaard (1986), Vasistas et al. (1989), Hite and Mih (1994), Mujib et al. (2008, 2012). The findings of above studies are mentioned in

Table 1 Name of investigators with their study

S. No.	Investigator	Related study
1	Anwar (1965)	Derived the expression for tangential velocity and water surface elevation in a vortex flow at the entrance of an outlet pipe
2	Cecen (1977)	Made investigations for the flow pattern in a vortex chamber-type-settling basin using the dye injection method
3	Rea (1984)	Studied the secondary flows in a vortex chamber
4	Julien (1985a, b)	Studied the variation of concentration of fine sediment particles in Rankine vortex system
5	Mashauri (1986)	Made a detailed investigation about the particle trajectory and distribution of tangential and radial velocities in a vortex-type-settling basin
6	Vatistas (1989)	Studied the variation of concentration of fine sediment particles in Rankine vortex system
7	Hite and Mih (1994)	Studied the flow structures by taking the data on radial, tangential, and vertical velocities in a sand funnel
8	Mujib et al. (2008, 2012)	Studied the flow structures by taking the data on radial, tangential, and vertical velocities in a vortex settling basins with tangential inlet and outlet

Table 1. A brief review presented herein indicates that most of the investigators mainly observed the tangential velocity inside the vortex chamber. A smaller number of studies are, however, available in which both the radial and tangential velocities were measured for studying the flow pattern in the vortex chamber. Hence, in present paper the emphasis is given to collect more and more data on velocity distribution for radial as well as tangential directions.

The flow mechanism inside the vortex chamber-type sediment extractor is very complicated due to the effect of the inflow, underflow, and overflow conditions. Since the variation of sediment concentration within the chamber of a vortex extractor is greatly affected by variations in the velocity components in vertical, radial, and tangential directions of the chamber, a complete knowledge about the flow field inside the chamber is, therefore, necessary in modeling of the vortex chamber-type sediment extractor for its effectiveness in removing the sediment from the flow. This paper is intended to present the flow field structure in the vortex chamber-type sediment extractor at high water abstraction ratio by laboratory measurements.

Theoretical Treatment

It is evident from the extensive literature review that the expressions for velocity distribution in the vortex chambers have been derived by assuming axisymmetric flows and by approximating the turbulence by mixing length model; it is not easy to model turbulence even in simplest of the flow condition, whereas the vortex flow

that occurs in the chamber of an extractor is quite complex. Keeping these points in mind, it is decided to derive the velocity distributions in the chambers of the extractors studied herein by making use of experimental observations.

Following functional relationships are assumed to hold good for the radial and tangential velocity components.

$$v_r = f_1(V_i, R_T, r, \theta, Q_u, Q_i) \tag{1a}$$

$$vt = f_2(V_i, R_T, r, \theta, Q_u, Q_i). \tag{1b}$$

Here, v_r and vt are the radial and tangential velocities, R_T is the radius of the chamber, r is the radial spacing, Q_u is the underflow discharge, and Q_i is discharge in the inlet channel. Carrying dimensional analysis for above variables using Bakingham's pi-theorem method, following equations in terms of nondimensional variables are obtained as follows.

$$v_r/V_i = \phi_1(Q_u/Q_i, \theta, r/R_T) \tag{2a}$$

$$vt/V_i = \phi_2(Q_u/Q_i, \theta, r/R_T). \tag{2b}$$

Experimental Program

The experimental work being reported herein was part of major program on study of vortex chamber-type sediment extractor. Details on these are available in Athar (2001). These experiments were conducted in the hydraulics laboratory of the University of Roorkee, India (presently I.I.T. Roorkee).

Circular cylinder vortex chamber-type extractor having internal diameter equal to 1.0 m with geometric configuration as shown in Fig. 1a, b is used. The vortex chamber is made of 6-mm-thick perspex sheet. The bottom of the chamber is made of painted steel, and it is given to aslope of 1:10 toward the center to facilitate the sediment movement toward the outlet orifice at the center. The internal diameter and over all height of the chamber are kept as 1 and 0.45 m, respectively. These dimensions are chosen on the basis of the space and discharge available in the laboratory and also considering the investigations of Sullivan (1972), Cecen and Bayazit (1975), Salakhov (1975), Mashauri (1986), Paul et al. (1991). Circular railing is provided along the top of the vortex chamber for supporting the equipment used in the measurement. A sharp-edged orifice with internal diameter of 0.10 m is provided at the center of the chamber. The orifice is further connected to an underflow outlet pipe with diameter equal 0.10 m for flushing out the sediment collected at the center of the vortex chamber. A gate valve is provided at the outlet of this pipe to regulate the flow through it.

The inlet channel used in the extractor is 6.5-m long, 0.20-m wide, and 0.25-m deep and has adjustable slope. The inlet channel bed and walls are made up of

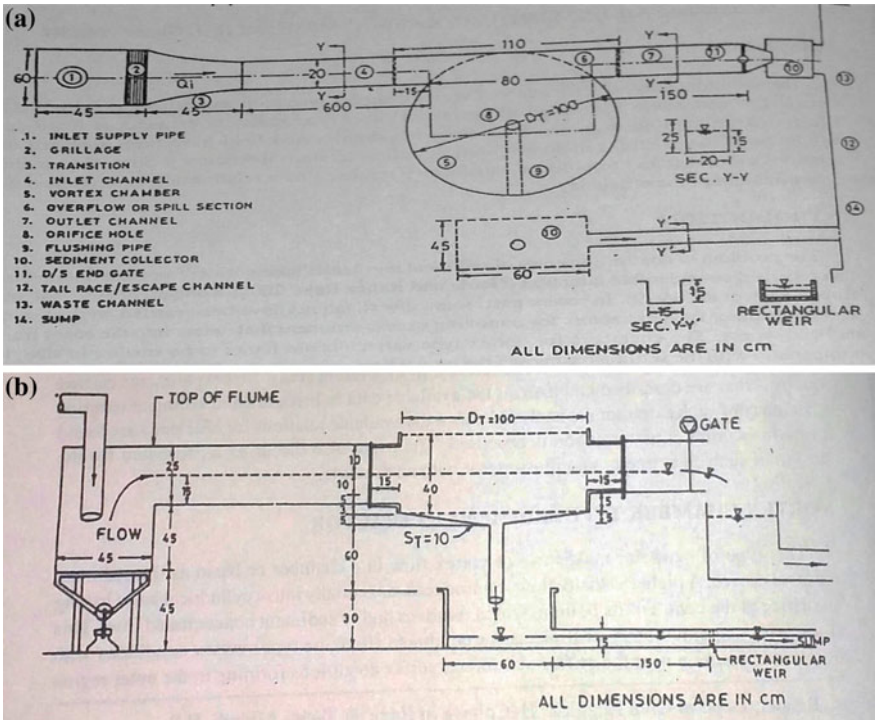

Fig. 1 **a** Plan of experimental setup, **b** plan of experimental setup

painted steel. The outflow outlet channel provided in the extractor is 2.5-m long, 0.20-m wide, and 0.25-m deep and has adjustable slope. Circular steel pipes are used as the railing in the inlet and the overflow outlet channels, and they are made parallel to the channel beds by adjusting the railing screws. The straight inlet channel joined the vortex chamber tangentially at its one side. The straight outlet channel was taken off tangentially to the chamber but from the point that was diametrically opposite to the junction of the inlet channel with the vortex chamber (see Fig. 1a). The detailed dimensions of the extractor are shown in Fig. 1b. The extractor received water supply from a constant head water supply tank. A pre-calibrated sharp-edged circular orifice meter was used to regulate the discharge into the inlet channel. Three half brick size grill walls and a floating wooden wave suppressor were provided at the entrance of the inlet flume for breaking large eddies and damping the disturbances at the free surface. The discharge of overflow outlet channel was measured by using a pre-calibrated sharp-edged rectangular weir. Outflow from the overflow outlet channel was collected in a rectangular tank having sides and bottom made of the fine wire mesh. This tank had a hopper for collecting the flow at the downstream of the channel. Outflow of this tank joined a sump provided at the downstream most end.

Electromagnetic Liquid Velocity Meter (PEMS)

A programmable electromagnetic liquid velocity meter (Fig. 2) manufactured in the Delft Hydraulics Laboratory is used for measuring the velocity components of the flow in the vortex chamber. This instrument consists of a disk-type probe, which is placed vertically in the flow. The P.E.M.S. employs Faraday's induction law for measurement of velocity of a conductive liquid moving through the magnetic field. The magnetic field is introduced by a pulsed current through a small coil inside the body of the sensor. Two pairs of diametrically opposed platinum electrodes available on the disk of the P.E.M.S. sense the Faraday-induced voltages produced by the flow past the sensor. This enables the instrument to simultaneously measure the two velocity components of the flow in the directions perpendicular to each other and in the plane of the disk containing sensors. For taking measurements, the P.E.M.S. probe is held in vertical position so that the pairs of platinum electrodes and the disk containing them occupy position in horizontal plane. The electrodes are rotated in the horizontal plane so that they produce velocity measurements in the directions tangential and radial to the flow. Mean values of the velocity components at 20 s interval are selected for use herein as the mean over still larger time is not found to be any different. Measurements taken by the instrument are displaced on its LCD display panel where from they could be noted for further use.

Measurements by P.E.M.S.

The chamber of the extractor is first divided into eight sectors, i.e., angular segments. These all eight sectors are further subdivided into five annular segments (Fig. 2) thus forming about 40 nodal points in a horizontal planes. Further 240 nodal points were assumed for taking observations for velocities assuming five z values (depths measured from bottom). The P.E.M.S. probe is fixed with a vertical gauge, and the whole assembly is mounted on the horizontal circular railing fixed

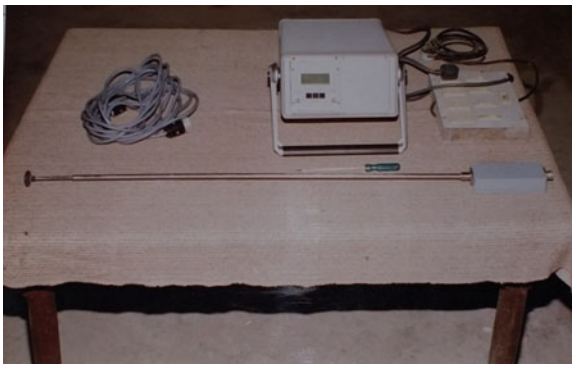

Fig. 2 PEMS meter

over the vortex chamber. The P.E.M.S. probe could be moved horizontally as well as vertically up and down. For measuring the velocity components, the P.E.M.S. moved to five different levels along the nodal points thus created. Electrodes in the P.E.M.S. probe are so oriented that the P.E.M.S. measured the velocity components in radial and tangential directions at the point where it is fixed.

The probe is also connected with the P.E.M.S. main cassette, which directly displays the observations. Before starting actual observations, the probe is generally kept in still water for about half an hour for zero setting of the instruments. The steady flow is established in the extractor by allowing known inflow and operating tailgate and outlet valve for establishing known underflow-flushing discharge. Fixing the P.E.M.S. probe at desired locations and orienting its probe in requisite directions measured radial and tangential velocities.

Detail measurements on velocity components for the vortex chamber are made. The range of the data collected in the present study is given in Table 2.

Analysis of Data

Velocity Distributions

Data for the velocity components along radial and tangential directions at various nodal points (240) within the vortex chambers were measured simultaneously using 2D-electromagnetic liquid velocity meter. Nondimensional velocity components, i.e., Vt (defined as vt/V_i) and V_r (defined as v_r/V_i) for different z values were plotted against nondimensional radial spacing r/R_T along each of the chamber diameter marked in Fig. 3 for all the runs. Many graphs for tangential and radial velocity distributions were obtained along various radius of the chamber.

1. Variations of Tangential and Radial Velocities along Vertical Direction

Figure 4 shows the variations of tangential and radial velocities along vertical direction. It is clear that these velocities are varying in vertical direction but effect is less pronounced.

Table 2 Range of data and dimensionless numbers used in present investigation

S. No.	Parameter	Symbol	Unit	Range
1	Inlet discharge	Q_i	m^3/s	$8 * 10^{-3}$–$22 * 10^{-3}$
2	Underflow discharge	Q_u	m^3/s	$0.696 * 10^{-3}$–$3.42 * 10^{-3}$
4	Radius of the chamber	R_T	m	0.50
5	Inlet flow depth	h_i	m	0.10–0.19
6	Flow depth at periphery	h_p	m	0.15–0.28
8	Water abstraction ratio	Q_u/Q_i	%	8–17
9	Angular spacing	θ	Degrees	0–315
10	Radial spacing	r/R_T	–	0.10–1.00

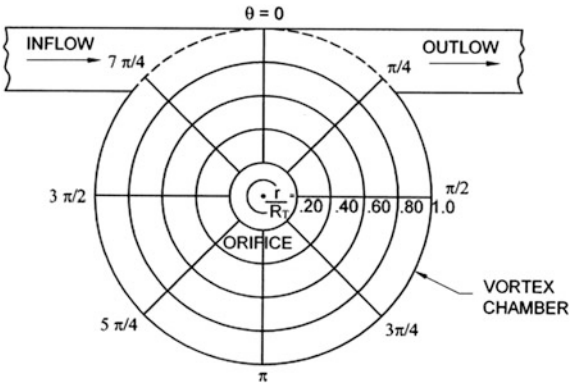

Fig. 3 Sectorization of vortex chamber

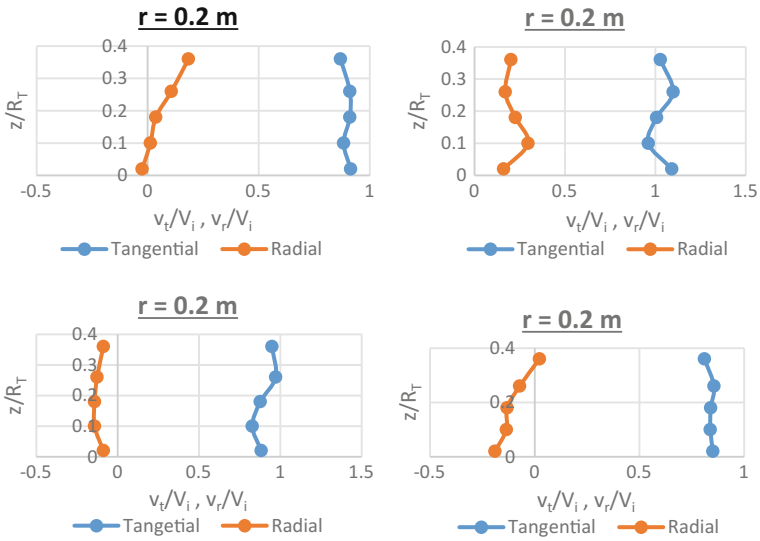

Fig. 4 Variation tangential and radial velocities along vertical at various r and θ

2. Variations of Tangential Velocities along Radial Direction

Figures 5, 6, 7, 8, 9, 10, 11, and 12 show the variations of tangential velocities along radial direction.

Almost from all these plots, it is clear that in many parts (θ values) tangential velocity compared well with that of the Rankine vortex (Julien 1985a; Vatistas et al. 1986; Mih et al. 1994). In many cases, the velocities values were not found ($r \leq 0.2$). The main reason was that at very high water abstraction ratio, air core was formed due to which depth of water was very small along the radius near the center of the chamber.

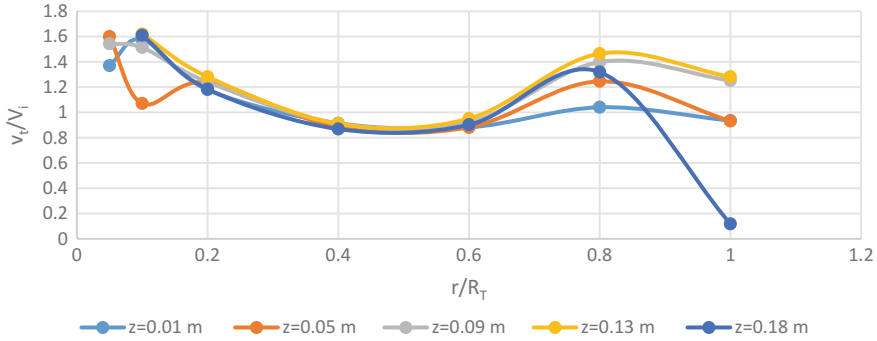

Fig. 5 Variation of tangential velocity along radius 0–1 ($\theta = 0°$)

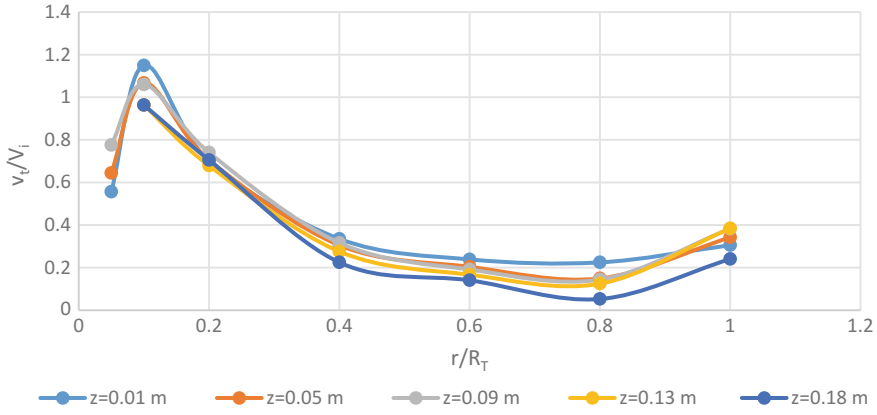

Fig. 6 Variation of tangential velocity along radius 0–2 ($\theta = 45°$)

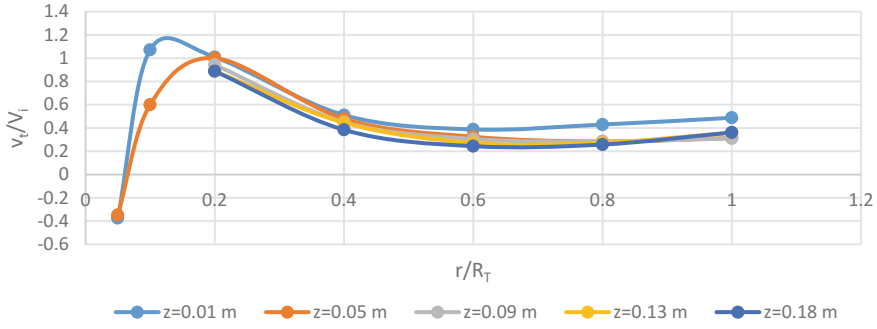

Fig. 7 Variation of tangential velocity along radius 0–3 ($\theta = 90°$)

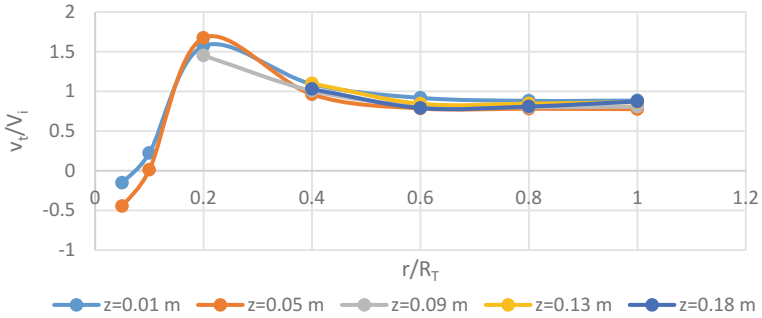

Fig. 8 Variation of tangential velocity along radius 0–4 (θ = 135°)

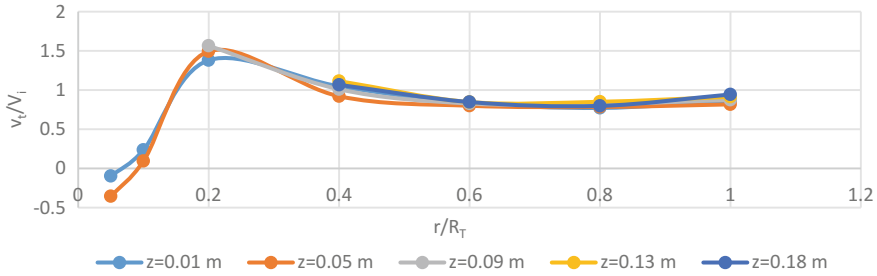

Fig. 9 Variation of tangential velocity along radius 0–5 (θ = 180°)

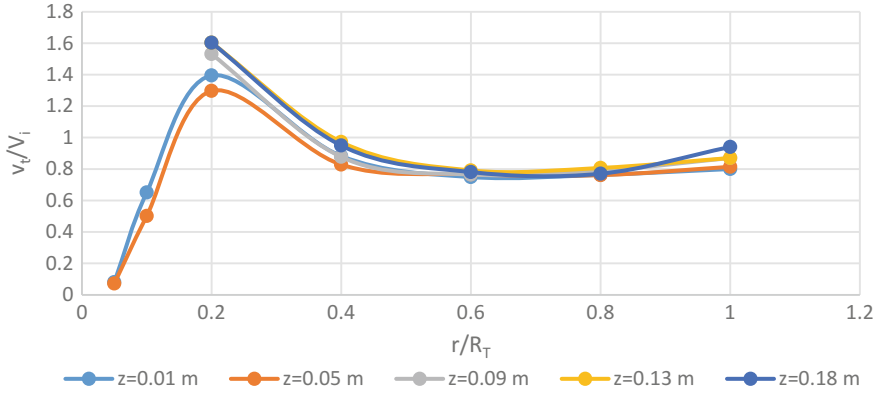

Fig. 10 Variation of tangential velocity along radius 0–6 (θ = 225°)

3. Variation of Radial Velocities in Radial Direction

Figures 13, 14, 15, 16, 17, 18, 19, and 20 show the variations of radial velocities along radial direction.

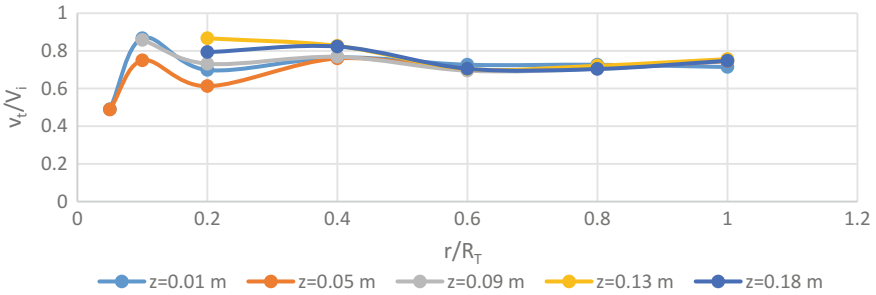

Fig. 11 Variation of tangential velocity along radius 0–7 (θ = 270°)

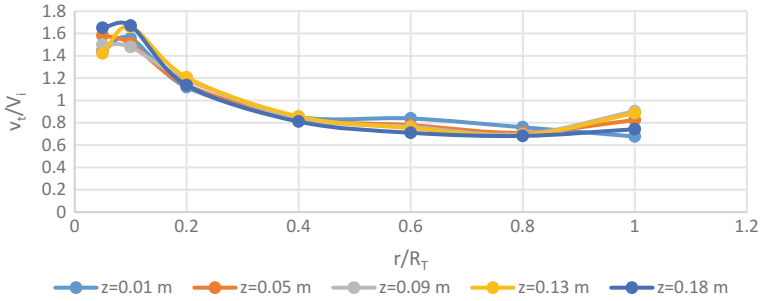

Fig. 12 Variation of tangential velocity along radius 0–8 (θ = 315°)

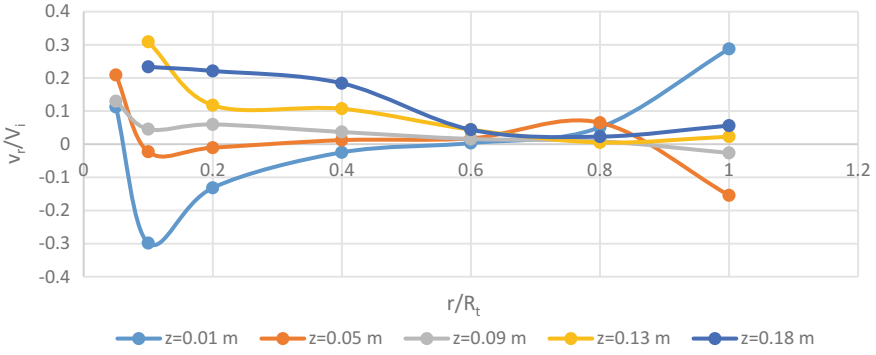

Fig. 13 Variation of radial velocity along radius 0–1 (θ = 0°)

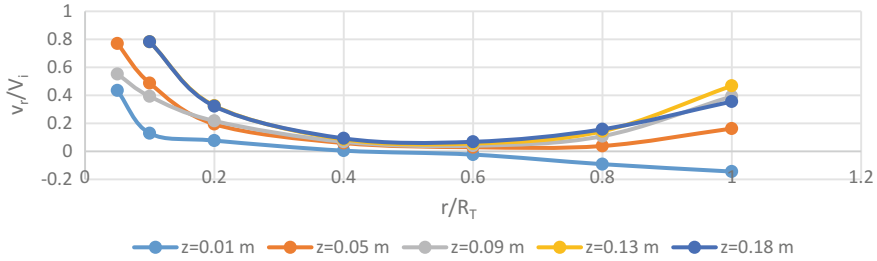

Fig. 14 Variation of radial velocity along radius 0–2 ($\theta = 45°$)

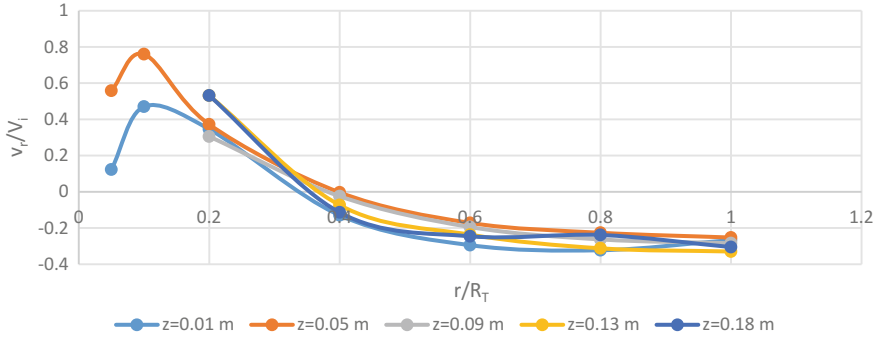

Fig. 15 Variation of radial velocity along radius 0–3 ($\theta = 90°$)

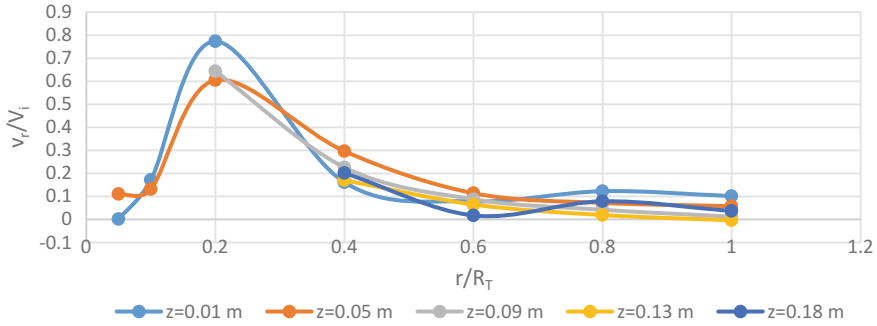

Fig. 16 Variation of radial velocity along radius 0–4 ($\theta = 135°$)

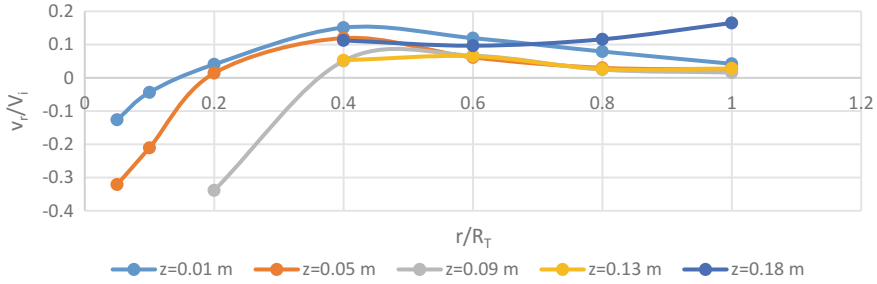

Fig. 17 Variation of radial velocity along radius 0–5 (θ = 180°)

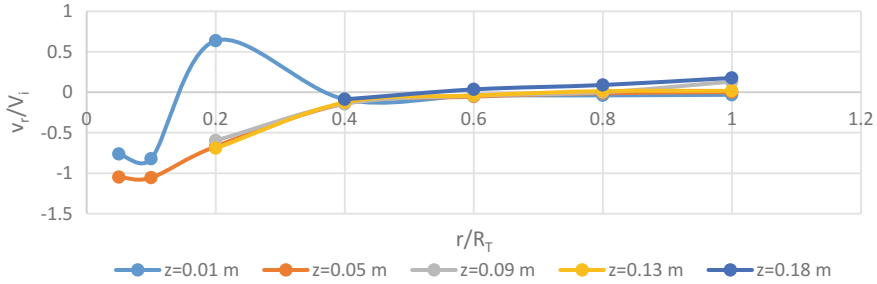

Fig. 18 Variation of radial velocity along radius 0–6 (θ = 225°)

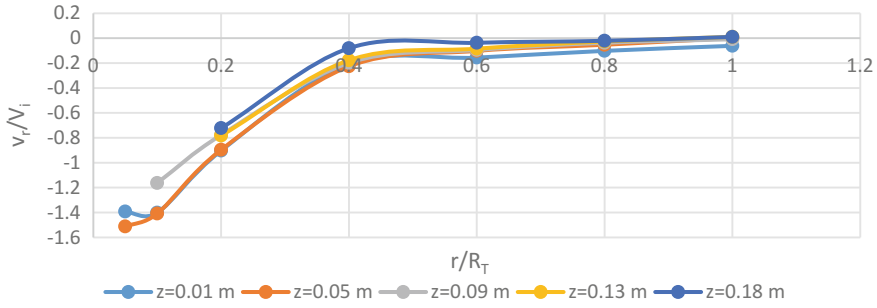

Fig. 19 Variation of radial velocity along radius 0–7 (θ = 270°)

It is found from all above plots that in some segment radial velocity also follows Rankine law. But in most of the other cases, the variation does not follow this law. It is also found that negative values of radial velocities were also obtained.

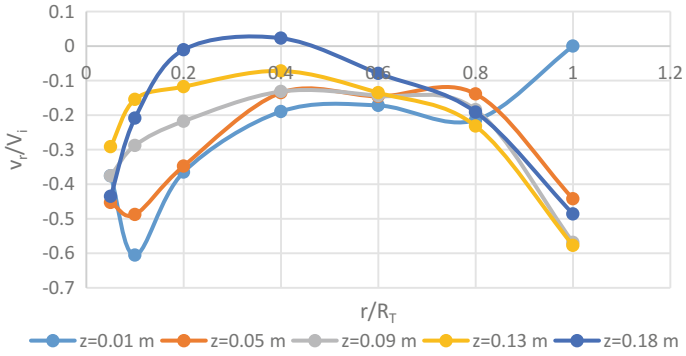

Fig. 20 Variation of radial velocity along radius 0–8 (θ = 315°)

Conclusions

Following conclusions are made:

1. Within the vortex chamber, the velocities in tangential and radial directions are found to vary along vertical direction but the effect is less pronounced.
2. Flow patterns are found to be different in the different segments of the vortex chamber. Segments of vortex chamber having flow pattern similar to that Rankine vortex extended only up to half diameter length of the vortex chambers.
3. Likewise tangential velocities and the radial velocities seem to follow Rankine vortex law in some segment of the chamber.

References

Ansari MA, Athar M (2012) Experimental study of flow structure inside vortex settling basin. In: Proceeding of national conference on hydraulics, water resources, coastal and environmental engineering (HYDRO-2012), Civil Engineering, Department, IIT Bombay, India, p 69

Anwar HO (1965) Flow in a free vortex. Water Power 153–161

Athar M (2001) Study of vortex chamber type sediment extractor. Ph.D. Thesis, presented for the award of the Degree of Doctor of Phelosphy, I.I.T. Roorkee

Athar M (2007) Experimental studies of flow mechanics inside the vortex chamber type sediment extractors. Paper accepted and due for the publication in the September Volume of the Journal of Indian Water Resources Society (IWRS), I.I.T. Roorkee, Sept 2007

Athar M, Kothari UC, Garde RJ (2002) Studies on vortex chamber type sediment extractor. J Hydraul Eng I.S.H. 8(2):1–16

Athar M, Kothari UC, Garde RJ (2003) Distribution of sediment concentration in the vortex chamber type sediment extractor. J Hydraul Res I.A.H.R. 41(4):427–438

Cleland JD (2001) Laboratory measurements of velocity profiles in simulated tornado-like vorticies. J Undergrad Res Phys 18(2):51–57

Daggett LL (1974) Similitude in free-surface vortex formations. J Hydraul Div ASCE 100 (HY-11):1565–1581

Hite JE Jr, Mih WC (1994) Velocity of air-core vortices at hydraulic intakes. J Hydraul Eng ASCE 120(3):284–297 (Paper No. 5252)

Jain AK, Ranga Raju KG, Garde RJ (1978) Vortex formation at vertical pipe intakes. J.H.D. ASCE 104(HY-10):1429–1445

Julien PY (1985a) Motion of sediment particles in a rankine-combined vortex. Report CER-84 PYJ6, Colarado State University, Fort Collins, p 37

Julien PY (1985b) Theoretical analysis of sediment particles in a rankine-combined vortex. In: Proceedings of the CSCE annual conference, Saskatoon, Canada, pp 89–105

Mashauri DA (1986) Modelling of a vortex settling basin for primary clarification of water. Ph.D. thesis presented to the Tampere University of Technology, Finland

Odgaard AJ (1986) Free air-core vortex. J.H.D. ASCE 112(7):610–620

Paul TC, Sakhuja VS, Dhillon GS (1991) Analytical models for free surface air-core vortex. Indian J Power River Valley Dev 161–170

Rea Q (1984) Secondary currents within the circulation chamber sediment extractor. M.Sc. Engineering dissertation, presented to Faculty of Engineering and Applied Science, Department of Civil Engineering, Institute of Irrigation Studies, University of Southampton, England

Richard F, Thomas PO (1996) Swirl technology: enhancement of design, evaluation and application. J Hydraul Eng ASCE 122(8):743–748 (Paper No. 10213)

Szalai L, Peter K, Rodi W (1994) Simulation of flow in circular clarifiers with and without swirls. JHE ASCE 120(1):4–21 (Paper No. 5169)

Vatistas CH, Lin S, Kwok CK (1986) Theoretical & experimental studies on vortex chamber flows. AIAA J 24(4):635–642

Zhou Z, Hou J, Tang Y (1991) Flow field measurement of sand funnel and its influence on sediment transport. In: Proceedings of 27th IAHR, Congress, pp 1–6

Performance Appraisal of Friction Factor Estimators

Abhishek Mishra, Aditya Deshpande and Bimlesh Kumar

Abstract Estimation of friction factor is essential for the analysis of flow conditions in pipes. Exact solution of the friction factor can be obtained from Moody diagram. The best approximation to Darcy friction factor for turbulent flow is given by Colebrook–White equation. In past few decades, a number of correlations have been proposed for the determination of friction factors in order to avoid iterations. The efficiency and applicability of these formulae should be estimated. In this research, the experimental results are compared with 27 different equations. The comparison of predicted with observed value has been expressed through Nash–Sutcliff efficiency coefficient, correlation coefficient R^2, slope, average discrepancy ratio, and standard deviation. For smooth pipes, Zigrang and Sylvester formulae are more efficient, to avoid cumbersome calculations. Barr, Avci and Karagoz equations can be suggested. For rough pipes, round equation is precision enough.

Keywords Friction factor · Explicit equations · Performance estimation

Introduction

An integral part of the frictional pressure drop due to fluid flow in pipes involves the determination of hydraulic resistances (i.e., friction factor *f*). The pressure loss in pipe flow is calculated by using the Darcy–Weisbach equation. The equation is given as follows:

A. Mishra · A. Deshpande (✉)
Department of Civil Engineering, Maulana Azad National Institute of Technology, Bhopal 462003, India
e-mail: deshpande1309@gmail.com

B. Kumar
Department of Civil Engineering, Indian Institute of Technology, Guwahati 781039, India
e-mail: bimk@iitg.ernet.in

V. P. Singh et al. (eds.), *Hydrologic Modeling*, Water Science and Technology Library 81, https://doi.org/10.1007/978-981-10-5801-1_33

$$\Delta P = f\frac{L}{D}\rho\frac{V^2}{2} \tag{1}$$

where ΔP is the pressure drop, f is friction factor, is density of the fluid, D is hydraulic diameter of pipe, and V is average velocity. The friction factor (f) depends on the flow regime. For a fully developed laminar flow (Reynolds number $Re < 2300$), the friction factor can be determined from the Hagen–Poiseuille equation as follows:

$$f = \frac{64}{Re} \tag{2}$$

where Re is the Reynolds number. The definition of the Re number can be given as follows:

$$Re = \frac{\rho VD}{\mu} \tag{3}$$

where ρ is the density and μ is the dynamic viscosity of the fluid. In Eq. (2), the friction factor changes inversely with the Reynolds number. The friction factor f decreases with an increasing Reynolds number, and the rate of decrease becomes slower for greater relative roughness (ε/D). For certain roughness, the friction factor is independent of the Reynolds number. For a constant Reynolds number, f increases markedly for an increasing relative roughness. For the transition region ($2300 \leq Re \leq 4000$) and the turbulent region ($Re \geq 4000$) in smooth as well as rough pipe, the friction factor can be described by Colebrook–White equation. The friction factor f or the flow coefficient λ is not a constant and depends on the parameters. The friction factor is obtained either by empirical equations or by published charts. These charts are known as Moody diagram. The empirical equations are of two types, one implicit and the other explicit. The implicit equations are those in which iteration steps are involved. Due to these iterations, there is loss of data, and hence, explicit equations are preferred. While transfer of fluid through chemical reactors and in industrial processes involves single-phase, double-phase, and even more complicated pipe flow systems, pipe friction is critical. Nowadays, even in medical sciences and biomedical engineering, when high local velocities are attained in blood vessels while transporting physiological fluid through catheter tube into the body, analysis of friction factor in catheter is important. Over the decades, various scientists have given number of equations to calculate friction factor which allows us to found friction factor for flow in a circular pipe. The Prandtl equation (1949), which has also been known as the Karman–Nikuradse relation (Nikuradse 1932; Von Karman 1930), and the PKN correlation is regarded as an accurate equation for determining the friction factor. Many researchers have developed explicit approximations to the Prandtl equation. Blasius (1913) was the first to apply the similarity theory and formulate that the friction factor is a function of the Reynolds number in turbulent flow. Other scientists who gave their contributions are Wood (1966), Churchill (1973, 1977),

Eck (1973), Jain (1976), Swamee and Jain (1976), Chen (1979), Round (1980), Shacham (1980), Barr (1981), Zigrang and Silvester (Eqs. 11 and 12 in 1982), Haaland (1983), Serghides (Eqs. 2 and 3 in 1984), Tsal (1989), Mandilli (1997), Romeo et al. (2002), Sonnad and Goudar (2006), Rao and Kumar (2007), Buzzelli (2008), Avci and Karagoz (2009), Papaevangelo et al. (2010), Brkic (2011), Fang et al. (2011). This paper presents the accuracy of the available explicit equations on the data obtained by Nikuradse on the rough and smooth pipes and Mckeon's data on smooth pipe, suggesting the most appropriate equation on the basis of slope of the graph obtained by plotting simulated friction factor values on y-axis and experimental values on x-axis, coefficient of correlation (R^2), Nash–Sutcliffe model efficiency coefficient (E), and discrepancy ratio (D) with standard ratio and their applications in the field.

Nash–Sutcliffe model efficiency coefficient (E) is used to assess the predictive models and is defined as follows:

$$E = 1 - \left[\frac{\sum(\text{observed} - \text{simulated})^2}{\sum(\text{observed} - \text{Observed Mean})^2}\right] \tag{4}$$

The value of E can be in the range from $-\infty$ to 0, with higher values indicating a better overall fit and 1.0 for perfect fit. An efficiency of 0 ($E = 0$) indicates that the model predictions are as accurate as the mean of the observed data, whereas an efficiency less than 0 ($E < 0$) indicates that the indicated mean is better predictor than the model. Another performance criterion discrepancy ratio indicates the "goodness of fit" between the observed and the predicted values. One way of measuring the goodness is by using the average discrepancy ratio and standard deviation (Yang and Simoes) based on the average values of the logarithmic ratio between computed and observed.

$$\text{Mean } D_a = \frac{\sum\left[\log\left(\frac{\text{simulated}}{\text{observed}}\right)\right]}{n} \tag{5}$$

and

$$\sigma_a = \frac{\sqrt{\sum(\log(\text{simulated}/\text{observed}) - \text{mean } D_a)^2}}{(n-1)} \tag{6}$$

where n is the number of observation. For specific fit mean $D_a = 0$ and $\sigma_a = 0$.

Before choosing a formula, it is worth knowing that in the paper on the Moody chart, Moody stated the accuracy is about ±5% for smooth pipes and ±10% for rough pipes. If more than one formula is applicable in the flow regime under

consideration, the choice of formula may be influenced by one or more of the following:

1. Required precision.
2. Speed of computation required.
3. Available computation technology (calculator with minimum strokes or spreadsheet with single cell formula).

Previous Literature

The Colebrook–White equation can be defined as follows (Colebrook and White 1937).

$$\frac{1}{\sqrt{f}} = -2\log_{10}\left[\frac{(\varepsilon/D)}{3.7} + \frac{2.51}{Re\sqrt{f}}\right] \tag{7}$$

where ε/D is the relative roughness which is the ratio of the mean height of roughness of the pipe to the pipe diameter. As seen from Eq. (4), the friction factor is a function of the Reynolds number and pipe roughness (ϵ). The Colebrook–White equation cannot be solved directly due to its implicit form as the value of f appears on both side of the equation. Colebrook (1939) presented a simple explicit equation valid for the wide range of Re. This equation was also recommended by Haaland (1983), with prediction error within 1.7% for $4000 < Re < 104$ and about 0.6% for $10^4 < Re < 10^7$. Chen (1985) presented a systematic study on the Prandtl equation and formulated two approximation equations.

Recently, Goudar and Sonnad (2003) derived a representation of the PKN correlation using the Lambert-W function. The derived equation is presented explicitly in Reynolds number; however, since the Lambert-W function is inherently implicit, the solutions to the Lambert-W function often need iteration methods. The relative difference of the derived approximation equation to the PKN correlation was not reported. More recently, Avci and Karagoz (2009) proposed a novel explicit friction factor based on a new logarithmic velocity profile. The derived equation was claimed to be indistinguishable from the solution of the PKN correlation. The maximum errors of this equation are around 0.5% for $4000 \leq Re < 10^4$ and 1% for $10^4 \leq Re \leq 10^7$. The original Prandtl equation (1949) is given by:

$$\frac{1}{\sqrt{f}} = 2\log_{10}\left(Re\sqrt{f}\right) - 0.8 \tag{8}$$

where f is the friction factor. Mises et al. (1914) did a very valuable piece of work, treating all of the then-known test results from the viewpoint of similarity. He obtained, chiefly from the observations of Darcy and Bazin with circular pipes, the

following formula for the friction factor f in terms of the Reynolds number and the relative roughness

$$\lambda = 0.0024 + \sqrt{\left(\frac{\varepsilon}{r}\right)} + \frac{0.3}{\sqrt{Re}} \tag{9}$$

This formula for values of Reynolds numbers near the critical, that is, for small values, assumes the following form:

$$\lambda = \left(0.0024 + \sqrt{\frac{\varepsilon}{r}}\right)\left(1 - \frac{1000}{Re}\right) + \frac{0.3}{\sqrt{Re}}\sqrt{1 - \frac{1000}{Re}} + \frac{8}{Re} \tag{10}$$

The term "relative roughness" for the ratio ε/r in which ε is the absolute roughness was first used by Mises. Proof of similarity for flow through rough pipes was furnished in 1911 by T.E. Stanton. He studied pipes of two diameters into whose inner surfaces two intersecting threads had been cut. In order to obtain geometrically similar depths of roughness, he varied the pitch and depth of the threads in direct proportion to the diameter of the pipe. He compared for the same pipe the largest and smallest Reynolds number obtainable with his apparatus and then the velocity distributions for various pipe diameters. Perfect agreement in the dimensionless velocity profiles was found for the first case, but a small discrepancy appeared in the immediate vicinity of the walls for the second case. Stanton thereby proved the similarity of flow through rough tubes. More recently, L. Schiller made further observations regarding the variation of the friction factor f with the Reynolds number and with the type of surface. His tests were made with drawn brass pipes. His observations indicate that the critical Reynolds number is independent of the type of wall surface. He further determined that for greatly roughened surfaces the quadratic law of friction is effective as soon as turbulence sets in. In the case of less severely roughened surfaces, he observed a slow increase of the friction factor with the Reynolds number. Schiller was not able to determine whether this increase goes over into the quadratic law of friction for high Reynolds numbers, since the Göttingen test apparatus at that time was limited to about $Re = 10^5$. His results also indicate that for a fixed value of Reynolds number, the friction factor ε increases with an increasing roughness.

The following equations were used in the work:

Moody Correlation: Moody (1947) developed a relationship that is valid for all ranges of the Reynolds numbers and the relative roughness as follows and applicable in the range of $Re \geq 4 \times 10^3$, $Re \leq 10^8$ and $\epsilon/D \geq 0 \leq 10^{-2}$.

$$\lambda = 0.0055\left[1 + \left(2 \times 10^4 \frac{\epsilon}{D} + \frac{10^6}{Re}\right)^{\frac{1}{3}}\right] \tag{11}$$

Altshul Correlation: Altshul which is cited in Genić et al. gave a friction factor correlation.

$$f_d = 0.11 \times \left[\frac{68}{Re} + \frac{\varepsilon}{D}\right]^{0.25} \tag{12}$$

Wood correlation: This correlation was proposed in the year 1966. Its validation region extends for $Re > 10,000$ and $< \varepsilon/D < 0.04$,

$$f_d = 0.094\left(\frac{\epsilon}{D}\right)^{0.225} + 0.53\left(\frac{\epsilon}{D}\right) + 88\left(\frac{\epsilon}{D}\right)^{0.4}(Re)^{-A1} \tag{13}$$

where $A1 = 1.62\left(\frac{\epsilon}{D}\right)^{0.134}$.

Churchill Correlation: Correlation proposed by Churchill (1973) is valid only for the turbulent regime, and it is similar to the Swamee and Jain correlation (1976).

$$\frac{1}{\sqrt{f_d}} = -2 \times \log_{10}\left[\frac{\varepsilon}{3.7D} + \left(\frac{7}{Re}\right)^{0.9}\right] \tag{14}$$

Eck correlation: It is given by

$$\frac{1}{\sqrt{f_d}} = -2 \times \log_{10}\left[\frac{\epsilon}{3.715D} + \frac{15}{Re}\right] \tag{15}$$

Jain: The applicable range of the equation is

$$Re \geq 5 \times 10^3 \text{ and } 10^7, \quad \epsilon/D \geq 4 \times 10^{-5} \leq 5 \times 10^{-2}$$
$$Re \geq 5 \times 10^3 \text{ and } 10^7, \quad \epsilon/D \geq 4 \times 10^{-5} \leq 5 \times 10^{-2}$$

$$\frac{1}{\sqrt{f_d}} = -2\log_{10}\left[\frac{\epsilon}{3.715D} + \left(\frac{6.943}{Re}\right)^{0.9}\right] \tag{16}$$

Jain and Swamee: The applicable range of the equation is

$$Re \geq 5 \times 10^3 \text{ and } 10^8, \quad \epsilon/D \geq 10^{-6} \leq 5 \times 10^{-2}$$

$$\frac{1}{\sqrt{f_d}} = -2\log_{10}\left[\frac{\epsilon}{3.7D} + \frac{5.74}{Re^{0.9}}\right] \tag{17}$$

Churchill (1977):

$$\lambda = 8\left[\left(\frac{8}{Re}\right)^{12} + \frac{1}{(A1+A2)^{1.5}}\right]^{12} \tag{18}$$

where

$$A1 = \left[-2.457\ln\left[\left(\frac{7}{Re}\right)^{0.9} + 0.27\frac{\epsilon}{D}\right]\right]^{16}$$

$$A2 = \left(\frac{37530}{Re}\right)^{16}$$

Chen: This equation is applicable in the range of $Re \geq 4 \times 10^3$ and $\leq 4 \times 10^8$, $\epsilon/\mathrm{D} \geq 10^{-7} \leq 5 \times 10^{-2}$

$$\frac{1}{\sqrt{f_d}} = -2\ \log_{10}\left[\frac{\epsilon}{3.7065D} - \frac{5.0452}{Re}\log_{10}\left[\frac{1}{2.857} \times \left(\frac{\epsilon}{D}\right)^{1.1098} + \frac{5.8506}{Re^{0.8981}}\right]\right] \tag{19}$$

Round: This equation is applicable in the range of $Re \geq 4 \times 10^3$ and $\leq 10^8, \epsilon/D \geq 0 \leq 5 \times 10^{-2}$

$$\frac{1}{\sqrt{f_d}} = 1.8\ \log_{10}\left[\frac{Re}{0.135\,Re\left(\frac{\epsilon}{D}\right) + 6.5}\right] \tag{20}$$

Shacham: This equation is applicable in the range of $Re \geq 4 \times 10^3$ and $\leq 4 \times 10^8$

$$\frac{1}{\sqrt{f_d}} = -2\log_{10}\left[\frac{\epsilon}{3.7D} - \frac{5.02}{Re}\log_{10}\left[\frac{\epsilon}{3.7D} + \frac{14.5}{Re}\right]\right] \tag{21}$$

Barr (1981).

$$\frac{1}{\sqrt{f_d}} = -2\ \log_{10}\left[\frac{\epsilon}{3.7D} + \frac{\left(5.158\log_{10}\left(\frac{Re}{7}\right)\right)}{Re\left[\left(1 + \left(\frac{Re^{0.52}}{29}\right)\left(\frac{\epsilon}{D}\right)^{0.7}\right)\right]}\right] \tag{22}$$

Zigrang and Sylvester: The equation is applicable in the range of

$$Re \geq 4 \times 10^3 \text{ and } \leq 10^8, \quad \epsilon/D \geq 4 \times 10^{-5} \leq 5 \times 10^{-2}$$

$$\frac{1}{\sqrt{f_d}} = -2\ \log_{10}\left[\frac{\epsilon}{3.7D} - \frac{5.02}{Re}\log_{10}[A5]\right] \tag{23}$$

where

$$A5 = \frac{\epsilon}{3.7D} + \frac{13}{Re}$$
$$A6 = \frac{\epsilon}{3.7D} - \frac{5.02}{Re}\log_{10} A5$$

Zigrang and Sylvester: The equation is applicable in the range of

$$Re \geq 4 \times 10^3 \text{ and } \leq 10^8, \quad \epsilon/D \geq 4 \times 10^{-5} \leq 5 \times 10^{-2}$$

$$\frac{1}{\sqrt{f_d}} = -1.8 \times\ \log_{10}\left[\frac{6.9}{Re} + \left(\frac{\epsilon}{3.7D}\right)^{1.11}\right] \tag{24}$$

Serghides: The applicable range of the equation is in the range of

$$f_d = \left[A7 - \frac{(A8 - A7)^2}{A9 - 2A8 + A7}\right]^{-2} \tag{25}$$

where,

$$A7 = -2\ \log_{10}\left(\frac{\epsilon}{3.7D} + \frac{12}{Re}\right)$$
$$A8 = -2\ \log_{10}\left(\frac{\epsilon}{3.7D} + \frac{2.51A7}{Re}\right)$$
$$A9 = -2\ \log_{10}\left(\frac{\epsilon}{3.7D} + \frac{2.51A8}{Re}\right)$$

Serghides (2):

$$f_d = \left[4.781 - \frac{(A7 - 4.781)^2}{A8 - 2A7 + 4.781}\right]^{-2} \tag{26}$$

where

$$A7 = -2\ \log_{10}\left(\frac{\epsilon}{3.7D} + \frac{12}{Re}\right)$$
$$A8 = -2\ \log_{10}\left(\frac{\epsilon}{3.7D} + \frac{2.51A7}{Re}\right)$$

Tsal: The applicable range of this equation is

$$Re \geq 4 \times 10^3 \text{ and } \leq 10^8, \quad \epsilon/\mathrm{D} \geq 0 \leq 5 \times 10^{-2}$$

$$A = 0.11\left(\frac{68}{Re} + \frac{\epsilon}{D}\right)^{0.25} \tag{27}$$

$$\text{If } A \geq 0.018 \text{ then } f_d = A$$
$$\text{If } A < 0.018 \text{ then } f_d = 0.0028 + 0.85A$$

Manadilli: The applicable range of this equation is

$$Re \geq 5.235 \times 10^3 \text{ and} \leq 10^8, \quad \epsilon/D \geq 0 \leq 5 \times 10^{-2}$$

$$\frac{1}{\sqrt{f_d}} = -2\log_{10}\left[\left(\frac{\epsilon}{3.7D}\right) + \left(\frac{95}{Re^{0.983}}\right) - \left(\frac{96.82}{Re}\right)\right] \tag{28}$$

Romeo et al.: The applicable range of this equation is

$$Re \geq 3 \times 10^3 \text{ and } \leq 1.5 \times 10^8, \quad \epsilon/D \geq 0 \leq 5 \times 10^{-2}$$

$$\frac{1}{\sqrt{f_d}} = -2\log_{10}\left[\frac{\epsilon}{3.7065D} \times \frac{5.0272}{Re} \times \log_{10}\left[\frac{\epsilon}{3.827D} - \frac{4.567}{Re} \times \log_{10}\left(\left(\frac{\epsilon}{7.7918D}\right)^{0.9924} + \left(\frac{5.3326}{208.815 + Re}\right)^{0.9345}\right)\right]\right] \tag{29}$$

Sonnad and Goudar: The applicable range of the equation is

$$\mathrm{Re} \geq 4 \times 10^3 \text{ and } \leq 10^8$$
$$\epsilon/\mathrm{D} \geq 10^{-6} \leq 5 \times 10^{-2}$$

$$\frac{1}{\sqrt{f_d}} = 0.8686 \ln\left(\frac{0.4584\,Re}{S^{\left(\frac{S}{S+1}\right)}}\right) \tag{30}$$

where

$$S = 0.124 \times \frac{\epsilon}{D} \times Re + \ln(0.4587\,Re)$$

Rao and Kumar:

$$\frac{1}{\sqrt{f_d}} = 2\ \log_{10}\left(\frac{\left(\frac{2\epsilon}{D}\right)^{-1}}{\left(\frac{0.444+0.135\,Re}{Re}\right)\beta}\right) \tag{31}$$

where $\beta = 1 - 0.55e^{-0.33\left(\ln\left(\frac{Re}{6.5}\right)\right)^2}$

Buzzelli:

$$\frac{1}{\sqrt{f_d}} = B1 - \left[\frac{B1 + 2\log_{10}\left(\frac{B2}{Re}\right)}{1+\frac{2.18}{B2}}\right] \tag{32}$$

where

$$B1 = \frac{[0.744\ln(Re) - 1.41]}{\left(1+1.32\sqrt{\frac{\epsilon}{D}}\right)}$$
$$B2 = \frac{\epsilon}{3.7D} \times Re + 2.51 \times B1$$

Avci and Karagoz: The applicable range of the equation is

$$Re \geq 10^4 \text{ and } \leq 10^7, \quad \epsilon/D \geq 10^{-5} \leq 10^{-3}$$

$$f_d = \frac{6.4}{\left[\ln(Re) - \ln\left[1 + 0.01\,Re \times \frac{\epsilon}{D} \times \left(1 + 10 \times \sqrt{\frac{\epsilon}{D}}\right)\right]\right]^{2.4}} \tag{33}$$

Papaevangelo et al. equation:

$$f_d = \frac{0.2479 - 0.0000947 \times (7 - \log_{10} Re)^4}{\left(\log_{10}\left\{\frac{\epsilon}{3.615D} + \frac{7.366}{Re^{0.9142}}\right\}\right)^2} \tag{34}$$

Brkic (1):

$$f_d = \left(-2 \times \log_{10}\left(10^{-0.4343\,\beta} + \frac{\epsilon}{3.71D}\right)\right)^{-2} \tag{35}$$

where $\beta = \ln\left(\frac{Re}{1.816\ln\left(\frac{1.1\,Re}{\ln(1+1.1\,Re)}\right)}\right)$.

Brkic (2):

$$f_d = \left(-2 \times \log_{10}\left(\frac{2.18\,\beta}{Re} + \frac{\epsilon}{3.71D}\right)\right)^{-2} \tag{36}$$

where

$$\beta = \ln\left(\frac{Re}{1.816\,\ln\left(\frac{1.1\,Re}{\ln(1+1.1\,Re)}\right)}\right)$$

Fang et al.: The applicable range of the equation is

$$f_d = 1.613\left(\ln\left[0.234 \times \left(\frac{\epsilon}{D}\right)^{1.1007} - \frac{60.525}{Re^{1.1105}} + \frac{56.291}{Re^{1.0712}}\right]\right)^{-2} \tag{37}$$

The data used came from three sources:

The experiments of Nikuradse on flow in smooth pipes.
The experiments of Nikuradse on flow in rough pipe.
McKeon, Morrison, Smits, Li, and Jiang have given the data in the article.

Results and Discussion

In this study, a comprehensive review of 27 explicit equations is conducted for friction factor that is used in the calculation of pressure drop in pipes. Explicit equations are used to avoid cumbersome iterative method for finding the friction factor, but the values obtained from these explicit equations lead to error. Nikuardse experimental data has been used to check the efficiency of the velocity predictors. And also McKeon's experimental data on smooth pipe is also taken into the account. Tables 1 and 2 show the values of all considered parameters, viz. m, R^2, σ_a, D_a, E for both rough and smooth pipes. Also, Table 3 shows the same values for the data obtained by McKeon on smooth pipe. For better insight of the work, it is worth mentioning the graph obtained for each explicit equation, showing the plot between simulated and experimental data. On the criterion already stated, it is worth stating that

1. For the value of slope m, the best-suited equation is the one that gives the value close to 1. On this basis, the best equations for rough pipe are Buzzelli (m = 0.963), Barr, Avci and Karagoz, Moody, Rao and Kumar, Romeo et al.,

Table 1 Rough pipe results

Author name	$y = mx$; $m=$	R^2	E	D_a	σ_a
Moody	1.0073	0.832	0.9864884	0.027343668	0.002485371
Altshul	0.9194	0.6655	0.97556468	−0.002734501	0.003178675
Wood	1.0851	0.9285	0.984461489	0.00487485	0.001984601
Churchill (1973)	0.9546	0.8711	0.982271021	0.0234572	0.003221911
Eck	0.9565	0.8683	0.982121394	0.02157632	0.003231054
Jain	1.0294	0.8594	0.98244373	0.022778885	0.003221548
Swamee and Jain	1.0703	0.9152	0.984797804	0.03943633	0.002082389
Churchill (1977)	1.0699	0.9147	0.984816601	0.039311604	0.00208703
Chen	1.0614	0.9247	0.98737905	0.03607903	0.001980336
Round	1.0273	0.8853	0.988464195	0.030321158	0.02223903
Shacham	1.061	0.9267	0.98765877	0.035731426	0.001955343
Barr	0.9634	0.8766	0.982301177	0.025065572	0.003214742
Zigrang and Sylvester	1.0613	0.9262	0.987571675	0.035868812	0.001960884
Zigrang and Sylvester	1.0613	0.9261	0.987531608	0.035815932	0.001961607
Haaland	1.0621	0.9286	0.987621877	0.035441008	0.001921253
Serghides	0.963	0.8773	0.9837886	0.0199293	0.00320518
Serghides	0.963	0.8773	0.9837878	0.01991712	0.0031781
Tsal	1.0902	0.795	0.983787808	−0.0138907	0.00381678
Manadilli	0.9549	0.8718	0.98238082	0.023482609	0.00320491
Romeo et al.	1.0226	0.8657	0.983801255	0.019851032	0.003178462
Sonnad and Goudar	0.9617	0.8768	0.983620232	0.020611071	0.003180256
Rao and Kumar	1.0091	0.8093	0.9769877	−0.01498531	0.004264896
Buzzelli	0.963	0.8773	0.983784776	0.01994493	0.003178075
Avci and Karagoz	0.9671	0.8814	0.984587524	0.014630532	0.003141327
Papaevangelo et al.	0.9625	0.8777	0.983790285	0.020756535	0.00318078
Brkic	0.9611	0.8733	0.983143184	0.020150916	0.00321477
Brkic	0.955	0.8713	0.982336171	0.023587857	0.003222637
Fang et al.	0.9629	0.8768	0.983711346	0.0197438	0.003180977

Round, and Jain. For smooth pipes, Barr, Avci and Karagoz, Zigrang and Sylvester equations have the value of slope close to 1.

2. For the values of Nash–Sutcliffe model efficiency coefficient E, the best equation is the one which gives the value close to 1 (for perfect fit, the value must be (1), and on this basis, the best equation for the rough pipes are Round, Shacham, Haaland, Zigrang and Sylvester, Chen.
3. For smooth pipes, Avci, Karagoz, Goudar and Sonnad, Barr, Zigrang and Sylvester (2). For the value of R^2, the best-suited equation is the one that gives the value close to 1. On this basis, the best equations for rough pipe are Haaland, Wood, Shacham, Zigrang and Sylvester.

Table 2 Nikuradse's smooth pipe

Equation	R^2	m (slope)	E	Discrepancy ratio (D)	Standard deviation (σ)
Moody (1947)	0.9758	0.9672	0.968386578	−0.019480747	0.002252998
Altshul	0.958	1.0284	0.95304784	−0.033367434	0.003785138
Churchill (1973)	0.9764	1.0082	0.976023876	−0.004296608	0.002145769
Eck (1973)	0.9594	1.022	0.956396175	−0.025492427	0.00254754
Jain (1976)	0.9765	1.0102	0.975838735	−0.00501973	0.00214551
Jain and Swamee (1976)	0.9765	1.0092	0.975933037	−0.004676539	0.002145623
Churchill (1977)	0.9769	1.0095	0.976328427	−0.004480329	0.002140627
Chen (1979)	0.9773	1.0104	0.976580299	−0.00305361	0.002134622
Round (1980)	0.9768	1.0263	0.972516536	−0.010828139	0.002146256
Shacham	0.9773	1.0104	0.976572574	−0.003118807	0.002134491
Barr (1981)	0.9772	1.0039	0.977081107	0.00057973	0.002138896
Zigrang and Sylvester (1982)	0.9772	1.0107	0.976496965	−0.003618096	0.002231976
Zigrang and Sylvester (1982)	0.9772	1.0039	0.977081107	0.00057973	0.002138896
Haaland [a][7]	0.9765	1.0117	0.975663796	−0.005568764	0.002368759
Serghides (1) (1984)	0.9772	1.01	0.976602736	−0.003223915	0.00221212
Serghides (2) (1984)	0.9772	1.0117	0.976367293	−0.004357291	0.002273305
Tsal (1989)	0.9745	1.0118	0.973643122	−0.008848113	0.002811415
Manadilli (1997)	0.9772	1.0099	0.976614323	−0.003097113	0.002206593
Sonnad and Goudar (2006)	0.9772	1.0035	0.977110211	−0.00114406	0.002143151
Buzzelli (2008)	0.9772	1.01	0.976605862	−0.003211186	0.002211519
Avci and Karagoz (2009)	0.9772	1.0036	0.977153699	0.000167381	0.00213522
Papaevangelou et al. (2010)	0.9772	1.0106	0.97647102	−0.003870136	0.002245316
Brkic	0.9772	1.0401	0.967530208	−0.014784092	0.002142425
Brkic (2)	0.9772	1.0059	0.976993943	−0.001878377	0.002133412
Fang et. al	0.9772	1.007	0.976932142	−0.001801965	0.002134722

Table 3 Mckeon's smooth pipe results

Equation	m (slope)	R^2	E	Discrepancy ratio (D)	Standard deviation (σ)
Moody (1947)	0.9455	0.9945	0.955935757	−0.022076359	σ = 0.0028769
Altshul	0.8605	0.9006	0.590563433	−0.102673187	σ = 0.0166109
Churchill (1973)	0.9819	0.9996	0.995297922	−0.008315910	0.000608723
Eck (1973)	0.9151	0.9944	0.899189546	−0.043707685	σ = 0.0094019
Jain (1976)	1.2948	0.982	−0.19135943	0.1018593778	σ = 0.0044768
Jain and Swamee (1976)	0.9811	0.9996	0.994936386	−0.008621923	0.000605785
Churchill (1977)	0.9817	0.9996	0.995197937	−0.008407622	0.000608723
Chen (1979)	0.9848	0.9992	0.996131781	−0.008228139	0.000961477
Round (1980)	0.9691	0.9997	0.987040322	−0.013580737	0.000586009
Shacham	0.9919	0.9993	0.998411403	−0.004951135	0.000917201
Barr (1981)	0.9846	0.9992	0.996051058	−0.00831759	0.000962815
Zigrang and Sylvester (1982)	0.994	0.9992	0.998716379	−0.004179499	0.000960564
Zigrang and Sylvester (1982)	0.9834	0.9993	0.9956095	−0.008723856	0.000909977
Haaland [a][7]	0.9794	0.9997	0.994029075	−0.009340673	0.000599638
Serghides (1) (1984)	0.9843	0.9993	0.995981949	−0.008354014	0.000923193
Serghides (2) (1984)	0.981	0.9992	0.99439685	−0.009942709	0.000972885
Tsal (1989)	0.958	0.9911	0.966813318	−0.025939531	0.003447446
Manadilli (1997)	0.9848	0.9993	0.996269431	−0.007995224	0.000879199
Sonnad and Goudar (2006)	0.9879	0.9991	0.997160957	0.047864101	0.056342899
Buzzelli (2008)	0.9861	0.9992	0.996606045	−0.007688372	0.000967817
Avci and Karagoz (2009)	0.9912	0.9986	0.997490831	−0.006284862	0.001346903
Papaevangelou et al. (2010)	0.9827	0.9993	0.995373178	0.046112363	0.055392709
Brkic	0.9605	0.9995	0.978879494	−0.018410094	0.00074916
Brkic (2)	0.9867	0.9992	0.996827017	−0.007417588	0.000967647
Fang et. al	0.9877	0.9993	0.997303436	−0.006750843	0.000892903

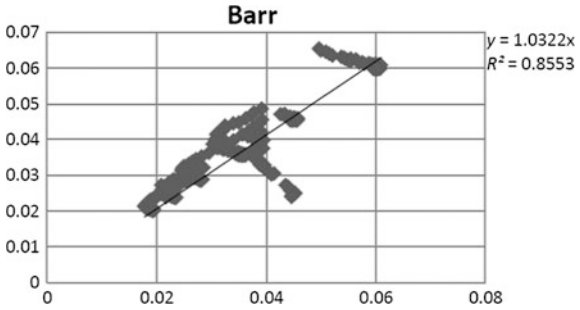

Fig. 1 Correlation of Barr's equation for rough pipe

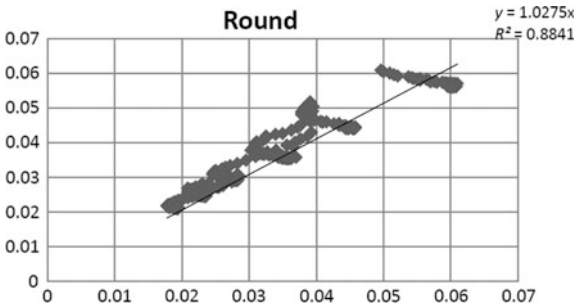

Fig. 2 Correlation of Round's equation for rough pipes

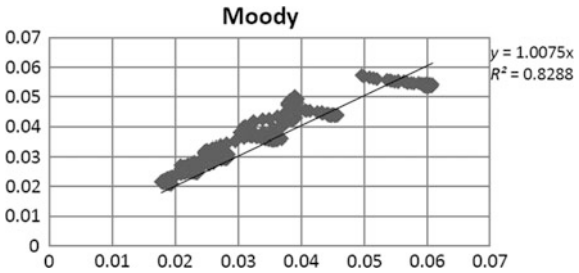

Fig. 3 Correlation factor for Moody's equation for rough pipes

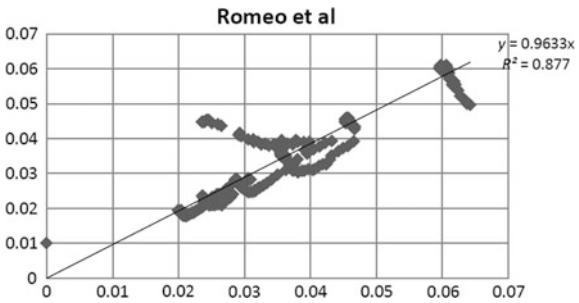

Fig. 4 Correlation factor for Romeo et al.'s equation for rough pipes

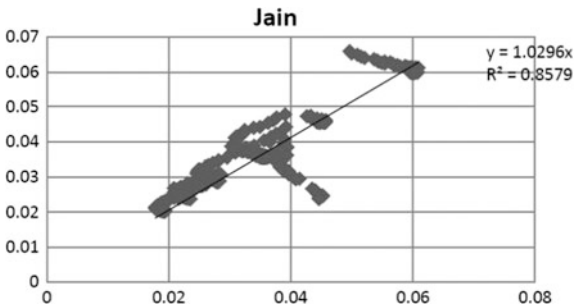

Fig. 5 Correlation factor for Jain's equation for rough pipes

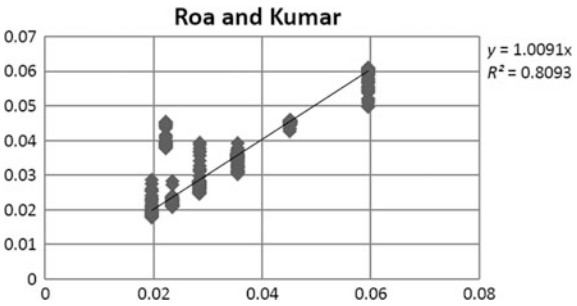

Fig. 6 Correlation factor for Rao and Kumar's equation for rough pipes

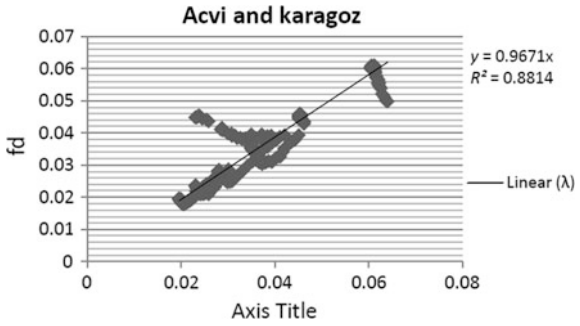

Fig. 7 Correlation factor for the Acvi and Karagoz's equation for rough pipes

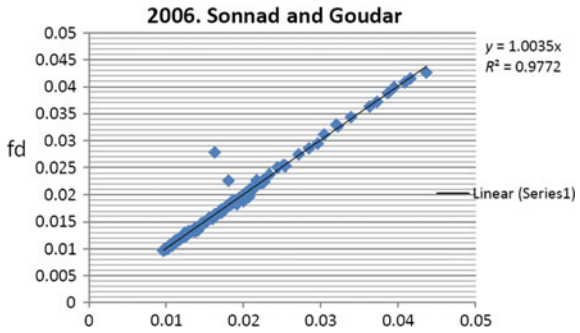

Fig. 8 Correlation factor for Sonnad and Goudar equation for smooth pipes

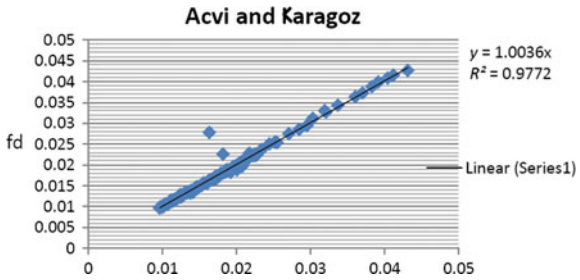

Fig. 9 Correlation factor Acvi and Karagoz's equation for smooth pipes

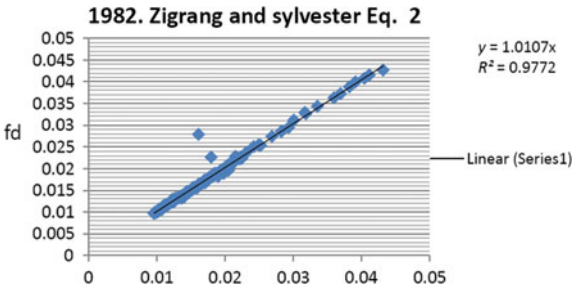

Fig. 10 Correlation factor for Zigrang and Sylvester's equation for smooth pipes

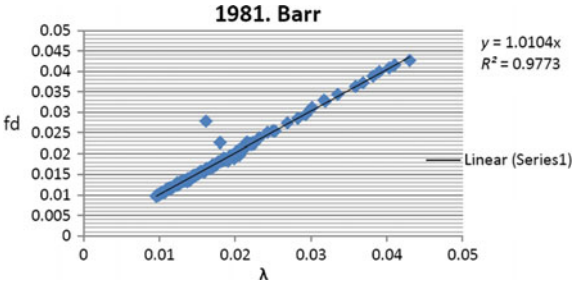

Fig. 11 Correlation factor for Barr's equation for smooth pipes

From Figs. 1, 2, 3, 4, 5, 6, 7, 8, 9, 10, and 11, f_d is represented on x-axis and l on y-axis

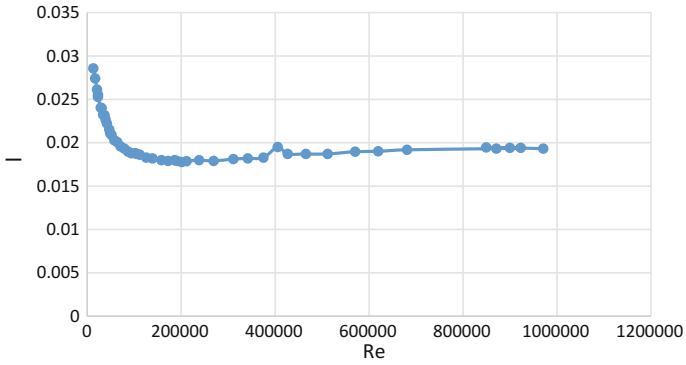

Fig. 12 l versus Re for $\varepsilon = 0.01$ and $D = 9.94$

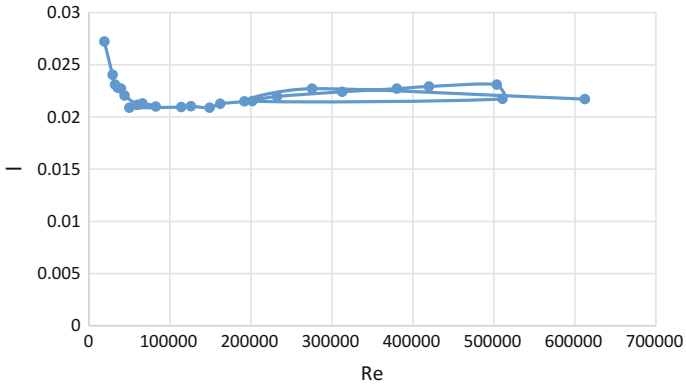

Fig. 13 λ versus *Re* for ε = 0.01 and *D* = 4.94

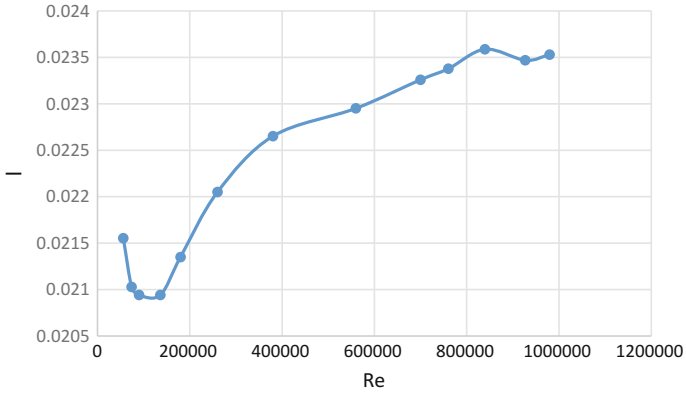

Fig. 14 λ versus *Re* for ε = 0.02 and *D* = 9.94

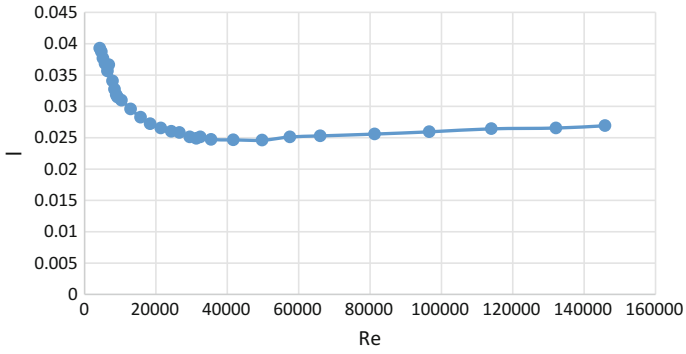

Fig. 15 λ versus *Re* for ε = 0.01 and *D* = 2.274

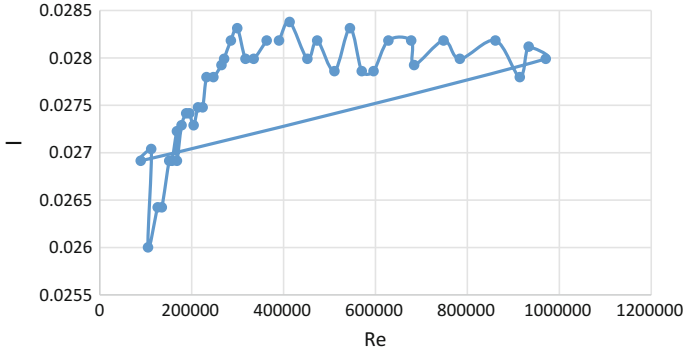

Fig. 16 l versus *Re* for ε = 0.04 and *D* = 9.92

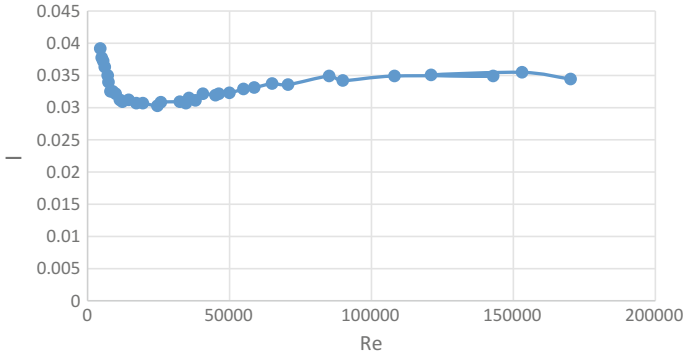

Fig. 17 l versus *Re* for ε = 0.02 and *D* = 2.434

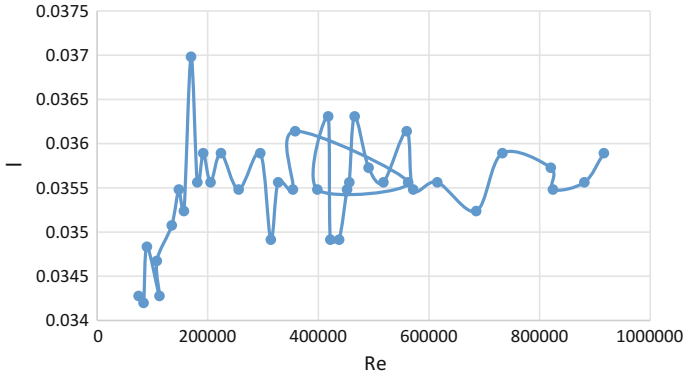

Fig. 18 l versus *Re* for ε = 0.08 and *D* = 9.8

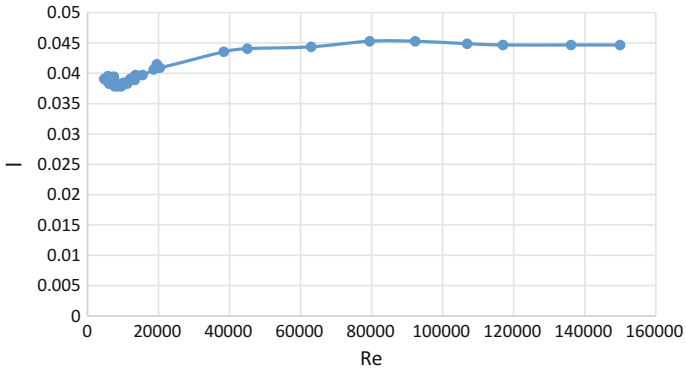

Fig. 19 l versus *Re* for $\varepsilon = 0.04$ and $D = 2.434$

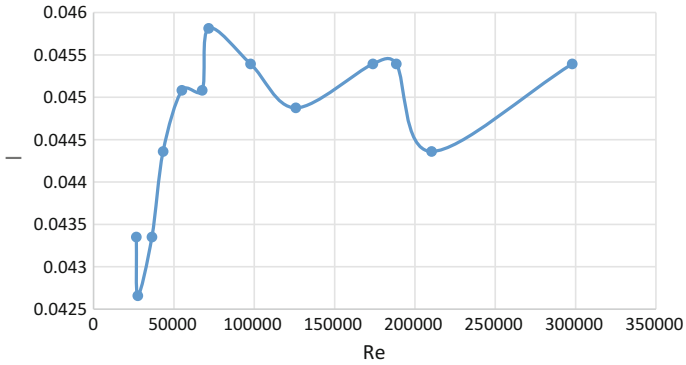

Fig. 20 l versus *Re* for $\varepsilon = 0.16$ and $D = 9.64$

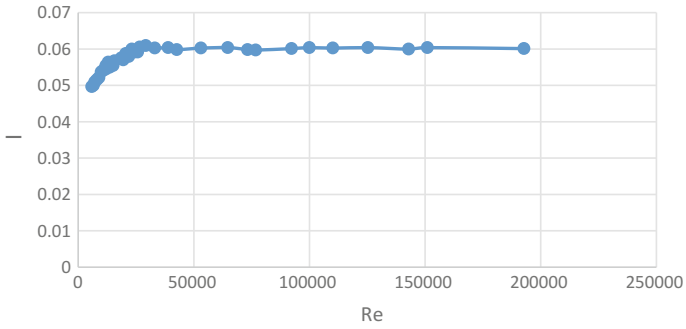

Fig. 21 l versus *Re* for $\varepsilon = 0.08$ and $D = 2.412$

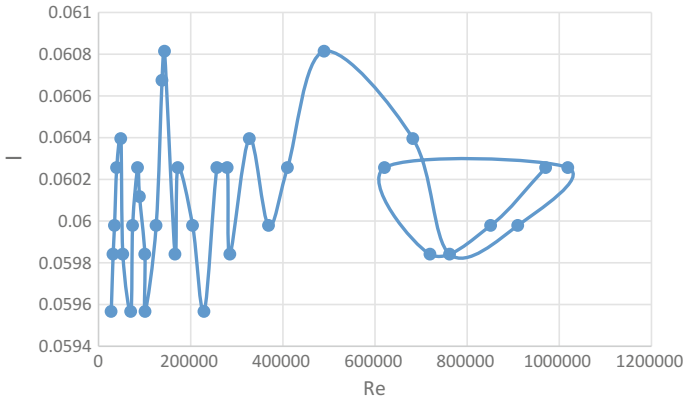

Fig. 22 l versus *Re* for ε = 0.16 and *D* = 4.82

Nikuradse's Experimental Data for Rough Pipe

See Figs. 12, 13, 14, 15, 16, 17, 18, 19, 20, 21 and 22.

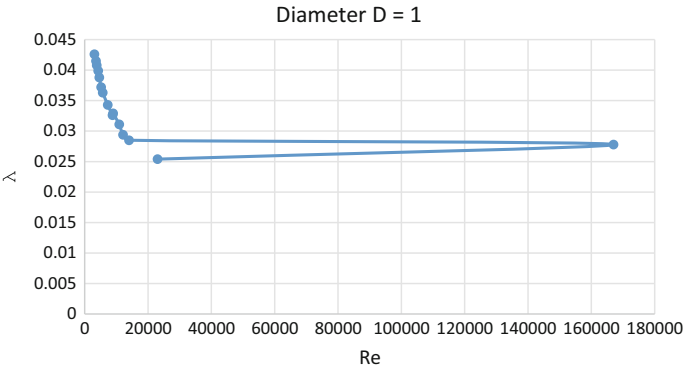

Fig. 23 *Re* versus l for pipe diameter *D* = 1

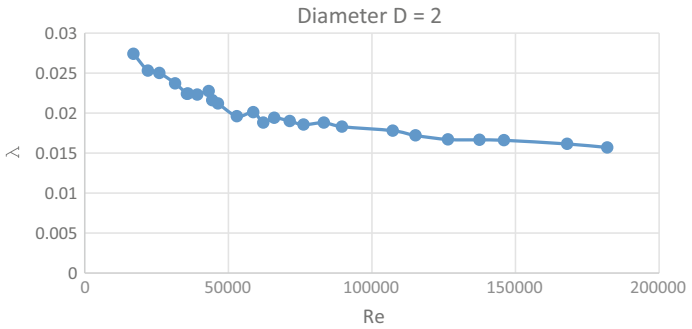

Fig. 24 *Re* versus l for pipe diameter $D = 2$

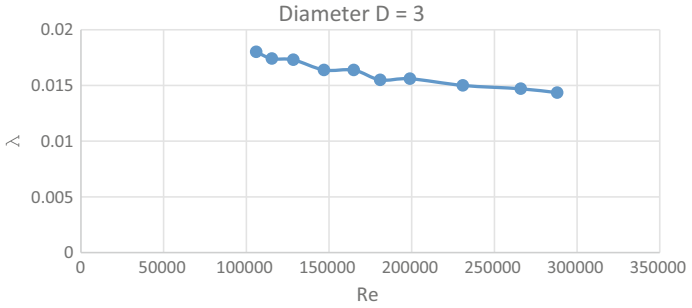

Fig. 25 *Re* versus l for pipe diameter $D = 3$

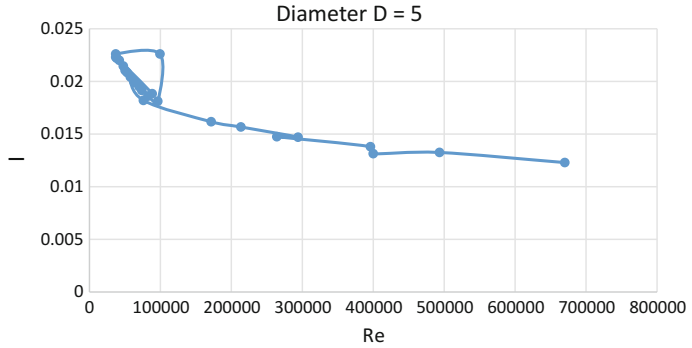

Fig. 26 *Re* versus l for pipe diameter $D = 5$

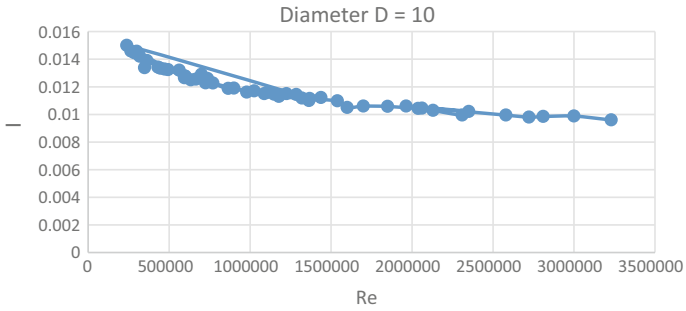

Fig. 27 *Re* versus l for pipe diameter $D = 10$

Nikurade' S Data for Smooth Pipes ($\epsilon/D = 0$)

See Figs. 23, 24, 25, 26 and 27.

Conclusion

In order to apply the explicit friction factor in the field, the equation should not be cumbersome to solve and should not contain too much variable. On this basis, Romeo et al. get eliminated.

Finally, considering all the above-stated criteria, we came to a conclusion that for smooth pipes Zigrang and Sylvester formulae are more efficient, to avoid cumbersome calculations. Barr, Avci and Karagoz equations can be suggested. For rough pipes, round equation is precision enough.

References

Avci A, Karagoz I (2009). A novel explicit equation for friction factor in smooth and rough pipes. J Fluid Eng ASME 131(6):061203 (1–4)

Barr DIH (1981) Solutions of the colebrook-white function for resistance to uniform turbulent flow. Proc Inst Civil Eng 71(2):529–536

Blasius PRH (1913) Das Aehnlichkeitsgesetz bei Reibungsvorgangen in Flüs sigk eiten. Forschungsheft 131:1–41

Brkić D (2011) An explicit approximation of the colebrook equation for fluid flow friction factor. Petrol Sci Technol 29(15):1596–1602

Buzzelli D (2008) Calculating friction in one step. Mach Des 80(12):54–55

Chen NH (1979) An explicit equation for friction factor in pipes. Ind Eng Chem Fundam 18 (3):296–297

Churchill SW (1973) Empirical expressions for the shear stress in turbulent flow in commercial pipe. AIChE J 19(2):375–376

Churchill SW (1977) Friction-factor equation spans all fluid flow regimes. Chem Eng 84(24): 91–92
Eck B (1973) Technische Stromungslehre. Springer, New York
Fang X, Xu Y, Zhou Z (2011) New correlations of single-phase friction factor for turbulent pipe flow and evaluation of existing single-phase friction factor correlations. Nucl Eng Des 241:897–902
Haaland SE (1983) Simple and explicit formulas for friction factor in turbulent pipeflow. J Fluid Eng ASME 105(1):89–90
Jain AK (1976). Accurate explicit equation for friction factor. J Hydraul Div ASCE102 (HY5):674–677
Manadilli G (1997) Replace implicit equations with signomial functions. Chem Eng 104(8): 129–130
Moody LF (1947) An approximate formula for pipe friction factors. Trans ASME 69(12): 1005–1011
Nikuradse J (1932) Gesetdssigkeiten der turbulenten Stromung in glatten Rohren. VDI-Forsch.-Heft 356
Papaevangelou G, Evangelides C, Tzimopoulos C, (2010) A new explicit equation for the friction coefficient in the Darcy–Weisbach equation. In: Proceedings of the tenth conference on protection and restoration of the environment: PRE10, Greece, Corfu, vol 166, July 6– 9, pp 1–7
Rao AR, Kumar B (2007) Friction factor for turbulent pipe flow. Division of Mechanical Sciences, Civil Engineering. Indian Institute of Science. Bangalore, India ID Code 9587
Round GF (1980) An explicit approximation for the friction factor—Reynolds number relation for rough and smooth pipes, Can J Chem Eng 58(1):122–123
Romeo E, Royo C, Monzon A (2002) Improved explicit equation for estimation of the friction factor in rough and smooth pipes. Chem Eng J 86(3):369–374
Serghides TK (1984) Estimate friction factor accurately. Chem Eng 91(5):63–64
Shacham M (1980) Comments on: 'An Explicit Equation for Friction Factor in Pipe'. Ind Eng Chem Fund 19:228–229
Sonnad JR, Goudar CT (2006) Turbulent flow friction factor calculation using mathematically exact alternative to the colebrook-white equation. J Hydraul Eng ASCE 132(8):863–867
Swamee PK, Jain AK (1976) Explicit equations for pipe flow problems. J Hydraul Div ASCE 102 (HY5):657–664
Tsal RJ (1989) Altshul-Tsal friction factor equation, Heating, Piping and Air Conditioning 8:30–45
Von Karman T (1930) Mechanische Ahnlichkeit und Turbulenz. Gogttinger Nachr., Math.-Phys. Klasse 1930 und Verh. d. 3. intern. Kongr. f.techn. Mech., Stockholm 1930 (Stockholm 1931), Bd. 1. (Available as NACA TM 611.)
Von Mises R (2014) Elemente der technischen Hydrodynamik. Leipzig, B. G. Teubner 1914
Wood DJ (1966) An explicit friction factor relationship. Civil Eng 36(12):60–61
Zigrang DJ, Sylvester ND (1982) Explicit approximations to the solution of Colebrook friction factor equation. AIChE J 28(3):514–515

Experimental Investigations of Wave Height Attenuation by Submerged Artificial Vegetation

Beena Mary John, I. Mohit Babu, Kiran G. Shirlal and Subba Rao

Abstract Coastal populations around the world are at a greater risk of damage from coastal hazards due to the unprecedented rise of global climate change characterized by sea-level rise, longer and frequent droughts and floods, heightened cyclonic and storm surge activities. The narrow fringe of vegetated coastal habitats along the shores of continents mainly acts as a buffer for the impacts of rising sea levels and wave action. The losses from natural disasters like the 2004 Indian Ocean tsunami, Hurricane Katrina, and others have reached an all-time high, and the decision-makers now realize that coastal habitats have an important role to play in risk reduction. Though coastal vegetation, as a shore protection method, is sustainable, environment friendly, and cost-effective, its behavior with wave is very complex, especially because of the coupling between the waves and vegetation motion and is therefore, not completely understood. Numerical modelling approach, having based on more assumptions and field study, being uneconomical fomented the need for the study in the form of physical modelling. This paper focuses on figuring out the effect of vegetation on wave attenuation through an experimental approach. The wave flume of length 50 m, height 1 m, and width 0.71 m is used to study the characteristic behavior of submerged heterogeneous vegetation of varying width for wave heights ranging from 0.08 to 0.16 m with an increment of 0.02 m and wave periods 1.8 and 2 s in water depths of 0.40 and 0.45 m. Measurements of wave heights at locations along the vegetation were observed to quantify wave attenuation and its trend.

B. M. John (✉) · I. Mohit Babu · K. G. Shirlal · S. Rao
Department of Applied Mechanics and Hydraulics, National Institute of Technology Karnataka, Surathkal, Mangalore 575025, India
e-mail: beena.marie.john@gmail.com

V. P. Singh et al. (eds.), *Hydrologic Modeling*, Water Science and Technology Library 81, https://doi.org/10.1007/978-981-10-5801-1_34

Introduction

Coasts are dynamic environments which are subjected to continuous and extensive changes in response to winds, waves, sea levels, and currents. These changes can become large and catastrophic during extreme events like cyclones, storm surges, and tsunami. High waves can result in erosion of beaches and inundation of low-lying lands. The forces of waves and currents can cause landward displacement of the shoreline which can in turn cause coastal erosion. An unprotected shoreline can easily be taken away by the sea. Man has continuously evolved methods to keep his settlements protected from the onslaught of the advancing sea. Hard methods of coastal protection including massive constructions was prevalent during the nineteenth and twentieth centuries, but alternative approaches harnessed from nature or natural resources have gained acceptance in the recent past (Charlier et al. 2005). The world's oceans are home to an abundance of important habitats ranging from seagrasses, coral reefs, and kelp forests to salt marshes and mangrove forests. Coastal vegetation aids in shoreline protection by damping the incoming waves and dissipating the energy. However, the hydrodynamics of vegetated coastal zones and the mechanism of wave attenuation through vegetation are still not fully understood (Massel 1999).

Pioneering studies on interactions between submerged vegetation and wave-induced flows include analytical solution of wave height attenuation due to a kelp farm, with kelp plants modelled as rigid cylinders (Dalrymple et al. 1984); experimental study on wave damping using artificial seaweed (Asano et al. 1988); effect of submerged or subaerial vegetation on wave activity expressed in terms of drag resistance against the fluid motion (Kobayashi et al. 1993); interaction between waves and vegetation motion with the analysis for the flow field and the swaying motion of an individual vegetation stand (Asano et al. 1992); and analytical solution for the vegetation motion of kelp fronds and kelp plant models (Dubi and Torum 1994).

Numerous experimental, numerical, and field studies have been conducted to investigate the effect of seagrasses (Gambi et al. 1990; Fonseca and Cahalan 1992; Ciraolo et al. 2006; Stratigaki et al. 2011; Koftis et al. 2012; Zeller et al. 2014), kelp forests (Dubi and Torum 1994; Elwany et al. 1995; Lovas and Torum 2001; Rosman et al. 2013), salt marshes (Bouma et al. 2005; Ozeren et al. 2013), and mangroves (Struve et al. 2003; Husrin et al. 2012; Strusinska-Correia et al. 2013) on wave activity. Gedan et al. (2011) presents a literature review and meta-analysis of wave attenuation data, which suggests that salt marsh and mangrove vegetation provides protection from erosion, storm surge, and potentially small tsunami waves. An experimental project which evaluated the wave energy attenuation associated with living shorelines (which included intertidal oysters and cordgrass) revealed that the living shoreline stabilization could attenuate a significant amount of wave energy produced by boat wakes (Manis et al. 2015).

The 2004 Indian Ocean tsunami which wreaked devastation across the Indian Ocean coastline, including the southeastern coast of India, marked a critical turning point for the scientists and administrators in India. The vulnerability of coasts to sudden catastrophic events gained importance, and measures to protect our coastline have become a prime concern. Kathiresan and Rajendran (2005), in their study of tsunami-hit regions, reported that agricultural fields suffered enormous loss due to intrusion of seawater in regions not protected by mangroves and other coastal vegetation and reiterated that mangroves prevent the entry of seawater inland, thus protecting the underground water systems essential for drinking water supply. Post-tsunami reconnaissance investigations along the most affected coastal stretches of India revealed that the thick forest of interwoven mangrove vegetation along the backwater canals of Pichavaram decelerated the gush of tsunami shoreward, thus greatly protecting the hamlet from the impact of tsunami (NIO 2005). Jayakumar et al. (2005) carried out a post-tsunami survey to ascertain the inundation limits at different locations along the tsunami-affected coastline. It was observed that the inundation values were lower at places where the coast is protected by dunes. However, the inundation values were higher wherever openings were found in dunes, as these openings provided a gateway for the water mass to travel through them to the hinterland. With reference to the Tamil Nadu coast (Southeast of Indian Peninsula), field observations with relevant measurements revealed that sand dunes and casuarina forests could aid in dissipating powerful waves (Mascarenhas and Jayakumar 2008). The soft measures of coastal protection thus gained importance in India during the post-tsunami years. Some of the early experimental works which shot up from this need were conducted in the 72 m long, 2 m wide, and 2.7 m deep wave flume at the Department of Ocean Engineering, Indian Institute of Technology Madras, India, by Sundar et al. (2011), Lakshmanan et al. (2012).

Sundar et al. (2011), from IIT Madras, India, in their detailed experimental investigations, studied the effect of vegetation in reducing the wave run-up and the variation of pressure on a wall fronted by different arrangements of vegetation, by varying the vegetative parameters such as diameter of stem, spacing between the stems, width of the green belt, and their rigidity. Lakshmanan et al. (2012) presented the variation of forces on a model building mounted over a slope, positioned at different distances from the vegetation belt, and subjected to the action of Cnoidal waves as a function of flow and vegetation parameters. The authors also studied the hydroelastic interaction of flow with vegetal stems and the resulting wave run-up on beach slopes (Noarayanan et al. 2012). The present paper aims to determine the wave height attenuation through varying widths of submerged artificial heterogeneous vegetation acted upon by varying wave parameters.

Methods

Experimental Setup and Instrumentation

The two-dimensional wave flume of Marine Structures Laboratory of the Department of Applied Mechanics and Hydraulics, National Institute of Technology Karnataka, Surathkal, is used to test the physical models of submerged artificial vegetation. The flume is 50 m long, 0.71 m wide, and 1.1 m deep. Figure 1 shows a schematic diagram of the setup of the present experiment.

The flume has a 6.3 m long, 1.5 m wide, and 1.4 m deep chamber with a bottom-hinged flap at one end which generates waves. The wave filter consists of a series of vertical asbestos cement sheets spaced at about 0.1 m center-to-center and parallel to length of the flume. A flywheel and bar-chain link the motor with the flap. By changing the eccentricity of bar chain on the flywheel, the wave height can be varied for a particular wave period. By changing the frequency through inverter, waves of desired wave period can be generated. The flap is controlled by an induction motor of 11 kW power at 1450 rpm, which in turn is regulated by an inventor drive (0–50 Hz), rotating in a speed range of 0–155 rpm. Monochromatic waves of heights 0.08–0.24 m and periods of 0.8–4.0 s in a maximum water depth of 0.5 m can be generated in this flume. In order to reduce reflection from the end of the flume, a rubble-mound wave absorber is in place at the other end of the flume. Four capacitance-type wave probes along with amplification units are used for data acquisition in the present experimental study. The spacing between probes is adjusted approximately to one-third of the wave length to ensure accuracy (Isaacson 1991). A MATLAB program based on the Isaacson's three-probe method is employed for separating the incident and reflected components of the signals recorded by the wave probes. Signals from wave probes are recorded by the computer through the data acquisition system.

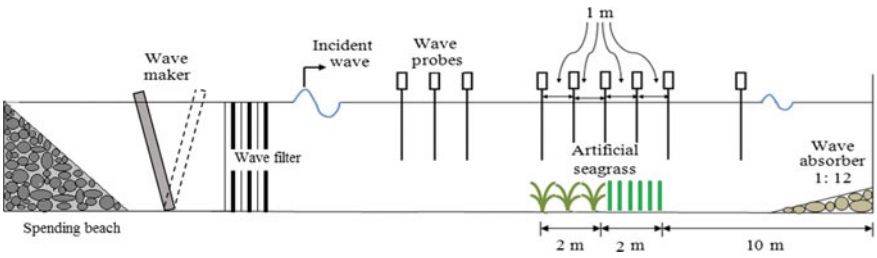

Fig. 1 Schematic diagram of experimental setup with submerged artificial vegetation

Test Models

To investigate the effect of width of vegetation on wave attenuation, two model scenarios are of interest in the present paper. The model scenarios include two cases of varying width of vegetation. The first case, represented by model 1, is a submerged artificial vegetation meadow of 3 m width, placed on the horizontal part of the flume bed. This is a combined heterogeneous model comprising of a 2 m wide seagrass meadow followed by a 1 m wide rigid vegetation meadow (rigid in the sense that the vegetation considered here is a submerged stem which may vibrate under the influence of passing waves, but this is very much less compared to the swaying motion of the seagrass leaves or kelp fronds). Model 2 is defined by a submerged artificial vegetation meadow of width 4 m; which also is a combined heterogeneous model, comprising of a 2 m wide seagrass meadow followed by a 2 m wide rigid vegetation meadow.

The submerged artificial seagrass is prepared from 0.1 mm thick polyethylene plastic sheets, whereas the submerged rigid plant model is made of nylon rods of diameter 0.010 m. In order to replicate the original vegetation in the field, a suitable material for the model is selected based upon the Young's modulus of natural vegetation. This is a measure of stiffness of the elastic material and is used to characterize the material property. The value of Young's modulus for seagrass is in the range 0.4–0.8 GPa (Folkard 2005), and that for common timber is in the range 10.05–15 GPa. In order to cover this range of E, a reference value of 0.7 and 11.5 GPa is assumed for the seagrass and the rigid vegetation, respectively, for the field condition. A reference value of 0.7 and 11.5 GPa, which falls in the above-mentioned range, is assumed for the seagrass and the rigid vegetation, respectively, for the field condition. A model scale of 1:30 is adopted in this experiment to scale down the prototype values. This would mean that the value of Young's modulus of the model material should be about 0.023 and 0.383 GPa, respectively. A material corresponding to this value is quite difficult to be identified for this type of vegetation model. Therefore, the stiffness property, EI, is modelled as a single parameter, instead of separately modelling Young's modulus, E, and the second moment of area, I. Thus, the appropriate material chosen for simulating seagrass leaves and the rigid vegetation trunks for this study is polyethylene with an E value of about 0.6 GPa and nylon with an E value of about 3 GPa, respectively. Accordingly, the prototype dimensions of seagrass leaves as well as the diameter of the rigid vegetal stems are fixed. The artificial vegetal models used for the experiments are shown in Fig. 2.

The seagrass model consists of a stipe of height 0.01 m, leaves of length 0.21 m, and placed at a spacing of 0.005 m. Each simulated plant is composed of 4–5 polyethylene leaves and is attached to 1 m $\times$ 0.73 m $\times$ 0.02 m concrete slabs in a staggered distribution. The rigid plant model is constructed by fixing rigid nylon

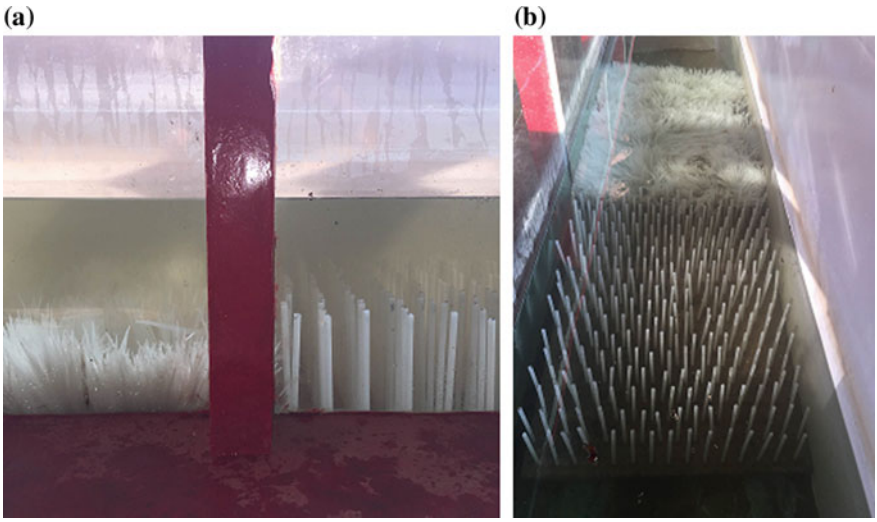

Fig. 2 Photo of model setup to study wave attenuation over a submerged heterogeneous artificial vegetation. **a** side view, **b** plan view

rods in holes drilled in 1 m × 0.73 m × 0.04 m concrete slabs. The rods are 0.010 m in diameter and 0.21 m long. Model scenario I of meadow width 3 m and model scenario II of width 4 m are placed over the flume bed, 30 m away from the wave flap and tested separately. Figure 2 illustrates a 1:30 scaled artificial heterogeneous vegetation model placed on the horizontal part of the flume bed.

Test Procedure

The models designed as submerged artificial vegetation are tested for the wave height attenuation when subjected to varying wave heights and wave periods in a water depth of 0.40 and 0.45 m in a two-dimensional wave flume. The vegetation test sections are subjected to normal attack of waves of characteristics as described in Table 1. The incident wave height, wave heights at locations within the meadow, and the wave transmission are recorded during the physical model investigation.

The wave flume is filled with ordinary tap water to the required depth. Before starting the experiment, the flume was calibrated to produce the incident waves of different combinations of wave height and wave periods. These models were tested for wave height attenuation in water depths (d) of 0.40 and 0.45 m with varying waves of heights (H) of 0.08–0.16 m, with an increment of 0.02 m and wave periods (T) of 1.8–2 s.

Table 1 Vegetation characteristics and experimental conditions

Artificial plant type	Vegetation model characteristics		Wave height (m)	Wave period, T (s)	Water depth, d (m)	Relative plant height (h_s/d)
Seagrass	Modulus of elasticity	0.6 GPa	0.08, 0.10, 0.12, 0.14, 0.16	1.8, 2	0.40, 0.45	0.525, 0.47
	Thickness of leaf	0.0001 m				
	Length of leaf	0.21 m				
	Width of leaf	0.004 m				
	Plant density	10,000 shoots/ m^2				
Rigid vegetation	Modulus of elasticity	2–4 GPa	0.08, 0.10, 0.12, 0.14, 0.16	1.8, 2	0.40, 0.45	0.525, 0.47
	Length of rod	0.21 m				
	Diameter of rod	0.010 m				
	Rod spacing	0.05 m				

Results

In this section, the variation of wave heights within the submerged vegetation meadow as well as the influence of relative plant height (h_s/d) on wave attenuation is analyzed for the two model scenarios, I and II.

Wave Height Attenuation

The measured wave heights at locations within the 3 m wide artificial submerged heterogeneous vegetation model (h_s/d = 0.525, 0.47) corresponding to wave periods, T = 1.8, 2 s are illustrated in Fig. 3.

It is observed that wave height attenuation along the meadow follows exponential decay, and the exponential curves obtained falls one below the other in decreasing order of wave heights. The percentage wave height at the exit point of the 3 m wide meadow for h_s/d = 0.525 is 44.8% and for that of h_s/d = 0.47, it is 53.3%. Figure 4 represents wave heights at locations within the 4 m wide meadow (h_s/d = 0.525, 0.47) corresponding to wave periods, T = 1.8, 2 s. The percentage wave height at the exit point of the 4 m wide meadow for h_s/d = 0.525 is 41.5% and that of h_s/d = 0.47 corresponds to 46%.

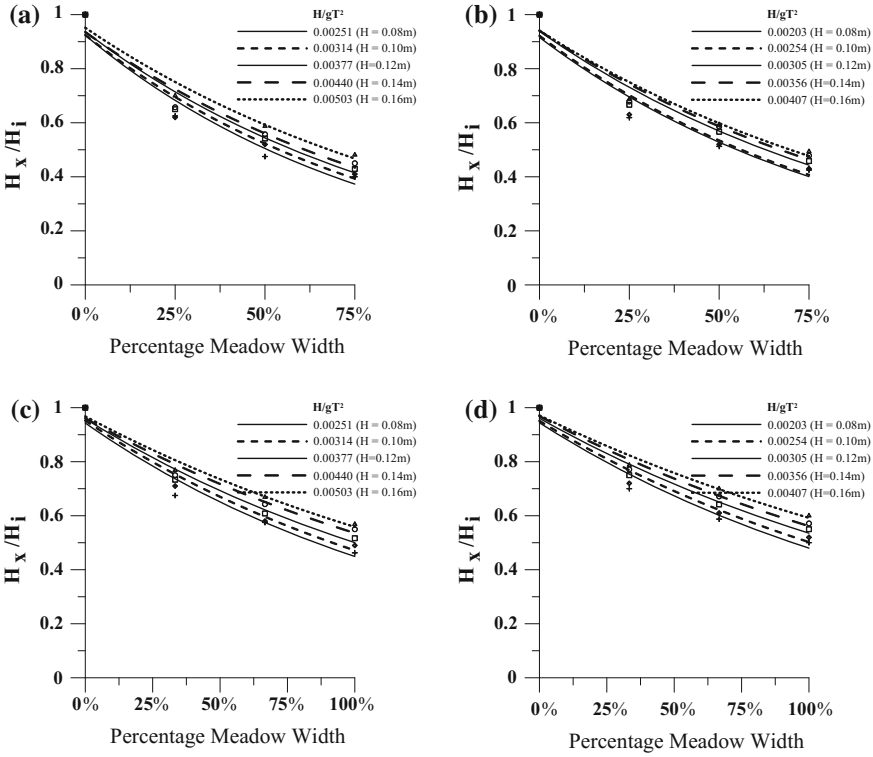

Fig. 3 Relative wave heights (H_x/H_i) at locations within the submerged heterogeneous vegetation model for **a** w = 3 m, T = 1.8 s, h_s/d = 0.525, **b** w = 3 m, T = 2 s, h_s/d = 0. 525, **c** w = 3 m, T = 1.8 s, h_s/d = 0.47, **d** w = 3 m, T = 2 s, h_s/d = 0. 47

Effect of Relative Plant Height ($\mathbf{h_s/d}$) *on Wave Attenuation*

The relative plant height represents the height of submergence of the vegetation with respect to the depth of water. An increase in relative plant height results in higher attenuation of incident wave height along the vegetated meadow. For the submerged vegetation model of 3 m width, the percentage wave height at the exit point of the meadow is nearly 44.8% for the case of higher relative plant height (h_s/d = 0.525) and 53.3% for h_s/d = 0.47; whereas, for the same vegetated meadow of width 4 m, it is nearly 41.5% for h_s/d = 0.525 and 46% for h_s/d = 0.47 (Fig. 5).

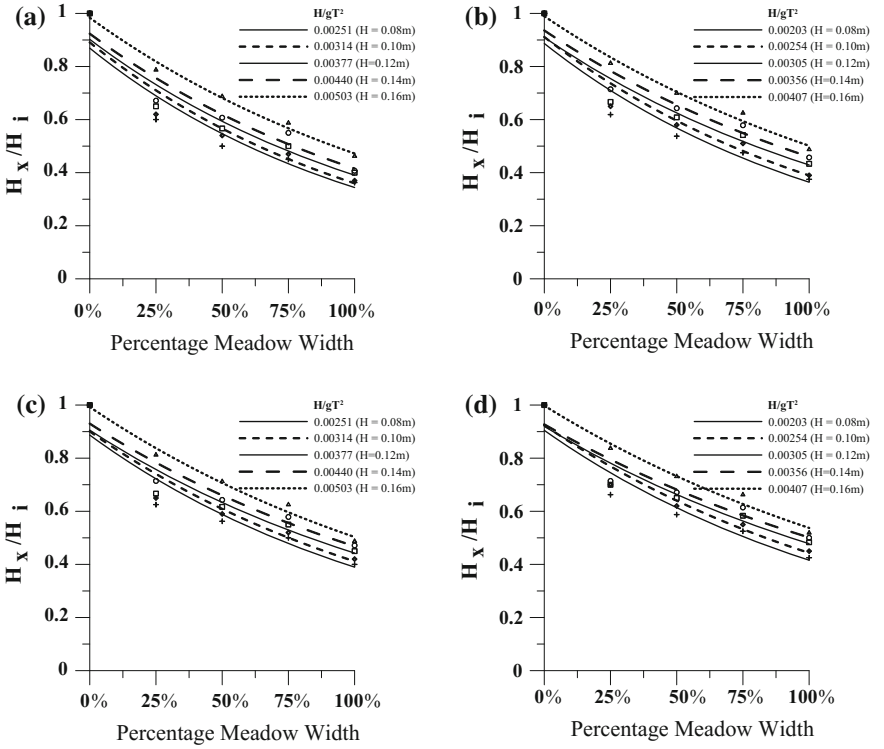

Fig. 4 Relative wave heights (H_x/H_i) at locations within the submerged heterogeneous vegetation model for **a** w = 4 m, T = 1.8 s, h_s/d = 0.525, **b** w = 4 m, T = 2 s, h_s/d = 0. 525, **c** w = 4 m, T = 1.8 s, h_s/d = 0.47, **d** w = 4 m, T = 2 s, h_s/d = 0. 47

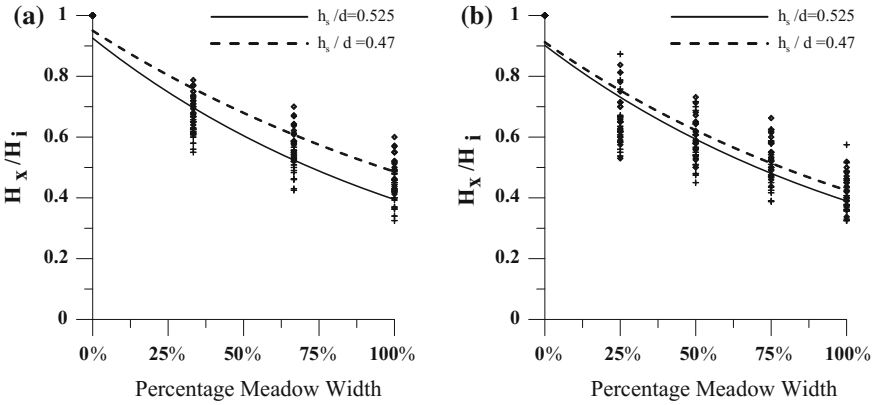

Fig. 5 Effect of relative plant height on wave attenuation for submerged heterogeneous vegetation model of width **a** w = 3 m, **b** w = 4 m

Conclusions

Wave heights decay exponentially as the wave propagates through the submerged vegetation. The wave orbital velocities are intercepted by the vegetation which results in increased turbulence, which in turn gives rise to loss of energy and reduction in wave heights.

As the relative plant height (h_s/d) increases from 0.47 to 0.525, both the model scenarios of width 3 and 4 m exhibit increased efficiency in wave height reduction. The percentage wave heights at the exit point of the meadow are 53.3 and 46% for a lower relative plant height of 0.47, when compared to 44.8 and 41.5% for a higher relative plant height of 0.525.

References

Asano T, Tsutsui S, Sakai T (1988) Wave damping characteristics due to seaweed. In: Proceedings of 35th coastal engineering conference in Japan, pp 138–142 (in Japanese)

Asano T, Deguchi H, Kobayashi N (1992) Interaction between water waves and vegetation. In: Proceedings of 23rd international conference on coastal engineering, Venice, Italy, pp 2710–2723

Bouma TJ, De Vries MB, Low E, Peralta G, Tánczos IC, van de Koppel J, Herman PJ (2005) Trade-offs related to ecosystem engineering: a case study on stiffness of emerging macrophytes. Ecology 86(8):2187–2199

Charlier RH, Chaineux MCP, Morcos S (2005) Panorama of the history of coastal protection. J Coastal Res 21(1):79–111

Ciraolo G, Ferreri GB, Loggia LG (2006) Flow resistance of *Posidonia oceanica* in shallow water. J Hydraul Res 44(2):189–202

Dalrymple RA, Kirby JT, Hwang PA (1984) Wave diffraction due to areas of energy dissipation. J Waterw Port Coast Ocean Eng 110(1):67–79

Dubi A, Torum A (1994) Wave damping by kelp vegetation. Coast Eng 142–156

Elwany MHS, O'Reilly WC, Guza RT, Flick RE (1995) Effects of Southern California kelp beds on waves. J Waterw Port Coast Ocean Eng 121(2):143–150

Folkard AM (2005) Hydrodynamics of model *Posidonia oceanica* patches in shallow water. Limnol Oceanogr 50(5):1592–1600

Fonseca MS, Cahalan JA (1992) A preliminary evaluation of wave attenuation by four species of seagrass. Estuar Coast Shelf Sci 35(6):565–576

Gambi MC, Nowell ARM, Jumars PA (1990) Flume observations on flow dynamics in *Zostera marina* (eelgrass) beds. Mar Ecol Prog Ser 61:159–169

Gedan KB, Kirwan ML, Wolanski E, Barbier EB, Silliman BR (2011) The present and future role of coastal wetland vegetation in protecting shorelines: answering recent challenges to the paradigm. Clim Change 106(1):7–29

Husrin S, Strusińska A, Oumeraci H (2012) Experimental study on tsunami attenuation by mangrove forest. Earth Planet Space 64(10):973–989

Isaacson M (1991) Measurement of regular wave reflection. J Waterw Port Coast Ocean Eng ASCE 117:553–569

Jayakumar S, Ilangovan D, Naik KA, Gowthaman R, Tirodkar G, Naik GN, Ganeshan P, ManiMurali R, Michael GS, Ramana MV, Bhattacharya GC (2005) Run-up and inundation limits along southeast coast of India during the 26 December 2004 Indian Ocean tsunami. Curr Sci 88(11):1741–1743

Kathiresan K, Rajendran N (2005) Coastal mangrove forests mitigated tsunami. Estuar Coast Shelf Sci 67(3):601–606

Kobayashi N, Raichle AW, Asano T (1993) Wave attenuation by vegetation. J Waterw Port Coast Ocean Eng 119(1):30–48

Koftis T, Prinos P, Stratigaki V (2012) Wave damping over artificial *Posidonia oceanica* meadow: a large-scale experimental study. Coast Eng 73:71–83

Lakshmanan N, Kantharaj M, Sundar V (2012) The effects of flexible vegetation on forces with a Keulegan-Carpenter number in relation to structures due to long waves. J Mar Sci Appl 11(1):24–33

Lovas SM, Torum A (2001) Effect of the kelp *Laminaria hyperborea* upon sand dune erosion and water particle velocities. Coast Eng 44:37–63

Manis JE, Garvis SK, Jachec SM, Walters LJ (2015) Wave attenuation experiments over living shorelines over time: a wave tank study to assess recreational boating pressures. J Coast Conserv 19(1):1–11

Mascarenhas A, Jayakumar S (2008) An environmental perspective of the post-tsunami scenario along the coast of Tamil Nadu, India: Role of sand dunes and forests. J Environ Manag 89 (1):24–34

Massel SR (1999) Fluid mechanics for marine ecologists. Springer, Berlin

NIO (2005) Observations of post tsunami reconnaissance investigations along eastern coastal tract of India following the devastating tsunami of 26th December 2004. National Institute of Oceanography Technical Report no. NIO/TR-08/2005

Noarayanan L, Murali K, Sundar V (2012) Role of vegetation on beach run-up due to regular and cnoidal waves. J Coast Res 28(1A):123–130

Ozeren Y, Wren DG, Wu W (2013) Experimental investigation of wave attenuation through model and live vegetation. J Waterw Port Coast Ocean Eng

Rosman JH, Denny MW, Zeller RB, Monismith SG, Koseff JR (2013) Interaction of waves and currents with kelp forests (*Macrocystis pyrifera*): insights from a dynamically scaled laboratory model. Limnol Oceanogr 58(3):790–802

Stratigaki V, Manca E, Prinos P, Losada IJ, Lara JL, Sclavo M, Amos CL, Caceres I, Sanchez-Arcilla A (2011) Large scale experiments on wave propagation over *Posidonia oceanica*. J Hydraul Res IAHR 49(Supplement 1):31–43

Strusinska-Correia A, Husrin S, Oumeraci H (2013) Tsunami damping by mangrove forest: a laboratory study using parameterized trees. Nat Hazard Earth Syst Sci 13(2):483

Struve J, Falconer RA, Wu Y (2003) Influence of model mangrove trees on the hydrodynamics in a flume. Estuar Coast Shelf Sci 58:163–171

Sundar V, Murali K, Noarayanan L (2011) Effect of vegetation on run-up and wall pressures due to cnoidal waves. J Hydraul Res 49(4):562–567

Zeller RB, Weitzman JS, Abbett ME, Zarama FJ, Fringer OB, Koseff JR (2014) Improved parameterization of seagrass blade dynamics and wave attenuation based on numerical and laboratory experiments. Limnol Oceanogr 59(1):251–266

Developing Rating Curves for Nubia Lake, Sudan, Using RS/GIS

Mohamed Elsahabi, Abdelazim Negm and Kamal Ali

Abstract Estimating the water capacity of any lake required an extensive measurements and complicated approximation manual methods, which consuming time, effort and money. Rating curves are considered a useful tool to estimate the capacity in a cost-effective way. In addition, generation of these rating curves using Remote Sensing (RS) data and GIS technique has led to save time, effort and money. In this paper, the measured available data of the Aswan High Dam Lake (AHDL) (particularly Nubia Lake) and the extracted data from processed satellite images for different years are used to develop rating curves for the lake by utilizing the created 3D profile of the lake. This profile is then used to estimate the relationship between the lake capacity and the level. Also, the relationship between the lake surface area and the level are developed for the active sedimentation zone of the lake for the years 2000, 2004, 2006, 2008, 2010, and 2012. Equations are presented for individual years and collectively. The accuracy of the developed relationships is assessed by comparing its results with the observed data for the lake. The root mean square error is found to range between 5–10 and 2–4% for (volume/level) relationship and (area/level) relationship respectively. Moreover, results indicated that the present approach overestimate the water capacity by less than 1% compared to the results of the method used by AHDA at year 2012 at the same water level (175 m amsl).

M. Elsahabi (✉) · K. Ali
Civil Engineering Department, Faculty of Engineering,
Aswan University, Aswan, Egypt
e-mail: moh_78_78@yahoo.com

K. Ali
e-mail: kamalabbas90@yahoo.com

A. Negm
Water and Water Structures Engineering Department, Faculty of Engineering,
Zagazig University, Zagazig 44519, Egypt
e-mail: amnegm@zu.edu.eg; amnegm85@yahoo.com

V. P. Singh et al. (eds.), *Hydrologic Modeling*, Water Science
and Technology Library 81, https://doi.org/10.1007/978-981-10-5801-1_35

Keywords Nubia lake · Sudan · Aswan high dam lake · Rating curve
Lake capacity · Remote sensing · GIS

Introduction

Estimating the storage capacity of the lakes is essential for the managers and decision makers of water management sector. But, estimating the capacity using the generated rating curves via labor-intensive manual methods need an extensive field measurement. Moreover, these manual computationally methods consume time, money and effort. Therefore, developing rating curves for lakes using GIS/RS techniques is needed to overcome most such problems when estimating the capacity of these lakes. In situ measurements and satellite observations data have been used to estimate the water storage quantity and variations in lakes and reservoirs, with successful application in different parts of the world among those lakes: Roseires reservoir in Sudan (Muala et al. 2014), Lake La Bure in the south–west of France (Baup et al. 2014), lake Izabal in Guatemala (Medina et al. 2010), lake Tana in Ethiopia and lake Mead (U.S.A.) (Duan and Bastiaanssen 2013), Lake Dongting in China (Zhang et al. 2006) and Randy Poynter Lake in Georgia (Lee 2013). Concerning the Aswan High Dam Lake (AHDL), several studies were conducted including those of Abileah et al. (2011), El Gammal et al. (2010), Muala et al. (2014). The AHDL is vital to Egypt; as it stores and regulates Nile water, being the main source of fresh water for about 85% of its population (Elsahabi et al. 2015). Therefore, it is of the outmost important to monitor the variations in its storage capacity. This will lead to improving the knowledge of the water mass balance of this lake, and consequently, enable this lake to fulfill its purpose efficiently. This paper aim to use the in situ measurements of Lake Nubia active zone for years 2000, 2004, 2006, 2008, 2010, and 2012 to develop its rating curves for the selected years individually and collectively based on remotely sensed data and GIS technique. Then the water capacity of this part of AHDL can be easily estimated and compared with the results obtained by the Aswan High Dam Authority (AHDA) based on the complementary cross sections method.

Study Area

The AHDL consists of two main parts. Egyptian part with a length of about 350 km and called Nasser Lake and Sudanese part with a length of 150 km. The study area of the present research extends between latitudes 21° 44′ 30″ and 22° 00′ 00″N (upstream AHD) within the Sudanese part (Lake Nubia) where most of the sediments were accumulated. It contains 6 cross sections (22, 24, 25, 26, 27 and 28) from North to South as indicated in Fig. 1.

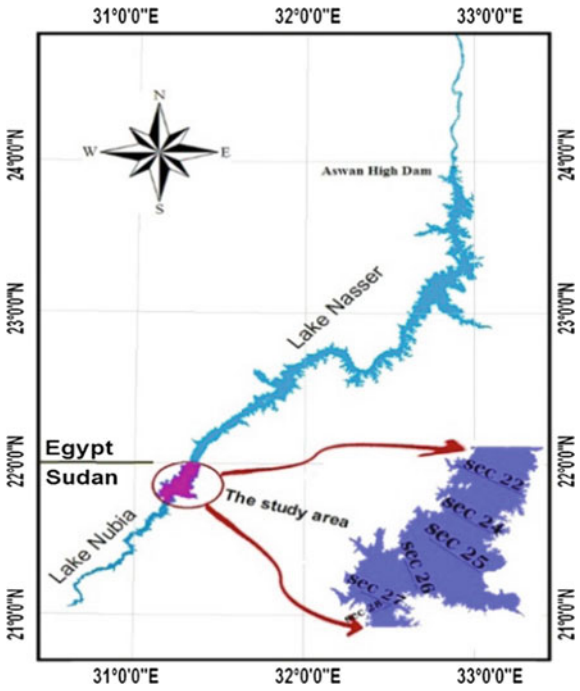

Fig. 1 Location map of the study area within the Aswan High Dam Lake (AHDL)

In addition, from the studies and observations done by the repetitive field survey missions, which were carried out through the joined efforts of the Aswan High Dam Authority (AHDA) and the Nile Research Institute (NRI), it is concluded that the cross sections have been enlarged and the water velocity have been decreased in the chosen portion of Lake Nubia (NRI 2012).This part represents the area with most intensive sediment deposition (about 50–70%) of the total amount of sediment in AHDL (NRI 2012), although this portion represents only about 5.96% of the total area of AHDL (MWRI 2012). This part called (the active sedimentation portion).

Data Collection

The following materials/data are collected to achieve the purpose of this paper:

Satellite Images

Three Landsat ETM+ images (Path/Row = 175/045) were used in this research. These images were acquired at different dates (September 2000, March 2006 and

March 2009) from the GLCF website in GeoTIFF (systematic correction) products (GLCF 2014). The acquired images are used to extract the lake boundaries. The satellite images were shot in September 2000 where the water level in the lake was (178 m) amsl, March 2006 where the water level was (173 m) and in March 2009 where the water level was 176.60 m.

Hydrographic Survey Data

The hydrographic survey data which describe the geometry of AHDL were conducted by (AHDA and NRI) using the Odom Hydrographic Echo Sounder device (Hydrotrac II) with accuracy up to 0.01 m ± 0.1% of the measured depth. The lake geometry presented by Easting, Northing, and Elevation (*E*, *N*, and *Z*) was used for the 3D bed surface generation (Elsahabi and Negm 2016). In this paper, the hydrographic survey data of the years 2000, 2004, 2006, 2008, 2010 and 2012 for the study area were used.

Water Levels Data

The water levels upstream AHD which had been daily recorded by AHDA gauge stations till the year 2010 (MALR 2010) were collected to help in detecting the water surface levels at the dates of acquiring the satellite images.

Methodology

To achieve the objective of the present paper, the methodology presented in Fig. 2 is used as explained in the next subsections.

Water Surface Areas Extraction

The water boundaries delineation from Landsat satellite images, using ArcGIS software are conducted by different techniques including:

- By image classification techniques (supervised and unsupervised techniques) (Ebaid and Ismail 2010; Lillesand et al. 2004).
- Normalized difference water index (NDWI) (Muala et al. 2014) as given by the following equation:

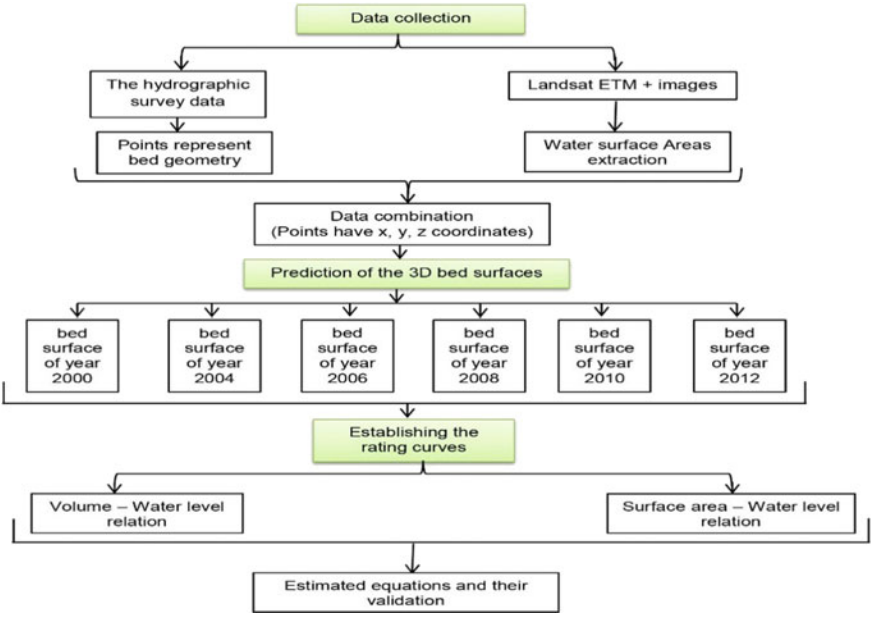

Fig. 2 Flowchart of the procedures adopted in the present study to develop the rating curves of Nubia Lake

$$\mathrm{NDWI} = \frac{\mathrm{Green} - \mathrm{NIR}}{\mathrm{Green} + \mathrm{NIR}} \tag{1}$$

In this method, the water bodies have positive values.

- By using the modified normalized difference water index (MNDWI) (Muala et al. 2014) which replaces the NIR band in the previous equation with the MIR band.
- Where water bodies have positive values.
- By normalized difference moisture index (NDMI) (Wilson and Sader 2002) which is given by the following equation:

$$\mathrm{NDMI} = \frac{\mathrm{NIR} - \mathrm{MIR}}{\mathrm{NIR} + \mathrm{MIR}} \tag{2}$$

Green, NIR, and MIR represent green, near-infrared and middle-infrared bands of the Landsat ETM+ images respectively. Also, water bodies have positive values.

Out of the above methods, the unsupervised image classification technique extracts the water bodies more accurately (Elsahabi et al. 2015, 2016, they concerned with lake Nasser and Lake Nubia as a study area respectively). Therefore, it was adopted as explained below and summarized in Fig. 3.

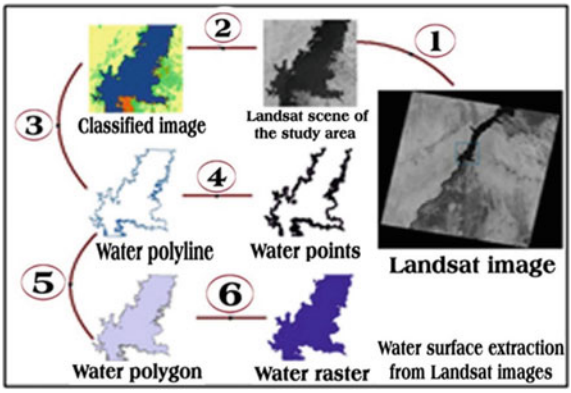

Fig. 3 Extraction of water boundaries from Landsat images

1. Detecting the Landsat scene of the study area by making a clip from the original image.
2. Making unsupervised classification, and then converting the final classified image (contain 4 classes) into features (vector layers).
3. Separating the water feature from the other features as a polyline.
4. Converting the polyline boundaries into water points layer, which have (x, y) coordinates and z from the water levels recorded by AHDA, which synchronized with the acquired dates of the satellite images.
5. Converting the water polyline layer into polygon layer.
6. Finally, converting the polygon layer into raster water scene to help in the interpolation method (predicting the 3D bed surface).

The derived water areas are overlaid with the reference water area to display the degree of misclassification error in water surfaces extraction. Finally, the overall accuracy (Story and Congalton 1986) is computed to support the accuracy assessment analysis. The extracted lake boundaries, obtained from the processed satellite images, were used to form the shape of the surface and also, to form a group of scattered points (x, y, z) using the WGS84, UTM Z36N as a defined projected coordinate system. These points are combined with the hydrographic survey points to generate the 3D bed surfaces of the study area for years 2000, 2004, 2006, 2008, 2010, and 2012.

Prediction of the 3D Bed Surfaces

To predict the original lake 3D bed surface for the selected years from 2000 to 2012, the available hydrographic survey data were combined with the data points derived from Landsat satellite images representing the water surface area for more accurate interpolation. The interpolation process was performed with the Radial

Base functions (RBF) method (ESRI 2008). The mean absolute error (MAE) was estimated to assess the accuracy of the interpolation methods (Elsahabi and Negm 2016).

Establishing the Rating Curves

The relationships between the three parameters of the lake (water volume/surface area/level changes) are estimated by using ArcGIS software version 9.3 (ESRI 2008). These relationships are generated to establish the rating curves for the selected years from 2000 to 2012.

Statistical Indicators

Table 1 presents the statistical indicators including RMSE (root mean square error) and R^2 (coefficient of determination) that are used to assess the accuracy of developed rating curves equations.

Results and Discussion

Extraction of Water Surfaces Areas

Among the several methods used to extract the water surface of the lake, the unsupervised classification technique performed significantly better than others with an overall accuracy of 98.90%. Therefore, the extracted water surfaces by the unsupervised technique from all available Landsat images from the year 2000 to 2012 were used in the next step.

Table 1 Statistics indicators for the equations of the developed rating curves

Concept	Name	Formula
Root m. square error	RMSE	$\sqrt{\sum (\text{Mes} - \text{calc.})^2 / N}$
Deter. coefficient	R^2	$\sum(\text{calc.} - \text{Avg. Mes})^2 / \sum(\text{Mes} - \text{Avg. Mes})^2$
Percent of root m. square error	RMSE (%)	$(\text{RMSE}/\text{Avg. Mes} \times 100)$

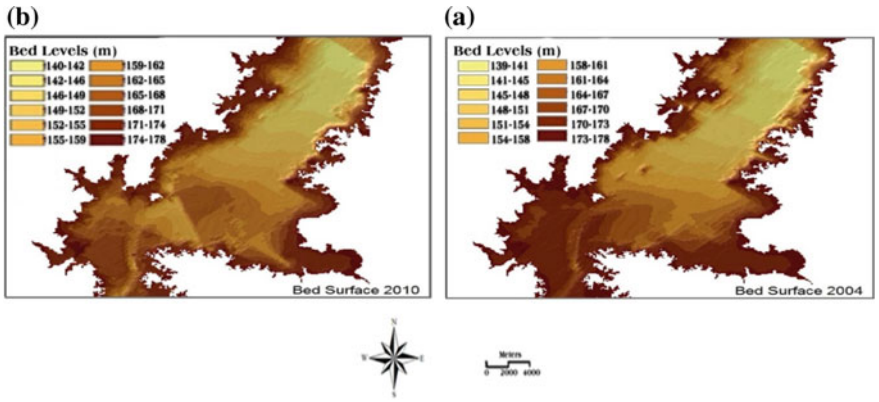

Fig. 4 Sample results of the predicted bed surfaces for the years **a** 2004 and **b** 2010

Creation of the 3D Profile of the Lake

The RBF interpolation function of ArcGIS is used to interpolate accurately the bed surface to create the 3D lake profile. The RBF generally produces good results for gently varying surfaces such as elevations (ESRI 2008). To assess the accuracy of the used RBF method, MAE was computed for all studied years. The biggest MAE was 0.21 m for year 2008 indicating high accuracy of the interpolation process (Elsahabi and Negm 2016). The 3D bed surfaces were predicted for the years 2000, 2004, 2006, 2008, 2010 and 2012. Sample results are presented in Fig. 4 for the year 2004 and year 2010.

Rating Curves and Their Validation

To understand the water capacity (volume) variations in the study area; various rating curves are developed between (volume or capacity, surface area, level changes), which are closely connected with lake's remotely sensed data and hydrographic survey data.

Volume/Level Relation

Figure 5a, b show samples of established rating curves that represent the relationships between (volume/level) for the year 2010 and collectively for the whole period from the year 2000 to the year 2012. It can be observed from these Figures that, the volume changes as a function of level changes presented a third polynomial relationship.

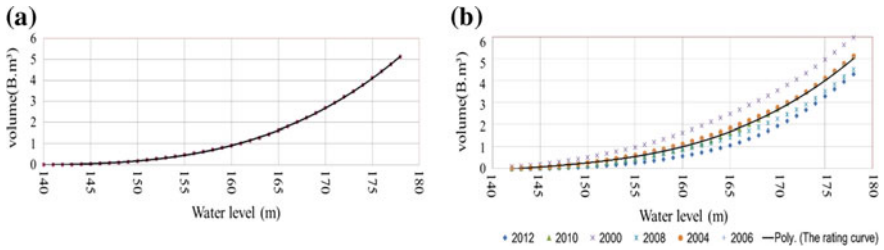

Fig. 5 Sample results of the rating curves (volume/level): **a** 2010 rating curve and **b** collective rating curve for the years (2000–2012)

Table 2 Developed relationships between volume and water depth for the period from 2000 to 2012, individually and collectively

Period of the estimated rating curve	Number of points	R^2	RMSE (Bm^3)	RMSE (%)	Rating curve equation (y = volume in $B.m^3$ and x = water level in m)
2000	45	0.99	0.091	5.2	$y = 4E-05x^3 - 0.0148x^2 + 1.817x - 74.04$
2004	40	0.99	0.084	5.6	$y = 7E-05x^3 - 0.0292x^2 + 4.0817x - 191.2$
2006	40	0.99	0.078	5.4	$y = 8E-05x^3 - 0.0337x^2 + 4.7562x - 224.92$
2008	38	0.99	0.070	5.5	$y = 9E-05x^3 - 0.0388x^2 + 5.6086x - 271.85$
2010	39	0.99	0.069	4.9	$y = 8E-05x^3 - 0.0332x^2 + 4.6016x - 213.06$
2012	37	0.99	0.058	5.3	$y = 0.0001x^3 - 0.0431x^2 + 6.1978x - 297.355$
2010 and 2012	74	0.97	0.099	7.6	$y = 0.0001x^3 - 0.043x^2 + 6.1793x - 296.7$
2000–2012	222	0.94	0.164	10.7	$y = 9E-05x^3 - 0.0386x^2 + 5.5358x - 265.35$

Table 2 shows the eight developed equations for the years (2000, 2004, 2006, 2008, 2010 and 2012), for two years (2010 and 2012) and for all years (2000–2012) of the relationship between (volume/level). From Table 2, it is clear that the computed volumes are in good agreement with the measured ones where R^2 varies from 0.94 to 0.99 and RMSE varies from 5 to 10% only.

As a quantitative indicator for above results; Fig. 6a, b show a comparison between the measured and the calculated water volumes from the derived rating curves equations at water level 178 and 175 m respectively. It is clear that the computed and the measured volume values are almost equal for individual years while a slight difference in the values of the volume for the whole years from 2000 to 2012.

Area/Level Relation

The relationship between (area/level) is clearly non-linear (a second—order polynomial function). Samples of the obtained results are presented in Fig. 7a, b for the year 2010 and for all years from 2010 to 2012.

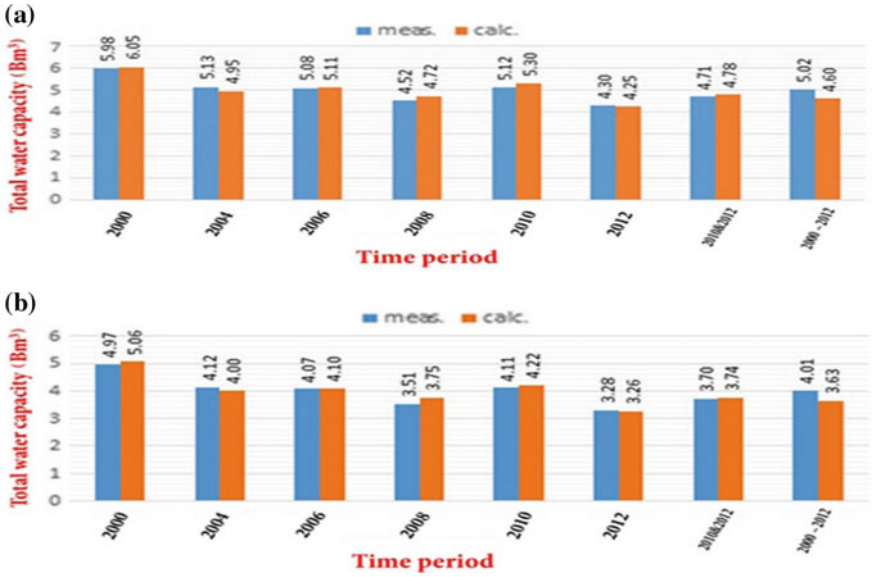

Fig. 6 Total water capacity computed from the individual and collective rating curves: **a** at water level (178 m amsl), **b** at water level (175 m amsl)

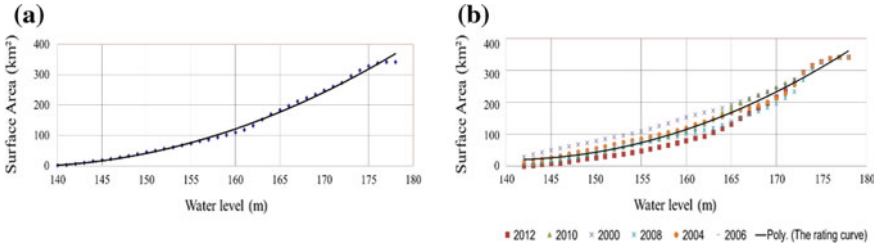

Fig. 7 Sample results of the rating curves (area/level): **a** 2010 rating curve and **b** collective rating curve for the years (2000–2012)

Similarly, Table 3 presents the eight developed equations for the relationship between area and level for the active sedimentation zone of Lake Nubia for the years (2000, 2004, 2006, 2008, 2010 and 2012), (2010 and 2012) and collectively for the period from (2000 to 2012). The value of R^2 is more than 0.97 while RMSE ranged between 2.7 and 5.4 km^2. The predicted surface area values using the developed equations are compared with the measured values as shown in Fig. 8 for the lake water level of 175 m.

Table 3 Developed equation for the rating curves of the area/level for the years from 2000 to 2012

Period of the estimated rating curve	Number of points	R^2	RMSE (km^2)	RMSE (%)	Rating curve equation (y = surface area and x = water level)
2000	45	0.99	2.76	2.1	$y = 0.1249\ x^2 - 31.068x + 1923$
2004	40	0.99	3.70	2.8	$y = 0.1972\ x^2 - 53.803x + 3682.3$
2006	40	0.99	3.06	2.3	$y = 0.2203\ x^2 - 60.939x + 4229$
2008	38	0.99	3.32	2.7	$y = 0.2642\ x^2 - 75.287x + 5379.2$
2010	39	0.99	3.03	2.2	$y = 0.2054\ x^2 - 55.65x + 3766.8$
2012	37	0.99	3.07	2.5	$y = 0.33\ x^2 - 95.598x + 6932.7$
2010 and 2012	74	0.98	4.52	3.4	$y = 0.2683\ x^2 - 75.816x + 5365.4$
2000–2012	222	0.97	5.38	3.8	$y = 0.2348\ x^2 - 65.673x + 4612.5$

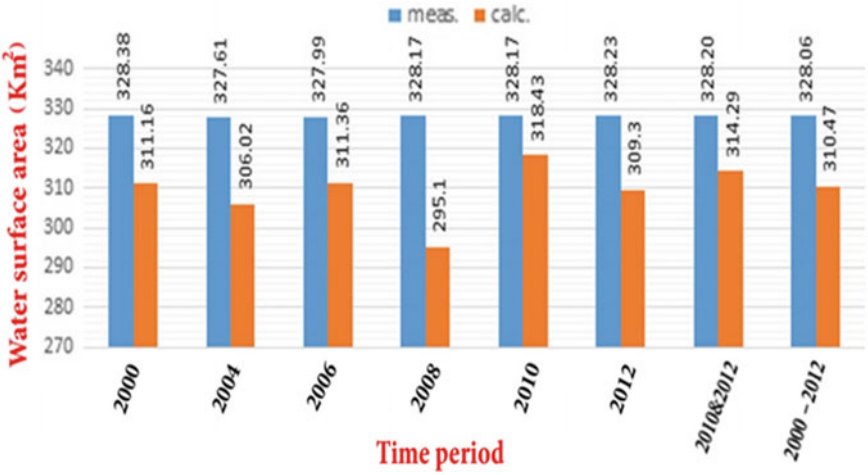

Fig. 8 Water surface area computed from the individual and collective rating curves at water level (175 m amsl)

Application and Comparisons

Table 4 illustrates that the sum of the water volume of AHDL active sedimentation portion that estimated by AHDA and NRI (the traditional method) was about 3.232 billion m^3at the year 2012 (NRI 2012) compared to 3.26 billion m^3 using the developed rating curves (see Fig. 6b). Consequently, the presented method overestimates the water capacity by less than 1%. Accordingly, the developed equations can be used to estimate the water volume (capacity) of this part of the lake instead of the costly measurements. However, field measurements by AHDA and NRI are necessary from time to another to update such equations and for other purposes as well.

Table 4 Calculated water volumes of the study area by AHDA at water level (175 m amsl) at the year 2012

Sec. code	Area (m^2)	Served length (km)	Volume (Bm^3)
22	190515.91	7.95	1.514
24	95818.63	7.25	0.695
25	98114.46	8.00	0.785
26	19233.31	6.00	0.115
27	8947.32	8.50	0.076
28	11884.96	4.00	0.047
$\sum$			3.232

Conclusions

This study developed several relationships between (water volume or capacity/surface area/water level) for the active sedimentation zone of Nubia Lake (part of Aswan High Dam Lake) for the selected years from 2000 to 2012 individually and collectively. The accuracy of the developed relationships was assessed by comparing the results with the field measurements and the existing rating curves for the lake. The RMSE was found to range between 5–10 and 2–4% for the relationships (volume/water level) and (surface area/water level) respectively. Also, the correlation coefficients were ranged from 0.94 to 0.99 (volume/water level) and from 0.97 to 0.99 (area/water level). It is recommended to use the remote sensing and in situ data jointly to provide accurate estimate of water capacity (volume) variations of the whole AHDL.

Acknowledgements Aswan University, Aswan High Dam Authority (AHDA) and the General Authority for AHDL Development are acknowledged for providing the facilities and data utilized during this research work.

References

Abileah R, Vignudelli S, Scozzari A (2011) A completely remote sensing approach to monitoring reservoirs water volume. In: Fifteenth international water technology conference, IWTC 15, Alexandria, Egypt, pp 1–17

Baup F, Frappart F, Maubant J (2014) Combining high-resolution satellite images and altimetry to estimate the volume of small lakes. Hydrol Earth Syst Sci 18:2007–2020

Duan Z, Bastiaanssen W (2013) Estimating water volume variations in lakes and reservoirs from four operational satellite altimetry databases and satellite imagery data. Remote Sens Environ 134:403–416

Ebaid H, Ismail S (2010) Lake Nasser evaporation reduction study. J Adv Res 1:315–322

El Gammal EA, Salem SM, El Gammal AA (2010) Change detection studies on the world's biggest artificial lake (Lake Nasser, Egypt). Egypt J Remote Sens Sp Sci 13:89–99

Elsahabi M, Negm A, El-Tahan MA (2015) Performances evaluation of surface water areas extraction techniques using landsat ETM+ data: case study Aswan High Dam Lake (AHDL).

In: 9th international conference inter disciplinarity in engineering, INTER-ENG, 8–9 Oct 2015, Tirgu-Mures, Romania

Elsahabi MA, Negm AA, ALi KA (2016) Performances evaluation of surface water areas extraction techniques using LANDSAT ETM+ data: case study of Lake Nubia, Sudan. In: Egypt Int J Eng Sci Technol 19(2):275–281

Elsahabi M, Negm A (2016) Building 3D profile for Lake Nubia, < Sudan > using RS/GIS for accurate estimation of Sediment. In: 10th international conference inter disciplinarity in engineering, INTER-ENG, 6–7 Oct 2016, Tirgu-Mures, Romania

ESRI (2008) Environmental Systems Research Institute. Help topics of ArcGIS version 9.3 Desktop developer center of geographic information systems (GIS) software, Redlands, California

GLCF (2014) The global land cover facility provides earth science data and products. Available from: http://glcfapp.glcf.umd.edu/data/landsat/, last accessed 09 May 2014

Lee K (2013) Estimation of reservoir storage capacity using terrestrial lidar and multibeam sonar, Randy Poynter lake, Rockdale County, Georgia In: Proceedings of the 2013 Georgia water resources conference, held 10–11 April 2013, at the University of Georgia

Lillesand T, Kiefer R, Chipman J (2004) Remote sensing and image interpretation (fifth edition). John Wiley and Sons, Inc

MALR (2010) The ministry of agriculture and land reclamation, Egypt, the general authority for AHDL development, AHDL levels (1978–2010)

Medina C, Gomez J, Alonso J, Villares P (2010) Water volume variations in Lake Izabal (Guatemala) from in situ measurements and ENVISAT radar altimeter (RA-2) and advanced synthetic aperture radar (ASAR) data products. J Hydrol 382:34–48

Muala E, Mohamed Y, Duan Z, Zaag P (2014) Estimation of reservoir discharges from Lake Nasser and Roseires Reservoir in the Nile Basin using satellite altimetry and imagery data Remote Sens 6:7522–7545

MWRI (2012): The ministry of water resources and irrigation, Egypt, Nile water sector annual report (2011–2012)

NRI (2012) Nile Research Institute annual report of sedimentation in Lake Nubia–Wadi Halfa field trips (1973–2012) National Water Research Center, Cairo, Egypt

Story M, Congalton R (1986) Accuracy assessment: a user's perspective. Photogram Eng Rem Sens 52(3):397–399

Wilson E, Sader S (2002) Detection of forest harvest type using multiple dates of Landsat TM imagery. Rem Sens Environ 80:385–396

Zhang J, Xu K, Yang Y, Qi L, Hayashi S, Watanabe M (2006) measuring water storage fluctuations in Lake Dongting, China, by Topex/Poseidon satellite altimetry. Environ Monit Assess 115:23–37

A Spreadsheet Approach for Prediction of Rating Curve Parameters

Mohammad Muzzammil, Javed Alam and Mohammad Zakwan

Abstract Streamflow data is required for planning and design of various hydraulic structures and water resource projects such as bridges, culverts, flood plain zoning, flood protection works, flood warning systems, and assessment of water resources potential. A reliable and continuous record of streamflow data is, therefore, of utmost importance. However, it is very difficult to maintain a continuous record of discharge and sometimes even impractical during floods. A continuous record of elevation of water surface in a stream above some arbitrary datum or the stage of river is rather easy and accurate as compared to discharge. A functional relationship between stage and discharge at a site in a river is called the rating curve. The accuracy of discharge estimated from the rating curve depends on the accuracy of stage measurement and development of the rating curve. The conventional method of regression analysis for the development of the rating curve often fails to give stage–discharge relationship accurately. In the present study, a simple and quick Excel solver technique has been used for the development of the rating curve accurately. The results of the solver in Excel are compared with conventional method of regression analysis. The statistical parameters such as root mean square error, correlation coefficient, and Nash criteria were computed for assessment of the performance of these methods for the rating curve development. It has been found that the performance of the Excel solver is better than that of the conventional method.

Keywords Streamflow · Rating curve · Excel solver · Conventional method

M. Muzzammil · J. Alam (✉) · M. Zakwan
Department of Civil Engineering, ZH College of Engineering & Technology,
AMU Aligarh 202002, Uttar Pradesh, India
e-mail: javedalamced@gmail.com

V. P. Singh et al. (eds.), *Hydrologic Modeling*, Water Science
and Technology Library 81, https://doi.org/10.1007/978-981-10-5801-1_36

Introduction

Streamflow measurements are the most important basic data of hydrologic studies required for the design and construction of hydraulic structures, flood management and flood forecasting. Accurate streamflow measurement is of paramount importance for economic and safe design of water resource project. Streamflow measurement techniques are broadly classified as direct determination of stream discharge and indirect determination of streamflow. For direct determination of discharge methods depending on the site conditions either of area velocity method, dilution method (chemical method), ultrasonic method, or electromagnetic method can be used. Indirect determination of streamflow requires construction of hydraulic structures such as flumes, notches, weirs, and gated structures or application of the slope-area method. However, continuous measurement of discharge at number of sections in a river is very costly and sometimes impractical. To eliminate this limitation, rating curve is commonly used. Development of the rating curve for a gauging site generally requires two step procedures. First step is to develop stage–discharge relationship using historical stage–discharge data of the gauging site by plotting the graph between the observed stage (G) and observed discharge (Q) at the gauging site. Second step involves the measurement of stages only, and the corresponding discharges are estimated from the rating curve. It is easy to maintain a continuous record of stages rather than maintaining continuous record of discharges in a river. Thus eliminating the need of rigorous, time-consuming, costly, and sometime impractical exercise of continuous discharge measurement, the rating curve has always been extensively used for discharge measurement in many artificial and natural channel as it represents the combined effect of many flow and channel parameters.

Stage–discharge relationship has always remained an area of interest for hydrologists, and many attempts have been made by hydrologists to establish reliable rating curves using graphical and numerical techniques. Stage–discharge relationship was established by graphical method by Herschy (1995), Fenton and Kellar (2001). Polynomial models for stage–discharge relationships were proposed by Herschy (1995), McGinn and Chubak (2002) Braca (2008). For extrapolating rating curve beyond the measured data range, various numerical methods have been proposed including regression method (Peterson-Øverlier 2004; Moyeed and Clarke 2005), polynomial regression model (Braca 2008), support vector machine (SVM) (Sivapragasam and Mutlie 2005), artificial neural network (ANN) (Tawfik et al. 1997; Jain and Chalisgaonkar 2000; Sudheer and Jain 2003; Bhattacharya and Solomatine 2005; Habib and Maselhe 2006), gene expression programming (GEP) (Guven and Aytek 2009), ANN with LMR (Bisht et al. 2010), and genetic algorithm (GA) with model tree (Ghimire and Reddy 2010). Least square fitting of rating curve using curvilinear asymptotes (Mir and Dubeau 2014) outlined the limitations of earlier approaches and proposed the use of curvilinear asymptotes rather than straight ones.

The accuracy of discharge estimated from the rating curve depends on the accuracy of stage measurement and development of the rating curve. The conventional method

of regression analysis for the development of the rating curve often fails to give stage–discharge relationship accurately. The main objective of the present study was, therefore, to implement a simple and quick optimization-based Excel solver to estimate the parameters of the stage–discharge relationship and assess the performance of conventional method as well as Excel solver approach for stage–discharge data.

Conventional Method

The stage–discharge relationship is generally a single-valued relation for majority of streams and rivers, especially non-alluvial rivers (Subramanya 2008), and it is represented as

$$Q = K(G - a)^n, \tag{1}$$

where Q = stream discharge; G = stage height; a = constant representing the gauge reading corresponding to zero discharge; K and n are rating curve parameters.

Being a hypothetical parameter, 'a' cannot be determined in field. The following methods are available to find the value of gauge height corresponding to zero discharge.

(1) To estimate the value of 'a,' Q versus G plot is prepared on arithmetical graph paper and best fit curve is drawn. By extrapolating the curve, the value of 'a' is found by eye judgment. This value of 'a' is then utilized to obtain a plot of log Q versus log $(G - a)$. If the plot obtained is a straight line, previously assumed value of 'a' is correct; otherwise, this process is repeated until an acceptable value of 'a' is obtained.

(2) A graph between Q and G is prepared on an arithmetical scale, and by the eye judgment a smooth best fit curve is drawn. Three discharges Q_1, Q_2, and Q_3 are selected in such a way that $Q_1/Q_2 = Q_2/Q_3$, and the corresponding values of stages G_1, G_2, and G_3 are noted from the curve. In such case, the following relation may be obtained using Eq. (1).

$$\frac{(G_1 - a)}{(G_2 - a)} = \frac{(G_2 - a)}{(G_3 - a)}, \tag{2a}$$

which may be reduced to

$$a = \frac{\left(G_1 G_2 - G_2^2\right)}{(G_1 + G_3 - G_3)}. \tag{2b}$$

(3) Apart from graphical and arithmetical methods, various optimization techniques can be used to obtain the best value of 'a.' The value of 'a' can be determined by trial-and-error method. The value of 'a' corresponding to correlation coefficient most close to unity is adopted.

As far as the estimation of the rating curve parameters K, n is concerned; they were obtained by the least square error method on the logarithmic plot between Q and $(G - a)$. Excel solver available in Microsoft Excel is a nonlinear optimization code, and its specific implementations have been proved in use over many years as one of the most robust and reliable approaches to solve difficult and highly nonlinear programming problems. A brief description on this solver is provided here.

Excel Solver

Excel solver is an optimization tool in Microsoft Excel basically used for optimization of profit and loss in business problems. Excel solver has the capability to optimize linear as well as nonlinear equations by changing specified parameters. It consists of linear programming solver (LPS) to optimize linear equations, generalized reduced gradient (GRG) solver, and evolutionary solver to optimize nonlinear equations. Rating curve equations are basically of nonlinear form, therefore, GRG nonlinear solver and evolutionary solver are used to obtain the optimum values of rating curve parameters. The GRG solver is a nonlinear optimization code developed by Leon Lasdon from University of Texas at Austin and Allan Waren from Cleveland University. GRG and its specific implementations have been proved in use over many years as one of the most robust and reliable approaches to solve difficult and highly nonlinear programming problems (Lasdon and Smith 1992). GRG solver uses two techniques for determination of search direction. The default choice is quasi-Newton method, a gradient-based technique, and the second choice is the conjugate gradient method. Depending on the available storage, GRG solver may utilize either of the quasi-Newton or conjugate gradient method. Evolutionary solver is a hybrid of genetic and evolutionary algorithms and classical optimization methods, including gradient-free direct search methods, classical gradient-based quasi-Newton methods, and simplex method (Premium Solver Platform 2010).

Analysis, Results, and Discussion

Two data sets of stage and discharge have been procured from literature (Subramanya 2008; Reddy 2011). The rating curve parameters a, K, and n were estimated using Excel solver on the spreadsheet for each data set separately and noted down in Tables 1 and 2 with other details of the results. The values of these parameters based on conventional approach are also provided in the same table just for reference. The difference in values obtained from both approaches may be observed.

Table 1 Comparison of performance evaluation criteria by Excel solver and conventional method (Subramanya 2008)

Stage (m)	Discharge (m^3/s)			Parameters	
	Observed	Predicted		Conventional method	Present study
		Conventional method	Present study		
7.65	15	17.41	10.28	a = 7.500	a = 7.522
7.70	30	26.46	17.29	K = 275.52	K = 261.03
7.77	57	40.96	29.14	n = 1.46	n = 1.57
7.80	39	47.75	34.87		
7.90	60	72.58	56.54		
7.91	100	75.24	58.91		
8.08	150	124.67	104.29		
8.48	170	267.53	243.85		
8.98	400	487.55	471.73		
9.30	600	648.30	644.29		
9.50	800	755.78	761.74		
10.50	1500	1363.79	1448.61		
11.10	2000	1778.35	1932.73		
11.70	2400	2225.77	2465.64		

Table 2 Comparison of performance evaluation criteria by Excel solver and conventional method (Reddy 2011)

Stage (m)	Discharge (m^3/s)			Parameters	
	Observed	Predicted		Conventional method	Present study
		Conventional method	Present study		
2.19	14.30	15.76	22.76	a = 0.85	a = 1.180
2.30	16.76	18.07	25.65	K = 9.50	K = 22.50
2.36	18.18	19.38	27.24	n = 1.73	n = 1.154
2.44	19.96	21.19	29.38		
2.47	25.49	21.89	30.19		
2.50	22.09	22.59	31.00		
2.96	36.95	34.57	43.77		
3.72	62.44	58.87	65.98		
3.87	69.23	64.29	70.50		
4.75	105.48	100.06	97.73		
4.88	111.14	105.90	101.85		
5.76	149.50	149.04	130.28		
5.85	153.62	153.79	133.24		
7.99	181.94	284.85	205.91		

The performance of both the methods for the parameter estimation was assessed with respect to the relation between the observed and the predicted discharges based on the following statistics

$$\text{Root Mean Square Error (RMSE)} = \sqrt{\frac{\sum_{i=1}^{n}\left(Q_{\text{o}}^{i} - Q_{\text{p}}^{i}\right)^{2}}{N}} \tag{3}$$

$$\text{Nash-Sutcliffe criteria } (E) = \left[1 - \frac{\sum_{i=1}^{N}\left(Q_{\text{o}}^{i} - Q_{\text{p}}^{i}\right)^{2}}{\sum_{i=1}^{N}\left(Q_{\text{o}}^{i} - \overline{Q}\right)^{2}}\right] \tag{4}$$

$$\text{Correlation coefficient } (r) = \frac{N\left(\sum Q_{\text{o}}Q_{\text{p}}\right) - \left(\sum Q_{\text{p}}\right)\left(\sum Q_{\text{o}}\right)}{\sqrt{\left(N\left(\sum Q_{\text{p}}^{2}\right) - \left(\sum Q_{\text{p}}\right)^{2}\right)\left(N\left(\sum Q_{\text{o}}^{2}\right) - \left(\sum Q_{\text{o}}\right)^{2}\right)}}, \tag{5}$$

where Q_{o} is the observed discharge; Q_{p} is the predicted discharge, and $\overline{Q}$ is mean of observed discharge.

The prediction method with lowest error and the highest correlation coefficient would be considered as the best models. The values performance indices have been provided in Tables 3 and 4 for both sets of data under considerations.

These tables indicate that the performance of the Excel solver method is better than that of the conventional method. A qualitative performance assessment of the both the approach for the parameter estimation of the rating curve was also made as shown in Figs. 1, 2, and 3. These figures also indicate that the present approach based on Excel solver is better than the conventional method.

Table 3 Performance indices of Excel solver and conventional methods for the data of Table 1

Method	RMSE	Det. coefficient (R^2)	Nash coefficient
Excel solver method	46.5	0.99	0.99
Conventional method	93.1	0.99	0.98

Table 4 Performance indices of Excel solver and conventional methods for the data of Table 2

Methods	RMSE	Det. coefficient (R^2)	Nash coefficient
Excel solver method	11.92	0.97	0.95
Conventional method	27.66	0.90	0.86

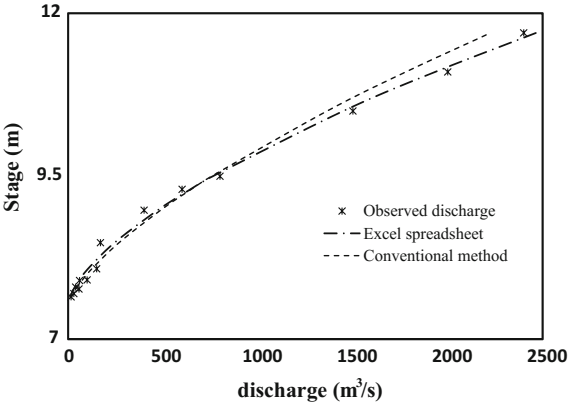

Fig. 1 A comparison of rating curves for data set 1

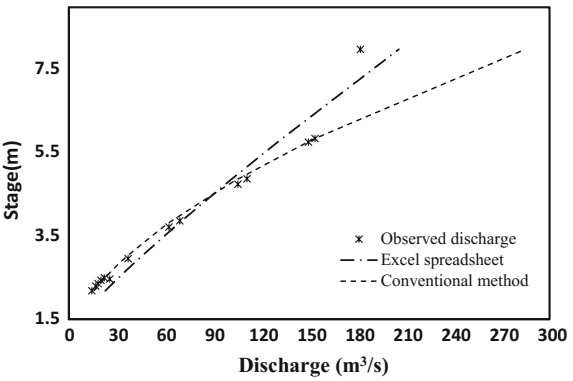

Fig. 2 A comparison of rating curves for data set 2

Conclusion

The parameters of the rating curves were estimated using conventional method and optimization-based Excel solver code for the two different sets of the data in the present study. The performance of both the methods was assessed quantitatively as well as qualitatively. It has been found that Excel solver is a promising tool for predicting parameters of the rating curves precisely. Further, it may be noted that the Excel solver eliminates the need of time-consuming and tedious process of trial and error for computation of stage–discharge relationships as in the case of the conventional method.

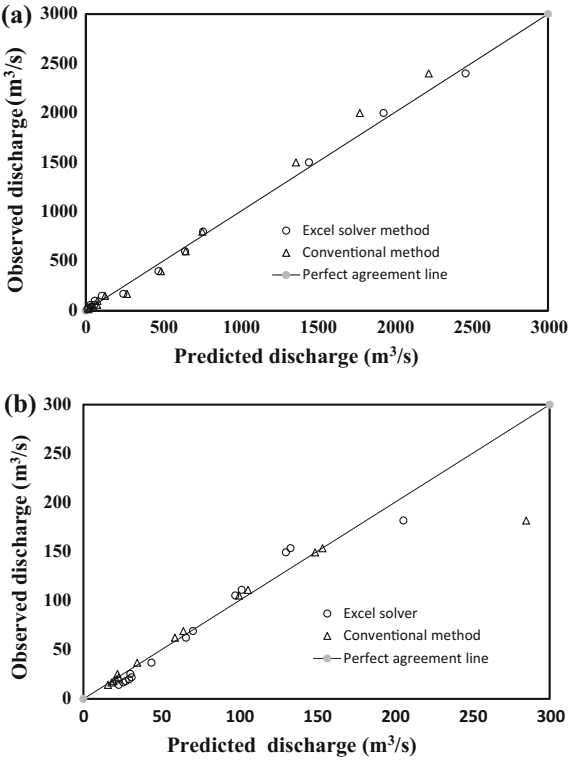

Fig. 3 A comparison of observed and predicted discharges for **a** data set 1 **b** data set 2

References

Braca G (2008) Stage-discharge relationships in open channels: practices and problems. FORALPS Technical Report, 11. Università degli Studi di Trento, Dipartimento di Ingegneria Civile e Ambientale. Trento, Italy

Bisht DCS, Raju MM, Joshi MC (2010) ANN based river stage-discharge modelling for Godavari river, India. Comput Modell New Technol 14(3):48–62

Bhattacharya B, Solomatine DP (2005) Neural networks and M5 model trees in modelling water level-discharge relationship. Neurocomputing 63(2005):381–396

Fenton JD, Keller RJ (2001) The calculation of streamflow from measurements of stage. CRC for Catchment Hydrology

Ghimire BNS, Reddy MJ (2010) Development of stage-discharge rating curve in river using genetic algorithms and model tree. In: International workshop advances in statistical hydrology. Taormina, Italy

Guven A, Ayetak A (2009) New approach for stage-discharge relationship: Gene expression programming. J Hydrol Eng, 14(8):482–492

Habib EH, Meselhe EA (2006) Stage-discharge relations for low-gradient tidal streams using data-driven models. J Hydraul Eng 132(5):482–492

Herschy RW (1995) Streamflow measurement, 3rd edn. E & FN Spon, London

Jain SK (2008) Development of integrated discharge and sediment rating relation using a compound neural network. J Hydrologic Eng 13(3):124–131

Jain SK, Chalisgaonkar D (2000) Setting up stage-discharge relations using ANN. J Hydrologic Eng 5(4):428–433

Lasdon LS, Smith S (1992) Solving sparse nonlinear programs using GRG. ORSA J Comput 4 (1):2–15

McGinn R, Chubak N (2002) A rating curve based on lake levels: evaluating outlet flow for clear creek, riding mountain national park, Manitoba. Prairie Perspect: Geogr Essays 5:17–29

Mir Y, Dubeau F (2014) Least square fitting of the stage-discharge relationship using smooth models with curvilinear asymptotes. J Hydrol Sci. doi:10.1080/02626667.2014.935779

Moyeed RA, Clarke RT (2005) The use of Bayesian methods for fitting rating curves, with case studies. Adv Water Resour. 28:807–818

Petersen-Øverleir A (2004) Modelling stage-discharge relationships affected by hysteresis using the Jones formula and nonlinear regression. J Hydrol Sci, 51(3):365–388

Premium Solver Platform, User Guide (2010) Frontline Systems, Inc

Reddy PJR (2011) A textbook of hydrology, 3rd edn. Laxmi publication, New Delhi, pp 154–200

Sivapragasam C, Muttil N (2005) Discharge rating curve extension—A new approach. Water Resour Manage, 19:505–520

Subramanya K (2008) Engineering Hydrology, 3rd edn. Tata McGraw-Hill, New Delhi, pp 101–133

Sudheer KP, Jain SK (2003) Radial basis function neural network for modelling rating curves. J Hydrol Eng 8(3):161–164

Tawfik M, Ibrahim A, Fahmy H (1997) Hysteresis sensitive Neural Network for modelling rating curves. J Computing Civ Eng, 11(3):206–211

Experimental Study on Role of Emergent Artificial Coastal Vegetation in Controlling Wave Run Up

Beena Mary John, R. T. Arun Vignesh, Kiran G. Shirlal and Subba Rao

Abstract Coastal vegetation can protect people and property from erosion and flooding, potentially providing a solution for conservation and development. Recently, there has been a substantial interest in the ability of natural vegetation to protect people and infrastructure from storm, wind, and wave damage. These ecosystem services provide new and powerful reasons for conservation of coastal habitats and may represent solutions that balance conservation and development. Since the costs of installing hard structures for coastal protection are very high; strong negative public reaction to rock emplacements along the coast often aggravate the problem; research in the field of soft measures of coastal protection is important which highlights the need and importance of a sustainable, environment friendly, and cost efficient solution such as coastal or beach vegetation. This paper tries to bring out the effect of artificial emergent vegetation of meadow widths 1 and 2 m on wave run up through an experimental study. The tests were carried out with emergent vegetation placed on the bed of a 50 m long wave flume. For wave heights ranging from 0.08 to 0.16 m at an interval of 0.02 m and wave periods ranging from 1.4 to 2 s in water depths of 0.40 and 0.45 m, measurements of wave run up over the beach slope were observed.

Introduction

Coastal populations around the world are at a greater risk of damage from coastal hazards due to the unprecedented rise of global climate change characterized by sea-level rise, longer and frequent droughts and floods, heightened cyclonic and storm surge activities. The vulnerability of coastal ecosystems to sea level rise increase with increases in population and development along the coast.

B. M. John (✉) · R. T. Arun Vignesh · K. G. Shirlal · S. Rao
Department of Applied Mechanics and Hydraulics, National Institute of Technology Karnataka, Surathkal, Mangalore 575025, India
e-mail: beena.marie.john@gmail.com

V. P. Singh et al. (eds.), *Hydrologic Modeling*, Water Science and Technology Library 81, https://doi.org/10.1007/978-981-10-5801-1_37

Wave run up over a beach determines the extent to which ocean waves acts on the shore. The extent of inundation due to wave activity is determined based on this important parameter called wave run up. In the last decade, there has been a significant rise in the number of experimental, numerical and field studies conducted to evaluate the role of coastal vegetation on wave energy reduction, which consequently leads to reduced inundation (Gambi et al. 1990; Dubi and Torum 1994; Elwany et al. 1995; Neumeier and Ciavola 2004; Augustin et al. 2009; Sundar et al. 2011; Ozeren et al. 2013; Yiping et al. 2015). Waves passing through the vegetated meadow lose energy while encountering the vegetation stems, which results in reduced wave heights within the meadow and the consequent reduction in inundation distances, which is indicated by the reduction in wave run up. Even though a lot of studies have been conducted on wave damping due to vegetation, there still exists a large variability which is largely due to the various factors such as vegetation characteristics which includes vegetation type, stiffness, density and geometry. In this chapter, results are presented for the effect of simulated emergent vegetation on wave run up over a beach slope.

Objectives

The objective of the present physical model study is to investigate the effect of emergent vegetation on wave run-up over a 1:12 sloped beach under the effect of varying incident wave characteristics.

Experimentation

The experiments are conducted with physical models of emergent vegetation in the two-dimensional wave flume of the Marine Structures Laboratory of the Department of Applied Mechanics and Hydraulics, National Institute of Technology Karnataka, Surathkal. The wave flume of the aforesaid department is 50 m long, 0.71 m wide and 1.1 m deep (schematized in Fig. 1). It has a 6.3 m long, 1.5 m wide and 1.4 m deep chamber with a bottom hinged paddle at one end which generates waves and a rock beach for wave absorption at the opposite end. The paddle is controlled by an induction motor of 11 kW power at 1450 rpm. This motor is regulated by an inverter drive (0–50 Hz), rotating with a speed range of 0–155 rpm. A flywheel and bar chain link the motor with the flap. The wave heights for the test runs can be varied for a particular wave period by changing the eccentricity of bar chain. The desired wave period is generated by changing of frequency through inverter.

Capacitance type wave probes along with amplification units are used for data collection during experiments. The spacing between probes is adjusted approximately to one third of the wave length as per the method proposed by Isaacson

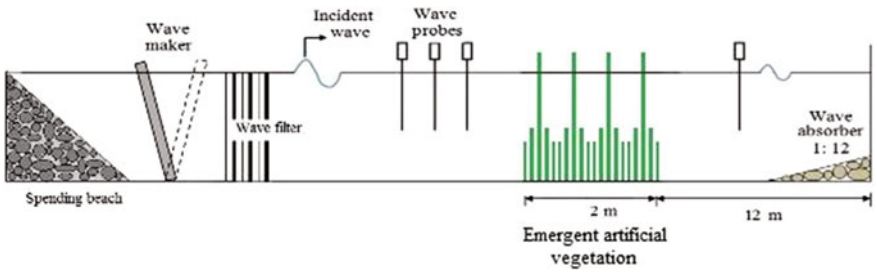

Fig. 1 Schematic diagram of experimental set up

(1991). For each wave period, six different wave heights ranging from 0.08 to 0.16 m at an interval of 0.02 m are generated. The wave surface elevation is converted to electrical signal and is stored in digital form by a software controlled 12-bit A/D converter.

To investigate the effect of emergent vegetation on wave run-up, two models namely, emergent trunk model and emergent trunk model with roots is of interest. The trunks of the emergent vegetation model are made of nylon rods selected for the most similar physical properties to real tree trunks (Table 1).The primary material property of interest is the stiffness or flexibility or rigidity of the trunk material, often reported as the modulus of elasticity or the Young's modulus (Ghisalberti and Nepf 2002; Freeman et al. 2000). The value of Young's modulus for natural tree trunks is in the range 10.05–15 GPa. A reference value of 15 GPa is assumed for the field condition. To scale down the prototype values, a model scale of 1:30 is adopted; which would mean that the value of modulus of elasticity would be about 0.5 GPa. A material of 0.5 GPa would be inappropriate to be used for modelling the trunks. Therefore, instead of scaling down the value of Young's modulus individually, it would rather be appropriate to scale down the stiffness property, EI as a single parameter. Nylon with an E value of about 2–4 GPa is selected for simulating the vegetation trunks. Having chosen the material for the model, the typical prototype diameter of the vegetal stems is in the range of 0.5–0.7 m. The emergent trunk model is made of nylon rods of diameter 0.016 m. The roots for model consists of nylon rods of diameter 0.010 and 0.006 m placed around the trunk. The model is constructed by fixing rigid nylon rods in holes drilled in 1 m $\times$ 0.73 m $\times$ 0.04 m concrete slabs. The photographs of the emergent models used for the present study is shown in Fig. 2.

Before starting the experiment, the flume is calibrated to produce incident waves of different combinations of wave heights and periods. The models are tested for its effect on wave run-up over a beach slope when subjected to varying wave heights and wave periods in a water depth of 0.40 and 0.45 m, as described in Table 1, in a two-dimensional wave flume. For studying the effect of emergent vegetation on wave run-up, the experimental test runs were conducted in two phases. During the first phase, the test runs were carried out with the emergent trunk model of widths 1 and 2 m; whereas, the second phase consisted of tests on the emergent trunk model

Table 1 Vegetation characteristics and experimental conditions

Simulated plant type	Vegetation model characteristics		Meadow width, w (m)	Wave height (m)	Wave period, T (s)	Water depth, d (m)	Relative plant height (h_s/d)
Emergent trunk model	Modulus of Elasticity	3 GPa	1, 2	0.08, 0.10, 0.12, 0.14, 0.16	1.4, 1.6, 1.8, 2	0.40, 0.45	1.25, 1.11
	Length of trunk	0.5 m					
	Diameter of trunk	0.016 m					
	Density	107 trunks/m^2					
Emergent trunk model with roots	Modulus of Elasticity	3 GPa	1, 2	0.08, 0.10, 0.12, 0.14, 0.16	1.4, 1.6, 1.8, 2	0.40, 0.45	1.25, 1.11; 0.525, 0.47; 0.4, 0.36
	Length of trunk	0.5 m					
	Diameter of trunk	0.016 m					
	Density of trunks	107 trunks/m^2					
	Length of Root 1	0.21 m					
	Diameter of Root 1	0.010 m					
	Density of Roots I	300 $roots_1$/m^2					
	Length of Root 2	0.16 m					
	Diameter of Root 2	0.006 m					
	Density of Roots 2	300 $roots_2$/m^2					

with roots of widths 1 and 2 m. The wave flume is filled with ordinary tap water to the required depth.

Results

The effect of wave steepness parameter (H/gT^2) on relative wave run-up (R_u/H) for the emergent models is discussed in this section. For the emergent trunk model of width 1 m, the extent of inundation on the beach represented by the wave run-up (R_u/H) decreases from 0.903 to 0.653 and from 0.923 to 0.659 for relative plant heights (h_s/d) 1.25 and 1.11, respectively for an increase in wave steepness parameter (H/gT^2) from 0.00203 to 0.00833, as illustrated in Fig. 3a, b. As the

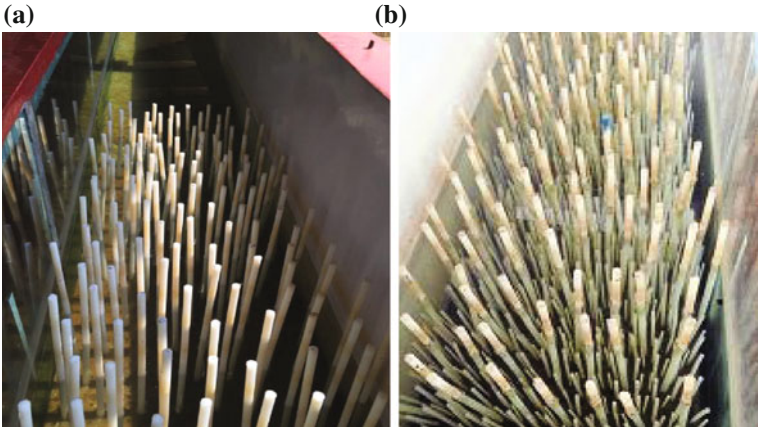

Fig. 2 Photos of emergent model setup **a** Emergent trunk model **b** Emergent trunk model with roots

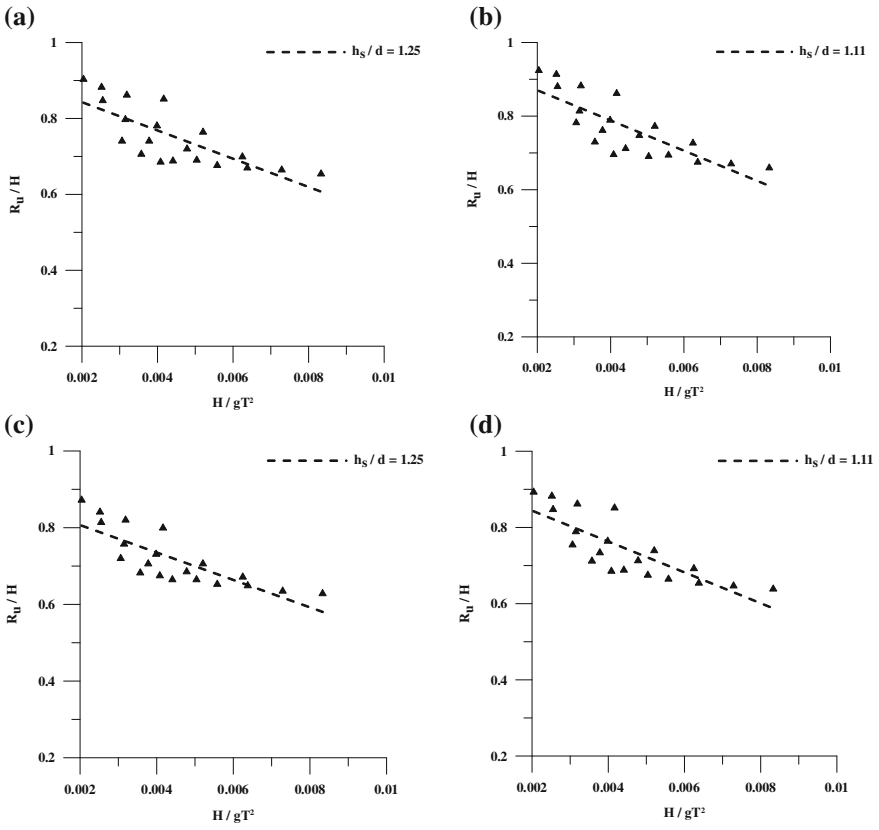

Fig. 3 Effect of H/gT^2 on R_u/H for emergent trunk model: **a** w = 1 m, h_s/d = 1.25; **b** w = 1 m, h_s/d = 1.11; **c** w = 2 m, h_s/d = 1.25; **d** w = 2 m, h_s/d = 1.11

width of the model increases to 2 m (100%), it is observed from Fig. 3c, d that as wave steepness parameter (H/gT^2) increases from 0.00203 to 0.00833, the relative wave run-up (R_u/H) decreases from 0.871 to 0.628 and from 0.892 to 0.638 for relative plant heights (h_s/d) 1.25 and 1.11, respectively. Therefore, for 100% increase in meadow width from 1 m to 2 m, the relative wave run-up decreases by 3.5–3.8% for $h_s/d = 1.25$; and by 3.35–3.18% for $h_s/d = 1.11$. A visual examination of the test runs indicates that as the wave propagates through the meadow, the presence of emergent trunks which interferes with the particle orbital velocities at the surface and further along the depth causes increased turbulence. Despite this turbulence owing to the emergence of the trunk, this model exhibits decreased reduction in wave height which results in a subsequent increase in wave run-up. This observation may be due to the role of plant density wherein the trunks interfere with the waves causing attenuation; while some energy passes through the gap between the emergent trunks.

As the wave propagates along the emergent trunk model with roots, the presence of the root system results in an increased turbulence, thereby resulting in an increased reduction in wave heights, which consequently results in a decreased wave run-up on the beach slope. For the emergent trunk model with roots of width 1 m, the extent of inundation on the beach represented by the wave run-up (R_u/H) decreases from 0.851 to 0.529 and from 0.871 to 0.534 for a relative plant height, $h_s/d = 1.25$ and 1.11, respectively as the wave steepness parameter (H/gT^2) increases from 0.00203 to 0.00833, as illustrated in Fig. 4a, b. For an increase in meadow width, w = 2 m for the same model, the wave run-up (R_u/H) decreases from 0.840 to 0.512 and from 0.851 to 0.519 for a relative plant height, $h_s/d = 1.25$ and 1.11, respectively as the wave steepness parameter (H/gT^2) increases from 0.00203 to 0.00833, as illustrated in Fig. 4c, d. It is therefore observed that as the meadow width increases from 1 to 2 m, the relative wave run-up decreases by 1.29–3.21% for $h_s/d = 1.25$ and by 2.29–2.8% for $h_s/d = 1.11$.

The results mentioned above indicates that as the relative plant height (h_s/d) increases from 1.11 to 1.25 (12.6%), there is a decrease in wave run-up from 0.923–0.659 to 0.903–0.653 for the emergent trunk model of width 1 m; and from 0.871–0.534 to 0.851–0.529 for the emergent trunk model with roots of width 1 m. For the 2 m wide models, a decrease in run-up from 0.892–0.638 to 0.871–0.628 for the emergent trunk model; and from 0.851–0.519 to 0.840–0.512 for the emergent trunk model with roots is observed. As the relative plant height increases, i.e., the depth of water is lower, as the wave passes along the meadow, the trunks successfully interfere with the waves and the entire distribution of energy field is interfered. This disturbs the particle orbital velocities, resulting in an increase in turbulence and loss of energy, which causes an increased attenuation of wave heights which directly leads to a decrease in wave run up over the beach slope.

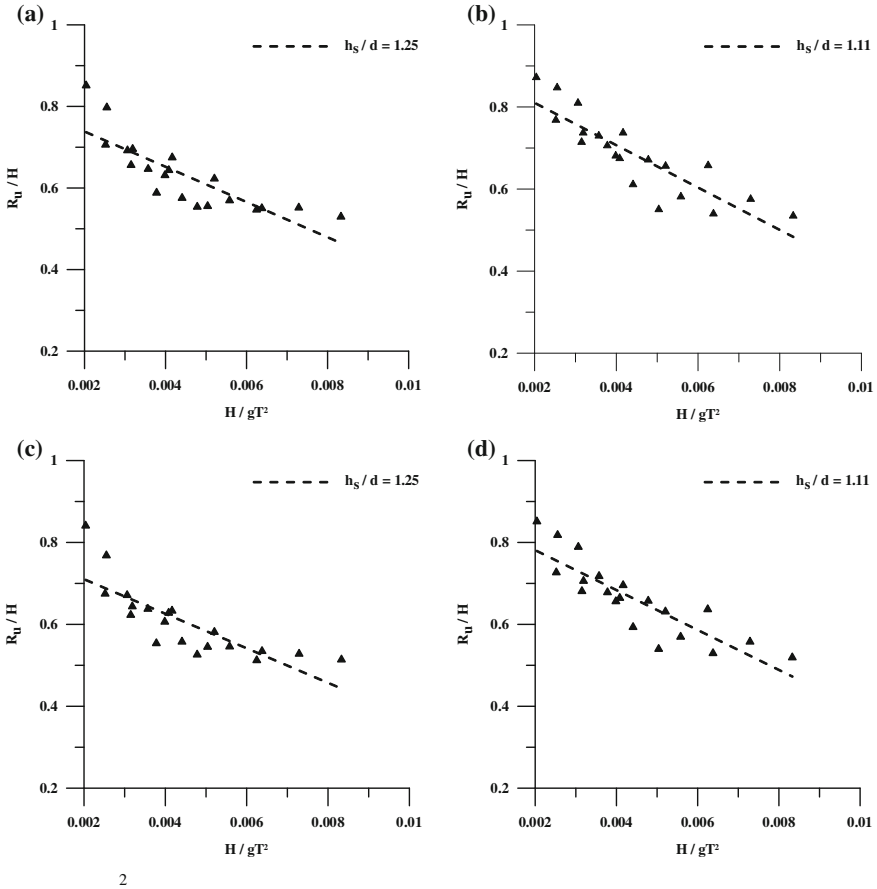

Fig. 4 Effect of H/gT^2 on R_u/H for emergent trunk model with roots: **a** w = 1 m, h_s/d = 1.25; **b** w = 1 m, h_s/d = 1.11; **c** w = 2 m, h_s/d = 1.25; **d** w = 2 m, h_s/d = 1.11

Conclusions

The loss of energy because of interference of the vegetation with the wave propagation causes a reduction in wave heights, leading to a reduction in wave run-up heights over the beach slope. As the width of the meadow increases from 1 to 2 m (100%) for the emergent trunk model, it is observed that the relative wave run-up decreases by 3.5–3.8% for h_s/d = 1.25; whereas it decreases by 3.35–3.18% for h_s/d = 1.11. For the emergent trunk model with roots, for the same increase in meadow width from 1 to 2 m, the relative wave run-up decreases by 1.29–3.21% for h_s/d = 1.25 and by 2.29–2.8% for h_s/d = 1.11. For an increase in relative plant height from 1.11 to 1.25, a decrease in relative wave run-up from 0.892–0.638 to 0.871–0.628 is observed for the emergent trunk model of width 2 m; and from 0.851–0.519 to

0.840–0.512 for the emergent trunk model with roots of width 2 m. The findings confirm the fact that the type of vegetation, plant density, meadow width and relative plant height plays a significant role in controlling the wave run-up over the beach slope.

References

Augustin LN, Irish JL, Lynett P (2009) Laboratory and numerical studies of wave damping by emergent and near-emergent wetland vegetation. Coast Eng 56:332–340

Dubi A, Torum A (1994) Wave damping by kelp vegetation. Coast Eng 142–156

Elwany MHS, O'Reilly WC, Guza RT, Flick RE (1995) Effects of Southern California kelp beds on waves. J Waterw Port Coast Ocean Eng 121(2):143–150

Freeman GE, Rahmeyer WJ, Copeland RR (2000) Determination of resistance due to shrubs and woody vegetation. ERDC/CHL TR-00-25. Engineer Research and Development Center, Vicksburg, MS

Gambi MC, Nowell ARM, Jumars PA (1990) Flume observations on flow dynamics in Zostera marina (eelgrass) beds. Mar Ecol Prog Ser 61:159–169

Ghisalberti M, Nepf HM (2002) Mixing layers and coherent structures in vegetated aquatic flows. J Geophys Res 107

Isaacson M (1991) Measurement of regular wave reflection. J Waterwa Port Coast Ocean Eng ASCE 117:553–569

Neumeier U, Ciavola P (2004) Flow resistance and associated sedimentary processes in a Spartina maritima salt-marsh. J Coastal Res 20(2):435–447

Ozeren Y, Wren DG, Wu W (2013) Experimental investigation of wave attenuation through model and live vegetation. J Waterw Port Coast Ocean Eng 04014019-1-12

Sundar V, Murali K, Noarayanan L (2011) Effect of vegetation on run-up and wall pressures due to cnoidal waves. J Hydraul Res, 49(4):562–567

Yiping L, Anim DO, Wang Y, Tang C, Du W, Lixiao N, Yu Z, Acharya K, Chen L (2015) Laboratory simulations of wave attenuation by an emergent vegetation of artificial Phragmites australis: an experimental study of an open-channel wave flume. J Environ Eng Landscape Manage 23(4):251–266

Development of Regional Soil Water Retention (SWR) Characteristics

R. K. Jaiswal, T. Thomas, R. V. Galkate, S. Singh and J. V. Tyagi

Abstract The unsaturated soil hydraulic properties may be considered the key factors governing the partitioning of rainfall and irrigation into soil water storage, evapotranspiration, and deep drainage. The understanding of regional parameters of soil water retention process with the most appropriate model is necessary for better understanding of water movement and supply of water for irrigation. In the present study, an attempt has been made to develop at-site and regional analytical models for computation of soil water retention curves for different soils in two adjoining commands of Benisagar and Rangawan reservoirs in Madhya Pradesh (India). The soil samples from seventeen different sites considering uniform distribution and all predominant soils were collected and analyzed for the determination of soil water retention at different pressures. The at-site and regional parameters of soil water retention (SWR) models suggested by Brooks and Corey (1964), Van Genuchten (1980), Durner (1994), Kosugi (1996), and Seki (2007) have been applied in the study to determine at-site and regional parameters. The performance of these models was evaluated using different statistical criteria including root mean square error (RMSE), coefficient of determination (R^2), adjusted coefficient of determination R^2_{adj}, and also the graphical representation. The soils in the study area can be divided into two distinct groups on the basis of simple graphical representation of SWR curves. The at-site and regional analysis concluded that SWR model suggested by Durner (1994) with different parameters may be considered the best-fit model for at-site and regional analysis of both soil groups (SG-1 and SG-2) in the study area.

R. K. Jaiswal (✉) · T. Thomas · R. V. Galkate
National Institute of Hydrology, Regional Centre, WALMI Campus, Bhopal 462016, MP, India
e-mail: rkjaiswal_sagar@yahoo.co.in

S. Singh · J. V. Tyagi
National Institute of Hydrology, Jal Vigyan Bhavan, Roorkee, Uttarakhand, India
e-mail: ssingh_nih@ernet.in

V. P. Singh et al. (eds.), *Hydrologic Modeling*, Water Science and Technology Library 81, https://doi.org/10.1007/978-981-10-5801-1_38

Introduction

The soil water is accepted as one of the most critical factors for agricultural communities owing to its importance in crop selection, planting strategies, fertilizer rates, and irrigation requirements (Lawford 1992). The movement of water through the soil is an important aspect of hydrological cycle, and relationship between soil moisture content (θ), soil water pressure (h), and unsaturated hydraulic conductivity (K) is necessary for mathematical modeling of hydrologic and agricultural system (Fredlund et al. 1997). The unsaturated hydraulic functions are key input data in numerical models of vadose zone processes. These functions may be either measured directly or estimated indirectly through prediction from more easily measured data based upon quasi-empirical models. Common conceptual models for unsaturated flow often rely on the oversimplified representation of medium pores as a bundle of cylindrical capillaries and assume that soil water pressure head is attributed to capillary forces only and ignores the adsorptive surface forces. Hence, it is often assumed that aqueous flow is negligible when a soil is near or at residual water content (θ_r). The reason for the finite value of θ_r is that the dominant historical water content measurements were in the wet range, and the typical soil water retention models assumed asymptotic behavior at low water content values. It is generally treated as a fitting parameter. Hence, an effective saturation was defined by Zhang (2010) with the help of following equation.

$$S_e = \frac{\theta - \theta_r}{\theta_s - \theta_r} \tag{1}$$

where θ is the water content and θ_s the saturated water content. Tuller and Or (2001) proposed a model of unsaturated hydraulic conductivity due to film and corner flow. The model is mathematically very complex and is not compatible with the commonly used retention models. Peters and Durner (2008) presented a new model that combines a simple film flow function with the capillary flow model of Mualem. To use the model, additional parameters must be known to quantify the contribution of film flow. Several functions have been proposed to empirically describe the soil water retention curve. These models were based on the equation given by Rechards (1931) for the flow of water in saturated or partly saturated soil. One of the most popular functions was the equation of Brooks and Corey (1964) to describe effective saturation (S_e) as follows:

$$S_e = \left[\frac{h_d}{h}\right]^{\lambda} \quad h > h_d \tag{2}$$

$$S_e = 1 \quad h \leq h_d \tag{3}$$

where h is the suction head, h_d and λ are the parameters referred to as the air entry head, and pore size distribution index, respectively, can be determined either by

graph fitting or using soil properties. By putting $h_d^{\lambda} = \alpha$, the Brooks and Corey (1964) equation can be written as the following for curve fitting:

$$S_e = (\alpha h)^{-\lambda} \quad h > 0 \tag{4}$$

$$S_e = 1 \quad h \leq 0 \tag{5}$$

After the model proposed by Brooks and Corey (1964), several differentiable equations of complex nature were suggested by researchers (King 1965; Visser 1968; Laliberte 1969; Su and Brooks 1975; Clapp and Hornberger 1978; Ross et al. 1991; Rossi and Nimmo 1994; Fayer and Simmons 1995; Morel-Seytoux and Nimmo 1999; Webb 2000; Groenevelt and Grant 2004; Hwang and Choi 2006; Khlosi et al. 2006; etc.), but most of them were complex in nature. Van Genuchten (1980) proposed a modification with a simple representation of soil water retention as given below:

$$S_e = \frac{1}{[1 + (\alpha h)^n]^m} \tag{6}$$

where α, n, and m are empirical constants with $m = 1 - 1/n$ as suggested by Genuchten (1980). Kosugi (1996) has suggested a lognormal fit model for soil retention data, and the equation can be expressed as follows:

$$S_e = Q\left[\frac{\ln(h/h_{m)}}{\sigma}\right] \tag{7}$$

where $Q(x)$ is the complementary cumulative normal distribution function, defined by $Q(x) = 1 - \Phi(x)$, in which $\Phi(x)$ is a normalized form of the cumulative normal distribution function, and h_m and σ are the parameters of the model. For fitting the soil water retention data more precisely, Durner (1994) and Seki (2007) presented two different models considering bimodal pore structure for heterogeneous soil pore space. The Durner models for representing S_e can be presented as follows:

$$S_e = w_1\left[\frac{1}{1 + (\alpha_1 h)^{n_1}}\right]^{m_1} + (1 - w_1)\left[\frac{1}{1 + (\alpha_2 h)^{n_2}}\right]^{m_2} \tag{8}$$

where $w_1, w_2, \alpha_1, \alpha_2, m_1, m_2, n_1$ and n_2 are the parameters of model with $m_i = 1 - 1/n_i$. The Seki's model is a lognormal bimodal that can be written as follows:

$$S_e = w_1 Q\left[\frac{\ln(h/h_{m1})}{\sigma_1}\right] + (1 - w_1)Q\left[\frac{\ln(h/h_{m1})}{\sigma_2}\right] \tag{9}$$

where $h_{m1}, h_{m2}, w_1, w_2, \sigma_1$ and σ_2 are the parameters of model, and $Q(x)$ is the complementary cumulative normal distribution function, defined by $Q(x) = 1 - (x)$, in which $\Phi(x)$ is a normalized form of the cumulative normal distribution function.

Study Area

Two adjoining commands of Benisagar and Rangawan reservoirs have been selected for the study located in Chhatarpur district of Madhya Pradesh, India (Fig. 1). The gross storage capacity and dead storage capacity of the Benisagar reservoir are 27.59 and 1.37 Mm^3, respectively. The gross command area of the project is 6802.46 ha, while the cultivated area is 6267 ha. The Rangawan project is a major interstate irrigation project of Madhya Pradesh (M.P.) and Uttar Pradesh (U.P.), situated near village Rangawan in Rajnagar Tahsil of Chhatarpur district. The project is 48 km away from Chhatarpur on Chhatarpur–Panna road.

Fig. 1 Location map of commands of Benisagar and Rangawan reservoirs in Chhatarpur district of Madhya Pradesh (India)

Fig. 2 Soil testing sites in Benisagar and Rangawan command areas

The Rangawan dam is an earthen dam located at 24° 41′N latitude and 79° 52′E longitude. The length of left bank main canal is 14 km having a head discharge of 8.27 m^3/s. Soil samples from seventeen different sites in both the commands considering different major soils in the study area have been collected, and pressure plate apparatus has been used to determine soil moisture at variable suctions on soil samples. The location map showing different sites in both the commands have been presented in Fig. 2.

Methodology

In the present study, an attempt has been made to apply analytical models of soil retention for the application of solute transport and water balance in command and determination of parameters of best-suited regional models for the study area. The soil samples collected from seventeen sites in the study area have been analyzed for the determination of soil moisture under variable suctions on pressure plate

apparatus. The soil moisture retention curves of soils revealed that the soils in the study area can be grouped into two broad classes. In the study, analytical-based models have been applied for the determination of at-site and regional parameters by grouping the observed information.

Analytical Models

A computer program SWRC Fit (http://swrcfit.sourceforge.net/) has been used that performs nonlinear fitting by Levenberg–Marquardt method for computation of parameters of the following models:

- Brooks and Corey (1964) model,
- Van Genuchten (1980) model,
- Kosugi (1996) lognormal model,
- Durner (1994) model,
- Seki (2007) model.

Regionalization Approach

For regionalization, all the data have been divided into two groups based on simple graphical representation, regional parameters of these models for both soil groups have been determined using clustering method, and SWRC Fit software was used to determine the parameters of regional models.

Performance Evaluation

The performance of different analytical models has been judged using different robust criteria including root mean square error (RMSE), coefficient of determination (R^2), and R^2_{adj}. The RMSE is an indicator for the representation of the overall error of the evaluated function and should approach to zero for best model performance. The R^2_{adj} was suggested to take the impact of number of parameters of model on the performance, and statistically, it can take any value ≤ 1 (Neter et al. 1996). The equation for computation of different performance evaluators has been given below.

$$\mathrm{RMSE} = \sqrt{\frac{\sum_{i=1}^{N}\left(\theta_i^{\mathrm{obs}} - \theta_i^{\mathrm{comp}}\right)}{N}} \tag{10}$$

$$R^2 = 1 - \frac{\text{SSE}}{\text{SST}} \tag{11}$$

$$R^2_{\text{adj}} = \frac{(N-1)R^2 - (p-1)}{N-p} \tag{12}$$

where θ_i^{obs},θ_i^{comp} are the ith observed and computed value of soil moisture, N is the number of data, SSE is the model sum of square, SST is the total sum of square, and p is the parameters in the model. The SSE and SST can be computed using the following equations:

$$\text{SST} = \sum_{i=1}^{N} \left(\theta_i^{\text{comp}} - \bar{\theta}\right) \tag{13}$$

$$\text{SSE} = \sum_{i=1}^{N} \left(\theta_i^{\text{obs}} - \theta_i^{\text{comp}}\right) \tag{14}$$

where $\overline{\theta}$ is the mean of computed values.

Analysis of Results

The soil, plant, and atmosphere act as a continuum along which soil water moves in response to gradients in energy. The energy potential of the water relative to that of pure water helps in determining the amount of water stored in the soil, moved through the soil, and moved into and through the plant to the transpiring surface of the leaf. In the present study, the soil samples from seventeen sites covering most of the soils in Benisagar and Rangawan commands have been analyzed for the determination of soil water retention at different pressures. The graphical representation showing variation of soil moisture on different suction heads has been presented in Fig. 3 which explained that the soil in the study area can be divided into two broad groups, namely SG-1 (Site-1, -2, -5, -6, -10, -11, -14, -15, and -17) and SG-2 (3, 4, 7, 9, 12, 13, and 16) from soil water retention point of view. Various analytical models have been applied, and the results obtained from the study have been compared with observed data using statistical criterions.

In case of analytical modeling, at-site and regional parameters of Brooks and Corey (1964), Van Genuchten (1980), Durner (1994), Kosugi (1996) lognormal model, and Seki (2007) models were estimated using SWRC Fit software. The clustering of observed data from Site-1, -2, -5, -6, -10, -11, -14, -15, and -17 in soil group SG-1 and Site-3, -4, -7, -9, -12, -13, and -16 in soil group SG-2 has been made to determine regional parameters of different models. The RMSE, R^2 and R^2_{adj} have been used to judge the best-fit at-site and regional models for the study area. The RMSE values of different models are given in Table 2. From the analysis of

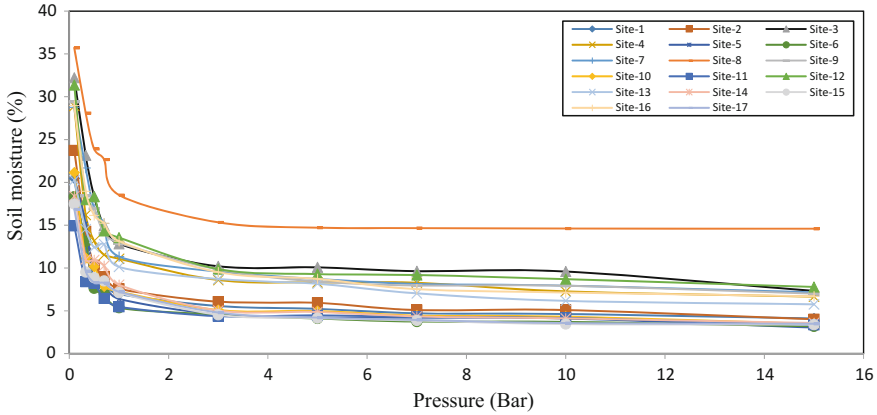

Fig. 3 Soil moisture retention curves for different sites in commands

Table 1 Best fit regional parameters for Durner (1994) model

Soil group	Best PTFs	θ_s	θ_r	w_1	α_1	n_1	α_2	n_2
SG-1	Durner (1994)	0.320	0.010	0.642	0.006	2.431	0.005	1.210
SG-2	Durner (1994)	0.547	0.003	0.572	0.149	1.145	0.006	2.221

goodness-of-fit measures, it has been observed that Durner (1994) model is the best-fit analytical model for at-site and regional modeling of soil moisture in the study area. The at-site and regional parameters of Durner (1994) model have been presented in Table 3. The equations derived for regional analysis to compute soil water retention curves using Durner (1994) model for soil groups SG-1 and SG-2 have been given in Table 1.

$$\theta = 0.01 + 0.199\left[\frac{1}{1+(0.006h)^{2.431}}\right]^{-1.431} + 0.111\left[\frac{1}{1+(0.005h)^{1.21}}\right]^{-0.21} \quad (15)$$

For SG-1

$$\theta = 0.003 + 0.311\left[\frac{1}{1+(0.149h)^{1.145}}\right]^{-0.145} + 0.233\left[\frac{1}{1+(0.006h)^{2.22}}\right]^{-1.22} \quad (16)$$

For SG-2

The best-fit models and their parameters for regional application of SWR modeling using analytical approach have been presented in Table 1.

Table 2 Performance evaluation of different models for analytical SWR curve

Site	Root mean square error for different models				
	Brooks and Corey (1964)	Van Genuchten (1980)	Kosugi (1996)	Durner (1994)	Seki (2007)
Site-1	0.049	0.032	0.216	0.002	0.154
Site-2	0.064	0.033	0.179	0.003	0.09
Site-3	0.124	0.048	0.117	0.007	0.092
Site-4	0.005	0.012	0.922	0.003	0.206
Site-5	0.27	0.051	0.084	0.004	0.091
Site-6	0.212	0.04	0.069	0.003	0.314
Site-7	0.108	0.043	0.095	0.006	0.081
Site-8	0.06	0.027	0.064	0.002	0.056
Site-9	0.005	0.007	0.629	0.005	0.616
Site-10	0.005	0.006	0.769	0.006	0.19
Site-11	0.006	0.01	0.177	0.006	0.064
Site-12	0.009	0.011	0.586	0.009	0.109
Site-13	0.008	0.008	0.189	0.007	0.147
Site-14	0.009	0.009	0.446	0.005	0.056
Site-15	0.006	0.006	0.301	0.002	0.058
Site-16	0.003	0.005	0.289	0.003	0.118
Site-17	0.005	0.005	0.351	0.002	0.054
SG-1	0.019	0.02	0.435	0.008	0.108
SG-2	0.02	0.02	0.196	0.002	0.192

Table 3 Best-fit at-site and regional analytical models and their parameters in Benisagar and Rangawan commands

Site	Best-fit analytical model	Model parameters						
		θ_s	θ_r	w_1	α_1	n_1	α_2	n_2
Site-1	Durner (1994) model	0.340	0.037	0.643	0.018	1.393	0.003	34.750
Site-2	Durner (1994) model	0.356	0.000	0.669	0.004	3.467	0.001	1.256
Site-3	Durner (1994) model	0.484	0.000	0.601	0.003	3.028	0.002	1.129
Site-4	Durner (1994) model	0.414	0.000	0.468	0.005	1.169	0.005	3.703
Site-5	Durner (1994) model	0.318	0.051	0.620	0.003	49.959	0.002	1.975
Site-6	Durner (1994) model	0.396	0.038	0.830	0.026	1.575	0.002	24.892
Site-7	Durner (1994) model	0.451	0.094	0.887	0.003	2.519	0.000	2.545
Site-8	Durner (1994) model	0.357	0.148	0.551	0.003	26.526	0.001	5.935
Site-9	Durner (1994) model	1.236	0.077	0.828	0.055	1.981	0.004	1.470
Site-10	Durner (1994) model	0.336	0.064	0.349	0.006	24.523	0.003	2.113
Site-11	Durner (1994) model	0.233	0.062	0.295	0.007	34.759	0.003	2.308
Site-12	Durner (1994) model	0.409	0.112	0.573	0.007	48.830	0.001	2.852
Site-13	Durner (1994) model	0.316	0.048	0.401	0.003	49.963	0.001	1.473

(continued)

Table 3 (continued)

Site	Best-fit analytical model	Model parameters						
		θ_s	θ_r	w_1	α_1	n_1	α_2	n_2
Site-14	Durner (1994) model	0.301	0.064	0.468	0.004	33.209	0.001	2.557
Site-15	Durner (1994) model	0.261	0.049	0.541	0.003	49.818	0.001	2.258
Site-16	Durner (1994) model	0.446	0.073	0.361	0.003	48.570	0.002	1.599
Site-17	Durner (1994) model	0.251	0.050	0.593	0.003	49.829	0.001	2.278
SG-1	Durner (1994) model	0.320	0.010	0.642	0.006	2.431	0.005	1.210
SG-2	Durner (1994) model	0.547	0.003	0.572	0.149	1.145	0.006	2.221

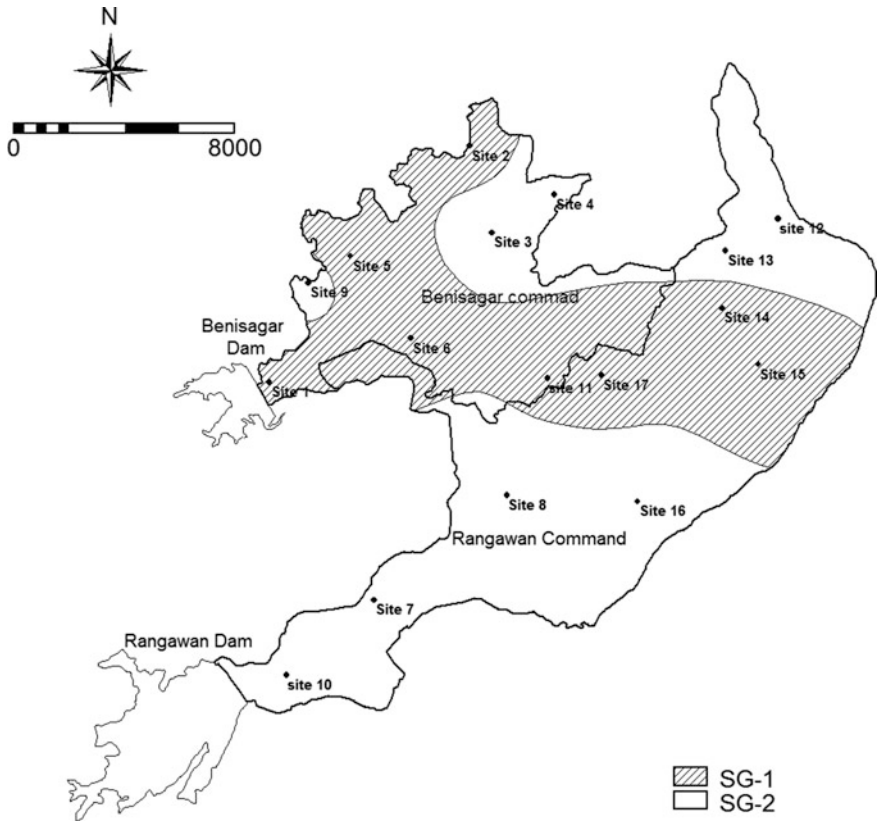

Fig. 4 Distribution of broad groups of soils identified in the commands

In the analysis, the area under both the commands has been demarcated spatially in two groups (SG-1 and SG-2) using interpolation technique in ILWIS geographic information system (GIS) and depicted in Fig. 4.

Conclusions

The water retention property of soil plays an important role in the movement of fertilizers, pesticides, contaminants in groundwater, and required water for irrigation. Various analytical and pedotransfer functions have been devised by scientists to compute soil water retention curves. In the present study, soil moistures at different pressures using pressure plate apparatus were computed on seventeen locations in Benisagar and Rangawan commands of Madhya Pradesh in India. Initially, two distinct groups were found in when all the data were plotted, and using clustering technique, average values were computed for two groups of soils (SG-1 and SG-2). Five different analytical models suggested by Brooks and Corey (1964), Van Genuchten (1980), Kosugi (1996) lognormal model, Durner (1994), and Seki (2007) were applied, site-specific and regional parameters were determined, and their performance was evaluated using root mean square error (*RMSE*), coefficient of determination (R^2), and R^2_{adj}. Durner (1994) model was found the most suitable analytical model for at-site as well as for the region. Two different regional models for soil groups SG-1 and SG-2 have been suggested that can be used for any other sites in the commands. From the spatial analysis, it may be concluded that 13,831 ha area falls under SG-1 group, while 16,473 ha under SG-2 from soil moisture point of view.

References

Brooks RH, Corey AT (1964) Hydraulic properties of porous media Hydrol Paper 3. Colorado State Univ., Fort Collins, CO, USA

Clapp RB, Hornberger GM (1978) Empirical equations for some soil hydraulic properties. Water Resour Res 14:601–604

Durner W (1994) Hydraulic conductivity estimation for soils with heterogeneous pore structure. Water Resour Res 30(2):211–223

Fayer MJ, Simmons CS (1995) Modified soil water retention functions for all matric suctions. Water Resour Res 31:1233–1238

Fredlund MD, Fredlund DG, Wilson GW (1997) Prediction of soil-water characteristic curve from grain-size distribution and volume-mass properties. In: Proceedings of third brazilian symposium on unsaturated soil, Rio de Janerio, Brazile, 22–25 Apr 1997, pp 1–12

Groenevelt PH, Grant CD (2004) A new model for the soil water retention curve that solves the problem of residual water contents. Eur J Soil Sci 55:479–485

Hwang S II, Choi S II (2006) Use of lognormal distribution model for estimating soil water retention curves from particle-size distribution data. J Hydrol 323(1–4):325–334

Khlosi M, Cornelis WM, Gabriels D, Sin G (2006) Simple modification to describe the soil water retention curve between saturation and oven dryness. Water Resour Res 42:W11501. doi:10.1029/2005WR004699

King LG (1965) Description of soil characteristics for partially saturated flow. Soil Sci Soc Am J 29:359–362

Kosugi K (1996) Lognormal distribution model for unsaturated soil hydraulic properties. Water Resour Res 32(9):2697–2703

Laliberte GE (1969) A mathematical function for describing capillary pressure-desaturation data. Bull Inter Assoc Sci Hydrol 14:131–149

Lawford RG (1992) An overview of soil moisture and its role in the climate system. In: Eley J et al (eds) Soil moisture modeling and monitoring for regional planning. Proceedings of the NHRI symposium, no. 9, National Hydrological Research Centre, Saskatoon, SK, pp 1–12

Morel-Seytoux HJ, Nimmo JR (1999) Soil water retention and maximum capillary drive from saturation to oven dryness. Water Resour Res 35:2031–2041

Neter J, Kutner M, Nachtsheim C, Wasserman W (1996) Applied linear statistical models. McGraw-Hill Companies Inc, NY

Peters A, Durner W (2008) A simple model for describing hydraulic conductivity in unsaturated porous media accounting for film and capillary flow. Water Resour Res 44:W11417. doi:10.1029/2008WR007136

Richards LA (1931) Capillary conduction of liquids through porous mediums. Physics 1(5): 318–333. doi:10.1063/1.1745010

Ross PJ, Williams J, Bristow KL (1991) Equation for extending water retention curves to dryness. Soil Sci Soc Am J 55:923–927

Rossi C, Nimmo JR (1994) Modeling of soil water retention from saturation to oven dryness. Water Resour Res 30:701–708

Seki K (2007) SWRC fit—a nonlinear fitting program with a water retention curve for soils having unimodal and bimodal pore structure. Hydrol Earth Syst Sci Discuss 4:407–437

Su C, Brooks RH (1975) Soil hydraulic properties from infiltration tests. In: Proceedings of watershed management, irrigation and drainage Div, ASCE, Logan, Utah, 11–13 Aug, pp 516–542

Tuller M, Or D (2001) Hydraulic conductivity of variably saturated porous media: film and corner flow in angular pore space. Water Resour Res 37:1257–1276

van Genuchten MT (1980) A closed-form equation for predicting the hydraulic conductivity of unsaturated soils. Soil Sci Soc Am J 44:892–898

Visser WC (1968) An empirical expression for the desorption curve. In: Rijtema P, Wassink H (eds) Water in the unsaturated zone. Proceedings of Wageningen symposium, IASH/AIHS, Unesco, Paris, vol I, pp 329–335

Webb SW (2000) A simple extension of two-phase characteristic curves to include the dry region. Water Resour Res 36:1425–1430

Zhang F (2010) Soil water retention and relative permeability for full range of saturation. U.S. Department of Commerce, Springfield, VA

Revision of Empirical Coefficients of Commonly Used Flood Formulae Using Flow Data from Karnataka Rivers

T. Chandramohan, Mathew K. Jose, B. K. Purandara and B. Venkatesh

Abstract The empirical formulae used for the estimation of flood peak are regionally developed, based on statistical correlation of the observed peak with important catchment and storm properties. Most of these formulae use the catchment area as a single parameter affecting the flood peak, and other factors are clubbed in a region specific coefficient. However, the changes in catchment conditions, river fluvial systems and global climate largely affect these empirical coefficients. Therefore, it is required to revise or modify these formulae as and when new data are available. In the present study, six commonly used empirical formulae: Rational, Riggs, Ryves, Inglis, Creager and Ali Nawbjung were revised and tested using the observed flood peak values and return period flood values for 21 gauge sites (covering different agro-climatic regions and varying catchment areas) in the State of Karnataka. For statistical comparison of the results from empirical run-off estimation methods with observed data, statistical indices such as RMSE, BIAS and MD were used. It is found that Ali Nawabjung formula gives comparable predictions. Inglis and Creager formulae are also yielding better predictions for Karnataka.

Keywords Empirical formula · Flood · Return period · Karnataka

Introduction

Flood peak values are required in the design of bridges, culvert, waterways, spillways for dams and estimation of scour at a hydraulic structure. To estimate the magnitude of a flood peak, various methods are being adopted. Empirical formulae are commonly used in ungauged catchments where an initial estimate of peak flood is required. These empirical formulae are essentially regional formulae based on

T. Chandramohan (✉) · M. K. Jose · B. K. Purandara · B. Venkatesh
National Institute of Hydrology, Regional Centre, Hanuman Nagar, Belgaum 590019, Karnataka, India
e-mail: cmohant@yahoo.com

V. P. Singh et al. (eds.), *Hydrologic Modeling*, Water Science and Technology Library 81, https://doi.org/10.1007/978-981-10-5801-1_39

statistical correlation of the observed peak and important catchment and storm properties (Ponce 1993). To simplify the form of the equation, only a few of the many parameters affecting the flood peak are used. Most of these formulae use the catchment area as a single parameter affecting the flood peak and other factors are clubbed in a region specific constant coefficient (Griffiths and McKerchar 2008).

Most of these formulae did not consider rainfall characteristics directly, which, undoubtedly, play a very important role in any flood formation process (Gholami 1991). Also, the return period of the flood, which is a major factor in the selection of design floods, is not considered in any of the available empirical formulae (Jha and Smakhtin 2008). Nevertheless, these formulae are generally being used by many State governments for minor/medium projects with catchment area up to around 1500 km^2.

These formulae give better results when applied for the catchment with conditions more or less similar to those for which it was derived. The formulae frequently used are Dickens, Ryes, Khosla, Myers, Inglis, Karpov and Kanwar and Rational formula (Kothyari 1995). The use of these equations depends on the accurate estimation and usage of coefficients used in these equations, which were derived during the formulation of those equations. Therefore, it is required to revise or modify the empirical coefficients as and when new data are available. Such efforts justify the use of empirical equations in water resources planning, design and management. The present study aims at analysing the applicability of few of the commonly used empirical equations for the State of Karnataka and to modify the empirical coefficients used. Peak flood series data for number of river basins were used here to revise six empirical equations which can be used for the estimation of return period floods.

The study area, Karnataka State, is situated between 11° 40′ and 18° 27′ north latitudes and 74° 5′ and 78° 33′ east longitudes in the centre of western peninsular India and accounts for 5.8% of the country's total geographic area. It has a 350-km-long coastline, which forms the western boundary. The average annual rainfall of the different regions of the State varies roughly from 50 to 350 cm. In the districts of Bijapur, Raichur, Bellary and southern half of Gulbarga, the rainfall is lowest varying from 50 to 60 cm. The rainfall increases significantly in the western part of the State and reaches its maximum over the coastal belt to more than 350 cm. The southwest monsoon is the principal rainy season during which the State receives 80% of its rainfall.

There are seven river systems in Karnataka which with their tributaries, drain the state, Krishna, Cauvery, and west flowing rivers form the major river systems of the State. Gauged river basins of different sizes and characteristics are selected for the present study. The location of gauge sites from the Karnataka State, for which the discharge data was available, is shown in Fig. 1, and the salient features of the gauge sites are given in Table 1.

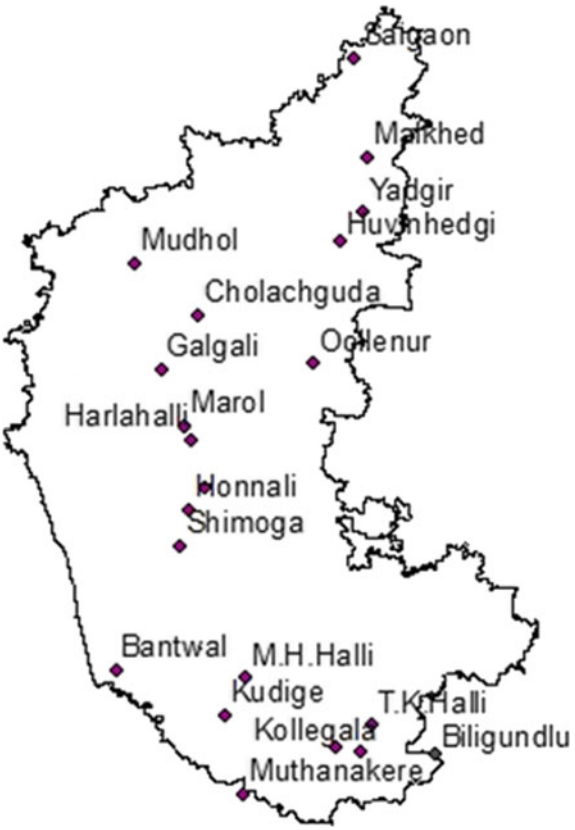

Fig. 1 Location of CWC gauge sites in Karnataka State

Table 1 CWC river gauge sites of Karnataka

River	Gauge site	Latitude (°, ′, ″)	Longitude (°, ′, ″)	Catch area A (km^2)	Av monsoon rainfall P (mm)
Cauvery	Biligundlu	12 10 48	77 43 48	36,682	286.7
Netravati	Bantwal	12 53 04	75 02 35	3184	3303.4
Kabini	Kollegala	12 11 21	77 06 00	21,082	304
Harangi	Kudige	12 30 09	75 57 43	1936	1716
Hemavati	M.H. Halli	12 49 06	76 08 00	3050	980.7
Bandigaduhalla	Muthanakere	11 50 00	76 07 00	1260	304
Malaprabha	Cholachguda	15 52 43	75 43 16	9373	427.3
Krishna	Galgali	15 25 00	75 25 00	22,560	365.9
Krishna	Huvinhedgi	16 29 25	76 55 23	55,150	478.2
Kagna	Malkheda	17 12 12	77 09 23	7650	640.1
Ghataprabha	Mudhol	16 19 00	75 12 00	6734	365.9

(continued)

Table 1 (continued)

River	Gauge site	Latitude (°, ′, ″)	Longitude (°, ′, ″)	Catch area A (km^2)	Av monsoon rainfall P (mm)
Tungabhadra	Oollenur	15 28 00	76 42 00	33,018	478.2
Manjira	Saigaon	18 03 00	77 03 00	9960	908.6
Bhima	Yadgir	16 44 15	77 07 31	69,863	640.1
Shimsha	T.K. Halli	12 25 00	77 11 36	7890	286.7
Kabini	T. Narasipura	12 13 48	76 53 46	7000	342.1
Haridra	Byaladahalli	14 26 00	75 46 47	2300	280
Tungabhadra	Harlahalli	14 49 50	75 40 33	14,582	478
Tungabhadra	Honnali	14 14 18	75 39 30	7075	1787.1
Varada	Marol	14 56 20	75 37 05	4901	478
Tunga	Shimoga	13 56 08	75 34 41	2831	1787.1

Methodology

The daily flow data were collected from the Central Water Commission (CWC) gauging sites for 21 rivers of Karnataka State and used for testing six commonly used empirical formulae and to modify the coefficients of these formulae. The duration of data availability varied from 15 to 33 years. The empirical formulae considered are:

- Ryves formula
- Rational formula
- Riggs formula
- Inglis formula
- Ali Nawabjung formula
- Creager formula.

Ryves and Dickens Formula

Ryves and Dickens formula takes the form of a power relation between run-off (Q) and catchment area (A) in the form:

$$Q = CA^b, \tag{1}$$

where C is the regional coefficient which is constant for all return period floods

Rational Formula

$$Q = CIA \quad \text{for } t > tc. \tag{2}$$

Inglis Formula

The general form of the Inglis Formula is

$$Q = 124A/(A + 10.4)^{0.5}. \tag{3}$$

For the present study, the formula is considered in the form of

$$Q = CA/(A + a)^{b}. \tag{4}$$

Creager Formula

$$Q = CA^{(aA)^{b}},$$

where 'a' and 'b' are the empirical coefficients for individual return period floods.

Ali Nawabjung Formula

$$Q = CA^{(a-(1/b)\log A)}. \tag{5}$$

Riggs Formula

$$Q_t = CA^{a}P^{b}. \tag{6}$$

The empirical coefficients are separated into two: C, representing a regional coefficient, which is kept constant for the individual equations for all the return period floods. The coefficients 'a' and 'b' are considered changing from each of the return period flood peaks (Salajegheh and Dastorani 2006). These coefficients were estimated in SYSTAT software using the peak flood series and return period flood values. The various steps involved in the study are:

- Collection of gauge data for all the river basins within the State.
- Processing the run-off data for each of the gauge sites to extract partial duration flood series.

- Estimation of return period floods for each of the river basin using L-moment approach.
- Collection/computation of catchment characteristics.
- Testing of empirical formulae using the discharge data and catchment characteristics.
- Modification of empirical coefficients to suit the local conditions and its verification by segregating the data set into two parts.
- Modify the existing equations to compute different return period floods.

To evaluate the applicability of various equations, statistical standards including mean square errors, oriental coefficient and mean difference were used. The empirical equation with lower RMSE, BIAS and MD would be the most suitable method.

Results

Partial duration flood series were derived for all the gauge sites. EV-I distribution has been identified as the robust distribution for analysing the peak flow; hence, this distribution was used in the present study. The flood peaks obtained were used to derive the parameters of the extreme value type I distribution. The model parameters were estimated using the L-moments (Hosking 1990; Rakesh et al. 2003). Flood values for different return periods were estimated using the fitted model. The relationship between the 100-year return period flood values of each of the basins with the corresponding catchment area is shown in Fig. 2.

Using flood discharge data series, the regional coefficients (C) and coefficients (a and b) for each of the equations were estimated using SYSTAT software and tested with one part of data series. Various empirical flood formulae were compared with the return period floods estimated for the basins. The estimated values of the

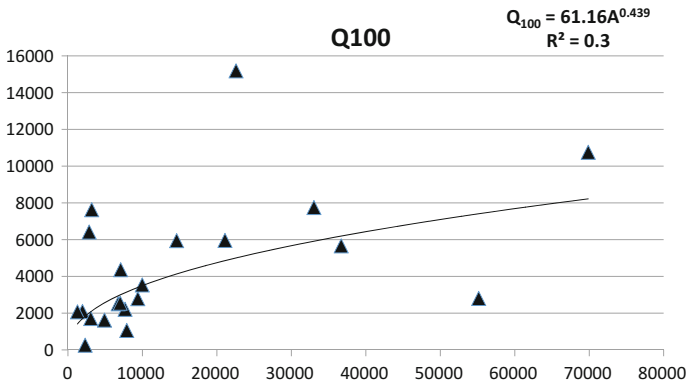

Fig. 2 Relation between Q_{100} and catchment area

Table 2 Empirical coefficients for Karnataka

Emp. formula	Coefficient	Return period flood						
		$Q2$	$Q5$	$Q10$	$Q50$	$Q100$	$Q200$	$Q500$
CREAGER	C	4	4	4	4	4	4	4
	a	24	22	21	20	19	17	14
	b	−0.03	−0.028	−0.027	−0.025	−0.022	−0.021	−0.018
RIGGS	C	11	11	11	11	11	11	11
	a	0.34	0.36	0.37	0.39	0.40	0.42	0.45
	b	0.42	0.41	0.40	0.38	0.36	0.35	0.33
RYVES	C	14	14	14	14	14	14	14
	a	0.53	0.54	0.55	0.57	0.58	0.61	0.62
RATIONAL	C	0.62	0.63	0.64	0.66	0.68	0.69	0.72
INGLIS	C	55	55	55	55	55	55	55
	a	11	15	16	18	19	21	22
	b	0.58	0.575	0.56	0.54	0.525	0.51	0.50
ALI NAWABJUNG	C	2.2	2.2	2.2	2.2	2.2	2.2	2.2
	a	1.20	1.24	1.26	1.29	1.33	1.35	1.40
	b	10.5	9	8.5	8	7	6.25	5.5

Table 3 Ranking of empirical formulae using statistical tests

Statistical standards	Creager	Riggs	Ryves	Rational	Inglis	Ali Nawbjung
MD	2	4	5	6	3	1
RMSE	1	5	4	6	3	2
BIAS	2	5	6	4	1	3

empirical coefficients for different return period floods were as shown in Table 2. With regard to the statistical comparison standards, for the best standard, a low rank and for the worst method, a high rank was considered in each standard. By tabulating these ranks, the method which has lowest rank in all standards, can be considered as the most proper method. Considering the conducted evaluation, the ranks for the three standards (RMSE, BIAS and MD) are shown in Table 3. It can be seen that the empirical formulae which can be used with better prediction efficiency for the State are as follows:

- Inglis
- Ali Nawabjung
- Creager

The comparison of the return period flood values (obtained using the observed discharge data) with the estimates using the empirical formulae is shown in Fig. 3. However, this figure gives only Q values for a particular return period and for a single gauging station, just for illustration purpose.

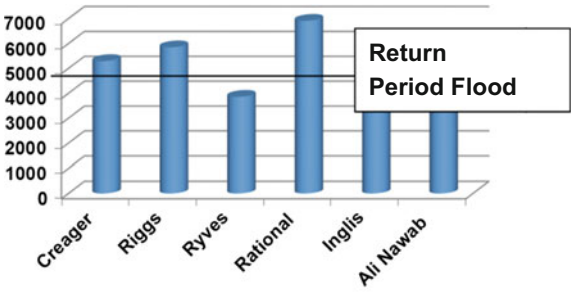

Fig. 3 Comparison of performance of empirical formulae

Conclusions

Empirical flood formulae are commonly used in water resources planning and management, where historical data are not adequately available for other methods such as flood frequency analyses or unit hydrograph techniques, or where an initial estimate of flood value for a return period is required. Most of the equations use catchment area as the variable for the calculation of peak flood value. However, it is very important to note that the coefficients used in such equations are site specific and evaluated with very few observations or data duration. Therefore, regular testing of these equations is required to revise the empirical coefficients, as and when more and more data are available.

In the present study, six commonly used empirical formulae were tested using the observed flood peak values and return period flood values for gauge sites (covering different agro-climatic regions and varying catchment areas) in Karnataka State. For statistical comparison of the results from empirical run-off estimation methods with observed data, statistical indexes such as RMSE, BIAS and MD were used.

Six formulae: Rational, Riggs, Ryves, Inglis, Creager and Ali Nawbjung were tested with the estimated flood values for different return periods. Ranks were assigned to each of these equations based on the statistical tests for standard prediction errors. It is found that Ali Nawabjung formula gives comparable predictions for the selected gauge sites. Inglis and Creager formulae are also yielding better predictions. Such revisions may be done regularly, as and when data pertaining to different seasons are available, which will give better accuracy for the computed peak flood/return period flood values.

References

Gholami S (1991) The survey of empirical methods using in instantaneous maximum discharges determining. M.Sc. thesis, University of Tehran, Iran

Griffiths GA, McKerchar AI (2008) Dependence of flood peak magnitude on catchment area. J Hyd (NZ) 47(2):123–131

Hosking JRM (1990) L-moments: analysis and estimation of distributions using linear combinations of order statistics. J Royal Stat Soc Series B 52:105–124

Jha R, Smakhtin V (2008) A review of methods for hydrological estimation at ungauged sites in India. IWMI Working Paper No. 130

Kothyari UC (1995) Estimation of monthly runoff from small catchments in India. J Hyd Sci 40:533–541

Ponce VM (1993) Engineering hydrology: principles and practices. Prentice Hall, Englewood Cliffs, NJ

Rakesh K, Chatterjee C, Sanjay K, Lohani AK, Singh RD (2003) Development of regional flood frequency relationships using L-moments for Middle Ganga Plains, Subzone 1(f) of India. J Wat Res Manag 17:243–257

Salajegheh A, Dastorani J (2006) Determining of regional coefficients of Fuller's empirical formula to estimate maximum instantaneous discharges in Dasht Kavir basin, Kalshour Sabzevar, Iran. BIABAN J 11(1):53–59

Reservoir Inflow Forecasting Using Extreme Learning Machines

Mukesh Kumar Tiwari and Sanjeet Kumar

Abstract Accurate and reliable forecasting of reservoir inflow is necessary for efficient and effective water resources' planning and management. In the present study, the capacity of recently developed extreme learning machines (ELMs) modeling approach in forecasting reservoir inflows is assessed and compared to that of equivalent traditional artificial neural network-based models. Performance of wavelet analysis technique is also explored by developing wavelet-based ELMs (WELMs) and wavelet-based ANNs (WANNs) models. Seven years of reservoir inflow data along with outflow data from two upstream reservoirs in the Damodar catchment along with rainfall data of 5 upstream rain gauge stations are considered in this study. Out of 7 years' daily data, 5 years' data are used for training the model, one-year data are used for cross-validation, and remaining one-year data are used to evaluate the performance of the developed models. Different performance indices indicated better performance of ELM and WELM models in comparison with MLR, ANN, WMLR, and WANN models. This study demonstrated the effectiveness of proper selection of wavelet functions and appropriate methodology for wavelet-based model development. ELM models were also computationally efficient as demonstrated by faster running time, and consequently, this study advocates the superiority of the WELM model and the significant role of wavelet transformation in order to improve the model's overall performance for reservoir inflow forecasting modeling.

Keywords Reservoir inflow · Extreme learning machine · Neural networks Wavelet analysis · Forecasting · Damodar catchment

M. K. Tiwari (✉)
Department of Soil and Water Engineering, College of Agricultural Engineering and Technology, Anand Agricultural University, Godhra 389001, Gujarat, India
e-mail: tiwari.iitkgp@gmail.com

S. Kumar
Department of Applied Engineering, Vignan's Foundation for Science, Technology & Research University, Vadlamudi, Guntur 522213, AP, India
e-mail: sanjeetiitkgp@gmail.com

V. P. Singh et al. (eds.), *Hydrologic Modeling*, Water Science and Technology Library 81, https://doi.org/10.1007/978-981-10-5801-1_40

Introduction

Accurate reservoir inflow forecasting is necessary for planning and management of available water resources. Inflow forecast can be applied for reservoir operation and management, flood control, drought management, water supply for irrigation, industrial and domestic uses, and hydropower generation. It emphasizes the development of a model that is accurate and can be easily applied for the operational reservoir inflow forecasting. Several approaches have been applied to map the nonlinear relationship between rainfall and runoff such as empirical, conceptual, physically, and data-driven (Verma et al. 2010; Paudel et al. 2011; Adamowski et al. 2013; Gad 2013). Data-driven models have been applied in different fields of water resources with promising results (Mukerji et al. 2009; Tiwari and Chatterjee 2010; Tiwari et al. 2013; Rath et al. 2013). In the previous years, complex nature of water resource variables has brought increased attention to the potential of soft computing technique methods including fuzzy logic and genetic programming (Kant et al. 2013), support vector regression (Herrera et al. 2010), and artificial neural networks (NNs) (Adamowski 2008; Tiwari and Chatterjee 2011). Neural network information processing system is capable of mimicking the functioning of human brain, and has been widely applied as an effective method for modeling highly nonlinear phenomenon in hydrological processes (Abrahart et al. 2012).

Recently, extreme learning machine (ELM) has gained popularity in hydrological forecasting as an improved artificial intelligence paradigm that requires significantly less computational time than the classical ANN model for training the datasets due to the fact that the input weights and hidden layer biases are randomly assigned (Huang et al. 2006). The forecasting problem is therefore reduced to a linear system of equations whose output weights are analytically determined with least squares method. ELM satisfies the universal approximation condition with good generalization performance (Huang 2003; Huang et al. 2015), and therefore appears to be a suitable ML approach for drought simulations. In an earlier study undertaken for a subset of stations in eastern Australia, Deo and Şahin (2015b) applied the ELM algorithm (without wavelet transformation) in a problem of modeling the monthly Effective Drought Index. Taormina et al. (2015) explored the ELM model for application in rainfall–runoff modeling and river forecasting, and Li and Cheng (2014) applied classical and wavelet ELM for streamflow discharge forecasting. Sun et al. (2014) compared ELM for flood forecasting in Daling River Basin, Yin et al. (2014) developed an ELM-based modular mechanism for real-time tidal prediction, and Abdullah et al. (2015) showed the ELM was efficient, simple in application, of high speed, and possessed good generalization performance for simulating Penman–Monteith evapotranspiration in Iraq. However, wavelet coupled ELM, ANN, and LSSVR to model the EDI has not been explored anywhere to date.

Although ANN methods have been used extensively as useful tools for prediction of hydrological variables, it has some limitations in dealing with non-stationary data (Cannas et al. 2006; Partal 2009). A non-stationary time series data has a variable variance and mean that does not remain constant or same to their

long-run mean over time, whereas the stationary time series data reverts around a constant long-term mean exhibits a constant variance independent of time. Daily flow time series data are often nonlinear and non-stationary (Rao et al. 2003; Wang et al. 2006). Non-stationarity such as seasonal variations and trends significantly affect modeling of time series and generally lead to poor predictability in practical applications (Francesco and Bernd 2000). Since the hydrological time series include several frequency components and have nonlinear relationships, hybrid model approaches, which include different data preprocessing and combine techniques, have been used to raise the prediction performance of neural networks. Wavelet analysis has emerged as an effective tool to simplify the non-stationarity in the dataset and has been widely applied by coupling with neural networks for water resource variables' forecasting (Zhou et al. 2008; Makwana and Tiwari 2014; Kisi and Shiri 2012; Sahay and Sehgal 2013; Sahay and Srivastava 2014; Sehgal et al. 2014). To develop WANN model, wavelet sub-time series generated using discrete wavelet transformation (DWT) are used as inputs to the ANN models. The DWT decomposes original time series data into many components, and each component has a distinct role in the original time series data. The low-frequency component or approximation generally reflects the identity (periodicity and trend) of the original data, whereas the high-frequency components (i.e., details) uncover sharp fluctuations (Kucuk and Oglu 2006). There are several applications of WANN models in water resource variables' forecasting and successful application inflow forecasting in the literature (Okkan 2012; Krishna 2014; Sehgal et al. 2014). More recently, Krishna (2014) developed and demonstrated the potential of wavelet analysis and moving average (MA) methods in conjunction with two types of neural networks, i.e., feedforward neural network and radial basis (RB) neural network, and multiple linear regression (MLR) models in the prediction of the daily inflow values of Malaprabha reservoir, Belgaum, India. The results showed that WANN model performs better compared to ANN and MLR models in forecasting the inflow hydrograph effectively. The author suggested undertaking further studies using data from upstream gauging stations to strengthen the findings. In this paper, we developed a wavelet extreme learning machine (WELM) model for inflow forecasting. ELM algorithm has a fast three-step method designed using a single-layer feedforward neural network with hidden neurons and randomly generated weights. The hidden layer parameters (hidden neurons and biases) are first randomized for a particular network architecture (governed by the number of input variables and the number of hidden neurons chosen optimally by the ELM network). Afterward, the input variables are propagated through the hidden layer and finally the output weights are solved as a linear system of equations (via the Moore–Penrose generalized inverse procedure) [details in Huang et al. (2006)].

Materials and Methods

Study Area

Damodar catchment, a part of the lower Ganges River, is located in the upper reaches of the Damodar River Basin in Jharkhand state of India (Fig. 1). The area lies between 23° 34′ to 24° 09′ North latitude and 84° 42′ to 86° 46′ East longitudes with an elevation variation between 122 and 1340 m above mean sea level. The catchment falls within sub-tropical climate, and daily mean relative humidity varies from 40 to 95% with alternating dry and wet periods. The daily mean temperature of the area ranges from 4 to 43 °C with average annual rainfall of 1390 mm, most of which occurs in months from July to September.

The study area comprises of mixed forest, mainly with deciduous and tropical moist forest along with many thorny bushes, and agricultural area. Damodar catchment consists of three reservoirs: Konar, Tenughat, and Panchet, and these reservoirs are constructed on Damodar River during 1955, 1972, and 1959, respectively, with the intention of hydropower generation, water supply for irrigation, industrial and domestic uses, and flood control. Damodar catchment is

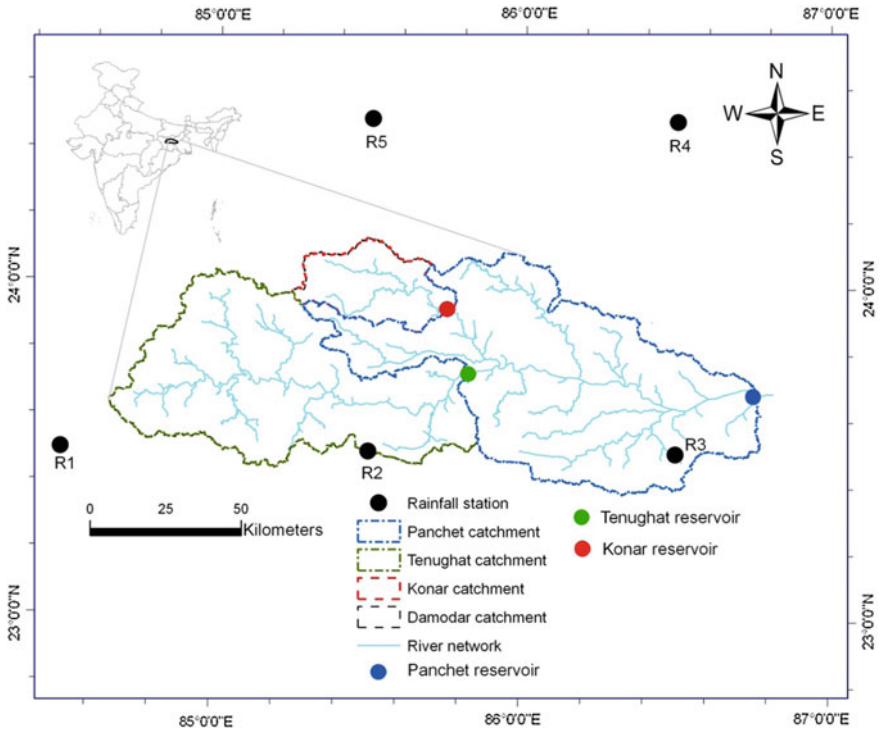

Fig. 1 Location map of study area along with reservoirs and rain gauge stations

further divided into three sub-catchments: Konar sub-catchment, Tenughat sub-catchment, and Panchet sub-catchment with area of 997, 4480, and 5401 km^2, respectively. The total area of the catchment area is about 10878 km^2 with the length of the main stream being 350 km draining into the Panchet reservoir.

Dataset Used in the Study

Daily rainfall data were collected from Indian Meteorological Department (IMD), Pune, for five stations covering the study area (i.e., R_1, R_2, R_3, R_4, and R_5); daily outflow reservoir data for Konar (K_O) and Tenughat (T_O) reservoirs and daily inflow data for Panchet reservoir (P_I) were collected for 7 years from January 01, 2001 to December 31, 2007, from the Reservoir Operation Department, Damodar Valley Corporation (DVC), Maithon, Jharkhand. From the available dataset, first five years of dataset (from Jan 01, 2001 to Jan 01, 2005) were considered for training, while data during the year 2006 were considered for cross-validation and data during the year 2007 were for the evaluation of the developed standard and combined ANN models (Table 1).

Artificial Neural Networks

Artificial neural network (ANN) is a strong mathematical approach, based upon imitation of human brain functioning by forming a model structure with the capability to map complex nonlinear relationships and processes that are inherent among several variables. In a simpler term, it is networks with nodes in form of feedforward neural network, consisting of different layers with computational nodes such as an input layer, one or more hidden layers, and an output layer as shown in Fig. 2a. As this approach is found very fast and efficient in highly complex and noisy environments to solve a wide range of problems, ANNs have been applied in numerous real-world applications including time series predictions (Abrahart et al. 2012). For detailed study on general properties of ANNs and its applications in water resource engineering, interested readers are directed to refer Bishop (1995), Haykin (1999), Maier and Dandy (2010), and Abrahart et al. (2012).

Table 1 Partitioning of data for ANN model development

Partition	Duration of the data	Number of data patterns
Training	01/01/2001–31/12/2005	1826
Cross-validation	01/01/2006–31/12/2006	365
Testing	01/01/2007–31/12/2007	365

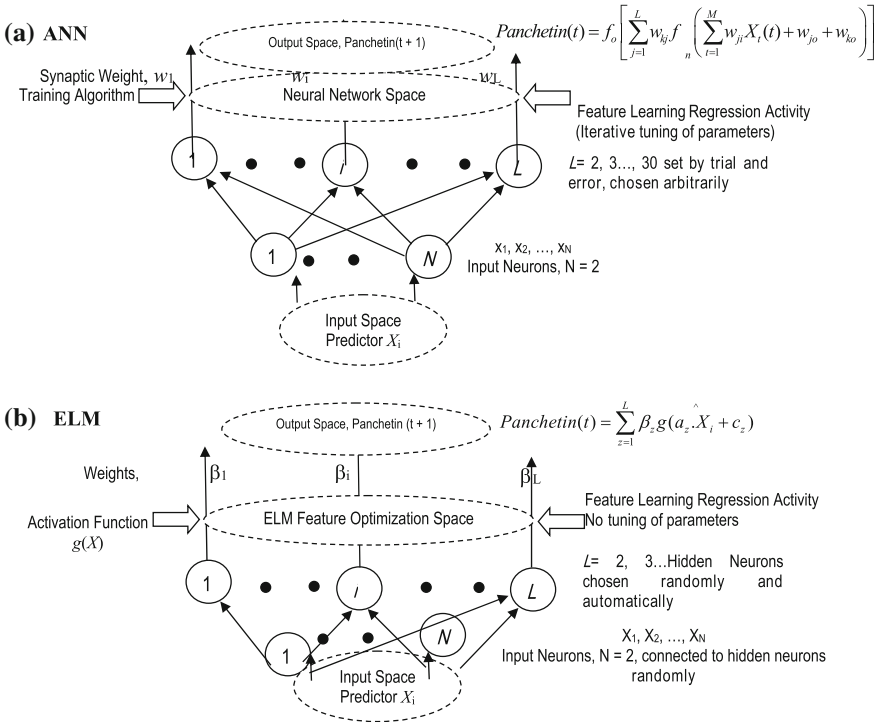

Fig. 2 Illustration of **a** extreme learning machine (ELM), and **b** artificial neural network (ANN) modeling frameworks used for the prediction of the inflow at Panchet reservoir

Extreme Learning Machine (ELM)

The ELM is a state-of-the-art single-layer feedforward network (SLFN) algorithm that operates similarly to feedforward backpropagation artificial neural network (FFBP-ANN) and least squares support vector regression (LSSVR) models. However, ELM has a better ability to solve regression problems with short modeling times compared to FFBP-ANN and LSSVR algorithms and has relatively better predictive performance (Acharya et al. 2013; Deo and Şahin 2015b). Also, the weights and hidden neuron selection are randomized, so that the output weights have a unique least squares solution solved by the Moore–Penrose generalized inverse matrix (Huang et al. 2006). Consequently, the ELM is a simple, three-step procedure requiring no parameterization except the randomization of hidden neurons which may be generated from a continuous probability distribution (e.g., the uniform distribution, normal distribution, triangular distribution). It has a distinct

advantage over conventional neural networks (e.g., ANN) that has slow convergence speed, lower generalizing performance, arriving at local minima, over-fitting problems, non-optimal solutions and iterative tuning of model parameters. In Fig. 2b, the schematic structure of ELM has been exemplified. Consider a set of N discrete samples $(x_i, t_i) \in R^n \times R^m$ and $(y_i, t_i) \in R^n \times R^m$, where n, m represent elements in respective domains, x is the input variable in model training data, y is the output variable in the test data, t is the time, and the subscript $i = 1, 2 \ldots N$ represents the subsequent samples. In our study the x comprised of inputs defined by lagged combinations of the inflows and rainfall time series and the y comprised of the forecasted inflow time series (target matrix).

In the ELM model network architecture, the SLFNs algorithm with L hidden neurons and a predetermined activation function, $G(a_i, b_i, x)$, can be described viz (Huang et al. 2006; Şahin et al. 2014):

$$f_L(x) = \sum_{i=1}^{L} \beta_i h_i(x), \tag{1}$$

where $\beta = [\beta_1, \beta_2, \ldots, \beta_L]^{\mathrm{T}}$ is the output weight matrix between hidden layer of L nodes and the $m > 1$ output nodes, and $h(x) = [h_1(x), h_2(x), \ldots, h_L(x)]$ is the nonlinear mapping space that comprises of the output row vector with respect to input variable x.

Note that $h_i(x)$ is the output of the ith hidden node. In optimization space, the ELM model's network is able to analyze the features present in the input data and "learn" the patterns or trends in those time series in order to simulate the objective variable which should intrinsically be related to the inputs. In accordance with Huang (2015), the output function for the hidden nodes may not be unique and different functions can be utilized with various neuron arrangements to determine the optimum model, as attempted by earlier work of Deo and Sahin (2015b). In this study, the $h_i(x)$ was of the form

$$h_i(x) = G(a_i.b_i.x), \quad a_i \in R^n, \quad b_i \in R, \quad i = [1, 2, \ldots, L], \tag{2}$$

where $G(a, b, x)$ was the activation function for ELM model with hidden parameters denoted as (a, b).

The $G(a, b, x)$ is a nonlinear piecewise continuous function that must satisfy the ELM universal approximation capability theorem (Huang et al. 2006), and therefore, it has to be optimized for the best unsupervised learning outcome. In the ELM model, the hidden node parameters (a, b) are randomly generated without any interference from the predictor data and may be deduced by continuous probability distribution instead of being explicitly trained. This can lead to remarkable computational efficiency compared to the traditional neural network models (e.g., ANN)

(Huang et al. 2006, 2015). The ELM model was developed using logarithmic sigmoid (G_{logsig}) equations viz:

$$G_{\text{logsig}}(a,b,x) = \frac{1}{1+\exp(-(ax+b))} \tag{3}$$

In this study, the logarithmic sigmoid equation was preferred as a common activation functions used in hydrological forecasting (Deo and Sahin 2015b; Adamowski et al. 2012) over bipolar logistic and Elliott sigmoids. Likewise, the linear transfer equation was found suitable for the output layer as a nonlinear transfer function in the output layer failed to improve performance values (Yonaba et al. 2010; Mubiru 2008). However, in a separate study, the effect of alternative activation functions based on sine, tangent sigmoid, radial basis and triangular basis equations (Tiwari and Chatterjee 2010; Deo and Sahin 2015a, b; Şahin 2012; Şahin et al. 2013) could also be trialed although these less common in hydrological forecasting.

After deducing the suitable weights for the hidden and output layer (β), the simulation of the inflow time series in the test period was performed by minimizing the approximation error:

$$\min_{\beta \in R^L} \|H\beta - y\|^2, \tag{4}$$

where $\|.\|$ denotes the Frobenius norm and h is the hidden layer (randomized) matrix produced by the activation function, mathematically defined viz:

$$H = \begin{bmatrix} h(x_1^L) \\ \vdots \\ h(x_N^L) \end{bmatrix} = \begin{bmatrix} h_1(x_1) \cdots h_L(x_1) \\ \vdots \\ h_1(x_N) \cdots h_L(x_N) \end{bmatrix}. \tag{5}$$

Note that $y(x)$ is the target output matrix that in our case represented the simulated drought index:

$$y(x) = \begin{bmatrix} t_1^L \\ \vdots \\ t_m^L \end{bmatrix} = \begin{bmatrix} (t_{11} \cdots t_{1m}) \\ \vdots \\ (t_{N1} \cdots t_{Lm}) \end{bmatrix}. \tag{6}$$

Finally, the optimal solution to Eq. (6) is given by

$$\beta^* = H^+ T, \tag{7}$$

where H^+ is the Moore–Penrose generalized inverse of the hidden layer matrix H.

Wavelet Analysis

Wavelet analysis utilizes a wavelet function known as mother wavelet defined as $\psi(t) = \int_{-\infty}^{+\infty} \psi(t)\mathrm{d}t = 0$, and successive wavelets can be derived as (Mallat 1989)

$$\psi_{a,b}(t) = |a|^{-\frac{1}{2}}\psi\left(\frac{t-b}{a}\right) \quad b \in R, a \in R, a \neq 0, \tag{8}$$

where a and b are the scale and time factor, respectively, and R is the domain of real numbers.

For a time series with a finite energy signal $f(t) \in L^2(R)$, the continuous wavelet transform is defined as (Kisi 2010)

$$W_f(a,b) = |a|^{-\frac{1}{2}} \int_R f(t)\psi^*\left(\frac{t-b}{a}\right)\mathrm{d}t \tag{9}$$

where $W_f(a, b)$ is the matrix of wavelet coefficient or a contour map known as scaleogram and ψ^* denotes a complex conjugate function.

To avoid generation of large number of coefficients, discrete wavelet transform (DWT) is applied as it is a convenient way and very useful for solving practical problems. DWT is obtained by constraining the wavelet dilation (a) and translation (b) parameters and defining the DWT as (Mallat 1989):

$$\psi_{m,n}\left(\frac{t-b}{a}\right) = a_0^{-m/2}\psi^*\left(\frac{t - nb_0a_0^m}{a_0^m}\right), \tag{10}$$

where integers m and n determine the magnitude of wavelet dilation and translation, respectively, a_0 represents a specified dilation step greater than 1 (most commonly $a_0 = 2$), and b_0 represents the location parameter which must be greater than zero (most commonly $b_0 = 1$).

Development of ANN Models

To develop a robust ANN model, different structures of ANN model were developed by using different combinations of input variables along with 1–10 numbers of hidden neurons with learning coefficient equal to 0.2 and momentum equal to 0.9 for which the generalization error is found to be minimum. The dataset were normalized to scale in the range of 0–1. The Levenberg–Marquardt method, considered as most efficient and fast second-order training method, is used to minimize the mean squared error between the forecast and observed reservoir inflows. To forecast inflows of Panchet reservoir at one-day (t) lead time, initially inflow of Panchet reservoir at previous time step (i.e., $t - 1$) is considered and then

subsequently other input variables of inflows of Panchet reservoir at longer lag time (i.e., $t-2$, $t-3$,...) were considered before performance of model start deteriorating.

Selection of suitable wavelet function called as mother wavelet and a suitable level of wavelet decomposition is a crucial issue, as there is no such study showing the best performance of model for a particular wavelet function or decomposition level. Another important property of wavelet function is its vanishing moment that limits wavelets' ability to represent polynomial behavior of the signal. It can be considered that higher vanishing moments should capture the variations more effectively and efficiently and should improve the model forecasting ability. Therefore, in this study, different wavelet functions with different vanishing moments such as db2, db5, db10, db20, Bior1.1, Bior3.3, Bior6.8, Haar, Coif1, Coif3, Coif5 were considered to develop WANN models.

Optimum number of decomposition level for DWT of the time series is estimated using the following formula (Nourani et al. 2008):

$$L = \text{int}[\log(N)], \tag{11}$$

where

L decomposition level
N number of time series data

This study uses $N = 1826$, which produces $L = 3$.

In this way for each wavelet function three level of decomposition is carried out such as approximation (A_3) and three details d_1, d_2 and d_3. Inflow data at Panchet reservoir, outflow data from Konar and Tenughat reservoir, and rainfall data at five gauging stations were initially decomposed using more frequently used mother wavelet *db5* into approximation (A_3) and details (d_1, d_2 and d_3) for each component. The time series data were also decomposed separately for training, cross-validation, and testing dataset. In spite of considering a selective method as discussed above to generate a new wavelet time series, all the combinations reported in previous studies along with some new approaches were tested in this study.

For several water resource variables' forecasting, wavelet analysis has improved the ANN model performance significantly, but there is no specific method for the selection of appropriate wavelet components for WANN model development and different studies have applied different approaches to develop WANN models. In this study, a comprehensive examination is carried out to compare and select the best approach for inflow forecasting. Five approaches tested in this study are as follows: (i) all the four components (i.e., A_3, d_1, d_2, and d_3) of eight input variables (i.e., R_1, R_2, R_3, R_4, R_5, K_O, T_O, P_I) with lag 1 (Approach 1); (ii) all the four components of input variables and lags found best for ANN model (i.e., A_3, d_1, d_2, and d_3 *of* P_I with lag 1; A_3, d_1, d_2, and d_3 of T_O with lag 1; A_3, d_1, d_2, and d_3 of R_1 with lag 1, 2, and 4; A_3, d_1, d_2, and d_3 of R_2 with lag 1 and 2) (Approach 2); (iii) all the significant wavelet components separately having correlation >0.10 with lag 1 (A_3 of R_1, R_2, R_3, R_4, R_5, K_O, T_O, P_I; d_1 of K_o, P_I, d_2 of K_O, T_O, P_I; d_3 of K_O, T_O, P_I) (Approach III); (iv) newly constructed time series adding significant

components of each parameter excluding d_1 component (lag input as best ANN) (A_3, d_2, and d_3 *of* P_I with lag 1; A_3, d_2, and d_3 of T_O with lag 1; A_3, d_2, and d_3 of R_1 with lag 1, 2, and 4; A_3, d_2, and d_3 of R_2 with lag 1 and 2) (Approach 4); and (v) newly constructed time series adding significant components having correlation >0.10 of each variable (A_3 of R_1, R_2, R_3, R_4, R_5, K_O, T_O, P_I; $A_3 + d_1 +$, $d_2 + d_3$ of K_O; $A_3 + d_2 + d_3$ of T_O; $A_3 + d_1 +$, $d_2 + d_3$ of P_I) (Approach 5).

In this study, MLR models are also developed to compare the performance of different ANN, ELM, and WELM models. The WANN and WELM models were developed using all the approaches discussed above.

Performance Indices

The performance of the developed ANN, WANN, ELM, WELM MLR, and WMLR models was evaluated using five performance indices defined below:

(i) The coefficient of determination (R^2):

$$R^2 = \left(\frac{\sum_{i=1}^{n} (O_i - \bar{O})(P_i - \bar{P})}{\sqrt{\sum_{i=1}^{n} (O_i - \bar{O})^2 \sum_{i=1}^{n} (P_i - \bar{P})^2}} \right)^2, \tag{12}$$

where O_i and P_i are the observed and forecasted inflow, respectively, $\overline{O}$ and $\overline{P}$ are the means of the observed and forecasted inflow, respectively, and n is the number of data patterns. Range of R^2 varies from 0 to 1, with 1 presenting a perfect forecasting model.

(ii) The Nash–Sutcliffe coefficient (E) is defined as

$$E = 1 - \frac{\sum_{i=1}^{n} (O_i - P_i)^2}{\sum_{i=1}^{n} (O_i - \bar{O}_i)^2} \tag{13}$$

The Nash–Sutcliffe efficiency varies from $-\infty$ to 1. The value of 1 shows the perfect model.

(iii) Root mean square error (RMSE):

$$\text{RMSE} = \sqrt{\frac{1}{n} \sum_{i=1}^{n} (O_i - P_i)^2}. \tag{14}$$

RMSE is always greater than 0; with value 0, the model fits the data perfectly.

(iv) Percentage deviation in peak (P_{dv}):

$$P_{dv} = \frac{P_p - O_p}{O_p} 100, \tag{15}$$

where O_p and P_p represent peak values of observed and forecasted inflow, respectively.

(v) Mean absolute error (MAE):

$$\text{MAE} = \frac{1}{n} \sum_{i=1}^{n} |O_i - P_i|. \tag{16}$$

MAE is always a positive number, with its minimum value 0 representing a perfect model.

Results and Discussion

Performance of ANN Models

The performance of ANN model for different input variables and for optimum number of hidden neurons in terms of different performance indices is shown in Table 2. Considering all the performance indices, performance of model #13 was found to be the best. Hydrograph and scatter plot between observed and forecasted values are shown in Fig. 3. It is observed that simulated values show the general behavior of the observed values, even though performance of model is not very good for medium and high inflow values' forecast. It can be considered that for best ANN model, outflow of Tenughat, inflow of Panchet reservoirs, and rainfall values at stations R_1 and R_2 are found effective, whereas some of the input variables are not found effective in simulating inflow forecast at Panchet reservoirs such as outflow of Konar, rainfall at stations R_3, R_4, and R_5. This may be due to the reason that these data have high colinearity with other hydro-climatic data and add negligible information for the improvement of daily inflow forecasts at Panchet reservoir. With $R^2 = 0.90$, $E = 78.32$, RMSE = 206.60 m^3/s and $P_{dv} = 15.91$ and MAE = 68.12 m^3/s, the performance of best ANN model can be considered satisfactory, but higher value of RMSE compared to MAE shows that model is not able to simulate high inflow values accurately. It may be due to the reason that ANN models are not able to extract non-stationarity from the training dataset.

Table 2 Best NN model structure for different input variables for testing dataset

Model	Input variables	Number of optimal hidden neurons	ANN architecture	Performance indices				
				R^2	E (%)	RMSE (m^3/s)	P_{dv} (%)	MAE (m^3/s)
1	$P_I(t-1)$	2	1-2-1	0.80	64.49	263.51	19.36	90.20
2	$P_I(t-1; t-2)$	3	2-3-1	0.81	64.21	264.84	62.34	113.11
3	$P_I(t-1)$; $T_O(t-1)$	2	2-2-1	0.86	69.55	244.03	47.46	74.05
4	$P_I(t-1)$; $T_O(t-1; t-2)$	9	3-9-1	0.86	71.68	235.59	33.01	74.94
5	$P_I(t-1)$; $T_O(t-1)$; $K_O(t-1)$	7	3-7-1	0.79	62.14	272.09	33.37	86.11
6	$P_I(t-1)$; $T_O(t-1)$; $K_O(t-2)$	7	3-7-1	0.84	70.49	240.49	0.09	75.63
7	$P_I(t-1)$; $T_O(t-1)$; $R_1(t-1)$	3	3-7-1	0.86	70.03	242.12	49.74	74.30
8	$P_I(t-1)$; $T_O(t-1)$; $R_1(t-1; t-2)$	5	4-5-1	0.87	73.20	229.17	29.17	73.77
9	$P_I(t-1)$; $T_O(t-1)$; $R_1(t-1; t-2; t-3)$	6	5-6-1	0.86	70.57	240.42	42.51	73.39
10	$P_I(t-1)$; $T_O(t-1)$; $R_1(t-1; t-2; t-4)$	9	5-9-1	0.89	75.01	221.80	15.38	71.80
11	$P_I(t-1)$; $T_O(t-1)$; $R_1(t-1; t-2; t-4; t-5)$	4	6-4-1	0.88	72.75	231.86	28.83	75.24
12	$P_I(t-1)$; $T_O(t-1)$; $R_1(t-1; t-2; t-4)$; $R_2(t-1)$	2	6-2-1	0.90	77.94	208.39	4.09	69.87
13	$\mathbf{P_I(t-1)}$; $\mathbf{T_O(t-1)}$; $\boldsymbol{R_1(t-1; t-2; t-4)}$; $\boldsymbol{R_2(t-1; t-2)}$	**7**	**7-7-1**	**0.90**	**80.74**	**194.74**	**2.85**	**68.10**
14	$\mathbf{P_I}(t-1)$; $\mathbf{T_O}(t-1)$; $R_1(t-1; \boldsymbol{t-2};$	7	7-7-1	0.89	79.06	203.04	3.62	72.28

(continued)

Table 2 (continued)

Model	Input variables	Number of optimal hidden neurons	ANN architecture	Performance indices				
				R^2	E (%)	RMSE (m^3/s)	P_{dv} (%)	MAE (m^3/s)
	$t-4$); $R_2(t-1)$; $R_3(t-1)$							
15	$\mathbf{P_I}(t-1)$; $\mathbf{T_O}(t-1)$; $R_1(t-1; t-2; t-4)$; $R_2(t-1)$; $R_4(t-1)$	4	7-4-1	0.90	78.32	206.60	15.91	68.12
16	$\mathbf{P_I}(t-1)$; $\mathbf{T_O}(t-1)$; $R_1(t-1; t-2; t-4)$; $R_2(t-1)$; $R_5(t-1)$	6	7-6-1	0.89	77.95	208.36	28.15	85.37

P_I, T_O, K_O, R_1, R_2, R_3, R_4, and R_5 represent inflow of Panchet, outflow of Tenughat, outflow of Konar, rainfall at stations 1, 2, 3, 4, and 5, respectively, whereas t represents at time t and $t-1$ represents at time $t-1$, etc

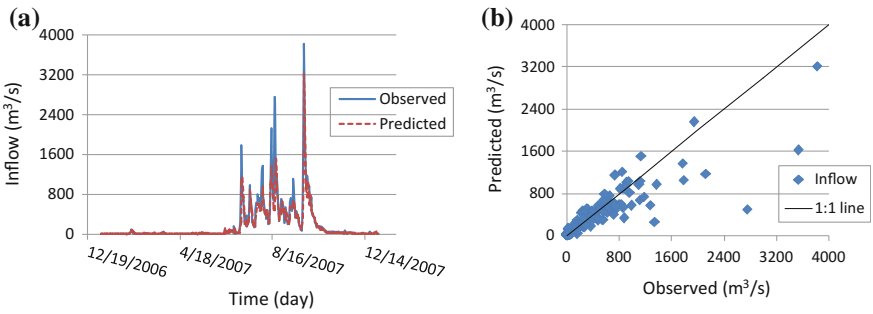

Fig. 3 Performance of NN model **a** hydrograph **b** scatter plot

Performance of WANN Models

WANN models were initially developed using all the wavelet sub-time series components of input variables, and lagged information for all the components was the same as found best for ANN model (Model #13) (i.e., Approach 2). Subsequently, the performance of several wavelet functions with different vanishing moments was considered to select an appropriate wavelet function. The performance of WANN models using different wavelet functions and vanishing moment is shown in Table 3. It can be observed that wavelet function *db5* performed best among all the wavelet functions considered. It can also be observed that

Table 3 Performance of WANN models developed using different approaches for one-day lead inflow forecasting

Input variables	Input variables	Hidden neurons	Performance indices				
			R^2	E (%)	RMSE (m^3/s)	P_{dv} (%)	MAE (m^3/s)
Approach 1	All the 4 components of 8 variables with lag 1	9	0.91	82.84	183.21	37.79	67.72
Approach 2	All the four components of input parameters and lags found best for ANN model	7	0.93	85.47	169.11	22.27	67.48
Approach 3	All the significant wavelet components separately having correlation >0.10 with lag 1	6	0.88	76.63	213.79	42.33	73.70
Approach 4	Newly constructed time series adding significant components of each parameter excluding d1 component (same lag input as found for best ANN)	7	0.93	87.15	159.05	11.31	65.83
Approach 5	Newly constructed time series adding significant components of each parameter	8	0.84	69.39	245.46	19.32	82.22

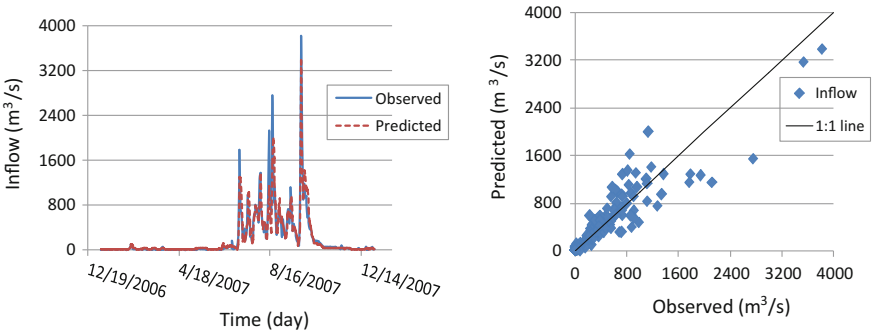

Fig. 4 Performance of WANN model **a** hydrograph **b** scatter plot using model

performance of WANN model developed using *db5* wavelet function with five vanishing moments performed better than standard ANN model in terms of different performance indices.

The performance of best found WANN modeling approach is also shown in form of hydrograph and scatter plot as shown in Fig. 4. It can be observed that the

observed values are simulated very well and the performance is considerably improved particularly for peak values as these are very close to 1:1 regression line. It can be observed that wavelet analysis with proper selection of wavelet function and vanishing moment along with suitable wavelet selection method can significantly improve the model performance.

Performance of ELM and WELM Models

WELM models were initially developed using all the wavelet sub-time series components of input variables, and lagged information for all the components was the same as found best for ANN model (Model #13) (i.e., Approach 2). Subsequently, the performance of several wavelet functions with different vanishing moments was considered to select an appropriate wavelet function. The performance of WANN models is shown in Table 4. It can be observed that performance of WELM model is better than standard ELM model in terms of different performance indices.

The performance of best found ELM and WELM modeling approach is also shown in form of hydrograph and scatter plot as shown in Fig. 5. It can be observed that the observed values are simulated very well and the performance is considerably improved particularly for peak values as these are very close to 1:1 regression line. It can be observed that wavelet analysis with proper selection of wavelet function and vanishing moment along with suitable wavelet selection method can significantly improve the model performance.

Performance of MLR and WMLR Models

Similar to several previous studies, developed ANN and WANN models are compared with MLR model to benchmark the performance. In this study in addition to MLR models, wavelet-based MLR models (WMLR) are developed and the performance is compared with ANN and WANN models. MLR and WMLR models are developed by using the same input variables as used for best ANN and

Table 4 Performance of ELM and WELM models for one-day lead inflow forecasting

Model	Input variables	Performance indices				
		R^2	E (%)	RMSE (m^3/s)	P_{dv} (%)	MAE (m^3/s)
ELM	Same input variables as used for best ANN model	0.85	85.14	104.86	20.06	35.92
WELM	Same input variables as used for best WANN model	0.94	87.79	95.04	14.56	32.62

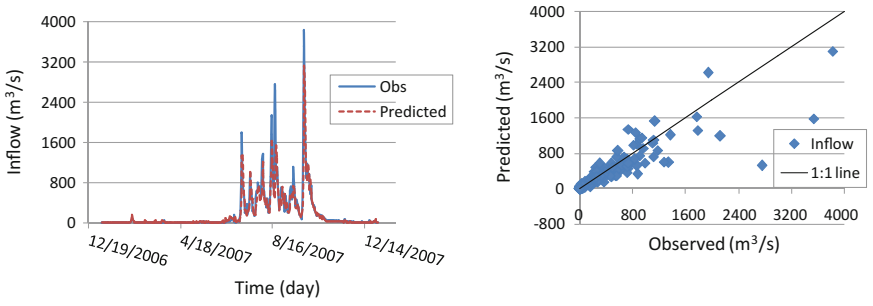

(a) ELM

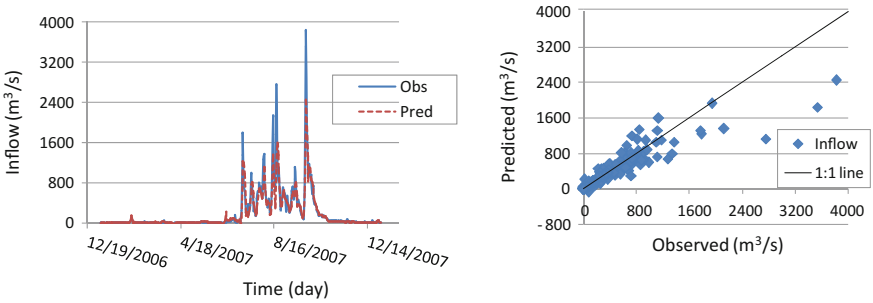

(b) WELM

Fig. 5 Hydrographs and scatter plots for performance comparison of **a** ELM and **b** WELM models

Table 5 Performance of MLR and WMLR models for one-day lead inflow forecasting

Model	Input variables	Performance indices				
		R^2	E (%)	RMSE (m^3/s)	P_{dv} (%)	MAE (m^3/s)
MLR	Same input variables as used for best ANN model	0.76	73.72	227.43	32.43	71.69
WMLR	Same input variables as used for best WANN model	0.80	77.41	210.88	32.36	66.28

WANN models, respectively, and the performance of both the models is shown in Table 5. It can be observed that the performance of WMLR models is better than MLR models, but WANN model performed better than both the MLR and WMLR models as these two models are not able to simulate medium and high inflow values satisfactorily (Fig. 6). This can also be observed from the higher RMSE values compared to MAE values for both the models.

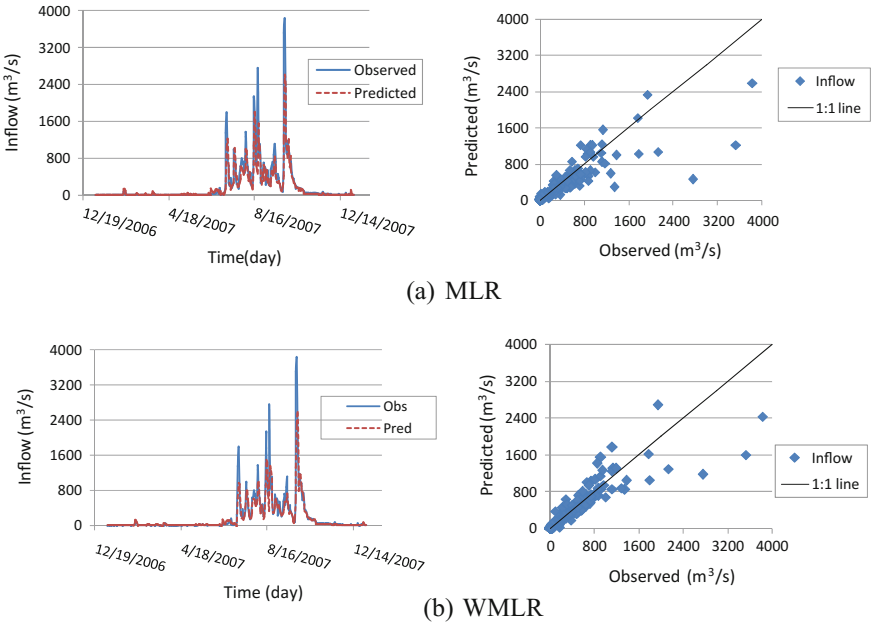

Fig. 6 Hydrographs and scatter plots for performance comparison of **a** MLR and **b** WMLR models

Conclusions

Wavelet-based ANN (WANN) and ELM (WELM) models are developed in this study for inflow forecasting of Panchet reservoir in India, and the performance is compared with standard ANN, ELM, wavelet-based MLR (WMLR) and MLR models. Robust ANN and ELM models were developed by considering several combinations of parameters such as input variables, optimization parameters, training algorithms, and hidden neurons. WANN and WELM models were developed by considering different wavelet functions and approaches to ensure efficient WANN and WELM models. Based on this study, following conclusions are drawn:

- Wavelet analysis with proper selection of wavelet function and vanishing moment along with suitable wavelet selection method can significantly improve the ANN model performance.
- WELM model performs better than WANN, WMLR, standard ANN, and MLR models for inflow forecasting.
- Optimum number of input selected for ANN model development is also best with different number of wavelet sub-time series excluding d_1 components for best WANN model development.

- Out of several wavelet functions and vanishing moments, *db5* wavelet function with five vanishing moments provides best WANN model for inflow forecasting.
- WANN model not only has capabilities to simulate all the observed values very well, but also it simulates peak inflow values far better compared to remaining models.
- The performance of ANN model is improved significantly by including reservoir outflow and rainfall information in the upstream and nearby areas.
- The selection of significant input is very crucial as inclusion of randomly selected input variables may significantly reduce the model performance.
- WELM and WANN models can deal with non-stationary dataset effectively and can be used as suitable tool for inflow forecasting. It has the potential to perform better for different non-stationary water resource variables' forecasting.
- Inflow forecasts can be improved by considering discharge releases from upstream reservoirs, and rainfall values in upstream and nearby locations in the upstream boundary.

Acknowledgments We acknowledge the Damodar Valley Corporation, Jharkhand, India for providing the necessary data and Information Technology Research Academy (ITRA), Media Lab Asia, Meity, Govt of India for the funding and encouragement to carry out the research work.

References

Abdullah SS, Malek M, Abdullah NS, Kisi O, Yap KS (2015) Extreme learning machines: a new approach for prediction of reference evapotranspiration. J Hydrol 527:184–195

Abrahart RJ, Anctil F, Coulibaly P, Dawson CW, Mount NJ, See LM, Shamseldin AY, Solomatine DP, Toth E, Wilby RL (2012) Two decades of anarchy? Emerging themes and outstanding challenges for neural network river forecasting. Prog Phy Geogr 36(4):480–513

Acharya N, Shrivastava NA, Panigrahi B, Mohanty U (2013) Development of an artificial neural network based multi-model ensemble to estimate the northeast monsoon rainfall over south peninsular India: an application of extreme learning machine. Clim Dyn 43(5):1–8

Adamowski JF (2008) Peak daily water demand forecast modeling using artificial neural networks. J Water Resour Plann Manage 134(2):119–128

Adamowski J, Adamowski K, Prokoph A (2013) A spectral analysis based methodology to detect climatological influences on daily urban water demand. Math Geosci 45(1):49–68

Adamowski J, Fung Chan H, Prasher SO, Ozga-Zielinski B, Sliusarieva A (2012) Comparison of multiple linear and nonlinear regression, autoregressive integrated moving average, artificial neural network, and wavelet artificial neural network methods for urban water demand forecasting in Montreal, Canada. Water Resour Res 48:W01528

Bishop CM (1995) Neural networks for pattern recognition. Clarendon Press, Oxford, UK

Cannas B, Fanni A, See L, Sias G (2006) Data preprocessing for river flow forecasting using neural networks: wavelet transforms and data partitioning. Phy Chem Earth 31(18):1164–1171

Deo RC, Şahin M (2015a) Application of the extreme learning machine algorithm for the prediction of monthly effective drought index in eastern Australia. Atmos Res 153:512–525

Deo RC, Şahin M (2015b) Application of the extreme learning machine algorithm for the prediction of monthly effective drought index in eastern Australia. Atmos Res 153:512–525

Francesco V, Bernd F (2000) Nonstationarity and data preprocessing for neural network predictions of an economic time series. Proc Int Joint Conf Neural Netw 5:129–134
Gad MA (2013) A useful automated rainfall-runoff model for engineering applications in semi-arid regions. Comput Geosci 52:443–452
Haykin S (1999) Neural networks: a comprehensive foundation, 2nd edn. Prentice Hall, Englewood Cliffs, NJ
Herrera M, Torgo L, Izquierdo J, Perez-Garcıa R (2010) Predictive models for forecasting hourly urban water demand. J Hydrol 387(1–2):141–150
Huang GB (2003) Learning capability and storage capacity of two-hidden-layer feedforward networks. Neural Netw IEEE Trans 14:274–281
Huang GB, Zhu QY, Siew CK (2006) Extreme learning machine: theory and applications. Neurocomputing 70:489–501
Huang G, Huang GB, Song S, You K (2015) Trends in extreme learning machines: a review. Neural Netw 61:32–48
Kant A, Suman PK, Giri BK, Tiwari MK, Chatterjee C, Nayak PC, Kumar S (2013) Comparison of multi-objective evolutionary neural network, adaptive neuro-fuzzy inference system and bootstrap-based neural network for flood forecasting. Neural Comput Appl 23(1):231–246
Kisi O, Shiri J (2012) Reply to discussion of precipitation forecasting using wavelet-genetic programming and wavelet-neuro-fuzzy conjunction models. Water Resour Manage 26 (12):3663–3665
Krishna B (2014) Comparison of wavelet based ANN and regression models for reservoir inflow forecasting. J Hydrol Eng 19(7):1385–1400
Kucuk M, Oglu NA (2006) Wavelet regression technique for stream flow prediction. J App Stat 33 (9):943–960
Li B, Cheng C (2014) Monthly discharge forecasting using wavelet neural networks with extreme learning machine. Sci China Technol Sci 57:2441–2452
Maier HR, Dandy GC (2010) Neural networks for the prediction and forecasting of water resources variables: a review of modeling issues and applications. Environ Model Softw 15:101–124
Mallat SG (1989) A theory for multi resolution signal decomposition: the wavelet representation. IEEE Trans Pattern Anal Machine Intell 11(7):674–693
Makwana JJ, Tiwari MK (2014) Intermittent streamflow forecasting and extreme event modelling using wavelet based artificial neural networks. Water Resour Manage 28:4857–4873
Mubiru J, Banda EJKB (2008) Estimation of monthly average daily global solar irradiation using artificial neural networks. Sol Energy 82:181–187
Mukerji A, Chatterjee C, Raghuwanshi NS (2009) Flood forecasting using ANN, neuro-fuzzy, and neuro-GA models. J Hydrol Eng 14(6):647–652
Nourani V, Alami MT, Aminfar MH (2008) A combined neural wavelet model for prediction of watershed precipitation, Ligvanchai, Iran". J Environ Hydrol 16(2):1–12
Okkan U (2012) Wavelet neural network model for reservoir inflow prediction. Sci Iran 19 (6):1445–1455
Partal T (2009) Modeling evapotranspiration using discrete wavelet transform and neural networks. Hydrol Process 23(25):3545–3555
Paudel M, Nelson EJ, Downer CW, Hotchkiss R (2011) Comparing the capability of distributed and lumped hydrologic models for analyzing the effects of land use change. J Hydroinf 13 (3):461–473
Rao AR, Hamed KH, Chen HL (2003) Nonstationarities in hydrologic and environmental time series. Kluwer, Dordrecht
Rath S, Nayak PC, Chatterjee C (2013) Hierarchical neurofuzzy model for real-time flood forecasting. Int J River Basin Manage 11(3):253–268
Sahay RR, Sehgal V (2013) Wavelet regression models for predicting flood stages in rivers: a case study in Eastern India. J Flood Risk Manage 6(2):146–155
Sahay RR, Srivastava A (2014) Predicting monsoon floods in rivers embedding wavelet transform genetic algorithm and neural network. Water Resour Manage 28:301–317

Şahin M (2012) Modelling of air temperature using remote sensing and artificial neural network in Turkey. Adv Space Res 50:973–985

Şahin M, Kaya Y, Uyar M (2013) Comparison of ANN and MLR models for estimating solar radiation in Turkey using NOAA/AVHRR data. Adv Space Res 51:891–904

Şahin M, Kaya Y, Uyar M, Yıldırım S (2014) Application of extreme learning machine for estimating solar radiation from satellite data. Int J Energy Res 38:205–212

Sehgal V, Sahay RR, Chatterjee C (2014) Effect of utilization of discrete wavelet components on flood forecasting performance of wavelet based ANFIS models. Water Resour Manage 28 (6):1733–1749

Sun M, Chen TT, Yu Y, Wang Z, Chi DC (2014) Extreme learning machine application in flood forecasting. J Shenyang Agric Univ 2:027

Taormina R, Chau KW (2015) Data driven input variable selection for rainfall runoff modeling using binary-coded particle swarm optimization and extreme learning machines. J Hydrol 529 (3):1617–1632

Tiwari MK, Chatterjee C (2010) Development of an accurate and reliable hourly flood forecasting model using wavelet-bootstrap-ANN hybrid approach. J Hydrol 394:458–470

Tiwari MK, Chatterjee C (2011) A new wavelet-bootstrap-ANN hybrid model for daily discharge forecasting. J Hydroinf 13(3):500–519

Tiwari MK, Song KY, Chatterjee C, Gupta MM (2013) Improving reliability of river flow forecasting using neural networks, wavelets and self-organizing maps. J Hydroinf 15(2):486–502

Verma AK, Jha MK, Mahana RK (2010) Evaluation of HEC-HMS and WEPP for simulating watershed runoff using remote sensing and geographical information system. Paddy Water Environ 8(2):131–144

Wang W, Vrijling JK, Van Gelder PHAJM, Ma J (2006) Testing for nonlinearity of streamflow processes at different timescales. J Hydrol 322(1–4):247–268

Yin JC, Li GS, Hu JQA (2014) Modular prediction mechanism based on sequential extreme learning machine with application to real-time tidal prediction. Extreme Learning Machines, Springer, pp 35–53

Yonaba H, Anctil F, Fortin V (2010) Comparing sigmoid transfer functions for neural network multistep ahead stream flow forecasting. J Hydrol Eng 275–283

Zhou HC, Peng Y, Liang GH (2008) The research of monthly discharge predictor-corrector model based on wavelet decomposition. Water Resour Manage 22(2):217–227

Quantifying Discontinuity, Connectivity, Variability, and Hierarchy in Overland Flow Generation: Comparison of Different Modeling Methods

Xuefeng Chu

Abstract Under the influence of surface topography, overland flow generation and surface runoff exhibit extremely high variability and discontinuity, featuring a hierarchical pattern of connectivity and threshold behavior. Quantifying these properties is crucial to better understand the intrinsic mechanisms of overland flow generation and further improve hydrologic and water quality modeling across varying spatiotemporal scales. This research focused on the theory of threshold hydrology, including new methods for delineation of depression-dominated land surfaces and new approaches for modeling of puddle filling-spilling-merging-splitting dynamics. Comparisons with traditional delineation and modeling approaches demonstrated the existence of threshold behavior in overland flow generation, nonuniformity in evolution of hydrologic connectivity and runoff initiation, and hierarchy in drainage network development. This research emphasized the dominance of surface topography on surface and subsurface hydrologic processes.

Introduction

At a broad regional scale, surface relief dominates the occurrence and evolution of drainage networks, as well as the spatiotemporal distributions and movement of water in both surface and subsurface systems. At a local scale, microtopography plays an important role in overland flow generation, surface ponding, and runoff processes, as well as infiltration and unsaturated/saturated flow. Surface microrelief controls the scales and distributions of depressions, which further affect the initiation timing of surface runoff, the depths and variations of surface runoff, retention of runoff water, and drainage patterns (Hansen et al. 1999; Govers et al. 2000; Darboux and Huang 2005; Abedini et al. 2006; Martin et al. 2008; Chu 2011; Chi et al. 2012; Chu et al. 2015). Surface roughness may significantly affect the

X. Chu (✉)
Department of Civil and Environmental Engineering, North Dakota State University, PO Box 6050, Fargo, ND 58108-6050, USA
e-mail: xuefeng.chu@ndsu.edu

V. P. Singh et al. (eds.), *Hydrologic Modeling*, Water Science and Technology Library 81, https://doi.org/10.1007/978-981-10-5801-1_41

magnitude and directions of overland flow and indirectly influence infiltration (Johnson et al. 1979; Govers et al. 2000; Kamphorst et al. 2000; Darboux and Huang 2005; Chu et al. 2015). Importantly, due to the topographic control, overland flow generation is characterized by a series of dynamic puddle-to-puddle (P2P) filling-spilling-merging-splitting processes, featuring intrinsic nature of discontinuity, variability, and hierarchy (Chu et al. 2013). Consequently, surface runoff exhibits a stepwise, intermittent increasing pattern (Chu 2011; Chu et al. 2015) and threshold behavior (Chu et al. 2013). Thus, characterization of surface microtopography and quantification of the resulting P2P dynamics and threshold behavior are critical to better understanding the mechanisms of overland flow generation and improving watershed hydrologic modeling.

Studies have been conducted to quantify depression filling and spilling processes and analyze hydrologic connectivity. Darboux et al. (2001) developed a conditional-walker method to simulate depression filling and water redistribution on rough surfaces, and to further evaluate the influence of surface microtopography on discharge and hydrologic connectivity. Antoine et al. (2009) proposed a functional connectivity indicator that linked surface connection to the surface storage filling. Antoine et al. (2011) further integrated the connectivity information of sub-grids to improve the prediction of a global runoff production. Appels et al. (2011) simulated the filling, merging, and connecting processes, evaluated the influence of microtopography on surface runoff, and quantified the development of hydrologic connectivity with simplified hydrographs. Chu et al. (2013), Yang and Chu (2015) developed a new modeling framework to simulate the microtopography-controlled P2P overland flow dynamics. Yang and Chu (2013) proposed a concept of P2P hydrologic connectivity to characterize the discontinuous overland flow processes and quantify the spatiotemporal variability in hydrologic connectivity. The importance of threshold behaviors in hydrologic, environmental, and ecological systems has been emphasized by many researchers (e.g., McDonnell 2003; Lehmann et al. 2007; Zehe and Sivapalan 2009). Leibowitz and Vining (2003) described the spilling process of prairie pothole wetlands and the potential biological effects. Wetlands were viewed as "isolated basins" and characterized by a "fill and spill" process (Winter and LaBaugh 2003; van der Kamp and Hayashi 2009). Spence (2007) applied a transfer function and storage threshold to predict the efficiency of runoff production. Lehmann et al. (2007) used a percolation theory to quantify the threshold processes and the relationship of rainfall input and outflow discharge.

Digital elevation models (DEMs) are widely utilized to represent topographic variations of a surface. A variety of methods have been developed for DEM-based surface delineation. O'Callaghan and Mark (1984) proposed the D8 method for basin delineation and identification of drainage networks from DEMs. Jenson and Domingue (1988) described their topographic analysis procedures for filling surface depressions, computing flow directions and accumulations, and determining drainage networks and watershed boundaries. Martz and Garbrecht (1993) proposed their algorithms for DEM-based watershed delineation, and Garbrecht and Martz (2000)

detailed the TOPAZ (TOpographic PArameteriZation) program for automated analysis of digital landscape topography. In addition to TOPAZ that has been incorporated in the WMS software (WMS 2015), many other digital terrain analysis tools and watershed delineation software packages, such as Arc Hydro (Maidment 2002) and HEC-GeoHMS (USACE 2013) have been developed to facilitate watershed hydrologic and water quality modeling. The D8 method (O'Callaghan and Mark 1984) is commonly implemented in most delineation methods. Tarboton (1997) proposed a new procedure to improve the D8 method featuring "fixed" eight directions and incorporated the D-infinity flow method in the TauDEM ArcGIS toolbox (Tarboton et al. 2015). In most existing DEM-based delineation approaches, filling depressions/sinks is performed as an essential preprocessing procedure that allows one to develop a depressionless surface and a single uniform drainage system, in which all DEM cells are well-connected and "unconditionally" contribute surface runoff to the basin outlet. Zhang and Chu (2015) evaluated different DEM-based delineation techniques and the effects of DEM resolutions.

The objective of this research is to examine the fundamentals of threshold hydrology, new methods for DEM-based delineation of depression-dominated land surfaces and modeling of the P2P filling-spilling-merging-splitting overland flow dynamics and the associated threshold behavior. Applications and comparisons with traditional delineation and modeling approaches are performed to demonstrate the threshold behavior in overland flow generation, the nonuniform progressive development of hydrologic connectivity, and the unique hierarchical drainage patterns.

P2P Overland Flow Dynamics and Threshold Behavior

Surface depressions dominate localized runoff concentration and hydrologic connectivity, exhibiting threshold behavior (Chu et al. 2013; Yang and Chu 2013). The entire overland flow generation and runoff process can be characterized by four major stages (Chu 2011): (1) infiltration-dominated stage, (2) P2P filling-spilling-merging stage, (3) transition stage, and (4) steady-state stage. During the early stage of a persistent rainfall event, rain water completely infiltrates into the soil. When the rainfall intensity exceeds the infiltration capacity, ponding occurs and excess water flows toward local minima (i.e., centers of depressions) and fills the depressions, forming numerous individual puddles (filling process). When an individual puddle is fully filled, the ponded water spills to the downstream puddle (s) (spilling process), and a hydrologic connection is established. Two puddles that share a common threshold may merge into a larger higher-level puddle (merging process). A hierarchical drainage system is eventually developed after all puddles at the highest level are fully filled (reaching the maximum depression storage). In contrast, a high-level puddle can be separated into a number of lower-level embedded puddles due to water loss caused by infiltration and/or evaporation during a dry condition (splitting process). This study is aimed at characterizing such

dynamic puddle filling, spilling, merging, and splitting processes, and quantifying the discontinuity, variability, hierarchy, and threshed behavior of overland flow.

Puddles and Puddle Delineation

Puddles and Puddle Types

A puddle, consisting of at least one center and one overflow threshold (Chu et al. 2010, 2013; Chu 2015), is a basic unit that stores ponded water and controls overland flow and distribution of runoff water over a land surface. Multiple centers form a flat (referred to as a "flat puddle" herein) that is able to transfer water, but has a zero storage volume. The threshold of a puddle controls the timing of spilling process, at which depression storage reaches its maximum. A puddle may have multiple thresholds, through which it connects to adjacent puddles. The characteristics of a puddle determine its hydrologic properties (e.g., storage and connectivity), which in turn affect overland flow generation and runoff-infiltration processes. According to the centers (C) and thresholds (T) of puddles and their relationships to others, puddles can be categorized as the following types (Fig. 1) (Chu et al. 2013; Chu 2015):

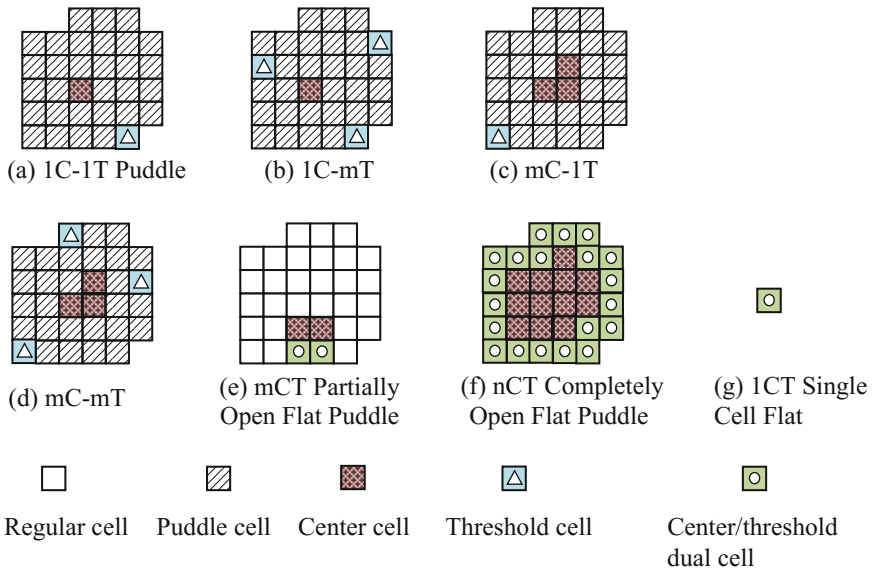

Fig. 1 Puddle definition and types

(1) 1C-1T Puddle (one center and one threshold, Fig. 1a): This is a basic type.
(2) 1C-mT Puddle (one center and multiple thresholds, Fig. 1b): Due to the multiple thresholds, 1C-mT puddles potentially spill water to more adjacent puddles, which improves its connectivity during the dynamic P2P processes.
(3) mC-1T Puddle (multiple centers and one threshold, Fig. 1c): This is a typical flat bottom puddle.
(4) mC-mT Puddle (multiple centers and multiple thresholds, Fig. 1d): This type of puddle has a flat bottom and connects to outside areas through its multiple thresholds.
(5) mCT Partially Open Flat Puddle (multi-center flat, Fig. 1e): Such a flat puddle has multiple centers and some of them also serve as a threshold, through which the puddle spills/transfers runoff water to its downstream area.
(6) nCT Completely Open Flat Puddle (multi-center and multi-threshold flat, Fig. 1f): In this case, the puddle simply becomes a flat surface with a zero storage volume and runoff water flows to the downstream areas through all boundary cells—thresholds.
(7) 1CT Single-Cell Flat Puddle (Fig. 1g): This is a special case—a topographic peak. The only cell serves as both a center and a threshold.

Puddle Levels and Hierarchical Relationships

Puddle levels are determined by a series of merging processes (Chu et al. 2010; Chu et al. 2013; Chu 2015). If two puddles share a common threshold, they potentially merge into a larger, higher-level puddle. Thus, a higher-level puddle may include numerous lower-level embedded puddles. Such hierarchical relationships dictate the P2P filling, spilling, merging, and splitting dynamics. In addition to the embedded relationship, puddles may also have an upstream-downstream relationship, depending on their thresholds and spatial characteristics, which form a cascaded P2P drainage system. Puddle relationships of a real topographic surface can be extremely complicated and vary with the stages of the P2P processes, depending on surface topographic characteristics, soil hydraulic properties, spatiotemporal distribution of rainfall, and other hydrologic conditions.

Algorithm for Automated Puddle Delineation

A new algorithm has been developed for DEM-based puddle delineation (PD) (Chu et al. 2010; Chu et al. 2013). The PD algorithm precisely characterizes surface topography by identifying the center(s) and threshold(s) of each puddle, searching for all contributing cells included in each puddle, checking the threshold-controlled

flow criteria for spilling and merging processes, determining the levels of all puddles and their hierarchical relationships, and computing their maximum depression storage (MDS), maximum ponding area (MPA), and other topographic parameters for each individual puddle and the entire surface.

Identification of centers and flats: Based on the DEM data, centers and flats are identified by comparing the elevations of an individual cell and its eight surrounding cells. The center of a puddle is determined if all of its eight neighboring cells have higher elevations. A flat is identified if two or more adjacent cells have the same elevation. Such cells are identified as centers, from which a searching process initiates and continues until at least one cell has a different elevation (either higher or lower). If all neighboring cells have higher elevations than the flat (centers) of the puddle, this flat puddle is categorized as a flat bottom puddle. If all neighboring cells have lower elevations than the flat, it becomes a completely open flat puddle (Fig. 1f). Otherwise, it is a partially open flat puddle (Fig. 1e). As a special case, 1CT single-cell flat puddle (Fig. 1g) consists of only one cell, which has an elevation higher than all surrounding cells.

Identification of thresholds and the first-level puddles: Following a set of criteria, a searching process is performed to identify all cells included in each puddle (Chu et al. 2010). The process continues until a threshold is found for the puddle. A first-level puddle is then determined. Specifically, the searching process for each puddle starts from the center of the puddle and its eight neighboring cells are added to a searching list. Then, the cell(s) with the lowest elevation in this searching list is identified, removed from the searching list, and added to the puddle. The neighboring cells of this new puddle cell are added to the searching list. By selecting the lowest cell(s) from the new searching list, expansion continues and more cells are added to the puddle. Such a searching-expanding process is repeated until a threshold cell is identified, and a first-level puddle is finalized. Note that multiple thresholds may exist for a puddle. A similar procedure is implemented for a flat puddle (multiple centers). In this case, all surrounding cells of the flat (more than eight cells) are added to the initial searching list. The searching process is then implemented by continuously adding the cell(s) that has the lowest elevation in the searching list to the puddle until a threshold cell is found and the flat puddle is determined.

Identification of higher-level puddles: As aforementioned, two or more puddles that share a common threshold can merge during the P2P processes. In this case, a new searching process for a second-level puddle initiates from the shared threshold. Note that this merged second-level puddle has a flat bottom of an elevation equal to that of the threshold of the lower-level embedded puddles. All cells that belong to this second-level puddle are then identified. The same procedure is performed until all higher-level puddles are delineated. The hierarchical relationships of puddles at different levels also are determined.

Modeling of the P2P Filling-Spilling-Merging-Splitting Dynamics

A new modeling framework has been developed to simulate the dynamic P2P filling-spilling-merging-splitting overland flow processes (Chu et al. 2013; Yang and Chu 2015). The incorporated PD algorithm provides essential puddle delineation details. The cascaded structure of the P2P model facilitates a series of simulations for basins, puddle-based units (PBUs) within each basin, and puddle-to-puddle and cell-to-cell (C2C) within each PBU. The full version of the P2P model is essentially a quasi-3D model to simulate the threshold-driven, discontinuous P2P overland flow dynamics for infiltrating surfaces with various microtopographic characteristics (Yang and Chu 2015). The P2P model provides modeling details on the dynamic C2C and P2P processes, puddle filling status, spatiotemporal ponded water distributions, infiltration and subsurface flow, discharges at basin outlets, and mass balance for all time steps.

Puddle-Based Units (PBUs)

PBU, a relatively independent unit associated with a highest-level puddle and its contributing area, has unique hydrologic characteristics (Chu et al. 2013; Yang and Chu 2015). Based on the information from the PD program (e.g., delineated puddles and flow directions), the P2P model tracks the PBUs for each basin and detects the upstream-downstream contribution relationships of the PBUs to generate a cascaded flow drainage system for the basin. The connectivity of each PBU to its downstream PBU is controlled by the threshold (unique threshold behavior). In the modeling, overland flow is routed for all PBUs by following their cascaded patterns in the hierarchical drainage system. To facilitate water routing within a PBU, two procedures (C2C and P2P routing) are implemented. The former (i.e., C2C) transfers water from upstream to downstream contributing cells, while the latter (i.e., P2P) simulates the dynamic behaviors of puddles and their interactions.

Cell-to-Cell (C2C) Water Routing Procedure

The C2C drainage network of a PBU is determined by the PD algorithm, which links all contributing cells to the centers of the highest-level puddle and its embedded puddles in the PBU. In the C2C modeling, runoff water is transferred from upstream to downstream cells until reaching a water-ponded cell, which leads to an increase in ponded water level and an expansion of the water-covered area of the PBU (Chu et al. 2013). The filling volume (FV) of water in the puddle is then computed. Depending on the quantity, the FV is used to determine the puddle status

(i.e., filling, spilling, merging, or splitting) in the following P2P water routing. In the full version of the P2P model, a 1D diffusion wave model is used to account for the C2C overland flow in each PBU (Yang and Chu 2015).

Puddle-to-Puddle (P2P) Water Routing Procedure

A PBU may include many embedded puddles at different levels. The P2P routing involves modeling of their filling, spilling, merging, and splitting dynamics (Chu et al. 2013; Yang and Chu 2015). To do so, a puddle routing (PR) list, including a group of "active" puddles to be routed, is created and continuously updated over time during the P2P routing until all puddles on the list are routed. Following the hierarchical relationships of puddles, the P2P routing is performed from one PBU to another downstream PBU in a basin and from one basin to another basin until the routing is completed for all basins of the entire area.

Modeling of Infiltration and Unsaturated Flow

In the full version of the P2P modeling system, a modified Green-Ampt (GA) model (Chu and Marino 2005) is coupled with the aforementioned P2P overland flow model. The GA model simulates infiltration and vertical unsaturated flow along a layered soil profile for each individual DEM cell under any complex rainfall patterns, as well as soil water drainage and redistribution during dry time periods. The GA model provides infiltration, surface ponding, rainfall excess, spatiotemporal distributions of soil moisture, soil water flow velocities, and deep subsurface drainage over the entire simulation domain.

A Case Study

A case study was conducted for a site in the Prairie Pothole Region (PPR) located in Stutsman County, North Dakota (Fig. 2) for testing the coupled PD and P2P modeling system, and demonstrating the microtopography-dominated threshold behavior and the critical role of real threshold-driven P2P dynamics in overland flow generation and hydrologic modeling. This PPR site has been used by the U.S. Geological Survey for long-term hydrologic and ecological monitoring studies (Winter and Carr 1980; Mushet et al. 2015). Chu (2015) delineated prairie potholes and the wetlands for this PPR site. The site has an area of 2.5515 km^2 (1,350 m 1,890 m). The surface topography of the study area, represented by a 10-m DEM obtained from the USGS (Fig. 2), is featured with numerous prairie potholes and the associated wetlands across varying scales.

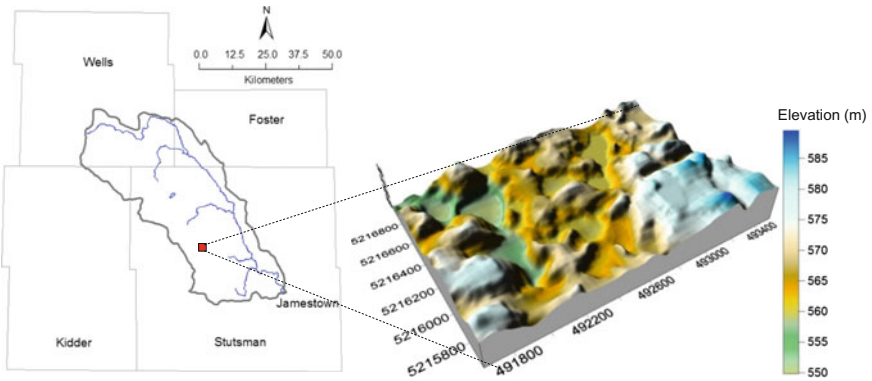

Fig. 2 Selected PPR site in Stutsman County, North Dakota

Importantly, two different surface delineation methods and two distinct overland flow modeling approaches were applied to the selected site and the results were compared to highlight the importance of quantifying the P2P overland flow dynamics and the resulting threshold behavior. The widely used TOPAZ in the Watershed Modeling System (WMS 2015) was used for traditional "depression-less" surface delineation, while the PD program was utilized for new depression-oriented, PBU-based surface delineation. Based on the delineation results from the two methods, HEC-HMS (USACE 2015) was used for traditional hydrologic modeling, and the P2P modeling was performed to simulate the P2P filling-spilling-merging-splitting overland flow dynamics. To be comparable, the initial and constant loss method was selected in the HEC-HMS modeling. The lumped depression storage (ratio of maximum depression storage to the basin area) was estimated for each basin using the exact depression storage delineated by the PD program. A 100-year, 24-h storm for Stutsman County, North Dakota from the USDA Natural Resources Conservation Service (126.24 mm/24 h) was selected for the HEC-HMS and P2P modeling. The total simulation time period was 36 h, which was further divided into 144 time steps (i.e., time interval was 15 min). Selection of this heavy storm and its duration for the modeling allows one to closely examine different phases of the P2P dynamics, the spatial and temporal variability in hydrologic connectivity, and the significant differences in simulation results from different modeling methodologies.

Surface Delineation for the PPR Site

The delineation results from the PD program are shown in Fig. 3 and Table 1. The surface with a maximum depression storage of 1,145,571 m^3consists of 17 basins (B1–B17) (Fig. 3a) and 126 puddles across 17 different puddle levels. The major

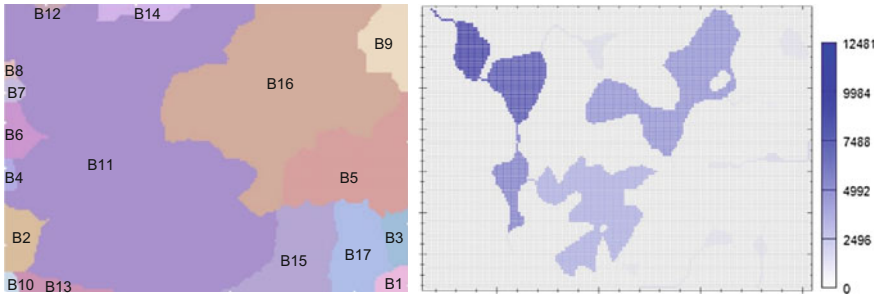

(a) Basins delineated byPD (b) Flow accumulations delineated by PD

Fig. 3 Delineation results from the PD program: **a** basins and **b** flow accumulations (the legend shows the accumulation numbers)

depressions with high flow accumulation numbers are clearly shown in Fig. 3b. Among the 17 basins, 11 "basins" are actually small drainage areas adjacent to the boundaries, which do not include any depressions or depressional areas (Table 1). The remaining 6 basins consist of both depressional and non-depressional areas. Particularly, the two largest basins (B11 and B16) include numerous puddles at different levels. B11 and B16 account for 48.92 and 23.43% of the surface area and 54.29 and 44.79% of the surface depression storage, respectively, (Table 1).

Figure 4 shows the delineation results from WMS. The six major sub-basins (B11, B16, B5, B15, B17, and B9) delineated by WMS (Fig. 4a) are similar to those from the PD program (Fig. 3a) although there are some minor differences. However, the real fundamental difference is the delineated drainage systems. The PD program identified all depressions/puddles, their levels, and their hierarchical drainage relationships. In WMS, however, all depressions were filled, forming a uniform channelized drainage network (Fig. 4b). The former (i.e., PD) implemented depression-oriented delineation for characterizing P2P dynamics, variable connectivity, and threshold behavior, while the latter (i.e., WMS) created a depressionless surface with complete connectivity.

Overland Flow Modeling for the PPR Site

Figure 5 shows the comparison of the hydrographs simulated by the P2P model and HEC-HMS. The discharges simulated by the P2P for the two largest basins (B11 and B16) under the 100-year 24-h storm are shown in Fig. 5a, b. Their peak flows are 1.071 and 0.0038 m^3/s, respectively, (Fig. 5a, b). For the HEC-HMS modeling, however, the simulated discharges from these two largest basins are zero for all time steps, which can be attributed to using the mean basin depression storage (49.83 and 85.85 cm, respectively, Table 1). Note that the rainfall excess never exceeded such large lumped values of surface depression storage for these two

Table 1 Surface topographic parameters for the 17 basins

Basin No.	Maximum depression storage (MDS) (m^3)	Depressional area (A_d) (m^2)	Non-depressional area (A_{nd}) (m^2)	Total basin area (A) (m^2)	Depression storage (MDS/A_d) (cm)	Mean basin depression storage (MDS/A) (cm)
11	621,946	1,248,100	100	1,248,200	49.83	49.83
16	513,124	597,600	100	597,700	85.86	85.85
5	3,808	132,200	70,800	203,000	2.88	1.88
15	1,119	70,600	60,200	130,800	1.59	0.86
17	1,375	70,000	26,000	96,000	1.97	1.43
9	4,199	69,600	100	69,700	6.03	6.02
2	0	0	44,400	44,400	0	0
6	0	0	31,800	31,800	0	0
3	0	0	28,900	28,900	0	0
14	0	0	27,700	27,700	0	0
13	0	0	24,000	24,000	0	0
1	0	0	17,000	17,000	0	0
7	0	0	9,900	9,900	0	0
4	0	0	7,800	7,800	0	0
10	0	0	6,100	6,100	0	0
12	0	0	4,300	4,300	0	0
8	0	0	4,200	4,200	0	0
Sum	1,145,571	2,188,100	363,400	2,551,500	52.36	44.90

Note The outlet cell is included in the non-depressional area

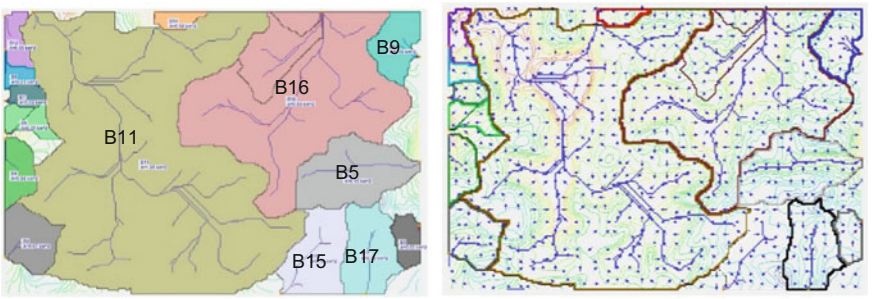

(a) Subbasins delineated by WMS (b) Drainage networks delineated by WMS

Fig. 4 Subbasins and drainage networks delineated by WMS

basins. Comparison of the total discharges from the six major basins (B5, B9, B11, B15, B16, and B17) simulated by the P2P and HEC-HMS also indicates that HEC-HMS tends to underestimate surface runoff for depression-dominated basins. The total peak flow from HEC-HMS is only 63.4% of the one simulated by the P2P model (Fig. 5c, d).

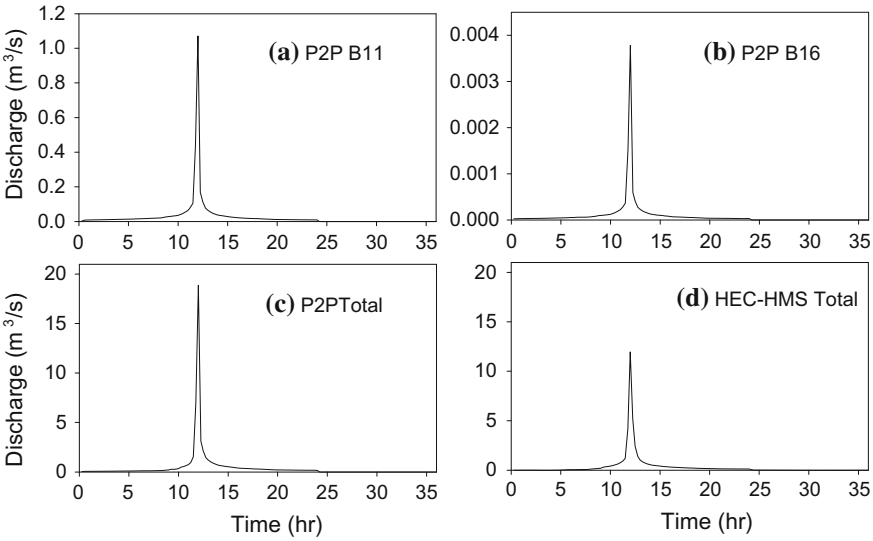

Fig. 5 Hydrographs simulated by the P2P model and HEC-HMS for the 100-year 24-h storm: **a** discharge simulated by P2P for B11; **b** discharge simulated by P2P for B16; **c** total discharge simulated by P2P for six major basins (B5, B9, B11, B15, B16, and B17); and **d** total discharge simulated by HEC-HMS for six major basins

Figure 6 shows the temporal variations of connected areas simulated by the P2P model for the 100-year 24 h storm (a) for the entire surface, (b) for four small basins (B5, B9, B15, and B17), (c) for the largest basin B11, and (d) for the second largest basin B16. Before t = 9 h, only 15.55% of the total area contributed surface runoff to the outlets (Fig. 6a). The connected area then exhibited stepwise increases and reached the highest (28.77%) at t = 12 h when the rainfall intensity reached the peak value. After the 24-h storm, the connected area decreased to 14.27% (Fig. 6a). The connected areas of four small basins (B5, B9, B15, and B17) reached 100% from t = 9 h for B15 to t = 12 h for B9 (Fig. 6b). Interestingly, due to the large numbers of depressions and significantly higher depression storages, very small portions of the two largest basins (B11 and B16) made runoff contributions to their outlets (Fig. 6c, d). The highest connected area percentage for B11 was 2.267% (Fig. 6c), while only 0.017% of the B16 area generated surface runoff for the outlet (Fig. 6d). Thus, surface runoff contributing areas vary spatially and temporally, depending upon the actually topographic characteristics, rainfall features, land covers, soil properties, and other factors. It is of practical importance to map the dynamic changes in contributing areas. In contrast, it is often assumed in traditional watershed hydrologic modeling (e.g., HEC-HMS) that 100% of the surface area contributes runoff through a well-connected drainage system over the entire simulation period, which accounts for static, complete connectivity.

Figure 7 shows the dynamic changes in normalized discharge (ratio of discharge to rainfall), normalized contributing area (ratio of connected area to the total area),

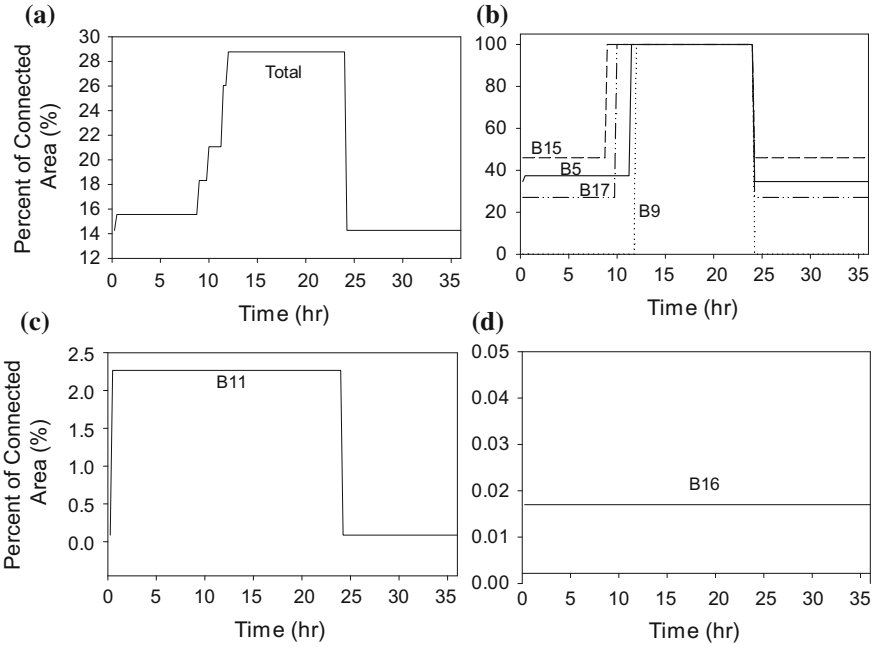

Fig. 6 Temporal variations of connected areas (the area contributing surface runoff to outlet) simulated by the P2P model for 100-year 24-h storm for **a** entire surface; **b** four small basins (B5, B9, B15, and B17); **c** largest basin B11; and **d** second largest basin B16

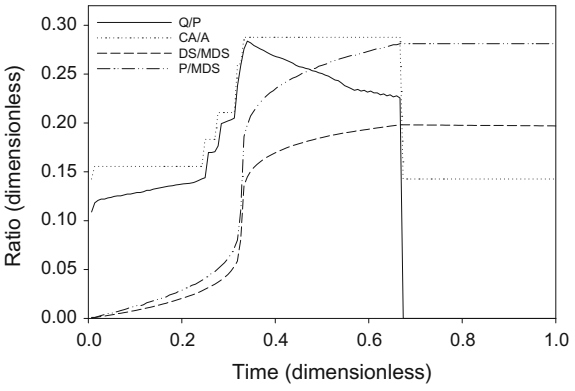

Fig. 7 Dynamic changes in normalized runoff discharge, contributing area, surface depression storage, and rainfall for the 100-year 24-h storm

normalized depression storage (ratio of depression storage to maximum depression storage), and normalized rainfall (ratio of rainfall to maximum depression storage) simulated by the P2P model for the 100-year 24-h storm. Both the normalized contributing area and outlet discharge curves display stepwise increases before the dimensionless time of 0.33 (i.e., t = 12 h) due to the P2P dynamics and threshold

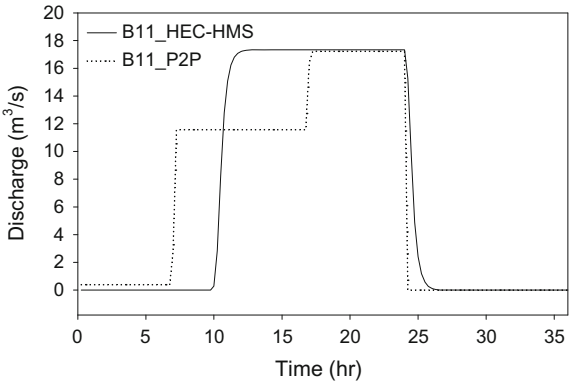

Fig. 8 Comparison of hydrographs simulated by the P2P model (with dynamic P2P threshold control) and HEC-HMS (with lumped depression storage control) for the largest basin B11 under a uniform steady 24-h storm with an intensity of 50.0 mm/h

behavior of the system (Fig. 7). From the time of 0.33–0.67 (i.e., t = 24 h), the normalized contributing area maintains the maximum value of 0.29 and the ratio of discharge to rainfall decreases from 0.28 to 0.23 (Fig. 7). A significant increase in depression storage can be observed within the time period from t = 12 h (or 0.33) to t = 24 h (or 0.67). After the normalized depression storage reaches the maximum value (0.20) at t = 24 h, it slowly decreases until the end of the modeling due to the losses in the dry time period from 0.67 to 1.0. The modeling results indicate that depressions were not fully filled and only 19.8% of the maximum depression storage was filled. Similar changes can be observed for the ratio of rainfall to maximum depression storage. The maximum percent of rainwater used to fill surface depressions is 28.1% (Fig. 7).

To further examine the threshold behavior of overland flow generation, a uniform steady 24-h rainfall with an intensity of 50.0 mm/h was applied in both P2P and HEC-HMS modeling. The former (i.e., P2P) accounted for the dynamic P2P threshold control while the latter (i.e., HEC-HMS) simulated the depression storage as a lumped depth of water for each basin (e.g., 49.83 cm for B11, Table 1). Comparison of the hydrographs simulated by the P2P and HEC-HMS for the largest basin B11 is shown in Fig. 8. Two major stepwise increases can be clearly observed for the hydrograph from the P2P model. HEC-HMS, however, tends to delay the initiation of surface runoff. The P2P modeling results demonstrate that surface runoff commences before all depressions are fully filled, which has been verified by many experimental studies (e.g., Chu 2011).

Summary and Conclusions

The theory of threshold hydrology was outlined in this study. Specifically, new methods were described for characterizing surface topography, delineating land surfaces, and simulating the dynamic puddle-to-puddle filling, spilling, merging, and splitting processes. The new PBU delineation algorithm took full consideration

of the hydrotopographic properties of puddles, their hierarchical relationships, and different filling conditions, and eliminated the artificial "fill sinks" preprocessing required for most existing "static" delineation methods. The new modeling approach facilitated simulation of the P2P dynamics through C2C and P2P routing across all PBUs in the cascaded drainage system.

The application of the new delineation and modeling methods to the PPR site and the comparison with traditional delineation and watershed modeling approaches demonstrated the existence of threshold behavior in overland flow generation, nonuniformity in evolution of hydrologic connectivity, variability in spatiotemporal distributions of surface runoff, and hierarchy in drainage patterns. This study emphasized the dominance of surface topography on surface and subsurface hydrologic processes and highlighted the potential issues associated with the traditional depressionless delineation methods. Traditional watershed hydrologic modeling based on depressionless surface topography, complete hydrologic connectivity, and uniform drainage networks may misrepresent the actual hydrologic system and provide inaccurate, even incorrect, simulation of hydrologic processes in both space and time. Using a lumped depression storage (depth of water) in traditional hydrologic modeling tends to delay initiation of surface runoff and underestimate surface runoff, especially for depression-dominated basins.

Importantly, not the entire watershed is "active" making runoff contribution to the outlet. Also, the "inactive" areas (in terms of runoff contribution) are not always inactive. Depending on the stages of the dynamic puddle filling, spilling, merging, and splitting processes, such non-contributing areas may become active and contribute surface runoff. In addition, overland flow may exhibit stepwise changes (either increase in a wet period or decrease in a dry period) due to the depression-driven threshold control.

Acknowledgements This material is based upon work supported by the National Science Foundation under Grant No. EPSCoR Award IIA-1355466 and EAR-0907588. The author would like to thank Jianli Zhang and Jun Yang for their various contributions to the related research.

References

Abedini MJ, Dickinson WT, Rudra RP (2006) On depressional storages: the effect of DEM spatial resolution. J Hydrol 318(1–4):138–150

Antoine M, Javaux M, Bielders C (2009) What indicators can capture runoff-relevant connectivity properties of the micro-topography at the plot scale? Adv Water Resour 32(8):1297–1310

Antoine M, Javaux M, Bielders C (2011) Integrating subgrid connectivity properties of the micro-topography in distributed runoff models, at the interrill scale. J Hydrol 403:213–223

Appels WM, Bogaart PW, van der Zee SEATM (2011) Influence of spatial variations of microtopography and infiltration on surface runoff and field scale hydrological connectivity. Adv Water Resour 34(2):303–313

Chi Y, Yang J, Bogart D, Chu X (2012) Fractal analysis of surface microtopography and its application in understanding hydrologic processes. Trans ASABE 55(5):1781–1792

Chu X (2011) Characterization of microtopography and its hydrologic significance. In: Wang X (ed) Modeling hydrologic effects of microtopographic features. Nova Science Publishers Inc., pp 1–14

Chu X (2015) Delineation of pothole-dominated wetlands and modeling of their threshold behaviors. J Hydrol Eng D5015003

Chu X, Marino MA (2005) Determination of ponding condition and infiltration into layered soils under unsteady conditions. J Hydrol 313:195–207

Chu X, Zhang J, Chi Y, Yang J (2010) An improved method for watershed delineation and computation of surface depression storage. In: Potter KW, Frevert DK (eds) Watershed management 2010: innovations in watershed management under land use and climate change, Proceedings of the 2010 watershed management conference. American Society of Civil Engineers, pp 1113–1122

Chu X, Yang J, Chi Y, Zhang J (2013) Dynamic puddle delineation and modeling of puddle-to-puddle filling-spilling-merging-splitting overland flow processes. Water Resour Res 49(6):3825–3829

Chu X, Padmanabhan G, Bogart D (2015) Microtopography-controlled overland flow generation: laboratory and field experiments. Appl Environ Soil Sci 2015:11 (Article ID 642952)

Darboux F, Huang C (2005) Does soil roughness increase or decrease water and particle transfer? Soil Sci Soc Am J 69(3):748–756

Darboux F, Davy P, Gascuel-Odoux C, Huang C (2001) Evolution of soil surface roughness and flowpath connectivity in overland flow experiments. Catena 46(2–3):125–139

Garbrecht J, Martz LW (2000) TOPAZ: an automated digital landscape analysis tool for topographic evaluation, drainage identification, watershed segmentation and subcatchment parameterization: TOPAZ User Manual. Grazinglands Research Laboratory, USDA Agricultural Research Services, El Reno, OK

Govers G, Takken I, Helming K (2000) Soil roughness and overland flow. Agronomie 20(2): 131–146

Hansen B, Schjonning P, Sibbesen E (1999) Roughness indices for estimation of depression storage capacity of tilled soil surfaces. Soil Tillage Res 52(1–2):103–111

Jenson SK, Domingue JO (1988) Extracting topographic structure from digital elevation data for geographic information system analysis. Photogramm Eng Remote Sens 54(11):1593–1600

Johnson CB, Mannering JV, Moldenhauer WC (1979) Influence of surface roughness and clod size and stability on soil and water losses. Soil Sci Soc Am J 43:772–777

Kamphorst EC, Jetten V, Guerif J, Pitkanen J, Iversen BV, Douglas JT, Paz A (2000) Predicting depression storage from soil surface roughness. Soil Sci Soc Am J 64(5):1749–1758

Lehmann P, Hinz C, McGrath G, Tromp-van Meerveld HJ, McDonnell JJ (2007) Rainfall threshold for hillslope outflow: an emergent property of flow pathway connectivity. Hydrol Earth Syst Sci 11:1047–1063

Leibowitz SG, Vining KC (2003) Temporal connectivity in a prairie pothole complex. Wetlands 23(1):13–25

Maidment DR (2002) Arc hydro GIS for water resources. ESRI Press, Calif

Martin Y, Valeo C, Tait M (2008) Centimetre-scale digital representations of terrain and impacts on depression storage and runoff. Catena 75(2):223–233

Martz LW, Garbrecht J (1993) Automated extraction of drainage network and watershed data from digital elevation models. Water Resour Bull 29(6):901–908

McDonnell JJ (2003) Where does water go when it rains? Moving beyond the variable source area concept of rainfall-runoff response. Hydrol Process 17:1869–1875

Mushet DM, Goldhaber MB, Mills CT, McLean KI, Aparicio VM, McCleskey RB, Holloway JM, Stockwell CA (2015) Chemical and biotic characteristics of Prairie Lakes and Large Wetlands in South-Central North Dakota—effects of a changing climate, Scientific Investigations Report 2015-5126, U.S. Geological Survey, Reston, VA

O'Callaghan JF, Mark DM (1984) The extraction of drainage networks from digital elevation data. Comput Vis Graph Image Process 28:323–344

Spence C (2007) On the relation between dynamic storage and runoff: a discussion on thresholds, efficiency, and function. Water Resour Res 43:W12416
Tarboton DG (1997) A new method for the determination of flow directions and contributing areas in grid digital elevation models. Water Resour Res 33(2):309–319
Tarboton DG, Sazib N, Dash P (2015) TauDEM 5.3 quick start guide to using the TauDEM, ArcGIS, Toolbox. Available at http://hydrology.usu.edu/taudem/taudem5/documentation.html
USACE (2013) HEC-GeoHMS geospatial hydrologic modeling extension, User's Manual, Version 10.1, CPD-77. U.S. Army Corps of Engineers, Hydrologic Engineering Center, Davis, CA
USACE (2015) Hydrologic modeling system HEC-HMS, User's Manual, Version 4.1, CPD-74A. U.S. Army Corps of Engineers, Hydrologic Engineering Center, Davis, CA
Van der Kamp G, Hayashi M (2009) Groundwater-wetland ecosystem interaction in the semiarid glaciated plains of North American. J Hydrogeol 17(1):203–214
Winter TC, Carr MR (1980) Hydrologic setting of wetlands in the Cottonwood Lake Area, Stutsman County, North Dakota. Water-Resources Investigations, U.S. Geological Survey, Denver, CO, pp 80–99
Winter TC, LaBaugh JW (2003) Hydrologic considerations in defining isolated wetlands. Wetlands 23(3):532–540
WMS (2015) Watershed modeling system, User Manual, v10.0. Aquaveo, LLC, Provo, Utah
Yang J, Chu X (2013) Quantification of the spatio-temporal variations in hydrologic connectivity of small-scale topographic surfaces under various rainfall conditions. J Hydrol 505:65–77
Yang J, Chu X (2015) A new modeling approach for simulating microtopography-dominated, discontinuous overland flow on infiltrating surfaces. Adv Water Resour 78:80–93
Zehe E, Sivapalan M (2009) Threshold behaviour in hydrological systems as (human) geo-ecosystems: manifestations, controls, implications. Hydrol Earth Syst Sci 13:1273–1297
Zhang J, Chu X (2015) Impact of DEM resolution on puddle characterization: comparison of different surfaces and methods. Water 7:2293–2313

Nondimensional UH-Based Smoothing of *S*-Curve-Derived UH Oscillations

P. R. Patil, S. K. Mishra, Nayan Sharma and Vijay P. Singh

Abstract This paper proposes nondimensional unit hydrograph (UH)-based procedure for eliminating the oscillations frequently observed in the recession part of altered duration UHs derived from conventional *S*-curve approach. Such occurrence of oscillations and/or even negative ordinates cannot be ignored or left unadjusted, and therefore, their elimination by often suggested manual/visual adjustments is attempted, which is quite cumbersome and time-consuming. Proposed procedure employs the peak (Q_p) and time to peak (t_p) of altered duration (τ-h) UH for its derivation, which is derived by using analytical *S*-shaped model-efficient enough to exactly reproduce the oscillation-free *S*-curve. The suggested approach is found to be superior to the conventional *S*-curve approach. On the whole, the complexity associated with the lagging of *S*-curve, interpolation—if altered UH duration is not a multiple of parent UH duration (*D*-h), manual/visual adjustments to eliminate oscillations in derived *S*-curve or altered duration UHs and also for reasons of maintaining unit volume of UH has been fully resolved.

P. R. Patil (✉) · S. K. Mishra · N. Sharma
Department of Water Resources Development & Management, Indian Institute of Technology Roorkee, Roorkee 247667, Uttarakhand, India
e-mail: prpatil25@gmail.com

S. K. Mishra
e-mail: skm61fwt01@gmail.com

N. Sharma
e-mail: nayanfwt@gmail.com

V. P. Singh
Department of Biological and Agricultural Engineering and Zachry Department of Civil Engineering, Texas A&M University, College Station, TX 77843-2117, USA
e-mail: vsingh@tamu.edu

V. P. Singh et al. (eds.), *Hydrologic Modeling*, Water Science and Technology Library 81, https://doi.org/10.1007/978-981-10-5801-1_42

Introduction

In surface water modeling/simulation, if a UH is developed for a specific duration of effective rainfall while dealing with a longer or shorter duration, a new UH must be derived for that specific duration. The linearity property implicit in the UH theory can be used to serve the purpose, and this procedure is sometimes referred to as the *S*-curve method. The *S*-hydrograph invented in classical UH theory is an elegant technique that could be used as an intermediate hydrograph to alter a UH from one unit duration to any other desired unit duration (Dooge 1973). Forward-backward *S*-curve method (Tauxe 1978) or *S*-curve method (Chow et al. 1988; Singh 1992) is frequently used for extending the duration of a UH. Shortening the duration of a UH, however, can lead to troubles. The *S*-hydrograph or *S*-curve or summation curve is the hydrograph corresponding to continuous rainfall excess at a uniform rate for an infinite period.

The derivation of a finite-period UHs from an *S*-hydrograph is more complicated than it appears at first glance as each computation depends on all preceding computations and the *S*-curve may not be known continuously, but only at certain intervals of time. For example, if we initiate with a parent UH defined only for a particular time interval, the derived *S*-curve will be defined for the same time interval. If altered UH duration is not a multiple of parent UH duration, interpolation of parent UH is must and then only parent *S*-curve can be derived. Though the available interpolation schemes are expedient, they lack theoretical as well as physical basis, which can lead to undesirable results which are difficult to justify from a physical standard (Boufadel 1998). Once the *S*-curve has been obtained from its parent UH, a new UH of the desired duration can be derived from it by displacing the *S*-curve by the same time step (may be an integer multiple or fraction), taking the difference of the two *S*-curves, and then normalizing the volume. If the derived hydrograph is normalized to unit volume, the resulting *t*-h UH corresponds to rain falling at a rate of l/*t* depth units per h for *t*-h.

Theoretically, the *S*-hydrograph is a smooth curve because the input rainfall excess is assumed to be a continuous and of uniform rate. However, the numerical processes of the procedures may result in an oscillatory form that may require smoothing or adjustment. If there are inaccuracies in the parent UH, there will probably be oscillations in what would be a smooth *S*-curve. Its ordinates sometimes tend to fluctuate on both the rising and equilibrium stages, frequently termed as hunting of *S*-curve. There is no guarantee that the *S*-curve derived from a smooth finite-period UH will itself be smooth. The correctness of the parent UH can be further improved if a smooth *S*-curve is drawn manually in such a manner that it reaches the equilibrium value at the end of base width of parent UH. Using this *S*-curve, UH is derived back. Finally, a check is required to be made for the area under the modified UH to be unity. It is possible that the *S*-curve oscillations may also lead to grossly erroneous ordinates of the derived altered duration UH showing an abnormal sequence of discharges (sometimes even negative values) at the tail end

(Subramanya 2013). Therefore, in practice, the *S*-curve obtained by summation is smoothed out graphically before taking the *S*-curve differences. In addition to this, the resulting altered duration UH is also adjusted manually, which is quite complicated, cumbersome, and time-consuming for maintaining unit volume.

Numerous hydrologists have noticed that the derived UH ordinates are distorted by high-frequency oscillations during the solution of various inverse problems associated with UH applications. Blank et al. (1971) described and discussed these oscillations in finite-period UH. In addition to this, they suggested an application low-pass digital data filter and moving average procedure as a mean to avoid oscillations. Hall (1977) suggested a simple extension of the basic harmonic method algorithm as a mean of smoothing oscillations in UHs derived from complex storms. The occurrence of such oscillations has also been attributed to the derivation of a shorter duration UH from a longer duration parent UH (Sangal 1986). According to Linsley et al. (1975), oscillations can be expected to occur in a derived *S*-curve whenever the parent UH time step is less than the effective rainfall pulse duration. Hunt (1985) used Duhamel's superposition integral-based UH solutions and numerical examples to explain the Linsley et al. phenomena, if the hydrograph is not the exact solution of a linear differential equation with time independent coefficients. If the actual effective duration of runoff is not same as of UH duration, using a shorter or longer duration causes the summation process to result in a runoff diagram with either periodic gaps or periodic increases to a doubled runoff magnitude in the same duration. Alternatively, *S*-curve serves as an approximate check on the assumed duration of the effective rainfall for the original UH. A duration which causes minimum oscillations in the *S*-curve can be found by trial and is quite lengthy. These fluctuations can also result from nonuniform runoff generation, unusual areal distribution of rain, or errors in the basic data.

The oscillation-free shape of parent *S*-curve to its lagged versions can be well represented mathematically by mean value function of the inflection *S*-shaped (IS) software reliability growth model (Ohba 1984) developed to analyze the software failure detection process, by modifying popularly used logistic population growth model (Verhulst 1838, 1845, 1847). Its underlying concept is that the observed software reliability growth becomes *S*-shaped if faults in a program are mutually dependent, i.e., some faults are not detectable before some others are removed. The law of growth assumes that systems grow exponentially until an upper limit or maximum capacity inherent in the system is approached, at which point the growth rate slows and eventually saturates or levels off, producing the characteristic *S*-shape curve (Stone 1980). Here, IS model is employed to estimate Q_p and t_p of τ-h UH analytically.

Nondimensional/dimensionless/index UH developed by Mockus (1957) to represent several UHs is plotted using the ratio of the basic units time to peak and peak rate. It has its ordinate values expressed in a dimensionless ratio Q/Q_p and its abscissa values as t/t_p. Gamma distribution has a long past in the hydrologic engineering applications and is thoroughly considered for fitting the hydrographs by Edson (1951), Nash (1957), (1958), (1960), Aron and White (1982), Singh (2004),

(2005), (2006), (2007), Nadarajah (2007), Rai et al. (2009). Bhunya et al. (2003) developed nondimensional form of UH based on the simplified two-parameter gamma distribution (2-PGD) employing two parameters, i.e., λ (which is dependent on the nondimensional shape factor β) and scale parameter t_p. These forms of UH relationships are similar to those presented by Singh (1988), (2000), but exhibit greater reliability. It is prerequisite for altered UH derivations that Q_p and t_p are to be known. Following such approaches, a procedure is suggested to eliminate the oscillating part of UH derived from *S*-curve maintaining the UH area as unity, which is the primary objective of this paper. An alternate procedure suggested by Patil et al. (2016) employing the relationships dependent only on β and t_p is also of comparable accuracy.

Inflection *S*-Shaped (IS) Model

The mean value function of this model is defined as (Ohba 1984):

$$f(t) = \frac{a}{1 + ce^{-bt}}\left(1 - e^{-bt}\right) \quad \text{for } t \geq 0; \quad a, b, c > 0, \tag{1}$$

$$\text{when } t = 0,\ f(t) = 0; \quad \text{and if } t = \infty, f(t) = a,$$

where the parameter a represents the asymptotic limit that bounds the function past which the output cannot grow (NakiCenovic 1988). e = 2.71828, b is a growth rate parameter which specifies 'width' or 'steepness' of *S*-curve, i.e., as b increases, the curve approaches the asymptote $f(t) = a$ more rapidly. The parameter c is the point of inflection, if $c > 0$; a function increases when $b > 0$ and decreases when $b < 0$.

The *S*-curve derives the name from its own shape which comes out like alphabet '*S*' though slightly deformed. Due to the shape similarity, IS model can be utilized for *S*-hydrograph fitting. With suitable change of notations (i.e., $a = Q_{\text{eq}}$), the mean value function of IS model (Eq. 1) can be transformed into hydrologic form as:

$$S_{(t)} = \frac{Q_{\text{eq}}}{1 + ce^{-bt}}\left(1 - e^{-bt}\right) \quad \text{for } t \geq 0; \quad Q_{\text{eq}},\ b,\ c > 0. \tag{2}$$

The curve defined by Eq. (2) is the time-varying *S*-curve due to *D*-h parent UH. It represents one pulse of growth as the *S*-curve proceeds from initial rapid growth to slow growth as the maximum capacity is approached. The maximum or equilibrium discharge (Q_{eq}) of the *S*-curve is defined as (CWC 1984; Subramanya 2013):

$$Q_{\text{eq}} = \frac{Ad}{0.36D} = \frac{2.778Ad}{D}\ \text{m}^3/\text{s}, \tag{3}$$

where A = catchment area (km^2), d = 1 cm depth, and D = unit duration of the parent UH (h). Q_{eq} is also referred as the volume of 1-cm direct runoff depth over

the entire catchment or the volume of direct runoff graph (i.e., UH). Alternatively, this volume can also be derived as the sum of all UH ordinates, i.e., ΣQ_i m^3/s at a time step $\Delta t = D$-h. If $\Delta t \neq D$-h, then the volume can be estimated as $\Sigma Q_i \times (\Delta t/D)$ m^3/s.

Mathematically, *S*-curve (Eq. 2) can be lagged by τ-h as follows:

$$S_{(t-\tau)} = \frac{Q_{\text{eq}}}{1 + ce^{-b(t-\tau)}}\left(1 - e^{-b(t-\tau)}\right) \quad \text{for } t \geq 0; \quad Q_{\text{eq}}, b, c, \tau > 0. \tag{4}$$

Here, location parameter (τ) shifts the function in time without affecting its shape (Meyer 1994).

The difference (z) of the two *S*-curves [$S_{(t)}$ and $S_{(t\,-\,\tau)}$] displaced by τ-h denotes the ordinates of an altered duration (τ-h) UH.

$$z = S_{(t)} - S_{(t-\tau)} = Q_{\text{eq}}\left[\frac{1 - e^{-bt}}{1 + ce^{-bt}} - \frac{1 - e^{-b(t-\tau)}}{1 + ce^{-b(t-\tau)}}\right]. \tag{5}$$

On differentiating Eq. (5) and equating to zero and on further simplifying the resultant, one obtains

$$t = t_p = \frac{\tau}{2} + \frac{1}{b}\log c. \tag{6}$$

Equation (6) gives the value of t in terms of τ, b, and c, which represents the t_p of τ-h UH. Substituting the estimate of t in (Eq. 5) leads to

$$Z_{\max} = Q_{eq}\left(1 + \frac{1}{c}\right)\left[\frac{e^{b\tau/2} - 1}{e^{b\tau/2} + 1}\right], \tag{7}$$

$$Q_p = Z_{\max}/(\tau/D). \tag{8}$$

Equation (7) gives the maximum difference ($z_{\max}$) between the ordinates of *S*-curves displaced by desired τ-h duration for known values of Q_{eq}, b, c, and τ, which can be further used to estimate the Q_p of τ-h UH when divided by the ratio (τ/D) as shown in Eq. (8). The shape of the UH can be further obtained by employing the 2-PGD-based nondimensional relationships, as described below.

Nondimensional UH

For the different ranges of λ, Bhunya et al. (2003) developed 2-PGD-based simplified relations to obtain dimensionless ratio Q/Q_p as:

$$Q/Q_p = \exp\left[\left(0.158/\lambda^2 - 0.169\right)f(t/t_p)\right] \quad \text{for} \quad (\lambda < 0.27), \tag{9a}$$

$$Q/Q_p = \exp\left[\left(21.834\lambda^2 - 23.58\lambda + 6.716\right)f\left(t/t_p\right)\right] \quad \text{for} \quad (\lambda \geq 0.27), \tag{9b}$$

where f is a function of (t/t_p) is given by (Singh 2000)

$$f\left(t/t_p\right) = \left[1 - \left(t/t_p\right) + \ln\left(t/t_p\right)\right]. \tag{10}$$

Bhunya et al. (2003) expressed λ in terms of nondimensional parameter β, which is defined as a product of q_p and t_p.

$$\lambda = \frac{0.636}{1 + 4.13(\beta)^{1.52}} + 0.029 \quad \text{for} \quad \beta \geq 0.54 \ \text{ and } \ \lambda \leq 0.27. \tag{11}$$

Procedure in Steps

Conventional *S*-Curve Approach

1. Derive *S*-curve by adding a series of unit duration parent UHs lagged by unit duration successively. The sum of parent UH ordinates in a series reaches a constant value, i.e., equilibrium discharge (Q_{eq}) at a time equal to the time base of parent UH. Sometimes, *S*-curve may exhibit hunting effect in this region.
2. Estimate the difference between two *S*-curves with their initial points displaced by the duration equal to the desired duration of altered UH.
3. Compute the ordinates of the altered duration UH by dividing the *S*-curves difference by the ratio of 'altered UH duration to parent UH duration' at each time step. The derived UH may also exhibit oscillations in its receding part.

Oscillations in derived *S*-curve and altered duration UHs are the problematic features of the conventional *S*-curve approach which are wiped out using the suggested approach.

Nondimensional UH Approach

For known Q_{eq}, the oscillation-free UH of the desired durations can be derived as follows:

1. Fit the parent duration *S*-curve using Eq. (2) to determine b and c of Eq. (2).
2. For known Q_{eq}, above estimated b and c and desired altered UH duration (τ-h) derive t_p of the altered duration UH using Eq. (6).

3. Derive $z_{\max}$ between the ordinates of *S*-curves displaced by the duration of altered UH using Eq. (7).
4. Derive Q_p of the altered duration UH using Eq. (8). Convert this Q_p (m^3/s) to q_p (h^{-1}).
5. Assume dimensionless ratio t/t_p with equally spaced ordinates.
6. Compute the nondimensional shape parameter β ($=q_p \times t_p$) and determine $f\,(t/t_p)$ and λ from Eqs. (10) and (11), respectively.
7. Derive ordinates of dimensionless ratio Q/Q_p from Eq. (9a) or (9b) considering range of λ with $f\,(t/t_p)$.
8. Plot the nondimensional UH by multiplying the value of Q_p with Q/Q_p and t_p with t/t_p.

Application

Three unit duration UHs of 6, 4, and 4 h given in textbook (Ojha et al. 2008; Subramanya 2013; Raghunath 1995) were used as parent UHs to test the proposed approach. The performance of the proposed and conventional *S*-curve approach is evaluated using Nash–Sutcliffe (1970) efficiency (η_{NS}) criterion expressed mathematically as:

$$\eta_{NS} = \left[1 - \left(\frac{\sum_{i=1}^{p}\left(Q_i - \hat{Q}_i\right)^2}{\sum_{i=1}^{p}\left(Q_i - \bar{Q}_i\right)^2}\right)\right] \times 100. \tag{12}$$

Here, Q_i = observed discharge for *i*th pulse (m^3/s), $\hat{Q}_i$ = computed discharge for *i*th pulse (m^3/s), $\bar{Q}_i$ = overall mean observed discharge (m^3/s), and p = total number of observations. The η_{NS} varies at the scale of 0–100%. The η_{NS} of 100% implies a perfect fit between the observed and computed values. In this study, the parameters b and c have been calibrated using SOLVER routine of EXCEL based on the generalized reduced gradient nonlinear programming algorithm (Lasdon et al. 1978) with the objective function of maximizing η_{NS} to obtain a reliable fit.

Analysis and Discussion of Results

Derivation of 3- and 9-h UHs from 6-h Parent UH (Ojha et al. 2008)

First, the derivation of 3- and 9-h UHs from known 6-h parent UH is described in detail in the following text, and then, the results are presented on similar lines for other parent UHs.

Conventional *S*-curve approach: To alter, 6-h parent UH (Table 1) into 3- and 9-h UHs, its ordinates were lagged continuously at an equal interval of 6 h till 54 h, which is the time base of the parent UH. The 6-h *S*-curve is derived by summing up a series of 6-h parent UHs which is termed as 'parent or conventional *S*-curve' (Table 1 and Fig. 1). As expected, the resultant *S*-curve exhibits hunting effect. Hence, a best-fit curve is plotted through these points manually in order to reach a constant equilibrium value, i.e., Q_{eq} = 16,250 m^3/s at t = 54 h (Table 1; Fig. 1). The 'manually adjusted 6-h *S*-curve' is comparatively smoother than the conventional 6-h *S*-curve, and hence, used in further analysis hereafter. The adjusted 6-h *S*-curve is lagged by 3 and 9 h. The difference between ordinates of adjusted 6-h *S*-curve and its lagged versions at 3 and 9 h yields the ordinates of 3-h UH and 9-h UH when divided by the ratio of τ/D = 3/6 and 9/6, respectively, and termed as altered duration conventional UHs (Table 1; Figs. 2 and 3). The estimated volume [$\Sigma Q_i \times (\Delta t/D)$ = 16,250 m^3/s] is identical for both the altered duration UHs.

Elimination of the hunting effect of *S*-curve through manual adjustments (Fig. 1) does not mean that the issue of oscillation is fully resolved, as the altered duration conventional UHs derived from the manually adjusted *S*-curve still exhibit oscillations (Figs. 2 and 3).

Nondimensional UH approach: For known Q_{eq} = 16,250 m^3/s and optimized b = 0.20 and c = 60.92, the complete shape of 'analytical IS 6-h *S*-curve' has been reproduced using Eq. (2) with Q_{eq} = 16,224 m^3/s achieved at t = 54 h. It closely resembles the manually adjusted conventional 6-h *S*-curve with η_{NS} = 99.99% (Eq. 12) and does not exhibit oscillations as in case of conventional *S*-curve (Fig. 4).

For known Q_{eq}, estimated b and c, and desired τ; the altered duration UHs Q_p and t_p were derived from the equations obtained through the differentiation of IS functions representing displaced *S*-curves. These have been used for conversion of UH to the desired duration using the proposed approach as follows.

The given 6-h parent UH is converted to 3- and 9-h UHs, respectively, to exemplify the utility of the proposed nondimensional UH approach in eliminating oscillations. For 3-h UH derivation (i.e., τ = 3 h), the z_{max} (=2402 m^3/s) is derived using Eq. (7) for known Q_{eq} = 16,250 m^3/s, b = 0.20, and c = 60.92. Q_P (=4803 m^3/s) estimated using Eq. (8) for τ/D = 3/6 and is further converted to q_p (=0.049 h^{-1}), for β-estimation. This conversion needs a catchment area (A = 35,097 km^2) to be known, and if it is not available, it can be derived from Eq. (3) for Q_{eq} and D as mentioned above. From Eq. (6), t_p is estimated as 22.55 h. β ($=q_p t_p$) is estimated as 1.11. Function f (t/t_p) is estimated using Eq. (10) for the assumed dimensionless ratio t/t_p. Since $\beta \geq 0.54$, λ is derived as 0.14 from Eq. (11). Thus, with known λ and f (t/t_p), ordinates of dimensionless ratio Q/Q_p were estimated from Eq. (9a) or (9b). Finally, nondimensional 3-*h* UH is developed by multiplying the value of Q_p with Q/Q_p and t_p with t/t_p.

For 9-h UH derivation (i.e., τ = 9 h), a similar approach is followed considering the same values of Q_{eq} = 16,250 m^3/s, b = 0.20, c = 60.92, and D = 6 h. The parameters calculated are z_{max} = 6823 m^3/s, Q_P = 4548 m^3/s, q_p = 0.047 h^{-1}, t_p = 25.55 h, β = 1.19, and λ = 0.13. It is observed that the oscillations in the

Table 1 Ordinates of *S*-curves and altered duration UHs derived by different approaches

Time (h)	6-h parent UH (m^3/s)	6-h *S*-curve (m^3/s)			Conventional		Nondimensional			
		Conventional	Manually adjusted conventional	Analytical IS	3-h UH (m^3/s)	9-h UH (m^3/s)	Time (h)	3-h UH (m^3/s)	Time (h)	9-h UH (m^3/s)
0	0	0	0	0	0	0	0.00	0.00	0.00	0.00
3	200	200	200	206	400	133	4.51	6.55	5.11	2.25
6	500	500	500	564	600	333	9.02	364.57	10.22	232.44
9	1000	1200	1200	1168	1400	800	13.53	1946.13	15.33	1604.39
12	1600	2100	2100	2144	1800	1267	18.04	3977.24	20.44	3658.92
15	2400	3600	3600	3613	3000	2067	22.55	4803.02	25.55	4548.40
18	3500	5600	5600	5604	4000	2933	27.06	4158.43	30.66	3851.85
21	4200	7800	7900	7953	4600	3867	31.57	2861.64	35.77	2502.92
24	5200	10,800	10,400	10,308	5000	4533	36.08	1664.57	40.88	1339.76
27	4400	12,200	12,400	12,314	4000	4533	40.59	851.61	45.99	618.44
30	3100	13,900	13,800	13,800	2800	3933	45.10	393.73	51.10	254.01
33	2300	14,500	14,700	14,790	1800	2867	49.61	167.72	56.21	94.92
36	1500	15,400	15,300	15,404	1200	1933	54.12	66.77	61.32	32.81
39	1000	15,500	15,700	15,768	800	1267	58.62	25.11	66.42	10.62
42	650	16,050	15,900	15,978	400	800	63.13	9.00	71.53	3.25
45	400	15,900	16,100	16,098	400	533	67.64	3.09	76.64	0.95
48	250	16,300	16,200	16,165	200	333	72.15	1.03	81.75	0.27
51	150	16,050	16,230	16,202	60	220	76.66	0.33	86.86	0.07
54	0	16,300	16,250	16,224	40	100	81.17	0.10	91.97	0.02
57			16,250	16,224	0	33	85.68	0.03	97.08	0.00
60			16,250	16,224		13	90.19	0.01	102.19	0.00
63			16,250	16,224		0	94.70	0.00	107.30	0.00
Volume of UH = $\Sigma Qi \times (\Delta t/D)$ m^3/s					16,250	16,250		16,010		15,973

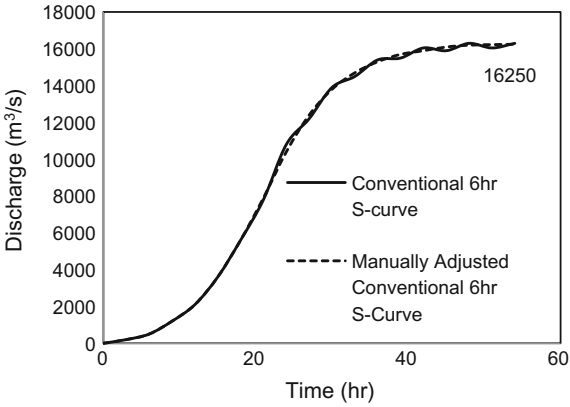

Fig. 1 Manual elimination of hunting effect observed in conventional 6-h *S*-curve (Ojha et al. 2008)

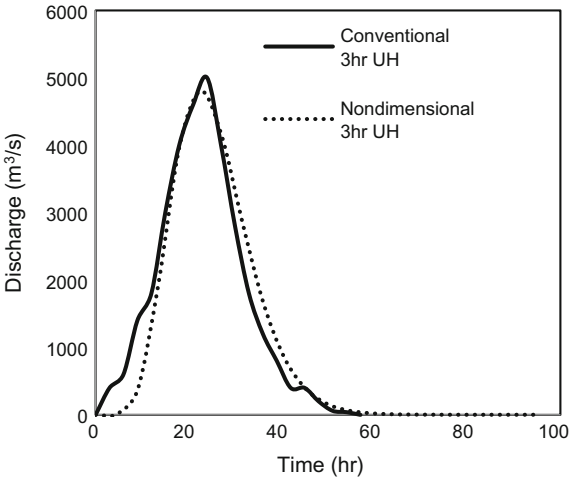

Fig. 2 3-h UH derived from 6-h parent UH (Ojha et al. 2008) using conventional and nondimensional approach

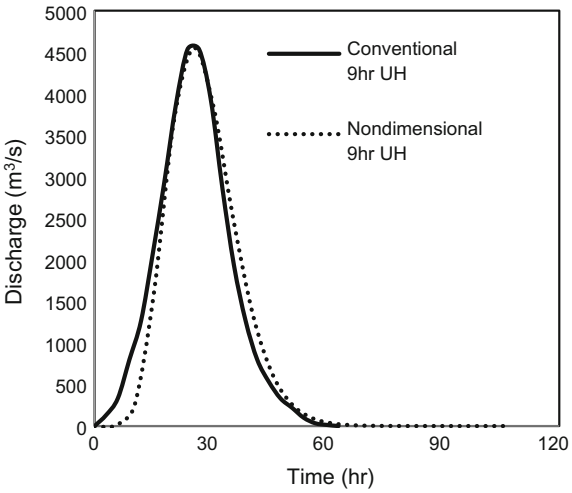

Fig. 3 9-h UH derived from 6-h parent UH (Ojha et al. 2008) using conventional and nondimensional approach

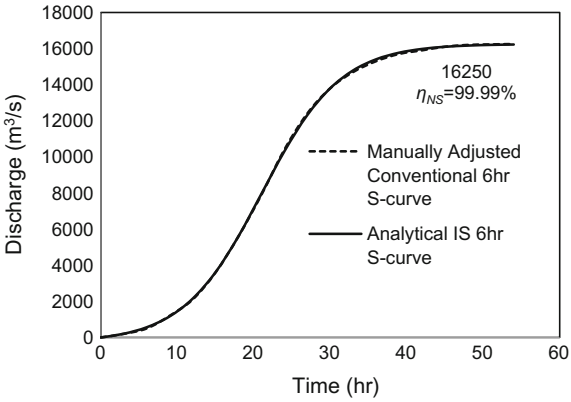

Fig. 4 6-h *S*-curve derived by the manually adjusted conventional (Ojha et al. 2008) and analytical IS approach

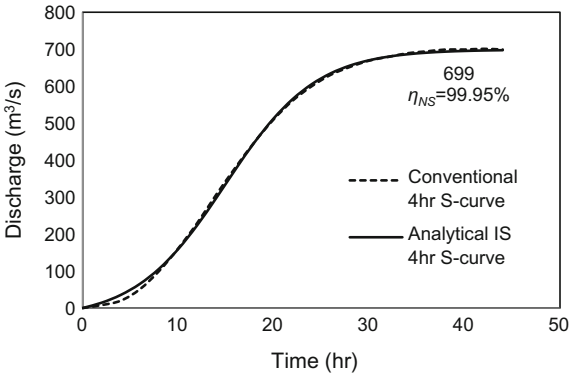

Fig. 5 4-h *S*-curve derived by the conventional (Subramanya 2013) and analytical IS approach

conventional 3-h and 9-h UHs are smoothed out completely by the derived nondimensional 3-h and 9-h UHs (Table 1; Figs. 2 and 3), satisfying volumetric equality with estimated $\Sigma Q_i \times (\Delta t/D)$ = 16,010 and 15,973 m^3/s, respectively.

Derivation of Altered Duration UHs from Other Two Parent UHs

Similarly, the altered duration (i.e., 2 and 6 h) UHs were derived from two different 4-h parent UHs (Subramanya 2013; Raghunath 1995) using the conventional and nondimensional approaches. Here, hunting effect of conventional *S*-curve has not been removed manually as even after these adjustments oscillations still continue to occur in the resultant altered duration UHs. The 4-h *S*-curves derived by the conventional and analytical IS approaches with respect to two different 4-h parent UHs are shown in Figs. 5 and 6, respectively. The resulting altered duration oscillation-free UHs are depicted in Figs. 7, 8, 9, and 10, respectively, satisfying volumetric equality.

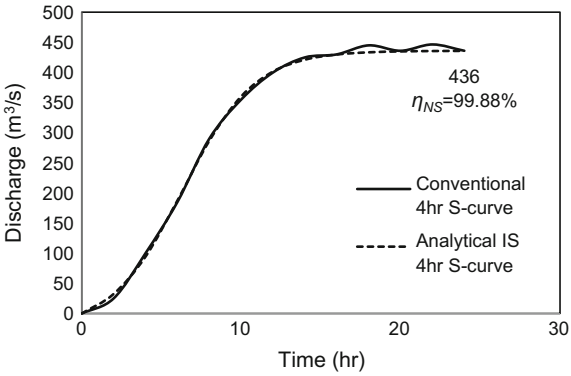

Fig. 6 4-h *S*-curve derived by the conventional (Raghunath 1995) and analytical IS approach

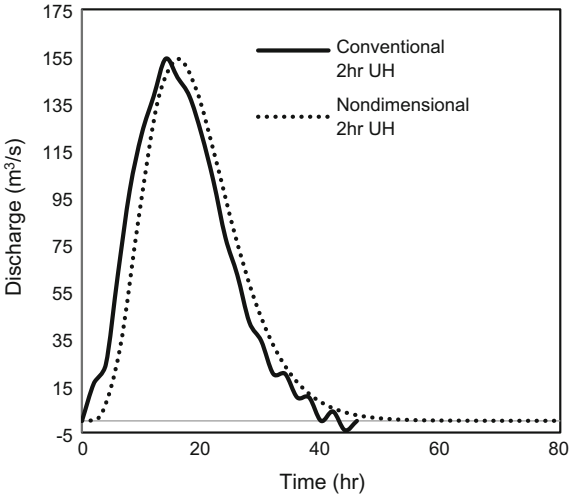

Fig. 7 2-h UH derived from 4-h parent UH (Subramanya 2013) using conventional and nondimensional approach

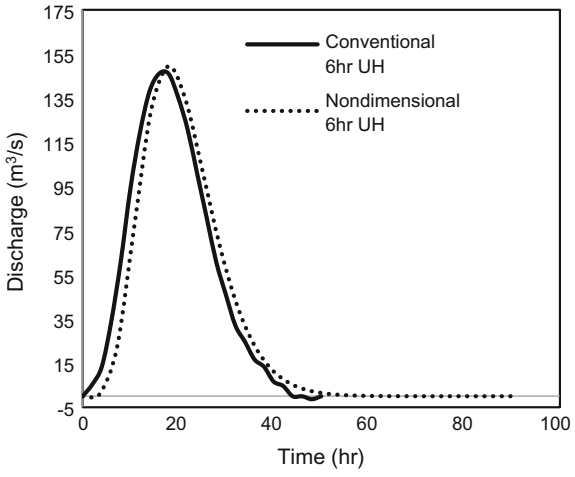

Fig. 8 6-h UH derived from 4-h parent UH (Subramanya 2013) using conventional and nondimensional approach

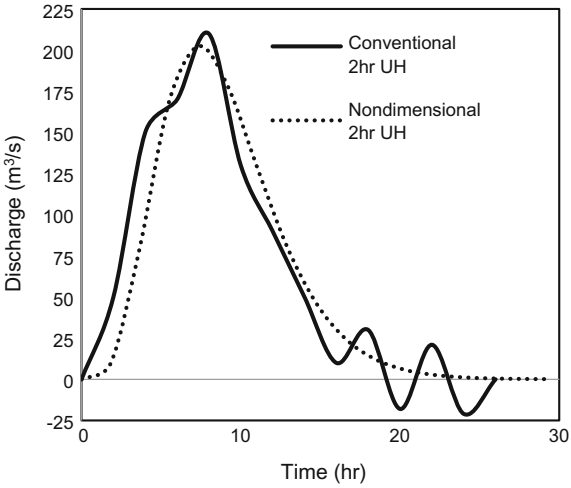

Fig. 9 2-h UH derived from 4-h parent UH (Raghunath 1995) using conventional and nondimensional approach

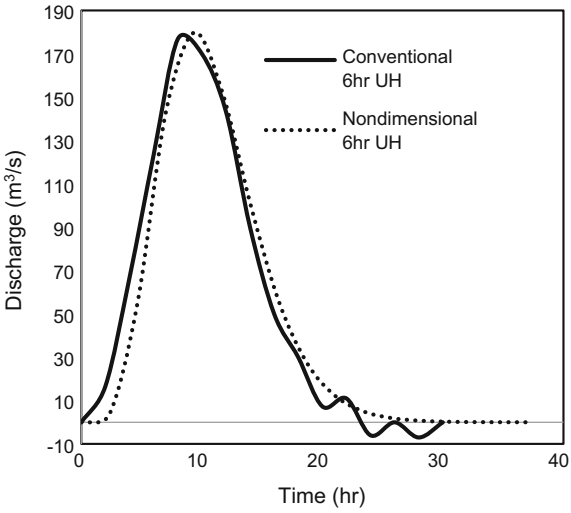

Fig. 10 6-h UH derived from 4-h parent UH (Raghunath 1995) using conventional and nondimensional approach

Conclusions

1. The proposed easily executable nondimensional approach yields reliable results in terms of the UH reproduction and outperforms the conventional *S*-curve based UH approach avoiding tail-end oscillations, automatically taking care of the volume and nonnegativity constraints, and reducing the computational complexity.
2. The need of manual adjustment has been completely eliminated by the proposed approach which in turn reflects its time-saving ability.

3. The suggested analytical IS model which has the efficacy to exactly reproduce the oscillation-free *S*-curve obviates the need for synthetic relationships in estimation of UH parameters (Q_p and t_p).
4. Estimation of Q_p and t_p is simple because of the absence of empirical coefficient that may require calibration, and involves computations of only exponential and logarithmic functions, which can easily be accomplished using Spreadsheet.
5. The convenience and sound theoretical basis of the proposed approaches assure of its practical applicability.

References

Aron G, White EL (1982) Fitting a gamma distribution over a synthetic unit hydrograph. Water Resour Bull 18(1):95–98

Bhunya PK, Mishra SK, Berndtsson R (2003) Simplified two-parameter gamma distribution for derivation of synthetic unit hydrograph. J Hydrol Eng, ASCE 8(4):226–230

Blank D, Delleur JW, Giorgini A (1971) Oscillatory kernel functions in linear hydrologic models. Water Resour Res 7(5):1102–1117

Boufadel MC (1998) Unit hydrographs derived from the Nash model. J Am Water Resour Assoc 34(1):167–177

Chow VT, Maidment DR, Mays LW (1988) Applied hydrology. McGraw-Hill, New York

CWC (1984) Flood estimation report for upper Indo-Ganga plains subzone-1(e)-a method based on unit hydrograph principle. Hydrology Directorate, CWC, New Delhi, India

Dooge JCI (1973) Linear theory of hydrologic systems. USDA-ARS Tech. Bull. No. 1968. U.S. Govt. Printing Office, Washington

Edson CG (1951) Parameters for relating unit hydrograph to watershed characteristics. Trans—Am Geophys Union 32(4):591–596

Hall MJ (1977) On the smoothing of oscillations in finite-period unit hydrographs derived by the harmonic method. Hydrol Sci Bull 22(2):313–324

Hunt B (1985) The meaning of oscillations in unit hydrograph *S*-curves. Hydrol Sci J 30(3): 331–342

Lasdon LS, Waren AD, Jain A, Ratner M (1978) Design and testing of a generalized reduced gradient code for nonlinear programming. ACM Trans Math Softw 4(1):34–50

Linsley RK, Kohler MA, Paulhus JLH (1975) Hydrology for engineers, 2nd edn. McGraw-Hill, New York

Meyer PS (1994) Bi-logistic growth. Technol Forecast Soc Chang 47:89–102

Mockus V (1957) Use of storm and watershed characteristics in synthetic hydrograph analysis and application. Am Geophys Union, Pacific Southwest Region, Sacramento, CA

Nadarajah S (2007) Probability models for unit hydrograph derivation. J Hydrol 344:185–189

Naki Cenovic N (1988) U.S. transport Infrastructures in cities and their vital systems. National Academy Press, Washington, D.C

Nash JE (1957) The form of the instantaneous unit hydrograph. Int Assoc Sci Hydrol Publ 45 (3):114–121

Nash JE (1958) Determining runoff from rainfall. Inst Civ Eng Proc 10:163–184

Nash JE (1960) A unit hydrograph study with particular reference to British catchments. Inst Civ Eng Proc 17:249–282

Nash JE, Sutcliffe JV (1970) River flow forecasting through conceptual models part I-A discussion of principles. J Hydrol 10(3):282–290

Ohba M (1984) Software reliability analysis models. IBM J Res Dev 28(4):428–443

Ojha CSP, Bhunya P, Berndtsson R (2008) Engineering hydrology. Oxford University Press, New Delhi, India

Patil PR, Mishra SK, Sharma N (2016) Oscillation free altered duration UH derivation using nondimensional approach. Perspect Sci. doi:10.1016/j.pisc.2016.06.059

Rai RK, Sarkar S, Singh VP (2009) Evaluation of the adequacy of statistical distribution functions for deriving unit hydrograph. Water Resour Manage 23(5):899–929

Raghunath HM (1995) Hydrology: principles, analysis, design. New Age International Publishers, New Delhi, India

Sangal BP (1986) Recursion formula for unit hydrographs. Can J Civ Eng 13(3):386–388

Singh VP (1988) Hydrologic systems: rainfall-runoff modeling, vol 1. Prentice-Hall, Englewood Cliffs, N.J.

Singh VP (1992) Elementary hydrology. Prentice Hall, New York

Singh SK (2000) Transmuting synthetic unit hydrographs into gamma distribution. J Hydrol Eng 5 (4):380–385

Singh SK (2004) Simplified use of gamma-distribution/nash model for runoff modeling. J Hydrol Eng 9(3):240–243

Singh SK (2005) Clark's and Espey's unit hydrographs vs the gamma unit hydrograph. J Hydrol Sci 50(6):1053–1067

Singh SK (2006) Optimal instantaneous unit hydrograph from multistorm data. J Irrig Drainage Eng 132(3):298–302

Singh SK (2007) Use of gamma distribution/nash model further simplified for runoff modeling. J Hydrol Eng 12(2):222–224

Stone R (1980) Sigmoids. Bull Appl Stats 7(1):59–119

Subramanya K (2013) Engineering hydrology, 4th edn. McGraw Hill Education, India

Tauxe GW (1978) S-Hydrographs and change of unit hydrograph duration. J Hydraulics Div, ASCE 104(3):439–444

Verhulst PF (1838) Notice sur la loi que la population poursuit dans son accroissement. Corresp Math Phys 10:113–121

Verhulst PF (1845) Recherches mathématiques sur la loi d'accroissement de la population [Mathematical researches into the law of population growth increase]. Nouv. M´em Acad R Sci B-Lett Brux 18:1–45

Verhulst PF (1847) "Deuxième mémoire sur la loi d'accroissement de la population. M´em Acad R Sci Lett B-Arts Belg 20:142–173

Fuzzy-Based Comprehensive Evaluation of Environmental Flow Alteration

Kairong Lin, Fan Zhang, Qiang Zhang, Xinjun Tu and Yang Hu

Abstract Environmental flow alterations of the key factors influencing aquatic health of a river basin, and it is particularly true for highly-fragmented rivers. In this paper, a new comprehensive evaluation technique using the fuzzy theory was developed. The evaluation index system of environmental flow alteration was firstly established including the relative change of median and deviation, degree of alteration quantifies from range of variability approach (RVA), and histogram matching approach (HMA). Then, the weight of each evaluation index was determined using the entropy theory and order dualistic comparison method. Finally, the overall alteration degree of the 32 IHA (Indicators of Hydrologic Alteration) parameters was generated by fuzzy comprehensive method. Two main control stations, the Yichang station located at the outlet of the Upper Yangtze basin and the Gaoyao station located at the outlet of the west river of Pearl River basin, were selected as case study stations. The results showed that each evaluation index only reflects parts of characteristics of alteration in each parameter, and their contributions to comprehensive alteration of each IHA parameter were different over the stations. The developed comprehensive evaluation method can make the weight determination more scientific and credible, and effectively overcome the shortcomings of traditional single-factor evaluation and offer more reasonable quantitative evaluation of environmental flow alteration.

Keywords Environmental flow · Hydrologic alteration · Comprehensive evaluation · Fuzzy · Entropy

K. Lin (✉) · F. Zhang · Q. Zhang · X. Tu · Y. Hu
Department of Water Resources and Environment, Sun Yat-Sen University, Guangzhou 510275, China
e-mail: linkr@mail.sysu.edu.cn

K. Lin · Q. Zhang · X. Tu
Key Laboratory of Water Cycle and Water Security in Southern China of Guangdong High Education Institute, Sun Yat-Sen University, Guangzhou 510275, China

V. P. Singh et al. (eds.), *Hydrologic Modeling*, Water Science and Technology Library 81, https://doi.org/10.1007/978-981-10-5801-1_43

Introduction

In recent years, a bunch of publications appeared addressing environmental flow alterations and related impacts on ecosystems (e.g., Gao and Vogel 2009; Home et al. 2013; Kim and Singh 2014; Lin et al. 2014; Shiau and Huang 2014; Zhang et al. 2014a, b). Indicators of hydrologic alteration (IHA) developed by The Nature Conservancy in the United States (Richter et al. 1996) is one of the techniques widely used in detection of hydrological alterations. IHA includes 33 parameters computed based on historic flow or stage records (Table 1). In order to quantify the degree of alteration for each hydrologic parameter in IHA, the range of variability approach (RVA) was established accordingly (Richter et al. 1997). Although the RVA is also well applied to determine the flow regime targets by using IHA (Lian et al. 2012), it is subject to potential limitations (Gippel 2001; Richteret al. 2006). Shiau and Wu (2008) pointed out that variations of the parameter value within the target range, and the value and frequency of the hydrologic parameter falling beyond the target range (the interval between 25 and 75% frequency) are not explicitly taken into account in the RVA method. To solve this problem, Shiau and Wu (2008) adopted a histogram matching approach (HMA) for assessment of flow regime alteration, which uses the degree of histogram dissimilarity, employing the quadratic-form distance between frequency vectors of the pre- and post-impact histograms based on IHA, and describes the whole variance of hydrologic alterations (Yang et al. 2012). In addition, Kim and Singh (2014) proposed an entropy-based multi-criteria decision method for hydrologic alteration assessment of biologically relevant flow regimes. Virtually, these assessment methods only describe some characteristic of alteration in every IHA parameter. For example, RVA concerns the frequency of a hydrologic parameter falling in the target range, and HMA considers the frequency distribution of the whole series, while variations of median value and coefficient of deviation are also not taken into account. Therefore, it is necessary to synthetically evaluate the alteration of every IHA parameter. In this paper, we proposed a comprehensive method based on the theory of fuzzy mathematics, to synthetically evaluate environmental flow alteration.

Methodology

Our objective is to compute overall alteration degree which involves the following steps, as shown in Fig. 1: (1) Calculation of IHA parameter; (2) Selection of evaluation index; (3) Computation of membership matrix; (4) Determination of evaluation index weight; and (5) Computation of overall membership degree.

Table 1 Evaluation of environmental flow alteration at Yichang and Gaoyao stations

IHA No.	Indicator	Yichang					Gaoyao				
		RCM/%	RCD/%	RVA/%	HMA/%	OAD	RCM/%	RCD/%	RVA/%	HMA/%	OAD
Magnitude of monthly river flow (*in* m^3/s)											
1	January	1.42	12.69	29.58	43.13	0.19	1.66	84.87	35.00	25.73	0.32
2	February	1.53	16.37	5.93	37.88	0.01	11.43	88.15	40.00	29.57	0.50
3	March	2.10	11.20	21.73	36.58	0.07	46.39	18.19	45.45	36.32	0.87
4	April	8.02	5.35	25.59	39.98	0.14	3.54	47.41	10.00	14.04	0.04
5	May	5.70	8.89	17.00	40.85	0.07	14.63	0.86	10.00	30.84	0.24
6	June	2.69	8.24	19.86	45.05	0.13	15.76	6.92	50.00	30.89	0.58
7	July	1.93	15.57	11.47	36.55	0.02	27.39	9.83	20.00	34.83	0.48
8	August	8.96	21.62	8.76	46.11	0.10	0.45	8.74	20.00	16.95	0.06
9	September	3.52	10.82	3.03	39.87	0.02	17.54	48.63	20.00	13.96	0.12
10	October	11.23	16.96	5.93	45.99	0.09	28.14	71.49	25.00	37.60	0.62
11	November	5.48	16.51	37.03	41.16	0.27	21.14	11.40	10.00	36.25	0.38
12	December	2.54	1.59	0.61	43.56	0.04	8.26	2.45	25.00	13.03	0.08
Magnitude and duration of annual extreme conditions (*in* m^3/s)											
13	1-day minimum	6.49	2.48	1.44	51.91	0.14	1.37	12.50	35.00	14.43	0.14
14	3-day minimum	5.07	2.53	2.69	40.45	0.02	4.90	14.55	35.00	28.72	0.33
15	7-day minimum	4.18	0.00	8.41	39.70	0.03	2.04	15.78	5.00	7.44	0.002
16	30-day minimum	4.02	22.73	25.59	39.67	0.13	3.94	11.07	5.00	18.70	0.04
17	90-day minimum	4.99	18.58	31.31	42.91	0.23	5.18	21.26	25.00	21.36	0.15
18	1-day maximum	9.18	25.50	11.47	42.44	0.07	22.28	18.97	40.00	34.30	0.61
19	3-day maximum	5.82	5.25	2.69	36.03	0.01	19.69	17.79	10.00	21.32	0.14
20	7-day maximum	4.46	1.99	25.93	43.57	0.17	12.07	2.82	35.00	21.15	0.25
21	30-day maximum	4.12	9.61	20.21	43.41	0.12	9.97	8.33	40.00	24.64	0.34

(continued)

Table 1 (continued)

IHA No.	Indicator	Yichang					Gaoyao				
		RCM/%	RCD/%	RVA/%	HMA/%	OAD	RCM/%	RCD/%	RVA/%	HMA/%	OAD
22	90-day maximum	2.90	10.50	19.86	42.52	0.10	5.30	14.96	5.00	21.75	0.08
23	Base flow	0.12	22.09	31.31	36.81	0.16	3.35	32.23	25.00	29.85	0.27
Time of annual extreme conditions (in days)											
24	Date of minimum	0.00	14.85	31.66	41.62	0.20	52.83	12.03	40.00	20.90	0.65
25	Date of maximum	3.50	8.26	48.48	34.88	0.32	4.47	57.19	65.00	42.88	0.72
Frequency and duration of high and low pulses											
26	Low pulse count	50.00	55.55	19.89	41.40	0.45	40.00	46.43	7.14	14.28	0.23
27	Low pulse duration	32.26	98.57	14.14	34.12	0.23	59.38	21.01	3.85	37.70	0.61
28	High pulse count	20.00	25.00	15.49	35.76	0.10	20.00	44.45	15.63	11.44	0.09
29	High pulse duration	25.00	80.91	51.81	37.98	0.58	9.52	58.58	42.31	31.36	0.50
Rate and frequency of change in conditions											
30	Rise rate	20.00	3.93	48.13	54.06	0.67	0.99	9.26	3.57	13.00	0.01
31	Fall rate	11.43	12.92	38.23	41.50	0.32	6.36	29.08	12.50	24.99	0.14
32	Number of reversals	23.78	135.68	58.50	63.01	0.93	7.17	9.33	25.00	30.19	0.29

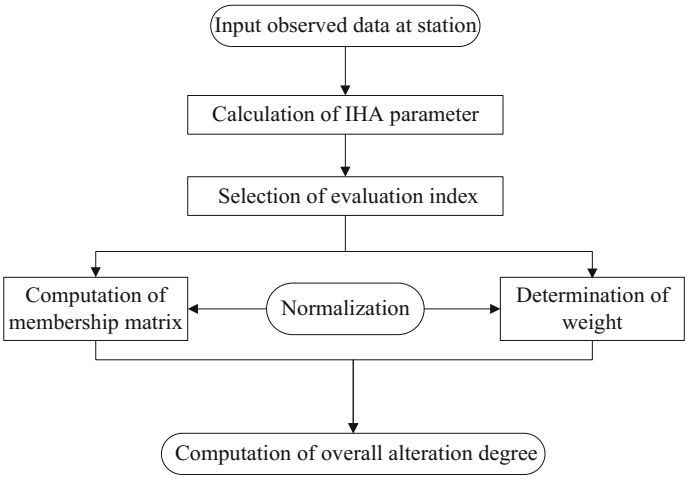

Fig. 1 Working flow for computation of overall alteration degree based on fuzzy evaluation method

Calculation of IHA Parameter

The IHA statistical package, developed by Richter et al. (1996) and supported by the nature conservancy (TNC), was used to calculate the hydrological alteration, in which 32 IHA parameters from historic flow records are selected in this study, including five characteristics of flow regimes, which are called magnitude of monthly water conditions, magnitude and duration of annual extreme conditions, timing of annual extreme conditions, frequency and duration of high and low pluses, and rate and frequency of condition changes.

Selection of Evaluation Index

In this study, four indices, i.e., the relative change of median (RCM), the relative change of deviation (RCD), degree of alteration calculated by RVA (DRVA), and degree of histogram dissimilarity calculated by HMA (DHMA), are adopted aiming to evaluate the alteration of each hydrologic parameter in IHA. Degree of alteration calculated by RVA (DRVA) is defined as the relative change of the number of the flow regime falling within the target range (the 25th- and 75th-percentile values) between the pre- and post-impact periods, and the detail calculation steps can be seen in Richter et al. (1996). While degree of histogram dissimilarity calculated by HMA (DHMA) is defined as the relative change of histogram dissimilarity between the pre- and post-impact periods, and the detail calculation steps can be seen in Shiau and Wu (2008).

Thus, the evaluation index matrix was established as follow:

$$X = \begin{bmatrix} x_{11} & x_{12} & \cdots & x_{1n} \\ x_{21} & x_{22} & \cdots & x_{2n} \\ \cdots & \cdots & \cdots & \cdots \\ x_{m1} & x_{m2} & \cdots & x_{mn} \end{bmatrix} = x_{ij} \tag{1}$$

where x_{ij} is the eigenvalue of the ith evaluation index of the jth hydrologic parameter in IHA, $i = 1, 2, \cdots m; \quad j = 1, 2, \cdots n$. In which, m is equal to 4 and n is equal to 32 in this study.

Computation of Membership Matrix

To unify the standards for comparison, we adopted the method of range transformation for the normalization of the evaluation index matrix. Because the bigger the evaluation index is, the higher the indicating extent of hydrologic alteration is, the following equation was adopted for normalization.

$$r_{ij} = \frac{x_{ij} - \bigwedge\limits_{j=1}^{n} x_{ij}}{\bigvee\limits_{j=1}^{n} x_{ij} - \bigwedge\limits_{j=1}^{n} x_{ij}} \tag{2}$$

where $\bigvee\limits_{j=1}^{n} x_{ij}$ and $\bigwedge\limits_{j=1}^{n} x_{ij}$ are the maximum and minimum eigenvalue of the ith evaluation index in the decision set. Thus, the relative membership matrix was established after normalization as follow:

$$R = \begin{bmatrix} r_{11} & r_{12} & \cdots & r_{1n} \\ r_{21} & r_{22} & \cdots & r_{2n} \\ \cdots & \cdots & \cdots & \cdots \\ r_{m1} & r_{m2} & \cdots & r_{mn} \end{bmatrix} \tag{3}$$

Determination of Evaluation Index Weight

Determination of Objective Weight

The objective weight of the evaluation index is determined by using the entropy theory after the relative membership matrix is got through the fuzzy evaluation.

Firstly, the information entropy is calculated as follow, which is a measurement of system disorder degree.

$$IE_i = -\sum_{j=1}^{n} a_{ij} \ln a_{ij} \tag{4}$$

where $a_{ij} = \frac{r_{ij}}{\sum_{j=1}^{n} r_{ij}}$.

Then, the output entropy can be calculated as follow, which is a measurement of the importance of the evaluation index.

$$\mathrm{OE}_i = \frac{\mathrm{IE}_i}{\ln n} \tag{5}$$

After that, the difference degree can be calculated as follow:

$$\mathrm{DD}_i = 1 - \mathrm{OE}_i \tag{6}$$

Finally, the objective weight of the evaluation index can be calculated as follow:

$$\mathrm{OW}_i = \frac{\mathrm{DD}_i}{\sum_{i=1}^{m} \mathrm{DD}_i} \tag{7}$$

Determination of Subjective Weight

The subjective weight of the evaluation index is determined by the order dualistic comparison method (Chen and Guo 2006), which depends on the relative importance of each evaluation index.

Firstly, an evaluation index was selected as the most important index, which important degree (ID) is set as 1. Then important degree (ID) of the equal important index to the most important index is also set as 1. Important degree (ID) of the least important index is set as 0. Four more levels of important degree were set between 0 and 1, which value are 0.667, 0.428, 0.25, and 0.11, respectively. After that, the subjective weight of the evaluation index can be calculated as follows:

$$\mathrm{SW}_i = \frac{\mathrm{ID}_i}{\sum_{i=1}^{m} \mathrm{ID}_i} \tag{8}$$

Determination of Overall Weight

The overall weight of the evaluation index is determined by the combination of the objective weight and subjective weight, which can be calculated as follows:

$$W_i = \frac{\mathrm{OW}_i \cdot \mathrm{SW}_i}{\sum_{i=1}^{m} \mathrm{OW}_i \cdot \mathrm{SW}_i} \tag{9}$$

Computation of Overall Alteration Degree

Firstly, let $r_{gi} = \bigvee_{j=1}^{n} r_{ij}$ and $r_{bi} = \bigwedge_{j=1}^{n} r_{ij}$, then $r_g = \left(r_{g1}, r_{g2}, \cdots, r_{gm}\right)^{\mathrm{T}}$ and $r_b = (r_{b1}, r_{b2}, \cdots, r_{bm})$, which represent the maximal and minimal alteration decision set. After that, an optimization criterion was established to find the optimum relative membership as follow:

$$\mathrm{Min}\left\{ F(u_j) = u_j^2 \left[\sum_{i=1}^{m} \left(w_i\left(\bigvee_{j=1}^{n} r_{ij} - r_{ij}\right)\right)^2 \right] + (1-u_j)^2 \sum_{i=1}^{m} \left(w_i\left(r_{ij} - \bigwedge_{j=1}^{n} r_{ij}\right)\right)^2 \right\} \tag{8}$$

where u_j is the relative membership degree of the jth hydrologic parameter in IHA.

Finally, let $\frac{\mathrm{d}F(u_j)}{\mathrm{d}u_j} = 0$, then the optimum relative membership degree can be gained as follow:

$$u_j = \frac{1}{1 + \frac{\sum_{i=1}^{m} \left[w_i\left(\bigvee_{j=1}^{n} r_{ij} - r_{ij}\right) \right]^2}{\sum_{i=1}^{m} \left[w_i\left(r_{ij} - \bigwedge_{j=1}^{n} r_{ij}\right) \right]^2}} \tag{9}$$

where u_j is the overall alteration degree (OAD) of the jth hydrologic parameter in IHA.

Case Study

In this study, two main control stations, Yichang station located at the outlet of the Upper Yangtze basin and Gaoyao station located at the outlet of the west river of Pearl River basin, are chosen as case study (as shown in Fig. 2). The Yangtze River

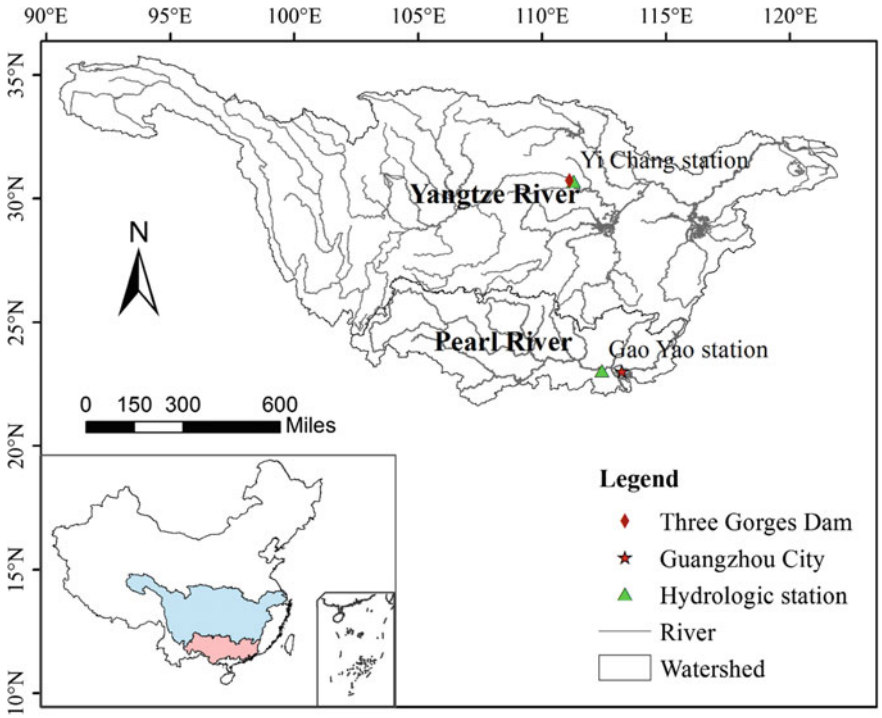

Fig. 2 Location of the study river basin and also hydrological stations

originates from the Tibetan Plateau and follows a sinuous west-to-east route before emptying into the East China Sea, and the basin is home to 33% of China's population and plays an important role in China's economic development (Gao et al. 2012). Yichang station has a drain age area of approximately 1.0 million km^2, and the upstream of this station is abundant in hydropower potential. Since the 1960s, large reservoirs were constructed in the Upper Yangtze basin, such as Hongfeng reservoir constructed in 1960, Heilongtan reservoir constructed in 1971, Wujiangdu reservoir constructed in 1982, and Three Gorges constructed in 2003. Therefore, the long-term flow records were divided into the pre-impact period of 1878–1960 and the post-impact period of 1961–2010 for the IHA analyses in this study.

The west river is the largest tributary of the Pearl River, which has a mainstream length of 2,214 km and a catchment of 351,500 km^2. The west river has the highest water discharge and sediment load, which represent 77 and 89% of the Pearl River's total water discharge and sediment load, respectively (Liu et al. 2014). Presently, the Pearl River provides the essential water supply to several major cities such as Guangzhou, Foshanin the Pearl River Delta region. Since the 1990s, large reservoirs were also constructed in the West River, such as Yantan constructed in 1992, Bailongtan reservoir constructed in 1996, and Tianshengqiao reservoir

constructed in 1997, with a total storage capacity of 138.8×10^8 m^3. In addition, another human activity, uneven sand dredging began in the late 1980s. Therefore, the long-term flow records were divided into the pre-impact period of 1960–1989 and the post-impact period of 1990–2009 for the IHA analyses in this study.

Results and Discussion

The 32 parameters selected to analyze the hydrologic alteration at Yichang and Gaoyao stations include the monthly average flow; 1-, 3-, 7-, 30-, 90-day minimum and maximum average flows and base flow; the date when minimum and maximum stage and flow occurred; low and high pulses and their durations; and number of reversals. The results for IHA analyses are listed in Table 1. Table 1 includes the relative change of median (RCM), the relative change of deviation (RCD), degree of alteration calculated by RVA (DRVA), and degree of histogram dissimilarity calculated by HMA (DHMA) of each hydrologic parameter in IHA.

Analysis of Evaluation Indexes

Four evaluation indexes' values of each IHA parameter were compared, as shown in Fig. 3. It can be seen that there were much difference between these four evaluation indexes' values at both Yichang and Gaoyao stations. Figure 4 shows the flow series and frequency histogram of high pulse duration and low pulse count between pre- and post-impact periods at Yichang station, respectively. Refer to Fig. 4a and Table 1, it can be seen that frequency histogram varies not too much between pre- and post-impact periods, the value of DHMA is 37.98%, while the value of the relative change of median and deviation, while the DRVA are 25, 80.91, and 51.81%, that is, the flow series had change a lot although the value of DHMA is not too large. On the contrary, for low pulse count at Yichang station, the value of DRVA is not too large, only 19.89%, while other three evaluation indexes are relative high, which values are 50%, 55.55, and 41.4%. As shown in Fig. 4b, frequency histogram of low pulse count varies a lot although the numbers falling beyond the RVA bound between pre- and post-periods have not too much different.

In addition, for Rise rate and Date of maximum at Yichang station, their values of DRVA are 48.13 and 48.48% separately, which appears to indicate a close hydrologic alteration between Rise rate and Date of maximum. However, it can be seen from Fig. 5a, c that there is a great difference between the flow series of these two indicators. As we compare their frequency histograms, which of Rise rate has changed greater than that of Date of maximum, as shown in Fig. 5b, d. And the relative change of median of these two indicators is also different, in which value of

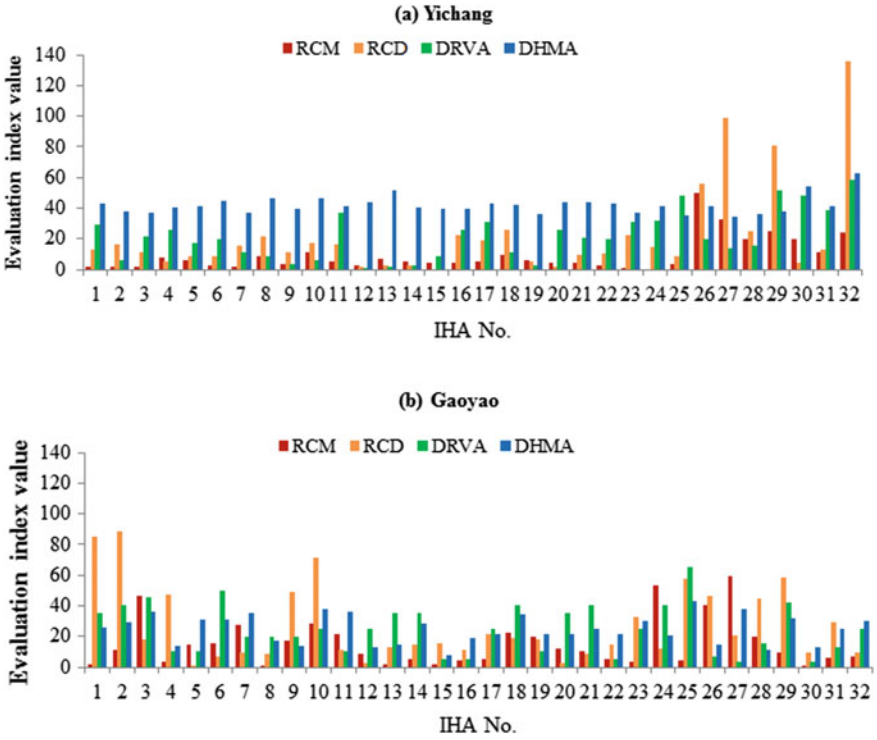

Fig. 3 Comparison of four evaluation indices at Yichang station (**a**) and Gaoyao station (**b**)

Rise rate is 20%, while that of Date of maximum is only 3.5%. On the contrary, for Date of maximum and Low pulse duration, their values of DHMA are 34.88 and 34.12%. It is also found from Fig. 5d, f, there are both small change between the frequency histograms of pre- and post-periods. However, it can be seen from Fig. 5c, e that there is a great difference between the series of these two indicators. As we compare their relative change of deviation, which value of Low pulse duration is 98.57%, while that of Date of maximum is only 8.26%.

The same patten can be found at Gaoyao station. For 90-day minimum and October, their values of DRVA are both 25%, which indicate that they may have the same hydrologic alteration degree. However, it can be seen from Fig. 6a, c that the post-impact series of 90-day minimum is more upwards deviation to RVA bound, while that of October is more downwards deviation to RVA bound. As we compare their frequency histograms, which of October has changed greater than that of 90-day minimum, as shown in Fig. 6b, d. And the relative change of deviation of these two indicators are also different, which value of October is 71.49%, while that of Date of maximum is only 21.26%. On the contrary, for

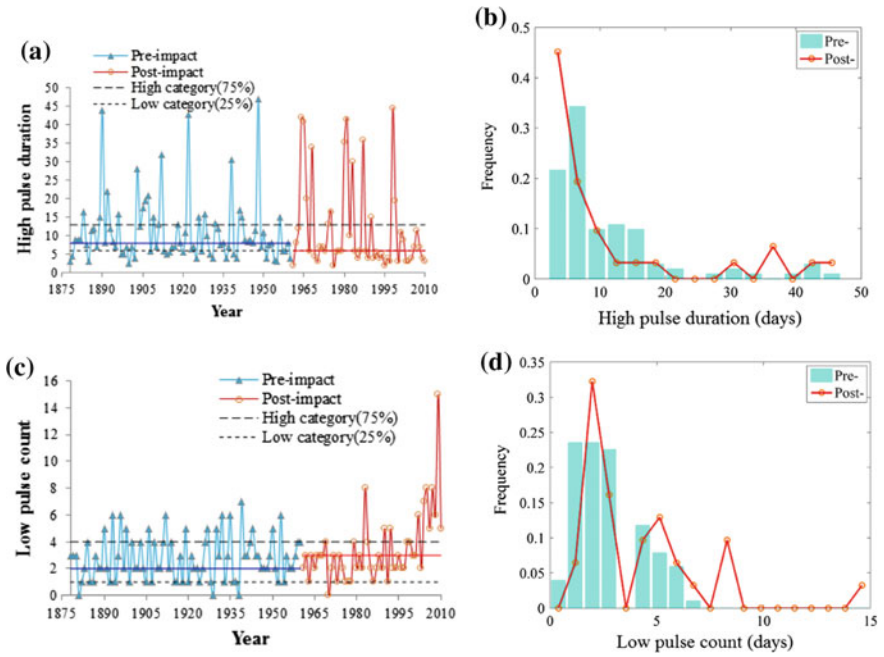

Fig. 4 Temporal variations of low pulse count and low pulse count versus frequency relations

October and Low pulse duration, their values of DHMA are 37.6 and 37.7% separately, which appears to indicate a close hydrologic alteration between October and Low pulse duration according to DHMA value. However, it can be seen from Fig. 6c–d, e–f that there is a great difference between the series of these two indicators. As we compare their values of DRVA, which of October is 25%, while that of Low pulse duration is only 3.85%. And the relative change of median and deviation of these two indicators are also different, in which values of October are 28.14 and 71.49%, while those of Low pulse duration are 59.38 and 29.01%.

These above results indicated that each evaluation index only reflects some characteristic of hydrologic alteration of each parameter, so it is necessary to synthetically evaluate the alteration of every hydrologic parameter in IHA.

Determination of Weigh Vector

Based on the method presented in Sect. 2.4, evaluation Index matrix was firstly normalized by using Eq. (2). Then, the information entropy, output entropy, difference degree, and objective weight of the evaluation index were determined by the entropy theory. After that, the subjective weight of each evaluation index was calculated by the order dualistic comparison method based on the importance of

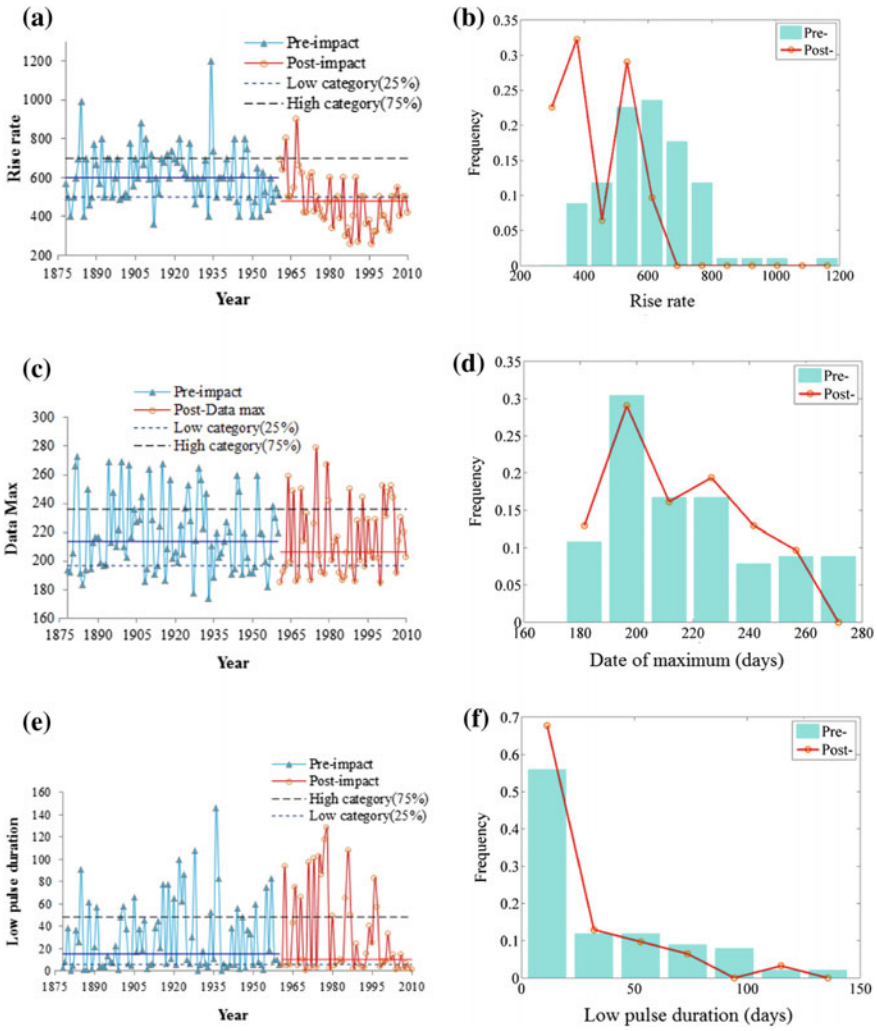

Fig. 5 Variation and frequency distribution of Rise rate **a**, **b** Date of maximum **c**, **d** and low pulse duration **e**, **f** at Yichang station

each evaluation index. Finally, the overall weight of the evaluation index is determined by combination of the objective weight and subjective weight, and the results were listed in Table 2. Traditional weight determination method mainly depends on expert's experience. The weight determination by using the entropy theory in this study not only considers the difference information of each evaluation index, but also the importance of each evaluation index, which can make the weight determination more scientific and credible.

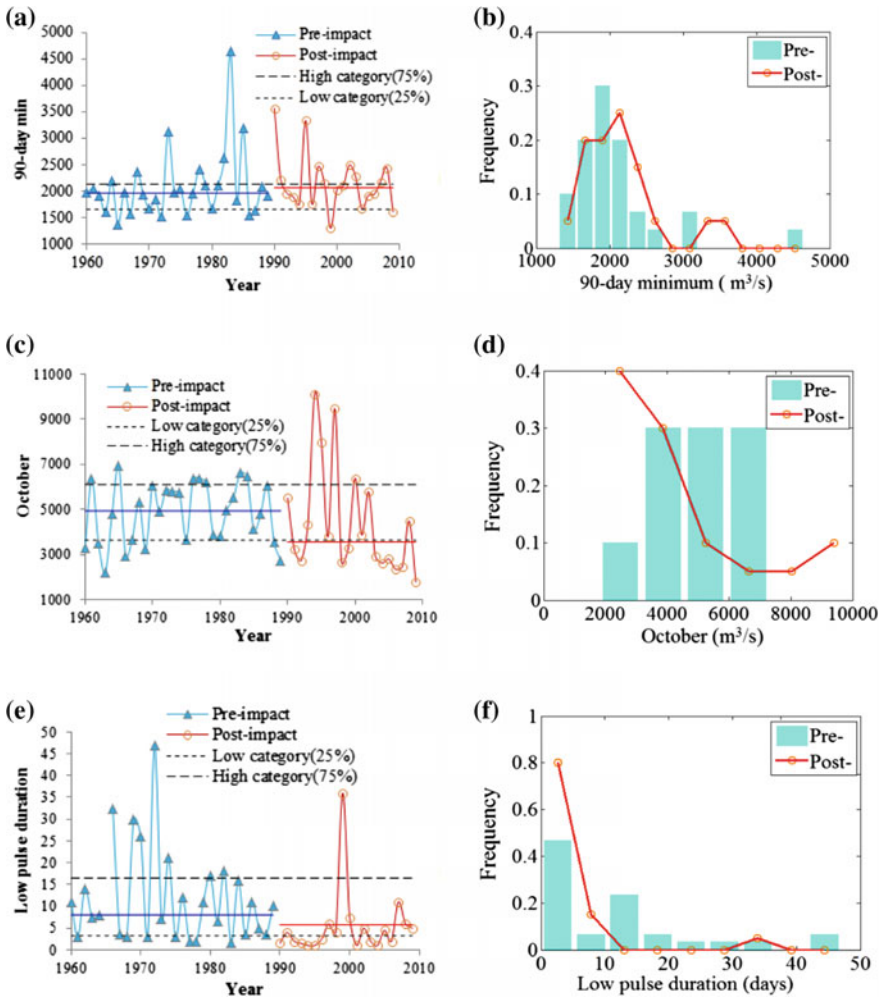

Fig. 6 Variation and frequency distribution of 90-day minimum **a**, **b** October **c**, **d** and low pulse duration **e**, **f** at Gaoyao station

Comprehensive Evaluation Results

Based on the weights for the evaluation index system determined in Sect. 4.2, we evaluated the comprehensive alteration of 32 IHA parameter according to the procedure detailed in Sect. 2.2, and the results are listed in Table 1. It can be seen from Table 1, number of reversals and 3-day maximum are identified as the greatest and smallest alteration index among the 32 IHA parameters at Yichang station, and overall alteration degree of them are 0.93 and 0.01, respectively. While March and

Table 2 Weights of the four evaluation indices

Station	Index	Entropy method				Order dualistic comparison method		Weight
		IE	OE	DD	OW	ID	SW	
Yichang	RCM	2.95	0.85	0.15	0.31	0.25	0.16	0.24
	RCD	2.87	0.83	0.17	0.36	0.428	0.09	0.16
	DRVA	3.17	0.92	0.08	0.18	1	0.37	0.32
	DHMA	3.22	0.93	0.07	0.15	1	0.37	0.27
Gaoyao	RCM	2.75	0.79	0.21	0.40	0.25	0.16	0.29
	RCD	3.01	0.87	0.13	0.25	0.428	0.09	0.11
	DRVA	3.15	0.91	0.09	0.18	1	0.37	0.30
	DHMA	3.14	0.91	0.09	0.18	1	0.37	0.30

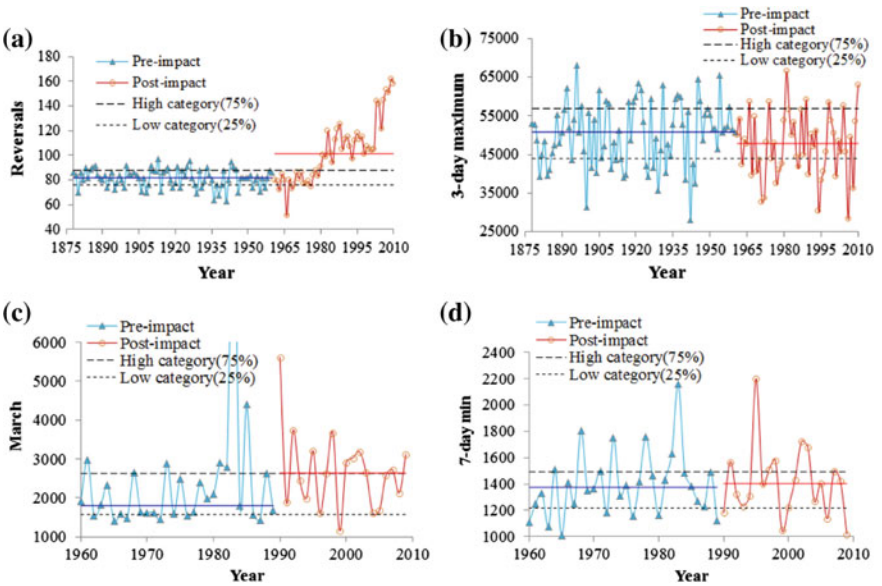

Fig. 7 Pre- and post-impact series of number of reversals **a** and 3-day maximum **b** at Yichang station and March **c** and 7-day minimum **d** at Gaoyao station

7-day minimum are identified as the greatest and smallest alteration index among the 32 IHA parameters at Gaoyao station, and overall alteration degree of them are 0.87 and 0.002, respectively. Figure 7a, b shows the series of number of reversals and 3-day maximum at Yichang station for the pre- and post-impact periods, and Fig. 7c, d shows the series of March and 7-day minimum at Gaoyao station for the pre- and post-impact periods. Refer to Fig. 7a, c, it can be seen that number of reversals at Yichang station and March at Gaoyao station for the post-impact period

have changed greatly when compared to the pre-impact period. It can be also seen from Fig. 7b, d that 3-day maximum at Yichang station and 7-day minimum at Gaoyao station for the post-impact period are close resemblance to the pre-impact period. This implies that the result of Fuzzy Comprehensive Evaluation Method is reasonable.

In addition, correlation analysis is conducted to further analyze the relationship between overall alteration degree and the four evaluation indexes, and the results are shown in Figs. 8 and 9. The correlation coefficients between overall alteration degree and RCM, RCD, DRVA, and DHMA are 0.35, 0.47, 0.68, and 0.33, respectively, which is significant at 0.05 level (larger than 0.2875 or less than −0.2875), in which the correlation coefficient between OAD and DHMA is the smallest. It can be seen from Fig. 2a and Table 1, the value of DHMA varies not too much among 32 IHA parameters at Yichang station. For Gaoyao station, the correlation coefficients between OAD and RCM, DRVA, and DHMA are 0.37, 0.45, 0.68, respectively, which is significant at 0.05 level (larger than 0.2875 or less than −0.2875), while the correlation coefficient between OAD and RCD is only 0.05.

These above results indicated that each evaluation index can contribute to comprehensive alteration of each IHA parameter, but their contributions were different according to different station.

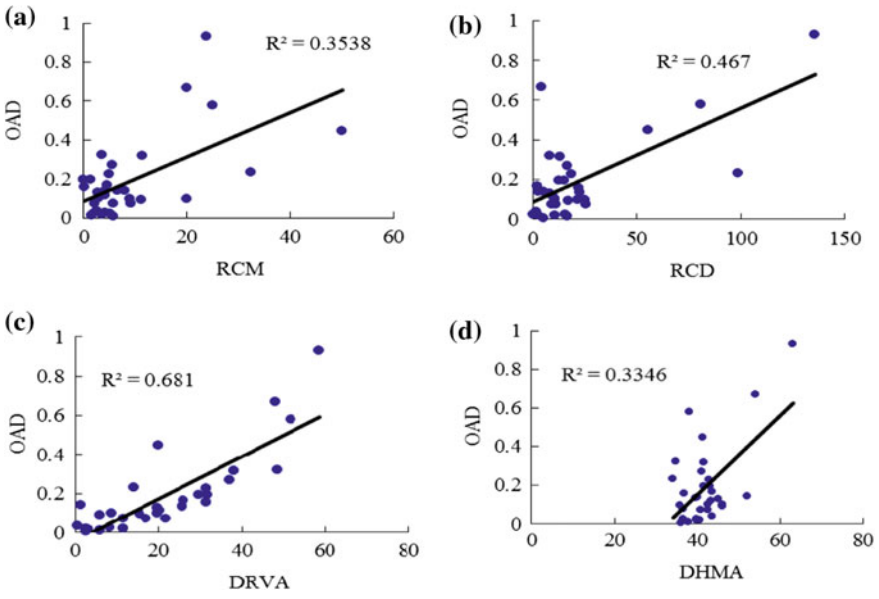

Fig. 8 Relations between membership degree and these four evaluation indices at Yichang station

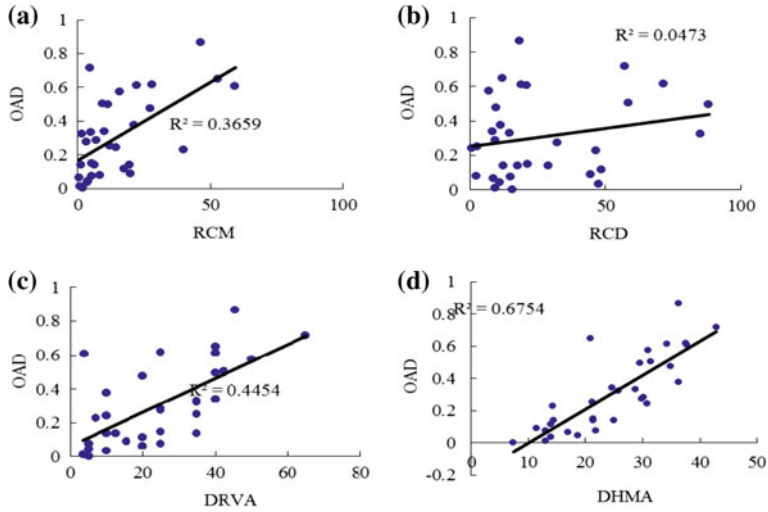

Fig. 9 Scatter plots between membership degree and the four evaluation indexes at Gaoyao station

Conclusion

In this paper, based on the theory of fuzzy mathematics, we proposed a comprehensive method for the evaluation of environmental flow alteration. Two control stations of the Yangtze River and Pearl River in China are selected as case study. Major findings from this study include the following:

(1) The four evaluation indexes, the relative change of median and deviation, and degree of alteration calculated by RVA and HMA are selected to form an evaluation index system, and the entropy theory and order dualistic comparison method are used to calculate the weights of these four evaluation indexes, which can make the weight determination more scientific and credible.
(2) Each evaluation index only reflects some characteristic of hydrologic alteration of each parameter, and the comprehensive evaluation method can effectively overcome the shortcomings of traditional single-factor evaluation and offers more reasonable quantitative evaluation of environmental flow alteration.
(3) Each evaluation index can contribute to comprehensive alteration of each IHA parameter, but their contributions were different according to different station.

The fuzzy-based evaluation method can be also used to comprehensively assess hydrologic alteration of different stations in a region. This study only chooses four evaluation indexes for comprehensive evaluation of environmental flow alteration. More suitable evaluation index should be studied and included into the fuzzy-based evaluation method in the future.

Acknowledgements This study was financially supported by the National Natural Science Foundation of China (Grant No. 51379223 and 51210013).

References

Chen S, Guo Y (2006) Variable fuzzy sets and its application in comprehensive risk evaluation for flood-control system. Fuzzy Option Decis Mak 5(2):153–162

Gao B, Yang DW, Zhao TGT, Yang H (2012) Changes in the eco-flow metrics of the upper Yangtze river from 1961-2008. J Hydrol 448–449:30–38

Gao YX, Vogel RM, Kroll CN, Poff NL, Olden JD (2009) Development of representative indicators of hydrologic alteration. J Hydrol 374:136–147

Gippel CJ (2001). Hydrological analyses for environmental flow assessment. In: Ghassemi F, Whetton P (eds) Proceedings MODSIM 2001, International congress on modelling and simulation, modelling and simulation society of Australia and New Zealand, The Australian National University, Canberra, Australia, pp 873–880

Homa ES, Brown C, McGarigal K, Compton BW, Jackson SD (2013) Estimating hydrologic alteration from basin characteristics in Massachusetts. J Hydrol 503:196–208

Kim Z, Singh VP (2014) Assessment of environmental flow requirements by entropy-based multi-criteria decision. Water Resour Manage 28:459–474

LianY YouJ, SparksR DemissieM (2012) Impact of human activities to hydrologic alterations on the Illinois River. J Hydrol Eng 17:537–546

Lin K, Lian Y, Chen X, Lu F (2014) Changes in runoffs and eco-flows in the Dongjiang river of the Pearl river basin. China Front Earth Sci 8(4):547–557

Liu F, Yuan L, Yang Q, Ou S, Xie L, Cui X (2014) Hydrological responses to the combined influence of diverse human activities in the pearl river Delta, China. CATENA 113:41–55

Richter BD, Baumgartner JV, Powell J, Braun DP (1996) A method for assessing hydrologic alteration within ecosystems. Conserv Biol 10:1163–1174

Richter BD, Baumgartner JV, Wigington R, Braun DP (1997) How much water does a river need? Freshw Biol 37:231–249

Richter BD, Warner AT, Meyer JL, Lutz K (2006) A collaborative and adaptive process for developing environmental flow recommendations. River Res Appl 22:297–318

ShiauJT WuFC (2008) A histogram matching approach for assessment off low regime alteration: application to environmental flow optimization. River Res Appl 24:914–928

Shiau JT, Huang CY (2014) Detecting multi-purpose reservoir operation induced time-frequency alteration using wavelet transform. Water Resour Manage 28:3577–3590

Yang ZF, Yan Y, Liu Q (2012) Assessment of the flow regime alterations in the lower Yellow river, China. Ecolog Inform 10:56–64

Zhang Q, Gu X, Singh VP, Xiao M (2014a) Flood frequency analysis with consideration of hydrological alterations: changing properties, causes and implications. J Hydrol 519:803–813

Zhang Q, Xiao M, Liu CL, Singh Vijay P (2014b) Reservoir-induced hydrological alterations and ecological in stream flow in the East river, the Pearl river basin, China. Stoch Env Res Risk Assess 28:2119–2131

Part VII
Watershed Modeling

Spatial Characters of a Tropical River Basin, South-West Coast of India

Girish Gopinath, N. Ramisha, Ajith G. Nair and N. P. Jesiya

Abstract An evaluation of drainage network of Mahe river basin (394 km^2), Kerala, India, with a humid tropical setting is carried out using geospatial techniques. The streams of the basin generally conform to Horton's laws. However, the correlation between mean stream length and stream order is low ($r = +0.55$), probably due to an abrupt increase in mean stream length in the highest orders of the subwatersheds. The Subwatersheds in the extreme eastern part of the basin are characterized by maximum relief, and gradients exhibit highest runoff and susceptibility to flooding and inundation. The lineament zones and associated tectonic activity control the drainage patterns and disposition of subwatersheds. The various linear and spatial morphometric parameters of each subwatershed are ranked based on their susceptibility to flooding. Subwatersheds III–VI are environmental hot spots, where implementation of flood control and mitigation measures should be urgently focused. The other subwatersheds steady are found to be in steady state equilibrium with components like climate, lithology, tectonics and topography that determine origin and development of a drainage basin. Major flooding rarely occurs in Mahe, in spite of favourable morphometric characters in other parts of the basin, and is attributed to permeable lateritic nature and dominant areal extent of SW IX in the western most extreme.

Keywords SRTM DEM · Mahe river basin · Morphometry · CalHypso Erosional signature

G. Gopinath (✉) · N. Ramisha · N. P. Jesiya
Geomatics Division, CWRDM, Kozhikode 673571, Kerala, India
e-mail: gg@cwrdm.org

A. G. Nair
Government Engineering College, Trivandrum, India

V. P. Singh et al. (eds.), *Hydrologic Modeling*, Water Science and Technology Library 81, https://doi.org/10.1007/978-981-10-5801-1_44

Introduction

Watershed is a natural hydrological entity which allows surface run off to define channel, drain, stream or river at a particular point (Kalyanjit et al. 2012). Morphometric analysis of a watershed provides a tool to characterize the watershed through the quantitative description of the drainage system (Strahler 1964). The morphometric assessment helps to elaborate a primary hydrological diagnosis in order to predict approximate behaviour of watershed if correctly coupled with geomorphology and geology. The hydrological response of a river basin can be interrelated with the physiographic characteristics of the drainage basin such as such as size, shape, slope, drainage density, size and length of streams (Chorley 1969). Hence morphometric analysis of watershed is an essential first step, towards basic understanding of watershed dynamics. To effectively interpret the morphometric parameters, the remote sensing and geographic information system-based techniques have been used. Remote sensing techniques are rapid, precise and effective in modern day morphometric studies (Kalyanjit et al. 2012). Geomorphic analysis from space has the advantage of allowing the use of quantitative methods for both data gathering and information extraction. Thus, satellite images are becoming useful and necessary in geomorphology, especially quantitative measurements performing geomorphic analysis. GIS have enhanced the applicability of geologic mapping when integrated with data obtained by remote sensing using a wide range of formats and scales.

Hypsometric analysis is the study of the distribution of horizontal cross-sectional area of a land mass with respect to elevation (Sivakumar et al. 2011). Morphology of a river basin plays primary role in the dynamics of surface and subsurface water runoff generation. It is also an essential tool to measure and represent the form of a watershed and its evolution. Hypsometric data were derived and analysed for each of the divided zone of Mahe river basin from 90 m SRTM DEM. Naturally, hypsometric analysis has been used to differentiate between erosional landforms at different stages during their evolution (Strahler 1952). Hypsometric integrals and hypsometric curves are important indicators of watershed conditions. The Shuttle Radar Topography Mission obtained elevation data on a near-global scale to generate the most complete high resolution digital topographic database of earth. Digital elevation model is a digital model or 3D representation of a terrain surface, commonly for a planet created from terrain elevation data. Present work focused on to evaluate the characteristics of Mahe river basin and to understand erosional topography of subwatersheds of river basin using advanced spatial technology in order to enhance the utilization of water resources for sustainable development of the basin area.

Study Area

Mahe River (also known as Mayyazhipuzha) flows through the state of Kerala and the coastal exclave of Mahe in Pondicherry. The river originates in the hills of Wayanad in the Western Ghats and traverses a total length of 54 km before culminating in the Arabian Sea at Mahe. The river passes through the villages of Naripetta, Vanimel, Iyyancode, Iringanoor, Tripangathur, Peringalam, Edachery, Kacheri, Eramala, Parakkadavu, kariyad, Olavilam, Kunnumakara, Azhiyoor and Mahe, thus covering an area of 394 km^2. Figure 1 shows the location map of Mahe river basin.

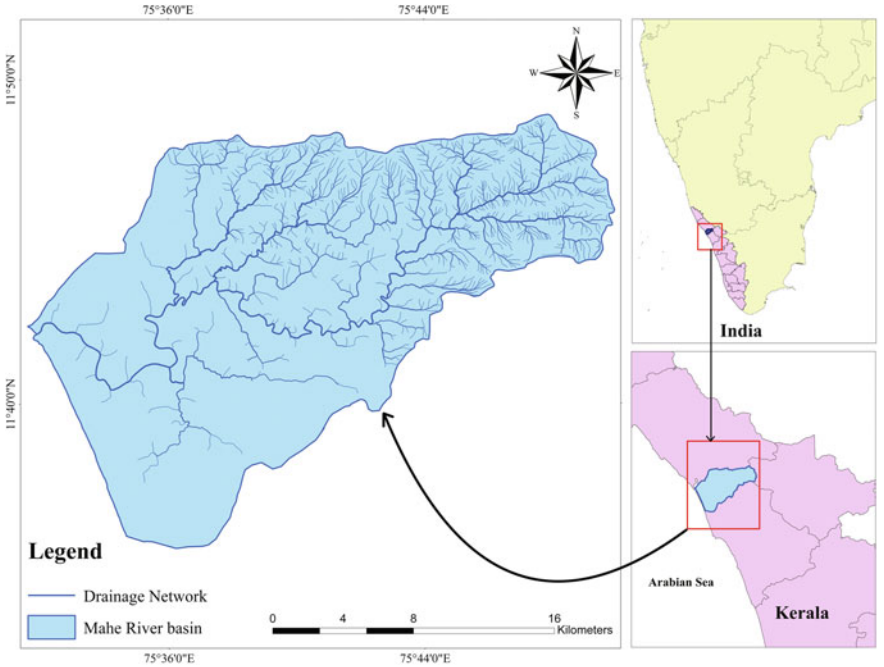

Fig. 1 Location map of Mahe river basin

Climate

The river basin has a wet and maritime tropical climate influenced by the seasonal heavy rains of the south-west summer monsoon and north-east winter monsoon. About 65% of the rainfall occurs during the first season (June to August), corresponding to the south-west monsoon, and the rest during the second season (September to December), corresponding to north-east monsoon. The average annual rainfall is 3,266 mm. The mean daily temperature ranges from 19.8 to 36.7 °C. Mean annual temperatures range from 25.0 to 27.5 °C in the coastal lowlands.

Materials and Methods

Survey of India toposheets at scale of 1: 50,000 (Toposheet No. 49 M/9, 49 M/6 & 10, 49 M/13 and 49 M/14) and SRTM DEM with a resolution of 90 m were used for the generation of data in the study. The NASA Shuttle Radar Topographic Mission (SRTM) has a resolution of 90 m at the equator and is provided with digital elevation data (DEMs) for over 80% of the globe. This data is currently distributed free of charge by USGS and is available for download from the National Map Seamless Data Distribution System, or the USGS ftp site. The SRTM data is available as 3 arc second (approx. 90 m resolution) DEMs. The DEM files have been mosaiced into a seamless near-global coverage (up to 60° north and south) and are available for download as 5° × 5° tiles, in geographic coordinate system—WGS84 datum. These files are available for download in both Arc-Info ASCII format and as GeoTiff, for easy use in most GIS and Remote Sensing software applications. In addition, a binary Data Mask file is available for download, allowing users to identify the areas within each DEM which has been interpolated.

The topographic maps were georeferenced and mosaiced using ERDAS IMAGINE 9.1. The shape files of Mahe river basin were delineated using Arc GIS 9.2. Entire networks of Mahe River get edited and various subwatersheds get separated using the editor tool as shape files. Calculation of areal and linear morphometric parameters of river basin using Arc GIS 9.2 gets preceded. For calculating relief parameters, DEM from SRTM 90 m resolution extracted using the extraction by Mask in Spatial Analyst tool of Arc GIS 9.2 was used. Filling of the DEM as reconditioning is used for filling the sinkholes in the DEM. It is done by fill in the hydrology option of Spatial Analyst tool. Subwatershed-wise extractions of DEMs get undergone to done the relief parameter calculation. Computation of basic characteristics required for morphometric analysis,

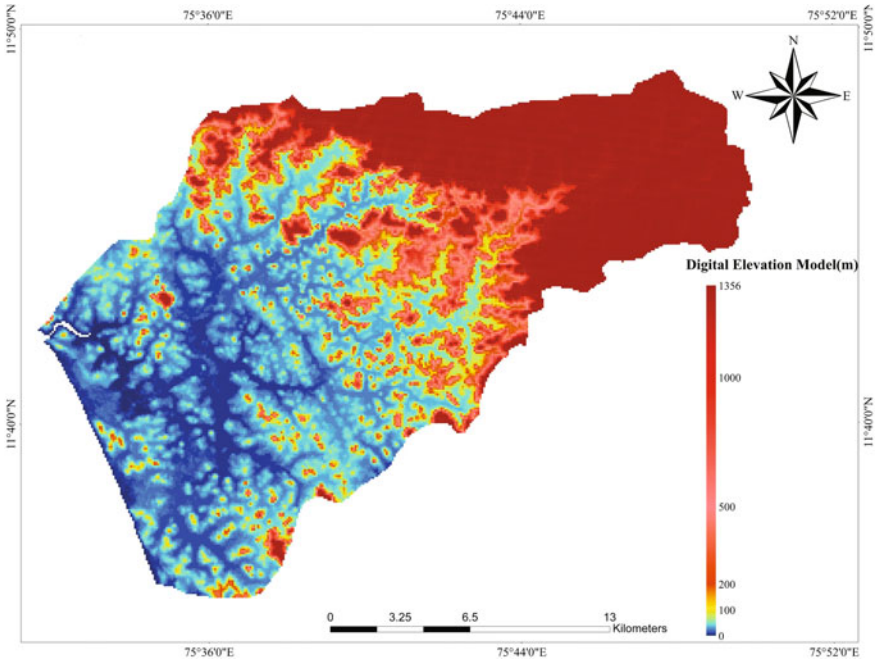

Fig. 2 Digital elevation model (DEM) of the river basin

ordering, lengths, area etc. were done in a GIS platform and using established mathematical equations (Gopinath et al 2015) parameters such as Stream Length Ratio (RL), Bifurcation Ratio (Rb), Drainage Density (Dd), Stream Frequency (Fs), Drainage Texture (T), Form Factor (Ff), Circularity Ratio (Rc), Elongation Ratio (Re), Constant of Channel Maintenance (C), Length of Overland Flow (Lo), Relief Ratio (Rr), Gradient Ratio (Gr) and Ruggedness number (Rn) were derived for each sub-watershed. Input for the hypsometric analysis is obtained from the shape files of dam for subwatersheds. Figures 2, 3 and 4 show DEM, slope and drainage pattern of the Mahe river basin; the CalHypso extension tool is used to perform hypsometric analysis. Hypsometric curves were automatically generated and hypsometric integral were calculated from DEM using Arc GIS extension known as CalHypso, makes the estimation process becomes easy and more accurate (Gopinath and Ashitha 2014).

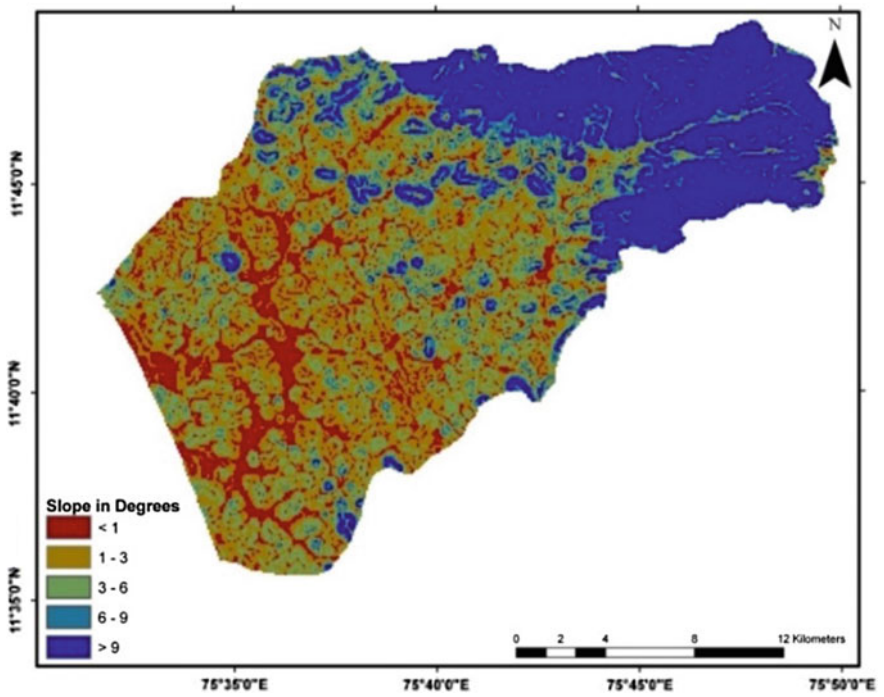

Fig. 3 Slope map of the study area

Results and Discussion

The present investigation includes morphometric analysis of drainage network and hypsometric analysis for studying the evolutionary development of landforms. Morphometric parameters calculated were grouped under (i) Linear parameters, (ii) Relief parameters and (iii) Areal parameters.

Basic Parameters

The total area projected upon a horizontal plane of basin contributing to cumulate of all order of basins is 431.06 km^2 and the areas of the each subbasin are as given in Table 1. Perimeter is the length of the boundary of the basin which can be drawn from topographical maps. The perimeter of the each subwatershed and basin length is given in Table 1. Basin area is hydrologically important because it directly affects the size of the storm hydrograph and the magnitudes of peak and mean runoff. The maximum flood discharge per unit area is inversely related to size (Chorley et al. 1957).

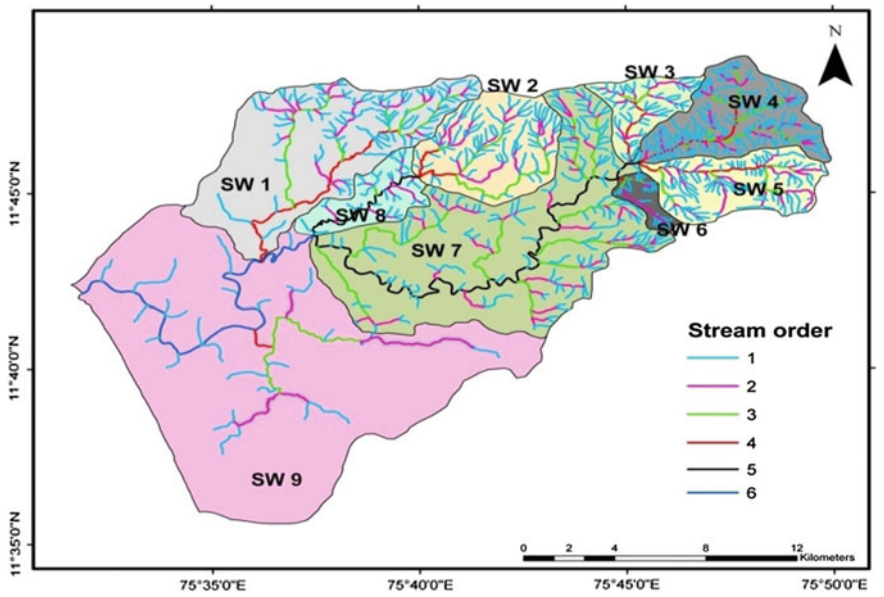

Fig. 4 Drainage network of Mahe river basin

Table 1 Basic parameters of the Mahe river basin

Subwatersheds	SW I	SW II	SW III	SW IV	SW V	SW VI	SW VII	SW VIII	SW IX	Basin
Area (A) km^2	59.61	28.69	11.42	27.44	22.81	4.27	96.41	12.93	167.48	431.06
Perimeter (P) km	38.83	20.58	16.80	25.34	21.90	10.26	58.40	18.67	66.99	100.06
Basin length (Lb) km	9.31	6.96	4.64	8.07	8.01	3.69	15.88	6.47	20.49	33.64

Linear Aspects

The linear aspect of the drainage network such as stream order (Nu), stream length (L), mean stream length (Lsm), stream length ratio (RL), bifurcation ratio (R) and mean bifurcation ratio were calculated and summarized in Tables 2a and b.

Morphometric analysis of Mahe River reveals it to be a sixth order basin with a total stream length of about 686 km and comprising of 909 stream segments (Fig. 4) of which, 693 are of first order, 159 are of second order, 40 are of third order, 8 are fourth order, two in fifth and one is indicating sixth order streams. First order stream segments contribute 76%, second order of 17% and the remaining stream segments include 7%. According to Chithra et al. (2011), the highest number of first order streams indicates the intensity of permeability and infiltration. The order wise total numbers of stream segments are known as the stream number.

Table 2 Linear aspects of the Mahe river basin

(a)

Subwatersheds		SW I	SW II	SW III	SW IV	SW V	SW VI	SW VII	SW VIII	SW IX	Basin
Total stream length of order u in km (L)	1	58	47.72	24.81	63.41	48.77	8.44	87.98	14.18	32.8	386.1
	2	15.05	13.63	8.24	11.81	14.68	3.45	29	6.43	11.73	114
	3	16.74	3.67	1.04	11.33	6.37	1.44	35.93	0.53	9.53	86.6
	4	12.09	4.04	4.08	5.93	5.92	0.284			1.55	33.9
	5							35.53	7.87		43.4
	6									21.46	21.5
	£Lu	101.88	69.06	38.17	92.48	75.74	13.614	188.44	29.01	77.07	685.5
Mean stream length in km (Lu/Nu)	1	0.6	0.7	0.5	0.5	0.5	0.4	0.6	0.4	1.1	0.58
	2	0.5	1.0	0.6	0.4	0.7	0.7	0.8	0.8	2.3	0.88
	3	1.9	0.9	0.3	1.6	1.1	0.7	0.4	0.5	4.8	1.76
	4	12.1	2.0	4.1	5.9	5.9	0.3			1.6	3.54
	5							35.5	7.9		4.82
	6									2.39	2.39
Number of streams (Nu) of different stream order (u)	1	100	73	55	131	95	22	154	33	30	693
	2	29	13	14	31	20	5	37	8	5	162
	3	9	4	3	7	6	2	9	1	2	43
	4	1	2	1	1	1	1			1	8
	5							1	1		2
	6									1	1
	£Nu	139	92	73	170	122	30	201	43	39	909
Nu/A		1.68	2.54	4.82	4.77	4.16	5.15	1.59	2.55	0.18	3.05

(b)

Parameters		SW I	SW II	SW III	SW IV	SW V	SW VI	SW VII	SW VIII	SW IX	Basin
Bifurcation ratio (Rb)	½	3.4	5.6	3.9	4.2	4.8	4.4	4.2	4.1	6.0	4.5
	2/3	3.2	3.3	4.7	4.4	3.3	2.5	4.1	8.0	2.5	4.0
	¾	9.0	2.0	3.0	7.0	6.0	2.0			2.0	3.44
	4/5										
	5/6										
	Mean	5.2	3.6	3.9	5.2	4.7	3.0	4.1	6.1	3.5	3.9
Stream length ratio (RL)	2/1	0.26	0.29	0.33	0.19	0.30	0.41	0.33	0.45	0.36	0.32
	3/2	1.11	0.27	0.13	0.96	0.43	0.42	1.24	0.08	0.81	0.61
	4/3	1.38	1.10	3.92	0.52	0.93	0.20			0.16	1.17
	5/4										
	6/5										
	Average	0.92	0.55	1.46	0.56	0.55	0.34	0.79	0.27	0.44	0.35

Horton (1945) laws of stream numbers state that the numbers of stream segments of each order form an inverse geometric sequence when plotted against order, and most drainage networks show a linear relationship with small deviation from a straight line.

Bifurcation Ratio (RB)

The average bifurcation ratio of area is 4.37. This means that on an average, there are 4.37 times as many channel segments to any given order as of the next higher order. A lower Rb range between 3 and 5 suggests that structure does not exercise a dominant influence on the drainage pattern (Table 2b). If the Rb is low, the basin produces a sharp peak in discharge and if it is high the basin yields low, but extended peak flow (Agarwal 1998). In this basin, the Rb values have been computed for the individual sub-basins of all orders. The average Rb values for first, second, third, fourth, fifth, sixth, seventh, eighth and ninth subwatersheds are 4.7, 3.62, 3.87, 5.22, 4.69, 2.97, 4.14, 6.06 and 3.5. Irregularities in the Rb values is due to the geological and lithological influence of the drainage basin (Strahler 1964). High bifurcation ratio might be expected in regions of steeply dipping strata and also may be due to more number of streams forming lesser number of higher order streams. Deviation from normal bifurcation ratios is noted in first, second, fourth, fifth, eighth and ninth subwatersheds. It indicates the effect of structures in the drainage pattern.

Total Stream Length (Lu)

Stream length is one of the most significant hydrological features of the basin as it reveals surface runoff characteristics. Streams of relatively smaller lengths are characteristics of areas with larger slopes and finer texture. Longer lengths of streams are generally indicative of flatter gradients. Generally, the total length of stream segments is more in first order streams and decreases as stream order increases. The total length of Mahe river basin is 685.5 km. Of this highest length is contributed by first order streams and the lowest by sixth order streams

Mean Stream Length (Lum)

Mean stream length is a dimensional property revealing the characteristic size of components of a drainage network and its contributing watershed surfaces (Strahler 1964). In the study area, mean stream length varies from 0.6 to 21.7.

Stream Length Ratio (RL)

The stream length ratio has an important relationship with the surface flow and discharge. Subwatersheds 1, 5 and 7 show an increasing trend in the stream length ratio from lower order to higher order indicating their mature geomorphic stage. Change in RL from one order to another indicates the late youth to mature stage of geomorphic development (Singh and Singh 1997).

The area of watershed is 431.06 km^2. Basin area is the direct outcome of the drainage development in a particular basin. The length of Mahe watershed has determined as 33.64 km.

Out of nine subwatersheds of Mahe river basin, SW III–VI possess high relief and gradient, with higher values for drainage density, stream frequency and drainage texture as well as lower values for length of overland flow and constant of channel maintenance (Table 3). The subwatershed IX comprising of coastal plain is the gentlest sloping (0.45). SW II and SW IV exhibit similar values of relief ratio,

Table 3 Areal aspects of the drainage basin

Parameters	SW I		SW II	SW III	SW IV	SW V	SW VI	SW VII	SW VIII	SW IX	Basin
Area (A) km^2	59.61		28.69	11.42	27.44	22.81	4.27	96.41	12.93	167.48	431.06
Perimeter (P) km	38.83		20.58	16.80	25.34	21.90	10.26	58.40	18.67	66.99	100.06
Basin length (Lb)	9.31		6.96	4.64	8.07	8.01	3.69	15.88	6.47	20.49	33.64
Drainage density (D)	1.71		2.41	3.34	3.37	3.32	3.19	1.95	2.24	0.46	2.44
Stream frequency (Fs)	2.33		3.21	6.39	6.20	5.35	7.03	2.08	3.33	0.23	4.02
Drainage texture (T)	3.99		7.72	21.37	20.88	17.76	22.40	4.07	7.46	0.11	11.75
Form factor (Ff)	0.69		0.59	0.53	0.42	0.36	0.31	0.38	0.31	0.40	0.44
Circularity ratio (Rc)	0.50		0.85	0.51	0.54	0.60	0.51	0.36	0.47	0.47	0.53
Elongation ratio (Re)	0.94		0.87	0.82	0.73	0.67	0.63	0.70	0.63	0.71	0.74
Basin shape (Bs)	0.16		0.24	0.41	0.29	0.35	0.86	0.16	0.50	0.12	0.34
Length of overland flow (Lo)	0.29		0.21	0.15	0.15	0.15	0.16	0.26	0.22	1.09	0.30
Constant of Channel Maintenance (C)	0.59		0.42	0.30	0.30	0.30	0.31	0.51	0.45	2.17	0.59

but the values of their drainage density, stream frequency, drainage texture, length of overland flow and constant of channel maintenance are different.

It happens due to the presence of larger proportion of regions with higher slope and elevation in SW IV compared to SW II (Figs. 2 and 3). The stream numbers, mean stream lengths and total lengths are related to stream orders in a geometric series. Such relations are in agreement with observations made by Horton (1945), Schumm (1956), Chorley et al. (1957) and other works. Strong correlation ($r = -0.990$, $r = -0.892$) are shown in the relations of stream number and total stream length with stream orders (Figs. 5 and 6). The strong relationship of these parameters with stream order indicates the uniformity of geological material particularly in the high relief portions of the basin. It is suggested that such a close correlation points to steady state equilibrium reached between the different morphometric parameters with components like climate, lithology and topography that determine origin and development of drainage basin (Strahler 1957).

However, the relationship between mean stream length and order deviates significantly from the ideal Hortonian trend as evidenced from the drop in correlation ($r = +0.55$) between these two parameters. The mean stream length abruptly increases from the theoretical trend in the higher orders of the basin (Fig. 6; Table 2a). These factors may account for the lower correlation between mean stream length and stream order in SW VII and SW VIII. The sixth order stream occurs only in the subwatershed IX, which has lower relief and gradient. Thus, the fundamental characters of a drainage basin (size, length, relief etc) are used to

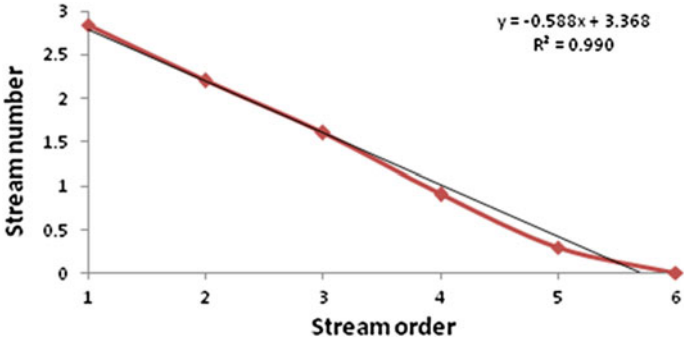

Fig. 5 Interrelationship between the stream order and stream number

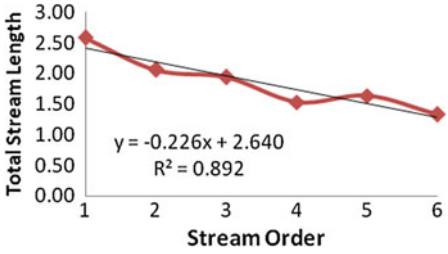

Fig. 6 Interrelationship between the stream order and total stream length

generalize features of landscape geometry which are then interpreted for the various fluvial processes. The Mahe river as a whole is characterized by fine texture, relief, ruggedness number, low drainage density (<5 km/km^2), constant of channel maintenance and length of overland flow and substantial values of stream frequency (>2 km^2) (Table 3). These features suggest that Mahe basin has relatively high spacing of streams, high run off, erosion potential and sediment load, low base flow, low percolation rate of water, low capacity for surface water storage. The resistant charnockite terrain of Western Ghats that forms the high relief parts of the basins is expected to spawn low drainage density (hence Lo and C) and stream frequency in SW III–VI. This is further enhanced by a humid climate that establishes a thick humus rich soil cover supporting lush canopied tropical evergreen forests that increase the infiltration of surface water. However, high values of Fs reveal the control of structural features in influencing the trend and number of lower order channels, consequently producing high surface run off in these subwatersheds. The subwatersheds VII and IX fall almost exclusively in terrain of lower relief that is dominant by Guruvayoor and Kadapuram sedimentary formations and patches of laterite. The less resistant nature of these materials accounts for the low stream number, stream frequency and drainage density of these subwatersheds.

Ruggedness number and drainage texture are the two vital indices of dissection and run off and resultant erosion and flooding susceptibility in drainage basin (Table 4). Drainage texture values of all high relief sub-basins III (21.37), IV (20.88), V (17.76) and VI (22.40) are >10 making them ultra fine textured. Ruggedness number too follows a similar trend exhibiting high value for SW V. In Mahe basin, this parameter is more influenced by the high relief of the subwatershed than drainage density. SW IX possesses lower value for these indices and is coarse textured. The slope values too, more or less correlate with the above parameters, signifying their influence in run off correlate with the above parameters signifying their influence in run off and flood potential of the subwatersheds. Vegetation encourages high permeability and consequently subdues surface run off and flood potential of the subwatersheds. Vegetation encourages high permeability and consequently subdues surface run off. However, the impact caused by dense vegetation in the basin particularly in the upper part is offset by high run off and low infiltration and base flow. Mahe basin as a whole is fine textured (11.75). The drainage pattern of the Mahe River shows dendritic and rectangular pattern (Fig. 4).

Table 4 Relief parameters of Mahe river basin

Parameters	SW I	SW II	SW III	SW IV	SW V	SW VI	SW VII	SW VIII	SW IX	Full basin
Relief (m)	781	980	950	1071	1266	926	1001	126	181	1356
Gradient	625	641	807	981	158	739	908	126	62	1356
Relief ratio	85.39	144.11	218.97	142.38	169.29	269.38	63.92	22.10	8.83	40.31
Gradient ratio	67.13	92.10	173.92	121.56	158.05	200.27	57.18	19.47	3.03	40.31
Ruggedness number	1.36	2.42	3.39	3.87	4.50	3.17	1.98	0.32	0.08	3.31

The dendritic nature is mainly exhibited along northern region, whereas south-western and north-eastern portions are characterized by rectangular pattern. Strong structural control is influenced by the dominance of rectangular pattern. The structural control on the drainage systems of the south-west coast of India is well known. At least five periods of tectonogenesis have occurred in the Pre-Cambrian terrain of the area resulting in different sets of fracture zones (Soman 2002). SW IX forms 39% of the total area of the Mahe watershed. The sudden fall in velocity and energy suffered by runoff and permeable nature results in the absorption and storage of significant amount of water in this subwatersheds. Major flooding occurs commonly in rivers of Kerala during the annual monsoonal rains causing destruction of life, property and inundation of large swaths of land. However, occurrence of major floods seldom occurs in Mahe River. As discussed, a large number of subwatersheds of this river are morphometrically conducive for high peak floods. Still, the relative rarity of floods in this river could be attributed to large areal extent and low gradient of SW IX which acts to inbuilt flood control mechanism. The velocity and energy of the surface flow from the high relief subwatersheds are checked when run off enter SW IX.

Hypsometric Attributes

Quantitative measurements allow geomorphologists to objectively compare different landforms and to calculate less straight forward parameters that may be useful for identifying a particular characteristic of an area (Keller and Pinter 1996). For each basin, hypsometric curves and hypsometric integral values are calculated in order to investigate erosional stage of the basins and the tectonic and lithological factors controlling it. The hypsometric curve of a catchment represents the relative area below a given altitude (Strahler 1952). It describes the distributions of elevations across an area of land, from one drainage basin to entire planet. These curves have been used to infer the stage of development of the drainage network (Keller and Pinter 1996).

The statistical characteristics of hypsometric analysis include hypsometric integral (Ea), hypsometric curve, coordinates of slope inflection points, hypsometric skewness, kurtosis (Luo 2000) as shown in Table 5. Hypsometric analysis has been carried out for the nine subwatersheds of Mahe river basin. The Hypsometric curves are shown in Fig. 7. Among the nine subwatersheds, I, II, VII, VIII and IX are in old age; whereas SW III–VI are in young stage. Hypsometric curves of old age basins are concave and curves of young stage basins are convex. Based on the hypsometric integral values, SW III–VI show values in the range of 0.3–0.6 indicating the young stage, while other subwatersheds have lower values indicating the old age. Higher hypsometric head (>0.61) is shown by SW III–VI pointing to

Table 5 Hypsometric parameters-hypsometric integral (HI), normalized height of hypsometric curve (*h*) at 0.2, 0.5, 0.8 and 0.9, maximum concavity (Eh) and coordinates of slope inflection point (*I*) given by a* and h*—of all the Nine subwatersheds of Mahe river

Subwatershed	Area (km^2)	HI (Ea)	Height of hypsometric curve				Eh	Coordinate of I		Geologic stage
			0.2	0.5	0.8	0.9		h*	A*	
1	59.61	0.097	0.11	0.05	0.04	0.01	0.72	0.14	0.13	Old
2	28.69	0.20	0.43	0.10	0.03	0.02	0.41	0.12	0.46	Old
3	11.42	0.48	0.67	0.49	0.29	0.18	0.12	0.27	0.83	Young
4	27.44	0.42	0.64	0.43	0.23	0.14	0.16	0.70	0.13	Old
5	22.81	0.42	0.61	0.42	0.27	0.17	0.19	0.61	0.20	Old
6	4.27	0.36	0.65	0.29	0.11	0.07	0.23	0.35	0.41	Young
7	96.41	0.08	0.09	0.05	0.04	0.03	0.72	0.08	0.20	Old
8	12.93	0.17	0.25	0.13	0.07	0.05	0.53	0.25	0.20	Old
9	167.48	0.14	0.19	0.13	0.10	0.09	0.69	0.23	0.08	Old

erosive processes at the upper reaches of these subwatersheds, whereas the other five subwatersheds show lower erosive processes. Hence subwatersheds of younger stage are prominent with erosion. But results of hypsometric integral values are in contradiction with other measurements. Integral values indicate a mature stage of development for SW III–VI, while the remaining (SW I, II, VII, VIII and IX) show old stage. Maximum concavity (Eh) of the nine subwatersheds are positive indicating highly eroded upland areas.

The results of hypsometric integral analysis are in contradiction to those of morphometric measurements, that indicates a young topography for the SW III–VI. While other hypsometric methods (curves and head values) largely corresponds to the trend of morphometric analysis with respect to stage of development of these subwatersheds. Integral values reveal an old highly eroded stage of landform development. These mutually incongruent results obtained could only be explained when further detailed studies into influence of parameters like landform, tectonics and climate on river basins are carried out. It is generally considered that higher values of morphometric parameters like drainage density, stream frequency, drainage texture, relief, and gradient and ruggedness number are indicative of younger topography where the stream activity is high. In the present study SW III–VI belongs to this category of high elevation and stream gradient which results in high erosion activity of streams. However, hypsometric analysis reveals a mature stage for these subwatersheds (III, IV, V and VI). The study was preliminary in nature; therefore, detailed studies are required before any concrete conclusion could be drawn on these aspects.

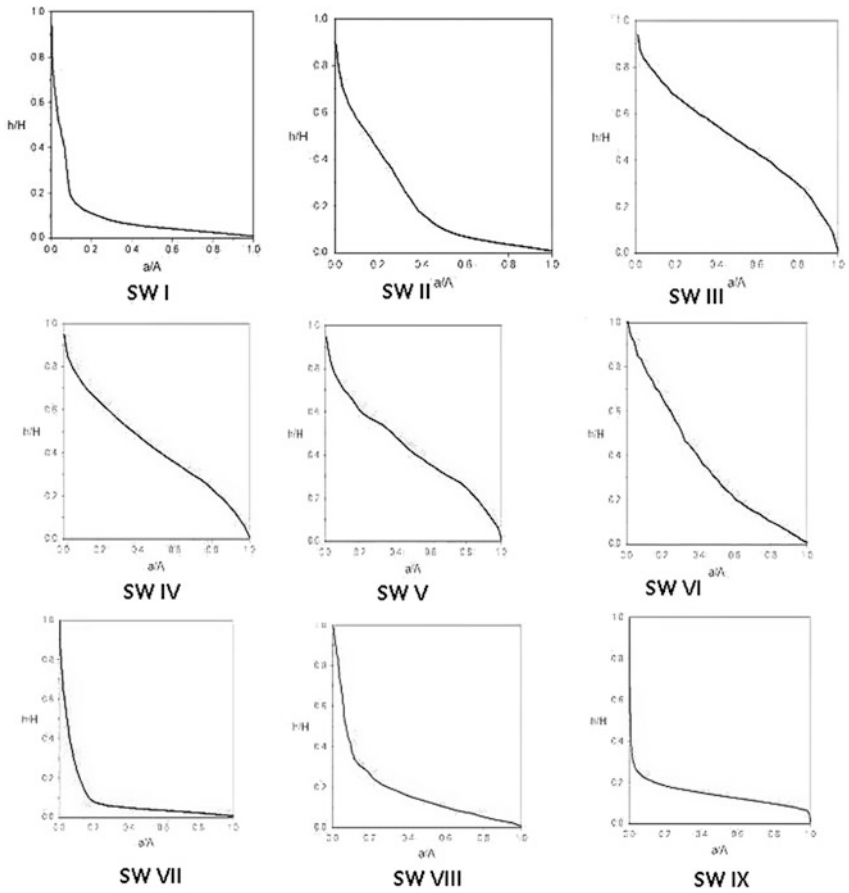

Fig. 7 Hypsometric curves of subwatersheds of Mahe river basin

Conclusion

The Mahe basin is identified as a sixth order basin with dendritic and rectangular patterns follows Hortonian laws are exhibiting a strong correlation ($r = -0.990$, $r = -0.892$) in relations of stream number and total stream length with stream orders. The correlation between mean stream length and stream order is lower ($r = -0.55$), probably due to an abrupt increase in mean stream length in the highest orders of the subwatersheds. This trend is more reflected in SW VII and VIII. Morphometric analysis of Mahe river basin reveals high run off, erosion potential and sediment load, low base flow, low percolation rate and low capacity for ground water storage. SW III–VI are characterized by highest surface run off and erosion, shortest time of concentration of surface flow, lowest base flow and infiltration for ground water recharge, rendering them most susceptible to high peak flooding and

inundation. On the other hand, SW I, II, VII, VIII and IX exhibit a reverse trend in the above parameters. The low relief and gradient of SW IX with its thick covering of permeable laterite and alluvium account for its lowest run off and susceptibility to flooding. The uncommon occurrence of major flooding in the Mahe in spite of favourable morphometric characters is attributed to permeable nature and dominant areal extent of SW IX. Thus, the subwatersheds III and IV are environmental hotspots where the focus of flood control and mitigation measures is to be urgently implemented. Hypsometric analysis of drainage basin development reveals that SW III–V are in youth stage of development, while remaining SW I, II and VI–IX show characters of old age. Hypsometric heads values also follow same trend. Morphometric and hypsometric analyses are indicative of younger topography for SW III–VI. It is suggested that in these subwatersheds, a steady state equilibrium is set up between different morphometric parameters and components like climate, lithology, tectonism and topography that control the origin and development of Mahe river basin.

Acknowledgements The authors are very thankful to the Executive Director, CWRDM (Centre for Water Resources Development and Management), Kozhikode, Kerala, India, for providing the facilities and guidance for preparation of the manuscript.

References

Agarwal CS (1998) Study of drainage pattern through aerial data in Naugarh area of Varanasi district, UP. J Indian Soc of Remote Sensi 26(4):169–175

Chithra C, Alaguraja P, Ganesh K, Yuvaraj D, Manvel M (2011) Watershed characteristics of Kundah sub basin using remote sensing and GIS techniques. Int J Geomat Geosci 2:311–335

Chorley RJ (1969) Introduction to physical hydrology. Methuen and Co., Ltd., Suffolk, p 211

Chorley RJ, Malm DE, Pogorzelski HA (1957) A new standard for estimating drainage basin shape. Amer J Sci 225:138–141

Gopinath G, Ashitha MK (2014) Elicitation of erosional signature of a tropical river basin with high-resolution stereo data. Appl Geomat 6:149–157. doi:10.1007/s12518-014-0127-

Gopinath G, Nair AG, Ambily GK, Swetha TV (2015) Watershed prioritization based on morphometric analysis coupled with multi criteria decision making. Arab J Geosci 2(2):01–17. doi:10.1007/s12517-015-2238-0

Horton RE (1945) Erosional development of streams and their drainage basins: Hydrophysical approach to quantitative morphology. Geolog Soc Am Bull 56:275–370

Kalyanjit S, Jha LK, Tiwari BK (2012) Morphometric analysis of a highland micro watershed in East Kasi hills district of Meghalaya India: using remote sensing and GIS techniques. J Geogr Reg Plan 5:142–150

Keller EA, Pinter N (1996) Active tectonics earthquake uplift and landscapes. Prentice Hall, New Jersey

Luo W (2000) Quantifying groundwater sapping processes with a hypsometric analysis technique. J Geophys Res 105:1685–1694

Schumm SA (1956) The relation of drainage basin relief to sediment loss. Int Assoc Sci Hydrol 36:216–219

Sivakumar V, Biju C, Deshmukh B (2011) Hypsometric analysis of Varattaru river basin of Harur Taluk, Dharmapuri district, Tamil Nadu, India, using geomatics technology. Int J Geomat Geosci 2:241–246

Singh S, Singh MC (1997) Morphometric analysis of Kanhar river basin. Nat Geogr J India 43 (1):31–43

Soman K (2002) Geology of Kerala. Geological Society of India, Bangalore, p 335

Strahler AN (1957) Dynamic basics of geomorphology. Bull Geol Soc Am 63:923–928

Strahler AN (1952) Hypsometric analysis of erosional topology. Geolog Soc Am Bull 63 (11):1117–1142

Strahler AN (1964) Quantitative geomorphology of drainage basins and channel networks. In: Chow VT (ed) Handbook of applied hydrology (Network; Mc Graw hill) section, pp 4–11

Streamflow Estimation Using SWAT Model Over Seonath River Basin, Chhattisgarh, India

Sabyasachi Swain, Mani Kant Verma and M. K. Verma

Abstract Water availability is one of the major issues that need attention from the present generation across the whole world to attain sustainability. Spatial variation of water resources and further climatic changes are main reasons for extremes such as droughts and floods. This urges for the quantification and forecasting of availability of the basic need of life. At the river basin level, streamflow is considered as the most crucial parameter to assess water availability, which can be estimated by simulation or modelling approaches. This article presents about the hydrological modelling using a semi-distributed model, namely soil and water assessment tool (SWAT), applied to Seonath river basin, Chhattisgarh, India. The climate forecasting system reanalysis (CFSR) meteorological data for the period of 1979–2014 (35 years) is used and the runoff is generated, which is calibrated using the observed flow at the basin outlet. The results reveal the observed flow and modelled flow to be very poorly correlated. The major causes of such mismatch are identified, and possible improvement options are discussed.

Introduction

Seonath basin is the largest sub-basin of Mahanadi river basin, and it covers a significant portion of the state Chhattisgarh, India. The various problems related to the basin are not being given much attention. Like most parts of India, majority of

S. Swain (✉)
Inter-Disciplinary Programme in Climate Studies, Indian Institute of Technology Bombay, Mumbai 400076, India
e-mail: sabyasachiswain16@gmail.com

M. K. Verma · M. K. Verma
Department of Civil Engineering, National Institute of Technology Raipur, Raipur 492010, India
e-mail: manikverma.ce@nitrr.ac.in

M. K. Verma
e-mail: mkseem670@gmail.com

V. P. Singh et al. (eds.), *Hydrologic Modeling*, Water Science and Technology Library 81, https://doi.org/10.1007/978-981-10-5801-1_45

population in Chhattisgarh is also directly dependent on agriculture for fulfilling their basic amenities. Although Mahanadi basin is highly vulnerable to flooding, the impacts of flood are never so thought provoking for Chhattisgarh. But the rainfall anomalies leading to erratic streamflow may be a cause of concern and responsible for the problems of water scarcity. According to the report of the National Commission for Integrated Water Resources Development, Government of India, various countries have been classified for water scarcity on basis of per capita annual water resource (AWR). The countries with per capita AWR less than 1000 m^3 are regarded to be in water stressed conditions. The number of countries in water stressed condition in 1990 was 20, which is expected to be detrimental to cause two-third of world population to face water stressed condition by 2050 (Gosain et al. 2006). Furthermore, according to IPCC (2007) reports, the global surface warming has occurred at a rate of 0.56–0.92 °C during the period 1906–2005, and impact of climate change may become severe to cause reduction in the freshwater availability. They have also predicted the decrease in annual average runoff and availability of water up to 30% by middle of the twenty-first century. Also, the impact of climate changes will be severe for developing countries like India (Gosain et al. 2006; Swain 2014; Swain et al. 2015).

At the river basin level, streamflow is considered to be the measure for estimating the water availability. For estimation of streamflow, various models have been developed. In the last two decades, the hydrological models are extensively used to assess the water availability and prediction of extremes. Soil and water assessment tool (SWAT) is one such model, which incorporates on Digital Elevation Model, land use map, soil map, and meteorological parameters to generate runoff at basin scale. The model uses two basic equations for estimating runoff i.e. soil conservation services—curve number (SCS-CN) method and Green Ampt–Mein Larsen equations (Arnold et al. 1998; Abbaspour et al. 2009; Setegn et al. 2010; Bekele and Knapp 2010).

Study Area and Data Used

The study area is Seonath basin, having an area of 30,560 km^2. The entire basin is within Chhattisgarh state, India. This basin is situated between 20° 16′N to 22° 41′ N Latitude and 80° 25′E to 82° 35′E Longitude. The predominant soil of watershed is sandy clay loam. Sandy loam, loam, and clay are also found in the watershed. Seonath basin has a tropical wet and dry climate, and temperatures remain moderate throughout the year, except from March to June, which can be extremely hot (Verma et al. 2016). The area under Seonath basin is mainly fertile plains.

The meteorological data (rainfall, maximum and minimum temperature, wind speed, solar radiation and relative humidity) are collected for 24 stations, as shown in Fig. 1. These data were downloaded from climate forecasting system reanalysis (CFSR) database simulated by National Centers for Environmental Prediction (NCEP) and Texas A & M University, USA. Digital elevation model (DEM) is

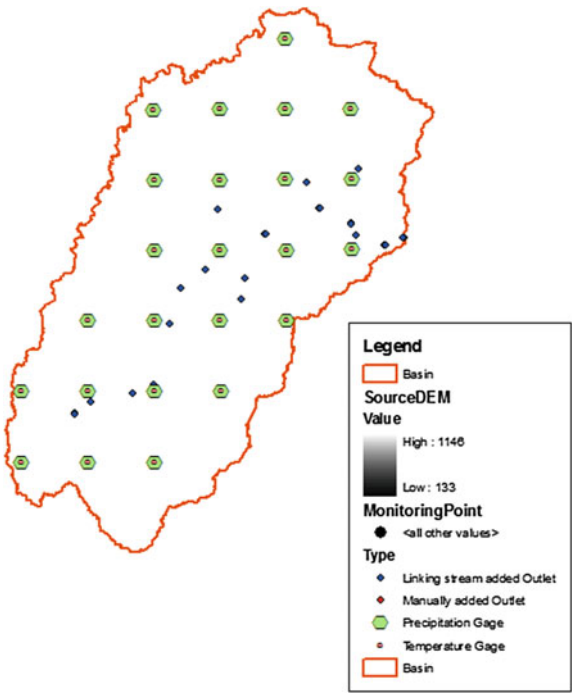

Fig. 1 Location of CFSR stations in Seonath basin

downloaded from ASTER website (30 m Resolution) which was used in watershed delineation. Soil map is collected from Chhattisgarh Council of Science and Technology (CCOST), Raipur (C.G.), which was used in HRU analysis. Land use/land cover map is downloaded from BHUVAN (LISS III), National Remote Sensing Centre (NRSC). Topographical sheets (for creating shape files) were collected from Survey of India.

Methodology

The various steps of running SWAT model are as follows: (1) automatic watershed delineation, (2) hydrological response unit (HRU) analysis, (3) write input tables, and, (4) SWAT simulation. (5) calibration using SWAT-CUP.

First of all, the SWAT project is set up with ArcGIS as an interface. Then, automatic watershed delineation is carried out from the DEM provided as input file. Figure 2 shows the process of delineating the watershed from DEM. The outlet point of the basin is also fixed by SWAT automatically based on DEM. In the second step, analysis of hydrologic response units is carried out through the model. The land use and soil map of the basin is provided as input, and based on these, the whole basin is subdivided into various homogenous units. The HRU is obtained

based on the response of soil and land use of different parts of the basin. The reclassification of both the maps is done in this step. Figures 3 and 4 present the reclassification of the input land use/land cover and soil map, respectively. Tables 1 and 2 represents the attribute table of the LULC map before and after reclassification, respectively. After HRU analysis, comes the writing of input tables. In this step, the weather generator data and all the input meteorological data are written in specified tabular format, for the simulation to run.

In the next step, the model is run for the required period i.e. from January 1979 to July 2014. The simulation is carried for the duration whose required data are already provided as input for SWAT simulation. We have to provide the starting and ending date of the streamflow that we require as output. The streamflow data can be generated as hourly, daily, monthly or annually output. Here, it has been printed for daily output, where the rainfall distribution is chosen as skewed normal distribution. At the end of this step, when the execution is successfully completed, the output file of streamflow at basin outlet for the required duration will be generated, which needs to be checked with that of actual observed runoff at the outlet so as to calibrate the model.

The calibration of the SWAT model is made by a software soil and water assessment tool—calibration and uncertainty procedures (SWAT-CUP), which is used for the auto-calibration of SWAT simulated outputs. The software uses various types of tools out of which Glue, Sufi2 and ParaSol are widely used. For the auto-calibration of the SWAT model for Seonath basin, Sufi2 is used here. The number of simulations carried was 50, and out of them, the closest values to that of observed data is considered.

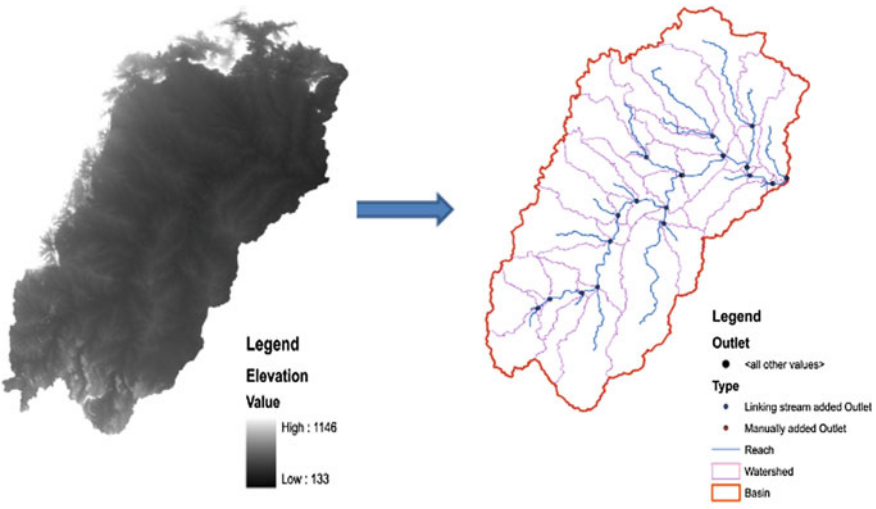

Fig. 2 Automatic watershed delineation from DEM through SWAT

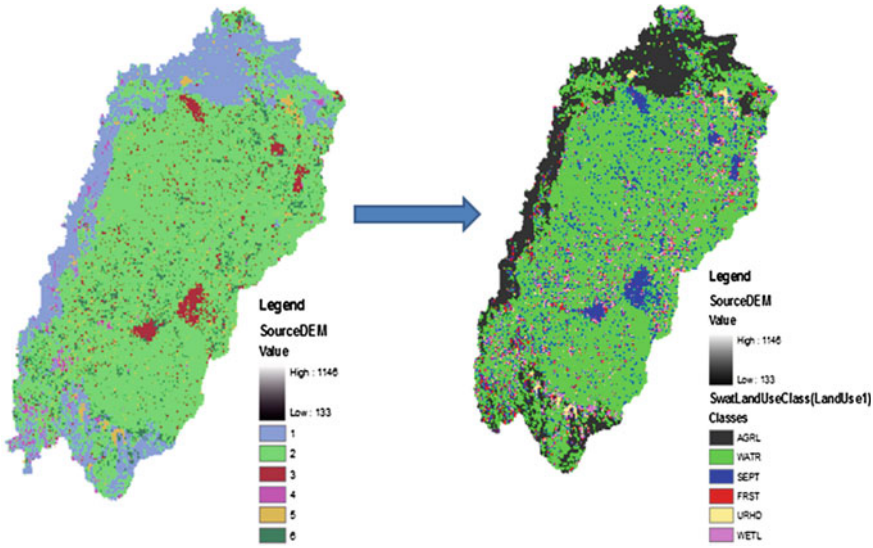

Fig. 3 LULC map reclassification in HRU analysis

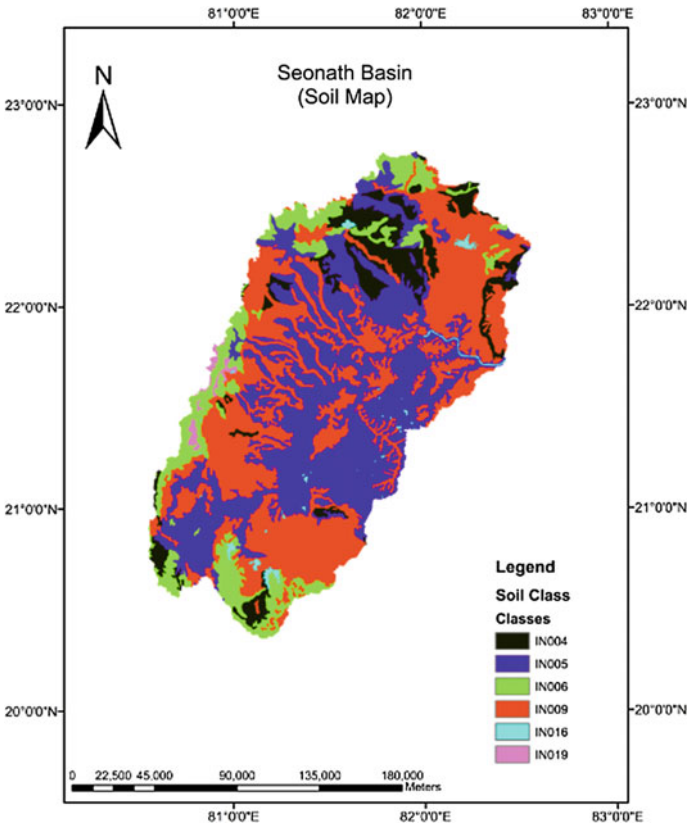

Fig. 4 Reclassified soil map through HRU analysis

Table 1 Attribute table before reclassification of LULC

Row ID	Value*	Count	LU_CODE
0	1	8439	Forest
1	2	27,232	Agricultural land
2	3	2277	Build up
3	4	579	Tree clad area
4	5	1139	Water bodies
5	6	2170	Wastelands

Table 2 Attribute table after reclassification of LULC

Row ID	Value*	Count	Object ID	LUArea1.Area	LUArea1.LUSWAT
0	1	6,677,863	0	19.843	AGRL
1	2	22,033,842	1	65.472	WATR
2	3	1,843,005	2	5.476	SEPT
3	4	428,189	3	1.272	FRST
4	5	917,401	4	2.726	URHD
5	6	1,753,325	5	5.21	WETL

Results and Discussion

Out of the 24 sub-basins, the runoff is generated at sub-basin numbered 15 (i.e. the outlet of the entire basin is located in sub-basin 15 after SWAT auto-delineation). The actual observed values of runoff at the outlet and number of simulations required have to be provided as input for SWAT-CUP, and it was given 50 for this case. More the number of simulations, more accurate is the calibration. At the end of the simulation, the model gives the 43rd simulation as the best simulation, which is closest to the observed values. But the results are having a clear mismatch with respect to that of observed data. The Nash–Sutcliffe efficiency and the coefficient of determination are found to be 0.07 and 0.31, respectively, which denotes that the model does not produce satisfactory results for the basin.

There are some prominent reasons for such a disagreement between the observed and the model generated streamflow. First of all, the meteorological data used are collected from CFSR, and the observed runoff data is collected from Water Resources Department, Chhattisgarh. As there was no meteorological data available for temperature, wind speed, etc., from WRD, the CFSR data were used for analysis. This might have accounted for the mismatch. Secondly, the observed data is collected at Jondhra outlet, whose location is not congruent to that of the outlet denoted by SWAT after automatic watershed delineation. Although they are close, since their exact locations are different, addition or loss to the streamflow may occur in the distance between these two points, which may definitely affect the final

output. Thirdly, the default values of HRU thresholds have been used in the model, which may contradict to the original case. Moreover, there might also be errors in streamflow data during collection due to lack of updated instruments and human errors.

Conclusion

The problem of water availability has raised itself as a crucial issue, which is addressed by assessing the runoff over Seonath river basin, Chhattisgarh, India. SWAT model was applied to the basin for a period of 35 years to check if the model can be used for future application. With a number of assumptions and using default values, the model was run and the streamflow generated by the model clearly showed disagreement with that of observed runoff values. The Nash–Sutcliffe efficiency and coefficient of determination were less than 0.5, for the best-matched simulation. The various causes of the mismatch have been discussed, which needs to be focused upon before the application of the model for further use over the basin.

Acknowledgements We would like to express our gratitude to the reviewers whose suggestions were immensely helpful to improve the quality of this article. We also acknowledge the organisations who have provided valuable data for this research work. Finally, we would like to thank all those individuals who have directly or indirectly helped us to complete this work.

References

Abbaspour KC, Faramarzi M, Ghasemi SS, Yang H (2009) Assessing the impact of climate change on water resources in Iran. Water Resour Res 45:W10434

Arnold JG, Srinivasan R, Muttiah RS, Williams JR (1998) Large area hydrologic modeling and assessment part I: model development, no 1, pp 73–89

Bekele EG, Knapp HV (2010) Watershed modeling to assessing impacts of potential climate change on water supply availability. Water Resour Manage 24(13):3299–3320

Gosain AK, Rao S, Basuray D (2006) Climate change impact assessment on hydrology of Indian river basins. Curr Sci 90(3):346–353

IPCC (2007) Fourth assessment report. Intergovernmental panel on climate change

Setegn SG, Srinivasan R, Melesse AM, Dargahi B (2010) SWAT model application and prediction uncertainty analysis in the Lake Tana Basin, Ethiopia. Hydrol Process 24:357–367

Swain S (2014) Impact of climate variability over Mahanadi river basin. Int J Eng Res Technol 3 (7):938–943

Swain S, Verma M, Verma MK (2015) Statistical trend analysis of monthly rainfall for Raipur district, Chhattisgarh. Int J Adv Eng Res Stud IV(II):87–89

Verma M, Verma MK, Swain S (2016) Statistical analysis of precipitation over Seonath river basin, Chhattisgarh, India. Int J Appl Eng Res 11(4):2417–2423

Revisiting the Soil Conservation Service Curve Number Method

S. K. Mishra, Vijay P. Singh and P. K. Singh

Abstract The Soil Conservation Service Curve Number (SCS-CN) [now called as Natural Resource Conservation Service Curve Number (NRCS-CN)] method is globally popular for estimating runoff from rainfall events because of its simplicity and ease of application for gauged and ungauged watersheds. Its popularity lies in its simplicity as well as its ability to account for some key runoff-producing watershed characteristics, such as soil type, land use, hydrologic condition, and antecedent soil moisture condition (AMCs). Recently, the method has undergone through a number of hydrologic and structural modifications through (i) soil moisture accounting (SMA) procedures; (ii) curve number (CN) estimation and their conversion techniques; (iii) linear/nonlinear initial abstraction (I_a) and maximum soil moisture retention relationships (S); (iv) storm duration and dynamic versus static infiltration; (v) slope and CN relationships; and finally (vi) overall renewal of SCS-CN methodology through different concepts and theories. This paper revisits the popular SCS-CN methodology in the context of recent modifications along with various applications based on these modifications and much beyond that it explores the newer fields of application in hydrologic sciences.

Keywords SCS-CN method · Soil erosion and sedimentation · Sediment graph Water quality and metal partitioning

S. K. Mishra (✉)
Department of Water Resources Development & Management,
Indian Institute of Technology Roorkee, Roorkee 247667, UK, India
e-mail: skm61fwt@gmail.com

V. P. Singh
Department of Biological and Agricultural Engineering and Zachry Department
of Civil Engineering, Texas A&M University, College Station, TX 77843-2117, USA

P. K. Singh
Water Resources Systems Division, National Institute of Hydrology,
Roorkee 247667, UK, India

V. P. Singh et al. (eds.), *Hydrologic Modeling*, Water Science
and Technology Library 81, https://doi.org/10.1007/978-981-10-5801-1_46

Introduction

The USDA soil conservation service (SCS) (now called as the natural resources conservation service, NRCS) curve number (CN) method, often designated as the SCS-CN method, was first published in 1956 in Sect. 4 of the *National Engineering Handbook* (SCS 1956). The SCS-CN method was originally developed for predicting runoff from small agricultural watersheds for individual rainfall events but has since been revised several times and extended to rural, forest, and urban watersheds and is now applied to a range of environments, including soil erosion and water quality modeling (Walker et al. 2006; Mishra et al. 2006b; Singh 2013). Although many hydrologic models are available for the estimation of direct runoff from storm rainfall, most models are limited because of their intensive input data and calibration requirements, and, therefore, the SCS-CN method seems to fulfill our demands with few data requirements and clearly stated assumptions. The method has also been coupled with several standard hydrologic software packages such as storm water management model (SWMM) (Metcalf and Eddy 1971); constrained linear simulation (CLS) (Natale and Todini 1976a, b); hydrologic engineering center-1 (HEC-1) (HEC 1981); agricultural nonpoint source model (AGNPS) (Young et al. 1989); chemicals, runoff, and erosion from agricultural management systems (CREAMS) (Smith and Williams 1980); areal nonpoint source watershed environment response simulation (ANSWERS) (Beasley and Huggins 1980); and soil and water assessment tool (SWAT) (Neitsch et al. 2002).

Since its inception, the method has witnessed myriad applications in various fields of hydrology, even for those it was not originally intended to be applied. A curve number (CN) that is descriptive of major runoff-producing characteristics of watershed such as soil type, land use/treatment classes, hydrologic soil group, hydrologic condition, most importantly the antecedent moisture condition (AMC) is required in the method. The wider applicability of the SCS-CN methodology can be attributed to its multifaceted characteristic inherited such as its simplicity, ease of use, major runoff-producing characteristics (as enumerated above), widespread acceptance, and the significant infrastructure and institutional momentum for this procedure within NRCS (Garen and Moore 2005). Recently, Singh (2013) revisited SCS-CN methodology using entropy theory (Kapur and Kesavan 1992; Singh 2013). More recently, the SMA procedure has been a key component of transmutation of the existing SCS-CN method to various improved variants (Michel et al. 2005; Sahu et al. 2007, 2010; Ajmal et al. 2015; Singh et al. 2015).

Therefore, keeping in view of the aforementioned discussion, this paper revisits the popular SCS-CN methodology in the context of recent modifications along with various applications based on these modifications and different fields of applications and much beyond that it also explores the newer fields of application in hydrologic sciences.

Background of SCS-CN Methodology

The SCS-CN method was developed in 1954, and it is documented in Sect. 4 of the National Engineering Handbook (NEH-4) published by the Soil Conservation Service (now called as Natural Resource Conservation Service), US Department of Agriculture in 1956. The document has since been revised in 1964, 1965, 1971, 1972, 1985, and 1993. It computes the volume of surface runoff for a given rainfall event from small agricultural, forest, and urban watersheds (SCS 1986). The SCS-CN method is the result of exhaustive field investigations carried out during the late 1930s and 1940s and the works of several investigators, including Mockus (1949), Sherman (1949), Andrews (1954), and Ogrosky (1956). The passage of Watershed Protection and Flood Prevention Act (Public Law 83-566) in August 1954 led to the recognition of the method at the Federal level, and the method has since witnessed myriad applications all over the world.

The SCS-CN method is a conceptual model of hydrologic abstraction of storm rainfall, supported by empirical data. Its objective is to estimate direct runoff volume from storm rainfall depth, based on a curve number CN (Ponce and Hawkins 1996). Its popularity is rooted in convenience, simplicity, authoritative origin, and responsiveness to four readily grasped catchment properties, viz., soil type, land use/treatment, surface condition, and antecedent moisture condition. To date, there has been no alternative that possesses so many advantages, which is why it has been and continues to be commonly used, whether or not it is, in a strict scientific sense, appropriate. Though appealing to many practising hydrologists by its overwhelming simplicity, the method contains some unknowns and inconsistencies (Chen 1982). Due to its origin and evolution as agency methodology, it is effectively isolated from the rigors of peer review. The information given in NEH-4 was not intended to be exhaustive. No complete account of the method's foundation is available to date, despite some noteworthy attempts made by Ponce and Hawkins (1996), Mishra and Singh (2003a), and Garen and Moore (2005), Chung et al. (2010). The method has been structurally diagnosed and critically reviewed by several researchers worldwide for its enhanced performance without disfiguring its inherent simplicity. The diagnostic works of Rallison and Miller (1982), Chen (1982), Ponce and Hawkins (1996), Mishra and Singh (1999, 2002a, b, 2003a, b, 2004a, b), Michel et al. (2005), and Chung et al. (2010) are noteworthy. Based on the works of Ponce and Hawkins (1996) and Mishra and Singh (2003a), it was concluded that the SCS-CN method is a conceptual model of hydrologic abstraction of storm rainfall supported by empirical data dedicated to estimate direct runoff volume based on a single numeric parameter CN.

The SCS-CN method is based on the water balance equation along with two fundamental hypotheses. The first hypothesis equates the ratio of actual amount of direct surface runoff (Q) to the total rainfall (P) (or maximum potential surface runoff) to the ratio of actual infiltration (F) to the amount of the potential maximum retention (S). The second hypothesis relates the initial abstraction (I_a) to S, also described as potential post-initial abstraction retention (McCuen 2002).

(a) Water balance equation

$$P = I_a + F + Q \tag{1}$$

(b) Proportional equality (first hypothesis)

$$\frac{Q}{P - I_a} = \frac{F}{S} \tag{2}$$

(c) I_a–S relationship (second hypothesis)

$$I_a = \lambda S \tag{3}$$

where P = total rainfall; I_a = initial abstraction; F = cumulative infiltration excluding I_a; Q = direct runoff; and S = potential maximum retention or infiltration. The values of P, Q, and S are in depth or volumetric dimensions, while the initial abstraction coefficient (λ) is dimensionless. In a typical case, a certain amount of rainfall is initially abstracted as interception, evaporation, infiltration, and surface storage before runoff begins. A sum of these four elements at initiation of surface runoff is usually termed "initial abstraction."

The first hypothesis (Eq. 2) is primarily a proportionality concept, and the second hypothesis (Eq. 3) is a linear relationship between initial abstraction I_a and potential maximum retention S. Coupling Eqs. (1) and (2), the expression for Q can be written as:

$$\begin{aligned} Q &= \tfrac{(P-I_a)^2}{P-I_a+S}; \quad \text{for } P \geq I_a; \\ &= 0; \qquad\quad \text{otherwise} \end{aligned} \tag{4}$$

Equation (4) is the general form of the popular SCS-CN method and is valid for $P \geq I_a$; $Q = 0$ otherwise.

For $\lambda = 0.2$, the coupling of Eqs. (3) and (4) results in:

$$Q = \frac{(P - 0.2S)^2}{P + 0.8S} \tag{5}$$

Equation (5) is well recognized as a popular form of the existing SCS-CN method. Thus, the existing SCS-CN method with $\lambda = 0.2$ is a one-parameter model for computing surface runoff from daily storm rainfall, having versatile importance, utility, and vast untapped potential. The parameter S of the SCS-CN method depends on soil type, land use, hydrologic condition, and antecedent moisture condition (AMC). Similarly, the initial abstraction coefficient λ is frequently recognized as a regional parameter depending on geologic and climatic factors. Many other studies carried out in the USA and other countries (SCD 1972; Springer et al.

1980; Cazier and Hawkins 1984; Ramasastri and Seth 1985; Bosznay 1989) report λ to vary in the range of (0, 0.3). Hawkins et al. (2001) suggested that the value of $\lambda = 0.05$ gave better fit to data and is more appropriate for use in runoff calculations. Since the existing SCS-CN method assumes λ to be equal to 0.2 for practical applications, it has frequently been questioned for its validity and applicability (Hawkins et al. 2001), invoking many researchers to carry out a critical examination of the I_a–S relationship for pragmatic applications (Mishra and Singh 2004b).

Mockus (1949) described the physical significance of parameter S of Eq. (6) as "it is a constant and is the maximum difference of (P − Q) that can occur for the given storm and watershed characteristics". The parameter S is limited by either the rate of infiltration at the soil surface or the amount of water storage available in the soil profile, whichever gives its smaller value. Since S can vary in the range of $0 \leq S \leq \infty$, it is mapped onto a dimensionless curve number CN, varying in a more appealing range $0 \leq \text{CN} \leq 100$, as:

$$S = \frac{25400}{\text{CN}} - 254 \tag{6}$$

where S is in mm. The difference between S and CN is that the former is a dimensional quantity (L), whereas the latter is nondimensional. The highest possible numerical value of CN (i.e., 100) symbolizes a condition of zero potential maximum retention ($S = 0$), which in a real physical situation represents an impermeable watershed. On the contrary, the lowest possible numerical value of CN indicates a situation of highest potential maximum retention ($S = \infty$), reflecting a physical situation of an infinitely abstracting watershed, which remains an unlikely situation in real-world conditions.

Advantages and Disadvantages of SCS-CN Methodology

The major advantages and disadvantages of SCS-CN methodology are summarized as below.

Major advantages:

- It is a simple, predictable, stable, and lumped conceptual model.
- It relies on only one parameter, CN, and is well suited for ungauged situations.
- It is the single available technique for wider applications in the majority of computer-based advanced hydrologic simulation models (Singh 1995).
- It responds to four readily grasped catchment properties: soil type, land use/treatment, surface condition, and antecedent moisture condition.
- It requires only a few basic descriptive inputs that are convertible to numeric values for estimation of direct surface runoff.
- The technique has tremendous capabilities for its adoption toward environmental and water quality modeling.

- It is well compatible with recent GIS and remote sensing tools in hydrologic applications.

Major disadvantages:

- Choice of fixing the initial abstraction coefficient $\lambda = 0.2$ leads to preempted regionalization based on geologic and climatic conditions.
- The method has no explicit provisions for spatial scale effects on CN, which remains highly sensible and truly governs the runoff.
- The discrete relationship between CN and AMC classes permits a sudden jump in CN, resulting in an equivalent quantum jump in computed runoff.
- It does not have any expression of time and ignores the impact of rainfall intensity and its temporal distribution.
- It lacks the expression for antecedent moisture, which plays a crucial and significant role in governing runoff generation process.

CN Estimation Techniques

The errors in CN may have much more consequences on runoff estimation than errors of similar magnitude in storm rainfall P (Hawkins 1975). This indicates the importance of accurate CN estimation in SCS-CN methodology. However, despite widespread use of SCS-CN methodology, an accurate estimation of CN has been a topic of discussion among hydrologists worldwide (Hawkins 1978; Chen 1982; Bonta 1997; Mishra and Singh 2006). In hydrologic literature, there are three different procedures available to compute CN for a given rainfall-runoff records, i.e., (i) using NEH-4 Table, (ii) ordered P and Q data (asymptotic CN estimation), and (iii) derived frequency distribution (Hjelmfelt 1980; Bonta 1997). A detailed diagnosis and description of these methods can be found in Mishra and Singh (2003a). Still, there has been no agreement advocating a single-CN procedure based on rainfall-runoff data (Soulis and Valiantzas 2013).

For any change in AMC (say from AMC_I to AMC_{III}) on a given catchment, a sudden jump in CN value (i.e., from CN_I to CN_{III}) invariably occurs, and this variability is discontinuous in nature, which ultimately results in a sudden jump in computed runoff. Thus, indirectly, it gives a reflection of the discrete nature of CN–AMC relationship. Depending on five-day antecedent rainfall, CN_{II} is convertible to CN_I and CN_{III} using the relationships given by Sobhani (1975), Hawkins et al. (1985), Neitsch et al. (2002), and Mishra et al. (2008) and also directly from the NEH-4 tables (SCS 1972; McCuen 1982, 1989; Ponce 1989; Singh 1992; Mishra and Singh 2003a). Mishra et al. (2008) compared CN conversion formulae (Table 1) developed by Sobhani (1975), Hawkins et al. (1985), Chow et al. (1988), and Neitsch et al. (2002) and found the Neitsch formulae to exhibit poorest correspondence with NEH-4 values taken as target values. The Sobhani formula best corresponded in CN_I-conversion, and the Hawkins formula in CN_{III}. However,

Table 1 CN conversion formulae

Model	AMCI	AMC III
Sobhani (1975)	$CN_I = \frac{CN_{II}}{2.334 - 0.01334 CN_{II}}$	$CN_{III} = \frac{CN_{II}}{0.4036 + 0.005964 CN_{II}}$
Hawkins et al. (1985)	$CN_I = \frac{CN_{II}}{2.281 - 0.01281 CN_{II}}$	$CN_{III} = \frac{CN_{II}}{0.427 + 0.00573 CN_{II}}$
Chow et al. (1988)	$CN_I = \frac{4.2 CN_{II}}{10 - 0.058 CN_{II}}$	$CN_{III} = \frac{23 CN_{II}}{10 + 0.13 CN_{II}}$
Neitsch et al. (2002)	$CN_I = CN_{II} - \frac{20(100 - CN_{II})}{\{100 - CN_{II} + \exp[2.533 - 0.0636(100 - CN_{II})]\}}$	$CN_{III} = CN_{II} \exp\{0.0067\,3(100 - CN_{II})\}$
Mishra et al. (2008)	$CN_I = CN_{II} - \frac{20(100 - CN_{II})}{2.274 - 0.012754 CN_{II}}$	$CN_{III} = \frac{CN_{II}}{0.430 + 0.0057 CN_{II}}$

in field application, Mishra et al. (2008) model performed best of all. However, more recently, to negate the classic problem of quantum jump in runoff computations (due to AMC change), the concept of soil moisture accounting (SMA) procedure has nowadays been at the forefront of the research community (Michel et al. 2005; Sahu et al. 2010; Ajmal et al. 2015; and Singh et al. 2015).

Slope Considerations in CN Estimation

In the standard NRCS model, the CN values for runoff estimation have been obtained experimentally from the measured rainfall-runoff data over a wide range of geographic, soil, and land management conditions. However, the watershed slope adjustment has not been taken into account and it is an important factor determining water movement within a landscape (Huang et al. 2006). The slope-adjusted CN can improve the runoff estimation capabilities of the NRCS model. The CNs obtained from the NRCS handbook (NRCS 2004) are usually assumed to correspond to a 5% slope (Sharpley and Williams 1990; Huang et al. 2006; Mishra et al. 2014).

Few attempts have been made in the past to incorporate watershed slope in CN estimation. Sharpley and Williams (1990) assumed that CN_{II} obtained from NEH-4 (SCS 1972) corresponds to a slope of 5%. The slope-adjusted CN_{II} (named as CN2α) was expressed as:

$$CN_{II\alpha} = \frac{1}{3}(CN_{III} - CN_{II})\left(1 - 2e^{-13.86\alpha}\right) + CN_{II} \tag{7}$$

Huang et al. (2006) tested Eq. (7) and found that it had limited applications, and, therefore, he developed an improved version for climatic and steep slope conditions observed in Loess Plateau of China as:

$$CN_{II\alpha} = CN_{II}\left[\frac{322.79 + 15.63\alpha}{(\alpha + 323.52)}\right] \tag{8}$$

More recently, Ajmal et al. (2016) developed an improved version of $CN_{II\alpha}$ using a large amount of measured rainfall-runoff data from 39 mountainous watersheds in South Korea. The developed relationship can be expressed as:

$$CN_{II\alpha} = CN_{II}\left[\frac{1.927\alpha + 2.1327}{(\alpha + 2.1791)}\right] \tag{9}$$

However, the credibility of the above equation needs to be validated for other regions having similar climatic and slope conditions. The constant α is the watershed slope in m/m.

C–I_a^*–λ Spectrum (I_a–S Relationship)

According to Plummer and Woodward (2002), the I_a was not a part of the SCS-CN model in its initial formulation; however, as the developmental stages continued, it was included as a fixed ratio of I_a to S. Because of the larger variability, the $I_a = 0.2S$ relationship has been the focus of discussion and modification since its very inception (Mishra and Singh 2003a). As an example, Aron et al. (1977) suggested $\lambda \leq 0.1$ and Golding (1979) provided λ values for urban watersheds depending on CN as $\lambda = 0.075$ for CN $\leq$ 70, $\lambda = 0.1$ for 70 < CN $\leq$ 80, and $\lambda = 0.15$ for 80 < CN $\leq$ 90. Hawkins et al. (2001) found that a value of $\lambda = 0.05$ gives a better fit to data and would be more appropriate for use in runoff calculations.

Mishra and Singh (1999) suggested that the initial abstraction component accounts for the short-term losses such as interception, surface storage, and infiltration before runoff begins, and, therefore, λ can take any nonnegative value. Mishra and Singh (2004a) developed a criterion for validity of the SCS-CN method with λ variation using the following relationships:

$$\lambda = \frac{CI_a^*}{\left(1 - I_a^*\right)\left(1 - I_a^* - C\right)} \tag{10a}$$

and

$$S \leq \frac{(P - Q)}{\lambda} \tag{10b}$$

where $I_a^* = I_a/P$; varies as $0 \leq I_a^* \leq 1$, and for $I_a^* > 1$, $C = Q/P = 0$.

Graphically, Eqs. (10a) and (10b) are shown in Fig. 1. It can be inferred from the figure that λ can take any nonnegative value $(0, \infty)$; for a given value of I_a^*, λ increases with C and reaches ∞ as $(C + I_a^*)$ approaches 1; for a given value of C, λ increases with I_a^*; as $I_a^* \to 0$, $\lambda \to 0$. It is due to this reason, the existing SCS-CN method performs poorly on very low runoff-producing (or low C values) lands, such as sandy soils and forest lands. Figure 1 also shows that the existing SCS-CN method has widest applicability on those watersheds exhibiting C values in the approximate range of (0.4–0.6) and the initial abstraction amount of the order of 10% of the total rainfall. On the basis of Fig. 1, they defined the applicability bounds for the SCS-CN method as: $\lambda \leq 0.3$; $I_a^* \leq 0.35$; and $C \geq 0.23$.

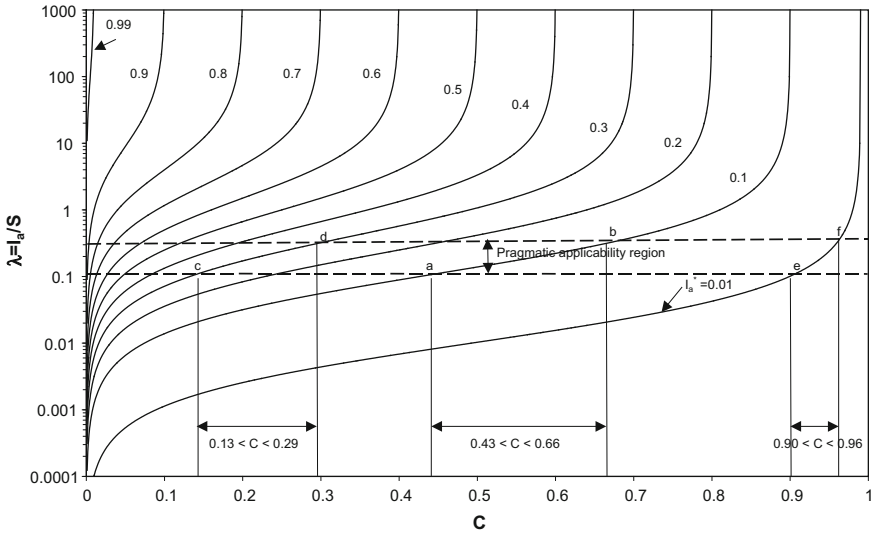

Fig. 1 Variation of initial abstraction coefficient λ with runoff factor C and nondimensional initial abstraction I_a^*

The I_a–S relationships developed by Jain et al. (2006) and Mishra et al. (2006a) are the improvements over the existing $I_a = 0.2S$ relationship. Considering to the fact that P is an implicit function of climatic/meteorological characteristics, Jain et al. (2006) developed a more general nonlinear I_a-S relation, expressed as:

$$I_a = \lambda S\left(\frac{P}{(P+S)}\right)^{\alpha} \tag{11}$$

where α is a constant. Equation (13) reduces to $I_a = 0.2S$ for $\lambda = 0.2$ and $\alpha = 0$ and hence could be taken as a generalized form of I_a–S relationship. Based on the hypothesis that I_a largely depends on initial soil moisture M, as Mishra et al. (2006a) developed a modified nonlinear I_a–S relationship:

$$I_a = \frac{\lambda S^2}{(S+M)} \tag{12}$$

The generalized nature of the above equation can be seen as, for $M = 0$ or a completely dry condition, Eq. (12) reduces to Eq. (3), which is the basic I_a–S relationship. Therefore, it can be concluded that these relationships (or their modification) can be further explored in different hydro-climatological regions for their enhanced applicability and versatility.

Soil Moisture Accounting (SMA) Procedure

A sound soil moisture accounting procedure (SMA) in combination with the CN procedure is needed to predict runoff from rainfall realistically, because CN is not a constant, but varies from event to event. Under wet soil conditions, much of the rainfall is converted to runoff. Therefore, the CN value has to be high for realistic prediction of runoff and vice versa. A sound SMA has to incorporate all soil moisture conditions (Mishra et al. 2004a; Mishra and Singh 2004a; Michel et al. 2005; Kannan et al. 2008).

The SMA concept was for the first time introduced by Williams and LaSeur (1976) to develop a continuous water yield model using the existing SCS-CN methodology. Here, the SMA procedure was based on the concept that the "Curve Number" (CN) should vary continuously with soil moisture, and thus there should be many values of CN instead of only three, i.e., CN_I, CN_{II}, CN_{III}. Later on, a good attempt was further made by Hawkins (1978) to account soil moisture on continuous basis. However, their models ignore the inherent structural deficiency of the existing SCS-CN methodology to account for SMA procedure.

The structural deficiency in terms of SMA of the existing SCS-CN method was highlighted by Mishra et al. (2004a) and an improved SMA-inspired SCS-CN model was developed and evaluated using large data set of US watersheds. Later on based on this concept, Mishra and Singh (2004a) developed versatile SCS-CN model (VSCS-CN) using soil moisture budgeting on continuous basis. Here, the SMA procedure was based on the notion that "higher the antecedent soil moisture amount before start of rainfall in the soil, higher will be the runoff and lesser will be the void space available for storage of rainfall." This was also well addressed by Michel et al. (2005) through SMA procedure. A brief discussion about SMA procedure explicit in SCS-CN method is being discussed here as follows (Mishra et al. 2004a).

Using the C = Sr concept, where C is the runoff coefficient (= $Q/(P - I_a)$) and Sr = degree of saturation (F/S), Mishra and Singh (2002a) modified Eq. (2) for antecedent moisture M as:

$$\frac{Q}{(P - I_a)} = \frac{F + V_0}{S + V_0} \tag{13}$$

which upon substitution into Eq. (2) leads to

$$Q = \frac{(P - I_a)(P - I_a + V_0)}{(P - I_a + V_0 + S)} \tag{14}$$

Here V_0 is computed as:

$$V_0 = \frac{(P_5 - 0.2S_1)S_1}{P_5 + 0.8S_1} \tag{15}$$

where P_5 is the antecedent 5-d precipitation amount, and SI (= $S + V_0$) is the potential maximum retention corresponding to AMC I. Equation (15) assumes the watershed to be dry 5 days before the onset of the rainstorm. Based on this concept, a no. of improved SCS-CN-based models (e.g., Sahu et al. 2007, 2010; Geetha et al. 2008; Durbude et al. 2011; Jain et al. 2012; Ajmal et al. 2015; Singh et al. 2015) have been developed with changed degree of complexities in mathematical structure and parameterization to address the issue of quantum jump of runoff estimation.

SCS-CN Method Using Entropy Theory

In an attempt to provide an analytical treatment to the SCS-CN method, Mishra and Singh (2002a) derived it from early rainfall-runoff models such as Mockus (1949) and Zoch (1934, 1936) with Horton infiltration model and first- (linear) and second- (nonlinear) order hypotheses. Recently, Singh (2013) derived the SCS-CN method using the entropy theory and developed probability distributions of its variables CN, S, P, F, I_a, and Q, assuming they are random in nature. It was found that the SCS-CN method requires no information for the probability distribution of runoff associated with it, other than obeying the total probability law. The entropy associated with SCS-CN method can be expressed using following expressions as follows:

$$H(Q) = \int_0^{P-I_a} \frac{1}{P - I_a} \ln\left[\frac{1}{P - I_a}\right] dQ = \ln(P - I_a) \tag{16}$$

or

$$H(Q) = \ln S - \ln F + \ln Q \tag{17}$$

Equation (16) can also be expressed in terms of CN as:

$$H(Q) = \ln\left[P - \lambda\left(\frac{25,400}{\text{CN}} - 254\right)\right] \tag{18}$$

Likewise, Eq. (17) can be cast as

$$H(Q) = \ln\left[\left(\frac{25,400}{\mathrm{CN}} - 254\right)\right] - \ln F + \ln Q \tag{19}$$

where $H(Q)$ is the Shannon entropy (Shannon 1948) of Q, expressed as:

$$H(Q) = -\int_0^{P-I_a} f(Q)\ln[f(Q)]\mathrm{d}Q \tag{20}$$

in which $f(Q)$ is the probability density function of Q, expressed as: $[F/QS]$. Equations (16)–(19) provide alternative ways of expressing the uncertainty or entropy associated with the SCS-CN method. The study shows that the gamma distribution represents the "best" distribution of CN, Q, P, S, $Q/(P - I_a)$, and F/S. The uncertainty in Q depends mainly on $(P - I_a)$ and the infiltration acts as a filter to this uncertainty, and, therefore, the quantities, P and I_a (which depends upon S or CN), must be determined as accurately as possible.

Some Advanced Applications of SCS-CN Methodology

Although the SCS-CN method was originated as an empirical, event-based procedure for flood hydrology, however, it has witnessed myriad and variety of applications throughout the spectrum of hydrology, due to the reason of its simplicity, stability, and accountability for most runoff-producing watershed characteristics: soil type, land use treatment, surface condition, and antecedent moisture condition. Singh and Frevert (2002) edited a book titled "Mathematical Models of Small Watershed Hydrology and Applications," in which at least 6 of the 22 chapters have the models based on SCS-CN approach. This reflects the robustness and versatility of SCS-CN methodology.

Though primarily intended for event-based rainfall-runoff modeling of the ungauged watersheds, the SCS-CN method has been applied successfully in the realm of hydrology, watershed management, and environmental engineering, such as long-term hydrologic simulation (LTHS) (Williams and LaSeur 1976; Hawkins 1978; Choi et al. 2002; Mishra et al. 2004a; Mishra and Singh 2004a; Michel et al. 2005; Sahu et al. 2007; Geetha et al. 2008; Kannan et al. 2008; Durbude et al. 2011; Sahu et al. 2010; Williams et al. 2012), hydrograph simulation (Aron et al. 1977; Mishra and Singh 2002a, 2004b); evapotranspiration (Mishra et al. 2014), soil moisture accounting (Mishra et al. 2004a; Michel et al. 2005; Sahu et al. 2010; Ajmal et al. 2015; Singh et al. 2015), sediment yield modeling (Mishra et al. 2006b; Tyagi et al. 2008; Singh et al. 2008; Bhunya et al. 2010), metal partitioning (Mishra et al. 2004b, c), urban hydrology (Pandit and Gopalakrishnan 1996; Singh et al. 2013), and river bank filtration and water quality (Ojha 2012).

The conceptualization and prevailing status of SCS-CN methodology has become so popular and versatile that many researchers have integrated it into their new hydrologic models, besides its direct applications (Singh et al. 2010). According to Walter and Stephen (2005), the criticisms of SCS-CN method should not be interpreted as "negative reflections" on its developer(s), rather these are enticements to engage the same creative effort that those early "developers" invoked to find appropriate approaches to current problems based on current science', which fortifies ongoing developmental efforts toward SCS-CN methodology. A brief description on some of these applications is being discussed here as follows.

Long-Term Hydrologic Simulation (LTHS) Models

Long-term hydrologic simulation is used for augmentation of hydrologic data, water resources planning, and watershed management. Long-term daily flow data are specifically needed for analysis of water availability, computation of fortnightly or monthly flows for reservoir operation, and drought analysis (Mishra and Singh 2004a). This section discusses some of the important and widely used LTHS models based on SCS-CN method.

Williams–LaSeur (1976) Model

Williams and LaSeur (1976) were probably the first to introduce the concept of soil moisture accounting (SMA) procedure to develop a model based on the existing SCS-CN methodology. The model is based on the notion that CN varied continuously with soil moisture, and thus considering many values of CN instead of only three (CN_I, CN_{II}, CN_{III}). The model computes a soil moisture index (SMI) depletion parameter that forces an agreement between the measured and predicted average annual runoff. The model eliminates sudden jump in the CN values while changing from one AMC.

Hawkins ET-CN Model

Hawkins (1978) developed a continuous hydrologic simulation model by linking evapotranspiration (ET) and CN. The model uses the volumetric concept for accounting the site moisture on a continuous basis. The model accounts the soil moisture on continuous basis and thus eliminates the problem of sudden jump in CN. The model yields Q equal to $0.05S$ for no rainfall condition, which is impossible and, therefore, violates the law of mass conservation. Furthermore, it

considers the SCS-CN method to be based on ($I_a + S$) scheme, whereas Ia is separate from S in the existing SCS-CN method (Mishra and Singh 2004a, b).

Versatile SCS-CN (VSCS-CN) Model

Mishra and Singh (2004a) critically reviewed of the long-term hydrologic simulation models such as Hydrologic Simulation Package Fortran (HSPF), US Department of Hydrograph Laboratory (USDAHL) (Holtan and Lopez 1971), William–LaSeur (1976) model, Hawkins (1978) model, Systeme Hydrologique European (SHE) (Abbott et al. 1986a, b), and Hydrologic Engineering Centre-Hydrologic Modeling System (HEC-HMS) (HEC 2000) in terms of their architecture and structure, degree of complexity of inputs, time interval used in simulation, and their applicability particularly in the context of developing countries. They developed a four parameter versatile SCS-CN (VSCS-CN) model to remove the inconsistencies and complexities associated with the existing long-term hydrologic simulation models. The developed model obviates the sudden jumps in CN values, exclusively considers the soil moisture budgeting on continuous basis, evapotranspiration, and watershed routing procedures. These characteristics make the model versatile. The model paved the way for structural diagnosis of the existing SCS-CN method, and since then, a plethora of SMA-based models have been developed in hydrologic literature.

The model exclusively accounts for dynamic and static components of infiltration and expresses the evapotranspiration ET in terms of pan coefficient (PANC) and absolute maximum potential retention $S_{abs} = (S + S_a)$, where S_a is the threshold soil moisture = $(V_0 + I_a)$. The pan coefficient was found to be the ratio of the S, to the absolute potential maximum retention, S_{abs}. Table 2 shows the different variants of the VSCS-CN model. These models could be further explored for their applicability and improved understanding of the processes involved in their formulations.

Michel SCS-CN Model

An enhanced version of SCS-CN model was developed by Michel et al. (2005) based on the analysis of the continuous soil moisture accounting (SMA) procedure implied by the SCS-CN equation. In model development, it was hypothesized that the SCS-CN model is valid not only at the end of the storm but at any instant along a storm. The SMA procedure is based on the notion that higher the moisture store level, higher the fraction of rainfall will be converted into runoff. The Michel SCS-CN model eliminates initial abstraction (I_a) and introduces a new parameter (threshold soil moisture) $S_a = (I_a + V_0)$ to compute the direct surface runoff.

Table 2 VSCS-CN model and its variants (Mishra and Singh 2003a, b)

S. No.	Case	Basic hypothesis	Q =	S/P =	Condition for	
					$I_a^* \geq 0$	$I_a^* \leq 1$
1	$M = F_c = I_a = 0$	$\frac{Q}{P} = \frac{F}{S}$	$\frac{P^2}{P+S}$	$\frac{1-C}{C}$	As $C \to 0$, $S \to \infty$ and As $C \to 1$, $S \to 0$	
2	$F_c = I_a = 0$	$\frac{Q}{P} = \frac{F+M}{S+M}$	$\frac{P(P+M)}{P+M+S}$	$\frac{(1-C)(1+M^*)}{C}$		
3	$M = F_c = 0$	$\frac{Q}{P-I_a} = \frac{F}{S}$	$\frac{(P-I_a)^2}{P-I_a+S}$	$\frac{1}{2\lambda^2}\left[2\lambda + (1-\lambda)C - \sqrt{(1-\lambda)^2C^2 + 4\lambda C}\right]$	$C \leq 1$	$C \geq 0$
4	$F_c = 0$	$\frac{Q}{P-I_a} = \frac{F+M}{S+M}$	$\frac{(P-I_a)(P-I_a+M)}{P-I_a+M+S}$	$\frac{1}{2\lambda^2}\left[(2+M^*)\lambda + (1-\lambda)C - \sqrt{(\lambda M^*)^2 + (1-\lambda)^2C^2 + 2\lambda C\{2+(1+\lambda)M^*\}}\right]$	$C \leq 1$	$\lambda \geq 0$, $C \geq 0$
5	$M = I_a = 0$	$\frac{Q}{P-F_c} = \frac{F_d}{S}$	$\frac{(P-F_c)^2}{P-F_c+S}$	$\frac{(1-F_c^*)(1-C-F_c^*)}{C}$	$F_c^* \leq 1$ for $C \geq 0$	$F_c^* \geq 0$ for $C \leq 1$
6	$M = 0$	$\frac{Q}{P-I_a-F_c} = \frac{F_d}{S}$	$\frac{(P-I_a-F_c)^2}{P-I_a-F_c+S}$	$\frac{1}{2\lambda^2}\left[2\lambda(1-F_c^*) + (1-\lambda)C - \sqrt{(1-\lambda)^2C^2 + 4\lambda C(1-F_c^*)}\right]$	$F_c^* \leq 1$ for $C \leq 1$	$F_c^* \geq 0$ for $C \geq 0$
7	$I_a = 0$	$\frac{Q}{P-F_c} = \frac{F_d+M}{S+M}$	$\frac{(P-F_c)(P-F_c+M)}{P-F_c+M+S}$	$\frac{(1-F_c^*+M^*)(1-C-F_c^*)}{C}$	For $S \geq 0$, $0 \leq F_c^* \leq 1$	
8	$M = F_c = I_a \neq 0$	$\frac{Q}{P-I_a-F_c} = \frac{F_d+M}{S+M}$	$\frac{(P-I_a-F_c)(P-I_a-F_c+M)}{P-I_a-F_c+M+S}$	$\frac{1}{2\lambda^2}\left[\lambda M^* + 2\lambda(1-F_c^*) + (1-\lambda)C - \sqrt{(\lambda M^*)^2 + (1-\lambda)^2C^2 + 4\lambda C(1-F_c^*) + 2\lambda(1+\lambda)CM^*}\right]$	$M^* \leq F_c^* \leq 1$ for $C \leq 1$	$F_c^* \geq M^* \geq 0$ for $C \geq 0$

NOTATIONS $F_c^* = F_c/P$; $V_0^* = V_0/P$; $I_a^* = I_a/P$; where F_c and F_d = static and dynamic components of infiltration

Sahu et al. SCS-CN Model

Sahu et al. (2007) developed a continuous hydrologic simulation model using SCS-CN method based on advanced SMA procedure. They hypothesized that the initial soil moisture (V_0) depends not only on antecedent five-day precipitation (P_5), but also on S. The dependency on S is based on the fact that the watershed with larger retention capacity S must retain higher moisture compared to the watershed with lesser S for a given P_5. The developed model obviates sudden jump in runoff computations and is an improvement over MSCS-CN model (Michel et al. 2005) based on SMA procedure.

SCS-CN-Based MLTHS ASMA Model

Jain et al. (2012) proposed modified long-term hydrologic simulation advance soil moisture accounting (MLTHS ASMA) model by suitably amalgamating the advanced soil moisture accounting (ASMA) procedure, the modified subsurface drainage flow concept, and curve number (CN)-based model for simulating daily flows. The proposed model uses the ASMA procedure both for surface and sub-surface flows.

Modified Michel SCS-CN Model

Based on sound hydrologic perception of soil moisture accounting procedure (SMA) and changed parameterization with improved relationships for estimation of parameters, Singh et al. (2015) developed modified Michel SCS-CN (MMSCS-CN) model for runoff computations. Simple expressions of V_0 and S_a were provided to obviate the manual adjustments in V_0 to accommodate all the three AMCs and fixation of S_a with S.

Parsimonious SCS-CN Model

Based on in-depth structural diagnosis of the SCS-CN model and implicit inconsistencies in model parameterization, Ajmal et al. (2015) developed a parsimonious SCS-CN model based on soil moisture proxies (SMP) (a synonym for SMA) and developed improved relationships for V_0 and S_a. The model is very simple in use and has only one parameter as the existing SCS-CN method.

CN-Based PET and IWR Models

The proportionality concept (C = Sr concept) of the SCS-CN method was used by Mishra et al. (2014) in the simple water balance equation to derive a power relationship between CN and mean PET using the usually available long-term daily rainfall-runoff data. The general form of the CN (S) versus PET (ET) model can be expressed as:

$$\mathrm{ET} = \alpha S^{\beta} \tag{21}$$

where α and β are the coefficient and exponent, respectively. Because there exists an inverse relationship between S and CN (Eq. 4), Eq. (16) suggests ET to be high for the watersheds of low CN and vice versa. This ET-CN rationale was based on the following relationship as expressed here:

$$E = I_{\mathrm{a}} + \frac{(P - I_{\mathrm{a}})(E^{*} - I_{\mathrm{a}})}{(P - I_{\mathrm{a}} + S)} \tag{22a}$$

$$E = \mathrm{ET} + \mathrm{ES} + \mathrm{EI} \tag{22b}$$

where ET is the daily transpiration (moisture transferred from the soil to the atmosphere through the root-stem-leaf system of vegetation); ES is the daily soil evaporation (moisture transferred from the soil to the atmosphere by hydraulic diffusion through the pores of the soil); EI is the daily interception loss (water evaporated from the wet surface of the vegetation and wet surface of the soil) during rainstorm; and E* is the daily potential evapotranspiration. The concept was applied to eight catchments falling under different climatic and geographic settings of India, and a high correlation coefficient (= 0.96) was observed between S (CN) and PET values as shown in Fig. 2a, b.

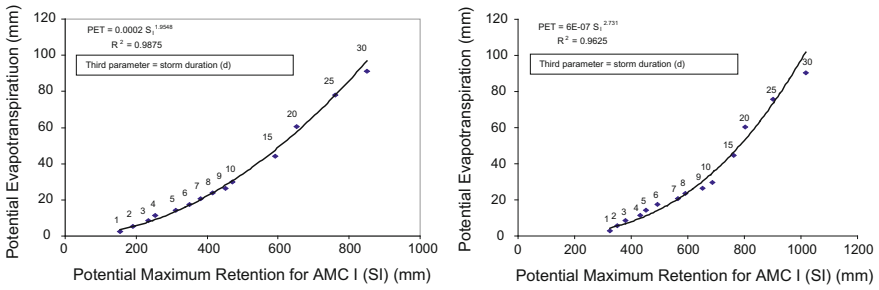

Fig. 2 Relation between Penman–Monteith PET and potential maximum retention for dry condition (SI) for Hemavati and Ghodahado catchments, India

Erosion, Sedimentation, and Water Quality Models

This section briefly discusses some of the recently developed models based on SCS-CN method for erosion, sedimentation, and metal partitioning in hydrologic and environmental engineering. As discussed previously, most of the computer-based sedimentation simulation models such as AGNPS (Young et al. 1989), CREAMS (Knisel 1980), SWRRB (Arnold et al. 1990), SWAT (Neitsch et al. 2002), EPIC (Sharpley and Williams 1990), and GWLF (Haith and Shoemaker 1987) use the SCS-CN method as a component model for runoff estimation. However, as a model itself, the SCS-CN method has not witnessed many applications in the field of soil erosion, sedimentation, and water quality, despite some noteworthy works of Mishra et al. (2006b), Tyagi et al. (2008), Singh et al. (2008), and Bhunya et al. (2010).

Garen and Moore (2005) explored the applicability of SCS-CN methodology in water quality modeling and named it as "Curve Number Hydrology," which signifies the versatility of the model itself. Therefore, the SCS-CN method has enormous potential and it is one of the "hydrological modeling techniques" available to the scientific community with its broad applicability.

SCS-CN-Based Metal Partitioning Models

The basic proportionality concept (C = Sr; where C = runoff coefficient = $Q/(P - I_a)$ and Sr = degree of saturation = (F/S); where F = cumulative infiltration) of the SCS-CN method was used by Mishra et al. (2004b) for partitioning of 12 metal elements, i.e., Zn, Cd, Pb, Ni, Mn, Fe, Cr, Mg, Al, Cu, and Na between dissolved and particulate-bound form. In metal partitioning analogy, two parameters, namely (i) the potential maximum desorption (Ψ) and (ii) the partitioning curve number (PCN) were postulated as analogous to the parameters S and CN of the SCS-CN model, respectively. These parameters were introduced, along with Ψ-PCN and Ψ-ADP, where ADP is the antecedent dry period similar to the AMC. The governing equations of the PCN model can be expressed as:

$$C_p = \frac{(C_T - i_f)^2}{C_T - i_f + \psi}; \quad \text{for } C_T \geq i_f \tag{23}$$

$$\text{if-}\Psi \text{ hypothesis} : i_f = \lambda_i \psi \tag{24}$$

$$\Psi\text{-CN mapping PCN} = \frac{1000}{1000 + \psi} \tag{25}$$

where C_P = particulate-bound metal; C_T = total metal; C_d = dissolved metal; Ψ = potential maximum desorption; and i_f = initial flush. Further, a new partitioning curve number (PCN) approach was also developed for partitioning heavy

Table 3 Formulation of rainfall-sediment yield and rainfall-runoff models (Mishra and Singh 2003a, b)

Model	Rainfall-sediment yield models	Model	Rainfall-runoff models
*S*1	$Y = \frac{AP}{P+S}$	*R*1	$Q = \frac{P^2}{P+S}$
*S*2	$Y = \frac{A(P-0.2S)}{P+0.8S}$	*R*2	$Q = \frac{(P-0.2S)^2}{P+0.8S}$
*S*3	$Y = \frac{A(P-\lambda S)}{P+(1-\lambda)S}$	*R*3	$Q = \frac{(P-\lambda S)^2}{P+(1-\lambda)S}$
*S*4	$Y = \frac{A[P-\lambda S+M]}{P+(1-\lambda)S+M}$	*R*4	$Q = \frac{(P-\lambda S)(P-\lambda S+M)}{P+(1-\lambda)S+M}$
*S*5	$Y = \frac{A[P-0.2S+M]}{P+0.8S+M}$	*R*5	$Q = \frac{(P-0.2S)(P-0.2S+M)}{P+0.8S+M}$
*S*6	$Y = \left[\frac{(1-\lambda_1)[P-0.2S+M]}{P+0.8S+M} + \lambda_1\right]A$	*R*6	$Q = \frac{(P-0.2S)(P-0.2S+M)}{P+0.8S+M}$
*S*7	$Y = \left[\frac{(1-\lambda_1)[P-\lambda S+M]}{P+(1-\lambda)S+M} + \lambda_1\right]A$	*R*7	$Q = \frac{(P-\lambda S)(P-\lambda S+M)}{P+(1-\lambda)S+M}$
*S*8	$Y = \left\{(1-\lambda_1)\alpha\left[\frac{[P-0.2S+M]}{P+0.8S+M}\right]^{\beta} + \lambda_1\right\}A$	*R*8	$Q = \frac{(P-0.2S)(P-0.2S+M)}{P+0.8S+M}$
*S*9	$Y = \left\{(1-\lambda_1)\alpha\left[\frac{[P-\lambda S+M]}{P+(1-\lambda)S+M}\right]^{\beta} + \lambda_1\right\}A$	*R*9	$Q = \frac{(P-\lambda S)(P-\lambda S+M)}{P+(1-\lambda)S+M}$

metals into dissolved and particulate-bound forms from urban snow melt, rainfall/runoff, and river flow environments using the analogy between SCS-CN method-based infiltration and metal sorption processes.

USLE Coupled SCS-CN-Based Sediment Yield Model

The popular and widely used models of SCS-CN method and universal soil loss equation (USLE) were coupled by Mishra et al. (2006b) for modeling rainstorm generated sediment yield from a watershed. The coupling is based on three hypotheses: (i) the runoff coefficient (C) is equal to the degree of saturation (Sr); (ii) the potential maximum retention (S) can be expressed in terms of the USLE parameters, and (iii) the sediment delivery ratio (DR) is equal to the runoff coefficient (C). Table 3 shows the summary of the developed models for different conditions. The developed models have ample potential for application to the ungauged watersheds.

SCS-CN-Based Conceptual Sediment Graph Model

The popular and extensively used Nash model (Nash 1957) -based instantaneous unit sediment graph (IUSG), SCS-CN method, and Power law (Novotny and Olem 1994) were coupled by Singh et al. (2008) to develop conceptual sediment graph models to get time distributed sediment yield on storm basis. The developed models

Table 4 Formulation of conceptual sediment graph models

S. No.	Model	Model expression
1	SGM1	$Q_s(t) = \left[\alpha A A_w [kt/(1+kt)]^{\beta} (n_s-1)^{n_s}/t_{ps}\Gamma(n_s)[(t/t_{ps})e^{-(t/t_{ps})}]^{n_s-1}\right]$
2	SGM2	$Q_s(t) = \left[\alpha A A_w [(kt-\lambda)/(1+kt-\lambda)]^{\beta} (n_s-1)^{n_s}/t_{ps}\Gamma(n_s)[(t/t_{ps})e^{-(t/t_{ps})}]^{n_s-1}\right]$
3	SGM3	$Q_s(t) = \left[\alpha A A_w [(kt+V_0/S)/(1+kt+V_0/S)]^{\beta} (n_s-1)^{n_s}/t_{ps}\Gamma(n_s)[(t/t_{ps})e^{-(t/t_{ps})}]^{n_s-1}\right]$
4	SGM4	$Q_s(t) = \left[\alpha A A_w [(kt-\lambda+V_0/S)/(1+kt-\lambda+V_0/S)]^{\beta} (n_s-1)^{n_s}/t_{ps}\Gamma(n_s)[(t/t_{ps})e^{-(t/t_{ps})}]^{n_s-1}\right]$

consider different factors responsible for soil erosion and sediment yield. The sediment graph models (SGMs) for four different cases, depending on the number of model parameters, and these are designated as SGM1 through SGM4, respectively, as shown in Table 4. For SGM1, both the initial soil moisture V_0 and initial abstraction I_a are assumed to be zero, i.e., $V_0 = 0$ and $I_a = 0$. For SGM2, $V_0 = 0$, but $I_a \neq 0$. For SGM3, $V_0 \neq 0$ and $I_a = 0$. Finally, for SGM4, $V_0 \neq 0$ and $I_a \neq 0$.

The models could be very useful in computation of time distributed sediment yield as well as total sediment yield and can be successfully applied for ungauged conditions as well. The models can be very useful for computing dynamic pollutant loads in water quality modeling if the sediment transports the pollutants that are toxic at high concentrations, requiring determination of peak, rather than average sediment flow rate.

SCS-CN-Based River Bank Filtration Model

The SCS-CN method was applied by Ojha (2012) in water quality modeling of the river bank filtration (RBF) process through coupling of the curve number (CN), filtration/kinetic coefficient (K), and the input applied to the system. It was found that the CN is related with the performance (output to input ratio, R) of a water quality system. Therefore, CN is dependent on all the parameters that influence the filtration/kinetic coefficient such as filtration velocity, medium properties and the distance between source water and abstraction point, and the source water quality. The model could be further explored for similar applications for its enhanced applicability and understanding.

Future Applications

Looking into diversified applications of SCS-CN methodology, including for the disciplines it was neither structured nor instituted, however, it has ample scope and should be explored for its' greater role and applicability in the following fields of hydrology such as:

Environmental flow studies
Climate change studies
Irrigation scheduling
Surface and subsurface drainage studies
Droughts and Flood studies
Water resources vulnerability and reliability
Water quality modeling

Conclusions

With the versatile applications of the SCS-CN methodology throughout the spectrum of hydrologic problems, including for those it was neither structured nor instituted by its' developers, this paper critically examines the hydrologic and structural modifications through which this methodology has undergone such as: (i) C = Sr concept and SMA procedure; (ii) CN estimation and their conversion techniques; (iii) linear/nonlinear initial abstraction (I_a) and S relationships; (iv) storm duration and dynamic vs static infiltration; (v) slope and CN relationships; (vi) overall renewal of SCS-CN methodology through different concepts and theories. Some of the most recent and advanced applications of SCS-CN method were also discussed in this paper. Lastly, looking into its vast applicability, the future fields of applications were also explored to maintain its hierarchy in hydrologic models.

References

Abbott MB, Bathurst JC, Cunge JA, O'Connell PE, Rasmussen J (1986a) An introduction to the European hydrologic system-Systeme Hydrologique Europeen, SHE, 2: Structure of a physically-based, distributed modeling system. J Hydrol 87:61–77

Abbott MB, Bathurst JC, Cunge JA, O'Connell PE, Rasmussen J (1986b) An introduction to the European hydrologic system-Systeme Hydrologique Europeen, SHE, 1: History and philosophy of a physically-based, distributed modeling system. J Hydrol 87:45–59

Ajmal M, Waseem M, Wi S, Kim Tae-Woong (2015) Evolution of a parsimonious rainfall–runoff model using soil moisture proxies. J Hydrol 530:623–633

Ajmal M, Waseem M, Ahn J-H, Kim T-W (2016) Runoff estimation using the NRCS slope-adjusted curve number in mountainous watersheds. J Irrig Drain Eng. 10.1061/(ASCE)IR.1943-4774.0000998

Andrews RG (1954) The use of relative infiltration indices in computing runoff (unpublished). Soil Conservation Service, Fort Worth, Texas, p 6

Arnold JG, Williams JR, Griggs RH, Sammons NB (1990) SWRRB—a basin scale simulation model for soil and water resources management. A&M Press, Texas

Aron G, Miller AC, Lakatos DF (1977) Infiltration formula based on SCS curve numbers. J Irrig Drain Div ASCE 103(4):419–427

Beasley DB, Huggins LF (1980) ANSWERS (Area nonpoint-source watershed environment simulation): User's manual. Purdue University, Department of Agricultural Engineering, West Lafayette, Ind

Bhunya PK, Jain SK, Singh PK, Mishra SK (2010) A simple conceptual model of sediment yield. J Water Resour Manage 24(8):1697–1716

Bonta JV (1997) Determination of watershed curve number using derived distributions. J Irrig Drain Eng 123(1):234–238

Boszany M (1989) Generalization of SCS curve number method. J. Irrig Drain Eng 115(1): 139–144

Cazier DJ, Hawkins RH (1984) Regional application of the curve number method, Water Today and Tomorrow. In: Proceeding of ASCE, irrigation and drainage division special conference. ASCE, New York, NY, p 710

Chen CL (1982) Infiltration formulas by curve number procedure. J Hydraul Div ASCE 108 (7):828–829
Choi JY, Engle BA, Chung HW (2002) Daily streamflow modeling and assessment based on the curve number technique. Hydrol Process 16(16):3131–3150
Chow VT, Maidment DR, Mays LW (1988) Applied hydrology. Mc-Graw-Hill, New York
Chung W, Wang I, Wang R (2010) Theory based SCS-CN method and its applications. J. Hydrol Eng 15(12):1045–1058
Durbude DG, Jain MK, Mishra SK (2011) Long-term hydrologic simulation using SCS-CN based improved soil moisture accounting procedure. Hydrol Process 25:561–579
Garen D, Moore DS (2005) Curve number hydrology in water quality modeling: use, abuse, and future directions. J Am Water Resour Assoc 41(2):377–388
Geetha K, Mishra SK, Eldho TI, Rastogi AK, Pandey RP (2008) SCS-CN based continuous model for hydrologic simulation. Water Resour Manag 22:165–190
Golding BL (1979) Discussion of runoff curve numbers with varying soil moisture. J Irrig Drain Div ASCE 105(IR4):441–442
Haith DA, Shoemaker LL (1987) Generalized watershed loading functions for streamflow nutrients. J Am Water Resour Assoc 23:471–478
Hawkins RH (1975) The importance of accurate curve numbers in the estimation of storm runoff. Water Resour Bull 11(5):887–891
Hawkins RH (1978) Runoff curve number with varying site moisture. J Irrig Drain Eng 104 (4):389–398
Hawkins RH, Hjelmfelt AT Jr, Zevenbergen AW (1985) Runoff probability, storm depth and curve numbers. J Irrig Drain Eng 111(4):330–340
Hawkins RH, Woodward DE, Jiang R (2001) Investigation of the runoff curve number abstraction ratio. Paper presented at USDA-NRCS hydraulic engineering workshop, Tucson, Arizona
HEC (1981) The new HEC-1 Food hydrograph package. US Army Corps of Engineers. Institute for Water Resources, Hydrologic Engineering Centre, 609, Second street, Davis, CA, 95616
HEC (2000) Hydrologic modeling system HEC-HMS, User's manual, version 2. Hydrologic EngineeringCenter, U. S. Army Corps of Engineers, Davis, California
Hjelmfelt AT Jr (1980) Empirical investigation of curve number technique. J Hydraul Div ASCE 106(9):1471–1477
Holtan HN, Lopez NC (1971) USDHAL-70 model of watershed hydrology, USDA, Tech Bull, 1435
Huang M, Gallichand J, Wang Z, Goulet M (2006) A modification to the soil conservation service curve number method for steep slopes in the Loess Plateau of China. Hydrol Process 20: 579–589
Jain MK, Mishra SK, Babu S, Singh VP (2006) Enhanced runoff curve number model incorporating storm duration and a nonlinear Ia–S relation. J Hydrol Eng 11(6):631–635
Jain MK, Durbude DG, Mishra SK (2012) Improved CN-based long-term hydrologic simulation model. J Hydrol Eng 17(11):1204–1220
Kannan N, Santhi C, Williams JR, Arnold JG (2008) Development of a continuous soil moisture accounting procedure for curve number methodology and its behavior with different evapotranspiration methods. Hydrol Process 22:2114–2121
Kapur JN, Kesavan HK (1992) Entropy maximization principles with applications. Academic Press, New York
Knisel WG (1980) CREAMS: a field-scale model for chemical, runoff and erosion from agricultural management systems. Conservation Research Report No. 26, South East Area, US Department of Agriculture, Washington, DC
McCuen RH (1982) A guide to hydrologic analysis using SCS methods. Prentice Hall, Englewood Cliffs, NJ
McCuen RH (1989) Hydrologic analysis and design. Prentice Hall, Englewood Cliffs, NJ
McCuen RH (2002) Approach to confidence interval estimation for curve numbers. J Hydrol Eng 7 (1):43–48

Metcalf and Eddy, Inc., University of Florida, and Water Resources Engineers, Inc. (1971) Storm Water Management Model, Vol. I. Final Report, 11024DOC07/71 (NTIS PB-203289), U.S. EPA, Washington, DC, 20460
Michel C, Vazken A, Charles P (2005) Soil conservation service curve number method: How to mend among soil moisture accounting procedure? Water Resour Res 41(2):1–6
Mishra SK, Singh VP (1999) Another look at the SCS-CN method. J Hydrol Eng 4(3):257–264
Mishra SK, Singh VP (2002a) SCS-CN method: part-I: derivation of SCS-CN based models. Acta Geophys Pol 50(3):457–477
Mishra SK, Singh VP (2002b) SCS-CN-based hydrologic simulation package. In: Singh VP, Frevert DK (eds) Mathematical models in small watershed hydrology, Water Resources Publications, Littleton, Colo, Chap 13, pp 391–464
Mishra SK, Singh VP (2003a) Soil conservation service curve number (SCS-CN) methodology. Kluwer, Dordrecht, The Netherlands. ISBN 1-4020-1132-6
Mishra SK, Singh VP (2003b) SCS-CN method: part-II: analytical treatment. Acta Geophys Pol 51 (1):107–123
Mishra SK, Singh VP (2004a) Validity and extension of the SCS-CN method for computing infiltration and rainfall-excess rates. Hydrol Process 18:3323–3345
Mishra SK, Singh VP (2004b) Long-term hydrological simulation based on soil conservation service curve number. Hydrol Process 18(7):1291–1313
Mishra SK, Singh VP (2006) A re-look at NEH-4 curve number data and antecedent moisture condition criteria. Hydrol Process 20:2755–2768
Mishra SK, Jain MK, Singh VP (2004a) Evaluation of SCS-CN based models incorporating antecedent moisture. Water Resour Manage 18:567–589
Mishra SK, Sansalone JJ, Singh VP (2004b) Partitioning analog for metal elements in urban rainfall-runoff overland flow using the soil conservation service curve number concept. J Environ Eng 130(2):145–154
Mishra SK, Sansalone JJ, Glenn DW III, Singh VP (2004c) PCN based metal partitioning in urban snow melt, rainfall/runoff, and river flow systems. J Am Water Resour Assoc 40(5):1315–1337
Mishra SK, Sahu RK, Eldho TI, Jain MK (2006a) An improved Ia–S relation incorporating antecedent moisture in SCS-CN methodology. Water Resour Manage 20:643–660
Mishra SK, Tyagi JV, Singh VP, Singh R (2006b) SCS-CN based modeling of sediment yield. J Hydrol 324:301–322
Mishra SK, Jain MK, Babu PS, Venugopal K, Kaliappan S (2008) Comparison of AMC-dependent CN-conversion formulae. Water Resour Manage 22:1409–1420
Mishra SK, Rawat SS, Chakraborty S, Pandey RP, Jain MK, Chaube UC (2014) Relation between runoff curve number and PET. J Hydrol Eng 9(2):355–365
Mockus V (1949) Estimation of total (peak rates of) surface runoff for individual storms. Exhibit A of Appendix B, Interim Survey Report Grand (Neosho) River Watershed, USDA, Dec 1
Nash JE (1957) The form of the instantaneous unit hydrograph, Publication 42. International Association Scientific Hydrology, Wallingford, England, pp 114–112
Natale L, Todini E (1976a) A stable estimation for linear models-1. Theoretical development and Monte-Carlo experiments. Water Resour Res 12:667–671
Natale L, Todini E (1976b) A stable estimator for linear models-2. Real world hydrologic applications. Water Resour Res 12:672–675
Neitsch SL, Arnold JG, Kiniry JR, Williams JR, King KW (2002) Soil and water assessment tool (SWAT): theoretical documentation, Version 2000. Texas Water Resources Institute, College Station, Texas, TWRI Report TR-191
Novotny V, Olem H (1994) Water Quality: prevention, identification, and management of diffuse pollution. Wiley, New York
NRCS (2000) USDA-NRCS soils data. Natural Resources Conservation Service,http://www.ftw.nrcs.usda.gov/soils_data.html
Ogrosky HO (1956) Service objectives in the field of hydrology. Unpublished, Soil Conservation Service, Lincoln, Nebraska, p 5

Ojha CSP (2012) Simulating turbidity removal at a river bank filtration site in India using SCS-CN approach. J Hydrol Eng 17(11):1240–1244
Pandit A, Gopalakrishnan G (1996) Estimation of annual storm runoff coefficients by continuous simulation. J Irrig Drain Eng 122(4):211–220
Plummer A, Woodward DE (2002) The origin and derivation of Ia/S in the runoff curve number system. Available at the NRCS website: http://www.wcc.nrcs.usda.gov/water/quality/common/techpaper/don1.pdf
Ponce VM (1989) Engineering hydrology: principles and practice. Prentice-Hall, Englewood Cliffs, NJ
Ponce VM, Hawkins RH (1996) Runoff curve number: has it reached maturity? J Hydrol Eng 1 (1):11–19
Rallison RE, Miller N (1982) Past, present, and future. In: Singh VP (ed) Proceeding international symposium on rainfall-runoff relationship. Water Resources Pub., P.O. Box 2841, Littleton, CO
Ramasastry KS, Seth SM (1985) Rainfall-runoff relationships. Rep. RN-20, National Institute of Hydrology, Roorkee, India
Sahu RK, Mishra SK, Eldho TI, Jain MK. (2007) An advanced soil moisture accounting procedure for SCS curve number method. Hydrol Process 21:2827–2881
Sahu RK, Mishra SK, Eldho TI (2010) An improved AMC-coupled runoff curve number model. Hydrol Process 21(21):2834–2839
SCD (1972) Handbook of hydrology. Soil Conservation Department, Ministry of Agriculture, New Delhi, India
SCS (1956) National engineering handbook. Supplement A, Section 4, Chapter 10, Soil Conservation Service, USDA, Washington, DC
SCS (1972). Hydrology national engineering handbook. Supplement A, Section 4, Chapter 10, Soil Conservation Service, USDA, Washington, DC
SCS (1986) National engineering handbook. Supplement A, Section 4, Chapter 10, Soil Conservation Service, USDA, Washington, DC
Shannon CE (1948) A mathematical theory of communications. Bell Syst Tech J 27(3):379–443
Sharpley AN, Williams JR (1990) EPIC—Erosion/productivity impact calculator: 1. model documentation. US Department of Agriculture Technical Bulletin No. 1768. US Government Printing Office, Washington, DC
Sherman LK (1949) The unit hydrograph method. In: Meinzer OE (ed) Physics of the earth. Dover Publications Inc, New York, pp 514–525
Singh VP (1992) Elementary hydrology, Prentice Hall, Englewood Cliffs
Singh N (1995) Watershed modeling. In: Singh VP (ed) Computer models of watershed hydrology. Water Resources Publications, Littleton, CO, pp 1–22
Singh VP (2013) SCS-CN method revisited using entropy theory. J ASABE 56(5):1805–1820
Singh VP, Frevert DK (2002) Mathematical models of small watershed hydrology and applications. Water Resources Publications, Highlands Ranch, CO
Singh PK, Bhunya PK, Mishra SK, Chaube UC (2008) A sediment graph model based on SCS-CN method. J Hydrol 349:244–255
Singh PK, Gaur ML, Mishra SK, Rawat SS (2010) An updated hydrological review on recent advancements in soil conservation service-curve number technique. J Water Clim IWA 1 (2):118–134
Singh PK, Yaduwanshi BK, Patel S, Ray S (2013) SCS-CN based quantification of potential of rooftop catchments and computation of ASRC for rainwater harvesting. Water Resour Manage 27(7):2001–2012
Singh PK, Mishra SK, Berndtsson R, Jain MK, Pandey, RP (2015) Development of a modified MSCS-CN model for runoff estimation. J Water Resour Manage 29(11):4111–4127
Smith MC, Williams JR (1980) Simulation of surface water hydrology. In: Knisel WG (ed) CREAMS: a field-scale model for chemical, runoff, and erosion from agricultural management systems. Washington, DC: U.S. Dept. Agric., Science and Education Administration, pp 13–35, Conservation Research Report No. 26

Sobhani G (1975) A review of selected small watershed design methods for possible adoption to Iranian conditions. MS Thesis, Utah State University, Logan, Utah

Soulis KX, Valiantzas JD (2013) Identification of the SCS-CN parameter spatial distribution using rainfall-runoff data in heterogeneous watersheds. Water Resour Manage 27(6):1737–1749

Springer EP, McGurk BJ, Hawkins RH, Goltharp GB (1980) Curve numbers from watershed data. In: Proceeding of irrigation and drainage symposium on watershed management, pp 938–950. ASCE, New York, NY

Tyagi JV, Mishra SK, Singh R, Singh VP (2008) SCS-CN based time distributed sediment yield model. J Hydrol 352:388–403

Walker WR, Prestwich C, Spofford T (2006) Development of the revised USDA-NRCS intake families for surface irrigation. Agric Water Manage 85(1–2):157–164

Walter MT, Stephen BS (2005) Discussion: curve number hydrology in water quality modeling: uses, abuses, and future directions by David C. Garen and Daniel S. Moore. J Am Water Resour Assoc (JAWRA) 41(6):1491–1492

Williams JR, LaSeur V (1976) Water yield model using SCS curve numbers. J Hydraul Eng 102 (9):1241–1253

Williams JR, Kannan N, Wang X, Santhi C, Arnold GJ (2012) Evolution of the SCS runoff curve number method and its application to continuous runoff simulation. J Hydrol Eng 17 (11):1221–1229

Young RA, Onstad CA, Bosch DD, Anderson WP (1989) AGNPS: a nonpoint-source pollution model for evaluating agricultural watersheds. J Soil Water Conserv 44(2):18–173

Zoch RT (1934) On the relation between rainfall and streamflow. Month Weather Rev 62:315–322

Zoch RT (1936) On the relation between rainfall and streamflow-II. Month Weather Rev 64: 105–121

Hydrological Impacts of Rejuvenating Degraded Hilly Watershed in Shivalik Region

A. K. Tiwari and V. K. Bhatt

Abstract The Shivaliks of northwest states (Haryana, Himachal Pradesh, Jammu and Kashmir, Punjab, and Uttarakhand), spread over an area of more than three million hectares, perhaps represent the one of the most fragile ecosystems of India. The flora and fauna in these hills has been recklessly destroyed during the last two generation resulted in present state of severe degradation. The rainfall is satisfactory and seemingly the potential of restoration of these denuded hills. It was with a view to explore this potential and simultaneous creation of a database for the collection of quantified scientific information on the existing and changing pattern of water and sediment yields from degraded hilly watershed. A watershed of 21 ha almost devoid of vegetation was rehabilitated through control of erosion and improved vegetation and protection. The long-term (1964–2000) hydrological experiment could provide information about the hydrological behavior of hilly forest watershed with respect to temporal rainfall, and the impact of vegetation cover and the treatment of the watershed. The water yield from the watershed sustained at 10–15% of rainfall on an average basis. Sediment yield declined (from 37 to 3.7 Mg/ha) as a result of soil conservation measures and increased vegetation cover, suggesting the entirely positive impact of the recommended measures to restore the ecological environment in these hills.

Introduction

The Shivaliks of northwest states (Haryana, H.P., Jammu and Kashmir, Punjab, and Uttaranchal/UP), spread over an area of more than three million hectares, perhaps represent one of the most fragile ecosystems in the country. The elevation varies from 280 to 1500 m. The average annual rainfall of the region is 1100 mm where about 82% is received during monsoon, with average annual pan evaporation about

A. K. Tiwari (✉) · V. K. Bhatt
Indian Institute of Soil & Water Conservation,
Research Centre, Chandigarh (UT) 160019, India
e-mail: gmaruntiwari@gmail.com

V. P. Singh et al. (eds.), *Hydrologic Modeling*, Water Science
and Technology Library 81, https://doi.org/10.1007/978-981-10-5801-1_47

2110 mm (Agnihotri 2000). Temperature varies from 2 to 43 °C. The Shivaliks are characterized by low hills, undulating topography, steep slopes, erodible soils and are dissected by numerous seasonal streams. In general, soils are coarse-textured and deep with pebbles and boulders on slopes near the foothills. The rain-fed areas of Shivaliks have no possibility of providing irrigation through conventional methods, and large amount of runoff not only goes waste from such lands but also creates problem of soil erosion and land degradation. Management of water resources in its various forms is key to environmental, economical, and social sustainability in Shivalik region. To address the above problems and to restore the ecological environment in this area, a hilly watershed typical of the region of 21 ha was brought under study in 1963 (year of start of Project).

Location of the Watershed

The selected watershed is located at the research farm of IISWC, Research Centre, Chandigarh, in Pinjore block of Panchkula district in Haryana. It is located at elevation of about 450 m (msl), at 30° 45′N latitudes and 76° 52′E longitudes. The research farm lies in the watershed, which drains into the Ghaggar River. The area of watershed is 21 ha and had scrub forest land initially which was further converted to a protected and treated forest land. The land slope in the watershed varies from 10% in some pockets to almost vertical cliffs near the ridges. The main drainage channel drops by 50 m in the first 200 m, and thereafter, the bed gradient gradually decreases to about 1.5% near the dam, with 10% average slope in the watershed.

Climate

The average annual rainfall of the region is 1117 mm. About eighty percent of this rainfall (889 mm) is received through southwest monsoon (June–September). The monsoon sets in last week of June and withdraws by middle of September. There is a wide variation in distribution of rainfall not only from year to year but also between the months. Late start and early recession of monsoon and wide dry spells are of common occurrence. Rainfall of long duration and high intensity (120 and 100 mm/hr for 15 and 30 min duration) is common. About 165 mm of rainfall is received during winter season (November–March) through northeast monsoon. The summers are hot, windy, and dry with the maximum temperature going up to 46 °C (mean maximum 40.4 °C in June). The winters are extremely cold with temperature touching freezing point (mean minimum 5.6 °C in January).

Geology

Geologically, the Shivaliks are made of sand stone, grits, conglomerates, and clay having the characters of fluviate deposits of torrential streams and flood basin. The rocks are young, soft, and loose and are highly susceptible to erosion. The clay minerals are illite, chlorite kaolinite, and montmorillonite with quartz and feldspar in traces. Pink salt is dominant mostly in Haryana area, and coarse sediment composed of pebbles and sandstone is common in the foothills. The soils in the watershed are moderately to severely eroded, gravelly on the surface throughout the profile depth. Most of the area is under forests and rock outcrops. The pH varies from 7.2 to 7.5 in hilly areas. The soils in the watershed area are classified as Chandigarh Series 1, which are essentially sedimentary soils of marble with sandstone intrusions. The texture at the surface varies from sandy loam to loam with silty clay loam subsoils (Yadav et al. 2005a). The soils are well drained with organic carbon varying from 0.07 to 0.37% at the surface at the beginning. The land is mostly classified in class VII as per soil depth, topography, and extent of erosion.

Infiltration

Steady-state infiltration rates and cumulative infiltration were estimated at different reaches, viz. upper, middle, and lower. Litter deposition, soil texture, organic carbon, and clay content of soil were also measured to know the correlation between these soil properties with infiltration. Steady-state infiltration rates gradually decreased from upper to lower reaches as per the present data. Very slow-to-slow steady-state infiltration rates (0.11 and 0.14 cm/h), respectively, were observed in lower reaches of east- and north-facing slopes. Cumulative infiltration was also low (ranged from 0.61 to 5.2 cm) in east- and north-facing slopes than that of west- and south-facing slopes (ranged between 2.43 and 24.68 cm) (Yadav et al. 2005b).

Vegetation

Initially, it was a scrub forest land almost with very few trees of *Acacia catechu* (Khair) and *Dalbergia sissoo* (Shisham). Biotic interference in the area consisted of mostly scrub growth principally of *Hycanthes arbortristin* (Har singar), *Carissa opaca* (Karanda), and *Ziziphus numularia* (Ber). The scanty grass cover included *Heteropogon contortus, Chrysopogon fulvus, Dicanthium annulatum, Eulaliopsis binata,* and *Eucmopogon fovoolatus.* Afforestation was carried out predominantly by sowing of *A. catechu* (Khair) in pits and trenches. The tree species has proved to be very successful on the hillslopes. *D. sissoo* was also planted by seedlings and

root–shoot cuttings. *E. binata* (bhabhar) grass was sown on the berms of staggered trenches. Plantation also included *Dendrocalamus strictus* (bamboo), *Albizzia lebbek* (siris), and eucalyptus. The efforts for afforestation and imposition of soil and water conservation structures have resulted in covering whole of the watershed with dense forest rejuvenating the hilly watershed. At per present status of vegetation, *A. catechu* recorded the maximum frequency (75%) followed by *D. sissoo* (16.67%); however, ingress of *Lantana camara* shrub in the watershed area after the 1990s resulted in the depletion of ground cover in the watershed. Grewal et al. (1996) reported that during 1980–85 luxurious growth of *E. binata* grass was obtained with the yield varying from 3 to 6 Mg ha^{-1} (dry weight basis) giving a good revenue. After ingress of *L. camara,* there was an overall change in vegetation pattern with drastic reduction in grass yield.

Resource Conservation

The watershed was provided with full protection within the fencing of the research farm. The induced protection could eliminate the grazing as well as removal of shrubs and trees. Staggered contour trenches of size 30–45 cm deep with a length of 2–3 m were excavated along the contour for reducing the overland flow, moisture conservation, and survival of the vegetation. Brushwood wattling reinforced with *Agave bulbils* and *Arundo donax* was used to control the steep and long slopes. Brushwood check dams and traps were constructed across small gullies and drainage ways to arrest silt. Seven check dams were constructed in the upper watershed to act as debris trap. These check dams controlled the runoff and debris from the individual watersheds varying from 0.74 to 4.6 ha. In the year 1974, one more check dam of height 2.5 m and length 14 m with a watershed of 0.55 ha was constructed near the pondage area. The check dams helped to reduce the sediment yield into the storage reservoir downstream built under earthen dam (16 m length and a height of 5.5 m). These structures were provided with suitable spillways. Water spreaders were also provided with a 3-m-wide drains on the upstream side. These earthen embankments were sodded by *Cynodon dactylon* (Dub) and were provided with suitable spillways.

Runoff

Runoff and sediment flow from the watershed was recorded through weir was installed with an automatic water level recorder for measurement of the flow. Hydrographs were taken up and analyzed with the help of rating table to derive the discharge rate at different time, peak discharge, and total volume of runoff for each rainfall event. The runoff data were collected from the year 1964–2000. Observations of daily water level in the pond were taken to determine the total water yield of the watershed, the quantity retained, and storage losses from the pond.

Sediment Outflow

To compute the sediment yield in the pond every year, the contour survey was carried out to record the change in submergence area and capacity of the pond by getting the sediment yield accumulated in the pond.

The submergence area of the pond was surveyed in 1963 to determine the storage capacity and establish benchmark levels for the determination of the sediment trapped in the pond. As the pond bed was undulating with steep slope, the major portion of the ponding area was covered with 20 ft × 20 ft (6.1 m × 6.1 m) grid with permanent markers for monitoring the sediment deposited in the pond. This was supplemented with occasional analysis of runoff samples from the pond, the upstream channel, and outflow through the spillway.

Database

The annual rainfall, runoff, peak discharge, and the sediment yield were analyzed for the year 1964–65 to 1999–2000 and presented in Table 1. To have in-depth assessment of impact of the soil and water conservation measures and vegetative treatment, the data were analyzed on annual basis.

Table 1 Annual rainfall, runoff, peak discharge, and sedimentation yield from the watershed (Tiwari et al. 2012a)

S. No.	Water year	Rainfall	Runoff		Peak discharge (cumec/km^2)	Sediment (Mg/ha)
		mm	mm	As %of rainfall		
1	1964–65	1254.2	276.74	22.07	2.54	37.71
2	1965–66	718.2	119.23	16.60	2.62	26.27
3	1966–67	1174.6	166.51	14.18	5.52	12.38
4	1967–68	1455.5	165.76	11.39	0.00	9.66
5	1968–69	899.9	69.98	7.78	0.26	6.94
6	1969–70	885.3	58.44	6.60	1.24	5.54
7	1970–71	1122.8	165.10	14.70	5.52	6.94
8	1971–72	1664.5	168.67	10.13	4.81	8.26
9	1972–73	680.1	26.17	3.85	0.00	4.13
10	1973–74	1687.8	136.82	8.11	2.68	4.03
11	1974–75	813.9	60.98	7.49	0.93	2.91
12	1975–76	1197.3	159.76	13.34	1.24	2.81
13	1976–77	1092.7	93.72	8.58	3.20	2.72
14	1977–78	1214.5	93.77	7.72	2.08	2.53
15	1978–79	1592.9	112.05	7.03	4.54	1.66

(continued)

Table 1 (continued)

S. No.	Water year	Rainfall	Runoff		Peak discharge (cumec/km^2)	Sediment (Mg/ha)
		mm	mm	As %of rainfall		
16	1979–80	802.7	57.31	7.14	0.00	0.54
17	1980–81	1261.1	108.66	8.62	0.22	1.33
18	1981–82	1286.5	104.38	8.11	0.23	1.80
19	1982–83	1244.5	47.51	3.82	0.00	0.50
20	1983–84	1185.6	106.99	9.02	4.43	2.16
21	1984–85	673.9	29.94	4.44	0.00	0.30
22	1985–86	942.5	22.81	2.42	0.00	0.10
23	1986–87	1273.4	83.29	6.54	0.00	0.25
24	1987–88	423.0	4.22	1.00	0.00	0.01
25	1988–89	1732.3	267.56	15.45	1.78	1.45
26	1989–90	1326.7	177.45	13.38	4.68	3.43
27	1990–91	1509.2	206.84	13.71	2.77	2.80*
28	1991–92	912.9	64.09	7.02	0.00	2.80*
29	1992–93	918.1	91.19	9.93	2.18	2.80*
30	1993–94	887.2	81.00	9.13	0.00	2.80*
31	1994–95	1291.2	184.13	14.26	2.22	2.80*
32	1995–96	1572.7	328.60	20.89	6.57	9.50
33	1996–97	1354.7	272.40	20.11	7.40	7.20
34	1997–98	1279.7	152.90	11.95	1.68	3.90
35	1998–99	1433.8	202.40	14.11	2.77	5.40
36	1999–2000	1013.7	154.90	15.28	1.78	3.70

*Average value of the five years (1990–95) has been adopted

Results and Discussion

Water Yield

Variation of annual rainfall and water yield from the watershed is given in Fig. 1. The annual water yield varied between 4.22 mm (1% of rainfall) at low rainfall of 423 mm in the year 1987–88 to 328.60 mm (21% of rainfall) in the year 1995–96 and at high rainfall of 1527.7 mm. The data in the initial years were higher which had a declined trend there after up to 1987–88. Again, there was a rise in runoff for three consecutive high rainfall years 1988–1991, and then, again it declined to low level when the rainfall was less than 1000 mm. There was again a increasing trend in runoff from the year 1994 onward to 1999 being the year with rainfall more than 1000 mm. Year 1995–97 had again a runoff value of 20–21% of rainfall which rose the eyebrows of many people that how a treated and fully vegetated watershed can contribute the runoff up to 21% of rainfall (Fig. 2).

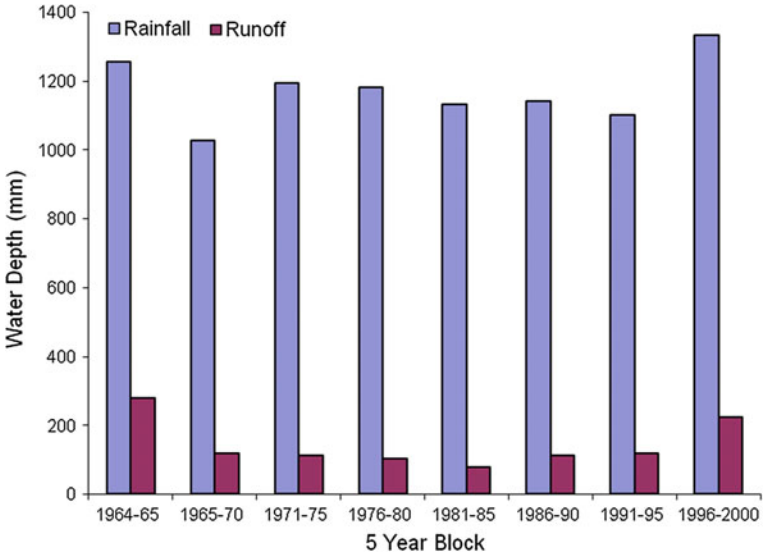

Fig. 1 Variation of average rainfall and runoff

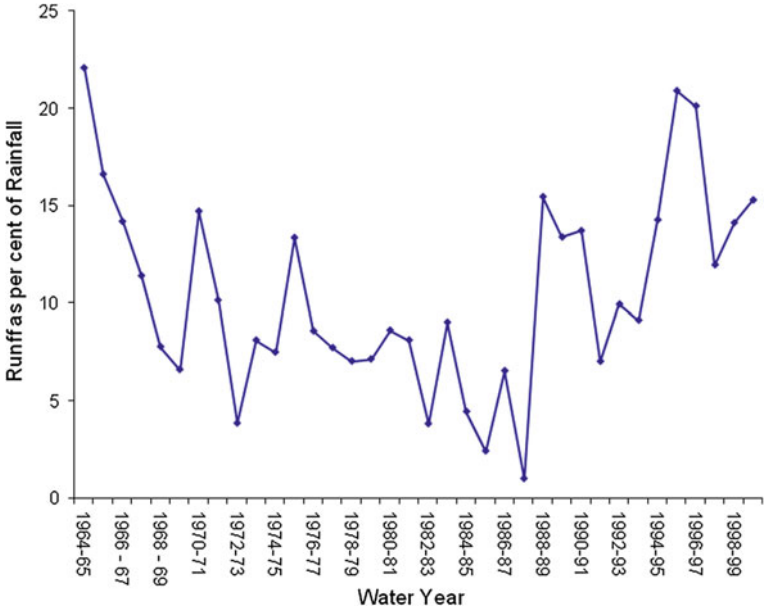

Fig. 2 Annual variation of runoff percentage of rainfall

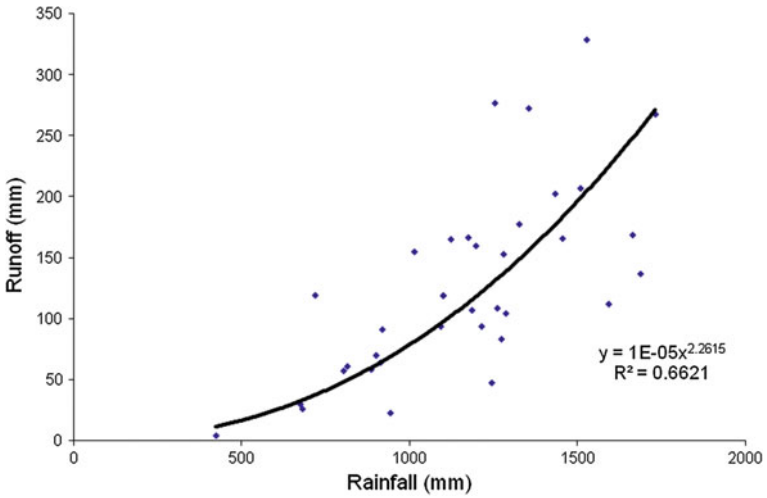

Fig. 3 Annual rainfall versus runoff in the watershed

Peak discharge did not show any trend as it totally depends upon the prior saturation, storm rain, and the intensity of rainfall. Discharge 7.40 cumec/km^2 was observed from the watershed being highest in the year 1996–97.

The annual values of runoff were plotted against the annual rainfall values (Fig. 3). The runoff was found to vary directly with the rainfall values. Following equation was obtained, in the exponential form

$$Y = 1E - 05 \times 2.2615(R2 = 0.6621)$$

where

Y Runoff (mm)
X Rainfall (mm)

Figure 3 shows that at rainfall above 1200 mm, the curve becomes steeper, depicting higher rate of runoff at higher rainfall, which was found to be in agreement with higher runoff during the years with higher rainfall (>1200 mm). However, in no case, the runoff was more than 21%, and on an average, these hilly protected forest watersheds can have the water yield of about 10–20% of annual rainfall (Tiwari et al. 2012b).

Sediment Yield

Sediment yield followed the same trend as that of the runoff, and it varied from a value of 37 Mg/ha before treatment to practically zero after the treatment. There has

been slight increase in the later stage, but it was found to be well within limits after the treatment. The initial observed value was found to be 37.71 Mg/ha in the year 1964–65 as 276.74 mm of runoff (22% of rainfall) came down to practically zero percent in the year 1979–80; however, in later years, it started increasing.

Looking into Fig. 4 wherein grouped average value of 5 years has been shown for sediment yield, there was sharp decline at the initial stage due to the check dams and the contour trenches (soil and water conservation measures). The little rise at the tail end of the curve may be either due to siltation of soil conservation structures, supplemented by the depletion of ground cover resulting from ever-increasing infestation of lantana enhancing a little more erosion from the hills.

The five-year average sediment yield values were related to the runoff. Following relationship was obtained for sediment yield.

$$Y = 0.1448 \times -12.092(R2 = 0.65)$$

where

Y Sediment yield (Mg/ha)
X Average 5-year runoff (mm)

Sediment yield was also compared with the peak discharge from the watershed. Usually, the heavy storms cause much erosion, and some times, even whole of the

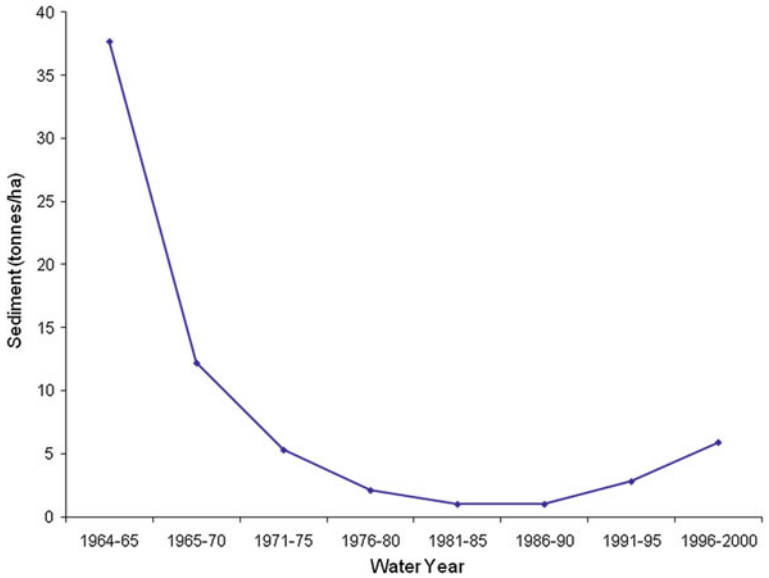

Fig. 4 Variation of sediment yield (1964–2000)

erosion might occur due to very few heavy storms. By analyzing the sediment yield and peak flow, it was seen that there was sharp rise in sediment yield beyond a peak discharge of 2.5 cumec/km^2.

Conclusions

The study provides the impact of resource conservation and afforestation on the long-term hydrology of the hilly watershed. Results indicate that the protected and treated hilly watersheds can provide the water yield to the tune of 10–20% of rainfall in the Shivalik belt. For rainfall up to 1000–1200 mm, the hydrological behavior does not have much change in the rainfall; however, for rainfall more than 1200 mm, this hilly watershed would contribute more runoff and become more vulnerable from the point of view of soil erosion. The soil conservation measures such as check dams and contour trenches combined with the plantations have a clear-cut impact on reducing the soil erosion from 37 Mg/ha/year to even less than 1 Mg/ha or within the permissible limits of soil erosion. Results further indicate that the barren hillocks even with the vertical cliffs can be rehabilitated through soil conservation measures and plantation activities along with protection. The increase of water yield and sediment yield (although within the permissible limit) in the later years has been due to the saturation of the sediment control structures. There might be a need to rejuvenate these structures through desilting and maintenance operations to keep their life effective. Infestation of lantana also needs to be controlled in these hilly watersheds, which is responsible for the depletion of ground cover in this watershed; the same may induce more of erosion. The rehabilitation process of the hills is to be watched carefully as the change in vegetation composition may also sometimes alter the hydrological behavior and increase vulnerability. The harvested rainwater from the hilly watershed in the pond can serve as good source of irrigation in the downstream areas through gravity flow. Water harvesting through these small structures assumes great importance in Shivaliks, where only 18% area is irrigated. For that, there has to be a sediment-free sustained water yield from these hilly watersheds in the Shivaliks.

References

Agnihotri Y (2000) Climatic trends vis-à-vis crop planning in Shivalik foothills. In: Mittal SP, Aggarwal RK, Samra JS (eds) Fifty years of research on sustainable resource management in shivaliks, Central soil and water conservation Research and Training Institute, Research Centre-Chandigarh pp 361–366

Grewal SS, Singh K, Juneja ML, Singh SC (1996) Relative growth, fuel wood yield, litter accumulation and conservation potential of seven Acacia species and an under story forestry grass on a slopping bouldry soil. Indian J For 19(2):174–182

Tiwari AK, Panwar P, Bhatt VK, Pal S, Bansal RC, Sharda VN (2012a) Resource conservation analysis of hilly forest watershed in Shivalik, Bulletin No. T-61/C-14. CSWCRTI, Dehradun pp 49

Tiwari AK, Bhatt VK, Bansal RC (2012b) Temporal variation of water yield from treated hilly watershed in lower Shivaliks. Indian For 138(3):257–264

Yadav RP, Aggarwal RK, Arya SL, Singh P, Prasad R, Bhattacharya P, Tiwari AK Yadav MK (2005a) Rainwater harvesting and reclycing technology for sustainable production in small agricultural watershed-Johranpur. CSWCRTI Bulletin No. T-50/C-11, pp 165

Yadav RP, Aggarwal RK, Bhattacharyya P, Bansal RC (2005b) Infiltration characteristics of different aspects and topographical locations of hilly watershed in Shivalik-lower Himalayan region in India. Indian J Soil Cons 33(1):44–48

Modeling of a River Basin Using SWAT Model

B. Venkatesh, T. Chandramohan, B. K. Purandara, Mathew K. Jose and P. C. Nayak

Abstract In the present study, process-based rainfall-runoff model namely Soil and Water Assessment Tool (SWAT) was calibrated for Manimala River basin in Kerala, with a catchment area of 780 km^2. The observed data of rainfall-runoff for a period of 8 years 2000–2007 were used for calibration and validation of the basin. Altogether, seven SWAT model parameters were calibrated with heuristic approach for the time frame of 2000–2005. Validation of these calibrated parameters was carried out in another independent timeframe (2006–2007). The results obtained show that the surface runoff is influenced by the parameters such as CN, ESCO, and SOL_AWC, whereas baseflow was influenced by lower values of GW_REVAP and ALPHA_BF. Further, the values of RMSE and NOF suggest for acceptance of rainfall-runoff model.

Keywords SWAT · Mainala River · Kerala · Calibration · Validation

Introduction

Understanding the water balance of a basin is the most important aspect in water resources development and management programmes. Major hydrological processes can be quantified with the help of water balance equations. The components of water balance of a basin are influenced by climate and the physical characteristics of the watershed such as morphology, land use, and soil. Understanding the relationship between these physical parameters and hydrological components is very essential for any water resources development related work. Since the hydrologic processes are very complex, their proper comprehension is essential, and for this,

B. Venkatesh (✉) · T. Chandramohan · B. K. Purandara · M. K. Jose
National Institute of Hydrology, Regional Centre, Visvesvaraya Nagar Main Road, Belgaum 590019, Karnataka, India
e-mail: bvenki30@gmail.com

P. C. Nayak
National Institute of Hydrology, Siddarth Nagar, Kakinada 533003, AP, India

V. P. Singh et al. (eds.), *Hydrologic Modeling*, Water Science and Technology Library 81, https://doi.org/10.1007/978-981-10-5801-1_48

watershed models are widely used. Most of the watershed models basically simulate the transformation of precipitation into runoff, sediment outflow, and nutrient losses.

Models which give a comprehensive picture of the various hydrologic processes are called as integrated watershed models. Choice of watershed development model depends upon the hydrologic components to be incorporated in the water balance. The most important hydrologic elements from the water management point of view are surface runoff, lateral flow, baseflow, and evapotranspiration. There are a number of integrated physically based distributed models. Among them, researchers have identified SWAT as the most promising and computationally efficient (Neitsch et al. 2005). Hence, in this study, an attempt has been made to identify the most sensitive parameters, of the SWAT model, and to determine the important hydrologic components of a river basin with focus on water conservation and management.

SWAT Rainfall-Runoff Model

The SWAT model is a long-term, continuous simulation watershed model. It operates on a daily time step and is designed to predict the impact of management on water, sediment, and agricultural chemical yields. The model is physically based, computationally efficient, and capable of simulating a high level of spatial detail by allowing the division of watersheds into smaller sub-watersheds. SWAT models water flow, sediment transport, crop/vegetation growth, and nutrient cycling. The model allows users to model watersheds with less monitoring data and to assess predictive scenarios using alternative input data such as climate, land use practices, and land cover on water movement, nutrient cycling, water quality, and other outputs. Major model components include weather, hydrology, soil temperature, plant growth, nutrients, pesticides, and land management. Several model components have been previously validated for a variety of watersheds.

In SWAT, a watershed is divided into multiple sub-watersheds, which are then further subdivided into hydrologic response units (HRUs) that consist of homogeneous land use, management, and soil characteristics. The HRUs represent percentages of the sub-watershed area and are not identified spatially within a SWAT simulation. The water balance of each HRU in the watershed is represented by four storage volumes: rain, soil profile (0–2 m), shallow aquifer (typically 2–20 m), and deep aquifer (more than 20 m). The soil profile can be subdivided into multiple layers. Soil water processes include infiltration, evaporation, plant uptake, lateral flow, and percolation to lower layers. Flow, sediment, nutrient, and pesticide loadings from each HRU in a sub-watershed are summed, and the resulting loads are routed through channels, ponds, and/or reservoirs to the watershed outlet. Detailed descriptions of the model and model components can be found in Arnold et al. 1998 and Neitsch et al. 2001.

SWAT Input Data: The model requires land use, soil, and topography data for simulating runoff from the watershed. The land use data were obtained from Food and Agricultural Organization (FAO) and the soil information from National Bureau of Soil Survey and Land Use Planning (NBSS and LUP). Topographic information was derived using digital elevation model (DEM) data (the shuttle radar topography mission (SRTM) DEM has been used). The DEM data were used to generate variations in sub-watershed configurations such as sub-watershed delineation, stream network delineation, and slope and slope lengths using the ArcView interface for the SWAT model. Land use categories provided in FAO land use files are relatively simplistic, including all categories such as forest and its variants, agricultural land, barren land, etc. In the present case, the watershed considered for the analysis is covered by 100% broad leaf natural forest. The soil data is available in NBSS and LUP, which contains soil maps at a 1:250,000 scale. Each map unit is linked to the Soil Interpretations Record attribute database that provides the proportionate extent of the component soils and soil layer properties. The soil map units and associated layer data were used to characterize the simulated soils for the SWAT analyses.

Study Area

Manimala River originates from Tatamala hills in Idukki district at an elevation of 1156 m above msl and drains through the highland, midland, and the lowland physiographic provinces of Kerala. It empties into the Vembanad Lake, after merging with the Pamba at Muttar in Alappuzha District. Owing to the steep topography, the stream network of the Manimala basin is very dense. The present analysis considers the river basin up to the gauge-discharge site at Thondara which covers a geographical area of 780 km^2. The location of the study area is shown in Fig. 1.

Manimala River basin receives major portion of rainfall during southwest monsoon period (June–September). The southwest monsoon forms around 80% of annual rainfall. The northeast monsoon (October–November) supplies the remaining portion of the rainfall. The average annual rainfall of the basin is around 2600 mm.

The major soil type found in the basin is gravelly clayey with good drainage characteristic. The basin is predominantly used for rubber plantation within the midland regions and part of highland and lowland regions. The lowlands are covered by paddy and other short-term crops and vegetables and shrubs. Highland regions are having forest areas (disturbed, semi-evergreen, and evergreen) and forest plantations.

Data Availability: Data from rainfall observation stations maintained by the state irrigation department is collected and used for the project. In this study, the

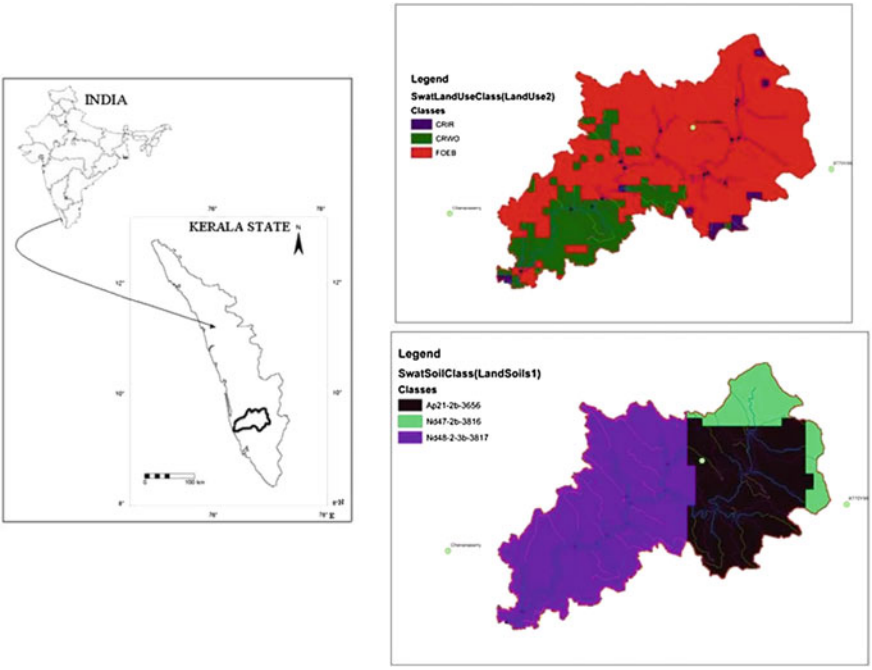

Fig. 1 Index map of Manimala basin with land use and soil maps

data of station such as Boyce estate (1990–2008) and Changanasserry (2000–2008) are used. The state irrigation department maintains gauge-discharge sites at three locations along the whole river stretch. The flow characteristics of highland reaches of the basin are measured at Mundakkayam, the Manimala gauge station represents the flow up to midland region, and the overall discharge till lowland area is measured at Thondara. In the present study, the rainfall and runoff at Thondara station data for a period of 2000–2007 have been used.

Results and Discussion

The SWAT modes was set-up for the Manimala basin using the observed daily data on rainfall at Boyce Estate and Chenganasserry and discharge data at Thondara which is maintained by state irrigaiton department. The data for these stations were collected for a period of 8 years starting from 2000 to 2007. The SWAT model was calibrated using the data for 2000–2005 and validated for a 2-year period (2006–2007). Calibration of the model was done by adopting the manual calibration procedure. Santhi et al. (2001) suggested a generalized manual calibration procedure, indicating the most sensitive input parameters, acceptable model evaluation

results, and sensible ranges of parameters uncertainty. As few of the model parameters are not possible to measure in the field and are need to be calibrated against the observed discharge, therefore, during the calibration period, the model parameters were varied within the physically allowed range and more realistic to the natural condition of the basin. As recommended by Coffey et al. (2004) to use the R^2 and modeling efficiency objective functions to evaluate the performance of the model, the following modeling evaluation indices were used in this study.

The root-mean-square error (RMSE) and the normalized objective function (NOF) were computed based on the following equation

$$\mathrm{RMSE} = \sqrt{\frac{\sum_{i=1}^{N}(P_i - Q_i)^2}{N}} \tag{1}$$

$$\mathrm{NOF} = \frac{\mathrm{RMSE}}{\bar{Q}} \tag{2}$$

where P_i are the model predicted values, Q_i are the observed values for the N observations, and $\bar{Q}$ is the mean of observed values. According to Kornecki et al. (1999), the ideal value of NOF is 0.0. However, a model is acceptable for NOF values in the range from 0.0 to 1.0 when site-specific data are available for calibration. In that case, the model can be used to test scenarios associated with management practices. The optimized values of the model parameters are tabulate in Table 1, and the time series data of discharge both for observed and simulated are plotted in Fig. 2, for the calibration period. Similarly, the validation period is plotted in Fig. 3.

The optimized curve number for the catchment is reported to be 78, which is indicative of generating higher runoff. As reported in the earlier paragraphs, the natural forest is one of the major land use of the basin (Fig. 1), which is further supported by the lower values of ESCO, as its value is close to the defaulted of 0.95. As this parameter (ESCO) adjusts the depth distribution for evaporation from the soil to account for the effect of capillary action. The higher values of ESCO cause lower soil evapotranspiration as entire soil layers is at the saturation and need

Table 1 Parameter ranges and values used in the sensitivity analysis

Model parameters	Variable name	Range	Model value
Curve number	CN	69–85	78
Soil evaporation compensation factor	ESCO	0.75–0.95	0.85
Plant uptake compensation factor	EPSO	0.01–1.0	0.55
Soil available water capacity (mm)	SOL_AWC	0–50	22
Baseflow alpha factor	ALPHA-BF	0.05–0.8	0.048
Groundwater revap coefficient	GW_REVAP	0.02–0.2	0.02
Groundwater delay time (days)	GW DELAY	0–100	31
Deep aquifer percolation fraction	RECHARGE_DP	0–1	0.05

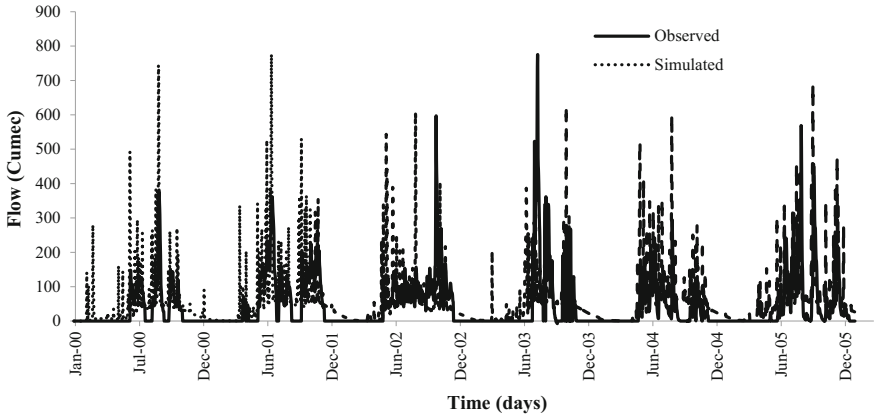

Fig. 2 Plot of observed and simulated discharge during calibration period

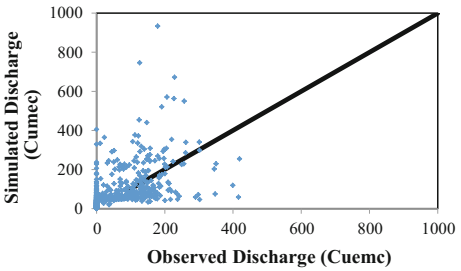

Fig. 3 Scatter plot for observed and simulated discharge during validation period

not to compensate for a water deficit in upper layers, which in turn increases both surface runoff and baseflow. ESCO was found to have a higher impact on baseflow than surface runoff. The groundwater delay parameter is responsible in enhancing the groundwater recharge after passing through the unsaturated zone (Srinivasan et al. 2010). These authors have reported the value of 31 days for groundwater delay in their application of SWAT to simulate the water balance and crop yield in upper Mississippi basin. In the present study, it is observed that the groundwater delay for Manimala is 31 days. The larger values of groundwater delay indirectly represent the average depth of the ground water as well as the hydraulic properties of the soils in the basin. Further, Rostamian et al. (2008) reported very large range values of groundwater delay (80–121 days) while simulating the discharge for mountainous catchments in Central Iran covered by 10% rocks and 50% agricultural activity.

The other most sensitive parameter as reported elsewhere (Jha 2011) is Base flow alpha factor (ALPHA-BF); any increase in the value will result in simulating steeper hydrograph recession. Numerous studies elsewhere (Srinivasan 2010; Zhang et al. 2009; Rostamian et al. 2008; Green et al. 2006) have reported a range of values 0.02–0.04. The optimized value of ALPHA-BF in this study matches with

Table 2 Performance indicator

Performance indicator	Calibration	Validation
Root-mean-square error (RMSE)	86.29	85.35
Normalized objective function (NOF)	01.98	01.68

that of the reported value. The GW_REVAP coefficient controls the amount of water that moves from the shallow aquifer to the root zone. This parameter was increased to allow more movement of water from shallow aquifer to the unsaturated zone. This parameter was used to adjust summer base flow.

The model evaluation statistics obtained for both calibration and validation period are tabulated in Table 2. Table 2 revealed that the RMSE values for calibration and validation are lower and are indicative of the higher efficiency of the model in simulating the flow. Similarly, the lower values were obtained for other evaluating parameter NOF.

Conclusion

This study assessed and identified hydrologic parameters of the SWAT model by the application to the forested catchment located in Kerala, India. The model was calibrated and validated using the observed runoff from an area of 770 km^2. The results obtained show that the surface runoff is influenced by the parameters such as CN, ESCO, and SOL_AWC, whereas baseflow was influenced by lower values of GW_REVAP and ALPHA_BF. Further, the values of RMSE and NOF suggest for acceptance of rainfall-runoff model; this calibration can be adjudged as good because of having lower values of RMSE and NOF, which is quite acceptable for water engineering problem assessment and application. The calibrated parameter values can also be used for further streamflow simulations in this catchment.

References

Arnold JG, Srinivasan R, Muttiah RS, Williams JR (1998) Large-area hydrologic modeling and assessment: part I. Model development. J Am Water Resour Assoc 34(1):73–89

Coffey ME, Workman SR, Taraba JL, Fogle AW (2004) Statistical procedures for evaluating daily and monthly hydrologic model predictions. Trans ASAE 47(1):59–68

Green CH, Tomer MD, Luzio MD, Arnold JG (2006) Hydrologic evaluation of the soil and water assessment tool for a large tile-drained watershed in Iowa. Am Soc Agric Biol Eng 49(2): 413–422

Jha MK (2011) Evaluating hydrologic response of an agricultural watershed for watershed analysis. Water 3:604–617. doi:10.3390/w3020604

Kornecki TS, Sabbagh GJ, Storm DE (1999) Evaluation of runoff, erosion and phosphorus modeling system—SIMPLE. J Am Water Resour Assoc 4:807–820

Neitsch SL, Arnold JG, Kiniry JR, Williams JR (2001) Soil and water assessment tool-version 2000-user's manual. Temple, Texas, USA

Neitsch SL, Arnold AG, Kiniry JR, Srinivasan JR, Williams JR (2005) Soil and water assessment tool user's manual: version 2005. TR–192: College Station, Tex: Texas Water Resources Institute

Santhi C, Arnold JG, Williams JR, Dugas WA, Srinivasan R, Hauck LM (2001) Validation of the SWAT model on a large river basin with point and nonpoint sources. J Am Water Resour Assoc 37(5):169–1188

Srinivasan R, Zhang X, Arnold J (2010) SWAT ungauged: hydrological budget and crop yield predictions in the upper Mississippi river basin. Am Soc Agric Biol Eng 53(5):1533–1546

Rostamian R, Jaleh A, Afyuni MJ, Mousavi SF, Heidarpour M, Jalalian A, Abbaspour KC (2008) Application of a SWAT model for estimating runoff and sediment. Hydrol Sci J (Special issue: Advances in Ecohydrological Modelling with SWAT) 53(5):977–988

Zhang X, Srinivasan R, Zhao K, Liew MV (2009) Evaluation of global optimization algorithms for parameter calibration of a computationally intensive hydrologic model. Hydrol Process 23(3):430–441

Performance of the Xinanjiang Model

A. Ahirwar, M. K. Jain and M. Perumal

Abstract The Xinanjiang rainfall–run-off model is a popular model applied extensively in the humid and sub-humid regions of the world for forecasting of flood, climate change studies and water resources assessment, planning and management. However, its performance in the Indian climatic conditions has not been extensively studied. In the present study, attempt is made to evaluate the performance of the Xinanjiang model for run-off simulation in six Indian watersheds having different climatic conditions (wet, average and dry). The results of the study indicate better model performance in wet catchments with average values of NSE = 0.88 and average R^2 = 0.89. The average values of NSE and R^2 on watersheds with average climatic condition obtained as 0.67 and 0.68, respectively, indicating average performance of the model. The performance of the model may be considered poor on watersheds with dry climatic conditions as the average estimated values of NSE and R^2 being 0.49 and 0.52, respectively. The results indicate the suitability of the application of Xinanjiang model in catchments characterised by wet and average climatic conditions and poor in dry climate conditions of India. However, extensive study is required to arrive at a final inference about the suitability of application of this model considering a number of catchments in the country.

Keywords Xinanjiang model · NSE · Wet · Average · Dry

Introduction

Hydrological processes operating on a landscape are affected by topography, variations in temperature, amount of rainfall, climatic conditions and landscape characteristics. For understanding the hydrological response of a catchment, a well-defined hydrological model framework is needed. Presently, a number of

A. Ahirwar (✉) · M. K. Jain · M. Perumal
Department of Hydrology, Indian Institute of Technology Roorkee, Roorkee 247667, India
e-mail: ajayahirwar2006@gmail.com

V. P. Singh et al. (eds.), *Hydrologic Modeling*, Water Science
and Technology Library 81, https://doi.org/10.1007/978-981-10-5801-1_49

well-established conceptual and physically based modelling approaches are available to model the rainfall–run-off response of a catchment. Although these models are applicable throughout the world, it is now understood that the basic failure of most of these models to represent the catchment response is essentially due to their inability to reproduce the dynamic variation of the saturated areas within the catchment with a minimum number of parameters (Beven et al. 1983). The highly nonlinear nature of catchment response to storm events can be attributed to the dynamic variation in accumulation and horizontal movement of water in the upper layer of soil (Todini 1996). Further, addition of more and more process components and parameters to the models may fail to reproduce the actual phenomena and reduce the models to extremely complex black boxes with an exceedingly high number of parameters to be estimated from historical data (Todini 1996). The newly developed conceptual models, either based on the concept of soil moisture replenishment, depletion and redistribution mechanism, like the Xinanjiang model and its modified versions (Zhao et al. 1980; Zhao 1992; Jayawardena ad Zhao 2000), the variable infiltration capacity (VIC) model and its transitions (Wood et al. 1992; Dumenil and Todini 1992; Liang et al. 1994, 1996a, b; Sivapalan and Woods 1995; Abdulla et al. 1996; Habets et al. 1999; Jayawardena and Mannama 2002), the ARNO model (Todini 1996) are capable of reproducing the catchment response with a smaller number of physically meaningful parameters even for large catchments.

The Xinanjiang model and its extensions could model the catchment response for any scale, including the scale required within the framework of global climate change models. This model has the capability to account for nonlinear spatial retention of the soil moisture in a lumped manner (Sahoo 2005). Gan et al. (1997) compared the performance of Xinanjiang model along with Pitman model of South Africa, Sacramento model of USA, NAM model of Europe and SMAR model of Ireland in three medium-sized, dry catchments located in Africa and USA and concluded that the Xinanjiang model performs better than these models. Nghi et al. (2008) compared the performance of Xinanjiang model with NAM model in the Nong Son catchment, in the Central Vietnam and concluded that the Xinanjiang model performs relatively better in run-off production. Li et al. (2009) evaluated the performance of Xinanjiang model on 210 catchments in south-east Australia and found that the inclusion of the leaf area index in the Xinanjiang model increases its performance in ungauged catchments. Similarly, many researchers like Ren et al. (2006), Bai et al. (2009), Chang et al. (2010), Hu et al. (2011), Yang et al. (2011), Liu et al. (2012), Ouyang et al. (2013), Yuanyuan et al. (2013), Shi et al. (2013), Duan and Mei (2014), Li et al. (2014), Lin et al. (2014), Si et al. (2015) and Zuo et al. (2015) applied the Xinanjiang model for different catchments of the world. However, not many studies are reported in the literature about the performance of the Xinanjiang model on Indian catchments. Kneis et al. (2014) used the Xinanjiang model for run-off generation process in the catchments of lower part of the Mahanadi River basin of India. In the present study, the performance of the

Xinanjiang model has been evaluated on six Indian catchments characterised by different climatic conditions (wet, average and dry).

Materials and Methods

Xinanjiang Model

The Xinanjiang model works on the concept of run-off formation on repletion of storage, i.e., the run-off is not produced until the soil moisture content of the aeration zone reaches field capacity and, thereafter, run-off equals the rainfall excess after deducting evaporation losses (Zhao et al. 1980). It has been applied to large basins in the humid and semi-humid regions of China and many other catchments elsewhere for rainfall–run-off modelling. The Xinanjiang model uses only two inputs, i.e., rainfall (P) and measured pan evaporation (EM). The outputs from the model are simulated discharge (Q), actual evapotranspiration (E) and daily soil moisture accounting (W) as water balance component. The structure of the model is shown in Fig. 1. The model consists of four basic sub-modules with 15 different parameters classified under four different heads, viz. evapotranspiration (K, C, UM, LM), run-off production (IM, WM, B), run-off separation (SM, Ex, KI, KG) and run-off concentration parameters (CG, CI, L, CS). The model accounts for nonlinear spatial retention of the soil moisture in a lumped manner using Eq. (1).

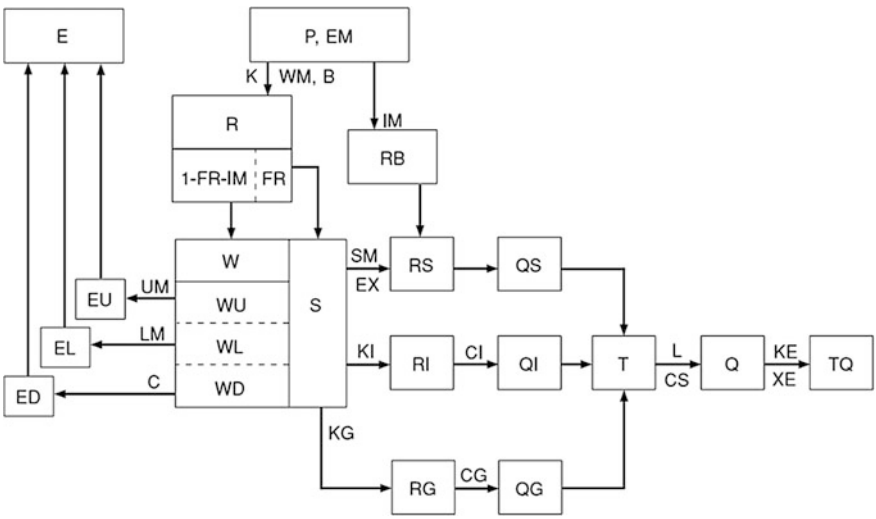

Fig. 1 The structure of the Xinanjiang model (adopted from Singh 1995)

$$1 - \frac{f}{F} = \left(1 - \frac{W'M}{\mathrm{MM}}\right)^{B} \cdot (1 - \mathrm{IM}) \tag{1}$$

where f is the fractional basin area, F is the total area of the basin, f/F is the proportion of the pervious area of the basin, $W'M$ is the point value of variable moisture storage capacity of soil, MM is the maximum moisture storage capacity of soil, B is a shape parameter describing the soil heterogeneity of the basin, and IM is the impervious area of the sub-basin. Detailed description of the model is available elsewhere (Zhao et al. 1980, 1992; Singh 1995).

Model Calibration

Almost all conceptual hydrological models require calibration of parameters before they could be used for simulation. The Xinanjiang conceptual rainfall–run-off model also contains large number of parameters which cannot be obtained directly from catchment characteristics (Xu et al. 2013), and therefore, an automatic optimisation technique is needed to calibrate the model parameters. In this study, the Shuffled Complex Evolution method developed at the University of Arizona (SCE-UA) by Duan et al. (1992) has been used for calibration of model parameters. The strategy of the SCE-UA method is to combine the strength of the simplex procedure (Nelder and Mead 1965) with the concepts of controlled random parameters search (Price 1987), competitive evolution (Holland 1975) and complex shuffling. SCE-UA method is capable to complete the searching of parameters even in one run (Gan and Biftu 1996). Zhang et al. (2015) showed that while applying SCE-UA method for optimising the hydrological model parameters, the parameter estimates are not get affected by the data length used which indicates the robustness of the SCE-UA algorithm. It may be noted that since the catchments studied herein are characterised by small catchments area, no channel routing component has considered in the modelling process, and accordingly, the parameters of the routing process of the model were not taken into consideration while calibrating the model.

Model Performance Criteria

The performance of the model has been judged based on the Nash–Sutcliffe efficiency (NSE) (Nash and Sutcliffe 1970) and R^2 (coefficient of determination). The NSE (Nash and Sutcliffe 1970) and R^2 can be expressed, respectively, as

$$\mathrm{NSE} = 1 - \frac{\sum \left(Q_{o,i} - Q_{e,i}\right)^2}{\sum \left(Q_{o,i} - \overline{Q}_o\right)^2} \tag{2}$$

$$R^2 = \left(\frac{\sum \left(Q_{e,i} - \overline{Q}_e\right)\left(Q_{o,i} - \overline{Q}_o\right)}{\sqrt{\sum \left(Q_{e,i} - \overline{Q}_e\right)^2 \sqrt{\sum \left(Q_{o,i} - \overline{Q}_o\right)^2}} \right)^2 \quad (3)$$

where $Q_{o,i}$ is the observed discharge (mm), $Q_{e,i}$ is the model simulated discharge (mm), $\overline{Q}_o$ is the mean observed discharge (mm), and $\overline{Q}_e$ is the mean simulated discharge (mm).

Study Area and Data Used

To evaluate the performance of the model, six watersheds situated in different agro-climatic conditions of India have been selected. As the measured pan evaporation data are not available for these catchments, the same were extracted from the mean monthly evaporation maps of India which are available at Indian Meteorological Department (IMD) website (http://www.imdagrimet.gov.in/node/92). The selected watersheds have been characterised into wet, average and dry categories on the basis of run-off coefficient. Salient features of the selected watersheds are given in Table 1. Locations of the selected watersheds are shown in Fig. 2.

The watersheds studied herein have been classified as wet, average and dry by Durbude et al. (2011) as per the following details:

1. **Wet watersheds**: The watershed having a run-off coefficient more than 0.65 has been classified as a wet watershed. Accordingly, the Hemavati and Kokkarne watersheds fall under this category.
2. **Average watersheds**: The watershed having a run-off coefficient between 0.36 and 0.65 has been classified as average watershed. Accordingly, the Khanpur and Anthroli watersheds fall under this category.
3. **Dry watersheds**: The watershed having a run-off coefficient less than or equal to 0.35 has been classified as a dry watershed. Accordingly, the Amachi and Hridaynagar watersheds fall under this category.

Results and Discussion

Model Performance in Calibration and Validation Processes

The performance of the model has been assessed using the statistical indices NSE and R^2. The calibration and validation have been performed using daily data at one-day time interval. Summary of the model performance is given in Table 2.

Table 1 Description of selected watersheds used in study

Watersheds Characteristics	Name of watersheds					
	Wet		Average		Dry	
	Hemavati	Kokkarne	Khanpur	Anthroli	Amachi	Hridaynagar
Basin	Cauvery	Sitanadi	Krishna	Kalinadi	Tungabhadra	Narmada
River	Hemavati	Sitanadi	Malaprabha	Dusginala	Mavinhole	Banjar
State	Karnataka	Karnataka	Karnataka	Karnataka	Karnataka	Chhattisgarh
District	Chikmagalur	Dakshina Kanada	Belgaum	Uttar Kanada	Shimoga	Durg
Area (km^2)	600	343	320	503	87	3370
Latitude	12° 55′ to 13° 11′N	13° 20′ to 13° 35′N	15° 20′ to 15° 40′N	15° 20′ to 15° 34′N	14° 10′ to 14° 16′N	21° 42′ to 22° 36′N
Longitude	75° 29′ to 75° 51′E	74° 49′ to 75° 10′E	74° 20′ to 74° 30′E	74° 35′ to 74° 55′E	75° 04′ to 75° 11′E	80° 28′ to 81° 36′ E
Topography	Low land, semi hilly and hilly	Hilly (western ghats)	Hilly (hilly crest and valley bottom)	Hilly (western ghats)	Hilly (western ghats)	Flat, undulating land
Discharge Gauging site	Sakleshpur	Kokkarne bridge in Udupi taluka	Belgaum-Goa road crosses Sitanadi river at Khanpur	Dusginala river crosses Khanpur-Haliyal road	Amachi village	Hridaynagar Gauging site of Central Water Commission, India
Agro-climatic subzone	Hilly zone of Karnataka	Coastal zone of Karnataka	Northern transition zone of Karnataka	Hilly zone of Karnataka	Southern transition zone of Karnataka	Northern hill region of Chhattisgarh
Land use/ cover	Forest, coffee plantation, agriculture	Fairly dense mixed jungle	Forest (63%), agriculture (17%)	Forest, agriculture, wasteland	Dense mixed jungle (forest)	Forest, agriculture, degraded land
Soil type		Laterite		Red loamy	Red loamy	Black to mixed red

(continued)

Table 1 (continued)

Watersheds Characteristics	Name of watersheds					
	Wet		Average		Dry	
	Hemavati	Kokkarne	Khanpur	Anthroli	Amachi	Hridaynagar
	Red loamy and red sandy		Red loamy and medium black			
Elevation (m) amsl	1240–890	1153–630	792–646	778–532	800–576	600–372
Average annual rainfall (mm)	2854	5079	3401	925	1785	1442
Mean evaporation (mm)	3.9	4.5	5.86	4.25	4.99	5.33
Calibration period	1975–1978 (3 years)	1985–1990 (5 years)	1985–1990 (5 years)	1985–1990 (5 years)	1985–1990 (5 years)	1985–1990 (5 years)
Validation period	1978–1980 (2 years)	1990–1994 (4 years)	1990–1994 (4 years)	1990–1994 (4 years)	1990–1994 (4 years)	1990–1994 (4 years)

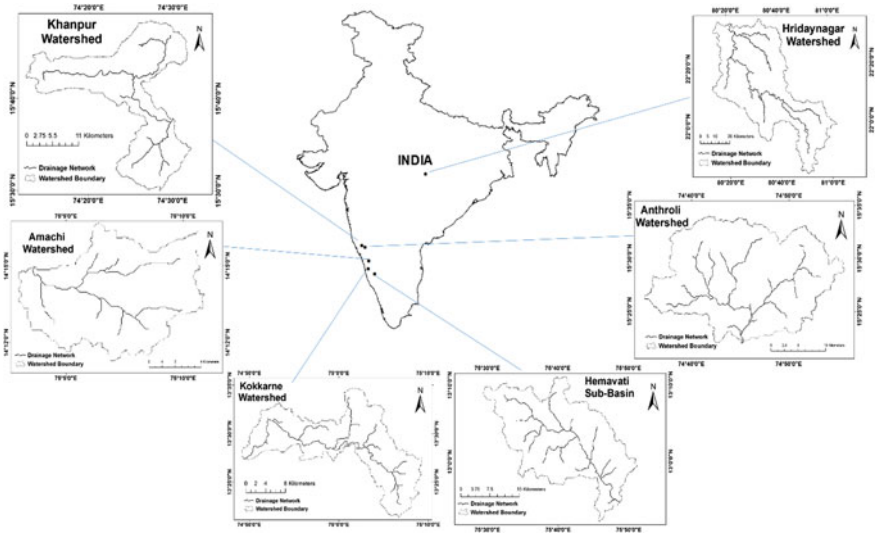

Fig. 2 Location map of study area

Table 2 The simulation results from the Xinanjiang model

Name of watershed	Run-off coefficient	Performance evaluation			
		Calibration		Validation	
		NSE	R^2	NSE	R^2
Kokkarne	0.79	0.90	0.90	0.90	0.91
Hemavati	0.78	0.87	0.87	0.85	0.89
Khanpur	0.60	0.77	0.77	0.72	0.72
Anthroli	0.37	0.71	0.71	0.50	0.51
Amachi	0.29	0.59	0.59	0.46	0.47
Hridaynagar	0.24	0.55	0.56	0.37	0.47

The plots between observed and model computed hydrographs both for calibration and validation processes are shown graphically in Fig. 3.

It can be seen from Table 2, the NSE for Kokkarne and Hemavati watersheds (both wet) are high as 0.90 and 0.87, respectively, and they are same or nearly the same in the calibration as well as in validation periods. The NSE for Khanpur (average) watershed is higher than that of the Anthroli (average) watershed, in the calibration period. But it may be noted that the NSE and R^2 estimates for Anthroli watershed in the verification period are significantly lower than the corresponding estimates of the Khanpur watershed. The NSE for Amachi (dry) watershed is slightly higher than that of Hridaynagar (dry) watershed in both the calibration and validation periods. The variation pattern of R^2 is different from the NSE estimates in the verification period of the Hridaynagar watershed.

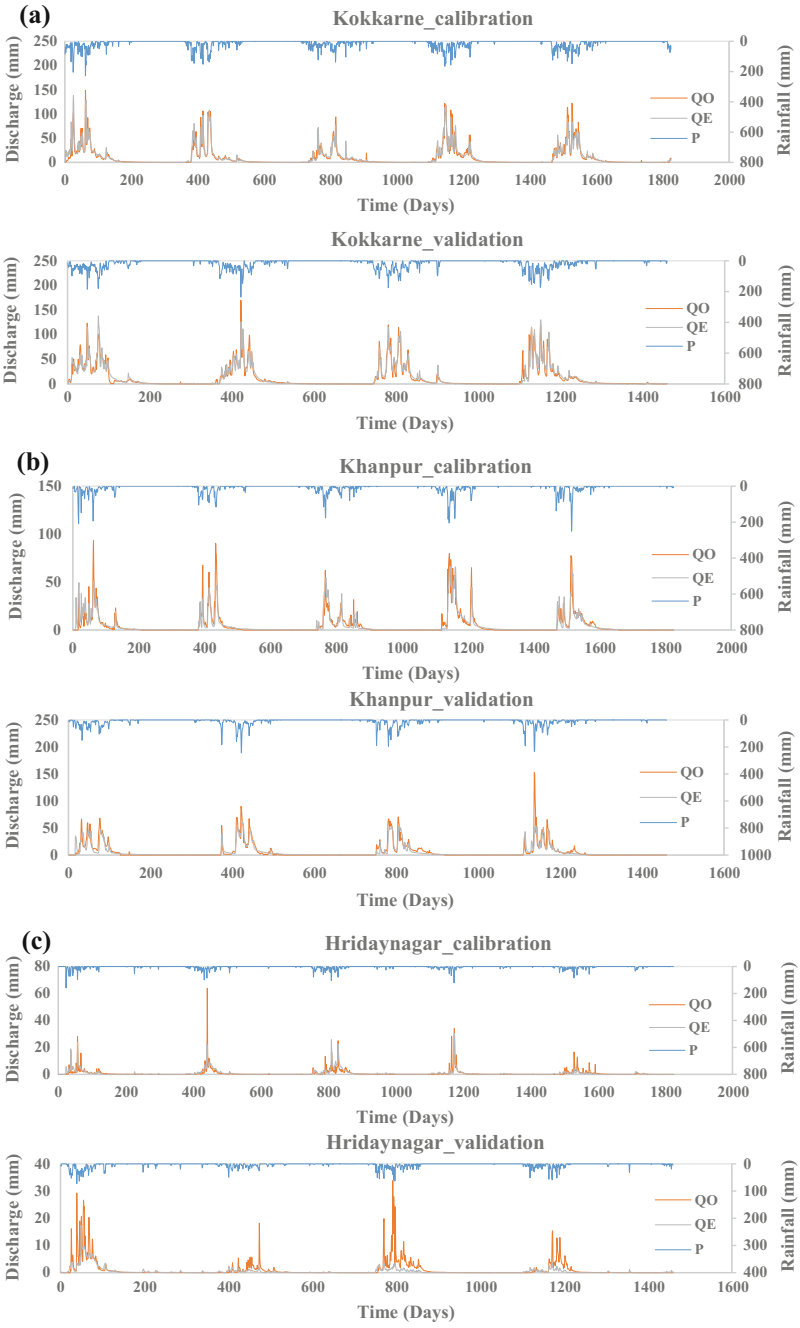

Fig. 3 Calibration and validation of the wet (**a**), average (**b**) and dry (**c**) watersheds

The run-off coefficients of the studied watersheds are also shown in Table 2. The run-off coefficient is an important factor to be considered because all the studied watersheds have been categorised on the basis of it. It is seen from Table 2 that the studied watersheds are arranged from wet to dry category as per different estimated ranges of run-off coefficients. The results presented in Table 2 confirm the general perception that the Xinanjiang model is suitable for application in wet and average catchments rather than for dry catchments. Overall, the performance of the model improves for the catchments with higher run-off coefficient suggesting that the model is more suitable for application in wet catchments.

Model Performance on Physical Basis

To show the model performance physically, the characteristics of the tension water capacity distribution curve can be studied.

Characteristics of Tension Water Storage Capacity Curve

Liu et al. (2001) showed that if the value of parameter B tends towards zero then the run-off decreases, and if it is zero, then catchment will behave like a tank, i.e., no run-off will be generated from pervious area. If the parameter B tends towards infinity, then the run-off will increase and the catchment will behave like a totally impervious surface, i.e., all the rainfall will become run-off after eliminating the evaporation losses. In this study, also the behaviour of the parameter B has been explored. Manfreda (2008) observed that the heterogeneity of the soil depends on the parameter B (Liu et al. 2001) which affects the average spatial soil moisture capacity (WM) which is the most important parameter in the run-off generation process. The tension water storage capacity curve obtained from the Xinanjiang model represents the physical performance of the model by means of its different shapes. The shapes and inclination of the curves towards different axis give an idea about the run-off generation characteristics of a watershed. If the inclination of the tension water storage capacity curve is towards the primary Y-axis and secondary X-axis, then the value of the parameter $B < 1$ which shows that the watershed has greater capacity to store the water, i.e., the run-off production will be less in this case. Alternatively, the inclination of the curve is towards secondary Y-axis and primary X-axis, and then the value of the parameter $B > 1$, which shows that the catchment has less capacity to store the water resulting in more run-off production. In Fig. 4 and Table 3, it can be seen that Kokkarne, Hemavati, Khanpur, Anthroli and Hridaynagar watersheds are characterised by the tension water capacity distribution curves having inclination towards the secondary Y-axis and towards primary X-axis with the estimates of $B > 1$, suggesting more run-off production. But it can be seen that Amachi watershed is characterised by the tension water capacity

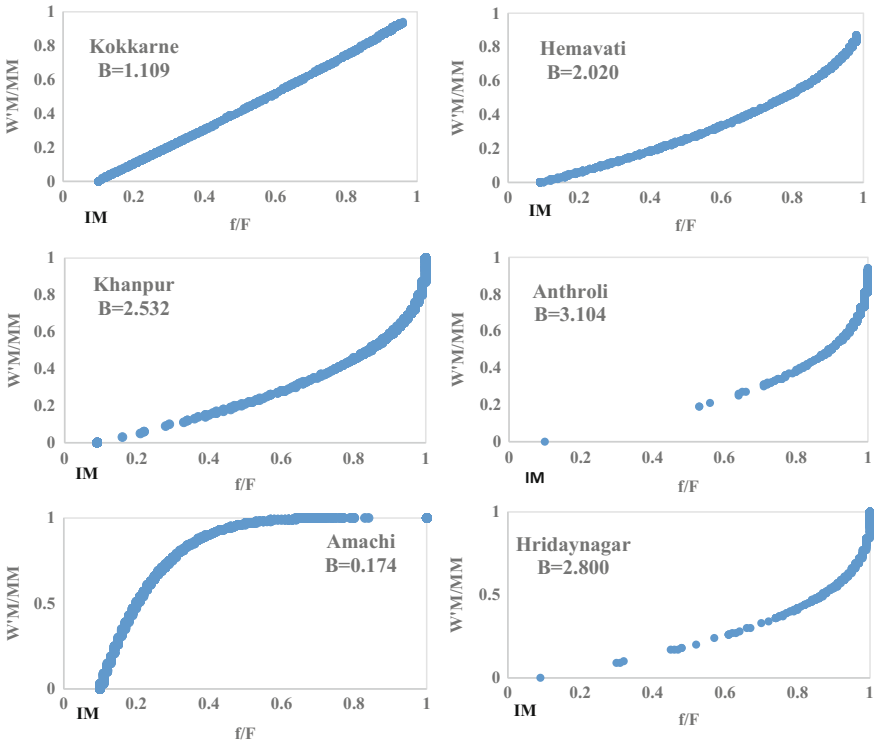

Fig. 4 Tension water capacity distribution curve of studied watersheds of the Xinanjiang model

Table 3 Physical performance of the Xinanjiang model

Name of watershed	Calibrated model parameters			Average annual evapotranspiration estimated during study period (mm)	Run-off produced	
	B	IM	WM (mm)		From impervious area (%)	From pervious area (%)
Kokkarne	1.11	0.10	549.65	1069.04	12.54	87.46
Hemavati	2.02	0.09	588.14	798.81	12.83	87.17
Khanpur	2.53	0.09	158.80	1515.08	16.06	83.94
Anthroli	3.10	0.10	175.02	667.10	37.53	62.47
Amachi	0.17	0.10	326.14	1227.69	34.15	65.85
Hridaynagar	2.80	0.09	306.03	1247.60	42.28	57.72

distribution curve having inclination towards the primary *Y*-axis and secondary *X*-axis which indicates higher moisture absorption due to presence of high soil moisture deficit as depicted in Table 4.

Table 4 Average soil moisture deficit of studied watersheds

Name of watershed	Run-off coefficient during calibration	Average soil moisture deficit per water year (fraction)				Average soil moisture deficit (fraction)
		1	2	3	4	
Kokkarne	0.79	0.54	0.54	0.50	0.58	0.54
Hemavati	0.74	0.35	0.34	0.37	–	0.35
Khanpur	0.56	0.79	0.81	0.75	0.78	0.78
Anthroli	0.31	0.50	0.46	0.39	0.46	0.46
Amachi	0.27	0.81	0.91	0.86	0.77	0.84
Hridaynagar	0.20	0.74	0.80	0.80	0.82	0.79

Factors Affecting Model Performance

Analysis of results obtained reveal that the model performance is affected by the average soil moisture capacity (WM) as it plays an important role in the run-off production process in the Xinanjiang model (Manfreda 2008). In catchments having dry and average run-off production characteristics, it is observed that generally these catchments have high evapotranspiration, and the precipitation occurs for short duration with high intensity. These catchments are, therefore, dominated by Hortonian run-off generation mechanism (infiltration excess run-off), and also run-off generation varies spatially and affected due to slope and surface topography (Ye et al. 1997; Li et al. 2015). In the Xinanjiang model, the average soil moisture capacity—obtained through optimisation—is kept constant throughout the model simulation, and it is relatively high in dry catchments. As the Xinanjiang model works on the concept of repletion of storage, and due to this concept, the model gets low efficiency in dry catchments due to higher evaporation and initial high moisture deficit.

During calibration and validation processes, it is seen that even the high value of rainfall does not generate high peak run-off due to high soil moisture deficit in dry catchments. While in wet catchments due to high rainfall for longer duration, the available soil moisture is more resulting in more run-off production. This could be a reason for the better performance of the Xinanjiang model, having saturation excess run-off mechanism as the only run-off generation mechanism in wet catchments instead of dry or average catchments. Now how the average soil moisture capacity (WM) affects the performance of the model is described in the next subsection.

Soil Moisture Profile

The soil moisture profile for wet, average and dry catchments is shown in Fig. 5. It can be seen from this figure that how the average soil moisture capacity (WM) affects the performance of the model. In the case of Hemavati and Kokkarne

watersheds which belong to wet category, the soil moisture deficit prevails for a shorter time implying that the saturation condition prevails for longer time, and therefore, the saturation excess run-off generation mechanism is happening without much problem; while for the Khanpur and Anthroli watersheds, which fall under the average category, the soil moisture deficit prevails for a longer time and thus reducing the surface run-off. Another interesting point can be seen from Fig. 5 pertaining to Khanpur watershed which shows why this watershed falls under the average category even though it receives more annual rainfall as compared to Hemavati watershed (Table 1). It can be seen from Tables 1 and 3 that this watershed is subjected to high evaporation, and also it can be seen from Table 4 that this watershed is characterised by high coefficient value of average soil moisture deficit, implying more soil moisture depletion which eventually reaches complete depletion, as depicted in Fig. 5. Therefore, this watershed has lower run-off production than the Hemavati watershed (Table 2). In the case of Amachi and Hridaynagar watersheds, the soil moisture deficit is more in comparison with the corresponding estimates of the wet and average watersheds. In dry watersheds, the soil moisture (W) is maintained as WM for a very short period of time, and

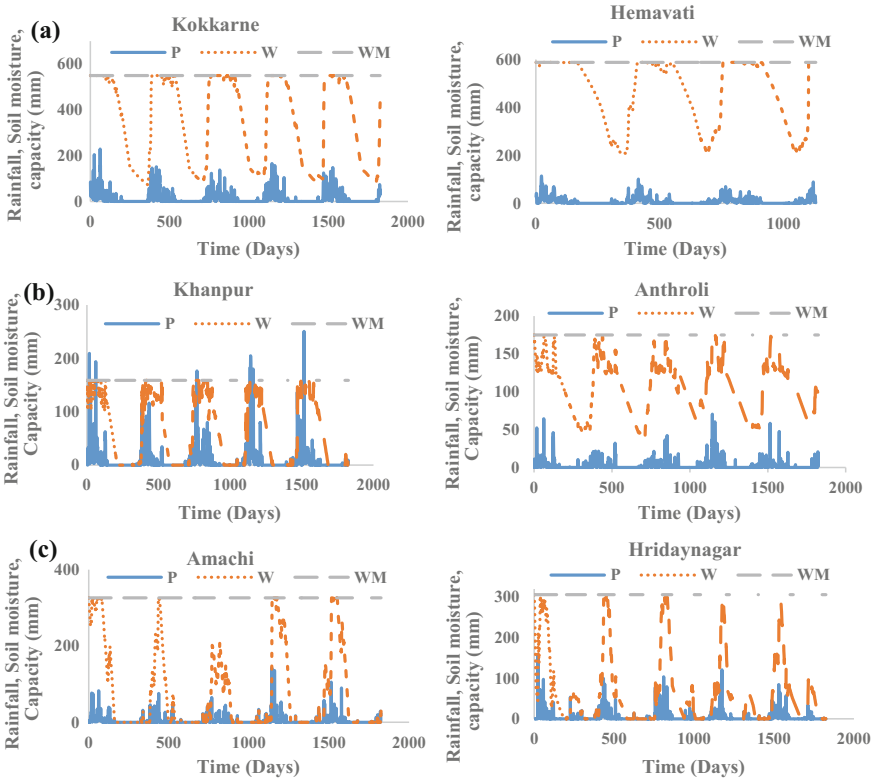

Fig. 5 Soil moisture profile of (**a**) wet, (**b**) average and (**c**) dry watersheds

therefore, the generated run-off getting low run-off peak in dry catchments results in low efficiency of the model. Figure 5 also depicts how the Xinanjiang model efficiency decreases from wet to dry watersheds, i.e., the difference between W and WM increases from wet to dry watersheds which causes low run-off leading to low model efficiency. So the sustained larger difference between W and WM for a longer period of time reduces the model efficiency.

Run-off Coefficient and Average Soil Moisture Deficit

The average soil moisture deficit is a non-dimensional coefficient like run-off coefficient and obtained by following relationship:

$$\text{Average soil moisture deficit} = \frac{\text{WM} - W}{\text{WM}} \tag{4}$$

It can be seen from Table 4 that the average soil moisture deficit has inverse relationship with the run-off coefficient, i.e., the watersheds having higher soil moisture deficit values are characterised by lower run-off coefficients which moves the watersheds from wet to average and dry category catchments. So it can be inferred from this study that the Xinanjiang model generated soil moisture deficit values/ coefficients can also be used for the categorisation of the watersheds as wet, average or dry catchments in addition to the use of the run-off coefficient as a criterion.

Conclusion

The performance of the Xinanjiang model has been evaluated by applying the model in six Indian watersheds having three different climatic conditions (wet, average and dry). It can be inferred from the study that how the nature of soil moisture profile presents in the watersheds of wet, average and dry categories and how the progression of the differences between W and WM affects the model efficiency. The results show that the performance of the model is mostly getting affected due to the parameter WM in the dry catchments. Overall, the performance of the model has been found to be best for wet catchments, good for average catchments and poor for dry catchments. A reconsideration of the categorisation of the watersheds as wet, average and dry is required considering also the prevailing wetness in the catchment for a longer period of time instead of categorising it only from the run-off coefficient criterion. As the Xinanjiang model adopts run-off generation mechanism based only on soil moisture saturation excess concept, the concept of incorporating infiltration run-off mechanism also needs to be introduced. Therefore, conceptual formulation present in the model for run-off generation needs modifications to make it amenable for use in average and dry catchments.

References

Abdulla FA, Lettenmaier DP, Wood EF, Smith JA (1996) Application of a macroscale hydrologic model to estimate the water balance of the Arkansas-Red river basin. J Geophys Res 101 (D3):7449–7459

Bai Y, Wagener T, Reed P (2009) A top-down framework for watershed model evaluation and selection under uncertainty. Environ Model Softw 24(8):901–916. doi:10.1016/j.envsoft.2008.12.012

Beven KJ, Wood E (1983) Catchment geomorphology and the dynamics of contributingareas. J Hydrol 65:139–158

Chang SHU, Suxia L, Xingguo M, Kun W, Chaolei Z, Shouhong Z (2010) The simulation of hydrological processes in an ungauged alpine basin by using Xinanjiang model. J Resour Ecol 1(2):186–192

Duan K, Mei Y (2014) Comparison of meteorological, hydrological and agricultural drought responses to climate change and uncertainty assessment. Water Resour Manage 28(14):5039–5054. doi:10.1007/s11269-014-0789-6

Duan QY, Sorooshian S, Gupta V (1992) Effective and efficient global optimization for conceptual rainfall-runoff models. Water Resour Res 28(4):1015–1031

Dumenil L, Todini E (1992) A rainfall-runoff scheme for use in the Hamburg climate model. In: O'Kane JP (ed) Advances in theoretical hydrology, a tribute to James Dooge. McGrah Hill, New York, p 462

Durbude DG, Jain MK, Mishra SK (2011) Long-term hydrologic simulation using SCS-CN-based improved soil moisture accounting procedure. Hydrol Process 25:561–579

Gan TY, Biftu GF (1996) Automatic calibration of conceptual rainfall-runoff models: optimization algorithms, catchment conditions, and model structure. Water Resour Res 32(12):3513–3524. doi:10.1029/95WR02195

Gan TY, Dlamini EM, Biftu GF (1997) Effects of model complexity and structure, data quality, and objective functions on hydrologic modeling. J Hydrol 192:81–103

Habets F, Noilhan J, Golaz C, Goutorbe JP, Lacarrere P, Leblois E, Ledoux E, Martin E, pttle C, Vidal-Madjar D (1999) The ISBA surface scheme in a macro scale hydrological model applied to the Hapex-mobility area part II: simulation of stream flows and annual water budget. J Hydrol 217:97–118

Holland JH (1975) Adaptation in natural and artificial system. University of Michigan Press, Ann Arbor

Hu L, Peng D, Tang S, Xiao Y, Chen H (2011) Impact of climate change on hydro-climatic variables in Xinanjiang River basin, China. In: 2011 international symposium on water resource and environmental protection, vol 4, pp 2559–2562. http://doi.org/10.1109/ISWREP.2011.5893400

Jayawardena AW, Zhou MC (2000) A modified spatial soil moisture storage capacity distribution curve for the Xinanjiang model. J Hydrol 227:93–113

Jayawardena AW, Mahanama SPP (2002) Meso-scale hydrological modeling: application to Mekong and Chao Phraya basin. J Hydrol Eng 7(1):12–26

Kneis D, Chatterjee C, Singh R (2014) Evaluation of TRMM rainfall estimates over a large Indian river basin (Mahanadi). Hydrol Earth Syst Sci 18(7):2493–2502. http://doi.org/10.5194/hess-18-2493-2014

Li H, Zhang Y, Chiew FHS, Xu S (2009) Predicting runoff in ungauged catchments by using Xinanjiang model with MODIS leaf area index. J Hydrol 370(1–4):155–162. doi:10.1016/j.jhydrol.2009.03.003

Li H, Beldring S, Xu C-Y (2014) Stability of model performance and parameter values on two catchments facing changes in climatic conditions. Hydrol Sci J 6667(Oct), 141023055853009. http://doi.org/10.1080/02626667.2014.978333

Li H, Beldring S, Xu C-Y (2015) Stability of model performance and parameter values on two catchments facing changes in climatic conditions. Hydrol Sci J 60(7–8). doi:10.1080/02626667.2014.978333

Liang X, Lettenmaier DP, Wood EF, Burges SJ (1994) A simple hydrological based model of land surface water and energy fluxes for general circulation models. J Geophys Res 99(D7) 14:1415–14, 428

Liang Z, Lettenmaier DP, Wood EF (1996a) One-dimensional statistical dynamic representation of subgrid spatial variability of precipitation in the two-layer variable infiltration capacity model. J Geophys Res 101(D16):21, 403–421,422

Liang X, Wood EF, Lettenmaier DP (1996b) Surface soil moisture parameterization of the VIC-2L model: evaluation and modifications. Global Planet Change 19:195–206

Lin K, Lv F, Chen L, Singh VP, Zhang Q, Chen X (2014) Xinanjiang model combined with curve number to simulate the effect of land use change on environmental flow. J Hydrol 519 (PD):3142–3152. http://doi.org/10.1016/j.jhydrol.2014.10.049

Liu S, Mo X, Leslie LM, Speer M, Bunker R, Zhao W (2001) Another look at the Xinanjiang model: from theory to practice. In: Proceedings of the MODSIM2001 congress, 10–13 Dec, Canberra, pp 137–142

Liu J, Chen X, Wu J, Zhang X, Feng D, Xu C-Y (2012) Grid parameterization of a conceptual distributed hydrological model through integration of a sub-grid topographic index: necessity and practicability. Hydrol Sci J 57(2):282–297. doi:10.1080/02626667.2011.645823

Manfreda S (2008) Runoff generation dynamics within a humid river basin. Nat Hazards Earth Syst Sci 8:1349–1357. doi:105194/nhess-8-1349-2008

Nash JE, Sutcliffe JV (1970) River flow forecasting through the conceptual models, 1: a discussion of principles. J Hydrol 10(3):282–290

Nelder JA, Mead R (1965) A simplex method for function minimization. Comput J 7(4):308–313

Nghi VV, Lam DT, DDD (2008) Comparison of two hydrological model simulations using nam and Xinanjiang for nong son catchment. Vietnam J Mech 30(1):43–54

Ouyang F, Lü H, Zhu Y, Zhang J, Yu Z, Chen X, Li M (2013) Uncertainty analysis of downscaling methods in assessing the influence of climate change on hydrology. Stoch Environ Res Risk Assess 991–1010. http://doi.org/10.1007/s00477-013-0796-9

Price WL (1987) Global optimization algorithms for a CAD work-station. J Optim Theory Appl 55 (1):133–146

Ren LL, Huang Q, Yuan F, Wang J, Xu J, Yu Z, Liu X (2006) Evaluation of the Xinanjiang model structure by observed discharge and gauged soil moisture data in the HUBEX/GAME Project. IAHS Publication 303:153

Sahoo B (2005) The Xinanjiang model and its derivatives for modeling soil moisture variability in the land- surface schemes of the climate change models: an overview. In: Proceedings of the international conference on hydrological perspectives for sustainable development

Shi P, Zhou M, Qu S, Chen X, Qiao X, Zhang Z, Ma X (2013) Testing a conceptual lumped model in Karst Area, Southwest China. J Appl Math 2013 827980:10 p. http://dx.doi.org/10.1155/2013/827980

Si W, Bao W, Jiang P, Zhao L, Qu S (2015) A semi-physical sediment yield model for estimation of suspended sediment in loess region. Int J Sedim Res. doi:10.1016/j.ijsrc.2015.10.002

Singh VP (1995) The Xinanjiang model. Computer models of watershed hydrology. Water Resources Publication, pp 215–232

Sivapalan M, Woods RA (1995) Evaluation of the effects of general circulation model's subgrid variability and pachiness of rainfall and soil moisture on land surface water balance fluxes. In: Kalma JD, Sivapalan M (eds) Scale issues in hydrological modeling. Wiley, Chichester, UK, pp 453–473

Todini E (1996) The ARNO rainfall-runoff model. J Hydrol 175:339–382

Wood EF, Lettenmaier DP, Zartarian VG (1992) A land-surface hydrology parameterization with subgrid variability for general circulation models. J Geophys Res 97(D3):2717–2728

Xu D, Wang W, Chau K, Cheng C, Chen S (2013) Comparison of three global optimization algorithms for calibration of the Xinanjiang model parameters. J Hydroinf 15(1):174. doi:10.2166/hydro.2012.053

Yang S, Dong G, Zheng D, Xiao H, Gao Y, Lang Y (2011) Coupling Xinanjiang model and SWAT to simulate agricultural non-point source pollution in Songtao watershed of Hainan, China. Ecol Model 222(20–22):3701–3717. doi:10.1016/j.ecolmodel.2011.09.004

Ye W, Bates BC, Viney NR, Sivapalan M, Jakeman AJ (1997) Performance of conceptual rainfall-runoff models in low-yielding ephemeral catchments. Water Resour Res 33(1):153–166. doi:10.1029/96WR02840

Yuanyuan M, Xuegang Z, Zhijia L (2013) Coupled simulation of Xinanjiang model with MODFLOW. J Hydrol Eng 18(11):1443–1449. http://doi.org/10.1061/(ASCE)HE.1943–5584.0000706

Zhang C, Wang R, Meng Q (2015) Calibration of conceptual rainfall-runoff models using global optimization. Adv Meteorol 2015:1–12. http://doi.org/10.1155/2015/545376

Zhao RJ (1992) The Xinanjiang model applied in China. J Hydrol 135(1–4):371–381

Zhao RJ, Zhang YL, Fang LR, Liu, Zhang QS (1980) The Xinanjiang model. In: Hydrological forecasting proceeding Oxford symposium, IASH 129, pp 351–356

Zuo D, Xu Z, Zhao J, Abbaspour KC, Yang H (2015) Response of runoff to climate change in the Wei River basin, China. Hydrol Sci J (Jan 2015), 1–15. http://doi.org/10.1080/02626667.2014.943668